



21st

**International Metallurgy
and Materials Congress**

21. Uluslararası Metalurji
ve Malzeme Kongresi

CONGRESS PROCEEDINGS E-BOOK KONGRE BİLDİRİLER E-KİTABI

**6-8 October / Ekim
2022, ISTANBUL**

TÜYAP Fair and Congress Center
TÜYAP Fuar ve Kongre Merkezi

 www.immc-mtm.com

 immc@immc-mtm.com

“Global Warming,
Climate Crisis
Küresel Isınma,
İklim Krizi”

    [immc2022](https://www.immc2022.com)

 **METEM**



21st International Metallurgy and Materials Congress
21. Uluslararası Metalurji ve Malzeme Kongresi

CONGRESS PROCEEDINGS E-BOOK

KONGRE BİLDİRİLER E-KİTABI

**UCTEA Chamber of Metallurgical
and Materials Engineers Training Center**
TMMOB Metalurji ve Malzeme
Mühendisleri Odası Eğitim Merkezi

Kocatepe Mah. Hatay Sok No: 10/9
06420 Çankaya - Ankara
Mobile: +90 537 527 07 90
Phone: +90 312 425 41 60

2022

 **METEM**

    immc2022





21st International Metallurgy and Materials Congress

21. Uluslararası Metalurji
ve Malzeme Kongresi

6-8 October / Ekim
2022, ISTANBUL

TÜYAP Fair and Congress Center
TÜYAP Fuar ve Kongre Merkezi

www.immc-mtm.com

immc@immc-mtm.com

CONGRESS SPONSORS / KONGRE SPONSORLARI



 **Çolakoğlu Metalurji**



 **sarkuysan**
ELEKTROLİTİK BAKIR SANAYİ VE TİCARET A.Ş.

COFFEE BREAK SPONSOR / COFFEE BREAK SPONSORU

SÜPERREF

Prof. Dr. Gehan A. J. Amaratunga	Cambridge University	England
Dr. Khalil Amine	Argonne National Laboratories	USA
Prof. Dr. Diran Apelian	Worcester Polytechnic Institute	USA
Dr. Csaba Balazsi	Hungarian Academy of Sciences	Hungary
Dr. Paola Bassani	CNR ICMATE	Italy
Prof. Dr. Joachim Bill	University of Stuttgart	Germany
Prof. Dr. Simona Cavalu	University of Oradea	Romania
Prof. Dr. Manish Chhowalla	Rutgers University	USA
Prof. Dr. Dan Eliezer	Ben-Gurion Univ. of the Negev	Israel
Prof. Dr. Ahmed Elmarakbi	Northumbria University	UK
Prof. Dr. David Embury	The Univ. of British Columbia	Canada
Prof. Dr. Ing. Bernd Friedrich	IME RWTH Aachen University	Germany
Prof. Dr. Bernd Friedrich	RWTH Aachen University	Germany
Prof. Dr. Maria Pau Ginebra	Univ. Politecnica de Catalunya	Spain
Dr. W. D. Griffiths	University of Birmingham	England
Prof. Dr. Bernd H. Günther	Heinrich-Heine-Univ. Düsseldorf	Germany
Prof. Dr. Fathi Habashi	Laval University	Canada
Prof. Dr. Makoto Hasegawa	Yokohama National University	Japan
Prof. Peter Hodgson	Deakin University	Australia
Dr. Antoniac Vasile Iulian	Univ. Politecnica of Bucharest	Romania
Dr. Florian Kongoli	Flogen Technologies Inc.	Canada/USA
Matthew J. Kramer	Iowa State University	USA
Prof. Dr. R. Vasant Kumar	University of Cambridge	UK
Dr. Thomas Luebben	Foundation Inst. of Materials Sci.	Germany
Prof. Dr. Rodrigo Martins	European Academy of Sciences	Portugal
Dr. Toshio Maruyama	Tokyo Institute of Technology	Japan
Prof. Dr. Sanjay Mathur	University of Cologne	Germany
Dr. Meyya Meyyappan	NASA Ames Research Center	USA
Mathieu Morcrette	Reactive et Chimie des Solides	France
Prof. Dr. Frank Mücklich	Saarland University	Germany
Dr. Pance Naumov	New York University Abu Dhabi	UAE
Prof. Mitsuo Niinomi	Tohoku University	Japan
Dr. Sanin Vladimir Nikolaevich	Russian Academy of Science	Russia
Prof. Dr. Besim Ben Nissan	University of Technology	Australia
Dr. Maria Omastova	Slovak Academy of Sciences	Slovakia
Dr. Julietta V. Rau	Istituto di Struttura della Materia	Italy
Prof. Dr. Simion Simon	Babes-Bolyai University	Romania
Dr. Abdelilah Slaoui	European Materials Research Soc.	France
Prof. Dr. Marcel A. J. Somers	Technical University of Denmark	Denmark
Prof. Dr. Michael Stelter	INEMET, TU Freiberg	Germany
Prof. Dr. Mingyue Sun	Chinese Academy of Sciences	China
Prof. Dr. Nickolas J. Themelis	Columbia University	USA
Dr. George E. Totten	Texas A&M University	USA
Prof. Dr. Cong Wang	Northeastern University	China



Prof. Dr. Gökhan ORHAN

Istanbul University-Cerrahpaşa



Prof. Dr. Özgül KELEŞ

Istanbul Technical University



Prof. Dr. Caner DURUCAN

Middle East Technical University



Biomaterials Symposium

Biyomalzemeler Sempozyumu

Doç. Dr. İpek AKIN KARADAYI, Istanbul Technical University

Doç. Dr. Salih DURDU, Giresun University

Doç. Dr. Batur ERCAN, Middle East Technical University

Prof. Dr. Gültekin GÖLLER, Istanbul Technical University

Steel Symposium

Çelik Sempozyumu

Prof. Dr. Arcan DERİCİOĞLU, Middle East Technical University

Prof. Dr. C. Bora DERİN, Istanbul Technical University

Prof. Dr. Ender KESKİNKILIÇ, Atılım University

Non-Ferrous Metals Symposium

Demir Dışı Metaller Sempozyumu

Dr. Öğr. Üyesi Murat ALKAN, Dokuz Eylül University

Prof. Dr. Cem KAHRUMAN, Bursa Technical University

Dr. Öğr. Üyesi Ahmet Orkun KALPAKLI, Istanbul Uni.-Cerrahpaşa

Doç. Dr. Ahmet TURAN, Yeditepe University

Casting Symposium

Döküm Sempozyumu

Yaşar Uğur AKI, Demisaş Döküm

Dr. Arda ÇETİN, Ekstra Metal

Prof. Dr. Ali KALKANLI, Middle East Technical University

Doç. Dr. Necip ÜNLÜ, Istanbul Technical University

Energy Materials Symposium

Enerji Malzemeleri Sempozyumu

Dr. Öğr. Üyesi Gökçe HAPÇI AĞAOĞLU, Istanbul Uni.-Cerrahpaşa

Doç. Dr. Tuğrul ÇETİNKAYA, Sakarya University

Doç. Dr. Burak ÜLGÜT, Bilkent University

Dr. Öğr. Üyesi B. Deniz KARAHAN, Istanbul Technical University

Recycling and Sustainability Symposium

Geri Dönüşüm ve Sürdürülebilirlik Sempozyumu

Dr. Mertol GÖKELMA, Izmir Institute of Technology

Doç. Dr. M. Şeref SÖNMEZ, Istanbul Technical University

Dr. Öğr. Üyesi Mert ZORAĞA, Istanbul University-Cerrahpaşa

Failure Analysis and Heat Treatment Symposium

Hasar Analizi ve Isıl İşlem Sempozyumu

Prof. Dr. Murat BAYDOĞAN, Istanbul Technical University

Utku İNAN, Alpha Metalurji



Aerospace Materials Symposium

Havacılık Malzemeleri Sempozyumu

Prof. Dr. Mustafa GÜDEN, İzmir Institute of Technology
Prof. Dr. Benat KOÇKAR, Hacettepe University
Doç. Dr. Havva KAZDAL ZEYTİN, TÜBİTAK MAM
Dr. Hakan YAVAŞ, TUSAŞ-TAİ

Welding and Non-Destructive Testing Symposium

Kaynak ve Tahribatsız Muayene Sempozyumu

Dr. Öğr. Üyesi Caner BATIGÜN, Middle East Technical University
Prof. Dr. Emel TABAN, Kocaeli University

Composite and Polymer Materials Symposium

Kompozit ve Polimer Malzemeler Sempozyumu

Prof. Dr. Cevdet KAYNAK, Middle East Technical University
Prof. Dr. Bora MAVIŞ, Hacettepe University
Doç. Dr. M. Reza NOFAR, İstanbul Technical University

Corrosion and Wear Symposium

Korozyon ve Aşınma Sempozyumu

Dr. Öğr. Üyesi Levent ORGAN, Yeditepe University
Dr. Öğr. Üyesi Çiğdem TOPARLI, Middle East Technical University
Doç. Dr. Fatih TOPTAN, İzmir Institute of Technology

Nanomaterials Symposium

Nanomalzemeler Sempozyumu

Doç. Dr. Z. Göknur BÜKE, TOBB-ETU
Prof. Dr. Sebahattin GÜRMEN, İstanbul Technical University
Prof. Dr. Burak ÖZKAL, İstanbul Technical University
Prof. Dr. H. Emrah ÜNALAN, Middle East Technical University

Ceramics, Glass, Refractory Materials Symposium

Seramik, Cam, Refrakter Malzemeleri Sempozyumu

Prof. Dr. Abdullah ÖZTÜRK, Middle East Technical University
Prof. Dr. Ender SUVACI, Eskişehir Technical University
Prof. Dr. Filiz ÇINAR ŞAHİN, İstanbul Technical University
Prof. Dr. Çekdar Vakıf AHMETOĞLU, İzmir Institute of Technology

Surface Treatment and Coating Symposium

Yüzey İşlemler ve Kaplama Sempozyumu

Doç. Dr. Ekrem ALTUNCU, Sakarya University of Applied Sciences
Doç. Dr. Metehan ERDOĞAN, Ankara Yıldırım Beyazıt University
Prof. Dr. Kürşat KAZMANLI, İstanbul Technical University
Dr. Alper YEŞİLÇUBUK, Arçelik

RSS

Recycling and Sustainability Symposium

Geri Dönüşüm ve Sürdürülebilirlik Sempozyumu

AMS

Aerospace Materials Symposium

Havacılık Malzemeleri Sempozyumu

STCS

Surface Treatment and Coating Symposium

Yüzey İşlemler ve Kaplama Sempozyumu

STS

Steel Symposium

Çelik Sempozyumu

NFMS

Non-Ferrous Metals Symposium

Demir Dışı Metaller Sempozyumu

CWS

Corrosion and Wear Symposium

Korozyon ve Aşınma Sempozyumu

CGRS

Ceramics, Glass, Refractory Materials Symposium

Seramik, Cam, Refrakter Malzemeleri Sempozyumu

EMS

Energy Materials Symposium

Enerji Malzemeleri Sempozyumu

FAHTS

Failure Analysis and Heat Treatment Symposium

Hasar Analizi ve Isıl İşlem Sempozyumu

CPS

Composite and Polymer Materials Symposium

Kompozit ve Polimer Malzemeler Sempozyumu

WNTS

Welding and Non-Destructive Testing Symposium

Kaynak ve Tahribatsız Muayene Sempozyumu

BMS

Biomaterials Symposium

Biyomalzemeler Sempozyumu

NMS

Nanomaterials Symposium

Nanomalzemeler Sempozyumu

CSS

Casting Symposium

Döküm Sempozyumu

6 October 2022, Thursday / 6 Ekim 2022, Perşembe
10.15-12:00
Hall Marmara / Salon Marmara

Deepening Climate Crisis and Solutions

Ümit ŞAHİN
Sabancı University
Türkiye

Why Does Humanity Need New Energy Materials,
and Where Will We Find Them?

Taylor SPARKS
University of Utah
USA

Assessment of Net Zero Emissions Targeting
against the Global Climate Crisis and the Problem
of Climate Justice

Alp Erinç YELDAN
Kadir Has University
Türkiye

8 October 2022, Saturday / 8 Ekim 2022, Cumartesi
Hall Büyükada / Salon Büyükada

13.30-14.00 Industrial Welding Applications of S690QL Grade Steels
Tanıl ATICI
Cimtas Steel Research & Development Center
Türkiye

7 October 2022, Friday / 7 Ekim 2022, Cuma
Hall Karadeniz / Salon Karadeniz

13.30-14.00 Multi-Materials 3D Printing Of Ceramics
Lisa BIASETTO
University of Padova
Italy

6 October 2022, Thursday / 6 Ekim 2022, Perşembe
Hall Karadeniz / Salon Karadeniz

14.40-15.10 Carbon-Based PVD Coating Solutions for a Sustainable Future
Ivan KOLEV
IHI Hauzer Techno Coating B.V.
Netherlands

6 October 2022, Thursday / 6 Ekim 2022, Perşembe
Hall Marmara / Salon Marmara

13.00-13:30 The Enabling Role of Materials Chemistry Towards Net-Zero Carbon
Ramachandran Vasant KUMAR
University of Cambridge
United Kingdom

8 October 2022, Saturday / 8 Ekim 2022, Cumartesi
Hall Karadeniz / Salon Karadeniz

14.00-14.30 New Polymorphs of Compounds With A Complex, Layered Crystal Structure Stabilized At The Nanoscale: Magnetic Strontium-Hexaferrite Nanoplatelets And Ferroelectric Bismuth-Titanate Nanowires
Darko MAKOVEC
Jožef Stefan Institute
Slovenia

7 October 2022, Friday / 7 Ekim 2022, Cuma
Hall Karadeniz / Salon Karadeniz

11.20-11.50 Tribocorrosion Degradation of Osteointegrated Biomedical Implants: Mechanisms, Biological Implications and (Possible) Solutions
Luis Augusto ROCHA
Digital Transformation CoLAB
Portugal

6 October 2022, Thursday / 6 Ekim 2022, Perşembe
Hall Büyükada / Salon Büyükada

16.20-16.50 Materials for Extreme Environments: On The Outside Looking in
Ali SAYİR
Air Force Office of Scientific Research
USA

8 October 2022, Saturday / 8 Ekim 2022, Cumartesi
Hall Marmara / Salon Marmara

10.40-11.10 Transition Metal Free: Dual Ion and Dual-Carbon Batteries
Martin WINTER
University of Münster & Helmholtz-Institute Münster
Germany

**Tanıl ATICI**

Tanıl Atıcı was born in Ankara in 1983. He was graduated from Middle East Technical University Metallurgical and Materials Engineering Department as BSc in 2006. In 2009, he was graduated from Welding Engineering course given by Middle East Technical University Welding Technologies Center. Since 2007, he is working as a welding engineer in Cimtast Steel company. He holds CWI (certified welding inspector) certificate of AWS (American Welding society). He is the director of Cimtast Steel Research & Development Center.

**Lisa BIASETTO**

Lisa Biassetto is Associate Professor at the Department of Management and Engineering of University of Padova since 2018, where she teaches Materials Science and Technology and Polymers Technology at the bachelor and master's degree Program of Product Innovation Engineering.

In 2007 she earned a PhD in Materials Engineering from University of Bologna-Italy. After the PhD she has been post doc researcher at Istituto Nazionale di Fisica Nucleare and researcher at UNIPD. Her collaborations over the years span from CERN-Geneve, ORNL-Tennessee-USA, TRIUMF-Vancouver-Canada, University of Colorado at Boulder-Colorado-USA, Technical University of Darmstadt, Germany, EPFL-Lousanne-Switzerland, Loughborough University-UK, Saarland University-Germany, Maribor University-Slovenia, Fraunhofer-IFAM, Germany..

Her major field of interest includes synthesis, processing, and characterization of porous components (ceramics, metallic and mixture thereof), coating technologies, non-energy deposition additive manufacturing technologies, biomaterials and ultra-high temperature ceramics for production of isotope beams.

She published more than 60 papers in international peer reviewed journals. She has coordinated or she has been involved as principal investigator in several research projects funded by EU, Italian Government, and private companies.

**Ivan KOLEV**

Professional Experience

2008 - Present: IHI Hauzer Techno Coating B.V.
Van Heemskerckweg 22
5928 LL - Venlo, The Netherlands

2018 - Present Process Technology Manager
2016 - 2018 Process Manager Strategical R&D
2009 - 2016 Process Manager Deco and Special
2008 - 2009 Senior Process Engineer

2007 - 2008 University of Antwerp, Belgium
Position: Research fellow, member of staff

Education

Doctor of Philosophy in Plasma Physics (PhD), 2006 University of Antwerp, Belgium
Master of Science in Engineering Physics (MSc), 1999 University of Sofia, Bulgaria
Bachelor of Science in Engineering Physics (BSc), University of Sofia, Bulgaria

**R. Vasant KUMAR**

R Vasant Kumar is Professor and the Head of Materials Chemistry Group and a Fellow of the Institute of Energy and a Fellow of the Institute of Materials, Mining and Metallurgy. He has published over 370 papers, 20 patents, 12 Chapters in Handbooks and 1 edited book (High energy density Li batteries, Wiley-VCH 2010- also translated in Chinese, 2013, 2nd Edition in 2022). He has supervised 40+ PhD students, 40+ post-doctoral researchers, 20 visiting students and hosted over 15 visiting professors.

He is Honorary/Guest Professor in 5 overseas Universities (2008, 2012, 2016, 2019, 2021). Has received Honorary Engineering Degree in University of Malaysia (2011), Kroll Medal from IOM3; Armourers & Brasiers Enterprise Award for translating research into industrial applications (2014).

He is the Editor-in-Chief of IOM3 journal, "Mineral Processing & Extractive Metallurgy" from 2004, Editorial Board Member of (i) "Advances in Nanoparticles" of Scientific Research Publishing from 2012; (ii) "Materials Today Chemistry" of Elsevier Ltd from 2017; (iii) Materials Circular Economy, Singapore from Oct 2018, and a Board Member of IOM3's Technical Division. He is Advisory Board Member of TECHMET Ltd, London (from 2019) and Korea National Lithium Research Centre (from 2020).

Many of his research has led to licenses and industrial practices and he has founded four start-up companies which are commercialising some of his inventions. Currently, Professor Kumar's research group is working on several research projects underpinned by harnessing of chemical reactions in a variety of applications that range from energy devices such as batteries and fuel cells to environmental research in mineral carbonation, sensors, sustainability and recycling of materials and photocatalytic reactions. rialization, and economics of climate change, and on empirical, dynamic general equilibrium models.

**Darko MAKOVEC**

Prof. dr. Darko Makovec is full professor, head of Department for Materials Synthesis and scientific chancellor at Jožef Stefan Institute. He has defended his PhD from chemistry at the University of Ljubljana in year 1995. In 2001-2002 he worked as a Fulbright senior scholar at University of Illinois at Urbana-Champaign, USA. His scientific interests are focused on synthesis and characterization of the inorganic and hybrid nanomaterials, especially materials containing magnetic nanoparticles. He is also expert in advanced electron microscopy. Prof Makovec has published over 200 peer-review articles.

**Luís A. ROCHA**

Luís Augusto Rocha is a Leading Researcher at DTx - Digital Transformation CoLAB, Campus de Azurém, Guimarães, Portugal. Formerly he was Associated Professor with Habilitation (Livre-Docente) at UNESP - Univ. Estadual Paulista, Faculdade de Ciências de Bauru, Brazil (2013-2018) and Associated Professor at the Department of Mechanical Engineering of University of Minho, in Portugal (1985-2013). He is the coordinator of the IBTN/Br, Brazilian Branch of the Institute of Biomaterials, Tribocorrosion and Nanomedicine, and co-founder of its European Branch.

He has a strong involvement in research on the biomaterials field, namely on the development of functionally graded materials (FGM), surface functionalization of metallic biomaterials and on the investigation of the degradation mechanisms of those materials, essentially from the tribocorrosion point-of-view, and its influence on biological systems. He published more than 100 papers in SCI Journals (h-index=39, according to Google Scholar). In 2021, he was ranked in the World's Top 2% Scientists List, compiled by Stanford University (Materials).

He is a member of WP18 on Tribocorrosion (European Federation of Corrosion), LGM-AS - Int. Assoc. for Layered and Graded Materials (World Academy of Ceramics) and International Advisory Board on Functionally Graded Materials (FGM Forum, Japan).

At DTx he is the Director of the Human Factors technical-scientific area, where he coordinates a multidisciplinary team, including Designers, Social Scientists, Economists, Psychologists etc. This team is building the DTx Living Lab focused on the involvement of humans in the process of co-creation of cyber-physical systems.

**Ali SAYİR**

Dr. Ali Sayir is currently the Program Manager for Materials with Extreme Properties portfolio within the Air Force Office of Scientific Research (AFOSR) in Arlington, VA. As a senior program officer Dr. Sayir has concerted effort on mathematic quantification of microstructures for DOD and leads major national programs in computational material science. He has responsibility for planning, directing, and securing long-term program support in extreme environment electronics and materials for quantum information sciences.

As a Program Officer, Dr. Sayir proactively evaluates materials for extreme environments, and judiciously sponsors innovative scientific opportunities in materials that can be integrated in the ab-initio design process for far-from equilibrium effects, and extreme non-linearity's, and ultra-fast control. He is in forefront in the development and execution of basic research on materials far from equilibrium for high-power systems and interested in new capabilities in materials that can adapt to external stimuli of electric-, magnetic-, acoustic-, thermal fields and combined loads. He is proactive member of DOD and scientific community, and coordinates research programs within the Air Force, DOD, and Army, Navy, DARPA, NASA and other national and international organizations.

Prior to joining AFOSR, Dr. Sayir managed materials and structures for NASA Hypersonic program at NASA Glenn Research Center, Cleveland, OH. He coordinated materials and structures projects between NASA centers, Department of Defense, Industry and Academia. Since 2008 he has held a Professor Faculty appointment at Case Western Reserve University in the Department of Materials Science of Engineering and has been founding member of a small company.

Dr. Sayir conducted research in areas such as eutectic solidification, electron emitters, high temperature piezoelectric materials, and materials for thermoelectric and thermophotovoltaic energy conversion, and proton conducting ceramics. He published 137 peer reviewed publications, 2 book chapters, received 3 patents, have over 40 invited presentations, and was selected a Fellow of the American Ceramic Society since 2009 for his scientific contributions and fellow of AFRL since 2020.

**Taylor SPARKS**

Dr. Sparks is an Associate Professor of Materials Science and Engineering at the University of Utah. He holds a BS in MSE from the UofU, MS in Materials from UCSB, and PhD in Applied Physics from Harvard University. He was a recipient of the NSF CAREER Award and a speaker for TEDxSaltLakeCity.

When he's not in the lab you can find him running his podcast "Materialism" or canyoneering with his 4 kids in southern Utah.

**Ümit ŞAHİN**

Ümit Şahin is Senior Scholar and the Coordinator of Climate Change Studies at Istanbul Policy Center. Şahin teaches courses on Global Environmental Challenges, Climate Change and Environmental Politics at Sabanci University Faculty of Arts and Social Sciences.

Since the early 1990s, Şahin has been part of the green political movement and climate, ecology and environmental movements, and an active contributor to anti-nuclear and human rights movements. Şahin was the editor-in-chief of the green political journal “Üç Ekoloji” (Three Ecologies) that he has founded in 2003.

Şahin is one of the founders of the Association of the Doctors for the Environment, serving as the organization's president, Şahin coordinated the “Turkey sign Kyoto!” campaign, which was carried out by Turkey's Green Party, for whom he was one of the founders and served as co-spokesperson between 2010 and 2012. He also has participated as an observer to the UNFCCC Climate Conferences (COPs) since 2008. He served as a member of Steering Committee of the Istanbul City Council.

Together with Ömer Madra, Şahin has been the producer and host of the “Açık Yeşil” (Open Green) radio program on Açık Radio since 2008. In addition, he edits and writes on climate change and environmental issues for “Yeşil Gazete” (Green Newspaper).

Şahin authored and edited several books, such as “Why We Can't Wait: Global Warming and Climate Crisis”, 2007 (with Ömer Madra, as interviewer and editor), “Green Economy”, 2012 (as co-editor with Ahmet Atıl Aşıcı), Open Green 1 - An Ecology Guide with Its Theory and Practice, 2019, and Open Green 2 - Climate Crisis, Politics, and Activism, 2020 (as co-author with Ömer Madra). Şahin has also several book chapters, policy papers and articles related to climate change, energy transition, environmental health, green politics, and human rights.

Ümit Şahin graduated from Cerrahpaşa Medical School in 1991, completed his Master of Public Health in Hebrew University and received his Ph.D. degree in public health from Istanbul University in 2000. His public health works has focused on environmental health.

**Martin WINTER**

Martin Winter has been researching in the field of electrochemical energy storage and conversion for more than 30 years. His focus is on the development of new materials, components and cell design for lithium ion, lithium-metal batteries and alternative battery systems. Martin Winter currently holds a professorship for “Materials Science, Energy and Electrochemistry” at the Institute of Physical Chemistry at the University of Münster, Germany. The full professorship developed from an endowed professorship funded by the companies Volkswagen, Evonik Industries and Chemetall (today Albemarle) from 2008 to 2012.

Martin Winter is founder and scientific director of MEET Battery Research Center at the University of Münster. MEET stands for “Münster Electrochemical Energy Technology “. At MEET, an international team of about 150 scientists, engineers and technicians is working on research and development of innovative electrochemical energy storage devices with higher energy density, longer durability and maximum safety. Since 2015, he is also founding director of the Helmholtz-Institute Münster (HI MS) “Ionics in Energy Storage”, a division of Forschungszentrum Jülich, with about 70 employees. MEET and HI MS are internationally leading institutions in the research and development of innovative electrochemical energy storage systems.

**Alp Erinç YELDAN**

A. Erinç Yeldan, Professor of Economics and Dean at Kadir Has University. He is one of the executive directors of the International Development Economics Associates (IDEAs), New Delhi; and serves as a member-elect of the International Resource Panel of the UN Environment Programme (UNEP). He is also a member-elect of the Science Academy (Bilim Akademisi) in Turkey.

Dr Yeldan received his Ph.D. from University of Minnesota, USA, and joined the Department of Economics at Bilkent in 1988. During 1994/95 he was a visiting scholar at the University of Minnesota, and during 2007/2008 he was a Fulbright scholar at University of Massachusetts, Amherst and at Amherst College. Dr. Yeldan's recent work focuses on development macroeconomics, vulnerability and fragmentation of labor markets, de-industrialization, and economics of climate change, and on empirical, dynamic general equilibrium models.



AÇILIŞ TÖRENİ / OPENING CEREMONY

ANKIROS 2022 - TURKCAST 2022
21. ULUSLARARASI METALURJİ VE MALZEME KONGRESİ / 21st INTERNATIONAL
METALLURGY & MATERIALS CONGRESS
11. ULUSLARARASI DÖKÜM KONGRESİ / 11th INTERNATIONAL FOUNDRY CONGRESS
YER / VENUE: TÜYAP- Fuar ve Kongre Merkezi, İstanbul - Hol 2-3 Fuaye / TUYAP Fair
and Convention Center, İstanbul - Halls 2-3 Foyer
TARİH / DATE: 05 EKİM 2022, 18:30 / 05 OCTOBER 2022, 18:30

AÇILIŞ KONUŞMALARI / OPENING SPEECHES

İbrahim ANIL

HANNOVER MESSE ANKIROS FUARCILIK A.Ş.
MURAHHAS AZA VE GENEL MÜDÜR / EXECUTIVE DIRECTOR AND GENERAL MANAGER

Dr. Timo WÜRZ

CECOF / CEMAFON
GENEL SEKRETER / GENERAL SECRETARY
EUnited Metallurgy
DİREKTÖR / DIRECTOR

Prof. Dr. Gökhan ORHAN

21. ULUSLARARASI METALURJİ VE MALZEME KONGRESİ
21st INTERNATIONAL METALLURGY & MATERIALS CONGRESS
ORGANİZASYON KURULU BAŞKANI / CHAIRMAN OF THE ORGANIZING COMMITTEE

Ata ÖZDEMİRLER

TMMOB METALURJİ VE MALZEME MÜHENDİSLERİ ODASI EĞİTİM MERKEZİ (METEM)
UCTEA CHAMBER OF METALLURGICAL AND MATERIALS ENGINEERS TRAINING CENTER
YÜRÜTME KURULU BAŞKANI / CHAIRMAN OF EXECUTIVE BOARD

Ahmet İrfan TÜRKOLU

TMMOB - METALURJİ VE MALZEME MÜHENDİSLERİ ODASI
UCTEA - CHAMBER OF METALLURGICAL AND MATERIALS ENGINEERS
YÖNETİM KURULU BAŞKANI / CHAIRMAN OF EXECUTIVE BOARD

Dr. Veysel YAYAN

"TÇÜD"- TÜRKİYE ÇELİK ÜRETİCİLERİ DERNEĞİ
TURKISH STEEL PRODUCERS ASSOCIATION
GENEL SEKRETER / SECRETARY GENERAL

Kadir EFE

"TÜDÖKSAD"- TÜRKİYE DÖKÜM SANAYİCİLERİ DERNEĞİ
TURKISH FOUNDRYMEN'S ASSOCIATION
YÖNETİM KURULU BAŞKANI / CHAIRMAN OF THE BOARD



CONGRESS SESSIONS

KONGRE OTURUMLARI



Opening Session

Açılış Oturumu

Opening Session

Session Chairman / Oturum Başkanı: **CANER DURUCAN**

10.15-12.00

Deepening Climate Crisis and Solutions

Ümit ŞAHİN

Sabancı University
Türkiye

Assessment of Net Zero Emissions Targeting Against The Global Climate Crisis and The Problem of Climate Justice

Alp Erinç YELDAN

Kadir Has University
Türkiye

Why Does Humanity Need New Energy Materials, and Where Will We Find Them?

Taylor SPARKS

The University of Utah
USA



RSS

Recycling and Sustainability Symposium

Geri Dönüşüm
ve Sürdürülebilirlik
Sempozyumu

RSS

Session 1

Session Chairman / Oturum Başkanı: **M. ŞEREF SÖNMEZ**

13.00-13.30

The Enabling Role Of Materials Chemistry Towards Net-Zero Carbon

R. Vasant KUMAR

University of Cambridge
United Kingdom

(Invited Speaker)

13.30-13.50

Investigating The Effect of Mechanical Pretreatment on The Recovery Rate of Critical Raw Materials from Discarded Hard Disc Drives

Alireza HABİBZADEH, Mehmet Ali KÜÇÜKER, Mertol GÖKELMA

Izmir Institute of Technology
Türkiye

13.50-14.10

Iron Removal from NdFeB Waste Magnet Solutions Using Sodium Alginate Solution

Emircan UYSAL¹, Elif EMİL KAYA^{1,2,3}, Serhat AL¹, Sebahattin GÜRME¹

¹Istanbul Technical University, ²RWTH Aachen University, ³Turkish-German University
Türkiye, Germany

14.10-14.30

Investigation of Dissolution Parameters of Rare Earth Elements in Fluorescent Wastes by Microwave Leaching

Ayşegül BİLEN, Utku HATİPOĞLU, Muhlis Nezihi SARİDEDE

Yıldız Technical University
Türkiye

RSS

Session 2

Session Chairman / Oturum Başkanı: **MERTOL GÖKELMA**

14.40-15.00

Characterization and Extraction of Heavy Metals from Municipal Solid Waste Incineration Fly Ash

Jonas SCHUSTER^{1,2}, Burçak EBİN¹

¹Chalmers University of Technology,

²Hamburg University of Technology

Sweden, Germany

15.00-15.20

Production of Metal Sulfides from Ferrochrome Flue Dusts and Investigation of Their Electrochemical Properties

Ozan AYDIN, Metin GENÇTEN, Burak BİROL

Yıldız Technical University

Türkiye

15.20-15.40

Li-Ion Battery Recycling for Industrial Scale

**Safiye TANRIVERDİ^{1,2}, Berk GÜLÖRTEN²,
Mahmut KARADAŞ²**

¹Istanbul University - Cerrahpasa,

²Proses Makine

Türkiye

15.40-16.00

Recovery of End-Of-Life Lithium-Ion Battery Cathode Materials in Acidic Media

**Elif GÜLOĞLU¹, Mert ZORAĞA¹,
Gökçe HAPÇI AĞAOĞLU¹, Ş. Samet KAPLAN²,
M. Şeref SÖNMEZ², Sebahattin GÜRMEZ²,
Gökhan ORHAN¹**

¹Istanbul University-Cerrahpasa, ²Istanbul Technical University
Türkiye

RSS

Session 3

Session Chairman / Oturum Başkanı: **SEDAT İLHAN**

16.20-16.40

Is Sustainability a Paradigm for Occupational Health and Safety?

Murat Can OCAKTAN

UCTEA Chamber of Metallurgical and Materials Engineers
Türkiye

16.40-17.00

Remelting Behaviour of Pure and AZ63 Magnesium Chips

Pınar YÖRÜK¹, Bora DERİN², Mertol GÖKELMA¹

¹İzmir Institute of Technology,
²Istanbul Technical University
Türkiye

17.00-17.20

Scrap-Salt Flux Interactions During Recycling Processes

**İrem Yaren ÇAPKIN¹, Adamantia LAZOU²,
Gabriella TRANELL², Mertol GÖKELMA¹**

¹İzmir Institute of Technology,
²Norwegian University of Science and Technology
Türkiye, Norway

17.20-17.40

Tin Recovery from Electrolytic Tinning Line (ETL) Scraps

**Gizem KAVUK¹, Anıl AGADANGİL¹,
Miyase Özlem KÖYBAŞI ÖZUÇAK¹,
S. Samet KAPLAN¹, M. Şeref SÖNMEZ²**

¹TOSÇELİK, ²Istanbul Technical University
Türkiye



AMS

Aerospace Materials Symposium

Havacılık Malzemeleri
Sempozyumu

AMS

Session 1

Session Chairman / Oturum Başkanı: **HAKAN YAVAŞ**

13.00-13.20

Dynamic Recrystallization in Directional Solidified CM247 LC Alloys

Müge AKDEMİR¹, Belgin ATAMAN¹, Aylin ŞAHİN KAHRAMAN², Havva KAZDAL ZEYTİN², Hüseyin AYDIN²

¹Istanbul Technical University, ²TUBITAK Marmara Research Center
Türkiye

13.20-13.40

Cold Spray Effect on Oxide Dispersion Strengthening of Inconel 718

Bayram Berk TANRISEVDİ, Eda AYDOĞAN

Middle East Technical University
Türkiye

13.40-14.00

Flowforming and Heat Treatment Effect of IN718 Alloy

Aptullah KARAKAŞ

Repkon Machine and Tool Industry
Türkiye

AMS

Session 2

Session Chairman / Oturum Başkanı: **HÜSEYİN AYDIN**

14.40-15.00

A Numerical Analysis of the Effect of Electro-Beam-Melt Ti6Al4V Cover Plate on the Ballistic Performance of SiC Armor**F. Murat YILDIZTEKİN¹, Mustafa GÜDEN¹,
Alper TAŞDEMİRCİ¹, A. Kaan TOKSOY²,
Gülden ÇİMEN¹, S. Burçin ÇELLEK¹**¹Izmir Institute of Technology, ²Roketsan Missiles Industries
Türkiye

15.00-15.20

Effect of Solution Heat Treatment on the Anisotropy of Microstructure, Texture and Mechanical Properties of Hastelloy X Fabricated by Laser Powder Bed Fusion**Seren ÖZER^{1, 2}, M. Alp YALÇIN¹, Güney Mert BİLGİN²,
Kemal DAVUT³, Ziya ESEN⁴, Arcan F. DERİCİOĞLU²**¹Atılım University, ²Middle East Technical University,
³Izmir Institute of Technology, ⁴Çankaya University
Türkiye

15.20-15.40

Effects of Heat Treatment and Hot Isostatic Pressing on High Temperature Mechanical Properties of Ti-48Al-2Cr-2Nb Alloy Produced by Electron Beam Melting**Güney Mert BİLGİN^{1,2}, Seren ÖZER^{2,3} Ziya ESEN⁴,
Arcan F. DERİCİOĞLU²**¹TUSAS Engine Industries, ²Middle East Technical University,
³Atılım University, ⁴Çankaya University
Türkiye

15.40-16.00

The Effect of Powder Bed Fusion and Direct Deposition Methods on Metallic Materials**Murat ISIK**
Uludağ University
Türkiye

AMS

Session 3

Session Chairman / Oturum Başkanı: **BENAT KOÇKAR**

16.20-16.50

Materials for Extreme Environments: On The Outside Looking in

Ali SAYİR

Air Force Office of Scientific Research
USA

(Invited Speaker)

16.50-17.10

Evaluation of Proficiency Test Results in Fatigue Test in Aerospace Metallic Materials

**Bülent AYDEMİR¹, Hüseyin AYDIN², Fatih GÜLER²,
Aygün GÜNGÖR², İbrahim KÜÇÜKOĞUL², Havva
KAZDAL ZEYTİN²**

¹Tübitak UME, ²Tübitak MAM
Türkiye

17.10-17.30

Mechanical Behavior of Repaired Carbon Fiber Reinforced Polymer Composite Laminates

Evren SONAT^{1,2}, Mete BAKIR^{2,3}, Sezer ÖZERİNÇ¹

¹Middle East Technical University,
²Turkish Aerospace Industries,
³Yıldırım Beyazıt University
Türkiye

17.30-17.50

Microstructural Evolution of CMSX-4 SLS Single Crystal Superalloys during Creep Rupture Tests

**Aylin ŞAHİN KAHRAMAN¹, Burak HORASAN², Havva
KAZDAL ZEYTİN¹, Hüseyin AYDIN¹,
Cevat Fahir ARISOY³**

¹Tübitak MAM, ²Sakarya University,
³İstanbul Technical University
Türkiye



STCS

Surface Treatment and Coating Symposium

Yüzey İşlemler ve Kaplama
Sempozyumu

STCS

Session 1

Session Chairman / Oturum Başkanı: **KÜRŞAT KAZMANLI**

13.00-13.20

ZnO Nanowire Growth via Anodization

Yiğithan TUFAN, İpek Tuğçe DÖŞ, Batur ERCAN

Middle East Technical University
Türkiye

13.20-13.40

Production and Characterization of Gold Nanofilms on Transparent Substances by Electrodeposition Method

Uğur BARUT, Metehan ERDOĞAN

Ankara Yıldırım Beyazıt Üniversitesi
Türkiye

13.40-14.00

Effect of Substrate Bias on Mechanical Properties of Magnetron Sputtered AlTiN-B₄C Films

Özden KISACIK^{1,2}, Cennet YILDIRIM^{1,3}, Erkan KAÇAR^{1,4}, Servet TURAN², Sedat SÜRDEM⁵

¹Boron Research Institute, ²Eskisehir Technical University, ³Istanbul Technical University, ⁴Hakkari University, ⁵Gazi University
Türkiye

14.00-14.20

Effect of Micro Arc Oxidation and Precipitation Hardening on The Corrosion Resistance of 7075 Al Alloy Fabricated by Flow Forming

Belgin ATAMAN¹, Serra BAYRAM¹, Mertcan KABA¹, Aptullah KARAKAŞ^{1,2}, Murat BAYDOĞAN¹, Hüseyin ÇİMENOĞLU¹

¹Istanbul Technical University, ²Repkon Makina ve Kalıp
Türkiye

STCS

Session 2

Session Chairman / Oturum Başkanı: **EKREM ALTUNCU**

14.40-15.10

Carbon-Based PVD Coating Solutions for a Sustainable Future

Ivan KOLEV

IHI Hauzer Techno Coating B.V.
Netherlands

(Invited Speaker)

15.10-15.30

Effect of Aluminizing on the High Temperature Oxidation Behavior of Inconel 718 Superalloy

Y. Burak TELBAKİROĞLU, Erkan KONCA

Atılım University
Türkiye

15.30-15.50

Improving Fracture Toughness of AlTiN Hard Coatings by W Additions

Burçin KAYGUSUZ¹, Amir MOTALLEBZADEH², Özcan Doğu KARADAYI³,

Muhammed Kürşat KAZMANLI⁴, Sezer ÖZERİNÇ¹

¹Middle East Technical University, ²Koç University, ³Ionbond Turkey Yüzey Teknolojileri, ⁴Istanbul Technical University
Türkiye

15.50-16.10

Performance and Wear of Vacuum Brazed Diamond Cutting Tools With Reinforced Electrolysis Coating

Berrak BULUT¹, Yunus Emre ERBAY², Isil KERTİ², Murat BAYDOĞAN¹

¹Istanbul Technical University, ²Yıldız Technical University
Türkiye

STCS

Session 3

Session Chairman / Oturum Başkanı: **ALPER YEŞİLÇUBUK**

16.20-16.40

For More Sustainable Cold Forging Process: Use of Sand Blasting Instead of Pickling and Rinsing

Baybars SARICA, M. Burak TOPARLI, Dođuş ZEREN, Umut İNCE

Norm Cıvata
Türkiye

16.40-17.00

Investigation of Mechanical and Corrosion Properties of Electroless Ni-W-Co-SiC Multicomponent Coatings

İsmail Deniz Kağın DEMİR¹, Göksel HIZLI², Selim ERTÜRK², Kürşat KAZMANLI²

¹TR Mekatronik Sistemler, ²Istanbul Technical University
Türkiye

17.00-17.20

Sol-Gel Spray Coating of Aluminium Alloys for The Automotive Applications

Çisem ÇELİK KURTULAN^{1,2}, Ş. Samet KAPLAN¹, M. Şeref SÖNMEZ¹

¹Istanbul Technical University,
²Turkish Energy, Nuclear and Mineral Research Agency (TENMAK)
Türkiye

17.20-17.40

Wear and Corrosion Performance Evaluation of Laser Claded Brake Disc

Ekrem ALTUNCU¹, Recep AKYÜZ², Çiğdem DİNDAR², Cem ÖZTÜRK²

¹Sakarya University of Applied Sciences, ²Tofas Automotive
Türkiye

17.40-18.00

A Comparative Study On Corrosion Properties of Decorative Chromium and PVD Evaporated Aluminium Coated ABS Parts

Aleyna BAYATLI¹, Arif AKILLILAR², Mustafa KOCABAŞ¹

¹Konya Technical University, ²Tosunogulları Mobilya
Türkiye



STS

Steel Symposium

Çelik Sempozyumu

STS

Session 1

Session Chairman / Oturum Başkanı: **BORA DERİN**

10.00-10.20

Evaluation of Chromite Ores by Metallothermic Process in EAF

Hasan GÜNEY, Selçuk KAN, Kağan BENZEŞİK, Onuralp YÜCEL

Istanbul Technical University
Türkiye

10.20-10.40

Determining Optimum Roasting Conditions of Hematite Magnetization with Temperature-Coke Mixture Copula

Zeynep Hazal YAZĞAN¹, Mikail BAŞYİĞİT¹, Abdullah BUHUR², Elif UZUN KART¹

¹Marmara University, ²ARGETEST
Türkiye

10.40-11.00

Effect of Ladle Furnace Slag on Steel Cleanliness of Tirecord Steel in Isdemir Plant

İlker AYÇİÇEK¹, Nuri SOLAK², Memduh Kağan KELER³

¹İskenderun Demir ve Çelik A.Ş., ²İstanbul Teknik Üniversitesi,
³Ereğli Demir ve Çelik A.Ş.
Türkiye

STS

Session 2

Session Chairman / Oturum Başkanı: **ENDER KESKİNKILIÇ**

11.20-11.40

Synthesis of Nanocrystalline Stainless Steels by Mechanical Alloying: Grain Growth, Phase Transformation, Thermal Stability and Mechanical Properties

Hasan KOTAN

Necmettin Erbakan University
Türkiye

11.40-12.00

Design and Investigation of The Mechanical Properties of Light Alloys For Electric Vehicles

**Ayşen Ceren DERELİ^{1,2}, Ahmet Salih YILMAZ²,
Ufuk BALIKÇI², Onuralp YÜCEL¹**

¹Istanbul Technical University, ²Anadolu Isuzu Otomotiv
Türkiye

12.00-12.20

Coil Slumping in Peritectic Steels

**Koray ARAY¹, Ahmet SAĞLAM¹, Metin KATRANCI¹,
Hasan YILDIRIM¹, Burcu SOYSAL ATAN¹,
Fatih ÇELİK¹, Abdurrahman Mesud ÇAKIR¹,
Erhan SAKALLI²**

¹İskenderun Demir ve Çelik A.Ş., ²Ereğli Demir ve Çelik A.Ş.
Türkiye

12.20-12.40

Reducing Quality Cost by Reducing Transverse Surface Crack Defect in Slab Grades

**Kübra AKGÜN, İlker AYÇİÇEK, Hakan KAPUSUZ,
Burcu Soysal ATAN, Murat SARIOĞLU**

İskenderun Demir ve Çelik A.Ş.
Türkiye

STS

Session 3

Session Chairman / Oturum Başkanı: **ARCAN DERİCİOĞLU**

13.30-13.50

Investigation of Microstructural Properties of Fish Scale Resistant Low Carbon Enamel Steel Grades

Ramazan UZUN, Mehmet Bulut ÖZYİĞİT, Yasemin KILIÇ, Oğuz GÜNDÜZ

Eregli Iron and Steel
Türkiye

13.50-14.10

The Role of Thermomechanical Rolling in Petroleum Pipe Steels and Its Effects on Mechanical Properties

Serdar GÜNBAY, Cemre KEÇECİ, Koray ARAY

İskenderun Demir ve Çelik A.Ş.
Türkiye

14.10-14.30

Effect of Isothermal Transformation on Microstructural and Mechanical Properties of a Low Carbon Microalloyed Bainitic Forging Steel

M. Mustafa BALÇILAR, Bilgehan ÖGEL

Middle East Technical University
Türkiye

14.30-14.50

Experimental Investigation and Theoretical Expression of The Effect of Steel Wire Rope Parameters on Breaking Load

Emre BAŞER^{1,2}, Yıldız ŞAHİN², Murat POLAT¹

¹Çelik Halat ve Tel Sanayii A.Ş., ²Kocaeli University
Türkiye

STS

Session 4

Session Chairman / Oturum Başkanı: **KELAMİ ŞEŞEN**

15.10-15.30

Thermodynamic Investigation of Kappa-Carbide Phase Change in Low-Density Steels**Memduh Kağan KELER^{1,2}, Sibel DAĞLILAR¹,
Oğuz GÜNDÜZ², Özcan BAHAROĞLU², Onur KART²**¹Yıldız Technical University, ²Eregli Iron and Steel
Türkiye

15.30-15.50

The Modeling of Mechanical Properties of Low-Carbon Grade (SAE J403:2014 1006, SAE J403:2014 1008, SAE J403:2014 1010) Wire Rod Steels**Ahmet SAĞLAM, Burcu SOYSAL ATAN, İlker
AYÇİÇEK, Hamdi GÜL, Mustafa TÜRKMANİ, Mehmet
Eriş DURUMUŞOĞLU, Abdurrahman Mesud ÇAKIR**İskenderun Demir ve Çelik A.Ş.
Türkiye

15.50-16.10

Modelling of Monoblock Loads by Quality Based Process Parameters to Ensure Optimum Production Speed at Wire Rod Mill**Hamdi GÜL¹, Hasan Ozan TEMİZ¹, Mustafa Özden
ÖZDEMİR¹, Tayfun KOCABAŞ², Abdurrahman Mesud
ÇAKIR¹, Fatih ÇELİK¹, Burcu SOYSAL ATAN¹**¹İskenderun Demir ve Çelik A.Ş., ²Oyak Maden Metalurji
Türkiye

16.10-16.30

Reduction of Emissions While Removing Dust From Isdemir New Blast Furnace Dust Catcher**Onur Hüseyin MEMİŞ, Ümit GEBENLİ, İbrahim
ÇAKMAK, Mustafa BAŞSU**İskenderun Demir ve Çelik A.Ş.
Türkiye

STS

Session 5

Session Chairman / Oturum Başkanı: **FATİH GÖKÇE**

16.50-17.10

Understanding Carbon Dioxide Emissions in Electric Arc Furnace Operations

Mehmet Fatih GÖKÇE¹, Bora DERİN²

¹Diler Demir Çelik, ²Istanbul Technical University
Türkiye

17.10-17.30

Emissions Occuring in The Coking Process in Steel Manufacturing and Methods of Struggle Against Emissions

Hüseyin KALAY, Zekeriya ÖZER, Kenan AKDEMİR

İskenderun Demir ve Çelik A.Ş.
Türkiye

17.30-17.50

Decarbonization and Green Steel Production in Iron and Steel Industry

Aziz KILIÇ

BCS Enerji Mühendislik
Türkiye



NFMS

Non-Ferrous Metals Symposium

Demir Dışı Metaller
Sempozyumu

NFMS

Session 1

Session Chairman / Oturum Başkanı: **AHMET TURAN**

10.00-10.20

Production of Functionally Graded Materials Based on FLG Reinforced Al-4.5Cu-1.5Mg by Powder Metallurgy

Gökçe BORAND, Deniz UZUNSOY

Bursa Technical University
Türkiye

10.20-10.40

Effect of Anodizing Thickness on Corrosion Behaviour of 2011 Aluminium Alloy

**İlyas Artunç SARI^{1,2}, Görkem ÖZÇELİK¹,
Onuralp YÜCEL²**

¹ASAS Aluminium, ²Istanbul Technical University
Türkiye

10.40-11.00

Investigation and Fe Analysis of Earing Amount and Direction of Deep Drawing Process of an Aluminium Sheet Under Various Condition

**Melih ÇAYLAK, Koray DÜNDAR, Yusuf ÖZÇETİN,
Görkem ÖZÇELİK, Ali ULUS**

ASAŞ Alüminyum
Türkiye

NFMS

Session 2

Session Chairman / Oturum Başkanı: **TANER AKBAY**

11.20-11.40

Reducing Energy Consumption During Heat Treatment of Cast Aluminum Alloys - Optimization of Process Parameters Through CALPHAD

Emre ÇINKILIÇ¹, Esra DOKUMACI ALKAN², Bilge Nur KAVALCI², Şevval ANAVATAN², Başak YAŞAR², Gizem AMMAS²

¹Hakkari University, ²Dokuz Eylul University
Türkiye

11.40-12.00

Investigation of Microstructure of Homogenized Aluminum Alloys in The Batch Homogenization Plant and Continous Homogenization Plant

Murat DOĞAN^{1,2}, Deniz KAVRAR ÜRK^{2,3}, Büşra GEDİK^{4,5}, Gökçen GÖKÇE²

¹Yıldız Technical University, ²Sistem Teknik, ³Istanbul Technical University, ⁴Şeyh Edebalı University, ⁵Arslan Aluminum
Türkiye

12.00-12.20

Parametric Approach of a Novel Heat Treatment on Al-Mg-Si Alloys: Retrogression and Re-Aging

Almina DEVECİ¹, Nilgün BÖYÜKULUSOY¹, Mehmet Buğra GÜNER^{1,3}, Görkem ÖZÇELİK^{2,3}, Ridvan GECÜ¹

¹Yıldız Technical University,
²Sakarya University of Applied Sciences, ³ASAŞ Aluminum
Türkiye

12.20-12.40

Influence of Mg Content on The Microstructure and Mechanical Properties of EN AW 6082 Alloys

Aleyna GÜMÜŞSOY, Hilal ÇOLAK, Işık KAYA, Emrah Fahri ÖZDOĞRU

TRI Metalurji A.Ş.
Türkiye

NFMS

Session 3

Session Chairman / Oturum Başkanı: **AHMET TURAN**

13.30-13.50

Gold Extraction from Oxide Gold Ores by Glycine Leaching**Umay ÇINARLI¹, Gabriel UĞURGEL¹, M. Barış DARYAL², M. Hakan MORCALI³, Ahmet TURAN¹**¹Yeditepe University, ²Gama Composite Engineering & Products, ³Gaziantep University
Türkiye

13.50-14.10

An Update for Critical Raw Materials (CRMs)**Erman CAR¹, Umay ÇINARLI², Ahmet TURAN², Onuralp YÜCEL³**¹Insertec Thermal Solutions, ²Yeditepe University, ³Istanbul Technical University
Türkiye, Spain

14.10-14.30

Environmental Impact of Hydrometallurgical Zinc Production**Georgi PATRONOV**University of Plovdiv "Paisii Hilendarski"
Bulgaria

14.30-14.50

Industrial Scale Extraction of Lithium Carbonate and Rare Earth Elements From Domestic Sources**Arzu S. SATILMIŞ¹, Herkail ÖZEN¹, Furkan E. ÖZEL¹, M. Şeref SÖNMEZ²**¹ASOS Process Engineering, ²Istanbul Technical University
Türkiye

NFMS

Session 4

Session Chairman / Oturum Başkanı: **AHMET ORKUN KALPAKLI**

15.10-15.30	Transformation in Mining and Green Metals Fevzi YILMAZ Fatih Sultan Mehmet Vakıf University Türkiye
15.30-15.50	Effect of Heat Treatment on Microstructure and Corrosion Behaviors of Additive Manufactured Ti-6Al-4V Using SLM Type 3D Printer Yusuf Atilla SADIKOĞLU¹, Şeyma KÜÇÜK¹, Özkan GÖKÇEKAYA², Takayoshi NAKANO¹, Hakan YILMAZER¹ ¹ Yıldız Technical University, ² Osaka University Türkiye, Japan
15.50-16.10	Effect of Hf Addition on the Structural Properties, Microhardness and Oxidation Behaviour of Co-Al-W Superalloys Emre DAMAR, Mehmet Şahin ATAŞ, Mehmet YILDIRIM Konya Technical University Türkiye
16.10-16.30	Homogenization of The CuNi12Zn24 Alloy Produced by Horizontal Continuous Casting Umut YILDIZ¹, Alptekin KISASÖZ², Çağlar YÜKSEL³, Mustafa YILDIZ¹, Serdar Osman YILMAZ⁴ ¹ Kayalar Bakır Alaşımları, ² Kırklareli University, ³ Atatürk University, ⁴ Namık Kemal University Türkiye

NFMS

Session 5

Session Chairman / Oturum Başkanı: **MURAT ALKAN**

16.50-17.10

Thermodynamic and Experimental Approach of The Phase Formations in Ti-Nb-Ta-Zr-Mo High Entropy Alloys

Gökhan POLAT¹, Yunus Eren KALAY²

¹Necmettin Erbakan University,
²Middle East Technical University
Türkiye

17.10-17.30

Integrated Processing of Al_xCoCrFeNi-Cu_a (0.5 ≤ x ≤ 3, a = 0.5, 1) High-Entropy Alloys: from Master Alloy Synthesis to Shaping

**Faruk KAYA¹, Albek ERŞAN², Sajjad ALİAKBARLU¹,
Gül İpek SELİMOĞLU², Bora DERİN¹**

¹Istanbul Technical University, ²Eskisehir Technical University
Türkiye

17.30-17.50

Thermodynamic and Experimental Investigation of AlCoCrFeNiTi based High-Entropy Alloys

**Murat ALKAN¹, Esra DOKUMACI ALKAN¹,
Saadet GÜLER^{1,2}**

¹Dokuz Eylul University, ²Izmir Katip Celebi University
Türkiye



CWS

Corrosion and Wear Symposium

Korozyon ve Aşınma
Sempozyumu

CWS

Session 1

Session Chairman / Oturum Başkanı: **ÇİĞDEM TOPARLI**

10.00-10.20

Investigation of The Influence of Age Hardening on The Corrosion Resistance and Hardness of a Nanocrystalline AA2024 Alloy

**Furkan ÖZDEMİR¹, Hasan OKUYUCU¹,
Rajeev GUPTA²**

¹Ankara Yıldırım Beyazıt University,
²North Carolina State University
Türkiye, USA

10.20-10.40

Can High-Strength Steel Become Stainless Also with Low Chromium Content?

Beste PAYAM, Mustafa Kamil ÜRGEN, Cem ÖRNEK

Istanbul Technical University
Türkiye

10.40-11.00

Effect of B and Sr Addition to Trivalent Chromium Process (TCP) Coated Al-Si Cast Alloys on Corrosion Resistance

**Berkay SAVAŞKAN^{1,2}, Muammer MUTLU², Özgül
KELEŞ¹**

¹Istanbul Technical University, ²Mita Kalıp ve Dokum Sanayii
Türkiye

CWS

Session 2

Session Chairman / Oturum Başkanı: FATİH TOPTAN

11.20-11.50

Tribocorrosion Degradation of Osteointegrated Biomedical Implants: Mechanisms, Biological Implications and (Possible) Solutions

Luis Augusto ROCHA

Digital Transformation CoLAB
Portugal

(Invited Speaker)

11.50-12.10

Tribocorrosion Properties of Electroless Nickel-Boron Coatings from Stabilizer-Free Bath

Muslum YUNACTI¹, Alex MONTAGNE², Mariana Henriette STAIA², Véronique VITRY¹

¹Université de Mons, ²Arts et Métiers Institute of Technology
Belgium, France



CGRS

Ceramics, Glass, Refractory Materials Symposium

Seramik, Cam, Refrakter
Malzemeleri Sempozyumu

CGRS

Session 1

Session Chairman / Oturum Başkanı: **ABDULLAH ÖZTÜRK**

13.30-14.00	<p>Multi-Materials 3D Printing of Ceramics</p> <p>Lisa BIASETTO University of Padova Italia</p> <p>(Invited Speaker)</p>
14.00-14.20	<p>Synthesis of Li_4SiO_4 as a Solid Sorbent for Carbon Capture via Solution Combustion Route</p> <p>Kagan BENZESİK¹, Ahmet TURAN², Şeref SÖNMEZ¹, Maria Teresa IZQUIERDO³, Onuralp YÜCEL¹ ¹Istanbul Technical University, ²Yeditepe University, ³Instituto de Carboquímica ICB-CSIC Türkiye, Spain</p>
14.40-15.00	<p>Nb-Co co-doped Barium Titanate Dielectric Ceramics for Multilayered Ceramic Capacitors</p> <p>Berkay ÖZGÜR¹, N. Kaan ÇALIŞKAN¹, Abdullah ÖZTÜRK² ¹Tübitak SAGE, ²Middle East Technical University Türkiye</p>

CGRS

Session 2

Session Chairman / Oturum Başkanı: **ONURALP YÜCEL**

15.10-15.30

Production of Activated Carbon from Olive Seed

Derya AKBULUT, Ali Osman KURT

Sakarya University
Türkiye

15.30-15.50

The Use of Olivine in The Production of Mineral Wool

Akın ODABAŞI¹, Gökhan BAŞMAN², Hülya KAFTELEN ODABAŞI¹, Hande ARDIÇOĞLU²

¹Firat University, ²Etikrom Inc.
Türkiye

15.50-16.10

The Utilization of Citrate Gel Method in Cobalt Boride Synthesis

Buse BİTİKÇİ, Çağan Berker İYİ, Hülya BİÇER

Kütahya Dumlupınar University
Türkiye

CGRS

Session 3

Session Chairman / Oturum Başkanı: **FİLİZ ÇINAR ŞAHİN**

16.50-17.10

Effect of Hot Isostatic Pressing on Densification, Microstructure and Electrical Properties of Mg_{0.95}Ca_{0.05}TiO₃ Ceramic

Selin GÜNTOP^{1,2}, Hakan DER¹, N. Kaan ÇALIŞKAN¹, M. Kaan PEHLİVANOĞLU¹, Abdullah ÖZTÜRK²

¹Tübitak SAGE, ²Middle East Technical University
Türkiye

17.10-17.30

Production and Characterization of Ceramics for Microwave Applications

Melike DÖNMEZ, Cihangir DURAN

Ankara Yıldırım Beyazıt University
Türkiye

17.30-17.50

Phase Analysis and Dielectric Characteristics of BST Ceramics Produced by Conventional and Microwave Assisted Solid-State Reactions

Başar SÜER, Özlem AYDIN ÇİVİ, Arcan F. DERİCİOĞLU

Middle East Technical University
Türkiye

17.50-18.10

Experimental Phase Studies in The Quasi-Binary BaCeO₃-SrCeO₃ System

Hanifi Eray KORKMAZ^{1,2}, Nuri SOLAK²

¹TRMotor Power Systems, ²Istanbul Technical University
Türkiye



EMS

Energy Materials Symposium

Enerji Malzemeleri
Sempozyumu

EMS

Session 1

Session Chairman / Oturum Başkanı: **BİLLUR DENİZ KARAHAN**

09.40-10.00

The Effect of Iron Concentration in Electrodeposited Solution and PH of Electrolyte on Photoelectrochemical Hydrogen Production Efficiency of Hematite (α -Fe₂O₃) Photoanode

Ersan DOĞAÇ, İlkan KARUL, Seyedsina ALYASİN, Ömer DOĞAÇ, Fatma Betül YILMAZ, Cevat SARIOĞLU

Marmara University
Türkiye

10.00-10.20

The Thermochemical Heat Storage Properties of Composite Structures Produced Different Matrix and Sorbent Salts

Behiye YÜKSEL¹, Esra AYAN², Gökhan ORHAN²

¹Halic University, ²Istanbul University-Cerrahpasa
Türkiye

10.20-10.40

Advanced Material Solutions for Safer and Long-Lasting High Capacity Cobalt Free Batteries for Stationary Storage Applications (CoFBAT)

Kamil Burak DERMENÇİ, Kato DAEMS, Joeri Van MIERLO, Maitane BERECIBAR

Vrije Universiteit Brussel
Belgium

EMS

Session 2

Session Chairman / Oturum Başkanı: **BURAK ÜLGÜT**

10.40-11.10

Transition Metal Free: Dual Ion and Dual-Carbon Batteries

Martin WINTER

University of Münster, Helmholtz Institute Münster
Germany

(Invited Speaker)

11.10-11.30

Material Supply Risk for Thin Film Solar Cells and Importance of Recycling

Ioanna TEKNETZI, Burçak EBİN

Chalmers University of Technology
Sweden

11.30-11.50

An Industrial Ecology Perspective of Battery Technologies for Electromobility: LCA Of Solid-State Lis Battery

Burak ŞEN¹, Ahsen AKBULUT¹, Abdulkadir KIZILASLAN¹, Mahmud TOKUR¹, Murat KÜÇÜKVAR², Nuri Cihat ONAT², Hatem AKBULUT¹

¹Sakarya University, ²Qatar University
Türkiye, Qatar

11.50-12.10

Electrochemical Noise Measurement in Batteries with Metallic Lithium Anodes

Gözde KARAOĞLU, Burak ÜLGÜT

Bilkent University
Türkiye

EMS

Session 3

Session Chairman / Oturum Başkanı: **TUĞRUL ÇETİNKAYA**

12.10-12.30

Investigating The Electrochemical Performance of Double Shell Cathode Active Materials for Lithium Ion Batteries

Elif SARIKAS, Ipek TUNC, Ozgul KELES

Istanbul Technical University
Türkiye

12.30-12.50

Composite Electrodes Production Using Nickel-Titanium Orthodontic Waste and Investigation of Their Uses in Lithium Ion Batteries (Libs)

Humza ASHRAF¹, B. Deniz KARAHAN^{1,2}

¹Istanbul Medipol University, ²Istanbul Technical University
Türkiye

12.50-13.10

Modulation of Cation Composition for Lithium Storage of Spinel-Structured High Entropy Oxides

**Deniz Okan BAYRAKTAR^{1,2}, Ersu LÖKÇÜ³,
Çiğdem TOPARLI¹**

¹Middle East Technical University, ²ASPİLSAN Enerji,
³Eskişehir Osman Gazi University
Türkiye

13.10-13.30

Investigation of Ni Effect on Mn-Fe-Based Multi-Transition Metal Layered Cathode Materials for Sodium-Ion Batteries

**Burcu KALYONCUOĞLU¹, Sebahat ALTUNDAĞ²,
Serdar ALTIN², Metin ÖZGÜL¹**

¹Afyon Kocatepe University, ²Inonu University
Türkiye



FAHTS

Failure Analysis and Heat Treatment Symposium

Hasar Analizi ve Isıl İşlem
Sempozyumu

FAHTS

Session 1

Session Chairman / Oturum Başkanı: **UTKU İNAN**

13.30-13.50

Determination of The Austenization Temperature via Computational Metallurgy Approach for an Alloyed Ductile Iron

**Bariş ÇETİN¹, Ayşe ERKAN², Ümmihan T. YILMAZ³,
Buğra ATASOY¹, Caner YALÇINER¹, Caner ŞİMŞİR^{4,5}**

¹FNSS Savunma Sistemleri, ²Döksan Isıl İşlem,
³Kırıkkale University, ⁴Middle East Technical University,
⁵Simultura Malzeme Teknolojileri
Türkiye

13.50-14.10

The Damage Analysis of The Diamond Particle in The Cutting Natural Stone Process

Berrak BULUT

Istanbul Technical University
Türkiye

14.10-14.30

Investigation of EPDM Materials Used in Milk Tanker

Yıldız YARALI ÖZBEK¹, Emin Emre GÖKTEPE^{1,2}

¹Sakarya University, ²Tırsan Treyler
Türkiye

14.30-14.50

Failure Evaluation of Compression Steel Spring Wires and Factors Affecting Breaking

Y. Ziya SALIK¹, Ekrem ALTUNCU²

¹Çelik Halat ve Tel Sanayii,
²Sakarya University of Applied Sciences
Türkiye



CPS

Composite and Polymer Materials Symposium

Kompozit ve Polimer
Malzemeler Sempozyumu

CPS

Session 1

Session Chairman / Oturum Başkanı: **EKREM ALTUNCU**

10.00-10.20

Surface Modification of Glass Fiber Woven Fabrics by Indium Tin Oxide Coatings and Electromagnetic Characterization of Their Multilayered Graded Composites in X-Band Frequency Range

Merve ÖZDİL DARICIOĞLU, Caner DURUCAN, Arcan F. DERİCİOĞLU

Middle East Technical University
Türkiye

10.20-10.40

Synthesis and Characterization of Graphene Reinforced Al-7.5 wt.% Zn Matrix Composites

Berk ŞENYURT¹, Gökçe BORAND¹, Duygu AĞAOĞULLARI², Nazlı AKÇAMLI¹, Deniz UZUNSOY¹

¹Bursa Technical University, ²Istanbul Technical University
Türkiye

10.40-11.00

Mechanical Properties of Si₃N₄ Reinforced Ti6Al4V Composite Foam

Ömür Ekrem GÜNTÜRK, Mevlüt GÜRBÜZ

Ondokuz Mayıs University
Türkiye

CPS

Session 2

Session Chairman / Oturum Başkanı: **CANER DURUCAN**

11.20-11.40

Biodegradable Polymer Nanocomposites Using Modified Cellulose Nanocrystals

Onur Nuri ARSLAN, Yonca ALKAN GÖKSU, Mohammadreza NOFAR

Istanbul Technical University
Türkiye

12.00-12.20

Investigation of The Effect of Copper Alloy Reinforcement on The Physical Properties of Polymer Matrix Composite

Ömer Alparslan KAYA¹, Talip ÇITRAK¹, Serdar TOZKOPARAN¹, Edanur KASAP¹, Münir TAŞDEMİR², Feriha BİROL¹

¹Sağlam Metal, ²Marmara Üniversitesi
Türkiye

12.20-12.40

Microcellular Hemp Fibre Reinforced Polypropylene Matrix Composites

Yeşim ASLAN¹, Munir TAŞDEMİR², Yeliz ALBRECHTSEN¹, İsmail MUTLU¹

¹Tekkan Plastik, ²Marmara University
Türkiye



WNTS

Welding and Non- Destructive Testing Symposium

Kaynak ve Tahribatsız
Muayene Sempozyumu

WNTS

Session 1

Session Chairman / Oturum Başkanı: **CANER BATIGÜN**

13.30-14.00

Industrial Welding Applications of S690QL Grade Steels

Tanıl ATICI

Cimtas Steel Research & Development Center
Türkiye

(Invited Speaker)

14.00-14.20

Investigation of Microstructure and Mechanical Properties of DP Quality Steels Welded with Different Heat Inputs

**Kardelen YILMAZ¹, Bilgehan ÖGEL²,
Caner BATIGÜN²**

¹Middle East Technical University,

²METU Welding Technology and Non-Destructive Testing Centre
Türkiye

14.20-14.40

The Effect of Process Parameters on Bead Geometry, Hardness and Microstructural Properties of Armour Steel Welds Performed by Robotic Gas Metal Arc Welding

**Ceren ÇELİK¹, Recep Murat KURT¹, Ozan ÇOBAN¹,
Hakan BAYKAL², H. Kübra AKBEN¹, Uğur GÜROL^{1,2}**

¹Istanbul Gedik University, ²Gedik Welding
Türkiye

14.40-15.00

Design of High Strength and High Torque Resistance Wire Rope

Fatih DUMAN¹, Emel TABAN², Sevim Gökçe ESEN¹

¹Çelik Halat ve Tel Sanayii A.Ş., ²Kocaeli University
Türkiye

WNTS

Session 2

Session Chairman / Oturum Başkanı: **EMEL TABAN**

15.20-15.40

Effects of Build Orientation and Process Parameters on Mechanical Behavior of IN718 Components Manufactured by Selective Laser Melting Method

Tuğçe KALELİ¹, Aydın YAĞMUR², C. Hakan GÜR¹

¹Middle East Technical University,
²EOS GmbH Electro Optical Systems
Türkiye, Germany

15.40-16.00

The Effect of Heat Input on Mechanical Properties of TRIP Steels in GMAW and TIG Welding

Gökhan ERİAN¹, Adem KURT²

¹Turkish Accreditation Agency, ²Gazi University
Türkiye

16.00-16.20

The Effect of Brazing Parameters on The Microstructural Features of Alumina-Copper Joints

**Ece Naz YURTSEVEN^{1,2}, N. Kaan ÇALIŞKAN¹,
M. Kaan PEHLİVANOĞLU¹**

¹Tübitak SAGE, ²Middle East Technical University
Türkiye

16.20-16.40

Non-Destructive Detection of Flaws in Conductive Sealant Applications With a Metamaterial Based Antenna

Elif Gaye ERKİ¹, Mete BAKIR¹, Oğuzhan AKGÖL²

¹TUSAS, ²İskenderun Technical University
Türkiye

16.40-17.00

Properties of Laser Welded 3003 Aluminum Alloy

Abdullah CEBEÇİ¹, Emel TABAN²

¹Assan Hanil Otomotiv, ²Kocaeli Üniversitesi
Türkiye



BMS

Biomaterials Symposium

Biyomalzemeler
Sempozyumu

BMS

Session 1

Session Chairman / Oturum Başkanı: **BATUR ERCAN**

10.00-10.20

Surface Modification of 3D-Printed Porous 316L Stainless Steel

Azade YELTEN^{1,2}, Batur ERCAN²

¹Istanbul University-Cerrahpasa,
²Middle East Technical University
Türkiye

10.20-10.40

Characterization of Copper Nanoparticle-Deposited Bioceramic Coatings Fabricated on Zirconium

**Tuba YILDIZ^{1,2}, Salih DURDU³, Kadriye OZCAN³,
Metin USTA¹**

¹Gebze Technical University, ²Samsun University,
³Giresun University
Türkiye

10.40-11.00

Production and Characterization of Bioactive Glass-Ceramics From Soda-Lime-Silica and Borosilicate Waste Glasses

**Merve Şeyma SÜREL¹, İremnur AKÇAKOCA¹,
Şeniz Reyhan Kuşhan AKIN², Gülsüm TOPATEŞ¹**

¹Ankara Yıldırım Beyazıt University, ²Çankaya University
Türkiye

11.00-11.20

Essential Oil-Loaded Polymeric Foams via Green Route

Fatma Nur PARIN

Bursa Technical University
Türkiye



NMS

Nanomaterials Symposium

Nanomalzemeler
Sempozyumu

NMS

Session 1

Session Chairman / Oturum Başkanı: **GÖKNUR CAMBAZ BÜKE**

12.10-12.30

Production of Nano Strontium Hexaferrite by Solution Combustion Synthesis

Ceren ÇALIŞKAN, Raşit SEZER

Karadeniz Technical University
Türkiye

12.30-12.50

Phase Engineering of Semiconductor Nanoscale Materials

Selim DEMİRCİ, Mehmet Masun TÜNÇAY

Marmara University
Türkiye

12.50-13.10

Effect of Starting Composition on the Morphology of Sol-Gel Synthesized Boron Carbide (B₄C) Particles

Selin TÜMKAYA, Suna AVCIOĞLU, Figen KAYA, Cengiz KAYA

Yıldız Technical University
Türkiye

13.10-13.30

The Synthesis & Characterization of Homogenous High-Quality Graphene Encapsulated Metallic Powders via Plasma Enhanced Rotating CVD

Deniz ÇAKIR¹, Ömer Refet ÇAYLAN^{1,2}, Tarık Can TÜRKÖĞLU¹, Oğulcan AKGÜN³, Günce DUGAN³, Halil Onat TUĞRUL³, Benat KOÇKAR³, Göknuur CAMBAZ BÜKE¹

¹TOBB University of Economics and Technology,
²Bilkent University, ³Hacettepe University
Türkiye

NMS

Session 2

Session Chairman / Oturum Başkanı: **M. ŞEREF SÖNMEZ**

14.00-14.30

New Polymorphs of Compounds With a Complex, Layered Crystal Structure Stabilized at The Nanoscale: Magnetic Strontium-Hexaferrite Nanoplatelets and Ferroelectric Bismuth-Titanate Nanowires

Darko MAKOVEC

Jožef Stefan Institute
Slovenia

(Invited Speaker)

14.30-14.50

Production of Tin Nanowires via AAO Template Method and Investigation of Their Performance As Catalysis for Electrochemical CO₂ Reduction

Dilan ER^{1,2}, Eleni ROSOLYMOU³, Mustafa URGEN¹

¹Istanbul Technical University, ²Arcelik Global,
³National Technical University of Athens
Türkiye, Greece

14.50-15.10

The Synthesis and Characterization of MO₂CTx Mxene by Hydrothermal Etching with Different Fluoride Salts for EMI Shielding Applications

**Elif OKAY¹, Ömer Refet ÇAYLAN¹,
Begüm Beril İNCECİK², Gökür CAMBAZ BÜKE¹**

¹TOBB University of Economics and Technology,
²Roketsan Missiles Industries
Türkiye

15.10-15.30

Effect of Calcination Temperature on MgAl₂O₄ Nanoparticles Production by Sol-Gel Method

Duygu YEŞİLTEPE ÖZÇELİK, Sebahattin GÜR MEN

Istanbul Technical University
Türkiye



CSS

Casting Symposium

Döküm
Sempozyumu

CSS

Session 1

Session Chairman / Oturum Başkanı: **NECİP ÜNLÜ**

15.50-16.10

Circular Economy in Metal Foundry Sector: From Europe to Türkiye

**Semih ATEŞ¹, Kerem Can DİZDAR¹,
Tunçağ Cihangir ŞEN², Serter Koray HATİPOĞLU²,
Cevat Fahir ARISOY¹**

¹Istanbul Technical University, ²Turkish Foundry Association
Türkiye

16.10-16.30

Optimizing The Amount of Flux Used in The Casting Process of EN AW 6082 Aluminum Alloy in Profile Production

**Sena ERDOĞAN^{1,2}, Selçuk ERKUL¹, Zekeriya MUTLU¹,
Rabia Şevval AKAN^{2,3}, Ayberk UZER^{2,3},
Muhammet ULUDAĞ^{2,3}**

¹PMS Metal Profile Aluminum, ²Bursa Technical University,
³ULUCON R&D and Consulting
Türkiye

16.30-16.50

Reducing The Energy Costs for Green Conversion by Coating the Surfaces of the Crucibles Used in HPDC Method with Boron Reinforcement Cellulose

Ümmet AYYILDIZ^{1,2}, Songül KILINÇ^{1,3}

¹Prometal, ²Bilecik Şeyh Edebali University,
³Bursa Technical University
Türkiye

16.50-17.10

Microstructure Evolution of The Three-Phase Al-Al₂Cu- Ag₂Al Eutectic System Upon Directional Solidification

**Merve KEVKİR¹, Arash KAZAZİ²,
Samira MOHAGHEGHİ³, Melis ŞEREFİOĞLU¹**

¹Marmara University, ²Koç University, ³İstinye University
Türkiye



POSTER PRESENTATIONS

POSTER SUNUMLARI

Recycling and Sustainability Symposium

Geri Dönüşüm ve Sürdürülebilirlik Sempozyumu

RSS-1

Investigation of Dissolution Conditions of Yttrium (Y) and Europium (Eu) in Fluorescent Wastes

**Utku HATİPOĞLU, Ayşegül BİLEN,
Muhlis Nezih SARIDEDE**

Yıldız Technical University
Türkiye

RSS-2

The Recycling Model of Zirconia & Alumina Waste in Iron - Steel Plants

Oğuzhan SAKARYA, Uğur CENGİZ

Bilecik Demir Çelik A.Ş.
Türkiye

RSS-3

An Investigation on Calcium Aluminate Cement Production Using Two Types of Bauxite, Alumina and Marble Waste

**C. Betül EMRULLAHOĞLU ABİ, Esra ÖZGÜVEN,
Serkan KESKİN**

Afyon Kocatepe University
Türkiye

RSS-4

Aluminium Black Dross Utilization via Pyrometallurgical and Hydrometallurgical Operations

Umay ÇINARLI, Ahmet TURAN

Yeditepe University
Türkiye

RSS-5

Recycling of Aluminium Used Beverage Cans: Decoating and Self-Heat Generation

**Musa ORUÇ¹, Emine Bengü KAYA¹, Umay ÇINARLI²,
Tuğçe ERGÜL², Ahmet TURAN², Onuralp YÜCEL³,
Erman CAR⁴**

¹Yalova University, ²Yeditepe University,
³Istanbul Technical University, ⁴Insertec Thermal Solutions
Türkiye, Spain

RSS-6

Circular Economy Approach for Evaluation of Mill Scale Using Al Residue as Reductant

Selçuk KAN, Kağan BENZEŞİK, Onuralp YÜCEL

Istanbul Technical University
Türkiye

RSS-7

Lean Sustainable Green Supply Chain Management In Light Metals Casting Industry

Ümmet AYYILDIZ^{1,2}

¹Prometal, ²Bilecik Şeyh Edebali Üniversitesi
Türkiye

Aerospace Materials Symposium

Havacılık Malzemeleri Sempozyumu

AMS-1

Evaluation of Proficiency Test Results in High-Temperature Tensile Test in Aerospace Metallic Materials

**Bülent AYDEMİR¹, Hüseyin AYDIN², Fatih GÜLER²,
Aygün GÜNGÖR², İbrahim KÜÇÜKOĞUL²,
Havva KAZDAL ZEYTİN²**

¹Tübitak UME, ²Tübitak MAM
Türkiye

AMS-2

The Effect of The Johnson Cook Damage Parameters on The Crushing Modes of an Electro-Beam Melt Additive Processed Ti6Al4V Body-Centered-Cubic Lattice Structures

**H. İrem ERTEN, Burak HIZLI, M. Arslan Bin RIAZ,
Samed ENSER, Mustafa GÜDEN**

Izmir Institute of Technology
Türkiye

AMS-3

Influence of Platform Dimensions on The Secondary Grain Formation in Production of Single Crystal Turbine Blade

**İbrahim BERBER, Sertaç ALPTEKİN, Lütfi YAKUT,
Bülent BAHADIR, Havva KAZDAL ZEYTİN**

Tübitak MAM
Türkiye

AMS-4

Microstructural Characterization of Forged Inconel 718 Superalloy After Long Term High Temperature Exposure

**Burak HORASAN¹, İbrahim BERBER¹, Fatih GÜLER²,
Havva KAZDAL ZEYİN², Hüseyin AYDIN²**

¹Sakarya University, ²TUBITAK Marmara Research Center
Türkiye

Surface Treatment and Coating Symposium Yüzey İşlemler ve Kaplama Sempozyumu

STCS-1

Simulation and Fabrication of Thin Film Notch Filter

Eray HUMALI^{1,2}, M. Kürşat KAZMANLI¹

¹Istanbul Technical University, ²Roketsan Missiles Inc.
Türkiye

STCS-2

Cone Shaped Parts Manufacturing by Electroforming Process

**Tutku TURGUTLUGİL GÖKÇE, N. Kaan ÇALIŞKAN,
M. Kaan PEHLİVANOĞLU**

Tübitak SAGE
Türkiye

STCS-3

Tribological Performance of Electrochemically Borided AISI H13 Hot Work Die Steel

Ümmet AYYILDIZ^{1,2}, Harun MİNDİVAN²

¹Prometal R&D Center, ²Bilecik Şeyh Edebali University
Türkiye

STCS-4

Optimization of Electroless Silver Coating on Calcium Based Ceramics

Kardelen GÜNDOĞDU, Metehan ERDOĞAN

Ankara Yıldırım Beyazıt University
Türkiye

STCS-5

Investigation of Formation of Au-Ag-Cu Alloys by Electrodeposition from Cyanide Based Electrolyte

Berkay ÇAĞAN¹, Metehan ERDOĞAN¹, İshak KARAKAYA²

¹Yıldırım Beyazıt University, ²Middle East Technical University
Türkiye

Steel Symposium
Çelik Sempozyumu

STS-1

The Use of Boron Element for Cost Reduction in Teeth Made of Low Alloy Steel Used in Excavators

Muhammed KIRICI^{1,2}

¹Motus Automotive, ²Konya Technical University
Türkiye

STS-2

Modelling and Simulation Studies for Optimization of Laboratory Scaled Steel Casting Mold Designs

**İ. İrfan AYHAN¹, Caner GÜNEY¹, Emre ALAN¹,
N. Başak DÜRGER¹, M. Fatih KAYADEĞİRMENİ¹,
Muhammet ULUDAĞ², Nursina ŞENSOY²,
Beyza GÜNAYDIN², Gülşah KURT²**

¹ÇEMTAŞ Çelik, ²Bursa Technical University
Türkiye

STS-3

Development of New Steel Grade with Improved Hardenability for Renewable Energy Industry

**İ. İrfan AYHAN¹, Caner GÜNEY¹, Emre ALAN¹,
N. Başak DÜRGER¹, M. Fatih KAYADEĞİRMENİ¹,
Nazlı AKÇAMLI²**

¹ÇEMTAŞ Çelik, ²Bursa Technical University
Türkiye

STS-4

Use Of Green Hydrogen in Iron and Steel Industry

Caner TUNA¹, Celal Erkal KAHRAMAN¹, Hakan ERÇAY¹, Tuncay DİKİCİ²

¹Özkan Demir Çelik, ²Dokuz Eylül Üniversitesi
Türkiye

STS-5

Sinter Plant Ignition Furnace Burning Optimization

**Erol AKKÜLAH, Cenk KAYA, Seyithan ÇEVİK,
Mehmet AYGÜN, Bengü TAŞDELEN**

Ereğli Demir ve Çelik
Türkiye

STS-6

Efficiency Improvement via Optimizing Secondary Cooling in a Heavy-Duty Gas Turbine

Mehmet YILDIZ, Mustafa Mert ÇAKA, Cenk BAYENDER, Tansu KUKUL, Özgür AKGÜN

Ereğli Iron and Steel
Türkiye

STS-7

Increasing Hot Rolled Mill Production by Increasing Coil Weights Under 1,80 mm Thickness

**Muhammet BİLEN¹, Koray ARAY¹, Serdar GÜNBAY¹,
Erhan SELVI¹, Hasan YILDIRIM¹, Burak Emre IŞIK¹,
İskender GÖK¹, Ahmet Mithat AVŞAR¹,
Tayfun KOCABAŞ², Abdurrahman Mesud ÇAKIR¹,
Burcu SOYSAL ATAN¹**

¹İskenderun Demir ve Çelik A.Ş., ²Oyak Maden Metalurji
Türkiye

STS-8

The Evaluation Potential of Basic Oxygen Furnace (BOF) Slag and The Recycling of Calcium Carbonate by Hydrometallurgical Methods

Muhammet BİLEN

İskenderun Demir ve Çelik A.Ş.
Türkiye

STS-9

Estimating Tap Hole Clay Consumption in Blast Furnace by Fuzzy Logic Method

Mehmet GÖKOĞLU, Ramazan YARAŞIR

İskenderun Demir ve Çelik A.Ş.
Türkiye

STS-10

Comparison of Manganese Oxide (MnO) and Iron Oxide (FeO) Analyzes in Steel Production Slag with Different Analysis Methods

**Barış SAĞLAR¹, Aydan GÜLSÜREN¹, Onur OREL¹,
Ramazan BİLGİN², Memduh Kağan KELER³**

¹İskenderun Demir ve Çelik A.Ş., ²Çukurova Universtiy,
³Ereğli Demir ve Çelik
Türkiye

STS-11

Water Management in Iron and Steel Industry

**Mehmet Burak ATAN, Erkin Y. GEDİK, Onur MARTI,
Gökhan GÜNGÖR, Arif AKSOY, İbrahim SARI**

İskenderun Demir ve Çelik A.Ş.
Türkiye

STS-12

**The Effect of Maintenance Activities on
Environmental Management in Iron and Steel
Facilities**

**Hasan BULUT, Ayşe ÇELİK, Merih YAMAN,
Gökçe ARSLAN**

İskenderun Demir ve Çelik A.Ş.
Türkiye

STS-13

**Management of Ferroalloys Stocks in Iron and Steel
Production**

Erman KAYA, Beril BİRİNCİ, Ece DAL YALÇIN

İskenderun Demir ve Çelik A.Ş.
Türkiye

STS-14

**Investigation of Castability of DIN EN 10089 38Si7
Steel Grade in Billet Casting Machine**

**İlker AYÇIÇEK¹, Kübra AKGÜN¹, Memduh Kağan
KELER²**

¹İskenderun Demir ve Çelik A.Ş., ²Ereğli Demir ve Çelik
Türkiye

STS-15

Pressure Vessel Detection System with Image Processing Techniques

Zekeriya SARIKOL, Semiramis GÜLKESEN

İskenderun Demir ve Çelik A.Ş.
Türkiye

STS-16

Modernization and Replacement of Isdemir 4th Blast Furnace Clay Gun and Drill Equipment

Recep GÜNEŞOĞLU, Osman FİDAN, Ökkeş CİĞERLİ, Ali Hikmet CAN, Hasan İŞLER, Evren ŞAHİN

İskenderun Demir ve Çelik A.Ş.
Türkiye

STS-17

Improvement of The Siphon Opening Process in The Isdemir New Blast Furnace No.1

Mustafa BAŞSU, Onur Hüseyin MEMİŞ, Ümit GEBENLİ, İbrahim ÇAKMAK

İskenderun Demir ve Çelik A.Ş.
Türkiye

STS-18

Distribution of Coil and Wire Rod Products Manufactured at Isdemir According to Areas of Usage, Standards and Customer Expectations

Muhammet BİLEN, Nalan Gül UĞUR

İskenderun Demir ve Çelik A.Ş.
Türkiye

STS-19

Establishing a Billet Quality Recommendation System (Digitalization)

Gökhan BİLMEZ, Erhan KORKMAZ, Erman KAYA

İskenderun Demir ve Çelik A.Ş.
Türkiye

STS-20

Minimizing The Consumption of Temperature Probe by Prediction of Liquid Steel Temperature During Ladle Furnace Process

**Mustafa SAĞLAM¹, Esra KÜPELİ¹,
Abdurrahman Mesud ÇAKIR¹, Burcu SOYSAL ATAN¹,
Alper KURTOĞLU¹, Alperen TERZİ¹,
Eyüp Veysel ÖZDEMİR¹, Hikmet ŞAHİN¹,
Mehmet Mustafa YILDIRIM¹, Bekir Burak
YAMANOĞLU¹, Tayfun KOCABAŞ²**

¹İskenderun Demir ve Çelik A.Ş., ²Oyak Maden Metalurji
Türkiye

STS-21

Coil Movement Optimization

**Metin KATRANCI, Hasan YILDIRIM,
Mahmut KAYHAN, Uğur OKTAY, Koray ARAY,
Abdurrahman Mesud ÇAKIR, Burcu SOYSAL,
Fatih ÇELİK**

İskenderun Demir ve Çelik A.Ş.
Türkiye

STS-22

Improvement of Scale Print Defect in Cut-To-Length Plants for S600 MC Steel Grade

**Serdar GÜNBAŞ, Koray ARAY, Erhan SELVİ,
Ahmet SAĞLAM**

İskenderun Demir ve Çelik A.Ş.
Türkiye

STS-23

Sinter Plant Circular Cooler Medium Voltage Fan Motor Conversion from DOL System To VFD System

Cengiz ABUKAN, Fatih DÜZLÜ, Volkan KIZILAY

İskenderun Demir ve Çelik A.Ş.
Türkiye

STS-24

Effect of Dunit and Dolomite Auxiliary Raw Materials on SiO₂ Output in Product Sinter and Cost Advantage in The Sinter Process

**Orkun HASDEMİR, Sadi BALABAN, Berkay DELAY,
Burhan Erkan KESEMEN, Volkan KIZILAY**

İskenderun Demir ve Çelik A.Ş.
Türkiye

STS-25

Mapping Slab Defects, Conceptualizing Digital Twins

Fatih Mehmet AYDIN, Serdar GÜNBAY, Hikmet ŞAHİN, Serkan DURSUN, İlker AYÇİÇEK

İskenderun Demir ve Çelik A.Ş.
Türkiye

STS-26

Advantage at Ladle Furnace Processing Time by Developing a Model That Calculates Liquid Steel %Al Value Closer to The Spectral Sample Result

Mustafa SAĞLAM¹, Memduh Kağan KELER², Esra KÜPELİ¹, Eyüp Veysel ÖZDEMİR¹, Alperen TERZİ¹, Hikmet ŞAHİN¹, Mehmet Mustafa YILDIRIM¹, Tayfun KOCABAŞ³, Abdurrahman Mesud ÇAKIR¹, Burcu SOYSAL ATAN¹, Deniz YAZICI¹

¹İskenderun Demir ve Çelik A.Ş., ²Ereğli Demir ve Çelik,
³Oyak Maden Metalurji
Türkiye

STS-27

Wire Rod Surface Examination by Non-Destructive Liquid Penetrant Testing Method

Cemre KEÇECİ, Erdem TAN, Mustafa ÖZDEMİR

İskenderun Demir ve Çelik A.Ş.
Türkiye

STS-28

The Effect of Debinding Parameters on Additive Manufactured 316L Stainless Steel Parts with Cold Metal Fusion Technology

Burcu Aslı ÖZKAN¹, Burak KÜÇÜKELYAS¹, Erkan ATEŞ², Cihan KABOĞLU¹, Deniz UZUNSOY¹

¹Bursa Technical University, ²3D Design Technologies
Türkiye

STS-29

Effect of Continuous Cooling on Microstructural and Mechanical Properties of a Low Carbon Microalloyed Mn-Si Bainitic Steel

Esra KADERLİ, Bilgehan ÖGEL

Middle East Technical University
Türkiye

STS-30

The Effect of Chemical Composition and Ratio of Deformation on Mechanical Properties in High Carbon Steel Wire Production

Sevim Gökçe ESEN, Muhammet Fatih DUMAN

Çelik Halat ve Tel Sanayii A.Ş.
Türkiye

STS-31

Experimental Investigation of Mechanical Performance Tests of Impregnated Plastic Core Steel Wire Rope and Impregnated Plastic Core Swaged Steel Wire Rope

Zeynep Şeyma SERDAROĞLU, Zehra ALTINIŞIK

Çelik Halat ve Tel Sanayii A.Ş.
Türkiye

STS-33

Comparison of Breaking Load and Service Life of Steel Wire Ropes with Parallel Wire Rope Core (PWRC) and Independent Wire Rope Core (IWRC)

Murat POLAT, Emre BAŞER

Çelik Halat ve Tel Sanayii A.Ş.
Türkiye

STS-34

Reducing The Amount of Slag Carry Off From The Ladle in The Continuous Casting Process

Ahmet Şafak ÇAKMAK, Hakan KAPUSUZ,

Emin Serkan EMİNOĞLU, Fatih ASLAN

İskenderun Demir ve Çelik A.Ş.
Türkiye

Non-Ferrous Metals Symposium Demir Dışı Metaller Sempozyumu

NFMS-2

The Effect of Coolants on The Surface Quality of Aluminium Pressure Die-Casting Alloys in Machning Process

Edin NURAY¹, Kaan GENÇER¹, Alptekin KISASÖZ², Çağlar YÜKSEL³

¹PTC Kimya, ²Kirklareli University, ³Ataturk University
Türkiye

NMFS-3

The Effect of Jet-Cooling Application on Microstructural Properties of The Overheating Areas in High Pressure Die Casting Parts

Kaan GENÇER¹, Yasin AYYILDIZ², Süleyman ŞENTÜRK³, Alptekin KISASÖZ⁴, Çağlar YÜKSEL⁵

¹PTC Chemical, ²Arslan Makina Döküm, ³PTC Technic,
⁴Kirklareli University, ⁵Ataturk University
Türkiye

NMFS-4

The Effect of Nitrogen Gas Purging on the Mechanical Properties of Vertical Semi-Continuous Casting

Mustafa YILDIZ¹, Çağlar YÜKSEL², Alptekin KISASÖZ³, Umut YILDIZ¹, Serdar Osman YILMAZ⁴

¹Kayalar Bakır Alaşımları, ²Atatürk University, ³Kirklareli University, ⁴Namık Kemal University
Türkiye

NFMS-6

Nickel Recovery from Olivine by Hydrometallurgical Method

Şeyma YÜKSEL SAĞMAN¹, Hande ARDIÇOĞLU¹, Hasan NİZAMOĞLU², Mehmet Deniz TURAN², Ali KESKİN¹, Erdoğan KARİP¹, Gökhan BAŞMAN¹

¹Eti Chrome, ²Firat University
Türkiye

NFMS-7

Investigation of Roasting Behavior and Mineralogical Transformation of Titanomagnetite Concentrate at Different Temperatures

**İsmail Emre YILDIZ¹, Zeynep Hazal YAZĞAN¹,
Mikail BAŞYİĞİT¹, Elif UZUN KART¹, Abdullah BUHUR²**
¹Marmara Üniversitesi, ²ARGETEST
Türkiye

NFMS-8

The Effect of The Scale Factor on AlCoCrFeNi based High-Entropy Alloys Produced via a Self-Propagating High-Temperature Synthesis Method

Murat ALKAN¹, Esra DOKUMACI ALKAN¹, Emre ÇİNKİLİÇ²
¹Dokuz Eylül University, ²Hakkari University
Türkiye

NFMS-9

Thermodynamic and Microstructural Investigations of AlCoCrFeNi(Ti)_x Based High-Entropy Alloys

**Esra DOKUMACI ALKAN, Murat ALKAN,
Oğuzhan DİRİCAN, Mehmet Nurullah KÖSE,
Abdulkafi KARTOPU**
Dokuz Eylül University
Türkiye

NFMS-10

Development of Oxide Dispersion Strengthened Inconel 718 Alloy by Calphad Method and Production of Designed Novel ODS Alloy by Laser Powder Bed Fusion

**M. Yeşim YALÇIN¹, A. Alkım GÖKBAYRAK¹,
C. Bora DERİN², Eda AYDOĞAN¹, Bahattin KOÇ³**
¹Middle East Technical University, ²Istanbul Technical University,
³Sabancı University
Türkiye

NFMS-12

Comparison of Microstructure and Mechanical Properties of CoCrFeNiMn High-Entropy Alloys by Uniaxially Pressing-Sintering and Vacuum Hot Pressing-Sintering Methods

Burak KÜÇÜKELYAS^{1,2}, Cantekin KAYKILARLI¹, İhsan ÇAHA³, Alexandra C. ALVES³, Fatih TOPTAN⁴, Sebahattin GÜRME², Deniz UZUNSOY¹

¹Bursa Technical University, ²Istanbul Technical University, ³University of Minho, ⁴Izmir Institute of Technology
Türkiye, Portugal

Corrosion and Wear Symposium

Korozyon ve Aşınma Sempozyumu

CWS-1

The Effect of Boron Addition on The Microstructure and Mechanical Properties of HCx Tool Steel

N. Şeyma NEVCANOĞLU, Akay NEVCANOĞLU, H. Özkan GÜLSOY

Marmara University
Türkiye

CWS-2

Corrosion Behaviour of Few-Layered-Graphene (FLG) Reinforced Al-4 Wt.%Cu Metal Matrix Composites Processed by Mechanical Alloying

Cantekin KAYKILARLI, Burak KÜÇÜKELYAS, Taha Yasin EKEN, Nazlı AKÇAMLI, Deniz UZUNSOY

Bursa Technical University
Türkiye

CWS-3

Change in Friction Coefficient of Cu15Ni8Sn Material in Dry and Oily Environment According to Casting Method

Talip ÇITRAK, Orçun ZİĞİNDERE, Edanur KASAP, Feriha BİROL, Ümit KAPLAN

Sağlam Metal
Türkiye

Ceramics, Glass, Refractory Materials Symposium Seramik, Cam, Refrakter Malzemeleri Sempozyumu

CGRS-1

Effect of h-BN Amount on Al₂O₃/Glass Composites for LTCC Applications

Oğuzhan BİLAÇ, Cihangir DURAN

Ankara Yıldırım Beyazıt University
Türkiye

CGRS-2

Methylene Blue Removal by Phase Separated Porous Glass

**Emre Burak ERTUŞ¹, Çekdar Vakıf AHMETOĞLU²,
Abdullah ÖZTÜRK³**

¹KTO Karatay University, ²İzmir Institute of Technology,
³Middle East Technical University
Türkiye

CGRS-3

Valuable Sources of Raw Material for Activated Carbon; Hazelnut Husk and Pumpkin Shell

Mürüvet Hazel UYSAL, Ali Osman KURT

Sakarya University
Türkiye

CGRS-4

The Effect of Sintering Parameters on the Properties of IR Transparent ZnS Produced by Spark Plasma Sintering

**Zeynep ÖZTÜRK, M. Kaan PEHLİVANOĞLU,
N. Kaan ÇALIŞKAN**

Tübitak SAGE
Türkiye

CGRS-5

Improvement of Oxidation Resistance of Carbon Fiber with BN-B₄C Coatings

**Cennet YILDIRIM^{1,2}, Muhammet Nasuh ARIK¹,
Nuri SOLAK²**

¹Boron Research Institute (TENMAK), ²Istanbul Technical University
Türkiye

CGRS-6

Synthesis of B₄C-Al₂O₃ Composite Powder via Aluminothermic Reduction

Emre TOY, Oğuz KARAAHMET, Buğra ÇİÇEK
Yıldız Technical University
Türkiye

Energy Materials Symposium

Enerji Malzemeleri Sempozyumu

EMS-1

The Effect of Impregnation Conditions on Active Metal Size and Distribution Profiles of Ni/Al₂O₃ Supported Catalyst

Emine ERSEZER¹, Cem AÇIKSARI², Elif ERDİNÇ², Serdar ÇELEBİ², Servet TURAN¹, Umut SAVACI¹
¹Eskisehir Technical University, ²TUPRAS R&D Center
Türkiye

EMS-2

Temperature-Dependent Galvanostatic EIS of Spiral and Bobbin Li/SOCl₂ Batteries

Gökberk KATIRCI, Fazlı Eren CİVAN, Burak ÜLGÜT
Bilkent University
Türkiye

EMS-3

An Innovative Approach for Electrolyte Recycling from Lithium-Ion Batteries

Nils ZACHMANN, Burçak EBİN
Chalmers University of Technology
Sweden

Failure Analysis and Heat Treatment Symposium

Hasar Analizi ve Isıl İşlem Sempozyumu

FAHTS-1

Investigation of Forging Process Failures and Solutions in the Production of Steering and Suspension System Parts

Sefer KOÇAK
Ditaş Doğan Yedek Parça
Türkiye

FAHTS-2**Investigation of The AA6005-A Alloy's Corrosion Behavior in Different Aging Conditions****Murat DOĞAN^{1,2}, İbrahim TÜTÜK¹, Kubilay ÖZTÜRK¹, Serhat ACAR¹, Kerem Altuğ GÜLER¹**¹Yıldız Technical University, ²Sistem Teknik
Türkiye**FAHTS-3****Failure Analysis of a Broken Reducer Shaft****M. Eriş DURMUŞOĞLU, Ali KOCA**İskenderun Demir ve Çelik A.Ş.
Türkiye**FAHTS-4****Failure Analysis of a Broken Descaler Pump Shaft at The Hot Strip Mill Facilities****Mehmet Eriş DURMUŞOĞLU, Ali KOCA**İskenderun Demir ve Çelik A.Ş.
Türkiye**FAHTS-5****Investigation of The Austempering Duration at 400°C on Silicon Solution Strengthened Ductile Iron****Soner Özden ERTÜRK¹, Levent Cenk KUMRUOĞLU², Ahmet ÖZEL³**¹HEMA Otomotiv Sistemleri, ²İskenderun Teknik Üniversitesi, ³Sakarya Üniversitesi
Türkiye**Composite and Polymer Materials Symposium**
Kompozit ve Polimer Malzemeler Sempozyumu**CPS-1****A Study on the Material Properties of Carbon Nanotubes Doped Glass Fiber Reinforced Nano Composites****Bahadır TÜRKYAMAN¹, Mehmet Fatih ÖKTEM²**¹Tübitak SAGE, ²Ankara Yıldırım Beyazıt University
Türkiye

CPS-4

**Investigation of The Mechanical Properties o
Thermoplastic Based Sandwich Structures Produced
by Fused Deposition Modeling (FDM) Technique**

Hurşit Sefa AYDIN, Cihan KABOĞLU, Deniz UZUNSOY
Bursa Technical University
Türkiye

CPS-5

**Mechanical Characterization of Graphene
Nanoplatelets/Al₂O₃ Reinforced Epoxy Hybrid
Composites**

**Cantekin KAYKILARLI^{1,2}, Aygül YEPREM²,
Deniz UZUNSOY¹**
¹Bursa Technical University, ²Yıldız Technical University
Türkiye

Biomaterials Symposium

Biyomalzemeler Sempozyumu

BMS-1

**Production and Characterization of Ti-6Al-4V
Slurry for Trabecular Dental Implants Produced by
Replica Impregnation Method**

**Aynur İNAN ÜSTÜN, Gülsüm TOPATEŞ,
Yasin Sinan ERTEM, Hasan OKUYUCU**
Ankara Yıldırım Beyazıt University
Türkiye

BMS-2

**Surface Investigation of Antibacterial Copper-
Incorporated Bioactive Surfaces Fabricated on
Commercially Pure Titanium**

**Salim Levent AKTUĞ¹, Kemal KORKMAZ¹,
Sıtkı AKTAŞ², Salih DURDU²**
¹Gebze Technical University, ²Giresun University
Türkiye

BMS-3

**Antimicrobial Properties of Electrospun Nano-
Sized Ag and TiO₂ Blended PVA Nanofibers**

**Merve OCAKTAN¹, Fatih ÇİFTÇİ²,
Nilüfer EVCİMEN DUYGULU¹**
¹Yıldız Technical University, ²Fatih Sultan Mehmet Vakif University
Türkiye

BMS-4

A Green Manufacturing Method in Skin Tissue Engineering

**Merve SIRTIKARA, Emir ERİŞÇİ,
Sevda Nur TEBERDAR, Mustafa ŞENGÖR**
Marmara University
Türkiye

Nanomaterials Symposium
Nanomalzemeler Sempozyumu

NMS-1

Comparative Study of Microstructural Changes and Hardness of Nanostructured FeCoCrNi High Entropy Alloys After Different Consolidation Routes

Mustafa TEKİN¹, Ali Rıza BALOĞLU², Hasan KOTAN²
¹KTO Karatay University, ²Necmettin Erbakan University
Türkiye

NMS-2

Development of Graphene/Silicon Composite Based Lithium Ion Battery Anode

Tarık Can TÜRKOĞLU, Eren ATLI, Ömer Refet ÇAYLAN, Göknur CAMBAZ BÜKE
TOBB University of Economics and Technology
Türkiye

NMS-4

Photoluminescence Property of NaYF₄: Yb/ Er/ Pr Upconversion Nanoparticles in the Near Infrared Region

Mahla SHAHSAVAR, Ayşe DULDA
Yeditepe University
Türkiye

NMS-5

The Synthesis & Characterization of Carbon Nanotubes on SiC via Vacuum Decomposition

**Erhan GÜRPINAR, Ömer Refet ÇAYLAN,
Derya KARADENİZ, Erkin Köseoğlu,
Göknur CAMBAZ BÜKE**
TOBB University of Economics and Technology
Türkiye

Casting Symposium Döküm Sempozyumu

CSS-1

Optimization of The Heat Treatment Parameters Depending on The Thickness in Plate Products Made of EN AW 1050 Al Alloy

**Sena ERDOĞAN^{1,2}, Selçuk ERKUL, 'Zekeriya MUTLU¹,
Rabia Şevval AKAN^{2,3}, Ayberk UZER^{2,3},
Muhammet ULUDAĞ^{2,3}**

¹PMS Metal Profile Aluminum, ²Bursa Technical University,
³ULUCON R&D and Consulting
Türkiye

CSS-2

Understanding The Solidification Dynamics of Commercial Aluminium Alloys Produced by Twin-Roll Casting

**Arash KAZAZI¹, Onur MEYDANOĞLU²,
Cemil IŞIKSAÇAN², Hatice MOLLAOĞLU ALTUNER²,
Melis ŞEREFİOĞLU³**

¹Koç University, ²Assan Alüminyum, ³Marmara University
Türkiye

CSS-3

Effect of Chromium on Wear Resistance of Carbide Austempered Ductile Iron (CADI)

Barbaros SENSES¹, Ummihan T. YILMAZ², Ayse ERKAN¹, Gökhan SAĞLAM¹

¹Döksan Heat Treatment and R&D Center A.S.,
²Kırıkkale University
Türkiye



PROCEEDINGS

BİLDİRİLER



CONTENTS / İÇİNDEKİLER

Investigating The Effect of Mechanical Pretreatment on The Recovery Rate of Critical Raw Materials from Discarded Hard Disc Drives	111
Alireza HABIBZADEH, Mehmet Ali KUÇUKER, Mertol GÖKELMA Izmir Institute of Technology Türkiye	
Iron Removal from NdFeB Waste Magnet Solutions Using Sodium Alginate Solution	112
Emircan UYSAL ¹ , Elif EMİL KAYA ^{1,2,3} , Serhat AL ¹ , Sebahattin GÜRME ¹ ¹ Istanbul Technical University, ² RWTH Aachen University, ³ Turkish-German University Türkiye, Germany	
Investigation of Dissolution Parameters of Rare Earth Elements in Fluorescent Wastes by Microwave Leaching	114
Ayşegül BİLEN, Utku HATIPOĞLU, Muhlis Nezih SARIDEDE Yıldız Technical University Türkiye	
Characterization and Extraction of Heavy Metals from Municipal Solid Waste Incineration Fly Ash	118
Jonas SCHUSTER ^{1,2} , Burçak EBİN ¹ ¹ Chalmers University of Technology, ² Hamburg University of Technology Sweden, Germany	
Production of Metal Sulfides from Ferrochrome Flue Dusts and Investigation of Their Electrochemical Properties	119
Ozan AYDIN, Metin GENÇTEN, Burak BİROL Yıldız Technical University Türkiye	
Li-Ion Battery Recycling for Industrial Scale	120
Safiye TANRIVERDİ ^{1,2} , Berk GÜLÖRTEN ² , Mahmut KARADAŞ ² ¹ Istanbul University - Cerrahpasa, ² Proses Makine Türkiye	
Recovery of End-Of-Life Lithium-Ion Battery Cathode Materials in Acidic Media	121
Elif GÜLOĞLU ¹ , Mert ZORAĞA ¹ , Gökçe HAPÇI AĞAOĞLU ¹ , Ş. Samet KAPLAN ² , M. Şeref SÖNMEZ ² , Sebahattin GÜRME ² , Gökhan ORHAN ¹ ¹ Istanbul University-Cerrahpasa, ² Istanbul Technical University Türkiye	
Is Sustainability a Paradigm for Occupational Health and Safety?	122
Murat Can OCAKTAN UCTEA Chamber of Metallurgical and Materials Engineers Türkiye	
Remelting Behaviour of Pure And Az63 Magnesium Chips	125
Pınar YÖRÜK ¹ , Bora DERİN ² , Mertol GÖKELMA ¹ ¹ Izmir Institute of Technology, ² Istanbul Technical University Türkiye	
Scrap-Salt Flux Interactions During Recycling Processes	127
İrem Yaren ÇAPKIN ¹ , Adamantia LAZOU ² , Gabriella TRANELL ² , Mertol GÖKELMA ¹ ¹ Izmir Institute of Technology, ² Norwegian University of Science and Technology Türkiye, Norway	
Tin Recovery from Electrolytic Tinning Line (ETL) Scraps	129
Gizem KAVUK ¹ , Anıl AĞADANGİL ¹ , Miyase Özlem KÖYBAŞI ÖZUÇAK ¹ , S. Samet KAPLAN ¹ , M. Şeref SÖNMEZ ² ¹ TOSÇELİK, ² Istanbul Technical University Türkiye	
Investigation of Dissolution Conditions of Yttrium (Y) and Europium (Eu) in Fluorescent Wastes	130
Utku HATIPOĞLU, Ayşegül BİLEN, Muhlis Nezih SARIDEDE Yıldız Technical University Türkiye	
The Recycling Model of Zirconia & Alumina Waste in Iron - Steel Plants	135
Oğuzhan SAKARYA, Uğur CENGİZ Bilecik Demir Çelik A.Ş. Türkiye	
An Investigation on Calcium Aluminate Cement Production Using Two Types of Bauxite, Alumina and Marble Waste	137
C. Betül EMRULLAHOĞLU ABI, Esra ÖZGÜVEN, Serkan KESKİN Afyon Kocatepe University Türkiye	
Aluminium Black Dross Utilization via Pyrometallurgical and Hydrometallurgical Operations	141
Umay ÇINARLI, Ahmet TURAN Yeditepe University Türkiye	
Recycling of Aluminium Used Beverage Cans: Decoating and Self-Heat Generation	142
Musa ORUÇ ¹ , Emine Bengü KAYA ¹ , Umay ÇINARLI ² , Tuğçe ERGÜL ² , Ahmet TURAN ² , Onuralp YÜCEL ³ , Erman CAR ⁴ ¹ Yalova University, ² Yeditepe University, ³ Istanbul Technical University, ⁴ Insertec Thermal Solutions Türkiye, Spain	
Circular Economy Approach for Evaluation of Mill Scale Using Al Residue as Reductant	143
Selçuk KAN, Kağan BENZEŞİK, Onuralp YÜCEL Istanbul Technical University Türkiye	



Lean Sustainable Green Supply Chain Management In Light Metals Casting Industry Ümmet AYYILDIZ ^{1,2} ¹ Prometal, ² Bilecik Şeyh Edebali Üniversitesi Türkiye	144
Dynamic Recrystallization in Directional Solidified Cm247 Lc Alloys Müge AKDEMİR ¹ , Belgin ATAMAN ¹ , Aylin ŞAHİN KAHRAMAN ² , Havva KAZDAL ZEYİN ² , Hüseyin AYDIN ² ¹ Istanbul Technical University, ² TUBITAK Marmara Research Center Türkiye	148
Cold Spray Effect on Oxide Dispersion Strengthening of Inconel 718 Bayram Berk TANRISEVDİ, Eda AYDOĞAN Middle East Technical University Türkiye	152
Flowforming and Heat Treatment Effect of IN718 Alloy Aptullah KARAKAŞ Repkon Machine and Tool Industry Türkiye	153
A Numerical Analysis of the Effect of Electro-Beam-Melt Ti6Al4V Cover Plate on the Ballistic Performance of SiC Armor F. Murat YILDIZTEKİN ¹ , Mustafa GÜDEN ¹ , Alper TAŞDEMİRÇİ ¹ , A. Kaan TOKSOY ² , Gülden ÇİMEN ¹ , S. Burçin ÇELLEK ¹ ¹ Izmir Institute of Technology, ² Roketsan Missiles Industries Türkiye	157
Effect of Solution Heat Treatment on the Anisotropy of Microstructure, Texture and Mechanical Properties of Hastelloy X Fabricated by Laser Powder Bed Fusion Seren ÖZER ^{1,2} , M. Alp YALÇIN ¹ , Güney Mert BİLGİN ² , Kemal DAVUT ³ , Ziya ESEN ⁴ , Arcan F. DERİCİOĞLU ² ¹ Atılım University, ² Middle East Technical University, ³ Izmir Institute of Technology, ⁴ Çankaya University Türkiye	158
Effects of Heat Treatment and Hot Isostatic Pressing on High Temperature Mechanical Properties of Ti-48Al-2Cr-2Nb Alloy Produced by Electron Beam Melting Güney Mert BİLGİN ^{1,2} , Seren ÖZER ^{2,3} , Ziya ESEN ⁴ , Arcan F. DERİCİOĞLU ² ¹ TUSAS Engine Industries, ² Middle East Technical University, ³ Atılım University, ⁴ Çankaya University Türkiye	159
The Effect of Powder Bed Fusion and Direct Deposition Methods on Metallic Materials Murat İSİK Uludağ University TürkiyeTürkiye	160
Evaluation of Proficiency Test Results in Fatigue Test in Aerospace Metallic Materials Bülent AYDEMİR ¹ , Hüseyin AYDIN ² , Fatih GÜLER ² , Aygün GÜNGÖR ² , İbrahim KÜÇÜKOĞUL ² , Havva KAZDAL ZEYİN ² ¹ Tubitak UME, ² Tubitak MAM Türkiye	161
Mechanical Behavior of Repaired Carbon Fiber Reinforced Polymer Composite Laminates Evren SONAT ^{1,2} , Mete BAKIR ^{2,3} , Sezer ÖZERİNÇ ¹ ¹ Middle East Technical University, ² Turkish Aerospace Industries, ³ Yıldırım Beyazıt University Türkiye	164
Microstructural Evolution of CMSX-4 SLS Single Crystal Superalloys during Creep Rupture Tests Aylin ŞAHİN KAHRAMAN ¹ , Burak HORASAN ² , Havva KAZDAL ZEYİN ¹ , Hüseyin AYDIN ¹ , Cevat Fahir ARISOY ³ ¹ Tubitak MAM, ² Sakarya University, ³ Istanbul Technical University Türkiye	165
Evaluation of Proficiency Test Results in High-Temperature Tensile Test in Aerospace Metallic Materials Bülent AYDEMİR ¹ , Hüseyin AYDIN ² , Fatih GÜLER ² , Aygün GÜNGÖR ² , İbrahim KÜÇÜKOĞUL ² , Havva KAZDAL ZEYİN ² ¹ Tubitak UME, ² Tubitak MAM Türkiye	169
The Effect of The Johnson Cook Damage Parameters on The Crushing Modes of an Electro-Beam Melt Additive Processed Ti6Al4V Body-Centered-Cubic Lattice Structures H. İrem ERTEN, Burak HIZLI, M. Arslan Bin RIAZ, Samed ENSER, Mustafa GÜDEN Izmir Institute of Technology Türkiye	172
Influence of Platform Dimensions on The Secondary Grain Formation in Production of Single Crystal Turbine Blade İbrahim BERBER, Sertaç ALPTEKİN, Lütfi YAKUT, Bülent BAHADIR, Havva KAZDAL ZEYİN Tubitak MAM Türkiye	176
Microstructural Characterization of Forged Inconel 718 Superalloy After Long Term High Temperature Exposure Burak HORASAN ¹ , İbrahim BERBER ¹ , Fatih GÜLER ² , Havva KAZDAL ZEYİN ² , Hüseyin AYDIN ² ¹ Sakarya University, ² TUBITAK Marmara Research Center Türkiye	177
ZnO Nanowire Growth via Anodization Yiğithan TUFAN, İpek Tuğçe DÖŞ, Batur ERCAN Middle East Technical University Türkiye	179
Production and Characterization of Gold Nanofilms on Transparent Substances by Electrodeposition Method Uğur BARUT, Metehan ERDOĞAN Ankara Yıldırım Beyazıt Üniversitesi Türkiye	180



Effect of Substrate Bias on Mechanical Properties of Magnetron Sputtered AlTiN-B₄C Films	181
Ozden KISACIK ^{1,2} , Cennet YILDIRIM ^{1,3} , Erkan KAÇAR ^{1,4} , Servet TURAN ² , Sedat SÜRDEM ⁵ ¹ Boron Research Institute, ² Eskisehir Technical University, ³ Istanbul Technical University, ⁴ Hakkari University, ⁵ Gazi University Türkiye	
Effect of Micro Arc Oxidation and Precipitation Hardening on The Corrosion Resistance of 7075 Al Alloy Fabricated by Flow Forming	185
Belgin ATAMAN ¹ , Serra BAYRAM ¹ , Mertcan KABA ¹ , Aptullah KARAKAŞ ^{1,2} , Murat BAYDOĞAN ¹ , Hüseyin ÇİMENOĞLU ¹ ¹ Istanbul Technical University, ² Repkon Makina ve Kalıp Türkiye	
Effect of Aluminizing on the High Temperature Oxidation Behavior of Inconel 718 Superalloy	189
Y. Burak TELBAKİROĞLU, Erkan KONCA Atılım University Türkiye	
Improving Fracture Toughness of AlTiN Hard Coatings by W Additions	194
Burçin KAYGUSUZ ¹ , Amir MOTALLEBZADEH ² , Özcan Doğu KARADAYI ³ , Muhammed Kürşat KAZMANLI ⁴ , Sezer ÖZERİNÇ ¹ ¹ Middle East Technical University, ² Koç University, ³ Ionbond Turkey Yüzey Teknolojileri, ⁴ Istanbul Technical University Türkiye	
Performance and Wear of Vacuum Brazed Diamond Cutting Tools With Reinforced Electrolysis Coating	195
Berrak BULUT ¹ , Yunus Emre ERBAY ² , Isil KERTİ ² , Murat BAYDOĞAN ¹ ¹ Istanbul Technical University, ² Yıldız Technical University Türkiye	
For More Sustainable Cold Forging Process: Use of Sand Blasting Instead of Pickling and Rinsing	199
Baybars SARICA, M. Burak TOPARLI, Doğuş ZEREN, Umut İNCE Norm Cıvata Türkiye	
Investigation of Mechanical and Corrosion Properties of Electroless Ni-W-Co-SiC Multicomponent Coatings	200
Ismail Deniz Kağan DEMİR ¹ , Göksel HIZLI ² , Selim ERTÜRK ² , Kürşat KAZMANLI ² ¹ TR Mekatronik Sistemler, ² Istanbul Technical University Türkiye	
Sol-Gel Spray Coating of Aluminium Alloys for The Automotive Applications	202
Çisem ÇELİK KURTULAN ^{1,2} , Ş. Samet KAPLAN ¹ , M. Şeref SÖNMEZ ¹ ¹ Istanbul Technical University, ² Turkish Energy, Nuclear and Mineral Research Agency (TENMAK) Türkiye	
Wear and Corrosion Performance Evaluation of Laser Claded Brake Disc	203
Ekrem ALTUNCU ¹ , Recep AKYÜZ ² , Çiğdem DINDAR ² , Cem ÖZTÜRK ² ¹ Sakarya University of Applied Sciences, ² Tofas Automotive Türkiye	
A Comparative Study On Corrosion Properties of Decorative Chromium and PVD Evaporated Aluminium Coated ABS Parts	207
Aleyna BAYATLI ¹ , Arif AKILLILAR ² , Mustafa KOCABAŞ ¹ ¹ Konya Technical University, ² Tosunogulları Mobilya Türkiye	
Simulation and Fabrication of Thin Film Notch Filter	212
Eray HUMALI ^{1,2} , M. Kürşat KAZMANLI ¹ ¹ Istanbul Technical University, ² Roketsan Missiles Inc. Türkiye	
Cone Shaped Parts Manufacturing by Electroforming Process	216
Tutku TURGUTLUGİL GÖKÇE, N. Kaan ÇALIŞKAN, M. Kaan PEHLIVANOĞLU Tübitak SAGE Türkiye	
Tribological Performance of Electrochemically Borided AISI H13 Hot Work Die Steel	220
Ümmet AYYILDIZ ^{1,2} , Harun MİNDİVAN ² ¹ Prometal R&D Center, ² Bilecik Şeyh Edebali University Türkiye	
Optimization of Electroless Silver Coating on Calcium Based Ceramics	224
Kardelen GÜNDOĞDU, Metehan ERDOĞAN Ankara Yıldırım Beyazıt University Türkiye	
Investigation of Formation of Au-Ag-Cu Alloys by Electrodeposition from Cyanide Based Electrolyte	225
Berkay ÇAĞAN ¹ , Metehan ERDOĞAN ¹ , İshak KARAKAYA ² ¹ Yıldırım Beyazıt University, ² Middle East Technical University Türkiye	
Evaluation of Chromite Ores by Metallothermic Process in EAF	230
Hasan GÜNEY, Selçuk KAN, Kağan BENZEŞİK, Onuralp YÜCEL Istanbul Technical University Türkiye	
Determining Optimum Roasting Conditions of Hematite Magnetization with Temperature-Coke Mixture Copula	231
Zeynep Hazal YAZĞAN ¹ , Mikail BAŞYİĞİT ¹ , Abdullah BUHUR ² , Elif UZUN KART ¹ ¹ Marmara University, ² ARGETEST Türkiye	



Effect of Ladle Furnace Slag On Steel Cleanliness of Tirecord Steel in Isdemir Plant	235
Ilker AYÇIÇEK ¹ , Nuri SOLAK ² , Memduh Kağan KELER ³ ¹ İskenderun Demir ve Çelik A.Ş., ² İstanbul Teknik Üniversitesi, ³ Ereğli Demir ve Çelik A.Ş. Türkiye	
Synthesis of Nanocrystalline Stainless Steels by Mechanical Alloying: Grain Growth, Phase Transformation, Thermal Stability and Mechanical Properties	238
Hasan KOTAN Necmettin Erbakan University Türkiye	
Design and Investigation of The Mechanical Properties of Light Alloys For Electric Vehicles	242
Ayşen Ceren DERELİ ^{1,2} , Ahmet Salih YILMAZ ² , Ufuk BALIKÇI ² , Onuralp YÜCEL ¹ ¹ İstanbul Technical University, ² Anadolu Isuzu Otomotiv Türkiye	
Coil Slumping in Peritectic Steels	243
Koray ARAY ¹ , Ahmet SAĞLAM ¹ , Metin KATRANCI ¹ , Hasan YILDIRIM ¹ , Burcu SOYSAL ATAN ¹ , Fatih ÇELİK ¹ , Abdurrahman Mesud ÇAKIR ¹ , Erhan SAKALLI ² ¹ İskenderun Demir ve Çelik A.Ş., ² Ereğli Demir ve Çelik A.Ş. Türkiye	
Reducing Quality Cost by Reducing Transverse Surface Crack Defect in Slab Grades	246
Kübra AKGÜN, İlker AYÇIÇEK, Hakan KAPUSUZ, Burcu Soysal ATAN, Murat SARIOĞLU İskenderun Demir ve Çelik A.Ş. Türkiye	
Investigation of Microstructural Properties of Fish Scale Resistant Low Carbon Enamel Steel Grades	249
Ramazan UZUN, Mehmet Bulut ÖZYİĞİT, Yasemin KILIÇ, Oğuz GÜNDÜZ Ereğli Iron and Steel Türkiye	
The Role of Thermomechanical Rolling in Petroleum Pipe Steels and Its Effects on Mechanical Properties	250
Serdar GÜNBAY, Cemre KEÇECİ, Koray ARAY İskenderun Demir ve Çelik A.Ş. Türkiye	
Effect of Isothermal Transformation on Microstructural and Mechanical Properties of a Low Carbon Microalloyed Bainitic Forging Steel	254
M. Mustafa BALÇILAR, Bilgehan ÖGEL Middle East Technical University Türkiye	
Experimental Investigation and Theoretical Expression of The Effect of Steel Wire Rope Parameters on Breaking Load	259
Emre BAŞER ^{1,2} , Yıldız ŞAHİN ² , Murat POLAT ¹ ¹ Çelik Halat ve Tel Sanayii A.Ş., ² Kocaeli University Türkiye	
Thermodynamic Investigation of Kappa-Carbide Phase Change in Low-Density Steels	263
Memduh Kağan KELER ^{1,2} , Sibel DAĞLILAR ¹ , Oğuz GÜNDÜZ ² , Özcan BAHAROĞLU ² , Onur KART ² ¹ Yıldız Technical University, ² Ereğli Iron and Steel Türkiye	
The Modeling of Mechanical Properties of Low-Carbon Grade (SAE J403:2014 1006, SAE J403:2014 1008, SAE J403:2014 1010) Wire Rod Steels	267
Ahmet SAĞLAM, Burcu SOYSAL ATAN, İlker AYÇIÇEK, Hamdi GÜL, Mustafa TÜRKMANI, Mehmet Eriş DURUMUŞOĞLU, Abdurrahman Mesud ÇAKIR İskenderun Demir ve Çelik A.Ş. Türkiye	
Modelling of Monoblock Loads by Quality Based Process Parameters to Ensure Optimum Production Speed at Wire Rod Mill	271
Hamdi GÜL ¹ , Hasan Ozan TEMİZ ¹ , Mustafa Özden ÖZDEMİR ¹ , Tayfun KOCABAŞ ² , Abdurrahman Mesud ÇAKIR ¹ , Fatih ÇELİK ¹ , Burcu SOYSAL ATAN ¹ ¹ İskenderun Demir ve Çelik A.Ş., ² Oyak Maden Metalurji Türkiye	
Reduction of Emissions While Removing Dust From Isdemir New Blast Furnace Dust Catcher	274
Onur Hüseyin MEMİŞ, Ümit GEBENLİ, İbrahim ÇAKMAK, Mustafa BAŞŞU İskenderun Demir ve Çelik A.Ş. Türkiye	
Understanding Carbon Dioxide Emissions in Electric Arc Furnace Operations	277
Mehmet Fatih GÖKÇE ¹ , Bora DERİN ² ¹ Diler Demir Çelik, ² İstanbul Technical University Türkiye	
Emissions Occuring in The Coking Process in Steel Manufacturing and Methods of Struggle Against Emissions	278
Hüseyin KALAY, Zekeriya ÖZER, Kenan AKDEMİR İskenderun Demir ve Çelik A.Ş. Türkiye	
Decarbonization and Green Steel Production in Iron and Steel Industry	282
Aziz KILIÇ BCS Enerji Mühendislik Türkiye	
The Use of Boron Element for Cost Reduction in Teeth Made of Low Alloy Steel Used in Excavators	284
Muhammed KIRICI ^{1,2} ¹ Motus Automotive, ² Konya Technical University Türkiye	



Modelling and Simulation Studies for Optimization of Laboratory Scaled Steel Casting Mold Designs	285
İ. İrfan AYHAN ¹ , Caner GÜNEY ¹ , Emre ALAN ¹ , N. Başak DÜRGER ¹ , M. Fatih KAYADEĞİRMENİ ¹ , Muhammet ULUDAG ² , Nursina ŞENSOY ² , Beyza GÜNAYDIN ² , Gülşah KURT ² ¹ ÇEMTAŞ Çelik, ² Bursa Technical University Türkiye	
Development of New Steel Grade with Improved Hardenability for Renewable Energy Industry	289
İ. İrfan AYHAN ¹ , Caner GÜNEY ¹ , Emre ALAN ¹ , N. Başak DÜRGER ¹ , M. Fatih KAYADEĞİRMENİ ¹ , Nazlı AKÇAMLI ² ¹ ÇEMTAŞ Çelik, ² Bursa Technical University Türkiye	
Use Of Green Hydrogen in Iron and Steel Industry	290
Caner TUNA ¹ , Celal Erkal KAHRAMAN ¹ , Hakan ERÇAY ¹ , Tuncay DİKİCİ ² ¹ Özkan Demir Çelik, ² Dokuz Eylül Üniversitesi Türkiye	
Sinter Plant Ignition Furnace Burning Optimization	291
Erol AKKÜLAH, Cenk KAYA, Seyithan ÇEVİK, Mehmet AYGÜN, Bengü TAŞDELEN Ereğli Demir ve Çelik Türkiye	
Efficiency Improvement via Optimizing Secondary Cooling in a Heavy-Duty Gas Turbine	294
Mehmet YILDIZ, Mustafa Mert ÇAKA, Cenk BAYENDER, Tansu KUKUL, Özgür AKGÜN Ereğli Iron and Steel Türkiye	
Increasing Hot Rolled Mill Production by Increasing Coil Weights Under 1,80 mm Thickness	298
Muhammet BİLEN ¹ , Koray ARAY ¹ , Serdar GÜNBAY ¹ , Erhan SELVİ ¹ , Hasan YILDIRIM ¹ , Burak Emre IŞIK ¹ , İskender GÖK ¹ , Ahmet Mithat AVŞAR ¹ , Tayfun KOCABAŞ ² , Abdurrahman Mesud ÇAKIR ¹ , Burcu SOYSAL ATAN ¹ ¹ İskenderun Demir ve Çelik A.Ş., ² Oyak Maden Metalurji Türkiye	
The Evaluation Potential of Basic Oxygen Furnace (BOF) Slag and The Recycling of Calcium Carbonate by Hydrometallurgical Methods	301
Muhammet BİLEN İskenderun Demir ve Çelik A.Ş. Türkiye	
Estimating Tap Hole Clay Consumption in Blast Furnace by Fuzzy Logic Method	305
Mehmet GÖKOĞLU, Ramazan YARAŞIR İskenderun Demir ve Çelik A.Ş. Türkiye	
Comparison of Manganese Oxide (MnO) and Iron Oxide (FeO) Analyzes in Steel Production Slag with Different Analysis Methods	309
Barış SAĞLAR ¹ , Aydan GÜLSÜREN ¹ , Onur OREL ¹ , Ramazan BİLGİN ² , Memduh Kağan KELER ³ ¹ İskenderun Demir ve Çelik A.Ş., ² Çukurova Universtiy, ³ Ereğli Demir ve Çelik Türkiye	
Water Management in Iron and Steel Industry	312
Mehmet Burak ATAN, Erkin Y. GEDİK, Onur MARTI, GÖkhan GÜNGÖR, Arif AKSOY, İbrahim SARI İskenderun Demir ve Çelik A.Ş. Türkiye	
The Effect of Maintenance Activities on Environmental Management in Iron and Steel Facilities	315
Hasan BULUT, Ayşe ÇELİK, Merih YAMAN, GÖkçe ARSLAN İskenderun Demir ve Çelik A.Ş. Türkiye	
Management of Ferroalloys Stocks in Iron and Steel Production	318
Erman KAYA, Beril BİRİNCİ, Ece DAL YALÇIN İskenderun Demir ve Çelik A.Ş. Türkiye	
Investigation of Castability of DIN EN 10089 38S17 Steel Grade in Billet Casting Machine	322
İlker AYÇIÇEK ¹ , Kübra AKGÜN ¹ , Memduh Kağan KELER ² ¹ İskenderun Demir ve Çelik A.Ş., ² Ereğli Demir ve Çelik Türkiye	
Pressure Vessel Detection System with Image Processing Techniques	325
Zekeriya SARIKOL, Semiramis GÜLKESEN İskenderun Demir ve Çelik A.Ş. Türkiye	
Modernization and Replacement of Isdemir 4th Blast Furnace Clay Gun and Drill Equipment	330
Recep GÜNEŞOĞLU, Osman FIDAN, Okkeş CİĞERLİ, Ali Hikmet CAN, Hasan IŞLER, Evren ŞAHİN İskenderun Demir ve Çelik A.Ş. Türkiye	
Improvement of The Siphon Opening Process in The Isdemir New Blast Furnace No.1	339
Mustafa BAŞSU, Onur Hüseyin MEMİŞ, Umit GEBENLİ, İbrahim ÇAKMAK İskenderun Demir ve Çelik A.Ş. Türkiye	
Distribution of Coil and Wire Rod Products Manufactured at Isdemir According to Areas of Usage, Standards and Customer Expectations	342
Muhammet BİLEN, Nalan Gül UÇUR İskenderun Demir ve Çelik A.Ş. Türkiye	



Establishing a Billet Quality Recommendation System (Digitalization)	347
Gökhan BİLMEZ, Erhan KORKMAZ, Erman KAYA İskenderun Demir ve Çelik A.Ş. Türkiye	
Minimizing The Consumption of Temperature Probe by Prediction of Liquid Steel Temperature During Ladle Furnace Process	349
Mustafa SAĞLAM ¹ , Esra KÜPELİ ¹ , Abdurrahman Mesud ÇAKIR ² , Burcu SOYSAL ATAN ¹ , Alper KURTOĞLU ¹ , Alperen TERZİ ¹ , Eyüp Veysel ÖZDEMİR ¹ , Hikmet ŞAHİN ¹ , Mehmet Mustafa YILDIRIM ¹ , Bekir Burak YAMANOĞLU ¹ , Tayfun KOCABAŞ ² ¹ İskenderun Demir ve Çelik A.Ş., ² Oyak Maden Metalurji Türkiye	
Coil Movement Optimization	352
Metin KATRANCI, Hasan YILDIRIM, Mahmut KAYHAN, Uğur OKTAY, Koray ARAY, Abdurrahman Mesud ÇAKIR, Burcu SOYSAL, Fatih ÇELİK İskenderun Demir ve Çelik A.Ş. Türkiye	
Improvement of Scale Print Defect in Cut-To-Length Plants for S600 MC Steel Grade	355
Serdar GÜNBAŞ, Koray ARAY, Erhan SELVİ, Ahmet SAĞLAM İskenderun Demir ve Çelik A.Ş. Türkiye	
Sinter Plant Circular Cooler Medium Voltage Fan Motor Conversion from DOL System To VFD System	360
Cengiz ABUKAN, Fatih DÜZLÜ, Volkan KIZILAY İskenderun Demir ve Çelik A.Ş. Türkiye	
Effect of Dunit and Dolomite Auxiliary Raw Materials on SiO₂ Output in Product Sinter and Cost Advantage in The Sinter Process	364
Orkun HASDEMİR, Sadi BALABAN, Berkay DELAY, Burhan Erkan KESEMEN, Volkan KIZILAY İskenderun Demir ve Çelik A.Ş. Türkiye	
Mapping Slab Defects, Conceptualizing Digital Twins	367
Fatih Mehmet AYDIN, Serdar GÜNBAŞ, Hikmet ŞAHİN, Serkan DURSUN, İlker AYÇİÇEK İskenderun Demir ve Çelik A.Ş. Türkiye	
Advantage at Ladle Furnace Processing Time by Developing a Model That Calculates Liquid Steel %Al Value Closer to The Spectral Sample Result	371
Mustafa SAĞLAM ¹ , Memduh Kağan KELER ² , Esra KÜPELİ ¹ , Eyüp Veysel ÖZDEMİR ¹ , Alperen TERZİ ¹ , Hikmet ŞAHİN ¹ , Mehmet Mustafa YILDIRIM ¹ , Tayfun KOCABAŞ ³ , Abdurrahman Mesud ÇAKIR ¹ , Burcu SOYSAL ATAN ¹ , Deniz YAZICI ¹ ¹ İskenderun Demir ve Çelik A.Ş., ² Ereğli Demir ve Çelik, ³ Oyak Maden Metalurji Türkiye	
Wire Rod Surface Examination by Non-Destructive Liquid Penetrant Testing Method	375
Cemre KEÇECİ, Erdem TAN, Mustafa ÖZDEMİR İskenderun Iron and Steel Co. Türkiye	
The Effect of Debinding Parameters on Additive Manufactured 316L Stainless Steel Parts with Cold Metal Fusion Technology	379
Burcu Aslı ÖZKAN ¹ , Burak KÜÇÜKELYAS ¹ , Erkan ATEŞ ² , Cihan KABOĞLU ¹ , Deniz UZUNSOY ¹ ¹ Bursa Technical University, ² 3D Design Technologies Türkiye	
Effect of Continuous Cooling on Microstructural and Mechanical Properties of a Low Carbon Microalloyed Mn-Si Bainitic Steel	380
Esra KADERLİ, Bilgehan ÖGEL Middle East Technical University Türkiye	
The Effect of Chemical Composition and Ratio of Deformation on Mechanical Properties in High Carbon Steel Wire Production	384
Sevim Gökçe ESEN, Muhammet Fatih DUMAN Çelik Halat ve Tel Sanayii A.Ş. Türkiye	
Experimental Investigation of Mechanical Performance Tests of Impregnated Plastic Core Steel Wire Rope and Impregnated Plastic Core Swaged Steel Wire Rope	387
Zeynep Şeyma SERDAROĞLU, Zehra ALTINIŞIK Çelik Halat ve Tel Sanayii A.Ş. Türkiye	
Comparison of Breaking Load and Service Life of Steel Wire Ropes with Parallel Wire Rope Core (PWRC) and Independent Wire Rope Core (IWRC)	391
Murat POLAT, Emre BAŞER Çelik Halat ve Tel Sanayii A.Ş. Türkiye	
Reducing The Amount of Slag Carry Off From The Ladle in The Continuous Casting Process	394
Ahmet Şafak ÇAKMAK, Hakan KAPUSUZ, Emin Serkan EMİNOĞLU, Fatih ASLAN İskenderun Demir ve Çelik A.Ş. Türkiye	
Production of Functionally Graded Materials Based on FLG Reinforced Al-4.5Cu-1.5Mg by Powder Metallurgy	399
Gökçe BORAND, Deniz UZUNSOY Bursa Technical University Türkiye	



Effect of Anodizing Thickness on Corrosion Behaviour of 2011 Aluminium Alloy Ilyas Artunç SARI ^{1,2} , Görkem ÖZÇELİK ¹ , Onuralp YÜCEL ² ¹ ASAS Aluminium, ² Istanbul Technical University Türkiye	400
Investigation and Fe Analysis of Earing Amount and Direction of Deep Drawing Process of an Aluminium Sheet Under Various Condition Melih ÇAYLAK, Koray DÜNDAR, Yusuf ÖZÇETİN, Görkem ÖZÇELİK, Ali ULUS ASAŞ Alüminyum Türkiye	404
Reducing Energy Consumption During Heat Treatment of Cast Aluminum Alloys – Optimization of Process Parameters Through CALPHAD Emre ÇINKILIC ¹ , Esra DOKUMACI ALKAN ² , Bilge Nur KAVALCI ² , Şevval ANAVATAN ² , Başak YAŞAR ² , Gizem AMMAS ² ¹ Hakkari University, ² Dokuz Eylül University Türkiye	408
Investigation of Microstructure of Homogenized Aluminum Alloys in The Batch Homogenization Plant and Continous Homogenization Plant Murat DOĞAN ^{1,2} , Deniz KAVRAR ÜRK ^{2,3} , Büşra GEDİK ^{4,5} , Gökçen GÖKÇE ² ¹ Yıldız Technical University, ² Sistem Teknik, ³ Istanbul Technical University, ⁴ Şeyh Edebalı University, ⁵ Arslan Aluminium Türkiye	409
Parametric Approach of a Novel Heat Treatment on Al-Mg-Si Alloys: Retrogression and Re-Aging Almina DEVECİ ¹ , Nilgün BÖYÜKULUSOY ¹ , Mehmet Buğra GÜNER ^{1,3} , Görkem ÖZÇELİK ^{2,3} , Ridvan GECÜ ¹ ¹ Yıldız Technical University, ² Sakarya University of Applied Sciences, ³ ASAŞ Aluminium Türkiye	410
Influence of Mg Content on The Microstructure and Mechanical Properties of EN AW 6082 Alloys Aleyna GÜMÜŞSOY, Hilal ÇOLAK, Işık KAYA, Emrah Fahri ÖZDOĞRU TRI Metalurji A.Ş. Türkiye	414
Gold Extraction from Oxide Gold Ores by Glycine Leaching Umay ÇINARLI ¹ , Gabriel UĞURGEL ¹ , M. Barış DARYAL ² , M. Hakan MORCALI ³ , Ahmet TURAN ¹ ¹ Yeditepe University, ² Gama Composite Engineering & Products, ³ Gaziantep University Türkiye	418
An Update for Critical Raw Materials (CRMs) Erman ÇAR ¹ , Umay ÇINARLI ² , Ahmet TURAN ² , Onuralp YÜCEL ³ ¹ Insertec Thermal Solutions, ² Yeditepe University, ³ Istanbul Technical University Türkiye	419
Environmental Impact of Hydrometallurgical Zinc Production Georgi PATRONOV University of Plovdiv “Paisii Hilendarski” Bulgaria	420
Industrial Scale Extraction of Lithium Carbonate and Rare Earth Elements From Domestic Sources Arzu S. SATILMIŞ ¹ , Herkail ÖZEN ¹ , Furkan E. ÖZEL ¹ , M. Şeref SÖNMEZ ² ¹ ASOS Process Engineering, ² Istanbul Technical University Türkiye	424
Transformation in Mining and Green Metals Fevzi YILMAZ Fatih Sultan Mehmet Vakıf University Türkiye	425
Effect of Heat Treatment on Microstructure and Corrosion Behaviors of Additive Manufactured Ti-6Al-4V Using SLM Type 3D Printer Yusuf Atilla SADIKOĞLU ¹ , Şeyma KÜÇÜK ¹ , Özkan GÖKÇEKAYA ² , Takayoshi NAKANO ¹ , Hakan YILMAZER ¹ ¹ Yıldız Technical University, ² Osaka University Türkiye, Japan	429
Effect of Hf Addition on the Structural Properties, Microhardness and Oxidation Behaviour of Co-Al-W Superalloys Emre DAMAR, Mehmet Şahin ATAŞ, Mehmet YILDIRIM Konya Technical University Türkiye	430
Homogenization of The CuNi12Zn24 Alloy Produced by Horizontal Continuous Casting Umut YILDIZ ¹ , Alptekin KISASÖZ ² , Çağlar YÜKSEL ³ , Mustafa YILDIZ ¹ , Serdar Osman YILMAZ ⁴ ¹ Kayalar Bakır Alışmaları, ² Kırklareli University, ³ Atatürk University, ⁴ Namık Kemal University Türkiye	431
Thermodynamic and Experimental Approach of The Phase Formations in Ti-Nb-Ta-Zr-Mo High Entropy Alloys Gökhan POLAT ¹ , Yunus Eren KALAY ² ¹ Necmettin Erbakan University, ² Middle East Technical University Türkiye	435
Integrated Processing of Al_xCoCrFeNi-Cu_a (0.5≤x≤3, a=0.5,1) High-Entropy Alloys: from Master Alloy Synthesis to Shaping Faruk KAYA ¹ , Albek ERŞAN ² , Sajjad ALİAKBARLU ¹ , Gül İpek SELİMOĞLU ² , Bora DERİN ¹ ¹ Istanbul Technical University, ² Eskisehir Technical University Türkiye	439
Thermodynamic and Experimental Investigation of AlCoCrFeNiTi based High-Entropy Alloys Murat ALKAN ¹ , Esra DOKUMACI ALKAN ¹ , Saadet GÜLER ^{1,2} ¹ Dokuz Eylül University, ² İzmir Katip Celebi University Türkiye	440



The Effect of Coolants on The Surface Quality of Aluminium Pressure Die-Casting Alloys in Machning Process	441
Edin NURAY ¹ , Kaan GENÇER ¹ , Alptekin KISASÖZ ² , Çağlar YÜKSEL ³ ¹ PTC Kimya, ² Kırklareli University, ³ Ataturk University Türkiye	
The Effect of Jet-Cooling Application on Microstructural Properties of The Overheating Areas in High Pressure Die Casting Parts	443
Kaan GENÇER ¹ , Yasin AYYILDIZ ² , Süleyman ŞENTÜRK ³ , Alptekin KISASÖZ ⁴ , Çağlar YÜKSEL ⁵ ¹ PTC Chemical, ² Arslan Makina Döküm, ³ PTC Technic, ⁴ Kırklareli University, ⁵ Ataturk University Türkiye	
The Effect of Nitrogen Gas Purging on the Mechanical Properties of Vertical Semi-Continuous Casting	447
Mustafa YILDIZ ¹ , Çağlar YÜKSEL ² , Alptekin KISASÖZ ³ , Umut YILDIZ ¹ , Serdar Osman YILMAZ ⁴ ¹ Kayalar Bakır Alaşımları, ² Atatürk University, ³ Kırklareli University, ⁴ Namık Kemal University Türkiye	
Nickel Recovery from Olivine by Hydrometallurgical Method	448
Şeyma YÜKSEL SAĞMAN ¹ , Hande ARDIÇOĞLU ¹ , Hasan NİZAMOĞLU ² , Mehmet Deniz TURAN ² , Ali KESKİN ¹ , Erdoğan KARIP ¹ , Gökhan BAŞMAN ¹ ¹ Eti Chrome, ² Firat University Türkiye	
Investigation of Roasting Behavior and Mineralogical Transformation of Titanomagnetite Concentrate at Different Temperatures	451
Ismail Emre YILDIZ ¹ , Zeynep Hazal YAZĞAN ¹ , Mikail BAŞYİĞİT ¹ , Elif UZUN KART ¹ , Abdullah BUHUR ² ¹ Marmara Üniversitesi, ² ARGETEST Türkiye	
The Effect of The Scale Factor on AlCoCrFeNi based High-Entropy Alloys Produced via a Self-Propagating High-Temperature Synthesis Method	455
Murat ALKAN ¹ , Esra DOKUMACI ALKAN ¹ , Emre ÇINKILIÇ ² ¹ Dokuz Eylül University, ² Hakkari University Türkiye	
Thermodynamic and Microstructural Investigations of AlCoCrFeNi(Ti)X Based High-Entropy Alloys	456
Esra DOKUMACI ALKAN, Murat ALKAN, Oğuzhan DIRİCAN, Mehmet Nurullah KÖSE, Abdulkafi KARTOPU Dokuz Eylül University Türkiye	
Development of Oxide Dispersion Strengthened Inconel 718 Alloy by Calphad Method and Production of Designed Novel ODS Alloy by Laser Powder Bed Fusion	457
M. Yeşim YALÇIN ¹ , A. Alkim GÖKBAYRAK ¹ , C. Bora DERİN ² , Eda AYDOĞAN ¹ , Bahattin KOÇ ³ ¹ Middle East Technical University, ² Istanbul Technical University, ³ Sabancı University Türkiye	
Comparison of Microstructure and Mechanical Properties of CoCrFeNiMn High-Entropy Alloys by Uniaxially Pressing-Sintering and Vacuum Hot Pressing-Sintering Methods	458
Burak KÜÇÜKELYAS ¹ , Cantekin KAYKILARLI ¹ , İhsan ÇAHA ² , Alexandra C. ALVES ³ , Fatih TOPTAN ⁴ , Sebahattin GÜRMEZ ² , Deniz UZUNSOY ¹ ¹ Bursa Technical University, ² Istanbul Technical University, ³ University of Minho, ⁴ Izmir Institute of Technology Türkiye, Portugal	
Investigation of The Influence of Age Hardening on The Corrosion Resistance and Hardness of a Nanocrystalline AA2024 Alloy	460
Furkan ÖZDEMİR ¹ , Hasan OKUYUCU ¹ , Rajeev GUPTA ² ¹ Ankara Yıldırım Beyazıt University, ² North Carolina State University Türkiye, USA	
Can High-Strength Steel Become Stainless Also with Low Chromium Content?	461
Beste PAYAM, Mustafa Kamil ÜRGEN, Cem ÖRNEK Istanbul Technical University Türkiye	
Tribocorrosion Properties of Electroless Nickel-Boron Coatings from Stabilizer-Free Bath	462
Muslum YUNACTI ¹ , Alex MONTAGNE ² , Mariana Henriette STAIA ² , Véronique VITRY ¹ ¹ Université de Mons, ² Arts et Métiers Institute of Technology Belgium, France	
Effect of B and Sr Addition to Trivalent Chromium Process (TCP) Coated Al-Si Cast Alloys on Corrosion Resistance	463
Berkay SAVAŞKAN ^{1,2} , Muammer MUTLU ² , Özgül KELEŞ ¹ ¹ Istanbul Technical University, ² Mita Kalıp ve Döküm Sanayii Türkiye	
The Effect of Boron Addition on The Microstructure and Mechanical Properties ff HCx Tool Steel	464
N. Şeyma NEVCANOĞLU, Akay NEVCANOĞLU, H. Özkan GÜLSOY Marmara University Türkiye	
Corrosion Behaviour of Few-Layered-Graphene (FLG) Reinforced Al-4 Wt.%Cu Metal Matrix Composites Processed by Mechanical Alloying	470
Cantekin KAYKILARLI, Burak KÜÇÜKELYAS, Taha Yasin EKEN, Nazlı AKÇAMLI, Deniz UZUNSOY Bursa Technical University Türkiye	
Change in Friction Coefficient of Cu15Ni8Sn Material in Dry and Oily Environment According to Casting Method	471
Talip ÇITRAK, Orçun ZİĞİNDERE, Edanur KASAP, Feriha BİROL, Ümit KAPLAN Sağlam Metal Türkiye	
Synthesis of Li₂SiO₄ as a Solid Sorbent for Carbon Capture via Solution Combustion Route	475
Kagan BENZESİK ¹ , Ahmet TURAN ² , Şeref SÖNMEZ ¹ , Maria Teresa IZQUIERDO ³ , Onuralp YÜCEL ¹ ¹ Istanbul Technical University, ² Yeditepe University, ³ Instituto de Carboquímica ICB-CSIC Türkiye, Spain	



Nb-Co co-doped Barium Titanate Dielectric Ceramics for Multilayered Ceramic Capacitors	476
Berkay ÖZGÜR ¹ , N. Kaan ÇALIŞKAN ¹ , Abdullah ÖZTÜRK ² ¹ Tübitak SAGE, ² Middle East Technical University Türkiye	
Production of Activated Carbon from Olive Seed	480
Derya AKBULUT, Ali Osman KURT Sakarya University Türkiye	
The Use of Olivine in The Production of Mineral Wool	481
Akın ODABAŞI ¹ , Gökhan BAŞMAN ² , Hülya KAFTALEN ODABAŞI ¹ , Hande ARDIÇOĞLU ² ¹ Fırat University, ² Etikrom Inc. Türkiye	
The Utilization of Citrate Gel Method in Cobalt Boride Synthesis	485
Buse BİTİKÇİ, Çağan Berker İYİ, Hülya BİÇER Kütahya Dumlupınar University Türkiye	
Effect of Hot Isostatic Pressing on Densification, Microstructure and Electrical Properties of Mg_{0.95}Ca_{0.05}TiO₃ Ceramic	487
Selin GÜNTOP ^{1,2} , Hakan DER ¹ , N. Kaan ÇALIŞKAN ¹ , M. Kaan PEHLIVANOĞLU ¹ , Abdullah ÖZTÜRK ² ¹ Tübitak SAGE, ² Middle East Technical University Türkiye	
Production and Characterization of Ceramics for Microwave Applications	491
Melike DÖNMEZ, Cihangir DURAN Ankara Yıldırım Beyazıt University Türkiye	
Phase Analysis and Dielectric Characteristics of BST Ceramics Produced by Conventional and Microwave Assisted Solid-State Reactions	496
Başar SÜER, Özlem AYDIN ÇİVİ, Arcan F. DERİCİOĞLU Middle East Technical University Türkiye	
Experimental Phase Studies in The Quasi-Binary BaCeO₃-SrCeO₃ System	497
Hanifi Eray KORKMAZ, Nuri SOLAK Istanbul Technical University Türkiye	
Effect of h-BN Amount on Al₂O₃/Glass Composites for LTCC Applications	498
Oğuzhan BILAÇ, Cihangir DURAN Ankara Yıldırım Beyazıt University Türkiye	
Methylene Blue Removal by Phase Separated Porous Glass	499
Emre Burak ERTUŞ ¹ , Çekdar Vakıf AHMETOĞLU ² , Abdullah ÖZTÜRK ³ ¹ KTO Karatay University, ² Izmir Institute of Technology, ³ Middle East Technical University Türkiye	
Valuable Sources of Raw Material for Activated Carbon; Hazelnut Husk and Pumpkin Shell	503
Mürüvet Hazel UYSAL, Ali Osman KURT Sakarya University Türkiye	
The Effect of Sintering Parameters on the Properties of IR Transparent ZnS Produced by Spark Plasma Sintering	504
Zeynep ÖZTÜRK, M. Kaan PEHLIVANOĞLU, N. Kaan ÇALIŞKAN Tübitak SAGE Türkiye	
Improvement of Oxidation Resistance of Carbon Fiber with Bn-B₄C Coatings	508
Cennet YILDIRIM ^{1,2} , Muhammet Nasuh ARIK ¹ , Nuri SOLAK ² ¹ Boron Research Institute (TENMAK), ² Istanbul Technical University Türkiye	
Synthesis of B₄C-Al₂O₃ Composite Powder via Aluminothermic Reduction	509
Emre TOY, Oğuz KARAAHMET, Buğra ÇİÇEK Yıldız Technical University Türkiye	
The Effect of Iron Concentration in Electrodeposited Solution and PH of Electrolyte on Photoelectrochemical Hydrogen Production Efficiency of Hematite (α-Fe₂O₃) Photoanode	514
Ersan DOĞAÇ, İlkan KARUL, Seyedsina ALYASIN, Ömer DOĞAÇ, Fatma Betül YILMAZ, Cevat SARİOĞLU Marmara University Türkiye	
The Thermochemical Heat Storage Properties of Composite Structures Produced Different Matrix and Sorbent Salts	518
Behiye YUKSEL ¹ , Esra AYAN ² , Gökhan ORHAN ² ¹ Halic University, ² Istanbul University-Cerrahpasa Türkiye	
Advanced Material Solutions for Safer and Long-Lasting High Capacity Cobalt Free Batteries for Stationary Storage Applications (CoFBAT)	519
Kamil Burak DERMENÇİ, Kato DAEMS, Joeri Van MIERLO, Maitane BERECİBAR Vrije Universiteit Brussel Belgium	



Material Supply Risk for Thin Film Solar Cells and Importance of Recycling Ioanna TEKNETZI, Burçak EBİN Chalmers University of Technology Sweden	520
An Industrial Ecology Perspective of Battery Technologies for Electromobility: LCA Of Solid-State Lis Battery Burak ŞEN ¹ , Ahsen AKBULUT ¹ , Abdulkadir KIZILASLAN ¹ , Mahmud TOKUR ¹ , Murat KÜÇÜKVAR ² , Nuri Cihat ONAT ² , Hatem AKBULUT ¹ ¹ Sakarya University, ² Qatar University Türkiye, Qatar	521
Electrochemical Noise Measurement in Batteries with Metallic Lithium Anodes Gözde KARAOĞLU, Burak ÜLGÜT Bilkent University Türkiye	522
Investigating The Electrochemical Performance of Double Shell Cathode Active Materials for Lithium Ion Batteries Elif SARIKAS, Ipek TUNC, Ozgul KELES Istanbul Technical University Türkiye	523
Composite Electrodes Production Using Nickel-Titanium Orthodontic Waste and Investigation of Their Uses in Lithium Ion Batteries (Libs) Humza ASHRAF ¹ , B. Deniz KARAHAN ^{1,2} ¹ Istanbul Medipol University, ² Istanbul Technical University Türkiye	524
Modulation of Cation Composition for Lithium Storage of Spinel-Structured High Entropy Oxides Deniz Okan BAYRAKTAR ^{1,2} , Ersu LÖKÇÜ ³ , Çiğdem TOPARLI ¹ ¹ Middle East Technical University, ² ASPILSAN Enerji, ³ Eskişehir Osman Gazi University Türkiye	529
Investigation of Ni Effect on Mn-Fe-Based Multi-Transition Metal Layered Cathode Materials for Sodium-Ion Batteries Burcu KALYONCUOĞLU ¹ , Sebahat ALTUNDAĞ ² , Serdar ALTIN ² , Metin ÖZGÜL ¹ ¹ Afyon Kocatepe University, ² Inonu University Türkiye	530
The Effect of Impregnation Conditions on Active Metal Size and Distribution Profiles of Ni/Al₂O₃ Supported Catalyst Emine ERSEZER ¹ , Cem AÇIKSARI ² , Elif ERDİNÇ ² , Serdar ÇELEBİ ² , Servet TURAN ¹ , Umut SAVACI ¹ ¹ Eskişehir Technical University, ² TUPRAS R&D Center Türkiye	531
Temperature-Dependent Galvanostatic EIS of Spiral and Bobbin Li/SOCl₂ Batteries Gökberk KATIRCI, Fazlı Eren CIVAN, Burak ÜLGÜT Bilkent University Türkiye	532
An Innovative Approach for Electrolyte Recycling from Lithium-Ion Batteries Nils ZACHMANN, Burçak EBİN Chalmers University of Technology Sweden	533
Determination of The Austenization Temperature via Computational Metallurgy Approach for an Alloyed Ductile Iron Barış ÇETİN ¹ , Ayşe ERKAN ² , Ümmihan T. YILMAZ ³ , Buğra ATASOY ¹ , Caner YALÇINER ¹ , Caner ŞİMSİR ^{4,5} ¹ FNS Savunma Sistemleri, ² Döksen Isıl İşlem, ³ Kırıkkale University, ⁴ Middle East Technical University, ⁵ Simultura Malzeme Teknolojileri Türkiye	535
The Damage Analysis of The Diamond Particle in The Cutting Natural Stone Process Berrak BULUT Istanbul Technical University Türkiye	539
Investigation of EPDM Materials Used in Milk Tanker Yıldız YARALI ÖZBEK ¹ , Emin Emre GÖKTEPE ^{1,2} ¹ Sakarya University, ² Tırsan Treylar Türkiye	543
Failure Evaluation of Compression Steel Spring Wires and Factors Affecting Breaking Y. Ziya SALIK ¹ , Ekrem ALTUNCU ² ¹ Çelik Halat ve Tel Sanayii, ² Sakarya University of Applied Sciences Türkiye	547
Investigation of Forging Process Failures and Solutions in the Production of Steering and Suspension System Parts Sefer KOÇAK Ditaş Doğan Yedek Parça Türkiye	550
Investigation of The AA6005-A Alloy's Corrosion Behavior in Different Aging Conditions Murat DOĞAN ^{1,2} , İbrahim TÜTÜK ¹ , Kubilay ÖZTÜRK ¹ , Serhat ACAR ¹ , Kerem Altuğ GÜLER ¹ ¹ Yıldız Technical University, ² Sistem Teknik Türkiye	554
Failure Analysis of a Broken Reducer Shaft M. Eriş DURMUŞOĞLU, Ali KOCA İskenderun Demir ve Çelik A.Ş. Türkiye	555



Failure Analysis of a Broken Descaler Pump Shaft at The Hot Strip Mill Facilities Mehmet Eriş DURMUŞOĞLU, Ali KOCA İskenderun Demir ve Çelik A.Ş. Türkiye	558
Investigation of The Austempering Duration at 400°C on Silicon Solution Strengthened Ductile Iron Soner Özden ERTÜRK ¹ , Levent Cenk KUMRUOĞLU ² , Ahmet ÖZEL ³ ¹ HEMA Otomotiv Sistemleri, ² İskenderun Teknik Üniversitesi, ³ Sakarya Üniversitesi Türkiye	562
Surface Modification of Glass Fiber Woven Fabrics by Indium Tin Oxide Coatings and Electromagnetic Characterization of Their Multilayered Graded Composites in X-Band Frequency Range Merve ÖZDİL DARICIOĞLU, Caner DURUCAN, Arcan F. DERICIOĞLU Middle East Technical University Türkiye	567
Synthesis and Characterization of Graphene Reinforced Al-7.5 wt.% Zn Matrix Composites Berk ŞENYURT ¹ , Gökçe BORAND ¹ , Duygu AĞAOĞULLARI ² , Nazlı AKÇAMLI ¹ , Deniz UZUNSOY ¹ ¹ Bursa Technical University, ² İstanbul Technical University Türkiye	568
Mechanical Properties of Si₃N₄ Reinforced Ti6Al4V Composite Foam Ömür Ekrem GÜNTÜRK, Mevlüt GÜRBÜZ On dokuz Mayıs University Türkiye	569
Biodegradable Polymer Nanocomposites Using Modified Cellulose Nanocrystals Onur Nuri ARSLAN, Yonca ALKAN GÖKSU, Mohammadreza NOFAR Istanbul Technical University Türkiye	573
Investigation of The Effect of Copper Alloy Reinforcement on The Physical Properties of Polymer Matrix Composite Ömer Alparslan KAYA ¹ , Talip ÇİTRAK ¹ , Serdar TOZKOPARAN ¹ , Edanur KASAP ¹ , Münir TAŞDEMİR ² , Feriha BİROL ¹ ¹ Sağlam Metal, ² Marmara Üniversitesi Türkiye	574
Microcellular Hemp Fibre Reinforced Polypropylene Matrix Composites Yeşim ASLAN ¹ , Munir TAŞDEMİR ² , Yeliz ALBRECHTSEN ¹ , İsmail MUTLU ¹ ¹ Tekkan Plastik, ² Marmara University Türkiye	578
A Study on the Material Properties of Carbon Nanotubes Doped Glass Fiber Reinforced Nano Composites Bahadır TÜRKYAMAN ¹ , Mehmet Fatih ÖKTEM ² ¹ Tübitak SAGE, ² Ankara Yıldırım Beyazıt University Türkiye	582
Investigation of The Mechanical Properties of Thermoplastic Based Sandwich Structures Produced by Fused Deposition Modeling (FDM) Technique Hürşit Sefa AYDIN, Cihan KABOĞLU, Deniz UZUNSOY Bursa Technical University Türkiye	586
Mechanical Characterization of Graphene Nanoplatelets/Al₂O₃ Reinforced Epoxy Hybrid Composites Cantekin KAYKILARLI ^{1,2} , Aygül YEPREM ² , Deniz UZUNSOY ¹ ¹ Bursa Technical University, ² Yıldız Technical University Türkiye	587
Investigation of Microstructure and Mechanical Properties of DP Quality Steels Welded with Different Heat Inputs Kardelen YILMAZ ¹ , Bilgehan ÖGEL ² , Caner BATIGÜN ² ¹ Middle East Technical University, ² METU Welding Technology and Non-Destructive Testing Centre Türkiye	588
The Effect of Process Parameters on Bead Geometry, Hardness and Microstructural Properties Armour Steel Welds Performed by Robotic Gas Metal Arc Welding Ceren ÇELİK ¹ , Recep Murat KURT ¹ , Ozan ÇOBAN ¹ , Hakan BAYKAL ² , H. Kübra AKBEN ¹ , Uğur GÜROL ^{1,2} ¹ İstanbul Gedik University, ² Gedik Welding Türkiye	589
Design of High Strength and High Torque Resistance Wire Rope Fatih DUMAN ¹ , Emel TABAN ² , Sevim Gökçe ESEN ¹ ¹ Çelik Halat ve Tel Sanayii A.Ş., ² Kocaeli University Türkiye	595
Effects of Build Orientation and Process Parameters on Mechanical Behavior of IN718 Components Manufactured by Selective Laser Melting Method Tuğçe KALELİ ¹ , Aydın YAĞMUR ² , C. Hakan GÜR ¹ ¹ Middle East Technical University, ² EOS GmbH Electro Optical Systems Türkiye	599
The Effect of Heat Input on Mechanical Properties of TRIP Steels in GMAW and TIG Welding Gökhan ERİAN ¹ , Adem KURT ² ¹ Turkish Accreditation Agency, ² Gazi University Türkiye	601
The Effect of Brazing Parameters on The Microstructural Features of Alumina-Copper Joints Ece Naz YURTSEVEN ^{1,2} , N. Kaan ÇALIŞKAN ¹ , M. Kaan PEHLİVANOĞLU ¹ ¹ Tübitak SAGE, ² Middle East Technical University Türkiye	605



Non-Destructive Detection of Flaws in Conductive Sealant Applications With a Metamaterial Based Antenna Elif Gaye ERKI ¹ , Mete BAKIR ¹ , Oğuzhan AKGÖL ² ¹ TUSAS, ² İskenderun Technical University Türkiye	609
Properties of Laser Welded 3003 Aluminum Alloy Abdullah CEBECİ ¹ , Emel TABAN ² ¹ Assan Hanil Otomotiv, ² Kocaeli Üniversitesi Türkiye	613
Effect of Post Weld Stress Relieving Heat Treatment on 6xxx Series Aluminum Alloys Furkan YALÇINKAYA ¹ , Barış KARA ² , Cem KAHRUMAN ¹ ¹ Bursa Technical University, ² Yeşilova Holding Türkiye	617
Surface Modification of 3D-Printed Porous 316L Stainless Steel Azade YELTEN ^{1,2} , Batur ERCAN ² ¹ Istanbul University-Cerrahpasa, ² Middle East Technical University Türkiye	622
Characterization of Copper Nanoparticle-Deposited Bioceramic Coatings Fabricated on Zirconium Tuba YILDIZ ^{1,2} , Salih DURDU ³ , Kadriye OZCAN ³ , Metin USTA ¹ ¹ TUSAS, ² İskenderun Technical University Türkiye	625
Production and Characterization of Bioactive Glass-Ceramics From Soda-Lime-Silica and Borosilicate Waste Glasses Merve Şeyma SÜREL ¹ , İremnur AKÇAKOCA ¹ , Şeniz Reyhan Kuşhan AKIN ² , Gülsüm TOPATEŞ ¹ ¹ Ankara Yıldırım Beyazıt University, ² Çankaya University Türkiye	626
Essential Oil-Loaded Polymeric Foams via Green Route Fatma Nur PARIN Bursa Technical University Türkiye	627
Production and Characterization of Ti-6Al-4V Slurry for Trabecular Dental Implants Produced by Replica Impregnation Method Aynur İNAN ÜSTÜN, Gülsüm TOPATEŞ, Yasin Sinan ERTEM, Hasan OKUYUCU Ankara Yıldırım Beyazıt University Türkiye	631
Surface Investigation of Antibacterial Copper-Incorporated Bioactive Surfaces Fabricated on Commercially Pure Titanium Salim Levent AKTUĞ ¹ , Kemal KORKMAZ ¹ , Sıtkı AKTAŞ ² , Salih DURDU ² ¹ Gebze Technical University, ² Giresun University Türkiye	632
Antimicrobial Properties of Electrospun Nano-Sized Ag and TiO₂ Blended PVA Nanofibers Merve OCAKTAN ¹ , Fatih ÇİFTÇİ ² , Nilüfer EVCİMEN DUYGULU ¹ ¹ Yıldız Technical University, ² Fatih Sultan Mehmet Vakıf University Türkiye	633
A Green Manufacturing Method in Skin Tissue Engineering Merve SIRTİKARA, Emir ERIŞÇİ, Sevda Nur TEBERDAR, Mustafa ŞENGÖR Marmara University Türkiye	634
Production of Nano Strontium Hexaferrite by Solution Combustion Synthesis Ceren ÇALIŞKAN, Raşit SEZER Karadeniz Technical University Türkiye	636
Phase Engineering of Semiconductor Nanoscale Materials Selim DEMİRÇİ, Mehmet Masun TUNÇAY Marmara University Türkiye	640
Effect of Starting Composition on the Morphology of Sol-Gel Synthesized Boron Carbide (B₄C) Particles Selin TÜMKAYA, Suna AVCIOĞLU, Figen KAYA, Cengiz KAYA Yıldız Technical University Türkiye	643
The Synthesis & Characterization of Homogenous High-Quality Graphene Encapsulated Metallic Powders via Plasma Enhanced Rotating CVD Deniz ÇAKIR ¹ , Ömer Refet ÇAYLAN ^{1,2} , Tarık Can TÜRKÖĞLU ¹ , Oğulcan AKGÜN ³ , Günce DUGAN ³ , Halil Onat TUĞRUL ³ , Benat KOÇKAR ³ , Göknur CAMBAZ BÜKE ¹ ¹ TOBB University of Economics and Technology, ² Bilkent University, ³ Hacettepe University Türkiye	647
Production of Tin Nanowires via AAO Template Method and Investigation of Their Performance As Catalysis for Electrochemical CO₂ Reduction Dilan ER ^{1,2} , Eleni ROSOLYMOU ³ , Mustafa URGEN ¹ ¹ Istanbul Technical University, ² Arcelik Global, ³ National Technical University of Athens Türkiye, Greece	648
The Synthesis and Characterization of MO₂CTx Mxene by Hydrothermal Etching with Different Fluoride Salts for EMI Shielding Applications Elif OKAY ¹ , Ömer Refet ÇAYLAN ¹ , Begüm Beril İNCEÇİK ² , Göknur CAMBAZ BÜKE ¹ ¹ TOBB University of Economics and Technology, ² Roketsan Missiles Industries Türkiye	652



Effect of Calcination Temperature on MgAl₂O₄ Nanoparticles Production by Sol-Gel Method	653
Duygu YEŞİLTEPE ÖZÇELİK, Sebahattin GÜRMENT Istanbul Technical University Türkiye	
Comparative Study of Microstructural Changes and Hardness of Nanostructured FeCoCrNi High Entropy Alloys After Different Consolidation Routes	654
Mustafa TEKİN ¹ , Ali Rıza BALOĞLU ² , Hasan KOTAN ² ¹ KTO Karatay University, ² Necmettin Erbakan University Türkiye	
Development of Graphene/Silicon Composite Based Lithium Ion Battery Anode	655
Tarık Can TÜRKÖĞLU, Eren ATLI, Ömer Refet ÇAYLAN, Göknur CAMBAZ BÜKE TOBB University of Economics and Technology Türkiye	
Laser Induced Graphene Structures for Electrochemical Sensing Devices	656
Murat DEMİREL, Ömer Refet ÇAYLAN, Tarık Can TÜRKÖĞLU, Göknur CAMBAZ BÜKE TOBB University of Economics and Technology Türkiye	
Photoluminescence Property of NaYF₄: Yb/ Er/ Pr Upconversion Nanoparticles in the Near Infrared Region	657
Mahla SHAHSAVAR, Ayşe DULDA Yeditepe University Türkiye	
The Synthesis & Characterization of Carbon Nanotubes on SiC via Vacuum Decomposition	658
Erhan GÜRPINAR, Ömer Refet ÇAYLAN, Derya KARADENİZ, Erkin Köseoğlu, Göknur CAMBAZ BÜKE TOBB University of Economics and Technology Türkiye	
Circular Economy in Metal Foundry Sector: From Europe to Türkiye	660
Semih ATEŞ ¹ , Kerem Can DIZDAR ¹ , Tunçağ Cihangir ŞEN ² , Serter Koray HATİPOĞLU ² , Cevat Fahir ARISOY ¹ ¹ Istanbul Technical University, ² Turkish Foundry Association Türkiye	
Optimizing The Amount of Flux Used in The Casting Process of EN AW 6082 Aluminum Alloy in Profile Production	664
Sena ERDOĞAN ^{1,2} , Selçuk ERKUL, Zekeriya MUTLU ¹ , Rabia Şevval AKAN ^{2,3} , Ayberk UZER ^{2,3} , Muhammet ULUDAĞ ^{2,3} ¹ PMS Metal Profile Aluminum, ² Bursa Technical University, ³ ULUCON R&D and Consulting Türkiye	
Reducing The Energy Costs for Green Conversion by Coating the Surfaces of the Crucibles Used in HPDC Method with Boron Reinforcement Cellulose	668
Ümmet AYYILDIZ ^{1,2} , Songül KILINÇ ^{1,3} ¹ Prometal, ² Bilecik Şeyh Edebali University, ³ Bursa Technical University Türkiye	
Microstructure Evolution of The Three-Phase Al-Al₂Cu- Ag₂Al Eutectic System Upon Directional Solidification	672
Merve KEVKİR ¹ , Arash KAZAZI ² , Samira MOHAGHEGH ³ , Melis ŞEREFÖĞLU ¹ ¹ Marmara University, ² Koç University, ³ Istinye University Türkiye	
Optimization of The Heat Treatment Parameters Depending on The Thickness in Plate Products Made of EN AW 1050 Al Alloy	673
Sena ERDOĞAN ^{1,2} , Selçuk ERKUL ¹ , Zekeriya MUTLU ¹ , Rabia Şevval AKAN ^{2,3} , Ayberk UZER ^{2,3} , Muhammet ULUDAĞ ^{2,3} ¹ PMS Metal Profile Aluminum, ² Bursa Technical University, ³ ULUCON R&D and Consulting Türkiye	
Understanding The Solidification Dynamics of Commercial Aluminium Alloys Produced by Twin-Roll Casting	678
Arash KAZAZI ¹ , Onur MEYDANOĞLU ² , Cemil İŞIKSAÇAN ² , Hatice MOLLAOĞLU ALTUNER ² , Melis ŞEREFÖĞLU ³ ¹ Koç University, ² Assan Alüminyum, ³ Marmara University Türkiye	
Effect of Chromium on Wear Resistance of Carbide Austempered Ductile Iron (CAD)	679
Barbaros SENSES ¹ , Ummihan T. YILMAZ ² , Ayşe ERKAN ¹ , Gökhan SAĞLAM ¹ ¹ Döksen Heat Treatment and R&D Center A.S., ² Kırıkkale University Türkiye	





RSS

Recycling and Sustainability Symposium

Geri Dönüşüm
ve Sürdürülebilirlik
Sempozyumu



INVESTIGATING THE EFFECT OF MECHANICAL PRETREATMENT ON THE RECOVERY RATE OF CRITICAL RAW MATERIALS FROM DISCARDED HARD DISC DRIVES

Alireza HABIBZADEH, Mehmet Ali KÜÇÜKER, Mertol GÖKELMA

Izmir Institute of Technology
Türkiye

Keywords: Recycling of WEEE, NdFeB magnet, Manual Disassembly, Pre-treatment

Abstract

Waste Electrical and Electronic Equipment (WEEE) is an important secondary source of Critical Raw Materials (CRM) essential in developing novel high-tech applications. The presented study aims to track the rare earth elements, along with gold, and aluminium in the end-of-life hard disk drives (HDDs) during recycling by using two different pre-treatment procedures. The recovery rates through manual disassembly and shredded HDDs have been compared.

1. Introduction

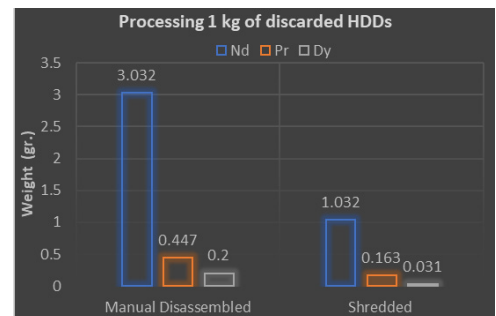
HDDs are considered one of the most accessible WEEE for recycling due to their short lifetime. 2 wt.% of each HDD is NdFeB permanent magnet (PM) which includes two critical REEs; Nd and Dy. Grinding and shredding, as the routine pretreatment of every recycling company might cause magnetic content, especially neodymium powders attached to iron, and get diluted in a ppm concentration in large ferrous streams which can be lost forever. While by doing efficient manual separation pretreatment, there is a chance to prevent this loss.

2. Materials and Method

Two different kinds of discarded hard disk drives were provided by Exitcom company. Seventy-five intact discarded HDDs with 36800 grams in weight and seven shredded HDDs with 3600 grams in weight were collected. The intact HDDs were subjected to manual disassembly and then mass balance, while the shredded one were sieved, demagnetized, sieved again, and finalaly mass balanced. Both kinds of discarded HDDs were divided to similar fractions after mechanical pretreatment. Each fraction was characterized by ICP-MS to determine the metal content, especially the rare earth elements (REEs).

3. Result and Discussion

The results shows, by employing manual dismantling as the mechanical pretreatment, losing of REEs and gold can be prevented, and provide a valuable secondary source of these elements. Recycling of aluminium shows also a higher efficiency in comparison to shredded HDDs. In terms of REEs, almost all of them might be lost during the shredding, while for manual disassembled one, the recovery rate in over 90%. In terms of gold digging, the gold fraction in manual disassembled one has 2218 ppm concentration while in shredded one is around 120 ppm. Finally, the aluminium yield is higher by melting lower amount of scrap which directly affect the efficiency.



4. Conclusion

The recovery rate of REEs, gold and aluminium is severely affected by the mechanical pretreatment. Recycling of neodymium, gold, and aluminium through manual dismantling shows higher value of efficiency in comparison to shredded one.

Acknowledgment

This research was funded by the Scientific and Technological Research Council of Turkey (TÜBİTAK) under the BİDEB-2232 program with grant number 118C311. The authors would like to thank to Exitcom Recycling for providing all samples.



IRON REMOVAL FROM NDFEB WASTE MAGNET SOLUTIONS USING SODIUM ALGINATE SOLUTION

Emircan UYSAL¹, Elif EMİL KAYA^{1,2,3}, Serhat AL¹, Sebahattin GÜR MEN¹

¹Istanbul Technical University, ²RWTH Aachen University, ³Turkish-German University
Türkiye, Germany

Abstract

In this study, waste NdFeB magnets were leached with sulfuric acid. Incorporation of Fe ions from the leach solution obtained, was done *via* using the organic molecule sodium alginate. Sodium alginate solution was prepared and mixed with the leaching solution. Fe ions constitute approximately 70.93% of the metal ions abrogated from the leach solution. The metal-alginate structures were determined by FTIR analysis.

Introduction

One of strongest permanent magnets is NdFeB magnets with highest energy products BH_{max} (200-400 kJ/m³) (Dahmen et al., 2001). NdFeB magnets include critical metals, such as neodymium, dysprosium, praseodymium and etc., in their chemical structure. Both economic and environmental issues necessitate to recycling of NdFeB magnets. The most general sense, REEs (Rare Earth Element), contained in NdFeB magnets, can be recovered by pyrometallurgical or hydrometallurgical methods (Zhang et al., 2020). Hydrometallurgical recycling processes consist of two steps; leaching and metal recovery from leaching solution. It is known that among mineral and organic acids, mineral acids are more effective (Bandara et al., 2014), and among mineral acids, sulfuric acid is the most effective mineral acid to dissolve Nd (Binnemans et al., 2013). Alginate is a biopolymer, which have anionic COO⁻ functional group. It can be extracted from brown algae, like sodium alginate (SA). In this study, we tried to remove Fe²⁺ ions from the leaching solution *via* ionic interaction between the COO⁻ group and Fe²⁺ ions.

Methods

Leaching of NdFeB magnets was carried out as stated in our previous study (Uysal et al., 2022). Briefly, 1 M sulfuric acid, 1/15 solid to liquid ratio, 200 rpm, 30 min and room temperature are used as parameters to dissolving NdFeB magnets. After leaching process, 2 g SA was dissolved in 100 ml deionized water. For the best absorption efficiency, Taguchi L₉(3³) experimental design was used. Parameters were chosen as time, temperature and leach solution to SA solution ratio. Levels were 1, 4 and 12 hours for time; 4, 24 and 44 °C for temperature; 0,5, 1 and 1,5 solution ratios. After the absorption experiments, the leaching solutions were determined *via* ICP analysis and the gels obtained were examined *via* FTIR analysis.

Results

Fe and Nd concentrations of the leaching solution were determined by ICP analysis. The metal ion concentrations of the sorption solutions were determined by ICP. Approximately 70% of the absorbed metal ions consists of Fe²⁺. The optimum conditions for absorption have been determined. The metal-alginate structures, which were obtained, were shown to be Fe-alginate by FTIR.

Funding

The research leading to these results has received funding from the German Federation of Industrial Research Associations, Germany and TÜBİTAK- Scientific of Technological Research Council of Turkey (Call identifier CORNET 29th Call) under grant agreement EN03193/20. The authors would like to greatly acknowledge TÜBİTAK/Turkey (Project No: 120N331) for financial support.



References

- Bandara, H.M.D., Darcy, J.W., Apelian, D., Emmert, M.H., 2014. Value Analysis of Neodymium Content in Shredder Feed: Toward Enabling the Feasibility of Rare Earth Magnet Recycling. *Environ. Sci. Technol.* 48, 6553–6560. <https://doi.org/10.1021/es405104k>
- Binnemans, K., Jones, P.T., Van Acker, K., Blanpain, B., Mishra, B., Apelian, D., 2013. Rare-Earth Economics: The Balance Problem. *JOM* 65, 846–848. <https://doi.org/10.1007/s11837-013-0639-7>
- Dahmen, K.A., Sethna, J.P., Kuntz, M.C., Perković, O., 2001. Hysteresis and avalanches: phase transitions and critical phenomena in driven disordered systems. *J. Magn. Magn. Mater.* 226–230, 1287–1292. [https://doi.org/10.1016/S0304-8853\(00\)00749-6](https://doi.org/10.1016/S0304-8853(00)00749-6)
- Uysal, E., Al, S., Emil-Kaya, E., Stopic, S., Gürmen, S., Friedrich, B., 2022. Hydrometallurgical recycling of waste NdFeB magnets: design of experiment, optimisation of low concentrations of sulphuric acid leaching and process analysis. *Can. Metall. Q.* 1–12. <https://doi.org/10.1080/00084433.2022.2058152>
- Zhang, Y., Gu, F., Su, Z., Liu, S., Anderson, C., Jiang, T., 2020. Hydrometallurgical Recovery of Rare Earth Elements from NdFeB Permanent Magnet Scrap: A Review. *Metals* 10, 841. <https://doi.org/10.3390/met10060841>

INVESTIGATION OF DISSOLUTION PARAMETERS OF RARE EARTH ELEMENTS IN FLUORESCENT WASTES BY MICROWAVE LEACHING

Ayşegül BİLEN, Utku HATİPOĞLU, Muhlis Nezih SARIDEDE

Yıldız Technical University
Türkiye

Keywords: Rare Earth Elements, Fluorescent Waste, Microwave, Leaching

Abstract

Rare earth elements (REEs) are found in a wide range of high-tech products. The recovery of rare earth elements from used fluorescent lamps is important in terms of regulating the supply-demand imbalance in the market, eliminating toxic products, and making fluorescent phosphorus powder rich and cheap REE source. Microwave leaching is being studied increasingly in addition to traditional leaching methods. Because of its selective-volume heating and high heating rate, the microwave process is frequently viewed as an alternative to traditional high-temperature processes for complex materials. It is possible to dissolve minerals containing rare earth elements by this method. In this study, the metals La, Tb, and Ce collected in green and blue phosphorus powders, as well as Y and Eu found in red phosphorus powder in the waste fluorescent powder were dissolved using the microwave method. The effects of amount of solid (0.1, 0.3, and 0.5 g) in 50 ml HNO₃ and acid concentration (2, 4, 6 M) on the leaching efficiency of waste fluorescent powder were investigated. In addition, the data obtained through experimental studies were mathematically modeled with the response surface statistical design method. When the waste fluorescent powder was subjected to microwave-assisted leaching at 140°C for 60 minutes using 0.1 g of material in 6M HNO₃, the leaching efficiency of Y, Eu, Ca Tb, La and Ce metals reached their maximum values. The leaching efficiencies were 98%, 99%, 77%, 94%, 78% and 91%, respectively. Additionally, using the Response Surface Box-Behnken approach, a mathematical model has been developed. The model correlation coefficients for the concentrations of dissolved Y, Eu, Ca, Tb, La, and Ce were determined as 98.31, 99.82, 99.86, 95.33, 87.23, and 94.51, respectively.

1. Introduction

REEs are strategic raw materials. Tons of REE wastes with varying properties emerge as a result of its use in so many different sectors. It is possible to recover REEs from these wastes. Recycling meets only about 2% of the world's REE demand. It is possible to recycle REE-containing materials, particularly used fluorescent lamps and hard disks, at a much lower cost than the ore-based primary production method. There are red, blue and green phosphor powders within the phosphor powder on the inner surface of fluorescent glasses. It is known that approximately 50-55% of the dust is red phosphorus. Red phosphorus powder contains yttrium oxide (Y₂O₃) and europium oxide (Eu₂O₃). Terbium oxide (Tb₂O₃), lanthanum oxide (La₂O₃), and Ce₂O₃ phases are attached to aluminate or phosphate radicals in blue and green phosphorus powders.

Leaching is the first applied chemical process for the recycling of rare earth elements from phosphorus powder. Sulfuric acid (H₂SO₄), nitric acid (HNO₃) and hydrochloric acid (HCl) are used for leaching process [1]–[3].

Microwave leaching as an alternative to traditional leaching methods is an increasingly popular method in recent years [4]. The principle of dissolution by microwave effect is based on that the metals in the mineral are more permeable than the gangue minerals such as CaO, CaCO₃ and SiO₂ under the microwave effect [5]. This leads to heating in and around metal-containing minerals, thereby locally altering the leaching kinetics. As the dissolution kinetics generally increase with increasing temperature, the dissolution efficiency of metal-containing minerals is higher, and the leaching of these minerals is terminated earlier. Thus, the concentration of gangue minerals or unwanted ions in the solution can be limited. Another effect of localized and rapid heating is that the surfaces of metal-containing minerals can be fractured by thermal stresses, thereby effectively expanding the surface area. In this way, the penetration rate of REEs (such as phosphates) that are difficult to dissolve is increased [4].

There are few studies on the microwave process for the extraction of rare earth concentrates. Thanks to the microwave process provides selective-volume heating and high heating rate, this method is often seen as an alternative to traditional high temperature processes for complex materials. Huang et al. [5] heated the concentrate consisting of a mixture of bastnasite and monazite with a grade above 70% in a microwave oven with NaOH and applied water leaching to the solid obtained at the end of the process. The solid that remained undissolved was subjected to acid leaching with HCl and 93.22% of the rare earth elements in the concentrate dissolved.

Lie et al. [6] in their study carried out microwave assisted leaching of Y and Eu from waste phosphorus powder. At the end of the experiment, using 2 M H₂SO₄, 400 W microwave power, 10 g/ml solid liquid ratio and 60 minutes, the leaching efficiency of Y and Eu was calculated as 78.08% and 100%, respectively.

In this research, leaching of rare earth elements in waste fluorescent lamp powder by microwave method was investigated by considering the effects of acid concentration and amount of solid on leaching efficiency. The obtained data were mathematically modeled using the Box-Behnken statistical analysis method.

2. Experimental Procedure

2.1. Materials

Waste fluorescent lamp powder was provided by Exitcom Recycling. The waste powder was sieved from 45 μm to separate any broken glass particles present. The powder below 45 μm was dried for 8 hours at 107°C. Table 1 shows the chemical composition of the waste powder analyzed by ICP-MS.

Table 1. Chemical composition of the fluorescent waste phosphor powder.

Y	Ca	Eu	La	Tb	Ce	Gd	Al
10,3	18,59	0,79	1,47	0,71	1,37	0,79	26,64

2.2. Method

Experimental studies were carried out in the CEM Mars 5 microwave device. Experiments were performed by dissolving 0.1, 0.3 and 0.5 g solids in 50 ml of HNO_3 solution at 140°C for 60 min. The leach residues were separated by filtration. Pregnant solutions (leach liquor) were analyzed by ICP-MS. Leaching efficiencies were calculated based on the concentration data obtained by ICP-MS. The formula used is shown in Equation 1.

$$\% \text{REE} = \frac{\text{REE from ICP-MS (ppm)}}{\text{Initial REE (ppm)}} \times 100 \quad (1)$$

In this study, the effect of amount of solid (0.1, 0.3, and 0.5 g) and acid concentration (2, 4, 6 M) on the leaching efficiency of Y, Eu, Tb, La, Ce and Gd were determined. In addition, experimental studies were mathematically modeled using the Box-Behnken statistical design method using MINITAB 18.

3. Results and Discussion

The figures showing the leaching efficiency of Y, Eu, Tb, La, Ce metals are given in Fig. 1. As can be seen in Fig. 1, although the leaching efficiency decreased with the increase in the amount of solid, the increase in the acid concentration positively affected the leaching efficiency. The highest leaching efficiency for all the metals studied was obtained at 6 M HNO_3 concentration and using 0.1 g solid.

It is known that with the increase in the amount of acid, the pH decreases and the concentration of H^+ ions in the solution increases. When product formation with low solubility product is prevented, in case of high H concentration, oxidation potential will increase and leaching efficiency will be positively affected [7].

The increase in the solid amount has a negative effect on the leaching efficiency. Because at the end of the critical time in the leaching process, cation saturation occurs in the solution. Nitrate salts and higher solubility products tend to be ionic in solution. In addition, this situation can be determined by considering kinetic factors [7].

As can be seen from Fig. 1 a, b and c, the leaching efficiency is relatively higher in conditions with high solids and low acidity than in d, e and f. The lowest efficiency was calculated as 54% for Y, 77% for Eu and 24% for Ca. For Tb, La and Ce, the leaching efficiency is below the lowest 10%. This is because La, Ce and Tb metals form complex oxides

with stable A_2O_3 . Such complex oxides are difficult to chemically treat, and strong physical effects are required for dissolving. The leaching efficiency was achieved as 94%, 78%, and 91% for Tb, La, and Ce, respectively, thanks to the high acid concentration and working with low solid content. The highest Y, Eu, and Ca yields were determined as 98%, 99%, and 77%, respectively. The reason for the relatively low Ca yield is that the Ca in the blue and green phosphorus is hard to dissolve.

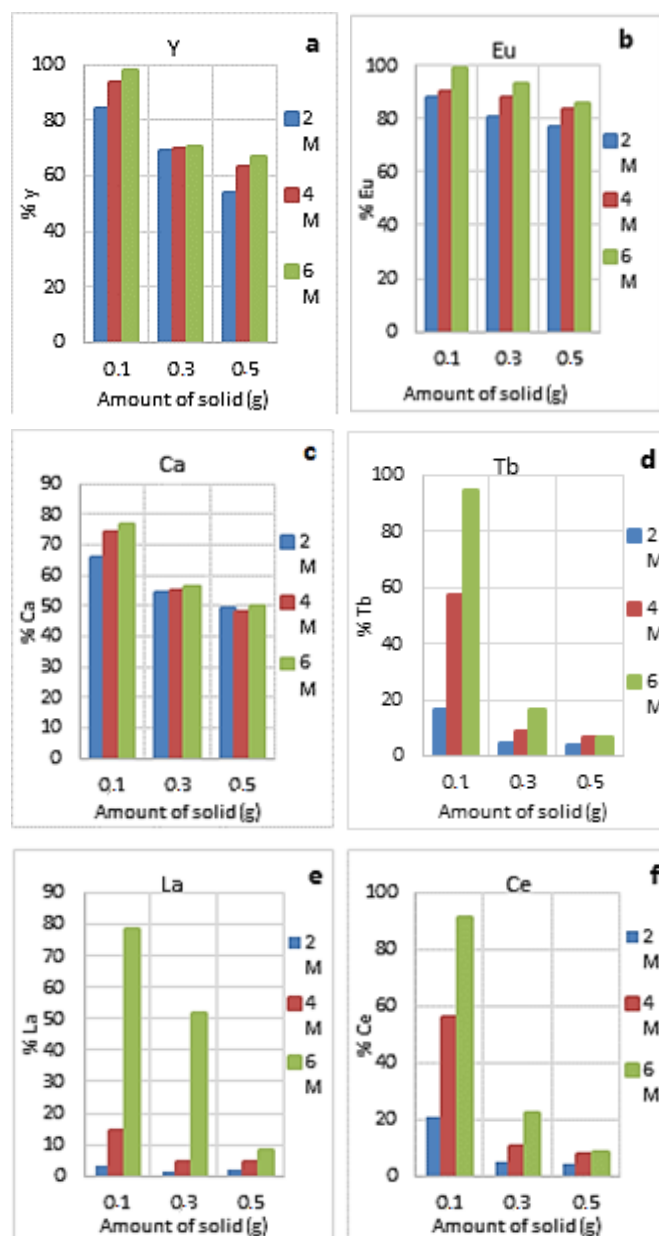


Figure 1. Leaching efficiencies of a) Y, b) Eu, c) Ca, d) Tb, e) La and f) Ce.

3.1. Mathematical modeling results

In this study, mathematical modeling was performed with MINITAB 18 using the response surface Box-Behnken method.

Table 2. Variance analysis of modelling for Y.

Source	DF	Adj SS	Adj MS	F-Value	P-Value
Model	5	971124	194225	94,24	0,002
Linear	2	958918	479459	232,65	0,001
Amount of Solid	1	942798	942798	457,48	0,000
Acid Concentration	1	16120	16120	7,82	0,068
Square	2	3408	1704	0,83	0,518
Amount of Solid*Amount of Solid	1	2748	2748	1,33	0,332
Acid Concentration*Acid Concentration	1	660	660	0,32	0,611
2-Way Interaction	1	8798	8798	4,27	0,131
Amount of Solid*Acid Concentration	1	8798	8798	4,27	0,131
Error	3	6183	2061		
Total	8	977307			

Table 3. Variance analysis of modelling for Tb.

Source	DF	Adj SS	Adj MS	F-Value	P-Value
Model	5	263,861	52,772	33,66	0,008
Linear	2	196,807	98,403	62,77	0,004
Amount of Solid	1	56,059	56,059	35,76	0,009
Acid Concentration	1	140,747	140,747	89,79	0,002
Square	2	17,211	8,605	5,49	0,099
Amount of Solid*Amount of Solid	1	16,781	16,781	10,71	0,047
Acid Concentration*Acid Concentration	1	0,429	0,429	0,27	0,637
2-Way Interaction	1	49,844	49,844	31,80	0,011
Amount of Solid*Acid Concentration	1	49,844	49,844	31,80	0,011
Error	3	4,703	1,568		
Total	8	268,564			

Variance analysis of modelling for Y and Tb were shown in Table 2 and 3. According to these values, both the acid concentration and the solid amount greatly affected the leaching efficiencies since the p values were less than 0.05. Model correlation coefficients were obtained as 98.31, 99.82, 99.86, 95.33, 87.23 and 94.51 in modeling on dissolved Y, Eu, Ca, Tb, La and Ce concentrations respectively. These data show that inferences can be made with high accuracy with the selected model.

Considering the contour plots drawn (Figure 2-7), it can be said that the acid concentration affects the metal ion concentration less for Y, Eu and Ca metals. However, the acid concentration is a more effective parameter for Tb, La and Ce.

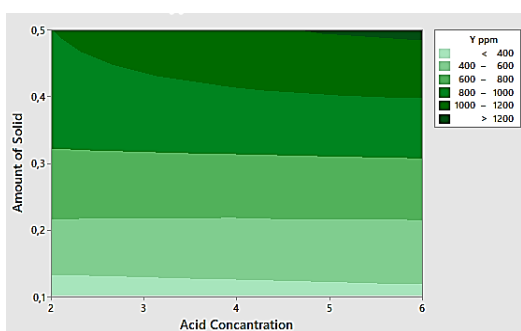


Figure 2. Contour plot of dissolved Y depending on solid amount and acid concentration.

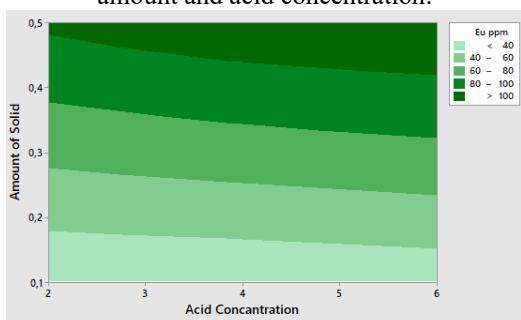


Figure 3. Contour plot of dissolved Eu depending on solid amount and acid concentration.

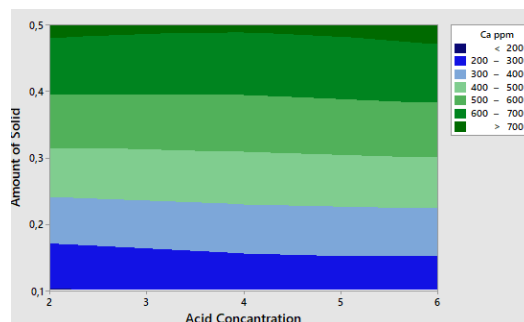


Figure 4. Contour plot of dissolved Ca depending on solid amount and acid concentration.

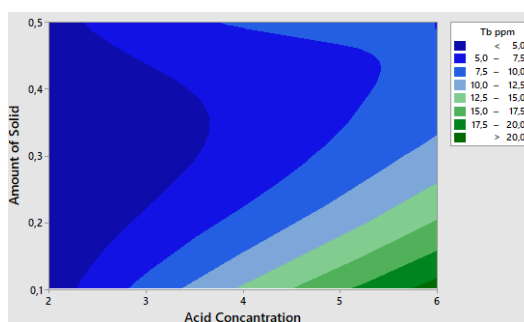


Figure 5. Contour plot of dissolved Tb depending on solid amount and acid concentration.

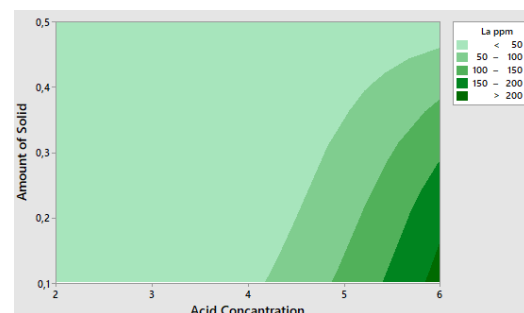


Figure 6. Contour plot of dissolved La depending on solid amount and acid concentration.

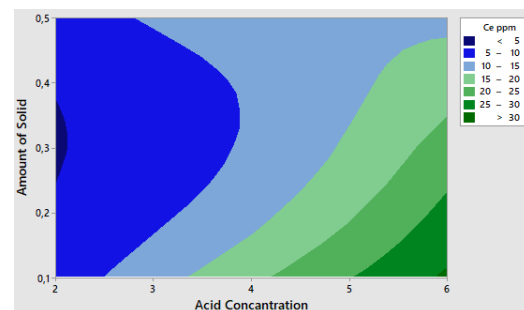


Figure 7. Contour plot of dissolved Ce depending on solid amount and acid concentration.

4. Conclusion

In this study, the effects of acid concentration and amount of solid on microwave-assisted leaching of fluorescent powder were examined, and the efficiency of the parameters was investigated with the mathematical model created.

The highest efficiency values were obtained when 6M HNO₃ and 0.1 g amount of solid were used in microwave assisted leaching process performed at 140°C and for 60 minutes to dissolve Y, Eu, Ca, Tb, La and Ce metals in the waste fluorescent powder. The leaching efficiencies were 98%, 99%, 77%, 94%, 78% and 91%, respectively.

In addition, a mathematical model has been created with the Response Surface Box-Behnken method. In the modeling performed for the dissolved Y, Eu, Ca, Tb, La and Ce concentrations, the model correlation coefficients were obtained as 98.31, 99.82, 99.86, 95.33, 87.23 and 94.51 respectively. For Y, Eu, and Ca metals, the acid concentration has less of an impact on the metal ion concentration. For Tb, La, and Ce, the acid concentration is a more effective parameter.

Thanks to the microwave-assisted leaching process, besides Y and Eu metals, Tb, La, and Ce metals bound to stable oxides can also be dissolved. Thus, there is no need for high-temperature processes such as alkali fusion for the solid that remains undissolved in the traditional leaching process. After performing the microwave-assisted leaching process, the metal ions that dissolved can be separated by solvent extraction.

Acknowledgment

Many thanks for material support to Exitcom Recycling and for raw material analysis support to Assoc. Dr. Şeref SÖNMEZ and Res. Asst. Samet KAPLAN.

This work is supported by YTU BAP 4691 project.

References

- [1] V. Innocenzi, I. De Michelis, F. Ferella, F. Beolchini, B. Kopacek, and F. Vegliò, "Recovery of yttrium from fluorescent powder of cathode ray tube, CRT: Zn removal by sulphide precipitation," *Waste Manag.*, vol. 33, no. 11, pp. 2364–2371, 2013, doi: 10.1016/j.wasman.2013.07.006.
- [2] S. G. Zhang, M. Yang, H. Liu, D. A. Pan, and J. J. Tian, "Recovery of waste rare earth fluorescent powders by two steps acid leaching," *Rare Met.*, vol. 32, no. 6, pp. 609–615, Dec. 2013, doi: 10.1007/s12598-013-0170-6.
- [3] Y. Wu, X. Yin, Q. Zhang, W. Wang, and X. Mu, "The recycling of rare earths from waste tricolor phosphors in fluorescent lamps: A review of processes and technologies," *Resour. Conserv. Recycl.*, vol. 88, no. 100, pp. 21–31, 2014, doi: 10.1016/j.resconrec.2014.04.007.
- [4] M. Al-Harashsheh and S. W. Kingman, "Microwave-assisted leaching - A review," *Hydrometallurgy*, vol. 73, no. 3–4, pp. 189–203, 2004, doi: 10.1016/j.hydromet.2003.10.006.
- [5] K. E. Haque, "Microwave energy for mineral treatment processes - A brief review," *Int. J. Miner. Process.*, vol. 57, no. 1, pp. 1–24, 1999, doi: 10.1016/s0301-7516(99)00009-5.
- [6] J. Lie, S. Ismajli, and J. C. Liu, "Microwave-assisted leaching of rare earth elements (Y and Eu) from waste cathode ray tube phosphor," *J. Chem. Technol. Biotechnol.*, vol. 94, no. 12, pp. 3859–3865, 2019, doi: 10.1002/jctb.6184.

- [7] N. N. Greenwood and A. Earnshaw, *Chemistry of the Elements 2nd Edition*. Butterworth-Heinemann, 1997.



CHARACTERIZATION AND EXTRACTION OF HEAVY METALS FROM MUNICIPAL SOLID WASTE INCINERATION FLY ASH

Jonas SCHUSTER^{1,2}, Burçak EBİN¹

¹Chalmers University of Technology, ²Hamburg University of Technology
Sweden, Germany

Keywords: municipal solid waste incineration, fly ash, hazardous waste, metal extraction, valuable metals

Abstract

This research focuses on the characterization of the fly ashes, determination of the metal species, extraction of the valuable metals, and reducing the leachability of heavy metals during landfilling. The results showed that 83 w% zinc, 100w% copper and 65w% antimony recovery is possible from the fly ash by a one stage leaching. In the case of low acidic leaching conditions, the leachate residue still contains a significant amount of leachable heavy metals which keeps the fly ash in hazardous waste classification. The heavy metal mobility are reduced after high acidic leaching conditions due to high extraction yield.

1. Introduction

Municipal solid waste incineration (MSWI) is the backbone of the waste management system in many countries to reduce the waste volume and produce energy. However, this approach comes with some drawbacks concerning the generated ash. The incineration process waste is separately collected as bottom and fly ash. Bottom ash (80wt%) is the main solid residue of the process that collected in the bottom of combustion chambers and mainly contains glass, metals, ceramics, and minerals. Meanwhile, fly ash consists of smaller particles, collected in the flue gas filtering sections and contains toxic chemical species such as metal compounds.

The fly ash is accepted as hazardous waste and thus treated and landfilled in specific conditions to eliminate the leachability of the heavy metals and minimize the environmental impact. Although MSWI fly ashes contain a high amount of metals, there is no industrial process to extract the metals due to limited knowledge of the metal compounds in the structure. Additionally, stabilization of the toxic metals in the MSWI fly ashes to minimize their leachability is another challenge.

2. Materials Methods

Fly ash samples were supplied by MSWI plants located in Sweden. Scanning electron microscopy, X-ray diffraction and X-ray absorption spectroscopy methods were used to characterize the fly ash.

Sulphuric acid and organic acid were used to extract metals including zinc (Zn), copper (Cu), aluminum (Al), magnesium (Mg), antimony (Sb), lead (Pb), etc. at room temperature for different leaching durations.

3. Conclusion

Characterization studies showed that the sample contains almost 0.6w% Zn, 0.7w% Cu, 2.8w% Al, 1.1w% Mg, 0.04w% Sb and 0.3 w% Pb together with CaSO₄, CaCl(OH), SiO₂, and their compounds as the main content as well as other metals in minor amounts. The valuable and toxic metals are mainly in complex oxide form together with other elements. However their chlorinated and sulphate compounds are also exist in the structure.

High extraction yields were reached for Zn, Cu, Mg, Al, Sb and Cd in one step leaching using both sulphuric acid and citric acids at room temperature. Pb was efficiently leached by only citric acid solution as expected due to insolubility properties of PbSO₄ which forms under sulphuric acid leaching.

After extraction of heavy metals by two different acids, the standard leachability test reveal that toxic metals in the fly ash are partly stabilized and their solubilities are lower than the standard limit. However, leachabilities of Zn and Cu are still higher than the limit and thus additional extraction stages are needed to recover them and reduce their mobilization.

Acknowledgment

This research was funded by Sweden's Research Council for Sustainable Development, FORMAS, Sweden (Project No: 2018-00947).

PRODUCTION OF METAL SULFIDES FROM FERROCHROME FLUE DUSTS AND INVESTIGATION OF THEIR ELECTROCHEMICAL PROPERTIES

Ozan AYDIN, Metin GENÇTEN, Burak BİROL

Yıldız Technical University
Türkiye

Keywords: Ferrochrome Flue Dusts, Metal Sulfides, Recycling, Supercapacitors, Electrode Materials

Abstract

In the present study, flue dusts obtained from ferrochrome alloys were treated with acidic solutions. Precipitation process was conducted by using thioacetamide as sulphur source. Electrochemical properties of the produced metal sulfides were analyzed.

1. Introduction

Recycling of metal oxides (MO) from the flue dust wastes generated during the production of ferrochrome alloys as value added products would increase the both importance and industrial applicability of these wastes. Recently, energy storage technologies emerge to higher efficiencies depending on the varying electrode materials. Although, the commercial electrode materials are composed of MO, currently metal sulfides (MS) gain importance depending on their specific electrochemical properties. Additionally, obtaining these sulfides from industrial wastes is a novel and significant process for the reduction of production costs of energy storage systems as well as the environmental pollution.

2. Materials and Methods

In the preliminary tests, flue dusts were treated with 1M HNO₃ solution at 50°C for 3 hours at 400 rpm. Leaching efficiencies of the metal oxides present in the flue dust were investigated by Atomic Absorption Spectroscopy (AAS). The dissolved metal ions were precipitated as their sulfides by the utilization of 0.5M thioacetamide at 70°C for 6 hours. Electrochemical properties of the produced MS were characterized by using of cyclic voltammetric (CV) method by preparing of coin cell type asymmetric supercapacitor. The tests were carried out between -0.4 and 1.5 V with 10 mV.s⁻¹ scanning rate.

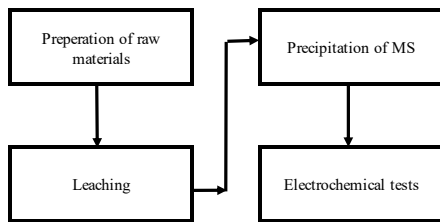


Figure 1: Flow chart of the experimental procedure

Table 1. Chemical analysis of the ferrochrome flue dust (wt %)

MgO	SiO ₂	Al ₂ O ₃	Cr ₂ O ₃	K ₂ O	ZnO	Fe ₂ O ₃	CaO	MnO	SO ₃ ⁻	Cl ⁻
37.9	28.8	8.5	6.1	6.0	4.4	2.8	0.6	0.5	2.4	1.0

3. Conclusions

Leaching efficiencies of ZnO and FeO from the flue dusts were determined as 91% and 53% respectively. Specific capacitance of the prepared asymmetric type supercapacitors consisting of ZnS anode was determined as 232.14 F.g⁻¹. Obtained results demonstrate that, the MS recovered from ferrochrome flue dusts has the potential to be used in supercapacitors as electrode materials.

References

- [1] J. Basson and J. Daavittila, High Carbon Ferrochrome Technology, Handb. Ferroalloys, Elsevier, (2013): pp. 317–363.
- [2] H. Estay, L. Barros and E. Troncoso, Metal Sulfide Precipitation: Recent Breakthroughs and Future Outlooks, Minerals, (2021)
- [3] R. Barik and P.P. Ingole, Challenges and prospects of metal sulfide materials for supercapacitors, Curr. Opin. Electrochem. 21 (2020) 327–334.

LI-ION BATTERY RECYCLING FOR INDUSTRIAL SCALE

Safiye TANRIVERDI^{1,2}, Berk GÜLÖRTEN², Mahmut KARADAŞ²

¹Istanbul University - Cerrahpasa, ²Proses Makine
Türkiye

Keywords: Li-ion Battery, Recycling, Lithium, Cobalt, Industrial Machinery

Abstract

Lithium-ion batteries are the most common type of battery today. It appears in many fields from electrical-electronic devices to electric vehicles. The raw material, waste, and recycling of a product with such high usage become important. Storing lithium batteries, which are classified as hazardous waste, is also a problem. For this reason, it must be recycled. And it requires special recycling line. In this study, the process of obtaining lithium carbonate from manually decomposed electric vehicle battery and renewable energy (solar energy, wind energy) storage battery will be discussed. The amounts of metallic copper and lithium carbonate obtained from two different battery types will be covered.

1. Introduction

There are different types of lithium-ion batteries according to their usage areas and desired performances. It basically consists of anode, cathode, and electrode. On average, lithium-ion batteries contain 1-15% Li, 6-60% Co, 15-50% Ni, 5-62% Mn, 10% Al, 15-20% Cu. ^[1] While one cell of the electric battery used in this study is approximately 320 g, one cell of the renewable energy storage battery is 498 g.

2. Materials and Methods

In this study, metallic copper and lithium carbonate amounts obtained from black mass separated from two different battery types were investigated. The battery cells, which were discharged to the appropriate limits, were dismantled manually. Aluminum foil, copper foil and plastic parts were dismantled from each other. The separated parts were dried at 230°C for 1 hour. The dried copper foils were grinded in the grinder for 60 seconds to provide a suitable environment for the separation of the black masses from the foil. When sieved with a 1 mm sieve, the bottom of the sieve consists of copper foil over the black mass sieve. However, this separation did not occur with 100% efficiency. In this study, the material on the sieve was melted in the induction furnace and recovered as copper metallic ingots, and the black mass was completely separated from the copper without passing into the molten metal.



*Li₂CO₃ from EV
Battery*

In the study on the electric vehicle battery, 162, 31 g of sieve material was melted in an induction furnace at 1000 degrees for 1 hour. As a result of the process, 77.87 gr metallic 99.95 purity copper was obtained, and 77.11 gr black mass powder was obtained separately from copper. This black mass was leached under suitable conditions and 1.90 g of lithium carbonate was recovered.

In the study on the renewable energy storage battery, 80.80 g of sieve material was melted in an induction furnace at 1000 degrees for 1 hour. As a result of the process, 49.88 gr metallic 99.95 purity copper was obtained, and 23.92 gr black mass powder was obtained separately from copper. This black mass was leached under suitable conditions and 2.30 g of lithium carbonate was recovered.



*Li₂CO₃ from Renewable
Energy Storage Battery*

3. Conclusion

Although physical separation of black mass is possible to a certain extent, pyrometallurgical separation of the entire black mass from the copper foil part is ensured. However, whether the process is adaptable to the industry can only be said by creating a feasibility report. Proses Makina, which is only mentioned as a part of industry-adaptive R&D studies, apart from lithium carbonate recovery; It also recovers cobalt, nickel, and manganese according to battery type by applying all of its chemical processes.

Reference

^[1] Gaines, L., Richa, K., Spangenberg, J., “Key Issues for Li-ion Battery Recycling”, Argonne National Laboratory, 2018.



RECOVERY OF END-OF-LIFE LITHIUM-ION BATTERY CATHODE MATERIALS IN ACIDIC MEDIA

Elif GÜLOĞLU¹, Mert ZORAĞA¹, Gökçe HAPÇI AĞAOĞLU¹, Ş. Samet KAPLAN²,
M. Şeref SÖNMEZ², Sebahattin GÜRMEZ², Gökhan ORHAN¹

¹Istanbul University-Cerrahpasa, ²Istanbul Technical University
Türkiye

Keywords: Recovery, Hydrometallurgy, Lithium-ion Batteries, Leaching

1. Introduction

Global lithium-ion battery (LIB) market has increased due to rapid growth of electric vehicle demands and energy storage industry. Besides the advantages of LIBs such as large energy density, high efficiency, high voltage, long cycle life, low self-discharge rate and being environmentally friendly; LIBs contain several toxic chemical components to disallow storage or incineration for dispose. Also, the metals contained in the battery have an important economic impacts, metallurgical values and critical primary sources due to several reasons.

2. Materials and Methods

In this study, 90 spent LIBs were collected and completely discharged in 1:1 CH₃COOH:H₂O solution for 24 hours. Then, components of the batteries were dismantled manually and cathode active powder striped from aluminium foil for further experiments. XRD, TG/DTA, ICP-MS analyses were carried out to characterize the cathode active powder which is the raw material of this study. The XRD pattern of the cathode powder shows the characteristic peaks of typical NMC materials (LiCo_{1/3}Ni_{1/3}Mn_{1/3}O₂). Leaching processes were performed in water-heated flask with 500 mL capacity with mechanical stirrer. Leaching experiments were carried out in H₂SO₄ medium in the range of 0.5-3 M concentration (with/without H₂O₂ addition), 25-80°C temperature and 250 rpm for 3 hours. Samples were taken from the reactor at 5-180 minutes and the samples were analyzed by ICP-MS to calculate leaching efficiency of Li, Co, Mn and Ni. When process was completed, the solution in the flask was filtered to separate the leach residues and the solution. To investigate the leaching efficiency depending on the process parameters, ICP-MS analyses were carried out. According to ICP-MS analyses, the leaching efficiency of Li, Co, Mn and Ni, were obtained. TG/DTA and XRD analyses were performed to investigate morphological and chemical properties of the leach residue.

3. Conclusion

The effect of leaching efficiencies of metals were investigated under the acid concentration, time, reaction temperature and H₂O₂ addition. With the increase of temperature and time, leaching behaviour of cathode materials affected positively.

Acknowledgements

This work was financially supported by the Scientific Research Projects Coordination Unit of Istanbul University-Cerrahpasa (Project number: 36028).



IS SUSTAINABILITY A PARADIGM FOR OCCUPATIONAL HEALTH AND SAFETY?

Murat Can OCAKTAN

UCTEA Chamber of Metallurgical and Materials Engineers
Türkiye

1. Introduction

Sustainability or sustainable development has become a threshold for the organizations that want to make sure social, economical or environmental diffractions during production process[1]. Sustainability is simply defined as “ability of being permanent”. “Sustainability and sustainable development” is mentioned thus and so, according to description of Bruntland Commission which is approved by academy[2]:

“Sustainable development is to provide current development without taking risks for future generations’s own abilities to development needs”

On the other hand paradigm concept was oftenly used in professional life. It is defined as “values sequence” in TDK dictionary[3]. It is not so wrong to say that , whole experiences and memories of an organization is relevant with cultural paradigm of an organization. It is not difficult to anticipate that paradigm shift is difficult as cultural transformation. “Paradigm Shift” concept was firstly used by Thomas Kuhn. Basic assumptions, key concepts and methodology of any kind of task can be supported by paradigm theory.Route map and basic goals of the task is also relevant with paradigm theory[4]. New business models are managed by different processes. Tasks are also accepted as a part of processes.

Nowadays, occupational health and safety is started to take into account as a managerialial process. Thus, sustainability has become an important issue for occupational health and safety process.

2. Sustainability and Paradigm

Sustainability can be defined as a paradigm for considering the future in the terms of social and economical diffractions[5]. Sustainability is simply used for keeping the current status. The concept that is being tried to be kept may become feared to make changes over time, and it transformed as a value for the organization. By managing the whole like this, this concept might turn into a paradigm.

Since occupational health and safety is a part of a professional life , social and economical status of working life can be affected by it. In order to manage an effective occupational health and safety

process, it is needed to manage fluctuations. Change management requires strong touches that will change the current status. Changing the current status means collapse of some structures or go out from comfort zone. In other words, it may be explained as touching to cultural values, so paradigms.

3. Sustainability in Occupational Health and Safety

Since current occupational health and safety philosophy needs to be pro-active, it strongly fits to bussiness format of sustainability. Interruption of decided activities in the field is the biggest enemy for sustainability. Sustainable management in terms of occupational health and safety can be proceeded under the perspective of organizational culture. Safety culture and organizational culture had an organic bond with each other. “Pro-active” term is also used for denoting the one level of organizational culture. Cultural classification of organizations was first made by Ron Westrum and expanded by James Reason [6,7]. Organizations were classified into three classes by Westrum. Westrum’s classification was given in below:

- ✓ Pathological
- ✓ Bureaucretic
- ✓ Generative

The main difference of classification of organizational culture is based on flow of information. Power oriented structure is observed in pathological cultures. In this culture knowledge is hidden, responsibilities are shrinked, novelty is crushed and poor cooperation is detected. Bureaucretic culture has a rule based structure. In bureaucretic cultures knowledge can be neglected, responsibilities are limited, novelty is evaluated as a problem and moderate cooperation is observed. Performance oriented structure belongs to generative culture. In this kind of culture, knowledge and risks are shared, responsibilities are defined clearly and high cooperation is present.

“Reactive” and “Proactive” culture levels were put in organizational culture classification. Reactive class is put between pathological and bureaucretic classes, proactive one is put between bureaucretic and generative classes. So new classification is listed as:

- ✓ Pathological
- ✓ Reactive
- ✓ Bureaucratic
- ✓ Proactive
- ✓ Generative

In order to discuss sustainability in the field of occupational health and safety, organizational culture level should be first examined.

4. Paradigm Change Stages in OHS Field

Implementation of new occupational health and safety issues by the intention of improvement in the field are not successful all the time. Individual and organizational readiness should be absolutely investigated before making interventions. State of change concept should be well built up regarding the organizational context. The stage of change concept should be well defined taking into account organizational contexts. Encouraging the top and middle management levels in terms of safety management are needed in order to make an efficient state of change assessment. Thus, conflict issues between production and safety may be depicted easily. There are different state of change models in the literature. The state of change model which is developed by Urlings and friends (1990) was based on social psychology and communication theory. This model consists of six separate stages given below [8].

- I. Giving attention to information
- II. Understanding information
- III. Changing attitudes
- IV. Changing intentions
- V. Changing behavior
- VI. Maintaining of new behavior

5. Obstacles in Front of Sustainability

In the upper part it is discussed that “how can we provide a paradigm change?”. Effective development cannot be expected to be observed without touching the person who is the hidden subject of the field. Generally sustainable development aim is to integrate social, economical and cultural policies in all scale. On the other hand it is not so wrong to say that “there are some obstacles in front of this aim”. These are listed as [8]:

- ✓ Economical and financial barriers,
- ✓ Innovational barriers,
- ✓ Social barriers,
- ✓ Poor monitoring and evaluation systems,
- ✓ Cultural barriers

6. Results

Continuous improvement concepts are an important element of the new occupational health and safety philosophy. Occupational safety and health studies carried out in the field by interacting the individuals. Old occupational health and safety philosophy were based on the solutions only initiated by technical improvements. After world war II, the importance of qualified individuals started to notice. And then requirement of a systematic approach was appeared. The establishment of each new system means that a paradigm shift. New systems also mean an improvement and the hardest side of the field studies is the protection of the improvements.

The issues in occupational health and safety area can be easily related to the sustainable development approach. The obstacles in front of sustainable development are also valid for occupational health and safety issues. Again mentioning the assessment of cultural level of the organization before starting to talk about sustainability. This aspect can be evaluated as cultural barrier from the view of sustainability. Another important issue is to include modern philosophies used in every function of an organization such as innovation in the work we do. Innovation barrier can be explained by lack of innovation initiated research philosophy. Poor monitoring and evaluation system's reflection on occupational health and safety area can be explained by inconvenient audit and observation system. Especially this mechanism is very important for feeding the management levels from the point of occupational health and safety philosophy. Social barriers can be related with unplanned growth of the organization, and they can cause unsustainable consumption and production patterns among the wealthy.

Finally, there is no doubt to say that each permanent improvement in occupational health and safety area can be named as a paradigm change. The main thing is not to constantly change the paradigm, but to make it permanent and sustainable.

References:

- 1- Jum'a L, Zimon D, Ikram M, Madzik P; “Towards a sustainability paradigm; the nexus between green practices, sustainability-oriented innovation and Triple Bottom Line”; International Journal of Production Economics 245 (2022), pp:1-13
- 2- <https://indigodergisi.com/2017/12/surdurulabilirlik-serisi-101/>, access date: 21.06.2022
- 3- <https://sozluk.gov.tr/>, access date: 13.05.2022



- 4- <https://www.thoughtco.com/what-is-a-paradigm-shift-2670671> , access date:23.05.2022
- 5- Basera N, “Sustainable Development: A Paradigm Shift with a Vision for Future”,International Journal of Current Research, Vol 8, Issue 09, pp:37772-37777, september 2016
- 6- Westrum R, “A Typology of Organizational Cultures”, Qual safety Health Care 2004, 13(SuppII),pp:22-27
- 7- METU PSY 662 Lecture Notes by Özkan, T; 2018
- 8- Barret, J,H; Haslam,R,A; Lee,G,K; Ellis,M;J; “Assesing attitudes and beliefs using the state of change paradigm- case study of health and safety appraisal within a manufacturing company”; International Journal of Industrial Ergonomics, 35 (2005), pp: 871-887
- 9- <https://www.researchgate.net/post/What-are-some-of-the-barriers-towards-achieving-sustainability>, access date: 22.06.2022



REMELTING BEHAVIOUR OF PURE AND AZ63 MAGNESIUM CHIPS

Pınar YÖRÜK¹, Bora DERİN², Mertol GÖKELMA¹

¹İzmir Institute of Technology, ²Istanbul Technical University
Türkiye

Keywords: Magnesium Recycling, Salt Flux, Oxidation

Abstract

Magnesium is widely used in many areas such as the automotive, aerospace, and medical industries. It has remarkable mechanical properties such as lightweight, strength, and creep resistance. The use of magnesium increases however the high oxidation tendency is a challenge in processing. Recycling of magnesium scraps is important due to the limited raw material accessibility, as well as environmental concerns. Magnesium is typically remelted under a salt flux (chloride and fluoride mix) which removes the surface oxides and other contaminants from the metal. This research focuses on the remelting behaviour of pure and AZ63 magnesium alloy in the form of chips. Magnesium chips were remelted under a salt flux to observe the effect of salt, temperature, and the salt factor. Fluxes with CaF₂, MgCl₂, KCl and NaCl were used and remelted at different temperatures (700°C, 750°C, 800°C and 850°C). Metal yield and coagulation efficiency were reported XRD (X-ray diffraction analysis), EDX (Energy Dispersive X-Ray Analysis), and TGA (Thermogravimetric Analysis) analysis were performed for the characterization of chips and remelted samples. The melting point and density of the salt fluxes were determined by the FactSage software.

1. Introduction

The use of magnesium and magnesium alloys has noticeably increased in recent years. Although magnesium has poor corrosion resistance and high cost, it is used in several fields due to its machinability, good creep resistance and strength [1]. Magnesium alloys have a variety of uses, including the automotive, aerospace, electronics, and aircraft industries [2]. Recycling of metals has gained importance due to the rising economic and environmental concerns [3]. The most important challenge in recycling of magnesium is metal losses during remelting due to its high oxidation tendency [4]. Therefore, magnesium is recommended to remelt under a salt flux. Flux 5 is commonly used in recycling processes which consists of a mix of chlorides (56% MgCl₂, 24% NaCl, 15% KCl) and fluorides (5% CaF₂) [5]. The use of the salt flux helps to increase the coalescence of metal droplets and to reduce the oxidation by covering the surface of the melt [6]. In addition, salt fluxes remove the oxide layer and other contaminants from the metal [7]. Machining waste of these alloys need an extra attention due to the large surface areas covered with the magnesium oxide and/or hydroxide [4]. This research focuses on the remelting behaviour of pure and AZ63 magnesium alloy in the form of chips.

2. Materials and Methods

Magnesium chips were created from the ingots (Pure and AZ63 shown in Table 1) to increase the surface area. Salt composition, temperature and stirring were selected as the parameters. The samples were remelted in a clay-bonded graphite crucible by a resistance heating chamber furnace at 700°C to 850°C. Flux5 was used for the remelting experiments in addition, five different amounts of CaF₂ addition were investigated (4wt%, 4.5wt%, 5wt%, 5.5wt%, 6wt%) at 850°C with a holding time of 15 minutes, to observe the effect of the F⁻ amount in the salt. The trials were performed with and without stirring to observe its effect on the coagulation and yield. After the remelting trials, the salt dross was washed out and the metal droplets were collected and dried to calculate the metal yield and the coagulation efficiency according to Eq. 1&2:

$$\text{Metal Yield(\%)} = \frac{\text{Mass of recovered metal}}{\text{Mass of the remelted scrap}} \times 100 \quad (\text{Eq. 1})$$

$$\text{Coagulation Efficiency (\%)} = \frac{\text{Mass of the biggest droplet}}{\text{Mass of recovered metal}} \times 100 \quad (\text{Eq. 2})$$

Table 1. Chemical compositions of the starting samples (wt%)

AZ63	Mg	Be	Fe	Mn	Al	Si	Ni	Cu	Zn
	90,2834	0,0012	0,0032	0,6628	5,6007	0,0033	0,0008	0,0003	3,4386
Pure Mg	Mg	Be	Fe	Mn	Al	Si	Ni	Cu	Zn
	99,9607	0,0001	0,0038	0,0181	0,0045	0,0048	0,0005	0,0019	0,0033

3. Conclusions

- Stirring caused heavy oxidation due to the contact with air and reduced the metal yield while it increased the coagulation due to the increasing contact between droplets.
- Behaviour of pure and alloyed magnesium is the same due to the differences of the melting temperature and the oxidation behaviour. The used salt flux (Flux5) showed higher metal yield for the pure magnesium.
- Although fluorine ion is known to increase the coalescence of metal droplets, increasing CaF_2 over 5% decreased the coagulation due to the oversaturation.

Acknowledgement

This research was funded by the Scientific and Technological Research Council of Turkey (TÜBİTAK) under the BİDEB-2232 program with the grant number 118C311.

References

- [1] Zhang, L. F. & Dupont, T. State of the Art in the Refining and Recycling of Magnesium, Trans Tech Publications, May 2007, Switzerland.
- [2] Tan, J. & Ramakrishna, S. Applications of Magnesium and Its Alloys: A Review, Applied Sciences, July 2021, Basel – Switzerland.
- [3] Luccia, R., Padillaa, L.R., Canteroa, S., Barilesa, R., & Oldanib, C. Refining of AZ91 Magnesium Alloy Obtained in Machining Chips Recycling, Procedia Materials Science, December 2015, Córdoba Capital – Argentina.
- [4] Ohmann, S., Ditze, A., & Scharf, C. Semi-Solid Remelting of Magnesium Chips, JOM, February 2018, Germany.
- [5] Rapiejko C., Mikusek D., Andrzejczak A., & Pacyniak T. Effect of Inoculant Emgesal® Flux 5 on the Microstructure of Magnesium Alloy AZ91C, Archives of Foundry Engineering, April 2019, Łódź – Poland.
- [6] Akbari, S. & Friedrich, B. Salt-Metal Interaction in Magnesium Recycling, International Workshop on Metal-Slag Interaction, September 2010, Yalta, Crimea – Ukraine.
- [7] Akbari, S. Göknelma, M. & Friedrich, B. Potential of Minimizing Magnesium Losses in Black Dross through Optimization of Salt Fluxes, IME Process Metallurgy and Metal Recycling, RWTH Aachen University, June 2009, Aachen – Germany.



SCRAP-SALT FLUX INTERACTIONS DURING RECYCLING PROCESSES

Irem Yaren ÇAPKIN¹, Adamantia LAZOU², Gabriella TRANELL²,
Mertol GÖKELMA¹

¹İzmir Institute of Technology, ²Norwegian University of Science and Technology
Türkiye, Norway

Keywords: Aluminium, Magnesium, Recycling, Salt flux

Abstract

Due to increasing environmental and economic concerns, the recycling of metals has been increasing in the last decades. Especially aluminium is one of the most common metals, saving up to 95% of energy when recycled. Magnesium is one of the most common alloying elements in aluminium alloys, contributing to oxidation behaviour. Both aluminium and magnesium have a high oxidation tendency, and this rises the necessity of salt flux usage during remelting. Salt fluxes remove oxides and other surface contaminants from the target metal. Salt fluxes allow molten metal pieces to coagulate and form the molten bath. Furthermore, it prevents further oxidation of the metal. The presence of fluorides increases the metal yield by promoting coalescence. Although metals and salts are frequently interacting in such processes, there is still a lack of knowledge of the final and intermediate products of the interaction reactions. This study aims to contribute to the literature with metal-salt interaction trials. This study investigates the interaction of aluminium and magnesium scraps with a salt flux. The salt flux consists of KCl, NaCl, and CaF₂. 5 different scrap categories were selected which are beverage can body and lid alloy, coffee capsule, aluminium foil, and magnesium AZ63 alloy chips. Remelting under the salt flux was performed at 800°C in a chamber electric resistance furnace in a carbon crucible. Metal-salt interactions were studied under XRD (X-ray diffraction analysis), and XRF (X-ray fluorescence spectroscopy) analysis.

1. Introduction

Recycling of metals has become more important due to rising economic and environmental concerns. Recycling aluminium saves up to 95% of energy when recycled. The global aluminium production was 56 Mtons in 2009 and increased to 97 Mtons in 2020.¹ The rate of this increase can be reduced by secondary production. Magnesium is a common alloying element in aluminium which unfortunately affects the oxidation behaviour of the melt significantly. The remelting of both aluminium and magnesium is generally performed under a salt flux due to their oxidation tendency.² Salt fluxes remove the contaminants from the metal and protect the melt from oxidation. In addition, it provides the coalescence of metal droplets in the molten bath.^{3,4}

Typically, chlorides (NaCl, KCl, MgCl₂) and fluorides (CaF₂, Na₃AlF₆, KF, NaF, MgF₂) are used in salt fluxes. The addition of fluoride promotes coagulation by separating the oxide film and reducing the interfacial tension between the molten salt and the metal.⁵ However, fluoride does not dissolve in water and the NaCl/KCl system but the mixture of NaCl/KCl salts dissolves in water.³ This study aims to understand the reactions occurring between the metal and salt during the recycling processes.

2. Materials and Methods

KCl, NaCl, and CaF₂ are used as the salt flux in this study. NaCl/KCl ratio was chosen as 70:30wt% and CaF₂ was added 2wt%. The remelting trials were performed at 800°C in a chamber electric resistance furnace. 5 different scraps were selected with different alloys.

The samples: beverage can body (3104 alloys), beverage can lid (5182 alloys), coffee capsule (1000series alloy), aluminium foil (8011 alloys), magnesium AZ63 alloy.



The samples were separately remelted under the salt flux in a graphite crucible. After melting the salt dross was washed out on a filter paper which filtered the non-metallic inclusions which formed during the remelting. After the filter cake (inclusions) were dried, they have examined under XRD and XRF analysis.

3. Conclusions

The following conclusions are drawn after analysing the XRD and XRF results:

- AlF_3 and MgF_2 were observed because of the reactions between oxides and F^-
 $2\text{Al}_2\text{O}_3(\text{s}) + 12\text{F}^- = 4\text{AlF}_3(\text{l}) + 3\text{O}_2(\text{g})$
 $2\text{MgO}(\text{s}) + 4\text{F}^- = 2\text{MgF}_2(\text{l}) + \text{O}_2(\text{g})$
- MgO and MgAl_2O_4 were observed in Mg containing aluminium scraps in addition to Al_2O_3
- CaF_2 doesn't dissolve in water unlike chlorides and accumulates on the filter after washing, therefore CaF_2 was observed in all XRD results

Acknowledgement

This research was funded by the Scientific and Technological Research Council of Turkey (TÜBİTAK) under the BİDEB-2232 program with the grant number 118C311

References

- [1] Global Aluminium Recycling, <https://greenbuilding.world-aluminium.org/uploads/media/1257424460GlobalAluminiumRecyclingBrochure.pdf>
- [2] Hiraki T, Miki T, Nakajima K, Matsubae K, Nakamura S, Nagasaka T. Thermodynamic Analysis for the Refining Ability of Salt Flux for Aluminum Recycling. *Materials* (Basel). 2014 Jul 30;7(8):5543-5553. doi: 10.3390/ma7085543
- [3] Gül, S., Dittrich, R. & Friedrich, B. KCl-reduced salt application in aluminium recycling, European Metallurgical Conference 2013 (EMC), Weimar/Germany
- [4] Akbari, S. & Friedrich, B. Salt-Metal Interaction in Magnesium Recycling, International Workshop on Metal-Slag Interaction, September 2010, Yalta, Crimea - Ukraine
- [5] Roy, R. R. & Sahai, Y. Interfacial tension between aluminum alloy and molten salt flux. *Materials Transactions, JIM* 38, 546–552 (1997)

TIN RECOVERY FROM ELECTROLYTIC TINNING LINE (ETL) SCRAPS

Gizem KAVUK¹, Anıl AGADANGİL¹, Miyase Özlem KÖYBAŞI ÖZUÇAK¹,
S. Samet KAPLAN¹, M. Şeref SÖNMEZ²

¹TOSÇELİK, ²Istanbul Technical University
Türkiye

Abstract

In the current study, Sn containing scraps from Toscelik tin plating plant was recovered almost completely by pyrometallurgical methods. Two different scraps were evaluated in this study. One is slag from Sn melting furnace, the second one is anode slime from tin coating. Sn slag contained around 85 wt% Sn while anode slime contained around 43 wt% Sn. These two scraps were recovered alone, and also by mixing at different ratios. At both scenario, Sn was recovered at 99% efficiency having suitable purity of use as Sn anodes.

Introduction

In electrolytic tinning line (ETL), tin is coated on stainless steel surface for durability, and corrosion protection purposes. In this process, two different Sn coating scraps (anode slime, and Sn melting slag) were obtained. Anode slime mainly consisted of SnO₂, and slag contained Sn metal itself. In this study, it was aimed to recover Sn from these scraps using pyrometallurgical methods [1, 2].

Materials and Methods

Carbon black was used as reductant, while Na₂CO₃ and SiO₂ were used as fluxing agent. Experiments were conducted in a muffle furnace at temperature range of 900°C-1100°C. Fireclay pots were used to recover metallic tin from these scraps.



Figure 1. Sn recovered from the scrap.

Table 1. Chemical analysis of recovered tin.

Element	Weight %
Sn	99,6691
Ag	0.00529
Bi	0.05627
Co	0.00076
Cr	0.00049
Cu	0.05053
Fe	0.05256
Sb	0.10214

Conclusion

Tin scraps from ETL process were recovered. It was casted as anode that was suitable for tinning process was given in Figure 1. In addition, chemical analysis of recovered Sn was shown in Table 1.

References

1. Habashi, F., (1997), Handbook of Extractive Metallurgy, V. II, Primary Metals, Tin, Wiley-VCH, p. 683.
2. Pollnow, D. L. B., (1977) Tinplate, and electrolytic tinning at the Iscor works, Vanderbijlpark, Journal of The South African Institute of Mining and Metallurgy, p. 126-131.



INVESTIGATION OF DISSOLUTION CONDITIONS OF YTTRIUM (Y) AND EUROPIUM (EU) IN FLUORESCENT WASTES

Utku HATİPOĞLU, Ayşegül BİLEN, Muhlis Nezih SARIDEDE

Yıldız Technical University
Türkiye

Keywords: Rare Earth Elements, Recovery, Fluorescent powder, Leaching

Abstract

Rare earth elements (REEs) are used in a variety of applications, including electronic devices, rechargeable batteries, magnetic equipment, and optical products. In the production of REEs from ore or secondary sources, hydrometallurgical methods are preferred. One of the main secondary REE sources are waste fluorescent lamp powders. Because the phosphor powders in fluorescent lamps contain a high concentration of REE, they are excellent raw materials for recycling. In this study, the leaching with various acids was carried out to extract Y and Eu from REEs in the phosphor powders in fluorescent lamps. The effect of acid type (HNO₃, H₂SO₄, HCl), acid concentration (0.5, 1, 2, 4, 6M), H₂O₂ concentration (0.5, 2, 4M), temperature (25, 52.5, 80 °C), leaching time (30, 60, 180, 270, and 360 min), and solid/liquid ratio (1/100, 3/100, 5/100) on the leaching efficiency were investigated. The results showed that increasing the acid concentration, time, and temperature had a positive effect on leaching efficiency, whereas increasing the solid/liquid ratio had a negative effect. The highest Y extraction yield was obtained after 360 minutes of leaching at 80°C using 6M HNO₃ and a 1/100 solid/liquid ratio. Sulfuric acid gives high Y and Eu efficiency and low Ca dissolution. Therefore, it is the most suitable solvent.

1. Introduction

REEs are elements in the periodic table with atomic numbers 57-71, also known as lanthanides, along with scandium and yttrium. REEs are elements that have become crucially significant in our technological world due to their unique magnetic, phosphorescent, and catalytic properties, and they are used in magnetic products, rare earth phosphor production, catalysts, and hydrogen storage materials. They are also widely used as they play various roles in metallurgical production. Materials containing REE as an additive are generally stable, corrosion-resistant, and lightweight [1,2].

The demand for rare earth elements is increasing as technology advances. Considering the increase in consumption, an increase in the amount of waste produced

is also expected. REEs can be recycled from NdFeB magnets, red mud, electronic waste, and fluorescent lamps. Inorganic acid leaching methods are widely used in the recovery of REE from these wastes [3,4]. Advantages of leaching methods are; creation of selective reactions with the use of different leaching agents, low energy consumption, no waste gas and flue dust formations and provide economic benefit from waste materials [5].

Takahashi et al. [6] applied a single step leaching process to fluorescent lamp powders. They applied dissolution at 70°C for 1 hour, with a pulp density of 3% w/v and acid concentration of 3N H₂SO₄, and as a result, Y 92%, Eu 98% and Ca 24% yield were obtained.

Wu et al. [7] applied leaching to fluorescent lamp powders for 4 hours at 50 °C. Pulp density of 2% w/v, stirring speed of 360 rpm and acid concentration of 1N HCl + 2 mL H₂O₂/500 mL was used. As a result of the study, 99.9% Y, 61.2% Eu and 35.8% Ca efficiencies were obtained.

Lee et al. [8] applied leaching process with different acids at same conditions. At 70 °C, 1 hour leaching time and 0.02 g/mL solid/liquid ratio conditions; 1N HCl gives Y 15.5% and Eu 95.5 %, 1N HNO₃ gives Y 13.68% and Eu 96.35%, 1N H₂SO₄ gives Y 23.72 and Eu 100% yield.

The aim of this research is to examine the effects of leaching parameters on the leaching efficiency of REEs in the extraction of compounds containing rare earth elements from fluorescent wastes.

2. Experimental Procedure

2.1 Materials and Equipment

Waste fluorescent lamp powder was provided by Exitcom Recycling. The waste powder was sieved from 45 µm to separate any broken glass particles present. The powder below 45 µm was dried for 8 hours at 107°C. Table 1 shows the chemical composition of the waste powder analyzed by ICP-MS.

Table 1. Chemical composition of the fluorescent waste phosphor powder

Y	Eu	La	Tb	Ce	Gd	Ca
10.30	0.79	1.47	0.71	1.37	0.79	25.9

Dissolving acids used in the experiments are H₂SO₄, HCl, and HNO₃. Hydrogen peroxide was used as oxidizing agent. All chemicals are Merck quality.

Leaching tests carried out in the incubator. Pregnant solution after leaching was analyzed by Perkin Elmer AA800 Atomic Absorption Spectrometer.

2.2 Experimental Studies

The weighed fluorescent powder were mixed with various acids and dissolved in 250 mL glass bottles by mechanical agitation in an incubator under controlled temperature. The operating parameters examined in the leaching tests were temperature, leaching time, acid type, acid concentration, hydrogen peroxide concentration and solid/liquid ratio. Table 2 summarizes the variable parameters used in the leaching processes.

Table 2. Leaching parameters

Parameters	Values
Temperature (°C)	25, 52.5, 80
Time (min)	30, 60, 180, 270, 360
Acid type	HNO ₃ , H ₂ SO ₄ , HCl
Acid concentration (M)	0.5, 1, 2, 4, 6
H ₂ O ₂ concentration (M)	0.5, 2, 4
S/L ratio (g/mL)	1/100, 3/100, 5/100

Glass bottles were agitated at 200 rpm during the experiment. Samples were taken at determined intervals and filtered by a filter paper. Filtered solution were prepared for AAS analysis by diluting with pure water.

The leaching efficiency was calculated based on the Y and Eu content in the sample as follows:

$$\text{Leaching efficiency (\%)} = \frac{w_f}{w_i} \times 100 \quad (1)$$

where w_f weight of metal in the final solution and w_i weight of metal contained in the initial sample.

3. Results and Discussion

The results of the experiments were compared depending on the acid types. The conditions that provide the highest Y and Eu yield and the lowest Ca yield were determined for each acid type.

Leaching efficiencies of Y, Eu, and Ca at 52.5°C using 5/100 with HNO₃ can be seen in Figs. 1, 2, and 3. According to the figures, leaching efficiencies increased

with increasing the acid concentration values. Also, an increase in reaction time increases leaching efficiency, but after 270 min. the efficiencies almost stay steady. Because the dissolving capacity of the acid is nearly completed after that time. Acid can dissolve more ions at higher acid concentrations and so higher efficiency can be obtained. H₂O₂ addition to the solution is increases leaching efficiency, but increasing H₂O₂ concentration decreases leaching efficiency.

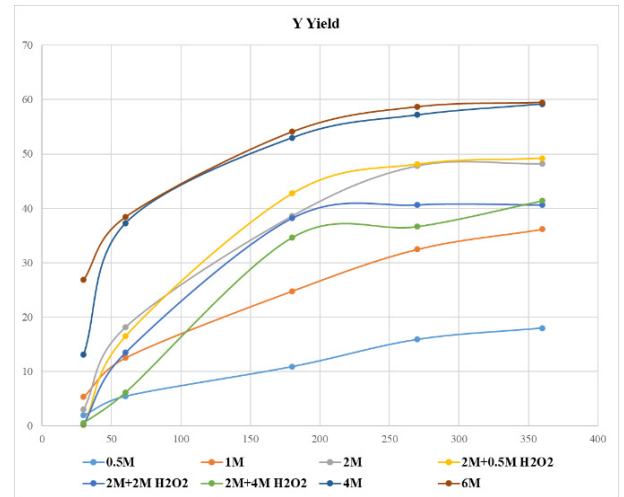


Figure 1. Leaching efficiency of Y at 52.5 °C 5/100 with HNO₃

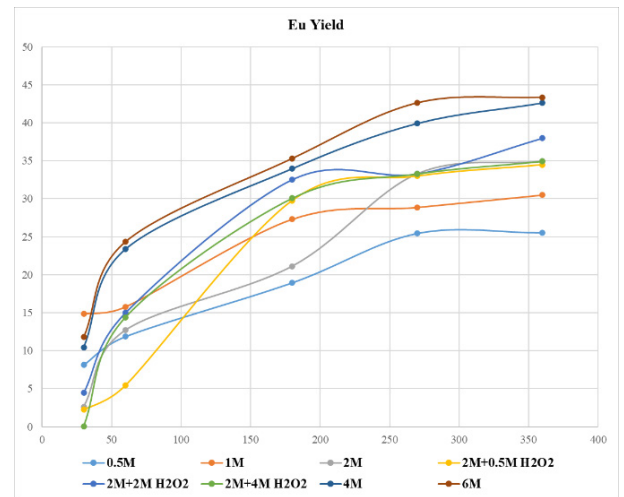


Figure 2. Leaching efficiency of Eu at 52.5 °C 5/100 with HNO₃

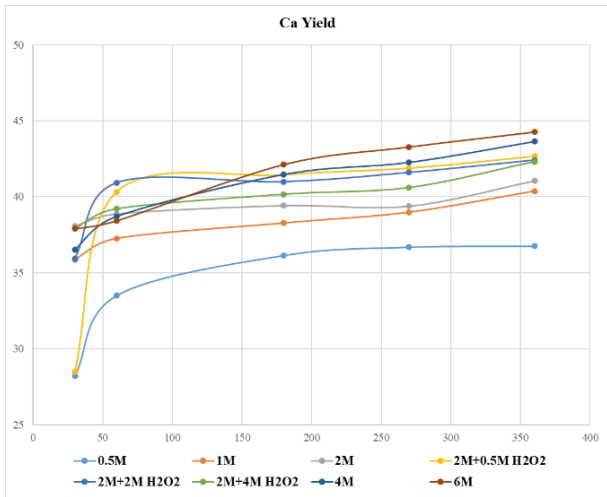


Figure 3. Leaching efficiency of Ca at 52.5 °C 5/100 with HNO₃

The effect of acid type on leaching efficiency is compared in Figs. 4, 5 and 6 under the same conditions. Accordingly, higher Y and Eu efficiencies and lower Ca efficiency were obtained in the dissolution process with H₂SO₄ compared to the others. As can be seen from Fig. 4, the dissolution of Ca is not much affected by the leaching time, but according to Figs. 5 and 6, the efficiency of Y and Eu increases with the dissolution time.

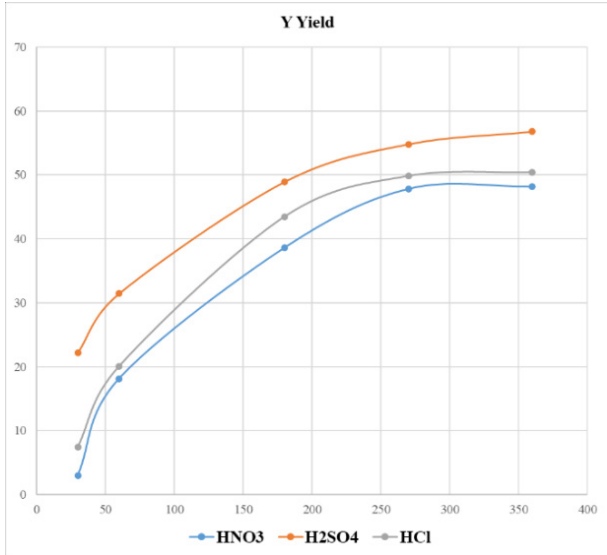


Figure 4. Leaching efficiency of Y at 52.5 °C 5/100 with 2M acid concentration

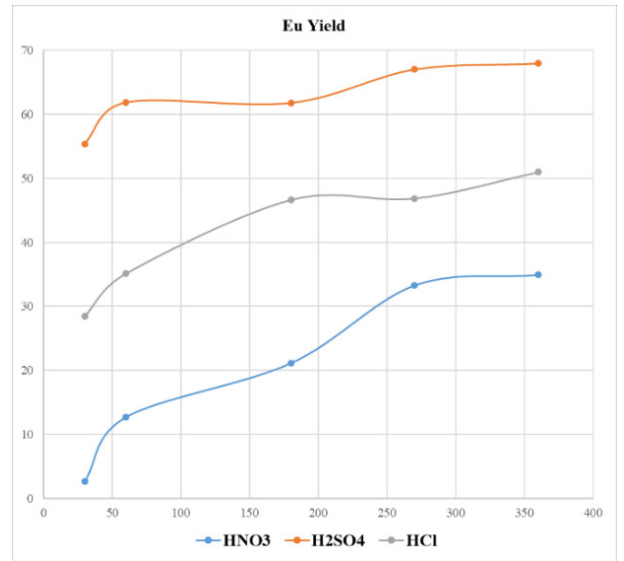


Figure 5. Leaching efficiency of Eu at 52.5 °C 5/100 with 2M acid concentration

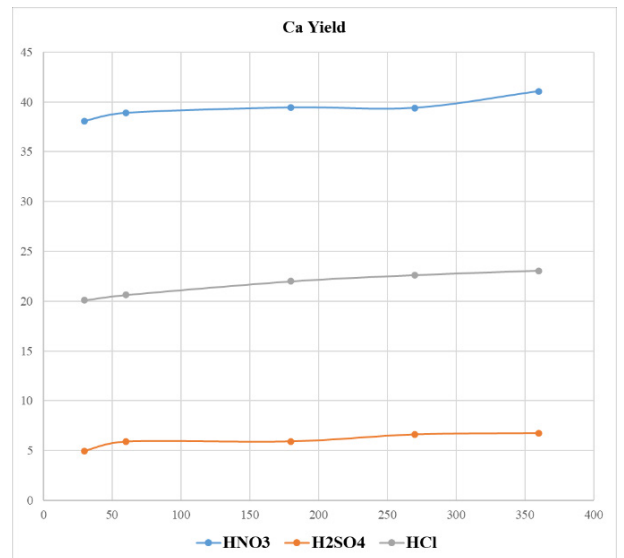


Figure 6. Leaching efficiency of Ca at 52.5 °C 5/100 with 2M acid concentration

The lowest Ca efficiency was obtained with H₂SO₄ (Fig. 4). In addition, as H₂SO₄ concentration increases, Ca efficiency decreases (Fig. 7). This can be explained by the low solubility product of calcium. Accordingly, Ca²⁺ ions interact with SO₄²⁻ ions in the solution, and CaSO₄ is

formed. When the solution contains a high amount of SO_4^{2-} , the precipitation of Ca^{2+} ions is further increased.

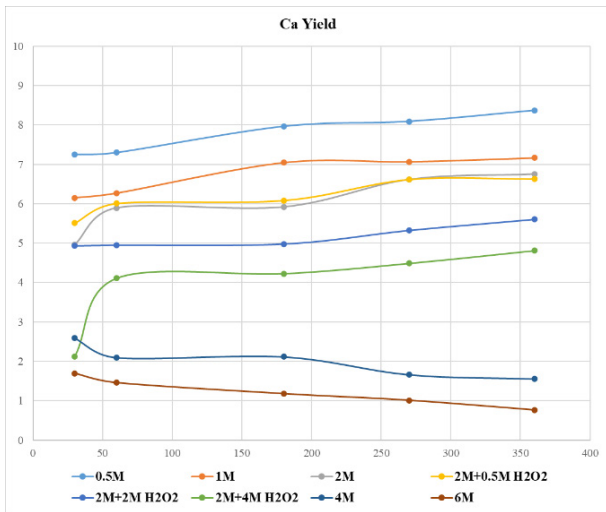


Figure 7. Leaching efficiency of Ca (H_2SO_4 , 52.5°C, 5/100)

The effects of temperature on leaching efficiency are shown in Fig. 8. Increasing temperature has a positive effect on leaching efficiencies. The highest yield values were obtained at 80°C. This is because temperature increases the rate of movement of ions in solution. Fast-moving ions interact more with each other. As a result, higher efficiency values are achieved.

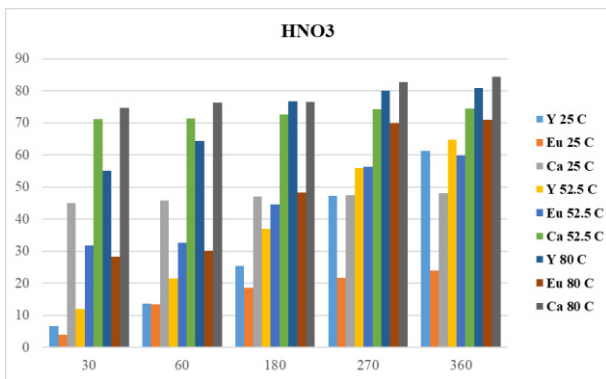


Figure 8. Leaching efficiency of Y, Eu, and Ca (2M HNO_3 , 1/100)

The effect of the solid/liquid ratio on leaching efficiency is shown in Fig. 9. The highest yield was obtained at a 1/100 solid/liquid ratio. The higher amount of acid per unit of solid waste powder in the solution increases the dissolving capacity. When a large amount of powder is present, it remains undissolved in the solution. This reduces efficiency.

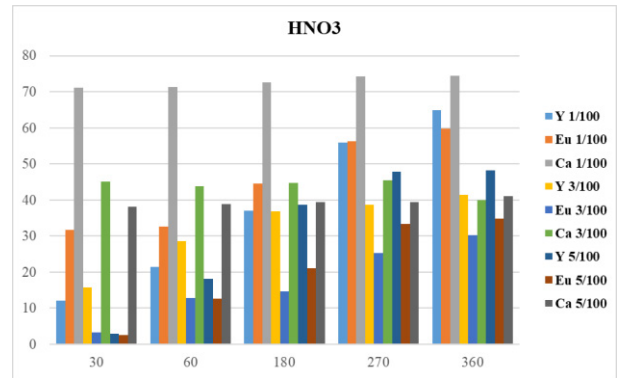


Figure 9. Leaching efficiency of Y, Eu, and Ca (2M HNO_3 , 52.5°C)

4. Conclusion

The results show that increasing acid concentration and dissolution time increase the leaching efficiency of Y, Eu and Ca. However, as time progresses, the rate of increase in efficiency slows down and after a while, increasing the time has no effect.

Low solid/liquid ratio and high temperature also positively affect the leaching efficiency for each acid type.

H_2SO_4 is the most effective acid type compared to HNO_3 and HCl. The reason for this is that sulfuric acid gives high Y and Eu efficiencies as well as the lowest Ca efficiency. It is desirable that the dissolution of Ca is low because high cation concentration in the medium will adversely affect the SX yield to be made later.

Acknowledgment

Thanks to Exitcom Recycling for raw material support. Also, thanks to Berfu Demirtaş, Çiğdem Ece Can, Derya Şahin, İlke Üçer, Sefa Umut Kaya and Şevval Gençal for their support to experimental process.

References

- [1] V. Balaram (2019). Rare earth elements: A review of applications, occurrence, exploration, analysis, recycling, and environmental impact. *Geoscience Frontiers*, 10(4), 1285-1303.
- [2] M. Şahiner, vd. *Dünyada ve Türkiye’de Nadir Toprak Elementleri (Nte)*. Maden Tetkik Ve Arama Genel Müdürlüğü Fizibilite Etütleri Daire Başkanlığı, Ankara, Türkiye, Maden Serisi, 5.
- [3] A. Erdem, vd. (2021). Nadir Toprak Minerallerinin Fiziksel Ayrılması ve Flotasyonu: Derleme", *International Journal of Pure and Applied Sciences*, vol. 7, no. 2, pp. 321-345, Jul., doi:10.29132/ijpas.922811

- [4] İ. H. Arslan (2001). Madencilik Özel İhtisas Komisyonu Raporu: Nadir Toprak Elementleri-Kıymetli ve Yarı Kıymetli Taşlar (DPT: 2620- ÖİK: 631). Endüstriyel Hammaddeler Alt Komisyonu Genel Endüstri Mineralleri III (Nadir Toprak Elementleri-Kıymetli ve Yarı Kıymetli Taşlar)
- [5] C. Tunsu, M. Petranikova, M. Gergorić, C. Ekberg, and T. Retegan, “Reclaiming rare earth elements from end-of-life products: A review of the perspectives for urban mining using hydrometallurgical unit operations,” *Hydrometallurgy*, vol. 156, pp. 239–258, 2015, doi: 10.1016/j.hydromet.2015.06.007.
- [6] T. Takahashi et al., “Separation and Recovery of Rare Earth Elements from Phosphor Sludge in Processing Plant of Waste Fluorescent Lamp by Pneumatic Classification and Sulfuric Acidic Leaching,” 2001.
- [7] Y. Wu et al., “Selective recovery of Y and Eu from rare-earth tricolored phosphorescent powders waste via a combined acid-leaching and photo-reduction process,” *Journal of Cleaner Production*, vol. 226, pp. 858–865, Jul. 2019, doi: 10.1016/j.jclepro.2019.04.137.
- [8] C. H. Lee et al., “Integrated process development for the recovery of Europium and Yttrium from waste fluorescent powder,” *Journal of Material Cycles and Waste Management*, vol. 19, no. 3, pp. 1235–1243, Jul. 2017, doi: 10.1007/s10163-016-0515-y.



THE RECYCLING MODEL OF ZIRCONIA & ALUMINA WASTE IN IRON - STEEL PLANTS

Oğuzhan SAKARYA, Uğur CENGİZ

Bilecik Demir Çelik A.Ş.
Türkiye

Keywords: Zirconia, Alumina, Circular Economy, Steel, Sustainable Production

Abstract

According to the steel production data of 2021, Turkey is the 7th largest steel producer in the world and the largest steel producer in Europe. The consumption and production demand of the iron and steel industry causes the problem of raw material and energy availability. However, it creates serious opportunities in terms of demand for alternative raw materials and sustainable waste management & reduction of environmental impacts. According to the data of the Turkish Statistical Institute (TUIK), it has been stated that approximately 25,000 tons of zircon has been used in our country in 2020, and the refractory and ceramics industry has been explained as two important sectors in which the use of zircon is intense, 98% of which is imported. Zircon is a very important raw material for these two sectors in terms of high temperature and mechanical properties. In Bilecik Iron and Steel, 15,000 zirconia nozzle (~24,9 tons) waste is generated annually, approximately 3,5 tons is zirconia waste and 16,7 tons is alumina waste.

In this study, 1) minimizing the waste of the zirconia nozzles used and creating less waste, one step closer to our goal of being a green production facility, 2) ensuring the transition from the linear economy model to the circular economy model, 3) to provide raw materials to the completely imported zircon & alumina market and to contribute to the country's economy by reducing foreign dependency, 4) to expand zircon & alumina recycling or recycling activities in another field and to ensure that other companies create a recycling culture, 5) it is aimed to reduce environmental effects such as CO₂ emission, energy using and pollution of water resources, which occur as a result of the synthesis of zircon by the Kroll Method, by recycling zircon. 6) it is aimed to reduce environmental effects such as CO₂ emission, red mud, bauxite, sodium hydroxide (NaOH) energy use and pollution of water resources, which occur as a result of the synthesis of alumina with the Bayer process, by alumina recovery. In order to achieve the above-mentioned goals, firstly, the zirconia nozzle changing parameters in the continuous casting machine (CCM) were checked and new parameters were determined in order to reduce the waste at the out point.

Then, zirconia nozzle wastes were collected with a qualified waste collection approach and these wastes were categorized as alumina, zirconia and metal sheet wastes suitable for their purpose. Post-mortem analyzes were carried out for the collected zirconia & alumina wastes, and the product classes were determined and the feedback of the sector representatives was evaluated. As a result of this study, a total of \$ 195,000 financial gain was obtained from the recycled waste. In terms of the environmental aspect (Life Cycle Assessment), 113,9 tons of water, 63 MWh of energy were recovered, and 43,9 tons of carbon emissions and 35 tons red mud, 30 tons sodium hydroxide were prevented.

1. Introduction

1.1. Zirconia & Alumina Wastes in Iron and Steel Plants Formation

In this project, where we adopt the boutique symbiosis approach instead of heap recycling, our priority is to reduce waste on site. For this reason, field studies were carried out at the source in order to minimize the waste of tundish zirconia nozzles. At the same time, the hybrid structure, which is basically formed by the combination of 3 different materials, has been separated in a controlled manner and categorized within itself. Undesirable impurities such as slag and steel stuck to the body were detected and cleaned. As a result of the separation, three types of products emerged as indicated in Figure 1: alumina, zirconia and metal waste. Alumina and zirconia constitute the refractory materials of the structure and their qualities are preserved during separation. With the qualified separation method, which is one of our main goals of the project, it is ensured that the useful and the useless parts of the material are not mixed.



Figure 1. Zirconia & Alumina Wastes in Iron and Steel Plants Formation

2. Conclusion

The result of this study, zirconia nozzle wastes were collected with a qualified waste collection approach and these wastes were categorized as alumina, zirconia and metal sheet wastes suitable for their purpose. Post-mortem analyzes were carried out for the collected zirconia & alumina wastes, and the product classes were determined and the feedback of the sector representatives was evaluated. As a result of this study, a total of \$ 195,000 financial gain was obtained from the recycled waste. In terms of the environmental aspect (Life Cycle Assessment), 113,9 tons of water, 63 MWh of energy were recovered, and 43,9 tons of carbon emissions and 35 tons red mud, 30 tons sodium hydroxide were prevented.

3. References

- [1] M. Lundberg, Environmental Analysis of Zirconium Alloy Production, Uppsala Üniversitesi (Uppsala University, December 2011, İsveç.
- [2] V. Köroğlu, Refrakter Üretimine Yönelik Olarak Zirkonya Stabilizasyon Çalışmaları, Y. Lisans Tezi, İstanbul Teknik Üniversitesi, 2013, İstanbul, Türkiye.

AN INVESTIGATION ON CALCIUM ALUMINATE CEMENT PRODUCTION USING TWO TYPES OF BAUXITE, ALUMINA AND MARBLE WASTE

C. Betül EMRULLAHOĞLU ABİ, Esra ÖZGÜVEN, Serkan KESKİN

Afyon Kocatepe University
Türkiye

Keywords: Bauxite; Marble Waste; Calcium Aluminate Cement

Abstract

In this study, calcium aluminate cement production was investigated using two types of bauxite, calcined alumina, and marble waste. The laboratory work essentially consists of characterization of the raw and tailing materials, crushing, grinding, preparation of different recipes, heat treatment at different temperatures and finally characterization of the products by XRD analysis. The samples containing Seydişehir bauxite ore and China sinter bauxite were sintered at 1100, 1200 and 1300 °C. The mixtures containing alumina were sintered at 1250 and 1320 °C. Compositions of two types of bauxite and marble tailing having Al₂O₃: CaO molar ratio of 1:1, 2:1, 3:1, 4:1, 5:1 and 6:1 was formulated. In the products containing Seydişehir bauxite ore and sintered at 1100 and 1200 °C; the XRD patterns confirmed the presence of free CaO, C₂AS, C₁₂A₇, CA, CA₂ and Al₂O₃ phases. The higher the Al₂O₃: CaO molar ratio of the samples sintered at 1100 °C the smaller the free CaO, C₁₂A₇ and CA₂ peaks intensities while the higher the C₂AS peaks intensities. There is no important change at the peaks of CA and Al₂O₃ phases. SiO₂ content of the ore caused to C₂AS and CAS₂ formation. The higher the sintering temperatures, the higher C₂AS peaks intensities. In the products containing China sinter bauxite and sintered at 1100, 1200 and 1300 °C; the XRD patterns confirmed the presence of free CaO, C₂AS, CAS₂, CA, C₁₂A₇ and Al₂O₃ phases. The higher the Al₂O₃: CaO molar ratio, the smaller the gehlenite and free CaO peak intensities and the higher the anortite and alumina peak intensities. The higher the sintering temperatures, the higher C₂AS and Al₂O₃ peaks intensities. In the products containing Seydişehir bauxite ore and China sinter bauxite and sintered, iron element may be replaced in the atomic structure of the C₂AS and CAS₂ phases in the form of C₂(A, Fe) S and C (A, Fe) S₂. In the products containing calcined alumina and sintered at 1320 °C, the XRD patterns confirmed the presence of free CaO, CA, CA₂ and Al₂O₃ phases. The higher the Al₂O₃ %, the smaller the free CaO and CA peak intensities while the higher the CA₂ and Al₂O₃ peak intensities as expected. Since there is very small amount of silica in the materials C₂AS and CAS₂ phases were not found in sintered samples.

1. Introduction

High Alumina Cement (HAC) was investigated almost 150 years ago, and its high early strength development behavior was discovered in the early 1900's. Commercial exploitation of HAC commenced in the 1920's as a binder for sea water resistant concrete. The usage of HAC of HAC, as a refractory binder, was first made by Atlas Aluminate Cement Co. of USA through the introduction of a castable product. HAC, however,

till the 1950's, implied a product based on limestone and bauxite which, in today's terminology, is a moderate purity HAC. High purity HAC, which is based on high purity limestone and alumina, was developed, and introduced to the market by Lafarge and Alcoa [1-3]. The Associated Cement Cos. Ltd, (ACC) started commercial production of high alumina cement (HAC) in the beginning of the 1970 is commercial production commenced with the manufacture of moderate purity HAC and subsequently, in the middle of the 1970's high purity HAC was added to the product range [4]

Bauxite has been used in increasing quantities for the manufacture of special quick-hardening high-alumina cements. These cements are prepared in blast furnaces, rotary kilns, or electric furnaces by the fusion of bauxite and limestone. The resulting product consists of a mixture of calcium aluminate and calcium - aluminum silicates with some iron oxide and possibly some calcium silicates. Hydraulic, high-purity calcium aluminate cement for applications requiring high refractoriness is made from Bayer-process alumina and high-grade limestone with 2 % or less impurities; contains 70-80 % Al₂O₃ and 18-25 % CaO. Calcium aluminate (high alumina) hydraulic cements are designed for use as binders in monolithic refractory concrete construction [5].

HAC's are considerably expensive than Portland Cements (approx. fifteen times expensive than PC in Turkey). Therefore, during the last three decades, extensive works has been carried out by the researchers. The effect of raw materials, the process parameters and pyro-processing technique on the quality of both moderate and high purity HAC has been reviewed. The role of additives in broadening the sintering range of HAC, particularly for moderate purity product, is discussed [4]. The utilization of ferronickel electro reduction furnace slag to produce HAC is investigated through laboratory and pilot-scale tests. The process followed consisted of smelting reduction of slag mixture with low-grade diasporic bauxite and limestone. In the laboratory-scale trials the main process parameters were defined, concerning raw materials proportions, kinetics of the reduction and cooling rate of the product. The presence of a carbon-containing iron bath enhances FeOx reduction from slag. According to the results of the laboratory tests, pilot-scale heat treatments were carried out in a 5-t electric arc furnace (EAF) and about 4 t of final mixture were produced [6].

In this study, HAC production was investigated using two types of bauxite, calcined alumina, and marble waste The laboratory work essentially consists of characterization of the raw and tailing materials, crushing, grinding, preparation of different recipes, heat treatment at different temperatures and finally characterization of the products by XRD analysis.

2. Experimental Procedure

The raw materials of China sinter bauxite, Seydişehir raw bauxite and gibbsite were supplied by Sörmaş Refractory (Bilecik, <math><90\mu\text{m}</math>), Seydişehir Aluminum (Konya, <math><4\text{ cm}</math>) respectively. Seydişehir bauxite ore taken from stockpile of Eti Aluminum Seydişehir Plant contains boehmite, hematite, clay, quartz, and minor amounts of residual minerals. Bauxite ore sample was crushed by jaw and roll crushers and then ground in the porcelain mill containing alumina ball for two hours. Gibbsite calcined at 400 °C for 2 h. was used in the experiments. Fine marble tailing from Reis Marble Factory (Afyon) was used as a source of limestone additive. It contains calcite and minor amounts of dolomite. Marble tailings in the form of original and calcined at 900 °C for 4 h were used at recipes containing bauxites and gibbsite calcined at 400 °C respectively. All materials were screened using sieve (90 μm) Chemical analysis of the materials used in this study are given in Table 1.

Table 1. Chemical analysis of the materials used in CAC production

%	China Sinter Bauxite	Seydişehir Bauxite ore	Seydişehir Gibbsite	Marble Tailing
Al ₂ O ₃	88.50	57.04	65.10	0.67
Fe ₂ O ₃	1.50	17.97	0.011	0.44
SiO ₂	5.40	7.23	-	0.18
TiO ₂	3.50	2.36	0.005	-
CaO	0.20	0.86	-	51.70
MgO	0.20	-	-	0.40
Na ₂ O	0.07	-	0.32	-
K ₂ O	0.13	-	-	0.21
CO ₂	-	0.75	-	-
V ₂ O ₅	-	0.025	0.0016	-
P ₂ O ₅	-	0.114	-	-
S	-	0.051	-	-
LOI	-	12.49	34.56	46.04
Total	99.50	98.89	100.00	99.64

Compositions of two types of bauxite and marble tailing having Al₂O₃: CaO molar ratio of 1:1, 2:1, 3:1, 4:1, 5:1 and 6:1 were formulated. The powders were mixed by dry milling using ball mill with alumina ball for 30 minutes, added 5% water, granulated, and then shaped using dry press. The samples were sintered at 1100, 1200 and 1300 °C sintering temperatures for 2 h. The mixtures containing calcined alumina and marble tailing were also applied the same procedures and sintered at 1250 and 1320 °C. The phases in the sintered samples were identified by XRD analysis (Cu K α , Model XRD 6000, Shimadzu, Kyota, Japan).

3. Results and Discussion

X-ray diffraction studies of the samples containing Seydişehir bauxite ore. XRD patterns of the sintered samples at 1100 °C containing Seydişehir bauxite ore are presented in Fig.1.

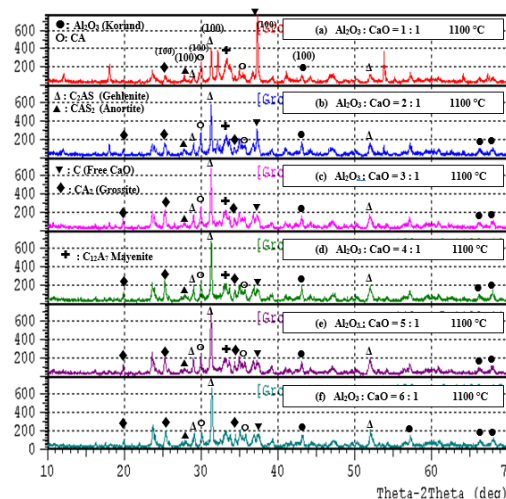


Figure 1. XRD patterns of the sintered samples at 1100 °C containing Seydişehir bauxite ore

The phases identified in figure 1. are free CaO (C, $2\theta=37.5^\circ$), gehlenite (C₂AS, $2\theta=31.5^\circ$), mayenite (C₁₂A₇, $2\theta=33.8^\circ$), grossite (CA₂, $2\theta=25^\circ$), anortite (CAS₂, $2\theta=28^\circ$) and CA (CaO, $2\theta=30^\circ$). The higher the Al₂O₃: CaO molar ratio, the smaller the free CaO, C₁₂A₇ and CA₂ peaks intensities while the higher the C₂AS peaks intensities. There is no important change at the peaks of CA and Al₂O₃ phases. SiO₂ content of the ore caused to gehlenite and anortite formation.

XRD patterns of the sintered samples at 1200 °C containing Seydişehir bauxite ore are presented in Fig.2.

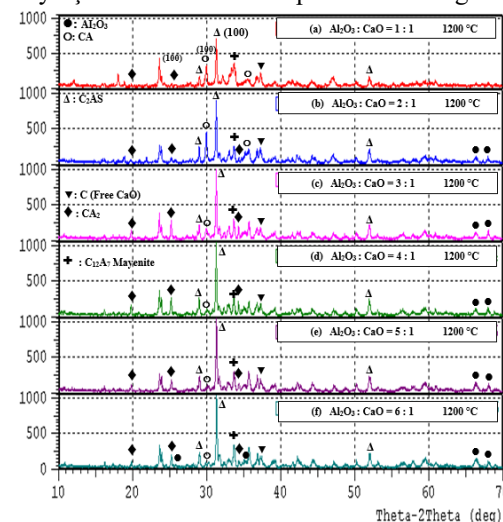


Figure 2. XRD patterns of the sintered samples at 1200 °C containing Seydişehir bauxite ore

The phases identified in Figure 2. are also free CaO, A, CA, CA₂, C₁₂A₇ and C₂AS. The higher the Al₂O₃: CaO molar ratio, the smaller the CA peaks intensities while the higher the CA₂ and C₂AS peaks intensities. There is no important change at the peak intensities of C₁₂A₇, free CaO and Al₂O₃ phases. SiO₂ content of the ore caused to gehlenite formation. The higher the sintering temperatures, the higher C₂AS peaks intensities.

Iron element may be found in the atomic structure of the C₂AS and CAS₂ phases in the form of C₂(A, Fe)S and C(A, Fe)S₂. X-ray diffraction studies of the samples containing China sinter bauxite

XRD patterns of the sintered samples at 1300 °C containing

China sinter bauxite are presented in Fig 3.

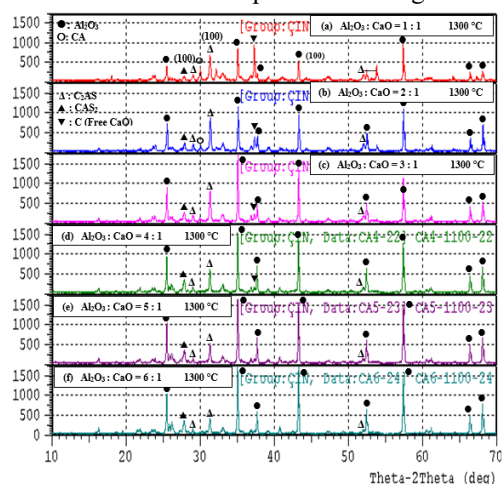


Figure 3. XRD patterns of the sintered samples at 1300 °C containing China sinter bauxite

The phases identified in figure 3. are free CaO, A, CA, CAS₂ and C₂AS. The higher the Al₂O₃: CaO molar ratio, the smaller the CA and free CaO peaks intensities while the higher the CA, A and CAS₂ peaks intensities. Peak intensity of the C₂AS phase increased first but then decreased. SiO₂ content of the bauxite ore and sinter bauxite caused to C₂AS and CAS₂ formation.

XRD patterns of the sintered samples at 1200 °C containing China sinter bauxite are presented in Fig.4.

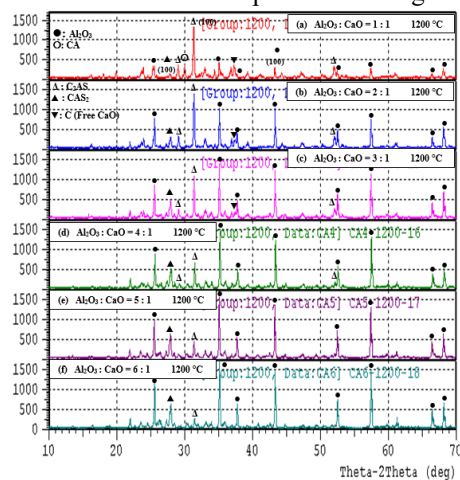


Figure 4. XRD patterns of the sintered samples at 1200 °C containing China sinter bauxite

The phases identified in figure 4. are also free CaO, A, CA, C₂AS and CAS₂. The higher the Al₂O₃: CaO molar ratio, the smaller the CA and C₂AS peaks intensities while the higher the Al₂O₃ and CAS₂ peaks intensities. SiO₂ content of the bauxite ore and sinter bauxite caused to C₂AS and CAS₂ formation. The higher the sintering temperatures, the higher C₂AS and CAS₂ peaks intensities.

Iron element may be found in the atomic structure of the C₂AS and CAS₂ phases in the form of C₂(A, Fe)S and C(A, Fe)S₂. XRD patterns of the sintered samples at 1300 °C containing China sinter bauxite are presented in Fig.5.

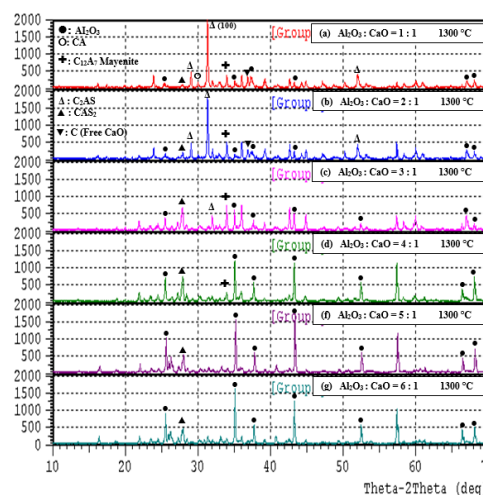


Figure 5. XRD patterns of the sintered samples at 1300 °C containing China sinter bauxite

The phases identified in figure 5. are free CaO, A, CA, C₁₂A₇, C₂AS and CAS₂. The higher the Al₂O₃: CaO molar ratio, the smaller the CA and CA peaks intensities while the higher the A and CAS₂ peaks intensities. Peak intensity of the C₁₂A₇ phase increased first but then decreased. C₂AS phase is shown only at Al₂O₃: CaO, 1:1 and 2:1 molar ratio. SiO₂ content of the bauxite ore and sinter bauxite caused to C₂AS and CAS₂ formation. The higher the sintering temperatures, the higher C₂AS and A peaks intensities.

3.1. X-ray diffraction studies of the samples containing Seydişehir Bayer Process Alumina

XRD patterns of the sintered samples containing Seydişehir Bayer Process alumina are presented in Fig.6.

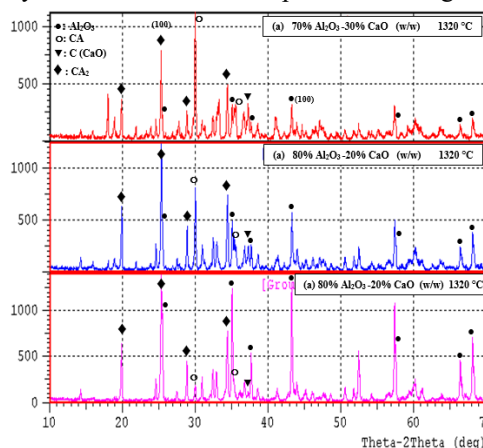


Figure 6. XRD patterns of the sintered samples containing Seydişehir Bayer Process Alumina

In the products containing Seydişehir Bayer process alumina and sintered at 1320 °C, the XRD patterns confirmed the presence of free CaO, CA, CA₂ and alumina (Al₂O₃) phases. The higher the Al₂O₃ %, the smaller the free CaO and CA peak intensities while the higher the CA₂ and Al₂O₃ peak intensities as expected.

Since there is very small amount of silica in the materials C₂AS and CAS₂ phases were not found in sintered samples.

4. Conclusion

The conclusion of this study was made as follows:

1. In the products containing Seydişehir bauxite ore and sintered at 1100 and 1200 °C; the XRD patterns confirmed the presence of free CaO, C₂AS, C₁₂A₇, CA, CA₂ and Al₂O₃ phases. The higher the Al₂O₃: CaO molar ratio of the samples sintered at 1100 °C the smaller the free CaO, C₁₂A₇ and CA₂ peaks intensities while the higher the C₂AS peaks intensities. There is no important change at the peaks of CA and Al₂O₃ phases. SiO₂ content of the ore caused to C₂AS and CAS₂ formation. The higher the sintering temperatures, the higher C₂AS peaks intensities.
2. In the products containing China sinter bauxite and sintered at 1100, 1200 and 1300 °C; the XRD patterns confirmed the presence of free CaO, C₂AS, CAS₂, CA, C₁₂A₇ and Al₂O₃ phases. The higher the Al₂O₃: CaO molar ratio, the smaller the gehlenite and free CaO peak intensities and the higher the anortite and alumina peak intensities. The higher the sintering temperatures, the higher C₂AS and Al₂O₃ peaks intensities.
3. In the products containing Seydişehir bauxite ore and China sinter bauxite and sintered iron element may be replace in the atomic structure of the C₂AS and CAS₂ phases in the form of C₂(A, Fe)S and C(A, Fe)S₂.
4. In the products containing calcined alumina and sintered at 1320 °C, the XRD patterns confirmed the presence of free CaO, CA, CA₂ and Al₂O₃ phases. The higher the Al₂O₃ %, the smaller the free CaO and CA peak intensities while the higher the CA₂ and Al₂O₃ peak intensities as expected. Since there is very small amount of silica in the materials C₂AS and CAS₂ phases were not found in sintered samples

References

- [1] Robson, T.D.; High alumina cements and concretes, Wiley and Sons, New York, 1962
- [2] G. Maczura, L. D. Hart, R. P. Heilich and J. E. Kopanda; Refractory Cements, Ceramics Science Engineering Proceedings, 1983.
- [3] W. H. Gitzen, L. D. Hart and G. Maczura; Properties of Some Calcium Aluminate Cement Composition, J. of American Ceramic Society, 40(5), 1957, pp, 158-167
- [4] Chakraborty I.N., Chattopadhyay A.K., Manufacture of high alumina cement an Indian experience, Calcium Aluminate Cements 2001, Proceedings of the International Conference on Calcium Aluminate Cements (CAC), held at Heriot-Watt University, Edinburgh, Scotland, UK, 16-19 July 2001, pp, 25-33
- [5] Ceramic Industry, January 1995, pp.78
- [6] E. Dourdoines, V. Stivanakis, G.N. Angelopoulos, E. Chaniotakis, E. Frogoudakis, D. Papanastasiou, D.C. Papamantellos; High Alumina Cement Production from FeNi-ERF Slag, Limestone and Diasporic Bauxite, Cement and Concrete Research, 34 (2004) 941-9



ALUMINIUM BLACK DROSS UTILIZATION VIA PYROMETALLURGICAL AND HYDROMETALLURGICAL OPERATIONS

Umay ÇINARLI, Ahmet TURAN

Yeditepe University
Türkiye

Keywords: Aluminium, Alumina-based ceramic, Black dross, Hydrometallurgy, Pyrometallurgy

Abstract

Aluminium dross has two subgroups as white dross and black dross according to metallic aluminium content. White dross is a secondary source of aluminium because of its high metallic aluminium content. However, black dross has a low metallic aluminium content (<25wt.%) and, it is usually disposed in dumping areas. In this study, it is aimed to develop a simple technique for the evaluation of aluminium black dross in the form of alumina-based ceramic materials by pyrometallurgical and hydrometallurgical processes.

1. Introduction

High energy consumption is required in the production of primary aluminium from bauxite ores, which makes secondary aluminium production very critical. Aluminium dross is a waste of pyrometallurgical processes and, it contains metallic Al, Al₂O₃, other metal oxides, metal halides and some other compounds such as AlN. The aim of this study was to determine the optimum conditions for the evaluation of black dross through hydrometallurgical and pyrometallurgical operations. Investigated process is the combination of calcination and leaching operations and, experimental studies were conducted with different acids to see their effects on product quality and recoveries [1-3].

2. Materials and Methods

In the first series of the experimental studies, the black dross was calcined at temperatures between 700 °C and 1100 °C to remove halide-based impurities by evaporation and to convert its metallic Al content into Al₂O₃. In the second series of the experiments, both the original black dross and the calcined black dross were leached in different solutions such as distilled water, HCl, H₂SO₄ and HNO₃ to obtain a pure alumina-based filter cake. In addition, the sinterability of the alumina-based ceramics (between 1350 °C and 1550 °C, 600 MPa uniaxial compaction pressure) was investigated under argon atmosphere and for 60 minutes.

3. Conclusion

After leaching experiments, an alumina-based ceramic containing approximately 36.8% Al₂O₃, 61.4% MgAl₂O₄ with 1.8% Na₂FeO₄, which might be available to use as a spinel refractory in steel smelting furnaces, was obtained in the experiment carried out in a solution containing 10 mL H₂SO₄ and 40 mL distilled water (3.5 M). According to the results obtained in the sintering studies, the density value of the sample sintered at 1550 °C was 3.15 g·cm⁻³ and the hardness value was 69.58 HV.

Acknowledgment

The authors are pleased to acknowledge the financial support for this research from Yalova University, Scientific Research Projects Department under grant number 2019/YL/0002.

References

- [1] O. Yücel, E. Car, UCTEA Metallurgy Journal, 175 (2015) 35-43.
- [2] K. Tripathy, S Mahalik, C. K. Sarangi, B. C. Tripathy, K. Sanjay, I. N. Bhattacharya, Minerals Engineering, 137 (2019) 181-186.
- [3] P. E. Tsakiridis, P. Oustadakis and S. A. Leonardou, Journal of Environmental Chemical Engineering 2013; 23-32.



RECYCLING OF ALUMINIUM USED BEVERAGE CANS: DECOATING AND SELF-HEAT GENERATION

Musa ORUÇ¹, Emine Bengü KAYA¹, Umay ÇINARLI², Tuğçe ERGÜL²,
Ahmet TURAN², Onuralp YÜCEL³, Erman CAR⁴

¹Yalova University, ²Yeditepe University, ³Istanbul Technical University,
⁴Insertec Thermal Solutions
Türkiye, Spain

Keywords: Used beverage cans; Aluminium; Decoating; Rotary tilting furnace

Abstract

Aluminium used beverage can (UBC) is one of the most important resources to produce aluminium metal in upstream secondary aluminium production. Beverage cans have organic-based dye and lac layers (VOC, volatile organic compounds) which provide visual quality and protection on underlying metal. One option on UBC recycling is the application of smelting after decoating operation which is a pyrolysis at high temperatures in special furnaces. Another option is the directly smelting of UBCs without decoating operations. In the present study, self-heat formation values, which arise because of the burning of those organic layers, during the direct smelting were tried to calculate. Laboratory scale experiments were carried out with increasing smelting temperature and, TGA and DSC systems were used to measure emitted and consumed heat and weight changes during the smelting of UBCs. Furthermore, modern decoating methods were investigated in this study as well in comparison to direct smelting.

1. Introduction

Currently, the aluminium industry has always been at the top due to the need for materials that are lightweight and easy to form, suitable for their intended use. Manganese (Al-Mn) AA3104 and magnesium (Al-Mg) AA5182 alloys in aluminium beverage cans provide features such as wear resistance, corrosion resistance, hardness and strength. Worldwide, approximately 1.5 million tons of aluminium beverage cans are consumed every year. The recycling of aluminium beverage cans started in the seventies as a result of the "Ban the Can" campaign. Direct smelting is usually preferred by smelters by using tilting rotary furnaces. Rotary furnaces are very popular particularly in the smelting of VOC-containing aluminium scraps because of two reasons; (1) various types of scraps (and their blends) can be smelted by means of rotary furnaces without any previous scrap preparation steps and (2) it is possible to use the energy coming from the burning of VOCs through both feeding oxygen by lances and by using oxy-burners. As reported in the literature and in industrial practice, direct smelting without decoating of UBCs causes the loss of aluminium metal. Burning results in the oxidation of the aluminium (and the formation of slag phase) and, it is a unreversible reaction. Pre-melting preparation processes of UBCs have an important place in the valorisation of aluminium. Pre-smelting preparation processes are as the following; classification, degreasing, lac-dye removal (decoating), separation of ferrous parts, compacting and preheating. Lac-dye coating layers on cans are usually removed (decoated) before smelting of UBCs to prevent the effects of burning of VOCs and inclusion formation. Decoating is briefly the pyrolysis of VOCs under controlled atmosphere and, it is done in special furnaces in particularly large-scale plants. It has some advantages: smelting efficiency increases, removed moisture prevent blasting in following smelting stage, smelting off gas is cleaner, less flux use for smelting and less slag (dross) formation. However, the most important disadvantage of the process is the cost of decoating furnaces.

2. Materials and Methods

In the experimental studies for the direct smelting of UBCs, samples were heated-smelted at the temperatures from 300 °C to 800 °C for 60 minutes in a muffle furnace with/without 50% KCl-50% NaCl flux addition. Moreover, a TGA-DSC system was utilized to observe both lac-dye removal temperature and generated heat which can be useful as an additional heat source to smelt UBCs. The TGA-DCS tests were done under nitrogen atmosphere up to 1000 °C.

3. Conclusion

Direct smelted samples showed a remarkable weight loss (5.92wt.%, up to 400 °C). With increasing temperature, weight loss values decreased because of the oxidation of aluminium (2.32% at 800 °C). In this experiment, slag formation was observed. On the other hand, TGA-DSC tests (under nitrogen at 600 °C) resulted in the obtaining of an aluminium structure, which did not contain oxide, with a weight loss value of 3.28% by weight after VOC removal.



CIRCULAR ECONOMY APPROACH FOR EVALUATION OF MILL SCALE USING AL RESIDUE AS REDUCTANT

Selçuk KAN, Kağan BENZEŞİK, Onuralp YÜCEL

Istanbul Technical University
Türkiye

Keywords: mill scale, recycle, aluminum dross

Abstract

With the increasing high production amounts in the iron-steel and aluminium industries the amount of waste and slag is increasing. In iron and steel production, iron oxide-based waste materials called mill scale are formed in the processes before hot rolling and continuous casting. In aluminum production and melting processes, aluminum is highly trapped in slag called dross. In this study, the iron in mill scale was recovered by the aluminothermic reduction method.

1. Introduction

Mill scale is a by-product of the iron and steel industry. It occurs on the surface of the material after heat process and it contains mainly iron oxides and low amount of metallic iron. Total iron composition is nearly 70% wt. depending on the process.

Aluminum dross is basically the oxide on the melted aluminum. Due to the movement of the aluminum bath during the degassing process, aluminum oxide breaks and entraps the metallic aluminum in it. In this study, mill scale is reduced by aluminum via self-propagating high temperature synthesis (SHS) method. Addition of aluminum obtained from dross as reductant and CaO are investigated.

2. Materials and Methods

Mill scale contains 70 wt.% Fe, Al (99 wt.% purity), Al dross contains 65 wt.% Al and CaO that obtained from CaCO₃ (96.78 wt. % purity) are used in this study.

The effect of aluminum amount on reduction efficiency was investigated. Afterward, CaO was added to increase the iron reduction yield. The purpose of adding CaO is to form calcium aluminate (CA) containing slag, which has a lower melting point, by combining CaO with Al₂O₃. Later, the amount of metallic Al was reduced, and the missing part was completed by using Al dross which is aluminum rich byproduct obtained by recycling aluminum melting drosses.

All experiments are aimed to produce 120 g Fe. Therefore, stoichiometric amount of reductant was determined by calculating the amount of Al sufficient to reduce the mill scale. Excess Al was used in some experiments. Al dross was used to reduce the cost as excess Al.

3. Conclusion

All the experiment parameters and the results are given in Table 1. Iron content was analyzed with optic emission spectroscopy (OES) device.

Table 1. Experiment parameters and the results.

Experiment	Stoichiometric Al (%wt.)	CaO (% wt.)	Stoichiometric Al Dross (%wt.)	Product (g)	Iron Content (wt. %)
1	110	-	-	100.7	96.5
2	120	-	-	109.3	94.4
3	110	5	-	95.6	97.2
4	110	10	-	101	96.6
5	120	5	-	105.8	94.6
6	120	10	-	106.4	95.0
7	100	-	10	84.3	96.7
8	100	-	20	97.1	93.4

4. References

- [1] B.T. Polat, İ.E. Öner, S. Kan, K. Benzeşik and O. Yücel, Journal of Sustainable Metallurgy, 8 (2022) 851-862.
- [2] M. Buğdaycı, M. Alkan, A. Turan and O. Yücel, High Temperature Materials and Processes, 37 (2018) 889-898
- [3] N. Gade, G. Verma, R. Sen and U. Pandel, Procedia Earth and Planetary Science, 11 (2015) 319-324



LEAN SUSTAINABLE GREEN SUPPLY CHAIN MANAGEMENT IN LIGHT METALS CASTING INDUSTRY

Ümmet AYYILDIZ^{1,2}

¹Prometal, ²Bilecik Şeyh Edebali Üniversitesi
Türkiye

Keywords: Global Warming, Sustainability, Green Transformation, Carbon Footprint, Supply Chain Management in Light Metals

Abstract

The world continues to warm rapidly. This global warming poses a serious threat to all living things. Against this threat, 200 states came together with the Climate Change Conference under the some roof of the United Nations and aimed to take measures against this problem. In Turkey, especially as one of these 200 states, it has started awareness studies in all sectors for the problem of global warming. The casting industry is one of the sectors with high energy use and carbon emissions. Therefore, it has become important for the future of the world to create action plans for climate change in the casting industries of developing countries and to ensure positive integration into the fight. In this context, it is necessary to optimize efficiency and energy use in the realization of casting activities. We, too, take into account the sustainability commitments of our customers as part of our operational excellence and sustainability efforts. In this direction, in order to increase our production efficiency, efficiency increases are aimed with lean production methods and transition to ISO 50001 energy management model is planned. In addition, the energy points to be followed in production were determined by taking digitalization steps for the control and development of energy use and, accordingly, energy efficiency through data. In addition to all these, it is aimed to reduce carbon emissions by evaluating alternative energy methods in high electricity and natural gas use in the casting sector. State incentives are used to ensure that the machinery infrastructure is suitable for green energy as the financial resources of the studies. In order to make all these works sustainable, awareness studies are carried out by training all working teams. Awareness of green transformation has been provided in the supply chain, and the carbon footprint has been taken into account in the total quality management targets of the enterprise. Thus, in order to reduce the carbon footprint to minimum levels,

integration with green transformation and the fight against climate change has been ensured by all process owners under the continuous control and supervision of the management.

Introduction

Sustainability and sustainable development are contestable concepts, like democracy, truth and justice [1]. There is an increasing acknowledgment that organizations must address the issue of sustainability in their operations. Sustainability is commonly described as utilizing resources to meet the needs of the present without compromising future generations' ability to meet their own needs [2]. In the early few years, sustainability initiatives focused on environmental issues only, but they have now moved to adopting triple topic (i.e. environment, economic and social) approach. There are two locution that link sustainability and SCM concepts closely: sustainable supply chain management (SSCM) and green supply chain management (GSCM) [3]. Wagner, Schaltegger, and Wehrmeyer [4] believe that SSCM strategies' effects are still unclear and may cause positive or negative economic performance. Because it does not clearly discriminate between different types of economic structure, it seems to support growth in the use of materials and energy, a form of economic growth that damages the natural environment. But sustainable definition does not mention the natural environment clearly, focusing only upon human needs or wants. However, the report as a whole makes it clear that these 'needs' include the conservation of the natural environment [5]. An institution is considered to be "an association of individuals, created by law, having a continuous existence irrespective of that of its members, and powers and liabilities distinct from those of its members". So, institutions contribute to the sustainability or unsustainability of a society and the planet as a whole, but do not totally establish it [6].

Sustainable development is advancement which meets the needs of the present without compromising the capability of future generations to meet their own requirements.

Procedure and Results

For the success of the green sustainable supply chain, especially in the foundry industry, high determination and managerial discipline come to the fore under 5 basic headings. These 5 titles;

- Management Decisions and Responsibilities
- Business Operational Process Management
- Human and Environmental Impacts
- Human Resources Value Management
- Social Responsibility and Level of Integration

In this context, let's consider the headings in a lean (free from waste) green supply chain (GSC) targeting.

Management Decisions and Responsibilities

When we define the supply chain, it is imperative that the keywords of #lean #green #sustainability constitute a key value for management and show high determination in this direction.

It is important for the success of the business management to make a decision by evaluating the activity, strategy and situation in these 3 key headings and to direct the teams during the decision-making phase. The spirit of the management, the management's point of view and the vision will help the company to establish its existence, competitiveness and value structure.

Transparency and management's understanding for sustainability in senior management decision-making processes will provide a significant advantage in the value, sustainability and profitability parameters of the enterprise.

Top management should pay attention to lean process management, environmentally friendly evaluations and determination of success points within the framework of sustainability, free from wastes revealed in short, medium and long-term strategies.

In the process of creating strategic goals and action plans, it should take managerial decisions with a stakeholder acquisition model, taking into account human and socio-economic parameters. In all these activities, business ethics, value management, duty of care, environment and human impact management should be prioritized.

Top management should determine business principles, working life rules and behavior models, principles and standards, ensure their implementation and monitor their sustainability, especially in business management. In the most basic titles;

- Business ethics and ethics
- Social and individual benefit management
- Organizational culture and solidarity
- Employee motivation and continuity
- Impartiality, Equality, Justice and Discrimination
- Ethical and Opportunistic Leadership
- Lean management

Issues should be dealt with strategically with high discipline. Thus, the senior management should maintain the company's vision, mission and values in an environmentally and human-friendly manner by determining the management style on social values rather than individual benefits.

Social and Individual Benefit Management

Operational steps should be structured to ensure the continuity of operational goals from design to delivery, in line with the strategic goals of the senior management.

In this context, operational processes should be transformed from minimum inputs to maximum output in a way that is free from waste management, risk management and waste starting from the design stage. It should have the capacity to analyze its impact on future generations, which is human in its center and protects this person from all kinds of mental and physical negativities.

Most of the issues that need to be considered in the use of energy and labor, which are the biggest inputs of process management, which we often see in the casting industry, especially in the casting of light metals, should be foreseen and eliminated at the design stage.

Delay, skipping or low efficiency of the design phase will lead to high energy use in operational processes, resulting in an increase in emission values, high levels of harmful fumes as environmental waste, and occupational diseases due to ergonomic difficulties.

In order to ensure human and environmental harmony at the center of the efficiency of operational processes, digital transformation should be adopted at the highest level and it should be aimed to reduce losses and emissions.

Process parameters such as the use of clean and renewable energy sources, recycling, zero waste, occupational safety and occupational disease should be constantly observed.

In the management of processes, green management should be constantly observed and the factors affecting the emission values should be taken into account in the choice of input products and equipment.

Especially for efficiency and environmental awareness, converting the hot air released into the environment into energy in casting operations and transforming environmental waste in a value-added way should be among the strategies.

Equipment efficiency (OEE), especially operational casting activities, should be constantly observed and lean management systems should be implemented and maintained with discipline. Thus, climate crisis studies should be supported by aiming to reduce the carbon footprint by producing maximum value with minimum resource use.

Thanks to the lean processes designed with the determination and vision of the senior management, COP26 and UN activities should be integrated into the world's warming problem.

Environmental risk management should be carried out and monitored continuously with the management of risks and impacts on air, soil and water in operations. These activities and policies should be carried out with all stakeholders, especially suppliers and employees of the enterprises, and the responsibilities should be expanded and activities should be carried out by the main stakeholder.

In the execution of these activities, the human resources of the enterprises should be constantly observed in terms of competency and they should be informed about the studies in the PDCA cycle. Lean sustainable green supply chain awareness of organizations should be kept alive continuously by identifying missing competencies and establishing collaborations with NGOs and universities.

The strategic goals and policies created for the lean sustainable green supply chain of the enterprise should be disseminated to all employees.

The enterprise has taken measures against all kinds of discrimination in human resources such as religion, language, race and gender and should establish an independent complaint mechanism in this direction. It should avoid employing child labor in its activities and

should constantly monitor and audit all its activities by independent companies and share the action plans it will reveal with the stakeholders with a transparency.

With this and effective management, the management of the supply chain should be managed in a human and environment-centered structure that continuously improves profitability and competitiveness.

References

- [1] Jacobs, M. (2012). *Green growth: Economic theory and political discourse* (Vol. 92). London: Grantham Research Institute on Climate Change and the Environment.
- [2] Brundtland, G. H., & Khalid, M. (1987). *Our common future*. Oxford University Press, Oxford, GB.
- [3] Ashby, A., Leat, M., & Hudson-Smith, M. (2012). Making connections: a review of supply chain management and sustainability literature. *Supply chain management: an international journal*, 17(5), 497-516.
- [4] Wagner, M., Schaltegger, S., & Wehrmeyer, W. (2001). The relationship between the environmental and economic performance of firms: what does theory propose and what does empirical evidence tell us? *Greener Management International*, (34), 95-108.
- [5] Diesendorf, M. (2000). Sustainability and sustainable development. *Sustainability: The corporate challenge of the 21st century*, 2, 19-37.
- [6] Macquarie Dictionary, 1981. Macquarie Library, Sydney



AMS

Aerospace Materials Symposium

Havacılık Malzemeleri
Sempozyumu

DYNAMIC RECRYSTALLIZATION IN DIRECTIONAL SOLIDIFIED CM247 LC ALLOYS

Müge AKDEMİR¹, Belgin ATAMAN¹, Aylin ŞAHİN KAHRAMAN²,
Havva KAZDAL ZEYİN², Hüseyin AYDIN²

¹Istanbul Technical University, ²TUBITAK Marmara Research Center
Türkiye

Keywords: Superalloys, Heat Treatment, Creep, DRX

Abstract

In this study, the effects of dynamic recrystallization (DRX) on high temperature mechanical properties of directionally solidified CM247LC superalloys were investigated. Dynamic recrystallization behavior is related to hot deformation plasticity of superalloys which provides grain refinement and deformation inibitance. In this work, heat-treated CM247LC alloys were performed via interrupted creep rupture at elevated temperatures. After that, optical and electron microscopy techniques were used to examine the microstructural evaluation of CM247LC alloys.

1. Introduction

CM247LC is chemically modified version of Mar-M247 Ni-based superalloy and is originally designed as a cast alloy. Hence, CM247LC superalloy is a choice of material preferred in both IGT (Industrial Gas Turbines) and aviation turbine blades with its superior creep and fatigue strength as well as oxidation resistance at elevated temperatures. In general, microstructure of directionally solidified cast CM247LC alloy consists of columnar grains that their boundaries aline through growth direction. Previous studies about CM247LC alloys mostly focused on high temperature mechanical properties strengthened by γ' phases precipitated in γ matrix and their microstructure evolution. However, there are only few studies focused on their dynamic recrystallization (DRX) behavior and its effects on microstructural and mechanical behavior [1–4]. Wang et. al examined the transformation of the microstructure during hot deformation process in IN718 superalloy. Hot deformation process were applied by compression tests with a true strain rate of 10^{-3} s⁻¹ at 1000°C. It was demonstrated that continuous and discontinuous DRX both formed in IN718 during high temperature deformation. It is suggested that DRX were driven by strain-induced grain and twin boundaries [1]. Sun et.al. investigated the similar DRX concept in EP962NP nickel based superalloys. Isothermal interrupted compression tests of nickel-based superalloys leads to γ' dissolution and re-precipitation, with DRX supported nucleation [4].

2. Experimental Procedure

The CM247LC samples were heat treated with standard heat treatment recipe via vacuum heat treatment furnace.

Solution heat treatment were applied to DS samples at 1221°C to 1250°C for 2 hours in each steps which end up with argon gas cooling in the furnace. After that, precipitation hardening were carried out with double aging at 1080°C for 4h and 871°C for 20h with furnace cooling. The chemical composition of directional solidified CM247LC is given in Table 1.

Heat-treated CM247LC DS superalloys were prepared for creep rupture tests according to the ASTM E-139 standard. Interrupted creep rupture tests were conducted on a stress level amount of 248 MPa and a temperature at 984°C. Test were interrupted at 0.1%, 0.2%, 0.5%, 1%, and 2% strain ratios, temperature and strain data were collected using with lever type extensometer, respectively. After each step, samples were cut from gauged areas cross sections. Polishing were applied with 0.6 μ m diamond and diamond lubricant; then, 20% wt. H₃PO₄ and 80% wt water were used for etching γ matrix on purpose to observe and reveal γ' cuboidal structure.

Table 1. Chemical composition of CM247LC (wt%)

Ni	W	Co	Cr	Al
Bal.	9,5	9,3	8,16	5,6
Ta	Hf	Ti	Mo	Re
3,22	1,45	0,68	0,51	0,1
C	Fe	B	Nb	Zr
0,074	0,015	0,015	0,1	0,007

3. Results and Discussion

Microstructure evolution during deformation were investigated by interrupted creep tests. Figure 1 shows the micrographs of for each creep step microstructures at 500 μ m magnification.

Naturally, creep strain of samples increased with increasing creep time as shown in the Figure 2. Samples reached various strain ratios 0.1 % (19min.), 0.2% (50min.), 0.5% (3h 21min.), 1% (9hr 27min.), 2% (15hr. 33min.) with extended creep times, respectively. Finally, creep rupture occurred at 48h 8 min.

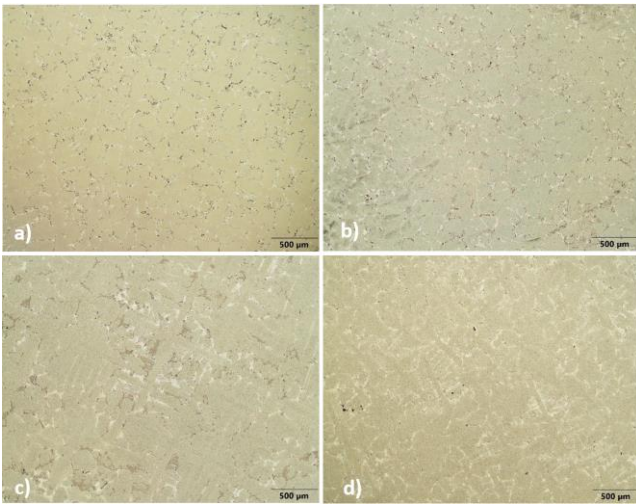


Figure 1. Etched microstructure of a) heat treated b) 0.2%, c) 1% strain and d) creep rupture samples

Naturally, creep strain of samples increased with increasing creep time as shown in the Figure 2. Samples reached various strain ratios 0.1 % (19min.), 0.2% (50min.), 0.5% (3h 21min.), 1% (9hr 27min.), 2% (15hr. 33min.) with extended creep times, respectively. Finally, creep rupture occurred at 48h 8 min.

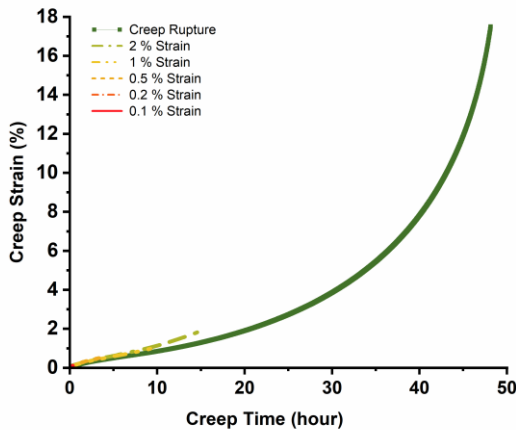


Figure 2. Creep strain-time curves

Creep rate-time curves are given in Figure 3. Higher strain ratios observed with accelerated creep rates due to increased plastic deformation. It is also reasonable with literature results that the creep rate decreases with increasing alternating creep stress (Fast Fourier Data) [5].

The elemental analysis of the microstructure shown in the Figure 4 and Table 2. According to SEM-EDS analysis, MC carbides (HfC, TaC) aligned through the grain boundaries while $M_{23}C_6$ dispersed mostly inside the grains. Coarser γ' were observed combined with the eutectic regions.

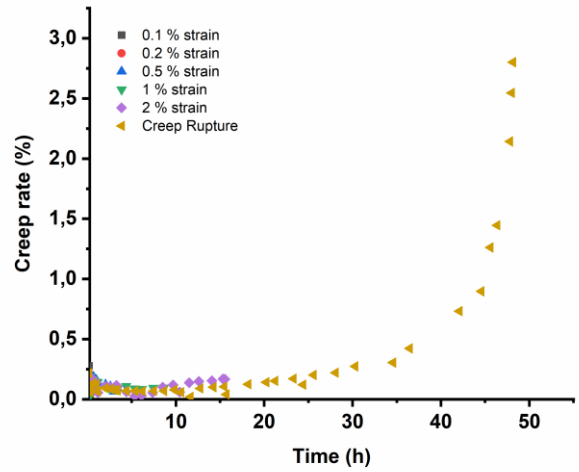


Figure 3. Creep rate curves

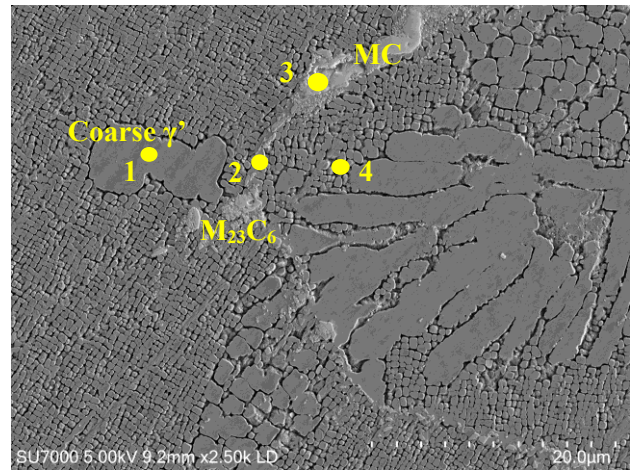


Figure 4. Microstructure of 0.2% strain ratio sample via SEM

Table 2. EDS analysis of phases in the microstructure of 0.2% strain ratio

1		2		3		4	
Element	Wt%	Element	Wt%	Element	Wt%	Element	Wt%
Ni	68.0	W	62.0	Hf	59.9	Ni	68.0
Co	7.4	Cr	27.1	Ta	24.5	W	8.8
W	6.6	Mo	6.2	C	8.7	Co	8.1
Al	6.4	Ni	2.6	W	6.2	Al	6.6
Ta	5.3	C	2.1	Ni	0.8	Ta	4.4
Hf	2.4					C	1.7
C	2.0					Hf	1.0
Cr	1.5						
Mo	0.4						

Increasing time with creep rate provides distortion in the morphology of γ' phases. Fine γ' precipitates of heat treated sample became coarser and agglomerated after 1%

creep rate as shown in Figure 5. The microstructure of heat treated sample had 82.63 % γ' phases in the matrix. Strain ratios of 0.2% and 1% had 82.60%, 87.27% γ/γ' , respectively while creep rupture sample increased to 91,28% γ/γ' phases. γ' dissolution and re-precipitation, with DRX supported nucleation the average size of secondary γ' increased, which is also related to the nucleation and growth of the secondary γ' due to increasing creep rate and plasticity at elevated temperatures [4].

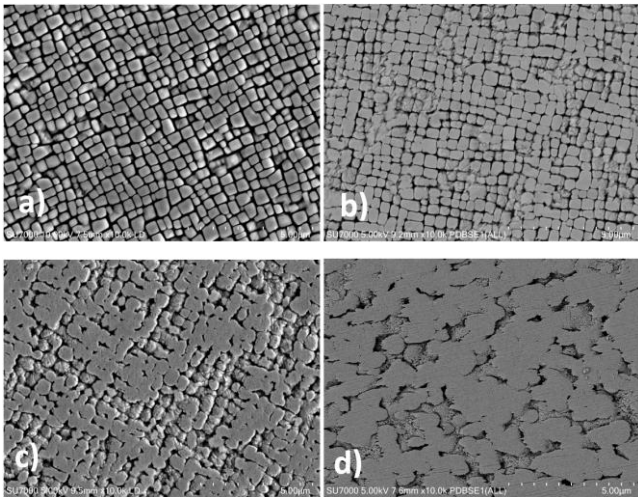


Figure 5. γ' phases of a) heat treated, b) 0.2 %, c) 1% strain rate, d) creep rupture samples.

Figure 6 and Figure 7 show the microstructure evaluation of CM24LC depending on the creep ratio. It becomes impossible to differentiate grain size in micro-level starting from the 0.2 % strain due to the extreme grain coarsening. Initially, heat treated samples have only few grains with an average grain size of 500 μ m. In creep ruptured CM247LC, the less and localized γ' phases coarsened due to severe plastic deformation and creep rate at the final stage of creep. In addition, it was observe that eutectic regions were coarsened and γ channels were narrowed.

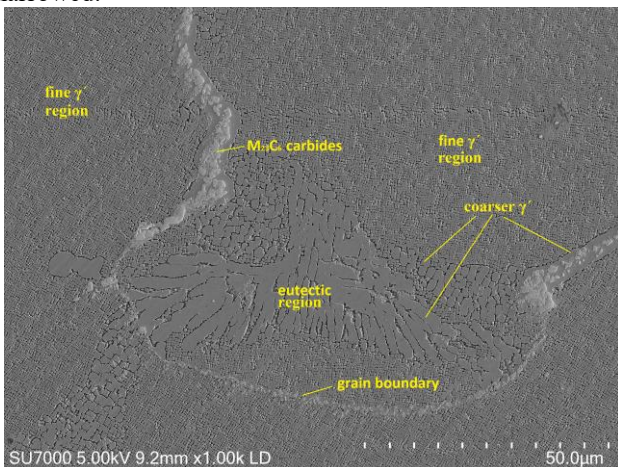


Figure 6. SEM images of 0.2% strain ratio sample

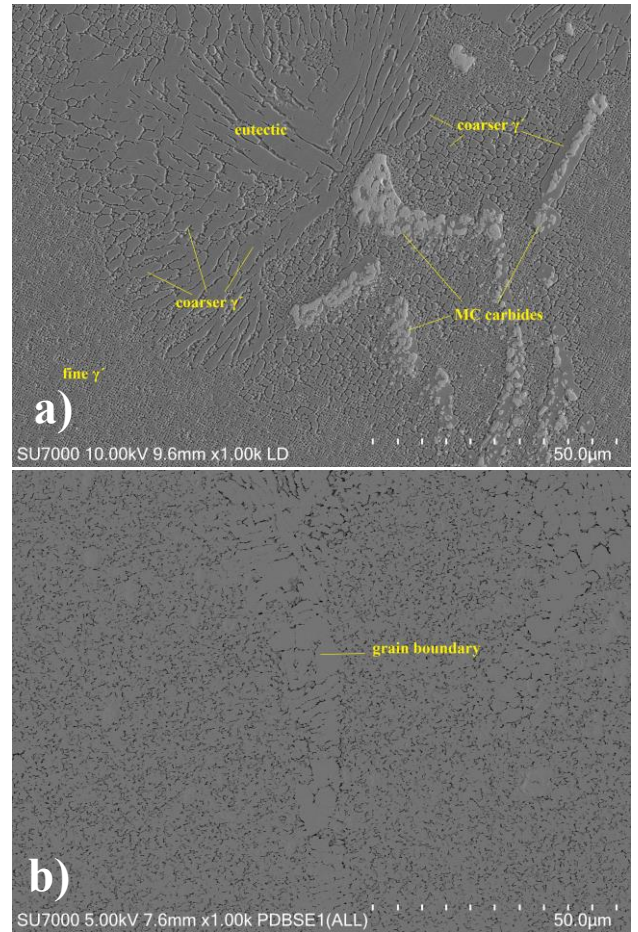


Figure 7. SEM images of a) 1% strain ratio and b) creep rupture sample

4. Conclusion

This investigations proved that creep life of the standard heat treated samples for CM247LC superalloy dependent on initial γ/γ' volume as well as morphology. It must be noted that with increasing creep rate, γ/γ' volume increases due to coarsening and agglomeration of primary γ' .

Although secondary γ' formations can be seen at extended creep ratios which is also effective for grain boundary strengthening due to DRX nucleation. Localize instability in the grain boundaries resulted with minor amount of $M_{23}C_6$ formation. Finally, it was observed that creep rupture has coarse γ/γ' formation with greater than 90% eutectic solutions without incipient melting.

Acknowledgment

The author wish to thank Metallic Materials Technologies Research Center for experimental infrastructure and studies.

Reference

- [1] K. Wang, Z. Sun, Y. Liu, Y. Lv, Investigation of microstructure and mechanical performance of



in738lc superalloy thin wall produced by pulsed plasma arc additive manufacturing, *Materials (Basel)*. 13 (2020) 1–19. <https://doi.org/10.3390/MA13183924>.

- [2] D. Li, Q. Guo, S. Guo, H. Peng, Z. Wu, The microstructure evolution and nucleation mechanisms of dynamic recrystallization in hot-deformed Inconel 625 superalloy, *Mater. Des.* 32 (2011) 696–705. <https://doi.org/10.1016/j.matdes.2010.07.040>.
- [3] Y. Li, Y. Zhang, Z. Chen, Z. Ji, H. Zhu, C. Sun, W. Dong, X. Li, Y. Sun, S. Yao, Hot deformation behavior and dynamic recrystallization of GH690 nickel-based superalloy, *J. Alloys Compd.* 847 (2020). <https://doi.org/10.1016/j.jallcom.2020.156507>.
- [4] B. Sun, T. Zhang, L. Song, L. Zhang, Microstructural evolution and dynamic recrystallization of a nickel-based superalloy PM EP962NP during hot deformation at 1150 °C, *J. Mater. Res. Technol.* 18 (2022) 1436–1449. <https://doi.org/10.1016/j.jmrt.2022.03.033>.
- [5] T. Bouchenot, On the Interaction of Creep and High-Cycle Fatigue in CM 247 LC, 2021. <https://stars.library.ucf.edu/etd2020/475>.

COLD SPRAY EFFECT ON OXIDE DISPERSION STRENGTHENING OF INCONEL 718

Bayram Berk TANRISEVDİ, Eda AYDOĞAN

Middle East Technical University
Türkiye

Keywords: Oxide dispersion strengthening, ODS, nano-oxides, Inconel 718, Cold-Spray, Coating

Abstract

Oxide dispersion strengthened Inconel 718- Y, F (IN718 – Y_2O_3 – FeO – Hf), ODS In718, produced by Low Pressure Cold Spray method. The Cold Spray was conducted with He / N pressure of 8 bar, max temperature of 165-330 °C. Mechanical alloying was applied to the powders using Argon atmosphere at a rate of 300 rpm. With and without the balls 1 hour tries are conducted up to 5 hours. Stainless steel 10 mm grinding balls are used with 1 to 1 ball to powder ratio. The samples heat treated for 1,2 and 3 hours at 1050 °C. The results obtained from EDX Mapping analysis satisfied the estimated composition as well as the distribution. TEM analysis of cold spray samples showed a homogeneous distribution of nano sized Y-Ti (Hf, Zr, Al) oxides through the microstructure of obtained material. Heat treatment of the cold sprayed samples effectively decreased the porosity of the coating while producing stress relief cracks. The observations of nano oxides showed comparable results with that of selective laser melting technique.

1. Introduction

It is well accepted that oxide dispersion strengthened alloys show high strength, creep resistance, thermal stability, oxidation and radiation resistance at high temperatures. The presence of Y-Ti (Hf, Zr, Al)-O nano-oxides in the microstructure of Inconel 718 stabilizes and improves the mechanical properties by pinning dislocations and grain boundaries at elevated temperatures [1]. During the cold spraying (solid state kinetic sintering method) pressurized and heated gasses are loaded with the micron size powders. The powders are accelerated to high speeds that results in kinetic sintering. The concurrence of severe plastic deformation along with adiabatic shear instability phenomenon results in mechanical locking of powder and substrate [2]. The mechanical alloying (MA) is necessary to incorporate the fine oxide particle of Y_2O_3 / FeO and Hf precursor to In-718 powder body. The objective of this study is to modify the composition of the Inconel 718 alloys by mechanical alloying and low-pressure cold spray methods to produce equiaxed grain structures with high volume fraction of nano-oxide dispersions.

2. Materials and Methods

The 3 layer of the material alloyed ODS In718 coating is applied with low pressure cold spray method used with the material alloyed powder. To achieve densification, the samples heat treated for 1,2 and 3 hours at 1050 °C. Microstructures of ODS alloys were examined by using optical microscopy, scanning electron microscopy and transmission electron microscopy.

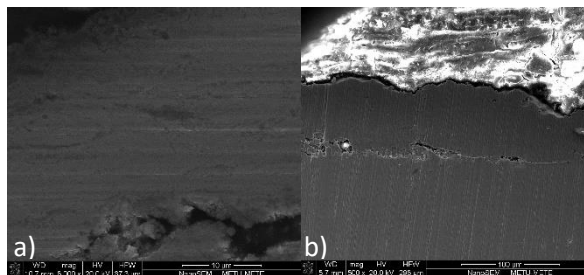


Figure 1. SEM images of IN718-YFH coating in heat treated condition; a) x8000, b) x500 back scattering.

3. Conclusion

It is confirmed from EDX Map and TEM analysis that the Y-Ti- (Al)-O nano particles are produced as a thin coating. Addition of Hf effect the morphology and size distribution of the nano-oxides. Hardness tests proves strengthening of the In 718.

Acknowledgement

The financial support provided by the L'Oréal- UNESCO “For Women in Science” is greatly acknowledged.

References

- [1] M. Yesim Yalcin, B. Derin, E. Aydogan, *J. Alloy. Compd.* 914 (2022), Article 165193
- [2] S. Singh, R. K. Raman, C. C. Berndt, and H. Singh, *Metals*. 11 (2021), 12-2016.

FLOWFORMING AND HEAT TREATMENT EFFECT OF IN718 ALLOY

Aptullah KARAKAŞ

Repkon Machine and Tool Industry
Türkiye

Keywords: Flow-forming, IN718, Heat Treatment, Microstructures

Abstract

The Flow-forming process has been used for several years to produce high-quality seamless, thin, and variable walled tubular components for aircraft, aerospace systems, nuclear, chemical, and petrochemical facilities, and many other major industries. IN718 alloy is often used in aviation industry and it is important to form and harden this material. The aim of this study is to analyze the effect of solution heat treatment and subsequently the Flow-forming process. Microstructure analysis by optical microscope and SEM and hardness measurements were applied to the initial preform manufactured in accordance with the AMS5662 standard, after solution heat treatment at 1066 °C/1h of the initial preform and after Flow-forming process of the solution heat treated part.

1. Introduction

Flow-forming is an advanced, often net-shape, cold metal-working process for manufacturing dimensionally precise tubular and other rotationally symmetric products. The process involves applying compression to the outside diameter of a cylindrical preform, attached to a rotating mandrel. Compression is applied by a combination of axial and radial forces using a set of three or more rollers that are simultaneously moved along the length of the rotating preform, flowing the material plastically in both radial and axial directions. The result is a dimensionally accurate, high quality cylindrical or tubular shaped product, having increased mechanical properties and fine surface finish [1].

The objective parameters of formability, improvement in mechanical properties and dimensional accuracy are influenced by various parameters such as process variables (feed rate, mandrel speed, etc.), tool geometry (mandrel shape, roller geometries, etc.) and work material. The main focus of this study is related to properties of work material such as hardness, ductility and microstructure.

IN718 is a precipitation hardenable Ni-based superalloy which is frequently used in aerospace industry because of its thermal and mechanical properties. This alloy contains gamma matrix (γ -mainly Ni), delta phases (δ -orthorhombic Ni_3Nb) on the grain boundaries and gamma double prime precipitations (γ'' -body center tetragonal Ni_3Nb). These

secondary phases and precipitations hinder the dislocation motion and they provide resistance to creep deformation up to 600°C, therefore this alloy could be used at this temperature range [2].

In this study, solution heat treatment was applied to IN718 (AMS5662) alloy in order to increase formability. After this treatment, Flow-forming process was carried out, subsequently, microstructure analysis and hardness measurements were applied.

2. Experimental Procedure

Firstly, Flow-forming processes were carried out on IN718 preforms that are solution heat treated at 968 °C and fracture was occurred during the process. Secondly, in order to increase formability of IN718 alloy, solution heat treatment was applied at 1066 °C/1h by a Protherm open atmosphere furnace. After solution heat treatment, Flow-forming process which is 50% thickness reduction ratio was carried out and the process was carried out without any failure. The pictures of the two pieces after Flow-forming operations are indicated in Fig.1, one is Flow-forming of the initial IN718 which failed (Fig.1-a), the other is the successfully Flow-formed piece (Fig.1-b).

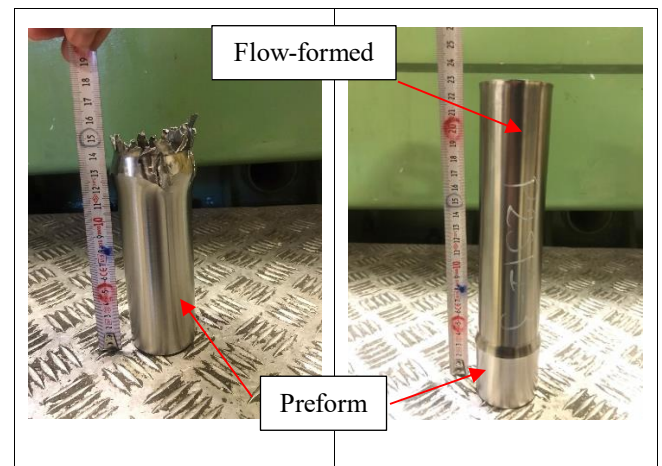


Figure 1: Failed (IN718 AMS5662) and successfully Flow-formed (solution heat treated at 1066°C/1h of IN718 AMS5662) parts after the Flow-forming processes.

First, solution heat treated and Flow-formed IN718 specimens were metallographically prepared and electrolytically etched using the A3 Struers solution. After etching, microstructure analysis was carried out with Olympus-BMX53 optical microscope and Zeiss-Merlin scanning electron microscope (SEM). Hardness is measured using Emco Test-Dura Scan 20 (HV0,3).

3. Results and Discussion

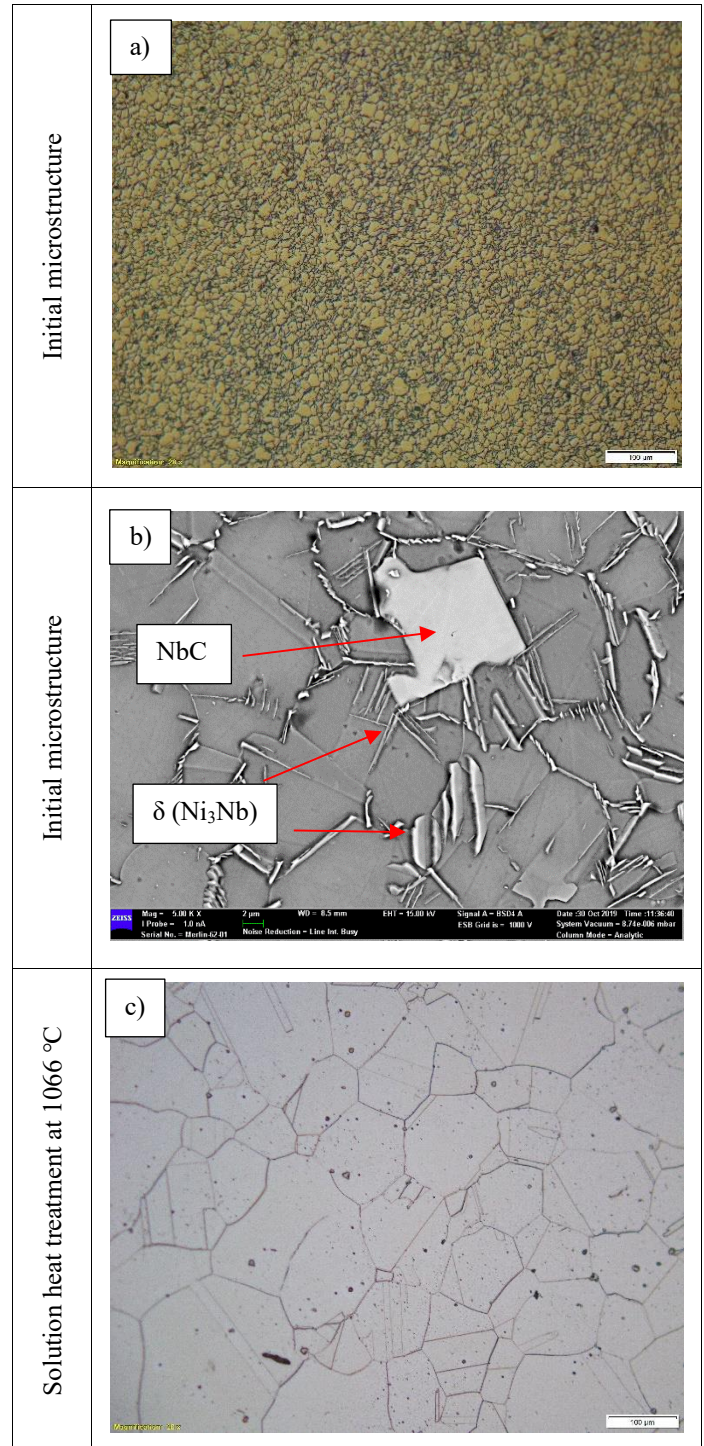
Chemical analysis is given in Table 1 and the results match with the AMS5662 standard.

Table 1. Chemical analysis of the IN718 (wt%)

Ni	Cr	Mo	Nb	Fe
53.04	18.41	3.04	5.25	18.40
Ti	Al	C	P	S
0.94	0.55	0.02	0.005	0.001

3.1. Microstructure Analysis

Microstructure images of the initial preform, solution heat treated preform and the Flow-formed IN718 specimens are indicated in Fig.2. According to Fig.1 a and b, the mean grain size is around 10 μm and microstructure contains NbC and δ phases on grain boundaries, this fitting to AMS5662 standard. After solution heat treatment at 1066 $^{\circ}\text{C}$, grain size increased to around 180 μm and all the δ phases dissolved in the matrix and NbC amount decreased as indicated in Fig.1 c and d. The grain growth was a result of solution δ phases. As for Fig.1 e and f, after Flow-forming operation, grain size decreased to 30-40 μm scales from 180 μm at the inner side because of dynamic recrystallization during the Flow-forming process and to almost submicron scales at the outer side and highly elongated grains could also be observed at the outer side. The reason the grain sizes change depending on the region is related to the Flow-forming mechanism. Maximum strain is created on the outer side where the rollers contact, the strain is decreases towards the inner side and minimum strain occurs on the inner side that contacts the mandrel [3].



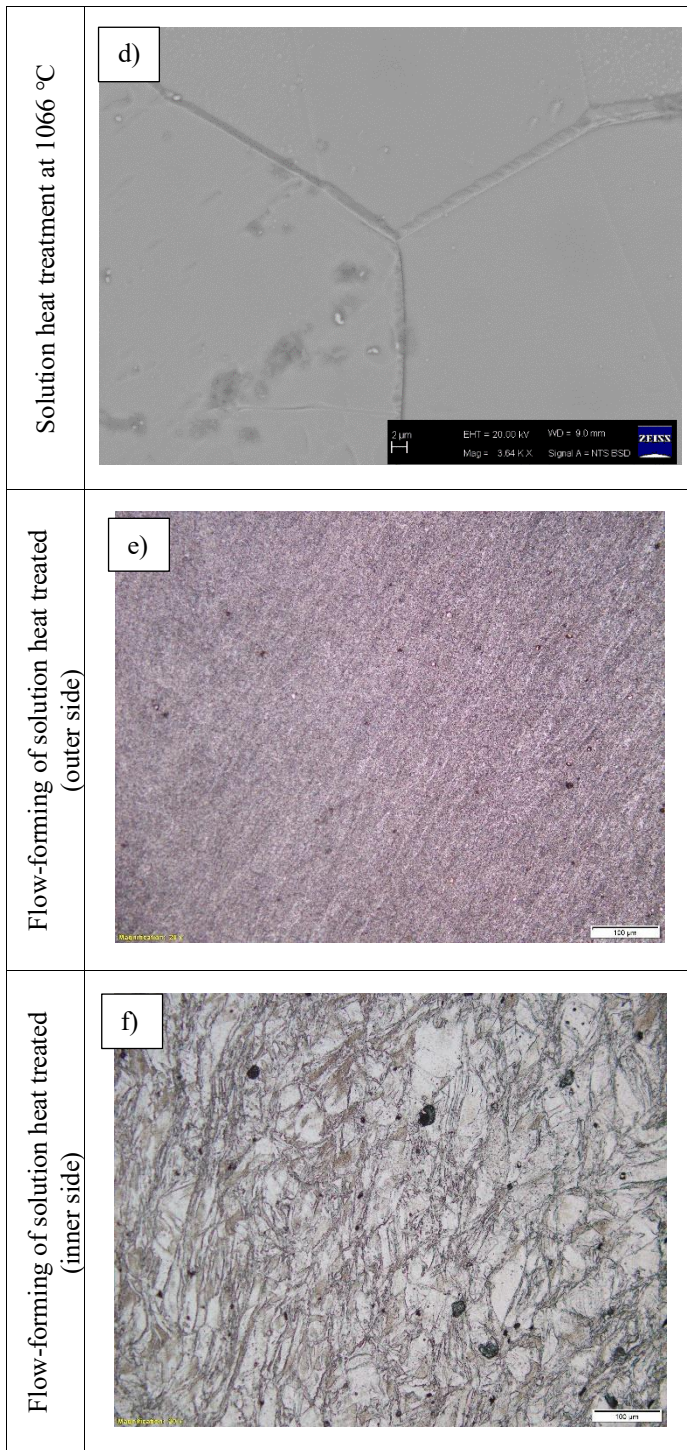


Figure 2: a) Initial microstructure of IN718 before solution heat treatment by optical microscope 200X magnified, b) Initial microstructure of IN718 before solution heat treatment by SEM 10000X magnified, c) microstructure of solution heat treated at 1066 °C by optical microscope 200X magnified, d) microstructure of solution heat treated at 1066 °C by SEM 10000X, e) outer side of Flow-formed specimen 200X magnified and f) inner side of Flow-formed specimen 200X magnified.

3.2. Hardness Measurement

Hardness measurements are indicated in Fig.3 and measurements were taken every 500 μm through the cross-section. Hardness values of initial IN718 is around 320 HV, this result is in accordance with AMS5662 standard and it decreased to around 200 HV after solution heat treatment because of solution of secondary phases and grain growth. Hardness levels of after Flow-forming of solution heat treated IN718 increased to around 600 HV at outer side and around 450 HV at inner side which is the softest region. The reason for this major increase of hardness is the strain hardening effect of Flow-forming process and low stacking fault energy of Ni metal.

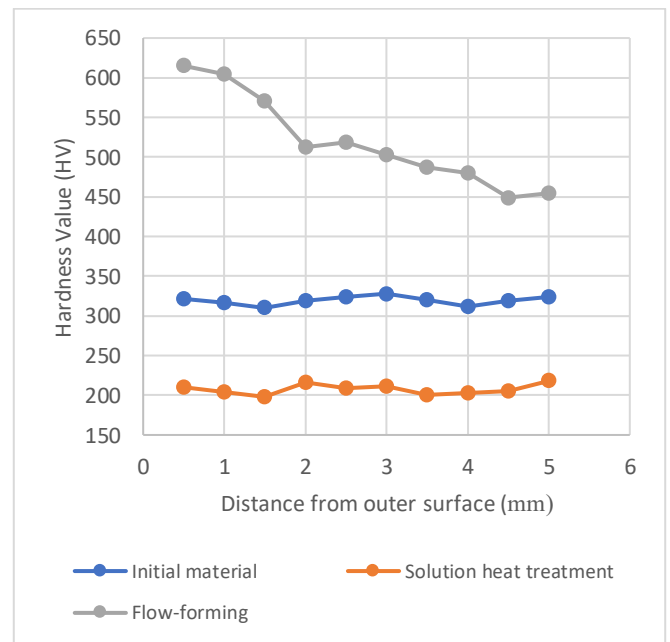


Figure 3: Hardness results of three different condition IN718

4. Conclusion

IN718 preform in AMS5662 condition could not be Flow-formed successfully. After this phenomenon, solution heat treatment was applied to IN718 at 1066 °C/1h in order to increase formability. After this solution heat treatment, Flow-forming operation was carried out successfully. The conclusions are specified;

- Initial mean grain size of IN718 is around 10 μm and it increased to 180 μm level after solution heat treatment at 1066 °C/1h because of dissolution of δ phases into the matrix.
- 180 μm grain size decreased to 30-40 μm and less after the Flow-forming process because of dynamic recrystallization during Flow-forming process even though it is a cold forming

application. Sufficient heat generates during Flow-forming of IN718 because of plastic deformation.

- A major increase in hardness, from 200 HV to 450-600 HV levels, is observed because of strain hardening.

4. Acknowledgment

The author acknowledges the management of Repkon Machine and Tool Industry for their kind support in carrying out this work.

References

- [1] G. Ray and D. Yilmaz, ASM Handbook Vol14A: Metalworking: Bulk Forming, 42 (2005) 516-521.
- [2] P. Maj, P. Blyskun, S. Kut, B. Romelczyk-Baishya, T. Mrugala, B. Adamczyk-Cieslak and J. Mizera, Flow forming and heat-treatment of Inconel 718 cylinders, Journal of Materials Processing Tech., Elsevier, Warsaw, Poland, 253 (2018), 64-71.
- [3] A. Karakas, T.O. Fenercioglu and T. Yalcinkaya, The influence of flow forming on the precipitation characteristics of Al2024 alloys, Elsevier, Istanbul, Turkey, 299 (2021).



A NUMERICAL ANALYSIS OF THE EFFECT OF ELECTRO-BEAM-MELT Ti6Al4V COVER PLATE ON THE BALLISTIC PERFORMANCE OF SiC ARMOR

F. Murat YILDIZTEKİN¹, Mustafa GÜDEN¹, Alper TAŞDEMİRCİ¹, A. Kaan TOKSOY²,
Gülden ÇİMEN¹, S. Burçin ÇELLEK¹

¹Izmir Institute of Technology, ²Roketsan Missiles Industries
Türkiye

Keywords: SiC Armor, Cover Plate, LS-Dyna, EBM-Ti6Al4V, Johnson Cook, Johnson-Holmquist 2

Abstract

Various cover plates, including high strength 4340, RHA alloys and ductile Al and Cu metals manufactured using conventional manufacturing methods, were numerically and experimentally investigated previously as cover plates in ceramic armors. This study, on the other side, focused on the use of an Electro-Beam-Melt processed Ti6Al4V alloy as a cover plate in the SiC ceramic armors. The use of Electro-Beam-Melt processed Ti6Al4V alloy was shown to increase the ballistic limit of SiC ceramic, showing a potential of application in ceramic armors. An optimization of the thickness of the cover plate was however needed in order to not to increase the weight of the armor significantly.

1. Introduction

In recent years there has been an increased interest in improving the ballistic performance of ceramic armors against the long rod kinetic impactors. The use of a thin layer of a metallic cover in the front of a ceramic armor has been shown to have a potential for increasing the ballistic limit. Cover plates prevent the separation of refracted ceramic tile and deform the long rod impactor radially [1]. Both result in an improved penetration resistance of ceramic armor. Various cover plates including high strength 4340 and RHA alloys and ductile Al and Cu metals were numerically and experimentally investigated previously as cover plates in ceramic armors, [2] while in the present study an Electro-Beam-Melt processed Ti6Al4V alloy (EBM-Ti64) plate was numerically investigated as a cover plate. The selection of this alloy was based on the fact that this alloy has a high strength and low density, dictating a higher specific strength. More it has an anisotropy in the building and transverse to the building direction, being more ductile in the transverse to the building direction. Higher ductility in the transverse direction is expected to distribute the impact load laterally more and hence increases the efficiency of cover plate.

2. Materials and methods

The long rod impact on the SiC armor with the EBM-Ti64 cover plate was simulated numerically in LS-Dyna. The used model consisted of a Tungsten (W) blunt long rod, EBM-Ti64 cover plate and SiC ceramic. The SiC ceramic was modelled using the Johnson-Holmquist 2 stress and damage model and EBM-Ti64 and W long rod were modelled using the Johnson and Cook model. The SiC ceramic and EBM-Ti64 cover plate were simulated in the model with the Lagrangian formulation, while the W rod was with the SPH method. The SPH method is well-suited for modelling the hydrodynamic behavior, which is an expected phenomenon for the metals under relatively high-pressure levels [3]. The material model parameters of the cover plate, ceramic and long rod were taken from the literature. The fidelity of the used model was initially verified with the experimental and numerical data in the literature on the selected metal covered SiC ceramic armors. Once the model was verified, the long rod impact simulations were implemented with and without EBM-Ti64 cover plate on the front of SiC armor at an impact velocity of 1500 m/s.

3. Conclusion

The ballistic performance of the SiC armors has been evaluated with and without EBM-Ti64 cover plate. Results showed an increase in the ballistic limit with the use of the EBM-Ti64 cover plate. The results also showed that the thickness of the cover plate played an important role on the ballistic performance. Although the 0.5-2 mm-thick cover plates showed no appreciable increase in the ballistic limit of the SiC ceramic, the use of 4-5 mm-thick cover plates increased the weight of the ceramic armor significantly. An optimization study on the thickness of the cover plate was therefore conducted and reported in the study.

References

- [1] Dresch, A. B., Venturini, J., Arcaro, O. R. K., & Bergmann, C. P. (2021). *Ceramics International*, 47(7), 8743–8761.
- [2] Zhai, Y. X., Wu, H., & Fang, Q. (2020). *Defence Technology*, 16(1), 50–68.
- [3] Tate, A. (1967). *Journal of the Mechanics and Physics of Solids*, 15(6), 387–399.



EFFECT OF SOLUTION HEAT TREATMENT ON THE ANISOTROPY OF MICROSTRUCTURE, TEXTURE AND MECHANICAL PROPERTIES OF HASTELLOY X FABRICATED BY LASER POWDER BED FUSION

Seren ÖZER^{1,2}, M. Alp YALÇIN¹, Güney Mert BİLGİN², Kemal DAVUT³, Ziya ESEN⁴, Arcan F. DERİCİOĞLU²

¹Atılım University, ²Middle East Technical University, ³Izmir Institute of Technology, ⁴Çankaya University
Türkiye

Keywords: Additive manufacturing, Laser powder bed fusion, Hastelloy X, Texture, Mechanical properties.

Abstract

In the present study, the effect of building direction and solution heat treatment on the microstructure, crystallographic texture and mechanical properties of Hastelloy X (HX) alloy fabricated by laser powder bed fusion (LPBF) method was investigated. The tensile test results revealed that vertically built samples showed higher ultimate tensile strength (UTS) value of 145 MPa with lower ductility than that of the horizontally built samples. Solution heat treatment caused a decrease in strength values while the ductility of both samples significantly enhanced by 62% and 32.8% for the vertically and horizontally built samples, respectively.

1. Introduction

HX is a solid solution strengthened, Ni-based superalloy containing high amounts of Cr, Fe and Mo along with low percentages of Co. This alloy is extensively utilized in gas turbine engines, automotive and petrochemical applications due to its good formability and combination of excellent high temperature strength along with oxidation resistance in aggressive environments. LPBF is one of the most well-known additive manufacturing (AM) techniques, which enables the fabrication of functional metallic components with complex geometries in a single production stage. However, some process-induced defects may occur in the microstructure of fabricated parts due to the high-temperature gradient and rapid solidification rate involved. Therefore, post-processing heat treatment becomes inevitable to enhance the mechanical properties of LPBF-processed HX alloy for fulfilling the service requirements by eliminating or minimizing the formation of defects/undesired phases.

2. Materials and Methods

HX samples were fabricated by Selective Laser Melting (SLM), a well-known LPBF method, in two different building directions such that their longitudinal axes were either parallel or perpendicular to the building platform. Subsequently, some of the samples were solutionized at 1175 °C for 2 hours and then air-cooled. Characterization of the samples was performed by scanning electron microscopy (SEM), electron back scattered diffraction (EBSD) and X-ray diffraction (XRD) methods. The samples were also subjected to the tensile and microhardness tests.

3. Conclusions

In the present study, solution heat treatment transformed the arc-shaped initial morphology into smaller recrystallized, equiaxed grains with the formation of annealing twinning. The results showed that vertically built samples showed higher UTS value of 145 MPa with lower ductility. Formation of textured columnar grains with different average grain size results in anisotropy in the tensile properties of the LPBF-produced samples. On the other hand, solution heat treatment significantly enhanced the ductility of both samples with respect to the building direction, while a decrease in strength was observed. Progress of recrystallization and reduction in dislocation density in heat-treated samples were also evidenced by analysis of kernel average misorientation (KAM) and grain orientation spread (GOS) obtained by EBSD.

References

- [1] S. Pourbabak, et al., (2019). Microscopic investigation of as built and hot isostatic pressed Hastelloy X processed by Selective Laser Melting. *Mater. Charact.*, 153, 366–371.
- [2] W. Zhang et al., (2021). Effect of solution temperature on the microstructure and mechanical properties of Hastelloy X superalloy fabricated by laser directed energy deposition. *Mater. Sci. Eng. A*, 820, 141537, 2021.



EFFECTS OF HEAT TREATMENT AND HOT ISOSTATIC PRESSING ON HIGH TEMPERATURE MECHANICAL PROPERTIES OF Ti-48Al-2Cr-2Nb ALLOY PRODUCED BY ELECTRON BEAM MELTING

Güney Mert BİLGİN^{1,2}, Seren ÖZER^{2,3}, Ziya ESEN⁴, Arcan F. DERİCİOĞLU²

¹TUSAS Engine Industries, ²Middle East Technical University, ³Atılım University, ⁴Cankaya University
Türkiye

Keywords: Additive Manufacturing, Electron Beam Melting, Ti-48Al-2Cr-2Nb, Microstructure, Mechanical Properties, Heat Treatment, Hot Isostatic Pressing

Abstract

In this study, Ti-48Al-2Cr-2Nb samples were produced by electron beam melting (EBM) method. Mechanical properties of as-built γ -TiAl produced by EBM significantly differ from those of the parts produced by conventional methods due to several issues including microstructural instabilities, porosity and residual stresses. Therefore, a subsequent heat treatment was found to be vital to eliminate those issues generated from the nature of the EBM layered process. The Ti-48Al-2Cr-2Nb alloy typically contains two main phases, γ -TiAl as the matrix and α_2 -Ti₃Al with various morphologies depending on the type of the processing and heat treatment history. The present study was conducted to characterize the microstructure and high temperature tensile strength behavior of EBM manufactured Ti-48Al-2Cr-2Nb samples in the as-built, heat-treated and hot isostatic pressed (HIP'ed) conditions within the purpose of utilizing this alloy for structural aerospace applications.

1. Introduction

The as-built microstructure needs to be stabilized through secondary treatments even if microcracks and porosity are avoided with an adequate EBM preheating temperature and well-developed process parameters. Therefore, post-processes like heat treatment and hot isostatic pressing (HIP) are required to follow EBM production to tailor the microstructure and to enhance the ductility. The present study was conducted to characterize the microstructure, high temperature tensile strength and stress rupture behavior of EBM manufactured Ti-48Al-2Cr-2Nb samples in the as-built as well as subsequently obtained heat treated and also HIP'ed conditions to render this alloy available for structural aerospace applications.

2. Materials and Methods

Ti-48Al-2Cr-2Nb samples were fabricated by EBM method being their longitudinal axes either parallel or perpendicular to the building platform. Subsequently, some of the samples were heat treated at two different temperatures of 1200 (HT-1) and 1400°C (HT-2) for 2 hours in vacuum, while some of them were HIP'ed at 1200°C under 100 MPa for 2 hours. Characterization of the samples was performed by scanning electron microscopy (SEM), optical microscopy (OM) and X-ray diffraction (XRD) methods. The samples were also subjected to tensile tests at room temperature and at 700 and 800°C.

3. Conclusions

The heat treatments were done at 1200 (HT-1) and 1400°C (HT-2) to obtain duplex and fully lamellar microstructures, respectively. It was determined that after HT-1 fine lamellar $\gamma + \alpha_2$ was still present along with coarse γ bands, while fully lamellar microstructure was seen after HT-2. The pores in the as-built sample were removed sufficiently as a result of HIP, where it was revealed that the duplex microstructure consisting of coarse grains and fine lamellae was present after the HIP process conducted at 1200°C. The average yield strength of EBM as-built Ti-48Al-2Cr-2Nb was found as 561 MPa along with 1.67% tensile elongation at room temperature. The yield strength of HT-1 alloy was 540 MPa, while the tensile elongation was 2.60% at room temperature. In the HIP'ed sample, the yield strength was found to be 505 MPa at room temperature, while the tensile elongation was 2.19%. HT-2 led to 34% decrease in yield strength with a value of 373 MPa at room temperature when compared to EBM as-built sample. In addition, the room temperature tensile elongation was 2.09% for HT-2 sample. A ductile transition at 800°C was not seen due to the fully lamellar microstructure formed as a result of HT-2 unlike other samples.

THE EFFECT OF POWDER BED FUSION AND DIRECT DEPOSITION METHODS ON METALLIC MATERIALS

Murat ISIK

Uludag University
TürkiyeTürkiye

Keywords: Directed Energy Deposition, Selective Laser Melting, Stainless Steel, Nickel-based Alloys,

Abstract

The current study brings an understanding of microstructure of metallic materials, e.g., stainless and Inconel 718 alloy. The general characteristics of Inconel 718 and stainless steel, fabricated using powder bed fusion and directed energy deposition methods, were investigated in this study. The main purpose of the current study is to reveal differences in fabrication of metallic materials such as Stainless Steel and Inconel 718 alloy using recent additive manufacturing methods. The variances in grain and sub-grain morphologies, such as size and shape, has been detected due to heat source and processing based thermal effects which are important for the resultant properties of the final product.

1. Introduction

Additive manufacturing is day by day attracting the attention of many scholars and industrial entrepreneurs. Among the additive manufacturing methods the directed energy deposition (DED) [1–3] and powder bed fusion based systems such as electron beam melting and selective laser melting are the most popular [4,5]. Inconel 718 has been in use in aerospace applications and engines stemming from their extraordinary mechanical properties under extreme temperatures. Stainless steel is known with great strength and toughness at elevated temperatures, and is of interest of various sectors, as well. Thus, it is important to better understand the differences in their production and resultant microstructure.

2. Materials and Methods

Inconel 718 powder was fabricated with different additive manufacturing methods; one batch was processed with directed energy deposition (DED), while the other one was made using selective laser melting (SLM). The stainless-steel powder was processed using electron beam melting (EBM) Subsequently, the heat-treated Inconel 718 samples were subjected to heat treatment based on AMS 5664 standard. Microstructure was investigated following the mirror polishing of mounted samples. The electrochemical polishing process was realized by applying an aqueous solution of HCl and potential of 5 V with a lead time of 5-10 seconds. Operation of microstructural observation was completed with an optical microscope (OM) and scanning electron microscope.

3. Results and Discussion

The microstructure of EBM processed stainless steel was shown in Figure 1. Very fine equiaxed grain structure was observed in the case of EBM specimen whereas none of the dendritic structure with δ ferrite and γ cells was spotted as in the case of DED steel. In the case of DED Inconel, elongated cellular structure aligned along the building direction was observed. On the other hand, a finer cellular structure, when comparing to DED, within the boundaries of few hundred-micron sized melt pools was detected for the SLM processed Inconel alloy. Based on experimental results of the current study and previous findings, this phenomenon is related to the cooling rate

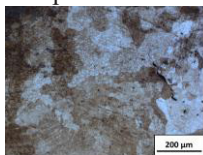


Figure 1 OM image of EBM steel.

differences of the used heat source and laser power between powder bed fusion and blown powder additive manufacturing techniques. For stainless steel, formation of equiaxed grains, are related to process induced heat input other than electron/laser heat source effect.

4. Conclusion

Producing by additive manufacturing manners conveys vital importance to next generation applications in several industries. The improvement of the part's quality is a long way process and understanding final microstructure via changing the additive technology and process parameters has a potential to contribute this challenge.

References

- [1] M. Isik, J.D. Avila, A. Bandyopadhyay, Alumina and tricalcium phosphate added CoCr alloy for load-bearing implants, *Addit. Manuf.* 36 (2020) 101553. <https://doi.org/10.1016/j.addma.2020.101553>.
- [2] J.D. Avila, M. Isik, A. Bandyopadhyay, Titanium–Silicon on CoCr Alloy for Load-Bearing Implants Using Directed Energy Deposition-Based Additive Manufacturing, *ACS Appl. Mater. Interfaces.* 12 (2020) 51263–51272. <https://doi.org/10.1021/acsami.0c15279>.
- [3] K. Dortkasli, M. Isik, E. Demir, A thermal finite element model with efficient computation of surface heat fluxes for directed-energy deposition process and application to laser metal deposition of IN718, *J. Manuf. Process.* 79 (2022) 369–382. <https://doi.org/10.1016/j.jmapro.2022.04.049>.
- [4] M. Isik, E. Kisa, B. Koc, M. Yildiz, B. Pehlivanogullari, Topology Optimization and Manufacturing of Engine Bracket using Electron Beam Melting, *J. Addit. Manuf. Technol.* 1 (2021) 583.
- [5] M.E. Balkan, E. A, M. I, B. Derin, B. K, Directed energy deposition process development for functionally gradient Copper-Inconel 718 materials, *J. Addit. Manuf. Technol.* 1 (2021) 581.



EVALUATION OF PROFICIENCY TEST RESULTS IN FATIGUE TEST IN AEROSPACE METALLIC MATERIALS

Bülent AYDEMİR¹, Hüseyin AYDIN², Fatih GÜLER², Aygün GÜNGÖR², İbrahim KÜÇÜKOĞUL², Havva KAZDAL ZEYTİN²

¹Tübitak UME, ²Tübitak MAM
Türkiye

Keywords: Proficiency test (PT), ASTM E606, fatigue test, EN ISO/IEC 17043

Abstract

An accredited test laboratory must take the proficiency test (PT) to ensure the reliability of its results. It is defined in TS EN ISO/IEC 17025, TS EN ISO/IEC 17043 standards, and TÜRKAK documents within the studies that need to be done to ensure the validity of results.

In this study, samples from the Inconel material used in the aerospace industry of the same specification are prepared according to the ASTM E606 standard. Test samples after a specific numbering have been sent to the participating labs. Each laboratory has applied a fatigue test to samples according to the method described in the ASTM E606 standard. The test results are reported accordingly. All results have been evaluated by TÜBİTAK UME Force Laboratory. The evaluation of the proficiency test results was made in accordance with the TS EN ISO / IEC 17043 standard and the results were presented.

1. Introduction

General conditions for the competence of test and calibration laboratories TS EN ISO / IEC 17025 standard has been defined. It includes the evaluation, approval, and subsequent inspection of the technical competence of the laboratory according to the necessary criteria by an internationally recognized and authorized organization to ensure that the tests and analyzes are carried out with TS EN ISO / IEC 17025 accreditation [1].

A proficiency test is defined as one of the accreditation requirements. Inter-laboratory comparisons and proficiency tests (PT) are important tools for assessing the technical competence of calibration and experimental laboratories. This issue is specified in TS EN ISO / IEC 17025, TS EN ISO / IEC 17043 standards [1,2], and the TURKAK document [3]. It is a requirement of TURKAK that accredited laboratories or laboratories applying for accreditation participate in the PT program and/or inter-laboratory comparisons regarding the measurement sizes within the scope of accreditation and achieve successful results.

In this study, the proficiency test was carried out in the field of fatigue testing of aerospace materials in accordance with ASTM E606 [4] standard. Participating laboratories have carried out the required experiments using their fatigue material testing machines. The measurement results were sent to the TUBITAK UME laboratory in the required

format, and TUBITAK UME prepared the proficiency test report by evaluating the results from the laboratories.

In this study, the results obtained during the proficiency test were discussed, in particular, an analysis was applied in accordance with the TS EN ISO / IEC 17043 standard to evaluate the differences between the average values of test results from different laboratories.

2. Technical Protocol

First of all, the proficiency test technical protocol was prepared and sent to all participating laboratories. The technical protocol is prepared to include the preparation of test samples, distribution to laboratories, timetable for tests, test reports, and test requirements.

2.1. Participants

Three different test laboratories in Turkey participated in this proficiency test. The proficiency test was started on 26.10.2020 and completed on 20.10.2021. Measurements were completed in accordance with the planned time schedule.

2.2. Samples and Test Conditions

The samples to be tested were prepared in accordance with the ASTM E606 standard. Samples were provided by TÜBİTAK MAM ME. Cylindrical specimens with a diameter of 6 mm, taken from the same bar of Inconel 718 superalloy material, were prepared in accordance with a certain numbering. 3 samples were sent to each participant by numbering appropriately. During the proficiency tests, the axial fatigue parameters given in ASTM E606 standards were used for the necessary conditions.

For fatigue test measurement at the room temperature, in order to avoid any difference between the participants, is given that the experimental frequency was 0.25 Hz and the R-value was 1.

For fatigue test measurement at a high temperature, each laboratory performed its measurements at 300 °C. Temperature variation tolerances have been checked in accordance with the ASTM E606 standard. In order to avoid any difference between the participants, is given that the experimental frequency was 0.25 Hz and the R-value was 0.9.

The force values of the machines used for measurements were calibrated according to ASTM E4 and ISO 7500-1 standards, and extensometer devices were calibrated

according to ASTM E83 and ISO 9513 standards. Oven systems are 3-zone and are in a structure to meet the requirements given in the ASTM E606 standard.

Laboratories that have the infrastructure and that are or will be accredited by TURKAK participated in the proficiency test. In order to keep their identities confidential, the results are given with the lab code



Figure 1. Fatigue Testing Machine of TUBITAK MAM

3. Results and Discussion

After completing the tests by each laboratory, the test reports were sent to the TUBITAK UME laboratory. TUBITAK UME laboratory evaluated all test reports according to TS EN ISO / IEC 17043 standard. In the given figures and tables, each laboratory is represented with a letter as A, B, C. The measurement results are prepared using documents from the laboratories participating in the proficiency test and the distributions between the values declared by the participants are given in the tables below.

Table 1. Distribution Ranges of Cycles to fracture of room temperature for the Participant Laboratories

	Mean value	Standard deviation	Max value	Min value	Distribution range (max-min)
Lab	cycle				
A	8286	140	8446	8189	257
B	8050	1126	9110	6868	2242
C	7502	774	8354	6843	1511

Table 2. Distribution Ranges of Cycles to fracture of 300°C temperature for the Participant Laboratories

	Mean value	Standard deviation	Max value	Min value	Distribution range (max-min)
Lab	cycle				
A	11443	2852	14725	9575	5150
B	0	0	0	0	0
C	11882	1179	13205	10942	2263

The average cycle of fracture in fatigue test of room temperature was found to be 7946 cycles. At the same time, the average standard distribution value of the laboratories was observed as 402,4 cycles in Table 1.

The average cycle of fracture in fatigue test at 300°C temperature was found to be 11662 cycles. Laboratory B did not participate in the measurement at 300 C. At the same time, the average standard distribution value of the laboratories was observed as 310,4 cycles in Table 2.

The test reports of all participant laboratories were sent to the TUBITAK UME the resulted proficiency test report was prepared as well. The test results of the participating laboratories were evaluated in according to ISO 17043 standard [3,4].

Measurement results of participating laboratories; Calculated according to the following formula specified in the standard of TS EN ISO / IEC 17043.

Z score is taken as an assessment method of the evaluated results. The Z score is calculated according to the below equation:

$$Z = \frac{x - \bar{X}}{\sigma} \quad (1)$$

- \bar{X} : Reference value
 x : Participating in the laboratory result
 σ : Standard deviation for proficiency testing evaluation

Criteria for performance evaluation should be established after taking into account whether the performance measure involves certain features. The features of z scores for performance evaluation are as follows;

- $|z| < 2.0$ shows adequate performance and does not generate a warning signal.
- $2.0 < |z| < 3.0$ shows questionable performance and generates a warning signal, the problem should be investigated.
- $|z| > 3.0$ shows poor performance and corrective action should be implemented.

Cycles to Fracture (cycle) Room temperature and 300°C temperature for the participated laboratories are given in Table 6 for the calculation of Z scores [5, 6].

Table 3. Calculated Z Score Parameters

Lab	Cycles to Fracture (cycle)	Cycles to Fracture (cycle)
	Room temperature	300°C temperature
A	0,8	-0,7
B	0,3	-
C	-1,1	0,7

4. Evaluation of Performance

Performance evaluation is based on the following performance criteria.

1) $|z| < 2.0$ shows adequate performance and does not generate a warning signal. $2.0 < |z| < 3.0$ shows questionable performance and generates a warning signal, the problem should be investigated. $|z| > 3.0$ underperforms and generates a signal of action and corrective action should be implemented. The differences between the participants are given in the result section of the participants.

2) In the case of the Z Score warning signal and activity signal, possible sources of error are given below.

- the test equipment has not been calibrated.
- the test equipment is not calibrated within its operating range,
- the test equipment did not carry out intermediate checks
- Test technical person is not getting enough education
- used a different method as a test method.

3) If the Z Score value is greater than 10, it makes it impossible to evaluate the results and interpret the performance. For this reason, participant values with a Z-Score value greater than 10 were not included in the calculations.

5. Conclusion

The laboratories, two of which is accredited by TURKAK and the other one of which will be accredited with existing infrastructure, participated in the proficiency test in order to perform the test. The experiments were carried out in accordance with the schedule. Based on the results obtained from the laboratories, this final report was prepared by the TUBITAK UME force laboratory.

As a result of the evaluation of the Z score, It has been determined that the proficiency test measurements of all laboratories in the parameters of the fatigue for room temperature and 300 °C temperature are as "z < 2 sufficient = successful"

In order to verify the testing capability of the test laboratories, the proficiency tests are very important for the assessment of the fatigue test measurement capabilities of all laboratories and they should be repeated periodically.

Table 4. Overall Z score assessment

Z-Score	$ z < 2$		$2 < z < 3$		$ z \geq 3$	
	Num.of Lab	%	Num.of Lab	%	Num.of Lab	%
F _{room}	3	100				
F _{300 C}	2	100				

References

- [1] EN ISO 17025 General requirements for the competence of testing and calibration laboratories, 2017
- [2] ASTM E606-04, Standard Practice for Strain-Controlled Fatigue Testing 2017
- [3] ASTM E4-21, Standard Practices for Force Calibration and Verification of Testing Machines, 2021
- [4] ASTM E83-16, Standard Practice for Verification and Classification of Extensometer Systems, 2017
- [5] EN ISO 7500-1:2018, Metallic materials - Calibration and verification of static uniaxial testing machines - Part 1: Tension/compression testing machines - Calibration and verification of the force-measuring system, 2018
- [6] EN ISO 9513:2012, Metallic materials — Calibration of extensometer systems used in uniaxial testing, 2012
- [7] EN ISO/IEC 17043, Conformity assessment - General requirements for proficiency testing, 2010
- [8] P704, TÜRKAK Yeterlilik Karşılaştırmaları ve Laboratuvarlararası Karşılaştırma Programları Prosedürü, Rev 11, 2020
- [9] Aydemir, B., Proficiency test report for High Temperature Fatigue Test in Metallic Materials, UME-KV-21-08, 2021
- [10] Aydemir, B., Proficiency technical protocol for High Temperature Fatigue Test in Metallic Materials, UME-KV-21-08, 2021



MECHANICAL BEHAVIOR OF REPAIRED CARBON FIBER REINFORCED POLYMER COMPOSITE LAMINATES

Evren SONAT^{1,2}, Mete BAKIR^{2,3}, Sezer ÖZERİNÇ¹

¹Middle East Technical University, ²Turkish Aerospace Industries, ³Yıldırım Beyazıt University
Türkiye

Keywords: Carbon fiber reinforced polymers, Composites, Bonded joints, Composite repair, Mechanical testing

Abstract

This study investigated the on-site repairs of carbon fiber reinforced polymer (CFRP) composites. As such repairs involve out-of-autoclave curing, the process takes place at atmospheric pressure and at relatively lower temperatures. As a result, the defect density tends to be higher, which reduces the mechanical properties. This work aims to investigate the relationships between the repair parameters and the mechanical response, providing data for the effective repair of critical aerospace components.

1. Introduction

Carbon fiber reinforced polymer (CFRP) composites are widely used in the aerospace industry due to their high specific strength. Structural repair is a commonly employed approach to recovering damaged components. Among many repair methods available, scarf and stepped bonded repairs are preferable as they provide superior strength recovery and an aerodynamically smooth finish [1]. The effective implementation of these repairs requires a better understanding of the mechanical performance of the repaired zone [2].

2. Materials and Methods

In this work, we focused on step-sanded flush repairs of composite laminates, performed through wet lay-up and prepreg routes. The process started with the manufacturing of the intact specimens using M21/AS4C carbon/epoxy fabric prepreps by HEXCEL. 18 mm-diameter holes drilled at the center of the panels simulated the damage, which were subsequently repaired by prepreg and wet lay-up patches. An Instron 5985 Mechanical Testing Machine performed the mechanical characterization according to ASTM D3039 on the repaired panels.

3. Results and Discussion

Table 1 shows the summary of the results. The intact specimens, as expected, exhibit the highest strength. Stepped specimens are carved-out versions of damaged specimens providing a baseline of the applied patch having no contribution to strength. The results show that prepreg repairs provide superior performance compared to wet repairs with recovery rates reaching 76%. This behavior is mainly due to the higher curing temperatures and smaller density of defects in pre-pregs compared to that of the wet layup.

Table 1. Summary of the tensile testing results.

Specimen Type	Average Tensile Strength (MPa)	CoV (%)	Recovery Rate (%)
Damaged	244	3.0	40.0
Stepped	149	2.5	24.8
Wet Repaired	398	4.0	66.0
Prepreg Repaired	455	5.4	76.0
Intact	600	2.0	-

4. Conclusions

The study showed that the repair process conditions have a significant impact on the strength of the composite. Prepreg repairs should be the first choice when the component to be repaired has critical load-bearing function.

References

- [1] Yoo J-S, Truong V-H, Park M-Y, Choi J-H, Kweon J-H. Parametric study on static and fatigue strength recovery of scarf-patch-repaired composite laminates. *Composite Structures* 2016;140:417–32.
- [2] Sonat E, Özerinç S. Failure behavior of scarf-bonded woven fabric CFRP laminates. *Composite Structures* 2021;258:113205.

Acknowledgments: We would like to thank the Turkish Aerospace Industries - Composite Manufacturing and Repair Department and the Material & Process Technologies Department for their support.



MICROSTRUCTURAL EVOLUTION OF CMSX-4 SLS SINGLE CRYSTAL SUPERALLOYS DURING CREEP RUPTURE TESTS

Aylin ŞAHİN KAHRAMAN¹, Burak HORASAN², Havva KAZDAL ZEYİN¹, Hüseyin AYDIN¹, Cevat Fahir ARISOY³

¹Tübitak MAM, ²Sakarya University, ³Istanbul Technical University
Türkiye

Keywords: Single Crystal Superalloys, CMSX-4, Creep, Microstructure

Abstract

In the present study, microstructural evolution of standard heat treated CMSX-4 SLS single crystal (SX) superalloy was investigated in different creep conditions via various temperature & stress conditions. To obtain a better understanding for the relationship between microstructure and creep properties of these alloys, samples were standard heat treated (HT) and then thermo-mechanically deformed by creep rupture (CR) tests. Creep tests were applied through with different temperature and stress conditions: at 982°C/221 MPa and at 871°C/620 MPa. Microstructural characterizations were done using with optical and electron microscopy techniques both on HT and CR samples. The investigations were focused on the variation of morphology, volume distribution and size of the γ and γ' phases. Due to different creep conditions, heat treated microstructures evolved similar to the service conditions. As a result, ongoing transformation mechanism of the γ and γ' phases in the matrix was examined via creep tests and a model was tried to suggested.

1. Introduction

Nickel based SX superalloys have unique crystal structure and outstanding high-temperature mechanical properties, thus they are widely used for aeroengine hot-end components which are exposed to high temperature creep deformation as a result of high temperature, long time and heavy service condition. Typical microstructure of SX alloys is consist of two phase: gamma (γ) matrix with face centered cubic crystal structure and gamma prime (γ' - Ni₃(Al,Ti,Ta)) precipitates with L1₂ ordered and coherently embedded in γ matrix. The microstructure of these SX alloys exhibits superior morphological characteristics and positional relationships between the γ' phase and the γ matrix. In addition, high temperature mechanical properties of these alloys highly depend on volume fraction, distribution, size and morphology of the γ' precipitates [1-2].

Due to high temperature exposes, creep deformation is observed in aero-engines (especially their hot-end componets) for a long periods of time . Hence, materials are used in aero-engines which provides extraordinary creep properties such as Ni-based SX superalloys.

It is clear from the literature that several factors can affect the creep properties of Ni-based SX alloys under prolonged temperature and stresses. Temperature and stress of different magnitudes, crystal orientation in the principal stress direction and lattice mismatch have important roles in the microstructural evolution of Ni-based SX [3-4]. In addition, two important deformation mechanisms lead the creep behavior on the microstructure:

i) Rafting: Coarsening of γ' phase in a given direction with a certain pattern is known as rafting. Various studies highlighted that the rafting in Ni-based SX is closely dependent on magnitude of the test temperature and stress value [5-7].

ii) Dislocation structure and dislocation motion of γ' phase: The motion of the dislocations during the creep process causes a nonuniform stress distribution accompanied by a decrease in the energy of the system, and this driving force is responsible for the directional coarsening of the γ' phase. Effect of dislocation density, structure and motion on the creep is discussed in several references [6-8].

One of the most common explanation to creep deformation at high temperatures is that instability of the γ' morphology and plastic deformation as a results of absence of extended stacking fault bands (i.e. twins) and a higher mobility of dislocations. *It is highlighted that high temperature and low stress conditions provides a primary creep followed by a long creep period with low and neary constant strain rate (aka. creep rate).* Moreover, deformation mechanism can active in completely rafted γ/γ' structure which is transverse climb & glide of $a/2\langle 101 \rangle$ interfacial dislocations. This climb behavior model can be seen at meso scale from a specimen elongation, while micro scale from occuring of vacancies and dislocations with $a\langle 100 \rangle$ Burgers vectors. *It is defined that vacancy annihilation and climb through the rafts are both relaxation mechanisms, allowing additional $a/2\langle 101 \rangle$ glide in the matrix channels* [8-9].

On the other hand, the creep deformation behaviour during low temperature creep is explained with shearing of γ' phase by a limited number of dislocations, while high temperature creep leads to accumulation of creep strains with high dislocation activities in γ' phase [10].

It is known that from the literature, γ' precipitate is hard to penetrate by dislocation during creep deformation, thus to increase the creep strength of the alloy volume fraction of the γ' is required between 60-80%. In service conditions, undesired coarsening of γ' precipitates occur due to long time exposures at high temperatures. Thus, creep resistance of the alloy is negatively affected due to loss of interfacial coherency [5-10].

In this study, high temperature/low stress and high stress/moderate temperature creep rupture effects on the microstructure of CMSX-4 SLS superalloy was investigated. Heat treated sample is defined as a reference, then evaluation of morphology, size and volume ratio of γ and γ' phases at 871°C/620 MPa and 982°C/221 MPa creep rupture conditions were examined.

2. Experimental Procedure

CMSX-4 SLS test bars were used in as-cast condition with a chemical composition given in Table 1. All samples were subjected to standard heat treatment procedure (Solution heat treatment (between 1277°C to 1321°C & Gas Fan Quenching) + two step aging (1140°C/6 h + 870°C/20 h & Furnace cooling). Then, Laue crystal misorientation were confirmed according to ASTM E82/E82M standart.

Table 1. Chemical composition of the CMSX-4 SLS (wt.%)

Ni	Co	W	Ta	Cr	Al	Re	Ti
Bal.	9.5	6.58	6.49	6.37	5.81	2.93	0.95
Mo	Hf	Si	Fe	Nb	Zr	Mn	
0.62	0.09	0.03	0.02	0.01	0.004	0.003	

[001] directed single crystal HT test samples (Figure 1) were specified as a reference materials for initial microstructure investigation. Figure 2 represents the cut off locations of HT and CR samples on a test bar.



Figure 1. Presentation of [001] directed HT test bar

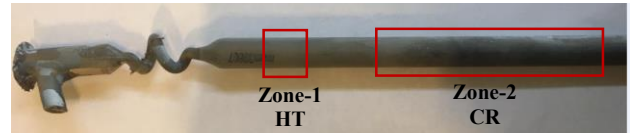


Figure 2. Cut off locations for HT and CR samples

As defined at Figure 2, cut off section Zone-1 used for the characterization of initial HT microstructures; while location Zone-2 were machined according to ASTM E139-11(2018) to obtain creep rupture test samples. Sample codes were defines as given in Table 2. Creep rupture tests were performed in two different conditions: (1) High temperature and low stress (at 982°C/221 MPa), (2) Low temperature and high stress (at 871°C/620 MPa).

Table 2. Sample codes according to the process conditions

Sample ID	Condition
HT	Heat treatment
CR-871	Creep rupture at 871°C/620 MPa
CR-982	Creep rupture at 982°C/221 MPa

Microstructural characterization of HT and CR samples were performed using Olympus BX53M digital optical microscope and Hitachi SU7000 scanning electron microscope equipped with a field emission gun (FEG-SEM) and Oxford Instruments AZteclive Ultim Max100 model energy dispersive spectroscopy (EDS). Samples were prepared and molded in [001] direction, ground and polished down to a mesh size of 0.5 μm . Finally, molded samples were etched with using Marble's Reagent (10 g CuSO_4 , 50 ml HCl , 50 ml H_2O) by immersion method.

3. Results and Discussion

Optical microstructures HT and CR samples were shown in Figure 3 as etched condition. Heat treated microstructure (Figure 3-a) consists of solutionized dendritic regions (DR) and ($\gamma+\gamma'$) eutectic phases at interdendritic regions (IR). Both gamma prime- γ' precipitates (white and nearly cubic formation) and gamma- γ channels (darker area behind the γ') can be clearly seen from higher magnification of optical micrographs. To understand the initial phase formation of the heat treated microstructure, both porosity (%) and ($\gamma+\gamma'$) eutectic phase formation were calculated with a ratio of 0.12% and 0.44% respectively by using optical microscope "Stream Basic" image analysis program.

At first insight from the microstructure of low temperature and high stress sample (CR-871) given at Figure 3-b showed coarser pore size than HT sample, and also some deformation marks can be recognized which is expected due to given temperature and loading creep conditions. However, the creep deformation and strain evidence is more obvious in high temperature/low stress sample CR-982 (Figure 3-c) even at meso scale micrographs due to specimen elongation & creep strain ratio.

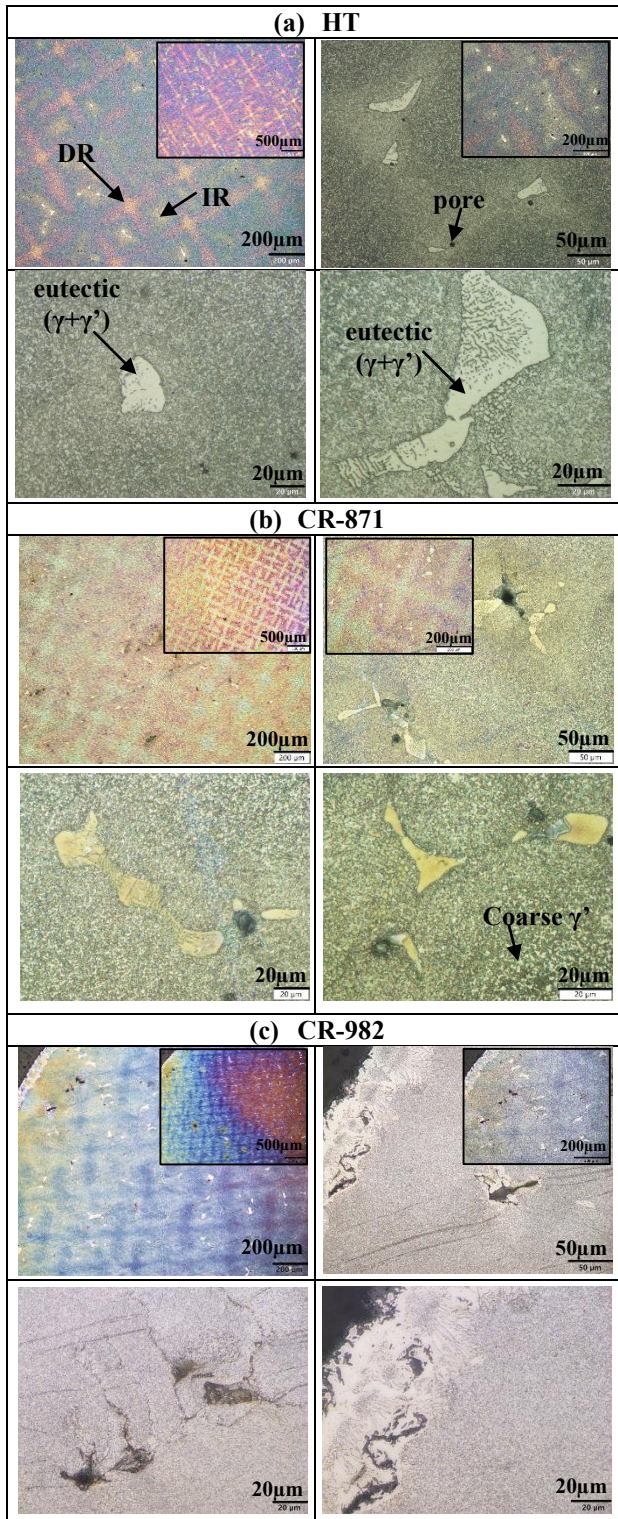


Figure 3. Optical microstructures after (a) heat treatment, (b) creep rupture at 871°C/620 MPa, (c) creep rupture at 982°C/221 MPa by optical microscopy at 5X, 10X, 20X, 50, 100X and 150X magnification

SEM investigation for gamma and gamma prime morphological measurement (γ' volume ratio (%), γ' size

(nm) and γ channel width (nm)) were represented in Figure 4. On the right side of the column, the evolution of gamma prime morphology can be clearly seen (x10.0k magnification) referenced to heat treated and different creep conditions.

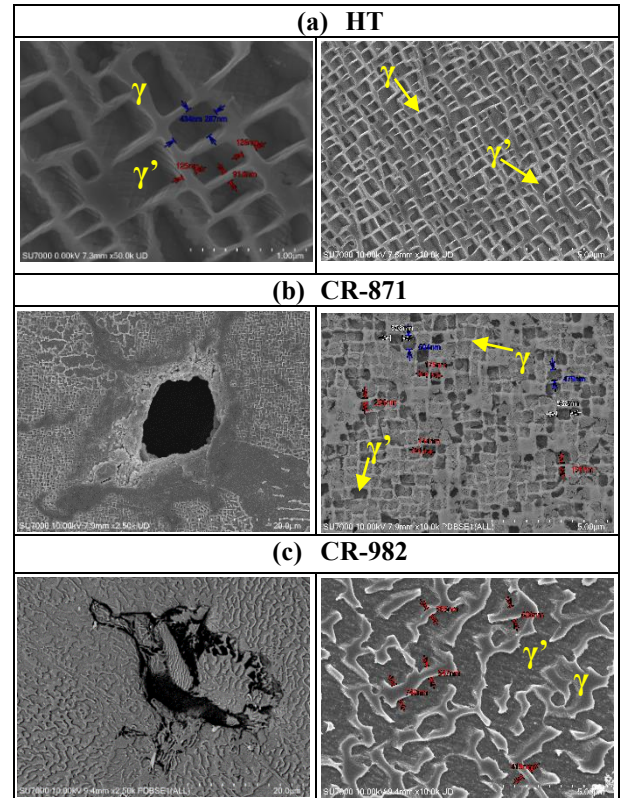


Figure 4. SEM microstructure after (a) heat treatment, (b) creep rupture at 871°C/620 MPa, (c) creep rupture at 982°C/221 MPa

To get better insight, characteristic change in morphology and γ' distortion is analysed by both SEM image analyser and Image-J program. Table 3 shows drastic change in γ' volume ratio which is decreased due to coarsening and agglomeration of primary γ' . Moreover, agglomerated γ' phases make γ channels way of separation resulting by coarsening of γ matrix as well. Although creep strain and total plastic strain ratios are close and in similar trends for both creep conditions as seen in Figure 5, microstructure characterization reveals that coarsening is distinctive at 982°C/221 MPa creep rupture tests. Due to rafting and temperature dependent dynamic strain aging, γ/γ' cuboidal structure evolved to the γ & γ' dual phase structure.

Table 3. Gamma and gamma prime phases morphological measurements

Sample ID	γ' vol. (%)	γ' size (nm)	γ channel width (nm)
HT	71.47	332.8	114.45
CR-871	68.46	534.08	185.25
CR-982	59.56	rafted	535.8

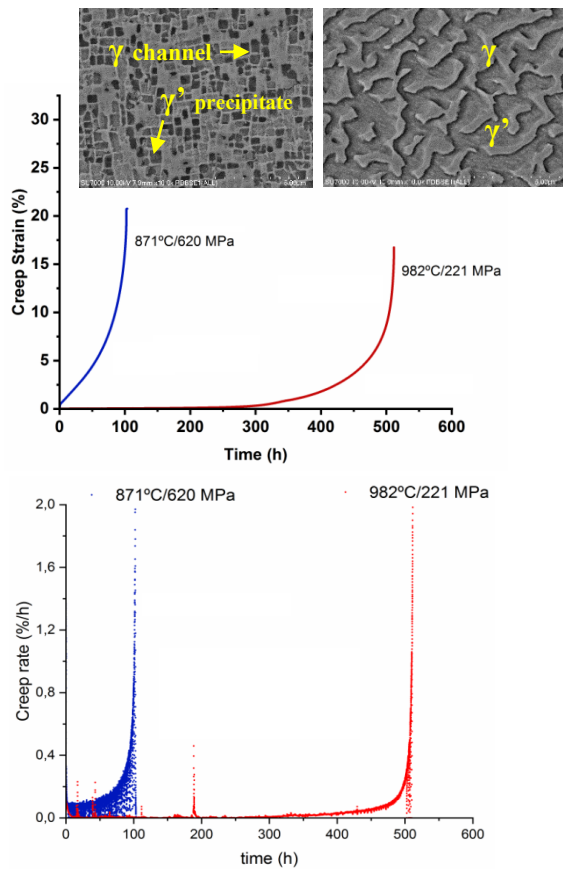


Figure 5. CR-871 and CR-982 samples creep strain and creep rate vs time graphs

4. Conclusion

In the present study, microstructural evolution of CMSX-4 SLS superalloy via two different creep rupture condition was tried to explained. HT sample was specified as a reference for cubic morphology, volume ratio and size of γ' precipitates. After creep rupture tests of both CR-871 and CR-982 samples, coarsened and strained γ and γ' phases observed in 982°C/221 MPa sample due to highly raftened microstructure with agglomerated γ' structure. On the other hand, an obvious distortion and deformation marks can be seen from the 871°C/620 MPa as a result of high stresses and moderated temperatures. Finally, it may concluded that high temperature is more effective on rafting mechanism which is also increase the total plastic strain ratio for a measures rupture time.

Acknowledgment

The authors wish to thank Metallic Materials Technologies Research Group in TUBITAK Marmara Research Center for experimental infrastructure and studies.

References

- [1] W. Xiong *et al.*, “Study of the Creep Behavior of Nickel-Based Single Crystal Superalloy Micro Specimens with Dimensional Effects,” *Crystals*, vol. 12, no. 5, 2022, doi: 10.3390/cryst12050592.
- [2] S. G. Tian, B. S. Wang, X. Ding, D. L. Shu, and J. Wu, “Creep behavior of a single crystal nickel-based superalloy containing Re/Ru at 1100°C/137MPa,” *Mater. Sci. Forum*, vol. 816, pp. 551–556, 2015, doi: 10.4028/www.scientific.net/MSF.816.551.
- [3] R. C. Reed, N. Matan, D. C. Cox, M. A. Rist, and C. M. F. Rae, “Creep of CMSX-4 Superalloy Single Crystals: Effects of Misorientation and Temperature,” *Acta Mater.*, vol. 47, no. 12, pp. 3367–3381, 1999, doi: 10.1016/S1359-6454(99)00217-7.
- [4] R. Wu and S. Sandfeld, “A dislocation dynamics-assisted phase field model for Nickel-based superalloys: The role of initial dislocation density and external stress during creep,” *J. Alloys Compd.*, vol. 703, pp. 389–395, 2017, doi: 10.1016/j.jallcom.2017.01.335.
- [5] P. Caron and T. Khan, “Creep Deformation Mechanisms in Nickel-base Single Crystal Superalloys,” in *Strength of Metals and Alloys (ICSMA 7)*, Jan. 1985, vol. 1, pp. 683–688, doi: 10.1016/B978-0-08-031642-0.50120-3.
- [6] G. Zhao, S. Tian, S. Zhang, N. Tian, and L. Liu, “Deformation and damage features of a Re/Ru-containing single crystal nickel base superalloy during creep at elevated temperature,” *Prog. Nat. Sci. Mater. Int.*, vol. 29, no. 2, pp. 210–216, 2019, doi: 10.1016/j.pnsc.2019.01.013.
- [7] T. M. Smith, R. R. Unocic, H. Deutchman, and M. J. Mills, “Creep deformation mechanism mapping in nickel base disk superalloys,” *Mater. High Temp.*, vol. 33, no. 4–5, pp. 372–383, 2016, doi: 10.1080/09603409.2016.1180858.
- [8] V. Sass, U. Glatzel, and M. Feller-Kniepmeier, “Creep Anisotropy in the Monocrystalline Nickel-Base Superalloy CMSX-4,” no. January, pp. 283–290, 2012, doi: 10.7449/1996/superalloys_1996_283_290.
- [9] A. Epishin and T. Link, “Mechanisms of high temperature creep of nickel-base superalloys under low applied stress,” *Proc. Int. Symp. Superalloys*, pp. 137–143, 2004, doi: 10.7449/2004/superalloys_2004_137_143.
- [10] W. Xia, X. Zhao, L. Yue, and Z. Zhang, “Microstructural evolution and creep mechanisms in Ni-based single crystal superalloys: A review,” *J. Alloys Compd.*, vol. 819, p. 152954, 2020, doi: 10.1016/j.jallcom.2019.152954.



EVALUATION OF PROFICIENCY TEST RESULTS IN HIGH-TEMPERATURE TENSILE TEST IN AEROSPACE METALLIC MATERIALS

Bülent AYDEMİR¹, Hüseyin AYDIN², Fatih GÜLER², Aygün GÜNGÖR², İbrahim KÜÇÜKOĞUL², Havva KAZDAL ZEYTİN²

¹Tübitak UME, ²Tübitak MAM
Türkiye

Keywords: Proficiency test (PT), High-temperature tensile test, EN ISO 6892-2, EN ISO/IEC 17043

Abstract

Test laboratories must verify test procedures and test capabilities for reliable results. Inter-laboratory comparisons (ILC) and proficiency tests (PT) are important tools for evaluating the technical competencies of calibration and test laboratories. This is detailed in the TS EN ISO/IEC 17025, TS EN ISO/IEC 17043 standards, and TURKAK documents. It is a requirement sought by TURKAK that accredited laboratories, or laboratories applying for accreditation, participate in the PT program and/or the ILCs related to tests in the accreditation scope and have achieved successful results.

In this study, samples from superalloy material used in the aerospace industry of the same specification were prepared according to the ISO 6892-2 standard. Test samples after a specific numbering have been sent to the participating labs. Each laboratory performed a tensile test on samples according to the method described in the ISO 6892-2 standard. The test results have been reported by participating laboratories according to the procedures described in the relevant standards. TÜBİTAK UME Force Laboratory there is a reporter laboratory where all the results are evaluated. Evaluation of qualification test conditions, test devices, and results shall be given in detail the calculations carried out in accordance with the TS EN ISO/IEC 17043 standard.

1. Introduction

Testing laboratories should obey the rules of ISO 17025 [1] for their recognition by the customer and increase the quality of their test services. In order to give traceable service in the testing and calibration area, National Accreditation System controls the laboratories in all countries. TURKAK is responsible for the organization of the accreditation system in Turkey.

Testing laboratories need to verify their own test procedures and testing capability. This verification and testing capability of the accredited laboratories can be achieved by coordinating proficiency testing among different laboratories. The TUBITAK MAM organizes proficiency testing to see the closeness and equivalency of the test results among the participating laboratories. Test samples were prepared in superalloy rod material. Each laboratory applied the high-temperature tensile test on the test samples according to procedures given in ISO 6892-2 [2]. All participant laboratories have performed the tests using their own test procedures and own test equipment. Their equipment especially material testing machines were

calibrated by an accredited laboratory in Turkey. Test results were evaluated according to the same procedures explained in related standards by the laboratories.

In this paper, the main results obtained during the proficiency test are discussed; in particular an analysis was applied to evaluate the differences in the mean values by the different laboratories. The calculated Z scores of the test results for the participant laboratories are presented.

2. Technical Protocol

First of all, the technical protocol was prepared and it was sent to all participant laboratories. It includes the preparation of the test samples, distribution of them to the laboratories, the timetable for the tests, test reports, and test requirements [5,6].

2.1. Participant Laboratories and Timetable

Four different test laboratories have participated in this proficiency testing in Turkey. All laboratories declared to provide all special requirements of tensile tests during measurements. Proficiency testing was started on August 12, 2020 and was completed on October 15, 2020. All measurements were completed according to time schedule declared in the technical protocol.

The test machines used in the measurements and their specifications are given in Table 1.

Table 1. The Machines Used in the Measurements and their Specifications

Lab code	Machine information	Specifications
A	Zwick, Z600 model, 600 kN force transducer	Hydraulic grips, clip-on extensometer
B	250 kN force transducer	Hydraulic grips, clip-on extensometer
C	Zwick, Z600 model, 600 kN force transducer	Hydraulic grips, Automatic clip-on extensometer
D	Zwick, Z100 model, 100 kN force transducer	Hydraulic grips, clip-on extensometer

2.2. Samples and Test Conditions

The test samples were prepared according to the description given in the technical protocol. The prepared samples were numbered and packed. Each packet was preserved in the same conditions and it was transferred to the laboratories. Each laboratory tested them on its own test equipment including material testing machine, calliper, and so on. The

test machine of TUBITAK MAM is shown in Figure 1. All testing equipment of the laboratories were calibrated by an accredited calibration laboratory before starting of the proficiency tests. The test conditions and parameters for the performed tests were conditioned and prepared according to standards of ISO 6892-2.



Figure 1. Material Testing Machine of TUBITAK MAM

3. Results and Discussion

After completing the tests by each laboratory, the test reports were sent to the reporter laboratory which is TUBITAK UME Force Laboratory. TUBITAK UME evaluated all test reports according to ISO 17043 standard [3]. In the given figures and tables, each laboratory is represented with a letter as A, B, C, or D. The mean values, standard deviations, and distribution ranges of the laboratories are given in tables 2,3,4,5.

The mean yield strength values were found 218,9 MPa in Table 2. In addition, the average distribution range of each laboratory was determined 35,1 MPa.

Table 2. Distribution Ranges of Yield Strengths (Rp0.2) for the Participant Laboratories

	Mean value	Standard deviation	Max value	Min value	Distribution range (max-min)
Lab	MPa				
A	217,7	21,5	240,0	197,0	43,0
B	220,7	15,5	236,0	205,0	31,0
C	216,3	17,0	236,0	206,0	30,0
D	220,9	14,2	233,5	197,0	36,5

Table 3. Distribution Ranges of Tensile Strengths (Rm) for the Participant Laboratories

	Mean value	Standard deviation	Max value	Min value	Distribution range (max-min)
Lab	MPa				
A	517,7	10,0	528,0	508,0	20,0
B	520,7	12,9	535,0	510,0	25,0
C	516,0	3,6	519,0	512,0	7,0
D	507,6	11,9	520,5	497,0	23,5

Table 4. Distribution Ranges of percentage elongation (A) for the Participant Laboratories

	Mean value	Standard deviation	Max value	Min value	Distribution range (max-min)
Lab	%				
A	62,1	6,3	69,3	57,8	11,5
B	64,8	9,0	73,2	55,4	17,9
C	63,3	1,6	64,5	61,5	3,0
D	68,0	2,9	70,5	64,0	6,5

Table 5. Distribution Ranges of percentage reduction of area (Z) for the Participant Laboratories

	Mean value	Standard deviation	Max value	Min value	Distribution range (max-min)
Lab	%				
A	60,3	1,5	62,0	59,0	3,0
B	60,2	2,0	62,4	58,8	3,6
C	60,7	2,5	63,0	58,0	5,0
D	60,8	3,3	64,0	56,0	8,0

In Table 3, the average distribution range of tensile strength was founded as 515,5 MPa.

The mean percentage elongation values were founded at 64,5 % in Table 4.

The average percentage reduction of the area was found to be 60.5%. At the same time, the average standard distribution value of the laboratories was observed as 2,3% in Table 5.

The test reports of all participant laboratories were sent to the TUBITAK UME the resulted proficiency test report was prepared as well. The test results of the participating laboratories were evaluated in according to ISO 17043 standard [3,4].

Z score is taken as an assessment method of the evaluated results. The Z score is calculated according to the below equation:

$$z = \frac{x - X}{\sigma} \quad (1)$$

where

X : the assigned value

x : the participant's result

σ : the standard deviation of test results

Criteria for performance evaluation should be established after taking into account whether the performance measure involves certain features. The features of z scores for performance evaluation are the following

- $|z| \leq 2$ indicates “satisfactory” performance and generates no signal
- $2 < |z| < 3$ indicates “questionable” performance and generates a warning signal
- $|z| \geq 3$ indicates “unsatisfactory” performance and generates an action signal

Yield strength (Rp0.2), tensile Strengths (Rm), percentage elongation (A), and percentage reduction of area (Z) for the participated laboratories are given in Table 6 for the calculation of Z scores [6,7]. The evaluations of the Z-scores are also given in Table 7.

Table 6. Calculated Z Score Parameters

Lab	Rp 0.2	Rm	A	Z
A	-0,5	0,4	-1,0	-0,6
B	0,8	0,9	0,1	-1,1
C	-1,1	0,1	-0,5	0,6
D	0,9	-1,4	1,4	1,1

Table 7. Evaluated Z-Scores

Z score	$ z \leq 2$		$2 < z < 3$		$ z \geq 3$	
	The number of Lab.	%	The number of Lab.	%	The number of Lab.	%
Rp 0.2	4	100				
Rm	4	100				
A	4	100				
Z	4	100				

4. Conclusions

Four (4) different laboratories have participated in the proficiency testing for high-temperature tensile tests for aerospace metallic material. TUBITAK MAM Material Testing laboratory has organized this proficiency testing.

Initially, technical protocol and test samples were prepared and sent to the participant laboratories. Test measurements were carried out in accordance with the timetable given in technical protocol. After each laboratory completed all tests, the test reports were sent to TUBITAK UME. All test reports were evaluated by TUBITAK UME according to ISO 17043 standard.

In yield strength, tensile strength, percentage elongation, and percentage reduction of area, the assessment method of Z score for all laboratories is determined as "success".

In order to verify the testing capability of the test laboratories, the proficiency tests are very important for assessment of the high-temperature tensile test measurement capabilities of all laboratories and it should be repeated periodically.

References

- [1] EN ISO 17025 General requirements for the competence of testing and calibration laboratories, 2017
- [2] EN ISO 6892-1:2019, Metallic materials - Tensile testing - Part 1: Method of test at room temperature, 2019
- [3] EN ISO 6892-2:2018, Metallic materials - Tensile testing - Part 2: Method of test at elevated temperature, 2018
- [4] EN ISO/IEC 17043, Conformity assessment - General requirements for proficiency testing, 2010
- [5] P704, TÜRKAK Yeterlilik Karşılaştırmaları ve Laboratuvarlararası Karşılaştırma Programları Prosedürü, Rev 11, 2020
- [6] Aydemir, B., Proficiency test report for High Temperature Tensile Test in Metallic Materials, UME-KV-20-03, 2020
- [7] Aydemir, B., Proficiency technical protocol for High Temperature Tensile Test in Metallic Materials, UME-KV-20-03, 2020



THE EFFECT OF THE JOHNSON COOK DAMAGE PARAMETERS ON THE CRUSHING MODES OF AN ELECTRO-BEAM MELT ADDITIVE PROCESSED Ti6Al4V BODY-CENTERED-CUBIC LATTICE STRUCTURES

H. İrem ERTEN, Burak HIZLI, M. Arslan Bin RIAZ, Samed ENSER, Mustafa GÜDEN

Izmir Institute of Technology
Türkiye

Keywords: Additive Manufacturing, Ti6Al4V, Body-Centered-Cubic Lattices, Damage Modes, Modelling

Abstract

Additively manufactured titanium alloys show an impressive energy absorption capacity and high specific mechanical strength. Variation in Johnson Cook damage parameters are quite effective for the crushing modes occurring in the compression simulation of electron-beam-melt (EBM) Ti6Al4V (Ti64) Body-Centered-Cubic lattices (BCC). In this study, the effects of these damage parameters were analyzed numerically and their convergence to the experimentally obtained crushing modes was investigated. Cells having 125 units with 10 mm size, 2 mm strut diameter and 2 mm face sheet thickness were fabricated for this particular study. After the lattice structures were subjected to the experimental compression test, they were simulated using the Johnson Cook damage model in the LS-DYNA program. The optimum value was obtained by comparing the crushing modes of the experimental samples and the numerical lattice models with different initial failure strains (D_1).

1. Introduction

Additively manufactured lattice structures produced from titanium and its alloys are being researched intensively due to their impressive properties like the strength of weight ratio and corrosion resistance. The current literature on the collapse modes of these structures are mixed in that the collapse mode varied between brittle strut fracture, a

sudden collapse of successive layers, shear location, cell extension mode and so on [1]. Noting characterizing the material behavior under the effects such as strain, flow stress and strain rate has become a very important issue, especially in industrial applications, the present study focused on obtaining a suitable/applicable stress and strain model formulation for such lattices [2]. In this study, experimental and numerical studies were carried out to investigate the effects of Johnson Cook damage parameters [3] of EBM- Ti64 BCC lattices on the fracture modes of these structures. Initially, quasi-static compression tests were performed on 125-unit cell EBM-Ti64 BCC lattice structure samples to obtain the material parameters to be used for modelling in the LS-DYNA commercial program. To be able to use lattice structures in various applications, mechanical property characterization of mechanical properties is required. Due to the properties of the EBM method, manufacturing defects, microstructure, loading conditions and building direction have a great effect on the mechanical properties of lattice structures [4]. For this reason, parameters obtained from bulk material tests do not always give accurate results in the characterization of lattice structures and determination of crushing mode when used in numerical analysis. Also, the initial failure strain values as it affects the crushing mode of the lattice structure were investigated.

2. Experimental and Finite Element Procedures

BCC Ti64 lattices were designed using SolidWorks and fabricated with producer-set parameters using 30-110 μm (57 μm mean size) powder on the Arcam Q20+ EBM device. As shown in Figures 1(a-c), the lattice structure is manufactured with 125-unit cells, a unit cell size of 10 mm, a strut diameter of 2 mm, and a face sheet thickness of 2 mm. The z-axis is the build direction, and the tests were carried out on the y-axis which is perpendicular to the build direction. Archimedes' method was used to determine the densities and to calculate the porosity of the Ti64 lattice structure specimens accordingly. The relative density of the BCC lattice structure was determined by CAD calculation. The Maxwell criterion [5] was used to decide whether the BCC lattice structure exhibits stretching or bending dominant behavior under the effect of stress. Calculation of this collapse strength in BCC lattice structures deformed by bending-dominated was calculated using the Ashby-Gibson equation [6, 7]. Then, the compression tests were performed in the Shimadzu AG-X Universal Test Machine at $1 \times 10^{-3} \text{ s}^{-1}$ with at least three tests.

The material properties obtained from the test results are shown in Figures 2(a, b) and their approximate values are used for modelling.

After the experimental compression tests, uniaxial quasi-static compression behaviors of 125 unit-cell lattices were modeled with a strain rate of $1 \times 10^{-3} \text{ s}^{-1}$ in the LS-DYNA program as shown in Figure 3.

The modified Johnson-Cook flow stress (1) and damage equation (2) were used to model the lattices:

$$\sigma = (A + B\varepsilon^n) \quad (1)$$

$$\varepsilon_f = [D_1 + D_2 \exp(D_3 \sigma^*)] \quad (2)$$

In this equation, ε and σ are the true plastic strain and equivalent true strain, respectively. A are the initial yield stress and B and n are strain hardening constant. D_1 , D_2 and D_3 are initial failure strain, exponential factor and

triaxiality constant, respectively. Initially, the upper and lower compression heads of the device were modeled using 500 solid elements to simulate the compression test environment. The lattice structure to be analyzed is meshed in hexahedron form with a 0.7 mm element size.

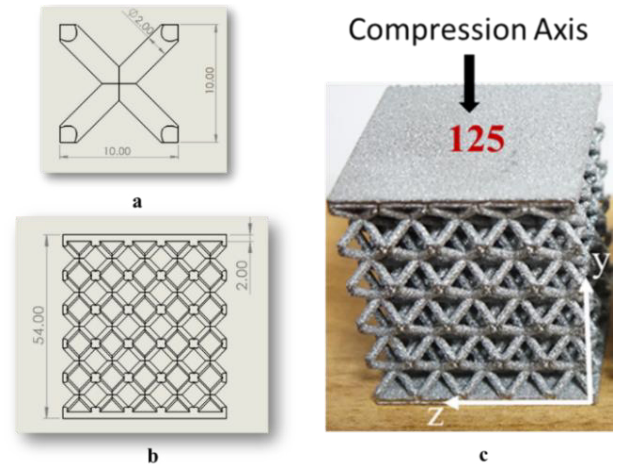


Figure 1. (a) CAD model of unit cell and (b) BCC Lattice Structure and (c) EBM-Ti64 BCC Lattice Structure

In addition, the Ti64 material was modeled with the Johnson Cook damage model using the A, B and n values in Figures 2(a, b) and the polynomial equation of state (Eos). According to the experimentally obtained data, the elastic modulus, Poisson ratio and Ti64 density in this model were entered as 107 GPa, 0.31 and 4317 kg m^{-3} , respectively. However, the low initial failure strain value (D_1) and geometric inhomogeneity obtained as a result of the test made the lattice structure very brittle resulting in sudden failure. For this reason, new initial failure strain values that comply with the experimental results have been studied.

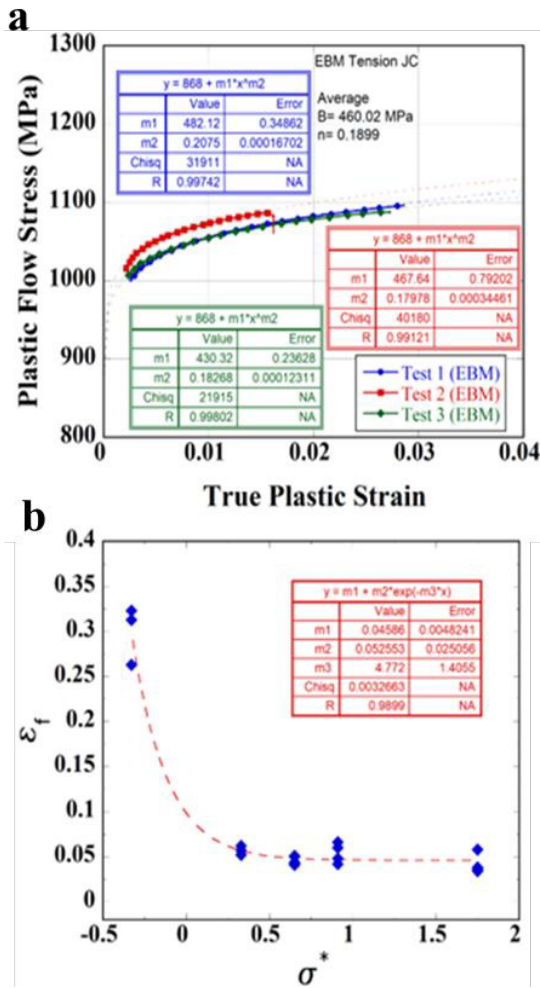


Figure 2. Determination of Johnson Cook parameters (a) A, B, n and (b) D_1 , D_2 D_3 values

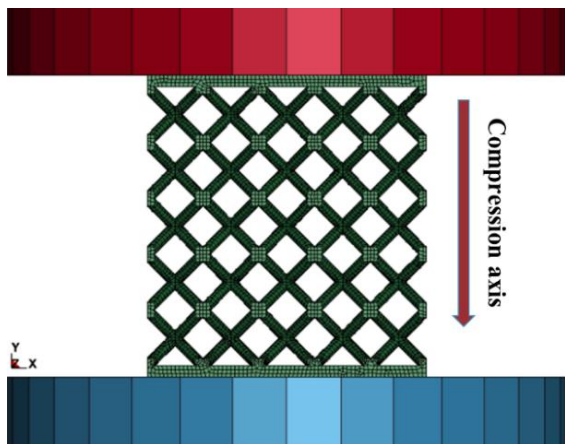


Figure 3. The compression test model of BCC lattice structure

3. Results and Discussion

The experimental and numerical stress-strain curves with different initial failure strains for BCC lattice as shown in Figure 4. As seen in the figure, the slump strength of the mesh decreases as the initial failure value decreases. Therefore, the deformation modes of lattices with different D_1 values are quite different.

It was obtained as $D_1=0.04$ from bulk material tests. However, the established model has not matched the test result by exhibiting a quite brittle crushing mode. Therefore, as a result of the analyzes made to obtain a reliable crushing mode in the model, the D_1 parameter was determined as 0.2. In addition, as can be seen from the figure, when $D_1=0.2$ in the model, the trends in experimental and simulation curves are similar.

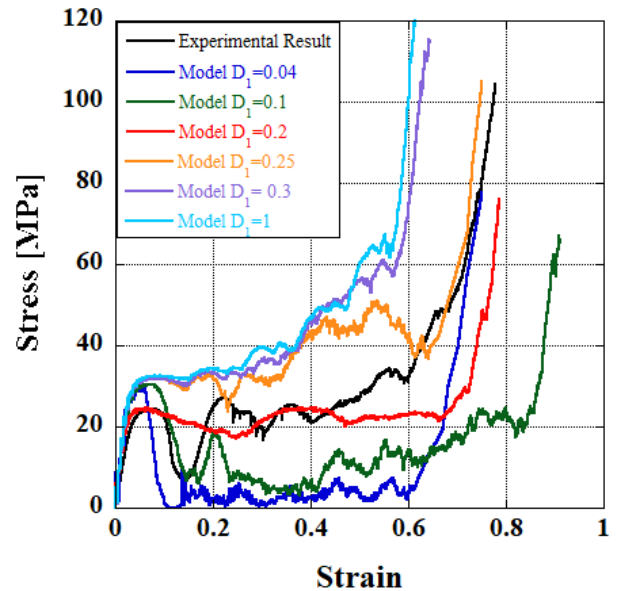


Figure 4. The stress-strain curves with different D_1 parameter

The deformation behaviour of BCC lattices with 125 cells can be seen in Figure 5. A comparison has been made between the deformation shapes for several initial failure strain (D_1) values at different strain rates. When the values of D_1 were 0.04 and 1 we can see no correlation between the experimental and numerical deformation behaviours. But for the D_1 value of 0.2, we see strong similarities in the bending behaviour of the lattices. This value of failure strain gives comparable results between experiments and simulations

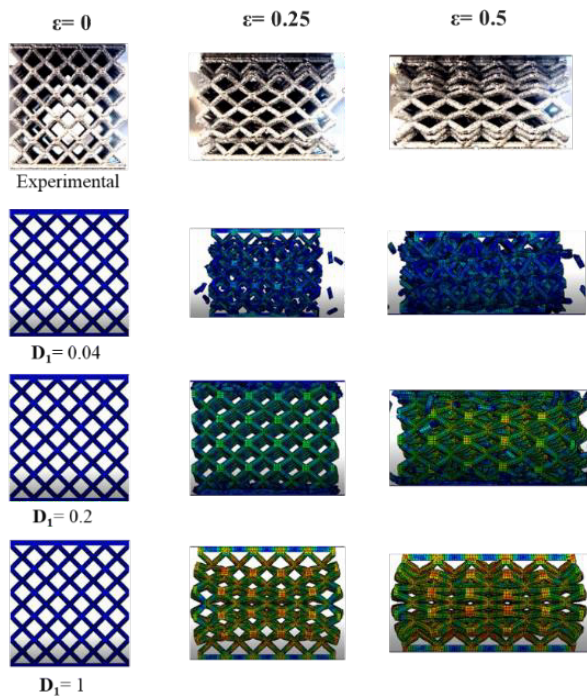


Figure 5 The experimental numerical deformation stage of Ti64 BCC lattices at different strains and initial failure strain

4. Conclusion

In conclusion, experimental and numerical studies were carried out to investigate the effect of Johnson-Cook damage parameters on the fracture modes of EBM-Ti64 BCC lattice structures. The Johnson-Cook damage model values obtained from the tests of a bulk material showed a crush mode mismatch between the model and the test. A correct material damage parameter is necessary for the reliable modelling of a lattice structure. Therefore, an optimization study was performed on the D_1 value (0.04) in order to capture the crush mode obtained from the test. As a result of the study, when the D_1 value was taken as 0.2, it was found that the test and model stress-strain curves converged with each other in a better way.

5. References

- [1] S. Drücker, M. Schulze, H. Ipsen, L. Bandegani, H. Hoch, M. Kluge, B. Fiedler, Experimental and numerical mechanical characterization of additively manufactured Ti6Al4V lattice structures considering progressive damage, *International journal of mechanical sciences* 189 (2021) 105986.
- [2] D. Herzog, V. Seyda, E. Wycisk, C. Emmelmann, Additive manufacturing of metals, *Acta Materialia* 117 (2016) 371-392.
- [3] G.R. Johnson, W.H. Cook, A constitutive model and data for metals subjected to large strains, high strain rates and high temperatures, *Proceedings of the 7th International Symposium on Ballistics* (1983).
- [4] S. Liu, Y.C. Shin, Additive manufacturing of Ti6Al4V alloy: A review, *Materials & Design* 164 (2019) 107552.
- [5] J.C. Maxwell, L. on the calculation of the equilibrium and stiffness of frames, *The London, Edinburgh, and Dublin Philosophical Magazine and Journal of Science* 27(182) (1864) 294-299.
- [6] M.F. Ashby, *Cellular Solids – Scaling of Properties*, Cellular Ceramics2005, pp. 1-17.
- [7] L.J. Gibson, M.F. Ashby, *Cellular solids: Structure and Properties*, Cambridge University Press (2. Edition) (1997).

INFLUENCE OF PLATFORM DIMENSIONS ON THE SECONDARY GRAIN FORMATION IN PRODUCTION OF SINGLE CRYSTAL TURBINE BLADE

İbrahim BERBER, Sertaç ALPTEKİN, Lütfi YAKUT, Bülent BAHADIR, Havva KAZDAL ZEYİN

Tübitak MAM
Türkiye

Keywords: Single crystal, Superalloy, Microstructure, Defect

Abstract

In this study, the relationship between the CMSX-4 single crystal turbine blade superalloy to be produced and the secondary grain defect that will occur on the platform surface when the turbine blade platform size parameters are changed is investigated. For this purpose, by determining the appropriate thermal gradient and withdrawal rate, solidification was carried out in the Vacuum Induction Melting (VIM) furnace with the Bridgman Method. Consequently, platforms of different sizes were created and their microstructures were analyzed.

1. Introduction

CMSX-4, which is a popular member of single-crystal super alloys used in the aerospace industry, provides superior performance with its ultra-high strength, low life cycle, and hot section durability. The production process is very important for the second generation nickel-based single crystal super alloy containing rhenium to be used under optimum conditions. The process, which starts with the investment casting process, continues depending on the parameters of thermal grandaunt, withdrawal, and cooling rate in the Bridgman furnace. In the single crystal alloy casting process, when the thermal gradient and withdrawal parameters cannot be controlled, it can cause dendrite deformation in the part and platform, and then secondary grain defects on the surface.

2. Materials and Method

In this study, four clusters were created with the help of plastic injection in order to perform the casting processes. After all the formed parts were combined, ceramic coating was applied on the model mold. After dewaxing and sintering in an autoclave, casting was carried out in Bridgman furnace with CMSX-4 second generation single crystal alloy. Platform dimensions in each cluster are given in figure 1 and table 1.

A(mm)		B(mm)		C(mm)		D(mm)	
A1	10x10x5	B1	14x14x3	C1	10x10x3	D1	14x14x4
A2	10x10x4	B2	12x12x3	C2	10x10x4	D2	12x12x4
A3	10x10x3	B3	10x10x3	C3	10x10x5	D3	10x10x4

Table 1. Platform Dimensions

Cr	Co	Al	Ta	W	Mo	Ta	Hf	Re	Ru
6.4	9.6	5.6	6.5	6.4	0.6	6.5	0.1	3.0	-

Table 2. CMSX-4 Material Chemical Ratio in %

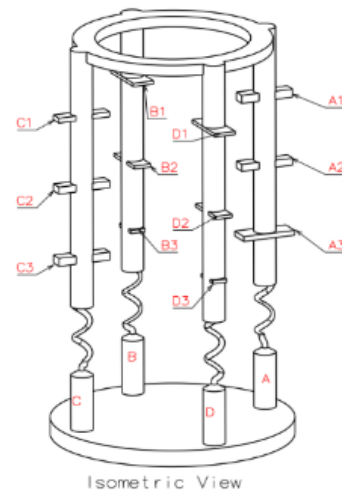


Figure 1: Single Crystal Production Mold

3. Conclusion

It was observed that with increasing platform dimensions, more nucleation occurred at the corner points and grew in the form of dendrites towards the centre. With the increase of the platform width, the possibility that the towing speed may be inversely proportional has been revealed. Secondary grain was observed on the surface.

References

Meng, X. B., et al. "Effect of platform dimension on the dendrite growth and stray grain formation in a Ni-base single-crystal superalloy." Metallurgical and Materials Transactions A 44.4 (2013): 1955-1965.

MICROSTRUCTURAL CHARACTERIZATION OF FORGED INCONEL 718 SUPERALLOY AFTER LONG TERM HIGH TEMPERATURE EXPOSURE

Burak HORASAN¹, İbrahim BERBER¹, Fatih GÜLER², Havva KAZDAL ZEYTİN², Hüseyin AYDIN²

¹Sakarya University, ²TUBITAK Marmara Research Center
Türkiye

Keywords: Thermal cycle, Hot deformation, Superalloy, Microstructure

Abstract

The aim of this study is to investigate the microstructure and mechanical evaluation of Inconel 718 superalloy after long thermal cycle oxidations. Inconel 718 superalloy, produced by triple melting, was deformed by radial forging at high temperatures and subjected to heat treatment. Thermal cycle tests carried out to examine the thermal stability of materials that will operate in service conditions similar to gas turbine conditions. Microstructural and mechanical characterizations were performed to provide the evaluation of $\gamma \rightarrow \gamma'$, γ'' formation after a long service of thermal cycle test.

1. Introduction

Inconel 718 is a Nickel-based superalloy preferred in the combustion chambers of gas turbine engines in the aviation industry due to its high temperature and oxidation resistance. In the austenitic γ matrix, various precipitates can be seen as γ' , γ'' , δ and laves. Among these precipitates, γ'' (Ni₃Nb) provides a significant role in high temperature strengthening of this alloy [1]. Considering the additional topological closed packet (TCP) formation in these superalloys during thermal cyclic oxidations, stability of γ' and γ'' becomes crucial. Therefore, material characteristics will be examined through thermal cycle tests.

2. Materials and Method

The casting of Inconel 718 superalloy was carried out by “Vacuum Induction Melting” (VIM) to prevent formation of inclusions as well as contamination. Then, in order to further reduce the inclusions, the casting ingot is remelted by “Electro Slag Remelting” (ESR) followed by “Vacuum Arc Remelting” (VAR) respectively. The part were cut from VIM + ESR + VAR ingot and deformed at elevated temperatures with radial forge. Then, applied to standard heat treatment. Each step was shown in Figure 1. After heat treatment, half of the samples were used to get reference creep behaviors. Finally, the other half of the heat-treated samples were subjected to thermal cycling test and planning to conduct creep tests to compare effect of service conditions.

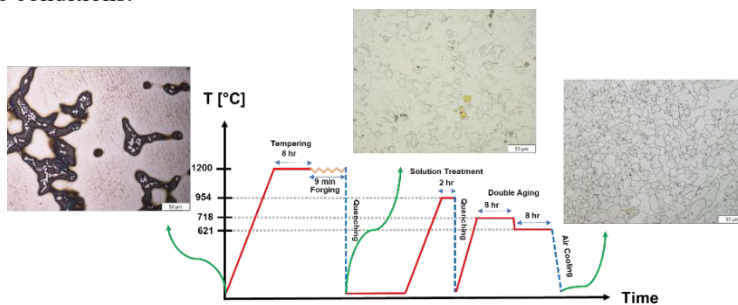


Figure 1. The processes until mechanical characterization

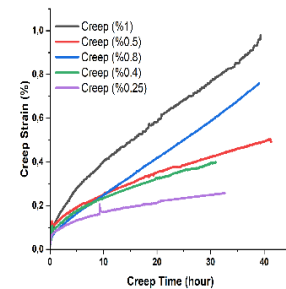


Figure 2. Creep Strain-Time curves

3. Conclusion

After the forging process, the dendritic structure has deteriorated. Niobium-rich laves phases dissolved. Dynamic recrystallized (DRX) grains were observed in the microstructure. The results of the creep test performed after heat treatment are given in Figure 2. Tests of the thermally cycled samples are still in progress will be presented in the conference. Finally, microstructures of creep tested and thermal cycle applied samples will be implemented.

References

- [1] Chamanfar, A., Sarrat, L., Jahazi, M., Asadi, M., Weck, A., & Koul, A. K. (2013). Microstructural characteristics of forged and heat-treated Inconel-718 disks. *Materials & Design* (1980-2015), 52, 791-800.



STCS

Surface Treatment and Coating Symposium

Yüzey İşlemler ve Kaplama
Sempozyumu

ZnO NANOWIRE GROWTH VIA ANODIZATION

Yiğithan TUFAN, İpek Tuğçe DÖŞ, Batur ERCAN

Middle East Technical University
Türkiye

Keywords: Surface Modification, Anodization, ZnO Nanowire, Implant, Antibacterial

Abstract

ZnO nanowires having three different sizes (70 ± 8 nm, 97 ± 7 nm and 140 ± 9 nm) were obtained via anodization. The effect of ZnO nanowire diameter on their antibacterial properties was assessed with both gram-negative *Escherichia coli* (*E. coli*) and gram-positive *Staphylococcus aureus* (*S. aureus*) bacteria. In addition, the effect of ZnO nanowires on bone cell proliferation was investigated *in vitro*. Our results showed that ZnO nanowire diameters could be controlled in the nanoscale by optimizing anodization parameters, and this, in turn, simultaneously enhanced antibacterial and biological properties of ZnO nanowires.

1. Introduction

One of the main problems in currently-used orthopaedic implants is surgical site infections which can gradually lead to permanent tissue damage, delayed healing and implant failure. Zinc-based materials, especially zinc oxide (ZnO) nanostructures (nanoparticles, nanopules and nanowires, etc.) are attracting significant attention in bone tissue engineering due to their antibacterial properties [1]. Anodization was extensively studied for the formation of nanostructures on metallic surfaces and to control the size and morphology of these nanostructures [2]. Therefore, the aim of this study was to obtain ZnO nanowires via anodization and control their size by optimizing the anodization parameters, including duration, potential and temperature. This allowed us to investigate the effect of ZnO nanowire size on its antibacterial and biological properties.

2. Materials and Methods

Zn plates were cut into 2 cm x 1 cm pieces, mechanically polished and ultrasonically washed in acetone, ethanol, and DI water, respectively (SEM image of polished Zn was given in Figure 1). Samples were anodized (platinum mesh was used as the cathode) for 2 min using 0.2 M NaHCO₃ solution. Three different ZnO nanowire sizes, 70 ± 8 nm (NW70), 97 ± 7 nm (NW100), and 140 ± 9 nm (NW140), were obtained under the applied voltages of 1V, 3V, and 5V, respectively (Figure 1). Morphologies and crystal structures of ZnO nanowires were also investigated under TEM. Moreover, their physical and chemical properties were characterized in detail. The effect of ZnO nanowire size on its antibacterial efficacy was investigated using both gram-negative *E. coli*, and gram-positive *S. aureus* bacteria. Finally, *in vitro* biological tests were carried out using osteoblasts.

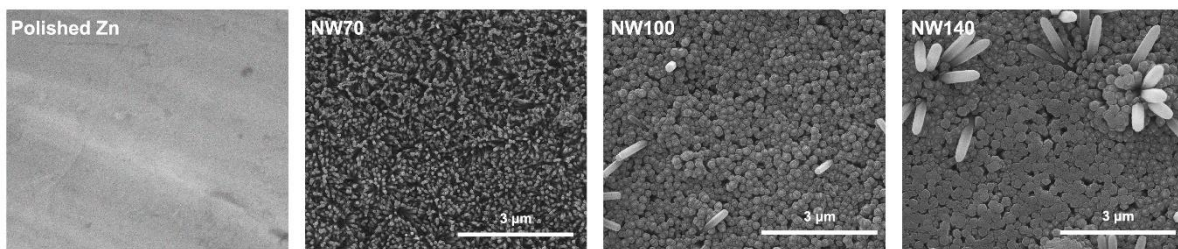


Figure 1. SEM images of polished and anodized Zn surfaces

3. Conclusions

ZnO nanowires were obtained via anodization and their sizes were altered at the nanoscale through the optimization of anodization parameters. Among all samples, NW70 exhibited the best antibacterial performance while maintaining osteoblast proliferation. Morphological, chemical and physical properties of ZnO nanowires, as well as their crystal structures were characterized to better understand nanowire formation mechanism and their biological interaction *in vitro*. It was anticipated that our findings might pioneer further studies to develop antibacterial implant surfaces.

References

- [1] Y. Su, I. Cockerill, Y. Wang, Y.X. Qin, L. Chang, Y. Zheng, and D. Zhu, Trends in Biotechnology, 37 (2019) 428-441.
- [2] S. Minagar, C. C. Berndt, J. Wang, E. Ivanova, and C. Wen, Acta Biomaterialia, 8(8) (2012) 2875-2888.



PRODUCTION AND CHARACTERIZATION OF GOLD NANOFILMS ON TRANSPARENT SUBSTANCES BY ELECTRODEPOSITION METHOD

Uğur BARUT, Metehan ERDOĞAN

Ankara Yıldırım Beyazıt Üniversitesi
Türkiye

Keywords: Electrodeposition, Au nanofilms, Pulse current, Optical properties

Abstract

In this study, deposition of gold nano films on indium tin oxide (ito)- coated glasses by pulse current electrodeposition method was examined. The gold nanofilms obtained on ito-coated glasses were characterized by focused-ion beam, thin film X-ray diffraction, scanning electron microscope, optical transmittance measurements and atomic force microscope.

1.Introduction

Thin film coatings have applications in many fields such as optics, chemistry, magnetics, electricity and mechanics. The most prominent of these are anti-reflective coatings applied to lenses and solar cells, reflective coatings used in mirrors, waveguide applications, diffusion-blocking layers, corrosion-resistant coatings, various sensor applications, films created to reduce friction or provide rigidity. In addition, coatings and piezoelectric applications can be included to provide conductivity and insulator to circuit elements such as resistors and capacitors [1].

2. Materials and Methods

In this study, gold nano films were produced on ito-coated glasses at different current densities by applying pulse current electrodeposition method. Table 1 shows ingredients and working conditions of gold electrolytes

Table 1. Ingredients and working conditions of gold electrolytes

	Potassium dicyanoaurate (g/L)	Citric Acid Monohydrate (g/L)	Ph	Temperature	Current Density (A/cm ²)
Gold Strike Electrolyte	0.08	18	3.5	30	10
Acid-Gold Cyanide Electrolyte	0.8	180	3.5	30	0.02, 0.04, 0.08

3. Conclusions

The thickness of the nanofilms obtained on ito-coated glasses was measured by focused-ion beam method and it was observed that the nanofilms were coated at all current densities and their thickness was around 10 nm. The results revealed that electrochemically produced gold nanofilms could be useful in various applications.

References

[1] Lee, Y., Kim, D., Jeong, J., Kim, J., Schmid, V., Korotchenkov, O., Vasa, P., Bahk, Y.M., Kim, D.S. 2019. "Enhanced terahertz conductivity in ultra-thin gold film deposited onto (3-mercaptopropyl) trimethoxysilane (MPTMS)-coated Si substrates", Sci. Rep., 9, 15025



EFFECT OF SUBSTRATE BIAS ON MECHANICAL PROPERTIES OF MAGNETRON SPUTTERED AlTiN-B₄C FILMS

Özden KISACIK^{1,2}, Cennet YILDIRIM^{1,3}, Erkan KAÇAR^{1,4}, Servet TURAN²,
Sedat SÜRDEM⁵

¹Boron Research Institute, ²Eskisehir Technical University, ³Istanbul Technical University,
⁴Hakkari University, ⁵Gazi University
Türkiye

Keywords: AlTiN-B₄C Coatings, Bias Voltage, Mechanical Properties, Tribology

Abstract

The primary objective of this research was to investigate the mechanical and tribological properties of AlTiN-B₄C hard coatings deposited by magnetron sputtering physical vapor deposition (PVD) method by employing different substrate bias voltages. In the present study, a pulsed dc magnetron sputtering PVD system was adopted to prepare AlTiN-B₄C coatings. The deposition was done on the Si wafers, AISI 304 SS and AISI 1.3343 M2 grade high speed steel substrates. Al_{0.67}Ti_{0.33} and B₄C were used as target sources for deposition. The chemical states in the coatings was observed through XPS analysis. Phase formations were detected by XRD. The surface morphology and the thickness of all the coatings were investigated by FE-SEM analysis. The hardness and Young's modulus were measured via nanoindentation test. Tribological behaviors of the coatings were examined by ball-on-disc tribometer at room temperature against Al₂O₃ ball. Overall, experimental results indicate that the changing the substrate bias voltage has an important effect on the structural, and morphological properties but there is no obvious effect on mechanical properties of AlTiN-B₄C coatings.

1. Introduction

As technology and engineering applications develop, it is a more practical and less costly method to improve the surface properties instead of modifying the entire material in order to give materials new properties or improve their behavior in different environments. For this reason, the interest in coating technologies is increasing day by day. When industrial applications are examined, it is seen that physical vapor deposition (PVD) and chemical vapor deposition (CVD) methods are commonly used [1]. The PVD coating process can be summarized as the process of coating (in a controlled manner) the surface of a base material by using the solid target material which is evaporated or sputtered turning it into the high-energy plasma in a vacuum environment without the need for very high temperatures. There are several PVD techniques were developed in order to modify the surface characteristics and also the properties of the base materials [2]. Deposition techniques and deposition parameters (working pressure, substrate temperature, bias voltage, reactive gases, deposition rate, etc.) directly affect the morphological, structural, and mechanical properties of the deposited films. Especially in the machining industry, hard and protective coatings such as

TiN are highly demanded. These hard and protective coatings enable the longer life time and effective machining performance of the tools. The addition of Al to TiN coating greatly improves its mechanical properties, oxidation resistance. In addition, AlTiN coatings exhibit a high age-hardening effect. On the other hand, the addition of the alloying elements such as boron and/or carbon to the AlTiN coatings enhances the mechanical, tribological properties, cutting performance, and thermal stability of the coating. Many studies show that the addition of carbon and/or boron to AlTiN coatings increases the mechanical properties effectively [3-5].

The primary objective of this research was to investigate the structural, mechanical and tribological properties of AlTiN-B₄C hard coatings deposited by magnetron sputtering PVD employing different substrate bias voltages. Observed differences on the properties of the coatings among the samples deposited with different process parameters were discussed and correlated with different deposition conditions.

2. Experimental Procedure

In the present study, a pulsed dc magnetron sputtering PVD system was adopted to prepare AlTiN-B₄C coatings. The deposition was done on the Si wafers, AISI 304 SS and AISI 1.3343 M2 grade high speed steel substrates. High purity Al_{0.67}Ti_{0.33} and B₄C were used as magnetron target sources for deposition. Before deposition, in order to obtain high quality films, substrate materials have been mirror finished and ultrasonically cleaned in acetone and ethanol for 15 min respectively. In the deposition process, first of all chamber was evacuated to less than 5×10^{-4} Pa and the process temperature was kept constant at 150°C for all coatings. In order to remove surface oxides and impurities on the samples, glow discharge process was done with Ar ions for 15 min at 1000 V substrate bias. During the deposition process, the revolution speed was set to 2 rpm, and target powers were adjusted 1.5 kW for both Al_{0.67}Ti_{0.33} and B₄C. The coating process began with deposition of chromium (Cr) primary layer for 5 min and then Chromium Nitride (CrN) interlayer for 10 min were done via cathodic arc PVD technique to improve adhesion between the main coatings and substrate. This interlayer coatings were carried out in an Ar and N₂ atmosphere at a pressure of 1 Pa. The bias voltage of -100 V was applied to the substrate and the target current was set to 80A. All these primary processes were fixed for all coatings. Four different sets of AlTiN-B₄C coatings were deposited

using different negative bias voltages (0V, 50V, 100V, and 150V) in fixed 67%-33% Ar-N₂ gas environment at a working pressure of 0.5 Pa. The deposition parameters was given in table 1.

Phase formations of the deposited films were determined by X-Ray Diffraction with CuK α radiation at 40 mA and 45 kV. The chemical states in the coatings was observed through XPS analysis. Prior to the XPS analysis, the specimens were etched by Ar ions. XPS survey scans were done in all coatings in order to check the overall compositions in 1300-0 eV binding energy range, with 1 eV step size. After the survey scan, the narrow scans were performed using 0.1 eV step size, and 50 eV pass energy for Al2p, B1s, N1s, Ti2p, and C1s. All these analysis were performed at the 400 μ m spot size. The surface morphological properties and the thickness of the deposited films were investigated by FE-SEM equipped with EDS. The hardness (H) and Young's modulus (E) of the coatings were measured via nanoindentation test equipped with Berkovich type indent under 30 mN load and 10 different indents per sample were performed for all specimens. Tribological behaviors of the coatings were examined by dry sliding tests using ball-on disc tribometer at room temperature against Al₂O₃ ball with a diameter of 6mm. The tests were carried out under a 5 N load, with a speed of 10 cm/s, and sliding distance of 100 m. Wear tracks were measured from four different parts using optic microscope and the average value of the cross-sectional area was determined. Lastly the wear rate (Ws) of each coating was calculated.

Table 1. Deposition parameters

Targets	Al _{0.67} Ti _{0.33} , B ₄ C, and Cr
Deposition Time	1.5 hours
Working Pressure	0.5 Pa
Deposition Temperature	150 °C
Gases	Ar and N ₂
Rotational Speed	2 rpm
Intermediate Coatings	Cr-CrN
Substrate Bias Voltage (V)	0V 50V 100V 150V
Ar-N ₂ Gas Ratio	67%- 33%
Magnetron target power (AlTi-B ₄ C Targets)	1.5-1.5 kW

3. Results and Discussion

3.1. Chemical compositions and crystalline structure

According to the XPS results the total amount of B and C is higher in the sample produced 100V bias voltage. Figure 1a shows that the XPS spectra of Al2p, B1s, N1s and Ti2p for the sample produced using 100V bias voltage. For components were assigned to the binding energies of 73.1 eV, 74.3 eV, 75.1 eV, and 74 eV corresponding to Al-B, Al-O-B, Al-O, and Al-N respectively [6,7]. Obviously, the Al-B bond that really exist for Al2p spectrum in the coating. The fitting results (Fig. 1(b)) show that the XPS spectrum of the B1s in composed of four components. It was seen that B bonds not only with Al, but also with Ti which is observed in

Ti2p spectrum (Fig.1 (d)). Due to the low amount of carbon in the environment, there are no bonds with C; but depending on the increased oxygen content, it was determined that B-O (192.53 eV), N-O (398.5 eV) and Ti-O-N (456.4 eV) and Ti-O-B (458.6 eV) bonds were examined [8,9]. Depending on the high amount of B in the deposited films the B1s spectrum show that the binding energies of 192.53 eV, 190.56 eV, 188.65 eV and 192 eV corresponding to B-O, B-N, Ti-B, and B-O-Al respectively [10,11].

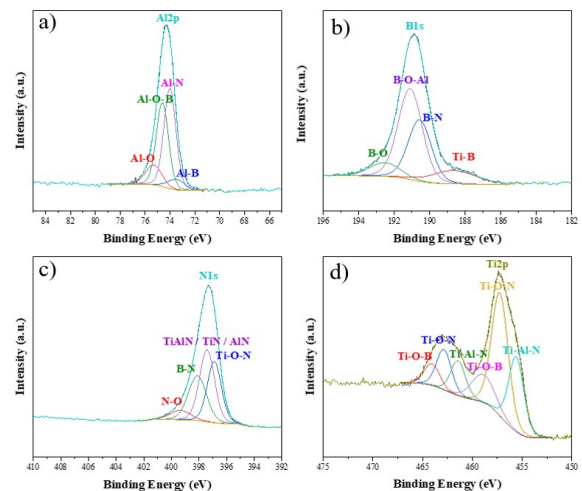


Figure 2. XPS spectra of (a) Al2p, (b) B1s, (c) N1s, and (d) Ti2p for the coating deposited using 100 V substrate bias voltage.

Besides, it has been observed that nitrated bonds are formed especially with Ti and Al due to the N₂ gas given to the environment, and the nitrated peaks in the Al2p, Ti2p and N1s graphs have the highest ratio among other bonds.

In addition to XPS fitting results, the depth profile analysis

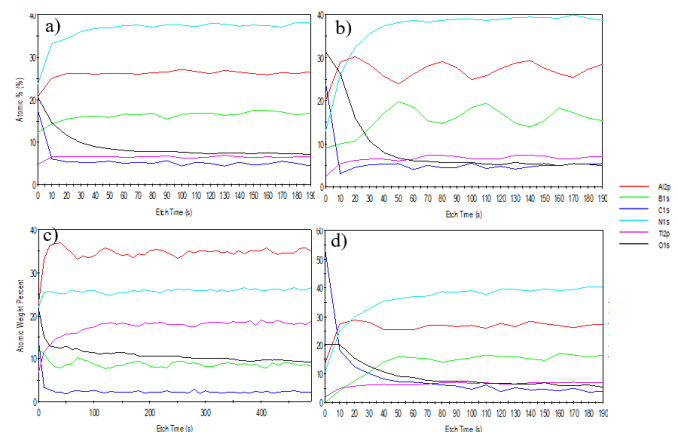


Figure 1. XPS Depth profile analysis of the coatings deposited using (a) 0V, (b) 50 V, (c) 100 V, and (d) 150V substrate bias voltage

(Fig. 2) was performed on all the deposited films. The main reason for this analysis is to measure the elements or chemical contents of the coatings depending on the coating depth. Since the magnetron targets are placed opposite to each other in the vacuum chamber layered coating was produced and this result is confirmed by depth profile analysis (Fig. 2). According to the XPS depth profile analysis, it was determined that while the amount of Al and Ti increased, both B and C content decreased. In summary, layered coatings model has been developed and boron content has been increased depending on the substrate bias voltage. Figure 3 shows that the XRD results

of the deposited films. Literature review indicate that the AlTiN coatings have a typical B1-NaCl crystal structure and the main phases are the fcc-AlN and fcc-TiN [5]. XRD results of the AlTiN coating (Fig.3 (a)) indicate that there are three different peaks located at 32.5°, 35.5°, and 37.5° corresponding to TiN and hexagonal AlN phases. It is possible that the hexagonal AlN phase is formed in the structure due to the lower formation energy of the AlN phase compared to the other phases and the high Al ratio of the target material used [12]. Since increasing the negative bias voltage results in internal stress in the films, XRD peak shift is observed. Figure 2 (b-e) shows the XRD patterns of the coatings produced using different substrate bias voltage. It can be clearly seen that all the deposited films have amorphous structure due to the boron and carbon. Both carbon and boron can promote the formation of hexagonal AlN phase, which is deteriorated the cutting performance of the tools [5]. Besides, it is possible that both carbon and boron present in the form of amorphous structure in the deposited films.

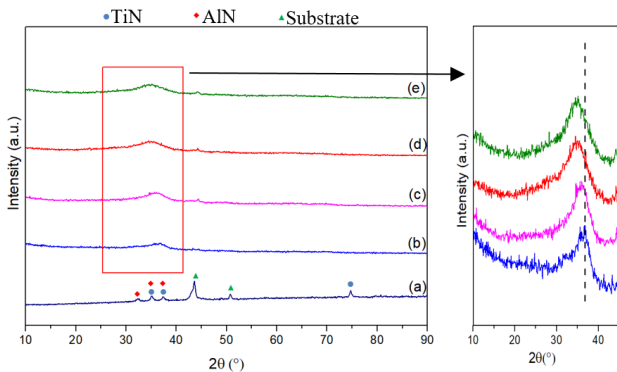


Figure 3. XRD patterns of deposited films; a) AlTiN coating, b) 0V, c) 50V, d) 100V, e) 150V substrate bias voltage.

3.2. Morphology of the coatings

The surface morphologies of the deposited films were examined using FE-SEM analysis. It was observed that all the coatings were homogeneous on the surface. The droplets with different sizes can be observed on the surface of all coatings, which are typical characteristics of cathodic arc deposition. Droplets are generally associated with inadequate reactions between metal and nitrogen [13] and the arcs formed on the cathode surface [14].

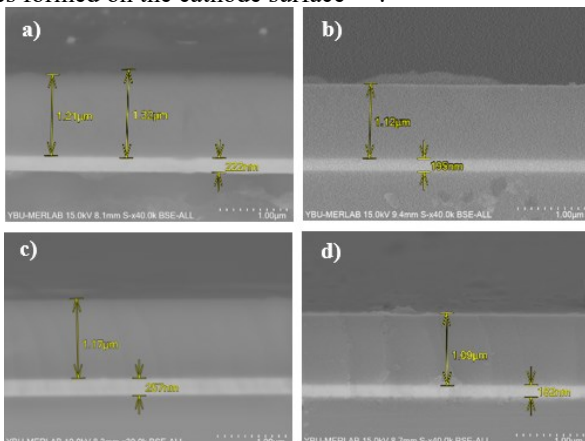


Figure 4. Cross-sectional SEM images of, a) 0V, b) 50V, c) 100V, d) 150V substrate bias voltage

Figure 4 shows the cross-sectional morphology of the deposited films using different bias voltages.

The thicknesses of the coatings were measured from Si wafer substrates. All samples have a 180-220 nm thick Cr-CrN interlayer coatings. Since the ionization rate in the magnetron sputtering method is low, the thickness does not increase significantly with increasing negative bias voltage as in the cathodic arc deposition. Therefore, substrate bias has no apparent effects on the thickness of the deposited films. The highest coating thickness was observed at 1.32 μm on the sample produced without a bias voltage. The further increase in the bias voltage may cause the re-sputter of deposited films. Therefore, the thickness of the deposited films decreases with increasing bias voltage.

3.3. Mechanical Properties

The main process parameters that affect the mechanical properties of coatings include negative bias voltage, target power, and reactive gas flow rate. Especially the bias voltage has a pronounced effect on either coating properties or adhesion. With the increase of bias voltage coating strength and endurance increase. However, increasing the bias voltage has a negative effect on the film adhesion [15]. To better understand the mechanical properties of these coatings, nanohardness and elastic modulus values should be evaluated together. Therefore, the effect of different bias voltages on the hardness and elastic modulus of the coatings is seen in Figure 5.

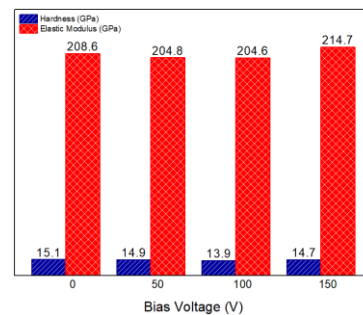


Figure 5. Nanohardness and Elastic Modulus of the coatings.

It has been observed that the lowest hardness value is obtained from the sample produced using 100 V substrate bias voltage (13.9 GPa). The reasons for the low coating hardness may be due to the effect of boron on the crystal structure of the coatings. Because boron causes the fraction of amorphous phase to increase in the structure (short-range ordered) [16]. As can be seen in the XRD results, it is seen that there is an amorphous structure in the coatings. Therefore, in the presence of amorphous structure, the hardness values remain below the expected. In addition, there is no obvious difference is observed in both hardness and the elastic modulus results depending on the different substrate bias voltage. Tribological behaviors of the deposited films were carried out under 5N load and dry sliding conditions at room temperature against 6mm diameter Al₂O₃ ball using the ball-on disc method. The wear rate of the deposited films were calculated and given in figure 6. Increasing the bias voltage may lead to the production of denser films due to ion bombardment, as well as increase the internal stresses and cause the re-sputtering effect.

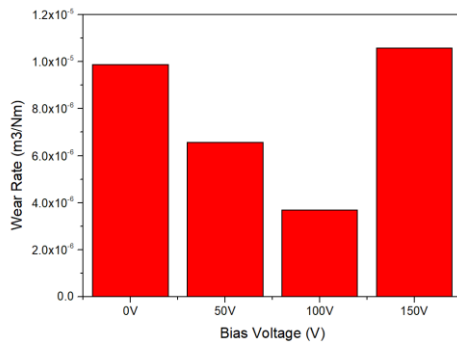


Figure 6. Wear rate of the coatings deposited using different bias voltages

Since the increasing the bias voltage is promote the re-sputtering effect and internal stress, higher wear rate, wear track width and friction coefficient was observed in the sample produced 150 V substrate bias voltage.

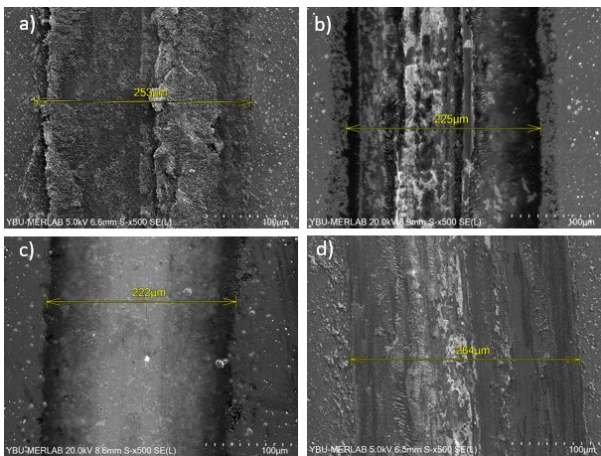


Figure 7. Wear track of the deposited films (a) 0V, (b) 50V, (c) 100V, and (d) 150V

4. Conclusion

In this research, AlTiN-B₄C hard coatings was produced using magnetron sputtering PVD by employing different substrate bias voltages and structural, mechanical and tribological properties of deposited films were examined. Layered coating model has been developed. All coatings exhibited the amorphous structure. Surface morphology of the all coatings have homogeneous morphology and the thickness of deposited films decrease with increasing bias voltage. There is no obvious effect of changing the bias voltage on the hardness and elastic modulus of the deposited films. Ball-on-disc tribological tests showed that higher wear rate, wear track width and friction coefficient was observed in the sample produced 150 V substrate bias voltage.

Acknowledgment

This work was supported by the TENMAK-Boron Research Institute within the scope of the project called “Development of Boron Containing Hard Coatings with PVD Method.

References

- [1] Baptista, A., Silva, F., Porteiro, J., Míguez, J., & Pinto, G. (2018). Sputtering physical vapour deposition (PVD) coatings: A critical review on process improvement and market trend demands. *Coatings*, 8(11), 402.
- [2] Mattox, D. M. (1998). *Handbook of Physical Vapor Deposition (PVD) Processing, Film Formation, Adhesion, Surface Preparation and Contamination Control*, 1998.
- [3] Rebholz, C., Schneider, J. M., Voevodin, A. A., Steinebrunner, J., Charitidis, C., Logothetidis, S. & Matthews, A. (1999). Structure, mechanical and tribological properties of sputtered TiAlBN thin films. *Surface and coatings technology*, 113(1-2), 126-133.
- [4] Rebholz, C., Leyland, A., Larour, P., Charitidis, C., Logothetidis, S., & Matthews, A. (1999). The effect of boron additions on the tribological behaviour of TiN coatings produced by electron-beam evaporative PVD. *Surface and Coatings Technology*, 116, 648-653.
- [5] Mei, F., Chen, Y., Zhang, H., Lin, X., Gao, J., Yuan, T., & Cao, X. (2021). Greater improvement of carbon and boron co-doping on the mechanical properties, wear resistance and cutting performance of AlTiN coating than that of doping alone. *Surface and Coatings Technology*, 406, 126738
- [6] Ghadimi, Z., Esfahani, H., & Mazaheri, Y. (2021). Control on nanostructured quaternary Ti–Al–O–B composite synthesized via electrospinning method, from nanoparticles to nanowhiskers. *Journal of Sol-Gel Science and Technology*, 98(1), 127-137.
- [7] Fu, Y., Richardson, P., Li, K., Yu, H., Yu, B., Donne, S., & Ma, T. (2020). Transition metal aluminum boride as a new candidate for ambient-condition electrochemical ammonia synthesis. *Nano-micro letters*, 12(1), 1-13.
- [8] Liu, J., Zhu, S. S., Deng, X., Liu, J. Y., Wang, Z. P., & Qu, Z. (2020). Cutting Performance and Wear Behavior of AlTiN-and TiAlSiN-Coated Carbide Tools during Dry Milling of Ti-6Al-4V. *Acta Metallurgica Sinica (English Letters)*, 33(3), 459-470.
- [9] Andrievskii, R. A., Shul’ga, Y. M., Volkova, L. S., Korobov, I. I., Dremova, N. N., Kabachkov, E. N., ... & Shilkin, S. P. (2016). Oxidation behavior of TiB₂ micro- and nanoparticles. *Inorganic Materials*, 52(7), 686-693.
- [10] Paiva, J. M., Shalaby, M. A. M., Chowdhury, M., Shuster, L., Chertovskikh, S., Covelli, D., & Veldhuis, S. C. (2017). Tribological and wear performance of carbide tools with TiB₂ PVD coating under varying machining conditions of TiAl6V4 aerospace alloy. *Coatings*, 7(11), 187.
- [11] Pshyk, A. V., Coy, L. E., Nowaczyk, G., Kempinski, M., Peplińska, B., Pogrebniak, A. D., & Jurga, S. (2016). High temperature behavior of functional TiAlBSiN nanocomposite coatings. *Surface and Coatings Technology*, 305, 49-61.
- [12] Santana, A. E., Karimi, A., Derflinger, V. H., & Schütze, A. (2004). The role of hcp-AlN on hardness behavior of Ti_{1-x}Al_xN nanocomposite during annealing. *Thin Solid Films*, 469, 339-344.
- [13] Aihua, L., Jianxin, D., Haibing, C., Yangyang, C., & Jun, Z. (2012). Friction and wear properties of TiN, TiAlN, AlTiN and CrAlN PVD nitride coatings. *International Journal of Refractory Metals and Hard Materials*, 31, 82-88.
- [14] Ljungcrantz, H., Hultman, L., Sundgren, J. E., Håkansson, G., & Karlsson, L. (1994). Microstructural investigation of droplets in arc-evaporated TiN films. *Surface and Coatings Technology*, 63(1-2), 123-128.
- [15] Skordaris, G., Bouzakis, K. D., Charalampous, P., Kotsanis, T., Bouzakis, E., & Bejjani, R. (2018). Bias voltage effect on the mechanical properties, adhesion and milling performance of PVD films on cemented carbide inserts. *Wear*, 404, 50-61.
- [16] Chang, Y. Y., & Cai, M. C. (2019). Mechanical property and tribological performance of AlTiSiN and AlTiBN hard coatings using ternary alloy targets. *Surface and Coatings Technology*, 374, 1120-1127

EFFECT OF MICRO ARC OXIDATION AND PRECIPITATION HARDENING ON THE CORROSION RESISTANCE OF 7075 Al ALLOY FABRICATED BY FLOW FORMING

Belgin ATAMAN¹, Serra BAYRAM¹, Mertcan KABA¹, Aptullah KARAKAŞ^{1,2},
Murat BAYDOĞAN¹, Hüseyin ÇİMENÖĞLU¹

¹Istanbul Technical University, ²Repkon Makina ve Kalıp
Türkiye

Keywords: Al 7075, Flow forming, corrosion resistance, micro arc oxidation (MAO)

Abstract

Flow forming is a cold deformation process to produce precision tubes for automotive and aerospace applications. During flow forming, the grains elongate along the deformation direction, and strength of the material increases due to strain hardening. Flow formed parts may work in corrosive environments during service. As it is a cold forming process, it may reduce the corrosion resistance of the formed parts, and hence improved corrosion resistance is required.

In this study, effect of various precipitation hardening conditions and micro arc oxidation (MAO) coating on the corrosion resistance of a flow formed Al 7075 alloy tube were investigated. Deformation ratio during the flow forming was 55% in terms of the thickness reduction of the tube. The MAO process was applied by using a bipolar DC power supply in an aqueous electrolyte solution. Immersion corrosion tests were conducted in 3.5 wt.% NaCl solution up to four weeks. The surface and cross sections of the coatings were examined by a scanning electron microscope (SEM), and the coating phases were identified by an X-ray diffraction (XRD) analysis. Electrical conductivity and hardness measurements were carried out to monitor the ageing effect on the microstructure of the samples. The results were evaluated to compare the corrosion resistance of the bare and the coated alloys with that of the untreated alloy.

1. Introduction

Aluminum and its alloys are widely used in aerospace, automobile and electronics industries. The flow forming process is a chipless metal forming process, in which plastic deformation is applied in a spiral form to produce axial tubes. Hollow tubes that can be produced by flow forming can also be produced by different methods such as extrusion or drawing. However, hot extrusion process does not provide high dimensional accuracy as the flow forming process does. The drawing process is cheaper and easier than extrusion, but is more susceptible to microcracks or other defects. Therefore, the flow forming process differs from other cold deformation processes and enables higher performance products to be produced [1].

MAO has many advantages as compared to the other coating processes. Sample preparation is less crucial in the MAO process than in other coating methods. As a result, the process may be completed in an easier and faster way, and the environmental effect of the solutions used for the preparation step is reduced. Another benefit of the MAO process is that a variety of materials, including aluminum, magnesium, titanium, niobium, and zirconium can be successfully coated [2].

In this study, the effect of MAO coating on the corrosion resistance of aluminum 7075 alloy fabricated by flow forming which were applied in combination with or without various ageing heat treatments was investigated.

2. Experimental Procedure

2.1. Materials

Flow formed tubes were produced by REPKON Makina ve Kalıp San. ve Tic. A.Ş in the following conditions: Untreated Al 7075, flow formed Al 7075, flow formed + T3 Al 7075 and flow formed + T8 Al 7075. Deformation ratio during the flow forming was 55% in terms of the thickness reduction of the tube. For the ageing heat treatments, the samples were first solutionized at 470 °C, flow formed by 55%, and aged at room temperature (T3) or at 121 °C for 24 h (T8) [3].

2.2. Micro-arc oxidation (MAO) process

Prior to the MAO process, the samples were cut with the dimensions of 11.6 mm x 3 mm x 15 mm from the tubes, and ground by 400, 800, 1200 and 2500 mesh SiC abrasive papers. The MAO process was conducted in an aqueous solution of electrolyte containing 10 g/L NaAlO₂, 2 g/L Na₃PO₄ and 2 g/L KOH (Figure 1). The process was conducted for 5 min. with 480 V positive and 70 V negative voltages.

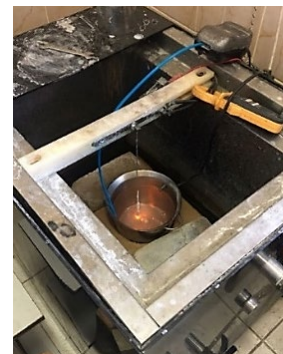


Figure 1. MAO process conducted in the present study.

2.3. Structural characterization

An X-ray diffractometer (GBC MMA 027, Figure 3.3) was used for qualitative identification of the phases in the bare alloys, and the coating layers formed during the MAO process. The XRD analysis was performed by using a CuK α radiation with a scan rate of 2°/min. over 2 θ angles of 10° and 90°. The acquired results were analyzed by using the X'Pert Highscore Plus program.

2.4. Microstructural examinations

The samples were prepared for microstructural

examinations using the standard metallographic preparation procedures and etched by the Keller's reagent (10 mL of HF, 15 mL of HCl, 25 mL of HNO₃, 50 mL distilled water). The microstructures of the bare alloys were examined by using optical microscope (Nikon Eclipse LV150L), and surface and cross sections of the coatings after the MAO process were examined by a scanning electron microscope (SEM, HITACHI – TM 1000).

2.5. Hardness measurement

Vickers hardness tests were conducted in Wilson Tukon 1102 hardness tester using a diamond pyramid indenter under a load of 1 kg (HV1). At least five values were taken in various locations, and the results were averaged.

2.6. Electrical conductivity measurement

Electrical conductivities of the samples were measured by an Auto Sigma 3000 model measuring device using the eddy current principle in the units of % IACS (International Annealed Copper Standards).

2.7. Immersion corrosion test

Prior to the immersion corrosion tests, the weight of the samples were measured. All of the samples, with and without the MAO process applied, were immersed in 3.5 wt.% NaCl solution, and the weight change was measured twice a week up to four weeks. After the samples were removed from the corrosion solution for the weight measurements, their surfaces were brushed with a toothbrush to remove the corrosion products from the surface, cleaned with water and alcohol, and then dried.

3. Results and Discussion

3.1. Structure of flow formed Al alloys

XRD patterns of untreated and flow formed Al 7075 alloys without the MAO process are shown in Figure 2. All peaks in the patterns belong to the Al rich phase. Beside small variations in the peak intensities of the untreated and the flow formed Al 7075 alloy, the major difference between them is that the flow formed sample exhibited a strong (220) peak, which is absent in the pattern of the untreated alloy. This may be attributed to a texture formation during the flow forming process, and hence should be further investigated

Optical micrographs of the untreated and flow formed Al 7075 samples were given in Figure 3. With the flow forming process, the grains are elongated along the deformation direction. Deformation direction of the grains can be seen in flow formed Al 7075.

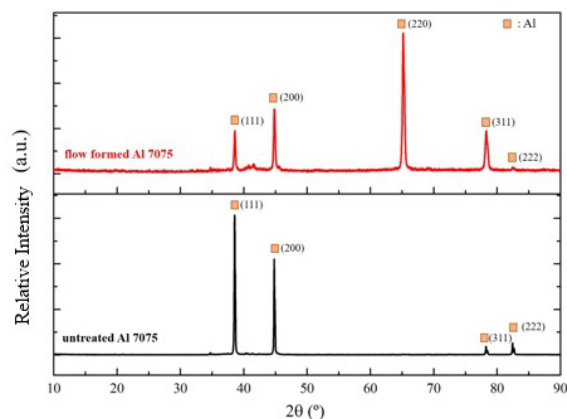


Figure 2. XRD patterns of the untreated and the flow formed samples.

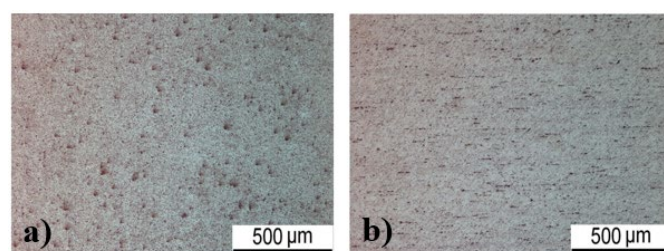


Figure 3. Optical micrographs of a) the untreated and b) the flow formed samples.

Figure 4 shows that the electrical conductivity decreased while the hardness increased. As it is well known, the precipitate phases during various ageing heat treatments (T3 and T8) increase the hardness and purify the matrix, and a higher electrical conductivity of the alloys indicates a higher purity of the matrix. However, the electrical conductivity of the samples in the present study generally increased with increasing hardness. This is attributed to the effect of the flow forming increasing hardness as a cold forming process when it is combined with the ageing heat treatments. Figure 4 also shows that the hardness of naturally aged alloy (T3) after the flow forming is higher than the artificially aged alloy with the combination of the flow forming (T8).

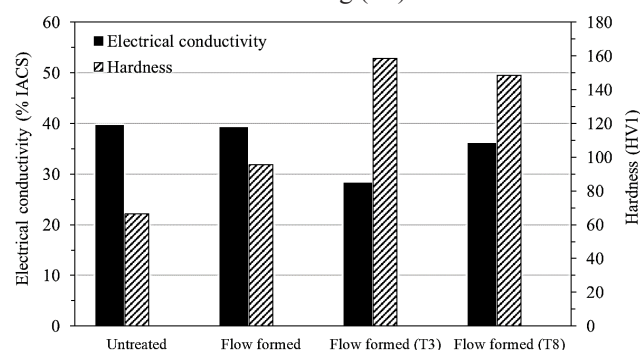


Figure 4. Electrical conductivity and hardness relationship.

3.2. Structure of MAO coated alloys

Figure 5 shows XRD patterns of the untreated and the flow formed Al 7075 samples after the MAO process. Beside γ -Al₂O₃ and α -Al₂O₃ phases as a results of the MAO process, the peaks coming from Al rich phase of the substrate were also seen. It was also shown that the intensity of the peaks of the flow formed Al 7075 alloy was higher than those of

untreated Al 7075 alloy. For each sample, on the other hand, the intensity of γ - Al_2O_3 phase was higher than that of α - Al_2O_3 phase.

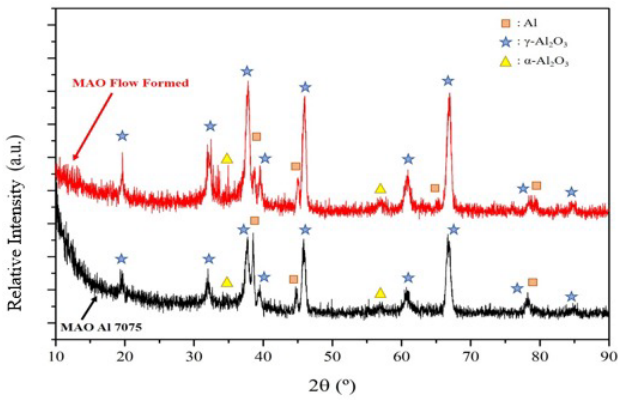


Figure 5. XRD patterns of the untreated and the flow formed Al 7075 alloy after the MAO process.

Surface SEM micrographs of the samples after the MAO process are given in Figure 6. The surface of all the samples has the characteristic morphology of the MAO process. That is distributed pores throughout the surface as a result of the discharge channels during the MAO process. Cross sectional SEM micrographs of the MAOed samples were given in Figure 7.

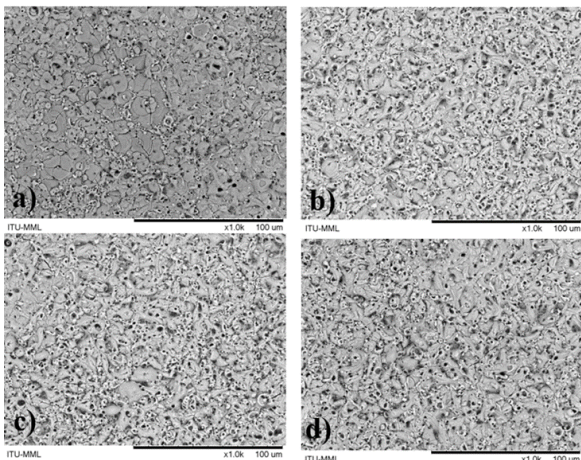


Figure 6. Surface SEM images of the samples after the MAO process a) the untreated sample, b) the flow formed sample, c) the flow formed (T3) sample, d) the flow formed (T8) sample.

As seen in Figure 7, the MAO coatings were well adhered to the substrate without any discontinuity between the coating and the substrate.

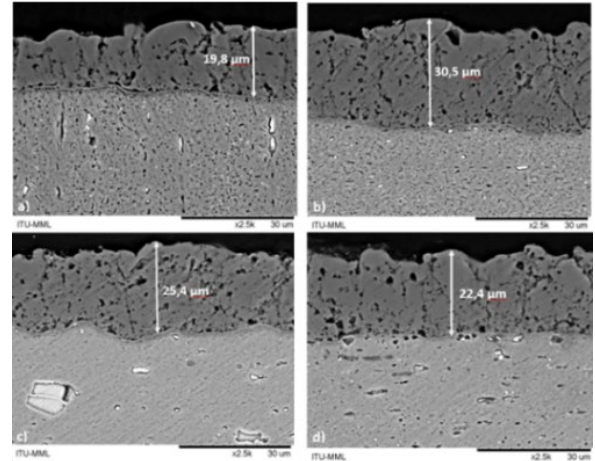


Figure 7. Cross sectional SEM micrographs of the samples after the MAO process a) the untreated sample, b) the flow formed sample, c) the flow formed (T3) sample, d) the flow formed (T8) sample.

The coating layers have pores which were uniformly distributed along the cross section of the coatings. From the cross sectional SEM micrographs, the coating thickness was also measured and given in Figure 8. The highest coating thickness was obtained in the sample subjected to flow forming process without any heat treatment, while the lowest coating thickness was obtained in the untreated Al 7075 sample. According to the results obtained, it is seen that the flow forming process has a positive effect on the coating thickness after the MAO process, and the ageing heat treatments (T3 or T8) applied in combination with the flow forming slightly reduced the coating thickness.

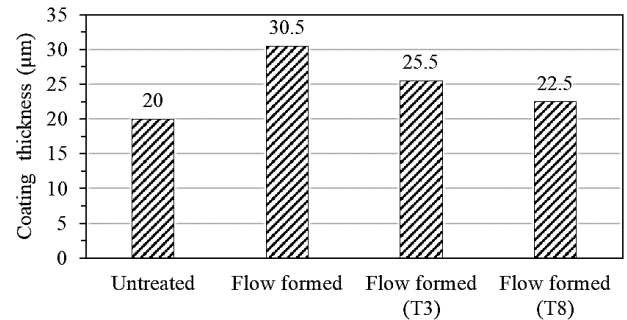


Figure 8. Coating thickness of the samples after the MAO process.

Figure 9 shows the area fraction of pores observed on the surface and the cross sections of the coatings, which were estimated by Image J image analysis software. Area fraction of the pores in the cross section was higher than those on the surface for each sample. The highest porosity sample was the flow formed Al 7075 alloy, which also exhibits the highest coating thickness.

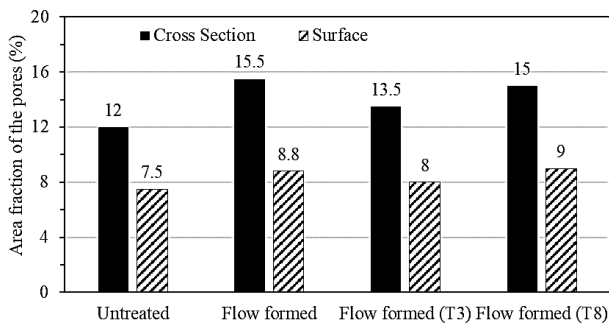


Figure 9. Area fraction of the pores on the surface and the cross section of the coatings.

3.3. Immersion corrosion test

Figure 10 shows the weight loss per unit area of the samples after four weeks of immersion corrosion tests. The lowest weight loss (as an indicator of the highest corrosion resistance) was obtained in the flow formed sample without any ageing heat treatment. The highest weight loss, on the other hand, was observed in the sample with natural aging and flow forming (T3 sample). The results suggest that the flow forming process improves corrosion resistance, while ageing heat treatments (T3 or T8) reduce the beneficial effect of the flow forming in terms of improved corrosion resistance.

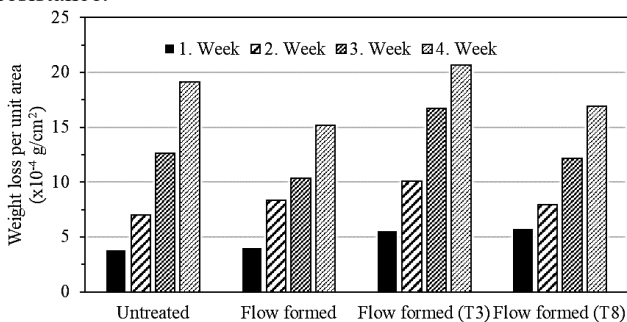


Figure 10. Immersion corrosion test results of samples before the MAO process.

Immersion corrosion test results of the MAO samples are given in Figure 11. It is seen that the MAO process provides a significant decrease in weight loss per unit area with respect to the uncoated bare alloys shown in Figure 10. The MAO process increased the corrosion resistance of the untreated and the flow formed samples. However, the weight loss of the flow formed and the aged samples after the MAO process was significantly higher than the untreated samples. It suggests that the flow forming process reduced the beneficial effect of the MAO process.

As seen in Figure 10, the weight loss per unit area continuously increased with time before the MAO process. However, it remained stable after the first week after the MAO process (Figure 11). This might be attributed to the presence of the loose outer layer at the top of the MAO coatings.

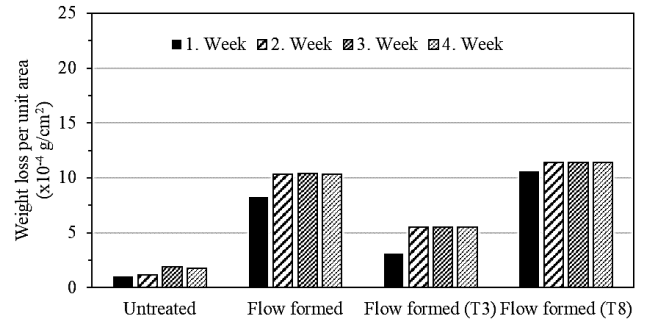


Figure 11. Immersion corrosion test results of the samples after the MAO process.

4. Conclusion

The effect of the MAO process on corrosion resistance of the untreated and the flow formed samples in combination with T3 or T8 ageing heat treatments was investigated in the present study, and the following conclusions were drawn:

1. The MAO process formed a well adhered coating layer on the untreated and the flow formed samples, which is mostly comprised of γ -Al₂O₃. The intensity of the peaks on the flow formed sample was higher than the untreated sample.
2. Flow forming results in the highest coating thickness after the MAO process. However, the ageing heat treatments in combination with the flow forming slightly reduced the coating thickness.
3. Flow forming increases the hardness of the untreated sample by approximately 45%. Additional hardness increment was achieved by ageing heat treatments which in combination with the flow forming process.
4. Flow forming improves the corrosion resistance of the sample without the MAO process. However, ageing heat treatments in combination with the flow forming reduces the corrosion resistance.
5. Corrosion resistance in terms of the weight loss per unit area decreases with increasing area fraction of the pores on the surface after the MAO process. It is also shown that area fraction of the porosity is more effective than the coating thickness on the corrosion resistance.

Acknowledgment

Authors greatly acknowledge the support provided by TUBITAK 2209-B program with the application Nr. 1139B412101777.

References

- [1] C. Kubilay, Flow Forming of Aeroengine Materials, PhD Thesis, University of Manchester (2014) pp. 1–224.
- [2] X. Shi-Gang, S. Li-Xin, Z. Rong-Gen, & H. Xing-Fang, Properties of aluminium oxide coating on aluminium alloy produced by micro-arc oxidation. Surface and Coatings Technology, (2005) 199(2-3), pp. 184-188.
- [3] K. Siadkowska, Z. Czyz, Selecting a Material for an Aircraft Diesel Engine Block, (2019).



EFFECT OF ALUMINIZING ON THE HIGH TEMPERATURE OXIDATION BEHAVIOR OF INCONEL 718 SUPERALLOY

Y. Burak TELBAKİROĞLU, Erkan KONCA

Atılım University
Türkiye

Keywords: Aluminizing, Aluminiding, Nickel, Superalloys, Oxidation.

Abstract

This study was undertaken to investigate the effect of aluminizing on the high temperature oxidation behavior of Inconel 718 nickel based superalloy. Bare and high activity chemical vapor deposition (CVD) aluminized Inconel 718 samples were oxidized in air at 925, 1000 and 1050°C for 200 hours. Detailed cross-sectional examinations, elemental analyses, weight change measurements, and x-ray diffraction studies were performed in order to investigate and evaluate the oxidation mechanisms of the samples. At 925°C it was observed that the oxidation resistance of Inconel 718 alloy was significantly improved by the protective Al₂O₃ layer formed on the NiAl phase that was created on the surfaces of the samples during aluminizing. The NiAl phase, on the hand, did not survive at higher test temperatures and therefore the beneficial effect of aluminizing started to decrease.

1. Introduction

Nickel base superalloys are favourable materials for high temperature applications such as gas turbine blades, discs, shafts etc. because of their unique combination of high strength, fatigue, creep, oxidation and corrosion resistance properties. Although they are strongly resistant to oxidation and corrosion, there is a certain upper temperature limit for the usage of these materials. In order to improve their oxidation performance, some special coatings such as diffusion coatings (aluminizing, PtAl etc.) [1], [2] and bond coatings (NiCrAlY, CoCrAlY) [3], [4] are applied on their surfaces. The main function of these coatings is to produce a protective layer on the surface of substrate material. When the substrate material is exposed to high temperatures, self oxidation of these layers occurs and the formed oxide layer slows the diffusion of oxygen into the superalloy substrate.

Aluminizing is the one of such processes applied on to the surface of the nickel based superalloys to form a protective β -NiAl layer. At high temperature applications, this β -NiAl layer oxidizes and forms oxidation resistant Al₂O₃ layer. By this way, penetration of oxygen through the nickel base superalloy substrate is slowed down and the service life of nickel base superalloy is improved. In literature, there are many different methods to produce aluminide coatings such as pack aluminizing [5], chemical vapour deposition high and low activity aluminizing [6], [1], slurry aluminizing [7] and hot dip aluminizing [8]. Each method produces different microstructure and properties which affect the service life of substrate material significantly.

The aim of this study was to investigate and compare the effect of aluminizing on the high temperature oxidation behavior of Inconel 718 superalloy in air. For this purpose, bare and high temperature high activity CVD aluminized Inconel 718 samples were used.

2. Experimental Procedure

2.1. Materials

Inconel 718 samples were supplied by TUBITAK Marmara Research Center (MAM) located in Gebze, Kocaeli, Turkey. The samples were 12.7 mm in diameter and 10 mm in height. Chemical composition of the samples are given in Table 1. High-activity CVD aluminizing of the Inconel 718 samples were carried out at TÜBİTAK MAM. %50Al-%50Cr ingot is used as the Al source. Aluminizing was conducted at 1070°C for 4 hours. After the aluminizing process, samples were heat treated for 2 hours between 1050-1090°C. The average thickness of aluminide layer was 25.4 μ m.

Table 1. Chemical composition of the Inconel 718 samples.

Material	C	Nb	Ti	Fe	Al	Cr	Mo	Co	Ni
Inconel 718	0.027	5.28	0.96	17.72	0.49	19.21	2.98	0.38	52.95

2.2. Oxidation Tests

Isothermal oxidation tests were done using the PROTHERM PLF 110/30 furnace at the Heat Treatment Laboratory of the Metallurgical and Materials Engineering Department of Atılım University (Ankara, Turkey). The furnace works at 1 atm air atmosphere. Samples were placed in the furnace at room temperature in order to prevent thermal shock which may cause spallation and failure of the coatings due to rapid thermal expansion. After each oxidation test, the power of the furnace was cut off to cool down the furnace to the room temperature before the samples were taken out. Temperature in the furnace was recorded by ORDEL DaLi 08 software. CVD aluminized 718 samples were tested at 925, 1000 and 1050°C. Bare 718 samples were tested at 925 and 1050°C. Duration of the isothermal oxidation tests was 200 hours for all samples.

2.3. Characterization of the Samples

Using a precision balance weight measurements of the samples were done before and after the oxidation tests. Cross-sectional microstructures were investigated by Carl Zeiss Merlin field emission scanning electron microscope (FESEM) located in Metal Forming Center of Excellence of Atılım University. The chemical composition of bare and oxidized samples were analysed by EDAX energy-dispersive spectroscope (EDS) detector. During SEM analysis EHT and probe current values are 15 kV and 1 nA, respectively.

3. Results and Discussion

3.1. Oxidation Rates of the Bare and Aluminized 718 Superalloy Samples

Surface areas, initial weights, final weights, weight changes and oxidation rates of bare and aluminized Inconel 718 samples are tabulated in Table 2 and Table 3, respectively. It was observed that increase in oxidation test temperature increases oxidation rate significantly from 925°C to 1050°C for bare Inconel 718 samples. For bare

sample, weight change value was negative at 1050°C because of CrO₃ volatilization [10].

Table 2. The oxidation test results of bare Inconel 718 samples.

Sample	Surface Area (cm ²)	Initial Weight (g)	Final Weight (g)	Weight Change (mg/cm ²)	Oxidation Rate x 1000 (mg/cm ² .hr)
718-925	6.628	10.5445	10.5501	0.845	4.23
718-1050	6.630	10.5306	10.4947	-5.416	-27.07

For aluminized Inconel 718 samples, weight change and oxidation rate values increased with increase in oxidation test temperature from 925°C to 1050°C as shown in Table 3.

Table 3. The oxidation test results of aluminized Inconel 718 samples.

Sample	Surface Area (cm ²)	Initial Weight (g)	Final Weight (g)	Weight Change (mg/cm ²)	Oxidation Rate x 1000 (mg/cm ² .hr)
Al-718-925	6.609	10.5788	10.5821	0.499	2.50
Al-718-1000	6.569	10.5145	10.5188	0.655	3.27
Al-718-1050	6.578	10.5143	10.5188	0.681	3.42

3.2. Cross-sectional Examination of the Bare Samples

Cross-sectional SEM image of the bare 718 sample oxidized at 925°C is seen in Figure 1a. A partial protective oxide layer is observed the sample surface. Although protective oxide formed on the top, intergranular oxidation was also observed. NiO occurred at the top of the sample. However, this NiO layer was non-uniform and cracked. The average thickness of the NiO layer is 3.4 µm. Fe-Ni oxide is occurred under the NiO layer. The average thickness of the Fe-Ni oxide is 5.0 µm. Cr₂O₃ layer is occurred under the Fe-Ni oxide. The average thickness of Cr₂O₃ layer is 6.3 µm. Ni-Nb oxide was created under the Cr₂O₃ layer at some regions. Internal oxidation of Ti-Ni-Cr-Al is also observed in this sample. The average depth of this internal oxidation reaches to 9.3 µm.

Cross-sectional SEM image of the bare 718 sample oxidized at 1050°C is seen in Figure 1b. Unstable oxide layer is observed on the top of 718-1050 sample. The formed oxide layers are cracked, broken, and separated. On the top Cr₂O₃ was formed. However, it is not stable over the whole surface. It can be seen from Figure 1b,

Cr₂O₃ layer is cracked and separated from the surface. Also, Nb₂O₇Ti is observed some top region of the surface. Intergranular oxidation occurred under surface oxides. Main oxides of intergranular oxidation are TiO₂ and Al₂O₃. The average length of internal oxides was 55.45 μm. The weight change of 718-1050 sample was -5.42 mg/cm². The reason of negative weight change is formation of volatile CrO₃ by the reaction of protective Cr₂O₃ and oxygen [10]. Also, other reason can be the formation of NiCr₂O₄ spinel by the transformation of Cr₂O₃. Formation of NiCr₂O₄ increases Pilling-Bedworth ratio which causes lateral spallation of the oxide layer due to increase in stress within oxide film [8].

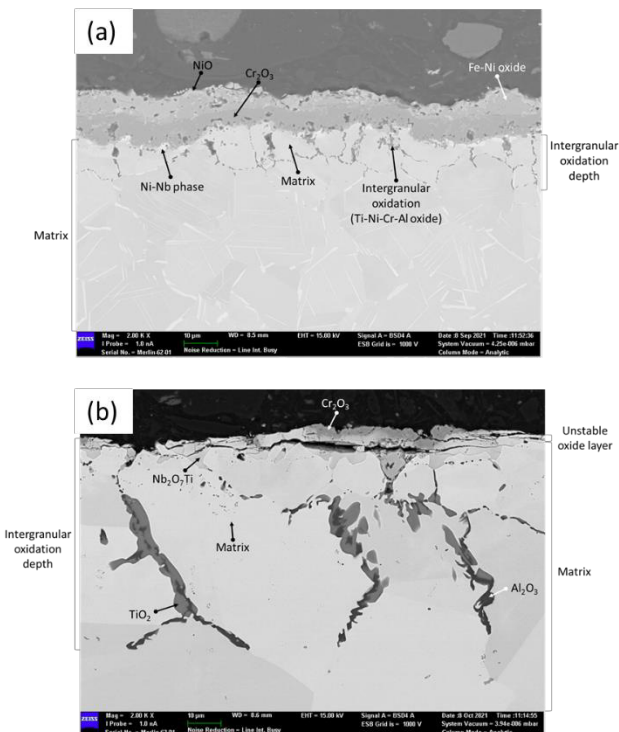


Figure 1. Cross-sectional SEM images of oxidized bare Inconel samples (a) 718 at 925°C (b) 718 at 1050°C.

Cross-sectional SEM image of the aluminized 718 sample in as-received condition is seen in Figure 2a. At the top surface, protective β-NiAl phase is observed. The average thickness of β-NiAl layer is 25.4 μm. An IDZ region is observed under the β-NiAl layer. The average thickness of IDZ is 11.9 μm. Two different phases observed at IDZ are Nb-Fe-Cr-Ni and Cr-Fe-Ni-Mo.

3.3. Cross-sectional Examination of the Aluminized Samples

Cross-sectional SEM image of the aluminized 718 sample oxidized at 925°C is seen in Figure 2b. It was observed that an Al₂O₃ layer was formed at the top surface. The average thickness of this Al₂O₃ layer is 2.8 μm. β-NiAl region stayed stable under the Al₂O₃ layer. The average thickness of β-NiAl region is 18.5 μm. A Cr-Fe-Ni-Mo region formed under the β-NiAl layer. The average thickness of Cr-Fe-Ni-Mo region is 7.4 μm. Nb-Cr-Mo-Ni particles are formed at between the Cr-Fe-Ni-Mo and β-NiAl regions.

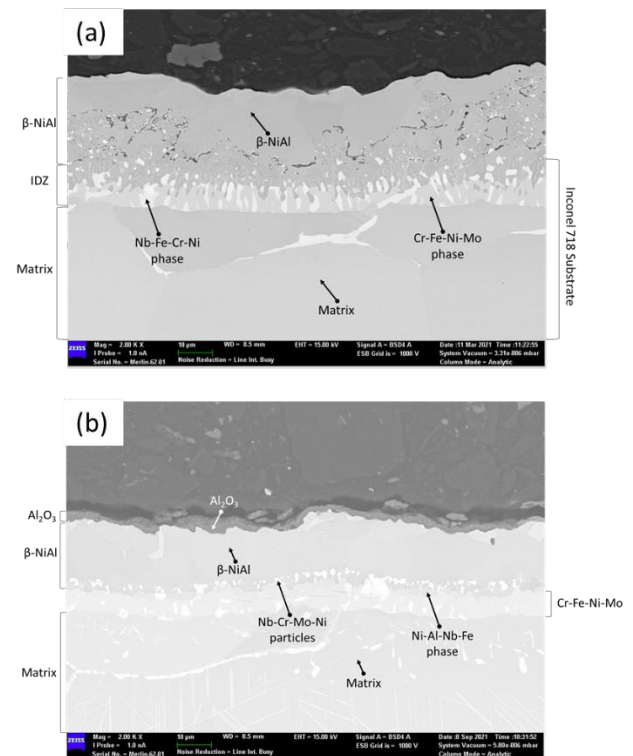


Figure 2. Cross-sectional SEM images of aluminized Inconel 718 samples (a) as-received (b) after oxidation test at 925°C.

Cross-sectional SEM image of the aluminized 718 sample oxidized at 1000°C is seen in Figure 3a. Similar to the 925°C test, an Al₂O₃ layer was formed at the top. There are cracks and voids observed in this Al₂O₃ layer. The average thickness of Al₂O₃ layer is 3.6 μm. A Ni rich and β-NiAl phases are observed under the Al₂O₃ layer. Nb-Mo-Cr particles were formed under the Ni rich and β-NiAl phases.

Cross-sectional SEM image of the aluminized 718 sample oxidized at 1050°C is seen in Figure 3b. At the top surface, Al₂O₃ was partially formed. Al₂O₃ layer has many cracks

and separated parts. The average thickness of Al₂O₃ layer is 3.3 μm. There are two Ni-Cr-Fe phases under the Al₂O₃ layer as detected by the EDS analyses. Also, some Nb-Mo-Cr particles are observed at the regions close to the surface.

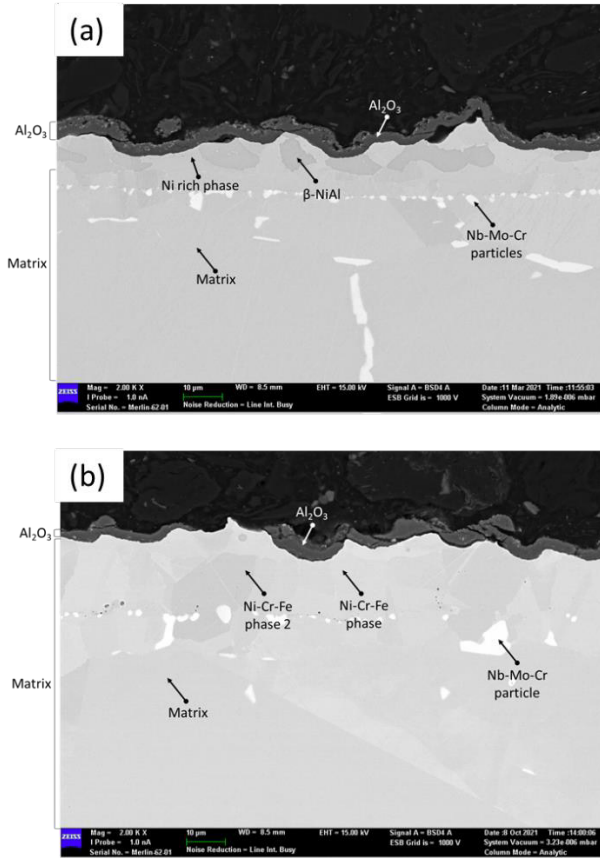


Figure 3. Cross-sectional SEM images of oxidized aluminized Inconel 718 samples (a) at 1000°C (b) at 1050°C.

Average oxide thicknesses of bare and aluminized Inconel 718 samples were tabulated at Table 4. For bare and aluminized Inconel 718 samples, oxide thicknesses increased with increase in oxidation test temperature from 925°C to 1050°C.

Table 4. Average oxide thickness of bare and aluminized Inconel 718 samples.

Sample	Average Oxide Thickness (μm)
718-925	22.5 ± 2.3
718-1050*	55.5 ± 8.0
Al-718-925	2.8 ± 1.0
Al-718-1000	3.6 ± 0.9

Al-718-1050	3.3 ± 1.2
-------------	-----------

*It is assumed that the weight loss of this sample shown in Table 2 was only due to the Cr volatilization and incorporated here as if it was solid Cr₂O₃.

4. Conclusion

Bare Inconel 718 alloy is vulnerable to significant oxidation even at 925°C. The weight changes of bare Inconel 718 samples were negative at temperatures higher than 1000°C. It is thought that this is most probably due to the chromium oxide volatilization during isothermal holding.

It is found that aluminizing process provides very good protection against the oxidation of Inconel 718 alloy at 925°C. However, the aluminide layer is not stable at 1000°C and 1050°C. The initial thickness of NiAl layer was 25.4 μm and it decreased to 18.5 μm after exposed to 925°C. The NiAl layer became discontinuous after the 1000°C oxidation test. At 1050°C, the NiAl layer completely disappeared. It is suggested that in addition to the Al that was consumed for the formation of Al₂O₃ layer, considerable loss of aluminum occurs by its diffusion from the aluminide layer into the substrate at 1000°C and 1050°C due to the large Al concentration difference between the aluminide layer and the Inconel 718 alloy substrate. Therefore the beneficial effect of aluminizing decreases with increasing test temperature.

Acknowledgement

I am thankful to TUBITAK MAM Critical Metallic Materials Unit especially Assoc. Prof. Dr. Havva Kazdal Zeytin, Gökhan Güven and Kaan Demiralay.

References

- [1] M. Zielińska, J. Sieniawski, M. Yavorska, and M. Motyka, Archives of Metallurgy and Materials, 56 (2011) 193-197.
- [2] G. M. Kim, G. H. Meier, and F. S. Pettit, Army Research Laboratory, (1993).
- [3] B. Wang, J. Gong, A. Y. Wang, C. Sun, R. F. Huang, and L. S. Wen, Surface and Coatings Technology, 149 (2002) 70-75.



[4] K. Kawagishi, H. Harada, A. Sato, and K. Matsumoto, EQ coating: A new concept for SRZ-free coating systems, Superalloys, 2008, pp. 761-768.

[5] K. M. Döleker et al., Surface Coatings and Technology, 412 (2021) 1-14.

[6] A. A. Inceyer, G. Güven, K. Demiralay, H. Kazdal Zeytin, and M. Usta, Journals of Materials Engineering and Performance, 31 (2022) 2341-2353.

[7] K. Shirvani, M. Saremi, A. Nishikata, and T. Tsuru, MATERIALS TRANSACTIONS, 43 (2002) 2622-2628.

[8] P. K. Koech and C. J. Wang, Oxidation of Metals, 90 (2018) 713-735.

[9] <https://www.crystalimpact.com/match> Dated: 14.06.2022.

[10] K. M. Doleker, O. Odabas, Y. Ozgurluk, H. Askerov, and A. C. Karaoglanli, Materials Research Express, 6 (2019) 1-9.

IMPROVING FRACTURE TOUGHNESS OF ALTiN HARD COATINGS BY W ADDITIONS

Burçin KAYGUSUZ¹, Amir MOTALLEBZADEH², Özcan Doğu KARADAYI³,
Muhammed Kürşat KAZMANLI⁴, Sezer ÖZERİNÇ¹

¹Middle East Technical University, ²Koç University, ³Ionbond Turkey Yüzey Teknolojileri,
⁴Istanbul Technical University
Türkiye

Keywords: hard coatings, fracture toughness, mechanical properties, micromechanical testing

Abstract

Hard coatings are widely utilized in the machining industry to increase the lifetime of cutting tools and allow higher cutting speeds. One of the primary drawbacks of conventional metal nitride hard coatings is their brittle nature. This study aimed at improving the fracture toughness of the coatings to overcome this problem. Our approach was to explore refractory elements additions to conventional AlTiN coatings, based on density functional theory predictions in the literature. The results showed that W additions can dramatically improve the fracture toughness.

1. Introduction

TiAlN is one of the most popular metal nitride coatings for reducing tool wear, due to its ultra-high hardness exceeding 30 GPa. However, its brittle nature makes the coating susceptible to cracking and premature failure [1]. Recent density functional theory calculations suggested that refractory metal additions can improve the fracture toughness of AlTiN dramatically [2]. In this study we explored this route through a series of experiments.

2. Materials and Methods

2 µm-thick TiAlN, TiAlMoN, and TiAlWN coatings were deposited on silicon substrates using reactive magnetron sputtering and cathodic arc evaporation. The coating microstructure was characterized by X-ray Diffraction and Scanning Electron Microscopy. Nanoindentation and ball-on-disc wear tests quantified the mechanical behavior of the coatings. Drilling experiments assessed the coating performance in practical use.

3. Results and Discussion

Figure 1a shows a cross-section of an AlTiMoN coating produced by cathodic arc evaporation. The image shows that the coating has a uniform and dense structure. Figure 1b shows the fracture toughness results of two example coatings. The results indicate that W additions can dramatically enhance the fracture toughness.

4. Conclusion

We demonstrated a feasible route to achieving high fracture toughness coatings for cutting tool applications. The results will guide further design and development studies toward the commercial use of these refractory metal-alloyed nitride coatings.

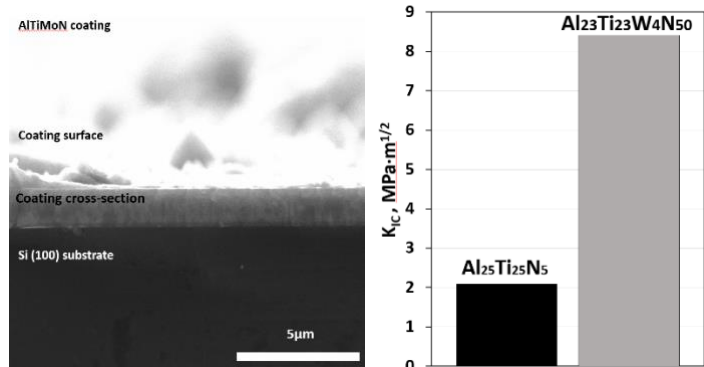


Figure 1. (a) A cross-sectional SEM image of an example AlTi-refractory alloy nitride coating. (b) Increase in the fracture toughness of AlTiN coating upon W additions.

Acknowledgments

This research was supported by the Scientific and Technological Research Council of Turkey Grant #118M201.

References

- [1] A. Leyland, A. Matthews, Design criteria for wear-resistant nanostructured and glassy-metal coatings, Surf. Coat. Technol. 177–178 (2004) 317–324. <https://doi.org/10.1016/j.surfcoat.2003.09.011>.
- [2] D. Music, R.W. Geyer, J.M. Schneider, Recent progress and new directions in density functional theory based design of hard coatings, Surf. Coat. Technol. 286 (2016) 178–190. <https://doi.org/10.1016/j.surfcoat.2015.12.021>.



PERFORMANCE AND WEAR OF VACUUM BRAZED DIAMOND CUTTING TOOLS WITH REINFORCED ELECTROLYSIS COATING

Berrak BULUT¹, Yunus Emre ERBAY², Isil KERTİ², Murat BAYDOĞAN¹

¹Istanbul Technical University, ²Yıldız Technical University
Türkiye

Keywords: Diamond, Diamond cutting tools, Vacuum brazing, Active brazing, Electrolysis coating.

Abstract

Synthetic diamond has been commonly used as abrasives of grinding or cutting tools. Traditional diamond tools mainly include sintered diamond tools and electroplated diamond tools. Active brazing has been recently recognized as a technique that offers high bonding strength of brazed diamond grits, and hence high protrusion and large chip storage space of abrasive tools. Active elements (Ti and Cr) are usually added to the alloy filler to make the active alloy that can braze the diamond. The high melting points of Ni-Cr alloys lead to high brazing temperatures typically above 1000 °C. During high-temperature brazing, C atoms from diamond grits are dissolved in liquid Ni, which could exaggerate the formation of graphite or amorphous C and impair the mechanical integrity of brazed diamond grits. Extensive research effort has been made to develop brazing strategies and methods in order to reduce the thermal damage of brazed diamond.

In this study, the combination of the active brazing and electrolysis process was investigated. The benefit of the electrolysis process is creating a cooling layer on the diamond cutting tools for improving the hardness and wear resistance. With this methodology, the disadvantages of the nickel in active brazing will be eliminated and at the same time the cutting performance-enhancing property of nickel will be utilized. Microstructures of the samples were determined by Scanning Electron Microscopy (SEM) and X-ray Diffraction (XRD) analysis. In order to examine the mechanical properties of the coatings, their hardness was measured by indentation method, micro-scratch analyzes and the wear tests were carried out. The trace formed as a result of the micro-scratch test was examined under an optical microscope and SEM. In the wear tests, natural stone was used as abrasive. No water was used during the test, and the resistance of the coating against heating was observed. Results showed the active brazing-electrolysis treated samples have high mechanical properties than active brazing samples. In the absence of the electrolysis layer, shape deformation occurred in the samples due to heating and the service life was lower than the samples with the electrolysis layer.

1. Introduction

Diamond is the most suitable abrasive for manufacturing ore, glass, ceramics, natural stones and other production tools. According to the bonding method, there are three types of diamond cutting tools, which are sintering, electroplating, and brazing [1]. Electroplated and sintered diamond tools are the traditional preparation methods of diamond tools. These methods have very limited control of diamond, because diamond and tool matrix are mechanically embedded rather than metallurgical bonding [2]. Electroplated diamond tools are made by depositing a layer of metal on the substrate by electroplating and consolidating diamond abrasive grains. Since the diamond is mechanically embedded, the plating layer has low holding strength and diamond abrasive grains are easy to fall off when the grinding load is heavy. The electroplating layer is only mechanically covered on the surface of the diamond, and the sharpness of the diamond is poor and the service life is low [3,4].

The brazing technique for single-layer diamond tools is recognized as a revolutionary invention since it produces a diamond tool with sharp surface morphology and excellent machining performance. At the brazing technology, the optimal arrangement of diamond grains can achieve high-strength chemical metallurgical bonding between abrasive grains and the matrix, showing high abrasive grain exposure, large chip holding space, and low grinding temperature [5]. According to the weldability of the diamond, it is known that the main reactive element systems suitable for brazing diamond are Ti and Cr. On this basis, the feasible solder particle mainly includes the Ni-Cr alloy system, Ag-Cu-Ti alloy system, and Cu-Sn-Ti alloy system. The Ag-based solder particle system is difficult for real industrial applications due to its expensive cost, and the strength of the silver-based solder particle is low. The Ni-based active brazing alloys have better brazing properties for diamond. The Ni-Cr alloy solution can infiltrate the diamond well and its active elements have a metallurgical chemical affinity with the diamond. However, the Ni-based brazing filler metal has a higher melting point, which causes thermal damage to the diamond when preparing diamond tools, which affects the performance.

The systematic research on Cu-based solder is of great significance to promote the development and application of

brazed diamond tools. For improving the bonding strength and hardness of the copper-based brazing filler metal, active elements such as Ti and Ga are added to the brazing filler metal to form an interface carbide reaction layer (the active element Ti is TiC), which increases wetting and bonding strength [5-7].

The diffusion and enrichment of Ti have a significant effect on brazing diamond, and the diffusion and enrichment of Ti will ultimately affect the mechanical properties of brazed joints. The diffusion and enrichment of Ti will break the carbon-carbon bonds existing in the diamond cubic structure [8]. Promote the formation of a strong metallurgical bond between the diamond and the matrix, thereby improving the mechanical properties of the welded joint. Holding time can also improve the fluidity of the solder on the diamond and improve the wettability and interface bonding strength of the solder [9].

This research aims to provide a comprehensive investigation of the combination of the active brazing and electrolysis process. With this methodology, the disadvantages of the nickel in active brazing will be eliminated and the electrolysis process is creating a cooling layer on the diamond cutting tools. By this way, the hardness and wear resistance of the diamond tools is improved and the cutting performance-enhancing property of nickel will be utilized.

2. Experimental Procedure

The active brazing alloys used in this research include commercial Cu-Sn-Ti metal powders (70 wt% Cu, 20 wt% Sn, and 10 wt% Ti). The purity of Cu-Sn-Ti alloy powder is 99.5%. The size of diamonds was ranged from 450 μm to 500 μm . AISI 1045 steel was used as brazing substrate. To prepare substrates, AISI 1045 steel was cut into a dimension of 10.0 (W) mm, 10.0 (L) mm, 1.0 (H) mm and polished using SiC sandpapers of a mesh size of 2000. The steel substrates were soaked in acetone, cleaned at ultrasonic bath for 10 min, and then dried in air. Firstly, the brazing alloy was uniformly distributed on the steel substrate with a thickness of about 500 μm . The diamonds were subsequently arranged onto the composite alloy powder as seen in Figure 1. The diamond grains were fixed on the upper layer of the substrate and brazed in a vacuum furnace at 900 $^{\circ}\text{C}$ with a dwell time of 10 min and a vacuum level below 5×10^{-5} Pa. The brazed diamond segments were obtained when the furnace temperature was cooled to below 90 $^{\circ}\text{C}$. After brazing process, one group of the samples was coated nickel with electrolysis process for one hour. The microstructure and mechanical properties of the brazing samples (metal single layer- MSL) and the brazing and electrolysis samples (MSL-Ni) were compared.

It was carried out using Panalitical XRD to determine the phases formed between the diamond-brazing alloy and the brazing alloy-steel substrate. In XRD measurements, using $\text{CuK}\alpha$ radiation with a wavelength of $\lambda = 1.54059 \text{ \AA}$, each sample was examined at a scanning interval of $2\theta = 5 - 110^{\circ}$, scanning speed of 3 degrees/min and scanning step of 0.05 degrees. The samples were examined with Zeiss Evo 18-SEM. In order to examine the mechanical properties of the coatings, their hardness was measured by indentation method, micro-scratch analyzes and the wear tests were carried out. The indentation process was carried out on a

Vickers penetrating depth precision hardness device. An indentation load of 25 mN was used for the hardness measurements of the coatings. In the selection of the indentation load, it was taken into account that the maximum immersion depth was below 10% of the examined pavement thicknesses. The micro-scratch tests at increasing load were applied to the coated surfaces of the samples. Scratch tests were performed at a speed of 5 mm/min and a length of 5 mm with from zero to 20 N loads. Rockwell-C diamond (100 μm diameter) was used as the insert. Wear tests were carried out using the linear opposing plane-pin wear method. In the wear tests, with the system developed in this study, the diamond cutting edge was applied as abrasive and the worn surface was applied as natural stone. Thus, the wear test became a prototype of field tests. During the wear test, a load of 30 N was applied, the worn stone is 20x30 mm black marble stone (stone hardness is 4 Mohs). The sliding speed is 1.9 cm/s, the sliding distance is 230 m and the stroke distance is 11.5 mm. After mechanical tests, the surfaces of the samples were investigated under optical microscopy and SEM.

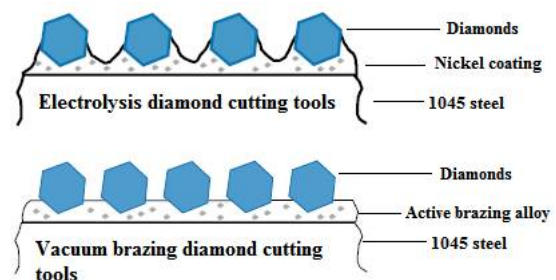
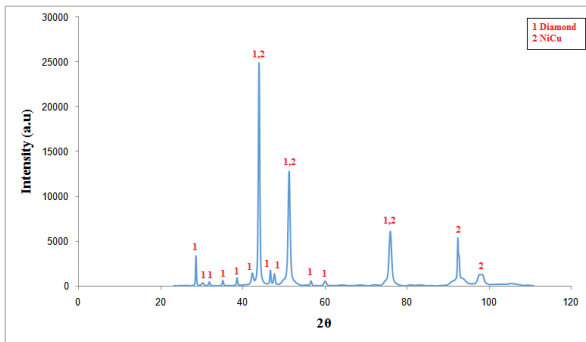


Figure 1. The schematic view of the coating diamond tools.

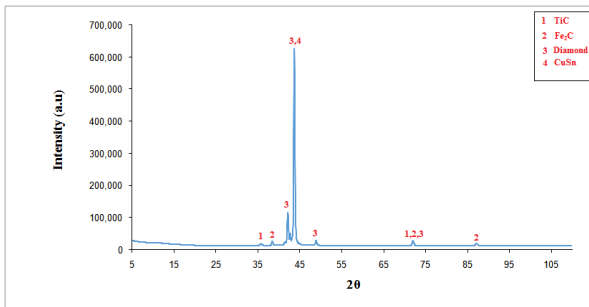
3. Results and Discussion

Figure 2 depict XRD patterns and corresponding phases obtained for the samples. The product phases of sample MSL are TiC, Fe_2C , Diamond and CuSn. The phases of sample MSL-Ni are Diamond and NiCu. When the phases were examined, it was determined that chemical bonds were formed between the diamond-brazing alloy and the brazing alloy-steel substrate as a result of vacuum brazing. Fe from the steel substrate and Ti from the brazing alloy formed C bonds with the diamond. When Ni was coated with electrolysis method after vacuum brazing process, high intensity Ni phases were determined in the structure. It has been determined by the results of the analysis that the Ni from the separate electrolysis process bonds with the existing Cu in the structure.

Figure 3 present the SEM images of the samples. When the SEM images are examined, it is seen that the brazing alloys have a high ability to wet the diamonds and the alloy covers the diamond surface in both sample groups. It is observed that there are no cracks or gaps between the diamond and the brazing alloy. When the two sample groups are compared, it is seen that all of the diamonds are coated with nickel in the MSL-Ni samples. Electrolysis process performed after vacuum brazing formed a protective layer on the diamonds.



(a)



(b)

Figure 2. The XRD pattern of the samples a)MSL b) MSL-Ni.

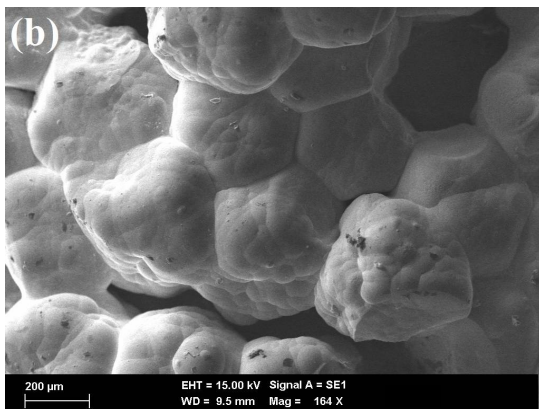
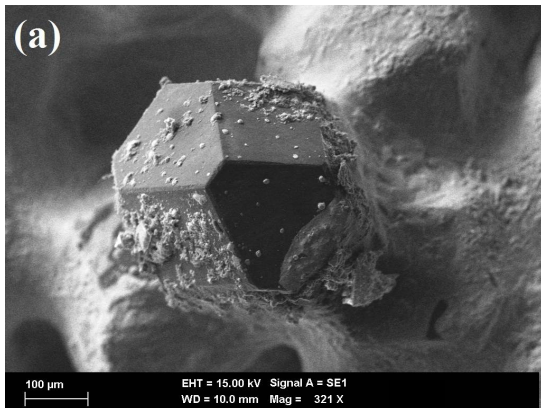
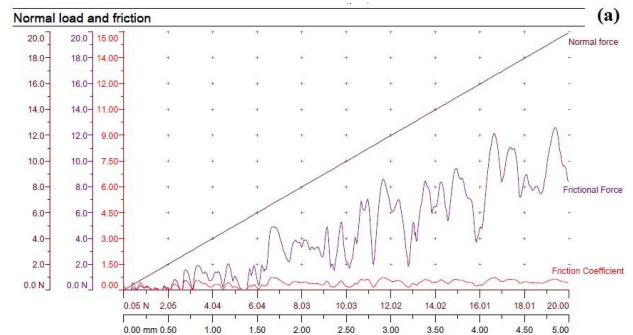


Figure 3. The SEM images of the samples a) MSL b) MSL-Ni.

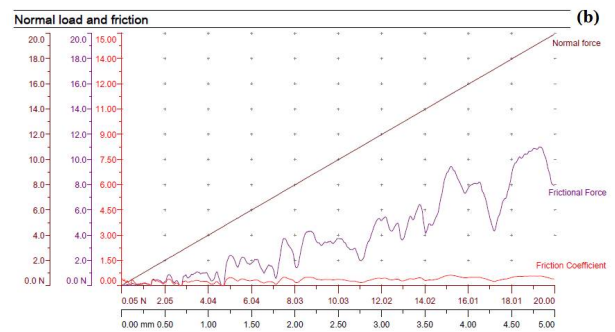
At the hardness measurements to determine the mechanical properties of the samples, indentation load (P)-penetration depth (h) and time curves were recorded in the computer environment. Ten hardness measurements were

made for each material under the same conditions. The average hardness values of the MSL and MSL- Ni samples are 150.7 ± 12.15 GPa and 255.2 ± 10.50 , respectively. It was determined that the hardness value of MSL-Ni samples was higher than the hardness value of MSL sample.

The friction coefficient-normal load graph of the samples obtained as a result of the increased load scratch test is given in Figure 4. When the graphs are examined, the amount of load where the increase in the friction coefficient occurs is determined as the first critical load where the coating starts to separate significantly from the base material, and this value is in the range of 6-6.5 N for the MSL sample, while it is in the range of 7.5-8 N for the MSL-Ni sample.



(a)



(b)

Figures 4. The numerical results of the scratch test a) MSL b) MSL-Ni.

The microscope and SEM images obtained from the increased load scratch test are given in Figure 5. When the images are examined, it is seen that cohesive cracks start from 5N in the MSL sample. At 8N load, it is very significant adhesive separations and ruptures are now beginning to occur. The film started to lose its bond on the base material from this load.

As a result of the abrasion test, 0.003 grams of weight loss occurred in the MSL sample. A weight loss of 0.002 grams occurred in the MSL-Ni sample. Weight loss of MSL-Ni sample is lower than that of MSL sample. SEM images of the samples after the wear test are given in Figure 6.

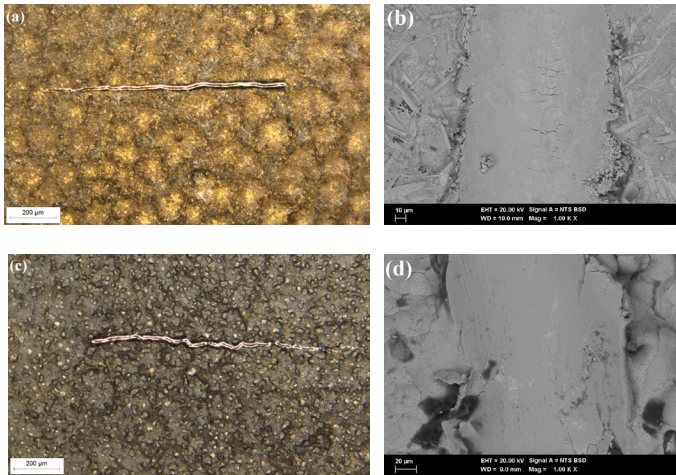


Figure 5. The optical microscope and SEM images of increased load scratch test a) optic microscope images of the MSL samples b) SEM images of the MSL samples c)optic microscope images of the MSL-Ni samples d) SEM images of the MSL-Ni samples.

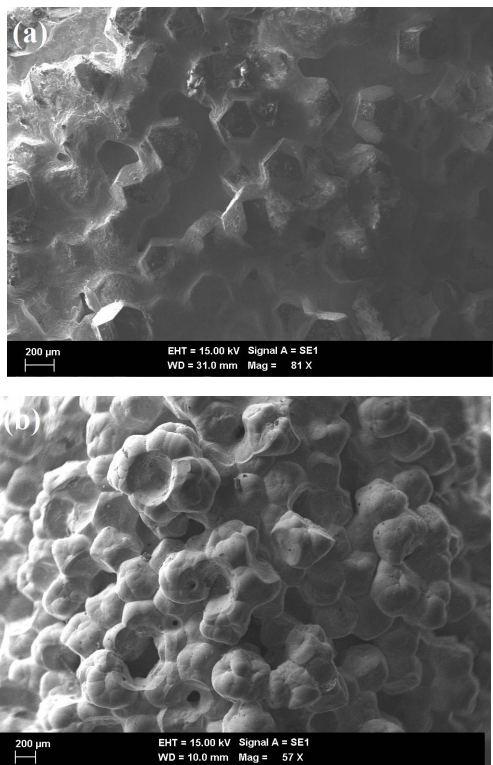


Figure 6. The SEM images of the samples after wear tests a) MSL b) MSL-Ni.

4. Conclusion

The purpose of this research was to produce vacuum brazed diamond tools with longer service life. This research was discussed the advantages and disadvantages of the brazing and electrolysis methods and try to combine these two methods to improving the coated diamond tools. According to the results of XRD and SEM analysis, the chemical bonds were formed between the diamond-brazing alloy and the brazing alloy-steel substrate and the brazing alloys have a high ability to wet the diamonds. The adverse effects of electrolysis coating performed after vacuum brazing was not observed. Moreover, the active brazing-electrolysis treated samples have high mechanical properties than active brazing samples. As seen in the SEM images after wear tests, in the absence of the electrolysis layer, shape deformation and pull-out diamonds were occurred in the samples due to heating and the service life was lower than the samples with the electrolysis layer. As a result of this review, a diamond cutting tool has been developed that has a longer service life and can cut under difficult field conditions with the electrolysis coating process performed after vacuum brazing.

References

- [1] Z.Chen, B. Xiao and B. Wang, *Diamond and Related Materials*, 115 (2021) 108352.
- [2] B. Cui, J. Chen, H. Li, R. Zuo, Z. Cheng, Z. Sun, Y. Li, B. Wang and D. Xu, *Diamond and Related Materials*, 123 (2022) 108826.
- [3] W. Ma, H. Xiao, S. Wang and S. Liu, *Vacuum*, 198 (2022) 110897.
- [4] H. Xiao, S. Wang and B. Xiao, *Ceramics International*, 48 (2022) 9258-9268.
- [5] Z. Liu, X. Liao, W. Fu, D. Mu, X. Xu and H. Huang, *Materials Science and Engineering A*, 790 (2020) 139711.
- [6] B. Cui, W. Zhao, R. Zuo, Y. Cheng, S. Zhong, H. Li, W. Li, Y. Fu and D. Xu, *Diamond and Related Materials*, 124 (2022) 108926.
- [7] S.Y. Wang, B. Xiao, S.C. Su, J.L. Wang and Y. Xiao, *Diamond and Related Materials*, 116 (2021) 108401.
- [8] D.Z. Duan, F. H, J.J. Ding, Q.J. Lin and C.S. Li, *Ceramics International* 47 (2021) 22854–22863.
- [9] J.B. Lu, H. Li, Y. Li, Z. Gong, S.J. Zhong and X.K. Qiu, *International Journal of Advanced Manufacturer Technology*, 91 (2017) 1453–146.



FOR MORE SUSTAINABLE COLD FORGING PROCESS: USE OF SAND BLASTING INSTEAD OF PICKLING AND RINSING

Baybars SARICA, M. Burak TOPARLI, Dođuş ZEREN, Umut İNCE

Norm Cıvata
Türkiye

Keywords: Sand blasting, polymer coating, pickling and rinsing

Abstract

Due to increasing environmental awareness and energy costs, alternative production methods have gained importance for the sake of sustainable manufacturing. In this study, use of sand blasting instead of pickling and rinsing was examined. Process parameters namely blasting time and blasting rate were investigated for metal wires with 8.0 mm diameter. Surface roughness and hardness measurements were carried out to characterize the effect of process parameters. Polymer-based coating was applied to sand blasted-surfaces and surface roughness measurements were repeated. Extrusion tests were conducted for final performance evaluations. In addition, a comparison was made between sand blasting and pickling and rinsing with respect to sustainable manufacturing. It was revealed that sand blasting offered less water and chemical agents usage compared to pickling and rinsing. Moreover, production efficiency was higher for sand blasting process.

1. Introduction

Cold forging is a method frequently used in the production of automotive parts. Low consumption of raw materials, superior material properties and narrow geometric tolerances provide cost savings for parts produced with cold forging. One of the most important factors affecting die life is tribological properties between the forged material and the die. Pickling and rinsing are commonly used in cold forging, as the initial stages of traditional metal wire surface cleaning and preparation operations. However, hazardous waste disposal and recycling issues, significant energy and water consumption and human health risks are some of the main problems of these traditional methods. Sand blasting can be considered as an alternative and more sustainable method for surface preparation.

2. Materials and Methods

In this study, sand blasting was investigated for metal wires in 8.0 mm diameter with polymer-based coating. Characterization tests including surface roughness and determination of extrusion peak force by using universal mechanical testing device were carried out. Extrusion tests were also conducted in order to determine the roughness effect on the material surface, which is very important parameter for forging. The extrusion tests were applied to all samples in lubricated and non-lubricated form with different sand blasting times and sand blasting speeds. As a result of this study, optimum process parameters of sand were determined to reduce forging loads.

3. Conclusion

In the characterization tests performed after the sand blasting and polymer coating, it has been observed that the polymer coating adheres homogeneously to the samples owing to sand blasting. As a result of the extrusion tests, it was determined that the extrusion peak force was reduced in non-lubricated samples and it can be stated that this process have a positive effect on the forging of the product. In addition, a comparison was made between sand blasting and pickling and rinsing considering sustainable manufacturing. It was observed that sand blasting offered significantly lower water and chemical agents usage compared to pickling and rinsing.



INVESTIGATION OF MECHANICAL AND CORROSION PROPERTIES OF ELECTROLESS Ni-W-Co-SiC MULTICOMPONENT COATINGS

İsmail Deniz Kağan DEMİR¹, Göksel HIZLI², Selim ERTÜRK²,
Kürşat KAZMANLI²

¹TR Mekatronik Sistemler, ²Istanbul Technical University
Türkiye

Abstract

Electroless nickel coatings are widely used in the defense and aerospace industry due to their superior properties such as high wear resistance, high hardness, corrosion resistance and homogeneous coating on the part surface. In this study, it was aimed to develop multicomponent electroless nickel coatings with good mechanical properties and high corrosion resistance under high temperature.

There are many studies on multicomponent nickel coatings in the literature, whereas there is limited number of studies, in which tungsten, cobalt and/or silicon carbide has been used by using different types of complexing agents and reducers.

In this study, 32CrMoV12-10 discs were used as substrate. Tungsten, cobalt and/or silicon carbide were added to electroless nickel plating bath with different reducers and complexing agents. The morphology of the coated surface will be investigated by using different techniques, also the composition and structure of the coating will be determined, microhardness tests and coating thickness measurements will be done. The corrosion properties of the coating will be described chemically.

Introduction

Electroless plating is a chemical reduction process and provides a very attractive method of coating single or multicomponent, since it is a low temperature process and by the proper choice of bath composition and operating compositions the properties of the deposits can be tailored to the particular application [1,2].

Electroless nickel coatings can be classified in two main categories, Ni-P and Ni-B. The co-deposition of a third element within the growing film has led to a new generation of electroless alloy coatings. The co-deposited metal is mainly chosen from transition metals such as W, Co, Mo, Re, etc. because of their superior properties. These coatings can also be customized for desired properties by selecting the composition of the coating to obtain specific requirements [3,4].

Experimental Procedure

In this work, it is aimed to study the effects of W (0.01-0.075 M), Co (2-5 g/l) and SiC (5 g/l) addition on deposit properties of electroless nickel coatings. Sodium tungstate ($\text{Na}_2\text{WO}_4 \cdot 2\text{H}_2\text{O}$) was used as tungsten source and cobalt sulphate ($\text{CoSO}_4 \cdot 6\text{H}_2\text{O}$) as cobalt source. Samples were cleaned ultrasonically in the acetone for 3 minutes. Then they were immersed in the alkaline bath which contains 24 g/l NaOH for 2 minutes. Before the coating process, samples' surfaces were activated in 30% HCl medium at 35-40°C for 2 minutes. Samples were washed with distilled water before every step. Bath temperature was kept constant at 70°C. pH value was in the range of 6.5-8.0 and measured during the coating process.

After the coating process, thickness measurements were done by both microscopic and XRF method using Nikon Eclipse MA100N Optic Microscope and Fisherscope Xray System XDL device. Morphology of the coating surface analyzed by XRD technique using Philips PW3710 & RE1806. Also, Hitachi X-MET8000 XRF analyzer was used to determine the chemical composition of the coated surface.

Samples were heat treated in a resistive heated furnace at 400°C for 1 hour to see the effect of the heat treatment on the hardness. Corrosion tests were carried out at room temperature for 72 hours in the salt bath that contains 5 g/l NaCl.



Conclusion

In the present study, results can be summarized as;

- Homogeneous and nearly with a rate of 10 microns per hour can be obtained.
- Hardness of the coating increases with the addition of tungsten to the bath. However, after 0.045 M it slightly decreases.
- When cobalt added to the bath with tungsten, change in the hardness in as plated and heat-treated circumstances increases.
- All of the samples passed from the chemical corrosion tests.

References

- [1] G.O. Mallory, Plating, 58 (1971) 319-322.
- [2] N. Arini and E. Maburi, Study of Electroless Ni-W-P Alloy Coating on Martensitic Stainless Steel, AIP Conference Proceedings, 1725 (2016) 020053.
- [3] J.N. Balaraju, S.M. Jahan, A. Jain and K.S., Rajam, Journal of Alloys and Compounds, 436 (2007), 319-327.
- [4] M. Wang, Z., Yang, C. Zhang and D. Liu, Transactions of Nonferrous Metals Society of China, 23 (2013) 3629-3633.

SOL-GEL SPRAY COATING OF ALUMINIUM ALLOYS FOR THE AUTOMOTIVE APPLICATIONS

Çisem ÇELİK KURTULAN^{1,2}, Ş. Samet KAPLAN¹, M. Şeref SÖNMEZ¹

¹Istanbul Technical University, ²Turkish Energy, Nuclear and Mineral Research Agency (TENMAK)
Türkiye

Abstract

In the automotive industry, light-weight alloy usage has been increased due to provide weight loss and thus fuel efficiency. Some of the aluminium alloys, especially the 5xxx and 6xxx series are utilized for the production of car bodies and decorative parts in the automotive industry [1]. However, the corrosion resistance of the bare alloys doesn't comply with the respective standards [2].

Introduction

Protection of the parts of car bodies is often obtained by anodization and cathodic coating. According to new developments in the automotive industry, alkaline resistance is one of the new requirements adopted by the standards. Consequently, another protective coating layer is essential. On the other hand, technological changes necessitate clean production, which means process and equipment to increase production efficiency and reduce waste and emissions [3]. The organometallic sol-gel coating is the most convenient method to meet the above-mentioned conditions [4, 5].

Materials and Methods

In this work, silane and titanium alkoxides were used as metal sources. Colloidal metal oxide materials were studied with multiple alkoxide solutions in order to prove the corrosion protection of automotive decorative parts. As a coating method, spray sol-gel coating was chosen. The chemical bonding was formed by hydrolysis and the following condensations of different alkoxide compounds. The addition of SiO₂ particles increased the barrier effect by increasing the coating thickness, density and reinforcement (Fig. 1) [6].

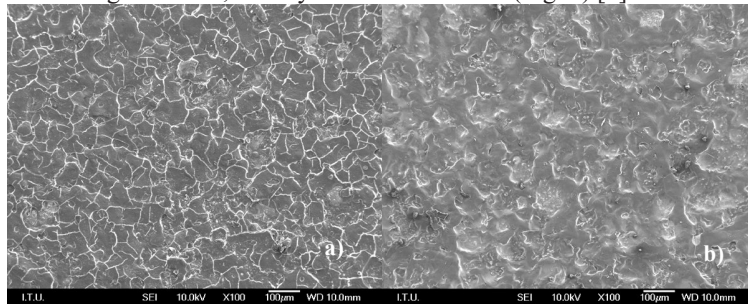


Figure 1. SEM images of different coatings. Solutions; a) silane alkoxide and colloidal SiO₂, b) silane and titanium alkoxide.

Conclusion

As a result, it was found that the solution which contained titanium and silane alkoxides could be applied directly on aluminium surfaces and provided surface quality and corrosion resistance that complies with automotive standards. Usage of colloidal SiO₂ caused cracking at the coating structure and deteriorated the corrosion resistance.

Acknowledgement

The authors would like to thank Arma Filtre Sistemleri San. ve Tic. A.Ş for their financial support.

References

- [1] Liu M, Guo Y, Wang J, Yergin M. PERSPECTIVE Corrosion avoidance in lightweight materials for automotive applications. doi:10.1038/s41529-018-0045-2
- [2] Choleridis A, Sao-Joao S, Ben-Mohamed J, et al. Experimental study of wear-induced delamination for DLC coated automotive components. *Surface and Coatings Technology*. 2018;352:549-560. doi:10.1016/J.SURFCOAT.2018.08.048
- [3] Almeida CMVB, Sevegnani F, Agostinho F, et al. Accounting for the benefits of technology change: Replacing a zinc-coating process by a water-based organo-metallic coating process. *Journal of Cleaner Production*. 2018;174:170-176. doi:10.1016/J.JCLEPRO.2017.10.192
- [4] Fotovvati B, Namdari N, Dehghanhadikolaei A. Manufacturing and Materials Processing On Coating Techniques for Surface Protection: A Review. doi:10.3390/jmmp3010028
- [5] Handbook, A. S. M. (1994). *Surface engineering*. ASM International, Handbook Committee, 5(s 346).
- [6] Tiringir, U., Milošev, I., Durán, A., & Castro, Y. (2018). Hybrid sol-gel coatings based on GPTMS/ TEOS containing colloidal SiO₂ and cerium nitrate for increasing corrosion protection of aluminium alloy 7075-T6. *Journal of Sol-Gel Science and Technology*, 85(3), 546-557.

WEAR AND CORROSION PERFORMANCE EVALUATION OF LASER CLADED BRAKE DISC

Ekrem ALTUNCU¹, Recep AKYÜZ², Çiğdem DINDAR², Cem ÖZTÜRK²

¹Sakarya University of Applied Sciences, ²Tofas Automotive Türkiye

Keywords: Brake disc, Laser cladding, Wear, Corrosion

Abstract

Investigations about both carbon-inducing brake discs and other related parts of automobiles are significant and necessary in terms of new regulations to reduce non-exhausted emissions coming into force day by day, and able to meet green expectations from the new-generation automobiles. Gray cast iron-based brake discs are safety and economical parts that are exposed to high wear and corrosion in the face of increasing vehicle speeds and road conditions. Disc life and brake performance are reduced due to varying harsh weather and aggressive road conditions. Trends and developments in electric vehicles; weight reduction, higher wear and corrosion resistance, lower replacement costs, minimum brake dust are desired without loss of brake performance on the new generation brake discs. Therefore, advanced surface treatment or coating applications on brake discs are an inevitable necessity for new generation vehicles.

In this study, the martensitic stainless steel used as a coating material is developed mainly to satisfy the property requirements for hardness, high strength, wear resistance, and corrosion resistance. Then pad-disc friction properties and the brake performance were measured in bench test at different temperatures. Test results are given comparatively. In addition, corrosion resistance performance for red rust occurrence was evaluated by performing salt spray test.

1. Introduction

Brake discs that is generally made of gray cast iron (GG15-25, DIN1561) [1,2] because of its low cost, excellent casting characteristics, good machinability and vibration damping ability etc., are critical parts for the safety of vehicles and often are subjected to harsh road conditions. In the literature, wear [3,4], and corrosion resistant [5,6] surface coatings can be obtained on coating the brake discs made of cast iron with various methods [7,8] which laser cladding is a great convenient method for this.

Laser cladding [9,10] is a metal deposition method through laser beam, and it has been used as a trend technology in recent years. Its typical applications are tool repairing, wear and corrosion resistance coating, thermal fatigue resistance necessity, etc. It has a wide range of material uses and the process performance is directly related to the selection of an appropriate coating material. Powders for use in laser cladding has included a extended range of material with a large choice of high quality nickel, cobalt and iron based powder solutions, as well as

carbide mixes. As the coating material for this investigation, AISI 431 martensitic stainless steel was selected because it offered the best optimal combination of corrosion and wear resistance.

2. Experimental Procedure

2.1 Laser Cladding process

The principle of laser cladding process is on based that both work piece surface and cladding material are molten using a high-power laser beam and formed a weld pool (Figure 1). In application, cladding material (metal powder or filler wire) is fed into process using a gas jet, an appropriate feed rate and deposition rate of the process is set for cladding application. The heat affected zone is limited since there is no high heat input to the part. Therefore, the process provides a great advantage as there is no change in material properties.

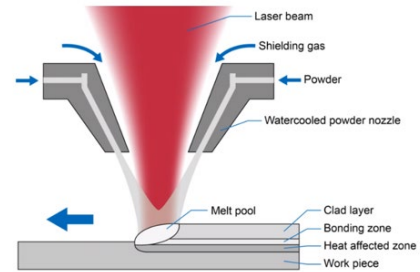


Figure 1. Laser cladding process

In the study, laser cladding process was applied in a coating thickness ~1 mm with the feedstock powders deposited on the substrate in the process parameters given in Table 1 and then the laser-coated disc surface was machined to create the desired surface roughness (Figure 2).

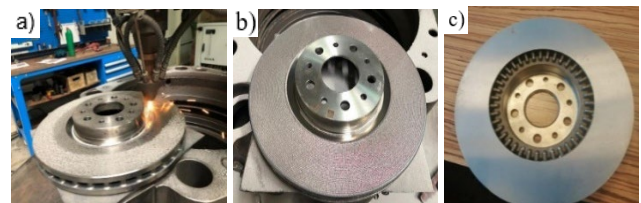


Figure 2. Laser cladding on brake disc a) during laser cladding process b) as laser cladded surface c) after machining.

Table 1. Laser cladding process parameter range.

Laser Cladding Parameters

Power (W)	Velocity (mm/s)	Powder (l/min)	Shielding gas (l/min)	Carrier gas (l/min)
1000-1350	10-13	4.5-5	15-20	5-7

Overlap (mm)	Spot width (r)	Apply time (dk)	Laser Cladding height (ort/mm)
1,5-1,8	1.5	60-75	1-1,5

The change of friction coefficient was observed for 1000 braking application on the dynamometer test system. After the test, the disc surfaces were examined visually, the disc coating and pad thickness change and wear losses were measured.

2.2. Wear Performance Test

The wear tests were performed in a full-scale dyno bench according to the relevant test procedure. The friction material used in the wear performance tests were selected from the same production batch of the original products. The measurements were carried out in accordance with relevant test standard and temperature, friction coefficient, braking torque, pressure, pad and rotor wear changes were recorded at each significant temperature step of the test. In order to provide realistic data, new brake pads were subjected to the brake bedding stage before the data acquisition.

2.3. Corrosion Test

This test was carried out in a salt spray test cabin until observing excessive red rust occurrence on the treated brake disc. After the test, the corrosion performance was evaluated visually since the performance criteria is the resistance during a period of use as specified in the performance standard.

3. Results and Discussion

3.1 Disc substrate and coating material (431L) examination results

The composition of the substrate material (DIN 1561: GG20) of brake disc is analysed by a spectrometer machine. The chemical composition is given in Table 2.

Table 2. Chemical analysis of the substrate material (wt%)

C	Si	Ni	Mo	Cu	S	P
3.52	2.3	0.038	0.007	0.17	0.12	0.03

Mn	Cr	Sn	Ti	V	C eq.
0.51	0.13	0.06	0.013	0.007	4.05

In the brake disc substrate characteristic examination, the microstructure included various phases with a matrix of the pearlitic max %5 ferrite and the cementite max %1. Graphite phase's distribution in the substrate was observed as given in Figure 3.

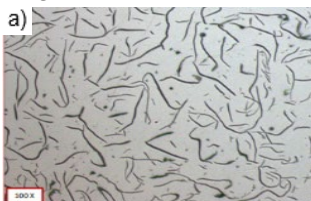


Figure 3. Graphite distribution in the microstructure of substrate material with a) 200X b) 500X

The microstructural characterization of the coatings after the production of the coatings was carried out in the electron microscope (SEM-EDX) with the top surface and cross-section examinations. Microhardness tests were carried out to determine the mechanical properties of the coatings on test samples. The surface roughness (Ra, Rz) of the coatings was measured by surface profilometry tool (Figure 4).

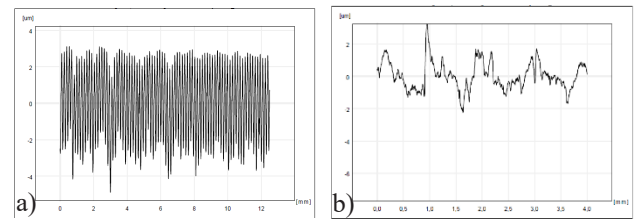


Figure 4. The surface roughness graphics a) inner surface radially in 1.58-7.17 b) outer surface circularly in Ra:0,66

The characterization of the coatings was carried out under the electron microscope (SEM-EDX). Fe, Cr, Mn, Si, O elements were detected in EDX analysis. At the end of the coating operation, unmelted and scattered spherical powder particles can be clearly seen in the melt pool on the upper surface (Figure 5). The desired surface quality can be obtained by removing this layer by machining or grinding.

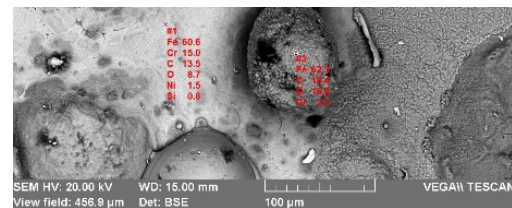


Figure 5. SEM Micrographs top view of laser cladded surface (as-cladded).

The coating section obtained with optimized process parameters is shown in Figure 6. The final thickness of the clad layer is about 1 mm. After the grinding process, the final coat thickness is 0.5 mm at section. There is agreement in the EDX analysis of the coating and the powder (Figure 7., Table 3). The surface hardness of the top coating is about 55 HRC and the substrate hardness is 208 ±10 HB.

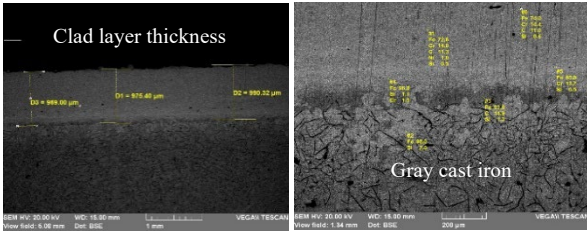


Figure 6. SEM Micrographs of the laser clad layer cross-section.

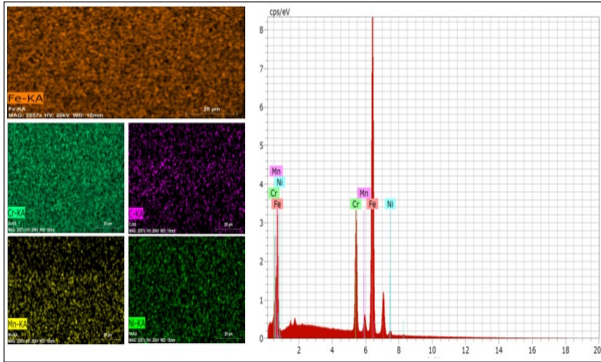


Figure 7. 431 Laser cladding layer EDX analysis.

Table 3. Laser cladding powder characteristic.

431 HC Laser Cladding Powder (+53-150μm)					
Fe Base %	Si %	C %	Cr %	Ni %	Mn %
Bal	0.75	0.2	16.0	1.8	<1

3.1 Wear Performance Test results

The change of friction behaviour between the original pad and the disc in different braking regimes and temperatures was investigated in the brake performance tests dynamometer device. After wear versus temperature test on test bench, the brake disc and brake pads surfaces have visually checked and evaluated in terms of coating deformation, crack formation and material loss in the braking surfaces (Figure 8).

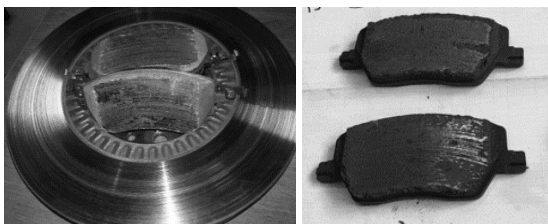


Figure 8. Brake disc and pad after performance testing

The brake pads in both couple (disc & original pads-coated disc& original pads) counter surfaces are damaged due to high temperature in the interface of the brake discs and pads. The original pad material is a low metal content compound, and it is expected to occurrence geometrical deformation at high temperatures (>400°C) and successive braking conditions. In the geometrical check, disc thickness variation (DTV) change is measured ~10 microns. In contrary, the DTV change is measured almost same as beginning in the coated discs. When the mass losses on the pad are compared, there is no significant difference in the brake test results made with the laser clad layer at low

temperatures. It has been observed that the wear of the laser clad layer-pad pair decreases at elevated temperatures (500°C). Approximately 3 times less wear was detected (Figure 9).

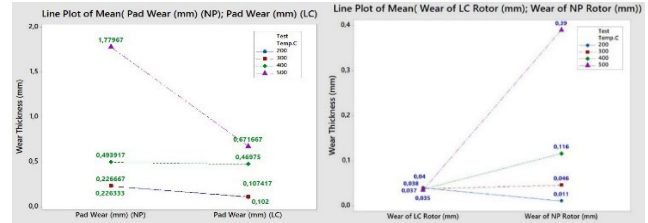


Figure 9. Wear comparison graph of pads & discs for uncoated disc-pad (NP) and coated disc-pad (LC) pairs at different temperatures.

While the disc wear was similar between coated and uncoated discs at low temperatures, the wear loss for coated discs decreased significantly at increasing temperatures. The friction behaviour of the uncoated disc-pad couple at different temperatures are shown in figure 10. No significant change is detected in the first 100 brakes. Afterwards, temperature changes and friction coefficient changes depending on the increasing number of brakes can be seen. As the temperature increases, the friction coefficient decreases after 500 brakes. Coefficient of friction decreases from 0.45 to 0.27.

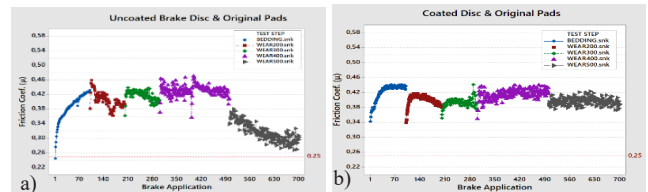


Figure 10. Uncoated (a) and coated (b) disc-pad friction coefficient trend at different temperatures.

The friction coefficient trend demonstration by increasing temperature of wear test is one of the well-known key characteristics which is considered in the brake efficiency evaluation. From the bedding stage in tests, friction coefficient has been measured and reported with the increasing testing temperature. In the NP disc-original pad couple, it can be evaluated that the coefficient remains stable up to 500 °C, after this temperature the friction coefficient is down dramatically. Even though the result is met the safe braking requirement for this brake configuration. In the laser clad coated disc-original brake pad couple, the friction coefficient is almost stable through the test when comparing with the NP disc-original pad couple. In contrast with the NP disc test, the friction coefficient is continued to stable in the high temperature (500 °C).

3.2 Corrosion Test results

The laser clad brake disc after the wear testing (Figure 11) on the vehicle was put in the salt spray corrosion test cabin to evaluate against to corrosion performance.

Corrosion occurrence was observed in planned time periods, the initial distinguishable red rust formed about the end of 24 hours and red rust occurred in almost each surface of the brake disc after 48 hours as shown in Figure 12. Uncoated discs are rapidly corroded under road conditions.

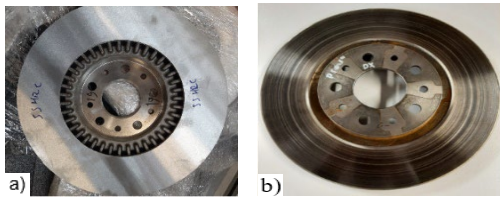


Figure 11. a) The laser-cladded brake disc before on the vehicle test on road conditions b) Used disc after the test.

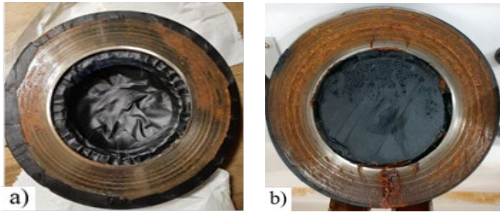


Figure 12. Corrosion performance of laser cladded disc after corrosion test a) internal surface of disc b) exterior surface.

4. Conclusion

Laser cladding operation can be implemented on the brake disc with process optimization by the robotic systems. By this way, the repeatable process results can be achieved. A grinding or machining operations should be done for reducing roughness when the surface roughness is not suitable for the pair of brake disc and pads. Thermal wear performance is highly effected successive brake applications and increasing friction surface temperature.

In this study, the martensitic stainless steel (AISI 431) coating demonstrates a great performance of thermal wear comparing with the normal production brake disc. Also, this coating shows a quite good results in the corrosion test assessed by the visual evaluation. The total brake dust emission is dramatically decreased (about 50%) with the coated brake disc since reducing wear amount both brake disc and pads. Further research is needed to understand the volumetric analysis of fine brake dust emissions in the coated rotor.

In the future brake systems, brake disc which is coated by laser cladding method will be used in the vehicles to increase the service life of brake components and decrease the environmental effects by limiting the dust emission during the braking time.

References

[1] W. Li, X. Yang, J. Xiao, and Q. Hou, "Effect of WC mass fraction on the microstructure and friction properties of WC/Ni60 laser cladding layer of brake discs," *Ceram. Int.*, vol. 47, no. 20, pp. 28754–28763, 2021, doi: 10.1016/j.ceramint.2021.07.035.

[2] G. Cueva, A. Sinatora, W. L. Guesser, and A. P. Tschiptschin, "Wear resistance of cast irons used in brake disc rotors," *Wear*, vol. 255, no. 7–12, pp. 1256–1260, 2003, doi: 10.1016/S0043-1648(03)00146-7.

[3] Zhu, Y., Liu, X. B., Liu, Y. F., Wang, G., Wang, Y., Meng, Y., & Liang, J. (2021). Development and characterization of Co-Cu/Ti3SiC2 self-lubricating wear resistant composite coatings on Ti6Al4V alloy

by laser cladding. *Surface and Coatings Technology*, 424, 127664.

[4] X. Liu, X. Meng, H. Liu, G. Shi, S. Wu, C. Sun, M. Wang, L. Qi, Development and characterization of laser clad high temperature self-lubricating wear resistant composite coatings on Ti-6Al-4V alloy. *Materials & Design*, 55, 404-409.

[5] Qi, K., & Yang, Y. (2022). Microstructure, wear, and corrosion resistance of Nb-modified magnetic field-assisted Co-based laser cladding layers. *Surface and Coatings Technology*, 434, 128195.

[6] Zhu, Q., Liu, Y., & Zhang, C. (2022). Laser cladding of CoCrFeNi high-entropy alloy coatings: Compositional homogeneity towards improved corrosion resistance. *Materials Letters*, 132133.

[7] X. Shi *et al.*, "Investigation on friction and wear performance of laser cladding Ni-based alloy coating on brake disc," *Optik (Stuttg.)*, vol. 242, no. May, p. 167227, 2021, doi: 10.1016/j.ijleo.2021.167227.

[8] J. Yu, B. Song, and Y. Liu, "Microstructure and wear behaviour of Ni-based alloy coated onto grey cast iron using a multi-step induction cladding process," *Results Phys.*, vol. 10, no. April, pp. 339–345, 2018, doi: 10.1016/j.rinp.2018.06.042.

[9] M. Federici, C. Menapace, A. Moscatelli, S. Gialanella, and G. Straffellini, "Pin-on-disc study of a friction material dry sliding against HVOF coated discs at room temperature and 300 °C," *Tribol. Int.*, vol. 115, no. March, pp. 89–99, 2017, doi: 10.1016/j.triboint.2017.05.030.

[10] L. Zhu, S. Wang, H. Pan, C. Yuan, and X. Chen, "Research on remanufacturing strategy for 45 steel gear using H13 steel powder based on laser cladding technology," *J. Manuf. Process.*, vol. 49, no. June 2019, pp. 344–354, 2020, doi: 10.1016/j.jmapro.2019.12.009.

[11] L. Zhu, S. Wang, H. Pan, C. Yuan, and X. Chen, "Research on remanufacturing strategy for 45 steel gear using H13 steel powder based on laser cladding technology," *J. Manuf. Process.*, vol. 49, no. June 2019, pp. 344–354, 2020, doi: 10.1016/j.jmapro.2019.12.009.

[12] X. Li, T. Li, B. Shi, D. Wang, M. Adnan, and H. Lu, "The influence of substrate tilt angle on the morphology of laser cladding layer," *Surf. Coatings Technol.*, vol. 391, no. March, p. 125706, 2020, doi: 10.1016/j.surfcoat.2020.125706.



A COMPARATIVE STUDY ON CORROSION PROPERTIES OF DECORATIVE CHROMIUM AND PVD EVAPORATED ALUMINIUM COATED ABS PARTS

Aleyna BAYATLI¹, Arif AKILLILAR², Mustafa KOCABAŞ¹

¹Konya Technical University, ²Tosunogulları Mobilya
Türkiye

Keywords: ABS, PVD evaporated aluminum coating, decorative chromium coating, corrosion resistance

Abstract

In this study, the corrosion behavior of coating which decorative chromium (Cr) and PVD (Physical Vapor Deposition) evaporation aluminum (Al) on Acrylonitrile butadiene styrene (ABS) furniture parts were comprised. The corrosion analysis was carried out with visual examination and electrochemical analysis. As a result, the decorative Cr is more resistant to dipped and electrochemical corrosion in contrast these analyses, PVD evaporated Al is more resistive in the salt spray test.

1. Introduction

Nowadays, plastic materials are replacing many metal parts, however, the plastic surfaces don't provide some properties expected by themselves like reflectivity and wear resistance [1]. At this point, surface metallization of polymers is a common, considerable process that obtained aesthetic, decorative, and reflective appearance in the furniture industry like chair-arms, door handle, clothes-hanger, armature, etc. [2-5]. Metallization is a technique that combined excellent properties of metallic and polymeric materials and enhances the wettability, reflectivity, electrical conductivity, and scratch-resistance of polymers [2,6,7]. Conventional metal plating one of these metallization processes has been widely used for more than 30 years and this method is generally expensive, toxic, and necessitates several complex steps [2,3,8]. These disadvantages are leading to new research about polymer surface metallization alternatively for conventional plating [4,9]. In this direction, PVD evaporation Al is drawn attention due to the simple, environmental, and tribological behavior improvement suitable for industrial applications and economical coating processes because aluminum has high reflectivity, low density, and good corrosive resistance [10,11].

The main aim of this study is to comprise on corrosive behavior of coating which produced decorative Cr and PVD evaporated Al. The comparison of corrosion resistance of these coatings was carried out with three different corrosion analyses. After corrosion analysis, visual examination and electrochemical results were observed and comprised. Decorative Cr coated ABS is more resistive to corrosion in all dipped-solution corrosive experiment than PVD evaporated Al coating however Al coated parts is better than Cr at the 5% wt. NaCl salt spray test. Similarly, electrochemical analysis is shown that Cr-coated samples are more resistive to corrosion.

2. Experimental Procedure

ABS of technical quality was obtained from Bürotime (Tosunogulları Mobilya A.S.) as common test samples used in the furniture industry. There is a difference between metallic and non-metallic surfaces which is the nature of the bond. Plastic material hasn't an atomic bond due to its nature therefore it is necessary to develop a proper surface that created a good adhesion [1]. In both PVD evaporating Al and decorative Cr process, a mechanical abrading procedure was employed to make the ABS surfaces smooth. For Cr-coating process, the surfaces were sensitized and activated with tin and palladium, respectively. The activated plastic surface is plated with electroless nickel to make it conducive for the electroplating step. The ABS electroless nickel-plated samples were electroplated with copper and bright nickel, respectively. Finally, decorative Cr plating is coated. For evaporation coating, the ABS surface was cleaned in isopropyl alcohol solution then ultraviolet (UV) lacquer was applied and dried. In the evaporation process, evaporated the particles accelerated in the reactor zone with plasma and deposited on the target [11]. The PVD evaporating

was applied for 10 minutes and coated ABS was lacquered UV and dried again. The coating processes of decorative Cr and PVD evaporated Al coatings of ABS plastics are summarized in Figure 1.

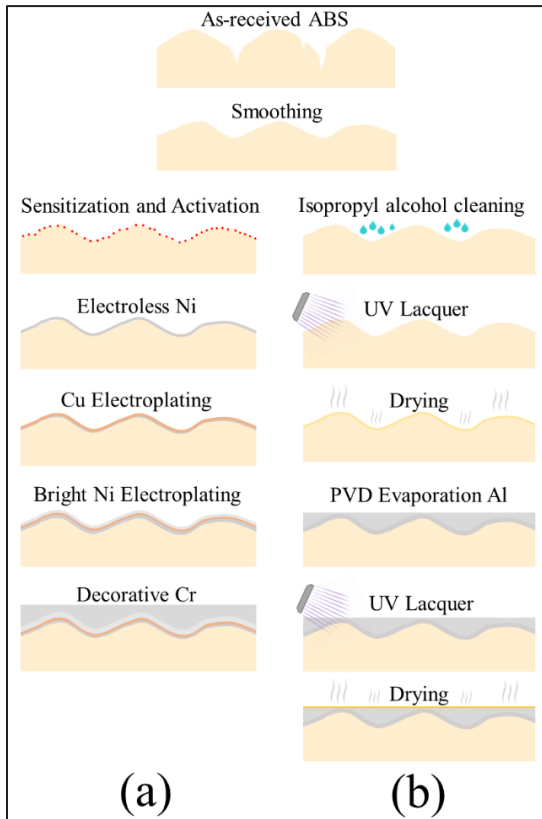


Figure 1. Coating process steps of (a) decorative Cr, (b) PVD evaporated Al

To investigate coating microstructure and homogeneity, the cross-sectional area of ABS was examined with optical microscopy and coating thickness was measured.

The electrochemical corrosion analysis was investigated by the open circuit potential (OCP) and potentiodynamic polarization (PDP) technique in 0.1 M NaCl solution at room temperature. For electrochemical analysis, coated ABS samples were masked with silicon as given in Figure 2c and electrochemical characterization of coatings was analyzed Gamry Interface 1010 Potentiostat with Ag/AgCl reference electrode and graphite counter electrode (Figure 2d). The OCP was monitored for 600 s to obtain the free potential of the surface, followed by PDP starting from the potential (-0.25 V vs. OCP) to ending potential (+1.5 V vs. OCP) with a scan rate of 1 mV/s. E_{corr} and i_{corr} values were obtained using the Tafel slope method.

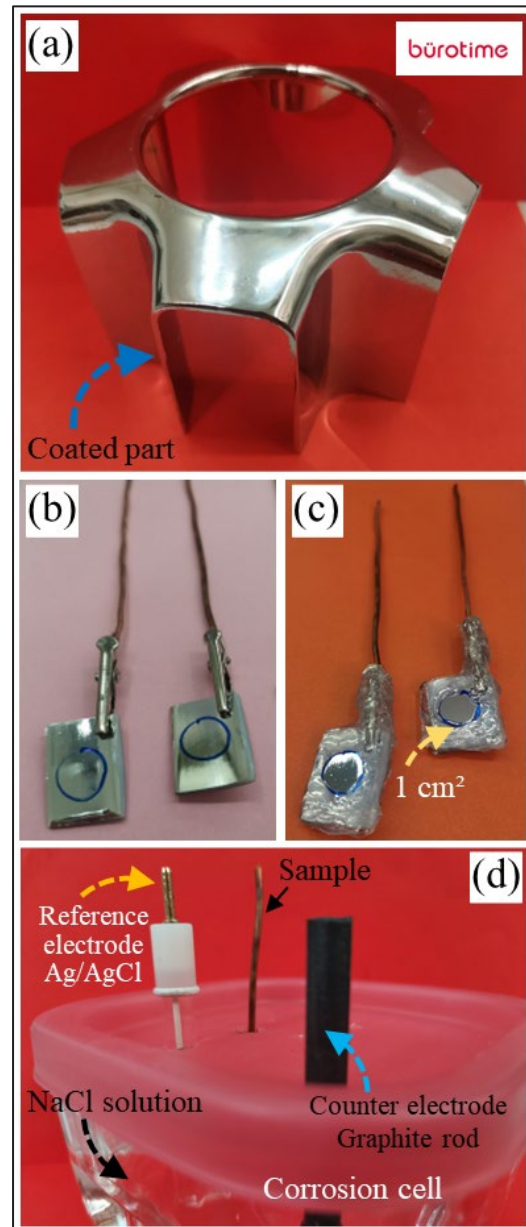


Figure 2. Coated furniture part (a), samples received from coated part (b), masked sample (c), and corrosion cell (d) for electrochemical corrosion analysis

The coated ABS components are mostly exposed to corrosive media by hand-contacting or cleaning because the material is designed for office or home furniture. For this purpose, the dipped-solution corrosion behaviors of these two coatings were examined in five different common furniture industrial corrosive media: (i) tap water, (ii) 0.1 M NaCl, (iii) 5% wt. commercial detergent solution, (iv) 5% wt. dilute bleach and (v) disinfectant solution. The coated ABS part was cut into small samples and dipped in the corrosive solution and observed for 14 days. Solution volumes are equal to in each corrosive media. The dipping corrosion experiment is shown in Figure 3.

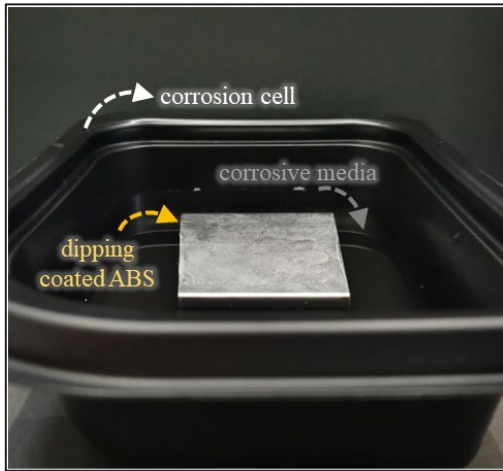


Figure 3. Image of dipped corrosion experiment

The third corrosion analysis is a salt spray test in 5% wt. NaCl solution for 30 days. The samples are fixed at 45° in a salt spray cabin. The visual examinations were observed and comprised.

3. Result and Discussion

Figure 4 illustrated the cross-sectional images with thickness of coated ABS parts. The decorative Cr coating thickness is $35 \pm 2 \mu\text{m}$ whereas PVD evaporated Al is $15 \pm 10 \mu\text{m}$. Decorative Cr is well-covered forming a continuous layer whereas Al coating wasn't homogeneously along the cross-section.

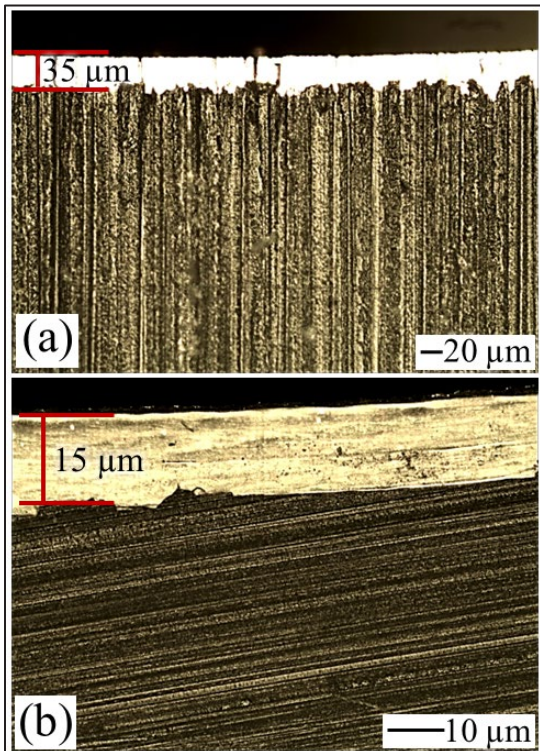


Figure 4. Cross-section image of (a) decorative Cr and (b) PVD evaporated Al coated ABS material

Figure 5 are shown digital images of PVD evaporated Al and decorative Cr coated samples after the dipped corrosion experiment. In this study, qualitative results were obtained by visual inspection of the specimen surface after exposure to the dipped corrosion experiment and salt spray test [12]. The corrosive behavior of plastic materials is different from metallic materials. Blistering and hazy appearance have occurred in some areas of the coated surface. Decorative Cr coated ABS is more resistant to corrosion in all dipped corrosive solutions because it protected its bright appearance in most corrosive media. The adhesion behavior of PVD evaporated Al is less than decorative Cr. The coated surfaces are resistive to corrosion in 0.1 M NaCl solution and any visual deterioration didn't occur however it was carried out in disinfectant solution. It can be said that disinfectant solution can be accepted as an aggressive media for metallic-coated ABS material.

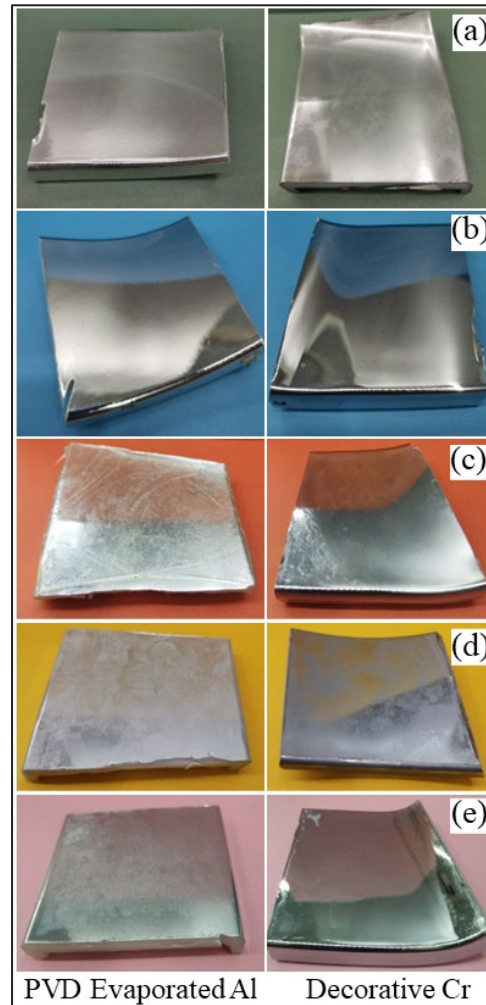


Figure 5. Digital image of PVD evaporated Al and decorative Cr coated ABS samples after dipped corrosion analysis (a) tap water, (b) 0.1 M NaCl, (c) disinfectant solution, (d) 5% wt. commercial detergent solution, (e) 5% wt. dilute bleach

Figure 6a and 6b are shown OCP and PDP curves of samples, respectively. The E_{corr} value of Cr is -229.5 mV and -384.2 mV for Al. The E_{corr} and OCP values of coated ABS has similarity however Cr is more positive side than Al. i_{corr} values were 22.5 nA/cm² 9.2 μ A/cm² for decorative Cr and PVD evaporated Al, respectively. It is known that a higher value of the i_{corr} and a more negative value for the E_{corr} indicates that the coating is less resistant to corrosion. In this situation, Cr is more resistant than to corrosion as to electrochemical corrosion tests.

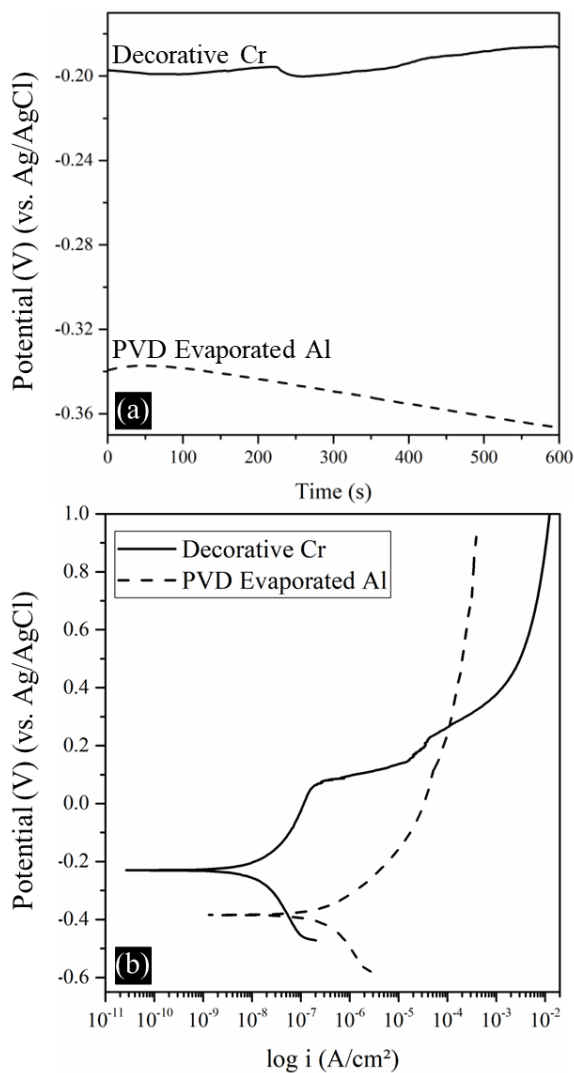


Figure 6. OCP (a) and PDP (b) graphs for coated ABS

The digital images of coated ABS after the salt spray test are given in Figure 7. The salt spray results are different from other corrosion analyses. PVD evaporated Al is more stable and resistant to corrosion in this method. The salt spray test provides a controlled corrosive environment and relative corrosion resistance information [13]. Al

layer was protected by its bright and metallic appearance but the decorative Cr-coated surfaces have blister and peeling point on the surface. The factors which most influenced salt spray test results are surface roughness and wettability [13]. In other words the surface which has low wettability and less roughness is more resistive to salt spray corrosion. The Al coated surface may be smoother compared to decorative Cr thus PVD evaporated Al coating can be more resistant to corrosion in the salt spray test.

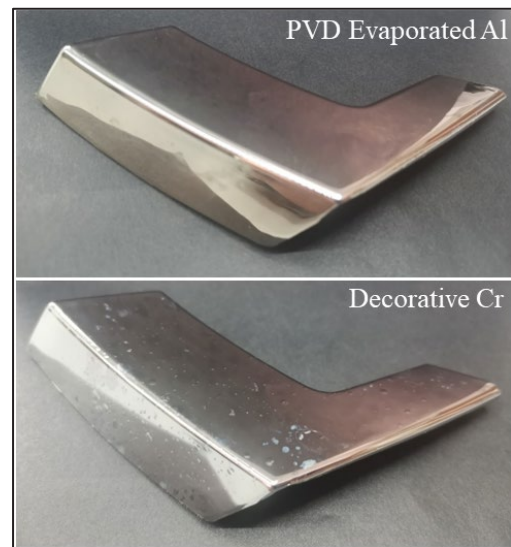


Figure 7. Salt spray test result for coated ABS sample after 30 days

4. Conclusion

- It successfully formed a uniform and continuous deposition of decorative Cr and PVD evaporated on the ABS surface. A shiny, bright, and decorative appearance was obtained in both coating methods.
- PVD evaporated Al process includes environmental and simple process and several steps are removed however its corrosion resistance is lower than conventional decorative Cr coating in dipped and electrochemical analysis.
- The corrosion resistance of coatings was estimated with three different corrosion analyses. The corrosion resistance of coated ABS material difference depends on corrosive media.

Acknowledgment

The authors would like to thank Bürotime (Tosunogulları Mobilya A.S.) for financial support.



References

- [1] V. Ijeri, S. Komal and B. Snehal, National Association for Surface Finishing, 78(2014), 1-8.
- [2] C. Eßbach, D. Fischer and D. Nickel, Journal of Manufacturing Processes, 68(2021), 1378-1386.
- [3] M. Bazzaoui, J. I. Martins, E. A. Bazzaoui, A. Albourine, R. Wang and P. Da Hong, Surface and Coatings Technology, 224(2013), 71-76.
- [4] M. Bazzaoui, J. I. Martins, E. A. Bazzaoui and A. Albourine, Applied Surface Science, 258(2012), 7968-7975.
- [5] J. P. Heinß and F. Fietzke, Surface and Coatings Technology, 385(2020), 1-8.
- [6] L. A. C. Teixeira and M. C. Santini, Journal of Materials Processing Technology, 170(2005), 37-41.
- [7] A. Garcia, T. Berthelot, P. Viel, A. Mesnage, P. Jégou, F. Nekelson, S. Roussel and S. Palacin, 2(2010), 1177-1183.
- [8] R. Suman, D. Nandan, A. Haleem, S. Bahl and M. Javaid, Materials Today: Proceedings, 28(2020), 1575-1579.
- [9] D. Zhang, X. Zuo, Z. Wang, H. Li, R. Chen, A. Wang and P. Ke, Surface Coatings Technology, 394(2020), 125890.
- [10] N. Arias and F. Jaramillo, Applied Surface Science, 505(2020), 144596.
- [11] A. Baptista, F. J. G. Silva, J. Porteiro, J. L. Míguez, G. Pinto and L. Fernandes, Procedia Manufacturing, 17(2018), 746-757.
- [12] ASTM Standard B-117, 1997, Standard Practice for Operating Salt Spray (Fog) Apparatus, ASTM International, West Conshohocken, Pennsylvania.
- [13] <<https://www.worldstainless.org>> Dated: 02.07.2022

SIMULATION AND FABRICATION OF THIN FILM NOTCH FILTER

Eray HUMALI^{1,2}, M. Kürşat KAZMANLI¹

¹Istanbul Technical University, ²Roketsan Missiles Inc.
Türkiye

Keywords: Notch Filter, Thin Film, Optical Coating, Electron Beam Evaporation Technique, Python

Abstract

Notch filters, a type of interference filter, block a narrow band on the electromagnetic spectrum. They are used in various fields such as in the defense industry, medicine, and Raman spectrometers. The filtering band of notch filters can be controlled by tuning their two cut-off frequencies. In thin films, controlling the filtering behaviour is possible to control the film materials and thickness of the thin-film layers. The dispersion phenomenon is the one of most outstanding parameters that influence the refractive index of the film materials. In this study, the Sellmeier dispersion equation of the selected film materials was used to create a mathematical model for thin-film notch filters. According to the results of the model, various thin-film notch filters which are composed of pre-determined film material combinations, were produced using the electron beam (E-beam) evaporation technique. The mathematical model and optical analysis results of the filters were compared to each other, and the effect of the material combination, film thickness, and the number of film layers on filtering performance was investigated.

1 Introduction

Nowadays, optical filters are well-developed and high-quality. They are used in various fields in crucial roles such as the glass industry, different spectroscopy applications, the defense industry, and neuroscience. Optical filters are used for providing desired optical behaviour of surfaces. They work on specific regions of the electromagnetic spectrum. Optical filters can be classified into two main groups absorptive and interference filters.

Absorptive filters are not allowed to reflect or transmit wavelengths of light by adding organic or inorganic substances to a substrate. Blocked wavelengths are generally unwanted parts to transmit or reflect of the spectrum. The absorption ratio of the filter is tuned by the amount of the added material [1]. In some applications, acrylic matrix and polycarbonate are chosen to reduce filter mass.

On the other hand, interference filters, namely dichroic filters, utilize constructive and destructive interferences between electromagnetic waves, so their structure is more complex than absorptive filters. Desired optical filtering behavior can be achieved by the control of the interferences between photons. Generally, dichroic filters are made of multilayer stacks of thin-films using physical vapor deposition (PVD) and chemical vapor deposition (CVD) techniques. The optical characteristics of the interference filters can be determined by adjusting the film thickness, the refractive index of the film material and substrate, and the number of thin-film layers that directly influence the interferences of the light. Besides, the wavelength of the incident photon, temperature, defects, and

impurities affect the refractive index, therefore filtering features of the thin film are influenced by these parameters. Wavelength dependency of refractive index is called dispersion and it has a dominant impact on optical properties. For example, generally, a refractive index of materials decreases between 10^{-4} and 10^{-3} per 1°C increase in temperature [2].

There are several types of dichroic filters with different filtering behaviour. Types of interference filters are usually named according to their filtering shape or working region on the electromagnetic spectrum like; monochromatic, low-pass, band-pass, ultraviolet, infrared, and notch filters. Notch filters block a certain spectral part of electromagnetic waves between their two cut-off frequencies. A narrow filtering region of the notch filter can be placed on any region of the electromagnetic spectrum.

In this study, a free simulation for thin-film notch filters has been created according to optical principles using Python software. Various thin-film coatings were produced according to the results of the simulation to verify simulation reliability, then three thin-film notch filters were fabricated using previous unused materials combination and film thicknesses. All notch filters can be used in different regions of the spectrum and applications such as Raman spectrometers, chronic migraine and photophobia treatment, and near-infrared spectrometers, respectively [3].

2 Numerical Modelling

Interference is the physics behind the working principle of the optical thin films. A phase difference (see Equation (1)), multiplication of wave number (k) and path difference (Δ), occurs when the incident light is reflected from surfaces because of the optical path difference, and it depends on the refractive index and thickness of materials.

$$\delta = k\Delta = (2\pi/\lambda)(2n_f t \cos \theta_t) \quad (1)$$

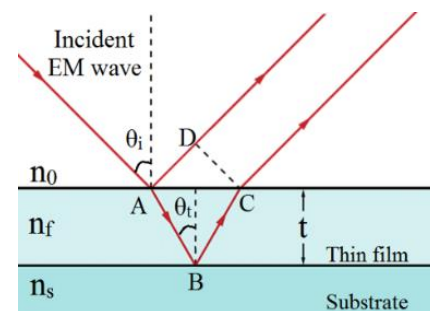


Figure 1. Optical path difference on surfaces

Since the wave-like nature of electromagnetic waves describes the optical characteristics of thin films, optical parameters can be derived using the Maxwell equations in

electrodynamics. All steps of derivations are not included in this paper, but one can find whole steps in [4]. Briefly, when Maxwell equations are solved according to boundary conditions of single-layer film and substrate considering the incident, transmitted, and reflected light, magnetic fields in terms of electric field and gamma parameters of film, substrate, and medium are derived as:

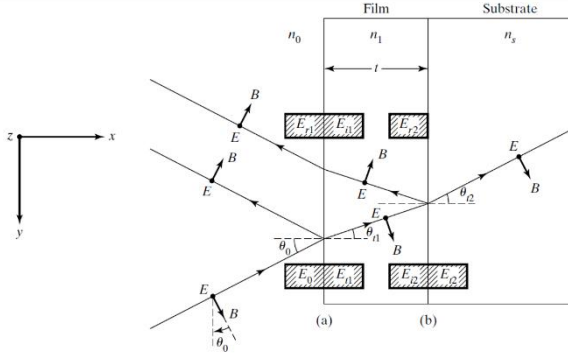


Figure 2. Transmission and reflection from a thin film [5]

$$B_a = \gamma_0(E_0 - E_{r1}) = \gamma_1(E_{t1} - E_{i1}) \quad (2)$$

$$B_b = \gamma_1(E_{i2} - E_{r2}) = \gamma_s(E_{t2}) \quad (3)$$

Where B_a and B_b are magnetic field components face medium–film and film–substrate interfaces, respectively. Gamma parameters that belong to medium, film, and substrate were defined for simplicity in the next calculations.

$$\gamma_0 = n_0 \sqrt{\mu_0 \epsilon_0} \cos \theta_0 \quad (4)$$

$$\gamma_1 = n_1 \sqrt{\mu_0 \epsilon_0} \cos \theta_{t1} \quad (5)$$

$$\gamma_s = n_s \sqrt{\mu_0 \epsilon_0} \cos \theta_{t2} \quad (6)$$

After several mathematical calculations, electric and magnetic fields on the surface (a) can be written in terms of these fields on the surface (b). Also, equations can be expressed in matrix form. An optical thin-film has a characteristic matrix which is shown in Equation (8).

$$\begin{pmatrix} E_a \\ B_a \end{pmatrix} = \begin{pmatrix} \cos \delta & \left(\frac{i \sin \delta}{\gamma_1} \right) \\ \gamma_1 i \sin \delta & \cos \delta \end{pmatrix} \begin{pmatrix} E_b \\ B_b \end{pmatrix} \quad (7)$$

$$M = \begin{pmatrix} m_{11} & m_{12} \\ m_{21} & m_{22} \end{pmatrix} \quad (8)$$

Using the elements of M , transmission and reflection coefficients, shortly t and r , of a single-layer thin-film can be calculated. Then, transmittance (T) and reflectance (R) are obtained by multiplication of these coefficients with their complex conjugates (see Equations (11) and (12)).

$$t = \frac{E_{t2}}{E_0} = \frac{2\gamma_0}{\gamma_0 m_{11} + \gamma_0 \gamma_s m_{12} + m_{21} + \gamma_s m_{22}} \quad (9)$$

$$r = \frac{E_{r1}}{E_0} = \frac{\gamma_0 m_{11} + \gamma_0 \gamma_s m_{12} - m_{21} - \gamma_s m_{22}}{\gamma_0 m_{11} + \gamma_0 \gamma_s m_{12} + m_{21} + \gamma_s m_{22}} \quad (10)$$

$$T = t^* t = |t|^2 \quad (11)$$

$$R = r^* r = |r|^2 \quad (12)$$

In the mathematical model, thin film filters have been assumed as non-absorbing structures, so the sum of the transmittance and reflectance equals 1. However, absorptance (A) was considered after the optical measurements; consequently, the sum of the transmittance, reflectance, and absorptance is equal to 1.

The Sellmeier dispersion formulas, a semi-empirical mathematical approach, can be used reasonably for thin-films and transparent glasses in order to examine wavelength dependency on the refractive index. The general representation of the Sellmeier formula can be shown as:

$$n_i^2 = A + \frac{B\lambda^2}{\lambda^2 - C^2} + \frac{D\lambda^2}{\lambda^2 - E^2} + \frac{F\lambda^2}{\lambda^2 - G^2} \quad (13)$$

In this study, the Sellmeier dispersion formula of selected film materials were used to simulate the optical properties of the coatings. The matrix power of the M was calculated for the periodically stacked multilayer thin-films.

$$M_{ij} = \underbrace{(M_i M_j)(M_i M_j) \dots (M_i M_j)}_{N\text{-times}} = (M_i M_j)^N \quad (14)$$



Figure 3. Schema of periodic multilayer thin film stacks

3 Materials & Methods

Created materials library for the simulation is completely user-defined and limitless, so the optical property of any kind of materials and substrates can be investigated. Three dielectric oxides were chosen to fabricate multilayer filters because of their good deposition property for the E-beam method, accessibility, and transparency range.

Table 1. Sellmeier formula constants of the materials [4]

Material	Al ₂ O ₃	Y ₂ O ₃	SiO ₂
A	1	1	1
B	1.4314	2.578	0.6962
C (nm)	72.6631	138.71	68.4043
D	0.6505	3.935	0.4079
E (nm)	119.3242	22936.0	116.2414
F	5.3414	-	0.8975
G (nm)	18028.3	-	9896.2

The Sellmeier formulas and general features of the selected oxides which are Al₂O₃, Y₂O₃, and SiO₂ are given in Table 1 and 2. Corning®-glass slides were used as substrate due to their uniform thickness and surface quality. Before fabricating multilayer stacks, single-layer films were deposited to compare the measurement thickness monitoring unit of the E-beam system and real thickness.

Thickness measurements of the single-layer coatings were performed using a KLA Tencor/P-7 surface profiler. According to thickness measurements, the thickness measurement unit of the deposition system was calibrated empirically using Equation (15).

Table 2. General features of selected film materials [4]

Coating Material	Al ₂ O ₃	Y ₂ O ₃	SiO ₂
Film Composition	Al ₂ O ₃	Y ₂ O ₃	SiO ₂
Mass Density (g/cm ³)	3.970	5.010	2.648
Transparency Range (μm)	0-1.0	0-8.0	0-9.0
z-ratio	0.336	1.000	1.000

$$\rho_{ad} = \rho_{th} \left(\frac{t_x}{t_m} \right) \quad (15)$$

Where ρ_{th} and ρ_{ad} were theoretical and adjusted mass densities of the materials, respectively. t_x and t_m are displayed by the thickness monitoring system and measured by surface profiler thicknesses. By using adjusted density, the thickness monitoring unit was calibrated practically. Periodically stacked multilayer thin film notch filters made of SiO₂-Al₂O₃ and Al₂O₃-Y₂O₃ combinations with different film thicknesses were deposited using the E-beam evaporation system under the 9×10^{-4} MPa vacuum level according to simulation results. The optical properties of the fabricated filters were measured by Shimadzu/UV-3600 spectrophotometer between 300 nm and 1200 nm in wavelength with an incident angle is 60°.

4 Results and Discussion

After the adjusting, the thickness monitoring system using the single-layer film thicknesses and mass densities of the chosen oxides, measured transmittance and reflectance behaviours of the single-layer coatings were compared with simulation outputs for the same film thicknesses. Figure 4 shows that simulation and experiment results are quite consistent with each other, so the mathematical model can be used in multilayer thin-film filters.

After this verification, fabrication of the periodically stacked multilayer thin-film notch filters had been started according to simulation results. 3-set notch filters were modelled to work on different regions of the electromagnetic spectrum. The center wavelengths of the notch filtering band (c_λ) of the modelled filters were determined as 480 nm, 620 nm, and 840 nm. Different binary combinations of the selected dielectric materials with appropriate film thicknesses were modelled to achieve aimed sophisticated notch filter behaviour. Moreover, the effect of the layer number on the filtering property was investigated during the fabrication process. All filters were produced with a 4.5 Å/s deposition rate to reach good surface quality because the average surface roughness of the film surface increases as the deposition rate increases according to atomic force microscopy examination [6].

First, the simulation revealed that a thin film notch filter in which c_λ is 480 nm, can be produced using Al₂O₃ and Y₂O₃ with layer thicknesses are 50 nm and 75 nm, respectively. This filter can be classified as a monochromatic filter that corresponds to the blue colour on the electromagnetic spectrum.

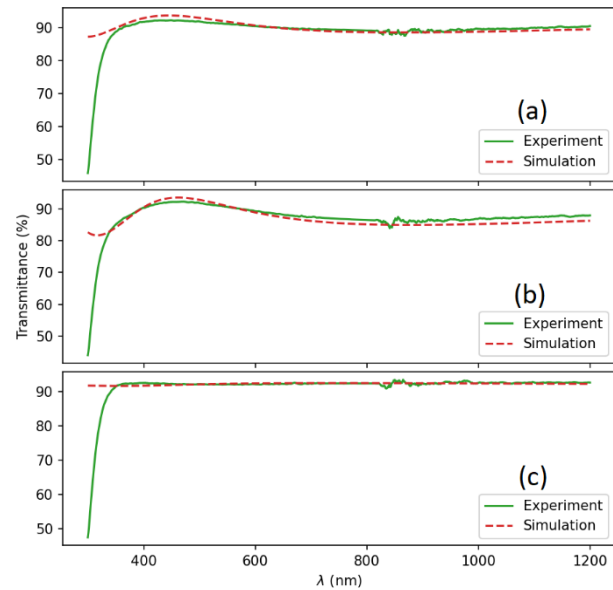


Figure 4. Comparison of the single-layer coatings with film thicknesses: (a) Al₂O₃ (136 nm), (b) Y₂O₃ (130 nm), and (c) SiO₂ (120 nm) on Corning®-glass substrates.

The number of periodic binary films was slightly increased to observe its effects. Figure 5 shows simulation results and optical measurements of filters with different layer numbers (N). It can be seen in the figure that the notch filtering characteristic becomes sharper as the layer number increases. c_λ of the $N=5$ coating was detected as 490 nm. When film thicknesses were checked, the thickness of the Y₂O₃ films was determined as 77 nm. So, 1 nm deviation in periodic Y₂O₃ films causes 5 nm red-shifting in c_λ of the filter. The simulation shows that the c_λ can be tuned by changing film thickness, so 514 nm of c_λ is achievable to use in Raman spectrometers.

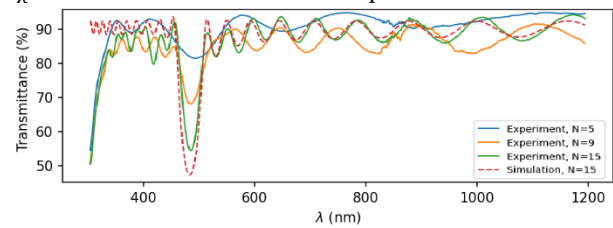


Figure 5. Al₂O₃ (50 nm) and Y₂O₃ (75 nm) thin-film notch filter with $c_\lambda = 480$ nm

The second filter set was simulated to obtain a monochromatic filter corresponding to the orange and yellow part of the spectrum to reduce the risks of photophobia and chronic migraine because the human eye is highly sensitive to this level of light [3]. For this reason, c_λ is determined as 620 nm, and the simulation outputs said that this filter can be produced using SiO₂ and Al₂O₃ materials with their film thicknesses are 70 nm and 110 nm, respectively. Figure 6 is presented to show the comparison of simulation and optical measurement results of the second set filter by increasing layer number. A mismatching between simulation and $N=4$ & $N=10$ filters appears in the figure. Simulation re-checking says that +3 nm deviation in SiO₂ layers caused 19 nm blue-shifting in c_λ of the $N=4$ structure. Similarly, 65 nm film thickness in Al₂O₃

layers is the reason for the fabrication of $N=10$ filter with the 597 nm of c_λ .

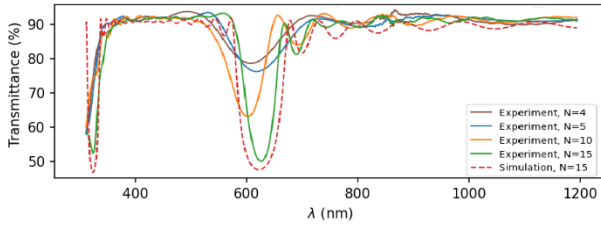


Figure 6. SiO₂ (70 nm) and Al₂O₃ (110 nm) thin-film notch filter with $c_\lambda = 620$ nm

The last notch filter was simulated for useability in near-infrared spectroscopies. For this filter, the c_λ was decided as 840 nm. Results of the simulation can be produced by deposition of SiO₂ and Al₂O₃ materials with 130 nm film thicknesses each. Transmittance results about to near-infrared notch filter are given in Figure 7. $N=10$ coating has a c_λ at 845 nm due to $t_{SiO_2} = t_{Al_2O_3} = 131$ nm layer thicknesses according to the simulation.

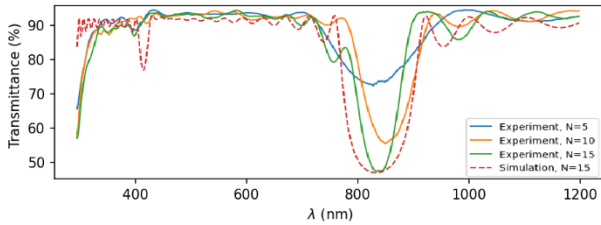


Figure 7. SiO₂ (130 nm) and Al₂O₃ (130 nm) thin-film notch filter with $c_\lambda = 840$ nm

Table 3 is composed of specifications of the 3 three fabricated thin-film notch filters with a 15-layer number. The number of the periodic stacked binary layers was limited to 15 due to features of the deposition system. The duration of the filter fabrication increases as the layer number increases obviously. This value was almost 10 hours for the 15-layer filters including vacuuming, deposition, and post-process durations. During the deposition, substrate temperature increases due to the emission current-related kinetic energy of adatoms. Low substrate and film temperatures are preferred because of having low diffusion ability among films, and whole films were assumed distinct from each other in the simulation.

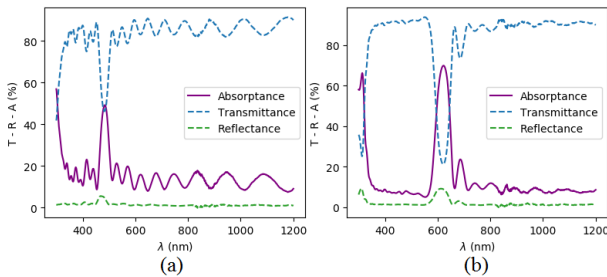


Figure 8. Absorbance of the (a) Al₂O₃(50 nm)-Y₂O₃(75 nm) and (b) SiO₂(70 nm)-Al₂O₃(110 nm)

After the T and R measurements, the A of the fabricated filter was examined. Absorbance ratios of the Al₂O₃-Y₂O₃ and SiO₂-Al₂O₃ structures are given in Figure 8 (a) and (b), respectively.

Figure 8 shows filtering band between cut-off frequencies has been absorbed by the structure instead of reflected. Both structures have approximately 10% average A except for the filtering band. Moreover, the A of the fabricated notch filters is weakly affected by material type and thickness because the average T of blank Corning®-glass has been measured as 91% between 300 nm and 1200 nm.

Table 3. Specifications of the fabricated notch filters

c_λ	480 nm	620 nm	840 nm
Dimensions	37.5 mm × 25 mm × 1 mm		
Substrate	Corning®-2947 glass		
Layer number (N)	15		
Thin film materials	Al ₂ O ₃ Y ₂ O ₃	SiO ₂ Al ₂ O ₃	SiO ₂ Al ₂ O ₃
Total thickness	1875 nm	2700 nm	3900 nm
Minimum T @ c_λ	46.004%	21.283%	15.985%
Cut-off wavelengths	457 nm – 508 nm	578 nm – 657 nm	771 nm – 902 nm
Bandwidth @FWHM	110 nm	220 nm	330 nm
Average T	84.751%	90.706%	91.001%
Average R	1.292%	2.014%	1.736%
Average A	13.957 %	7.280%	7.252%

5 Conclusion

In this study, it is aimed to create a thin-film notch filter simulation on Python utilizing optical principles. The simulation is completely free and limitless, so one can model the optical behaviours of any kind of material using the dispersion formulas, unlike commercial programs. Moreover, 3-set thin-film notch filters have been fabricated according to simulation outputs. The results show that fabricated notch filters have a using potential in various spectroscopies (such as Raman and near-infrared) and some neurobiology applications.

Also, any desired notch filter can be modelled and fabricated in terms of c_λ using previously unused materials combinations and film thicknesses.

6 Acknowledgment

The authors sincerely acknowledge the support of İ. G. Hızlı, and S. Çelik for this study.

7 References

- [1] E. Aydın, Notch Filter Design, MSc Thesis, Ankara University, 2011, Ankara, Turkey, pp. 1-2.
- [2] Y. Liu and P. H. Daum, Journal of Aerosol Science, 39(2008), pp. 974-986.
- [3] R.N. Hoggan et al, Journal of Clinical Neuroscience, 28(2016), pp. 71-76.
- [4] E. Humalı, Simulation and Fabrication of Thin Film Notch Filter, MSc Thesis, Istanbul Technical University, 2020, Istanbul, Turkey, pp. 7-35.
- [5] F. L Pedrotti, L. M Pedrotti, and L. S. Pedrotti, Introduction to Optics, Prentice Hall International Limited, 1993, London, United Kingdom, pp 477.
- [6] C. Stampfer, A. Jungen and C. Hierold, Sensor Journal, IEEE, 6(2006), pp. 613-617.

CONE SHAPED PARTS MANUFACTURING BY ELECTROFORMING PROCESS

Tutku TURGUTLUGİL GÖKÇE, N. Kaan ÇALIŞKAN, M. Kaan PEHLİVANOĞLU

Tübitak SAGE
Türkiye

Abstract

In this work, cone shaped copper parts manufacturing with electroforming method is studied. The effects of electroforming parameters such as solution concentration and pH, the stirring rate of the solution, the filtration state of anode material, pulsed forward to reverse current ratio, on the product properties such as grain size and surface uniformity and total production time are examined. Experiments had shown that, filtering the anode with silk aided in increasing the surface uniformity and refining microstructure of the cone shaped part. Increasing the HCl concentration from 0.05 ml/l to 0.1 ml/l, and hence varying the pH between 0.15-2, accelerated the electroforming process, but degraded the surface uniformity. Pulsed forward to reverse current ratio was found to be an important parameter in terms of shortening the process time and properties of the obtained product. As far as the results of this study is concerned, using an acid copper sulphate solution with additive of HCl concentration 0.05 ml, oxygen free copper anodes with filtration and pulsed forward and to reverse current ratio of 3 were the optimum parameters for cone shaped copper electroform parts.

1. Introduction

Electroforming is a variation of electroplating process in which metal is deposited on a mandrel which is then removed, the coating becoming the product. It is a process that evolve from electron exchange between anode and cathode. Metal salt solution anions are deposited to cathode surface help with electric current [1].

Even tough, it is similar with electroplating, the much thicker deposition from electroforming is the most important difference between them. Electroform is a metallic object that has been created from metal ion deposition to the mandrel [2]. Schematic of electroforming process is shown in Figure 1. There is a cathode which is usually a metallic material, and anode material which chosen for electroforming material. Electroform part made in an electrolytic solution by deposition of Cu^{+2} anions.

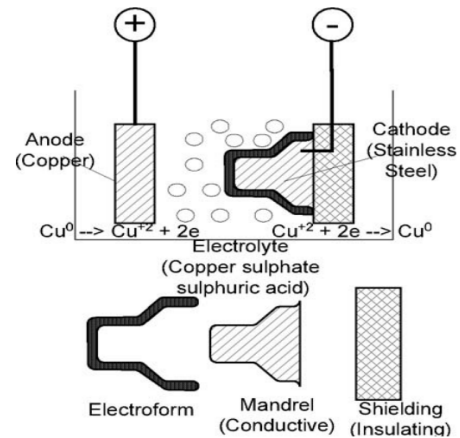


Figure 1. Schematic of electroforming process [3].

To obtain better performance from electroforming, electroforming parameters such as plating solution concentration, pH value, temperature, additives, and impurities should be controlled and optimized [4].

Electroforming method have many advantages over traditional production methods. Thanks to the electroforming method, parts that are very difficult or impossible to produce with traditional methods can be produced easily. The primary advantages of electroforming can be listed. Firstly, high dimensional precision if the mandrel is produced with the right tolerances and the surface is cleaned well, product can be dimensionally appropriate. Secondly, precise reproduction of surface detail and high accuracy. Reproduction of surface detail is hard for other conventional machining process. Furthermore, complex-shape or thin walled without joint line production with correct mandrel in single operation. In order to produce complex-shapes in conventional methods, many machining methods must be used together like pressing, drilling, machining, deburring while in electroforming final part is obtained with one process. The other advantage is different size and mass production can be achieve with electroforming process, it just be limited by batch dimensions [1] [3].

On the other hand, electroforming has some disadvantages like: non-uniform thickness, electroform mandrel separation, internal stress and longer deposition times.

Mandrel effects on dimensional precision and surface details for electroform is important. So that, design of mandrel and choosing mandrel material is vital. Mandrels can be divided in two groups which are permanent and expendable. Permanent mandrels can be used several times. They can also be grouped as conductor or non-conductor. Conductor mandrels can be used in pure metal depositions. Permanent or expendable mandrels can be chosen on the basis of their separation methods. For expendable mandrels, removing process can be chosen as heating and/or chemical dissolution [5].

Another important parameter for electroforming is the form of power supply. In electroforming or electroplating applications, direct current or pulse-reverse current can be used. Using pulse-reverse current gives finer, smaller grain size and lower porosity than using direct current [6] [7]. Therefore, they have different concepts in plating. There is a negatively charge layer around the cathode for both. When using the direct current that layer always charge the cathode. However, pulse-reverse current has a period which allows discharge of that layer [8].

Pulse-reverse current has off and on time. Using current on and current off time have effects on electroforming. If current is on, metal ions from cathode depleted the layer, if current is off metal ions from bulk diffuse the cathode layer. Because of that, in current off time gas bubbles and impurities can be desorbed from cathode. Thanks to off-on time in pulse-reverse current has advantages over to direct current in electroplating like; smooth surface that nearly free from pinholes and better current efficiency [9].

In pulse-reverse current plating there are important parameters like ratio between current densities of anode and cathode. P. Leisner, M. Fredenberg and I. Belov [10] reports that, anode current / cathode current (i_a/i_c) should be between 1 and 3.5 to obtain best results. It also says that time period of cathode / time period of anode (T_c/T_a) should equal to 20.

Cone shaped parts manufacturing with traditional ways have difficulties. Electroforming process gives great opportunities to get cone shaped parts with high dimensional accuracy with refiner microstructure than conventional manufacturing process. The aim of this study is obtaining highly pure copper cone shapes with smother surface and refiner grain size via electroforming process.

2. Experimental Procedure

In this study, copper sulphate in an acids condition was used as plating solution. Copper sulphate pentahydrate ($\text{CuSO}_4 \cdot 5\text{H}_2\text{O}$), sulphuric acid (H_2SO_4) and hydrochloric acid (HCl) used to prepare electroforming solution.

Table 1 shows the compositional parameters of the electroforming solution used in study. For all experiments copper sulphate pentahydrate ($\text{CuSO}_4 \cdot 5\text{H}_2\text{O}$) and sulphuric acid (H_2SO_4) ratios were kept as constant. HCl was used as an additive to adjust pH. So that, performed three different experiments where HCl concentration was 0.05 ml/l, 0.075 ml/l and 0.1 ml/l to see surface uniformity and process speed effects. Value of pH have changed in these experiments between 0.15-2.

Table 1. Electroforming solutions

Chemical	Amount
Copper sulphate pentahydrate ($\text{CuSO}_4 \cdot 5\text{H}_2\text{O}$)	220 gr/l \pm 20 gr/l
Sulphuric acid (H_2SO_4)	40 ml/l \pm 10 ml/l
Hydrochloric acid (HCl)	0.05, 0.075, 0.1 ml/l

In all experiments the temperature of solution was kept constant as 25°C degrees. All chemicals were used in highly purity state, to minimize the impurity in solution.

In this study, oxygen free copper was chosen as anode material. Silk fabric has been used to filter the anode. The anode material was completely covered with silk fabric before being placed in solution.

Permanent and conductor mandrel was chosen because of its reusability and suitability for electron exchange properties. As the mandrel material PH 17-4 stainless steel was chosen because it's suitable to copper ions deposition property. Cone shaped electroforms can be obtained with v shaped machined mandrel. Figure 2. Shows the v shaped mandrel. Electroforming formation begins corner sides of mandrel so that, surface finish of corner sides important.



Figure 2. V shaped mandrel [5]

The surface roughness and surface cleaning of mandrel is of vital importance as is reflected exactly to the shaped which have been coated. So, after the machining mandrel have been grinded for decreasing the surface roughness. Before all experiment the mandrel was grinded to remove contaminates from previous experiment. After grinding,

acid dipping and alkaline cleaning procedures were made to clean mandrel. Acid dipping with 20-30% H₂SO₄ solution for 3-5 min and 40-50% NaOH solution for 3-5 min applied to mandrels, before for all experiments.

In order to see the effect of pulse-reverse current ratios (i_a/i_c) on total process time, experiments carried out with $i_a/i_c=2$ and $i_a/i_c=3$. The experiments carried out $T_c/T_a=20$. For example, $i_a=4.62$, $i_c=1.54$ was chosen to obtain the ratio as 3. Figure 3 shows the schematic representation of current-time graph. As the forward current 4.62 ampere was applied, T_{on} of forward is 15 msec T_{off} is 5 msec so that, the $T_c=20$ msec. As the reverse current 1.54 ampere was applied. The reverse current was $T_{on}=1$ msec without T_{off} so the total $T_a=1$.

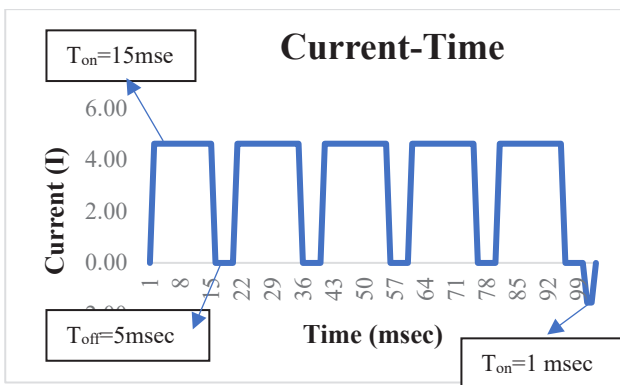


Figure 3. Schematically representation of current-time graph

Optical emission spectroscopy was used to analyse the electroform coppers chemical composition. Metallographic sample preparation was carried out to see microstructure of electroforms with optical microscope.

3. Results and Discussion

As far as the results of this study, value of pH changing with HCl concentration decreases the total process time but degraded the surface uniformity. So that, HCl concentration 0.05 was chosen. Anode to cathode current ratios have an effect of decreasing the total electroforming time. Such as, it was chosen as $i_a/i_c=2$ total electroforming process time was around 17-20 days, but when it was chosen as $i_a/i_c=3$ total process time was dropped around 12-15 days. The other result is stirring effects product surface quality. Electroforms which experiments was carried out with mixing rate 350-400 rpm has rough surfaces, however, the other electroform which was obtained with lower mixing speed like around 200-250 rpm has better surface uniformity.

Surface cleaning and surface properties of mandrel is vital for electroforming process, if mandrel surface has impurities or contaminates, electroform product can have some impurities and it can be rough.

Further result is, electron deposition begins at the tip and edge of V-shape mandrel. So, thickness from there is higher. Experiments also shown that its possible obtain 2-3 mm thickness in 7-12 days with optimum parameters.

Some characterizations were made in order to examine and compare the data obtained as a result of the experiments. Elemental analysis was carried out with optical emission spectroscopy. Table 2 shown the elemental analysis with optical emission spectroscopy for electroform product. Its copper content is nearly 99.97%. It contains trace amounts of elements such as iron, zinc etc. Chemical analysis says that electroforming method gives high pure material.

Table 2. Chemical analysis of product.

Cu %	Fe%	Zn%	Sn%	S%
99.977955	0.0022	0.0015	0.0023	0.0017

After metallographic sample preparation microstructure examination carried out with optical microscopy. Figure 4 and Figure 5 shows microstructure pictures of electroform unfiltered. Figure 6 shows the microstructure of electroform with filtration. All of microstructures have twinning and dendritic appearance. It is possible for grain growth to be dendritic as the electroforming process relies on electron exchange between the anode and cathode. When comparing the surface uniformity of electroforms with filtration and without filtration, silk filtration certainly increases uniformity of surface. There is a big difference between microstructures given in Figure 5 and Figure 6 in terms of their grain sizes, so that silk filtration might have effect on microstructures refinement.



Figure 4. Electroform unfiltered x50 magnification in optical microscope

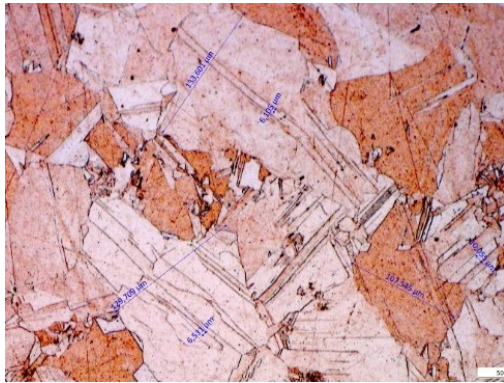


Figure 5. Electroform unfiltered x200 magnification in optical microscope



Figure 6. Electroform with filtration x200 magnification in optical microscope

4. Conclusion

As a conclusion of this work, copper cone shape parts successfully obtained with thickness in several millimetres via electroforming process. Value of pH is decreasing with increasing the HCl concentration. Decreasing of pH drops the total process time, but it gives lower surface uniformity. So that 0.005 ml/l is optimum for smother surface. Using anode with silk filtration gives smother surface and might have effect of grain size refinement. Experiment which have lower stirring rate gives smother surfaces for electroforms. Mandrel surface finish and surface cleaning is important to obtain electroforms with dimensional accuracy. i_a/i_c ratio affects total process time and surface uniformity. If the ratio of $i_a/i_c=2$ total electroforming process time was around 17-20 days, but when it was chosen as $i_a/i_c=3$ total process time was dropped around 12-15 days for 1-2 mm thickness.

Acknowledgment

I wish to acknowledge the help provided by financial and support staff in the TÜBİTAK SAGE.

5. References

- [1] P. Hernandez, D. Campos, A. Benitez ve P. Socorro, «Electroforming Applied to Manufacturing of Micro components,» *Procedia Engineering, Volume 132,*, pp. 655-662, 2015.
- [2] M. Sole, «Electroforming: Methods, materials, and merchandise,» *JOM*, cilt 46, p. 29–35, 1994.
- [3] J. McGeough, M. Leu, K. Rajurkar, A. De Silva ve Q. Liu, «Electroforming Process and Application to Micro/Macro Manufacturing,» *CIRP Annals*, cilt 50, no. 2, pp. 499-514, 2001.
- [4] C. Huang, H. Li, M. Zhu ve M. Yu, «Present Research Situation and New Trends of Electroforming,» *AMM*, 2013.
- [5] *Standard Guide for Electroforming with Nickel and Copper*, ASTM 832 (2013).
- [6] M. Chen, K.-W. Chen, T.-F. Liu, Y.-L. Wang ve H.-P. Feng, «Effects of direct current and pulse-reverse copper plating waveforms on the incubation behaviour of self-annealing,» *Thin Solid Films*, cilt 518, no. 24, pp. 7468-7474, 2010.
- [7] L. Holmbom ve B. Bacobson, *J. Electrochem. Soc.* 135, 1988.
- [8] M. Chandrasekar ve M. Pushpavanam, «Pulse and pulse reverse plating—Conceptual, advantages and applications,» *Electrochimica Acta*, cilt 53, no. 8, pp. 3313-3322, 2008.
- [9] C. V. Horn, «Pulse plating,» *Semi/microelectronics*.
- [10] P. Leisner, M. Fredenberg ve I. Belov, «Pulse and pulse reverse plating of copper from acid sulphate solutions,» *Transactions of the IMF*, cilt 88, no. 5, pp. 243-247, 2010.



TRIBOLOGICAL PERFORMANCE OF ELECTROCHEMICALLY BORIDED AISI H13 HOT WORK DIE STEEL

Ümmet AYYILDIZ^{1,2}, Harun MİNDİVAN²

¹Prometal R&D Center, ²Bilecik Şeyh Edebali University
Türkiye

Keywords: AISI H13 steel, Electrochemical Boriding, Hot work tool steel, Tribology

Abstract

DIN 1.2344 (AISI H13) steel was treated using electrochemically boriding with the intention of prevention unexpected die failure in hot metal forming. The treatment process was carried out in a molten salt based on 90 % borax ($\text{Na}_2\text{B}_4\text{O}_7$) and 10 % sodium carbonate (Na_2CO_3) at a constant temperature of 950 °C for 15 min and a current density of 200 mA/cm² in a stable and then soaking it in the melt (applied current having been terminated) for an additional 45 min. The steel test pieces were attached to the cathode holder of the electrolytic boriding cell while a graphite crucible served as the anode. The boride layer thickness, composition, and structural morphology were investigated using light optical microscopy (LOM) and X-ray diffraction (XRD) methods. The mechanical and tribological behaviors were assessed using microhardness and reciprocating wear tests, respectively. The thickness of the layer formed in the AISI H13 steel borided at 950 °C for ~60 min was about 25 µm. The composition of borided layer is composed of FeB and Fe₂B phases having 1800 ± 50 HV_{0.5} hardness. The composite layer consisting of FeB+Fe₂B displayed up to less wear 99 % and also lower coefficient of friction in comparison with untreated AISI H13 steel working in relative motions. This study showed that electrochemical boriding of die steels is feasible, and this method can be considered as a viable alternative to producing hard and protective layers on AISI H13 steel by other techniques.

1. Introduction

AISI H13 is one of the most popular hot work tool steels due to its high toughness and tempering resistance along with moderate wear resistance [1]. In the service process, the surface hardness of tool decreases, and wear will be accelerated by thermal softening, which shortens its service life [2]. In order to enhance the hardness of tool, surface engineering is a common practice in industry to protect the tool from plastic deformation,

wear and fatigue [3, 4], which has a positive effect on prolonging the lifetime of tool and reducing the production cost [5].

Boriding is a thermochemical surface hardening process with a great importance because it can increase the strength and service life of tool steels for tribological industrial applications [6]. In recent years, many different types of thin hard coatings are applied on tools and dies made from hot working tool steels by chemical vapor deposition (CVD), and duplex treatments consisting of plasma nitriding (PN) and physical vapor deposition (PVD) [7]. However, most of these techniques require process time range of 6-12 h to achieve sufficiently thick (i.e., 5 to 10 µm) hard coatings needed for good performance long durability in metal forming dies which are used in industry.

In this study, we explored the possibility of faster and more efficient boriding of AISI H13 tool steel using an electrochemical process. To the best of our knowledge, this is the first attempt on the electrochemical boriding of AISI H13 steel as there are no published papers or reports that we could find in open literature. In the work, we mainly concentrated on electrochemical boriding of AISI H13 steel in order to achieve thick and hard boride layers in very short process duration.

2. Experimental Procedure

Disc samples, with a diameter of 30 mm and thickness of 5 mm, were machined out of AISI H13 hot work tool steel. Before the boriding treatment, samples were ground up to 1200-grid emery paper and then polished using 1 µm alumina paste to obtain a good surface preparation. They were, then, cleaned ultrasonically in acetone and dried. The boriding of samples was carried out in borax based electrolyte composing of 90 % borax ($\text{Na}_2\text{B}_4\text{O}_7$) and 10 % sodium carbonate (Na_2CO_3) at the constant current density of 200 mA/cm² and the temperature of 950 °C for 15 min. The steel sample acted as a cathode while graphite crucible served as an

anode. After the electrochemical boriding, the applied current was turned off, and a post-processing or soaking treatment was started in which sample was left in the molten bath for an additional period of 45 min without any polarization. When the boriding process finished, borided sample was removed from the graphite crucible, cooled in air and rinsed by hot water to clean the surface for future examination. The samples were then sectioned and polished to mirror finish for further characterization.

The boride layer thickness and morphology were investigated in cross-section using a Nikon Eclipse LV150 Light Optic Microscope (LOM). XRD analysis was carried out by utilizing $\text{CuK}\alpha$ radiation with a Panalytical Empyrean diffractometer. Furthermore, the cross-sectional hardness distribution of the borided steel was carried out by Shimadzu HVM microhardness tester with a load 50 g and a dwell time of 15 s. Sliding wear tests were performed using a custom-built ball-on-flat configuration under dry conditions on a linear reciprocating wear tester at 25 °C room temperature and 35±5 % of relative humidity according to the ASTM G133-05 standard using a 10 mm diameter alumina ball, sliding speed of 1.9 cm s^{-1} , sliding distance of 57.5 m, track length of 11.5 mm and normal loads of 3.75, 7.5, 15 and 30 N. Penetration depth (d_i) and volume of removed material (V) was obtained across the wear tracks by a surface profilometer (Mitutoyo SurfTest SJ-400) and wear rate (K) was estimated using Archard's expression.

3. Results and Discussion

Borided AISI H13 steel presented a biphasic FeB-Fe₂B layer without a tooth-like structure similar to that obtained in pack borided AISI H13 steel [8]. (Fig. 1 a). The cross-section with the thickness of ~25 μm was composed of FeB and Fe₂B phases. This top (darker contrast) layer is made of FeB phase, while the bottom layer with lighter contrast is Fe₂B phase. The thickness of FeB layer was almost equal to that of the Fe₂B layer in the boride coating structure. Boriding of AISI H13 steel by pack boriding yields a 66 μm layer in 6 h at 950 °C [9], which is a growth rate of 0.183 $\mu\text{m}/\text{min}$. By comparison, a 25 μm layer was produced by electrochemically boriding in 60 min at 950 °C, yielding a growth rate of 0.42 $\mu\text{m}/\text{min}$. In the Fig. 1 a, the boride layer on the AISI H13 steel discloses smooth and compact morphology. XRD confirmed the formation of both phases (Fig. 1 b). FeB appeared to be the most predominant phase followed by Fe₂B phase.

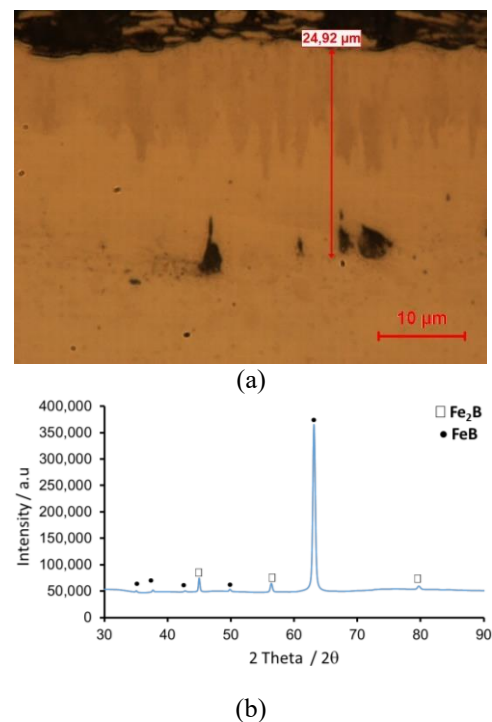


Figure 1. (a) Cross-section LOM microstructure and (b) XRD pattern of the borided AISI H13 steel.

Figure 2 shows the hardness distribution of borided layer cross-section. The boriding treatment increased the hardness of the surface of the AISI H13 steel. The hardness gradually increased in the depth direction of substrate-borided layer, in which the increase of hardness on the cross-section had a positive effect on improving its tribological performance. The highest hardness values are obtained for FeB (1805 $\text{HV}_{0.05}$) but the Fe₂B layers are also very hard (1550 $\text{HV}_{0.05}$) as compared to the steel substrate (530 $\text{HV}_{0.05}$).

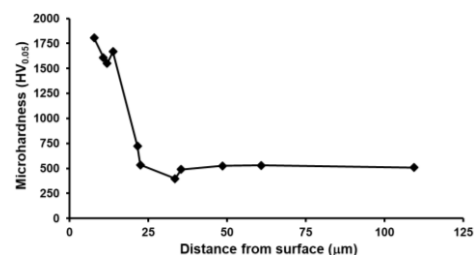


Figure 2. Cross-sectional hardness profile of the borided AISI H13 steel.

COF graphs of the untreated and borided AISI H13 steels, after dry sliding wear tests, are given in Figure 3. In the Fig. 3, the COF of the untreated AISI H13 steel was higher than those of the borided AISI H13 steel. This can be attributed to the severe damage as a result of low surface hardness. It could be seen from Fig. 3 (a) that the COF of untreated AISI H13 steel increased from 1.0 to 1.5 with an increase in the load from 3.75 N to 30 N and the fluctuation retained relatively high. The COF

of the untreated AISI H13 steel increased at the premier 5 m, and then retained stable. At 15 N and 30 N, a trend of gradually increasing COF of the borided AISI H13 steel was detected (Fig. 3 b), which is attributable to the formation of a fatigue crack on the material surface at 15 and 30 N loads and resultant failure of this layer with distance. However, the COF of the borided AISI H13 steel was stable under the loads of 3.75 N and 7.5 N. Meanwhile, the wear volume increased with an increase in the applied load for all the samples (Fig. 4). The values of the wear volume of the untreated AISI H13 steel under 3.75 N, 5 N, 15 N and 30 N were 0.0601, 0.1828, 0.5510 and 0.9348 mm³, respectively. On the other hand, the measured wear volumes for the borided surface under 3.75 N, 5 N, 15 N and 30 N were 0.0011, 0.0021, 0.0047 and 0.0093 mm³, respectively. The borided AISI H13 steel displayed up to 99 % less wear than untreated AISI H13 steel under the applied loads of 3.75-30 N.

Additionally, the worn surfaces of the untreated and borided AISI H13 steel under different applied loads are also illustrated Fig. 5 and Fig. 6, respectively. The worn surface of the untreated AISI H13 steel possess grooves with the thinner black zones when the applied loads were 3.75 N and 7.5 N. A larger number of black zones and few adhesions were present on the worn surface under the load of 15 N. As the load increased to 30 N, severe adhesion phenomena and cracks had appeared on the worn surface of the untreated AISI H13 steel. Meanwhile, crack initiation and its propagation due to structural defects on the borided AISI H13 steel surface had occurred, leading to spalling of the coating in the form of small particles. As the load increased (shown in Fig. 6), many cracks generated on the surface of the borided AISI H13 steel.

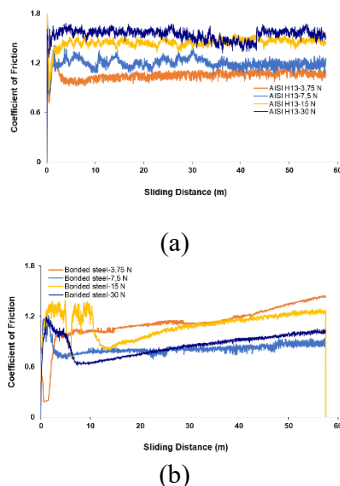


Figure 3. Variation of the coefficient of friction obtained at the surface of the (a) untreated and (b) borided AISI H13 steel during the dry sliding wear test.

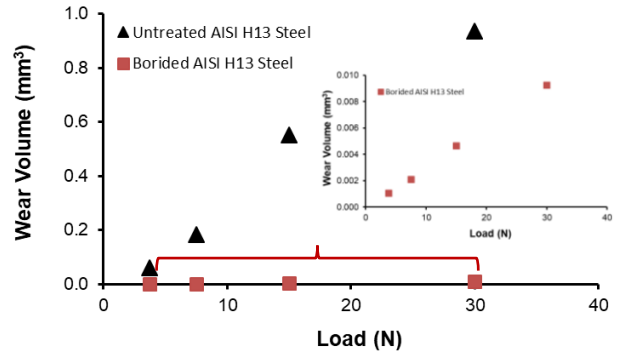


Figure 4. Wear volume (mm³) calculated at the untreated and borided AISI H 13 steel after the dry sliding wear tests.

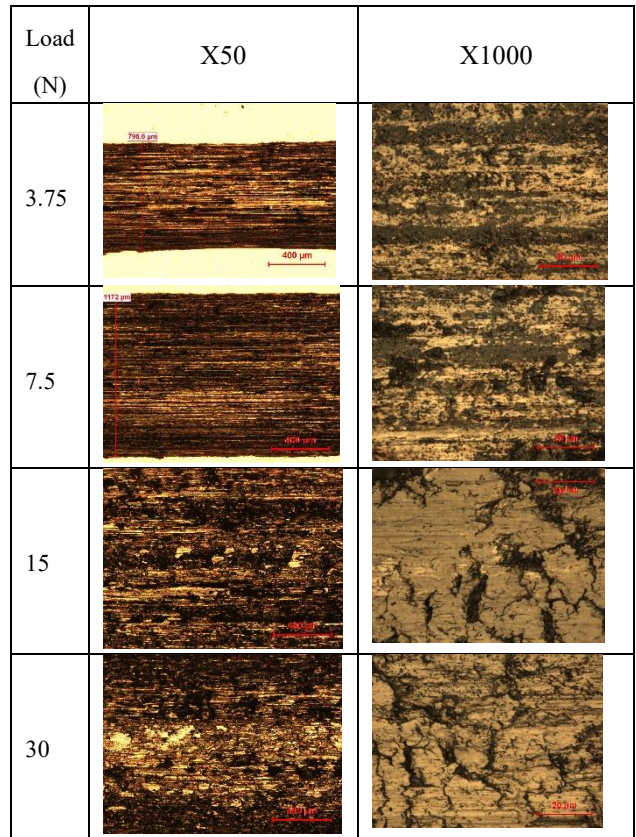


Figure 5. LOM micrographs obtained after the dry sliding wear test on the wear tracks of the untreated AISI H13 steel.

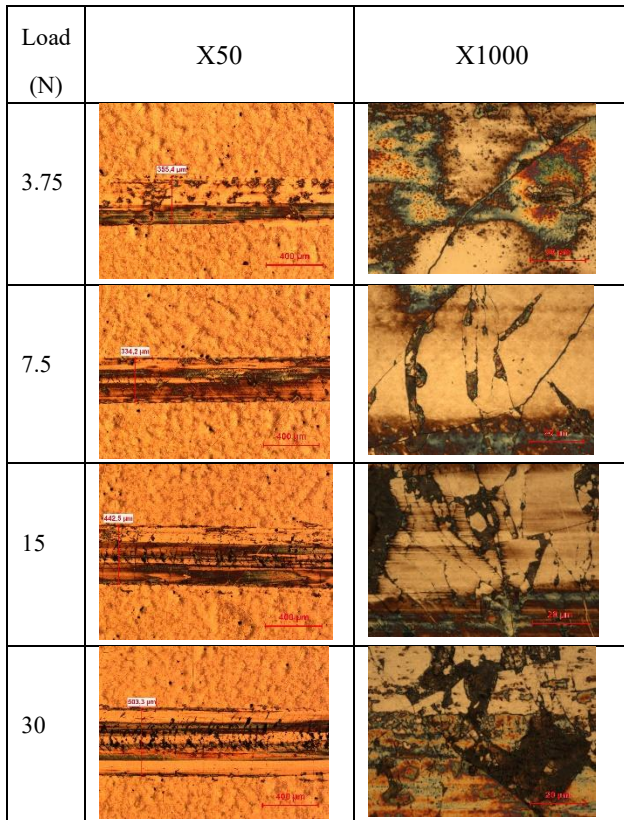


Figure 6. LOM micrographs obtained after the dry sliding wear test on the wear tracks of the borided AISI H13 steel.

4. Conclusion

When the above results are taken into consideration, the following conclusions can be derived:

-In our studies, we were able to produce a 25 μm thick layer in about an hour at 950 °C. The morphology of boride layer was not in a saw-tooth shape like boride layer obtained in pack borided AISI H13 steel.

-XRD analysis showed that FeB and Fe₂B phases exist on the AISI H13 steel surface because of the electrochemically boriding.

-The surface hardness of the borided AISI H13 steel is in the range of 1550–1805 HV_{0.5}, while the untreated AISI H13 steel substrate is 530 HV_{0.5}.

-The borided AISI H13 steel demonstrated 99 % less wear as compared to untreated AISI H13 steel.

Acknowledgment

The financial support of the research foundation of Bilecik Şeyh Edebali University (Project No.: 2022-01.BŞEÜ.03-01) is gratefully acknowledged. We would also like to thank the Eti Maden Operations General Directorate Technology Development Department, which sent samples to be used in electrochemical

boriding studies. Thanks are also due to Ms. Songül Kiliç for project works.

References

- [1] T. Shinde, N. B. Dhokey, *Surface Engineering*, 33 (2017) 944-952.
- [2] H. Yang, X. Wu, G. Cao, Z. Yang, *Surface & Coatings Technology*, 307 (2016) 506–516.
- [3] G. Riccardo, B. Rivolta, C. Gorla, F. Concli, *Engineering Failure Analysis*, 121 (2021).
- [4] S.P.Silva, A.M. Abrao, E.R.Silva, M. A. Camara, *Wear* 462-463 (2020).
- [5] B. Podgornik, V. Leskovšek, F. Tehovnik, J. Burja, *Surface & Coatings Technology*, 261 (2015) 253–261.
- [6] V. Sista, O. Kahvecioglu, O.L. Eryilmaz, A. Erdemir, S. Timur, *Thin Solid Films*, 520 (2011) 1582–1588.
- [7] K. Das, J. Alphonsa, M. Ghosh, J. Ghanshyam, R.Rane, S. Mukherjee, *Surfaces and Interfaces*, 8 (2017) 206–213
- [8] A. Günen, İ.H. Karahan, M. S. Karakaş, B. Kurt, Y. Kanca, V.V. Çay, M. Yıldız, *Metals and Materials International*, (2020) 26 1329–1340.
- [9] Y. Boonplook, P. Juijerm, *Advanced Materials Research*, 931-932 (2014) 296-300.



OPTIMIZATION OF ELECTROLESS SILVER COATING ON CALCIUM BASED CERAMICS

Kardelen GÜNDOĞDU, Metehan ERDOĞAN

Ankara Yıldırım Beyazıt University
Türkiye

Keywords: Silver, Metallization, Electroless plating, Dielectric resonators

Abstract

Coating technology has been carried out with the aim of reducing corrosion and surface friction, and also providing conductivity and aesthetic benefits. Silver plating is preferred due to its high electrical properties, thermal conductivity and low melting temperature. It can be carried out with or without the need for external electrical current. However, it is possible to make the homogeneous coating on metallic or non-metallic materials that do not have a smooth geometry with electroless silver plating. This study aimed to make the catalytically inactive materials electrically conductive by electroless silver plating. Conductive ceramics have many application areas. Dielectric oxide ceramics have been utilized as filters and oscillators within the microwave wireless communication industry. In this context, parameter optimization will be made that provides appropriate coating thickness, homogeneity, and adhesion properties to measure relative permittivity and dielectric loss of resonator ceramics.

1. Introduction

Nonmonotonic mixture of $(1-x)\text{CaTiO}_3-x\text{Ca}(\text{Mg}_{1/3}\text{Nb}_{2/3})\text{O}_3$ ceramics that have orthorhombic perovskite structure has a high dielectric constant and $Q \times f$ values with a near-zero temperature coefficient of the resonant frequency [1]. The electroless coating process refers to the deposition of an adhesive metal coating on a conductive, semiconductor, or non-conductive substrate by chemical methods without the need for any external electricity [2]. Electroless silver plating occurs because of cathodic reduction of cations and anodic oxidation of reducing agent, and as a result, silver ions are reduced on the catalyzed surface [3]. Coating processes on catalytically inactive materials necessarily require a pretreatment process, with SnCl_2 and PdCl_2 , catalytic sites can be formed on the substrate surface [4]. SnO_2 adheres to the sample surface, so the positively charged silver ions in the electroless silver-plating bath reduced by Sn^{2+} ions [5]. Pd sites form a catalytic site on the surface for the precipitation of silver ions [6].

2. Materials and Methods

0.68 CaTiO_3 -0.32 $\text{Ca}(\text{Mg}_{1/3}\text{Nb}_{2/3})\text{O}_3$ ceramics were prepared by tape casting. After alkali and acid cleaning, sensitization and activation processes were completed. AgNO_3 as a silver source, hydrazine monohydrate as a reducing agent, ammonium hydroxide, and ammonium carbonate as controlling agents were used in the electroless silver-plating bath.

3. Conclusion

0.68 CaTiO_3 -0.32 $\text{Ca}(\text{Mg}_{1/3}\text{Nb}_{2/3})\text{O}_3$ ceramics produced in this study had 97% relative density, 0.09% water absorption and 0.125 μm (Ra) surface roughness. Following the mentioned surface preparation, an average coating thickness of 2 μm was obtained in 1 hour between 55 and 65 °C.

References

- [1] H. Liu, H. Yu, Z. Tian, Z. Meng, Z. Wu, and S. Ouyang, Journal of the American Ceramic Society, 88(2) (2005) 453-455.
- [2] C. R. Shipley, Method of electroless deposition on a substrate and catalyst solution therefor, (2009).
- [3] B. Sodervall and T. Lundberg, DEPOSITION OF SILVER LAYER ON NONCONDUCTING SUBSTRATE,(1995).
- [4] J. P. Marton and M. Schlesinger, Journal of The Electrochemical Society, 115(1) 16 (1968)
- [5] G. Mallory, J. B. Hajdu, Electroless Plating: Fundamentals and Applications, Noyes Publications/William Andrew Publishing, 1996, Newyork, United States of America, pp. 317-322.
- [6] D. Hashimoto, K. Kitajima, and A. Okada, REDUCING ELECTROLESS SILVER PLATING SOLUTION AND REDUCING ELECTROLESS SILVER PLATING METHOD, (2014).

INVESTIGATION OF FORMATION OF Au-Ag-Cu ALLOYS BY ELECTRODEPOSITION FROM CYANIDE BASED ELECTROLYTE

Berkay ÇAĞAN¹, Metehan ERDOĞAN¹, İshak KARAKAYA²

¹Yıldırım Beyazıt University, ²Middle East Technical University
Türkiye

Keywords: Alloy electrodeposition, gold-silver-copper alloy

Abstract

Ternary Au-Ag-Cu alloys have multifunctional properties, such as high electrical conductivity, corrosion and wear resistance. Because of these properties, they are used in slip rings, which are crucial for electromechanical systems used mainly in aerospace, naval, and land defense systems or medical devices. In this study, static potential and cyclic voltammetry measurements were carried out to determine the appropriate amount of potassium cyanide and the reduction potentials of gold, silver and copper in gold-silver-copper cyanide solutions. The effects of applied voltage and bath composition on the produced alloy composition were studied. Electrodeposited layers were characterized by scanning electron microscopy (SEM) and X-ray fluorescence (XRF) to take cognizance about surface morphology, coating thickness and alloy compositions.

1. Introduction

Au-Ag-Cu alloys can be used in some critical applications, such as wind turbines, automation equipment, hydro-electric generator, the solar array drive mechanism of spacecraft, de-icing system of a helicopter, rotating table, magnetic resonance imaging (MRI), and so on, because of enhancing some properties of a material [1]. For example, these alloys can be used for easily oxidizable materials, such as pure copper and copper beryllium (CuBe₂), since the addition of Au in the alloy hinders the oxidation of material. Therefore, corrosion resistance is enhanced. In addition, electrical properties, wear resistance and service life of material can be improved by means of Au-Ag-Cu alloys [2].

Formation of Au-Ag-Cu alloy is possible with using different techniques such as cladding and deposition of alloying elements. Cladding method is preferred, but this technique has some drawbacks such as using mechanical forces, high budget process for production infrastructure and consumption of high level of precious metals. On the other hand, some deposition techniques can be used such as thermal spraying, chemical vapor deposition (CVD), physical vapor deposition (PVD) and electrochemical deposition. Electrochemical deposition has some advantages compared to other deposition techniques such as controlling the process parameters, cost-effectiveness, requiring less amount of precious metals, and no need to build production infrastructure [3].

In the light of this information, electrochemical deposition technique was carried out to achieve Au-Ag-Cu alloys with

different chemical compositions. In this work, reduction potentials of Au, Ag and Cu ions were investigated from reduction potential and cyclic voltammetry measurements. The effect of amount of KAu(CN)₂, AgCN, CuCN and KCN on composition of Au-Ag-Cu alloy were also given in the scope of this study.

2. Experimental Procedure

Initial composition of Au-Ag-Cu electrodeposition bath was determined from previous experiments [4]. Before the electrodeposition studies, the suitable amount of KCN and the reduction potentials of Au, Ag and Cu ions were investigated from static potential and cyclic voltammetry measurements, respectively. Parameters, such as reduction potentials, addition of KAu(CN)₂, AgCN, CuCN, and KCN were varied in the experimental studies. In order to observe the change in chemical compositions, XRF, EDS and SEM analyzes were carried out.

Static potential measurements were conducted in a system containing platinized titanium, saturated KCl (Calomel) electrode, hot plate and multimeter at 55°C for three electrolytes, as shown in Table 1. In addition, KCN (0-0.35 M) and 0.16 g/L thiourea were added for each electrolyte.

Table 1. Type and composition of electrolytes for static potential measurements

Electrolytes	Amount (g/L)
1) AgCN	0.5
2) CuCN	5
3) KAu(CN) ₂	3.88

Cyclic voltammetry measurements were conducted for different types of electrolytes. Firstly, measurements were done for each cyanide compound such as 0.5 g/L AgCN, 5 g/L CuCN, and 3.88 g/L KAu(CN)₂. Then, binary mixtures of 3.88 g/L KAu(CN)₂ – 5 g/L CuCN, 3.88 g/L KAu(CN)₂ – 0.5 g/L AgCN, and 0.5 g/L AgCN – 5 g/L CuCN were used for the measurements. Finally, a ternary mixture containing 0.5 g/L AgCN, 5 g/L CuCN and 3.88 g/L KAu(CN)₂ was prepared. Cyclic voltammetry measurements were carried out at 55°C. Experimental setup for the measurement was included saturated KCl (Calomel) reference electrode, two graphite electrode (used as a counter and working electrode), hot plate, and Gamry Instrument. The surface area of working electrode was 0.2826 cm². In addition, 0.18 M KCN and 0.16 g/L thiourea were added for each electrolyte. The scan rate for unary and binary mixtures of electrolyte was chosen as 100 mV/sec. On the other hand, the scan rate for ternary mixture

of electrolyte was determined as 150 mV/sec. Before the electrodeposition of Au-Ag-Cu alloy, Cu substrates were electrodeposited with nickel. Nickel is generally used as an interlayer to improve adhesion and prevent diffusion of Au and Cu. Nickel is electrodeposited from nickel sulphamate electrolyte. Composition and parameters are given in Table 2 [5]. Before the nickel electrodeposition, substrate surface was activated by H₂SO₄ solution (5 wt. %). Thickness of nickel layer was adjusted around 10-15 μm.

Table 2. Composition and operating parameters of nickel sulphamate electrolyte [5]

Ingredients	Compositions
Nickel Sulphamate Tetrahydrate (for 1 L solution)	0.35 L
Boric Acid	30 g/L
Sulphamic Acid	1.25 g/L
Parameters	Values
Temperature	50°C
Current Density	1.5 A/dm ²
Current Efficiency	95%
Agitation	Magnetic stirrer
Anode	Ni anode

The electrodeposition of Au-Ag-Cu alloy was conducted in different electrolytes and operating parameters. Constant parameters were determined as: pH: 10, temperature: 55°C, and current type: direct current (DC).

3. Results and Discussion

3.1 Static potential measurements

According to static potential values, 0.18 M KCN was found as the proper amount since cyanide compound of Au, Ag and Cu have similar potential values.

3.2 Cyclic voltammetry measurements

Cyclic voltammetry measurements were done for single cyanide compounds to determine reduction potentials of Au, Ag and Cu separately. Then, reduction potentials of Au, Ag and Cu in binary and ternary mixtures of cyanide compounds were observed. According to these measurements, a potential difference of at least -0.7 V at 55°C should be applied to reduce all ions simultaneously. Since the anode reaction, the polarizations and the voltage drops due to resistance exist in the electrochemical cell, the potential difference between two electrodes should be higher than this value.

3.3 Preliminary experiments

According to cyclic voltammetry measurements, reduction potential value was determined as 1.9 V, and experiments were conducted for 60 minutes. For these experiments, electrolyte consisting of 3.88 g/L KAu(CN)₂, 0.5 g/L AgCN and 5 g/L CuCN was used. Different KCN concentrations were used to understand the effect of addition of KCN on alloy composition at the same electrolyte composition. According to Figure 1, Cu (wt. %) composition was decreased by the addition of KCN, while Au and Ag (wt. %) contents had an increasing trend with increasing the amount of KCN.

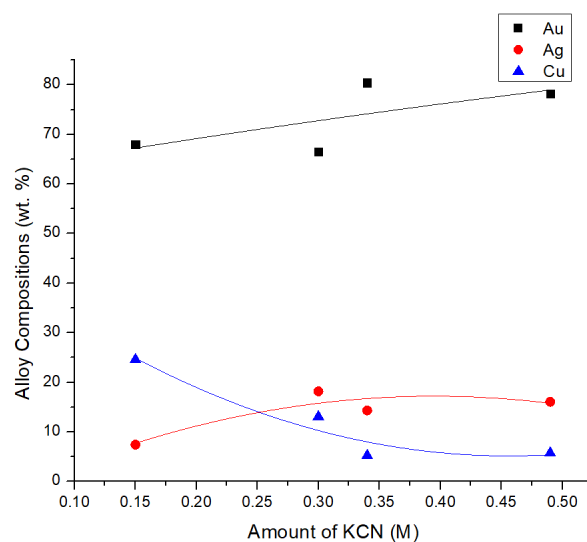


Figure 1. Change in alloy composition with addition of KCN at 1.9 V

After 60 minutes coating, Au-Ag-Cu layer was obtained as nearly 13 μm. Moreover, the effect of KCN on current density was investigated. As can be seen from Figure 2, current density also showed an increasing trend with the addition of KCN.

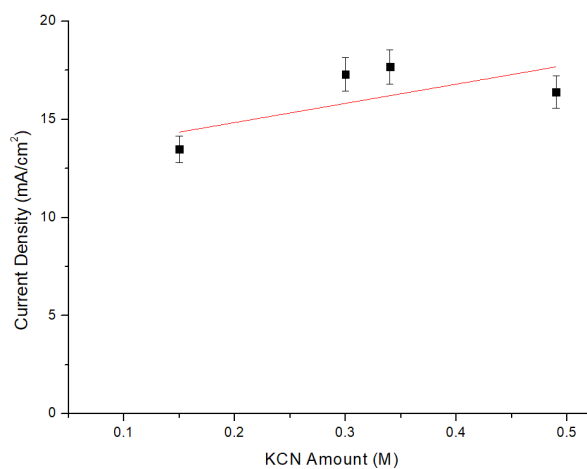


Figure 2. The effect of KCN on current density

While a relatively uniform coating surface without dendritic growth was achieved at low current density, dendritic growth was obtained at high current density as can be seen in Figure 3.

3.4 Effects of KCN on alloy composition at different reduction potential values

To observe the effect of KCN on alloy composition at different reduction potential values, an electrolyte containing 3.9 g/L KAu(CN)₂, 0.5 g/L AgCN, and 7.2 g/L CuCN was used. For these experiments, three different reduction potential values were selected as 1.7 V, 1.9 V, and 2.1 V. As can be seen in Figure 4, Au (wt. %) composition in the alloy increased with decreasing the reduction potential value at the highest and lowest amount of KCN.

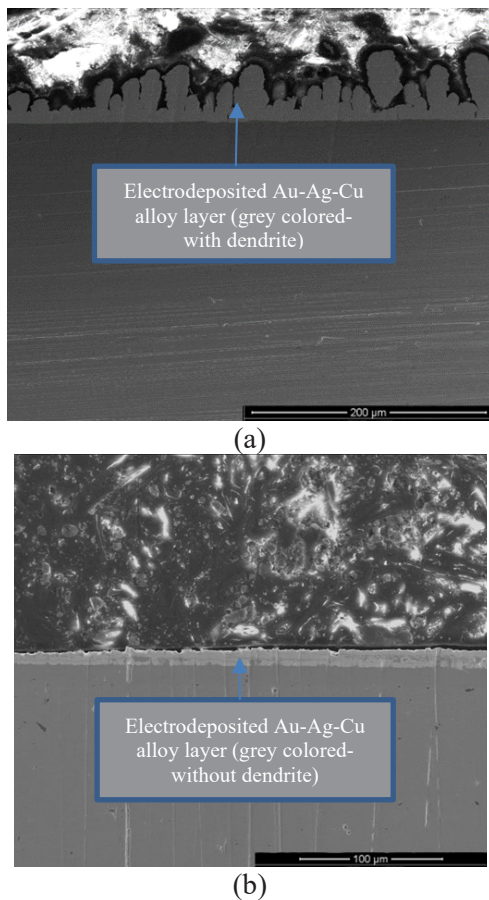


Figure 3. Coating images from cross section of the samples at different current density values (a) 17.5 mA/cm², (b) 13.5 mA/cm²

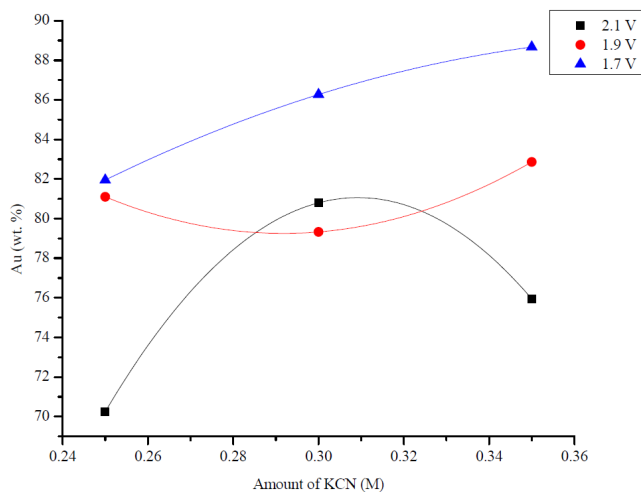


Figure 4. Variation in Au (wt. %) composition in the alloy with different amount of KCN and reduction potential values

Variations in Ag (wt. %) composition in the alloy with different amount of KCN and reduction potential value were found as given in Figure 5. Ag (wt. %) concentration in the alloy increased with decreasing reduction potential values at 0.3 M KCN. In addition, highest Ag (wt. %) concentration was achieved at 1.7 V with the addition of 0.3 M KCN.

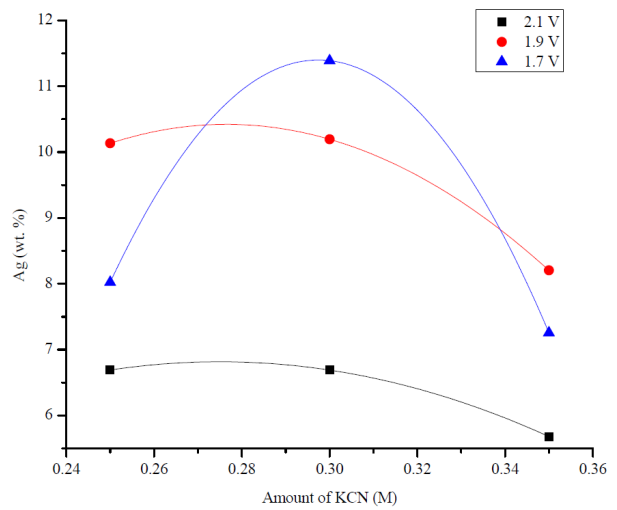


Figure 5. Variation in Ag (wt. %) composition in the alloy with different amount of KCN and reduction potential values

Cu (wt. %) compositions in the alloy were also variable with different amount of KCN and reduction potential values, as given in Figure 6. According to obtained values, Cu (wt. %) compositions in the alloy were increased by increasing reduction potential value at 0.3 M and 0.35 M KCN. However, the highest Cu (wt. %) composition was obtained at 0.25 M KCN and 2.1 V.

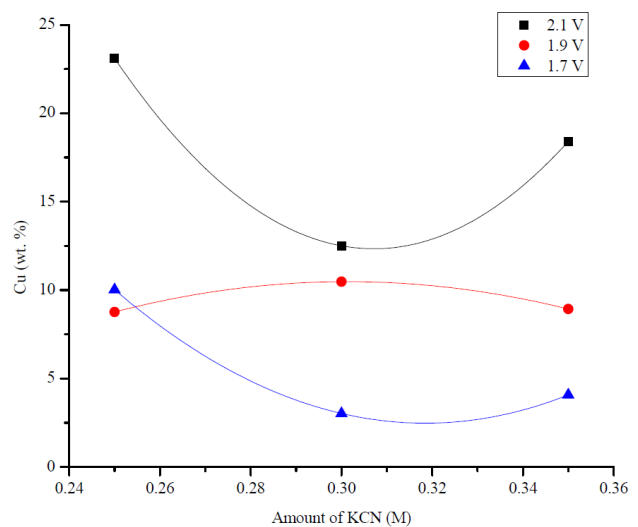


Figure 6. Variation in Cu (wt. %) composition in the alloy with different amount of KCN and reduction potential values

3.5 Effects of amounts of $\text{KAu}(\text{CN})_2$ and AgCN in plating bath

To understand the effect of addition of AgCN , three different AgCN amounts (0.5, 0.75, and 1 g/L) were studied in the determined electrolyte composition containing 3.9 g/L $\text{KAu}(\text{CN})_2$, 7.2 g/L CuCN and 0.3 M KCN. The reduction potential value was determined as 1.9 V. As can be seen in Figure 7, the additions of AgCN into the plating bath had a significant effect on alloy compositions.

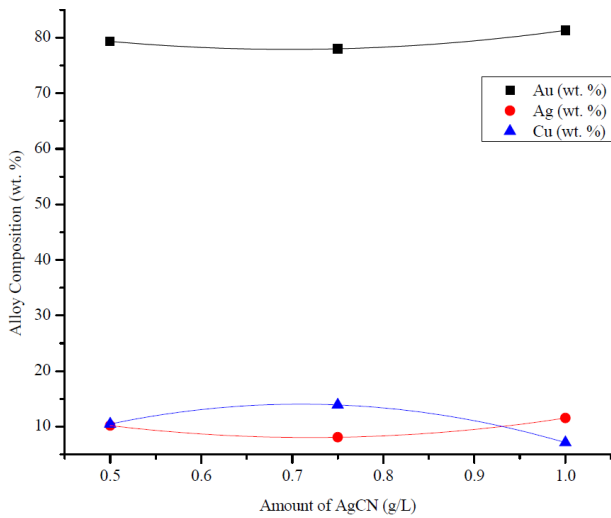


Figure 7. Variation of alloy composition by the addition of AgCN (g/L)

Five different amounts of $\text{KAu}(\text{CN})_2$ (0.25, 0.5, 0.75, 1.0, and 1.25 g/L) were studied to observe the effects on alloy compositions. The electroplating bath was composed of 1 g/L AgCN, 7.2 g/L CuCN, and 0.3 M KCN. The applied potential value was chosen as 1.9 V. According to given data in Figure 8, it was clearly observed that Cu (wt. %) compositions in the alloys had a decreasing trend by the addition of $\text{KAu}(\text{CN})_2$. However, Ag (wt. %) compositions in the alloys had different tendency towards the increasing amounts of $\text{KAu}(\text{CN})_2$. Ag (wt. %) compositions had decreasing trend up to 0.8 g/L $\text{KAu}(\text{CN})_2$. After this point, this trend showed an upward gradient.

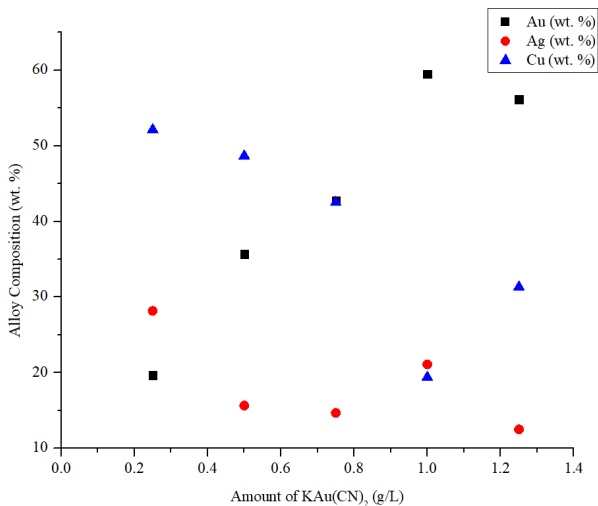


Figure 8. Variation of alloy composition by the addition of $\text{KAu}(\text{CN})_2$ (g/L)

3.6 Effects of reduction potentials on alloy compositions and microstructures

To observe the effect of applied potential on alloy composition, experimental studies were conducted in electroplating bath including 1.1 g/L $\text{KAu}(\text{CN})_2$, 1 g/L AgCN, 5 g/L CuCN, and 0.3 M KCN. As given in Figure 9, Au and Ag (wt. %) composition in the alloy reduced by increasing the applied potential while Cu (wt. %) composition had increasing trend.

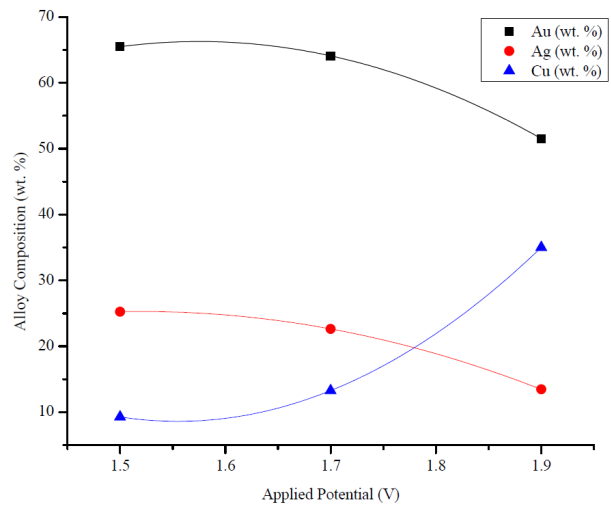


Figure 9. Variations in alloy compositions at different reduction potential values

Surface morphology of coating layer could be changed in terms of applied potential level. According to conducted studies, higher applied potentials lead to spherical and coarser grains while tetragonal shaped-like and finer grains could be obtained at lower applied potential levels.

4. Conclusion

From the experimental studies, following results were obtained: i) Au composition in the alloy decreased at low and high amount of KCN with higher potential values, ii) Ag composition in the alloy increased at 0.3 M KCN with lower applied potential values, iii) Cu composition in the alloy increased at 0.3 and 0.35 M KCN with higher applied potential values, iv) AgCN addition did not affect the alloy composition, and v) uniform, fine-grained without dendritic coating was achieved.

Acknowledgment

The authors would like to express the gratitude to financial support provided by The Scientific and Technological Research Council of Turkey (Project No. 118M346), and the laboratory and testing support provided by METU-TEMPLAB and MEGAP Inc.

References

- [1] N. Argibay, J. A. Bares, and W. G. Sawyer, "Asymmetric wear behavior of self-mated copper fiber brush and slip-ring sliding electrical contacts in a humid carbon dioxide environment," *Wear*, vol. 268, no. 3–4, pp. 455–463, 2010, doi: 10.1016/j.wear.2009.08.036.
- [2] X. L. Xie, L. Zhang, J. K. Xiao, Z. Y. Qian, T. Zhang, and K. C. Zhou, "Sliding electrical contact behavior of AuAgCu brush on Au plating," *Trans. Nonferrous Met. Soc. China (English Ed.)*, vol. 25, no. 9, pp. 3029–3036, 2015, doi: 10.1016/S1003-6326(15)63930-9.
- [3] Cetinöz, B., Erdogan, M., Karakaya, I., Yurdakul, E.B., "Electrochemical Deposition of Au-Ag-Cu Alloys on CuBe₂," in 19th International Metallurgy & Materials Congress, 2018, pp. 1057–1058.
- [4] W. R. Brash, "Electroplated gold-copper-silver alloys," 0566054A1, 1993.
- [5] A. Chateauinois, "ASM Handbook: Surface Engineering (Vol 5)," in ASM Handbook, vol. 5, no. 1, ASM International, 1998, p. 851.



NFMS

Non-Ferrous Metals Symposium

Demir Dışı Metaller
Sempozyumu



EVALUATION OF CHROMITE ORES BY METALLOTHERMIC PROCESS IN EAF

Hasan GÜNEY, Selçuk KAN, Kağan BENZEŞİK, Onuralp YÜCEL

Istanbul Technical University
Türkiye

Keywords: ferrochrome, Low CO₂ emission, aluminum dross

Abstract

In this study, reducing smelting of chromite concentrates by EAF assisted metallothermic method; the effect of Al_{Powder} and Al_{Dross} addition amount, time and the ratio of flux addition on the produced metal and slag compositions and metal recovery were investigated. As a result, it was seen that ferrochrome can be produced from fine-grained chromite concentrate by this method. At the end of EAF assisted semi-pilot smelting experiments using aluminum as reductant, the highest chromium content in produced alloys was 59.52 wt. %, while the highest chromium recovery from chromite concentrate to alloys was 76.73 wt. % in these experiments.

1. Introduction

Stainless steels (SS) are basically the alloys of iron and carbon which should contain at least 11% chromium. Chromium reacts with oxygen at the surface, forms a protective thin layer. This thin film prevents further rusting of stainless steel. These characteristics provide stainless steel a wide range of application areas; industries of chemical and power engineering, food and packages, transportation etc.

Chromium and nickel are responsible for the 34.9 and 23.8% of total CO₂ emission of the production respectively. The stages that cause most of the CO₂ emission in order to produce 1 ton of SS production can be listed as follows: 1.01 ton CO₂ (34.9%) from chromium production, 0.69 ton CO₂ (23.8%) for nickel production, 0.49 ton CO₂ (17.0%) for electricity and 0.44 ton CO₂ (15.2%) for direct emission.

As CO₂ emissions in stainless steel production are dominated by preparation stages of Cr and Ni alloys and these are the indispensable elements; new methods should be investigated in order to decrease the usage of electricity or energy and CO₂ emissions

2. Materials and Methods

KEF Chromite Concentrate (KCC) contains 40 wt.% Cr₂O₃, Al (99 wt.% purity), Al dross contains 65 wt.% Al and CaO that obtained from CaCO₃ (96.78 wt. % purity) are used in this study.

Metallothermic reaction is preferred to both reduce carbon emission and save electrical energy. Two types of aluminum sources are used as reductants. One of them is aluminum powders and since it is more economical, the other one is the metallic aluminum-rich part obtained by recycling aluminum melting drosses (Al_{Dross}).

CaO added in order to increase the slag fluidity.

In the experiments, the use of different stoichiometric ratios and reductants separately and together were tried.

3. Conclusion

All the experiment parameters and the results are given in Table 1. Chromium content was analyzed with optic emission spectroscopy (OES) device.

Table 1. Experiment parameters and the results.

Exp. No	KCC, g	Al _{Dross}		Al _{Powder}		CaO		Cr Recovery, %
		g	Stc, %	g	Stc, %	g	CaO/KCC	
1	5000	1390	100	-	-	-	-	56.61
2	5000	-	-	1280	140	-	-	64.13
3	11000	1710	120	1139	100	-	-	76.73
4	15000	2335	120	1475	100	1835	0.03	54.43
5	15000	2335	120	1475	100	535	0.03	36.08
6	15000	2335	120	1475	100	535	0.03	39.90
7	6000	-	-	1102	100	353	0.05	70.97
	6000	2000	100	-	-	353	0.05	70.36



DETERMINING OPTIMUM ROASTING CONDITIONS OF HEMATITE MAGNETIZATION WITH TEMPERATURE-COKE MIXTURE COPULA

Zeynep Hazal YAZĞAN¹, Mikail BAŞYİĞİT¹, Abdullah BUHUR², Elif UZUN KART¹

¹Marmara University, ²ARGETEST
Türkiye

Keywords: Türkiye's volcanic kafa ore, reduction roasting, magnetic separation, optimization

Abstract

In this study, the magnetization behavior of Türkiye's volcanic kafa ore (VKO) was investigated with reduction roasting. The Kafa ore contains mainly hematite which is the main source of iron along with a small amount of goethite and gangue minerals namely quartz and calcite. Since it is necessary to separate the gangue from iron-bearing ore and low magnetic susceptibility of hematite; the magnetization of hematite was carried out by reduction roasting. By doing so, it was aimed to separate the magnetized iron ore from the gangue by magnetic separation. In order to achieve this purpose, an experimental design was planned which has 5 different sets of temperature and 3 different sets of coke mixture ratios. The temperature ranges from 400°C to 900°C by 100°C increment in every set. Similarly, the coke that was used as a reducing agent mixture, takes values of 30, 40, and 50%. Following the experimental setup, roasted VKOs were subjected to low-intensity dry magnetic separation at 750 oersteds magnetic field strength. The effects of temperature and amount of coke on the transformation of hematite to magnetite and the determination of mineralization of the concentrate obtained after magnetic separation were investigated by X-ray diffraction. Fe grade and recovery were determined by using chemical analysis, and then the optimization of the experiments was determined with Fe% recovery that was obtained after magnetic separation. X-ray diffraction patterns show that magnetite transformation begins at 600 °C after reduction roasting. After magnetic separation, the effect of the temperature and the effect of the coke mixture on Fe% recovery were investigated. The relationship between Fe% recovery and temperature was shown as a linear correlation. The recovery rate can be expressed as $y = 0.2114x - 77,711$ where y is the recovery rate and x is the temperature. The fitness of the model is very high with an $R^2 = 0.886$. However, the effect of the coke mixture on Fe% recovery could not be detected. The fitness of the model confirms this indifference by $R^2 = 0.0078$. When the coke mixture was kept constant, iron recovery efficiencies were lower than 57% till 600°C and it sharply increased by temperature and peaked at 800°C. A peculiar condition was detected at 700°C and a 50% coke mixture with a 90% Fe-recovery rate. Another high-efficiency point was observed at 800°C and a 30% coke mixture with an 89% Fe-recovery. In conclusion,

two optimal conditions were found with different trade-offs. The first one requires a lower temperature while needs more coke. The second condition needs more temperature while the coke requirement is lower than the first one. These conditions can be traded regarding the following conditions: availability of energy, cost of marginal temperature increment, availability of coke, and cost of coke.

1. Introduction

Türkiye is one of the leading steel producer countries. In 2021 Türkiye produced 40.4 Mtons of steel with 13% growth compared to the previous year and took 7th place in the world despite the covid pandemic (WSA, 2022, 2021). However, in contrast to the production rate and capacity, Türkiye's iron resources are insufficient and far from the meeting demand. While Türkiye covers approximately 0.5% of the world's land area, it has only 0.045% of the world's iron reserves. Moreover, according to MTA, domestic iron resources will be depleted in 8-10 years (MTA, 2019, 2017). That asymmetrical distribution of iron resources caused Türkiye to import iron ore and scrap iron. The worth of imported materials cost approximately 13.18B\$ in 2021 (ITC, 2021). In order to soften the situation, alternative iron reserves have been under the investigation for a decade. These resources are not suitable for iron smelting without mineral dressing and/or pretreatment. While magnetic separation is usually effective against magnetite-bearing ore, the hematite-bearing ore with other low magnetic susceptibility is hard to separate. Therefore the reduction (magnetizing) roasting is a viable option to improve the magnetic properties of the hematite (Rath et al., 2014; Suthers et al., 2014; Uwadiale and Whewell, 1988; Yu et al., 2017; Zhao et al., 2021). With this respect, this study aims to investigate the effectiveness of magnetizing roasting and determine the optimum conditions.

2. Experimental Procedure

The iron ore used in the study was VKO taken from Middle Black Sea Region. The quantitative mineralogical and elemental analysis of the VKO sample was made by using X-ray diffraction (XRD) and inductively coupled plasma atomic emission spectroscopy (ICP-AES), respectively. The mineralogical composition of the VKO is given in Figure 1, and its chemical composition is given in Table 1. It has been determined that the VKO sample

mainly consists of hematite, quartz, goethite, and calcite phases (Figure 1). Mineralogical and petrographic analyses are given in Figure 2. According to the mineralogical and petrographic analyses, the matrix which fills the cracks and voids consists of quartz and calcite minerals. These minerals are in a microcrystalline structure. The major iron mineral is hematite while goethite presence is rather minor. Hematite is in massive form and there are goethite layers in between the hematite stratum. In the below, thin sections of two samples were given. The letter H represents massive hematite, the Go represents goethite while the letter G represents the gang minerals namely quartz and calcite.

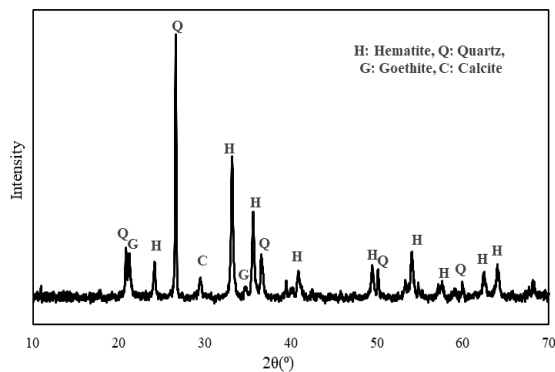


Figure 1. XRD pattern of raw sample

Table 1. Mineralogical and chemical compositions of the VKO

Fe (%)	SiO ₂ (%)	CaO (%)
49.44	20.92	3.24

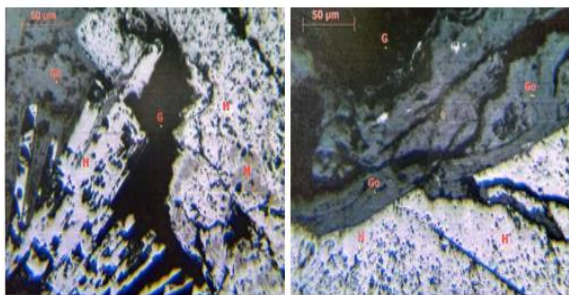


Figure 2. Mineralogical and petrographic analyses of the raw sample (G: Gangue mineral, H: Hematite, Go: Goethite)

The crushed hematite-bearing ore was mixed with graphite in three different proportions which graphite takes 30, 40, and 50% of the mixture. The weight of the mixture is 400 grams in total. Following the mixture composition step, the roasting conditions were determined. While the magnetic roasting usually is carried out at temperatures between 700-800°C, to investigate the effect of the mixing rates the temperature range was determined as from 400 to 800°C. Thus, 15 different conditions were created (Table 2).

Table 2. Variable Parameters

Temperature (°C)				
400	500	600	700	800
Mix Ratio (%)				
30		40		50

After the roasting, the samples were separated by a low-intensity dry magnetic separator at 750 oersteds magnetic field strength. Their performance and response to the magnetic field were checked via XRD patterns and via recovery rates empirically. In the following section, the results of the aforementioned analyses were given.

3. Results and Discussion

First of all, the recovery rates and their relationship with Fe ions were analyzed. The analysis showed that almost all the Fe recovery comes from Fe²⁺ as in the literature (Figure 3.) Their relationship is very strong and linear. Besides the Fe²⁺, a small amount of Fe³⁺ separated via DMS and included in total iron recovery. The correlation between Fe recovery and Fe³⁺ ions was given in Figure 4.

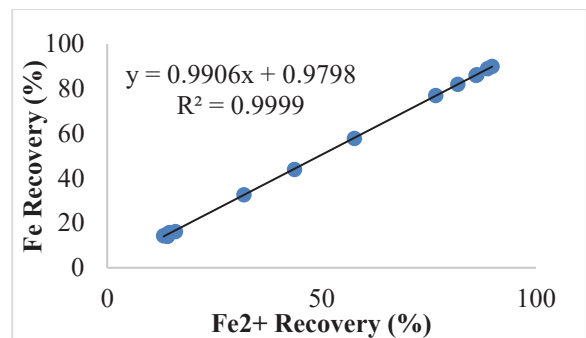


Figure 3. Iron recovery and Fe²⁺ ion relationship

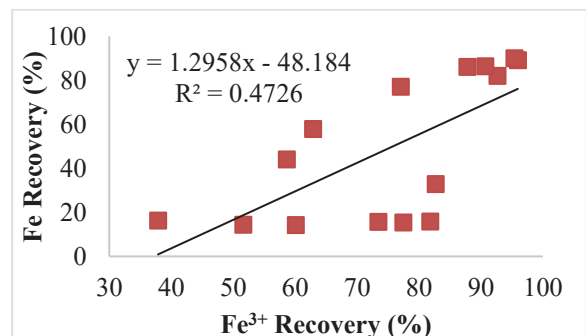


Figure 4. Iron recovery and Fe³⁺ ion relationship

After we confirmed that the majority of the Fe recovery comes from the Fe²⁺ which was Fe³⁺ before the reduction roasting, the effects of the experimental parameters were investigated. The temperature and the mix ratio of coke and ore were the variables of this study. It was determined that the temperature is the main engine of the reduction reactions. The relationship between temperature and Fe recovery was

given in Figure 5. The correlation is very strong ($R^2=0.886$) and linear.

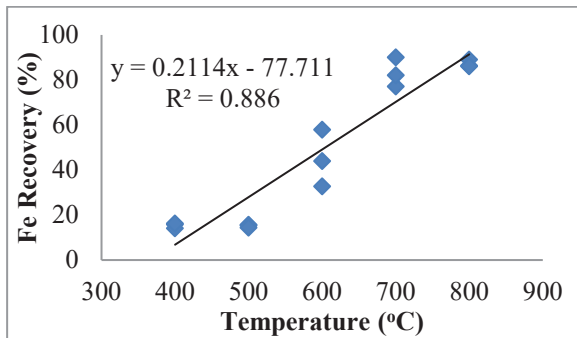


Figure 5. Effect of the temperature on Fe recovery

The other variable namely mixture ratio took values of 30%, 40%, and 50%. The impact of the mixing rates on Fe recovery was not detectable alone. Because the correlation between mixing proportions and iron recovery was not significant. The relationship between mix ratio and Fe recovery was given in Figure 6.

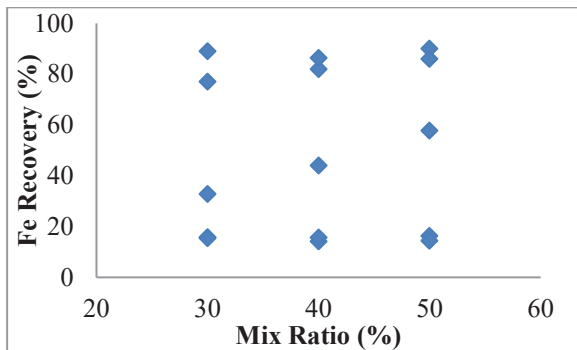


Figure 6. Iron recovery and mix ratio relationship

Subsequent to the correlation analyses, the optimum conditions were investigated. In accordance with the current literature, the magnetization did not completely occur prior to the 700°C. There were six conditions in which the recovery yield is higher than 70%. All these results were observed and obtained at 700°C and 800°C. Among these six best results two distinctive points came forward. The first one has 50% graphite and was roasted at 700°C. Under these conditions, 90.01% of the total iron was recovered. The second peak condition has only 30% graphite however the roasting temperature was 800°C. These experimental parameters provided 89.07% iron recovery. In addition to the comparative investigation, in order to represent the effect of the experimental parameters on iron recovery, a contour diagram was drawn. Since a strong and linear relationship was found between temperature and iron recovery, the linear inverse distance method was used to draw the diagram. Conforming to the literature and findings of the study, the iron recovery was significantly below the 700°C. At the 700°C, a peculiarity stands out at 50% of the mixing level. According to the diagram, all the conditions at 800°C emerge (Figure 7).

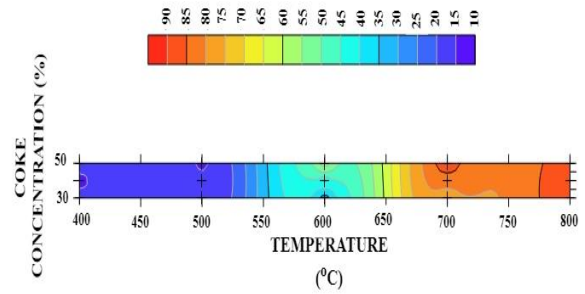


Figure 7. Contour diagram of the iron recovery

XRD patterns of concentrates (700°C-30% coke, 800°C-50% Coke) obtained under optimum conditions were given in Figure 8. When the XRD patterns were examined, no goethite peak was detected in the concentrates as a result of the roasting, and the new magnetite peaks at 18,30,35,43,56,62 2θ (ref. code: 01-079-0418) were formed at confirms the conversion of hematite and goethite into magnetite.

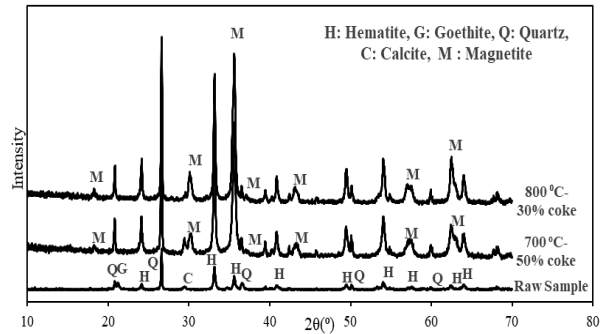


Figure 8. XRD patterns of concentrates (700°C-30% Coke, 800°C-50% Coke) obtained under optimum conditions

The conclusions of the results were given in the following section.

4. Conclusion

While iron resources of the Türkiye are the under the threat of depletion, finding alternative resources or deploying alternative methods to eliminate impurities are crucial to secure the supply. This study aims to find the optimum conditions for a magnetic reduction in most the effective way possible. For these reasons, 15 different experimental parameters were established by incorporating two working conditions namely temperature (°C) and mix ratio (%).

The findings of this study can be concluded as:

- The temperature is the main engine of the magnetic roasting
- Fe^{3+} ions were separated by DMS alongside Fe^{2+} because they coexist and cohabit.
- The reduction roasting of hematite-bearing ore starts around 700°C.
- Two optimum conditions were determined. The first one occurs at a lower temperature (700 °C) but the coke ratio is higher (50%). The second condition needs a higher temperature (800°C) but less coke ratio (30%).

- Since the iron recovery yields are almost identical, according to the microeconomic concept namely Isoquant Curve there will be a tradeoff between the variables.
- In the first case, it is possible to save fuel due to lower temperature requirement. In the second case, coke consumption will be almost half of the first scenario.
- The producers can choose according to their needs, necessities, accessibility of materials, and cost of the materials.

Zhao, B., Gao, P., Tang, Z., Zhang, W., 2021. The efficient improvement of original magnetite in iron ore reduction reaction in magnetization roasting process and mechanism analysis by in situ and continuous image capture. *Minerals* 11. <https://doi.org/10.3390/min11060645>

Acknowledgment

The authors would like to thank ARGETEST Cevher Zenginleştirme ve Analiz Hizmetleri due their precious support and contributions.

References

- ITC, 2021. Trade Map - Trade statistics for international business development [WWW Document]. Trade Stat. Int. Bus. Dev. URL <https://www.trademap.org/Index.aspx> (accessed 7.12.21).
- MTA, 2019. Dünyada ve Türkiye’de Demir, Krom ve Baz Metaller. Ankara.
- MTA, 2017. Dünyada ve Türkiye’de Demir. Ankara.
- Rath, S.S., Sahoo, H., Dhawan, N., Rao, D.S., Das, B., Mishra, B.K., 2014. Optimal Recovery of Iron Values from a Low Grade Iron Ore using Reduction Roasting and Magnetic Separation. *Sep. Sci. Technol.* 49, 1927–1936. <https://doi.org/10.1080/01496395.2014.903280>
- Suthers, S.P., Nunna, V., Tripathi, A., Douglas, J., Hapugoda, S., 2014. Experimental study on the beneficiation of low-grade iron ore fines using hydrocyclone desliming, reduction roasting and magnetic separation. *Trans. Institutions Min. Metall. Sect. C Miner. Process. Extr. Metall.* 123, 212–227. <https://doi.org/10.1179/1743285514Y.0000000067>
- Uwadiale, G.G.O.O., Whewell, R.J., 1988. Effect of temperature on magnetizing reduction of agbaja iron ore. *Metall. Trans. B* 19, 731–735. <https://doi.org/10.1007/BF02650192>
- WSA, 2022. World steel in figures.
- WSA, 2021. World Steel in Figures Report 2021.
- Yu, J., Han, Y., Li, Y., Gao, P., Sun, Y., 2017. Separation and recovery of iron from a low-grade carbonate-bearing iron ore using magnetizing roasting followed by magnetic separation. *Sep. Sci. Technol.* 52, 1768–1774. <https://doi.org/10.1080/01496395.2017.1296867>



EFFECT OF LADLE FRUNACE SLAG ON STEEL CLEANLINESS OF TIRECORD STEEL IN İSDEMİR PLANT

İlker AYÇİÇEK¹, Nuri SOLAK², Memduh Kağan KELER³

¹İskenderun Demir ve Çelik A.Ş., ²İstanbul Teknik Üniversitesi, ³Ereğli Demir ve Çelik A.Ş. Türkiye

Keywords: Steel Production, Slag, Steel Cleanliness, tire cord, Slag Basicity

Abstract

Cord wire steel, which is one of the group of tire reinforcement steels, is a steel grade with high steel cleanliness and the control of the inclusion morphology in the production processes must be carefully managed. Elements such as steel cleanliness, mechanical results and microstructure, which are the expectations of the customer in cord wire production, are among the main points to be considered. Cleanliness of tire cord steel is important due to the usage area of the cord wire. The cold drawing of the cord wire to very thin diameters (<0.18 mm) makes the inclusion types that will occur in the steel important as well as the cleanliness of the steel. It is critical that the inclusions of the Alumina type, which cannot be formed especially for the cold drawing process, remain at a very low level in the steel. Basically, ladle metallurgical slag has a significant impact for determining the type of inclusion in the steel. It is known in the literature that tire cord wire is produced with slag compositions with a slag basicity value of 0.6-1.5 and the desired inclusion type can only be achieved at these basicity values.

In this study, the effects of slag basicity on steel cleanliness and inclusion types in steel were investigated while tire cord wire production was carried out at İsdemir facilities. Basically, the differences between heats produced with low basic value, which is thought to be suitable for tire cord wire production, and heats made with classical basic slag composition, in terms of steel cleanliness and inclusion type are emphasized. In the heats made for the tire cord wire, it is ensured that the basicity of the slag remains at a maximum value of 1.5. In the heats produced with basic slag and intended to be used in the production of bead wire, the values remained

between 2.2-3.0. In both productions, soft stirring times were kept long in order to have a positive effect on steel cleanliness in the ladle metallurgy process. Flotation, which was done for 20-25 minutes in the production of tire cord wire, was made in 15 minutes in the production of bead wire. After the study, the steel cleanliness samples were examined with the Explorer 4 equipment. This device counts inclusions with the logic of scanning electron microscope and reports on the chemical composition, morphology, distribution and size of the inclusions. When the results were inspected, the inclusion composition of the steel produced in accordance with the production of tire cord wire was examined. It was observed that the Al_2O_3 type inclusions investigated in low levels. Hence it is interpreted that the final sample meets the requirements for tirecord steel. When the chemical composition of the steel grade for the bead wire is examined, it contains inclusions with high Ca-Al composition similar to the heats produced with classical basic slag.

1. Introduction

Steel cleanliness is an important issue for steelmakers. Steel cleanliness is depend on the grade and using area of steel. Tire cord is one of the most important steel grade according to steel cleanliness. Tire cord producers have strict demands for raw materials as steel wire. Requirements of tire cord steel low impurity level (Cu+Ni+Cr), low S level (less than 150 ppm), low P level (less than 150 ppm), low Al content (less than 30 ppm) and high level steel cleanliness. The reason of these strict requirements are reduction of wire diameter up to %99,95. In addition to this requirements, inclusion type is one of the most important factor to produce tire cord steel. Tire cord steel have high plastic

deformation rate therefore inclusions that in this steel must be deformable. Non-deformable inclusions that have high Al- Ca content cause breakage during plastic deformation of steel wire. Deformable inclusions are tolerated in the cold rolling of steel wire. These types of inclusions are sulfides and silicates. Type of inclusion in tire cord steel can be controlled with the basicity and composition of ladle furnace slag.[1-7] In this work, effect of ladle slag on tire cord steel production is investigated in İSDEMİR.

2. Experimental Procedure

In İSDEMİR steel produced with BF-DES-BOF-LF and CCM route. Steel grade and its composition is given below table.

Table 1 Grades Used in Experiment

İSD GRADE		1.1070 02	1.1072 00
TYPE OF EXPERIMENT		LOW BASICITY	HIGH BASICITY
C	Min	0,70	0,70
C	Max	0,74	0,74
Mn	Min	0,45	0,55
Mn	Max	0,55	0,65
P	Max	0,015	0,015
S	Max	0,012	0,015
Si	Min	0,15	0,15
Si	Max	0,25	0,25
Al	Max	0,003	0,010
Cu	Max	0,06	0,10
Cr	Max	0,06	0,10
Ni	Max	0,06	0,10
N (ppm)	Max	60,00	70,00
Cu+Cr+Ni+Mo	Max	0,15	

Two different grades are produced in İSDEMİR steel melt shop. After primary and secondary steel making process, heats are casted in Concast Steel Continuous Casting Machine.

İsdemir have 4 identical desulphurization stations, 3 identical basic oxygen furnaces, 2 identical twin ladle furnace stations and 2 identical continuous casting machines. Heats are 200 tons and tundish capacity is 35 tons in İsdemir steel melt shop.

In this work differences in production are secondary steel making process. 1.1070_02 is produced with low basicity ladle furnace slag, no calcium treatment and low stirring during 20 min. 1.1072_00 is produced high basicity ladle furnace slag, calcium treatment according to continuous casting machine conditions during casting and low stirring during 10 min.

After casting and rolling of these heats, sample are given from wire rod of these heats to analyze Thermo Scientific Explorer 4.0. These analyze result show that type, size, quantity and phase diagram where fit

in ternary. Thermo Scientific Explorer 4.0 work as SEM logic.

3. Results and Discussion

1.1070_02 grade produced with low basicity, CaO/SiO₂ ratio is 1,5. In contrast 1.1072_00 grade is produced with high basicity, CaO/SiO₂ ratio is in the range 2,4-3,6.

Inclusion analyze shows that low basicity heats in 1.1070_02 grade low Al and Ca content although inclusions content of high basicity slag shows that relatively high Ca-Al content.

Low-basicity practice presents that, 90.5% of inclusions are MnS, while Alumina type inclusions are less than 1.00 %. Inclusions per unit area are observed as 79,79 pcs/mm². It is detected that controlling Sulphur is crucial for formation of MnS. The length of MnS are also detrimental factor for next following steps of tire cord steel. Since there is no Calcium addition, it is detected that there is any Ca based complex inclusion type in steel. The overall steel cleanliness are inspected and graded as “good” for customer expectation.

High-basicity slag usage confirms that, inclusions are generally based on calcium-aluminate type. Hence, addition of Calcium in ladle furnace operation, some unmodified C3A and CA₂ type inclusions observed in steel. In this scenario, it is also detected that most of inclusions are C12A7 formation (40.1 %) which is ideal for castability and steel cleanliness. MnS inclusions constitute 20% of all inclusions. Inclusions per unit area are observed as 26,21 pcs/mm² at high basicity sample. On the other hand, the length of C12A7 inclusions are located between the ranges from 20-100 microns. This situation should be under controlled for automotive applications. In addition to this, MnS inclusions should also taken into a consideration with high basicity practice.

Investigating quantity of inclusions shows that 1.1072_00 grade relatively low Alumina inclusion content with compare the 1.1070_02 grade. This is an interesting result. These results explained with the effect of calcium treatment and stirring time. Calcium treatment decrease the level of inclusions but inclusion have high Al content. This shows that calcium treatment lowers the quantity of inclusions however lowering the quantity of inclusions may not the critical point in all steel grades. Using area is the key point to produce steel with suitable secondary metallurgical treatment.

After production of wire rod, 1.1070_02 grade used in tire cord production successfully. 1.1072_02 grade used in bead wire production.

[7] Zhiyin Deng, L. C. (2019). Effect of Refractory on Nonmetallic Inclusions in Si-Mn Killed Steel. *steel research international*, 1-12.

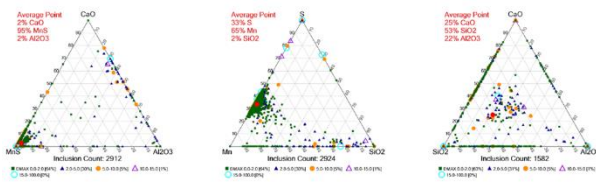


Figure 1 Low Basicity Ternary Diagram of Inclusions

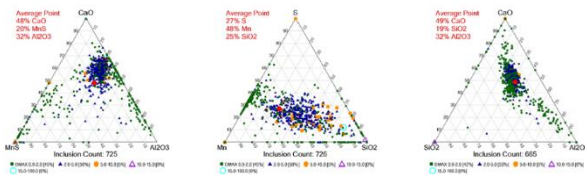


Figure 2 High Basicity Ternary Diagram of Inclusions

4. Conclusion

In sum up, every steel grade needs different treatments to used in its application. In contrast, classical steel making treatments, tire cord steel needs low basicity in secondary metallurgical treatment. Another key result of this work is bead wire steel can be produce with high basicity in ladle furnace slag with some clean steel production application like calcium treatment with suitable kg of Ca and at least 10 min soft stirring.

References

- [1] Cai-ping Xin, F. Y.-x.-f. (2016). Study on Control of Inclusion Compositions in Tire Cord Steel by Low Basicity Top Slag. *High Temp. Mater. Proc.*, 47-54.
- [2] SAKAMOTO, M. (2019). Wire Rod for High Tensile Strength Steel Cords. Kamaishi City: NIPPON STEEL.
- [3] Shu-hao Chen, M. J.-f.-h. (2012). Top slag refining for inclusion composition transform control in tire cord steel. *International Journal of Minerals, Metallurgy and Materials*, 490-498.
- [4] Silva, A. L. (2018). Non-metallic inclusions in steels – origin and control. *Journal of Material Research and Technology*, 283-299.
- [5] Wei Yan, W. C. (2019). Quality Control of High Carbon Steel for Steel Wires. *Materials*, 1-26.
- [6] Zhang, L. (2006). State of the Art in the Control of Inclusions in Tire Cord Steels - a Review. *Process Metallurgy - Steelmaking*, 158-169.



SYNTHESIS OF NANOCRYSTALLINE STAINLESS STEELS BY MECHANICAL ALLOYING: GRAIN GROWTH, PHASE TRANSFORMATION, THERMAL STABILITY AND MECHANICAL PROPERTIES

Hasan KOTAN

Necmettin Erbakan University
Türkiye

Keywords: Nanocrystalline stainless steels, Mechanical alloying, Grain growth, Phase Transformation, Thermal stability

Abstract

Nanocrystalline stainless steels often display a large grain size dependent improvements in mechanical properties as predicted by the Hall-Petch relationship. On the other hand, their production and wider structural and engineering applications may be limited by the high driving force for thermally induced grain growth even at low temperatures. Accordingly, thermal stability of nanostructured stainless steels is crucial for successful consolidation via powder processing routes and for high temperature structural applications. Here, recent research on grain size stability and hardness properties of nanostructured stainless steels are reported. Nanocrystalline austenitic stainless steels with solute additions were synthesized using high energy mechanical alloying. Structural and microstructural characterizations were carried out using x-ray diffraction (XRD) techniques and focused ion beam microscopy (FIB) as a function of solute additions. The dependence of hardness on the microstructure was utilized to study the mechanical changes. The relative importance of solute additions was discussed with respect to grain size stability, phase stability, and hardness after annealing at 1100 °C.

1. Introduction

The superior properties of nanocrystalline metals and alloys make them suitable candidates for the structural applications [1]. The austenitic stainless steels, which have features such as high corrosion resistance and biocompatibility, have relatively low yield strength. However, their strength can be increased by reducing the grain size, and the application of these materials can be widened [2, 3]. Powder metallurgy is known to be an effective method for the production of nanocrystalline materials, including stainless steels [4]. With this method, alloys that cannot be produced by traditional casting can be produced by mechanical

alloying, the mechanical properties of the materials can be improved by reducing the grain size to nanometer range, and the material properties can be controlled by creating complex phase transformations in the microstructure due to the severe plastic deformation induced during mechanical alloying [5, 6]. For example, the grain size of metastable austenitic stainless steels can be reduced to 20-30 nm by mechanical alloying while the severe plastic deformation induced during mechanical alloying causes the austenite-martensite phase transformation and alter the microstructure and the resultant properties [7].

It has been well-studied and well-known that the high grain boundary area in the nanocrystalline materials increases the internal energy and makes them unstable against grain growth during sintering or annealing and during application at elevated temperatures [8-10]. Additionally, unstable nature of the deformation induced martensitic microstructures tend to revert upon temperature exposures [11]. Thus, it is both scientifically and technologically important to determine the microstructural changes of nanocrystalline austenitic stainless steels upon temperature exposures.

In the present study, grain growth, phase transformation, and hardness of nanostructured austenitic stainless steels were studied as a function of solute additions (Y and Zr) after mechanical alloying and annealing at 1100 °C. Focused ion beam microscopy (FIB) studies were carried out to image the microstructures after annealing. X-ray diffraction (XRD) studies were conducted to determine the phase transformation after mechanical alloying and annealing. Additionally, hardness tests were applied to the as-milled and annealed steels to interpret the mechanical properties depending on the obtained microstructures.

2. Experimental Procedure

In the present study, nanostructured austenitic stainless steels were produced from commercially purchased elemental powders by mechanical alloying via high energy SPEX 8000D mixer mill. The chemical compositions of the produced stainless steels are given in Table 1. The Zr and Y solutes were added as stabilizing agents. For mechanical alloying, appropriate amounts of powders were mixed with stainless steel balls (440C) and sealed in a hardened steel vial under vacuum. 10:1 ball to powder ratio with 5.1g total powder charge was loaded into the vial without any process control agent (PCA) and milled for 20 h at room temperature. The as-milled nanostructured powders were then annealed at 1100 °C for 60 min in a 98% Ar + 2% H₂ gas atmosphere to investigate the effect of annealing on grain size stability, phase transformation, and hardness.

Table 1. The compositions of the produced stainless steels.

at %	Fe	Cr	Ni	Zr	Y
Base composition	74	18	8	0	0
+1 Zr	73	18	8	1	0
+1 Y	73	18	8	0	1

The structural stability and phase transformation as a function of solute additions and annealing were performed by x-ray diffraction (XRD) using Cu-K α radiation. The microstructural characterizations were carried out by using focused ion beam (FIB) microscopy. Additionally, the hardness of the samples was investigated using Vickers hardness test.

3. Results and Discussion

The XRD scans given in Figure 1 shows the structural evolution of the base composition as well as Y and Zr added stainless steels after mechanical alloying and annealing. It is clearly seen from the as-milled XRD scans that a BCC solid solution phase, which is also known as α' -martensite, became the dominant phase in the microstructure after mechanical alloying of all three stainless steel compositions, which is not expected based on the equilibrium phase diagram. The austenite-to-martensite phase transformation is a well-known phenomenon observed in some austenitic stainless steels during severe plastic deformation such as mechanical alloying, which depends on the stacking fault energy as well as the chemical composition of the stainless steels [12-14].

Additionally, broad crystalline diffraction peaks observed after mechanical alloying indicates the accumulated internal strain and reduction of the grain size during mechanical alloying process. The Scherrer approach was used to estimate the as-milled grain size resulting in around 25 nm grain size after mechanical alloying [15]. The as-milled stainless-steel powders were annealed at high temperature, at 1100 °C, to investigate the effect of temperature on the grain growth, phase transformation, and hardness of the studied stainless steels. As can be seen from the XRD patterns given in Figure 1, the initial broad crystalline diffraction peaks observed after high energy mechanical alloying sharpened upon high temperature annealing. This is a sign of grain growth and the relief of internal strain piled up during mechanical alloying. Additionally, although BCC phase remained the dominant phase in the microstructure, the nucleation of the FCC phase, which is the austenite, was also observed upon annealing at 1100 °C. This incomplete transformation, which is also known as the partial reverse transformation from martensite to austenite, after annealing is in agreement with the reported data in the literature [16, 17].

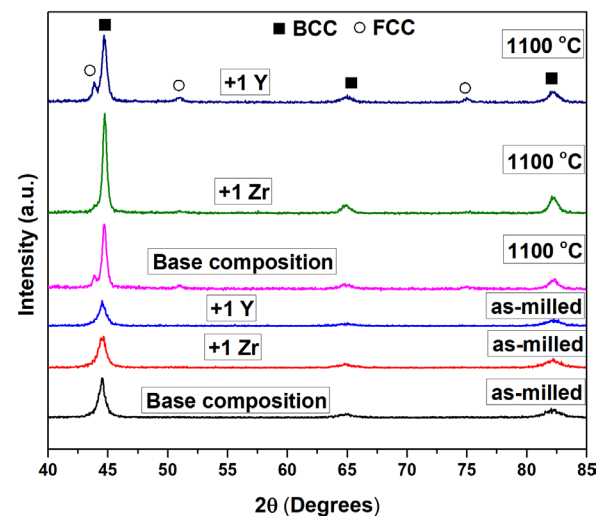


Figure 1. The XRD patterns of the as-milled and annealed stainless steels with solute additions.

Figure 2 shows the FIB micrographs of the stainless steels after annealing at 1100 °C. It is known that the channeling of incident ions between the lattice planes of the imaged specimen, stainless steels, creates the contrast seen in the figure. It is obvious from Figure 2 (A) that annealing of the initially nanostructured microstructure of the base composition caused a grain growth resulting a microstructure with an average grain size over few microns after 60 min annealing at 1100 °C. It indicates that as-milled nanostructured stainless steel of the base composition is not thermally

stable at high temperature, 1100 °C, because of the excessive grain boundary enthalpy stored in the large grain boundary area [18, 19].

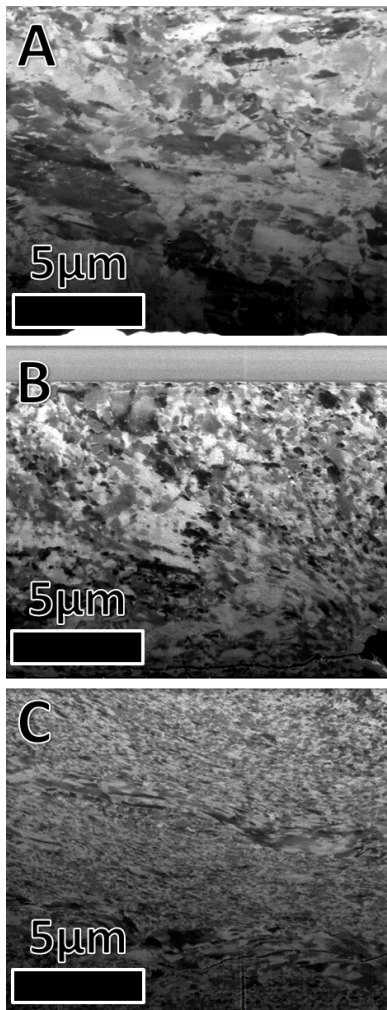


Figure 2. FIB images of initially nanocrystalline stainless steels after 60 min annealing at 1100 °C: (A) base composition, (B) +1Zr, (C) +1Y.

This result creates challenges for material processing through powder metallurgy. That is, grain growth of nanocrystalline microstructures limits the consolidation of nanocrystalline powders and prevent attaining the 100% theoretical density and good particle bonding. A large number of studies conducted in an attempt to retard the grain growth of nanocrystalline metals and alloys suggest that alloying can lower the driving force for grain growth by solute segregation, which is also called thermodynamic stabilization [20-23]. Accordingly, addition of 1 at% Zr and Y appeared to influence the grain growth at high temperature, as observed from Figure 2 (B) and (C). It is seen from the figure that alloying with 1at% Zr slows down the grain growth when compared to the base

composition. That is, the microstructure of the Zr added stainless steel shows smaller grains as the average grain size appears to be in the ultra-fine region (Figure 2B), whereas adding Y (Figure 2C) promotes even better stability after annealing at 1100 °C stabilizing the grain size around 150 nm. The effect of solute additions can be two-fold as the solute additions such as Zr and Y are expected to diffuse to the grain boundaries resulting in the reduction of the total grain boundary energy and / or form small second phases upon temperature exposures which reduce the grain boundary mobility, both of which promote better grain size stability in comparison to steel without Zr and Y additions.

The dependence of hardness on the microstructure is the easiest and convenient way to investigate the mechanical changes as a function of solute additions or annealing temperatures. Accordingly, hardness test was conducted and the results are given in Figure 3. The hardness results of the as-milled stainless steels are around 7 GPa, which is higher than those synthesized by other techniques due to the fact that mechanical alloying has the ability to form nano-sized grains with high density of defects as well as nano-sized martensite phase, both of which are correlated with the increase in the hardness.

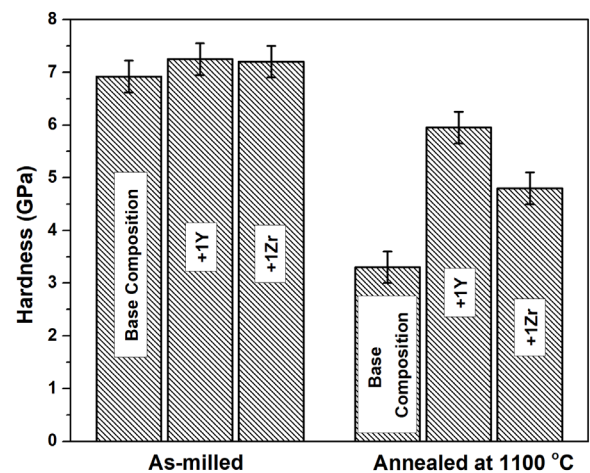


Figure 3. Hardness values of the as-milled and annealed stainless steels as a function of solute additions.

The changes in the hardness after annealing were also investigated as a function of solute additions and as expected, a reduction in the hardness was determined due to the grain growth as shown in Figure 2. As seen from Figure 3, the hardness of the base composition dropped from around 7 GPa to around 3.3 GPa after annealing at 1100 °C. Conversely, although reduction

in hardness was observed for the steels with Zr and Y additions lowering to around 5 GPa and 6 GPa for Zr and Y additions, respectively, the overall hardness still remained elevated in comparison to the base composition.

4. Conclusion

In this work, nanostructured austenitic stainless steels were produced by mechanical alloying and Zr and Y were added as stabilizing agents. The obtained powders were studied in terms of phase stability, thermal stability, and hardness as a function of solute additions after mechanical alloying and annealing at 1100 °C. The obtained results showed that the severe plastic deformation during high energy mechanical alloying induced phase transformation from austenite to martensite while reducing the average grain size down to around 25 nm. Annealing at 1100 °C was found to trigger partial reverse transformation from martensite to austenite leaving the martensitic phase the dominant phase in the microstructure after annealing. Microstructural investigations showed that base composition yielded an increase in the average grain size, which reached over few microns after annealing at 1100 °C. Nevertheless, alloying with Y and Zr additions promoted better grain size stability limiting the grain growth and keeping the average grain size around 150 nm and in the ultra-fine range, respectively, after annealing at the same temperature. As a result, the retarded grain growth behavior of the initially nanostructured stainless steels with Zr and Y additions upon high temperature exposures enhanced the limiting structural states in terms of hardness results.

Acknowledgment

This work is financially supported by TUBITAK under grant number 114M214. I would like to thank Dr. Kris A. Darling for FIB analysis.

References

- [1] K. H. Lo, C. H. Shek, and J. K. L. Lai, *Materials Science & Engineering R-Reports*, 65 (2009) 39-104
- [2] M. Shirdel, H. Mirzadeh, and M. H. Parsa, *Materials Characterization*, 103 (2015) 150-161.
- [3] H. Kotan, G. Polat, and A. B. Yildiz, *Advanced Powder Technology*, 32 (2021) 3117-3124.
- [4] H. Kotan, *Materials Science and Engineering A*, 647 (2015) 136-143.
- [5] M. H. Enayati, M. R. Bafandeh, and S. Nosohian, *Journal of Materials Science*, 42 (2007) 2844-2848.
- [6] B. Radiguet, A. Etienne, P. Pareige, X. Sauvage, and R. Valiev, *Journal of Materials Science*, 43 (2008) 7338-7343.
- [7] H. Kotan, *Journal of the Faculty of Engineering and Architecture of Gazi University*, 34 (2019) 1266-1272.
- [8] C. C. Koch, *Journal of Materials Science*, 42 (2007) 1403-1414.
- [9] C. Suryanarayana and C. C. Koch, *Hyperfine Interactions*, 130 (2000) 5-44.
- [10] A. R. Kalidindi and C. A. Schuh, *Acta Materialia*, 132 (2017) 128-137.
- [11] R. V. de Melo, C. A. S. de Oliveira, and C. A. Suski, *International Journal of Materials Research*, 107 (2016) 1147-1148.
- [12] A. Das, P. C. Chakraborti, S. Tarafder, and H. K. D. H. Bhadeshia, *Materials Science and Technology*, 27 (2011) 366-370.
- [13] D. Kaoumi and J. L. Liu, *Materials Science and Engineering A*, 715 (2018) 73-82.
- [14] K. Tomimura, S. Takaki, S. Tanimoto, and Y. Tokunaga, *ISIJ International*, 31 (1991) 721-727.
- [15] J. I. Langford, *Journal of applied crystallography*, 11 (1978) 102-113.
- [16] G. Cios, T. Tokarski, A. Zywczyk, R. Dziurka, M. Stepien, L. Gondek, et al., *Metallurgical and Materials Transactions A*, 48a (2017) 4999-5008.
- [17] S. J. Lee, Y. M. Park, and Y. K. Lee, *Materials Science and Engineering A*, 515 (2009) 32-37.
- [18] H. V. Atkinson, *Acta Metallurgica*, 36 (1988) 469-491.
- [19] T. R. Malow and C. C. Koch, *Synthesis and Processing of Nanocrystalline Powder*, (1996) 33-44.
- [20] N. Zhang, D. Gunderov, T. T. Yang, X. C. Cai, P. Jia, and T. D. Shen, *Journal of Materials Science*, 54 (2019) 10506-10515.
- [21] M. A. Atwater, S. Mula, R. O. Scattergood, and C. C. Koch, *Metallurgical and Materials Transactions A*, 44a (2013) 5611-5616.
- [22] T. Chookajorn, H. A. Murdoch, and C. A. Schuh, *Science*, 337 (2012) 951-954.
- [23] M. Saber, H. Kotan, C. C. Koch, and R. O. Scattergood, *Journal of Applied Physics*, 114 (2013).



DESIGN AND INVESTIGATION OF THE MECHANICAL PROPERTIES OF LIGHT ALLOYS FOR ELECTRIC VEHICLES

Ayşen Ceren DERELİ^{1,2}, Ahmet Salih YILMAZ², Ufuk BALIKÇI², Onuralp YÜCEL¹

¹Istanbul Technical University, ²Anadolu Isuzu Otomotiv
Türkiye

Keywords: Electric vehicles, lightweighting, roof design, topological optimization, structural analysis.

1. Introduction

Today, especially in the big cities, air pollution has become an important urban problem due to its negative impact on public health, economy and environment. Urban transportation, which has a large share in energy consumption, also increases this problem rapidly. A sustainable approach is needed to reduce such negative effects of transportation vehicles. Because of this problem, users have started to approach to alternative energy vehicle technologies. Studies so far have proven that electric vehicles have environmental compatibility and can be a good and powerful alternative to diesel vehicles in solving the problem. However, since there is a brand new power source addition to a bus, there is a massive weight increase. Lightweight studies should be carried out, in order to prevent the reduction of passenger capacity.

2. Materials and Methods

In the study carried out, the battery frame, which was located on the roof of an 8-meter-long fully electric urban transportation bus, was removed from use as part of the lightweighting studies and the modules of the battery were directly connected to the upper frame of the vehicle. By performing the analyzes before and after the changes, the stress and deflection values observed in the upper frame were evaluated, and design iterations were carried out until the appropriate value was found. Both the reinforcement of the frame structure consisting of P355NB HSLA steel profiles and 6063-T5 aluminum profiles were used for the connection of the modules. The mechanical and chemical tests of the steel material of the profiles used in the structure of the vehicle were carried out. Structural analysis on Hyperworks and fatigue analysis on nCode Design Life were carried out for the vehicle structure, which was designed in CATIA V6 platform.

3. Conclusion

Within the scope of this study, weight reduction was obtained in an 8-meter-long electric bus with the aim of optimizing the number of passengers and vehicle range.

The steel alloy used in the body structure of the bus was subjected to material characterization tests. Compliance was checked by comparing the information on the material provided by the manufacturer with the chemical analysis, hardness measurement and tensile tests performed.

In the static analysis of the designed bus body structure, it was accepted that the optimum value was reached for the stress and deflection values, the design was finalized, and then the fatigue analysis of the vehicle was carried out. In the fatigue analysis performed after the design changes on the ceiling and the addition of aluminum T-profiles, no crack initiation was observed in either the roof structure of the vehicle or the aluminum profiles.

After the vehicle was produced, it was tested on different road tracks, and measurements were taken on the aluminum T-profiles on the upper frame. The results showed that the yield strength of the aluminum alloy was not exceeded under any circumstances.

When the first design of the bus is compared with the last design in which weight reduction is obtained, the number of passengers has increased by 4 people. Thus, the ratio of the number of passengers to the gross vehicle weight of the bus increased from 0.38% to 0.41%.

COIL SLUMPING IN PERITECTIC STEELS

Koray ARAY¹, Ahmet SAĞLAM¹, Metin KATRANCI¹, Hasan YILDIRIM¹, Burcu SOYSAL ATAN¹, Fatih ÇELİK¹, Abdurrahman Mesud ÇAKIR¹, Erhan SAKALLI²

¹İskenderun Demir ve Çelik A.Ş., ²Ereğli Demir ve Çelik A.Ş.
Türkiye

Key Words: Rolling, Hot Strip Mill, Peritectic Steels, Coil Slumping, Binary Logistic Regression.

Abstract

Coil slumping can be observed after coiling or stock. This defect is a shape problem in hot strip mills. The coil slumping defect can be metallurgically associated with phase transformation, unsuitable tension and stacking conditions in peritectic steels. Defective coils are sent to the recoiling line for requested diameter. Recoiling line can affect additional cost, ready-to-ship product tonnage and coil's final quality. In this study, The probability of slumping defect was modeled using the binary logistic regression analysis method. Experiments were made by determining the factors affecting the probability of slumping defect and the levels of these factors. In 1.6050_40 Isdemir order quality, approximately %90 improvement was achieved by changing process temperatures and run out table practices in collapse rate.

1.Introduction

Slabs from continuous casting are annealed at high temperature and heated. The slabs are coiled by going through roughing mill, finishing mill, runout table and coiler, respectively. The schematic view of the hot rolling is given in Figure 1.

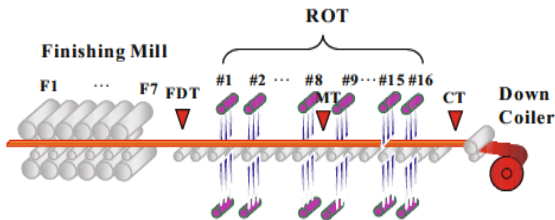


Figure 1. Schematic View of Hot Rolling

Slumping problem can occur by two different ways. The first is the defect that occurs as soon as it comes out of the coiler, and the other is the defect experienced in the coil stock area. While the coils are being stocked, they are stocked by

moving to the upper rows and systematically addressing after the lower rows are completed in a single row (Figure 2).



Figure 2. Coil Stockyard

In İsdemir, the internal diameter measurement values are targeted as 762 mm (+/- 7%). Coils outside the 7% tolerance of 762 mm are considered defected (Figure 3). If these defected coils are within the inner diameter size, they are sent to the recoiling line for recoiling, and others with the unsuitable inner diameter are considered as scrap.



Figure 3. Coil Slumping Photos

The slumping problem both creates a problem at the production exit and occupies the recoiling line. For the coils that cannot be recoil, it creates a higher cost of poor quality since the coil has been named as scrap.

2. Experimental Procedure

During the data analysis, the parameters affecting the coil slumping were determined by brainstorming method. The parameters are finishing delivery temperature, coiling

temperature, runout table cooling rate, slab length, strip thickness, chemical analysis etc. Considering these parameters may affect the slumping of coil, statistical data analysis has been started. A data set was prepared on approximately 86,000 coils, including the production of 2020. Pareto analysis was performed on the grades with the problem of coil slumping and the outstanding quality was determined (Figure 4).

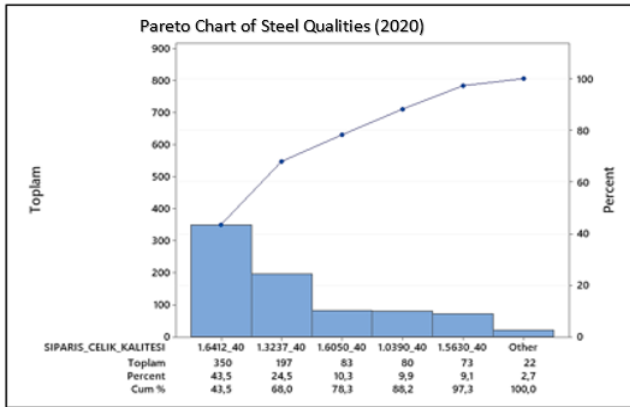


Figure 4. Pareto Chart of Steel Qualities by 2020

Our output factor which is -coil slumping is ok or not ok- is categorical, binary logistic regression analysis method was used. In this study, the probability of coil slumping was modeled (Figure 5).

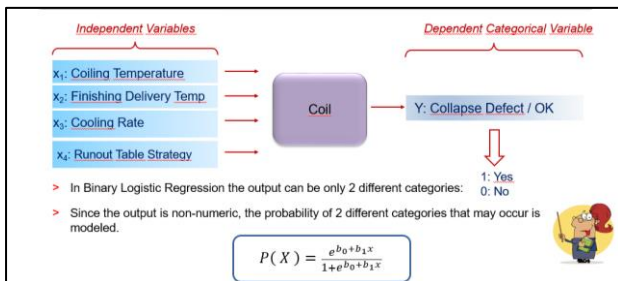


Figure 5. Method Selection (Binary Logistic Regression)

In the statistical analysis, Minitab software was used and the analysis results were interpreted. It has been determined that the thickness parameter is an effective factor on the defect (Figure 6, Figure 7).

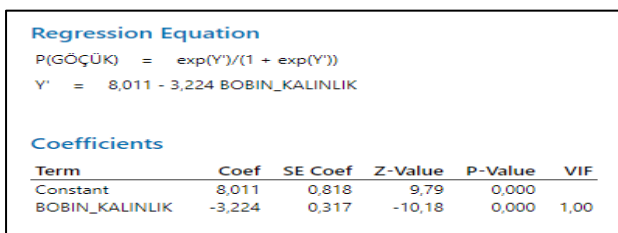


Figure 6. Binary Logistic Model of Coil Slumping

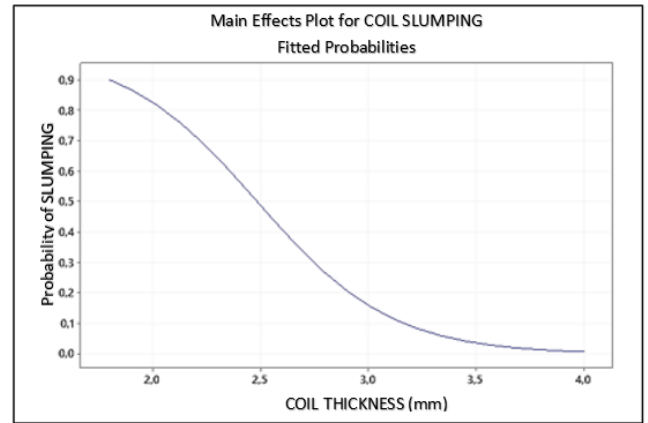


Figure 7. Main Effects Plot of Coil Thickness for Coil Slumping

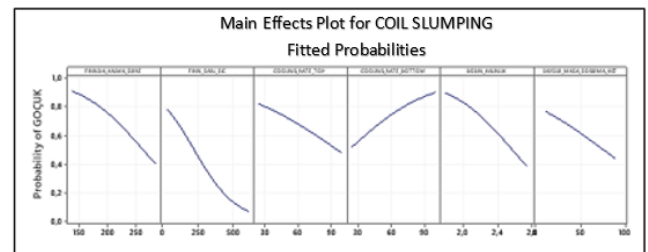


Figure 8. Main Effects Plot for Coil Slumping

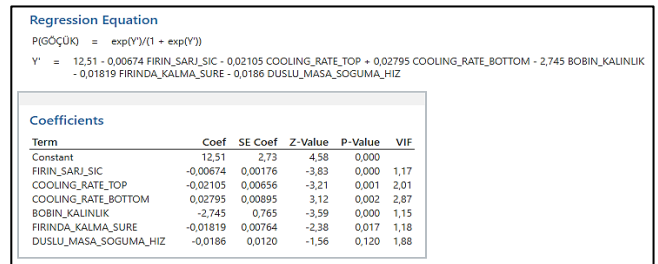


Figure 9. Binary Logistic Model of Coil Slumping

Regression analysis was performed with parameters such as residence time in the furnace, furnace discharge temperature, runout table strategy, coil thickness (Figure 8, Figure 9). It was decided to perform tests on the finishing delivery temperature, coiling temperature, runout table cooling rate, runout table cooling regime and F6-coiler tension values, which were determined to be effective in the analysis studies (Table 1).

Table 1. Chemical Analysis

QUALITY	C%		Mn%		Si%	
	Min	Max	Min	Max	Min	Max
4.6050_51	0,16	0,20	1,10	1,50	0,015	0,025

3. Results and Discussion

Experiments were carried out for 6 months by changing the coiling temperature, finishing delivery temperature, runout table strategy, tension values. After the trials were made, the coils were stored in a single row in the stock area and waited for cooling. After the cooling of the coils, one by one inner diameter measurements were taken from all of the coils and analyzed. Appropriate temperatures were checked from the JMATPro software and the minitab program (Figure 10).

As a result of the experiments, microstructure examinations and strength checks were made. The grain size was determined as 12.0 according to ASTM E-112. (Figure 11) The CCT diagram from the JMATPro software was checked. In order to prevent collapse, the coiling temperature should be chosen below the bainite transformation temperature of 598 °C or above the perlite transformation temperature of 701 °C. (Figure 10)

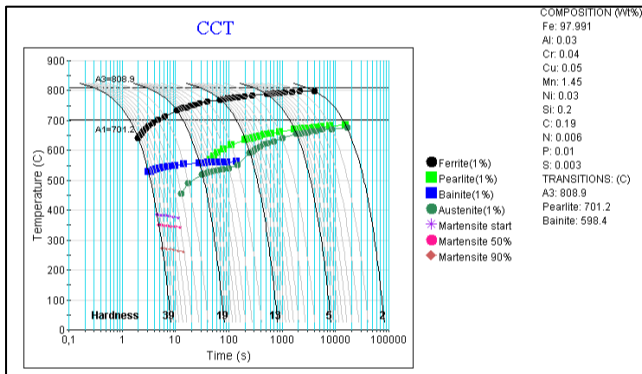


Figure 10. CCT Diagram

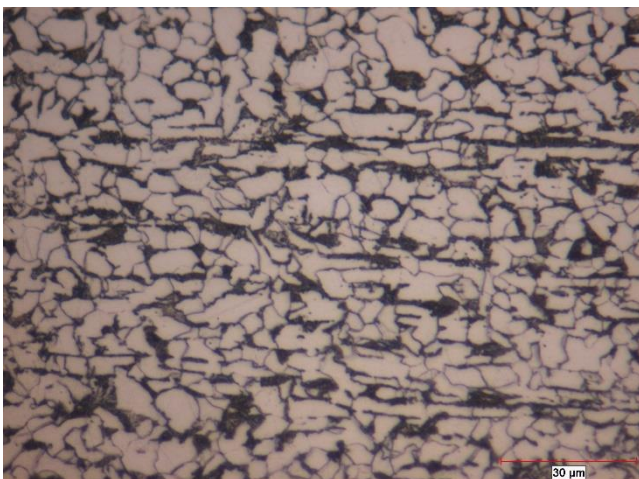


Figure 11. X-500 Microstructure

4. Conclusion

As a result of the trials, collapse were prevented. Details are in the Table 2 below.

Table 2. Trial result

Finishing Delivery Temperature (°C)	Coiling Temperature (°C)	Tension	Runout Table Strategy	Decision
x	t	a	A	Collapse
x-30	t-40	a x 1,5	B	OK

The rate of coil slumping problem decreased from 21.37% to 2.67% when we compare the periods of before-after.

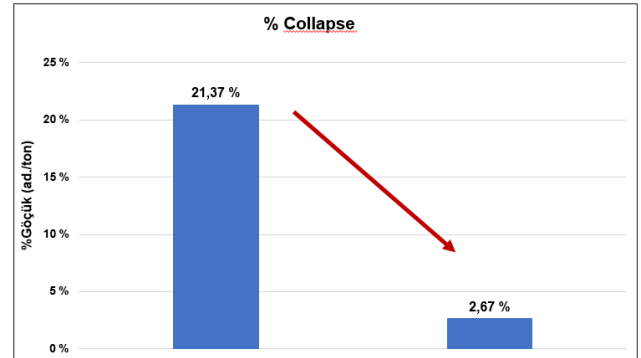


Figure 12. The Comparison of Coil Slumping by Project Term

References

- [1] B. Anderssen, N. Fowkes, R. Hickson, M. Mcguinness, Analysis of coil slumping,
- [2] A.K.Akela, P.T.Tripathi, M.Vastrad, R.Rao, G.Balanchardan, Optimization of runout table cooling parameters to control coil collapse in carbon-manganese steels (2021)
- [3] K. Banks, A. Tuling, B. Mintz, Influence of chemistry and runout table parameters on hot coil collapse in C-Mn steels
- [4] C.J. Parks, Journal of Mechanical Science and Technology, 2010, Vol 24, No 5



REDUCING QUALITY COST BY REDUCING TRANSVERSE SURFACE CRACK DEFECT IN SLAB GRADES

Kübra AKGÜN, İker AYÇİÇEK, Hakan KAPUSUZ, Burcu Soysal ATAN, Murat SARIOĞLU

İskenderun Demir ve Çelik A.Ş.
Türkiye

Key Words: Transverse Surface Crack, Secondary Cooling, Continuous Casting, Minitab, Binary Logistic Regression

Abstract

In Isdemir, an integrated iron and steel producer, liquid raw iron comes out of blast furnaces, passes through different facilities which are respectively desulfurization, basic oxygen furnace (converter), ladle furnaces and continuous slab casting plant and finally becomes semi-finished product “slab”. Cracks that occur transversely on the slab wide surface are called “Transverse Surface Crack”. The transverse surface crack is difficult to detect at the end of the continuous slab casting plant and can be detected after the scarf process or after the slab has cooled. In this study, peritectic grades and relatively high carbon grades should be charged above 300 0C in the reheating furnaces. 4237, 4252, 4250 and 3032 grades have been investigated in this research. Isdemir 4237 grade belongs to the EN 10025-2:2019 standard and is included in the hot rolled non-alloy structural steels group. Isdemir 4252-4050 peritectic grade belongs to the S355JR-J2 standard and is in the high strength structural steels group. Isdemir 3032 grade belongs to the EN 10083-2:2006 standard and is included in the hot rolled carbon steel group suitable for ring manufacturing after rolling and heat treatment. Data sets have been inspected according to 2021 production results of studied grades. Heat fluxes, Secondary cooling, superheat temperature, and chemical analyzes have been imported to data sets. The probability of transverse surface crack defect on the prepared data set was modeled through the Minitab program with the binary logistic regression analysis method. Factors that were found to be statistically effective were also evaluated from a metallurgical point of view in the light of process knowledge. As a result of the analyzes a trial procedure was established and the cost of quality caused by the transverse surface crack defect was reduced.

1.Introduction

The ladle which comes from the ladle metallurgical station is put into the slab machine turret in the slab continuous casting machine. The liquid steel in the turret is transferred to the tundish with the tube. The tundish used in slab casting machines has a capacity of 70 tons of liquid steel.

The mold is a place where the first solidification is started and the liquid steel forms a solid shell, also the mold is the last place where the liquid steel has the opportunity to get rid of inclusions. Due to the homogeneous heat flux in the mold, bleeding and quality defects of the semi-finished product is prevented. The continuous casting mold makes an oscillation during casting. The oscillation of the mould causes a relative movement between the mould and the hot strand. The purpose of this movement is to reduce the friction between the mold and the solid shell and to prevent sticking to the mold.

In addition, casting powder, which prevents sticking and helps to homogeneous heat flux, is poured into the mold at certain periods.

Liquid steel, which starts to solidify in copper molds whose width can be adjusted depending on customer demand, is transmitted to the area where it comes into direct contact with water.

The slab coming to the secondary cooling zone comes into direct contact with the conditioned water here and is transmitted to the cutting zone with the help of rollers.

The chemical analysis of the studied grades and the process parameters affecting transverse surface crack defects are given at Figure 1.

Grades	Chemical Analyses			Process Parameters		
	C	Al	N	Casting speed	Secondary Cooling Spray Plan No	Superheat
4.4252_52	0,17-0,20	0,020-0,060	0,012	1,1	5	25-35
4.4237_50	0,12-0,16	0,015-0,060	0,012	1,2	5	25-35
6.5031_53	0,28-0,32	0,020-0,060	0,01	1,1	5	25-35

Figure 1. Chemical composition and process parameters of the studied grades

2. Experimental Procedure

Within the scope of the study, a data set was created from parameters such as chemical analysis, secondary cooling parameters, casting speed in order to determine the factors affecting the formation of transverse surface crack sensitivity. Binary logistic regression analysis was performed with the data set according to yes/no condition of transverse surface crack defects.

6.5031_53 Grade

Within the scope of the study, a data set was created from parameters such as chemical analysis, secondary cooling parameters, casting speed in order to determine the factors affecting the formation of transverse surface crack sensitivity. Binary logistic regression analysis was performed with the data set according to yes/no condition of transverse surface crack defects.

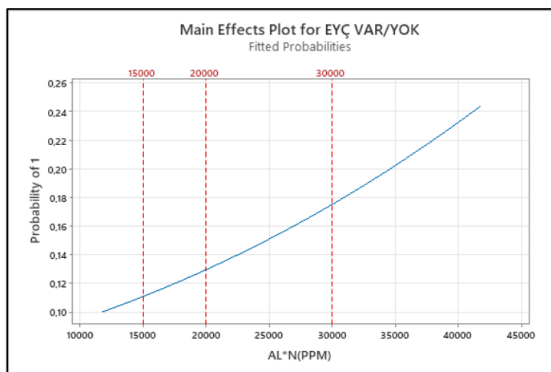


Figure 2. The effect of Al*N value to the yes/no condition on defect

When the binary logistic regression analysis was performed on the existing data set, it has been determined that Al*N value is effective, and as this value increases, the probability of transverse surface defect increases as seen at Figure 2. Secondary cooling, is classified from 4 to 9 depending on the amount of water given. The productions with defects for spray plan no 4 and 5 used in the production practice of the relevant quality were statistically compared with the 2-proportions test. It has been determined that the probability of a defect is statistically lower when working with the spray plan number 4 as seen at Figure 3.

Test and CI for Two Proportions				Estimation for Difference	
Method				Difference	95% CI for Difference
p1: proportion where Sample 1 = Event				-0,260355	(-0,310420; -0,210289)
p2: proportion where Sample 2 = Event				CI based on normal approximation	
Difference: p1 - p2				Test	
Descriptive Statistics				Null hypothesis	H0: p1 - p2 = 0
Sample	N	Event	Sample p	Alternative hypothesis	H1: p1 - p2 ≠ 0
Sample 1	382	10	0,026178	Method	Z-Value
Sample 2	349	100	0,286533	Normal approximation	-10,19
				Fisher's exact	0,000
					P-Value
					0,000

Figure 3. The effect of spray plan number to Yes/No condition on transverse surface crack

4.4237_50 Grade

In the study, it was determined that the defect was seen especially in the productions over 1,800 mm width.

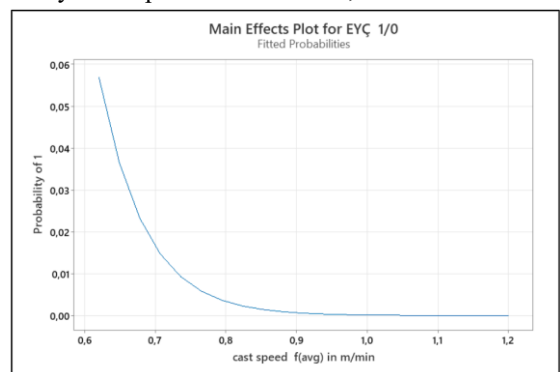


Figure 4. The effect of casting speed to YES/NO condition on transverse surface crack

When we look at the analysis made with the data set, it was seen that the probability of transverse surface defect in production decreased with a speed of 1-1.2 m/min. This point is determined at Figure 4.

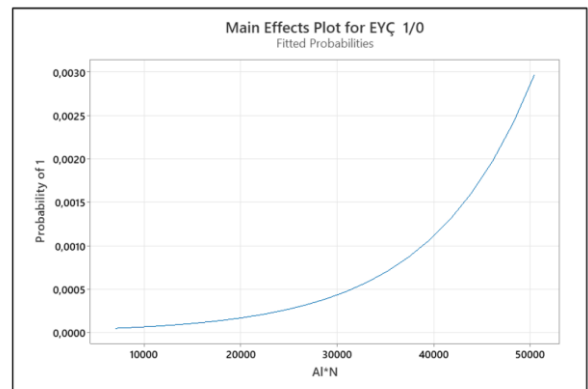


Figure 5. The effect of Al*N value to YES/NO condition on transverse surface crack

4.4252_52 Grade

Transverse surface crack defect was modeled with the data set created in the relevant quality.

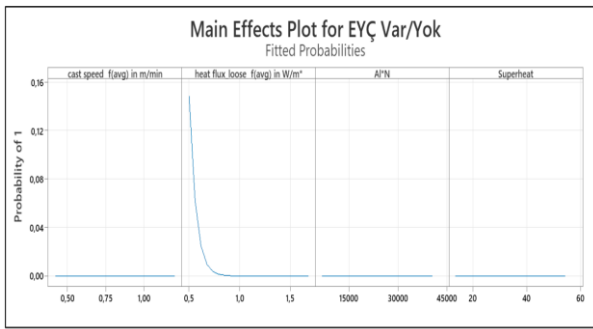


Figure 6. The effect of process parameters transverse surface crack defect

In the study, the effects of Al*N, casting speed, superheat and heat flux on the formation of transverse surface crack defects were investigated (Figure 6).

As a result of the investigations, three different trial procedures are established for three steel grades. In the trial procedures, casting speed, superheat, Al*N values are determined and production are taken.

3. Conclusion

According to the prepared procedure, surface crack was not experienced in the slabs.

6.5031_53 Grade

The relevant quality is 0.30 %C quality and it is charged without waiting in the oven with the mandatory hot charging regime.

- It has been determined that one of the reasons for being of the transverse surface crack defect is the change in the casting speed. By producing with a constant casting speed of 1.0 m/min, the min-max difference of the casting speed was aimed to be 0.
- Secondary cooling; soft cooling has a similar effect to the mechanism of increasing the casting rate.
- In addition, higher cooling rates cause finer sulfide precipitation at the austenite grain boundaries, reducing the spacing between particles, facilitating the coalescence and fracture of ductile cracks. The secondary cooling spray in grade 6.5031_53 has been reduced from plan number 5 to 4.
- Superheat: Temperatures above 30°C are harmful in terms of crack risk. In case of casting with high superheat, the risk of cracking increases due to the increase in the dendritic structure and thermal stress. Superheat degree should be aimed to be 20-25°C and below depending on the carbon degree
- Superheat is targeted between 25-35°C in trial productions. Al*N value; Al*N value is targeted below 30,000 ppm.

4.4237_50 Grade

Especially in 1,800 mm width size and above widths, transverse surface crack defect is seen.

- Secondary Cooling; In the examinations, it was observed that the probability of defect formation decreased when the edge waters were closed. Secondary cooling practice was softened from spray plan no 7 to spray plan no 5. No defects were encountered in trial productions.
- Casting speed: It is very important that the casting speed is constant for homogeneous heat flux, especially in large size productions. Slabs with speed reduction are sensitive to eaves defect formation due to inhomogeneous cooling regime.

4.4252_50 Grade

- Secondary Cooling; Cooling regime is softened by changing the spray plan from 5 to 4.
- Casting speed is limited to 1 m/min.
- Al*N value; Al*N value is targeted below 30,000 ppm.

As a result of all the work done, process parameters have been optimized according to the chemical analysis of each quality and the probability of defects has been reduced.



INVESTIGATION OF MICROSTRUCTURAL PROPERTIES OF FISH SCALE RESISTANT LOW CARBON ENAMEL STEEL GRADES

Ramazan UZUN, Mehmet Bulut ÖZYİĞİT, Yasemin KILIÇ, Oğuz GÜNDÜZ

Eregli Iron and Steel
Türkiye

Keywords: Hydrogen permeation properties, Enamel steels, Material characterization

Abstract

Enamel coated steels are widely used in high-temperature equipment, white goods, silos, water tanks chemical reactors, etc. thanks to their good formability, weldability and enameling behavior. Since these steel grades are susceptible to the fish-scale formation, microstructure of these materials needs to be specially designed. Fish scale is caused by excess hydrogen that dissolves into the steel during the enamel firing process. As expected, steel sheet production steps make some differences in the microstructure of the steel. In this study, the effect of two steps of production, cold rolling and annealing, on hydrogen permeability was investigated. It was observed that the hydrogen permeability properties are improved by decreasing the grain size of ferrite and increasing the area fraction of precipitates that are trapping sites for hydrogen atoms.

1. Introduction

Ultra-low carbon steels have drawn much attention because of their excellent deep drawability and sufficient fish-scale resistance [1]. Fish scale formation is occurred on the surface of enameled part due to hydrogen mobility [2]. It is expected for enameling steel grades to have excellent hydrogen absorption capacity to prevent from fish scale defect on the surface of enameled part. It is known that the fish scale formation occurs due to recombination of hydrogen at the sheet-enamel interface in curing process [3]. In the curing process, the atomic hydrogen diffuses into the steel. While cooling, the atomic hydrogen diffusion is starting from the bulk towards the steel-enamel interface and hydrogen atoms recombine as molecular hydrogen. After a while, fish scale problem occurs due to pressure of hydrogen at the interface of enamel and steel [4]. Trap sites are significant to prevent fish scale formation, the resistance of fish scaling could be enhanced by increasing the number of hydrogen traps. Nitrides, carbides, sulfides, carbonitrides, non-metallic inclusions, grain boundaries, dislocations, vacancies and microvoids are additional trap sides for enamel steel grades [5].

2. Materials and Methods

Different deformation ratios were applied on samples by cold rolling simulator. Annealing tests are performed by annealing simulator. Hydrogen diffusion coefficient was measured by Helios II system. Microstructure characterization studies were carried out with light optical microscopy (Nikon Epiphot 200). The automated inclusion/particle analyses were run in the ThermoScientific Explorer-4 (TSE-4).

3. Conclusions

In this study, the effect of cold rolling and annealing processed on microstructure and hydrogen permeability properties were investigated. The samples, in which 47% and 65% cold rolling were applied in the cold rolling simulator, were annealed in the annealing simulator at 725°C and 850°C. Microstructure characterization was performed on the samples simulated in the annealing simulator, and it was determined that the samples annealed at 725°C had a finer grain structure than the samples annealed at 850°C, and the hydrogen permeability value decreased. When evaluated in terms of the amount, size and distribution of the precipitate, it was determined that the dispersed precipitates instead of locally enlarged precipitates in the microstructure showed a better performance in terms of hydrogen permeability. Because the trapping capacity is higher in samples with higher precipitation ratio per unit area.

4. References

- [1] X. Chun, R. Dehuai, S. Quanshe, "Effect of precipitations on hydrogen diffusivity coefficient and fishscale resistance of ultra-low carbon vanadium microalloyed steels" 23rd International Enamellers Congress, 2015.
- [2] Fu-tao D., Lin-xiu D., Xiang-hua L., Jun H., Fei x., Effect of Ti(C N) Precipitation on Texture Evolution and Fish-Scale Resistance of Ultra-Low Carbon Ti-Bearing Enamel Steel, Journal Of Iron And Steel Research, 2013, No 20(4), pp.39-45.
- [3] Fábíán E., Szabó P., Effect of Texture on Hydrogen Permeability in Low Carbon Al-Killed Steels, Materials Science Forum Vol. 659 (2010) pp. 301-306.
- [4] Schöttler, V. Flaxa, K. Hulka, Influence of composition and processing conditions on mechanical properties and fishscale resistance of microalloyed steels for double-face vitreous enamelling, Mater. Sci. Forum 500–501, 527–534 (2005)
- [5] M.A. Mohtadi-Bonab, J.A. Szpunar, L. Collins, R. Stankievech, Evaluation of hydrogen induced cracking behavior of API X70 pipeline steel at different heat treatments, Int. J. Hydrogen Energy 39, 6076–6088 (2014)

THE ROLE OF THERMOMECHANICAL ROLLING IN PETROLEUM PIPE STEELS AND ITS EFFECTS ON MECHANICAL PROPERTIES

Serdar GÜNBAŞ, Cemre KEÇECİ, Koray ARAY

İskenderun Demir ve Çelik A.Ş.
Türkiye

Key Words: Thermomechanical rolling, petroleum pipe steels, TMP, micro-alloy steels

Abstract

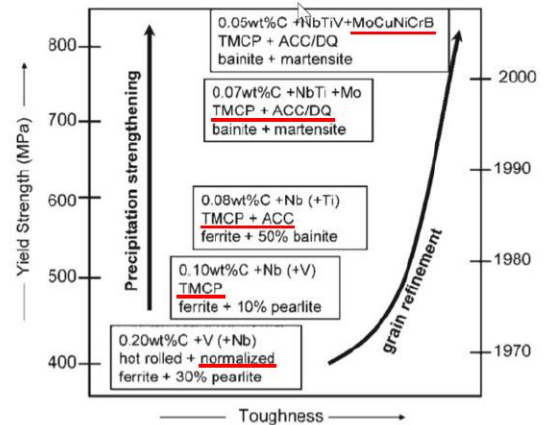
Thermomechanical rolling (TM) have a great importance in obtaining mechanical properties depending on the usage area of the product. It is a rolling method that is frequently used to obtain high strength, hardness and toughness values in low carbon and micro alloy steels. With the thermomechanical rolling process, it tries to change the microstructure by performing both mechanical treatment and heat treatment on the coil. In this study, the mechanical properties and microstructure changes of microalloyed steels after thermomechanical rolling were investigated. Chemical composition, microstructure, thermo-mechanical controlled process (TMP) metallurgical information is shared in order to achieve the targeted strength, ductility and toughness properties in different qualities and especially EN ISO 3183:2019 Annex A PSL2 L485ME quality petroleum pipe steels.

1. Introduction

In order to obtain excellent mechanical properties such as high strength and high toughness expected from new generation steels, steel production methods such as precipitation hardening and microstructure optimization are selected.

As it is known, depending on the increasing demands and the usage area, the mechanical properties required from steel can include hardness and toughness at high values. At this stage, methods such as precipitation hardening to give these properties to the steels, micro-alloying to create solid solution hardening, and thermomechanical rolling to improve the grain structure are used.

In this study, I will share the thermomechanical rolling method and sample investigation studies applied in İsdemir. The thermomechanical rolling method plays a leading role in obtaining the desired microstructure and mechanical properties by eliminating the need to use high amounts of micro alloy elements in quality design.



Vervynck et al., *International Materials Reviews* 2012 Vol 57 No 4, pp. 187-207

Figure 1 Hardening methods used according to quality requirements

At the same time, it is possible to produce steel at lower carbon ratios with the use of micro alloys and the increase in strength from the rolling process. In this way, customer expectations such as lower segregation and better weldability can be achieved successfully.

In the thermomechanical rolling process, the aim is to control the recrystallization phase and to obtain the smallest possible grain size, and to obtain high strength and toughness with a uniform distribution and grain size reduction.

In thermomechanical rolling, the final pass rolling processes are carried out below the T_{nr} temperature. This temperature range is usually below T_{nr} and above A_{r3} temperature. Since there is no recrystallization in deformations under T_{nr} , the austenite grains are crushed and deformed. Thus, the aspect ratios of the grains increase and they turn into a more elongated morphology (pancake structure). Of course, in order to reach this temperature range mentioned here, it is necessary to wait at the entrance of the strip mill. Hold rolling until the desired temperature is reached is one of the first materials of the thermomechanical rolling process.

TM controlled rolling process is done to obtaining the smallest grain size. Grain size control is provided with this two different points:

1. Very small particles formed during recrystallization to nucleate by deformation with low temperature
2. To prevent the growth of small particles formed.

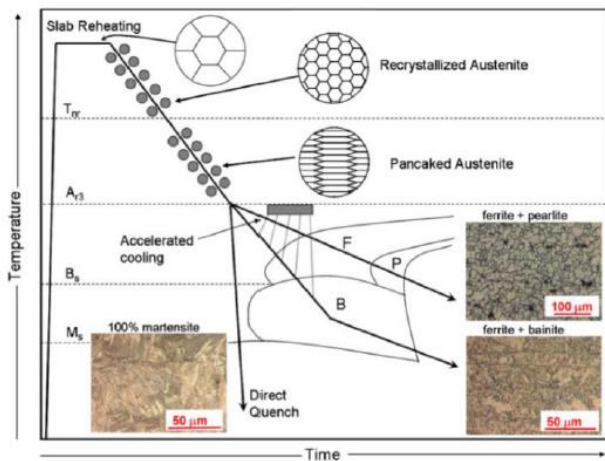


Figure 2 Formation behavior of grains under different temperature

There are many parameters that need to be evaluated in order to achieve the goal in the thermomechanical rolling process: These are;

- The amount of deformation,
- The temperature at which the deformation is performed
- Recrystallization Temperature, T_{nr}
- Effect of microalloying elements on T_{nr} temperature,
- Effect of alloying elements on phase transformations
- The temperature and time at which the product is cooled and held during rolling

As a result, a microstructure can be obtained from polygonal ferrite, bainite and their mixtures containing very low pearlite with improved toughness, formability and weldability.

2. Experimental Procedure

The diffusion of the thermomechanical rolling method at İsdemir started in 2014. For this purpose, the first trials of pilot productions were carried out on API X70 PSL2 steel grade, which is 14-17 mm thick x 1500 mm wide petroleum pipe steel. Due to the high strength required in these grades and high toughness at low temperatures, the need for thermomechanical rolling has arisen apart from conventional rolling. As it is known, depending on the climatic conditions used, the interest and demand for these steels, which are necessary for the transportation of liquid fossil fuels, are constantly increasing.

In İsdemir, our hot rolling mill starts the process with 2 walking beam furnaces. There are 2 coilers, edger, rough rolling and after the furnace exit, 6-stand strip mill, runout table cooling. It is also worth mentioning that there are 7 descalers with a capacity of 220 bar.

- Flow chart:
 - Slab Furnaces
 - Hydraulic Scale Breaker
 - Edger
 - Rough Rolling
 - Coilbox
 - Crop Shear
 - Finishing Scale Breaker
 - Strip Rolling
 - Runout Table
 - Down Coiler

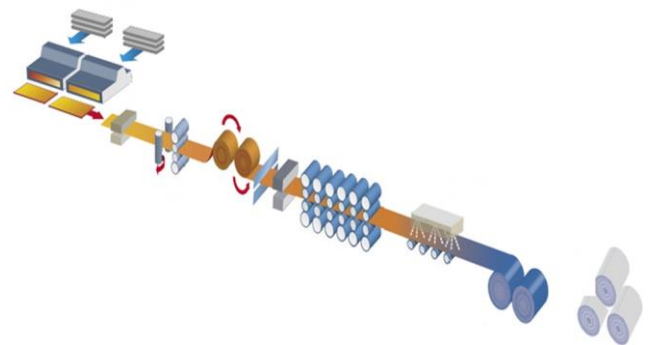


Figure 3 Hot Rolling Mill Scheme

In this study, mechanical properties and microstructural studies of the products rolled by thermomechanical process are carried out. Thermomechanical rolling studies were evaluated by examining the conventional rolled and thermomechanical rolled products by considering the hot rolling process. The hot rolling mill where the rolling is carried out includes the following process steps.

First of all, the optimum chemical composition was determined for one of the grades, EN ISO 3183:2019 Annex A PSL2 L485ME, which is the subject of our study. Nb and Ti alloys are of great importance in thermomechanical rolling for grain size control during austenitization and rolling. Again, T_{nr} , which is the most necessary temperature for the thermomechanical rolling process, was calculated according to the chemical composition. The T_{nr} temperature can be affected by the reduction rate and the addition of micro alloys to a large extent. Among the micro alloy elements, Nb has the highest increasing effect on T_{nr} .

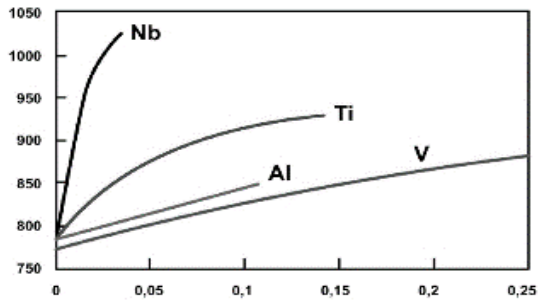


Figure 4 Effects of alloying elements in thermomechanical rolling

Table 1 Chemical Compositions of Slabs

Quality	C	Mn	Al	N	Ti	Nb
L485ME -1 TM	0,06	1,62	0,044	0,007	0,029	0,055
L485ME -2 C	0,08	1,69	0,048	0,005	0,033	0,055

TM: Thermomechanical Rolling (80 sec holding time before finishing mill)

C: Conventional Rolling

The process parameters used in the thermomechanical rolling method according to the chemical composition above. The holding time for thermomechanically rolled slab is 80 seconds. The thickness of the coil produces is 14,4 mm that the rolled slabs are 225 mm thickness. Tnr temperature is approximately 950 °C and L485ME quality production is produced at these temperatures. After the production of the coils, they are kept in the hot stack and the precipitation hardening is completed and the sampling process is started.

3. Results and Discussions

During rolling under Tnr temperature, deformation occurs without recrystallization. Since the austenite grains are not likely to recrystallize in deformations made under Tnr, they are deformed after reduction and become longer and more elongated morphology while the grains get smaller. We mentioned that the grains in this morphology are called pancake structure. As the cooling continues, pancake-shaped ferrite grains are formed within the austenite grains under Ar3 temperature. Ferrite grain cores from this type of morphology are much smaller than in classical recrystallization as they contain much more grain boundaries than coaxial grains.

The analysis of the results obtained was based on mechanical tests and metallographic studies. Samples were taken from the coils of the pilot batch after final cooling in air to evaluate the mechanical properties. The results of the mechanical tests comply with the requirement. Thus, thermomechanical rolling method can be applied to obtain high mechanical properties in Isdemir hot rolling mill conditions.

Table 2 Mechanical Results-1

Coils	Finishin Temp	Coiling Temp	Yield Strength	Tensile Strength	Elong.
TM Rolling	815	576	56,3	67,1	20
Conventional	820	564	61,8	72,4	20

Table 3 Mechanical Results-2

Coils	Charpy imp. Temp	Charpy 1	Charpy 2	Charpy 3	DWTT Temp	DWTT 1	DWTT 2
TM Rolling	-29	211	270	274	0	100	100
Conventional	-29	265	283	253	0	85	79

In the dwtt (drop weight tear test) performed after thermomechanical rolling, 100% ductility was achieved and the amount of ductility was lower in the conventional rolled coil. The notch impact test results were similar. The importance of the thermomechanical rolling process for success in dwtt test results visible with these results. Of course, it is also very important that the steel must be clean with low impurities, low nitrogen, hydrogen and free from segregation. At higher coil thicknesses, the thermomechanical effect on ductility can be seen more.

4. Conclusion

As seen in the study, the thermomechanical rolling method has been successfully applied for the production of L485 ME (14,4 mm) in Isdemir Hot Rolling Mill. With the requirements of EN ISO 3183:2019 Annex A PSL2, final rolling is critical to achieve the required mechanical results and desired microstructure. Although we have capabilities for higher strength steels and to make higher thicknesses of existing steel grades, there are issues to be worked on in the coming period in order to increase the line capacity in this regard.

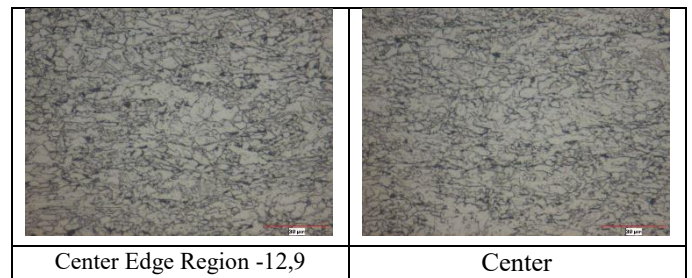


Figure 5 TM Rolling Micro Structure

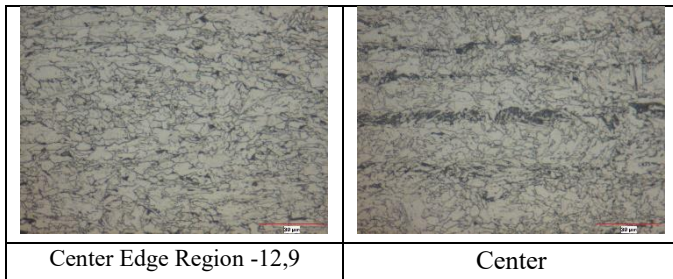


Figure 6 Conventional Rolling Micro Structure

After both rolling methods, samples were taken from the coils and etched with nital were investigated. A predominantly ferritic polygonal structure appeared in both microstructures and the measured grain sizes were 12.9.

The formation of perlite band in the micro building center manufactured by conventional rolling attracts attention. the same formation is not detected in the thermomechanical rolled product. At this point, annealing practices gain importance along with the presence of segregation in rolled slabs.

References

- [1] Uranga P., Ibabe J. M. R., Thermomechanical Processing of Steels, 2-3, 2020.
- [2] API Specification 5L. Specification for Line Pipe, Forty third edition March 2004.
- [3] Erdemir Product Catalogue 2017
- [4] ASM Handbook Heat Treating of Steel Volume 4
- [5] Development Of Thermo-Mechanical Control Process (TMCP) And High-Performance Steel In JFE Steel, ENDO Shigeru, NAKATA Naoki



EFFECT OF ISOTHERMAL TRANSFORMATION ON MICROSTRUCTURAL AND MECHANICAL PROPERTIES OF A LOW CARBON MICROALLOYED BAINITIC FORGING STEEL

M. Mustafa BALÇILAR, Bilgehan ÖGEL

Middle East Technical University
Türkiye

Keywords: Bainitic steels, Isothermal transformation, Retained austenite

Abstract

Bainitic forging steels have been developed as an alternative to Quench and Temper (Q&T) steels in recent decades due to their lower cost and energy needs, as well as their superior combination of strength, ductility, and toughness. The mechanical properties and fatigue performance of bainitic steels surpass those of their alternatives and with microalloying the mechanical properties, such as yield strength and ultimate tensile strength are further improved. Although the effect of continuous cooling on bainitic forging steels without microalloying has been investigated, the influence microalloying and isothermal transformation on the microstructure and mechanical characteristics of these steels remains to be investigated. For this purpose, a low carbon microalloyed bainitic forging steel (0.2C-1.3Si-1.5Mn-1.45(Cr+Mo), microalloyed with V-Ti-Nb) is isothermally transformed at a temperature just above M_s , 360 °C, for various isothermal holding times. The isothermal transformation routes are simulated by JMatPro® software, and the transformed steel is experimentally investigated by means of optical microscopy and scanning electron microscopy examinations, and mechanically characterized by hardness tests and tensile tests. In addition, XRD measurements are used for determination of retained austenite content. The results show that prolonged holding time does not have a significant effect on retained austenite content and hardness values are similar across various isothermal holding times. The mechanical tests show that a high ductility (>10%) and high strength (>1200 MPa) steel was obtained.

1. Introduction

In recent years, the steel industry has developed products with superior mechanical properties and lower energy consumption than its predecessors, such as conventional ferritic-pearlitic steel, in response to stringent energy and environment regulations and high safety demands from the automotive, aerospace, and defense industries. The steel industry requires improvements in yield strength, ultimate tensile strength, impact toughness, fracture toughness, fatigue resistance, machinability, and weldability, yet ferritic-pearlitic steels, even with microalloying, fall short [1-3]. To satisfy these requirements, the quench and temper (Q&T) method is used [3]. Nevertheless, the Q&T process is expensive and time-consuming, which raises the price and carbon footprint of steel products [4, 5]. In

order to replace the existing materials and procedures, bainitic forging steels were developed in the 1980s [6]. Microstructures of bainite can be generated by either continuous cooling or isothermal transformation. With or without microalloying, bainitic forging steels are often continually chilled to obtain bainitic microstructures. However, constant cooling regulation is challenging, and cooling system dependability is a challenge [6]. On the other hand, it has been demonstrated that obtaining bainite by isothermal transformation yields the best mechanical characteristics [3, 6, 7]. In addition to producing a bainitic microstructure with relative ease, carbide precipitation should be suppressed to obtain better mechanical properties because carbides, particularly cementite, act as a nucleation site for voids and cracks, which drastically reduce mechanical properties such as fatigue resistance and fracture toughness [8]. Retained austenite content is also a significant component in enhancing mechanical characteristics. Due to the transformation-induced plasticity (TRIP) effect [9], excessive quantities of residual austenite may increase ductility at the price of strength. Although bainitic forging steels without microalloying that have been subjected to continuous cooling and isothermal transformations have been studied, the effect of isothermal transformation on microalloyed bainitic forging steels has not yet been investigated. In this work, a microalloyed forging steel with V, Ti, and Nb is subjected to isothermal transformation at varying holding times to produce the carbide-free bainite described. The goal of this work is to examine the microstructure, bainite morphology, carbide precipitation, volume percentage of phases, and mechanical characteristics of isothermally heat-treated samples. Several characterization and testing methods, including optical and scanning electron microscopy, X-Ray Diffraction (XRD) Analysis, hardness measurements, and tensile tests, were used to accomplish this objective.

2. Experimental Procedure

In this study, a low carbon microalloyed bainitic forging steel is subjected to an isothermal heat treatment just above the martensite start (M_s) temperature, at 360 °C for various isothermal holding times. In order to determine the martensite start temperature, the composition is fed into the JMatPro® software. The composition is analyzed by Optical Emission Spectrometer (OES), which is listed in Table 1. The specimens are subjected to an austenitization of 1150 °C

for 45 minutes and isothermally heat treated in a salt bath for various durations at 360 °C.

Table 1. Chemical composition of bainitic forging steel in weight percent. Fe is balance.

%C	%Si	%Mn	%Cr +Mo	%P	%S	%V
0.22	1.30	1.46	1.45	0.01	0.066	0.01
%Ti	%Nb	%N	%Ni	%Al	%Cu	%B
0.0158	0.0360	0.003	0.04	0.01	0.03	0.003

The microstructural characterization was done by optical microscopy (OM) with Nikon Eclipse E200 and scanning electron microscopy (SEM) with FEI Nova NanoSEM 430. Standard metallographic sample preparation techniques were used for microstructural examination. 3 different etchants were used for color metallography and to identify phases formed: 2% Nital solution, LePera etchant, and 10% sodium metabisulfite for 10-30 seconds. X-Ray Diffraction (XRD) measurements were performed with Rigaku DMAX 2200 with Cu-K α for phase identification and retained austenite measurements by applying Rietveld Refinement to the XRD data. Repetitive polishing and etching is applied to the XRD samples. Hardness measurements were performed for mechanical characterization for all samples with EMCO Test M4U-025 Universal Hardness Tester using Vickers method. Tensile tests were performed for fully bainitic samples with BESMAK BMT-100E. All tests and characterization methods were compliant with their respective ASTM standards.

3. Results and Discussion

The simulated time-temperature-transformation (TTT) diagram of the steel is given in Figure 1. The JMatPro® software gives the Ms temperature as 357 °C. The isothermal transformation temperature to form bainite is then selected as 360 °C since it has been proven that a lower transformation temperature results in better mechanical properties for bainite [10]. For 360 °C, the simulated TTT diagram gives the bainite start and finish times as 0.58 hours (or 35 minutes) and 24 hours, respectively. To systematically study the effect of isothermal holding time to the phases formed in the microstructure, retained austenite content, and mechanical properties, intermediate holding times were selected as 1 hour, 2 hours, 4 hours, 8 hours, and 12 hours. To verify whether the bainite finish time was predicted correctly, an additional holding time of 30 hours was applied at 360 °C.

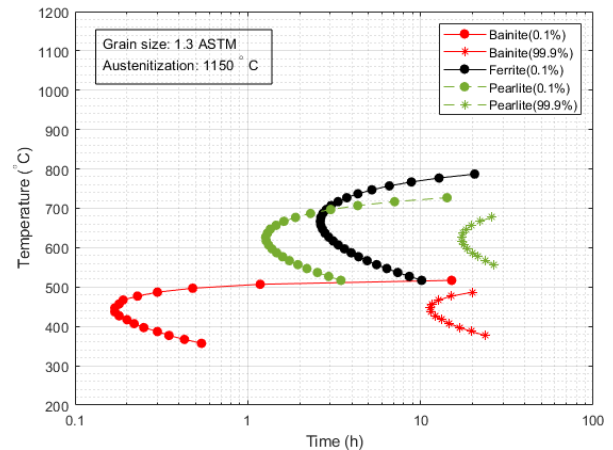


Figure 1. TTT diagram of low carbon microalloyed steel, simulated by JMatPro®.

Figures 2, 3, and 4 show the optical microscopy examination images taken at 200x. Figure 2 shows different bainite morphologies, such as lath and granular, and white blocky martensite/austenite (M/A) as indicated on the figure. Inclusions and second phase particles, formed by alloying and remnants of forging, are also present in the microstructure. The micrographs etched with nital in Figure 2 show that as the holding time increases, the area of white islands decreases. In Figure 3, the LePera etchant is used to distinguish the bainite from martensite, since nital etching is not sufficient. LePera etchant colors bainite as dark and martensite as bright white [11]. Although nital etching suggests that there is a high amount of martensite in the structure, the LePera etching suggests that the martensite inside the microstructure is minimal. Images in Figure 4 are prepared using 10% sodium metabisulfite and it also colors bainite and martensite in different colors, bainite is blue and martensite is brown [12]. The images in Figure 4 shows that as the holding time is increased, the microstructure becomes more bainitic, since the brown phases present in the 35-minute sample disappears as the holding time is increased.

SEM images of the samples are given in Figure 5, where the bainite morphology is more clearly observed as lower lath-like. Bainitic sheaves are present in all samples, with some amount of blocky M/A, such as in the 12-hour sample, indicated on the image. The SEM images show no sign of carbide precipitation, due to high Si content. In 30-hours sample, second phase particles are present at the prior austenite grain boundary, which might be a carbide-nitride particle, precipitated due to microalloying.

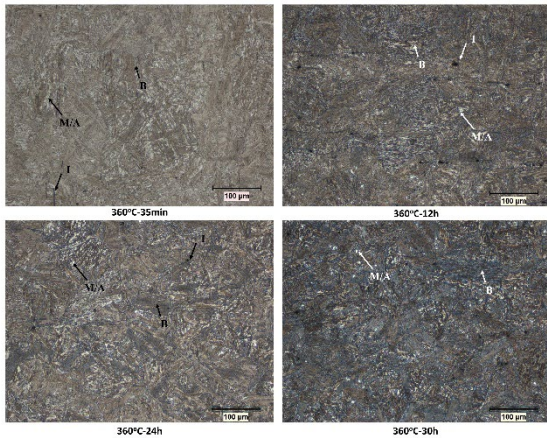


Figure 2. OM images (200x) of the steel isothermally transformed at 360°C, etched with 2% nital. B: bainite, M/A: martensite/austenite, I: inclusion.

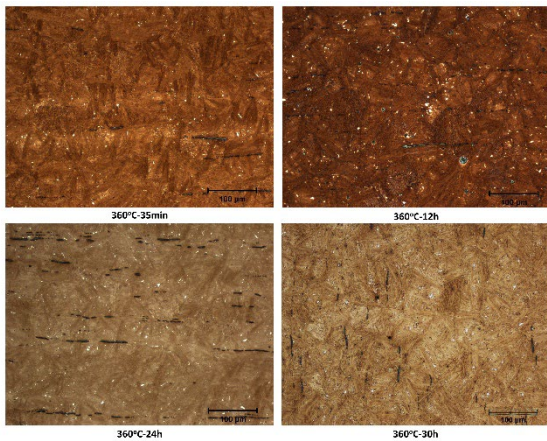


Figure 3. OM images (200x) of the steel isothermally transformed at 360°C, etched with LePera's etchant.

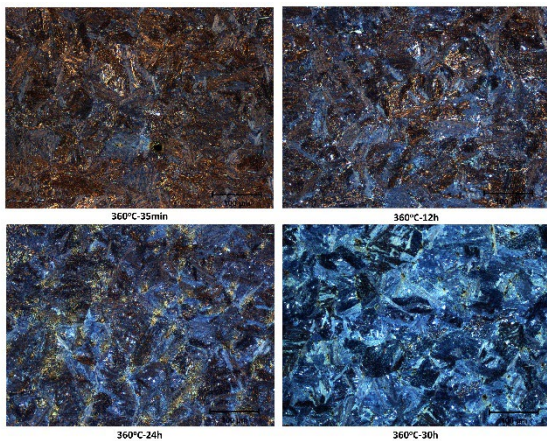


Figure 4. OM images (200x) of the steel isothermally transformed at 360°C, etched with 10% sodium metabisulfite.

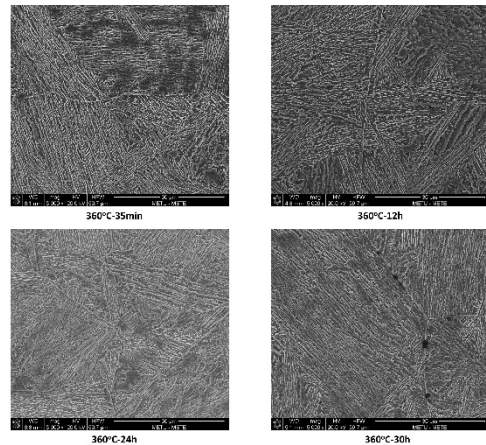


Figure 5. SEM images (5000x) of the steel isothermally transformed at 360°C, etched with 2% nital.

The retained austenite (RA) amount present in the steel could not be observed by color metallography, so XRD measurements were used to determine the RA content. Figure 6 shows the XRD pattern of all the isothermally heat-treated samples. The patterns show that both BCC and FCC phases are present in all samples, which are ferrite and austenite, respectively. The peaks shift in reasonable amounts, less than 0.1 degrees. Broadening is observed in all peaks. Although the austenite peaks are present, the intensities are quite weak, which suggests that the austenite data collected from the sample is not coming from the blocky M/A islands but rather between the bainite sheaves observed in SEM. The RA between bainite sheaves can only be resolved under transmission electron microscopy (TEM).

The results of the Rietveld Refinement are given in Figure 7. The retained austenite content is approximately the same across all samples, averaging around 5%, which confirms that the data collected must be coming from the RA sheaves in the bainite. The OM and SEM images show blocky M/A islands, which in turn would have increased the RA content observed by XRD. However, the measurement levels are much lower, which suggests that blocky M/A is completely transformed into martensite. Also, the RA amount is expected to be low since the carbon content is low. The largest RA content was measured in the 12-hour sample as 5.8% and the lowest was measured as 4.7% in the 35-minute sample. This result implies that as the holding time is increased, more carbon is rejected into the austenite, causing it to become more stable. The earlier the sample is quenched, the lesser the austenite is observed.

Mechanical characterization of isothermally heat-treated samples was done by hardness measurements and tensile tests. The hardness measurements show that the hardest specimen was obtained after a isothermal heat treatment of 2 hours, with an average hardness of 433 HV30 (± 9) and the softest specimen was obtained after a heat treatment of 24 hours, with an average hardness of 391 HV30 (± 6). The average hardness

measurements are given as a bar chart in Figure 7, with the RA content superimposed on the bar chart.

The trend between the RA content and hardness value shows a correlation, as the RA content decreases, the hardness increases, which implies that a harder microstructure is obtained when austenite is consumed, which is expected since bainite and martensite are harder phases compared to austenite.

The tensile test was applied to the sample heat-treated for 24 hours since the bainite reaction is shown to reach completion at that value, with optimum microstructure, amount of phases, and hardness. The tensile test results are given in Figure 8. The samples gave yield strength values of 1110 and 1145 MPa, and ultimate tensile strength values of 1255 and 1264 MPa with an elongation of 17.6% and 16.7%. The results show an optimum combination of strength and ductility.

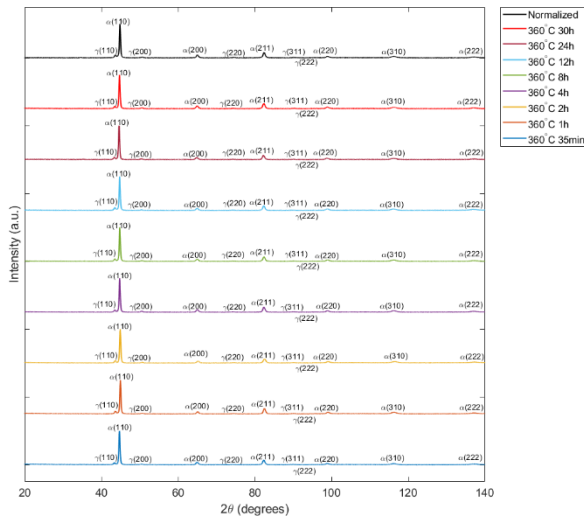


Figure 6. XRD patterns of samples isothermally heat-treated at 360°C, α : Ferrite, γ : Austenite.

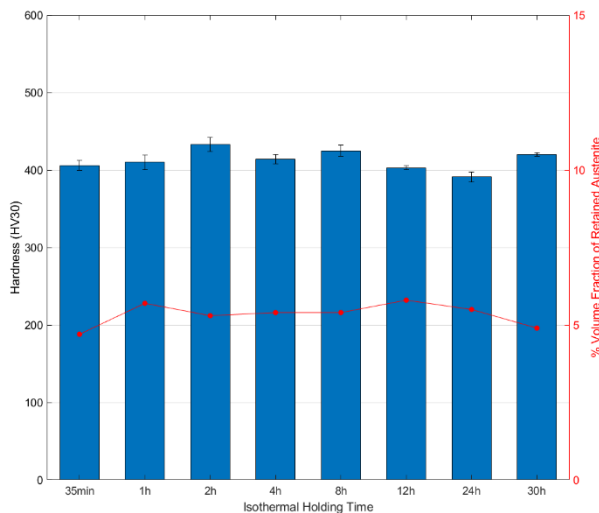


Figure 7. Retained austenite content (in red) and hardness measurements (plotted as a bar chart) of isothermally heat-treated samples at 360°C.

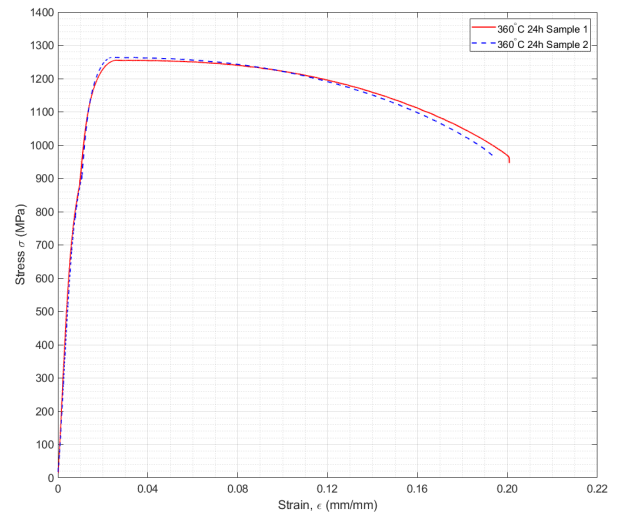


Figure 8. Stress-strain diagram of isothermally heat-treated samples at 360°C for 24 hours.

4. Conclusion

In this study, a bainitic forging steel, microalloyed with V-Ti-Nb with low carbon content was subjected to isothermal transformation at just above M_s , 360°C, to form bainite at varying isothermal holding times. Microstructural and quantitative phase studies were performed. The optimum mechanical properties were obtained after a transformation of 24 hours.

Acknowledgement

The authors would like to thank ÇEMTAŞ A.Ş. R&D Department, and specifically to Emre ALAN, İsmail İrfan AYHAN, Nurten Başak DÜRGER, Caner GÜNEY, and Fatih KAYADEĞİRMENİ for the procurement of the materials.

References

- [1] Wang, Z., Hui, W., Xie, Z., Zhang, Y., & Zhao, X. (2020). Enhancing mechanical properties of a V + Ti microalloyed bainitic forging steel via tailoring microstructure through controlled forging. *Journal of Materials Science*, 55(24), 10849–10862. <https://doi.org/10.1007/s10853-020-04695-3>
- [2] Matlock, D. K., Krauss, G., & Speer, J. G. (2001). Microstructures and properties of direct-cooled microalloy forging steels. *Journal of Materials Processing Technology*, 117(3), 324–328. [https://doi.org/https://doi.org/10.1016/S0924-0136\(01\)00792-0](https://doi.org/https://doi.org/10.1016/S0924-0136(01)00792-0)
- [3] Keul, C., Wirths, V., & Bleck, W. (2012). New bainitic steels for forgings. *Archives of Civil and Mechanical Engineering*, 12(2), 119–125. <https://doi.org/10.1016/j.acme.2012.04.012>
- [4] Buchmayr, B. (2016). Critical Assessment 22: bainitic forging steels. *Materials Science and Technology*, 32(6), 517–522. <https://doi.org/10.1080/02670836.2015.1114272>
- [5] Kesti, V., Kaijalainen, A., Väisänen, A., Järvenpää, A., Määttä, A., Arola, A. M., Mäntyjärvi, K., & Ruoppa, R. (2014). Bendability and Microstructure of Direct Quenched Optim® 960QC. *Materials Science Forum*, 783–786, 818–824. <https://doi.org/10.4028/www.scientific.net/MSF.783-786.818>



- [6] Sourmail, T., Maminska, Dipl.-I., Roth, Dipl.-I., D'eraimo, Dipl.-I., & Galtier, Dipl.-I. (2017). *30 years of bainitic forging steels*.
- [7] Sharma, S., Sangal, S., & Mondal, K. (2011). Development of New High-Strength Carbide-Free Bainitic Steels. *Metallurgical and Materials Transactions A*, 42, 3921–3933. <https://doi.org/10.1007/s11661-011-0797-6>
- [8] Bhadeshia, H. K. D. H. (2005). High Performance Bainitic Steels. *Materials Science Forum*, 500–501, 63–74. <https://doi.org/10.4028/www.scientific.net/MSF.500-501.63>
- [9] Adamczyk-Cieślak, B., Koralnik, M., Kuziak, R., Majchrowicz, K., Zygmunt, T., & Mizera, J. (2022). The Impact of Retained Austenite on the Mechanical Properties of Bainitic and Dual Phase Steels. *Journal of Materials Engineering and Performance*. <https://doi.org/10.1007/s11665-021-06547-w>
- [10] Sugimoto, K., Sato, S., Kobayashi, J., & Srivastava, A. K. (2019). Effects of Cr and Mo on Mechanical Properties of Hot-Forged Medium Carbon TRIP-Aided Bainitic Ferrite Steels. *Metals*, 9(10). <https://doi.org/10.3390/met9101066>
- [11] LePera, F.S. Improved Etching Technique to Emphasize Martensite and Bainite in High-Strength Dual-Phase Steel. *JOM* 32, 38–39 (1980). <https://doi.org/10.1007/BF03354553>
- [12] Zakerinia, Hossein & Kermanpur, Ahmad & Najafzadeh, Abbas. (2009). Color metallography; A suitable method for characterization of martensite and bainite in multiphase steels. *International Journal of ISSI*. 6. 14-18.



EXPERIMENTAL INVESTIGATION AND THEORETICAL EXPRESSION OF THE EFFECT OF STEEL WIRE ROPE PARAMETERS ON BREAKING LOAD

Emre BAŞER^{1,2}, Yıldız ŞAHİN², Murat POLAT¹

¹Çelik Halat ve Tel Sanayii A.Ş., ²Kocaeli University
Türkiye

Keywords: Steel Wire Rope, Breaking Load, Design of Experiment, Taguchi, Response Surface

Abstract

Steel wire ropes are critical carrying elements working under load used in a wide range of applications and various industries made of strands twisted around the core and many wires forming strands. Steel wire ropes are produced with appropriate designs and features to fulfil the expected performance according to the usage area and loading types. There is a minimum breaking load value, which is theoretically calculated with a formula determined by ISO 2408 standard, which is one of these performance properties and which steel wire ropes must provide. According to the existing conditions, the determination of the rope behaviour is only possible by experimentation. The scope of the study is the expression in terms of coefficients of the effects of the steel wire rope parameters on the breaking load. In this study, a suitable design of experiment was created to reveal the effects of the steel wire rope parameters; which are rope lay length ratio, preform ratio in percentage and rope grade in kg/mm² on the breaking load. Experimental and statistical data obtained by tensile tests by the ISO 6892-1 standard of steel wire ropes produced following the experimental design are determined and presented.

1. Introduction

Companies are increasingly taking corrective actions driven by executives. There is an interest in understanding whether by reducing raw material consumption and satisfying customer satisfaction. Steel wire ropes are expected to provide also minimum breaking load which is calculated with a formula determined by ISO 2408 standard due to regulatory requirements in the standard. When customer requirements are fully defined and standard values are provided, all that needs to be done is to reduce the consumption of raw materials and unnecessary labour and machine utilization that contribute to the sustainable profitability of the companies.

In this study, the design of experiment has been used to reveal the effects of parameters on the breaking load of steel wire rope. The study has been executed to give the output of statistical expression of the effect of parameters on the breaking load and solutions to

achieving the target value which is minimum breaking load to reduce the cost. The scope of this study also includes the effect of interaction. Thus, the interaction effects of a variable that is not known have been revealed in the presence of another variable.

2. Design of Experiment

In the design processes, the development of new methods or implementation of new technologies, and determining optimal values cause high cost and unnecessary utilization of machines and labour. Full factorial Design of Experiment (DOE), which is used to examine the effect of parameters, but Taguchi and Response Surface DOE methods are more cost-effective and alternative.

"The Taguchi design method utilises orthogonal arrays, which distribute the variables in a balanced manner, thus greatly reducing the number of experiments required [1]". Taguchi's approach, as a method of identifying the parameters that create variability in the final product, has been adopted worldwide at lower costs. This method aims to determine the optimal levels of the experimental design parameters (also known as control factors).

If there is a wonder about the possibility of improving the results by only changing the level of the parameters that affect the output. Using the response surface method (RSM) is required to explore controllable regions of parameters which vary. Carrying out experiments in some levels of parameters and obtaining the outputs helps to make a prediction of the result that would be obtained in other levels which is not conducted. This helps to better understand whether the system could be improved by varying the parameter levels for the researcher [2].

3. Steel Wire Ropes

Steel wire ropes are used in such industries as elevator, fishing, forestry, iron and steel, marine, industrial cranes and materials handling, building, port, mining, drilling, and oil and gas industries. Rope production should be carried out according to the requirements necessitated by special reasons such as environmental, mechanical and chemical conditions.

Wire ropes consist of wires, strands, and a core. A strand consists of individual wires that are helically twisted around the centre wire and wire rope consists of strands twisted around the core. Wire ropes are called by the number of strands and wires in each strand [3].

3.1. Minimum breaking load

The effects of parameters such as diameter, rope class, and construction on the breaking load, are defined as an MBL factor (K) which is an empirical value. The minimum breaking load is obtained by multiplying the MBL factor with these three parameters for ropes between 2 mm and 60 mm by ISO 2408:2017 standard:

$$F_{min} = \frac{d^2 \times R_r \times K}{1000} [kN] \quad (1)$$

where d is rope nominal diameter [mm]; R_r is rope class [kg/mm²] which determines the strength of each wire; K is the MBL factor empirically determined for each rope construction [4].

4. Steel Wire Ropes Parameters

Considering Byron says, “Generally, the more wires in the rope, the greater the flexibility; also, the smaller the wires, the less abrasion resistance.”, 6x36WS rope is expected to have more service life than 6x19S one [3].

Gerger and Tayanç (1998) confirmed that the fatigue life increased as the wire diameters decreased in their experimental study. Therefore, the service life of the rope made in a large number of small diameter wires instead of in a small number of large diameter wires will be higher. However, it is until the point where even though the tensile strength of the wires increases, the fatigue strength decreases [5].

It also shows that the effect of rope class on the breaking load should be carefully considered. Rope class is the expression of the breaking load of the wires in kg/mm². The processes that the wires go through to have 180 and 220 kg/mm² strength are different, and the effects on the breaking load of the rope are studied to be examined.

In this study, it is desired to reveal the effect of the lay length ratio and preform ratio on the breaking load used as a parameter while designing and producing the rope. The lay length ratio (n) for any strand in a rope twisted is calculated as follows:

$$n = (\text{length of lay}) / (\text{rope diameter}) \quad (2)$$

where l_a is a length of lay. The preform ratio is calculated as follows:

$$\% \text{ pref.} = \frac{(\text{height of twisted strand}) \times 100}{\text{rope diameter}} \quad (3)$$



Figure 1. ‘Lay length’ [6]; ‘preforming’ (respectively)

5. Experimental Procedure

Within the scope of the study, 16 mm steel wire ropes (6x36WS-FC and 6x19S-FC) in the appropriate parameter levels created using the Taguchi experimental design model given in Table 4 were manufactured in Çelik Halat ve Tel Sanayii A.Ş. The wire rods, with chemical composition given in Table 1 following the ISO 16120-2:2011 standard have been processed of wire drawing and patenting to produce steel wire rope.

Table 1. Chemical Composition of hot rolled wire rod.

% C	% Si	% Mn	% P	% S
0.45-0.83	0.20	0.59	0.009	0.009

5.1. Actual breaking load and tensile test

The breaking tests were carried out in the field of tensile testing of steel wire rope following ISO 2408:2017 and ISO 6892-1:2019 standards. Thus, the actual breaking loads (ABL) are obtained and ABL must provide (not below) the minimum breaking load.

The statement of the uncertainty of the 1000 kN tensile test device, in which the experimental studies were carried out, is reported with a coverage factor of $k=2$ (extended uncertainty), which indicates approximate 95% confidence following the document EA-4/02.

5.2. Setup

Experimental design using Taguchi Orthogonal Arrays was created via Minitab Statistical Software with the parameters and their levels as seen in Table 2.

Table 2. Levels of parameters using Taguchi O. Array.

	Lay Length Ratio	Preform Ratio (%)	Rope Class (kg/mm ²)
Level 1	6	75	180
Level 2	6.25	90	220
Level 3	6.5		
Level 4	6.75		

L8 (41; 22) orthogonal array has been selected for both steel wire rope constructions to keep the cost at a minimum. It offers eight models (as shown in Table 3) to explain the levels of the parameters given.

“The signal-to-noise ratio measures how the response varies relative to the nominal or target value under different noise conditions [7]”. The larger is a better option, which maximizes the response determined in the experimental design, was chosen:

$$SN \text{ ratio} = -10 * \log(\Sigma(1/Y^2)/n) \quad (4)$$

Table 3. Orthogonal array using Taguchi O. Array

Lay Length Ratio	Preform Ratio	Rope Class
6.00	75	180
6.00	90	220
6.25	75	180
6.25	90	220
6.50	75	220
6.50	90	180
6.75	75	220
6.75	90	180

6. Result and Discussion

It is seen that the rope class has a major impact on the breaking load of 6x36WS-FC rope in comparison with the preform ratio. Lay length ratio does not affect the breaking load. The model R-sq value was founded in the percentage of 99.99 and the standard deviation of regression is 0.0116. It shows that the P values explain the model consummately.

Table 4. Analysis of Variance for SN ratios

Source	DF	Seq SS	Adj SS	Adj MS	F	P
Lay L. Ratio	3	0.01992	0.0199	0.00664	49.15	0.020
Preform R.	1	0.13305	0.1330	0.13305	984.94	0.001
Rope Class	1	2.06079	2.0607	2.06079	15255.65	0.000
Residual Error	2	0.00027	0.0002	0.00014		
Total	7	2.21403				

The main effect plot describes the influence at selected levels of the parameters (as shown in Figure 2).

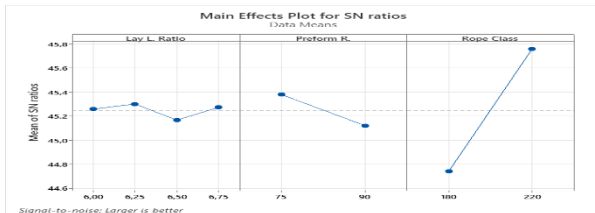


Figure 2. Main effects plot for SN ratios using Taguchi

The rope class which is should be used in the second level to increase the output is the most effective parameter to increase the breaking load of steel wire rope. While the second level of the preform ratio decreases the value of the response variable, the second level of the lay length ratio parameter, which has the least effect on the response variable, has an improving effect (Fig. 2).

The interaction plot explains the effects of the dependence between the parameters. Figure 3 shows that there is an interaction effect between the lay length ratio and the preform ratio. There is no interaction between the preform ratio and the rope class, but it can be seen that the rope class affects the response variable more than the preform ratio. There is also a small interaction effect between the lay length ratio and the rope class.

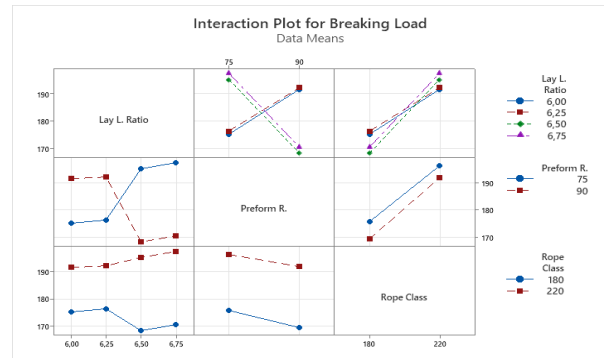


Figure 3. Interaction Plot for Breaking Load using Taguchi Orthogonal Array.

6.1. Custom RSM DOE including both construction

Due to an unexpected situation during manufacturing 220 kg/mm² class 6x19S-FC ropes, the tensile test could not be performed for that class of this construction. Thus, the design of experiment using the custom Response Surface Method which the construction parameter is used in addition to others has been run.

Table 5. Custom RSM DOE test samples

Constr.	Lay L.	Pref. R./Rope C.	Pref. R./Rope C.
6x36WS-FC	6	75-180	90-220
	6.25	75-180	90-220
	6.5	75-220	90-180
	6.75	75-220	90-180
6x19S-FC	6	75-180	-
	6.25	75-180	-
	6.5	-	90-180
	6.75	-	90-180

The breaking load formulas given in Table 6 were estimated for the given parameter levels from the tensile tests of the samples expressed in Table 5. The tensile tests have been performed almost 20 times for each composition expressed in Table 5.

Table 6. Breaking load formulas for given parameters

Const.	Lay L.	Class	Breaking
6x19S	6.00	180	Breaking = 156,47 + 0,0754 Preform Ratio
6x36WS	6.00	180	Breaking = 202,02 - 0,3579 Preform Ratio
6x19S	6.25	180	Breaking = 157,77 + 0,0754 Preform Ratio
6x36WS	6.25	180	Breaking = 203,31 - 0,3579 Preform Ratio
6x19S	6.50	180	Breaking = 155,34 + 0,0754 Preform Ratio
6x36WS	6.50	180	Breaking = 200,89 - 0,3579 Preform Ratio
6x19S	6.75	180	Breaking = 157,04 + 0,0754 Preform Ratio
6x36WS	6.75	180	Breaking = 202,59 - 0,3579 Preform Ratio
6x19S	6.00	220	Breaking = 177,85 + 0,0754 Preform Ratio
6x36WS	6.00	220	Breaking = 223,40 - 0,3579 Preform Ratio
6x19S	6.25	220	Breaking = 179,15 + 0,0754 Preform Ratio
6x36WS	6.25	220	Breaking = 224,69 - 0,3579 Preform Ratio
6x19S	6.50	220	Breaking = 176,72 + 0,0754 Preform Ratio
6x36WS	6.50	220	Breaking = 222,27 - 0,3579 Preform Ratio
6x19S	6.75	220	Breaking = 178,42 + 0,0754 Preform Ratio
6x36WS	6.75	220	Breaking = 223,97 - 0,3579 Preform Ratio

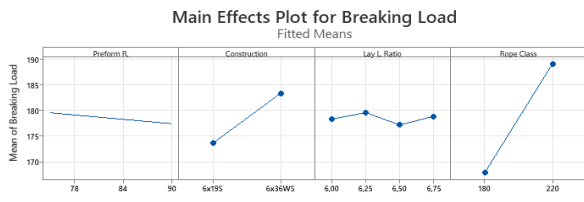
The coefficients of the levels of parameters are the determination of the size of additive or reductive effect on the breaking load. All levels of parameters influence the breaking load except 6 and 6.75 levels of lay length ratio as shown in P values in Table 7. The model R-sg

value is 99.37% and the standard deviation of regression is 1.13424. It shows that the result explains the model consummately.

Table 7. Coefficient of the levels using custom RSM.

Term	Coef	SE Coef	T-Value	P-Value
Constant	178.465	0.179	995.12	0.000
Preform R.	-1.06	0.179	-5.91	0.000
6x19S	-4.899	0.179	-27.31	0.000
6x36WS	4.899	0.179	27.31	0.000
6.00	-0.185	0.274	-0.68	0.502
6.25	1.111	0.274	4.06	0.000
6.50	-1.314	0.274	-4.8	0.000
6.75	0.388	0.274	1.42	0.163
180	-10.689	0.179	-59.6	0.000
220	10.689	0.179	59.6	0.000

The main effect plot describes the influence at selected levels of the parameters (as shown in Figure 4).



All displayed terms are in the model.

Figure 4. Main effect plot using custom RSM.

The rope class and the construction parameters which are should be used in the second level to increase the output are the most effective parameter respectively to increase the breaking load of steel wire rope.

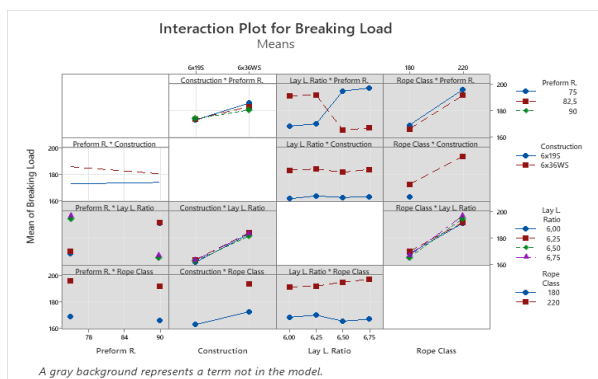


Figure 5. Interaction plot using custom RSM.

Due to the lack of the tensile test data of the 220-rope class of 6x19S-FC steel wire rope, all interaction effect is could not be shown in Figure 5. However, it is shown that between the lay length ratio and the preform ratio, there is an interaction effect in Figure 3. It is also seen that the construction parameter has a large effect compared with the lay length ratio. There is no interaction effect between these parameters.

6.2. Optimization of parameter levels

Considering the rope class which is 220 kg/mm²; the actual breaking load is expected to provide 182 kN which is the minimum breaking load for both constructions to reduce the cost for the manufacturer.

Minitab statistical software offers solutions to optimize the parameter level. The first solution is the desired situation in percentages of 97.9127.

Table 8. The solutions to achieve the minimum breaking load for 220 rope class

	Preform	Lay L. Rope	Breaking	Composite
Solution	Ratio	Constr. Ratio	Class Load Fit	Desirability
1	75	6x19S	6.5	220 182.376 0.978127
2	75	6x19S	6	220 183.505 0.912449
3	75	6x19S	6.75	220 184.078 0.879116

7. Conclusion

Wire ropes, which consist of wires, strands, and a core, must be provided the minimum breaking load following the ISO 2408 standard. The study is executed using the Taguchi and Response Surface Method Design of Experiment to show the optimal level of parameters to reduce costs and achieve the target value which is the minimum breaking load in the design process. Considering the rope class and the construction of steel wire ropes have a larger impact on the breaking load, the optimal parameter levels of 220-rope class are determined as 6x19S-FC, 6.5 lay length ratio, and 75% preform ratio to provide the minimum breaking load.

Acknowledgement

This study was financially supported by The Scientific and Technological Research Council of Turkey (TÜBİTAK) within the scope of the program called 2209-B Industry Oriented Research Project Support Programme for Undergraduate Students. The authors would like to acknowledge R&D Chief Sevim Gökçe Esen and Çelik Halat ve Tel Sanayii A.Ş.

References

- [1] Ballantyne, K. N., R. A. Van Oorschot, and R. J. Mitchell. "Reduce optimisation time and effort: Taguchi experimental design methods." *Forensic Science International: Genetics Supplement Series* 1.1 (2008): 7-8.
- [2] L.A. Sarabia, M.C. Ortiz, Response Surface Method, Ed. S. Brown, R. Tauler, B. Walczak, *Comprehensive Chemometrics*, Elsevier, 2009, 1, 345-390.
- [3] Byron, F. (2021). Failure analysis of galvanized rope in a marine environment. *Materials Performance*, 60(11), 48-51.
- [4] Pfaff, Manfred. "Hulls, Cordage, Superstructures, Anchor Gear, Corrosion Protection, and Deck Coverings." *Ship Operation Technology*. Springer, Wiesbaden, 2022. 13-76.
- [5] Gerger, M. N., and Tayanç M. "Çelik Tel Halatlarda Tel Çapı ve Redüksiyon Oranının Yorulma Dayanımına Etkisi." *Makina Tasarım ve İmalat Dergisi* 3.4 (1998): 167-173.
- [6] Feyrer, K. *Wire ropes*. Berlin: Springer-Verlag Berlin Heidelberg, 2007.
- [7] <https://support.minitab.com> Dated: 02.07.2022

THERMODYNAMIC INVESTIGATION OF KAPPA-CARBIDE PHASE CHANGE IN LOW-DENSITY STEELS

Memduh Kağan KELER^{1,2}, Sibel DAĞLILAR¹, Oğuz GÜNDÜZ², Özcan BAHAROĞLU², Onur KART²

¹Yıldız Technical University, ²Eregli Iron and Steel
Türkiye

Keywords: Low-density steels, Alloy design, Kappa-carbide, Casting, Microstructure

Abstract

Low-density steels are classified as steel grades with high entropy/low-density steels with Fe-Mn-Al-C basic alloying elements. Low-density steels with high Al content, developed since the early 1950s, are evaluated in the automotive industry, cryogenic applications and aerospace fields.

Kappa-carbide phases are one of the crucial structures in low density steels in austenite matrix. In this study, it is investigated that the change in as-cast structure depends on alloy design. Manganese, which is one of the alloying elements, triggers the main phase to be austenite in steel, while Al acts as a ferrite stabilizer. It has been determined that Kappa-carbide formation tends to transition to coarse structure at the grain boundaries as the Al content increases. In order to obtain as-cast structure with high equiaxed ratio, ingot mold casting was carried out in an air induction furnace and homogeneous cooling conditions (thermal insulation, exothermic casting feeder powder, etc.) were applied to the ingot. The activity of the Kappa-carbide phase and its relationship with Al, Mn and the oxygen activity of the liquid steel was evaluated, hereby the metallurgically ideal alloy design was achieved by using some thermodynamic software tool.

1. Introduction

Lightweight steels contain high Aluminum and the density of steel can be decreased with higher Al amount in steel. Due to lower density of the steel material, emissions can be reduced. In this regard, low-density steels are the primary research topic for next generation automotive industry and aviation. Low density steels can be specified into 4 groups as hot rolled microstructure. Ferritic, austenitic, ferrite based duplex and austenite based duplex grades have been categorized depending on the alloy design in literature [1]. Carbon is also variable in chemical

design and the relation between carbon and carbide maker elements (Mn, Al, Cr) are crucial for hot rolling, mechanical results, steel cleanliness and thermodynamic equilibrium.

During melting and solidification, it is important to analyze which carbide formation can occur with different alloying elements. Carbides tend to increase with Manganese and Aluminum amount.

FeMnX and FeMnAlC₃ structures affect the mechanical properties and ductility by optimizing the size and distribution in steel matrix. Keler and his friends found that fine carbides have potential to change their formation into coarser structure with increasing alloying amount in lightweight steels [2].

Some researchers [3-6] focused on carbides' crystal structure, thermodynamic equilibrium stability and their effect on general phases on Fe-Mn-Al-C lightweight system. Isothermal sections were characterized by thermodynamic databases and equilibrium triangles.

Figure 1 shows the effect of Al and C amount for final phase distribution with isothermal sections.

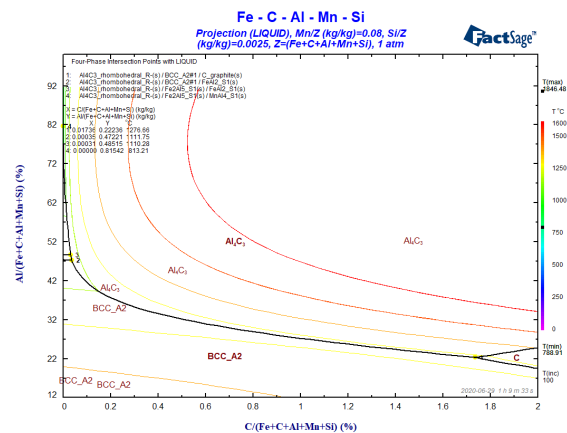


Figure 1. Isothermal Phase Changes in Fe-Mn-Al-C-Si System

In Figure 1, the Manganese amount is determined as 8%, Silicon is 0,25% while Aluminum and Carbon are variable.

Figure 2 indicates that Fe-C phase diagram with constant Al, Mn and Si values. In an addition to Figure 1, the Aluminum amount was chosen as 10% in low-density steel. It is shown that k-carbides tend to increase with Carbon amount. It is clear that below 400°C, more carbide-based precipitates can be occurred.

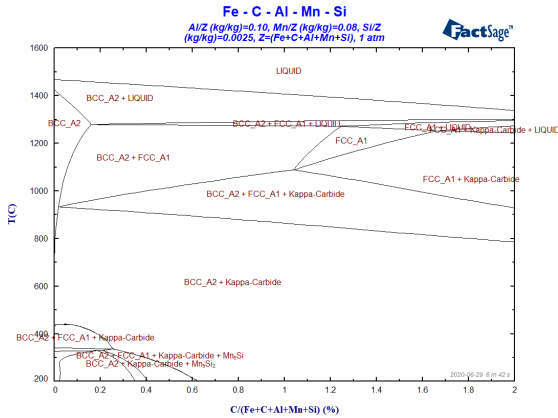


Figure 2. Phase Diagram of Fe-C System and the K-Carbide Formation

Figure 3 includes k-carbide phase transformation during solidification in reference alloy system of low-density steel. The concept of this steel contents of 0,15 % C, 8% Mn, 10% Al and 0,25% Si. It is observed that k-carbide phase components are Fe₃AlC, Fe₃MnC, Fe₃FeC, Mn₃FeC, Fe₃Mn and Mn₃C.

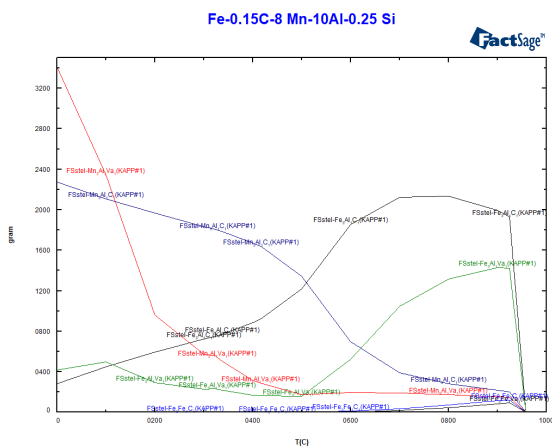


Figure 3. Phase Transformation of Kappa-Carbide in Fe-Mn-Al-C System During Solidification

2. Experimental Procedure

In order to determine under which conditions the kappa carbide phase distribution occurs, different

alloy designs were carried out by making an experimental design. Some metallurgical tools have been used for the chemical concept of low-density steel grades. For understanding the mechanism of kappa-carbide formation, FactSage 7.3 and JMatPro computational thermodynamic software have been used. After these calculations, casting and rolling studies have been finished.

For melting process, an induction melting furnace was used as heating equipment. The mold material was chosen as GGG-20 and the dimensions of the final product was 200x350x500 mm. Iron based-scrap was used for base material. Ingot aluminum was added to the furnace after melting and the yield of Aluminum was more than 70%. Ferro-manganese with high carbon content was used as an alloying element. The chemical composition of low-density steel ingot-1 was given in Table 1.

Liquidus temperature was calculated as 1372,17 °C and the phase transformations while solidification was identified with FactSage 7.3 computational simulation package. FStel database was selected and used to calculate phase activities and solidification patterns.

Table 1. Chemical Analysis of Lightweight Steel Alloy-I

C	Mn	Al	Si	Cr	V	Fe
0,75	11,9	14,2	0,33	0,08	0,05	Bal.

Solidus temperature was calculated as 1187,90 °C and k-carbide formation was detected below the temperature of 1214,27 °C. Figure 4 demonstrates the cooling reactions from liquidus point to solidus temperature.

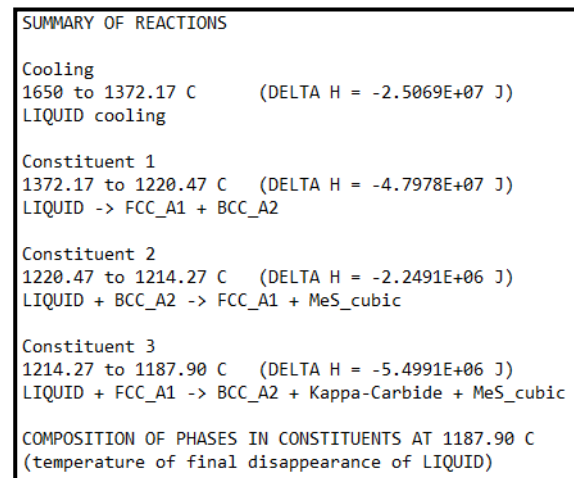


Figure 4. Cooling Transformations of Alloy-I

Chemical analysis of low-density steel ingot-2 (Alloy-II) was given in Table 2. Liquidus temperature of ingot-2 was calculated as 1517,17 °C.

Table 2. Chemical Analysis of Lightweight Steel Alloy-II

C	Mn	Al	Si	Cr	Nb	Fe
0,095	2,48	4,83	0,24	0,02	0,019	Bal.

Solidus temperature of ingot-2 was modelled as 1431,38 °C with the FactSage FSstel dataset. Phase transformations during solidification was specified below. Unlike Alloy-I material, the kappa carbide phase does not seem to occur between liquidus and solidus temperatures in Alloy-II material.

SUMMARY OF REACTIONS	
Cooling	
1655 to 1517.17 C	(DELTA H = -3.2956E+07 J)
LIQUID cooling	
Constituent 1	
1517.17 to 1438.06 C	(DELTA H = -1.0320E+08 J)
LIQUID -> BCC_A2	
Constituent 2	
1438.06 to 1431.38 C	(DELTA H = -2.2066E+06 J)
LIQUID -> BCC_A2 + MeS_cubic	
COMPOSITION OF PHASES IN CONSTITUENTS AT 1431.38 C (temperature of final disappearance of LIQUID)	

Figure 5. Cooling Transformations of Alloy-II

3. Results and Discussion

Alloy-I and Alloy-II materials produced in an induction furnace. Both alloy systems were produced to see the final results in as-cast structure and phase effect. The activity and final amount of k-carbide phases have been detected via Gibbs energy minimization principle at thermodynamic equilibriums. After pilot-scale melting and casting operations, studies have focused more on the Alloy-II system. Also, it is evaluated that Alloy-II system has more potential to use for industrial scale production and rolling due to its chemical concept.

Figure 6 shows the correlation between activity and total phase content at Alloy-II low-density steel. It is investigated that activity of k-carbide phase starts to initiate below 1000°C while the physical formation starts under 800°C. Hence, this formation relates with Fe_xAlC_x type of k-carbide. It is also observed that below 950°C, Fe_xMnC_x type of carbides also consist in Alloy-II cooling equilibrium system.

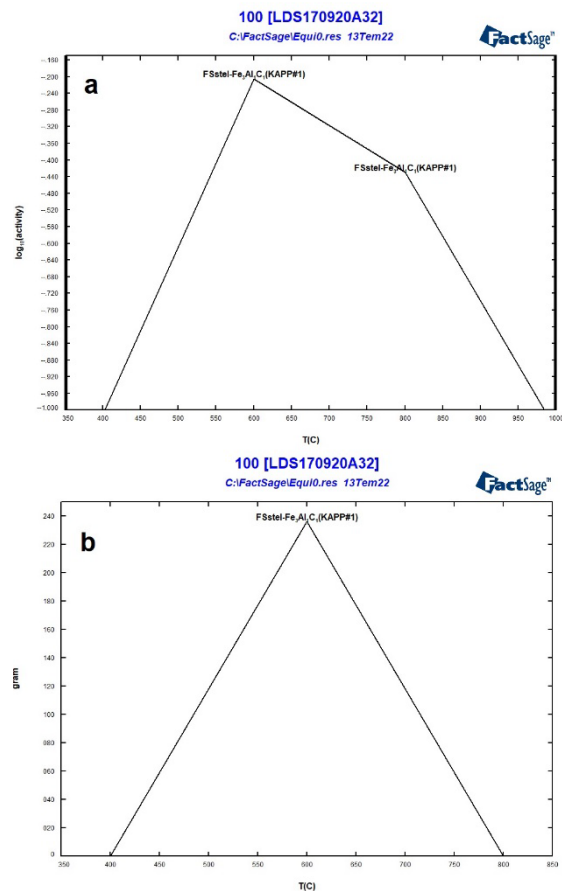


Figure 6. Relation between the K-carbide phase activity and phase weight in Alloy-II system; a) Activity Change of Fe_3AlC Phase in Logarithmic Scale, b) Total Change of Fe_3AlC Phase in 100 kg Low-Density Steel Sample

Phase diagram of Alloy-II system was given in Figure 7. The structure was observed as ferritic and austenitic duplex because of high Al and Mn content. In microstructure investigation, carbides and Al based k-carbides have been detected.

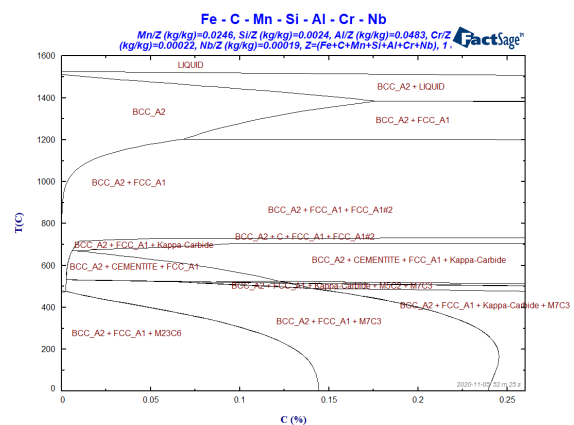


Figure 7. Phase Diagram of Alloy-II System

Microstructure inspections obligate that carbide formations occur in as-cast structures at austenitic-ferritic matrix. Figure 8 shows the coarser or needle type κ -carbide formations behind equiaxed grains. SEM results showed carbides include Mn, Al and C peaks with Si or Nb elements.

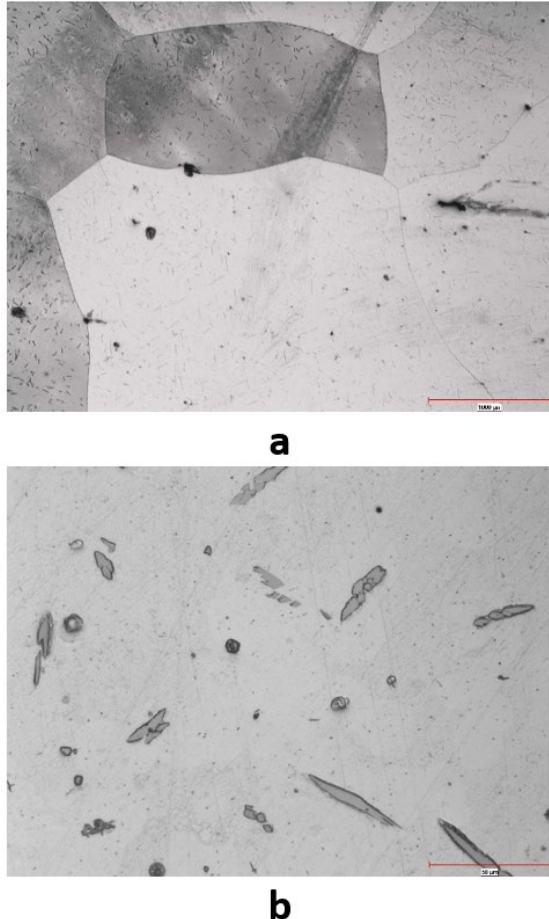


Figure 8. Optical Images with a)25X Magnification and b)500X Magnification

4. Conclusion

This study showed that the Manganese amount of steel affects the as-cast matrix with austenitic structure. It is investigated that the change in as-cast structure depends on alloy design. Manganese, which is one of the alloying elements, triggers the main phase to be austenite in steel, while Al acts as a ferrite stabilizer. It has been determined that Kappa-carbide formation tends to transition to the coarse structure at the grain boundaries as the Al content increases in the steel.

Acknowledgment

The authors would like to acknowledge that this paper is submitted in partial fulfilment of the requirements for PhD degree at Yildiz Technical

University. The authors also thank Ereğli Iron and Steel (ERDEMİR) Research and Development team for their support.

References

- [1] Chen, S., Rana, R., Haldar, A., & Ray, R. K. (2017). Current state of Fe-Mn-Al-C low density steels. *Progress in Materials Science*, 89, 345-391.
- [2] Keler, M. K., Daglilar, S., Kuskonmaz, N., Cetin, Z., Kart, O., Gunduz, O., & Gunduz, O. (2022). Casting of Fe-(2–12) Mn-(4–14) Al-(0.09–0.7) C low-density steel via artificial slag practice. *Materials Letters*, 319, 132277.
- [3] Chen, P., Li, X., & Yi, H. (2020). The κ -carbides in low-density Fe-Mn-Al-C steels: A review on their structure, precipitation and deformation mechanism. *Metals*, 10(8), 1021.
- [4] Chin, K. G., Lee, H. J., Kwak, J. H., Kang, J. Y., & Lee, B. J. (2010). Thermodynamic calculation on the stability of (Fe, Mn) 3AlC carbide in high aluminum steels. *Journal of alloys and compounds*, 505(1), 217-223.
- [5] Liu, D., Cai, M., Ding, H., & Han, D. (2018). Control of inter/intra-granular κ -carbides and its influence on overall mechanical properties of a Fe-11Mn-10Al-1.25 C low density steel. *Materials Science and Engineering: A*, 715, 25-32.
- [6] Bartlett, L. N., Van Aken, D. C., Medvedeva, J., Isheim, D., Medvedeva, N. I., & Song, K. (2014). An atom probe study of kappa carbide precipitation and the effect of silicon addition. *Metallurgical and Materials Transactions A*, 45(5), 2421-2435.

THE MODELING OF MECHANICAL PROPERTIES OF LOW-CARBON GRADE (SAE J403:2014 1006, SAE J403:2014 1008, SAE J403:2014 1010) WIRE ROD STEELS

Ahmet SAĞLAM, Burcu SOYSAL ATAN, İlker AYÇİÇEK, Hamdi GÜL, Mustafa TÜRKMANİ, Mehmet Eriş DURUMUŞOĞLU, Abdurrahman Mesud ÇAKIR

İskenderun Demir ve Çelik A.Ş.
Türkiye

Keywords: Statistical Modelling, Regression, Minitab, Optimization, Tensile Strength, Wire Rod, Low Carbon, Steel

Abstract

600.000 tons wire rod are produced in İskenderun Demir ve Çelik Inc. Co. (İSDEMİR) annually in 2020. In wire rod mill production are divided according to application of wire rod that are wire, high carbon, pin bolt, bolt and welding wire in the range of Ø 5,5 and Ø16 mm diameter. 15 % of total production is SAE J403:2014 1006, SAE J403:2014 1008, SAE J403:2014 1010 grades. İskenderun Iron and Steel Inc. (ISDEMİR) grades 1.1006_00, 1.1008_00 ve 1.1010_00, which belongs to SAE J403:2014; they are the class of carbon steels carbon steels for wire drawing manufacturing. In the study, experiments were made with different cooling rates and modeling was done with regression analysis. As a result of the experiments and analysis obtained with the experimental design, a mathematical model was obtained that explains the tensile strength at the rate of 66,6%. The optimum levels of the input factors were determined in line with the mathematical model obtained. When the production results are examined, an improvement of 49.4% in the standard deviation value of the tensile strength values in 1.1006_00 grade, 29.4% in 1.1008_00 grade and 50.2% in 1.1010_00 grade compared to previous productions.

1. Introduction

SAE J403:2014 1006, SAE J403:2014 1008, SAE J403:2014 1010 grade steels are suitable thin wire drawing and are used in many fields. İskenderun Iron and Steel Inc. (ISDEMİR) grades 1.1006_00, 1.1008_00 ve 1.1010_00 and produced between Ø5,5-16 mm.

The billet with 130X130 mm dimensions is annealed in the Wire Rolling Mill Reheating Furnace. It is reduced to Ø 40 mm diameter after 9 stands in roughing mill group, Ø25 mm diameter after 4 stands in 1st intermediate mill group, and Ø18 mm after 2 stands in group 2nd intermediate mill group.

The main customers' requirements for this grade are good wire drawability for the same steel grade, low variability and low tensile strength values are expected in different heats. Tensile strength directly affects drawability, formability and productivity in the customer process. Typical chemical composition and mechanical properties for this grade of the previous trials were given in Table 1.

Chemical Composition (%)				Mechanical Properties	
1.1006_00				Tensile Strength (MPa)	
Typical Range	Min		0,245	Min	-
	Max	0,075	0,355	Max	400

Chemical Composition (%)				Mechanical Properties	
1.1008_00				Tensile Strength (MPa)	
Typical Range	Min	0,035	0,295	Min	-
	Max	0,085	0,505	Max	410

Chemical Composition (%)				Mechanical Properties	
1.1010_00				Tensile Strength (MPa)	
Typical Range	Min	0,08	0,345	Min	-
	Max	0,125	0,455	Max	420

Table 1. Chemical composition and mechanical properties

Therefore, this study aims to provide customer requirements by optimizing process parameters.

1.1 Analysis of 1.1006_00 Grade

In the study, it is aimed to produce 1.1006_00 grade tensile strength value lower than 400 MPa with a production with a lower standard deviation and a lower total defect rate. According to the test results of the coils produced with a cooling rate of approximately 4.5 °C/sec before the study, the average tensile strength value is 395,52 MPa, the standard deviation value is 10.11 MPa, and the total defect rate is 32,87% (Figure 1).

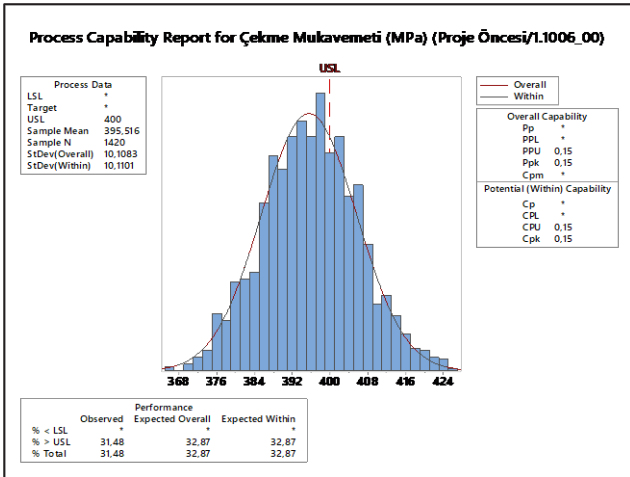


Figure 1. Process Capability Graph of 1.1006_00 Grade

1.2 Analysis of 1.1008_00 Grade

In the study, it is aimed to produce 1.1008_00 grade tensile strength value lower than 410 MPa with a production with a lower standard deviation and a lower total defect rate. According to the test results of the coils produced with a cooling rate of approximately 4.5 °C/sec before the study, the average tensile strength value is 402,91 MPa, the standard deviation value is 11,93 MPa, and the total defect rate is 27,62% (Figure 2).

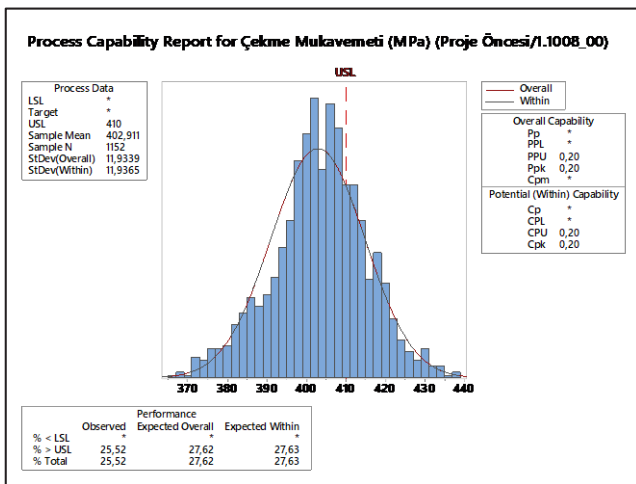


Figure 2. Process Capability Graph of 1.1008_00 Grade

1.3 Analysis of 1.1010_00 Grade

In the study, it is aimed to produce 1.1010_00 grade tensile strength value lower than 420 MPa with a production with a lower standard deviation and a lower total defect rate. According to the test results of the coils produced with a cooling rate of approximately 4,2 °C/sec before the study, the average tensile strength value is 427,78 MPa, the standard deviation value is 9,89 MPa, and the total defect rate is 78,43% (Figure 3).

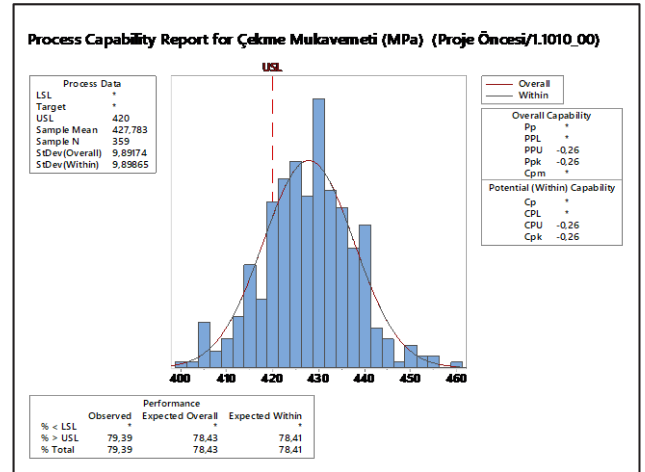


Figure 3. Process Capability Graph of 1.1010_00 Grade

2. Experimental Procedure

The effect of cooling rate on mechanical properties was examined. Advance CCT and TTT diagrams were created in JMatPro software in accordance with the chemical composition. According to the analysis of grades, the Advance CCT and TTT diagrams were created in Figure 4-6 in JMatPro software were prepared and possible phases and rates were determined according to the cooling ratio.

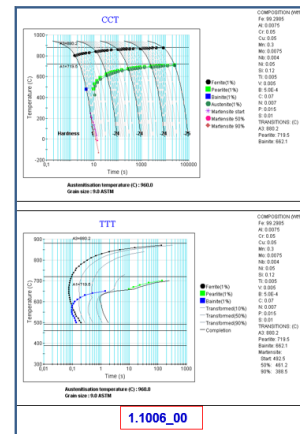


Figure 4. TTT and CCT diagrams of 1.1006_00

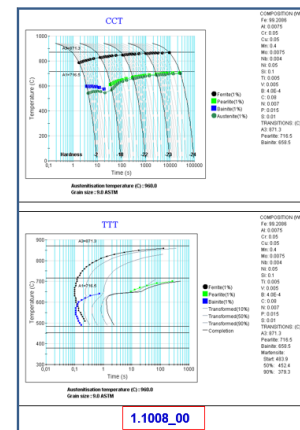


Figure 5. TTT and CCT diagrams of 1.1008_00

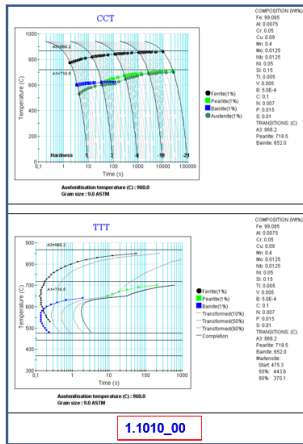


Figure 6. TTT and CCT diagrams of 1.1010_00

Industrial trials were done after preliminary studies. According to the diagrams obtained, wire rod produced with variable fan practices in similar chemical compositions, were subjected to cooling with a cooling rate of approximately 2,5°C/sec. As a result of the trial productions mechanical properties were evaluated.

3. Results and Discussion

A certain number of analysis samples were taken to determine the tensile strength of the coils produced within the scope of the experimental design. The experiments created for each grade were analyzed via MiniTab® software. Mechanical tests were performed on wire samples in accordance with TS EN ISO 6892-1 standard. The tensile strength values obtained together with the data created in the grade of 1.1006_00 were analyzed. According to the test results of the coils produced with different cooling rates depending on the analysis, the average tensile strength value is 388,91 MPa, the standard deviation is 5,12 MPa, and the total defect rate is 1,52%.

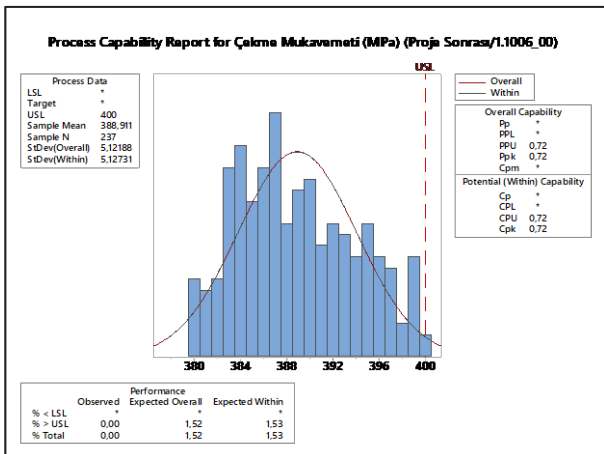


Figure 7. Process Capability Graph of Class 1.1006_00 After Project

According to the data of 1.1008_00 grade, the average tensile strength value is 396,75 MPa, the standard deviation is 8,42 MPa, and the total fault rate is 5,78%.

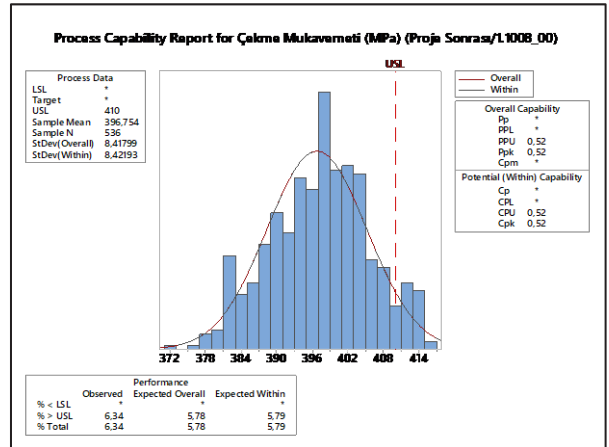
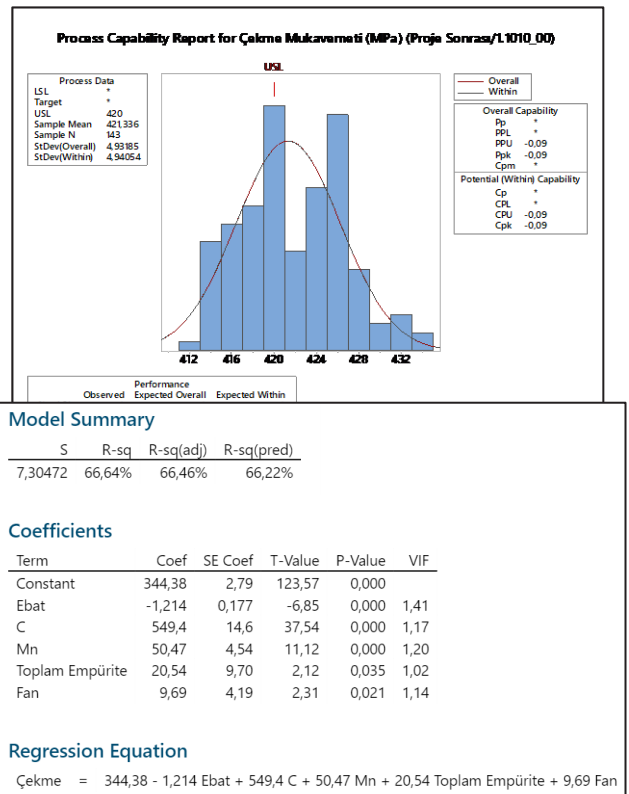


Figure 8. Process Capability Graph of Class 1.1008_00 After Project

According to the test results of 1.1010_00 grade coils, the average tensile strength value is 421,34, the standard deviation value is 4,93 MPa, and the total total defect rate is



60,07%.

Figure 9. Process Capability Graph of Class 1.1010_00 After Project

Figure 10. Regression Model of Tensile Strength (1.1006_00, 1.1008_00, 1.1010_00)

A strong mathematical model with an R_2 (adj) value of 66.46% was obtained for the tensile strength by analyzing the experiments created for these qualities via MiniTab® software. The standard deviation of the model is 7.3 MPa.

4. Conclusions

In this study, the tensile strength values obtained together with the mathematical modeling created for the grades 1.1006_00, 1.1008_00 and 1.1010_00 were analyzed. The trials are designed according to the cooling patterns determined according to Advance CCT and TTT diagrams of the JMatPro software.

With the wire rods produced with constant laying head temperature, trial productions were made with different sponge applications.

The results obtained within the scope of the study are summarized below (Table 2).

For 1.1006_00 grade;

- In the standard deviation value, 49,4% improvement was achieved compared to the pre-project situation.
- An improvement of 95,38% was achieved in the % total defect rate value.

For 1.1008_00 grade;

- An improvement of 29,4% was achieved in the standard deviation value compared to the pre-project.
- An improvement of 79,07% was achieved in the % total defect rate value.

For 1.1010_00 grade;

- In the standard deviation value, 50,2% improvement was achieved compared to the pre-project situation.
- An improvement of 23,41% was achieved in the % total defect rate value.

As a result;

- A mathematical model of tensile strength was created for the studied grades.
- Customer satisfaction was increased by reducing the variation in strength between castings.
- Deflection rate has decreased in coils due to strength.
- A mathematical model specific to ISDEMIR has been created.
- Systematic working conditions were provided in the field, depending on the mathematical model created.
- With Variable Fan practices, approximately 936,582 kWh/year energy savings were achieved.

Grade	Tensile Strength Average (MPa)		Tensile Strength Variability (MPa)	
	Before Project	After the Project	Before Project	After the Project
1.1006_00	395,52	388,91	10,11	5,12
1.1008_00	402,91	396,75	11,93	8,42
1.1010_00	427,78	421,34	9,89	4,93

Table 2. Comparison of Before and After Project

MODELLING OF MONOBLOCK LOADS BY QUALITY BASED PROCESS PARAMETERS TO ENSURE OPTIMUM PRODUCTION SPEED AT WIRE ROD MILL

Hamdi GÜL¹, Hasan Ozan TEMİZ¹, Mustafa Özden ÖZDEMİR¹, Tayfun KOCABAŞ²,
Abdurrahman Mesud ÇAKIR¹, Fatih ÇELİK¹, Burcu SOYSAL ATAN¹

¹İskenderun Demir ve Çelik A.Ş., ²Oyak Maden Metalurji
Türkiye

Key Words: Wire Rod Mill, Monoblock, Load, Vibration, CART Analysis (Classification and Regression Trees), Multiple Linear Regression Analysis.

Abstract

600.000 tons wire rod are produced in İskenderun Demir ve Çelik Inc. Co. (İSDEMİR) annually in 2021. In wire rod mill production are divided according to application of wire rod that are wire, high carbon, pin bolt, bolt and welding wire in the range of Ø 5,5 and Ø16 mm diameter. 130-130 mm billets pass through roughing mill, 1st intermediate mill and 2nd intermediate mill and monoblock and reach the final diameter. Both of rolling speed, vibration and load are related to each other. The vibration level of block stand is always monitored and when the vibration level is high, rolling speed is decreased to control the vibration. Due to the higher block loads and vibration level during the production of high carbon&low carbon steel qualities carried out in 2021, the rolling speed was lower than normal. In this study, the factors that affect monoblock loads of 5,5 mm diameter high carbon and low carbon steel quality are determined by CART analysis and multiple linear regression method and optimum rolling speed has been obtained. The total wire rod production of these steel qualities increased due to the increase in the rolling speed.

1. Introduction

Sudden peaks exceeding 110% in block loads and an average load of more than 85% during production can lead to a decrease in the service life of rolling equipment and sudden failure stops.

In order to prevent these situations from happening, block loads were kept under control by reducing the rolling speed at the moments when block loads increased.

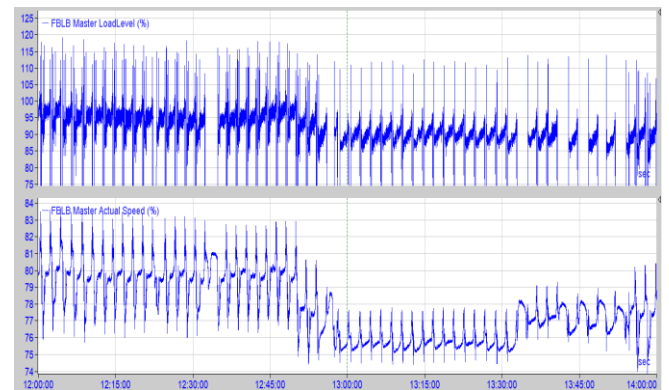


Figure 1. Relationship between FBLB master load and FBLB master actual speed in Iba Analysis

2. Experimental Procedure

In the production of Mesh and High Carbon quality products carried out in 2021; due to the high block loads and vibrations, the rolling speed is lower level than usual.

QUALITY	SIZE	Group	AVG SPEED	AVG LOAD	QUALITY	SIZE	Group	AVAGE SPEED	AVAGE BLOCK
5.3006_01	5,5	Mesh	77,8	70,2	5.1065_00	5,5	HS	77,3	77,2
5.3006_01	5,5	Mesh	77,8	70,5	5.1065_00	5,5	HS	76,9	77,5
5.3006_01	5,5	Mesh	77,9	71	5.1065_00	5,5	HS	76,9	77,6
5.3006_01	5,5	Mesh	77,9	71	5.1065_00	5,5	HS	76,8	77,6
5.3006_01	5,5	Mesh	77,8	70,1	5.1065_00	5,5	HS	76,8	77,5
5.3006_01	5,5	Mesh	77,7	71	5.1065_00	5,5	HS	77	77,5
5.3006_01	5,5	Mesh	77,6	69,7	5.1065_00	5,5	HS	77	77,8
5.3006_01	5,5	Mesh	77,7	69,7	5.1065_00	5,5	HS	77,1	77,9
5.3006_01	5,5	Mesh	77,8	70,8	5.1065_00	5,5	HS	77,1	77,3
5.3006_01	5,5	Mesh	77,6	70,7	5.1065_00	5,5	HS	77,4	77,1
5.3006_01	5,5	Mesh	77,8	70,1	5.1065_00	5,5	HS	77,1	77,2
5.3006_01	5,5	Mesh	77,6	70,3	5.1065_00	5,5	HS	77,2	77
5.3006_01	5,5	Mesh	77,9	70,7	5.1065_00	5,5	HS	77,5	76,9
5.3006_01	5,5	Mesh	77,7	69,7	5.1065_00	5,5	HS	77,1	76,6

Figure 2. Average speed and load in 5.3006_01 and 5.1065_00 quality

Block machine vibrations are constantly monitored during production. If the vibration rises, the rolling speed is reduced in a controlled way to keep the vibrations under control.

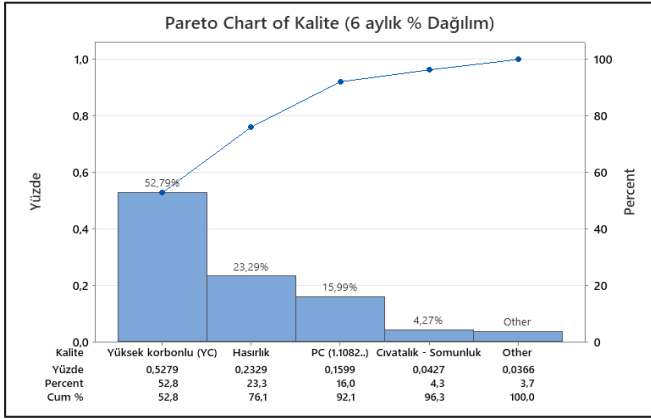


Figure 3. Pareto Analysis of Wire Rod Qualities (2021/2nd 6 months)

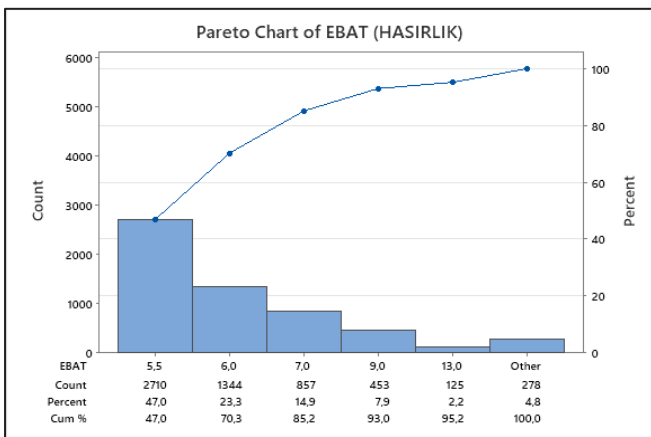


Figure 4. Pareto Analysis of Low Carbon Steels – Size Distribution (2021/2nd 6 months)

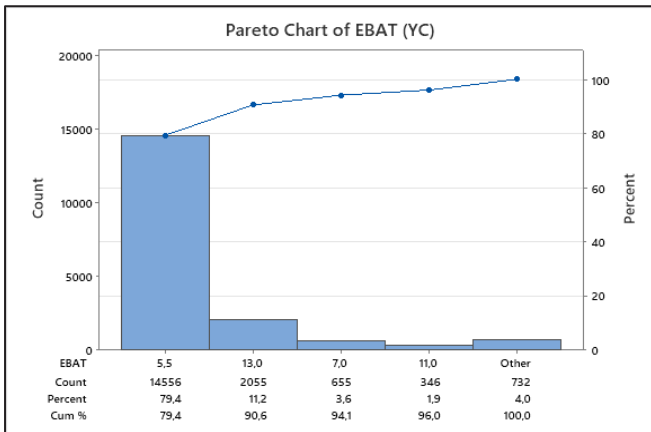


Figure 5. Pareto Analysis of High Carbon Steels – Size Distribution (2021/2nd 6 months)

A data set was prepared on approximately 53,000 process data including B line productions in 2021, and then statistical analysis was carried out on these parameters: monoblock inlet temperature, furnace exit temperature, monoblock inlet ring diameter, monoblock bench vibrations, rolling speed, size, quality, descaler pressure.

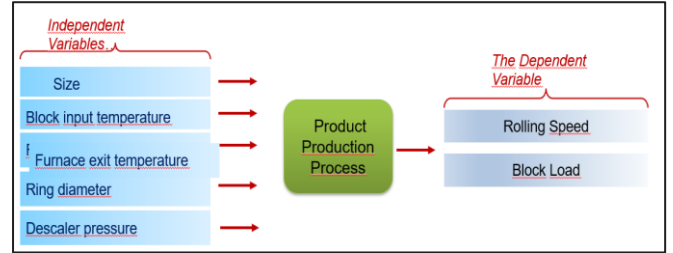


Figure 6. Multiple Linear Regression Analysis

For low carbon steels with the diameter 5,5 cm, multiple linear regression analysis method was carried out and mathematical models with R-sq (adj) is greater than 90% have obtained.

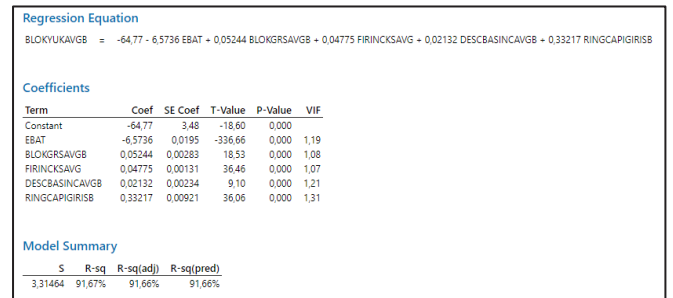


Figure 7. Statistical Model Studies B-Line Mesh Quality 5.5 mm Size (Low Carbon Steel Qualities-Block Load)

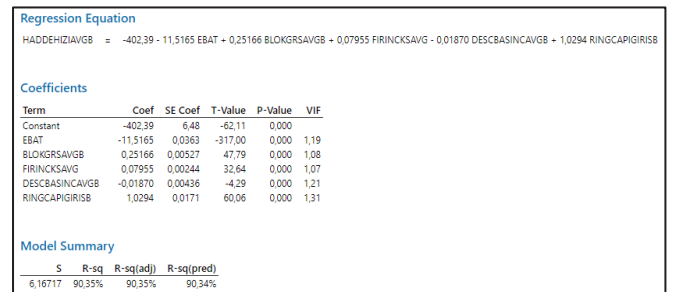


Figure 8. Statistical Model Studies B-Line Mesh Quality 5.5 mm Size (Low Carbon Steel Qualities-Rolling Speed)

At the same time, in the annual planned maintenance, the chassis anchors and studs of the monoblock reducer were checked. After that, the sections deemed necessary were repaired and the reducer connection points were strengthened by adding new anchors to some areas.

Within the scope of high carbon quality (5.5-6 mm, 5.1065 quality) production, vibration and process parameters were examined and CART analysis was performed.

Classification and regression trees are one of the methods used to analyze large and complex data sets. CART is a nonparametric statistical method that uses decision trees to solve classification and regression problems using both qualitative and quantitative variables. CART provides insights for a wide range of applications, including quality control studies in manufacturing, drug discovery, credit scoring, and loss forecasting.

As a result of the analysis, the levels of the factors were determined to achieve the optimum rolling speed that can be achieved compared to the block load and vibration effects.

3. Conclusion

- The mesh quality (5.5-6 mm, 1.1006); when the block inlet temperature is between 1000-1010°C, the rolling speed is increased to 81.3 m/s after the project while the speed was 78.9 m/s before the project. In this context, the gain obtained was 2.7 tons/hour for 5.5 mm and 3.1 tons /hour for 6 mm.
- High steel quality (5.5-6 mm, 5.1065); thanks to the CART analysis results, the speed increased from 78.5 m/s before the project to 79.6 m/s after the project. In this context, the gain obtained was realized as 1.2 tons/hour for 5.5 mm and 1.3 tons/hour for 6 mm.

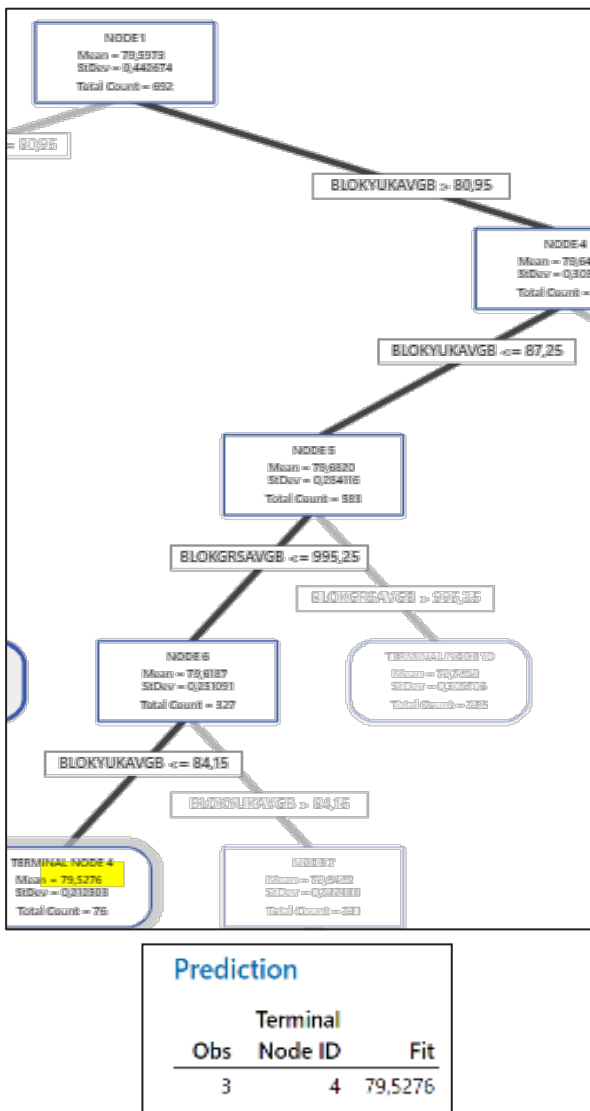


Figure 9. Statistical Model Studies – CART Analysis B-Line Mesh Quality 5.5 mm Size (High Carbon Steel Qualities)



REDUCTION OF EMISSIONS WHILE REMOVING DUST FROM ISDEMIR NEW BLAST FURNACE DUST CATCHER

Onur Hüseyin MEMİŞ, Ümit GEBENLİ, İbrahim ÇAKMAK, Mustafa BAŞSU

İskenderun Demir ve Çelik A.Ş.
Türkiye

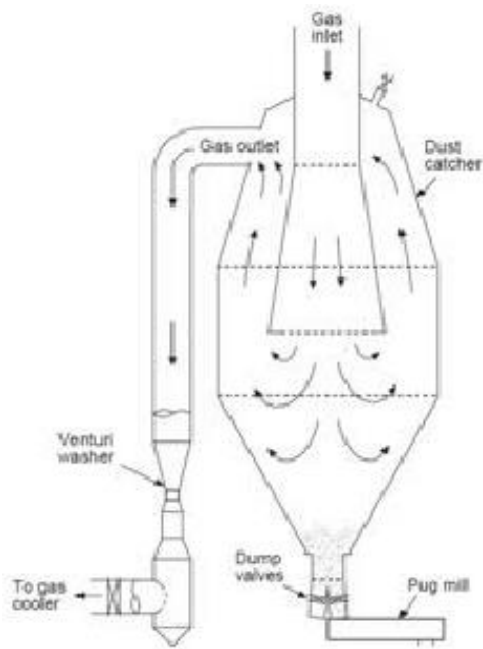
Key words: Blast Furnace, Emission, Dust Catcher, Occupational Health and Safety, Environment, Process Safety, Dust, Blast Furnace Gas, Top Gas

Abstract

İskenderun Iron and Steel Co. Inc. (ISDEMİR) New Blast Furnace No.1 will be commissioned as Turkey's largest blast furnace with a working volume of 3072 m³ and a daily production capacity of 7900 tons of liquid raw iron. It is important for the environment and process safety to keep the byproducts of this blast furnace, which has a large production capacity, under control. One of the outputs of the blast furnace is blast furnace gas. The gas, which comes under pressure to the dust catcher system, first hits an impact surface and spills some of the coarse dust it contains with the effect of gravity. At the same time, due to the shape of the dust trap, the pressurized blast furnace gas creates a vortex inside and leaves more dust. At the same time due to the shape of the dust trap, the pressurized blast furnace gas creates a vortex inside and leaves more dust. Blast furnace gas, which is a dirty gas, comes out as semi-dirty gas from the dust catcher and is cleaned by the other equipment of the gas cleaning system. It is very important for process safety to regularly discharge the dust left by the blast furnace gas to the dust catcher. While these dusts are being discharged, controlled irrigation is carried out by means of nozzles in order to minimize dust emission to the environment. In general applications, these dusts are taken into the truck bed. In ISDEMİR New Blast Furnace No.1, these powders will be taken to the bulk trailer as an alternative. In this way, minimum emission and minimum environmental pollution are foreseen and dust catcher design is made in this way. In this study, it will be explained how the dust emission is prevented and how it contributes to the environment and the blast furnace process with the improvements made in the design of the dust catcher system in the ISDEMİR New Blast Furnace No.1.

1. Introduction

ISDEMİR New Blast Furnace No.1, will be commissioned as Turkey's largest blast furnace with a working volume of 3072 m³ and a daily production capacity of 7900 tons of liquid raw iron. Keeping the outputs of Blast Furnace No. 1, which has a large production capacity, under control is important in terms of environment and process safety. One of the outputs of the blast furnace is blast furnace gas. Blast Furnace gas is cleaned in a few steps in the gas cleaning system and included in the system for reuse. The gas outlet pipes in the blast furnace top system are called trouser pipes/downcomers. Blast Furnace gas leaves the furnace through these pipes and comes to the dust catcher. The dust catcher is the first element of the gas cleaning system. The blast furnace gas is partially cleaned in the dust catcher. The gas from the dust catcher is called semi-contaminated gas. The dust catcher is similar in shape to a silo shape.



Picture 1. Dust Catcher Principle

2. How Does the Dust Catcher Work?

Dust catcher is a gas cleaning system that provides the removal of coarse-grained dusts when the gas is dry, based on the centrifugal principle. Efficiency is affected by particle size distribution, gravity or centrifugal force. It aims to get the gas free of dust as much as possible before wet cleaning. Blast Furnace gas from the top of the blast furnace enters the dust trap axially through a conical inlet section. A vortex is created in the separation chamber of the dust catcher by means of guide vanes. The resulting centrifugal force pulls the dust particles contained in the gas onto the chamber wall. The separated particles slide down the chamber wall into the dust collection chamber. The gas flow is directed upwards by the cone at the bottom of the separation chamber. The cleaned gas (semi-contaminated gas) exits the dust catcher via the inner outlet line above the separation chamber. The dust collection chamber must be emptied continuously. The dust discharge will stick through the dust discharge system. The dust catcher discharge system has a discharge line with an intermediate chamber. Thanks to a special valve added to the upper part of this intermediate chamber, the connection between the discharge chamber and the blast furnace line will be disconnected during the dust discharge process, and it will be possible to safely discharge. In this way, the process will be prevented from being affected. The dust accumulated in the intermediate chamber is discharged by means of the spiral (pug mill) at the bottom. Continuity of dust removal is important for process safety.



Picture 2: Main guide vanes and inner outlet at the top of the dust catcher separation chamber; (from bottom to up view) [1]



Picture 3. Conical inlet section of the axial dust catcher (axial cyclone) [1]

3. Advantages of İSDEMİR New Blast Furnace No.1 Dust Catcher System

İSDEMİR's new Blast Furnace No.1 will have a daily production capacity of 7900 tons of liquid raw iron. Therefore, the gas output and the amount of dust will be quite high. Therefore, the safety of the dust catcher system is important. At the same time, environmental safety should be ensured by keeping the environmental emissions at a minimum during the discharge of this system. In accordance with İSDEMİR's zero waste policy, some systems that prevent environmental emissions are foreseen in the New Blast Furnace No.1 dust catcher system. One of them is to take the dust accumulated in the dust catcher chamber into tankers called silobas. Normally, the dust discharge process is carried out in the form of unloading into the truck bed. During the discharge of the dust catcher system, gas inlet to the dust catcher and thus pressure input continues. When the amount of dust in the chamber is reduced to a minimum, gas and dust emission can occur by

blowing with this pressure effect. In order to minimize this, or even reduce it to zero, dust removal alternative has been added to the bin in the new Blast Furnace No.1 dust holder. A trailer is a tanker-shaped vehicle. The discharge line of the dust catcher is connected to the tanker inlet of the silo by means of a hose, allowing the dust to be discharged without emission to the environment. Thus, environmental pollution is prevented to a great extent during the realization of an operation that must be carried out continuously. Another advantage of İSDEMİR New Blast Furnace No.1 dust catcher is to prevent the furnace top pressure drop that will occur in case the dust catcher blows. The blowing of the dust catcher causes the furnace top to become open to the atmosphere. This will cause both gas emission to the environment and a sudden decrease in the furnace top pressure. The sudden drop in the furnace top pressure is a very risky situation for the blast furnace process. In order to prevent pressure drop, the dust discharge chamber is a separate section in the dust catcher discharge system. Thanks to the new valve placed on the upper part of this chamber, the connection of the chamber with the dust catcher can be disconnected. This means that it is no longer possible for the furnace to be exposed to the atmosphere during the dust discharging process. This situation minimizes the risks in terms of both environmental safety and process safety.

4. Conclusion

While the continuity and safety of production are of great importance for the İSDEMİR New Blast Furnace No.1, which will be the blast furnace with the largest production capacity in Turkey, environmental awareness is at the forefront. One of the measures taken to meet these criteria is the gas cleaning system that does not harm the environment and protects the process safety. It has been decided to use the new dust catcher system in İSDEMİR Blast Furnace No.1, together with the improvements made for environmental awareness and process continuity.

References

[1] Paul Wurth Gas Cleaning Plant Operation and Maintenance Plan

UNDERSTANDING CARBON DIOXIDE EMISSIONS IN ELECTRIC ARC FURNACE OPERATIONS

Mehmet Fatih GÖKÇE¹, Bora DERİN²

¹Diler Demir Çelik, ²Istanbul Technical University
Türkiye

Keywords: EAF, CO₂, emissions Carbon oxidation

Abstract

Direct emissions result from the reaction of carbon-containing fuels and raw materials with oxygen. Carbon dioxide emission amounts can be increased or decreased significantly with effective process management and raw materials used in the process. The carbon-oxygen balance in the EAF and how to maintain this balance for more efficient use of chemical energy are the factors that need to be known to reduce direct carbon dioxide emissions. This study focuses on discussing the improvement of CO₂-emitting reactions in EAF processes.

1. Introduction

In EAF melting, carbon is an indispensable part of the process and fulfills critical tasks from the beginning to the end of the process such as control of bath oxidation, homogenization, and foamy slag generation. Direct emissions of CO₂ in EAF processes are due to these oxidation reactions (for slag forming or chemical heating) of the carbon sources such as scrap/iron substitutes (in metallic form or as organic matter on the outer surface), charge or injected form of coke/coal, electrode, and natural gas. All of these reactions are responsible for about 80 % of the CO₂ emissions. Considering all these functions of carbon, its necessity in the steel production process in EAF is obvious. However, to reduce carbon emissions, it is necessary to carefully control the efficiency of the carbon used in the production process and the losses that occur during operation. Eq (1) shows the theoretical amounts of carbon by mass and oxygen by volume required for the formation of carbon monoxide at STP.

2. Natural gas combustion and electrode consumption in EAF operations

The burners, an integral part of today's arc furnaces, use natural gas and oxygen and generate approximately 2.06 kg CO₂ per Nm³ natural gas feed. With the proper operation of EAF burners and the use of quality scrap, it is possible to decrease CO₂ emissions. Figure 1 shows the modeling calculation of oxidation reactions of 1 mole of natural gas with pure oxygen by FactSage 8.1 [1]. As it is clear, CO₂ is not the only gas product to be emitted during EAF operation. Graphite electrode consumption in EAF process accounts for 10 % of the emissions. Almost 60 % of this consumption results from oxidation and the rest is from tip consumption. Those consumptions can be reduced if the right technical solutions are applied. With an improved electrode consumption, CO₂ emissions through electrode consumption can be reduced up to 1 kg CO₂/t steel.

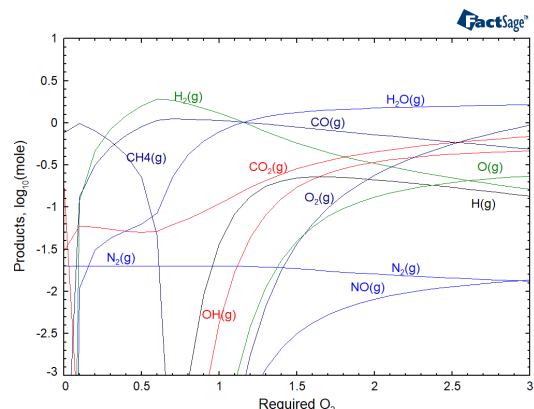
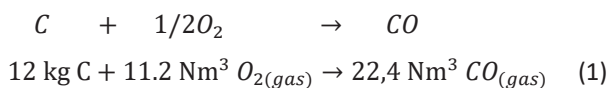


Figure 1. Modeling calculation for oxidation of natural gas by FactSage 8.1

3. Conclusion

Direct emissions can be brought down to the benchmark value of 0,058 t CO₂/t steel value. Nevertheless, this target requires tight, precise, and almost real-time control of raw materials and the whole process.



EMISSIONS OCCURRING IN THE COKING PROCESS IN STEEL MANUFACTURING AND METHODS OF STRUGGLE AGAINST EMISSIONS

Hüseyin KALAY, Zekeriya ÖZER, Kenan AKDEMİR

Iskenderun Demir ve Çelik A.Ş.
Türkiye

Keywords: Coking process, Steel production, Emission, Coke battery, Struggle emission

Abstract

Steel is the most widely used metal in the world, which is frequently used in the fields of construction and engineering, forms the basis of the industrial economy. The large amount of CO₂ released into the atmosphere during steel production is one of the most important factors causing global warming. For this reason, the role of steel in the climate crisis has been closely examined in recent years, as in the petroleum and coal sector. In the steel production process, liquid raw iron, scrap and other alloying elements are converted into liquid steel by pure oxygen blowing method. For the production of liquid raw iron, iron ore, sinter, pellets and coke are used as inputs. Coke, which is used as the most important input, is obtained by charging the coal carried by conveyor belts to battery ovens and burning in high temperature and oxygen-free environment. During the coking process, environmental polluting emissions occur at many different points. Some of these emissions can be discharged from the general chimneys connected to the batteries or they can be mixed into the air with different sources during various activities. In addition to fugitive emissions from the general chimney, emissions from ovens, oven doors and flanges occur. These emissions, which occur for various reasons, include dust, CO, volatile organic compounds, hydrocarbons, sulfur compounds, aromatic hydrocarbons and heavy metals such as mercury. The amount and types of emissions that occur vary according to each point.

The global iron and steel industry accounts for 11% of carbon emissions and 7% of greenhouse gas emissions. According to the Paris Agreement, carbon emissions in the industry are aimed to reach zero between 2050 and 2070. In this context, priority is given to struggle against emissions in iron and steel production, and related studies are continuing. Dust collection systems are one of the most important parameters in emission control methods. In these systems, fugitive emissions are controlled by using the bag filter method. Apart from dust collection systems, the damage to

the environment is minimized by struggle against emissions with many different methods. Temperature measurements are taken at certain intervals in battery ovens, and cleaning is done along the heating lines in ovens with low temperatures. The refractory team continues to work on oven doors, charging covers and damaged oven walls with daily routine controls. In this study, the emissions that occur in the coking process during steel production at the Iskenderun Iron and Steel Factory (ISDEMİR) and the methods of struggle against emissions are discussed.

1. Introduction

Iron and steel have played an important role in the development of human civilization for many years. It is frequently used in agriculture, construction, electricity generation and distribution, machine and tool production, and the automotive industry. In the 18th century, coal, iron and steel is considered the beginning of the industrial revolution. The globalization of the world economy has had a major impact on the steel industry. Competitive market conditions accelerated structural change and encouraged the steel industry to strengthen.

There are 4 different methods in steel production. The most complex of these methods is the classical blast oven method used in integrated steelworks. Integrated steelworks are characterized by the flow of energy between the various production units and the combination of interconnected materials. Examples of these units are sinter plants, pelletizing plants, coke oven plants, blast ovens and steel production plant [1-2].



Figure 1. ISDEMIR integrated iron and steel plant

The steel production process steps in the integrated iron and steel factory can be summarized as follows: Iron ore and coal, which are the main raw materials of iron and steel production, come to the plant by sea or by rail. Coal is sent to the coking plants for the coking process, and the fine ore is sent to the sinter plants for use in the blast ovens. The coal, which comes to the coke factory coal silo with the help of belts, is charged to the ovens and converted into coke in an oxygen-free environment under a certain temperature and pressure. The powdered ore is brought to the size that the blast ovens can use in the sinter factory, and sinter is produced and sent to the blast ovens. Liquid crude iron is produced in blast ovens using iron ore, sinter, pellets and coke. After being desulfurized in the desulfurization plant, the liquid crude iron is sent to the steel plant to enter production. In the steel plant, liquid raw iron is converted into liquid steel by reducing the carbon ratio by pure oxygen blowing method. The produced liquid steel is poured into molds in the casting facility and slabs or billets in desired dimensions are obtained. In Figure 2, the steel production process flow chart is outlined.

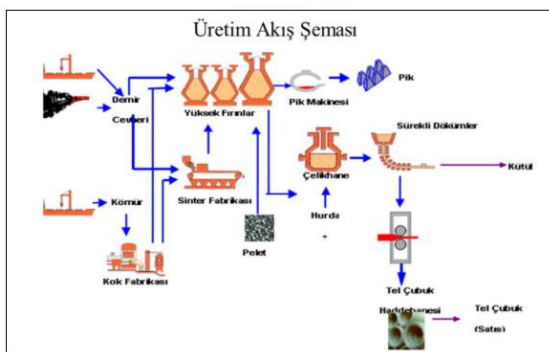


Figure 2. Steel production process steps

1.1. Main environmental issues in iron and steel production

Both materials and energy are used intensively in iron and steel production. Impurities such as rust, oil, plastic materials and paint in the scrap used in production are the main factors

in the formation of environmental pollution. The main emissions due to these factors are dust, heavy metals, carbon monoxide, nitrous oxide and furans. These are the emissions that need to be limited due to the serious pollution and health problems caused by these pollutants.

In addition, main environmental problems are encountered in the integrated iron and steel plant, depending on the units. For example, 50% of the total dust emissions occur in the sinter plant. The main cause of fugitive emissions to air in coking plants is emissions resulting from insufficient coking time. Also, many of the emissions are scatter emissions from discharge, storage, transport, oven walls and doors. The main environmental problems in blast ovens are dust, wastewater, emissions from slag processes [3]. Reducing these emissions, in accordance with the Kyoto protocol and the Paris Agreement, has an important place in the developing competitive environment. The amount of emissions can be reduced by the improvements to be made in the fields of operation, raw materials, equipment, storage and technique in the integrated iron and steel plant [4-5].

1.2. Emissions in the coking process and control methods

Coking is the process of obtaining coke, which occurs by the combustion of imported coals blended in certain proportions at high temperature and in an oxygen-free environment at a certain time interval. The main process steps of coke ovens are charging the coal, heating and burning the ovens, coking, pushing and extinguishing the produced coke. All of these processes constitute the main source of emissions from coke ovens. Figure 3 shows the main emissions occurring in coke plants.



Figure 3. Emissions from coke plants

Dust emissions are common during the transportation, preparation, unloading and storage of coal. In order to reduce emissions, coals containing less SO should be preferred, crushing and screening processes, storage and transportation processes should be carried out in closed environments. In addition to dust emissions during the charging of pulverized coal to batteries, organic compounds such as benzene, SO₂,

H₂S, NH₃ are emitted from the decomposition of coal. During oven charging, these emissions are mostly observed in the charging process, doors, covers and related process lines. Proper sealing of charging ports and systems is an important element in reducing charge emissions. In the case of combustion and heating of the coke oven, the fuel gas not completing the combustion regime or the gas leakage on the damaged oven walls cause fugitive emissions. The temperature measurements of all ovens are taken at the batteries in each shift, and the cleaning of the heating equipment in the ovens with low temperatures is carried out. Gaseous ovens are reported to the heating team and necessary cleaning is done. During the coking process, fugitive emissions may occur in the doors and charging holes due to the positive pressure in the ovens. For this, oven doors are taken into routine maintenance, if the refractory brick is damaged, it is replaced, if the oven frame is damaged, it is replaced and it is made ready for use again by general cleaning. For fugitive emissions occurring in the charging holes, necessary controls are made throughout the production and the charging frame is sprayed with special chemical mixture. This process prevents fugitive emissions, but since it does not provide continuity, the process continues as needed by making continuous observations. The special chemical mixture used consists of a mixture of lime and water and is used by making it denser than water.

During the pushing of the oven, whose coking process has been completed, the oven is emptied into the quenching car with the help of the guide car. Emissions and dust generated during pushing are not released to the environment thanks to the dust collection systems that are in operation throughout the production, but are accumulated in the dust collection bunkers.

During the extinguishing of the coke, the extinguishing process is carried out with cold water, which causes the particles to spread. The water vapor from the water in contact with the hot coke rises from the coke and pulls the dust from the coke mass. Dust, CO, NH₃, H₂S emissions come first among the emissions observed during the extinguishing of coke. In order to prevent these emissions, the spray method can be used in the extinguishing process. The extinguished coke is sent to the coke crushing and screening unit with the help of belts. While the coke is brought to the desired dimensions in the crushing and screening unit, some emissions and dusts occur in the system. At this stage, the dust collection system is activated again and the fugitive emissions are prevented and are not released into the environment [6].

2. Experimental Procedure

There are many different factors that cause emissions throughout the coke plant. Within the scope of struggle against emissions, studies are carried out both with maintenance and repair of existing equipment and with various ongoing improvement projects. Examination of the

refractory structure of ovens, especially in batteries, and making necessary repairs and maintenance are among the most important studies that can be evaluated within this scope.

Within the scope of refractory works in batteries, works are routinely carried out on oven doors and severely damaged oven door bricks are replaced with new ones. For less damaged door bricks, chemical mortar is made together with special glass slaked fireclay mortar. Chemical mortar made in sherbet consistency is applied to the oven door brick surfaces with the help of a brush. Renewing and repairing the refractory structure, which has completed its life in the batteries, provides the necessary support in preventing gas passages that cause fugitive emissions. Figure 4 shows the work done on the oven doors and door bricks. Ceramic ropes used between the casing and the armor in the ovens in the batteries are another method within the scope of struggle against emissions. The temperature resistance of the ceramic rope must be extremely high and its tightness must be good. The material of the ceramic rope should be ceramic fiber fully braided, Ni-Cr wire reinforced circular packing. Ceramic thread with the specified chemical and physical properties is used in batteries, and all emissions that occur in the doors are thus prevented.



Figure 4. Improvements to the coil oven doors

Within the scope of struggle against emissions, work continues on oven charging frames. Special chemical bricks used in the charging holes of the batteries are placed around the charging caps, acting as a frame and sealing around it with special chemical mortar materials. Therefore, the fugitive emissions that occur during production are prevented from being released to the environment. These damaged frame bricks are routinely replaced. Compliance of bricks with physical and chemical parameters cannot be ignored. Each parameter is directly related to the lifetime of the refractory structure of the bricks. In Figure 5, the change of the charging hole frame brick is shown.



Figure 5. Changing the charge frame bricks

Keeping dust collection systems active is extremely important within the scope of struggle against emissions. Many different improvements have been made in the dust collection system in the past. With the kaizen study performed in the dust collection system in the 4th battery, the differential pressures were reduced and the system performance was improved. The frequency of the pulses in the dust collection system has been increased, the diaphragms in the filters have been replaced by routine controls. As a result, the performance increase in the dust collection system led to a decrease in the emissions released directly to the environment. In addition, the dust collection filters and cages that are routinely changed can be evaluated as the studies carried out within this scope. Figure 6 shows the dust collection system in the 4th battery.



Figure 6. 4.Battery dust collection system

3. Results and Conclusion

Steel production continues rapidly in the world, crude steel production increased by 3.7% in 2021 compared to 2020 and exceeded 1.95 billion tons. Our country has become the 7th largest steel producing country in the world in 2021 with its steel production increasing compared to previous years [7]. CO₂ emissions in steel production in Turkey are below the average compared to other countries. For 1 ton of crude steel, 0.69 tons of CO₂ emissions occur. This is due to the greater use of electric arc oven methods. This method is more advantageous in terms of carbon emissions. However, this is a very high amount for our environment, as CO₂ constitutes the majority of this amount of greenhouse gases. The intense energy consumption of the iron and steel industry and the

environmental effects of production processes are being examined by various organizations. For this reason, studies are carried out on more environmentally friendly projects where emissions are reduced in the iron and steel industry.

More environmentally friendly production processes can be created by struggle against emissions with the improvement and innovative project studies that each company in the sector will make within itself. In this study, the causes of emissions occurring throughout the ISDEMIR coke plant and the methods of struggle against this emission are discussed. Work on improving the equipment in the current system and using innovative emission-reducing materials continues rapidly. Emission sources are determined by making both direct and detailed emission measurements and alternative studies are carried out. Filters are improved to reduce dust emissions and dust holding efficiency is increased. For other emission types, both process improvements and equipment improvements continue.

Acknowledgment

We would like to thank the ISDEMIR coke factory batteries operating chief engineer, dust collecting system teams and refractory teams who contributed to this study for their support in technical applications throughout the entire research.

References

- [1] Prospektif Teknolojik Araştırmalar Enstitüsü Sürdürülebilir Üretim ve Tüketim Birimi Avrupa IPPC Bürosu, Demir Çelik Üretimi için Mevcut En Uygun Teknikler (Met) Referans Belgesi, Endüstriyel Emisyon Direktifi, 75(2010).
- [2] Karbon Yönetimi Bülteni, OYAK, Mart-Nisan 2(2019) 39.
- [3] <<https://www.Isdemir.Com.Tr/Kurumsal/Celigin-Hikayesi>> Dated: 10.05.2022.
- [4] M. E. ERTEM, AB'ye Uyum Sürecinde Kyoto Protokolü ve Demir Çelik Sektörünün Yeri.
- [5] S. UÇAK, Avrupa Yeşil Mutabakatının Çelik Sektörüne Olası Etkileri, Uygulamalı Ekonomi ve Sosyal Bilimler Dergisi, 3 (2021) 94-113.
- [6] U. S. Environmental Protection Agency, Emission Factor Documentation for AP-42, May 2008, RTI International, pp. 2-10.
- [7] <https://www.cib.org.tr/files/Doc/files/CIB_CalismaRaporu2021.pdf> Dated: 10.05.2022.



DECARBONIZATION AND GREEN STEEL PRODUCTION IN IRON AND STEEL INDUSTRY

Aziz KILIÇ

BCS Enerji Mühendislik
Türkiye

Keywords: Hydrogen. Decarbonization, Iron & Steel

Abstract

Decarbonization and green energy production are very important in Iron-Steel industry which has high level of carbon emissions. In this scope, one of the important things that could be done is usage of renewable energy sources. Green Deal, announced by the Council of the European Union, exposes the importance of the green energy and decarbonization for the future. For the Iron-Steel industry which has a wide industrial and employment capacity, green steel production should be carried into action as quickly as possible.

The decrease in petroleum reserves in the world as a result of excessive use and consequently the increase of its price furthermore the damage it has caused to the environment have made us do a research on alternative fuels that are abundant in nature and environment friendly. The enormous damage to the environment caused by exhaust emissions from fossil fuels used in internal combustion engines has led countries to take precautions in this regard.

Studies show that hydrogen, which is abundant in the universe, has many of the required properties for a fuel. Hydrogen is potentially available wherever there is water and clean power source. It has more efficient combustion feature compared to the other fuel types. Since hydrogen does not contain carbon and sulfur, there is no CO, CO₂ and HC among the combustion products. Theoretically, water is the only substance formed when hydrogen is burned.

We can easily say that hydrogen has many advantages in many aspects ecologically. The fact that hydrogen, which is a secondary energy source, can be obtained with different and renewable primary energy sources, is considered to make this fuel type the most important energy carrier of the future.

In addition, hydrogen can be used with the other fossil fuels. With this feature it provides many advantages. These are:

1. Reduced NOX and CO emissions and increased thermal efficiency as a result of lowering the fuel/air mixture limit
2. Reduction of the pressure differences between cycles
3. Increasing the flame speed of the mixture

Hydrogen and other fuels

Hydrogen, which has an odorless, colorless, tasteless and transparent structure, is the lightest chemical element in nature. The heating value of unit mass of hydrogen in gas form is the same as hydrogen in liquid form, and it is 2.8 times that of natural gas. One of the most important features that will benefit the use of hydrogen as a fuel is that for different air-hydrocarbon mixture ratios, ignition can be achieved between 0.3-1.7 values of the air excess coefficient, while this limit reaches 0.15-4.35 values for hydrogen. The amount of energy required to ignite hydrogen-air mixtures is also very low compared to other fuels.

Since the smallest molecule is the hydrogen molecule, it is more likely to leak through small gaps than other liquid and gaseous fuels. Viscosity, diffusion coefficient in air and propensity to pass through holes are 1.26 to 2.8 times higher in hydrogen compared to natural gas. Since the energy of natural gas is about 3 times more than hydrogen, natural gas leaks cause more energy loss.

Fossil fuels still used in our world are oil, natural gas, coal and wood. After these fuels are combined with oxygen gas and burned, the gases that come out pollute the world. About 80% of our energy needs are provided by fossil fuels. People breathe the toxic gases emitted into the atmosphere. With the greenhouse effect of these gases, the world is warming, glaciers are melting, floods are happening, and the climate is changing. Nuclear energy increases our problems with heat even more. Despite the negativities created by our current energy system, hydrogen energy will be a savior as it is a renewable clean energy. The important thing is that hydrogen is produced without creating pollution.

In this context, the importance of the use of hydrogen in industrial combustion systems pioneered by our company has become more evident. It is aimed to have zero carbon footprint by using hydrogen fuel instead of natural gas fuel.

The use of hydrogen gas and hydrogen and oxygen as fuel in the industrial field is controlled by hydrogen and HHO burners. Compared to natural gas, hydrogen gas is a clean and environmentally friendly energy source. Hydrogen gas is obtained by different methods. The most known method is the separation of water by electrolysis or plasma technology. Hydrogen gas and oxygen gases are obtained by separating the components of water (H₂O). Hydrogen is dangerous when it reacts with some gases. It causes huge explosions. Hydrogen is offered as an alternative to the fuels available today. Some of these alternative fuels are; natural gas, fuel oil, diesel, LPG, LNG, biogas, propane, and coal-like solid fuels. It is very important to make the obtained hydrogen suitable for the combustion system. When combined with different gases, the risk of explosion is very high. For this reason, safety rules must be made at the highest level and used as fuel. The control system of hydrogen gas is important. Mixing with air should be given in the most ideal way. Flow control is carried out in this system. Hydrogen, oxygen, HHO air flow rates are read separately and combustion is carried out by proportioning them to each other.

Usage areas of hydrogen gas in industrial facilities

Hydrogen gas can be used in all systems with industrial burner combustion. It can be used in iron-steel furnaces, aluminum melting, aluminum

holding, sheet and billet, rotating and tilting, runner heating, homogenization, aging, casting, forging, annealing and heat treatment, rolling, ladle and tundish heating, bell and well type, stress relief, meltshop ladles, wire annealing, lead and zinc, ceramic and glass, frit, tunnel, drying and disposal, fire testing, pipe annealing, tempering, paint drying, enamel, rotary calciner, drying ovens and boiler systems.

Hydrogen gas minimizes the waste gases formed as a result of combustion. As a result of combustion with other fuels, environmentally harmful gases are discharged from the chimney. When combustion is made with natural gas and other types of fuel, the NO_x and CO amounts are very high. When we use hydrogen gas, it is an environmentally friendly fuel type as no harmful gases are formed as a result of the reaction. The flue gas value is at minimum levels, which is almost nonexistent. When burning with hydrogen gas, the carbon footprints are close to zero.

Now furnaces can be designed in accordance with the hydrogen fuel system. It is predicted that investment costs will reach more affordable levels over time. With our current technological structure, all data and information have been obtained so that it can be applied to all kinds of furnaces.

References

- [1] <https://www.bcsmuhendislik.com/hidrojen-bruloru-ve-yakma-sistemleri/> Dated: 24.01.2019

THE USE OF BORON ELEMENT FOR COST REDUCTION IN TEETH MADE OF LOW ALLOY STEEL USED IN EXCAVATORS

Muhammed KIRICI^{1,2}

¹Motus Automotive, ²Konya Technical University
Türkiye

Keywords: Boron Steel, Low Alloy Steel, Bucket Teeth of Excavator, Ground Engaging Tools

Abstract

The effects on the mechanical properties by reducing expensive alloying elements and adding boron (0.003-0.005 wt %) to alloy for excavator teeth were investigated. The study concluded that: the tensile strength of modified alloy was found to be 1757 ± 24 MPa, yield strength 1613 ± 29 MPa, % elongation value of 3. The amount of energy absorbed by the sample was found to be 27 ± 3 joules. Hardness measurements were made from the outside to the inside of a thick section of the tooth. While the hardness on the surface (under decarburized structure) was 51 HRC, the value of 47 ± 2 HRC was also obtained in the innermost region.

1. Introduction

Excavators are often used in the mining and construction projects. The most important parts used in excavators are the bucket teeth. They are generally produced from martensitic steels except for Hadfield steels. They are expected to have good penetration, strength, abrasion and impact resistance, as well as a long service life. Achieving all these properties together is costly for manufacturers. One of the ways to reduce these costs is modification in alloy. Therefore, in the study; reduction of Mo element has been studied by using boron element.

2. Materials and Methods

The chemical composition of the modified alloy by weight includes 0,3% C, 1,5% Si, 1,5% Mn, 1% Cr, 0,25% Ni, 0,10% Mo and 0,003% B. Normalizing, hardening and tempering heat treatments were applied to the teeth produced by sand casting method. Tensile, Charpy (notch) Impact and Hardness tests were applied to the samples. Tensile and impact tests were performed on samples obtained from Keel blocks and hardness measurements were also made from the surface of the bucket teeth to the center. All tests were performed at room temperature. Also, microstructure analysis was carried out.

3. Conclusion

As a result of experimental studies; the mechanical properties of the modified alloy were found to be very close the old alloy. When comparing the new alloy with the old alloy for mechanical tests; it was determined that the tensile strength decreased by 1% and the yield strength increased by 1,32%, as Figure 1-a. It was found that the impact absorption energy, decreased by 38,7%, as Figure 1-b. In microstructure analysis; it is noticed that in the outermost part of the tooth, lath martensite is formed, as shown in Figure 1-c. The hardness value of this region has already 51 HRC value. The average hardness value measured from the inner part in the same direction was determined as 47 ± 2 HRC. Considering efficient usage surface/depth of the tooth, it was concluded that the hardness decreasing in the inner region is not significant.

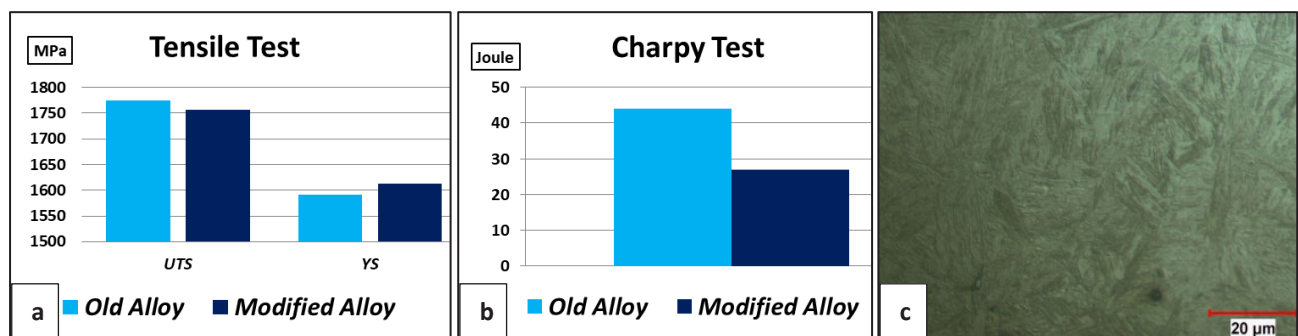


Figure 1. Results of experimental studies (a) Tensile test (b) Charpy Test (c) Microstructure

MODELLING AND SIMULATION STUDIES FOR OPTIMIZATION OF LABORATORY SCALED STEEL CASTING MOLD DESIGNS

İ. İrfan AYHAN¹, Caner GÜNEY¹, Emre ALAN¹, N. Başak DÜRGER¹, M. Fatih KAYADEĞİRMENİ¹, Muhammet ULUDAĞ², Nursina ŞENSOY², Beyza GÜNAYDIN², Gülşah KURT²

¹ÇEMTAŞ Çelik, ²Bursa Technical University
Türkiye

Keywords: Gravity Steel Casting, Mold Design, Simulation and Modelling.

Abstract

In this study, NovaCast software was used to determine the optimum mold design for steel casting applications with using laboratory scaled vacuum induction melting unit. The shrinkage volume of final products was compared that were produced via gravity die casting method with different mold designs. High strength low alloy steel was melted and cast while the permanent mold material was selected as cast iron. It was shown that shrinkage cavity is an unavoidable result for top-open vertical mold design. Additionally, the high amount of open and closed porosities in solidified steel for vertical mold designs were observed due to high turbulent flow of liquid steel while pouring directly into the mold cavity. Therefore, the mold design was optimized with adding a slope with different angle of gradients in order to reduce the turbulence effect. Furthermore, a neckdown typed exothermic sleeve was integrated to top of the mold to act as a pouring basin and a feeder. The mold with optimized design was physically produced and the trial productions were performed with laboratory scaled melting unit. The macro and microstructural investigations of solidified steel cast resulted with relatively lower amount of shrinkage cavity and porosities as estimated via casting software.

1. Introduction

“New Product Development” and “Process Development” R&D activities generally require a large number of trial production that is not always possible for many industrial production routes such as metal casting process. Therefore, laboratory scaled productions provide time and cost saving solutions. However, the samples that are produced with laboratory scaled physical prototype simulations need to be capable of representing the industrial products. For this reason, optimizing and precise-controlling of process parameters play an essential role in laboratory scaled productions.

Gravity and counter-gravity die castings have a significant share in the production of steel ingot casting process. In gravity casting, the liquid steel is directly poured into the cavity of vertically placed permanent mold while counter-gravity casting uses a bottom gating for reducing the

splashing due to uphill teeming and minimizes the possibility of defects in solidified product as shown in Figure 1. On the other hand, pouring the liquid steel directly into the mold cavity is a simple method and does not require any complex equipment. Moreover, the method provides faster production and the need of installation area is much less when compared with counter-gravity casting. Therefore, top poured permanent die gravity casting is preferred by many vacuum induction melting applications. Nevertheless, the process parameters and the design of the system have to be controlled with fine adjustments in order to reduce the casting defects.

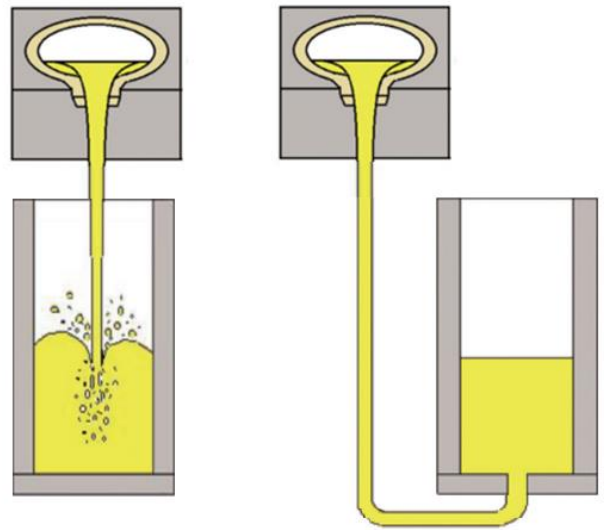


Figure 1. Comparison of gravity and counter-gravity casting methods [1].

The computer aided casting simulation technique becomes an efficient tool for not only predicting final properties of casting products, but also detecting and optimizing casting defects like turbulence behavior through the mold filling or shrinkage-related porosity after the solidification of liquid metal. The combination of both virtual and physical simulations allows more efficient processes while producing casting products with less defects.

In this study, NovaCast software was used to determine the optimum mold design for steel casting applications with using laboratory scaled vacuum induction melting unit. The shrinkage volume of final products was compared that were produced via gravity die casting method with different mold designs. High strength low alloy steel was melted and cast while the permanent mold material was selected as cast iron. It was shown that shrinkage cavity is an unavoidable result for top-open vertical mold design. Additionally, the high amount of open and closed porosities in solidified steel for vertical mold designs were observed due to high turbulent flow of liquid steel while pouring directly into the mold cavity. Therefore, the mold design was optimized with adding a slope with different angle of gradients in order to reduce the turbulence effect. Furthermore, a neckdown typed exothermic sleeve was integrated to top of the mold to act as a pouring basin and a feeder. The mold with optimized design was physically produced and the trial productions were performed with laboratory scaled melting unit. The macro and microstructural investigations of solidified steel cast resulted with relatively lower amount of shrinkage cavity and porosities as estimated via casting software.

2. Material and Method

3D CAD models of molds were designed by using SolidWorks v2020. The simulation of flow and solidification processes were performed with NovaCast Flow&Solid software.

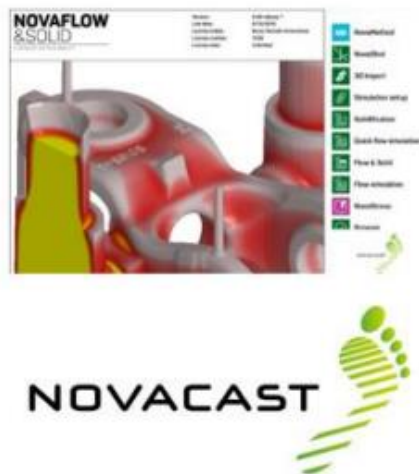


Figure 2. NovaCast NovaFlow&Solid software.

CARGEM B1200[®] grade high strength low alloy steel was chosen for both simulation studies and laboratory scaled productions. The chemical composition of steel was given in Table 1.

Table 1. The chemical composition of CARGEM B1200[®] [2].

C	Si	Mn	Cr + Mo	Other Elements
0.22%	1.4%	1.5%	1.45%	B, Ti, Nb

The required process parameters for simulation studies including mass of molten metal, flow rate, gravity coefficient influence and cooling rate were determined according to laboratory scaled vacuum induction melting system as shown in Figure 3.

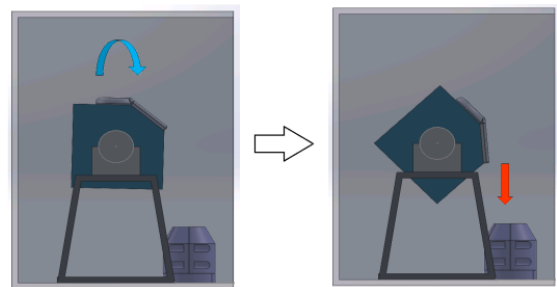


Figure 3. Pouring of liquid metal into permanent mold.

Firstly, the performance of top open Ø85 mm round and 80x80 mm square-sectioned ingot molds were analyzed by means of casting defects such as top shrinkage, micro and macro porosity via simulation software. The 3D CAD models of molds were given in Figure 4. In order to validate the results of casting simulations, the high strength low alloy steel was melted and cast by using laboratory scaled vacuum induction melting unit with using molds having dimensions as same with the ones that were used for simulations.

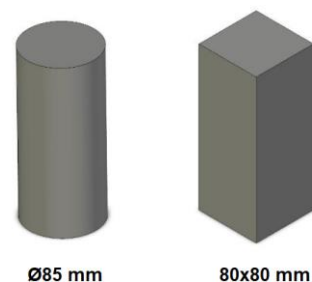


Figure 4. 3D CAD models of molds studied with simulation software.

3. Results

Figure 5 shows the comparison of shrinkage results of simulation and physically produced products with using 80x80 mm square-sectioned top open mold design. It was shown that the position and the amount of top shrinkage cavity in the laboratory scaled cast product matched with the simulation results.

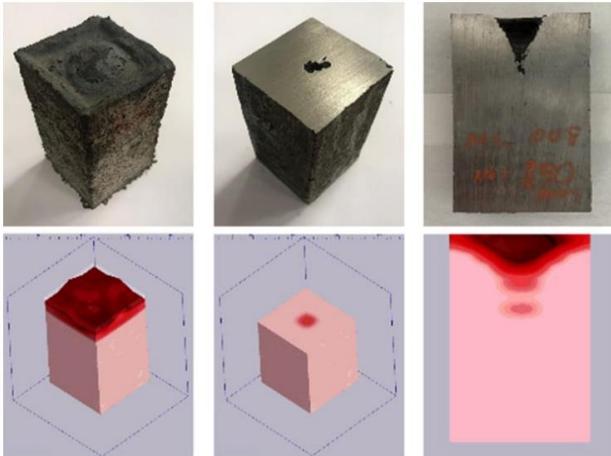


Figure 5. Comparison of the shrinkage results of simulation calculation and laboratory scaled cast product.

Figure 6 shows the results of mold filling performance and casting defects of round and square-sectioned top open molds calculated with simulation software. The volume fraction of shrinkage defect from the open top to the center of the mold found to be higher in product that produced with square-sectioned mold.

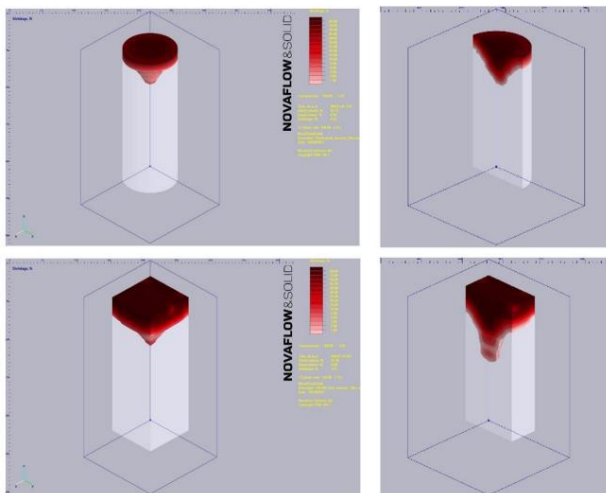


Figure 6. The calculated shrinkage performances of molds with different geometries.

The results indicated that the shrinkage defect is unavoidable for the top open molds regardless from its geometry but it is possible to reduce this kind of defects by optimizing the mold design.

The possible reason of detected casting defects is related with uncontrolled turbulent flow and the splashing behavior inside the mold cavity after pouring of liquid metal as the nature of the vertical gravity casting. The previous studies also proved that exothermic sleeves are beneficial tools to prevent the molten steel from shrinking by keeping the retardation of temperature fall during

solidification [3, 4]. Therefore, the mold design was optimized with adding a slope with different angle of gradients in order to reduce the turbulence effect. Additionally, a neckdown typed exothermic sleeve was integrated to top of the mold to act as a pouring basin and a feeder.

$$M = V/A \dots \dots \dots \text{Eq.1}$$

M: Modulus [cm], V: Volume [cm³], A: Area [cm²]

$$M_b = 1.2xM \dots \dots \dots \text{Eq.2}$$

M_b: The modulus of feeder [cm]

The required geometry and the size of exothermic sleeve in order to minimize the top shrinkage defect was calculated according to Eq. 1 and Eq. 2, respectively.

The modulus of exothermic sleeve is calculated as “0.210 cm”. The geometry and dimensions of the sleeve were chosen based on the calculated value.

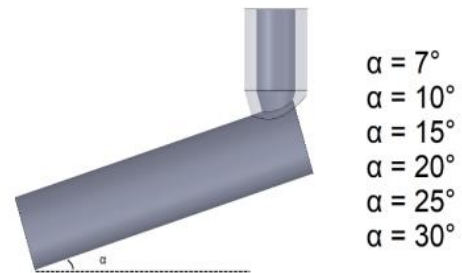


Figure 7. The 3D CAD model of optimized mold design with different sloping angles.

The 3D CAD model of optimized mold design is given in Figure 7. A variety of different sloping angles was analyzed with simulation software and performance results were compared. It was seen that the process suffers from turbulent flow due to increased falling height above 30° and below 10° angled slope designs. The best performance was obtained with the 15° angled design and the model results were confirmed with laboratory scaled production that has a negligible shrinkage defect as shown in Figure 8.

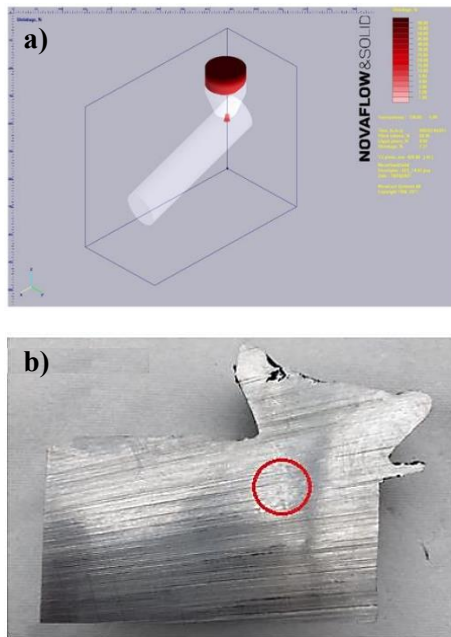


Figure 8. Shrinkage defects of 15° angled top open exothermic sleeve integrated mold design a) simulation results, b) laboratory scaled production.

4. Conclusion

Based on the result of this study, the following main conclusions can be drawn;

- The shrinkage defect is an unavoidable result for top open vertical mold designs but can be minimized by optimization of process parameters and mold design.
- The sloped design with an effective sloping angle is found to be a beneficial optimization to avoid splashing and turbulent flow.
- The top shrinkage cavity can be eliminated by integrating an exothermic sleeve to the top of the mold to act as a pouring basin and a feeder.
- In general, it is found that the computer aided simulation techniques are effective tools to improve process yield and product quality in casting process.

Acknowledgements

This work was supported by The Scientific and Technological Research Council of Turkey (TÜBİTAK) within the scope of “2209-B - Industry Oriented Research Project Support for Undergraduate Students” project programme.

References

- [1] Campbell, J. (2020). Perspective Chapter: A Personal Overview of Casting Processes. Casting Processes and Modelling of Metallic Materials.

- [2] Erişir, E., Ayhan, I. I., Güney, C., Alan, E., Dürger, N. B., & Ün, S. (2021). Microstructure and Phase Transformations in High-Strength Bainitic Forging Steel. *Journal of Materials Engineering and Performance*, 30(5), 3458-3467.

- [3] Lan, X. K., & Khodadadi, J. M. (2001). Fluid flow, heat transfer and solidification in the mold of continuous casters during ladle change. *International Journal of Heat and Mass Transfer*, 44(5), 953-965.

- [4] Idamayanti, D., Purwadi, W., Bandanadjaja, B., & Triadji, R. (2020). Rice husk waste as an exothermic material for a riser sleeve for steel casting. *International Journal of Technology*, 11(1), 71-80.



DEVELOPMENT OF NEW STEEL GRADE WITH IMPROVED HARDENABILITY FOR RENEWABLE ENERGY INDUSTRY

İ. İrfan AYHAN¹, Caner GÜNEY¹, Emre ALAN¹, N. Başak DÜRGER¹, M. Fatih KAYADEĞİRMENİ¹, Nazlı AKÇAMLI²

¹ÇEMTAŞ Çelik, ²Bursa Technical University
Türkiye

Keywords: Bolt Steel, Fasteners, Alloy Design, Heat Treatment, Mechanical Properties.

Abstract

In the near future, wind power is expected to be one of the most popular renewable energy sources. A rapid growth is also expected in the need of steel material with higher mechanical properties with a variety of sectional thicknesses by the increasing demand in wind power industry. Therefore, new alternative steel grades with higher hardenability will offer a solution to fulfill the need of material with desired properties. In this study, new alloying strategies were investigated in order to provide higher mechanical properties including hardenability as well as strength and toughness. The new steel alloys were designed by using computational thermodynamic software and laboratory scaled productions were performed with the selected chemical compositions. The mechanical test results showed that the required conditions for bolt and fasteners according to ISO 898-1 standard can be achieved by proper optimization in the alloying strategies.

1. Introduction

Steel is widely used in the renewable energy industry, for instance, a three-bladed wind power turbine consists of averagely 25.000 pieces of bolts and fasteners. The steel structures that are used in wind power applications are exposed to severe environments, even sub-zero temperatures. In such cases, the impact toughness of steel material needs to be adequate to prevent catastrophic failures due to brittle fracture at low temperatures. Therefore, the steels with property class of “10.9” and above are generally preferred according to ISO 898-1 standard. In addition to low temperature toughness, the hardenability is another important requirement, which enables the steel an opportunity to use at larger section thicknesses. The hardenability is directly affected by the chemical composition of steel.

The steel grades containing chromium (Cr) and molybdenum (Mo) additions such as 34CrMo4, 42CrMo4 are widely used in bolts and fasteners. The carbon (C) content of steels as well as chromium (Cr) and molybdenum (Mo) are intentionally increased with the increment of sectional thickness. In such cases, the impact absorbing energy of material tends to reduce that may result a usage limitation under lower temperatures. The microalloying elements such as niobium (Nb), vanadium (V), titanium (Ti) and boron (B) offer a significant potential solution to overcome the balance requirement between low temperature toughness and hardenability.

The purpose of this study is to investigate new steel designs with improved hardenability to provide alternative solutions for the bolts and fasteners in wind power industry as a replacement of conventional steel grades.

2. Materials and Methods

Thermodynamic and thermo-mechanical estimations of new alloy designs were calculated by using JMatPro v.10.2 software. The selected chemical compositions were produced in laboratory scale by using 10 kg vacuum induction melting unit. Quench and tempering (Q&T) heat treatment was applied to the hot deformed productions.

Light optical microscope (LOM) and scanning electron microscope (SEM) were used to reveal microstructural properties of heat-treated samples. Tensile test, Charpy impact test and hardness measurements were performed to determine the mechanical properties of newly developed steel and the results were compared with conventional Q&T steel grades.

3. Conclusion

In this study, a new alternative steel compositions consisting of microalloying additions was successfully developed. It is found that optimized contents of C, Mn, Cr, Mo and microalloying elements help to improve tensile properties as well as low temperature toughness of steel while providing a higher hardenability compared to conventional Q&T steel grades.

In general, it can be concluded that the required mechanical properties of bolts and fasteners in wind power industry can be achieved by proper alloying strategies within the higher hardenability. It is thought that the promising results of the new alloy design will provide an opportunity to reduce the need of different steel grade requirements depending on the sectional thicknesses for the wind power applications.



USE OF GREEN HYDROGEN IN IRON AND STEEL INDUSTRY

Caner TUNA¹, Celal Erkal KAHRAMAN¹, Hakan ERÇAY¹, Tuncay DİKİCİ²

¹Özkan Demir Çelik, ²Dokuz Eylül Üniversitesi
Türkiye

Keywords: Green hydrogen, energy, iron and steel, climate change

Abstract

Energy; is an important factor affecting environmental pollution, quality of life, national economy, and international relations. Due to the increasing population in the world, the increase in energy demand and energy costs, environmental pollution caused by consumed fossil fuels, and global climate change bring renewable energy to the fore. The iron and steel industry contributes negatively to the CO₂ emissions in the world in general, and in this context, it continues to operate as one of the important factors of climate change. Nowadays, a number of working technologies related to the production of hydrogen and hydrogen-enriched reduction technologies are widely carried out in the blast furnace and direct reduced iron process.

1. Introduction

The increasing consumption demand of humanity has caused the rapid depletion of resources, the increase in electricity need and environmental pollution. The world is facing the major challenge of climate change. Many sectors such as iron ore and steel, fertilizers, refining, methanol, and maritime shipping emit major amounts of CO₂, and carbon-free hydrogen will play a critical role in enabling deep decarbonization [1].

Considering that the 6% increase in global steel demand expected to occur until 2030 and 7% of global CO₂ emissions in the current situation is caused by the iron and steel industry, the green energy transition in the steel industry becomes imperative [2].

2. Results and discussion

Hydrogen energy, solar energy, wind energy, geothermal energy, hydroelectric energy, and biomass energy can be listed as renewable energy sources [3]. All these reasons, such as air pollution, climate change, acid rain, deterioration in ecological balance, depletion of the ozone layer, energy wars, and the increase in diseases due to environmental pollution, become almost mandatory for the use of hydrogen energy. Hydrogen is a synthetic fuel obtained from water, fossil fuels, and biomass using primary energy sources, and there are gray, blue, turquoise, and green codes in the commonly used color code terminology [4].

Green hydrogen is the most suitable one for a fully sustainable energy transition from renewable energy. Hydrogen is a useful as an energy carrier for applications requiring high energy density. Green hydrogen offers a combined solution between sustainable renewable electricity generation and hard-to-electrification sectors. However, high production cost, 35% loss in energy used to produce hydrogen by electrolysis, and lack of infrastructure are obstacles to green hydrogen.

3. Conclusion

Hydrogen has high calorific value, thermal conductivity, high reaction rate and also various sources. Because of these, it is considered both as the most promising clean energy source in the 21st century and provides great potential for applications in the iron and steel industry. The steel industry is committed to continuing to reduce the footprint from its operations and the use of its products.

References

- [1] K. Raj, A. P. Lakhina and C. Stranger, Green Hydrogen Opportunities For Deep Decarbonisation In India, June 2022, New Delhi India, pp.12.
- [2] L. Guevara Opinska, M. Mahmoud, C. Bene, K. Rademackers, Moving towards Zero-Emission Steel, December 2021, European Union, pp.7-9.
- [3] <https://www.nationalgeographic.com/environment/article/renewable-energy> Dated: 12.08.2022.
- [4] A. I. Osman, N. Mehta, A. M. Elgarahy, M. Hefny, A. Al-Hinai, A. A. H. Al-Muhtaseb and D. W. Rooney, (2021). Hydrogen production, storage, utilisation and environmental impacts: a review. Environmental Chemistry Letters, 1-36.

SINTER PLANT IGNITION FURNACE BURNING OPTIMIZATION

Erol AKKÜLAH, Cenk KAYA, Seyithan ÇEVİK, Mehmet AYGÜN, Bengü TAŞDELEN

Ereğli Demir ve Çelik
Türkiye

Keywords: Sintering Process, Ignition Furnace, Ignition and Combustion Quality, Coke Oven Gas Saving, Dust and CO₂ Emissions Reduction

Abstract

In this study, in Ereğli Demir ve Çelik Fabrikaları T.A.Ş. (ERDEMİR) Sinter Plant, the applications are made to optimize and improve the ignition furnace temperature and to determine the minimum furnace temperature that will not lose combustion efficiency, to save coke oven gas and reduce dust and CO₂ emissions, working automatically according to the furnace temperature determined for ideal combustion and monitoring the parameters related to the coke oven gas on the Level 1 screens are discussed.

1. Introduction

Sinter Plant is the plant where the fine iron ores that cannot be used directly in the Blast Furnaces are blended, fluxes, waste materials and coke breeze (as fuel) and pre-reduced in the physical and chemical properties required by the Blast Furnaces.

After the raw mixture is fed to the sinter machine, while passing under the ignition furnace, it is ignited from the surface by the flame obtained by the mixture of coke furnace gas and air.

After the ignition, the coke breeze in the raw mixture burns together with the vacuum provided by the main fan and provides the heat required for the process. In this way, the combustion zone on the surface moves towards the bottom with the air sucked by the main fan after the ignition furnace and sinter production takes place. The quality of ignition and combustion is the most important factor in the sintering process. When a good ignition and combustion cannot be achieved, the quality of sinter deteriorates, electro static filter performance decreases and sinter production is interrupted.

With this study, after determining the optimum furnace temperature, it is aimed to evaluate all parameters and to make the adjustment of the coke oven gas consumption amount independent of people and to work automatically according to the set with optimum furnace temperature.

2. Manual Adjustment of Coke Oven Gas Consumption

In the existing method before the improvement, the coke oven gas consumption value was manually set in m³/hour unit. The operator decided on the set value change by visually checking the machine surface at the furnace exit.

When there is no complete combustion on the surface of the bed, sinter plant dust emission increases and efficiency decrease occurs, waste materials are limited and the Sinter Plant is stopped if needed.

In the study, it is aimed to optimize and improve the ignition furnace temperature which is around 1050°C and to save coke oven gas by determining the minimum furnace temperature that will not lose combustion efficiency.

2.1. The Current Situation

In the current situation, the material surface of the ignition furnace outlet is visually inspected by the operators. If there is melting or slag on the upper surface of the material, it is decided that the coke oven gas is excessive.

If the upper surface of the material is not burned and if the surface is brown ore color, it is decided that the coke oven gas is not sufficient. After the control, the coke oven gas amount (m³/hour) set value is changed, and the surface of the sinter bed after furnace is checked again.

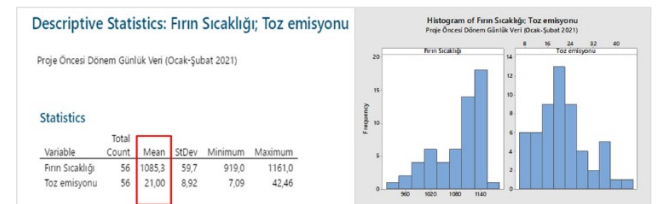


Figure 1. Sinter Ignition Furnace Temperature and Dust Emission Average Values

In the current situation, it is seen that the average value of the sinter ignition furnace temperature is 1085°C, and the average value of dust emission is 21 mg/Nm³. In the current

situation, it is seen that the temperature can go down to 960°C.

3. Improvement Practices

It is planned to work automatically according to the furnace temperature instead of the manual method, to transfer the TBYS (Facility Information Management System) data to Level-1 and make the data traceable with graphics, to optimize the ignition furnace temperature value, and to update the furnace temperatures with control charts according to the data to be obtained.

3.1. Transferring TBYS Data to Level-1

The TBYS system (facility information management system) is a system in which production and consumption information is collected and followed in different facilities in the factory. In the current situation, there was no system in the Sinter Plant in which the coke oven gas parameters could be monitored. By transferring TBYS data to Level-1, it was made traceable with graphics, and coke oven gas was monitored more effectively in Sinter Plant operator screens.

All desired values were first transferred to the Level-2 system database, and then written to the relevant points in the automation system, so that they could be followed as a retrospective trend in both systems.

3.2. Automatic operation according to ignition furnace temperature and determining the parameter settings of the program by tests.

Tests were performed to determine the parameters accurately. A trend was drawn according to the valve opening ratio, furnace temperature and coke gas flow, by putting the valve manually and then back to automatic. The coefficients of the PID system were calculated according to the data obtained over this trend.

Considering the variables used in the calculations and the trend graph, the P and I coefficients of the PID block were calculated with the first order PID system by using the system parameters. Initial parameters were determined as P value 0.012 and I value 90.000 ms.

For a while, the system was followed and observed in this way. For more accurate interpretations, a trend has been created in automation scadas showing furnace temperature set point, furnace temperature process value, and proportional valve opening data.

As a result of the examinations, it was concluded that the valve should respond more quickly. The valve response is accelerated by gradually reducing the I coefficient (If it accelerates too much, the valve oscillates and control becomes impossible over time).

Due to the non-standard movements in the temperature caused by the coke oven gas pressure or the calorie, the extinguishing of the furnace due to the automatic proportional control valve falling below 20% was prevented by the determined rule.

4. Gradually Lowering the Ignition Furnace Temperature Set Value

Furnace temperature set value was gradually decreased and data analysis was made for each stage. In the current situation, as a result of the improvement studies based on the days worked at 960°C furnace temperature, we reduced the furnace set value to 950°C degrees as the first step.

In the current situation, as a result of the improvement studies based on the days worked at 960°C oven temperature, we reduced the oven set value to 950°C degrees as the first step.

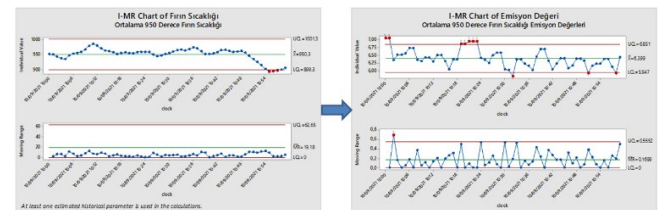


Figure 2. Reducing Set Values (950°C ± 50 °C)

In the work of gradually reducing the furnace temperature set values, we first updated it to be 950°C on average with ± 50 variability, and we did not encounter an out-of-control situation in both furnace temperature and emission values in the process.

After reducing the furnace set value to 950°C, we set the set value to 900°C with ± 50 degrees variability in the second stage and we worked at this furnace temperature for a certain period. At the third stage, we set the set value to 880°C with ± 50 degrees variation and we worked with the furnace temperature of 880°C for a certain period. When we examined the temperatures and emission values at the second and third stages, we did not encounter a problem in the process.

After reducing the furnace set value to 880°C, we adjusted the set value to 860°C with ± 50 degrees variability as the fourth stage, and we conducted trial studies for a while. When we examined the temperatures and emission values, we encountered values above 30 mg/Nm³ in emission values, and we observed that complete combustion could not be achieved at the exit of the sinter ignition furnace.

We set the value to 880°C because the ignition furnace temperature caused an increase in emissions at 860°C, and we did not encounter any problems in the process and

emission values in the verification study. No problem was observed in combustion efficiency either.

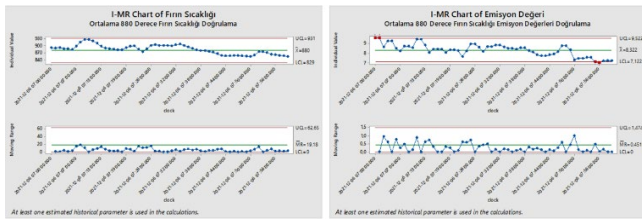


Figure 3. Optimum Set Value ($880\text{ }^{\circ}\text{C} \pm 50\text{ }^{\circ}\text{C}$)

5. Results and Discussion

In order to compare the pre- and post-project averages, we first looked at the normality of the distribution of the data. While the furnace temperature data before the project was not normally distributed, we observed that it was normally distributed after the project. Again, when we performed the normality analysis for the emission values, we observed that the data before and after the project were normally distributed. When we examined the variability of the furnace temperatures before and after, we saw that they were different from each other and that the emission values had different variability in the pre- and post-project periods. After the project, variability was reduced.

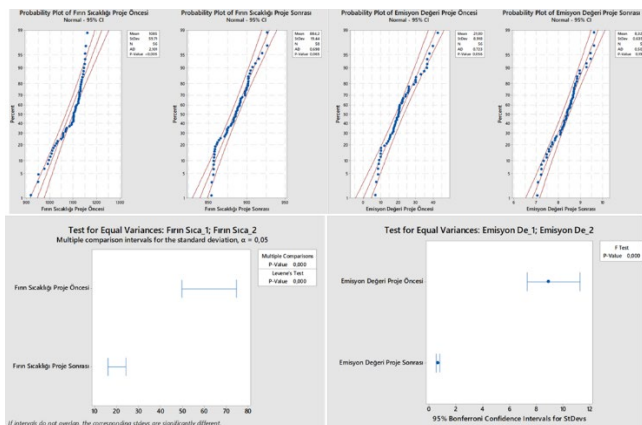


Figure 4. Normality distribution of data for comparison of means and variances before and after

We analyzed the pre-project ignition furnace temperature average and the post-project average with two sample t-tests and found out that the averages were different from each other. We also analyzed the average of the emission values before and after the project with two sample t-tests and we observed that they were statistically different from each other. The furnace temperature, which was an average of 1085°C and a standard deviation of about 60 before the project, decreased to an average of 884°C and about 19 standard deviations after the project.

6. Conclusion

With this project, the minimum furnace temperature value required for efficient combustion has been found through trials. After the project, ignition furnace combustion control was standardized. By working automatically according to the furnace temperature, efficient combustion and coke oven gas savings are achieved.

After determining the optimum temperature for ideal combustion in the ignition furnace, the average coke oven gas consumption decreased by $3.3\text{ Nm}^3/\text{ton}$ as a result of automatic coke oven gas flow instead of manual operator control. The amount of savings achieved means a decrease in CO_2 emissions by 5600 tons/year.

EFFICIENCY IMPROVEMENT VIA OPTIMIZING SECONDARY COOLING IN A HEAVY-DUTY GAS TURBINE

Mehmet YILDIZ, Mustafa Mert ÇAKA, Cenk BAYENDER, Tansu KUKUL, Özgür AKGÜN

Ereğli Iron and Steel
Türkiye

Keywords: Gas Turbine, Secondary Cooling, Wheel Space Temperature, Efficiency, Natural Gas Consumption, Outside Temperature, Statistical Data Analysis.

Abstract

In this study, heavy-duty gas turbines located in integrated iron and steel plants named Ereğli Demir ve Çelik Fabrikaları T.A.Ş. (ERDEMİR) efficiency increasing and power regaining by optimizing secondary cooling air somehow adjusting cooling fans working regime and increasing cooling air amount using external air source results evaluated in statistical data analysis will be explained.

1. Introduction

Gas turbines are exposed to heavy operating conditions, especially high operating temperatures. For this reason, gas turbines need to be taken into maintenance at certain intervals and their parts should be renewed according to the manufacturer's criteria. However, power loss (degradation) is experienced in gas turbines over time. There are many factors that cause this loss. It is possible to regain some power by carrying out improvement studies in a planned manner in order to identify, monitor and eliminate the effects of all these factors. Any improvements that can be made in gas turbines bring significant gains in terms of operating costs. Even the smallest activities for energy recovery have considerable importance, especially in our country, which is dependent on foreign energy. (Fig1)

Gas turbines, compress the air with the help of the compressor and increase the pressure. Injecting natural gas into the hot air trapped in the combustion chamber, it performs the combustion process. The kinetic energy generated by the high pressure and temperature released as a result of combustion generates electrical energy by driving the turbine blades. (fig2)

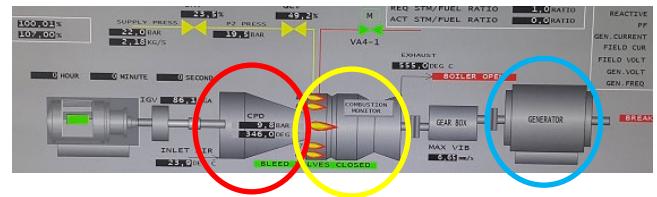


Fig2. Gas Turbines

- 1 – Compressor (Red Circle)
- 2- Turbine (Yellow Circle)
- 3- Generator (Blue Circle)

Unit	Produced Electricity	Natural Gas Flow	Pressure of the Cooling Fans
GT01	30.9 MW/h	11,290 m ³ /h	120 mbar
GT02	31.4 MW/h	11,345 m ³ /h	140 mbar

Table1. Productivity of Generators

2. Experimental Procedure

Flow Characteristics in Turbine Wheel Space Cavity paper is reviewed. This paper shows that increasing de secondary air flow and pressure by the limited value, it can affect Exhaust Temperature, 2nd Wheel Temperature and 3rd Wheel Temperature parameters that can be important impact to the producing the electricity rate. With that idea, a statistical model is created. In regression analysis, model is found having strong relationship with R-sq (adj.) %71,54 value. Mentioned regression model is;

$$\text{Electricity Generation} = 169.749 - 0.234025 \times (\text{Exhaust Temperature}) - 0.024551 \times (\text{3rd Wheel Temperature})$$

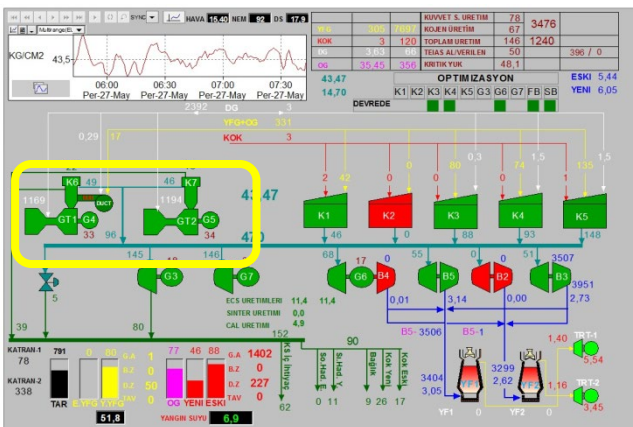


Fig1. Cogeneration Process

Model Summary

S	R-sq	R-sq(adj)	R-sq(pred)
0,617138	71,54%	71,54%	71,53%

Table2. Model Summary of the Regression Model.

3. Results and Discussion

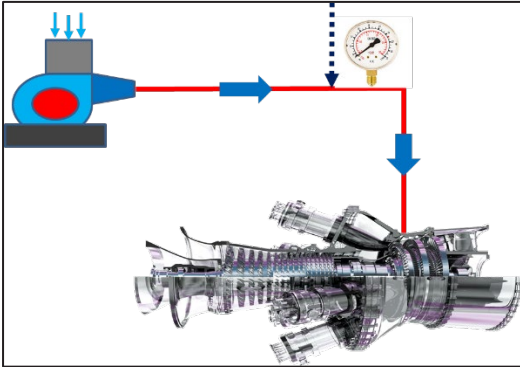


Fig3. The air diagram to be added to the air supplied with the compressors

Secondary air flow was changed adding externally air source by following pipe line pressure. An airline connected to the cooling fans outlet pipe line which go through to gas turbine casing. Actually, the pressure was 120mbar. Secondary air flow increased gradually using a hand valve installed on external air pipe line. After the increased amount of pressure, turbine consumption and power output data analyzed. First of all, the amount of air increased from 120 to 180. Doing this, the optimum cooling air pressure value found. The last value for the increased secondary air pressure is 220 mbar.

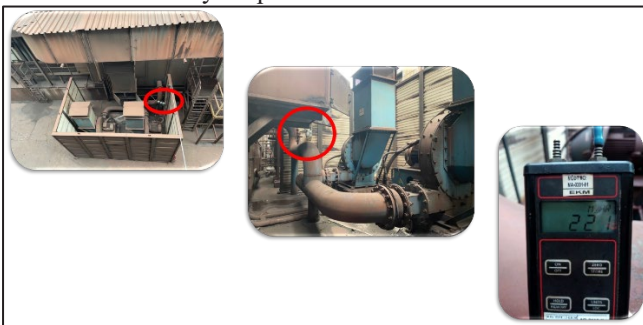
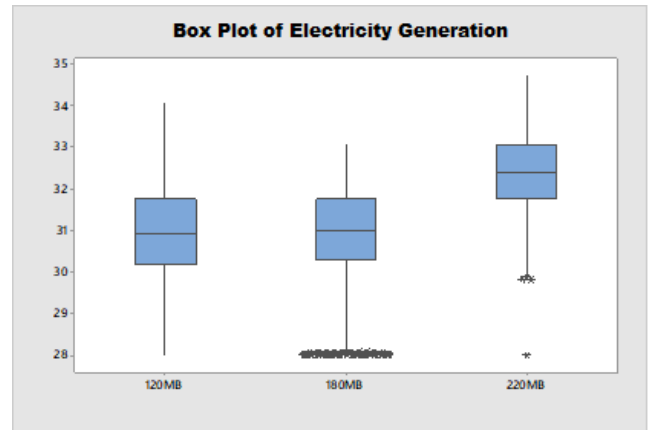
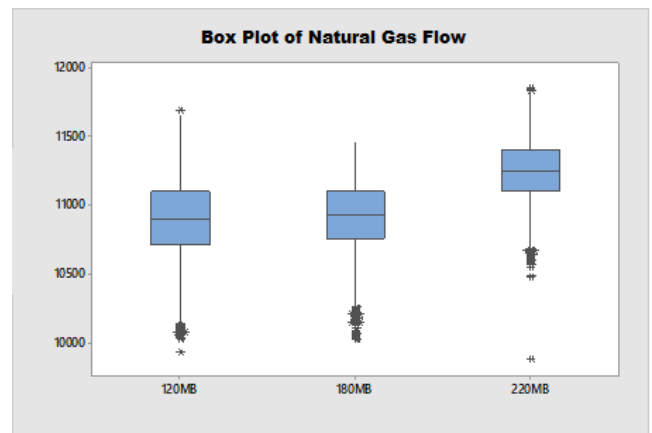


Fig4. Construction of planned transactions

The expectation is; natural gas usage rates to increase depending on the decrease in exhaust temperature. As a result, electricity production increases. But it is necessary to be sure whether this production is efficient or not.



Graph1. Electricity Generation with secondary air pressure



Graph2. Natural Gas Flow with secondary air pressure

As can be seen in the Box Plots drawn, electricity production also increases with the increase in natural gas flow. However, when the exhaust temperature is high, natural gas cannot be supplied, so electricity production does not increase. You can see that there is no differentiation in the graphics at 120 MB and 180 MB. But when the gas flow rises to 220 MB, the electricity production and boundedly the gas flow increase.

Descriptive Statistics: Electricity Generation

Statistics

Variable	Önce - Sonra	Total Count	Mean	Minimum	Median	Maximum
Electricity Generation	120MB	57463	30,917	28,000	30,930	34,070
	180MB	39690	30,952	28,000	30,980	33,090
	220MB	21544	32,445	28,010	32,390	34,740

Table3. Electricity Generation Calculation

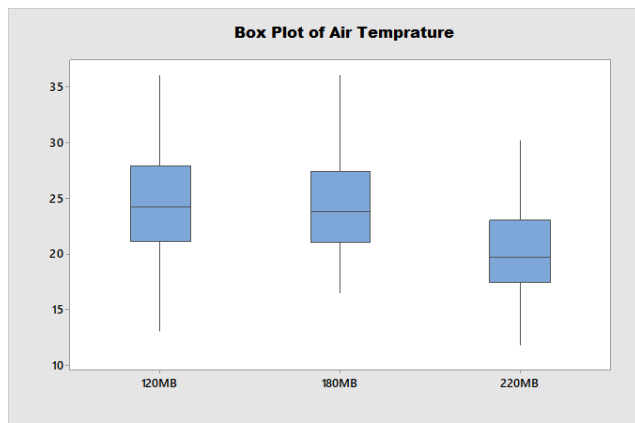
As a result, electricity generation increased significantly by 1.528 MW/h when looking at hourly averages. Whether this increase is a significant difference or not; was measured by performing 2 sample t-tests between the two data sets. It was observed that the data were statistically

significantly different from each other between 120 MB and 220 MB. (table4)

Test		
Null hypothesis	$H_0: \mu_1 - \mu_2 = 0$	
Alternative hypothesis	$H_1: \mu_1 - \mu_2 \neq 0$	
T-Value	DF	P-Value
-211,48	47804	0,000

Table4. 2 Sample t-test for 120 MB and 220 MB

We needed a new regression analysis since the outside temperatures showed a serious change in the data we collected during the 220 MB trials. (Graph3)



Graph.3 Air Temperature differences between 120-220 MB

We have created a regression analysis formula that can tell the electricity production increases depending on the air temperature. The R-sq (adj.) of this regression analysis was calculated as 80%. (Table5)

Model Summary			
S	R-sq	R-sq(adj)	R-sq(pred)
0,462479	80,60%	80,60%	80,60%

Table5. Regression Model Summary

Formulation of that calculation;

$$\text{Electricity Generation} = 36.4237 - 0.225462 \times (\text{Air Temp})$$

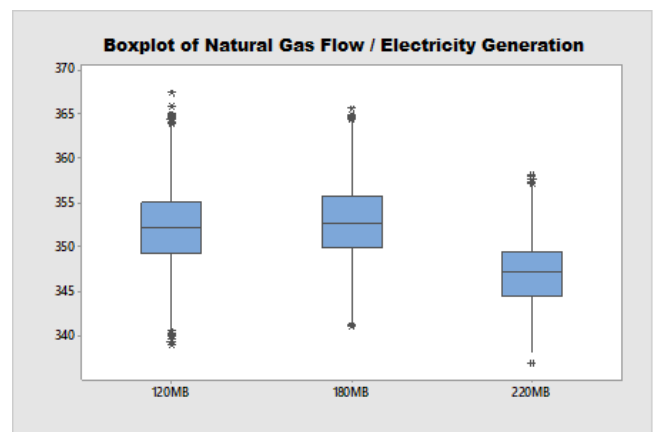
With that formula; how much electricity production would increase with only the outside temperature if we had not made any improvements, and we applied our formula with 80% R-sq (adj.).

Descriptive Statistics: Electricity Generation				
Once - Sonra	N	Mean	StDev	SE Mean
120MB	57463	30,917	0,943	0,0039
220MB	21544	31,889	0,866	0,0059

Table6. Electricity Generation without improvement

Calculation of without improvement electricity generation increased significantly by 0.97192 MW/h. (Table6)

Similarly, a formula was created with the natural gas flow. Natural gas is increasing, but the outside temperature was also decreasing at the time of the improvement. A formula was needed for this difference. An analysis was made on the amount of natural gas used per MW. This shows the production efficiency. (Graph4)



Graph4. Natural Gas used per MW

Statistics						
Variable	Once - Sonra	Total Count	Mean	Minimum	Median	Maximum
Natural Gas Flow per MW	120MB	57463	352,23	338,93	352,16	367,33
	180MB	39690	352,82	340,93	352,59	365,60
	220MB	21544	347,04	336,89	347,23	358,04

Table7. Mean of Natural Gas used per MW

As a result, Natural Gas used per MW increased significantly by 5.1823 m³/MW when looking at hourly averages (Table7). Whether this increase is a significant difference or not; was measured by performing 2 sample t-tests between the two data sets. It was observed that the data were statistically significantly different from each other between 120 MB and 220 MB. (table8)

Test		
Null hypothesis	$H_0: \mu_1 - \mu_2 = 0$	
Alternative hypothesis	$H_1: \mu_1 - \mu_2 \neq 0$	
T-Value	DF	P-Value
182,57	46641	0,000

Table8. 2 Sample t-test for 120 MB and 220 MB

Air temperature affects electricity production is similarly natural gas consumption. For this reason, if no improvement was made, it was calculated how much of a change in usage would be in the period of improvement. (Table9)

Model Summary			
S	R-sq	R-sq(adj)	R-sq(pred)
2,13316	72,42%	72,42%	72,42%

Table9. Regression Model Summary

Formulation of that calculation;

$$\text{Natural Gas Flow/MW} = 332.033 + 0.82679 \times (\text{Air Temp})$$

With that formula; how much electricity production would increase with only the outside temperature if we had not made any improvements, and we applied our formula with 80% R-sq. (Table10)

Descriptive Statistics: Natural Gas Flow per MW				
Önce - Sonra	N	Mean	StDev	SE Mean
120MB	57463	352,23	3,46	0,014
220MB	21544	348,66	3,17	0,022

Table10. Natural Gas Flow/MW without improvement

Calculation of without improvement Natural Gas Flow/MW decreased significantly by 3.5641 m³ /MW. (Table10)

4. Conclusion

With this study, the result obtained from the improvement made hourly electricity increase was subtracted from the figure of how much increase would have been if no improvement was made. Because the increase in electricity generation caused by the cooling of the air had to be subtracted from the improvement amount.

Thus, the secondary air support, which was brought in 220MB, increased the electricity production to 1.528 MW/h (Table3). Even if we did not make any improvements, the production amount would have increased to 0.97192 MW/h (Table6). As the effect of the improvement, it has been understood that the electricity production is 0.55668 MW/h.

Similarly, the amount of natural gas consumed to generate 1 MW of electricity increased by 5.19 m³/MW with the improvement (Table7). If no improvements were made, the difference in usage due to the increased production amount due to the cold weather would have been 3.5641 m³/MW (Table10). In this case, the amount of natural gas consumed to produce 1 MW of electricity, which is due to the improvement, decreased by 1.626 m³/MW.

For the entire remediation, 100 m³ of compressed air per hour was used.

In a nutshell; 8,000 hours of electricity is produced in 1 year. In addition, the difference between the price of electricity purchased from abroad and the cost of electricity produced in cogeneration plants is 31 USD per MW. An average of 30.9 Mw of electricity is produced per hour.

According to these assumptions, the total return after the study was calculated as 340,287 USD (Table11).

Natural Gas Savings	Electricity Generating Revenue	Compressed Air Consumption
1,626 m ³ /MW x 8000 h x 30,9 MWh x 0,527 USD/m ³ =	0,5567 MW/h x 8000 h x 31 USD/MW =	0,012 USD/m ³ x 100 m ³ /h x 8000 h=
211.826,18 USD	138.061,6 USD	9.600 USD

Table11. Total Return of the Improvement

References

[1] Flow Characteristics In Turbine Wheel Space Cavity (Nov.2021) -Lie Xie, Qiang Du- Energy Reports Vol7



INCREASING HOT ROLLED MILL PRODUCTION BY INCREASING COIL WEIGHTS UNDER 1,80 MM THICKNESS

Muhammet BILEN¹, Koray ARAY¹, Serdar GÜNBAŞ¹, Erhan SELVI¹, Hasan YILDIRIM¹, Burak Emre IŞIK¹, İskender GÖK¹, Ahmet Mithat AVŞAR¹, Tayfun KOCABAŞ², Abdurrahman Mesud ÇAKIR¹, Burcu SOYSAL ATAN¹

¹İskenderun Demir ve Çelik A.Ş., ²Oyak Maden Metalurji Türkiye

Key Words: Coil, Continuous Slab Casting, Production Increase, Efficiency, Carbon Footprint

Abstract

One of the most important parameters affecting production efficiency in hot rolled mill production is coil weight. Coil weight is calculated by slab length, thickness, width, density, slab to coil transition efficiency calculations. In İsdemir, slab thickness is 225 mm and it cannot be changed because of fixed casting mold is used. On the other hand, slab width cannot go beyond certain options depending on the opening and crushing situations in the hot rolling mill. The only parameter that can be optimized in coil weight is the slab length, since the yield calculation is not very variable and the density also varies according to the amount of some alloy and a constant density value is assumed. Each slab length below 12,000 mm reduces the production speed of the rolling mill and negatively affects many areas such as the number of samples, slab furnace fuel consumption, manipulation and packaging. Coils with a thickness of less than 1.80 mm were produced with a slab length max. 10,500 mm. In this study, the slab length has been gradually increased for coils with a thickness of less than 1.80 mm, considering and analyzing various factors such as order steel quality, customer, thickness, width, rolling process values and coil slumping risk. Thus, the production rate and production amount of hot rolled products increased, the number of truck transfers, slab furnace emissions, scrap amount and the number of manipulations were reduced, and also contributing to the carbon footprint positively.

1.Introduction

The slab casting facilities at İsdemir make casting from two channels for the width range of 800-880 mm and from a single channel for 980-2,050 mm.

While the slab furnace annealing the slabs between 5,200-6,250 mm in length in double rows, the slabs which are taller than this width are processed as a single row. Slabs between 6,250 and 12,000 mm create inefficiency in the furnace, and it is an undesirable situation in terms of both natural gas consumption and skid damage.

Each slab length below 12.000 mm reduces the production speed of the rolling mill and negatively affects many areas such as the number of samples, manipulation and packaging. For example, if a 1500 mm wide coil is produced from 8,000 mm slab, the production speed is 464 tons/hour, while for 12,000 mm this value becomes 584 tons/hour.

For coil, slit coil or truss products, our goal in the hot rolling mill is to produce from the longest and widest slabs as permitted by standards, laws, customers, quality criteria and most importantly customer demands.

Many regulations and systematics have been developed so as not to exceed 39 tons for coils that will not go on the highway and 29 tons for others.

Hot Rolling Mill coil production speed; product code varies depending on order thickness, width and quality and slab length.



Figure 1. Continuous Slab Casting



Figure 2. Hot Rolling Mill

In the study, it was aimed to increase the efficiency by producing with a slab length of 10,500 mm instead of a longer slab length on the thin side and to overcome the difficulties experienced in terms of the order management process.

2. Experimental Procedure

In the study, the thickness range of 1.39-1.79 mm was divided into 4 thickness ranges, 2 different width ranges, a total of 8 groups. Trials were planned in line with the evaluations, with a slab length of 11-11.5-12 m in each group. After each trial, quality defect, rolling loads, rolling temperatures, roll condition, coil slumping in the stockyard, customer evaluations were examined.

Within the scope of the 1st trial, 38 coils were produced from 11 m slab length for orders 1.3237_40 steel quality 1.71-1.73 mm thickness and 1,000-1,225 mm width target. Within the scope of the 2nd trial, 8 coils were produced from 11 m slab length for orders 1.3237_40 steel quality 1.6-1.73 mm thickness and 1,025-1,225 mm width target. Within the scope of the 3rd trial, 38 coils were produced from 11 m slab length for orders 1.4237_40, 1.6405_40 and 1.6412_40 steel quality 1.5-1.73 mm thickness target. Within the scope of the 4th trial; a total of 38 coils were produced from 1.4237_40 and 1.6222_40 grades with 1.42 to 1.50 mm thickness and 11 m slab length. Within the scope of the 5th trial; a total of 15 coils were produced from

1.4237_40, 1.3237_40 and 1.6224_40 grades with 1.42 to 1.73 mm thickness, 11,5 m and 12 m slab length.

3. Results and Discussion

When coil slumping problem of trials in the coil stockyard were examined, it was seen that there was no problem. It has been determined that the ones shipped to the customer from the trial productions do not have a negative result in terms of customer satisfaction.

In addition, when the rolling load distributions of the trial productions were examined on the PDA, it was seen that the target load on the stand basis and the actual load values were close to each other, and there was no negative situation compared to the pre-project.



Figure 3. Coil Slumping Control

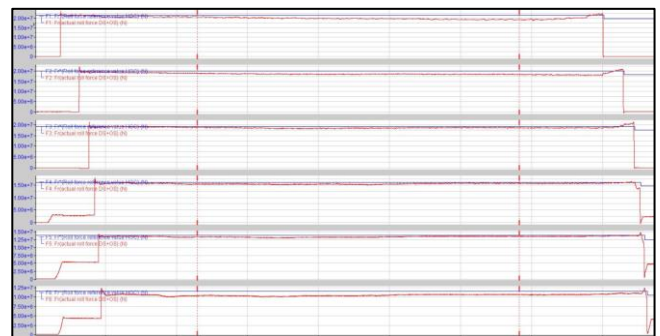


Figure 4. PDA Analysis of Rolling Load

When the trial productions were examined in terms of bed temperatures, temperatures reaching a maximum of 60°C were seen. At 65°C and above, the roller is disabled. It was observed that this temperature was not reached during the trials.

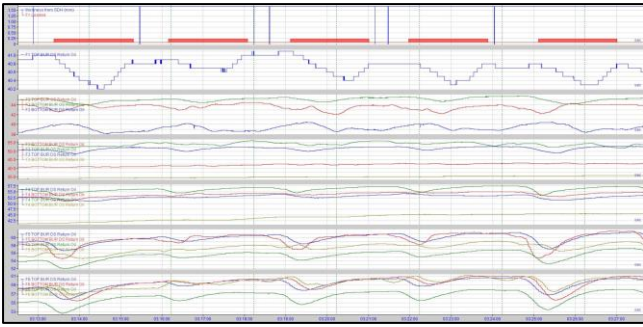


Figure 5. Analysis of Bearing Temperature

Work roller temperature is expected to be max 50°C at F5-F6 stands. This value was not exceeded in the experiments. If this temperature is 55°C and above, tail slip etc. increased likelihood of problems.

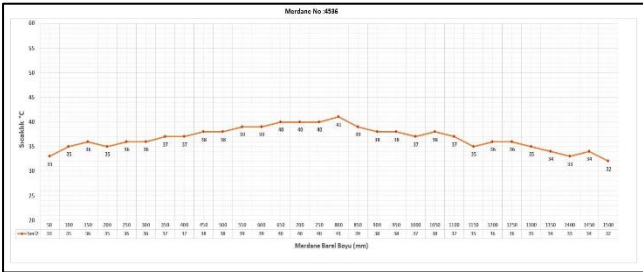


Figure 6. Temperature Profile of Roller

The edges, called shoulders, are the places where the material does not pass. The material passes through the core of the roller and roller wear occurs in this region. However, it takes the heat most at the navel point and makes the navel curved. A similar wear profile was observed in all materials at stands F5-F6.

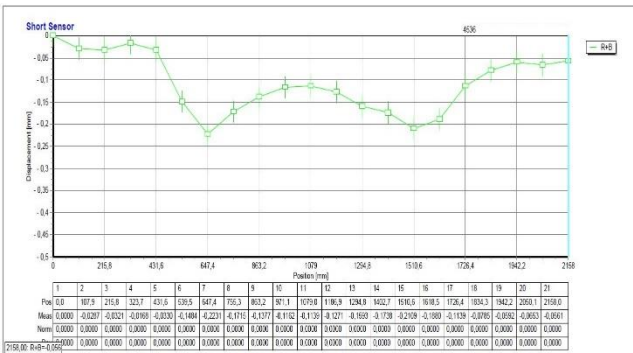


Figure 7. Wear Profile of Roller

4. Conclusion

As a result of the study;

- Hot rolling mill production rate increased by 15% on average. For example, if production is made with the new production rate for an order of 1000 tons, the amount of production to be obtained is

1,241 tons.

- In addition to this, reduction in the number of samples taken, a decrease in the damage rate of slab heating furnace skids, a positive effect on the carbon footprint due to the reduction in the number of truck transfers and reduction in slab furnace emissions, and ease of managing the process while taking orders.



THE EVALUATION POTENTIAL OF BASIC OXYGEN FURNACE (BOF) SLAG AND THE RECYCLING OF CALCIUM CARBONATE BY HYDROMETALLURGICAL METHODS

Muhammet BİLEN

İskenderun Demir ve Çelik A.Ş.
Türkiye

Keywords: Slag, Converter, BOF, Slag Recovery, Leaching, Precipitated Calcium Carbonate, İsdemir

Abstract

Steelwork slag is one of the waste material groups obtained from İsdemir basic oxygen furnace (BOF) facilities. Their chemical compositions and properties vary according to the produced quality and production conditions. Slag is obtained in the steelmaking process, during the purification of molten iron from impurities. Various researches are carried out for the use of steel slag in different industrial facilities. One of the most important factors in determining the usability of steelwork slag as raw material in different production areas is the economic contribution of the process. Today, a large part of the slag is used or discarded without fully exploiting its properties.

In this study, the general usage areas and potential sectors of the steel mill slags and recovery conditions of high purity calcium carbonate by injection of carbon dioxide into the leach solution in which Ca^{2+} ions were selectively extracted from the basic oxygen furnace (bof) slag of İsdemir by using acetic acid were studied.

1. Introduction

Slags are one of the waste material groups obtained from various metallurgical plants. Their chemical compositions and properties differ depending on the main product type and production method of the facility where they are obtained. Steelworks slag, which is one of the by-products of iron and steel factories, is obtained in the steel production process, during the purification of molten iron from impurities. Various researches are carried out for the use of steel slag in different industrial facilities. One of the most important factors in determining the usability of steelwork slag as raw material in different production areas is the economic contribution of the process. Today, most of the slags are used or discarded without using their properties. [1]

Blast furnace and steelwork slag constitutes 90% of the total solid waste generated in an integrated steel plant. Steel slags mainly consist of calcium silicate and alumino-ferrite formed by the melting of calcium, iron, magnesium and

manganese oxides. Making maximum use of converter slag is one of today's main driving forces. Efforts are underway on a global scale to increase the recovery of steelwork slag for use in various applications. [3]

2. Slag Evaluation Operation

Today, after a series of processes applied to steelwork slag in various countries:

- Metallics in pieces and granules obtained (magnetic scraps) as scrap input in the converter;
- Metallic products in powder form and finely crushed slag as charge material for the sinter blend;
- On the other hand, slags classified in various sizes with their metallics removed:

- ✓ As asphalt coating material on highways; (surface, foundation and fill material)
- ✓ As a material for improving agricultural soil;
- ✓ As raw material for cement clinker;
- ✓ As fine aggregate for reinforced concrete; (In case of rapid cooling of the slag)
- ✓ It is used as a filling material for some purposes [2]

Integrated iron and steel plants generate large amounts of solid waste. As many studies in this field have shown, approximately 400-450 kg of solid waste is produced during the production of one ton of steel. These solid wastes are generally blast furnace and steel mill slag, dust, mud, rolling mill scale, used refractories etc. The first trend today is the maximum use of steelwork slag.

After various treatments applied to the converter slag:

- Metallics in pieces and granules obtained (magnetic scraps) as scrap input in the converter;
- Metallic products in powder form and finely crushed slag as charge material for the sinter blend;

Slags classified in various sizes with their metallics removed are:

- ✓ As asphalt coating material on highways; (surface, foundation and fill material)
- ✓ As a material for improving agricultural soil;

- ✓ As raw material for cement clinker;
- ✓ As fine aggregate for reinforced concrete; (In case of rapid cooling of the slag)
- ✓ It is used as a filling material for various purposes [2]

2.1. Use of Slag in Cement Production

Research on the use of steelwork slags in the cement industry is still ongoing. Within the scope of these researches, two more methods have emerged in the use of steelwork slag as an additive in cement production. In the first of these methods, the slag of the steel mill is directly added to the cement raw material at a certain rate, and it is put into the process by grinding together in the kiln mill. In the second method, the slag of the steel mill with a grain size of up to 20 mm is fed into the furnace from the feed or outlet end of the rotary kiln and is put into the process. In the second method, an increase of up to 15% in clinker production is achieved and CO₂ and NO_x emissions decrease. [1]

Application areas of steel slag cement are listed below.

- Civil engineering applications
- Industrial building applications
- Dam construction applications
- Road construction applications [3]

According to the researches, the different properties of steel slag from conventional cement are as follows:

1. High strength with progressive time
2. Low temperature hydration
3. Good wear resistance
4. Good permeability
5. Micro-expansion
6. It has good freezing and corrosion resistance.

2.2. Use of Slag on Highways

Steelworks slag is used as an infrastructure material because of its high strength, as a filling and ballast material for land leveling, road construction, and water structures. Features that have an effect on the application in road construction; lime distribution, iron distribution, expansion due to free lime, pores, insufficient crystallization. Due to these properties, expansion due to free lime can be observed in practice. In order to prevent this and to lose the properties of the free lime naturally present in the structure of the slag, it should be waited for long time before it is laid on the road. [2]

Advantages of Asphalt Production Using Converter Slag: Converter slag is a very dense and hard material. Due to its high stability, it allows thinner asphalt to be laid in some cases. Their stability, hardness and good bonding properties make it possible to produce quality asphalt. The angular structure of the slag aggregates and thus the tighter interlocking of the particles increases the rutting resistance of slag asphalts. [4]

Disadvantages of Asphalt Production Using Steel Mill Slag: These are that transportation costs are about 20% more expensive than those of conventional aggregates due to their high specific gravity, and potential volumetric expansion problems because they contain free lime. However, due to

their very suitable physical properties, they allow the production of higher quality and long-lasting asphalt and can tolerate the increase in transportation costs. [4]

2.3. Use of Slag as Ballast Material

Ballast is the crushed stone layer in which the sleepers placed on the platform are embedded. It has been observed that the physical properties of the steelwork slag are compatible with both the standard values and the values specified in the DDY specification. It provides the necessary properties according to TSE and DDY specifications for the use of steelwork slag as a ballast material. [3]

2.4. Use of Slag in Fertilizer Production

BOF slag contains sufficient amount of CaO and MgO and is used as a natural acidity reducer in acidic soils. Phosphorus and various minerals in slag make the soil more useful as agricultural fertilizer and are dispersed in the soil. BOF slag is mostly used with this feature in Europe. In some applications, 20% of the slag is used as fertilizer. [6]

2.5. Use of Slag in the Sinter Plant

Addition of 2%, 4%, 6% and 8% steel mill slag to the sinter feed is done in Pohang plants in S. Korea. Since the average size of the slag is larger than the limestone, the flow of the sinter bed is improved and the sintering time is shortened. Adjusted slag additions up to 2% are optimal. [6]

Most steelmaking slags contain mainly CaO, MgO, SiO₂ and FeO. In low phosphorus steelmaking practices, the total concentrations of these oxides in the liquid slag are around 90%. BOF slag; In addition to its slag feature, it is a substance that has a certain value but is generally discarded because it contains significant amounts of Fe and Mn in its composition. In general, the chemical composition of this basic slag, which is formed in the conversion of liquid raw iron to steel in iron and steel production, is mainly 15-20% Fe, 4-9% SiO₂, 45-53% CaO, 3.7-5.7% MnO, 2% max MgO, 0.95% max P₂O₅ is found. In iron and steel production, phosphorus among these substances can create negativity. By adding BOF slag to the iron ore sinter blend; While the sintering requirement of the sinter can be met, significant amounts of Fe and Mn, which have become waste, can be recovered. (Mumu et al., 2001).

The slag taken from the steel mill is crushed and ground and passed through magnetic separation. After the metallic iron part is taken, it is added to the sinter blend. [5]

2.6. Use of Slag in Grit Production

Grit: The traditional method of cleaning material surfaces is sand blasting, in which a mixture of compressed air and abrasive particles (grit) is sprayed. Sand blasting is widely used for cleaning steel constructions before painting and ship hull surfaces that are newly built or under maintenance in shipyards from paint and corrosion products. Because of their low cost, slag-based grit has industrial use in the

shipbuilding industry, repair and maintenance shipyards, and cleaning underwater tanks. [4]

2.7. Use of Iron Separated Slag in BOF Plant

During the steel production and billet casting process, the scrap that has passed into the slag due to the system; It is recycled and used to be used in scrap charging to converters. The slag released during steel and billet production is collected in the slag area in order to be separated and recovered. The liquid slag poured from the slag ladle to the field solidifies and crystallizes when it encounters the controlled cooling water, and becomes a gray and less porous material. The slag, which is broken in the slag field and stored in certain sizes, is separated from its ferrous parts with a magnetic separator and these ferrous ones are charged to the converter as scrap. Smaller parts are used in the production of sinter at certain rates. Metallic iron ratio of scraps that can be used in the steel mill is required to be at least 80% by weight. In this respect, studies are continuing to increase the metallic ratio in the scrap obtained. There are slag particles on the magnetic scraps obtained from slag and in their pores, and these slag particles should be separated from the scrap as much as possible in order to increase the metallic ratio. [2]

2.8. Evaluation of Steelwork Slag in the World

Global efforts the use of BOF slag as recovery in various applications continues increasingly. The main purpose is 100% reuse of steelwork slag. It has always been studied for the correct evaluation of iron and steel slag in steelworks. The wide pattern of production and reuse of solid waste materials in different countries and India is illustrated in the examples below. Steel slag is stocked in separate areas and applied in many areas depending on its specific properties. For example;

- a) Sites in China submitted their declarations on cement production.
- b) Some Japanese sites are focused on road construction.
- c) Posco steel enterprises in S. Korea attach importance to the use of alloy as a material in blast furnaces and sinters.
- d) Steel mill slag was added as an alloy material to the sinter feed at the rate of 2%, 4%, 6% and 8% at the Pohong Enterprises in S. Korea. Adjusted slag addition up to 2% has been found to be optimal.
- e) In Europe, slag is used as fertilizer and soil aerator. It acts like a reversible cycle between blast furnaces and agricultural soils.
- f) Indian sites must follow a policy that maximizes the use of steel slag.
- g) In Japan, studies have been carried out for many years for the use of steel mill slag, which is dense, hard and similar to gravel, as aggregate. In the researches, the physical properties of steel slag, the change of these properties over

time, stabilization as aggregates were discussed. The roads made and in use using slags were examined.

h) Studies on the economic evaluation of blast furnace slag, which form large groups among industrial wastes, have been going on for many years in western countries. More than 12 million cubic meters of slag have been produced and used in glass ceramics in the United States.

1) 64% of the steel slag produced in Australia is used in road base material and asphalt. [7]

2.9. Evaluation of Steelworks Slag in Turkey

Activities at Erdemir A.Ş.: The steelmaking slag produced as a result of steel production at Erdemir is processed in the crushing-screening facility and the metallic part is evaluated as scrap in converters. The part in the size range of 0-10 mm is used in sinter production at 130-140 thousand tons/year. However, its use in sintering is limited because the blast furnace increases the hot metal phosphorus content. When high-phosphorus liquid metal is charged to the converter, the cleanliness of the steel deteriorates and the consumption of oxygen and lime increases. With a research project, the possibilities of using slag as road aggregate and railway ballast material were investigated. As a result of the characterization studies, it has been revealed that the slag has the necessary properties to be used as road aggregate and railway ballast material. [4]

Works at İsdemir A.Ş.: It is reported that an average of 300-500 thousand tons of scaling and slag material is produced annually in the steel mill unit and poured into the slag casting area. However, in recent years, in line with the technological development, the slag of the steelworks is added to the sinter after it is mixed with ore at a rate of 2.5%. In this way, the recovery of steelwork slag was achieved.

Almost all of the slag in the İsdemir slag field has been separated by the contractor. 3-5% iron from the steelwork slag is loaded into trucks with excavators just like an open pit, and separated into sterile slag with magnetic breakers and separators, and brought to the economy.

3. Recovery of Calcium Carbonate by Hydrometallurgical Methods

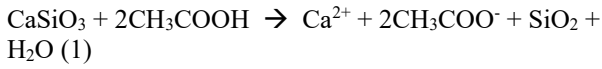
The chemical analyzes of the converter slag used in the study are given in the table below. Accordingly, it is seen that approximately half of the material to be leached into solution is calcium-based.

Table 1. Chemical analyzes of the converter slag

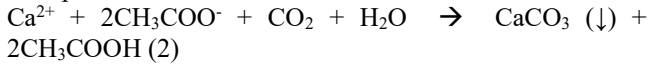
SiO ₂	CaO	Al ₂ O ₃	MgO	FeO	MnO	TiO ₂	Fe	P ₂ O ₅	Fe ₂ O ₃
14,1	48,8	2,1	4,0	17,7	4,9	0,6	17,3	1,9	6,9

Solution of Converter Slags with Acetic Acid:

As a result of leaching of steel mill slags with acetic acid, calcium extraction was carried out as a requirement of the basic reaction given below.



Precipitation of Calcium Carbonate:



After the solid-liquid separation of the solution formed by the dissolution of the steelwork slags with acetic acid is made, the precipitation of Ca^{2+} ions from the solution as CaCO_3 and the selective precipitation of other impurities in the solution (such as magnesium, iron, silica) form the most important part of the study. For this purpose, experiments were carried out under various conditions to precipitate Ca^{2+} ions as CaCO_3 from a clean solution containing calcium acetate ions, passed through 2-4 μm filter paper. Before and after these precipitation experiments, the pH value of the original solution sample was measured.

Recovery of calcium carbonate from steel mill slags by hydrometallurgical methods and especially İskenderun Demir ve Çelik Fabrikaları A.Ş. After the leaching of (İsdemir) steel mill slags with acetic acid (CH_3COOH), calcium is taken into a solution with a selective dissolution and the recovery conditions of high purity solid calcium carbonate (CaCO_3) by adding CO_2 to this solution were investigated. This study was carried out in two stages. While the slag of the steelworks, which has been purified as much as possible with a magnetic separator, is subjected to leaching with acetic acid, calcium ions are taken into solution, while other impurities such as iron, silica and magnesium are not extracted as much as possible. The other step, and the details described here, is the step in which calcium carbonate precipitation is carried out by giving CO_2 gas to the solution called carbonation. In the extraction phase, at 50 °C, 6.5% solid-liquid ratio, slag with a particle size of less than 0.1 mm and a solution with 0.7 M acid concentration, calcium ions were selectively taken into the solution with a yield of 61.38% at the end of the test period of 2 hours. Calcium ions in the liquid are in the form of calcium acetate. NaOH solution is needed to convert this compound into $\text{Ca}(\text{OH})_2$ form. In the carbonation experiments, the most suitable conditions were found to be 15 ml NaOH amount, 50 °C temperature, 2 bar pressure and 4 min reaction time. The NaOH solution used in the precipitation phase was recovered as sodium acetate at the end of the experiment, but since it could not be measured in XRF and ICP devices, its purity could not be commented on. As a result of these values, the precipitated calcium carbonate was obtained with 99.77% purity and 92.1% yield during the precipitation phase. It also contains 0.227% MgO , 0.016% Fe_2O_3 , 0.001% SiO_2 trace elements. When 100 gr of slag is used, 49.02 gr solid CaCO_3 is formed with 56.5% yield as a product. According to the XRD analyzes made at

the end of each experiment, it was determined that almost all of the solid contained calcite phase, and when SEM images of this solid were examined, it was scalenohedral (triangular hexagonal) crystal structure, and according to the grain size analyzes, it showed low grain size distribution in the narrow range required by the paint and paper industry. Although precipitated calcium carbonate has not started to be used in Europe, it has a large share of use in America. The reason for this is that it is a product whose grain size and crystal shape can be controlled. Although its cost is higher than micronized calcite, the use of good standards has increased the usage areas of precipitated calcium carbonate.

References

- [1] DÜNDAR, H., 2006, Farklı Sogutma Hızlarında Sogutulan Çelikhane Cürüflarının Ögütme Parametrelerinin İcelenmesi, Hacettepe Üniversitesi, Ankara www.posco.co.kr POSCO / Sustainability
- [2] ALTAN, E., 2001, Çelikhane Curufu İçerisindeki Hurdaların Değerlendirilmesi, I. Ulusal Demir-Çelik Sempozyumu ve Sergisi Bildiriler Kitabı, Zonguldak, 1003-1011, Ankara www.posco.co.kr POSCO / Sustainability
- [3] GÜNAY, E. ve KARA M., 2005, Erdemir Çelikhane Curuflarının Ekonomik ve Ekolojik Değerlendirilmesi, 3. Demir Çelik Kongresi, Zonguldak
- [4] İSDEMİR SİSTEM GELİŞTİRME MÜDÜRLÜĞÜ, 2004, Çelikhane ve Yüksek Fırın Cürüflarının Dünyadaki Uygulamaları, İskenderun Demir Ve Çelik A.Ş. Teknik Hizmetler Genel Müdür Yardımcılığı (Yayınlanmamış Rapor)
- [5] MUMCU, A., ARISOY F., ŞEŞEN K., 2001, Sinter Üretiminde Bazik Oksijen Fırını (BOF) Cürufunun Kullanılmasının Etkileri, I. Ulusal Demir-Çelik Sempozyumu ve Sergisi, Zonguldak
- [6] STEEL TIMES INTERNATIONAL, 2000 (Waste Management of Steel Slug)
- [7] TURAN, S. ve KAYA, G., Yüksek Fırın Cürufunun Seramik Sektöründe Katma Değeri Yüksek Ürünlerin Eldesinde Değerlendirilmesi, Mühendis ve Makina-Cilt: 45 Sayı 536



ESTIMATING TAP HOLE CLAY CONSUMPTION IN BLAST FURNACE BY FUZZY LOGIC METHOD

Mehmet GÖKOĞLU, Ramazan YARAŞIR

İskenderun Demir ve Çelik A.Ş.
Türkiye

Keywords: Blast Furnace, hearth, taphole clay, Level 2 expert system, fuzzy logic.

Abstract

Liquid hot metal (LHM) and slag are produced as a result of the reaction of the ferrous materials and coke charged in the blast furnace (BF) with the hot blast blown from the tuyere located at the bottom of the furnace and accumulates in the BF hearth. For the drainage of the LHM and slag accumulated in the hearth, the cast opening process is performed with a specially designed drill. After the LHM and slag drainage in the hearth is completed, the refractory-based taphole clay filled into the specially designed mud gun equipment is injected into the tap hole and the tap close process is carried out.

Another task of the taphole clay is to ensure the formation of mushroom around the taphole at the hearth. Thanks to the mushroom thus formed, BF contributes to the prolongation of the hearth life by minimizing the wear of the carbon blocks around the hearth during LHM and slag drainage.

The consumption of the taphole clay varies depending on the working conditions and taphole length of the BF, and the taphole clay quality. On the other hand, under ideal conditions, the use of taphole clay from the taphole is an important factor in terms of cost and life of the BF hearth.

In this study; Studies have been carried out on the estimation of the consumption of the taphole clay to be used in, by fuzzy logic method, depending on the taphole length, %Si value in LHM and slag arrival times. By applying the rules obtained by the fuzzy logic system on the Level 2 expert system, Taphole Clay Consumption Model was developed, which gives a taphole clay consumption recommendation in each tap.

1. Introduction

The blast furnace is a sophisticated operation that is difficult to control because all of its phenomena are not fully understood. Due to measurement challenges and considerable process delays, control is even more difficult. Operator experience and manual control procedures are used in numerous circumstances to operate blast furnaces. Expert systems, which comprise monitoring functions and advising systems that assist operators in maintaining stable and optimal process conditions, make use of operator expertise [1].

The slag and iron that has accumulated in the hearth of the blast furnace is drained by drilling the furnace open at certain tapholes and draining it. Gas will exit the taphole once the liquids have been removed (this is known as a gas blow), indicating that the liquid level elevation is lower than the taphole elevation. While this may seem self-evident, the slag and hot metal interfaces near the conclusion of a cast are not horizontal, as they would be when draining a bucket, because the blast furnace is under pressure. The liquid levels are contorted by the presence of gas pressure above the slag, the slag curves down to the taphole, and the hot metal level curves up to the taphole. (Figure-1). The degree of slag and hot metal level distortion is determined by the drainage speed and blast pressure. When the operator drills a large diameter taphole or the taphole clay erodes quickly, the rapid drainage pushes the slag layer down and a gas blow occurs, indicating that the hearth is empty when there is still a significant amount of slag and iron in the hearth. Casting the blast furnace slowly and reducing the iron and slag casting rate to as near to the output rate as possible is the best strategy to reduce "false blows." This is mostly determined by the quality of the taphole clay, the tapping schedule, and the ability to operate the blast furnace with several tapholes [2].

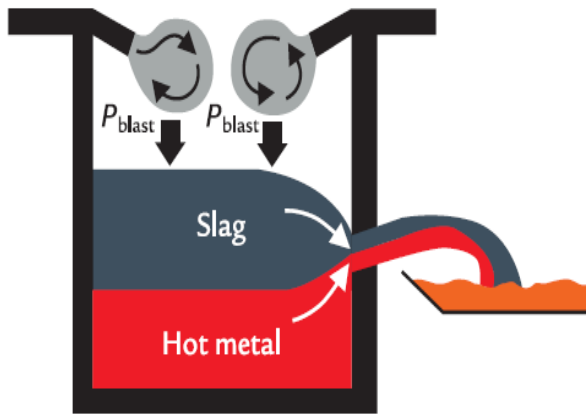


Figure 1. pig iron and slag levels in the blast furnace during casting [2]

One of the most essential consumables utilized in the blast furnace is taphole clay. Superior grade clay is required for a steady blast furnace operation because it ensures continuous removal of liquid hot metal and slag. Taphole clays are sophisticated and purpose-built to handle the needs of extracting molten iron and slag at temperatures as high as 1480- 152^oC for long periods of time, such as 13 hours, with minimum erosion (Fig.2).

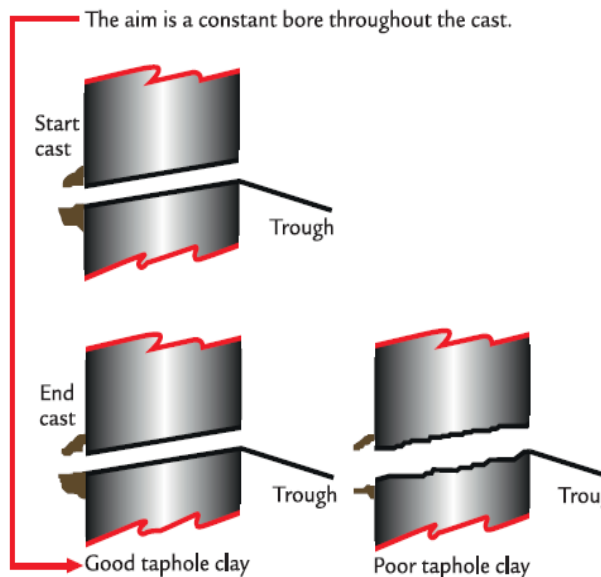


Figure 2. During the casting process, a good taphole clay has less erosion[3]

Fuzzy logic, a well-known method for dealing with ambiguous and erroneous data, is used by modern expert systems. It also provides a practical and educational way to express operator experience in language form [3].

2. Tapping Expert System in Blast Furnace

Iron tapping is often handled manually in mills, with activities based only on information from past tappings. When planning the next tapping, the

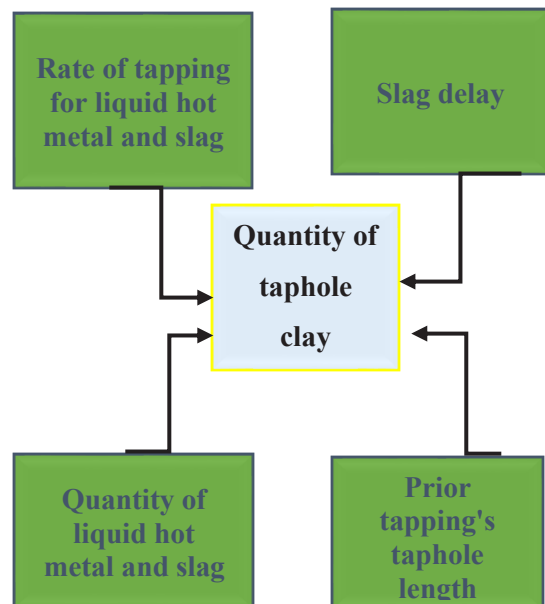
operator considers the temperature, tapping duration, and prior taphole length. These are primarily valid characteristics, although differences in other blast furnace operating factors, such as heat balance, can lead to incorrect conclusions in some cases. Iron tapping expert system alerts operators to changes in process variables and provides recommendations to assist reduce tapping time variances. This is done to keep the furnace running smoothly and to keep the hearth as empty as possible during tapping.

The iron tapping expert system is a modular system that includes the following modules:

- Casting opening time
- Casting
- Plugging
- Closed time.

The plugging module monitors past tapping and forecasts changes in taphole length, as well as advising on how much mass should be introduced. If the length of the taphole is shortening, the system instructs the operator to raise the amount of tapping mass in the next tapping, while in the opposite scenario, it suggests a reduction in the same amount. The key variables affecting the quantity of injected taphole mass are shown in Figure 1.

Figure 3. Variables that have an impact on the quantity of injected taphole clay



The plugging module monitors past tapping and forecasts changes in taphole length, as well as advising on how much mass should be introduced. If the length of the taphole is shortening, the system instructs the operator to raise the amount of tapping mass in the next tapping, while in the opposite scenario, it suggests a reduction in the same amount.

At Iskenderun Iron and Steel Corporation, there are three blast furnaces, two of them two tapholes, one of them three tapholes. The control of taphole length at blast furnace 2 is the subject of this research. On average, the closing time is between 25-30 minutes and the tapping time is 85 minutes. The ideal tapping hole length is 2.2 meters, with an inclination angle of roughly 10 degrees.

The Fuzzy Con-program package, initially developed in the Control Engineering Laboratory, was used to create the fuzzy plugging module (Juuso et al., 1994) [4].

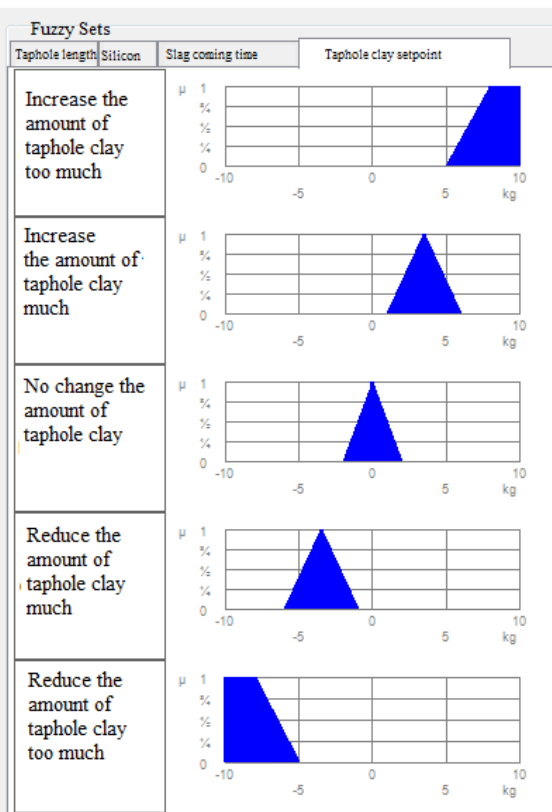


Table 2. Table of rules for estimating taphole clay consumption

It also provides adequate memory to define the number of variables and membership functions that are required in this type of application. It is possible to employ both triangular and trapezoidal membership functions.

The rule base can be created as a list or a matrix, and then verified using real-world data through simulation. The following method is commonly used when creating fuzzy models:

- Choosing input and output variables
- Choosing input and output variable membership functions
- Defining the rule base
- Testing and adjusting

Table 3: Input rules for fuzzy logic

Taphole length (m)	Si (%)	Slag Time	Taphole clay set
Taphole length too long	Si content too high	Slag coming time too long	Reduce the amount of taphole clay too much
Taphole length too long	Si content too high	Slag coming time long	Reduce the amount of taphole clay too much
Taphole length too long	Si content too high	Slag coming time normal	Reduce the amount of taphole clay too much
Taphole length too long	Si content too high	Slag coming time little	Reduce the amount of taphole clay too much
Taphole length too long	Si content too high	Slag coming time too little	Reduce the amount of taphole clay too much
Taphole length too long	Si content high	Slag coming time too long	Reduce the amount of taphole clay too much
Taphole length too long	Si content high	Slag coming time long	Reduce the amount of taphole clay too much
Taphole length too long	Si content high	Slag coming time normal	Reduce the amount of taphole clay too much
Taphole length too long	Si content high	Slag coming time little	Reduce the amount of taphole clay too much
Taphole length too long	Si content high	Slag coming time too little	Reduce the amount of taphole clay too much

Variables that predicted especially strong longitudinal wear of the taphole were prioritized. The following input variables were chosen as input variables:

- Taphole length (x1)
- Slag delay (x2)
- Si-content (average over the tapping period) (x3) [1]

Comprehensive work has been done to estimate the

taphole clay consumption of the taphole with fuzzy logic, and 125 rules have been developed. Every parameter in the rules; It was done in accordance with the fuzzy logic of very little, little, normal, more, too much.

The rules determined according to fuzzy logic systematics were loaded into the level-2 system (Table -3).

3. Results and Discussion

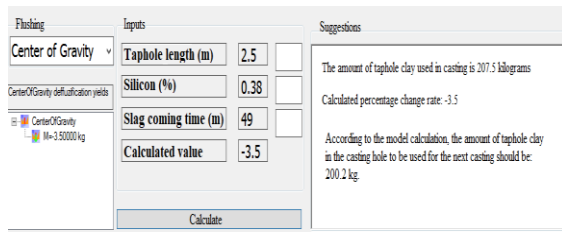


Figure 4: Taphole clay consumption recommendation based on forecasting model

With the fuzzy logic program, it was provided to give suggestions on the taphole clay consumption of the taphole for the next casting. Considering this recommendation, a great contribution was made in determining the number of taphole clay used. (Figure-4)

As a result of the model made for casting taphole clay consumption with fuzzy logic, the fuzzy model gave results as in figure-5.

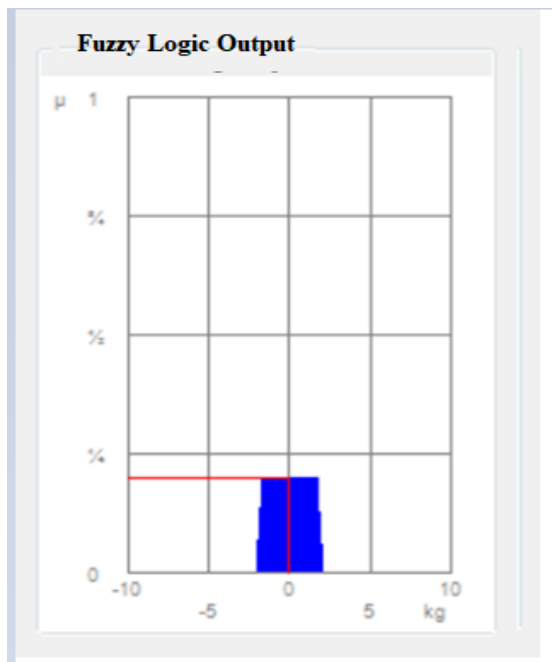


Figure 5: Suggestion change in taphole clay consumption according to the results of the specified rules, level-2 was calculated as Fuzzy Output

4. Conclusion

Results from the hand with the Taphole Clay Consumption Model;

- For Casting Hole consumption; amount of taphole clay used in casting, hole size, taphole clay leakage, etc. data has been entered correctly.
- By entering the data correctly, more real data about the taphole clay can be reached, and the taphole clay can be evaluated objectively on a brand basis.
- The model is constantly monitored and other factors affecting taphole clay consumption will also be evaluated.

References

- [1] Saarela, A., Leiviskä, K., & Ruuska, J. (2003). Expert system for taphole plugging in a blast furnace. IFAC Proceedings Volumes, 36(24), 65-70.
- [2] Cameron, I., Sukhram, M., Lefebvre, K., & Davenport, W. (2019). Blast Furnace Ironmaking: Analysis, Control, and Optimization. Elsevier.
- [3] Matsuda, K., Tamura, K., Konishi, M., Kitano, S., Kadoguchi, K., Takami, M. (1990). Application of artificial intelligence to operation control of Kobe No. 3 blast furnace. Proceedings, The Sixth International Iron and Steel Congress, Nagoya.
- [4] Juuso E. K., J. Myllyneva, and K. Leiviska, Adaptive Tuning of Fuzzy Logic Controllers. Preprints of the 2nd IFAC Workshop on Computer Software Structures Integrating AIKBS Systems in Process Control, August 10-12, 1994, Lund, Sweden, pp. 82-



COMPARISON OF MANGANESE OXIDE (MnO) AND IRON OXIDE (FeO) ANALYZES IN STEEL PRODUCTION SLAG WITH DIFFERENT ANALYSIS METHODS

**Bariş SAĞLAR¹, Aydan GÜLSÜREN¹, Onur OREL¹, Ramazan BİLGİN²,
Memduh Kağan KELER³**

¹İskenderun Demir ve Çelik A.Ş., ²Çukurova Universtiy, ³Ereğli Demir ve Çelik
Türkiye

Key Words: Slag, Iron oxide, Manganese oxide, ICP-OES, XRF, Titrimetric method

Abstract

Characterization of by-products is important in primary and secondary production facilities in steelmaking processes. The chemical and mineralogical determination of the output by-products (slag of the steel production process) has been evaluated within the scope of this study. The content of converter (BOF) slags consists of phases such as calcium oxide, magnesium oxide, manganese oxide in basic oxide structure, and silicon dioxide and iron oxides in acidic oxide structure.

Converter slag is generally in the form of Fe₂O₃ and Fe₃O₄. It has been determined that the general structure of ladle furnace (LF) slags is in the form of calcium aluminate, the total value of the minor phases such as FeO and MnO is high in the converter slag analysis, and these values are lower in the ladle furnace slag [1-2].

MnO and FeO becomes difficult in the processes where the final product is approached. The aim of the studies is to determine how the minor phase distribution changes with which process data, especially in ladle furnace slags.

1.Introduction

The aim of the studies was to determine how the minor phase distribution changes with which process data, especially in ladle furnace slags. In this context, it is expected that in the castings where the minor phase ratio is less than 5%, effective bottom mixing, steel slag reactions are at ideal levels, the Al₂O₃ ratio is between 25-30 and the steel cleanliness is in a clean status according to ASTM E (45) standards.

It is estimated that the ladle furnace operations are not at the desired level technically in castings where the minor phase ratio is greater than 5% and there may be areas open to improvement. With the high % FeO ratio in the slag,

steel loss occurs and it is known that the slag structure physiochemically reduces the inclusion capacity [3-4].

2.Materials and Methods

In research studies, XRF and ICP-OES instruments and titrimetric method were used as characterization methods. Since the slag composition consists of complex components with oxides, the elemental values obtained in the XRF and ICP OES method are multiplied by a certain coefficient. In the percentage calculation, the analysis results obtained from ICP-OES for the Mn element were verified by comparing them with the XRF results. In addition, the correlation coefficient was determined by associating FeO, which was determined by the titrimetric method, with the Fe output obtained from the XRF analysis.

2.1. MnO Determination of Slag Samples by Melting Method in XRF Device

Slag remaining in the ladle after being taken out of the ladle during the liquid steel production phase is poured into the slag ladle, and samples are taken from time to time. After the samples are sent to the laboratory, the sample is placed in the grinding bowl and ground to <150 µm for 90 seconds in a disc grinder. After the grinding process is completed, magnetite and metallic iron are removed with the chamber magnet. The sample is dehumidified in an oven at 105°C for 2 hours. The dehumidified sample is left to cool in the desiccator. Pt / Au 0.9 g of sample was weighed on a precision balance to the crucible and mixed by adding 9 g of 67% flux material. Pt / Aukroze was placed in the melting device and the melting process was started by setting the appropriate program in the XRF device and the results were observed.



Figure 1. XRF Zetium device which is used for industrial tests

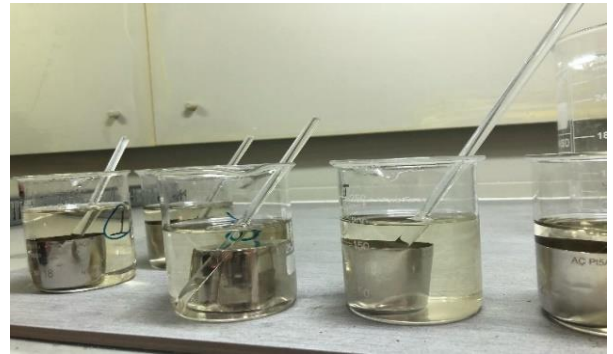


Figure 3. Dissolving the slag in the smelting process in acid

2.2. Determination of MnO and FeO in XRF Device by Press Method of Slag Samples

The incoming sample is first ground in the mill. The sample is prepared in the press machine with 150kN for 10 seconds, the press process is started and the results are observed.



Figure 2. XRF ARI9800xp device which is used for industrial tests

2.3. MnO Analysis of Slag Samples by Melting Method in ICP-OES Device

0.5 g of the ground slag samples were weighed and Pt 6 gr K_2CO_3 , Na_2CO_3 mixture and 1.5 gr $Na_2B_4O_7$ were put into the crucible. Platinum crucible was mixed with Platinum wire. Melting process was applied for 2 hours in 1000 °C ash furnace. Pt with the sample subjected to the melting process the crucible ash was removed from the furnace and left to cool in the desiccator. Platinum crucible was placed in to 250 ml beaker containing 50 ml of HCl and 50 ml of water and dissolved on the heating plate. After dissolving for 30 minutes, the beaker is left to cool at room temperature. The sample is transferred to 1000 volume flask with the help of a funnel and made up to 1000 ml with ultrapure water. The reading process was started on the ICP-OES device and the results were observed.



Figure 4. Reading the prepared slags in the ICP-OES 720 device

2.4. Dissolution of Slag Samples by Wet Method and Analysis of FeO

The ground slag sample was weighed 0.5 g and transferred to the flask. 0.5 g Na_2CO_3 , 0.5 g NaF and 100 ml HCl were added to the flask. The mouth of the flask was closed with a watch glass and the sample was completely dissolved on the heating plate. When the dissolution process was achieved, 100 ml of distilled water was added to the sample in the flask and cooled at room temperature. After cooling, 5 ml of phosphoric acid solution and 5 drops of sodium diphenylamine Added sulfonate indicator. The solution was titrated with $K_2Cr_2O_7$ and when the color transformation became dark violet, the titration process was terminated and the consumption was read and the calculation was made.



Figure 5. Titration of samples with $K_2Cr_2O_7$ titrant

$$\text{CALCULATION \%FeO} = \frac{S \cdot F \cdot M \cdot N \cdot 100 \cdot 1,29}{1000 \cdot T}$$

S: Consumption, F: Factor, M: Molarity: Normality, T: Weight, 1,29: Stoichiometric constant

3. Results and Discussion

Titrimetric method and ICP-OES methods in the slags released in iron-steel production processes. In this context, the composition of FeO and MnO phases in the slag was evaluated by titrimetric analysis method and compared with XRF.

The main purpose of the studies is to clearly determine the % FeO and % MnO values and to increase the metallurgical knowledge about steel cleaning, liquid steel oxygen activity, steel-slag interaction reactions, slag-refractory reactions. Steel cleanliness is a conceptual quality factor in the liquid steel production process, which is an in-depth research area in the literature and determined by advanced metallurgical characterization methods.

It is aimed to keep the complex phases with non-metallic oxide and/or sulfur in the steel at a certain scale. In this context, the effect of slag analysis on steel cleaning should be further evaluated.

Along with the thermodynamic investigations, it was determined that in the reaction equilibrium conditions, in an ideal slag composition at the exit of the ladle furnace (LF), at a temperature of 1600°C, total Fe is mostly in the FeO phase and negligibly in the Fe₂O₃ phase in the slag. When the process data and chemical analyze are examined, the chemical composition of the slag (basicity of CaO) is the composition that most affects the total FeO and MnO values. $MgO / Al_2O_3 + SiO_2$ was determined. However, in addition to the validation studies, the wet analysis outputs were used in the mineralogical phase structure. Subsequently, the obtained results were tested in

the XRF device to verify the new coefficients. When the results were examined, the titrimetric analysis outputs were evaluated for the detection of minor phases with more accurate coefficients of the XRF device.

% MnO value is directly related to the slag oxygen activity. It has been determined that alloying elements and slag-forming materials should be evaluated according to the slag oxygen activity and temperature.

% FeO and % MnO value, the higher the steel cleanliness value.

In addition to thermodynamic studies, kinetic factors were evaluated separately in the studies and in-depth information was obtained about steel production slags.

4. Conclusion

The results obtained from the ICP-OES device were tested in the XRF device to confirm the total FeO with more accurate coefficients. When the results were examined, the titrimetric analysis outputs were evaluated for the detection of minor phases with more accurate coefficients of the XRF device. In all analyses, the MnO ratio was found to be less than 5%. Analyzes greater than 5% were evaluated by R&D, laboratory and operation teams, and investigations were made on the slag escaping from the converter. In order to reduce the oxygen activity in the steel in castings with high % FeO and % MnO values, ferroalloys and granular aluminum were added to the slag as a reducing agent. It has been determined that the holding capacity of the inclusions in the slag is directly related to the FeO and MnO values. If the % Total FeO and MnO values are less than 2%, favorable results were obtained in terms of steel cleanliness (ASTM E-45).

Acknowledgment

The authors would like to acknowledge that this paper is submitted in partial fulfilment of the requirements for master's thesis at Çukurova University. The authors also thank Iskenderun Iron and Steel (ISDEMİR) Laboratory team for their support.

References

- [1] Günay, E., & Kara, M. (2005). Erdemir Çelikhane Cürufalarının BEkonomik Ve Ekolojik Değerlendirilmesi. *TÜBİTAK MAM, Malzeme Enstitüsü*.
- [2] Bilen, M. (2010). Çelikhane curuflarından liç-karbonatlaştırma prosesi ile kalsiyum karbonat kazanılması. *Yüksek lisans tez çalışması, Çukurova Üniversitesi, Adana*.
- [3] Altan, E. (2001). Çelikhane curufu içerisindeki hurdaların değerlendirilmesi. *I. Ulusal Demir-Çelik Sempozyumu ve Sergisi*.
- [4] Hasse, S., & Brunhuber, E. (2000). *Giesserei-Lexikon 2001*. Fachverlag Schiele & Schoen.

WATER MANAGEMENT IN IRON AND STEEL INDUSTRY

Mehmet Burak ATAN, Erkin Y. GEDİK, Onur MARTI, GÖkhan GÜNGÖR, Arif AKSOY, İbrahim SARI

İskenderun Demir ve Çelik A.Ş.
Türkiye

Keywords: Water Resources, Water Management

Abstract

The impact of climate change on water resources results in changes in the hydrological cycle and changes in water quality. Although the total amount of water in the world remains constant with the hydrological cycle, changes in the precipitation regime negatively affect the amount and quality of surface and underground water resources. Although water is one of the most important inputs in the Iron and Steel industry, production cannot be made without water, and it is one of the sectors with high water consumption. At Iskenderun Iron and Steel (ISDEMİR), water management is given the utmost importance as it is aware of the importance of water for both nature and production.

Although the principle of 'we cannot manage what we cannot measure' has been adopted in the management of water, measuring water is the basis. In total, measurement values are taken from 167 different points. These values can be monitored instantly on the PIMS (Plant Information Management System) installed in our factory and are reported daily, monthly and weekly in the ENYS (Energy Management System) through which these data flow. With established systematics, increases in consumption points and places in need of improvement throughout the factory are determined. The circulation rate of the facilities and the water consumption per production of the factory are monitored within the annual targets and necessary actions are taken in case of target deviations. In addition, ISDEMİR's water footprint calculations were made in 2021 and action items were determined

1. Introduction

Water is used in every shop of a steel plant and for practically all the functions of water. A steel plant cannot function without water. Because of this steel plants are normally built near to ample sources of fresh water to ensure the availability and quality of water needed by the steel plant. However these days, greater attention is given to the management of available water resources in the steel plant environment, particularly in terms of water quality, quantity, and how it is used.

A steel plant uses large quantity of water for steam generation, cooling, waste transfer, and dust control etc. The processes of the plant cannot take place without the availability of water. Enormous quantity of water is needed

at every stage of production. Less than 10 % of this water is actually consumed and balance water is usually is returned to the system [1].

Several factors make water a versatile material. It is normally easy to handle, readily available, and inexpensive. It can carry large amounts of heat per unit volume (high specific heat). It neither expands nor compresses significantly within ambient temperature ranges. It does not decompose. It can dissolve, entrain, suspend, and subsequently transport other materials.

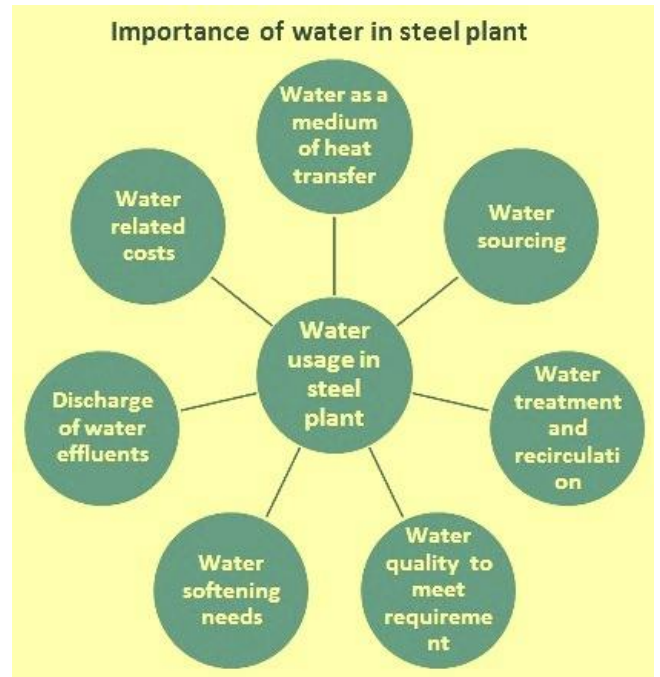


Figure 1: Importance of water in steel plant

The impact of climate change on water resources results in changes in the hydrological cycle and changes in water quality. Although the total amount of water in the world remains constant with the hydrological cycle, changes in the precipitation regime negatively affect the amount and quality of surface and underground water resources. Although water is one of the most important inputs in the Iron and Steel industry, production cannot be made without water, and it is one of the sectors with high water consumption. At Iskenderun Iron and Steel (ISDEMİR), water management is given the utmost importance as it is aware of the importance of water for both nature and

production.

2. Materials and Methods

At İSDEMİR, the process of water from the source to its discharge is meticulously monitored.

İsdemir's industrial fresh water resources; Mersin Stream Water, Well Water and Aslantaş Dam Water. In addition to these water sources, sea water is also used for condensation of steam at İsdemir.

In the industrial process, heat has to be removed or transported. Water is used as a heat transfer element in the systems. Systems can be divided into 3 main classes according to the way water is used. These:

- Single pass cooling,
- Open loop (multi-pass) cooling,
- It is closed circuit cooling.

All of these water usage patterns are monitored with established systematics and actions are organized according to the outputs.

In İsdemir, the consumption of water for the steel production was 1.1 billion m³ in 2021; consumption per ton of steel produced was 6.5 m³. These large water consumption shows that Water Management has become a very crucial requirement for the iron and steel industry.

One of the main requirements for the management of water is the presence of an effective measuring and reporting system.

In İSDEMİR, water monitoring infrastructure is mainly carried out on 2 systems.

- 1.Plant Information and Management System (PIMS)
2. Energy Management System (ENMS)

2.1 Plant Information and Management System (PIMS)

PPIMS systematic was established to measure all inputs and

Onayla		Dağıt Ve Onayla		Excel		Aylık Detay Excel	
Servis Suyu							
Üretim-Tüketim Dengesi							
05/2022							
Kcal/m ³		500					
Üretim (Beli)		2.216.262		84.463.183		889.461	
Kayıp		2.216.262		84.463.183		889.461	
Üretim (Net)		2.216.262		84.463.183		889.461	
Dağıtım		2.216.262		84.463.183		889.461	
Ünitesi Tüketim Değerleri :							
Matörler	Ünitesi	Mersin Csu1 m ³	Sirkülasyon Suyu m ³	Karşın Suyu m ³	İşeme Suyu m ³		
210111	KOK BAFARVALARI (1-2-3-4)	224.792	0	0	0		
210112	SİNERJİ FABRİKASI	22.354	0	0	0		
210113	1.YÜKSEK FIRIN	0	0	0	0		
210112	2.YÜKSEK FIRIN	46.180	3.224.000	0	0		
210113	1.YÜKSEK FIRIN	676.630	4.836.000	0	0		
210114	4.YÜKSEK FIRIN	86.250	7.615.903	124.448	0		
210114	PELVARIZZ KAMÜR ENJEKSİYON (PC)	87.666	0	0	0		
210114	PERVAKASISI	2.700	0	0	0		
210141	KİRCİ C FABRİKASI	0	0	0	0		
210245	7. KİRCİ C FIRINI TESİSİ	11.200	0	0	0		
210245	8. KİRCİ C FABRİKASI	11.200	0	20.750	0		
210245	1. SLAB DÖKÜM TESİSİ	0	5.641.068	0	0		
210274	KONİMLİKTİ ÜR DÖKÜM	418	2.228.716	6.464	0		
210311	SLAB İSTİHAR TESİSLERİ	0	20.739.069	0	0		
210321	KANGAL HADDEHANSİ	146.906	1.776.612	1.333	0		
210313	YAN ÜRÜNLER	72.590	3.720.000	0	0		
210314	KOK KURU SÖNDÜRME BEHARİ	1.737	0	0	0		
210321	HAM MADDE MANİPLASYON	43.133	837.000	0	0		
210314	CURRY İSLEME TESİSİ	31.000	0	0	0		
210322	ÇELİK HANE BEHAR KAZANI	0	0	0	0		
210214	KONVERTÖRLE R	76.000	942.674	132.226	0		
210215	POZİTİF ALKALİ BASAÜRENDİSİZLEŞTİRME	9	375.000	0	0		
210214	LOKOMOTİF, DEMİRYOLU VE SİYALİZASYON BAKIM İŞLERİNİN ARIZ VE ARIZLARTI ADI R BAKIM ATÖLYESİ	466	0	0	0		
210248		466	0	0	0		

outputs that affect the cost and to send these measurements automatically to the ERP system used by Cost Accounting.



In PIMS, measurement values are monitored instantly. There are 167 flow meters in total at İSDEMİR where water usage is monitored. Instant values collected in PIMS are transferred to ENMS system.

Figure 2: Flowmeter measuring points diagram

2.2. Energy Management System (ENMS)

It is a software designed for the preparation of Energy Balance Report and the reporting of energy items that will create data for Cost Accounting.

Within İSDEMİR;
Auxiliary Operations Directorate Energy Management,



Electronic Automation Department,
ENYS Coordinators and
Prepared by the Software Development Department.

Determined energy items are reported and monitored daily, monthly and annually. The data taken from 167 flow meters for water are classified according to their usage areas in this software and turned into a report.

Figure 3: Energy Management System (ENMS)

Daily, monthly and annual reports are examined by the relevant personnel, and the reasons for the increase in water consumption are investigated in order to ensure efficient use of water.

The results of the improvements made can also be observed with the measurement systematic that has been established. Within the scope of İSDEMİR improvement works in 2021, 56 Kaizens were made and completed.

2.3 Water Footprint

Corporate water footprint is a tool and concept that directly measures water consumption during the creation of a product or service. In order to ensure production continuity of industrial facilities, it is necessary to measure, monitor and improve their water consumption in line with the ISO 14046 Global Water Footprint Standard.

Within the scope of the study, the operational water footprint of İSDEMİR was calculated. The type and magnitude of water consumption and pollution at different stages of the production process are shown in detail.

İSDEMİR supplies water from two different basins. One of them is Ceyhan Basin and the other is Asi Basin. İSDEMİR is the dominant industrial water user in the basin with an overall blue water footprint of 16.3 million m³ /year for 2021. Most water use is concentrated in direct operations (93 percent). The product blue water footprint of steel is 6,5 m³ / ton.

The critical pollutant requiring the largest assimilation volume was determined as total suspended solids (TSS) and oil-grease. The total gray water footprint of the facility in 2021 is 43 million m³, and these issues will be given priority in the future projections.

3. Results and Discussion

Although the risk of drought is increasing day by day in our country and in the world, the effect of drought has been felt seriously in the basin where our factory supplies water in recent years.

From the point of view of both the continuation of life and the industry, water is indispensable for the continuity of production. In our factory, it is known how important water saving is with an environmental perspective, and all the steps taken are towards more efficient use of water.

4. Conclusion

Through to the systematics established by İSDEMİR, the impression of water from the source to the end use point can be made. In this way, efficient use of water, future projection and improvement works can be done better.



THE EFFECT OF MAINTENANCE ACTIVITIES ON ENVIRONMENTAL MANAGEMENT IN IRON AND STEEL FACILITIES

Hasan BULUT, Ayşe ÇELİK, Merih YAMAN, Gökçe ARSLAN

İskenderun Demir ve Çelik A.Ş.
Türkiye

Key Words: Asset management, environmental management, maintenance management, sustainability, energy efficiency

Abstract

As in every production facility, all systems and machines are expected to operate at the desired level in a sustainable, reliable and efficient manner in the integrated iron and steel production line. Achieving this situation is possible with an effective asset management. Asset management is a very complex structure provided with the participation of many organizations and individuals. Moreover, it interacts with other management tools. In this study, the relationship between asset management and environmental management will be discussed.

1. Introduction

In today's world, one of the most important agenda items in front of humanity is the protection and sustainability of the environment. Maintenance management interacts with environmental management in terms of both the effective operation of the assets established for environmental protection and the management of wastes generated during activities. In general, it does not seem possible to talk about a sustainable environmental management in businesses that do not have an effective maintenance management. At the same time, it contributes most directly to environmental management through energy efficiency studies.

2. Maintenance Activities Environmental Management Relationship

For a sustainable environmental management, the maintenance process is one of the indispensable issues in our businesses. Basically, the maintenance process should serve the environmental management process. This is possible by accepting the environmental issue as one of the main topics while managing maintenance activities. In line with this

approach, it is possible to examine the management of the impact of the maintenance process on the environment under three main headings;

- Environmental issue in care approach
- Environmental issue in maintenance activities
- Evaluation of maintenance activity results and development studies

2.1. Environmental Issue in Maintenance Approach: Each business likely to have its own maintenance management approach. This approach is often supported by a process flow and procedure. Therefore, the environmental issue should be included as a basic item in the maintenance work. In other words, a basic principle should be adopted in which the environmental dimension and the issue will be evaluated in every step to be taken regarding maintenance. This principle should be fully internalized and audited from time to time by all maintenance process workers in the field. The environmental issue should be emphasized in maintenance procedures.

After defining the maintenance approach and basic management rules in a company, the most important issue to be done is to create an asset tree structure. After the assets are created, the primary task is to classify these assets. The classification made will constitute the main input for all kinds of maintenance activities to be performed on the subject assets. The absolute online monitoring of critical assets is an example. In these classification studies, the "environment" dimension should be within the evaluation parameters. When evaluated in terms of the environment, all assets that become critical for the company will be classified as critical equipment and all preventive maintenance approach and spare parts will be managed as critical assets.

At İsdemir, equipment classifications are effectively used in all the studies listed below;

- Fault root cause studies
- Preventive maintenance planning and applications of assets
- Backup management
- Visual factory applications
- Job prioritization in maintenance activities
- Purchasing and investment processes

The maintenance of systems and equipment, which have become critical and important due to the impact of the environmental dimension, is carried out effectively within the current systematic maintenance approach.

2.2. Environmental Issue in Maintenance Activities: In this title, the most basic applications that should be done will be discussed one by one by highlighting the environmental issue in the maintenance process applications;

2.2.1. Systems, machinery and equipment within the scope of legal regulations should be followed specifically. Continuous emission measurement systems (CEMS) and continuous wastewater monitoring systems (CWMS) can be given as examples of systems that can be evaluated in this context. In order to ensure the sustainability and reliability of these systems, all necessary preventive maintenance approaches should be defined and implemented effectively.

At İsdemir, all preventive maintenance defined to these systems has been standardized and practices are effectively followed.

2.2.2. The maintenance management process of all systems and machines that are important in terms of environmental management should be closely followed. Examples of these systems are dust collection systems, oil scraper systems etc. In order to ensure the sustainability and reliability of these systems, all necessary preventive maintenance should be defined and implemented effectively.

At İsdemir, all preventive maintenance defined to these systems has been standardized and practices are effectively followed. The actual operating results of these systems are shared on all necessary platforms by the Maintenance Management and Environmental Chief Engineering every month.

No	Equipment Number	BAV'S Equipment Description	MTBF (h:mm)	MTTR (h:mm)	MDT (h:mm)	% Availability (Failure)	% Availability (Maintenance)	% Availability (Failure + Maintenance)	Reliability (%)	Equipment Downtime (Hours)
1	106963	WASTE GAS FİLTRE SİSTEMİ 7	1739:12	00:21	00:31	99,95	99,99	99,94	97,93	217,89
2	138300	TOZ TOPLAMA	00:00	00:00	00:00	100,00	100,00	97,63	100,00	42,50
3	127933	TOZ TOPLAMA	00:00	00:00	00:00	100,00	100,00	97,69	100,00	90,50
4	153256	3 YF TOZ TOPLAMA SİSTEMİ	00:00	00:00	00:00	100,00	100,00	98,18	100,00	63,00
5	129168	TOZ TOPLAMA	00:00	00:00	00:00	100,00	100,00	98,80	100,00	41,75
6	128814	TOZ TOPLAMA	00:00	00:00	00:00	100,00	100,00	99,20	100,00	27,75
7	132735	191 LAMİTE TOZ TOPLAMA	1737:07	01:55	01:55	99,83	99,83	99,25	99,83	24,25
8	152538	483-02 ELEKTROFİLTRE SİSTEMİ	00:00	00:00	00:00	100,00	100,00	99,31	100,00	24,00
9	110031	WASTE GAS FİLTRE SİSTEMİ 8	00:00	00:46	00:46	99,98	99,98	99,45	99,98	16,28
10	157863	2 NOLLU KURU TOZ TOPLAMA İSTASYONU	1734:57	02:33	03:21	99,71	99,71	99,71	97,93	19,08
11	586025	EPI TOZ TOPLAMA SİSTEMİ	00:00	00:00	00:00	100,00	100,00	99,54	100,00	16,00
12	157197	483-01 ELEKTROFİLTRE SİSTEMİ	00:00	00:00	00:00	100,00	100,00	99,54	100,00	16,00

Figure 1 Equipment performance chart

2.2.3. Effective maintenance management will prevent leakage and optimum use of maintenance materials that may cause environmental pollution.

A large number of spare parts and consumables are used in all maintenance activities in the field. The optimum use of these materials is only possible with a good maintenance method. In addition, preventing the leakage of polluting materials such as

oil on the equipment is important for environmental management, directly or indirectly.

For example, one liter of used engine oil; considering that 1 million liters of water is unusable and 5 million liters of water is undrinkable, the importance of these works cannot be overlooked.

The chart below shows the change in İsdemir used oil return rates. We aim to maximize this ratio by using all our means.

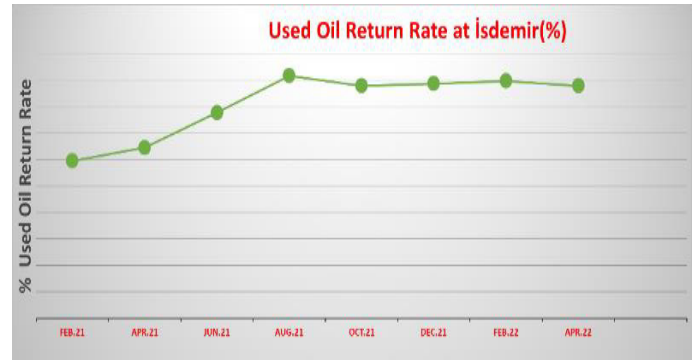


Figure 2 Used oil return rate graph at İsdemir



Figure 3 Used oil storage area in İsdemir

2.2.4. Energy efficiency is also directly related to the maintenance process. Effective maintenance management indirectly contributes to environmental management with its contribution to energy efficiency. Below are the main titles of the work that İsdemir has done on this subject;

- Paying attention to energy efficiency when purchasing the asset (via specifications)
- To follow the energy efficiency opportunities continuously by following the developing technologies
- Considering energy efficiency as a parameter in maintenance planning (such as arranging preventive maintenance with the aim of keeping boiler efficiency above a certain level)
- To eliminate situations that may cause energy loss in maintenance operations (such as lubricating electric motors in the ideal period, with the ideal amount and the most efficient oil)

- Detection and elimination of losses and leaks with autonomous maintenance
- Taking structural measures to prevent loss and leakage

significant impact on the environment. Global steps have been taken to prevent or reduce all negative environmental effects arising from industrial activities at the source, and many responsibilities have been imposed on industries in terms of environmental sensitivity.

2.2.5. The management of maintenance waste is also an important environmental issue. In addition to the efforts to reduce waste, it is necessary to collect, separate and properly return the waste that is generated in some way. These studies not only have very positive effects on the environment, but also create an input for the company's coffers.



Figure 4 Example of İsdemir waste collection point

Waste Type	Waste Code	Amount of Disposal in 2021 (Kg)	R/D Code
Scrap Conveyor Belt	07 02 13	901.420,00	R12
Used Oil (Hydraulic)	13 01 10	43.460,00	R9
Used Oil (Engine)	13 02 08	26.820,00	R9
Oily Water	13 05 07	105.740,00	R12
Plastic	15 01 02	203.220,00	R12
Maintenance Waste	15 02 02	91.700,00	R12
Battery	16 06 01	15.560,00	R4
Scrap Electric Motor	17 04 07	103.040,00	R12
Scrap Cable	17 04 10	94.460,00	R12

Figure 5 İsdemir 2021 waste declaration sample table

2.3. Evaluation of the results of maintenance activities and development studies: Developing the environmental impact dimension of the maintenance process is also an important topic. Here, first of all, maintenance should be taken that the systems and machines that affect the environment in the maintenance KPIs are within the institutional and individual target set. In this way, the subject will always be on the agenda, and the results of all the studies will be able to serve corporate goals. At İsdemir, the failure-induced usability rate of dust collection systems is added to the maintenance KPI target set every year in order to increase it to a better level. Again, after the analysis of the maintenance activities, the environmental pollution-reducing kaizen, improvement maintenance and fault root cause analysis studies are among the leading systematics of continuous development. In addition, environmentally friendly investments to replace systems that become inadequate or inefficient in the field should be triggered by environmental analysis of maintenance results and internal audit studies. One of the most important issues in the internal inspections of the maintenance process carried out every year at İsdemir is to control the level of work done by the units on the environment.

3. Conclusion

The use and maintenance of industrial machinery has a

One of the most important responsibilities is regular maintenance work, and it is to move sustainability forward in a positive way with improvement maintenance.

With the development of environmental awareness, it should be aimed to prevent environmental pollution at its source and to minimize the effects that will occur during production or maintenance and repair processes. The five strategies to be taken as a basis in the environmental management dimension in maintenance and repair activities should be as follows:

- Reduce pollution at source when applicable
- Earn and reuse on the spot
- Recycle in an environmentally friendly way at a facility
- Treat pollution with environmentally friendly method
- Dispose or release as a last resort

Natural life and the environment are the most important heritage we have and we need to show the necessary sensitivity to protect this heritage.

References

[1] IBM Maximo softwar

MANAGEMENT OF FERROALLOYS STOCKS IN IRON AND STEEL PRODUCTION

Erman KAYA, Beril BİRİNCİ, Ece DAL YALÇIN

Iskenderun Demir ve Çelik A.Ş.
Türkiye

Keywords: Iron and Steel, Ferroalloys, Stock Management, Production Planning, Quality

Abstract

The Planning and Coordination Unit of Production Planning Department in Iskenderun Iron and Steel Company (ISDEMIR) aims to keep stocks at optimum level by communicating with sales, raw materials, purchasing, inventory, quality and operating departments and making ferroalloy consumption estimates. In this direction, material consumption forecasts are obtained by loading data from the models created on Level 4 systems in ISDEMIR into the system. Model outputs are evaluated with inventories and data is provided to the supply chain. With this way, ferroalloy stocks are kept at optimal stock levels and inventory costs are minimized.

The fact that iron and steel prices are global is important in terms of increasing the competitiveness of our company with this study.

1. Introduction

Iron and steel production is one of the world's most important and biggest industry. Main usage areas of steel are construction, transportation, energy, packaging and industrial supplies. Integrated Steel Plants (Blast Furnace) and Electrical Arc Furnaces (Electrical process) are two main steel production processes which ferroalloys are important for both methods.

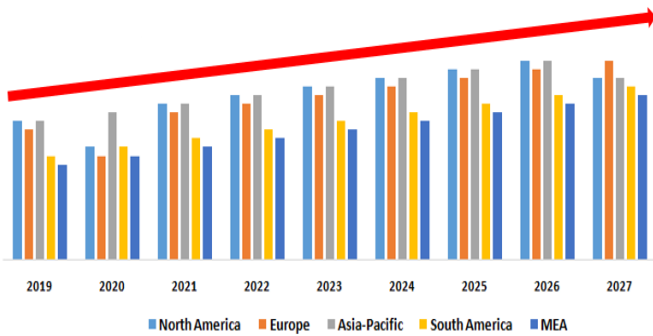
Ferroalloy refers to various alloys of iron with a high proportion of one or more other elements such as manganese (Mn), aluminium (Al), or silicon (Si). They are used in the production of steels and alloys. The alloys impart distinctive qualities to steel and cast iron or serve important functions during production and are, therefore, closely associated with the iron and steel industry, the leading consumer of ferroalloys.

Alloying element	Influence on structure	Influence on properties	Typical applications in steel
Mn	Austenite forming, Substitutional atom, carbide stabilizer	Increases harden – ability, strenght, toughness, hot workability	Deoxidation with Si (Al), forms MnS, alloying element in low – alloyed steels up to 1,6%. AISI 200 series stainless 5-20% Mn
Cr	Ferrite forming, Substitutional atom, forms carbide	Increases harden – ability, strenght, corrosion, resistivity	In low -alloyed steels up to 2% Cr, in stainless steels 11-25%. Heat resistant steels, tool steels.
Ni	Austenite forming, Substitutional atom	Increases strenght, toughness, impact and corrosion resistance	Case hardening steels up to 3-5% Ni. Stainless steel 8-20% Ni. Heat resistant alloys app. 25% Ni.
Si	Ferrite forming, Substitutional atom	Ferrite hardening	Deoxidation, slag reduction, typically 0,3-0,6% Si. Spring steels 1,7-2,2% Si. Electrical Si steels 1-4 % Si
Cr, Mo, W, Ti, Nb, V	Carbide formers	Increases hardness, strenght, wear resist	Tool steels, wear resistant steels
Nb, Ti, V, Ta, (B), Al	Nitride formers, Grain refinement	Increase strenght and ductility	Ine grained steels, high strenght low alloyed HSLA steels

Table 1 Common alloying elements in steel, their influences and applications.

The global ferroalloys market size was estimated at USD 43.02 billion in 2020 and is expected to grow a compound annual growth rate (CAGR) of 5.5% from 2020 to 2027 to reach USD 69.05 billion by 2027. The increasing steel production around the globe is the prominent factor driving market growth. Ferroalloys impart special characteristics to steel, such as improved hardness, resistance to corrosion, higher abrasion resistance, enhanced tensile strength at extreme temperatures, and significant creep strength.

Therefore they represent significant raw materials to the iron and steel industry. China emerged as the leading player in the global market in 2019. China produced approximately 53% of the global crude steel in 2019, according to the World Steel Association. As a result, there is a massive demand for ferroalloys in China. The emergence of the COVID-19 pandemic is likely to significantly affect the steel output in China, which, in turn, is expected to hamper the ferroalloys market in 2020. However, the quick economic recovery of the country since March 2020 is expected to soften the impact to some extent. By the end of April 2020, nearly all the steel-using end-use industries in China were reopened for production. However, the manufacturing firms were yet to operate at full capacity owing to weak domestic demand, as well as a sharp collapse in the exports. The second half of 2020 in China is likely to show more visible signs in the recovery of steel demand owing to the investments in infrastructure development, driven by several planned initiatives by the regional government and consequently, ferroalloy demand in China has recovered from June 2020.



Graph 1 Global Ferroalloys Market Forecast 2020 to 2027

Some of the key players operating in the ferroalloys market include Ferro Alloys Corporation Limited, Shanghai Shenjia Ferroalloys Co. Ltd, SAIL, Glencore, and Jindal Group.

The key factors that are driving the ferroalloys market include rising steel production particularly in emerging economies of Asia Pacific such as China and India.

2. Experimental Procedure

The main screen of the model prepared on İSDEMİR Production Management System (IUYS) for the estimation of ferroalloy material consumption is in Figure-1.

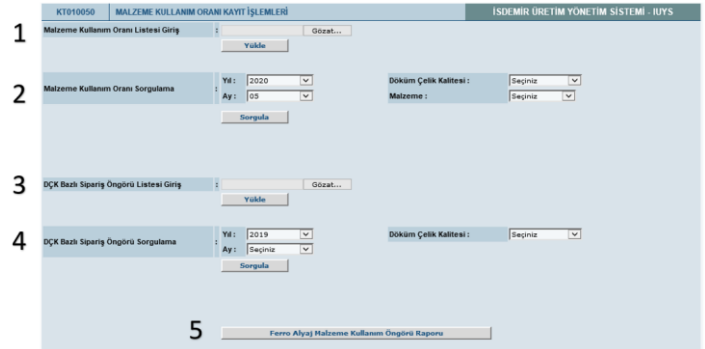


Figure-1 Main screen of model on İSDEMİR Production Management System (IUYS)

The main headings of the sections numbered on the main screen (Figure-1) are listed below.

1. Material consumption amount definition section
2. Material usage rate inquiry section
3. Steel quality based order entry section
4. Steel quality based order prediction inquiry section
5. Ferroalloy material usage forecast report

2.1. Material consumption amount definition section

Material usage rates are automatically transferred to the model from the quality cards in the Level 4 system. If there is a trial quality that is not defined in the system due to trial procedures, manual entry can be made from this section. Under normal condition, manual definition is not required. For manual identification, the format in Figure 2 should be used.

YEAR	MONTH	QUALITY	MATERIAL CODE	USAGE RATE

Figure-2 Manuel identification format for material consumption amount definition

2.2. Material usage rate inquiry section

This section is used to monitor the change in consumption rates by months and compliance with actual material consumption. The information in Figure-3 can be easily accessed by entering the year, month, steel quality and material type in this section.

YEAR	MONTH	QUALITY	MATERIAL CODE	USAGE RATE
2022	5	1.1005_01	4602	1,026
2022	5	1.1005_01	4600	4,822
2022	5	1.1005_01	2401	0,487
2022	5	1.1005_01	4400	0,615
2022	5	1.1005_01	4401	0,233
2022	5	1.1005_01	3400	0,739
2022	5	1.1005_01	2203	0,467
2022	5	1.1005_01	2204	0,233
2022	5	1.1006_00	2400	0,737
2022	5	1.1006_00	4602	1,538
2022	5	1.1006_00	4600	3,200
2022	5	1.1006_00	2401	0,428
2022	5	1.1006_00	4400	0,615
2022	5	1.1006_00	4401	0,237
2022	5	1.1006_00	3400	0,746
2022	5	1.1006_00	2200	0,001
2022	5	1.1006_00	2203	0,300
2022	5	1.1006_00	2204	0,150
2022	5	1.1006_01	2400	0,778
2022	5	1.1006_01	4602	2,564
2022	5	1.1006_01	4600	2,289

Figure-3 Material usage rate datas

2.3. Steel quality based order entry section

The sales department uploads the order forecasts to the system in the format shown in Figure 4. The data of the actual orders entered into the order system automatically flows into the model.

YEAR	MONTH	QUALITY	ESTIMATED ORDER TONNAGE
2020	1	1.1022_00	0
2020	1	1.1030_00	0
2020	1	1.1040_00	0
2020	1	1.1042_00	0
2020	2	1.1022_00	10.427
2020	2	1.1030_00	0
2020	2	1.1040_00	10.427
2020	2	1.1042_00	10.427
2020	3	1.1022_00	0
2020	3	1.1030_00	0
2020	3	1.1040_00	0
2020	3	1.1042_00	0
2020	4	1.1022_00	752
2020	4	1.1030_00	0
2020	4	1.1040_00	752
2020	4	1.1042_00	752
2020	5	1.1022_00	766
2020	5	1.1030_00	0
2020	5	1.1040_00	766
2020	5	1.1042_00	766

Figure-4 Quality based order prediction entry format

2.4. Steel quality based order prediction inquiry section

This section is used to quickly search the order forecast (based on year, month and steel quality) entered by sales department. The information in Figure-5 can be easily accessed by entering the year, month and steel quality in this section.

YEAR	MONTH	QUALITY	ESTIMATED ORDER TONNAGE
2020	6	1.1006_00	1.075
2020	6	1.1008_00	5.376
2020	6	1.1010_00	25.612
2020	6	1.1018_00	0
2020	6	1.1018_03	0
2020	6	1.1065_02	0
2020	6	1.1070_02	0
2020	6	1.1072_00	0
2020	6	1.1076_00	1.613
2020	6	1.1082_00	0
2020	6	1.1082_01	0
2020	6	1.1082_02	1.055
2020	6	1.1082_03	0
2020	6	1.1082_04	538
2020	6	1.1236_01	2.129
2020	6	1.1281_00	0
2020	6	1.1355_25	591
2020	6	1.2023_01	0
2020	6	1.2355_07	710

Figure-5 Order forecasts

2.5. Ferroalloy material usage forecast report

The main report is obtained with the material usage rates flowing to the model from the quality cards in the Level 4 system or manually defined from the main screen, the orders received from the sales system and the order predictions entered by the sales department.

The report output is in excel format and includes two tabs: summary and detail. While the summary tab contains ferroalloy-based total consumption information, the detail tab includes quality-based consumption. Figure-6 includes a summary, and Figure-7 a detailed report example.

Isdemir Ferroalloy Material Usage Forecast Report															
Material	Product Type	January	February	March	April	May	June	July	August	September	October	November	December	Sum	Average
2203 - CASI (CASI TEU)	Flat Product		16.270,71		1.172,71	1.194,65	4.630,66	2.729,06	7.669,63	5.316,34	11.834,27	4.198,28		54.406,12	4.534,01
2400 - YKEMIN (YKSEK KARBONLU FERROMANGAN)	Long Product		30.895,22		2.205,15	2.246,21	7.579,20	4.326,31	12.142,44	8.431,02	10.760,54	5.884,25		91.670,34	10.207,82
2401 - YKEMIN ORTA KARBONLU FERROMANGANEZ	Flat Product		3.756,74		270,77	275,01	930,64	681,58	1.912,96	1.328,25	2.955,59	930,71		13.043,05	1.449,23
3400 - CAFZ FLORIT	Long Product		41.985,91		2.961,23	3.016,38	10.177,91	7.833,53	21.985,09	15.265,81	33.969,18	8.378,07		146.674,91	16.074,96
4600 - PESIYS FERRO SILS	Long Product		113.085,72		8.150,64	8.302,43	28.914,16	18.436,04	51.743,52	35.927,75	79.945,73	28.541,70		372.147,69	41.340,74
4602 - PESIYN FERRO SILKUMMANGAN	Flat Product		282.011,85		18.884,46	19.236,16	64.906,89	47.536,41	133.418,10	92.637,83	206.136,08	29.830,40		874.586,28	97.177,59

Figure-6 Ferroalloy material usage forecast report (summary)

Material Number	Material Description	Quality	2020-01	2020-02	2020-03	2020-04	2020-05	2020-06	2020-07	2020-08	2020-09	2020-10
2203	CaSi (CaSi telli)	1.1022_00		5.635		406	414	1.396	1.022	2.869	1.992	
2203	CaSi (CaSi telli)	1.1022_01										
2203	CaSi (CaSi telli)	1.1040_00		4.588		331	337	1.137	832	2.336	1.622	
2203	CaSi (CaSi telli)	1.1042_00		6.048		436	444	1.498	874	2.454	1.704	
2400	YKFeMn (Yüksek karbonlu ferromangan)	1.1022_00		10.784		777	792	2.671	1.957	5.491	3.813	
2400	YKFeMn (Yüksek karbonlu ferromangan)	1.1022_01										
2400	YKFeMn (Yüksek karbonlu ferromangan)	1.1040_00		7.299		526	536	1.808	1.324	3.717	2.581	
2400	YKFeMn (Yüksek karbonlu ferromangan)	1.1042_00		12.612		902	919	3.100	1.046	2.935	2.038	
2401	OKFeMn Orta karbonlu ferromangan	1.1022_00		3.757		271	276	931	682	1.913	1.328	
2401	OKFeMn Orta karbonlu ferromangan	1.1022_01										
3400	CaF2 Florit	1.1022_00		24.402		1.759	1.792	6.045	4.427	12.426	8.628	
3400	CaF2 Florit	1.1022_01										
3400	CaF2 Florit	1.1040_00		8.342		601	612	2.066	1.513	4.248	2.948	
3400	CaF2 Florit	1.1042_00		8.342		601	612	2.066	1.893	5.313	3.688	
4600	FeSi75 Ferro silis	1.1022_00		37.664		2.715	2.765	9.330	6.833	19.179	13.31	
4600	FeSi75 Ferro silis	1.1022_01										
4600	FeSi75 Ferro silis	1.1040_00		32.137		2.316	2.359	7.961	5.830	16.364	11.36	
4600	FeSi75 Ferro silis	1.1042_00		43.285		3.120	3.178	10.723	5.772	16.201	11.24	
4602	FeSiMn Ferro silikomangan	1.1022_00		90.902		6.552	6.674	22.519	16.492	46.288	32.14	
4602	FeSiMn Ferro silikomangan	1.1022_01										
4602	FeSiMn Ferro silikomangan	1.1040_00		90.902		6.552	6.674	22.519	16.492	46.288	32.14	
4602	FeSiMn Ferro silikomangan	1.1042_00		80.208		5.781	5.889	19.869	14.562	40.842	28.36	

Figure-7 Ferroalloy material usage forecast report (detail)

3. Results and Discussion

After the model is created, the details of which are explained in the “Experimental Procedure”, the model is run every month and data is provided to the Raw Material Planning Department with the report output. In the light of this data, the Raw Material Planning Department takes the necessary actions to make purchases by considering the optimum stock levels. In this way, stock levels are kept at optimum level and stock costs are minimized.

4. Conclusion

In the Iron and Steel industry, product prices are determined by global markets, and profit margins can only be increased by reducing costs. Stock costs also have a considerable place among the costs. With this study, ferroalloy stock costs have been minimized, and actual and estimated usage rates have also become easily comparable.

References

- [1] Global Ferroalloys Market-Global Industry Analysis And Forecast (2020-2027) – By Type, End-Use Industry, And Region.
- [2] Rudolf Fichte. "Ferroalloys". Ullmann's Encyclopedia of Industrial Chemistry. Weinheim: Wiley-VCH. doi:10.1002/14356007.a10_305.
- [3] Aydın S., Arslan C., and Dikeç F., “Developments in Ferroalloy Production and Consumption of Türkiye”, The Proceedings INFACON 7, pp.297-306, Trondheim, Norway, 1995.
- [4] www.worldsteel.org The official web site of the International Iron and Steel Institute (IISI) on the internet.
- [5] Aydın S., Taptık Y., Arslan C., “Scrap Recycling and Steel Production – A General Perspective and Türkiye’s Standpoint”, Ironmaking and Steelmaking, Vol:23, No:3, 1996, pp.242-246.

INVESTIGATION OF CASTABILITY OF DIN EN 10089 38Si7 STEEL GRADE IN BILLET CASTING MACHINE

İlker AYÇİÇEK¹, Kübra AKGÜN¹, Memduh Kağan KELER²

¹İskenderun Demir ve Çelik A.Ş., ²Ereğli Demir ve Çelik
Türkiye

Keywords: Continuous Casting, Steel, Castability, Billet

Abstract

İsdemir is an integrated steel producer and the process route follows blast furnace, desulfurization, basic oxygen furnace (converter), ladle furnaces and continuous billet casting plant respectively. After casting, steel becomes semi-finished billet for wire rod rolling. In this study, it is investigated that the castability of 38Si7 steel grade in billet continuous casting plant. The usage area of this grade, which has high silicon content, is rail and fasteners. 38Si7 grade is produced according to DIN EN 10089 standard. During the casting of 38Si7 grade, clogging problems and level fluctuations are observed. Hence, number of heats in tundish was lower than other sub-merged casted grades and interruption of heat during casting was relatively high. In the preliminary studies, a data set was created with parameters such as stopper levels, chemical analysis, alloying elements, slag-former materials, calcium treatment process and casting time with clogging problems. The parameters that cause clogging in the nozzle were restricted at certain values and the deoxidation practice was revised. Finally, the average number of heats taken in the tundish has increased and level fluctuation problem has resolved at end of the studies.

1. Introduction

Castability is one of the most important problem in continuous casting of steel billet. Steel billets are generally killed by silicon and manganese. In addition to this some steel grades have high silicon content. Type of deoxidation practice determine type of indigenous inclusions generates in liquid steel [1].

Controlling ladle furnace operations is crucial for deoxidation products and inclusions [2]. Hence, Ca treatment for this steel grade, should be adjusted and thermodynamically modelled.

The equilibrium of Mn and Si in steel plays a significant role for steel-slag reactions and oxygen activity in steel [3-4]. While the liquid steel is almost solidified, the microsegregation of Mn and Si reduces the oxygen activity and manganese silicates precipitate as liquid inclusions. In addition, while the activity of oxygen increases, probability of formation Alumina type inclusions also rise.

In this work 38Si7 grade is investigated in aspect to castability performance. The basic problem of casting of this grade is number of heat per tundish. As high silicon grade generates high number of silicate inclusions, casting performance of 38Si7 grade relatively low.

Casting performance is related to many parameters in ladle furnace and continuous casting. Therefore, ladle furnace and continuous casting parameters are studied to increase casting performance of grade.

2. Experimental Procedure

In İSDEMİR steel produced with BF-DES-BOF-LF and CCM route. Steel grade and its composition is given below table.

Table 1 38Si7 Chemical Composition

38Si7 Grade(1.7038 00)		
C	Min	0,37
	Max	0,40

Mn	Min	0,60
	Max	0,70
P	Max	0,015
S	Max	0,004
Si	Min	1,55
	Max	1,70
Al	Max	0,02
Cr	Min	0,18
	Max	0,22
N (ppm)	Max	90
B	Min	0,0025
	Max	0,0040
Ti	Min	0,020
	Max	0,030

An production procedure is prepared before production of 38Si7 grade. The procedure is given below.

- In house scrap is used in BOF process.
- % S value is decreased as low as possible, aim is lower than 30 ppm.
- Carry slag over value should be minimum during tapping heat from BOF to ladle.
- FeSi with low Al should be used.
- Ladle must be used in billet grade before used in 38Si7 grade.
- Ladle furnace processing time should not exceed 50-60 min.
- Alloying must be done in Ti-B-Ca order and 5 min shall be waited after alloying of each element.
- % S value of last sample of ladle furnace must be lower than 40 ppm.
- Ca value should be lower than 15-20 ppm before ending ladle furnace process.
- Molds with low casting numbers should be used.
- Secondary cooling systems and lines should be checked before casting.
- High casting speed practice should be done in continuous casting.
- Soft cooling practice should be done.
- Covering the tundish surface with tundish covering powder should be done.

3. Results and Discussion

Before the procedure given in experimental procedure part, 15 heats are cast 12 different tundish. This means that tundish performance of this grade is 1,25 heats/tundish. After applying the rules given in procedure, 33 heats are cast in 9 different tundish and casting performance is 3,67 heats/tundish. In

addition to this, production is ended intentionally after applying procedure. In other word, after applying procedure heats are not ended because of high stopper level.

An important result of applying the procedure is lowering the aluminum content of heats. Average aluminum level decreased from 90 ppm to 64 ppm with applying new rules in production of 38Si7 grade. Low aluminum content in steel causes less alumina inclusion in steel and high casting performance. Alumina inclusions have bad effects on the tip of stopper in sub-merged entry nozzle casting.

Another important factor is Ca level in steel. Before applying casting procedure Ca level in steel was 24 ppm and after applying procedure Ca level decrease to 16 ppm. This gives that less Ca based inclusions. Ca based inclusions, especially CaS is accumulated on the tip of stopper. CaS has high melting temperature and after nucleation in steel, escaping from this inclusion is very hard. Therefore, the most important thing not to allow the formation of such inclusions. S level is important to production of this grade so average S level in steel is 40 ppm.

Ladle furnace processing time is important in production of high silicon steel grade. In contrast aluminum killed steel, Ca treatment is not efficient in high silicon grade to minimize silicate inclusions in steel. Increasing processing time means increasing the rate of reoxidation and increasing silicate inclusions. Ladle furnace processing time decrease from 79 min to 58 min after applying new production procedure. This gives low silicate level and less stopper blockage. The Si-SiO₂ equilibrium controls the oxygen activity at the steel-slag interface.

Average casting speed increases from 2,8 m/min to 2,9 m/min to increase to casting performance. Increasing casting speed lower stopper blockage.

4. Conclusion

In conclusion, casting performance in continuous casting is an important parameter to increase productivity and lower cost. Increasing casting performance varies from each type of quality and production conditions. In this work, 38Si7 grader has high silicon content and casting performance of this grade increased with optimizing ladle furnace and continuous casting parameter.

References



- [1] Turkdogan, E. T., & Fruehan, R. J. (1998). Fundamentals of iron and steelmaking. The Making, Shaping and Treating of Steel, Steelmaking and Refining Volume, 11th ed., RJ Fruehan, ed., AISE Steel Foundation, Pittsburgh, 11, 125-126.
- [2] Choudhary, S. K., & Chandra, S. (2007). Castability of Mn–Si killed low carbon wire rod steel. ISIJ international, 47(1), 190-192.
- [3] Papadopoli Tone, S. Non-Metallic Inclusion Changes in Si-Mn Killed Steels (Doctoral dissertation, Carnegie Mellon University).
- [4] Ghosh, P. K. (2019). Nozzle clogging for 'Si' killed steel. Steel Times International, 43(2), 32-36.



PRESSURE VESSEL DETECTION SYSTEM WITH IMAGE PROCESSING TECHNIQUES

Zekeriya SARIKOL, Semiramis GÜLKESEN

İskenderun Demir ve Çelik A.Ş.
Türkiye

Keywords: Image Processing, Artificial Intelligence, YOLOv4, Scrap Classification

Abstract

From time to time, a pressure vessel may be included in the scraps loaded into scrap box in the steel-making a scrap preparation facility. Human ingenuity is used to find and separate these. There is a chance of an explosion damaging the converter if the pressure vessels are scrapped and then transported to the converter. Before they are charged to the converter, it is crucial to identify and classify the pressure vessels in the scrap. In the scrap preparation facility, there are cameras for each scrap scale to check whether there is a pressure vessel in the scrap during the loading of the scraps with the help of polyps/magnets into the box, and these cameras record the image of the scrap inside the scrap boxes. This study, it is aimed to detect possible pressure vessels by scanning automatically taken images with image processing techniques.

1. INTRODUCTION

Turkey's only and largest factory producing long and flat products integrated iron and steel factory Isdemir produces steel from liquid row iron and scrap in steel making converters. The steel-making plant has a facility that scraps preparation. This facility has six scrap box and six cameras separately for a camera to a box.

While loading scrap with polyp and magnets whether pressure vessels detect, it is separated and thrown out of the box. If the crane operator or the control room operator misses the pressure vessel, it will be delivered to the converter with scrap in the box, potentially resulting in an explosion in the converter.

While the pressure vessels are determined by the human eye, the proposed method will be image processing with artificial intelligence techniques. In this method, we use the YOLOv4 object detection network. Pressure vessels are things that can be

defined as objects. Object detection subject has been studied in a few more ways such as R-CNN, Yolo, etc. Many subjects can be considered as objects such that a bird, person, table, phone also status or position any object.

Computer vision has become very common in real life, especially object detection with image processing. Many object detection algorithms have been developed with artificial intelligence, faces with cascade classifier [1] or traffic participants/road signalization with Yolo [2]. From the studies' results, we saw that the Yolo algorithm, based CNNs is the best way for object detection [3].

In this paper, we present the Isdemir Pressure Vessel Detector System. In this system, the YOLOv4 algorithm can help us with high accuracy to detect pressure vessels from scrap boxes in a variety of the scrap shape.

2. Material and Methods

2.1. YOLO

Yolo is called "You Only Look Once". The best object detection algorithm Yolo was designed by Joseph Redmon and friends [4]. Since Yolo was first announced, they publish five versions and we use version four in this work.

The original YOLO model network architecture consists of 24 convolutional layers and additional 2 fully connected layers [3]. Input image sizes automatically resized 416x416, so always 416x416x3 image size used for training. Yolo's working architecture as shown in Figure 1.

There is a pre-trained type of Yolo that includes lots of common objects. This model trained on Coco dataset [5]. There is no need to retrain for Coco dataset objects.

Yolo system predicts as output coordinates of the bounding box, confidence, and class id that has the highest confidence.

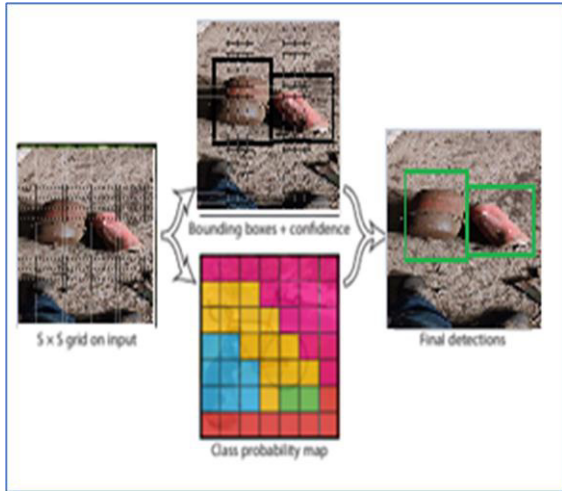


Figure 1. Yolo divides the input images $S \times S$ grid and then predict as output bounding box, confidence, and class probability that highest [3,4].

Labeling: Yolo network training with a labeled image. Labeling is the indicate wanted object location. There must be a .txt file with the same name as the image. The .txt file should have object information. The information starts with class id , x, y coordinate, and width and height. The information must be in Yolo format.

2.2. System Architecture and Design

This study's objective is to identify pressure vessels in a scrap box. Server software and client software make up the two components of the system. On the server, the picture is processed, and the information is then stored in the database. The client-side application's goals are to notify the operators and offer information about the edited photographs. The system architecture was displayed in Figure 2.

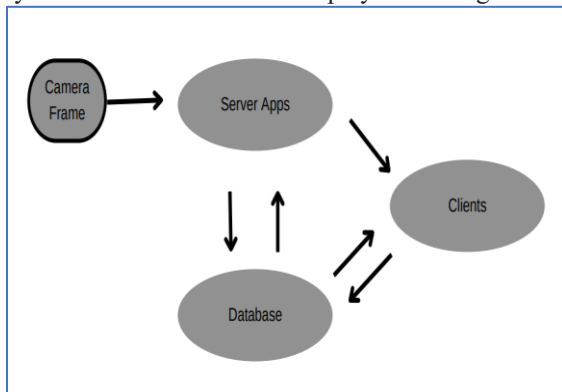


Figure 2. System Architecture

The steps in the presented system are as follows:

- Dataset collection
- Data preparation and labeling
- Train Yolov4 model
- Developing server and client-side software

Data Set Collection: Training Yolov4 is a bespoke object detection model that needs your own data to be detected. We gathered data for this system from the steel manufacturing plant's scrap preparation unit. Various pressure vessels were placed on or in a scrap pile and samples were taken. Pressure vessels are placed on each level of the box while it is being loaded, and each level receives a different sample picture. Numerous pressure vessels are depicted in boxes or without boxes in Figure 3. After working on dataset collection, a total of 372 samples were obtained.



Inside of the heap



Top of the heap



Single



More than one

Figure 3. Top or Inside of the heap and separately pressure vessel sample

Data preparation and labeling: Yolo algorithm requires labeling objects that wish to detect from images. To train a Yolov4 object detection model requires labeling images with Yolo format. There is some labeling tool with Yolo formats such as LabelImg [6] and online labeling. In this study, we used YoloTrainGuide which is shown in Figure 4

developed by the Isdemir level 2 team.

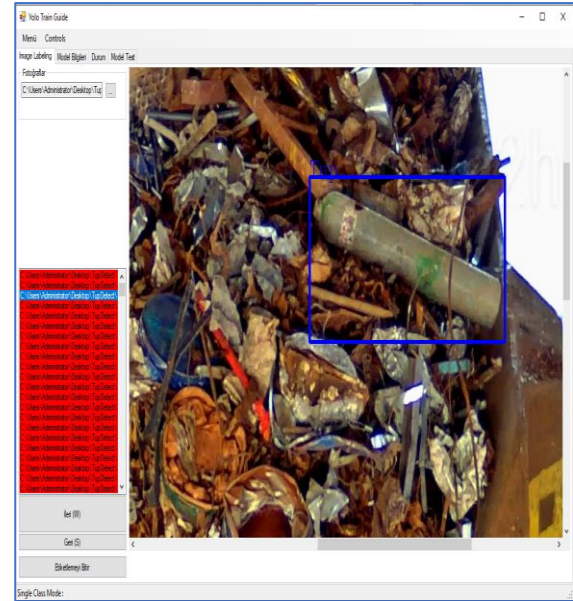


Figure 4. YoloTrainGuide is labeling and train application developed on .net by Isdemir Level 2 team

Training Yolov4 model: After completing labeling images, the train starts with the configuration of the “.cfg” file. The configurations due to the objects that you want to detect.” Class num, filters, max batch, etc.” must be adjusted before the training. The class file must contain your class names, and the data file contains the location of all files. Train platform works on darknet framework and operating system is Windows Server 2019, GPU unit is Nvidia RTX4000. Training time is related to the number of samples and classes. After training loss chart will be created also shown in Figure 5.

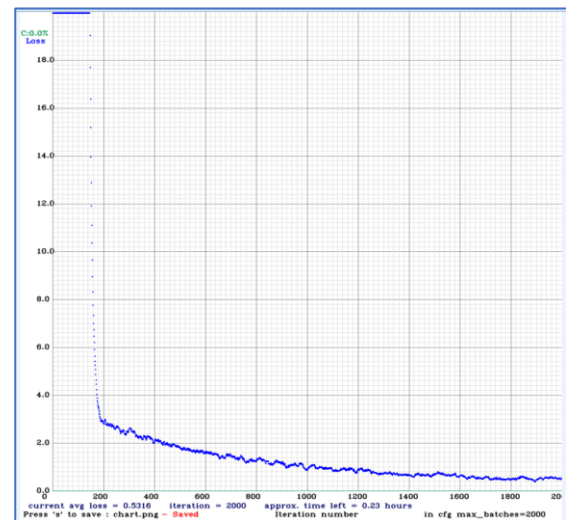


Figure 5. Loss Cart of Model

Developing server and client-side software: Server-side and client applications are developed by the Isdemir level 2 team. The applications were

developed on .Net platform with windows form and service. Client-side application developed also .net platform with WPF technology. The client app and alarm window are shown in Figure 6.

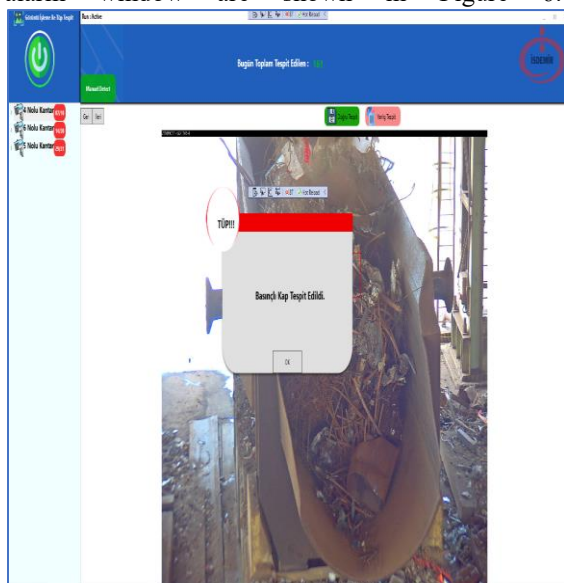


Figure 6. Client-Side application

2.3. Additional Features of the System

While loading scraps to box, whether detected a pressure vessel, all of working client applications gives a warning audible and visible.

Some features of the system are as follows:

- More than one pressure vessel is detected at the same time.
- Various pressure vessels are detected.
- Client application has manual detection that process loaded image via server side application.
- The client has a field that indicates whether the detections are true.
- Client application can run in many location at the same time.

3. Results and Discussion

The Isdemir Pressure Vessel Detection System provides us with a pressure vessel early warning system from a scrap box. As the system produced data, we tested it with 10 fresh samples, and the accuracy rate was 90%. Test method and the result is shown in Figure 7. We avoid that by using the system's real detection identification function, which the system may show incorrectly. If a pressure vessel is found during operation, the system issues an

auditory and visual alert, and the operator is then responsible for controlling the detection's outcome. With genuine identified images, the system will be retrained, and model accuracy will rise. The iron and steel sector can also identify and regulate a wide variety of objects using this technique.

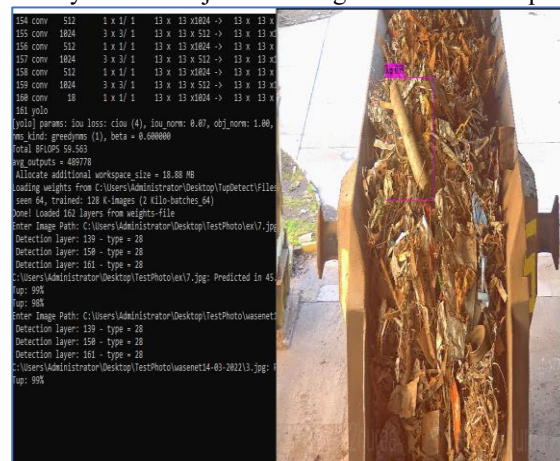


Figure 7. Image Test

The YoloV4 model is trained on a physical server with a GPU unit. Iteration number changes due to class number, so our model's train iteration number was 2000. Training time was approximately 8 hours. After the train, we used the model in the server-side application. After the system worked for about 2 months, we renewed the train with true detections that were identified by the operator during the operation time via the client. The second model was trained with 523 images.

4. Conclusion

In the presented system, we used image processing technics so, there is no need for any sensor or industrial equipment just a camera and computer. Before this system was developed, there were no detectors except the human eye. With the development of this system, a new detection system was commissioned and started to contribute to the operation regardless of its accuracy.

References

- [1] P.A. Viola, M.J. Jones, "Rapid object detection using a boosted cascade of simple features", in CVPR, issue 1, 2001, pp. 511–518.
- [2] Aleksa Ćorović, Velibor Ilić, Siniša Đurić, Mališa Marijan, and Bogdan Pavković – "The Real-Time Detection of Traffic Participants Using YOLO Algorithm" in 26th Telecommunications forum TELFOR 2018
- [3] Matija Buric, Miran Pobar, Marina Ivasic-Kos - "Ball detection using Yolo and Mask R-CNN" in 2018 International Conference on Computational Science and Computational Intelligence (CSCI)



[4] Joseph Redmon , Santosh Divvala, Ross Girshick , Ali Farhadi – “You Only Look Once: Unified, Real-Time Object Detection” in arXiv:1506.02640v5 [cs.CV] 9 May 2016

[5] T.-Y. Lin et al., “Microsoft coco: Common objects in context,” at a European conference on computer vision, 2014, pp. 740–755

[6] Christoph Sager, Christian Janiesch & Patrick Zschech (2021) “A survey of image labelling for computer vision applications”, Journal of Business Analytics, 4:2, 91-110, DOI: 10.1080/2573234X.2021.1908861



MODERNIZATION AND REPLACEMENT OF İSDEMİR 4TH BLAST FURNACE CLAY GUN AND DRILL EQUIPMENT

Recep GÜNEŞOĞLU, Osman FİDAN, Ökkeş CİĞERLİ, Ali Hikmet CAN, Hasan İŞLER, Evren ŞAHİN

İskenderun Demir ve Çelik A.Ş.
Türkiye

Keywords: Blast Furnace, Clay Gun (Mud Gun), Drilling Machine, İsdemir

Abstract

The clay gun and drill machine in İSDEMİR 4th Blast Furnace (4th YF) were modernized and replaced. In Blast Furnaces; iron ore, pellet, sinter, metallurgical coke etc. Liquid iron and blast furnace slag are obtained in the lower zone of the furnace by making the raw material charge from BLT (Bell Less Top System), blowing hot air in the furnace tuyere area and injection of pulverized coal (PCI). Liquid iron and slag are taken into the runner by drilling the mud from the casting hole by hammering and rotating from the casting opening hole using a hydraulic furnace opening drill machine. Liquid iron and slag are separated in the runner. After that, Liquid iron is taken to the torpedo and sent to the steel shop by rail for steel production. After the liquid iron and slag are removed from the furnace floor in the casting opened with a drill, the blast furnace casting hole is closed with a clay gun by pressing approximately 280 bar from the clay gun plugging mechanism. In order to adapt to today's conditions and technology, the clay gun and drill were redesigned, the hydraulic lines were revised, and the projects were designed and modernized by choosing the same as the 1st Blast Furnace clay gun and drill machine. Thus, the efficiency is increased by minimizing the furnace opening and furnace closing time losses caused by the drill machine and clay gun problems.

1. Introduction

The 4th Blast Furnace (DİLEK) is the largest blast furnace in Turkey, which was commissioned on August 17, 2011. It is a blast furnace with a useful volume of 2500 m³, a production capacity of 6250 tons/day of liquid iron and 2200 tons of slag [1].

In the 4th Blast Furnace, there are bellless top system, stove type cooling system, coke gas enrichment, 4 stoves that can give a temperature of 1200 C, and on-site granulation system, which are found in modern furnaces. In addition, there are two INBA systems, which are not available in other furnaces.

It has 2 working casting holes and 1 spare casting hole to be used in maintenance works and during the breakdown of one of the runners. It has 2 working casting holes and 1 spare casting hole to be used in maintenance works and during the breakdown of one of the runners.

There are belts carrying 10000 Tons ferrous material and 2000 Tons coke per day. The material carried with the help of belts is poured into the furnace by bellless overhead equipment.

The air coming from the turbo blower at 180 °C is further heated in the stoves heated by using coke gas and blast furnace gas, increased to 1200 °C and sent into the furnace with the help of 30 tuyeres. The air velocity entering the furnace through the tuyeres is 250 m/s. The temperature of this air in front of the tuyere is 2400 degrees Celsius. An average of 40 tons of PCI tuyeres are blown per hour. Our daily PCI consumption is around 800 – 1000 T/day.

- **Commissioning Date** 17.11.2011
- **Working Volume** 2500m³
- **Number of Casting Holes** 3 pcs
- **Number of Tuyers** 30 pieces
- **Daily Average Production Capacity** 6000 tshd/day

- **Casting Hall Information;**
- **Casting Hall:** 2 pcs. 1 spare
- **Main Runner:** 3 pcs. 1 spare
- **Casting Hole:** 3 pcs. 1 spare
- **Clay Gun and Drill Equipment:** 3 pcs Hydraulic system
- **Slag Granulation System:** On-site granulation system is used. Slag is transported to the stock area with belts.

Blast Furnace Operating Parameters;

No	Parameter	Values	Unit
1	Hot Air Pressure	3.9	Bar
2	Peak Pressure	2.30	Bar
3	Differential Pressure	1.52	Bar
4	Hot Air Flow	5500	Nm ³ /min
5	Hot Air Temperature	1200	°C
6	Number of Castings	10-12	per Day
7	Received Avg SHD	6000	t/day
8	Amount of Slag Received	350	kg/tshd

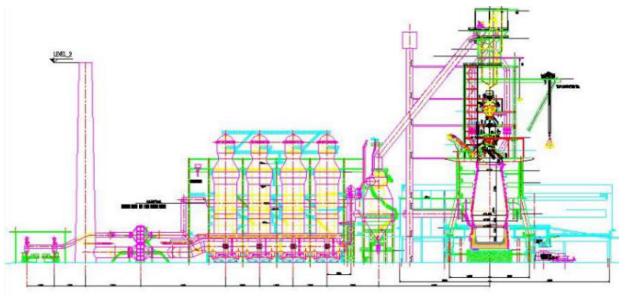


Figure-1: 4th Blast Furnace [2], [3].

2. Modernization and Replacement Of ISDEMIR 4th Blast Furnace Clay Gun And Drill Equipment

In Blast Furnaces; iron ore, pellet, sinter, metallurgical coke etc. Liquid iron and blast furnace slag are obtained in the lower zone of the furnace by making the raw material charge from BLT (Bell Less Top System), blowing hot air in the furnace tuyere area and injection of pulverized coal (PCI). Liquid iron and slag are taken into the runner by drilling the mud from the casting hole by hammering and rotating from the casting opening hole using a hydraulic furnace opening drill machine. Liquid iron and slag are separated in the runner. After that, Liquid iron is taken to

the torpedo and sent to the steel shop by rail for steel production. After the liquid iron and slag are removed from the furnace floor in the casting opened with a drill, the blast furnace casting hole is closed with a clay gun by pressing approximately 280 bar from the clay gun plugging mechanism.

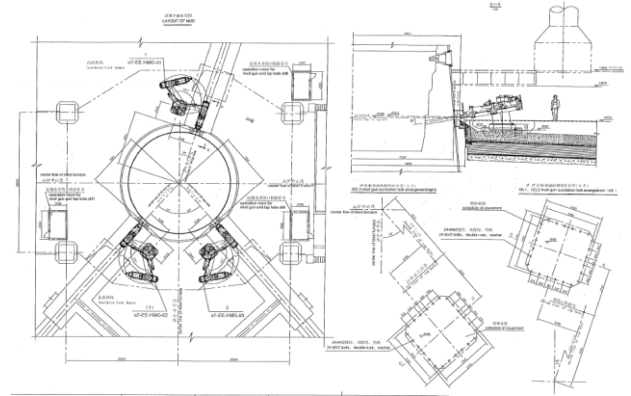


Figure-2: ISDEMIR 4th Blast Furnace, Hydraulic Clay Gun, Drill Equipment and Main Runner; 3 pcs. 1 spare

These equipments, which are among the most important equipment in the furnace process and enable the casting to be opened and then closed, must work with high efficiency. The timely and proper opening of the casting largely depends on the performance of these equipments. In cases such as the inability to open or close the casting, the furnace pressure is necessarily reduced and production losses are experienced. It has many negative effects in terms of both work safety and process, such as the inability to close the casting hole, opening a casting hole using oxygen. It has been decided to modernize the existing equipment because it is insufficient in terms of efficiency and performance, is far from today's technology and does not have an employee-friendly digital structure.

The purchasing process has started by choosing the most suitable and powerful equipment for today's technology and conditions. The equipment was supplied from TMT company located in Luxembourg. Afterwards, a work schedule was created and work started.



Figure-3: Available Mudball and Drill Equipment

Type	CG1625
Drive system	Fully hydraulic
Pressure on clay mass	160 bar (adjustable)
Hydraulic pressure for max. clay mass pressure	240 bar
Contact force against taphole	320 kN
Clay barrel volume nominal	0,25 m ³
Nozzle inside diameter	150 mm
Plugging speed	1-4 l/s (adjustable)
Ramming angle	3-10° (adjustable)
Slewing angle	According to layout drawing
Slewing time	~ 18 – 20 seconds (adjustable) (further reduction possible on request)
Vertical nozzle adjustment	upwards + 400 mm downwards - 200 mm
Horizontal nozzle adjustment	+/- 200 mm
Taphole following movement of the nozzle	Inwards BF: 150 mm Outwards BF: 200 mm
Cooling water flow per machine	8,75 m ³ /h at 8,5 bar
Supplied water cleanness	Impurities < 250 mg/l Grain size < 200 µm
Supplied water temperature	<45°C
Weight of ramming unit	~ 6,5 t
Total claygun weight	~ 24 t

Figure-4: Technical Information of The Supplied Clay Gun

Drive system	Fully hydraulic: slewing, rotation hammer, carriage feed
Stroke length	4.000mm
Taphole length	to be defined
Drill bit diameter	45 – 80 mm
Drill bar diameter	32 or 38 mm
Roller carriage speed backward	1 m/s
Drill angle	10° (range ±3°)
Slewing angle	According to layout drawing
Slewing time	~15-18 seconds, adjustable
Weight of chain feed	~ 3.000 kg
Hydraulic hammer:	HS500
Forward impact energy	max. 330 Nm, adjustable
Backward impact energy	max. 280 Nm, adjustable
Forward impact frequency	max. 1840 min ⁻¹ , adjustable
Backward impact frequency	max. 1785 min ⁻¹ , adjustable
Oil flow during drilling	~ 100 l/min
Operating pressure	max. 200 bar
Rotator	
Rotation speed	max. 300 min ⁻¹ , adjustable
Max. torque	max. 680 Nm, adjustable
Oil flow during drilling	~ 76 l/min
Operating pressure	max. 200 bar
Hydraulic feed motor	
Carriage speed backwards (no load)	max. 0,6 m/s, adjustable
Oil flow during drilling	~ 20 l/min
Operating pressure	max. 200 bar
Feed force forward	max. 25 kN, adjustable
Drill bit flushing	
Flushing air / N2	3,5 Nm ³ /min at 7 bar
Water	max 4 l/min at 4 - 5 bar
Supplied water cleanness	Impurities < 250 mg/l Grain size < 200 µm
Supplied water temperature	<45°C

Figure-5: Technical Information of The Supplied Drill Machine

The modernization works of clay gun and drill equipment, which started on April 14, 2022, were successfully completed on June 06, 2022.

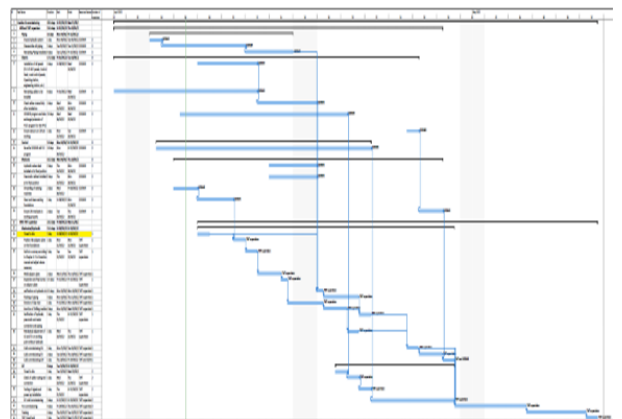


Figure-6: BF4 Taphole 1-Erection and Commissioning Schedule

2.1. The works carried out within the scope of modernization of the equipment are as follows;

Using the existing hydraulic power station, the hydraulic pipelines were revised according to the equipment. ASI312 stainless steel was chosen as the material for hydraulic pipes and fittings due to its high pressure. In addition, all connections were made as butt welded.



Figure-7: AISI 312 Stainless Steel Revised Hydraulic Pipelines

A new hydraulic valve desk was supplied for the clay gun and drill machines. The location of the hydraulic valve desk in the casting hall in the old system was revised. Next to the hydraulic power unit located on the ground floor, a room for the hydraulic valve desk was made. In this way, a clean, dust-free environment is provided for the working place of the hydraulic valves.



Figure-8: Hydraulic Valve Desk Room



Figure-9: Hydraulic Valve Desk

3. Assembly of Equipment

Close to the completion of the hydraulic piping works, the existing clay gun and drill machine were disassembled up to the main frame. The main frame surface was cleaned and ground to be smooth. Then, the holes of the intermediate foundation plate on which the equipment will be mounted were drilled. The intermediate foundation plate was mounted on the basic frame. One of the most critical tasks here was the assembly of the intermediate foundation plate at project values. It was required to be mounted with a maximum margin of error of 5mm in all axes after assembly and welding.

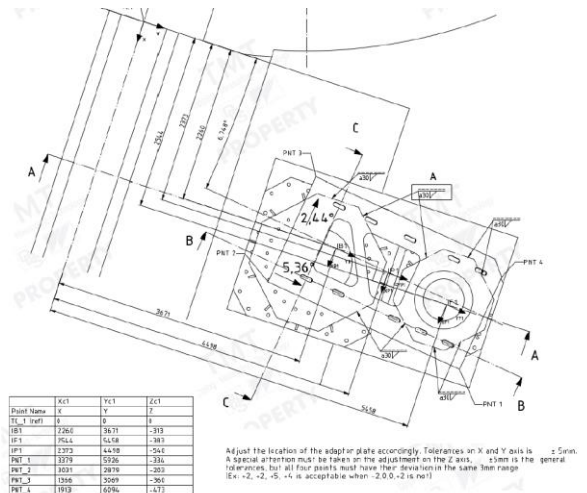


Figure-10: Project Values

	Zc1 Project value	Zc1 First Position after the assembly	Zc1 Difference	Put The Shim Plate	Zc1 After shim put	Zc1 Difference After The Weld	Zc1 FINAL Difference
PNT_1	-247	-263	-16	4mm	-259	-12	-12
PNT_2	-116	-129	-13	3	-128	-12	-12
PNT_3	-273	-284	-11	-	-284	-11	-12
PNT_4	-386	-401	-15	3	-397	-11	-12
	Yc1 Project value	Yc1 Position after the assembly	Yc1 Difference	After The Weld	Yc1 FINAL Difference		
PNT_1	5926	5927	1	5928	2		
PNT_2	2879	2880	1	2881	2		
PNT_3	3069	3070	1	3070	1		
PNT_4	6094	6095	1	6095	1		
	Xc1 Project value	Xc1 Position after the assembly	Xc1 Difference	After The Weld	Xc1 FINAL Difference		
PNT_1	3379	3378	-1	3379	0		
PNT_2	3031	3031	0	3029	-2		
PNT_3	1366	1366	0	1364	-2		
PNT_4	1913	1912	-1	1913	0		

Figure-11: After Assembly and Final Values

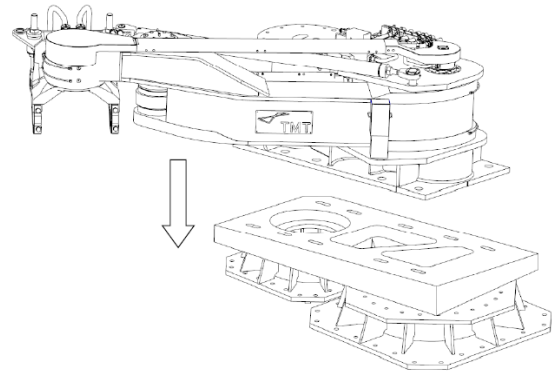


Figure-14: Intermediate Foundation Plate



Figure-12: Main Base Frame



Figure-15: Assembly of Clay Gun



Figure-13: Intermediate Foundation Plate



Figure-16: Assembly of Clay Gun Plugging Unit

After the welding of the intermediate foundation plate with the base frame was completed, the clay gun assembly started.

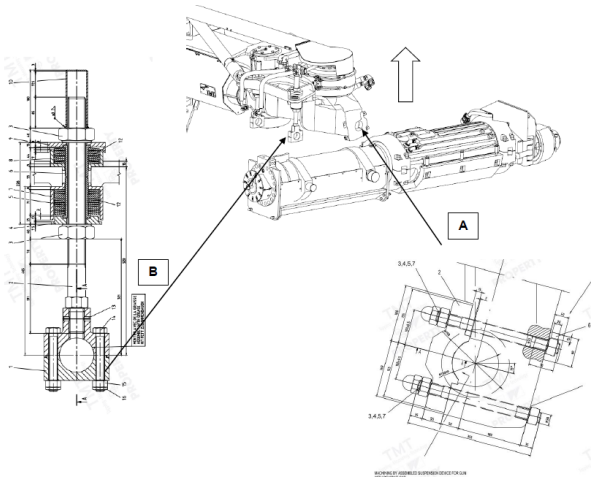


Figure-17: Assembly of Clay Gun Plugging Unit

After the clay gun installation, using a hydraulic test unit parallelism and alignment settings were made. Then the assembly of clay gun was completed, the drill machine assembly started.



Figure-18: Adjustment of Clay Gun

Drilling angle adjusted upon completion of drill machine assembly. After alignment and parallelism settings adjusted for the drill machine.

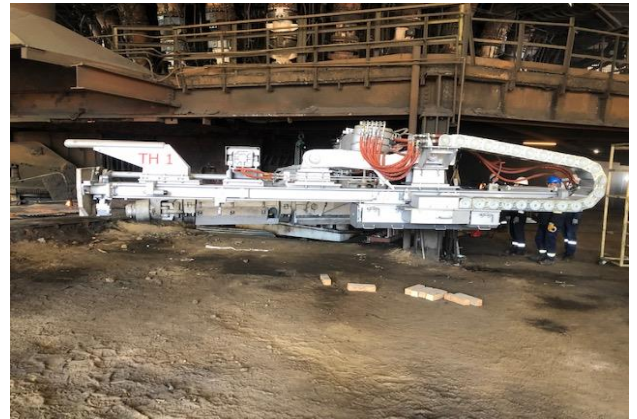


Figure-19: Assembly of Clay Gun Plugging Unit



Figure-20: Drilling angle adjusted

After the equipment installations and settings were completed, the flushing activity of the hydraulic pipes was performed. Afterwards, the pipe connections of the equipment and hydraulic valve desk were made. After the completion of all assemblies, cold tests were started. Adjustment of hydraulic proportional valves, control of pneumatic connections, electrical and automation adjustments were made during cold tests.

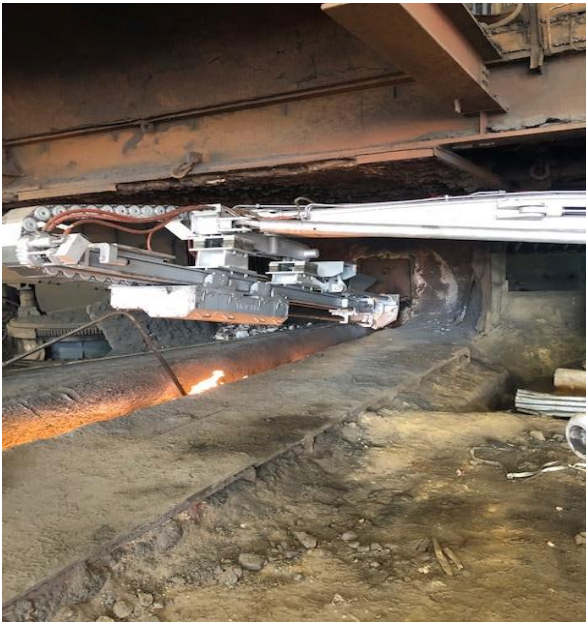


Figure-21: Cold Tests of Drill Machine



Figure-22: Cold Tests of Clay Gun

Cold tests were completed on 06.05.2022. All units are organized and the casting hole No. 1 has been activated. Equipments was used for the first time on 06.05.2022.

4. Modernization and Innovations Realized by Activating the Equipments

More powerful equipment was procured. In this way, situations such as opening the casting hole with oxygen

and not closing the casting hole were eliminated. In this way, an important step was taken in terms of production and furnace process health.

Equipments can be operated by means of a radio remote control.



Figure-23: The Radio Remote Control.

The strength of the equipment movements was preferred as adjustable according to the need. It is adjusted gradually from the control desk or the radio remote control according to the need.

Ensuring that the casting hole is closed automatically. In this way, the human-dependent workforce has been reduced.

Automatic opening of the casting hole. In this way, the human-dependent workforce has been reduced. These operations are done with a single button on the radio remote control. In this way, the difference in the use of operators is prevented.



Figure-24: The Control Desk

A lamp panel was placed in the casting hall. In this way, the tracking of movements can also be seen from here. It also shows how many pumps are activated in the hydraulic power unit.



Figure-25: The Lamp Panel

Automatic monitoring of the taphole depth from the control table.

Online tracking of the pressed hole mud amount from the control table.



Figure-26: The Amount Injected of Mud and The Depth of The Taphole

A knob is preferred instead of hook as a drill feed fixing element.



Figure-27: Drill Feed Fixing

The hydraulic valves that provide the equipment movement are proportionally selected.

It is ensured that water can be used together with air during taphole openings.

5. Conclusion

The old clay gun and drill machine were modernized and the following results were observed;

- Drill and clay gun related glitches have been reduced,
- Hydraulic efficiency has been increased by choosing thicker hydraulic pipes, which are insufficient,
- Manually controlled clay gun and drill machine were modernized and radio remote controlled, the operator was given a safer distance and a better viewing angle,
- Clay gun and drill machine digitization provided,
- Reduced clay gun problems rubbing the runner,
- The old non-proportional hydraulic valves were made proportional and they were operated more sensitively,
- Automated operations have been modernized,



- Clay gun nozzle and drill bar consumption has been reduced,
- Reduced mud freezing problems with cooling and refractory enclosures,
- Energy savings have been achieved,
- No extra expenditure was made by using the existing hydraulic power unit.

References

- [1] Özdemir, G., Can, A.H. ve Kartal V., 2011.” Çamur Topu Matkap Hidroliği (İsdemir 3. Yüksek Fırın Hidrolik Uygulamaları)”, VI. Ulusal Hidrolik Pnömatik Kongresi 12-15 Ekim 2011/İZMİR, s:128
- [2] Çelik, V. ve Fidan, O., (2021).” 4.YF Atık Isı Eşanjörü İyileştirme”, 6nd International Conference on Material Science and Technology in Cappadocia (IMSTEC'21), November 26-27-28, 2021, Cappadocia /TURKEY, s: 151
- [3] Çelik, V., Eken, K., ve Fidan, O., (2022).” Salamander Drilling Position And Salamander Runner Design Charging Into Torpedo Car”, 8. Uluslararası Demir ve Çelik Sempozyumu (EFRS-2022), 26 - 27 Mayıs 2022 İzmir p: 366



IMPROVEMENT OF THE SIPHON OPENING PROCESS IN THE ISDEMIR NEW BLAST FURNACE NO.1

Mustafa BAŞSU, Onur Hüseyin MEMİŞ, Ümit GEBENLİ, İbrahim ÇAKMAK

İskenderun Demir ve Çelik A.Ş.
Türkiye

Keywords: Blast Furnace, Emission, Dust Catcher, Occupational Health and Safety, Environment, Process Safety, Dust, Blast Furnace Gas, Top Gas

Abstract

ISDEMIR Blast Furnace No.1 will have a daily production capacity of 7900 tons of liquid raw iron. The furnace will be the largest blast furnace in Turkey with an internal volume of 3072m³ and will have 4 tapholes. In this study, it will be mentioned how the use of siphon drills (jack dam drill) in the blast furnace casthouse has a positive effect on environmental pollution, occupational health and safety, shortening maintenance times and production continuity. At the same time, the design and usage of the siphon drill will be explained.

Siphon zone, located at the end of the main runner in the blast furnace, is the zone where the pig iron and slag are separated. After the siphon is the pig iron secondary runner, the hole that allows the siphon region to open to the pig iron secondary runner is called the siphon hole. Siphon opening is an operation performed in blast furnaces during maintenance and emergencies. This process is part of the blast furnace operation. Its frequency is on average once or twice a month, but this number can increase or decrease. The construction methods of this process can cause occupational safety risks, loss of time, extra work force for personnel and environmental pollution due to dust emissions. In addition, failure to perform this process effectively and on time can lead to production losses.

In order to avoid the aforementioned risks and important problems, a new equipment called a jack dam drill was provided for the Blast Furnace No.1, which was rebuilt by ISDEMIR and is the largest blast furnace in Turkey. The Blast Furnace No.1 casthouse has been specially designed to be suitable for the installation and use of this equipment. It is

planned to contribute to reducing environmental pollution with the use of siphon drills, to contribute to occupational safety by making unmanned work, to prevent production losses by preventing prolongation of shut-down time and to contribute to production continuity.

1.Introduction

ISDEMIR Blast Furnace No.1 will have a daily production capacity of 7900 tons of liquid raw iron. The furnace will be the largest blast furnace in Turkey with an internal volume of 3072m³ and will have 4 tapholes.

Siphon zone, located at the end of the main runner in the blast furnace, is the zone where the pig iron and slag are separated. After the siphon is the pig iron secondary runner, the hole that allows the siphon region to open to the pig iron secondary runner is called the siphon hole. At the same time, in cases where the main runner needs to be drained, a siphon hole is opened and the hot metal in the main runner is taken directly into the tilting runner through the discharge runner. Siphon opening is an operation performed in blast furnaces during maintenance and emergencies. There are several ways to open the siphon hole. The most common method is to open it by hammering with a crusher-tipped excavator. If the siphon hole cannot be opened with a crusher, there are also applications where it is opened by hitting the hole with oxygen through oxygen lances.

Crusher machines are generally insufficient to open the siphon hole. Thus, the processing time is prolonged and causes loss of time. Especially if the runner concrete is to be crushed and then new concrete poured, this delay may prolong the shut-

down time and cause loss of production. In addition, the long duration of this process causes loss of labor for other works that need to be done in the shut-down time. On the other hand, drilling holes with oxygen is an undesirable and last preferred method. While siphon opening with oxygen, the lances are directed to the hole by human and their manipulation is done. During this process, heat and flame are released. Although there are equipment that will completely protect the personnel from these effects, the process of opening with oxygen is not preferred. At the same time, dust is emitted to the environment during the siphon opening process with oxygen, which is harmful to the environment. For these reasons, the need to use cleaner, safer and more useful equipment has arisen. Thus, it was decided to use equipment called siphon drill/Jack Dam Drill [1] in the newly built Blast Furnace No.1 casthouse.

2. What is a Jack Dam Drill (Siphon Drill)?

Siphon drill is the equipment that enables the siphon hole to be opened easily and from the same place every time. The principle and the bits used are similar to the blast furnace taphole drill, but the siphon drill is a smaller and more portable piece of equipment. There are four casting holes in ISDEMİR Blast Furnace No.1, so there are 4 runners and siphons. Siphon drill will be one and will be used for all runners. The drill will be transported and installed by crane around runners. The runners and casthouse of ISDEMİR Blast Furnace No.1 are designed in accordance with the use of siphon drill. At the edge of the runner, on the floor of the casthouse, there is a steel construction zone where the siphon drill will be installed. In addition, there is a hole whose angle and position is adjusted on the edge of the pig iron runner so that the drill can reach the siphon hole. The layout, location and view of the siphon drill from various directions are shown in Figure 1 and Figure 2.

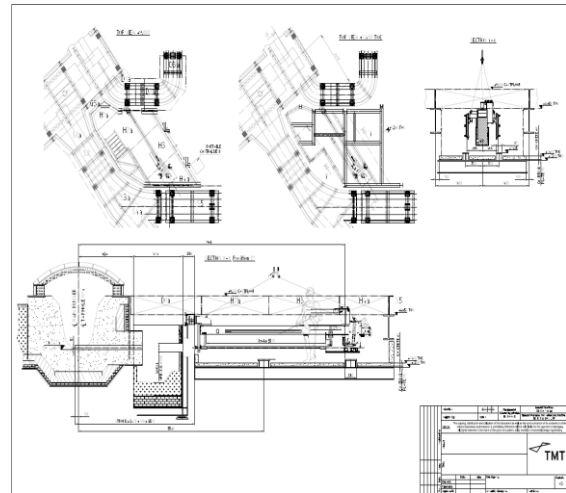


Figure 1: Siphon Drill Layout and Drawings [1]



Figure 2: View of Runners and Siphon Drill Area on 3D model

3. Advantages of Jack Dam Drill

It will contribute to the prevention of environmental pollution by minimizing dust emissions during the siphon opening process. Since there is no need for manpower in its installation and use, it will not pose a risk in terms of occupational safety and will ensure that the workforce is used more efficiently. Since it will shorten the siphon opening process, it will prevent production loss in cases where the ducts are of critical importance during shut-downs. In addition, it will extend the life of the refractory of siphon as it will ensure that the siphon hole is opened properly at the same angle and from the same point every time. In this way, it will also reduce the refractory consumption.

4. Installation and Use of Siphon Drill

As can be seen in Picture 3, the siphon drill can be lifted from three points and safely lifted by the overhead crane in the casthouse. Thanks to the automatic locking mechanism seen in Picture 4, no human intervention is required. As can be seen in Picture 5, there is a locking mechanism based on the tension and looseness of the lifting slings. In the left position, the system is unlocked when the lifting slings are tight. When the slings come loose, locking occurs.

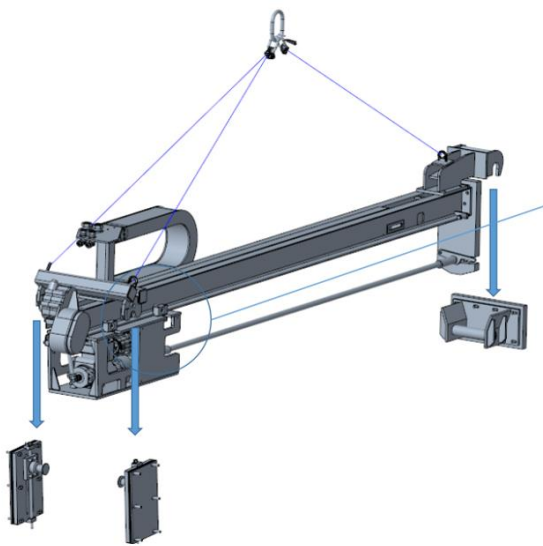


Figure 3: Lifting and Assembly of Equipment [1]

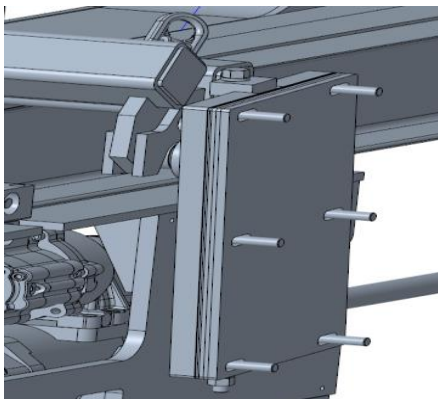


Figure 4: Automatic Locking Mechanism [1]

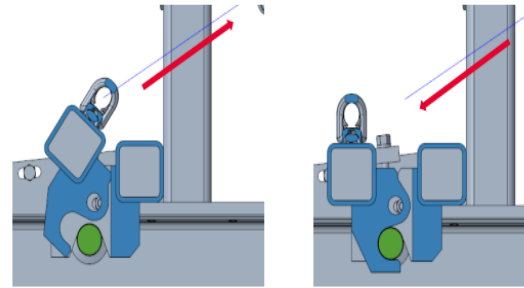


Figure 5: Lifting Points Locking Mechanism [1]

5. Conclusion

The use of Siphon Drill equipment in the blast furnace casthouse will be very beneficial in terms of environment, occupational safety, labor efficiency, maintenance time and prevention of production losses. By shortening the siphon opening process, it will shorten the shut-down time. By opening the siphon at the same angle and from the same point every time, the siphon hole will not require repair, the refractory consumption will be reduced, and it will save money. Since it is easy and practical to use and install, it will not require labor and will ensure efficient work by using the workforce in the foundry for other works. At the same time, it will prevent security weakness when opening the siphon. Thanks to these advantages and added value, it was decided to use a siphon drill in ISDEMIR Blast Furnace No.1, which will be the largest blast furnace in Turkey.

References

- [1] TMT Jack Dam Drill Technical Specification



DISTRIBUTION OF COIL AND WIRE ROD PRODUCTS MANUFACTURED AT ISDEMİR ACCORDING TO AREAS OF USAGE, STANDARDS AND CUSTOMER EXPECTATIONS

Muhammet BİLEN, Nalan GÜL UĞUR

İskenderun Demir ve Çelik A.Ş.
Türkiye

Keywords: İsdemir, Coil, Wire Rod, Standards, General Usage Areas, Customer Expectations

Abstract

ISDEMİR is an integrated iron and steel facility, which produces both long and flat products from production of iron ore. Wire rod, billet, coil with mill edge, slitted or trimmed coil and cut length plate can be stated İsdemir's product mix. Each of these products have different usage areas and customer expectations. ISDEMİR has a wide range of application areas with the hot rolled flat products or long products, which are expressed as wire rods-billets in order to respond to the customers', who operated in the industrial area and have different demands and expectations, requests. Micro-alloy high-strength steel grades with excellent results in high-strength applications for flat products are used in the production of wheel rim and chassis parts, which requires high strength and superior formability in the basic input of automotive. Boiler steels suitable for use under high temperature and pressure are used in the production of boiler and pressure vessels. Due to high formability, excellent weldability and toughness properties, tube steels are used production of LPG tubes, which are exposed to high temperature and pressure. Medium and high strength shipbuilding steels, which provide superior weldability and desired toughness values, are used in shipbuilding (ship parts, keel etc.). General structural steels, which can be welded by conventional methods and whose mechanical properties are guaranteed and ductility and toughness are optimized, are used in general construction manufacturing. In addition, there are also coil products used in the manufacture of bolts, nuts, springs, fine wire, electrode holders, welding wire and pre-stressed concrete wire. In this study, it is aimed to examine the long and flat products produced in İSDEMİR in terms of usage and customer expectations.

1. Introduction

ISDEMİR, the integrated iron and steel plant producing iron ore in Turkey, has both flat and long products in its product range. ISDEMİR, which has various products such as coils, billets, coils, slit-edge-cut-split coils, sheets and plates, produces products with a wide range of usage areas in order to respond to customer demands with different requests and expectations.

2. Flat Product Usage Areas

Usage areas for flat products; Structural Steels, Energy Sector, Construction Machinery and Crane Production, Tractors and Agricultural Machinery, Pipe and Profile, Spiral Pipe - Crude Oil and Natural Gas, ERW Pipe - Petroleum Drilling Steels, Automotive Industry - Wheels, Heavy Vehicle Chassis - Trailer, Safety Belt Systems can be examined in 14 different groups as Pressure Vessel Steel, LPG Cylinder – Pressure Vessel, Steel Suitable for Shipbuilding and Steel Used in Machine Construction.

2.1. Construction Steels Group

They are unalloyed or low alloyed steels defined by their tensile strength and yield limit. Mechanical properties are dependent on the amount of carbon. It is used for applications requiring high strength rather than forming and forming properties.

- Steel construction
- Business Machines
- Guardrail Systems
- Lighting Poles
- Machinery Manufacturing



Figure 1.

2.2. Energy Sector

The structural steels produced at İsdemir are also used in energy distribution lines.

- Steels suitable for galvanized coating are used.
- Galvanized coating is made according to Class1 or Class3.
- Grades conforming to Class 1: 4237 – 4244 – 4252 – 4437
- Grades conforming to Class 3 (confirmation required at the time of order): 3237 - 3244 – 3252 - 6237 - 6244 - 5252 - 6252 - 7252.



Figure 2.

2.3. Grades Used in The Production of Construction Machines And Cranes

- Cut-to-length product is used.
- Along with 6052 quality suitable for folding, 6252 and 6237 quality products are preferred.
- Thicknesses are between 8 – 20 mm. The width changes according to the cutting plan.
- Products are processed on laser cutting benches.
- The most important problem in the sector is the distortion of the material that occurs during laser cutting.
- It is not necessary to use products with cut edges.
- Firms put the products into sandblasting before processing.



Figure 3.

2.4. Tractor And Agricultural Machines

The steels used in agricultural machinery are divided into two as the body sheets of the machine and the parts in contact with the soil. The sector is clustered in the Aegean Region and Konya. Very high wear is expected from the part in

contact with the soil. 5630 grade is used. Bearing structural steels are used in the body parts of the machine.



Figure 4.

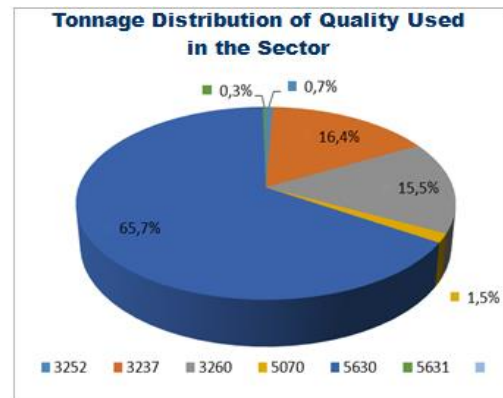


Figure 5.

• 3237, 6244, 4936, 6052 and 6252 quality materials are used in the tractor cabin.

• Thickness ranges vary between 3 – 12 mm. Cut-to-length products are laser cut.

5620-5630-5631 grades gain both hardness and strength provided that heat treatment is applied. The basic principle in heat treatment is that the material is heated to a certain temperature (over 850 °C), instantaneously cooled and hardened by quenching. The products work against wear.



Figure 6.

2.5. Pipe & Profile Grades

Spiral pipe production begins with the application of unrolling, ironing and edge milling processes to hot rolled coils. Afterwards, spiral forming and internal-external

welding processes are performed and ultrasonic control is applied.

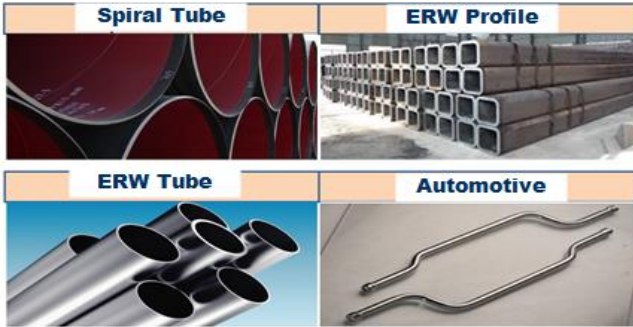


Figure 7.

2.6. Pipe – Spiral Pipe – Crude Oil and Natural Gas

Steels suitable for pipe manufacturing for crude oil and natural gas lines are produced according to API 5L standard. There are grades with different technical requirements, PSL1 and PSL2. While only minimum yield, minimum tensile, and minimum elongation guarantee is requested for PSL1 grades, features such as maximum yield, maximum tensile, maximum elongation, impact resistance, DWTT, etc. are also requested for PSL2 grades.

Table 1.

Standard Corresponding			İsdemir Steel Grade
Standard	Spec. Level	Quality	
API 5L/EN ISO 3183	PSL1	L245 / B	9035
API 5L/EN ISO 3183	PSL2	L245N / BN	9036
API 5L/EN ISO 3183	PSL1	L290 / X42	9042
API 5L/EN ISO 3183	PSL2	L290N / X42N	9043
API 5L/EN ISO 3183	PSL1	L320 / X46	9046
API 5L/EN ISO 3183	PSL2	L320N / X46N	9047
API 5L/EN ISO 3183	PSL1	L360 / X52	9052
API 5L/EN ISO 3183	PSL2	L360M / X52M	9053
API 5L/EN ISO 3183	PSL1	L390 / X56	9056
API 5L/EN ISO 3183	PSL2	L390M / X56M	9057
API 5L/EN ISO 3183	PSL1	L415 / X60	9060
API 5L/EN ISO 3183	PSL2	L415M / X60M	9061
API 5L/EN ISO 3183	PSL1	L450 / X65	9065
API 5L/EN ISO 3183	PSL2	L450M / X65M	9066
API 5L/EN ISO 3183	PSL1	L485 / X70	9070
API 5L/EN ISO 3183	PSL2	L485M / X70M	9071



Figure 8.

2.7. Pipe – Erw Pipe – Petroleum Drilling

In the oil drilling process, two intertwined pipes are used as casing and tubing. Medium and high strength steels suitable for oil drill pipe construction are produced according to API 5CT standard. There are usage areas as nongradable and upgradable. It is symbolized by the magnitudes of the yield strengths, such as J55, K55. The most used grade of Casing Tube (5CT) steels is J55. The tensile and yield strength of K55 quality does not show parallelism with other grades. The tensile strength and yield strength of K55 quality steel is wider. In these steels, strength increase should be provided during deformation with the composition design and these grades allow more plastic deformation.

Table 2.

Standard Corresponding			İsdemir Steel Grade
Standard	Spec. Level	Quality	
API 5CT	PSL1	H40	9240
API 5CT	PSL1	J55	9255
API 5CT	PSL1	J55 Special 1)	9256
API 5CT	PSL1	J55 (Special 2)	9257
API 5CT	PSL1	N80 Special	9275
API 5CT	PSL1	N80 Type1	9280

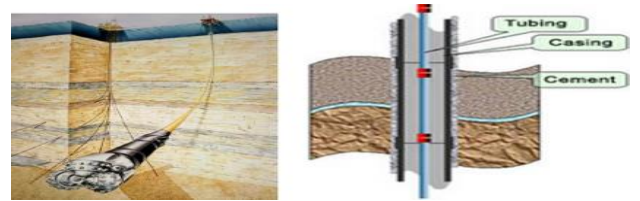


Figure 9.

2.8. Automotive Industry – Wheel

There is a production capacity of 15 million wheels in our country. 220,000 tons of steel is used annually in the sector. The sector is divided into two as passenger cars and heavy vehicles. Formability and weldability are very important in the wheel industry. For this reason, its internal structure has been specially cleaned 39 . . series materials are used. High strength grades are used in the disc area and lower grades are used in the pulley.



Figure 10.

Heavy Vehicle:

- 39.. Series materials are used in the pulley and disc.
- Thicknesses vary between 6 – 16 mm.
- Sliced product is used.
- Generally, RKK product is preferred.
- Large wheels are produced in diameter.

Passenger cars:

- 39.. Series is used in the pulley and 3660 (DP600) quality sheet is used in the disc.
- Thicknesses are between 2.7 mm and 5 mm.
- Sliced product is used.
- Acidified and tempered products are used because the floating expectation is very high.
- DP600 quality is dual phase and it is a low carbon and low alloy steel produced by thermomechanical rolling method.

2.9. Automotive Industry – Heavy Vehicle Chassis – Trailer

The expectation of this sector is easily shaped and high strength materials.

- MC group S335 MC, S420 MC, S460 MC, S500 MC, S550 MC, S600 MC, S700 MC
- 6052 and 6252
- Cut-to-length material is used.
- Plate products are processed by guillotine shears, laser cutting or plasma cutting.



Figure 11.

2.10. Automotive Industry – Seat Belt Systems

In the seat belt case;

- S550 MC and S500 MC grades are used.
- 2 – 2.5 mm RKK
- Sliced product
- Homogeneity of the material is very important since progressive mold is used.
- It is produced as BRKK to prevent head-end thickness difference.



Figure 12.

2.11. Pressure Container Steels

Pressure vessel steels are used in areas such as household LPG cylinders, vehicle LPG conversion systems, steam

boilers, water heaters, boilers, waste heat boilers, LPG transport tanks.

Table 3.

General Usage Area and Main feature	Standart Karşılığı		İsdemir Kalite No
	Standart	Kalite	
Steels suitable for the production of welded gas cylinders (LPG tube steels)	DIN EN 10120:2008	P245NB	6837
	DIN EN 10120:2008	P265NB	6842
	DIN EN 10120:2008	P310NB	6847
	DIN EN 10120:2008	P355NB	6852
At medium and low temperatures and under pressure	ASTM A516-10	55	6855
	ASTM A516-10	60	6860
	ASTM A516-10	65	6865
	ASTM A516-10	70	6870
For use under high temperature and pressure suitable boiler steels	DIN EN 10028-2:2009	P235GH	6335
	DIN EN 10028-2:2009	P265GH	6341
	DIN EN 10028-2:2009	16Mo3	6345
	DIN EN 10028-2:2009	P295GH	6347
	DIN EN 10028-2:2009	P355GH	6352
Non-alloy steel suitable for use under pressure	DIN EN 10028-2:2009	P355GH Özel	6350
Fine grain suitable for use under pressure normalized steels	DIN EN 10028-3:2009	P355NH	6353
	DIN EN 10028-3:2009	P355NL1	6355

2.12. Lpg Cylinder – Pressure Container

Product groups used in the industry

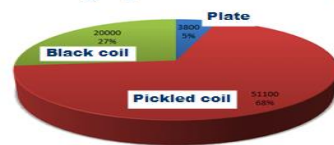


Figure 13.

2.13. Steels Suitable For Ship Building

- Generally, LKK or LRKK product is used
- 3.2 certificate is requested.
- ABS, BV, DNV, TL Lloyds
- Wide product is preferred
- There is the use of painted products.
- Traceability is important.
- Marking is done with punch



Figure 14.

2.14. Steels Used in Machine Building

The machinery sector is one of the areas where structural steels are used the most. 3237, 6252, 6052, 3244 quality materials are used. In this sector, the products are in the form of plates. LKK or LRKK product is preferred. Unrolled plate products can be supplied for thicknesses up to 22 mm.



Figure 15.



ESTABLISHING A BILLET QUALITY RECOMMENDATION SYSTEM (DIGITALIZATION)

Gökhan BİLMEZ, Erhan KORKMAZ, Erman KAYA

İskenderun Demir ve Çelik A.Ş.
Türkiye

Keywords: Production Planning, Stock Control, Wire Rod Mill, Quality Transformation, Level-4 Expert System

Abstract

An average of 30-40 different quality productions take place every month in İsdemir wire rod mill. For some grades, regular orders are entered every month, and for some, there is rarely an order entry. In the billet casting machines in the continuous casting facility, the castings are cast on a tundish basis and are produced in tundish with an average of 5 castings (1000 tons). For grades with rare order entry tightness, 1 tundish casting may result in a stock situation that is not produced for the customer. In İsdemir terminology, this stock is called customer waiting billet stock. For example, the quality 5.2600_05 is a quality entered at rare intervals with low customer potential. On average, orders are made between 300-500 tons in 4-5 month periods. When we buy 1 tundish (1000 tons) casting for this order group, an average of 500-700 tons of excess billet stocks are formed. These billets are in stock for a long time. As a result of the joint work of the Software and Production Planning departments, the billet quality recommendation systematic was created on the UYS (Production Management System). Thanks to this report, it is possible to see the quality of all the billets waiting in the stock, which can be connected in terms of analysis, based on casting. The report can be followed live instantly from the UYS (Production Management System) system. Thanks to the project, it is aimed both to bring the billets that have been waiting in stock for a long time to order, and to quickly deliver the grades with low casting tonnage (cannot be produced tundish) or for which less orders are entered to the customers.

1. Introduction

Billets coming out of the continuous casting machine in İsdemir coil rolling mill are rolled as coils in 23 different sizes and approximately 30-40 different qualities, with a thickness range of 5.5mm-16mm. The size of the billets to be rolled has a width of 130X130mm and a length of 12m. First, the billets from the continuous casting unit are subject to quality control approval at the billet stock area. The approved billets are

stacked in the front of the line stock area. Billets must be heated to a temperature of 1,200°C before rolling. This heating is done in the coil rolling mill reheating furnace. Afterwards, the billets are pre-shrunk in the rough group processing section, the thinning process is continued in the intermediate groups, and finally, they are reached to the final production size thickness in the machines called monoblock. Coils reaching the order thickness are subjected to cooling-forming-packaging processes and are made ready for shipment.

In İsdemir long product production group, production takes place with an average of 30-40 different quality – 6 product process groups per month. However, quality deviations during casting, analysis deviations, etc. may occur in non-order quality productions. These grades, produced out of order, are in stock for a long time and have a negative impact on stocking costs.

Before the project, manual follow-up was made for these grades produced out of order and the processes took a long time. After commissioning the project, the manual process was eliminated and significant time and unit labor savings were achieved.

2. Experimental Procedure

Casting Steel quality, Casting number, Casting Tonnage and Casting Analysis displays can be found with the reports received by entering the billet suggestion system from the UYS (Production Management Systems) screen. This system was created as a result of the integrated work of the production planning and software departments..

This software has been developed in Java using the Java Server Faces 2.0 technology used in the software department of ISDEMİR. In addition, Java Script was used to add dynamic features to the web page. The page shows data is stored in Oracle 19C database. During this study, the data received from different systems were combined and displayed

MINIMIZING THE CONSUMPTION OF TEMPERATURE PROBE BY PREDICTION OF LIQUID STEEL TEMPERATURE DURING LADLE FURNACE PROCESS

Mustafa SAĞLAM¹, Esra KÜPELİ¹, Abdurrahman Mesud ÇAKIR¹, Burcu SOYSAL ATAN¹, Alper KURTOĞLU¹, Alperen TERZİ¹, Eyüp Veysel ÖZDEMİR¹, Hikmet ŞAHİN¹, Mehmet Mustafa YILDIRIM¹, Bekir Burak YAMANOĞLU¹, Tayfun KOCABAŞ²

¹İskenderun Demir ve Çelik A.Ş., ²Oyak Maden Metalurji
Türkiye

Key Words: Ladle Furnace, Heating, Probe Consumption, Multiple Linear Regression Analysis, Digitalization, Minitab, Level-2

Abstract

In the blast furnace-based steel production plants, liquid iron desulfurization is carried out according to the target value on the basis of the steel quality to be produced at the desulfurization plant. Afterwards, in the basic oxygen furnace (BOF), liquid steel is obtained by blowing oxygen onto the bath consisting of liquid raw iron and steel scrap. The liquid steel produced taken to ladle furnaces for heating, alloying and steel cleaning processes before the continuous casting process. In ladle furnaces, temperature measurements both during and at the end of the treatments are important for the ladle furnace process. In İSDEMİR ladle furnaces, an average of four temperature measurements are taken per heating during the process. It is important to know the temperature value during the process steps in the ladle furnace. Liquid steel temperature is critical for production continuity, production efficiency and quality. In the study, the liquid steel temperature during the process in the ladle furnaces was calculated by means of a model obtained by the multiple linear regression analysis method. The R-sq (adj) value of the model is 92.34% and its power to explain the output is very high. The resulting regression model was integrated into the Level-2 system and made available to the operators. Thus, both the occupational health and safety risks occurred during the liquid steel temperature measurements and the amount of

temperature probe consumption per casting are reduced.

1.Introduction

In İSDEMİR, Liquid Hot Metal (LHM) coming from the Blast Furnaces via torpedoes is poured into the ladles in the steelmaking shop. The desulfurization process is done in the ladle. Heat, in the steelmaking shop begins with scrap charging into the BOF. The desulfurized hot metal is then charged. Pressurized oxygen is blown over the bath consisting of scrap and LHM by means of a lance.



Figure 1. Hot Metal Charging to BOF

The reactions of elements such as C, Si, Mn etc. in LHM



with oxygen are exothermic and heat is released. Scrap amount is determined according to LHM analysis. Scrap melts with the effect of heat generated. The liquid steel produced is discharged into the steel ladle by turning the converter. Deoxidation and the alloying materials are added during tapping. In the Secondary Metallurgy stage, processes are carried out to adjust the temperature of the liquid steel, to make the final alloying and to ensure the cleaning of the steel in the ladle furnaces.

Figure 2. Ladle Furnace

After the Ladle Furnace operations are completed, heat is transferred to the slab or billet casting machine in İSDEMİR. Afterwards, it is casted as a semi-finished product in continuous casting machines.



Figure 3. Slab Casting Machine

Liquid Steel Temperature

Liquid steel temperature is one of the most important parameters in the steel production process. It is important to measure the temperature value correctly and to reach this value at the desired frequency.

As a measurement method, it is carried out by immersing the probe containing the thermocouple into the liquid steel by means of a lance. Diving of the probe into the liquid steel is provided manually by the operator or by means of automatic systems.

2. Experimental Procedure

In order to provide advantages in Occupational Health and Safety, probe saving and time saving, it is aimed to create a model that predicts the temperature of liquid steel, taking into account the operations performed in LF.

At the beginning of the study, the current situation analysis was carried out by subtracting the average number of temperature measurements per heat in LF for the most common slab casting grade (Figure 4).

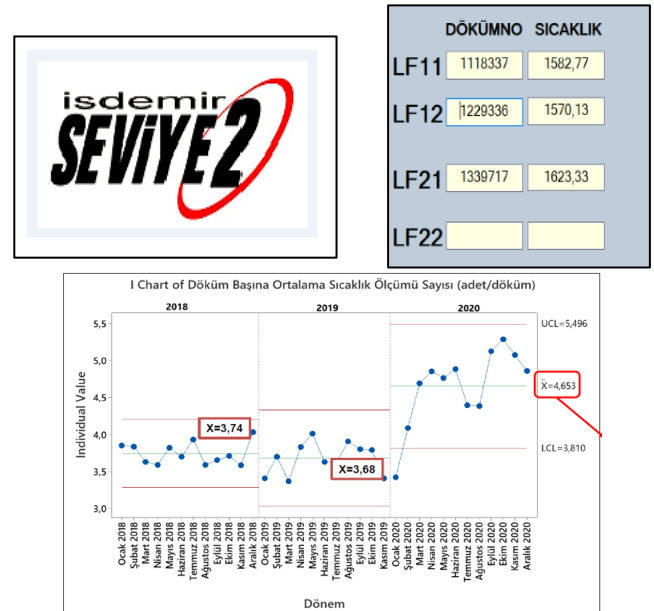


Figure 4. Chart of Average Temperature Measurements Per Heat

In the heat-based investigations, the factors affecting the liquid steel temperature were determined. During the analysis, the situations between two temperature measurements in the heat at LF were examined. The state between two temperature measurements was taken as a row in the dataset. Realization data of the determined factors for each line were recorded.

	C1	C2-T	C3	C4	C5	C6	C7	C8
	Döküm No	Kalite	İlk Sıcaklık	Karıştırma Toplam	Süre	Ark Süresi	Malzeme Verilme Durumu	Sıcaklık
1	8339651	2.7112_50	1573	693,0	7	0,0	0	1569
2	8339651	2.7112_50	1569	693,0	8	6,7	408	1581
3	8339651	2.7112_50	1581	693,0	10	9,2	0	1590
4	8339651	2.7112_50	1588	693,0	3	2,9	0	1592
5	8339651	2.7112_50	1592	280,0	4	0,0	108	1591
6	8339651	2.7112_50	1592	280,0	4	0,0	108	1591
7	8118283	2.7112_50	1616	1020,0	7	2,9	480	1602
8	8118283	2.7112_50	1602	903,0	5	0,0	0	1597
9	8118283	2.7112_50	1597	903,0	5	0,0	0	1594
10	8118283	2.7112_50	1594	212,0	4	0,0	144	1590

Figure 5. Data Set

Situations between two temperature measurements in casting were examined. Each of the states between two temperature measurements was taken as a row in the data set. Realization data of the determined factors for each line were recorded (Figure 5). After that, multiple linear regression analysis was performed to predict the temperature and we had a strong mathematical model which has 92,34% R²(adj) value (Figure 6).

Model Summary			
S	R-sq	R-sq(adj)	R-sq(pred)
3,50726	92,57%	92,34%	91,97%

Coefficients					
Term	Coef	SE Coef	T-Value	P-Value	VIF
Constant	144,1	32,8	4,39	0,000	
İlk Sıcaklık	0,9110	0,0206	44,23	0,000	1,22
Karıştırma Toplam	-0,002932	0,000795	-3,69	0,000	1,12
Süre	-1,037	0,101	-10,31	0,000	1,61
Ark Süresi	2,166	0,108	19,98	0,000	1,92
Malzeme Verilme Durumu	-0,00682	0,00129	-5,30	0,000	1,06

Regression Equation	
Sıcaklık	= 144,1 + 0,9110 İlk Sıcaklık - 0,002932 Karıştırma Toplam - 1,037 Süre + 2,166 Ark Süresi - 0,00682 Malzeme Verilme Durumu

Figure 6. Multiple Linear Regression Analysis

The developed model was adapted to the İSDEMİR Level-2 system. It has been put into use in a way that allows it to be used easily by the operators. The model, which is adapted to the Level-2 system, takes this temperature as a reference together with the first temperature measurement in LF, and the model recalculates the temperature prediction value at one minute intervals depending on the next operations and updates the value (Figure 7).

Figure 7. Level-2 Adaptation

3. Results and Discussion

With the commissioned model, the number of measurements in the steel quality in which the model was developed in LF was reduced, thus improving OHS risks, decreasing the average probe usage and gaining time. In order to verify the model, one sample t-test was carried out to determine the differences between the estimated temperature and the measured temperature (Figure 8).

One-Sample T: Tahmin Edilen-Ölçülen Sıcaklık				
Descriptive Statistics				
N	Mean	StDev	SE Mean	95% CI for μ
139	0,598	3,329	0,282	(0,040; 1,156)
μ : population mean of Tahmin Edilen-Ölçülen Sıcaklık				
Test				
Null hypothesis		$H_0: \mu = 0$		
Alternative hypothesis		$H_1: \mu \neq 0$		
T-Value	P-Value			
2,12	0,036			

Figure 8. X-500 Microstructure

As a result of the confirmation analyses, it was seen that there was no statistical difference between the measured temperature and the estimated value. The temperature predicted by the model is statistically 0.6°C higher than the measured temperature. Considering the operating temperatures, since the measurement accuracy of the probe

is +/- 4°C, the deviation value of the model shows a better value than the current situation.

4. Conclusion

Probe consumption was reduced for the slab casting grades determined as a result of the study.

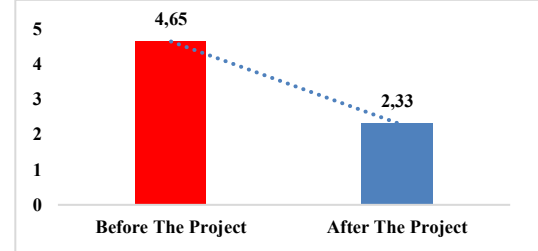


Figure 9. Probe Consumption

In addition to reducing probe consumption;

- Reducing OHS risks
- Know-how for İSDEMİR
- Not having a negative effect on our current achievements
- Potential to have a positive impact on quality

Model studies can be made for different qualities on a new data set.

In addition, new attempts can be made to expand the limit values of the current model.

COIL MOVEMENT OPTIMIZATION

Metin KATRANCI, Hasan YILDIRIM, Mahmut KAYHAN, Uğur OKTAY, Koray ARAY, Abdurrahman Mesud ÇAKIR, Burcu SOYSAL, Fatih ÇELİK

İskenderun Demir ve Çelik A.Ş.
Türkiye

Key Words: Coil Stockyard, Coil Movement, Stacking, Handling

Abstract

İsdemir coil stockyard is the place where the coils were stacked according to a certain systematic after production and then other necessary operations have been carried out in order to ship them to the customer. In addition to this main task, the coils are stacked in such a way to send to different lines. There are many criteria that need to be reviewed for stacking coils with different properties of coils. It is difficult for the operator to review all of them in terms of sustainability. To solve this, an automatic address suggestion algorithm has been created and implemented in the İsdemir coil stockyard. Bringing the coil to the best point where it could be stacked and picking it up from the best point had a positive effect on the entire field operation.

Due to the homogenization of the stacks (dimensional and steel quality); improvements have been provided in occupational safety, 5S and process safety. By stacking the coils according to a certain criterion, the number of unaddressed coils in the field has decreased. The time of making the coils ready for shipment and the number of crane manipulations have been improved. Since the control of the field stacking conditions was made automatically, the operators only started to act as operators.

Results had recorded and compared with historical data.

The number of repeated handling in the field has decreased. Coil stacks have become safer. The delivery process of the coils to the customer has been improved.

1. Introduction

İsdemir coil stockyard is the place where the coils from production are stacked before being sent to sampling, labeling and re-coiling lines.



Figure 1. General View of Stockyard

Heterogeneous stacks cause some problems like;

- Delay in delivery to customer.
- If there is a less width coil on the lower floor than the one on the upper floor, it may cause the upper one to fall.
- Slumping may be seen on coils which lower floor.
- There are coils whose address is not registered.

To solve these problems, an automated suggestion model has been created and implemented in coil stockyard field which is pointing the coil to the best point with the parameters, predetermined.

2. Implementation of Project

In the implementation phase of the project, the current situation analysis was first made. The variety of the coils, the variety of stock points and the stacking methods of the operators were reviewed. Then, address suggestion criteria and stacking control conditions were prepared. With the software studies, the suggestion algorithm was put into use in the coil stock field management application. The suggestion algorithm was made available to operator on crane monitoring system.

2.1 Analysis

To see the variation of coils;

- Sample state of coils,
- Next route (which re-coiling lines, labelling)
- Physical properties of coils (temperature, weight, diameter, width and steel grade) have been reviewed. (See Figure 2)

Regression Equation					
Sıcaklık = 95,7 - 1,303 Soğuma Süresi + 0,001091 B.AĞR. + 0,06118 SRM SIC.					
Coefficients					
Term	Coef	SE Coef	T-Value	P-Value	VIF
Constant	95,7	10,2	9,34	0,000	
Soğuma Süresi	-1,303	0,115	-11,34	0,000	1,11
B.AĞR.	0,001091	0,000186	5,87	0,000	1,01
SRM SIC.	0,06118	0,000872	7,02	0,000	1,12
Model Summary					
S	R-sq	R-sq(adj)	R-sq(pred)		
4,90535	75,80%	74,99%	73,64%		
Analysis of Variance					
Source	DF	Adj SS	Adj MS	F-Value	P-Value
Regression	3	6708,3	2236,09	92,93	0,000
Soğuma Süresi	1	3096,4	3096,36	128,68	0,000
B.AĞR.	1	828,3	828,33	34,42	0,000
SRM SIC.	1	1184,8	1184,77	49,24	0,000
Error	89	2141,6	24,06		
Total	92	8849,8			

Figure 2. Regression Model of Temperature Change

To see the conditions of stacking points;

- Proximity of stacking points to weighing zone, sampling machine and re-coiling lines,
- Whether there is a coil in the lower floor in the stacking point has been reviewed.

To see stacking methods of operator;

- Recorded manipulations have been reviewed.

2.2 The Way System Works

The crane monitoring system includes; X-Y lasers and reflectors inside the crane cabin, crane system (Level2 application) and Coil Stockyard Management System (Level-3 application). Coil stock space is coordinated by dividing it into symbolic addresses in specific x-y value ranges. (See Figure 3).

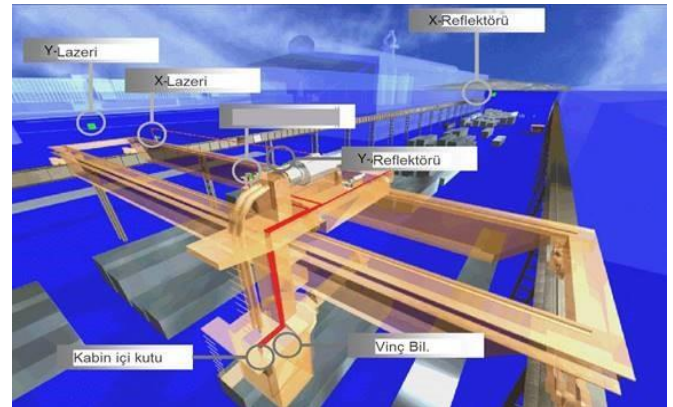


Figure 3. X-Y Lasers on which is being used for virtual mapping

Coil movements and positions from Level2 application, values read from X-Y lasers are transmitted to Level3 application and recorded in Coil Stock Field Management System. This transmitted information is displayed on the virtual site map. (See Figure 4)

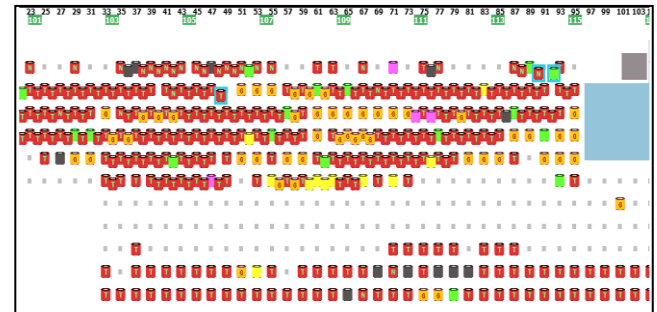


Figure 4. Level-3 Virtual Map of The Coil Stock Yard

As soon as the operator handles a newly produced coil or any coil, an address is suggested to the operator on the crane monitoring screen. This address is generated by the previously constructed algorithm. (See Figure 5)

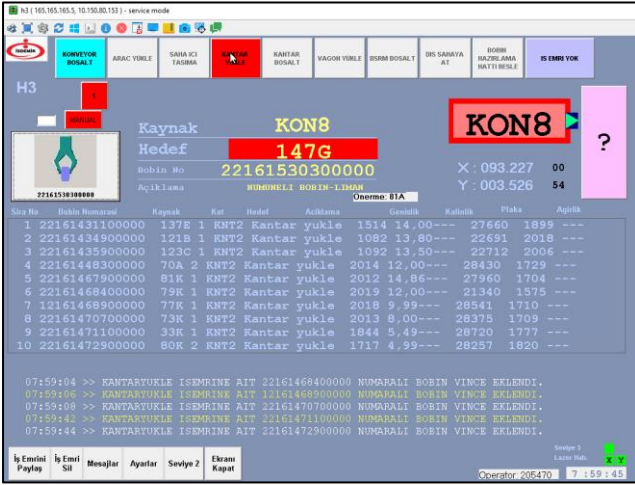


Figure 5. Crane Monitoring Screen

The operator performs the transfer operations according to the proposed address. All manipulations are recorded in the database on a daily basis for the realization of the decision mechanism. With these records, the full and empty status of the addresses are reviewed.

The field variability is examined by reviewing the generated data. The recommendation algorithm is enhanced by operational practices and operator feedback. This algorithm created can be easily controlled and changed on a page on the software.

3. Results and Discussion

With the commissioning of the automatic address suggestion system, improvement in field traffic has been achieved. In particular, an improvement has been achieved in the number of coils handled more than necessary. (See Figure 6)

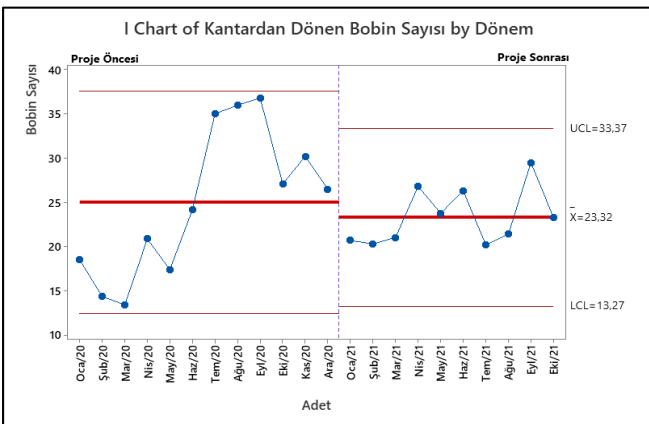


Figure 6. Individual Chart of Extra Handled Coils

An improvement has been achieved in the number of coils whose addresses are not registered in the field. (See Figure 7)

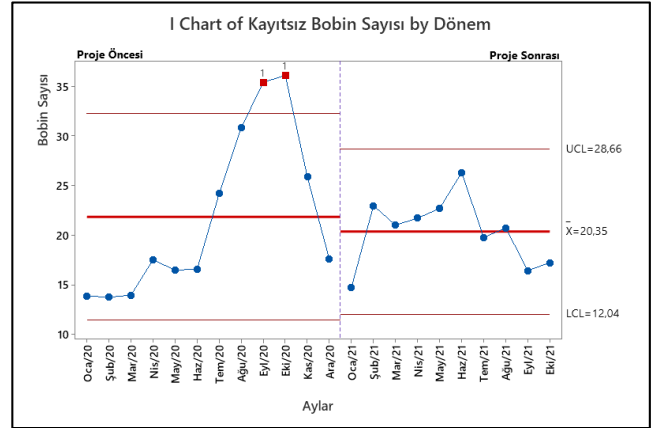


Figure 7. Individual Chart of Unaddressed Coils



Figure 8. General Field View After Project

4. Conclusion

In the study, which can be evaluated at the point of digitalization, it is aimed to prevent human-induced variables and errors. Additionally, the risks caused by irregular stacking have been eliminated. These risks are situations such as the falling of the coils, the coil slumping remaining on the lower floor. Effective use of field capacity was ensured.

IMPROVEMENT OF SCALE PRINT DEFECT IN CUT-TO-LENGTH PLANTS FOR S600 MC STEEL GRADE

Serdar GÜNBAY, Koray ARAY, Erhan SELVİ, Ahmet SAĞLAM

İskenderun Demir ve Çelik A.Ş.
Türkiye

Keywords: Scale Print, Powdering, Cooling Strategy, Hot Rolling Mill, Wustite, Manyetite, Scale

Abstract

In the production of high-strength S600 MC grade suitable for chassis production in the automotive sector at İsdemir facilities, the scale structure is a sensitive issue that needs to be managed in terms of surface quality. In chassis production, cut to length process from hot coil, mold forming, punching on sheet, and surface cleaning by sandblasting are performed respectively. When the scale formation of hot rolled coil has a thick and fragile formation, scale powdering is formed during uncoiling of the coils and it prints into the steel surface with the pressure of the straightening and leveller rollers, creating a defect. Although the chassis is not a visible part in the vehicle, the formation of submerged scale defects on the surface causes the requirement for additional sandblasting before painting. With an adhesive and thinner scale formation in hot rolled coil, it is possible to prevent scale printed defect in the cut-to-length systems.

In this study, the strengthening mechanism by affected rolling mill parameters and chemistry, scale formation, uncoiling and cut-to-length systems, and defect solving methods will be studied for the steel grade S600 MC. The ratios of Wustite(FeO), Magnetite(Fe₃O₄) and Hematite(Fe₂O₃) phases in scale formation vary according to hot rolling temperatures and run-out table cooling type. Scale thickness is the total thickness of all phases and it is preferred to have low thicknesses (7-8 microns). Wustite based scale formation which is more sticky and less fragile cause less powdering.

1. Introduction

Steel grade S600 MC is a steel grade with a minimum yield strength of 600 Mpa, and its primary use as hot rolled coil is crane booms, shipping container boxes and automotive structural parts. The metallurgical design that is successfully used by many to produce the HSM coil for 600 MPa

minimum yield strength is one that incorporates microstructure formation, grain size and precipitation strengthening. The desired microstructure is an acicular ferrite (low carbon bainite) with a small volume fraction of regular bainite and most likely some polygonal ferrite that is a very fine grain size packet. Cooling strategy is shown graph 1.

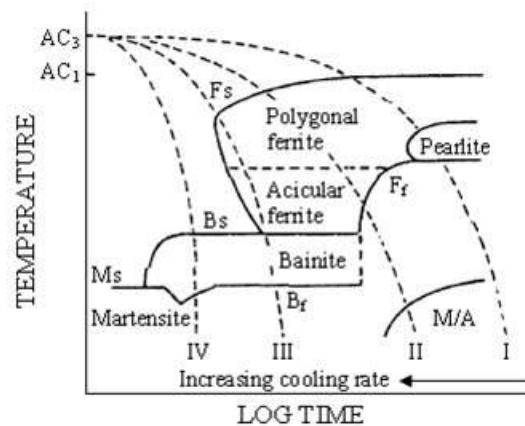


Figure 1 Number III cooling strategy is applied in order to reach polygonal ferrite, acicular ferrite and small volume fraction bainite

TiC precipitation strengthening mechanism that will form during final cool cooling. The desired precipitate is a fine, evenly dispersed TiC which means that we need the N₂, O₂ and S controlled to low levels to force the TiC formation.

In order to increase the efficiency of TiC precipitates together with the fine-grained microstructure, Finishing mill temperature (aim is < 860 °C), Coiling Temperature (aim is < 600 °C) and run out table cooling strategy (Late Soft cooling) parameters are applied. TiC precipitation mass fraction due to the temperature is shown Figure 2 [1]

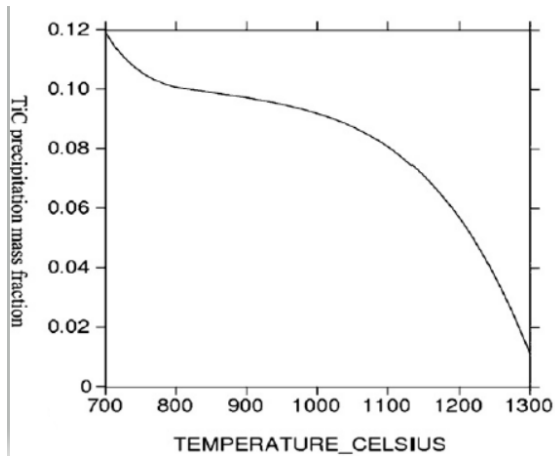


Figure 2 TiC Precipitation mass fraction increase below 800 C

By that metallurgical concept, scale powdering issue is observed on coils during unstraightening by rollers. The powdered scale immerse the steel surface by the pre-straightened rollers or leveller rollers. The resulting defect called as scale-print defect, shown Figure 3 and Figure 4.



Figure 3 Scale Powdering

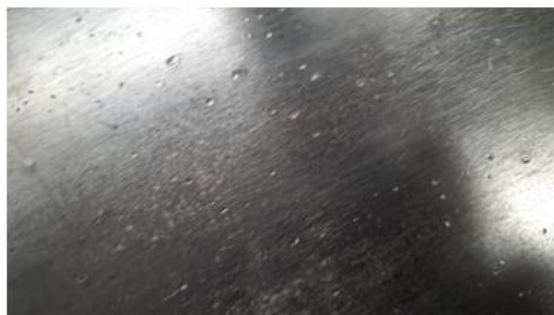


Figure 4 Scale Print Defect

In this study, it was aimed to reduce the total scale thickness and to reduce the amount of Wustite and hematite formation in order to reduce powdering. The results of the experiments with the run out table cooling strategy and the finishing mill entry strip thickness parameters will be examined.

2. Experimental Procedure

In İSDEMİR steel produced with BF-DES-BOF-LF and HSM route. Steel grade and its composition is given below table.

S600 MC	Min	Max
C		0,070
Mn	1,50	1,80
P		0,015
S		0,005
Si		0,100
Al	0,015	0,060
Cu		0,120
Cr		0,080
Ni		0,100
V		0,010
N(ppm)		70
B		0,001
Ti	0,100	0,120
Mo		0,020
Nb	0,070	0,080
Ca	0,0020	0,0060

Table 1 S600 MC ISD Steel Grade Chemical Analysis

HSM(Hot Strip Mill) has 2 walking beam type slab reheating furnaces, 1 four high roughing mill, 6 four high finishing mill stands, accelareted cooling unit and 2 coilers. Scale is removed by HSM(Hydraulic scale breaker), FSM(Finish Scale Braker) and Interstand Scale Braker equipments with a pressure of 220 bar. Layout of the equipments of HSM is shown Figure 5.

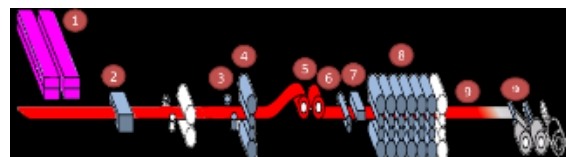


Figure 5 Flowchart: 1 – slab furnaces, 2 – hydraulic scale breaker, 3-edger, 4- roughing mill, 5 – coilbox, 6- rotary shear, 7- finish scale breaker, 8- finishing mill,9- cooling units, 10 – downcoilers

Coils belonging to the trial were recoiled and examined in İsdemir Recoil Line. There are pre-straightened rollers, leveller system to improve flatness and ACB system facilities in the Recoil line. There are no dust collector and any brushing systems in the line. The performance of the coils shipped to the customer after the production was followed on the customer lines. Scale powdering issue and scale print defect samples are shown Figure6 and Figure 7, after production on customers' cut to length line.



Figure 6 Scale Powdering Issue on Customers' cut to length line



Figure 7 Scale Print Defect On Customers' cut to length line

In this study, in order to reduce the scale structure and thickness, the finishing mill temperature and coiling temperature was kept constant in order to achieve strength, and experiments were carried out by changing the FM (finishing mill) entry thickness, FM entry temperature and run out table cooling strategy.

The FM temperature is aimed at 860 C to ease the rolling difficulty and to improve the wave defect, while the Coiling temperature is targeted as 590 C to provide polygonal ferrite and low amount of bainite together with fine microstructure.

The scale structure of the coils produced with the current practices declared above was examined on the samples taken from the recoil line. According to the results of the examination, it was seen that the scale thickness ranged from 12.54 micron to 14.97 micron in total, Fe₃O₄ (Magnetite) thickness was between 4.05-5.04 micron and FeO (Wustite) thickness was between 10-12 micron. Wustite/Magnetite ratio: 2,4-2.5. Shown Figure 8 and Figure 9.

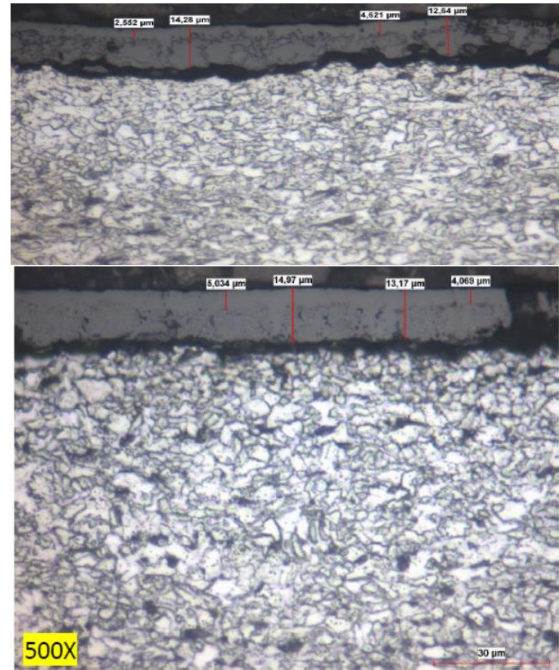


Figure 9 Wustite/Magnetite Thickness of Current Practice

The parameters included in the experiment are given in the table below. Dusting, scale amount (wüstite and magnetite amount) and scale printing defect on coils, cut-to-length lines were monitored.

Coil ID	Thickness	FM Entry Thickness	Finish Temp.(F)	Coiling Temp.	FM Entry Temp.	Cast Grade	Order Grade	Cooling Strategy
12252058200000	5,97	40,7	856	552	952	3,4960_51	1,4960_40	Late Cooling
12252058800000	5,97	40,7	857	570	959	3,4960_51	1,4960_40	Early Cooling
22252058900000	5,97	40,7	858	563	951	3,4960_51	1,4960_40	Early Cooling
22252058700000	5,97	40,7	857	577	958	3,4960_51	1,4960_40	Early Cooling
12252058400000	5,97	45,8	858	559	959	3,4960_51	1,4960_40	Late Cooling
12252058600000	5,97	45,8	857	572	964	3,4960_51	1,4960_40	Late Cooling
22252058500000	5,97	45,8	858	560	967	3,4960_51	1,4960_40	Early Cooling
22252058900000	5,97	45,8	858	581	963	3,4960_51	1,4960_40	Early Cooling

Table 2 Trial Parameters

Finish mill entry thickness is 45 mm, finish mill entry temperature is 963 C, cooling regime late cooling scale thickness has decreased to 7-10 microns. According to the results of the scale structure analysis, Magnetite was observed in the range of 3.26-4.64 microns, Wustite was observed in the range of 4-6.69 microns. Wustite/Magnetite ratio: 1.2-1.4. Figure 10

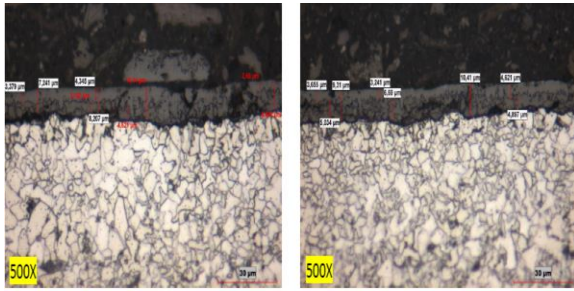


Figure 10 FM entry thickness 45mm, Late Cooling

Finish mill entry thickness is 45 mm, finish mill entry temperature is 967 C, cooling regime early cooling scale thickness has decreased to 8,48 microns. According to the results of the scale structure analysis, Magnetite was observed in the range of 3.37-4.0 microns and Wustite was observed in the range of 4-5 microns. Wustite/Magnetite ratio: 1.2-1.25. Figure 11

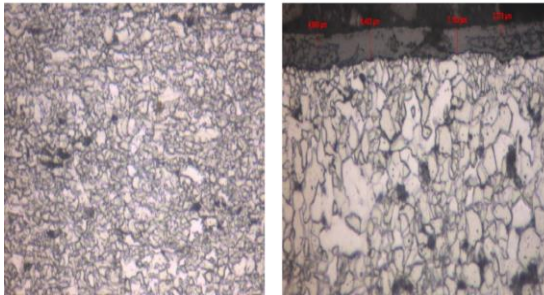


Figure 11 FM entry thickness 45mm, Early Cooling

Finish mill entry thickness is 40 mm, finish mill entry temperature is 967 C, cooling regime early cooling scale thickness has decreased to 8,48 microns. According to the results of the scale structure analysis, Magnetite was observed in the range of 3.37-4.0 microns and Wustite was observed in the range of 4-5 microns. Wustite/Magnetite ratio: 1.2-1.25. Figure 12

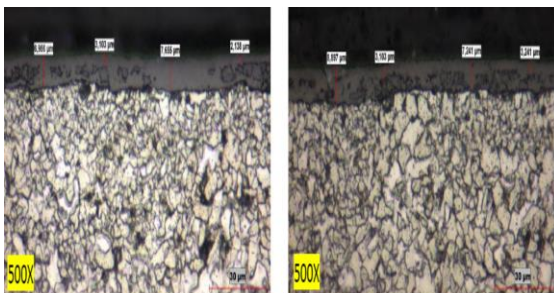


Figure 12 FM entry thickness 40mm, Early Cooling

Finish mill entry thickness is 40 mm, finish mill entry temperature is 952 C, cooling regime late cooling scale thickness was realized in the range

maximum 12-16 microns. Wustite and Hematite phases were not measured. Figure13

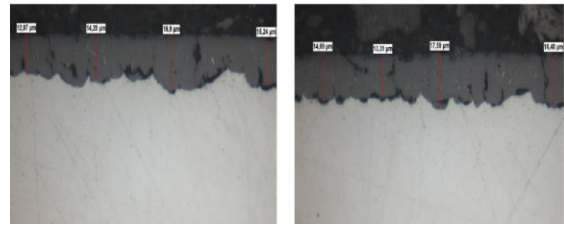


Figure 13 FM entry thickness 40mm, Late Cooling

The effect of Early Cooling (Figure14) and Late Cooling (Figure15) was investigated by scale powdering in the recoil line. When the surface is wiped with a cloth after stretching, powdering does not occur from the Early Cooling strategy, while powdering is observed when cooled with the Late cooling strategy. When dust collection and brushing are insufficient, the particles that are not removed from the material surface create submerged scale defects on the material surface by roller pressure.

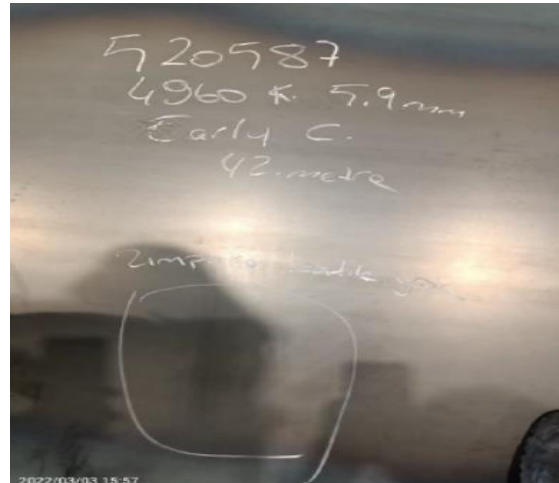


Figure 14 Early Cooling, Scale Powdering is not seen



Figure 9 Late Cooling, Scale Powdering is seen, when wipe with a cloth

3. Results and Discussion

It was determined that the scale thickness decreased by 35-40% in the early cooling strategy. In the Late Cooling strategy, the scale thickness is higher than Early Cooling Strategy(EC). As the fFM entry thickness increases, the FM entry temperature decreases. It is known that there is an increase in strength with high reduction ratio rolling made under TnR temperature. Although it is theoretically stated that the TiC precipitation hardening decreases in the Early Cooling Strategy, strength optimization was achieved by rolling under TNR.

The Early Cooling strategy was effective in reducing the scale thickness with the decrease of FM entry temperature. While the FM entry temperature was around 1000 C, it decreased to the range of 950-960 C at the trial.

In microscopic examination the scale thickness decreased from 13-16 microns to 7-10 microns. Wustite/Magnetite ratio decreased from 2.4 to 1.2 ratio.

It has been observed that the powdering problem is prevented or very little in the trial coils. It has been observed that there is no scale printing defect in the coils with low powdering issue.

The effectiveness of dust collector and brushing systems before straightening and leveler rollers on the cutting lines is an important parameter in improving the scale printing defect that occurs with powdering. The wetness of the produced coils causes the scale to agglomerate, which causes an increase in the defect rate.

4. Conclusion

In summary, since thinner and sticky scale type reduce the powdering, it is effective in improving the scale printing defect on the cut to length lines. Reducing the scale thickness can be achieved by increasing finishing entry thickness, reducing the finishing entry temperature and choosing the Early cooling strategy on the runout table. Especially successful results have been obtained for customers who demand high surface precision.

References

[1] Y. Han*, J. Shi, L. Xu, W.Q. Cao, H. Dong 2012 . Effect of hot rolling temperature on grain size and precipitation hardening in a Ti-microalloyed low-carbon martensitic steel

[2] Y. Han, J. Shi, L. Xu, W.Q. Cao, H. Dong. (2012). Effects of Ti addition and reheating quenching on grain refinement and mechanical properties in low carbon medium manganese martensitic steel

[3] David T. Blazevic 2005. Hot Strip Mill Operations Volume 5, Scale.

[4] Hikaru Okada, Deformation Behavior of Oxide Scale in Hot Strip Rolling

SINTER PLANT CIRCULAR COOLER MEDIUM VOLTAGE FAN MOTOR CONVERSION FROM DOL SYSTEM TO VFD SYSTEM

Cengiz ABUKAN, Fatih DÜZLÜ, Volkan KIZILAY

İskenderun Demir ve Çelik A.Ş.
Türkiye

Keywords: Sinter plant, circular cooler, medium voltage driver, energy saving

Abstract

Sintering of iron ore is the enlargement of powdered iron ores (0-10 mm.), which cannot be used directly in blast furnaces, by undergoing semi-reduction with the help of coke powder. The sinter at the temperature of 700-850 °C at the exit of the sinter machine must be cooled to temperatures of 100-120 °C in order to provide manipulation to the next process. For the cooling process, atmospheric air is applied to the hot sinter by means of fans. With the awareness of efficient use of resources, the continuity of energy saving and quality-oriented improvement studies in production lines is always one of the priority issues.

In this study; the conversion of the circular cooler cooling fan, which is one of the main components of the sinter plant, medium voltage DOL system to medium voltage VFD system, provided gains such as energy savings, process continuity and technology improvement.

1. Introduction

In the process of converting iron ore to pig iron, "Sintering" is required to make the ore suitable for processing in Blast Furnaces. The sintering process is the heat treatment of different types of ores with limestone and fuel to bring them to the physical and chemical properties required for the Blast Furnace. During this process, the blend to be sintered is laid on the sinter line by means of bunkers and heat treatment is applied by passing through the furnace. When the fuel in the blend is ignited by the furnace, the sintering process starts and the heat is transferred from top to bottom by suction from the bottom of the sinter line.

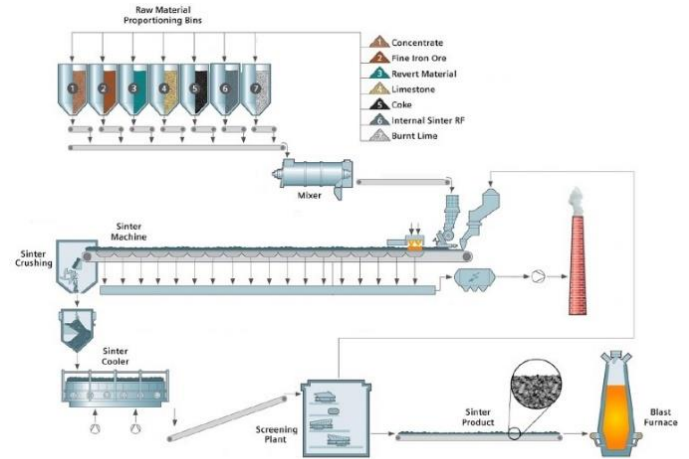


Figure 1. Sintering process

During the sintering process, dust and gases (CO₂, SO_x, NO_x...) go to the filtration units via wind boxes. The product formed as a result of the sintering process is crushed in the crusher so that it can be transported and cooled. The cooled sinter is screened in the desired size range according to the process needs of the blast furnaces and sent to the blast furnaces with the help of conveyor lines.

As per design the surface temperature of sinter shall be reduced down to 100 °C for easy handling by belt conveyor and downstream equipment. To achieve this performance a circular sinter cooler with effective cooling area is provided along with 5 Nos. of cooling blowers to supply sufficient cooling air to the cooler. Sinter coolers are based on the cross-flow cooling principle. The cooling air is pressed through the sinter bed perpendicular to the moving direction of the sinter bed. The particles at the bottom of the cooler are always exposed to the ambient cooling air, giving their heat to the cooling air. Thus, the particles in the top layers experience already warmed up air from the bottom layer. This results in an unequal effective cooling time over the height of the sinter bed, since the bottom layers are cooled faster than the top layers. Thus, the top layers of the sinter cooling bed experience a higher air temperature than the bottom layers. This effect is more pronounced in the first part of the cooler. Due to the cross-flow cooling principle the off-air of the cooler decreases with the length of the cooler. A part of the cooler is open and the cooling air goes to the ambient.

2. Experimental Procedure

Iron ore and coal are the main raw materials shipped to Isdemir plants by sea and rail. Shipped to the coke plant furnaces via conveyor belts, coal is converted into coke under high temperature and in an oxygen-free environment. This is the procedure of manufacturing coke, deemed necessary by blast furnaces. Production process commences, as the raw material is brought to the plants. Coal is shipped to the coke plants to be subjected to the coking process whereas fine ore is shipped to the sinter plant for the sintering process. Sinter is produced after fine ore, iron flue dust/fine and oxide are dimensioned to a correct size at the sinter plants so that they can be utilized by the high blast furnaces. Subsequently, they are transferred to the blast furnaces via the conveyor belt system. The blast furnaces produce liquid crude iron of which its production requires the use of iron ore, sinter, pellet and coke as the components. Liquid crude iron produced is kept in torpedoes after being cleared from slag. Liquid crude iron is transferred to the steel plant for the desulphurization treatment at the desulphurization plants. By making use of liquid crude iron, scrap and alloy elements varying in line with the desired quality, the carbon amount in the liquid crude iron is reduced by means of pure oxygen blowing method. Hence, liquid crude iron is converted into liquid steel. Liquid steel is then, interminably, casted into molds at the continuous casting plants. Subsequently, it is solidified at a desired size and converted into slabs or billets, which are semi-finished products. As for formed steel, the slabs are transferred to the hot rolling mills while the billets are transferred to the wired rod mill. The coils and sheets are flat steel products made from slabs, whereas, wired rods, a kind of long product, is derived from billets. The finished-products made at our plants are shipped to customers by road, rail or sea. (1)

The material coming out of the sintering machine is at high temperature. In order to manipulation of this material with conveyor belts, it must be cooled to a certain temperature. This cooling process is carried out in the circular cooler.

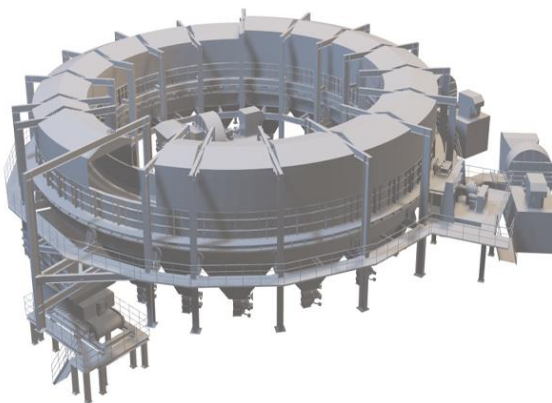


Figure 2. Circular cooler overview

There are five medium voltage squirrel-cage asynchronous motors in the circular cooler. These motors have direct start (DOL) in the existing system. In addition, there are dampers (electrical actuated) present for adjustment of each fan motor flow. In generally dampers are established for different usage purposes. Aim of dampers in the cooling

systems can be summarize as follows; cold air flow adjustment, current limitation of fan motors at startup, isolating the fan/motor from the system in fault/maintenance activities. Different cooling conditions may be required in the circular cooler due to atmospheric conditions, sinter process variables and etc. In the existing system, different cold air flow needs are met by changing the number of motors running or the damper opening ratios.

There are five pieces 710 KW, 750 rpm, 6300 KV asynchronous motors in the system and the fan motors are driven by direct starting (DOL). In this technology, it is necessary to prevent the motor from damaging the electrical network by drawing excessive currents during start-up. In order to prevent the motors damaging the electrical network by drawing excessive current at start-up, they are started while the dampers are closed. In this way, the motors are started without load and excessive current draw is prevented. In the current situation, since the motors are started with DOL, flow control cannot be done with the starter. Flow control in all motors in the system is provided by proportional actuated dampers. The total flow is adjusted in order to provide the required cooling regime in the system. In operational practices, it has been determined that the fans operate at approximately 50-70% dampers openings, depending on the process needs. Flow rate and efficiency calculation of the fans are determined by using the speed-flow rate curves of the fan. In order to determine the actual velocity-flow rate correlation, the electrical power consumed at various damper opening rates were measured under operating conditions to calculate the power consumed according to the damper opening ratios. The parameters were taken as follows in order to make the gain calculations;

- Annual working time: 8150 hours – working at a frequency corresponding to 80% damper opening,
- Annual downtime: 360 hours – 10hz frequency operation,
- Power and flow rates according to the damper opening rates determined by the measurements,

These data were used in affinity law formulas and theoretical payback periods were determined.

2.1. Field applications of conversion from DOL system to VFD system

Various MV drives have been thoroughly studied to ensure compatibility with our system. Electrical automation interface projects have been created in order for the driver to be supplied to work in harmony with the existing electrical and automation systems. After procuring suitable drivers, driver assemblies and MV/LV cables were assembled and terminated. PLC software has been completed so that the driver can be commissioned and remotely controlled by the operators. 6.3 breaker/relay settings have been made in the MCC. VFD application was applied for only one fan due to process conditions.

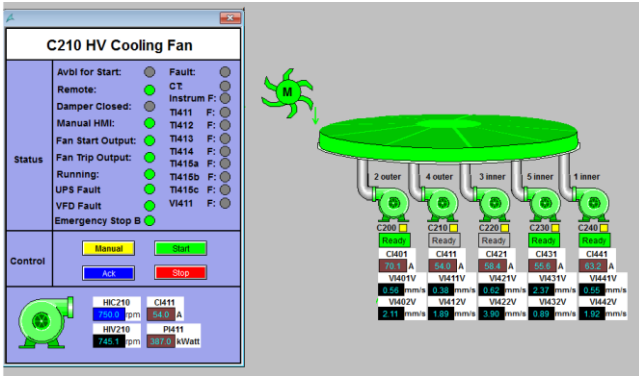


Figure 3. Scada page overview



Figure 4. VFD panel

3. Results and Discussion

The results were evaluated by taking into account the daily energy consumption reports. The energy consumption graph between the first month and the last month of the study is given below. As can be seen from the graph, energy consumption has decreased by approximately 30%.

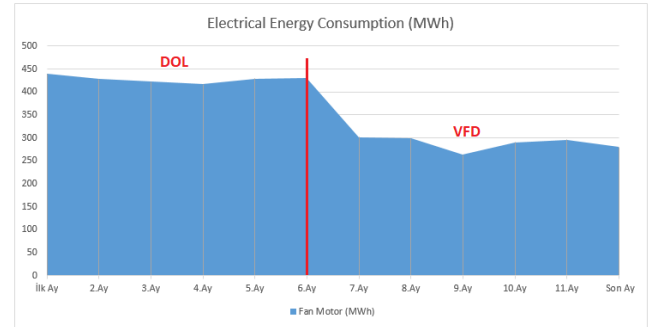


Figure 5. Electrical energy consumption

VFD application was applied for only one fan due to process conditions. Energy consumptions are determined for DOL and VFD operating states. In this direction; The annual average electrical energy saving is determined as 1,476 MWh.

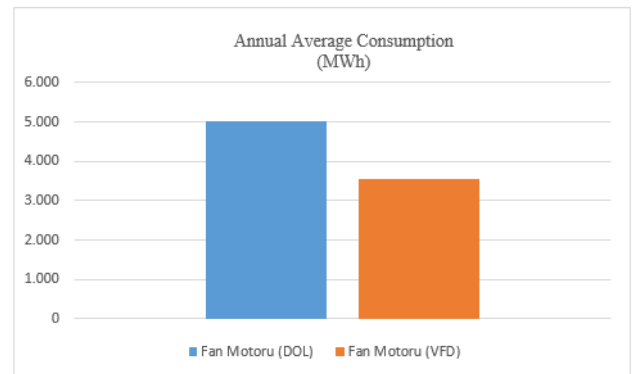


Figure 6. Annual consumption comparison

4. Conclusion

One of the most important issues of today is the efficient use of energy resources. At this point, energy saving provides a substantial benefit. The importance of reducing energy consumption as much as possible and applying it in the most economical way in industrial enterprises is increasing every year. Saving electrical energy, which is one of the important input parameters in iron and steel plants, makes it necessary to switch to alternative methods in various business practices.

In general, fan motors are selected at a power above the capacity, and a damper is used on the suction side of the fans in order to adjust the required air amount. In some cases, the flow requirements may change due to the process. In fan applications, the power is directly proportional to the cube of the flow rate or rotational speed (rpm or Hz). Energy savings can be achieved with variable speed drives. In this study, in which the operational application was made, the starting/driving systems of the fan motors were changed, resulting in savings of approximately 30% annually. Saving opportunities can be expanded by choosing similar methods



in different industrial applications.

References

- [1] <https://www.isdemir.com.tr/kurumsal/celigin-hikayesi/>

EFFECT OF DUNIT AND DOLOMITE AUXILIARY RAW MATERIALS ON SiO₂ OUTPUT IN PRODUCT SINTER AND COST ADVANTAGE IN THE SINTER PROCESS

Orkun HASDEMİR, Sadi BALABAN, Berkay DELAY, Burhan Erkan KESEMEN, Volkan KIZILAY

İskenderun Demir ve Çelik A.Ş.
Türkiye

Keywords: Sinter process, Dunite, Dolomite, SiO₂, Cost.

Abstract

Sintering of iron-containing ore is the agglomeration process of powdered iron ores (0-10 mm.), which can be used in blast furnaces, by reduction with the help of coke powder and/or anthracite. In the sinter process, sinter chemical analysis of the target product can be carried out by using auxiliary raw materials such as dunite, dolomite, olivine, limestone. Dosed dunite or dolomite is used as MgO input, and has an effect on SiO₂. The continuity of resources in quality and cost oriented improvement studies has always been one of the priority issues.

In this study; After the use of dolomite auxiliary raw material instead of dunite in the sinter process, the SiO₂ value in the sinter chemical analysis of the target product was improved and a cost advantage was achieved. In addition, due to the low CaO input due to the sinter alkalinity in the Blast Furnace process, the volume of the furnace slag decreased.

Summary

Sintering is an agglomeration (size enlargement) process, and it is the enlargement of the size of powdered iron ores (0-10 mm.), which cannot be used directly in blast furnaces, by undergoing partial melting (semi-reduction) with the help of coke powder. Optimization of auxiliary raw materials in the sinter plant has been one of the priority issues in terms of efficient operation of the plant. With the awareness of efficient use of resources, the continuity of quality-oriented improvement works is always one of the priority issues.

1. Introduction

In the process of converting iron ore to pig iron, "Sintering" is necessary to make the ore suitable for

processing in Blast Furnaces. Sinter process; by heat treatment of different types of ores with limestone and

fuel to gain the necessary physical and chemical properties for the furnace. During this process, the mixture to be sintered is laid on the sinter line by means of bunkers and heat treatment is applied by passing through the furnace. When the fuel in the blend is ignited by the furnace, the sintering process begins, and the heat is absorbed from the bottom of the sinter line and transferred from top to bottom. During the sintering process, dust and gases go to the filtration units via wind boxes.

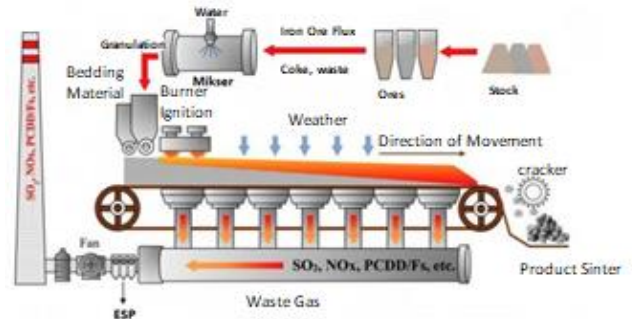


Figure 1. Schematic diagram of the iron ore sintering process. (1)

The purpose of sintering is to ensure that iron powders that cannot be used directly, as well as waste ferrous materials such as scale and flue dust, can be used while producing liquid raw iron in blast furnaces by giving them good properties. Dolomite consists of calcium magnesium carbonate, while dunite consists of magnesium silicate.

Dolomite gives basicity to sinter. It is added in order to provide acid-base balance in the sinter blend consisting of 0-30 mm in size. Also MgO-Al₂O₃ balance shall be provided. If ore with a high clay content is used, the

amount of dolomite must be calculated and added to achieve balance.

MgO/Al₂O₃ must be equal to 1 (MgO/Al₂O₃=1). The use of dolomite to compensate for the missing amount of MgO tolerates the high clay content in the ore.

Dunite is characterized by being a very homogeneous and tough auxiliary raw material used in the sinter plant. Dunite consist of 95-99% olivine and the remaining 1-5% pyroxene, serpentine, chlorite and spinel. Dunite has high heat and cold resistance to mechanical stresses such as fracture, crushing and abrasion. Dunite has a large porosity reaching 20% below 800°C, This situation provides great level of reactivity and absorption. In addition, dunite has stable components with low melting points.

2. Experimental Studies

Main raw materials such as iron ore and coal are transported by sea way and rail way at İsdemir Co. which is an integrated iron and steel plant. The production process begins when the raw material is brought to the facilities. Coal is transported by the use of conveyor belts to coke factories for the coking process; The fine ore is transported to the sinter factory for sintering so that it can be used in the blast furnaces. The coal, which is transported to the coke plant silo by the conveyor belt system, is charged to the furnaces and converted into coke at high temperature and in an oxygen-free environment, thus producing the coke needed by the blast furnaces. Iron ore fines, ferrous flue dusts and scale are brought to the size that blast furnaces can be used in the sinter factory, and sinter is produced and sent to the blast furnaces with the conveyor belt system. Blast furnaces produce liquid raw iron. For the production of liquid raw iron, iron ore, sinter, pellets and coke are used as inputs. The liquid produced is purified from the slag and taken to the torpedoes. The liquid raw iron in the torpedoes is desulfurized in the desulfurization plant and then transferred to the Steelworks to enter production. Steelworks ; By using liquid raw iron, scrap and various alloying elements that differ according to the desired quality and by pure oxygen blowing the carbon ratio in the liquid raw iron is reduced, thus liquid raw iron is converted into liquid steel. The liquid steel produced is poured into the molds continuously in the continuous casting facilities, solidified in the desired dimensions and turned into slabs or billets, which are semi-products. The shaped steel and slab is delivered to the hot rolling mills. Coil and sheet, which are flat hot products, are produced from slab, and wire rods, which are long products, are produced from billets. The products which are produced in the facilities reach the customers by ship, rail way and road. (2)

In Iskenderun Demir Çelik Co., Sinter and Raw Material Manipulation unit, industrial studies were carried out in order to examine the cost advantage of dunite and dolomite

auxiliary raw materials in the product sinter in the sinter process and their effect on SiO₂ output.

Before the plant trials, sinter pot tests were carried out. A total of 4 SPG trials were conducted, two with low ignition time (75 sec) and two high ignition time (100 sec). In order to examine the effect of dunite and dolomite auxiliary raw materials on SiO₂ output in the product sinter and the cost advantage, the results of sinter pot tests using dunite instead of dolomite were examined.

Sinter pot test result;

- Blend bulk density has been increased,
- The ratio of sintered FeO has been increased,
- Bed length flame velocity and accordingly increase in efficiency,
- It was determined that efficiency and drum index decreased at low ignition times, but there were no significant differences in these values at high ignition times.

In industrial plant trials, dunite and dolomite were dosed to the sintered blend as -6 mm and 1.6% of the sintered blend.

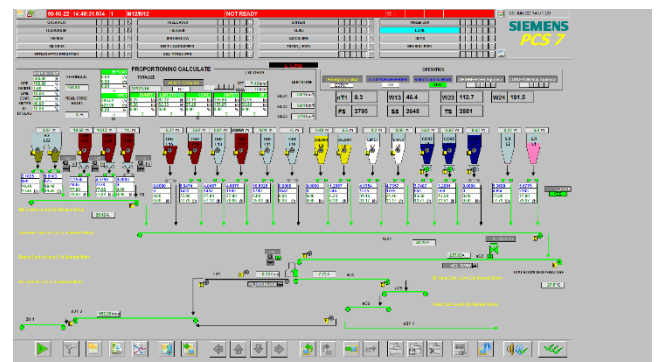


Figure 2. Dunite and Dolomite Dosing.

In order to evaluate the process output parameters of dunite and dolomite usages as auxiliary raw materials in the sinter blend, the SiO₂ output in the product sinter and the cost advantage in the sinter process were studied and recorded for about 1 month.

2.1. Plant use of dunite and dolomite as auxiliary raw materials

The work carried out in the sinter plant was examined by taking into account the sintering blend data used in the enterprise.

- Total Sinter Fines Ratio

- Internal Sinter Fines Ratio
- Blast Furnace Sinter Fines Ratio
- Coke Breeze Ratio
- FeO
- Al₂O₃
- SiO₂
- CaO
- Basicity
- Machine Speed
- Machine Efficiency
- Trommel
- Blast Furnace -5 mm Fines Ratio
- Blast Furnace Sinter Usage Rate

All these parameters were studied and evaluated.

3. Results and Discussion

Using dolomite as an auxiliary raw material instead of dunitite in the sinter process reduces the consumption of 0.15% SiO₂ and 15 kg/tss limestone. The advantage of the decrease in 0,15% of SiO₂ allowed to increase the consumption of waste material and increased the use of lower cost high SiO₂ iron ores in the sintering blends and all of these were reflected as a cost advantage. When the analysis of sintered ores are examined on a yearly basis, an average of 0.19% SiO₂ increase is observed in the purchased ores used in the sinter blend. The negative effect of this increase is offset by the use of Dolomite instead of Dunite in the Sintering Process. If in this period dunitite was going to be used instead of dolomite, then it was expected that at the same sinter rate the slag rate was going to rise by 6 kg/thm, which would also lead to a rise in the total fuel rate at the Blast Furnace.

4. Results

One of the most important issues of today is the efficient use of resources. At this point, saving on input costs provides a substantial benefit. The importance of the correct application of the optimization of the inputs in industrial enterprises is increasing every year. The use of equivalent auxiliary raw materials, which is one of the important input parameters in the iron and steel factories, necessitates the transition to alternative methods in various business applications. The management of costs in a way that does not create weakness in the processes, does bring profit has always been one of the most important issues of the enterprises. Saving opportunities and alternatives can be expanded by choosing similar methods in different industrial applications.

Reference

- [1] Y. Wang , L. Qian , Z.Yu, T. Chun, H. Long, X. Wu, J. Li Inhibition Behavior of PCDD/Fs Congeners by Addition of N-containing Compound in the Iron Ore Sintering, Wang et al., Aerosol and Air Quality Research, 20: 2568–2579, 2020.
- [2] <https://www.isdemir.com.tr/kurumsal/celigin-hikayesi/>



MAPPING SLAB DEFECTS, CONCEPTUALIZING DIGITAL TWINS

**Fatih Mehmet AYDIN, Serdar GÜNBAŞ, Hikmet ŞAHİN, Serkan DURSUN,
İlker AYÇİÇEK**

İskenderun Demir ve Çelik A.Ş.
Türkiye

Key Words: Continuous Caster, Slab Process Defects, Longitudinal Surface Cracks, Digital Transformation, Digital Twins.

Abstract

Process Defects that occur during casting, remain one of the most challenging obstacles in Slab Casting Plant, in terms of Quality and Casting Continuity. Slabs with process defects, in case of later detection and on their defect levels, are mostly re-processed by time-consuming and high-cost treatments, or even being sent to scrap in some cases, which causes much greater financial losses. Non-detected defects cause delay and breakdowns in subsequent plants with much greater and critical financial losses. Therefore, pre-detecting those defects via process parameters, predicting them via artificial intelligent systems, and detecting them with cutting-edge technologies, is one of the main focuses of Continuous Casting Technologies, in recent. Since, it is a known phenomenon that there is an important correlation between process defects and process parameters, observing, virtualizing, simulating them against each other, and eventually developing predictive models based on those studies, can give a better chance to foresee and prevent them before occurring. By Mapping Slab Defects, Digital Twin for Slab Casting process is being conceptualized, in İskenderun Iron and Steel Co. (İSDEMİR). By this application, slab process defects and crack warnings/detections, are digitally mapped against instantly stored process parameters, as regards selected *Plant, Sequence, Tundish, Heat, or Slab*.

1. Introduction

The Digital Twins concept was first coined at the University of Michigan in 2003. Defined by one of its contributors, Grieves[2014], as a virtual space representation of physically produced objects in physical space. Digital Twin pairs, as the name suggests, members from each space should resemble each other as far as possible. Such resemblance and linkage between two spaces can be provided with data and information. All physical measurements of physical objects in real space, from automation instruments are a matter of this goal. By related data, we can understand how each physical member of each twin was produced, which process events or

anomalies occurred during production, and how they did affect produced object quality[1].

Since, we know the metallurgical process(es), contains many interrelated complex processes [2], every new concept and technological development can give huge contributions to analyzing and understanding every single step of this process. Digital Twins is one of those newly introduced concepts that can be used for gaining a better understanding of the steelmaking process.

This paper aims to give an overview of ongoing Digital Twins work, in İSDEMİR, Continuous Slab Casting Machines.

2. Data Preparation: Production Process from an Object-Oriented Perspective

2.1. Collecting and Calculating Required Data

The continuous Slab Casting Process has many parameters that not only affect directly produced slab quality but also can cause directly or indirectly occurring slab defects. But, based on experiences, it is known that some of those parameters have a far stronger effect on quality defects and process anomalies. Some of such parameters; *Mold/spray water temperatures, liquidus/tundish steel temperatures, mold level standard deviations, casting speed variation, and tundish nozzle depth in steel* are provided for every processed slab. Mentioned parameters either were calculated on the Level 1 side as required and retrieved from there by Level 2 directly, or calculated by Level 2 based on data retrieved from Level 1. In either case, ultimately yielded data are recorded to the database table in a required frequency.

2.2. Creating Real-Time Process Anomalies Automatically Based On Data

With a strong collaboration of Level 2 Automation and Quality members, process anomalies and deviations are defined for each selected observing

data. Based on these rules and limits slabs are tagged in the Level 2 System with a priority level.

First of Sequence Slab: Each first slab of a new starting sequence is tagged as the first slab of the sequence

Last of Sequence Slab: Each last slab of the ending sequence is tagged as the last slab of the sequence

Grade Code Changing Slab: in case of the grade change during a sequence, mixed slabs with transition zone are marked as the rule suggests.

Low Cast Speed Slab: if the minimum cast speed of the slab, is lower than the defined ranges of speed, the slab is tagged as a low cast speed slab. With multi-range definitions, low cast speed is set with varying priorities. Low cast speed anomaly is also marked by its start and end points.

High Cast Speed Slab: Maximum cast speed of the slab is selected and if the selected maximum is higher than the defined range slab is tagged as a low cast speed slab. High cast speed is marked by its start-end points.

Cast Speed Changed Slab: Maximum and minimum cast speed difference is calculated and if the absolute difference is higher than the defined range, Slab is tagged as cast changed speed slab.

Width Changed Slab: Maximum and minimum slab widths are selected from stored values and if there is a higher absolute difference than the defined limit, the slab is tagged as width changed slab.

High Tundish Temperature Slab: Any given slab is marked as a high-temperature slab if only the maximum deviation from liquidus temperature is higher than defined limits.

Mold Level Standard Deviation Slab: Mold level standard deviations are calculated based on stored values and fall between head and tail cast lengths of the slab. If the deviation is higher than the defined range, the slab is tagged as the rule suggests.

Mold Water Temperature Low Slab: Mold water temperatures are selected within the range of head and tail cast length for each slab. If the lowest selected temperature is lower than the defined range slab is tagged as this rule suggests.

Mold Water Temperature High Slab: Mold water temperatures are selected within the range of head and tail cast length for each slab. If the highest selected temperature is higher than the defined range slab is tagged as this rule suggests.

Spray Water Temperature Low Slab: Spray water temperatures are selected within the range of head and tail cast length for each slab. If the lowest selected temperature is lower than the defined range slab is tagged as this rule suggests.

Spray Water Temperature High Slab: Spray water temperatures are selected within the range of head and tail cast length for each slab. If the highest selected temperature is higher than the defined range slab is tagged as this rule suggests.

Tundish Changed Slab: If tundish changing occurs during casting, regarded slab based on selection rule is tagged as tundish changed slab.

Tundish Changed-Short Slab: If tundish changing occurs during casting, regarded slab based on selection rule is tagged as tundish changed-short slab.

2.3. Manually Created Process Anomalies and Events

Level 2 Quality Observers can manually create process events and process anomalies during and after casting for necessary slabs, in case of any occurrence. Manual process anomalies and events are assigned to slabs, and they can be defined by exact location, i.e start, and end points if it is possible. Manual process events and anomalies, such as nozzle change, nozzle punched, slag taken from mold, etc., are also shown on regarded slabs with their start and end locations.

2.4. Slab Defect Warnings from Image Processing AI Model via YOLO Darknet

Since 2019, by installing a camera on each strand of both slab machines, ISDEMIR is doing a successful R&D to detect longitudinal cracks (LC) in slabs. For each slab, based on its length, and viewing area of the regarded camera, several images are saved to a predefined location. Pre-trained YOLO Darknet AI model immediately process stored images and stores processed images with required data, in case of any crack detection.

Crack warning images, with a confidence value of detection and detection rectangle(s), are shown to operators and quality observers immediately. On the other hand, defect warnings are stored with calculated location on the slab and with their further dimensions. These stored crack warning occurrences also are shown to users in the process map user interface.



Figure 1: Process Map Treview

2.5. Mapping Process Events, Anomalies and Defect Warnings with Respect To Cast Length

All mentioned process anomalies and deviations, and longitudinal crack warnings are shown all along cast length, per user selection.

In the user interface, Casting Process is shown as a treeview of the machine, sequence, tundish, heat, and, slab, as shown in Figure 1. Users can select one of the objects to view all related information on the process map, as shown in Figure 2.

The continuous casting process, all along its selected object length, is digitally twined in an object-oriented perspective and shown to the user. All

objects (anomalies and defect warnings) are shown as colored objects with varying intensities of color. Defect warnings with higher confidence levels are shown with high brown intensity, and process anomalies with higher priority are shown with higher red intensity.

Users can navigate between all sub-objects, including warnings and anomalies, easily via navigation buttons and observe related process parameters.

3. Results and Discussions

By developing a new user interface on WPF by Isdemir Level 2 team, users can observe the continuous casting process based on the framework defined by Quality Department. The continuous casting process is comprehended from the object-oriented perspective and interpreted as digital twins in the user interface.

With a user-friendly interface, all related parameters along the casting process are shown continuously. Width changes, grade changes, mold powder changes, and all other selected user parameters are mapped on the digital twin interface.

4. Conclusion

As one of the major contributors to the Digital Twins notion, Grieves [2014] suggests, that merging virtual products with real products via data and information can give an insight *perspective* about understanding the production process. Through this ongoing work in Isdemir Co., a virtual space for Digital Twins of the physical manufacturing process is still being developed and improved.

References

- [1] M. Grieves, Digital Twin: Manufacturing Excellence through Virtual Factory Replication, 2014, pp. 1-7.
- [2] A. P. V. S. P. & T. D. Galkin, «Integrated Simulation of Process of Steel Casting on the Continuous Steel Casting Unit,» 2020 2nd International Conference on Control Systems, Mathematical Modeling, Automation and Energy Efficiency (SUMMA), 2020.



Figure 2: Digital Twin Of Slabs

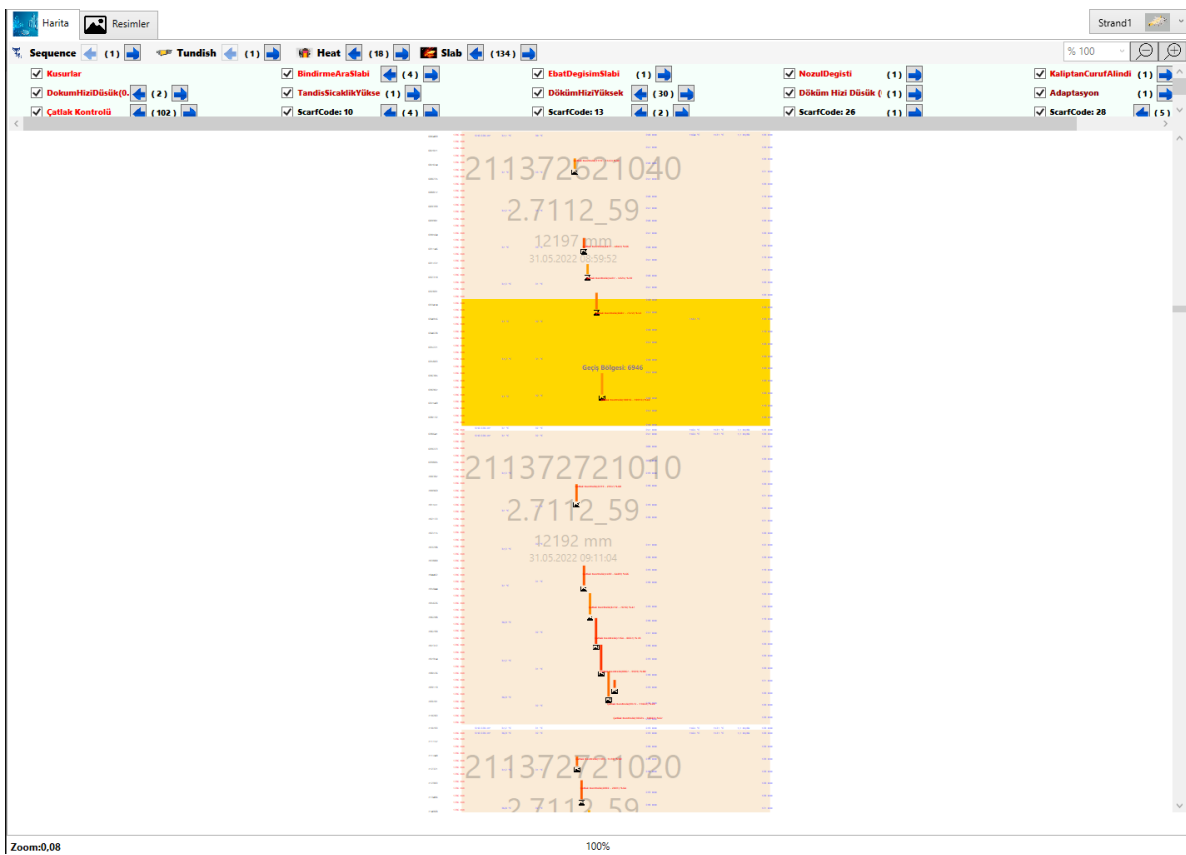


Figure 3: Zooming into Process



ADVANTAGE AT LADLE FURNACE PROCESSING TIME BY DEVELOPING A MODEL THAT CALCULATES LIQUID STEEL %Al VALUE CLOSER TO THE SPECTRAL SAMPLE RESULT

Mustafa SAĞLAM¹, Memduh Kağan KELER², Esra KÜPELİ¹, Eyüp Veysel ÖZDEMİR¹, Alperen TERZİ¹, Hikmet ŞAHİN¹, Mehmet Mustafa YILDIRIM¹, Tayfun KOCABAŞ³, Abdurrahman Mesud ÇAKIR¹, Burcu SOYSAL ATAN¹, Deniz YAZICI¹

¹İskenderun Demir ve Çelik A.Ş., ²Ereğli Demir ve Çelik, ³Oyak Maden Metalurji Türkiye

Key Words: Ladle Furnace, Deoxidation, Oxygen Probe, Basic Linear Regression Analysis, Digitalization, Minitab, Level2

Abstract

For the plants producing from ore, the steel production process starts with the charging of scrap metal to the BOF, adding hot metal onto it, and then ending with blowing oxygen at high flow rate for 13-15 minutes by means of an overhead lance. After this stage, the liquid steel in the converter is poured into the steel ladle, which is lined with refractory bricks. As a result of exothermic reactions in BOF, the ratio of elements that can react with oxygen in liquid steel decreases. Due to the nature of the process, some of the oxygen remains free in the liquid steel. In order to provide the chemical content of the casting in the production line, to avoid castability problems, to achieve the hot workability of the product and the targeted mechanical properties, the oxygen in the liquid steel must be removed. To reduce the oxygen solubility, alloy materials containing elements such as Al, Si, Mn, which have higher oxygen affinity than Fe, are used. The deoxidizers used for this purpose are ferromanganese, ferrosilic, ferrosilicomanganese and aluminum. After the oxygen blowing process in the converter is completed, aluminum is used for slab grades for the deoxidation of the dissolved oxygen remaining in the steel and for alloying at the tapping stage. Subsequently, final deoxidation and final

alloying with wire Al is carried out in ladle furnaces. After pre-oxidation in the steel tapping step, the final deoxidation and alloying is done in the ladle furnace.

It is important for the secondary metallurgy process that the percentage of aluminum in the liquid steel can be seen accurately and in a short time in ladle furnaces. The usage of aluminum above ideal conditions in liquid steel has a negative effect on steel cleanliness due to the increase in inclusions. In cases where there is not enough time to wait for the laboratory analysis result and/or this waiting period is not suitable in terms of steel cleanliness and castability, the need for quality change or the risk of loss of speed in casting machines may occur. In the study, a model estimating the %Al value of liquid steel was obtained with the simple linear regression analysis method and thermodynamic simulation programs. The model was adapted into the Level-2 application and presented to the use of operators. When needed, measurement was taken with an oxygen probe and 5 minutes of gain was achieved in the process time according to the current situation.

1.Introduction

In the production of liquid steel in ladle furnaces, the aluminum content of the liquid steel can be measured by two

different methods. In the first method, using the oxygen probe, the oxygen, temperature and $-mV$ values in the liquid steel are measured and the %Al value is calculated with the mathematical model. In the second method; after the steel filled into the mold with the sample probe freezes, the steel sample is sent to the spectral analysis laboratory to measure on solid steel.

In the measurements made with the oxygen probe, the oxygen probe; completed by attaching the sensor to a cardboard tube. The probe is mounted on a lance that is electrically connected to a signal processing unit. Cell potential and thermoelectric voltage signals are obtained simultaneously from the probe. When these signals reach stability, they transfer and record the dissolved oxygen content of the temperature and the steel bath and the aluminum values calculated according to this value to the monitor.

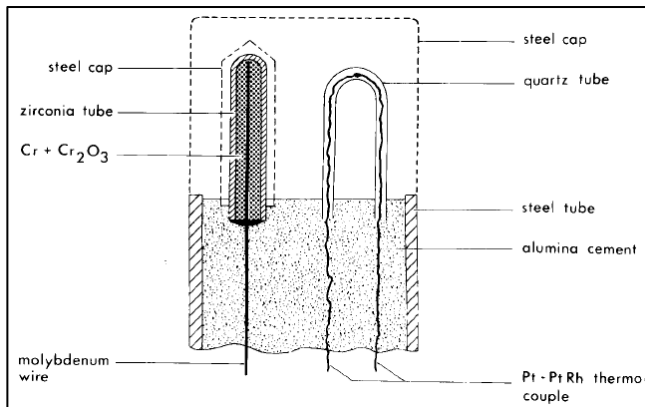


Figure 1. Schematic View of Oxygen Probe

2. Experimental Procedure

Within the scope of the project, the factors affecting the aluminum ratio in the liquid steel during the measurement by using an oxygen probe were determined. Measurement rules were determined in order to create a data set for the determined factors. The factors to be included in the data set were determined as follows: mV value, oxygen value, temperature, spectral analysis result. The rules to be considered while preparing the data set are listed as follows:

- The mixing flow rate from the bottom of the ladle will be reduced to the float level and the measurement will be taken after waiting for 1 minute.
- The steel sample will be taken immediately after the measurement with the oxygen cartridge and the %Al value found as a result of the spectral analysis will also be recorded.
- The $-mv$ graphs of the measurements will be

photographed and recorded and the measurements that do not form the appropriate curve will be removed from the data set.

- Afterwards, a comparison will be made with the spectral %Al value and the values calculated by the current company model.

In accordance with the determined rules, 84 trial heats were made, measurements were taken and the data set was prepared. Correlation analysis was performed to determine whether there is a strong linear relationship between the input factors over the prepared data set. Although the factors affecting the aluminum value are the mV value and the temperature, the effect was not evident since the temperature values did not change much in the 84 heats examined. By using the regression analysis method, the statistical model that best explains the spectral analysis aluminum value was obtained.

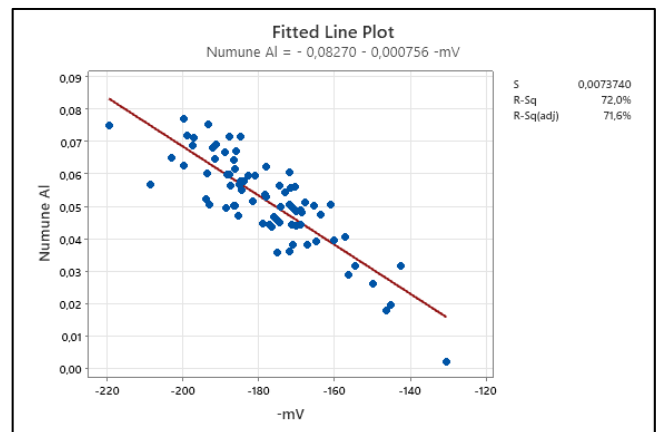


Figure 2. Liquid Steel %Al Statistical Model-Fitted Line Plot

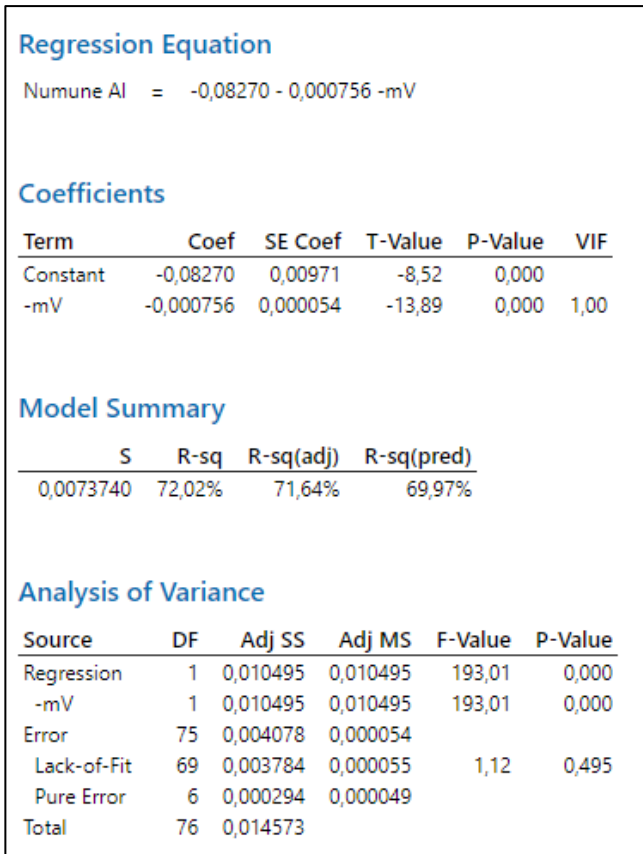


Figure 3. Liquid Steel %Al Statistical Model

In addition, with the literature study, how the oxygen activity in aluminum and liquid steel changes was investigated. A metallurgical model was created for the quality determined by FactSage thermodynamic software.

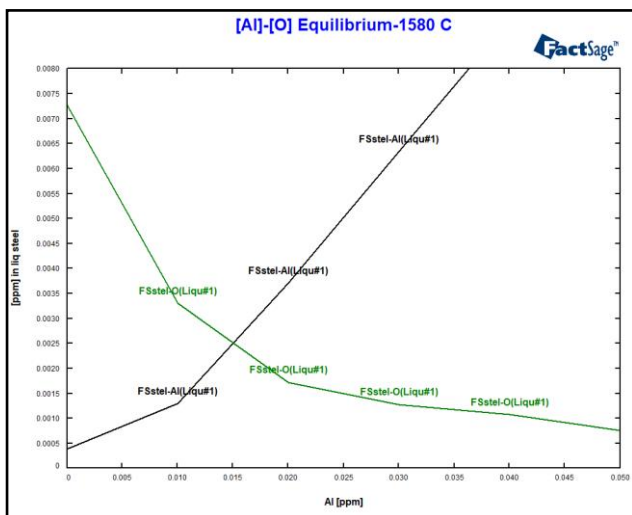


Figure 4. FactSage 7.3 Thermodynamic Model

In order to standardize the study, software integration work was carried out on Level-2 according to the created model.. An application has been developed that allows the estimation

of %Al over -mV measured after the oxygen probe is immersed, to be displayed on the Level-2 operator screen.

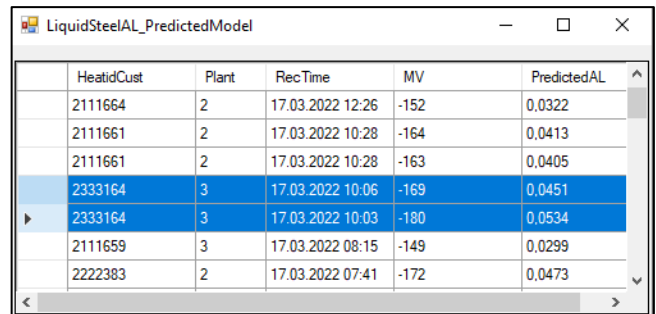


Figure 5. Level-2 - Liquid Steel %Al Statistical Model

3. Conclusion

In order to verify the regression model obtained, the trials were carried out considering the Level-2 application that was put into use.

A hypothesis test was performed to determine whether there was a statistical difference between the aluminum value predicted by the model and the spectral analysis laboratory measurement in the trial castings.

It has been observed that there is an acceptable level of difference between the laboratory analysis result and the model prediction in the castings carried out for the verification of the model.

With the study; in the ladle metallurgy process where the production rate is high, gains such as obtaining a decision support mechanism, reducing the speed losses of the casting machine, and contributing to the steel cleaning have also been achieved.

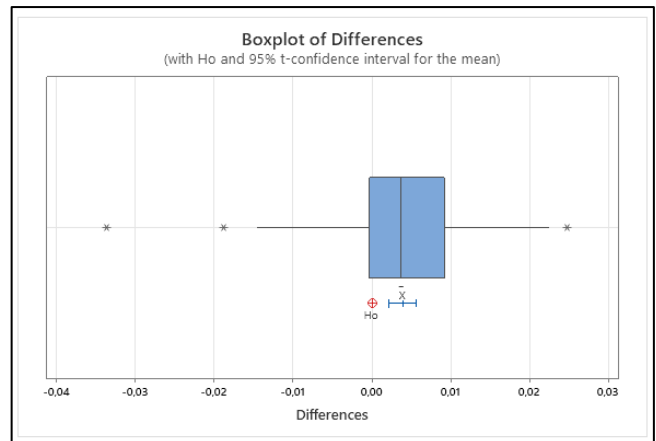


Figure 6. Boxplot of Differences-1 sample t-test

Descriptive Statistics				
Sample	N	Mean	StDev	SE Mean
Model AI Hesaplaması	101	0,04803	0,01151	0,00115
Numune AI	101	0,04413	0,01315	0,00131

Estimation for Paired Difference				
Mean	StDev	SE Mean	95% CI for $\mu_{\text{difference}}$	
0,003899	0,008584	0,000854	(0,002205; 0,005594)	

$\mu_{\text{difference}}$: population mean of (Model AI Hesaplaması - Numune AI)

Test	
Null hypothesis	$H_0: \mu_{\text{difference}} = 0$
Alternative hypothesis	$H_1: \mu_{\text{difference}} \neq 0$
T-Value	P-Value
4,57	0,000

Figure 7. Result of 1 sample t-test

WIRE ROD SURFACE EXAMINATION BY NON-DESTRUCTIVE LIQUID PENETRANT TESTING METHOD

Cemre KEÇECİ, Erdem TAN, Mustafa ÖZDEMİR

Iskenderun Iron and Steel Co.
Türkiye

Key Words: Wire rod defect examination, liquid penetrant testing, non-destructive testing, wire rod surface cracks.

Abstract

Although many data-based analyzes and models have been made to prevent the formation of defects with process control techniques in steel production processes, it has not been clearly provided to completely eliminate the formation of defects in the products produced. Despite controlled process, there are still defects that may occur due to systems and equipment or raw materials. Therefore, in addition to process control, it is necessary to physically control the manufactured product. Destructive testing methods are generally used at this stage, and particularly wire-shaped samples are cut for examination using hot or cold acid or a microscope. These examinations can cause additional time and wire rod mill process line downtime. In this study, liquid penetrant testing method has been included as an alternative to the eddy current method, which is frequently used in wire-rod production, and experiments have been performed considering that the method can enable the detection of wire rod surface cracks.

1. Introduction

Non-destructive inspection is the process of testing and measuring without damaging the material. Non-destructive inspection is used to determine the integrity of machinery and similar parts/components, or to measure the quantitative values of some properties of the objects.

Penetrant inspection is a method used to detect surface discontinuities such as cracks and pores applied to ferrous and non-ferrous materials. Penetrant testing (PT) is not applicable on high porous materials. In this method, the liquid that has high surface wetting property called penetrant is applied to the material that has suspected surface cracks or pores. The rest of excess liquid penetrant is carefully removed from the surface. After removing, the penetrant liquid which has penetrated the cracks is drawn to the surface by applying developer and thus surface cracks can be detected. The expected property in this testing is the surface-open defects or cracks for dye penetration into cracks. The

other expected property is that the temperature of the test piece should be between 5°C and 50°C.

The penetrant inspection process proceeds in several steps on the material to be examined.

1. First, the surface is cleaned for examination. In order not to prevent penetration of liquid penetrant into the material surface, the surface should be free of scale, rust, oil and dirt.
2. Penetrant spray is applied to cover the entire surface to be examined. It is waited between 5 and 60 minutes.
3. The control surface is cleaned again with a cleaning spray.
4. The developer spray is sprayed on the inspection surface.
5. The surface is examined under 500 lux light intensity and the surface is cleaned after the inspection.



Figure 1. Liquid penetrant application

2. Experimental Procedure

Penetrant test was applied to 400 mm long samples taken from 13 mm diameter wire rods rolled from 130x130 mm square billets. High carbon steels such as SAE 1080 were used in the examinations.

Before the examination, the samples were examined under the macro microscope and optical microscope and matched

according to the crack sizes. After sanding and polishing, the samples were etched with 2% nital solvent and examined under a optical microscope.

Order	Crack Size Range	Sample No	Measured Crack Size (micron)
1	Below 20 microns	19192	18,32
2	20-40 micron	19185	25,23
3	40- 60 micron	18847	47,35
4	60 – 80 micron	18436	70,85
5	80 – 100 micron	18888	88,48
6	100 – 120 micron	19190	114,40
7	120 – 140 micron	19169	134,40
8	140 – 160 micron	19249	153,10
9	160 – 180 micron	19184	171,80
10	180 – 200 micron	19188	188,00
11	200 – 220 micron	19187	209,80
12	220 – 240 micron	19189	230,50
13	240 – 260 micron	19245	248,50
14	260 – 280 micron	18922	265,80
15	Above 280 micron	19183	500,80

Table 1. Measured crack sizes of the samples

Liquid penetrant inspection was performed on 15 wire rod samples, which were detected between 20 microns and 500 microns under the optical microscope in the metallography laboratory, and the visibility of the defects was examined.

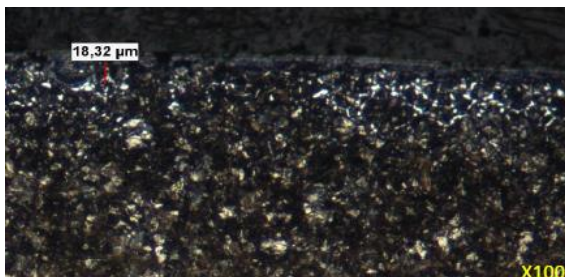


Figure 2. Micro image of 18 micron crack at x100 magnification

After the wire rod sample was kept in hot acid for 15 minutes, it was cleaned with an ultrasonic cleaning device and liquid penetrant inspection was carried out. The obtained image is shown in figure 3.

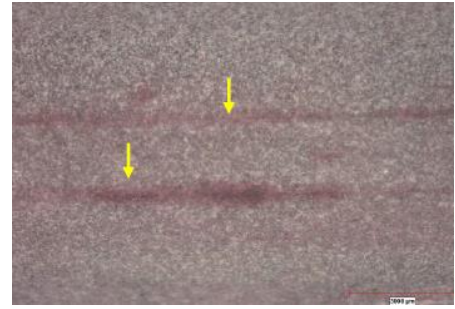


Figure 3. Penetrant inspection image of sample 18 micron crack detected

It is seen that defects can be detected by vomiting of liquid penetrating through the defect. In the same way, the study was carried out on samples above 20 microns. In the continuation of the study, liquid penetrant was applied up to the 500 micron cracked sample.

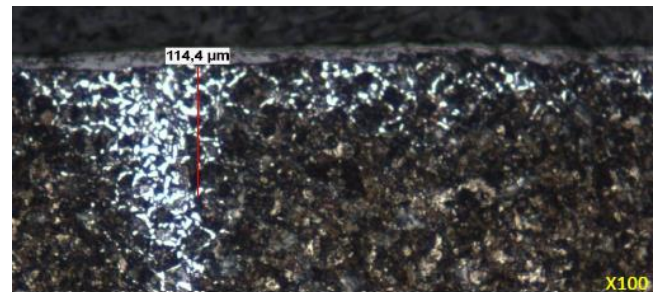


Figure 4. Micro image of 114 micron crack at x100 magnification



Figure 5. Penetrant inspection image of sample 114 micron crack detected

15 different crack sizes were determined in both micro and macro examination, and since the results were similar, low-medium and high-intensity defects were shown in the study.

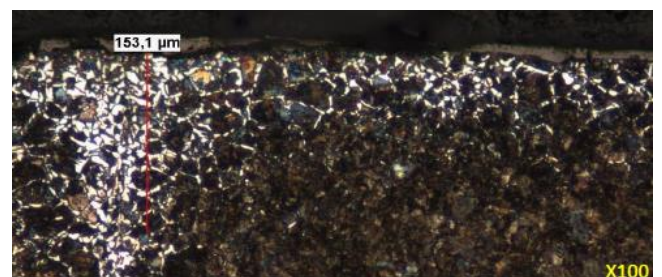


Figure 6. Micro image of 153 micron crack at x100 magnification

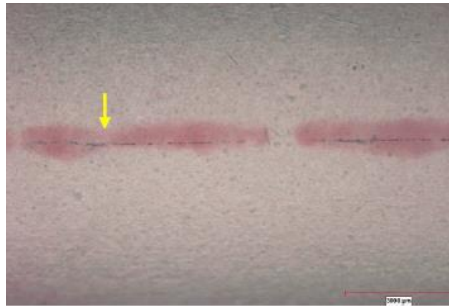


Figure 7. Penetrant inspection image of sample 153 micron crack detected

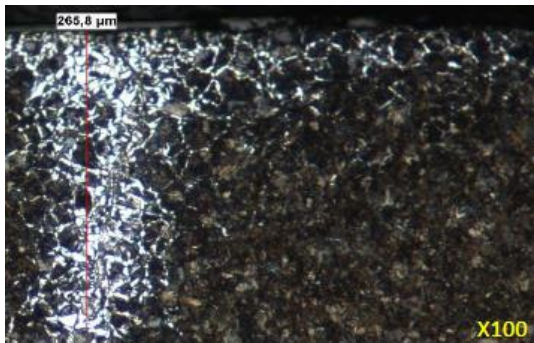


Figure 8. Micro image of 266 micron crack at x100 magnification

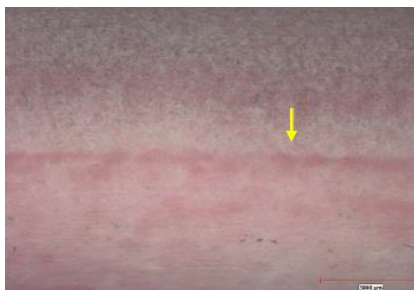


Figure 9. Penetrant inspection image of sample 266 micron crack detected

The highest crack size was determined as 501 microns and is shown in figure 10. Scale formations were also seen inside the crack due to the crack length and width.

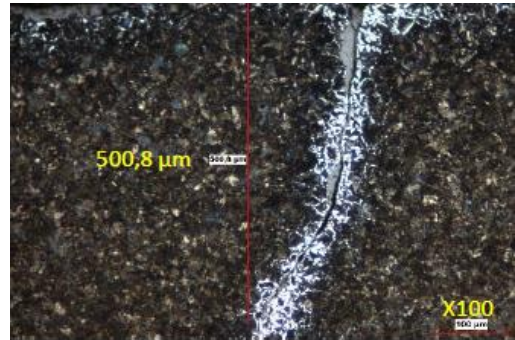
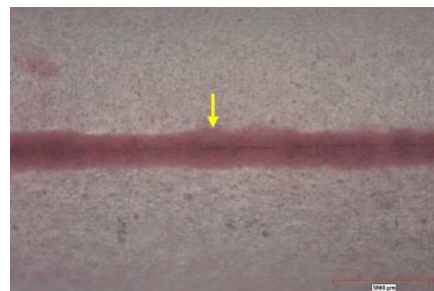


Figure 10. Penetrant inspection image of sample 501 micron crack detected



Şekil 11. Penetrant inspection image of sample 501 micron crack detected

3. Results and Discussions

In the study, different applications were made to reveal the difference between hot acid and cold acid. After the samples were kept in acid, the sample was kept in an ultrasonic cleaner with water and cleaned with alcohol and it was observed that the cracked parts were darkened by the vomiting effect of the acid.

Macro Examinations

It has been determined that the appearance of the defects after the hot acid application may be more detectable than the cold acid application.

Penetrant Inspections

The slight corrosion formation on the surface while waiting in the water inside the ultrasonic cleaner eliminates the shine on the surface of the sample and it provides a much clearer understanding of the cracks without applying PT.

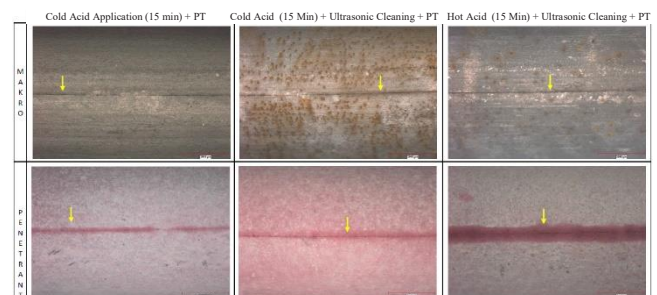


Figure 12. Cold and hot acid difference

4. Conclusion

Studies performed in the laboratory environment have shown that cracks formed on the wire rod surface can be detected by the non-penetrant inspection, which is non-destructive testing method after surface cleaning. The length and width of the crack, as well as the fact that the crack is empty or covered with scale, affects detectability significantly.

The accumulation of scale in the crack prevents the penetration of the liquid penetrant and may cause the application to fail. Despite this unfavorable situation, the presence of cracks can be detected in a sample taken from the wire rod section, even under the macro microscope.

This study was also performed in SAE 1065 grade and SG2 grade, which is suitable for electrode manufacturing, and the results were obtained similarly.

References

[1] ASM HANDBOOK, Nondestructive Evaluation and Quality Control 1989

THE EFFECT OF DEBINDING PARAMETERS ON ADDITIVE MANUFACTURED 316L STAINLESS STEEL PARTS WITH COLD METAL FUSION TECHNOLOGY

Burcu Aslı ÖZKAN¹, Burak KÜÇÜKELYAS¹, Erkan ATEŞ², Cihan KABOĞLU¹, Deniz UZUNSOY¹

¹Bursa Technical University, ²3D Design Technologies
Türkiye

Keywords: Metal Additive Manufacturing, Selective Laser Sintering, Cold Metal Fusion, Solvent Debinding,

1-Introduction

As with a conventional SLS (Selective Laser Sintering) system, the wiper deposits a new layer of unsintered powder on top of the previous layer, the laser fuses it, and the process is repeated until the part is complete. Cold Metal Fusion (CMF) is a powder-based indirect metal printing technique developed by the Germany-based company Headmade Materials. In cold metal fusion technology, metal powder is combined with a plastic binder matrix. The metal-polymer feedstock powder is suitable for use with an SLS system as well as the debinding procedures. There is no oxidation of the metal since the metal particles are enclosed in a polymer and are not exposed to any air. Moreover, it is also reportedly very simple to reuse old powder because the "cold" process has no heat impact on the unused powders. Put simply, the technology promises to enable users with polymer laser sintering machines to switch to the metal side of the industry. No study was found on the literature for CMF technology. In the present study, the commercial 316L stainless steel-polymer powder from Headmade Materials GmbH was Selective Laser Sintered and the obtained green parts were evaluated using Scanning Electron Microscopy (SEM) and Differential Scanning Calorimetry (DSC). The debinding process was conducted on the green parts.

2-Materials and Method

The 316L Stainless Steel (SS) powder mixture provided by Head Materials GmbH was subjected to SLS processing. Samples were produced with EOS Formiga P110 SLS machine. Obtained green part samples were treated in acetone, n-heptane, and n-propanol solvents at 30°C, 40°C, and 50°C for 4 to 60 hours, and their effects on weight loss and density values were examined. The DSC analysis was performed at 5 °C/min with a maximum temperature of 500 °C. SEM image analysis was done by Carl Zeiss/Gemini 300 scanning electron microscopy. Particle size distribution analysis was done by Malvern Mastersizer 3000E equipment. The final used solvents were n-heptane and acetone, which are from Merck with high purity (%99).

Conclusion

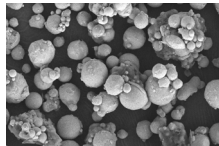


Figure 1: SEM image of 316L mixture powder after SLS

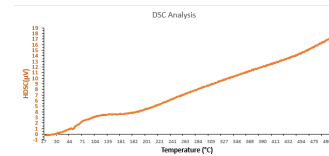


Figure 2: DSC analysis of mixture powder after SLS

- According to SEM examinations, the particles have a spherical morphology and an average grain size of 20 microns. Because of the metal and binder(polymer) differences, non-uniform particle size distribution was observed (Figure 1).
- In the DSC examination, exothermic peaks of the powders were observed at two different temperatures (50 °C and 189 °C) (Figure 2).
- According to the results of the solvent debinding experiments, weight loss rates in different solvents are between %1.30 - 11.88 wt.
- The green part samples kept in n-propanol could not maintain their strength and quickly broke apart.
- Weight loss increased for green parts with increasing dwelling time in both acetone and n-heptane at room temperature.
- While the temperature increase in acetone solvent did not significantly change the weight loss rates for green parts, the temperature increase in n-heptane solvent significantly increased the weight loss rates of green parts.

References

- [1] Zeng, K., Pal, D., & Stucker, B. (2012). A review of thermal analysis methods in laser sintering and selective laser melting. In 2012 International Solid Freeform Fabrication Symposium. University of Texas at Austin.
- [2] Xie, F., He, X., Cao, S., & Qu, X. (2013). Structural and mechanical characteristics of porous 316L stainless steel fabricated by indirect selective laser sintering. Journal of Materials Processing Technology, 213(6), 838-843.

EFFECT OF CONTINUOUS COOLING ON MICROSTRUCTURAL AND MECHANICAL PROPERTIES OF A LOW CARBON MICROALLOYED Mn-Si BAINITIC STEEL

Esra KADERLİ, Bilgehan ÖGEL

Middle East Technical University
Türkiye

Keywords: Bainitic steels, Continuous Cooling, Retained austenite, Isothermal transformation

Abstract

Steels with a bainitic microstructure offer great possibilities for highly stressed forged components. Various combinations of mechanical properties can thereby be adjusted in these steels, dependent on the morphology of the bainitic phase. Also, the bainitic structure obtained by continuous cooling offers an advantage since it can eliminate laborious and long heat treatment steps. The aim is to obtain the bainitic microstructure without using complicated heat treatment procedures. In this study, steels with a composition respectively (0.2% C, 1.35%Si, 1.5% Mn) and (0.2% C, 0.3%Si, 1.5% Mn) are investigated. The microstructural studies have been carried out in continuously cooled and isothermally transformed specimens. Optical and scanning electron microscopy were used to observe the microstructural morphology of all those steels. Mechanical properties were investigated by hardness test and retained austenite content was determined by XRD methods. It is shown that as silicon (Si) content increases retained austenite amount in the final microstructure is slightly reduced. High-strength steels (>900 MPa) with adequate ductility were obtained in continuously cooled specimens.

1. Introduction

In recent years, on the automotive industry, high-strength steel is used for more energy efficient and environmentally friendly[1]. Microalloying elements are added to obtain carbide-free bainitic steels. The bainitic microstructure can be obtained by applying either isothermal transformation or continuous cooling. Carbide precipitation is suppressed by the addition of microalloying elements to improve mechanical properties [2]. Cementite particles are undesirable due to the damage initiation effect on the microstructure.[3] Carbide precipitation is suppressed by the addition of microalloying elements to improve mechanical properties[3]. The addition of silicon retards cementite formation in steels and therewithal epsilon type carbides precipitate in the bainitic ferrite matrix [4], [5]. In this study, the different silicon content is used to understand the effect of

silicon on microstructure, morphology, and mechanical properties.

This work investigated the bainitic transformation of low carbon and low alloy steel. A detailed study showing the relationship between mechanical properties and microstructure for steels is presented.

2. Experimental Procedure

2.1. Chemical Composition

The steel alloys have been supplied by Çemtaş A.Ş and the compositions are given in Table 1.

Table 1. Chemical analysis of the specimens(wt%)

	C	Si	Mn	Cr	Mo	V	Ti	Nb	B	N
1.50%Si	0.17	1.35	1.80	0.74	0.14	0.0078	0.0343	0.0031	0.0033	0.0073
0.25% Si	0.17	0.30	1.75	0.79	0.13	0.0061	0.0236	0.0033	0.0021	0.0074

2.2. Heat Treatment Process

The CCT and TTT curves were simulated by JmatPro 7.0 software.

Two specimens were austenitized at temperature 1150°C then those samples were cooled to room temperature under air by continuously cooling. The CCT curves of samples were shown in Figures 1 and 2.

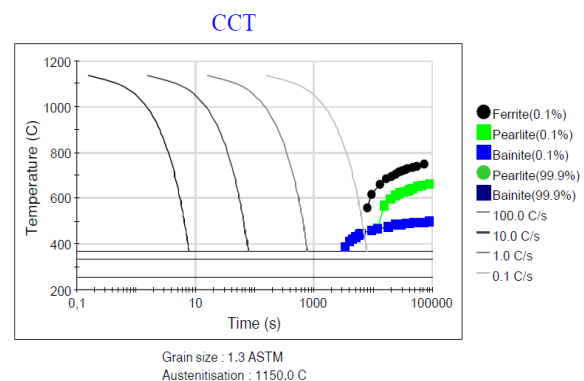


Figure 1. Simulated CCT diagram obtained from JMatPro of 1.50 % Si.

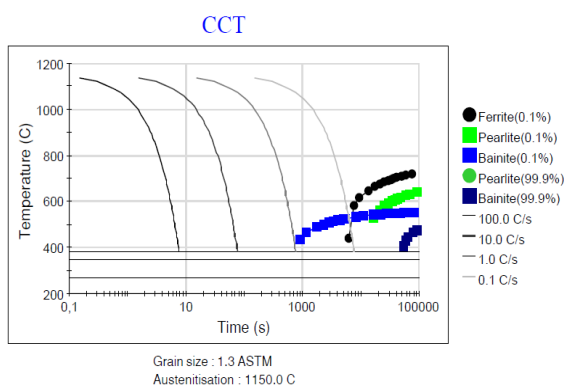


Figure 2. Simulated CCT diagram obtained from JMatPro of 0.25% Si

The isothermal transformation temperatures and holding times are determined by the simulated TTT curves. The TTT diagrams are shown in Figures 3 and 4. Two of the specimens were austenitized at 1150° C for 30 minutes. Then the samples cooled to Bs (0.1% bainite) and Bf (99.9% bainite) temperatures in a salt bath and those temperatures and holding times were obtained from Figures 3 and 4. According to the simulated TTT curve, Ms temperature is 383°C for 0.25% Si Steel and 366°C for 1.50% Si steel. Transformation temperatures are chosen just above the Ms temperature as 390°C and 370°C due to obtaining a lower bainitic microstructure. After isothermal treatments, oil quenched procedures were followed.

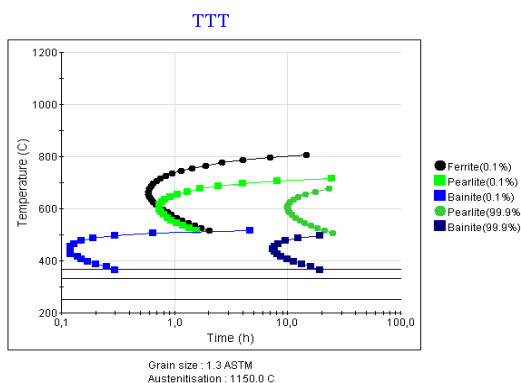


Figure 3. Calculated TTT diagram simulated from JMatPro of 1.50%Si

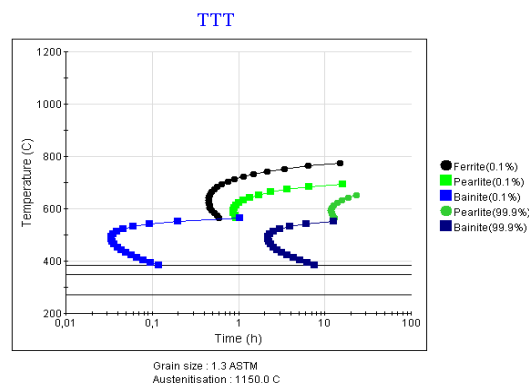


Figure 4. Calculated TTT diagram simulated from JMatPro of 0.25%Si

2.3. Microstructural Characterization

Metallography samples were investigated under optical microscope and SEM. The samples were grinded with abrasive paper 320 grit SiC followed by 400, 600, 800, 1200, and 2000 grit SiC. Then samples were polished with a 6 μm and 1μm diamond solution. The samples were etched with a nitral 2% solution to investigate the phases. Retained austenite, bainite, bainitic ferrite, and carbide morphologies were studied.

2.4. X-Ray Diffraction Samples and Retained Austenite Measurements

Rigaku DMAX-2200 diffractometer was used at a scan rate (2θ) of $0.5^\circ \text{ min}^{-1}$ over the range $2\theta = 20-140^\circ$ by using Cu-K α radiation $\lambda = 1.5406 \text{ \AA}$. The result was computed on a computer-based program called GSAS. According to integrated intensities of (111), (200), (220) austenite peaks, and the (110), (200), (211) ferrite peaks; the volume fraction of the retained austenite is calculated by the Rietveld refining method [6].

2.5. Mechanical Testing

The Vickers hardness of samples was measured using 1000 grams load. Five measurements were taken, and average values are given in the table.

3. Results and Discussion

The hardness values are given in Table 2. As shown in Table 2, hardness values increase as Si content increases for both isothermally transformed and continuously cooled samples. For the same Si compositions, isothermal transformed samples have higher hardness values than continuously cooled samples shown in Table 2. It is known that as retained austenite content decreases, the hardness values increase.

Table 2. Hardness data of samples

Sample	Hardness (HV)
0.25Si-1.75Mn- 0.8Cr- Continuous Cooled	283±10.5
0.25Si-1.75Mn- 0.8Cr- Isothermal Treated	336.4±11.4
1.50Si-1.8Mn- 0.8Cr- Continuous Cooled	382.3±2.08
1.50Si-1.8Mn- 0.8Cr- Isothermal Treated	426.6±6.9

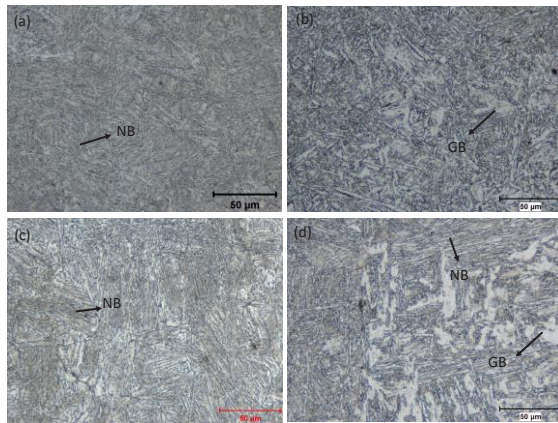


Figure 5. OM images of all bainitic steel; a) 0.25% Si isothermally transformed, b) 0.25% Si continuous cooling, c) 1.50% Si isothermally transformed, d) 1.50% Si continuous cooling

Figure 5 shows the optical microscopy images taken at 500x. All the micrograph shows samples etched with nital 2% solution. As it can be seen from images b and d, with continuous cooling needle and granular bainite can be observed, moreover the area of white islands increases. Isothermal transformed samples show needle-like bainite morphology as can be seen from images and c.

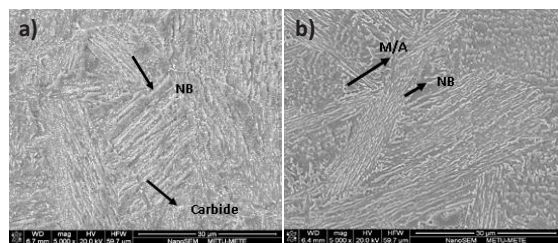


Figure 6. SEM micrographs of isothermally transformed samples; a) Isothermally Transformed at 390°C for 6.5 h (0.25%Si-1.75Mn- 0.8Cr), b) Isothermally transformed at 370°C for 19h (1.50%Si-1.75Mn- 0.8Cr)

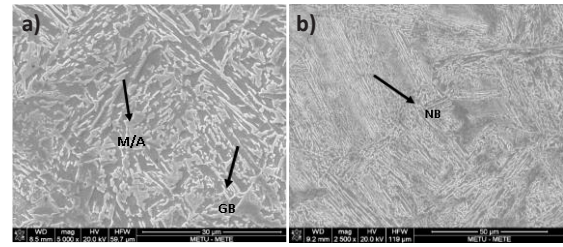


Figure 7. SEM micrographs of continuously cooled samples; a) Continuous cooled (0.25%Si-1.75Mn- 0.8Cr), b) Continuous cooled (1.50%Si-1.8Mn- 0.8Cr)

In SEM images bainitic morphology can be seen more clearly. Figures 6 and 7 show SEM micrographs of samples. 0.25% Si isothermally transformed sample shows needle-like bainite and carbide precipitation, whereas 0.25% Si continuous cooling sample shows granular bainite morphology. Samples with 1.50% Si show needle-like bainite morphologies with no sign of carbide precipitation.

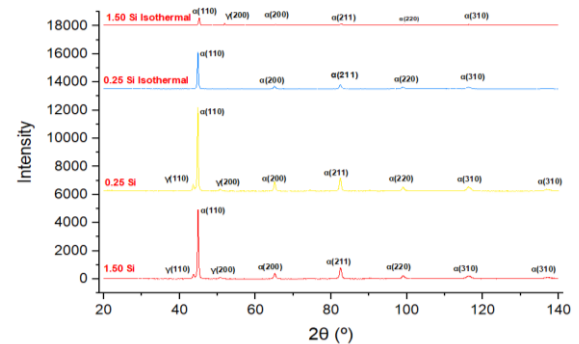


Figure 8. XRD patterns of samples

According to XRD results shown in Figure 9, austenite peaks have not existed for 0.25% Si isothermal treated sample. For 1.50% Si isothermal and continuous samples in Figure 9, retained austenite amount is not very significant. As shown in the XRD results in Figure 9, 0.25% Si continuously cooled sample shows the intense austenite peaks. For isothermal transformed samples, austenite transforms into bainite, and a trace amount of retained austenite was obtained in the final microstructure.

4. Conclusion

In this study, continuous cooling and isothermal heat treatments were applied to steels having different Si content, to obtain carbide-free bainitic steels. Isothermally transformed 1.50%Si and 0.25% Si steels show needle-like bainitic microstructure. Continuously cooled 1.50% Si shows needle-like bainite whereas 0.25% Si shows granular bainite. In continuous cooling samples, carbide precipitation was not observed whereas isothermally transformed 0.25% Si sample contain carbide precipitate. In the 1.50% Si isothermal

sample carbide precipitation was not observed. Carbide precipitation has a negative effect on steel's mechanical properties. Hence, with Si addition carbide free bainitic steels can be obtained. Hardness values of isothermally treated samples are higher than continuous cooling samples since bainite is harder than retained austenite.

Acknowledge

The authors would like to thank ÇEMTAŞ A.Ş. R&D Department for the procurement of the materials.

References

- [1] Z. Wang, W. Hui, Z. Xie, Y. Zhang, and X. Zhao, "Enhancing mechanical properties of a V + Ti microalloyed bainitic forging steel via tailoring microstructure through controlled forging," *Journal of Materials Science*, vol. 55, no. 24, pp. 10849–10862, Aug. 2020, doi: 10.1007/s10853-020-04695-3.
- [2] Caballero, F. G. (2012). Carbide-free bainite in steels. In *Phase transformations in steels* (pp. 436-467). Woodhead Publishing.
- [3] H. K. D. H. Bhadeshia, "BAINITE IN STEELS THEORY AND PRACTICE THIRD EDITION."
- [4] H. K. D. H. Bhadeshia, "High Performance Bainitic Steels," 2005. [Online]. Available: www.msm.cam.ac.uk/phase-trans
- [5] H. K. D. H. Bhadeshia and D. v. Edmonds, "MECHANISM OF BAINITE FORMATION IN STEELS.," *Acta Metallurgica*, vol. 28, no. 9, pp. 1265–1273, 1980, doi: 10.1016/0001-6160(80)90082-6.
- [6] ASTM, "ASTM E975-13 Standard Practice for X-Ray Determination of Retained Austenite in Steel with Near Random Crystallographic Orientation," *Astm*, vol. 03, pp. 1–7, 2009.



THE EFFECT OF CHEMICAL COMPOSITION AND RATIO OF DEFORMATION ON MECHANICAL PROPERTIES IN HIGH CARBON STEEL WIRE PRODUCTION

Sevim Gökçe ESEN, Muhammet Fatih DUMAN

Çelik Halat ve Tel Sanayii A.Ş.
Türkiye

Keywords: Steel Wire, Mechanical Properties, Wire Drawing, Deformation Ratio

Abstract

High carbon steel wires are used in many fields, especially in automotive, white goods, agricultural applications and wire ropes. Wire drawing, which is a cold deformation method, can vary in its mechanical properties according to the wire rod used, the total reduction ratio applied, the wire drawing process conditions and the wire drawing dies in process. Mechanical properties such as tensile strength, ductility, reduction in area after fracture and hardness, which are limited in production standards according to the targeted diameter and quality class, determine the performance of the wire in the field of end use. In this study, the effects of % reduction ratio and %C composition on mechanical properties were investigated in the production of 1.00 mm SM (medium tensile strength under static stress) quality steel wire are limited in production standards according to the targeted diameter and quality class, determine the performance of the wire in the field of end use.

1. Introduction

High carbon steel wires are used in different forms in automotive, white goods, steel ropes, agriculture and defense industries. Steel wires are produced by cold deformation of steel raw materials called wire rod with a minimum diameter of 5.50mm [1]. The wire drawing die used in wire drawing processes are selected according to the targeted wire properties and these die series determine the amount of deformation applied to the wire rod.

Wire drawing is different from conventional cold drawing methods by diameter reduction process with more than one drawing die and this process varies according to final wire diameter and lubricant change [1,2]. During wire drawing process, the surface and mechanical properties of the wire depend on the die angle, wire drawing speed, temperature, lubrication and reduction ratio [3]. Calculation of

reduction ratios and input-output diameters has great importance for determining the mechanical properties. Tensile and elongation properties are the most important mechanical properties that determine the identity of the material [4,5]. Deformation rate and strength are parameters that are proportional to each other. In wire drawing processes, there are basically two principles to achieve the targeted tensile strength. One of the principles is to increase of deformation rate (reduction ratio) and the other is to change the chemical structure of the selected raw material.

In this study, the mechanical properties of 1.00mm SM (medium tensile strength under static stress) quality class wires produced using two different methods were compared. Wire production was carried out by reducing high carbon steel wire rods (wt. 0.70% C and wt. 0.83% C) at different rate (90.23% reduction and 85.21% reduction), which were selected according to the target strength range determined in the wire drawing standards and other property specs (TS EN 10270). As a result of this study, the relationship between deformation and ductility was established.

2. Experimental Procedure

The chemical compositions of wire rods with a diameter of 5.50 mm (wt. 0.70% C and wt. 0.83% C) used in experimental studies are given in Table 1. Wire rods with different chemical compositions were drawn to 3.20 mm and 2.60 mm in order to examine the effect of low and high reduction in 1.00 mm wire production.

Table 1. Chemical composition of wire rods used in experimental studies

	C %	Mn%	Si%	P%	S%	Cu%	Cr%	Ni%	V%
C83	0.83	0.50	0.21	0.01	0.015	0.012	0.03	0.017	0.001
C70	0.70	0.48	0.18	0.01	0.014	0.012	0.03	0.016	0.001

After the wire rods are brought to the semi-finished product level by applying the first wire drawing procedure, the ability to take shape is gained by applying the industrial patenting heat treatment. After patenting, which is austenitizing heat treatment, pickling with HCl, phosphate and borax coating was applied to the wires. In this way, semi-finished products are prepared for final wire drawing in terms of surface and mechanical properties.

Wire drawing process was applied using the series specified in Table 2, taking into account the test matrix created to obtain the mechanical properties of SM quality wire specified in the standard.

Table 2. Experimental set-up

1 st Attempt		2 nd Attempt	
Wire rod	C70	Wire rod	C83
Die series			
Inlet	3.20 mm	Inlet	2.60 mm
1	2.76 mm	1	2.28 mm
2	2.39 mm	2	2.01 mm
3	2.09 mm	3	1.79 mm
4	1.84 mm	4	1.60 mm
5	1.64 mm	5	1.44 mm
6	1.46 mm	6	1.30 mm
7	1.31 mm	7	1.18 mm
8	1.19 mm	8	1.08 mm
9	1.09 mm	9	1.00 mm
10	1.00 mm		
TOTAL REDUCTION	90.23%	TOTAL REDUCTION	85.21%

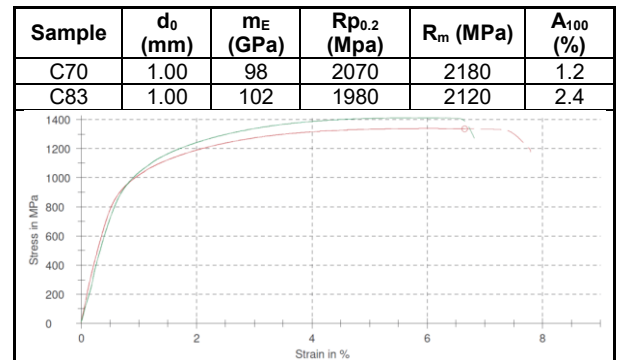
1.00 mm drawn wire samples were pulled with the universal tensile testing unit Zwick 5 kN with test speed: 0.006 sn-1, 250 mm jaw distance and 5 MPa pre-load according to TSE EN ISO 6892-1 Method B. Yield strength, tensile strength, elongation ratios were compared according to the result of tensile test. The torsion test was conducted with 300 mm sample length according to TS EN ISO 10218-1. (The fracture of the torsion test piece must be perpendicular to the wire axis). The hardness of the wire samples (from wire center to edge) was carried out with an emcotest branded instrument with HV 0.5.

3. Results and Discussions

SM quality wire samples with a diameter of 1.00 mm were produced under industrial conditions with different deformation rates. The tensile test results of the obtained wire samples are given in Table 3. Five consecutive tensile

tests were applied to the wire samples and the average strength values were shared.

Table 3. Tensile test results



In the wire drawing test results, it was seen that the cross-section and elongation (%) values of the wire obtained with high reduction were lower than the wire produced with raw material with a high C % ratio. From these results, it can be understood that the shaping potential of the wire decreases in response to the strength value obtained with the increase in the deformation rate.

The twist in the torsion tests and their visuals, which is another of the industrial mechanical tests, are shared in Table 4.

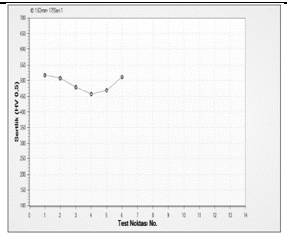
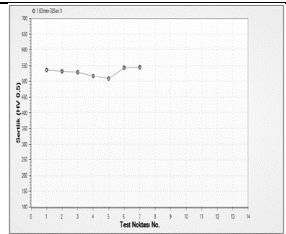
Table 4. Torsion test results

Sample	C70	C83
Number of twist	27	35
Form of fracture		

When the breaking shape of the samples in the torsion test is examined, the piecewise breaking shape, which is not suitable in the standard, was observed in the wire produced at high deformation rate. This fragmented fracture is caused by internal stress (dislocation), temperature and cementite precipitation during the production of the wire. Although the targeted number of twists in the torsion test was achieved, the wire produced with 90.23% reduction failed in the test due to the fracture type.

After the metallographic preparation of the wire samples, the hardness test was applied on the sections. Hardness test results are given in Table 5. The point results of measurements taken along a line over the cross-section of the wire are shown in the graph, the average of the points is given as the test value. Although it is expected that there will be surface hardening in wire drawing processes, this rate is not desired to be too high.

Table 5. Hardness test results

Sample	C70	C83
Hardness (HV _{0.5})	544	480
Difference between edge and center	±40	±10
Measuring points and values		

The difference in hardness between the center and the edge of the C70 sample produced by applying high reduction is quite high (recommended max. ±10). Also the hardness of C70 sample is higher than C83.

4. Conclusions

1.00mm SM quality wire was produced by applying different deformation ratios from steel raw materials with different chemical compositions. Although the final wire product is of the same quality class and the same product, the effects of the applied deformation rate on the mechanical properties of the wire were investigated. In this context, samples were produced with 90.23% reduction from wt. 0.70%C and 85.21% reduction from wt. 0.83%C. Although the strength of the wires obtained by high reduction application comes within the specification, the elongation and narrowing of the cross-section are lower than the other. Although the number of twist was suitable for the torsion test, the fracture mechanism was not found to comply with the standards. In the hardness test applied, a high hardness difference was observed between the center and the edges of the wires produced with high reduction.

Acknowledgment

Çelik Halat ve Tel Sanayii A.Ş provided information, opportunity and financial support to all test and experimental activities of the project. The authors would like to thank Çelik Halat ve Tel Sanayii A.Ş for opening up all its possibilities for experimental studies and the creation of process conditions.

References

- [1] Ünseren M., Tel çekme matrisleri üzerine bir araştırma, Süleyman Demirel Universty, Master thesis, 2006.
- [2] Chaudhary A., Kumar R., Aneja A., Rectification of Problem in Wire Drawing By Lean Way, International journal of emerging technology and advanced engineering, vol. 4, Issue1, 2014
- [3] Wright, R. N. Workability in Extrusion and Wire Drawing, in Workability Testing Techniques, ed. G. E. Dieter, p. 255, ASM International, Materials Park, Ohio, 1984.
- [4] Shemenski, R. M., M. A. Foster, and J. Walters. "Finite Element Analysis of Die Geometry for Drawing Steel Wire," Conference Proceedings, 74th Wire & Cable Technical Symposium, pp. 42–55, Cleveland, Ohio, The Wire Association International, Inc., Guilford, Connecticut, 2002.
- [5] Flanders, N. A. and E. M. Alexander. "Analysis of Wire Temperature and Power Requirements on Multi-Pass Drawing Productivity," Wire Journal International, Vol. 12, No. 4, pp. 60–64, The Wire Association International, Inc., Guilford, Connecticut, 1979

EXPERIMENTAL INVESTIGATION OF MECHANICAL PERFORMANCE TESTS OF IMPREGNATED PLASTIC CORE STEEL WIRE ROPE AND IMPREGNATED PLASTIC CORE SWAGED STEEL WIRE ROPE

Zeynep Şeyma SERDAROĞLU, Zehra ALTINIŞIK

Çelik Halat ve Tel Sanayii A.Ş.
Türkiye

Keywords: Steel Wire Rope, Impregnated Plastic Core Steel Wire Rope

Abstract

Steel wire ropes are lifting equipment of produced in different area according to the place of use. Equipment of steel wire ropes used in many areas such as fishing, oil&gas, marine and mining. Constructions of steel wire ropes effect of mechanical properties including bending fatigue, breaking load, and wear resistance.

Impregnated plastic core (EPIWRC) steel wire ropes extensively used in marine areas. Plastic coating between are steel core and another strands increases the corrosion resistance and wire rope fatigue life of the steel core. With the swaging process, the metallic fill factor in the unit cross section area and pulley contact surface increases an the impregnated plastic core steel wire rope. In this study, the differences in wear resistance, bending fatigue, corrosion performance, breaking load between plastic-filled swaged ropes and plastic-filled steel ropes were investigated.

1. Introduction

Steel wire ropes are lifting equipment with wide range of applications. Some of the common using areas are harbour cranes, bridges, oil&gas and offshore [1]. Steel wire ropes make of individual steel wires. Steel wire ropes are made up steel wire ropes spun into a strand. Steel wire ropes are made of strands and strands are made of steel wire. The number of wires used in the rope, wire diameter and arrangement affect the corrosion performance of the steel rope [2].

Rope core types vary according to the place and purpose of use of the steel wire ropes. Steel rope are produced with different core types according to their used areas. The commonly used fiber core (FC), independent wire rope core (IWRC) and impregnated plastic independent wire rope core (EPIWRC) [3]. Core types used in steel wire ropes are given Figure 1.

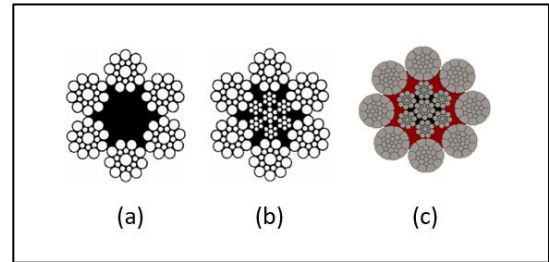


Figure 1. Core types of steel wire ropes; (a) fiber core (FC), (b) independent wire rope core (IWRC), (c) impregnated plastic independent wire rope core (EPIWRC) [3]

The coating of steel wire rope core with plastic is a feature that increases corrosion performance. Corrosion performance is an important parameter for steel rope that will operate in damp and wet areas.

During use of steel ropes, abrasion occurs due to pulley-rope friction, the contact of the strands with each other under load, and the contact of the wires in the strands with each other. In addition, corrosion of the galvanized layer in galvanized wires reduces the corrosion resistance of the rope. [4], [5].

Swage ropes are designed for heavy duty applications. These ropes have been reduced in diameter under tension. In addition, as the pulley-rope contact increases that fatigue life is longer than before the swage process [5]. Swage ropes have high wear resistance as the rope surface becomes almost smooth. Because they will not be attached anywhere during use. Swaged wire rope and non-swaged wire rope are given Figure 2.

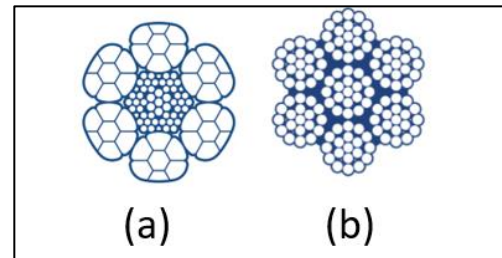


Figure 2. (a) Swaged wire rope, (b) non-swaged wire rope

In this study, corrosion, wear and fatigue performances between impregnated plastic independent wire rope and impregnated plastic independent swaged wire rope were

investigated.

2. Experimental Procedure

2.1. The Production of Prototype Ropes

In this study, 22.00 mm rope productions were completed with 8xK26WS composition and in the same strength class (1960MPa) with 2 different steel wire ropes. First one is impregnated plastic independent steel wire rope and second one is impregnated plastic independent swaged steel wire rope. The cross section view of these ropes are given Figure 3. Prototype ropes are given Figure 4.

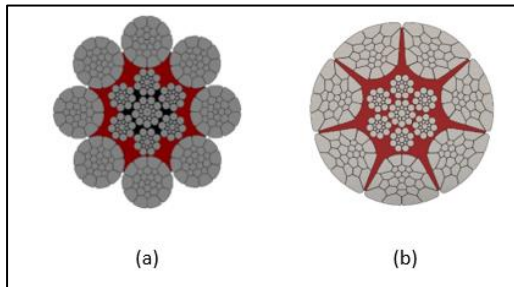


Figure 3. The cross section of ropes; (a) impregnated plastic independent steel wire rope, (b) impregnated plastic independent swaged steel wire rope



Figure 4. Prototype Ropes; (a) impregnated plastic independent steel wire rope, (b) impregnated plastic independent swaged steel wire rope

2.2. Comparative Corrosion Test

Comparative corrosion tests, samples were completed in pairs in the corrosion test cabinet shown in Figure 5, in accordance with ASTM B-117 standard.



Figure 5. Corrosion test cabinet

2.3. Tensile Test

All tensile tests were carried out in accordance with the TS EN ISO 6892-1 standard on the 100-ton tensile test machine in Figure 6.



Figure 6. 100-ton tensile test machine

2.4. Fatigue Test

Fatigue tests were carried out in the fatigue test device of the Çelik Halat ve Tel Sanayii A.Ş., as can be seen in Figure 7. Fatigue test was applied to both ropes and the test was completed according to wire fracture and service life. The maximum number of wire fracture that may occur during use is mentioned in the ISO 4309 standard.



Figure 7. Fatigue test machine

3. Results and Discussion

3.1. Tensile Test Results

Tensile tests were carried out for both steel wire ropes and the results are given in Table 1. The first sample is a impregnated plastic independent wire rope, and the second sample is impregnated plastic independent swaged wire rope.

Table 1. Tensile test results

Sample	Diameter (mm)	Actual Breaking Load (kN)
1	22	417
2	22	484

It was observed that the breaking load of the swaged rope was higher when two ropes with the same diameter were tensile test.

Swaged rope has %16 more strength then other rope.

3.2. Comparative Corrosion Test Results

The simultaneously initiated corrosion performance test was terminated at the 580th hours. Corrosion test results are given in Figure 8. When the figure is examined, it is observed that there is less corrosion in sample 1. Red rust started to form on sample 2 at the 425th hours. Red rust started to appear on the sample 1 at the 448th hours.



Figure 8. Corrosion test results; (a) impregnated plastic independent steel wire rope, (b) impregnated plastic independent swaged steel wire rope

3.3. Fatigue Test Results

In order to measure the wear resistance, the test machine was stopped at the 40000th cycle of the fatigue test device and the number of wire fracture was measured. Wear resistance is inversely proportional to the number of wire fracture. The number of wire fractures in the 40000th cycle is shared in the Table 2.

Table 2. 40000th Cycle of fatigue test results

Sample	Number of Cycle	Number of Wire Fracture
1	40000	7
2	40000	4

The abrasion resistance of the impregnated plastic independent swaged wire rope is %42,8 higher than the impregnated plastic independent wire rope.

The fatigue test result is given in Table 3. The product of the rope as a result of the test are shared in Figure 9.

Table 3. Fatigue test results

Parameters	Sample 1	Sample 2
Rope Diameter	22 mm	22 mm
Composition	8xK26 EPIWRC	8xK26 EPIWRC Swaged
Working Speed	10 RPM	10 RPM
Number of Cycle	56833	60981
Rope Temperature	Max. 50°C	Max. 50°C

The fatigue test results performed by keeping the constant ambient and test conditions are given in Table 3. When the test is complete, the fatigue cycle number of sample 2 is %7.3 higher than for sample 1.

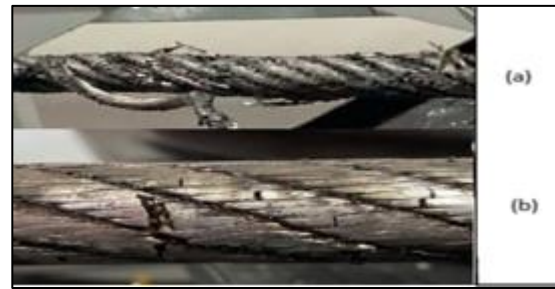


Figure 8. Fatigue test results; (a) impregnated plastic independent steel wire rope, (b) impregnated plastic independent swaged steel wire rope

4. Conclusion

In this study, performance tests between two different ropes were investigated. Tensile test result and fatigue test result are more successful in impregnated plastic independent swaged wire rope, but corrosion test performance is lower. Because earlier red rust was observed as a result of damage to the plastic coating of the steel core during the swaged process. All tests performed in the study were carried out under laboratory conditions and contain theoretical results.

Acknowledgment

Thanks to Çelik Halat ve Tel Sanayi A.Ş. for laboratory and test facilities in this project.

References

- [1] A. Güzey, "Demirsel teller üretim sürecinin incelenmesi" Msc thesis, Dept. Met. And Mat. Eng. Trakya University, Edirne



- [2] R. P. Singh, M. Mallick, and M. K. Verma, “Studies on failure behavior of wire rope used in underground coal mines”, *Engineering Failure Analysis*, vol. 70, pp: 290-304, 2016
- [3] A Anon. *Steel Wire Ropes and Fittings*. Bridon Ropes. 1992.
- [4] X. D. Chang, H. B. Huang, Y. X. Peng, and S. X. Li, “Friction, wear and residual strength properties of steel wire rope with different corrosion types”, *Wear*, vol. 458, pp.203-425, 2020.

COMPARISON OF BREAKING LOAD AND SERVICE LIFE OF STEEL WIRE ROPES WITH PARALLEL WIRE ROPE CORE (PWRC) AND INDEPENDENT WIRE ROPE CORE (IWRC)

Murat POLAT, Emre BAŞER

Çelik Halat ve Tel Sanayii A.Ş.
Türkiye

Keywords: Bending fatigue, Breaking load, Metallic cross section, Steel wire rope

Abstract

Steel wire ropes are load-lifting equipment with superior performance used in various industries. One of the most basic parameters of steel wire ropes is the breaking load. Breaking load can be increased by producing ropes with different properties. Steel wire ropes can be produced with fibre core, independent wire rope core and parallel wire rope core. There are 2 closing processes in ropes with IWRC are called steel core and rope closing. The operation in which the steel core and rope closing process is done at the same time is called the parallel closing method. One of the methods to increase the breaking load of rope is the parallel closing method. Steel wire ropes produced with parallel closing method are used as suspension ropes in industry. In this study, the breaking load increase was obtained by increasing the metallic cross section per unit area by producing with the parallel closing method. At the same time, ropes produced with the parallel closing method have a higher service life. In this study, the tests were carried out under laboratory conditions. Performance may vary depending on industrial usage conditions.

1. Introduction

Steel wire ropes are lifting equipment produced using high carbon pearlitic steel wire rods. Steel wire ropes, which are used in many areas, are especially preferred in elevator systems, fishing industry, port cranes and mining enterprises [1].

Steel wire ropes are elements consisting of many wires. The elements in the structure of the wire rope are given in Figure 1 [2].

There are different structures in the core of steel wire ropes. It can be classified as independent wire rope core (IWRC), wire strand core (WSC), fibre core (FC), parallel wire rope core (PWRC), impregnated plastic wire rope core (EPIWRC). FC ropes have flexibility and lubrication superiority. IWRC ropes provide high strength. PWRC ropes have higher metallic cross-sectional area. EPIWRC ropes have extra corrosion resistance. [3].

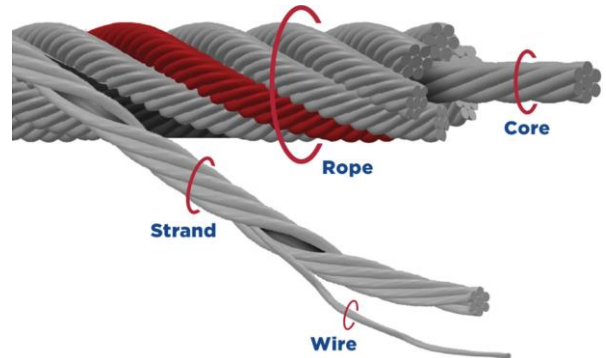


Figure 1. The elements of steel wire ropes

In steel wire ropes, the contact areas change according to the closing direction and lay length. While there are point contacts in IWRC ropes, linear contacts occur in PWRC ropes as all twists are made in equal lay length. This provides a more homogeneous pressure distribution. PWRC rope have rotation sensitivity due to their design [4]. The contact characteristic is given in Figure 2.

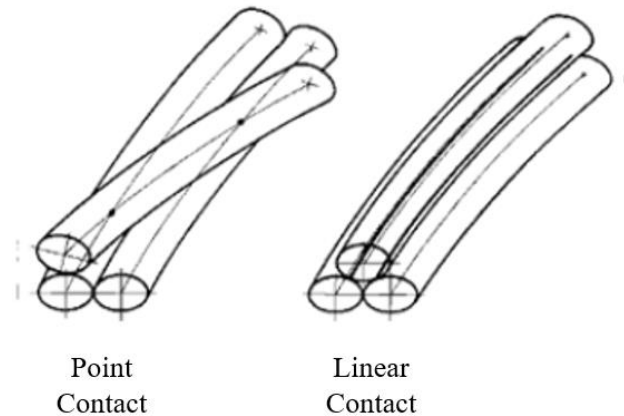


Figure 2. Contact characteristics of wires [4]

The desired feature of a rope during the transportation process is to have sufficient strength, to work on the pulleys without damage, to be protected from corrosion and not to rotate under load. In order to determine these properties, breaking load test, torque test, bending fatigue test and corrosion test can be applied to the ropes [2].

The fatigue behavior of steel ropes as a result of bending on the pulleys was investigated. As a result of the study, it was stated that tensile load, D/d ratio, pulley material, rope construction and quality of the wire are very important to increase the rope life [5]. The wear mechanism of steel ropes during working on cast iron pulleys has been investigated. A rope of 8x19S construction with a diameter of 8 mm was used in the study. As a result of the study, it was stated that fatigue fracture occurred as the propagation of cracks occurring in the contact areas. Increasing the contact pressure causes the crack depth to increase and the fracture to accelerate [6].

In this study, breaking load and bending fatigue life of ropes with IWRC and PWRC were investigated comparatively.

2. Experimental Procedure

For the study, an independent wire rope core (IWRC) and parallel wire rope core (PWRC) ropes of 8x26WS construction with a diameter of 22 mm, wire strength of 1960 MPa was used. Detailed information about the samples is given in Table 1.

Table 1. Sample information to be used in the study

Sample No	Construction	Diameter (mm)	Core Type	Tensile Grade (N/mm ²)
1	8x26WS	22	IWRC	1960
2	8x26WS	22	PWRC	1960

2D design studies were carried out for Samples 1 and 2. The theoretical cross-sectional views of the samples are given in Figure 3.

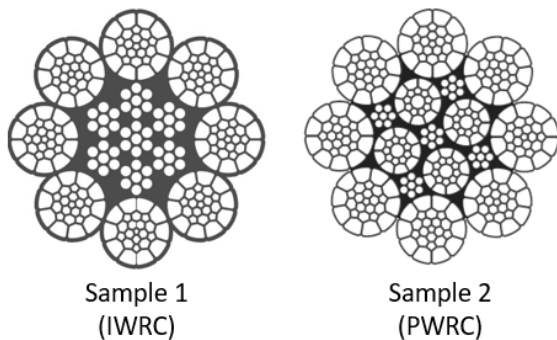


Figure 3. Cross-sectional views of samples

The expected breaking load values and theoretical cross-sectional areas of the samples are given in Table 2.

Table 2. Technical parameters of samples

Sample No	Construction	Core Type	Minimum Breaking Load (kN)	Cross-sectional Area (mm ²)
1	8x26WS	IWRC	385	233
2	8x26WS	PWRC	427	256

For the tensile tests, 1.20 meters samples were taken from the produced steel wire ropes. Both ends of the samples are terminated with a zinc head. Tensile tests were carried out according to ISO 6892-1.

Bending fatigue tests are performed on devices specially designed for steel wire ropes. Ropes mounted on the test device consisting of one drive sheave and one test sheave are subjected to cyclic motion. The test is completed when reference values such as diameter reduction and number of wire breaks in the ISO 4309 standard are reached. The bending fatigue test principle is given in Figure 4.

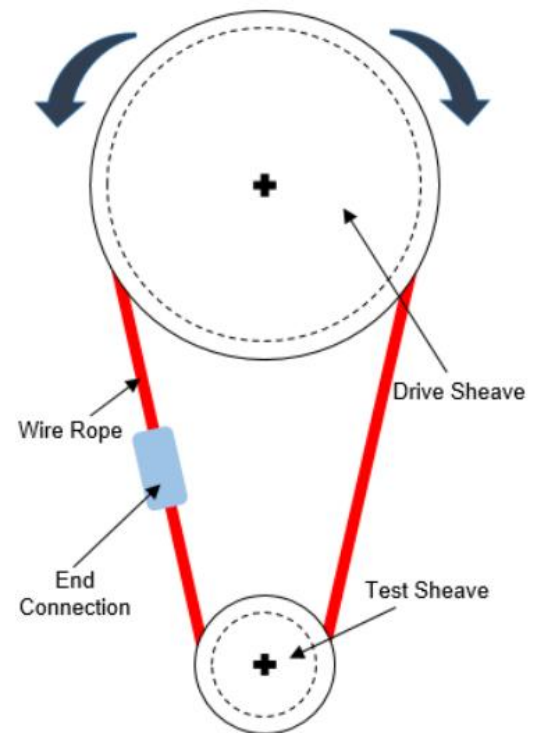


Figure 4. Test principle of bending fatigue test

3. Results and Discussion

Tensile tests were carried out on independent wire rope core (IWRC) and parallel wire rope core (PWRC) steel wire ropes. Detailed test results are given in Table 3 and tensile test diagrams are given in Figure 5. The tests of the samples were successfully completed and results above the targeted values were obtained for both samples. Actual breaking load values are 3.5% higher than the minimum breaking load values.

Table 3. Tensile test results of samples

Sample No	Construction	Core Type	Minimum Breaking Load (kN)	Actual Breaking Load (kN)
1	8x26WS	IWRC	385	400
2	8x26WS	PWRC	427	442

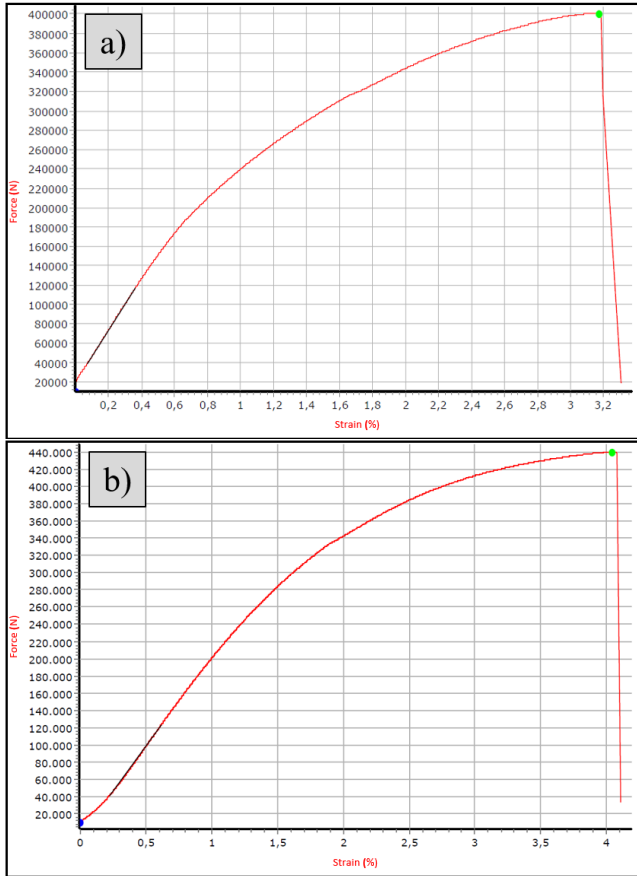


Figure 5. Tensile test diagrams of the samples: a)IWRC, b)PWRC

Tensile tests were carried out on a vertical type universal tensile testing device. In the test, the loading speed was determined as $0.1 \times F_m$ until 80% of the breaking load was reached, then $0.05 \times F_m$. F_m is the minimum breaking load of the sample.

Bending fatigue tests were performed on the samples. Temperature, force and elongation parameters were checked in the test. Temperature value was kept below 40 °C. Force value was kept constant with a deviation of $\pm 100N$. Test parameters and details of their results are given in Table 4. Tests were carried out in laboratory conditions, using appropriate test pulleys in the standard. Product performance may vary due to variable conditions in industry use.

Table 4. Bending fatigue test results of samples

Sample No	Diameter (mm)	Core Type	Safety Factor	Number of Cycles
1	22	IWRC	5	38.868
2	22	PWRC	5	42.126

The first wire breaks started at 30,000 cycles. The visuals of the products in this cycle number given in Figure 6.

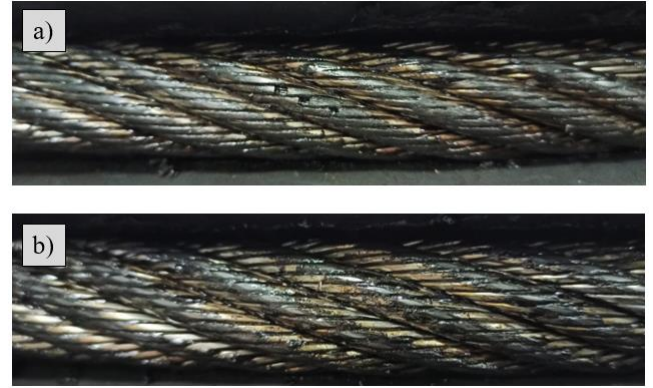


Figure 6. Visual of the samples at 30.000 cycle: a)IWRC, b)PWRC

4. Conclusion

Steel ropes are complex lifting elements that are preferred due to their superior flexibility, load carrying ability and safety in use. In the study, the breaking load and bending fatigue life of independent wire rope core(IWRC) and parallel wire rope core(PWRC) ropes were investigated. As a result of the study, it was determined that impregnated PWRC ropes provide 20% of higher strength and 8% of higher fatigue resistance compared to IWRC ropes. PWRC ropes are suitable for use in critical areas with higher performance expectations. As mentioned in the literature, due to the rotation sensitivity of PWRC ropes, attention should be paid on the usage area. Test activities in the study were carried out under laboratory conditions. In sectoral usage, product performance may vary as a result of the variable effects of human, machine and environmental factors.

Acknowledgement

The production and testing activities of the products used in this study are carried out by Çelik Halat ve Tel San. A.Ş. Thank you for their support.

References

- [1] A. Güzey, Demirsel Tellerin Üretim Sürecinin İncelenmesi, M.Sc. Thesis, Trakya Üniversitesi, 2009, Edirne, Türkiye.
- [2] <<https://www.celikhalat.com.tr>> Dated:28.06.2022
- [3] M. Polat, Investigation of bending fatigue behavior and mechanical properties of steel wire ropes with impregnated plastic core (EPIWRC), M.Sc. Thesis, Kocaeli Üniversitesi, 2022, Kocaeli, Türkiye
- [4] Ö.S. Çiçek, Modelling and Analysis Corrosion Fatigue Behaviour of Steel Wire Rope, PhD Thesis, İstanbul Teknik Üniversitesi, 2016, İstanbul, Turkey.
- [5] H. Zhihui, H. Jiquan, The Fatigue and Degradation Mechanisms of Wire Ropes Bending-over-sheaves, Applied Mechanics and Materials, 127 (2012), 344-349.
- [6] V. Oksanen, K. Valtonen, P. Andersson, A. Vaajoki, A. Laukkanen, K. Holmber and V.T. Kuokkala, Comparison of Laboratory Rolling-Sliding Wear Tests with In-service Wear of Nodular Cast Iron Rollers Against Wire Ropes, Wear, 340-341 (2015), 73-81.

REDUCING THE AMOUNT OF SLAG CARRY OFF FROM THE LADLE IN THE CONTINUOUS CASTING PROCESS

Ahmet Şafak ÇAKMAK, Hakan KAPUSUZ, Emin Serkan EMİNOĞLU, Fatih ASLAN

Iskenderun Demir ve Çelik A.Ş.
Türkiye

Keywords: Slab Casting Machine, Ladle, Slag, Tundish, Cost Study

Abstract

Continuous Casting process are aimed process safety, product quality and high production efficiency as well as production continuity. In this context, the integration of current technologies into the existing system is great importance in slab machines.

In the continuous casting process, the molten steel coming from the ladle is transferred to the steel tundish after that transferred from the tundish to the water-cooled mold to produce semi-finished products. Ladle slag is recognized as one of the most important factors ensuring steel quality and process safety in production of liquid steel. In the continuous casting process, a minimum amount of ladle slag is required to carry over the tundish. Currently, operators are responsible for controlling the steel flow from the ladle to the tundish. The slag passing from the ladle to the tundish is detected by the glow on the tundish surface and the ladle is closed. Depending on the experience of the personnel, a large amount of slag may flow from the ladle to the tundish, or useful steel may be scrap as a result of early closing of the ladle. Excess slag flowing into the tundish; It damages tundish walls, increases quality defects and puts process safety at risk. In the current situation, operating costs increase or decrease according to the person-based performance of the systematic that depends on the operator. In addition, this situation causes quality defects and a decrease in production efficiency.

Electromagnetic sensor was placed the bottom of the ladle for improvement work. The sensor detects the slag-liquid steel density difference; It prevents the slag carry out from the ladle to the tundish. The sensor detects the slag, closing the ladle slider and eliminating operator initiative. Accordingly, an improvement has been achieved in cost and labor issues.

1. Introduction

Since continuous casting technology is an important part of steel production, integrating and applying up-to-date technologies to improve casting conditions into the existing system provides a positive effect on the process by providing good results. The continuous casting process is a semi-

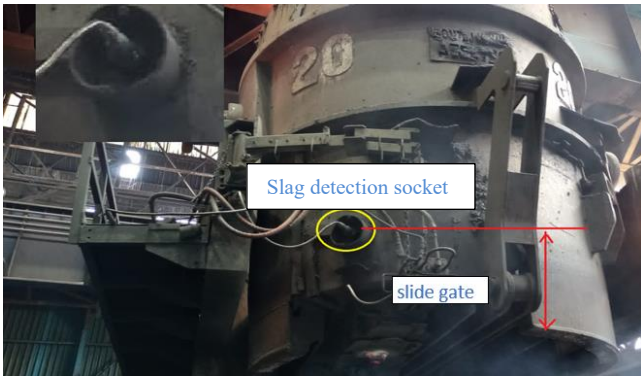
finished production process where solidification is the basic principle by continuing the casting for days with maintaining the occupational health and safety conditions with the optimum machine parameters, which is fundamental for liquid steel. The steel, which is poured from the ladle to the tundish with a minimum amount of slag, is one of the main factors affecting the process efficiency and reliability.

In the continuous casting process, the control of the steel flow from the ladle to the tundish is done by closing the ladle slider manually with traditional methods. This closing process is took place by closing the ladle slider after the casting personnel realizes the boiling on the tundish surface. On the other hand, the slag detection system enables the transfer of liquid steel from the ladle to the tundish, without the need for personnel, thanks to the parts in Figure 1, which are mounted to the ladle. The region where the ladle slag detection system is placed outside the ladle where its shown in Figure 2.



Installed slag detection system

Picture 1 Slag Detection System Equipment (Sensor, Socket)



Picture 2 Ladle-mounted Slag Detection System equipment

The slag detection system, which is placed on the ladles, works with the electromagnetic field principle. An electromagnetic measurement procedure is used to detect the accompanying slag. By means of an arrangement of coils concentrically surrounding the nozzle (figure 1), electrical eddy currents are induced in the melt and their electromagnetic fields are detected.

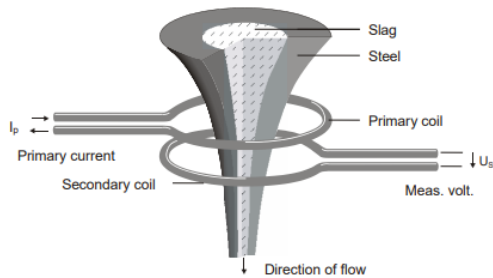


Figure 1 Slag Detection System Equipment (Sensor, Socket)

The system have include current supplier and secondary coil. When the current passes through the first coil an electromagnetic field is generated in the steel flowing through ladle nozzle. The electrical conductivity of slag is lower than that of liquid steel, the ratio is 1:10.000 at 1600°C. Before slag entering stage entire flowing composition is liquid steel having high electrical conductivity wherein larger magnetic field. When slag starts to come through coils, the magnetic field will decrease. The

magnetic field is converted and collected via secondary coil. The deviation in electrical conductivity of the flowing stream means the amount of slag. By online monitoring of magnitude and phase of voltage that is induced in secondary coil, carryover slag can be detected very early. This method is first used by AMEPA company and commonly used in steel plants (Figure 2)

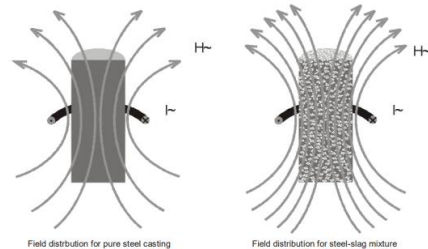


Figure 2 Slag Detection System Magnetic Field

2. Experimental Trials

Tests have been made to examine the effect of the use of the slag detection system on the process. Within the tests, the ladle was not closed when the slag came in the ladles, where the slag detection system was installed, and the ladles were closed manually. In Figure 3, the ladle closing alarm signal from the slag detection system and the ladle closing signal of the automatically closed ladles are given on the same graph.

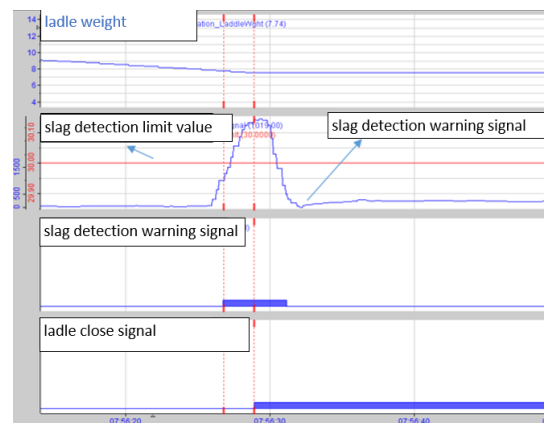


Figure 3 Application of Slag Detection System

In the graph in Figure 3, there are ladle tonnage, slag detection limit and slag detection warning signal, slag detection buzzer warning, ladle closing signal. A test was conducted with the aim of determining the state of the steel in the ladle running out and the slag in the ladle pouring into the tundish. In this context, the slag detection

sensor, which was installed in the area close to the ladle bottom, generated a warning alarm when the steel in the ladle ran out, informing that the ladle should be closed, and the ladle closed automatically in a short time.

However, during long-term tests, it was noticed that as a result of the early arrival of the slag detection signal, the ladle was closed early and the steel remained in the ladle, as the amount of steel escaping into the slag ladle increased. When the data of approximately one thousand castings were examined, it was determined that the slag detection sensor gave an early alarm about 2.14 seconds. For this reason, the ladles have started to be closed manually instead of automatically. In practice, the system detects the slag and gives an alarm, but closing the ladle is still done by the operators. It is not allowed to operate the system in a fully automatic state during routine production times, except for tests.

3. Final Results

3.1 Examination of Escaping Slag From Ladle to Tundish

In the steelmaking process, ladle slag is an integral part of adjusting the steel analysis. The slag is mostly composed of oxidized compounds such as Al_2O_3 , CaO , MgO , SiO_2 and FeO . Ladle slag, which was indispensable in previous plants, creates the opposite situation in terms of human and plant safety, quality and castability in terms of the continuous casting process. If these oxide compounds are transferred to the tundish and mold after the ladle, the amount of slag in the tundish increases at the end of long castings and causes undesirable results in different aspects.

In this direction, in the event that a large amount of slag passes from the ladle to the tundish; First of all, if the ladle slag cannot be caught at the right time, it constantly increases in the tundish and finds a weak area on the tundish surface, it can corrode the tundish wall and cause the liquid steel to come out of this area. However, even if the tundish is not punctured, the casting is finished as soon as the surface becomes flushed, thus shortening the life of the tundish.

The second undesirable aspect of ladle slag concerns castability. The slag passing from the ladle to the tundish and then to the mold affects the behavior of the casting powder in the mold and adversely affects the castability. The negative result in terms of quality is that it is an undesirable substance in the steel due to the oxidized structures in the slag content. Especially FeO and MnO , which are seen as weak oxide structures in the slag, prepare the ground for reoxidation. As the oxidized structures formed as a result of reoxidation are not deformed during rolling, they may cause

defects in the final product. In other words, it becomes a source of inclusions.

3.2 Summary

It is a big problem to determine the closing time of the ladle in the traditional method of closing the ladle. Inexperienced personnel may be undecided and close the ladle early or late. With the dehumanization of existing systems and the transition to an automated system, it is possible to increase efficiency and make more convenient castings in terms of occupational health and safety.

If a large amount of slag is taken from the ladle to the tundish, the possibility of cutting stopper will increase during casting, and the production efficiency will decrease due to strand loss in slab machines due to stopper cutting. In addition, in case of excess amount of slag taken into the tundish; Quality defects from continuous castings such as longitudinal surface crack, transverse surface crack, edge crust and macro inclusion will appear. The slag warning system will also take an active role in preventing the appearance of quality defects.

As it is known, if a large amount of slag is taken into the tundish, the tundish may be punctured, and serious accidents may occur as a result. In the iron and steel industry, near-misses and even fatal accidents have occurred due to tundish punctures. In this context, the contribution of the system in terms of occupational health and safety stands out indisputably.

In its current state, the slag detection system is used in determined crucibles. It has been determined that the production efficiency decreases due to the early closing of the ladle in the ladles where the slag detection system is used. Therefore, the system is not used in automatic mode, but in manual mode. That is, the system gives an alarm, but the ladles are closed manually.

By providing full alarm sensitivity of the system; It will be possible to obtain high quality castings in terms of occupational health and safety by reducing the amount of stopper cutting, increasing the production efficiency and increasing the life of the tundish.

The direct exposure of the slag warning system equipment to the liquid steel temperature increases the maintenance cost of the system. In this context, the slag detection system cable melts and deforms due to the high temperature on the tundish surface. Due to its deformation, the system cannot work from time to time. In this context, cable damage can be reduced by changing the place where the cable will pass. In the example, there is a photograph of the measure applied (Picture 3-4).



Picture 3 Slag Detection System Cable Route



Picture 4 Precaution Taken Against Damage To The Slag Detection System Cable

References

- [1] Tan D, S. Ji, P. Li, X. Pan, Development of vibration style ladle slag detection methods and the key technologies. Science China Technological Sciences, 2010
- [2] Chen D., H. Xiao, Q. Ji, Vibration Style Ladle Slag Detection Method based on Discrete Wavelet Decomposition. IEEE, 2014
- [3] Operating Instructions ESD 100 S, AMEPA,2016



NFMS

Non-Ferrous Metals Symposium

Demir Dışı Metaller
Sempozyumu

PRODUCTION OF FUNCTIONALLY GRADED MATERIALS BASED ON FLG REINFORCED Al-4.5Cu-1.5Mg BY POWDER METALLURGY

Gökçe BORAND, Deniz UZUNSOY

Bursa Technical University
Türkiye

Keywords: Aluminum Alloy, Arc Discharge, Functionally Graded Materials, Graphene, Powder Metallurgy

1. Introduction

Functionally graded materials (FGMs) are innovative materials whose properties varies on their position in line with functional requirements as composition, microstructure and so on throughout the volume. Aluminum (Al) alloys are generally used in many fields because of physical and mechanical properties such as light weight, high specific strength and high specific modulus. Graphene, one of the allotropes of carbon, is preferred as an ideal reinforcement due to its superior mechanical, electrical and thermal properties. In the present study, 0, 0.1, 0.2, 0.3, 0.5, and 0.7 wt% few layered graphene (FLG) which were synthesized by electric arc discharge (EAD) method were reinforced to the Al-Cu-Mg matrix by MA. According to the increased FLG content, FGM was designed as six layers. The effect of FLG content on FGM design is emphasized by investigating of its the structural and mechanical properties.

2. Materials and Methods

The FLG which were synthesized by EAD in our laboratory were added to the Al-Cu-Mg matrix 0, 0.1, 0.2, 0.3, 0.5 and 0.7 wt% by using planetary ball milling. These composite powders were formed by stacking in six layers using a uniaxial manual press at 450 MPa. The green bulk FGM was subjected to sintering at 590°C with a 5°C/min heating and cooling rate for 3 hours under Ar atmosphere. Microstructural observations of the FGM for each layer were determined via an optical microscope. Moreover, the microhardness measurements of the FGM were carried out for 15 seconds with a load of 200 g by taking five measurements from each of the six layers.

3. Conclusion

Functionally graded FLG reinforced Al-Cu-Mg alloy was successfully fabricated by powder metallurgy (P/M). Fig. 1(a) represents a schematic illustration of the design of the FGM. In Fig.1(b), the optical images of each layer for FGM represents how the FLG contents are graded from top to bottom. It is considered that the FLG acts as a barrier between the grains through the gradation of the Al-Cu-Mg FGM. Fig. 1(c) shows the graph with the error bar of microhardness (HV) values of FGM for each layer. According to the increasing FLG content design, a microhardness increase of approximately 45% was observed from the first layer (81 HV) to the last layer (117 HV).



Figure 1: (a) Schematic illustration of the design of the FGM, (b) Grading of FLG on Al-4.5Cu-1.5Mg alloys based from top to bottom, (c) The graph with error bar of microhardness (HV) values of FGM for each layer.

Acknowledgment

This study was financially supported by “The Scientific and Technological Research Council of Turkey (TÜBİTAK)” with the project number of 119M011.



EFFECT OF ANODIZING THICKNESS ON CORROSION BEHAVIOUR OF 2011 ALUMINIUM ALLOY

İlyas Artunç SARI^{1,2}, Görkem ÖZÇELİK¹, Onuralp YÜCEL²

¹ASAS Aluminium, ²Istanbul Technical University
Türkiye

Keywords: 2011, aluminium, lead, bismuth, anodizing, corrosion

Abstract

Elements with low melting points like Bi, Pb, Sn may increase machinability of alloys by precipitating directly at grain boundary with the compound they form. In this way, it is highly preferred in alloy composition where machinability is important. Natural gas valves are the product group in which materials with good machinability are preferred. Valves must have high corrosion resistance due to their intended use. Within this framework, effect of anodizing thickness on corrosion behaviour of 2011 aluminium alloy were investigated in this study. In experimental studies, EN AW 2011 aluminium alloy in T6 heat treatment condition were used as samples. Billets were cast in a prototype direct chill (DC) casting facility and optical emission spectrometry was used to determine the composition of the alloy. Then, homogenization process was carried out. As the next step, billets were extruded with the proper extrusion parameters determined by experimental studies. Produced profiles were cut into small pieces and brought to T6 heat treatment condition by solution heat treatment, quenching and artificial aging processes, respectively. The samples were then anodized at different thicknesses. Anodized and mill finish samples were kept in a corrosive environment. Optical microscope, SEM/EDS were used for characterization.

1. Introduction

Wrought aluminium alloys are classified according to main alloying element they contain. 2xxx series alloys can be strengthened by precipitation hardening. Copper, main alloying element of 2xxx alloys, forms Al₂Cu phase with aluminium and helps hardening mechanism. Frequently magnesium is used as a secondary alloying element [1]. In this way, 2xxx series alloys become a preferred alloy in sectors such as automotive and aerospace where strength and lightness are important. In 2011 alloy, low melting point metals such as bismuth and lead are added to the chemical composition to increase machinability [2].

Aluminium is resistant to corrosion under atmospheric conditions due to natural Al₂O₃ layer it forms [3]. However, intergranular corrosion is very common in 2xxx series

alloys, specifically in T6 condition [4]. Although it has a natural protection layer, aluminium alloys must be coated to prevent corrosion in aggressive environments. For this reason, anodized coating process is usually carried out and it can be performed as technical anodizing (~5 µm) and hard anodizing (~25 µm) [3]. In previous studies, effect of Mg and Ag on the corrosion behavior of 2xxx series alloys has been investigated and it has been observed that presence of appropriate proportions in chemical composition has a positive contribution to corrosion resistance [5].

In this study, effect of anodizing thickness on corrosion behavior of 2011 alloy was investigated. For this purpose, direct chill (DC) casting, homogenization, extrusion, heat treatment and anodizing processes were carried out, respectively. Samples were taken from produced profile and corroded in aggressive corrosion environment. Chemical composition was determined by optical emission spectroscopy (OES), microstructure examinations of the samples were carried out under optical microscope and scanning electron microscopy (SEM), elemental analysis of phases in microstructure was performed with energy-dispersive x-ray spectroscopy (EDS). It has been observed that the technical anodizing thickness is not sufficient for the aforementioned corrosive environment and hard anodizing is required to prevent corrosion.

2. Experimental Procedure

2011 alloy was produced by direct chill casting and then homogenization was performed. Chemical composition analysis of cast billet was carried out with Optical Emission Spectrometry (OES). Chemical composition of billet is shown in Table 1.

Table 1. Chemical composition of casted billet (wt%).

Cu	Bi	Pb	Al
5,01	0,43	0,22	Bal.

After homogenization, profiles were extruded using 62 MN extrusion press. Produced profiles are shown in Figure 1.



Figure 1. 2011 alloy profiles.

Profiles were cut into suitable lengths and heat treated in the T6 condition in lab-scale furnace. Solution heat treatment followed by quench, then artificial aging is the basic route of T6 condition. After heat treatment, the samples were anodized in different thickness. As shown in Figure 2, non-anodized, 5 and 25 μm anodized coated samples were prepared.

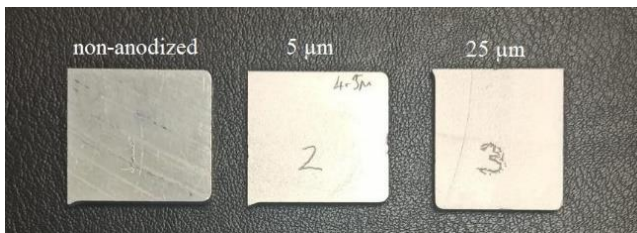


Figure 2. Non-anodized and coated samples.

In order to provide a corrosive environment, samples were taken into a solution containing 1 liter of water, 30 g of NaCl and 10 mL of HCl. Corroded specimens after waiting 24 hours are shown in Figure 3.

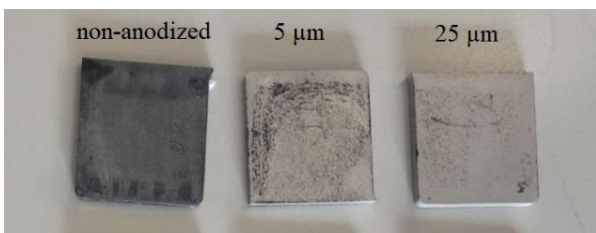


Figure 3. Corroded samples.

In order to carry out the metallographic examination, samples were first taken into bakelite. After that, samples were sanded with 2400 grit sandpaper starting from low grit. Afterwards, polishing process was performed and samples have become ready for optical examination. Polishing process is shown in Figure 4.

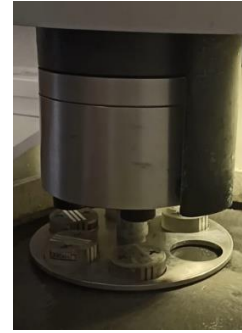


Figure 4. Polishing process

Lastly, microstructure examination of the samples was carried out on Zeiss Scope A1 optical microscope, and SEM/EDS analysis were carried out on ZEISS EVO MA15 Scanning Electron Microscope.

3. Results

Results obtained in optical microscope examinations are shown in Figure 5, Figure 6 and Figure 7.

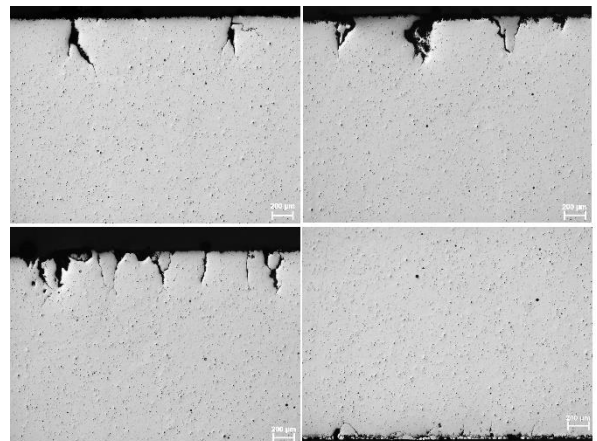


Figure 5. Corroded areas on non-anodized sample (Magnification: 5x).

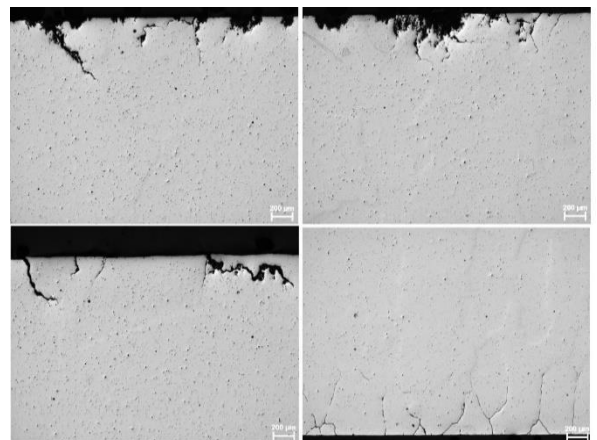


Figure 6. Corroded areas on technical anodized (5 μm) sample (Magnification: 5x).

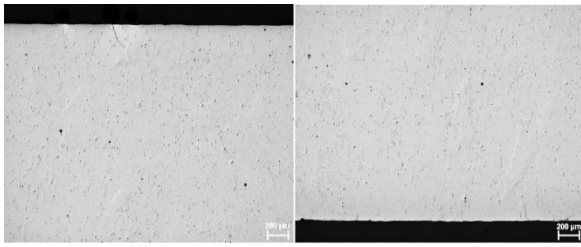


Figure 7. Corroded areas on hard anodized (25 μm) sample (Magnification: 5x).

Deepest corrosion length was measured as 562 μm in non-anodized sample. It was measured 505 μm in technical anodized sample and 201 μm in hard anodized one.

Optical examinations made under 5x magnification were further investigated under Scanning Electron Microscopy (SEM) and Energy-dispersive X-ray Spectroscopy (EDS) analysis was performed on the corroded areas. SEM images are shown in Figure 8, Figure 9 and Figure 10.

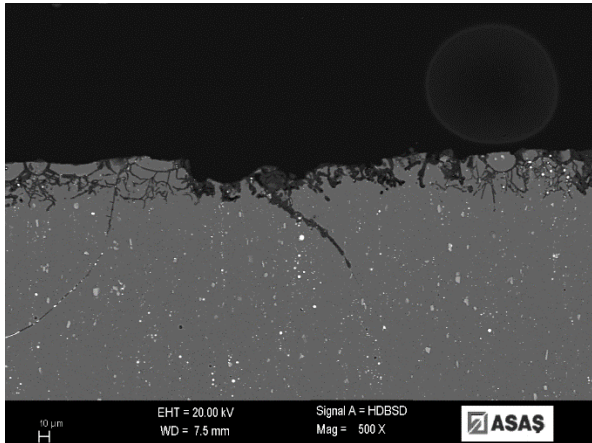


Figure 8. SEM image of non-anodized sample.

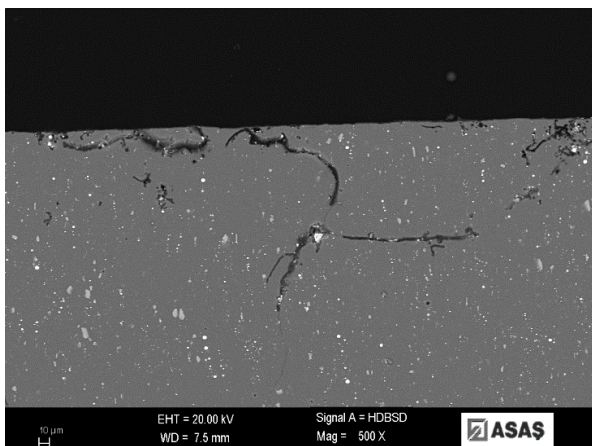


Figure 9. SEM image of technical anodized (5 μm) sample.

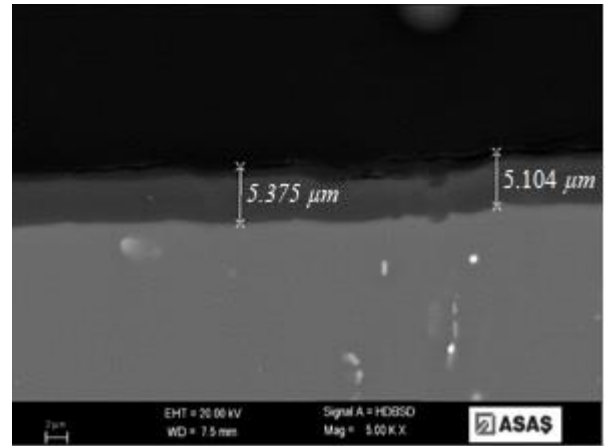


Figure 10. SEM image of hard anodized (25 μm) sample.

SEM examination of the hard anodized sample shows that the anodized layer is still preserved in most of the sample.

EDS analysis was performed on the deepest corrosion region of non-anodized sample. Analyzed areas are shown in Figure 11.

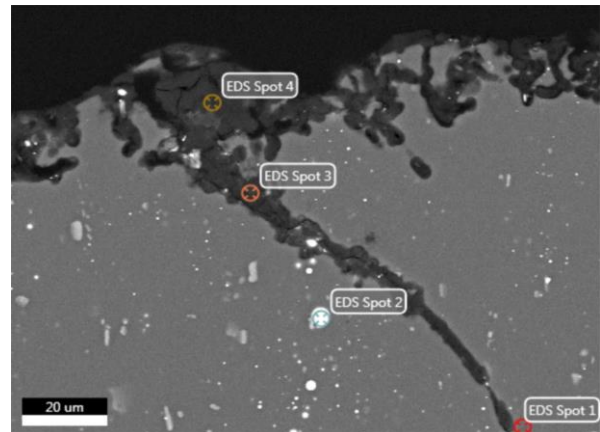


Figure 11. Areas where EDS analysis was performed.

Graphs obtained after EDS analysis are shown in Figure 12, Figure 13, Figure 14 and Figure 15.

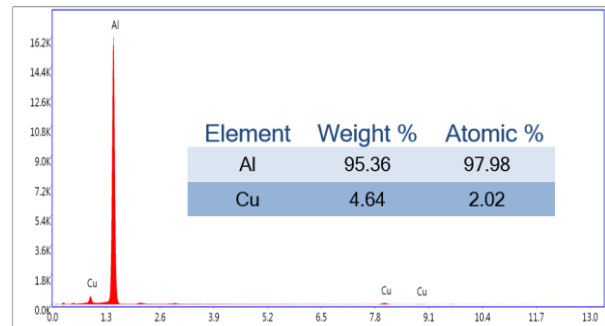


Figure 12. EDS Analysis - Spot 1.

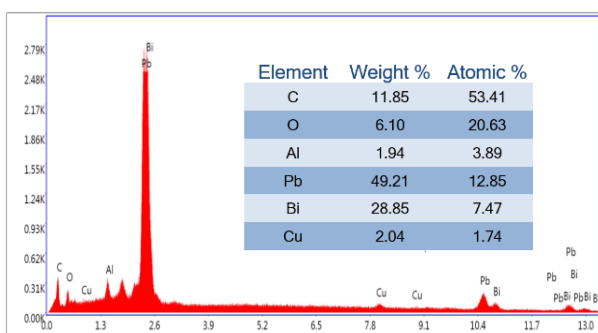


Figure 13. EDS Analysis - Spot 2.

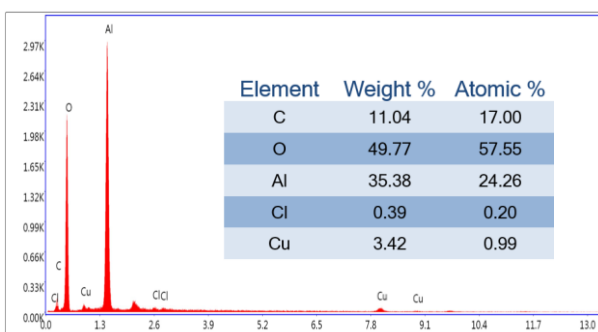


Figure 14. EDS Analysis - Spot 3.

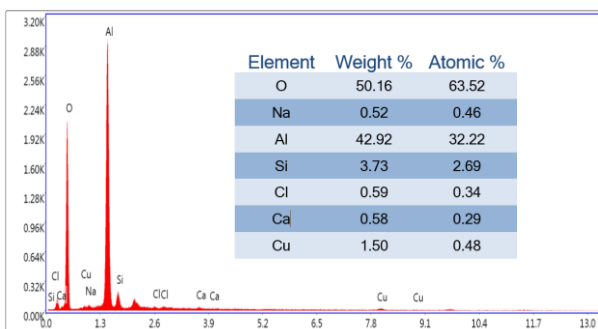


Figure 15. EDS Analysis - Spot 4.

4. Conclusion

The 2011 billets produced by the direct chill casting method were homogenized and then extruded. After extrusion, 2011 alloy profiles heat treated to get T6 condition. As the next step, the profiles were anodized in different thicknesses and then corroded in aggressive corrosive environment.

Optical emission spectrometry (OES) results show that the chemical composition obtained is within the limits of the 2011 alloy in EN 573-3 standard.

Cu, Pb and Bi elements observed in EDS analysis are due to chemical composition of 2011 alloy and Na, Cl is because of corrosion solution.

As a result of microstructure analysis, it was observed that the deepest corrosion in non-anodized sample is close to technical anodized sample. It shows that technical anodizing is not adequate for related corrosive environment. However, the maintenance of anodized layer in hard anodized sample and shallow corrosion depth indicate that hard anodizing can be used to protect 2011 alloy from corrosion.

Corrosion behavior of 2011 alloy in different corrosive environments can be investigated in future studies.

Acknowledgement

It's a great honor to thank Mrs. Esra Kaymak Aksu and Mr. Barış Akın for their support during the anodizing. Special thanks to Mr. Mustafa Serkan Özcan for his support in metallographic preparation.

References

- [1] Dixon, B. (n.d.) Extrusion of 2xxx and 7xxx alloys.
- [2] Davies, J.R., Aluminium & Aluminium Alloys, ASM, Materials Park, Ohio, 1993,
- [3] American Society for Metals. (1978). Asm Metals Handbook: Volume 13 corrosion.
- [4] Fu, J., & Cui, K. (2022). Effect of mn content on the microstructure and corrosion resistance of Al-Cu-Mg-Mn Alloys. Journal of Alloys and Compounds, 896, 162903. <https://doi.org/10.1016/j.jallcom.2021.162903>
- [5] Wang, J., Liu, Z., Bai, S., Cao, J., Zhao, J., & Zeng, D. (2020). Combined effect of Ag and MG additions on localized corrosion behavior of Al-Cu alloys with high CU content. Journal of Materials Engineering and Performance, 29(9), 6108–6117. <https://doi.org/10.1007/s11665-020-05072-6>

INVESTIGATION AND FE ANALYSIS OF EARING AMOUNT AND DIRECTION OF DEEP DRAWING PROCESS OF AN ALUMINIUM SHEET UNDER VARIOUS CONDITION

Melih ÇAYLAK, Koray DÜNDAR, Yusuf ÖZÇETİN, Görkem ÖZÇELİK, Ali ULUS

ASAŞ Alüminyum
Türkiye

Keywords: 1050, aluminium, deep drawing, finite element method, anisotropy, earing, formability

Abstract

Earing problem is the most known problem in the cup drawing process for sheet metals due to the anisotropic nature of blank materials. In this study, earing problem was investigated in deep drawing of cylindrical cups and punch from aluminium sheets both experimentally and numerically. For experimental studies, EN AW 1050-H0 aluminium sheet was determined as forming test material. Experimental sample sheets were produced by TRC (Twin Roll Casting) method. Two stage rolling process was applied to material during manufacturing process. At the last stage of manufacturing process final heat treatment process carried out. In order to observe mechanical properties and formability behavior of test specimen, tensile tests were performed taking cognizance of rolling direction. Several deep drawing tests were conducted to investigate earing amount and direction of the material with different sheet metal thickness and treatment process. Then, finite element studies were carried out with a finite element software. Hill anisotropic yield criterion was used during the FE studies. Experimental and numerical solutions were compared to examine the performance of material properties and yield criterion.

1. Introduction

According to the developments in the vehicle industry, aluminum alloys have started to attract attention thanks to their lightweight and strength-to-weight ratios [1]. When it comes to modelling aluminum alloys in finite element simulations, complex anisotropic behavior of these alloys came with some difficulties. In order to overcome this hardship, diverse anisotropic yield criteria have been composed in the literature. In 1948, Hill proposed a new criterion [2]. In this study, r-based Hill yield criteria was used. Experimental and Finite element studies have been carried out.

Deep drawing is the one of the popular manufacturing techniques. The deep drawing process is based on the production of engineered parts of specific shapes through large plastic deformation of flat metal sheets. This plastic

deformation exerts an external force on a metal sheet. This external force must be large enough to place the material in the plastic region and ensure that the metal part does not flex back or become elastically deformed again after the external force has displaced it. The final quality of the parts produced by this process depends on the final wall thickness and being wrinkle-free and unbreakable [3]. Fig.1 represents the schematic representation of the deep drawing process.

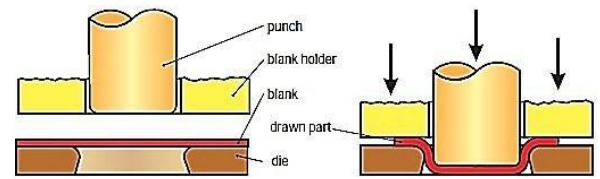


Fig. 1: Deep Drawing Process [4]

There are several studies in the literature. Ouchaâla et. al. investigated earing amount of deep drawn aluminum alloy is named after AA1050. Finite element method and r-based Hill yield criteria is used in the study. It is declared that, FEM results and published results are in conformity [5]. Sener et. al. investigated the effect of blank thickness and ear formation in cup drawing process with FE analysis. Yld91 yield criterion is used to define anisotropic behavior of material. AA 2090-T3 aluminum material was used as test material. It is concluded that Yld91 yield criterion could sufficiently define the anisotropic behavior of AA2090-T3 alloy and the computed earing profiles and thickness strain distributions from the simulations were compatible with the experiment [1]. Patel et al. conducted similar work about earing defect during deep drawing process. EN10130FeP06 mild steel sheet of 1mm thickness used as test material. Several FE analyses were composed and it is declared that deep drawing process can be effectively understood with FE simulation through accurate prediction of % earing height, contact force and maximum thickness [6]. Aksen et. al. performed several

FE simulations to predict hole expansion process. An AA6016 aluminum alloy was used as test material and Hill48 yield criteria was used as yield criterion. Experimental tests and Fe simulations were compared and it was concluded that, test results and FE results are consistent [7].

2. Description of Model

In the present study, Marc software is used as finite element software. Finite element model was created with fully integrated shell elements. Tool geometries are based on standard test tools. Fig.1 indicates basic dimensions of test tools.

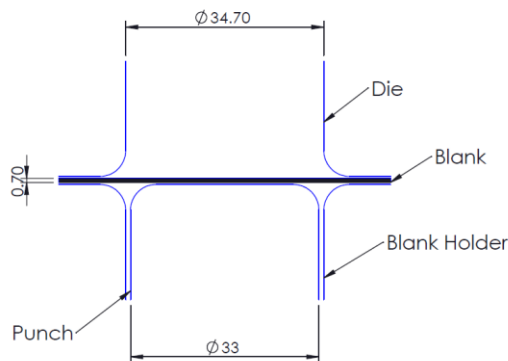


Fig 1: Basic dimensions of tools

Tools were simulated as rigid bodies in FE simulations. The die was fixed fully at its initial position. Punch moved through to die with 2250 N punch force with 25 mm displacement. Segment to segment contact algorithm was conducted for defining contact regions. Rolling direction of material was defined on FE model. Fig 2. indicates the FE model. Model was prepared as one fourth model thanks to symmetrical geometry of model.

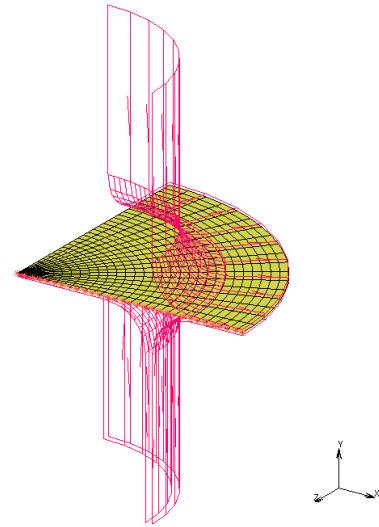


Fig 2: FE Model

Hill yield criteria was used to define anisotropic behavior of material. A yield function was proposed by Hill [2] was written in Eq. 1. In the equation, F, G, H, L, M and N are anisotropy parameters as known as Lankford parameters.

$$2f = F(\sigma_{yy} - \sigma_{zz})^2 + G(\sigma_{zz} - \sigma_{xx})^2 + H(\sigma_{xx} - \sigma_{yy})^2 + 2L\tau_{yz}^2 + 2M\tau_{zx}^2 + 2N\tau_{xy}^2 = 1 \quad [1]$$

In this study, anisotropy parameters were calculated according to yield stress ratios. Eq.2 determines the yield stress ratios.

$$F = \frac{1}{2} \left(\frac{1}{R_{22}^2} + \frac{1}{R_{33}^2} - \frac{1}{R_{11}^2} \right), G = \frac{1}{2} \left(\frac{1}{R_{11}^2} + \frac{1}{R_{33}^2} - \frac{1}{R_{22}^2} \right), H = \frac{1}{2} \left(\frac{1}{R_{11}^2} + \frac{1}{R_{22}^2} - \frac{1}{R_{33}^2} \right), \quad [2]$$

3. Material Description and Modelling

An AA1050 – H0 aluminum alloy was used as test material. This material was manufactured with Twin Roll Casting method. Continuous casting of aluminum-like metals is commonly accomplished using the twin-roll casting method. This method; In addition to the benefits such as good surface quality, no need for an additional hot rolling process and production of materials close to the final product, there are also certain disadvantages. Energy and production costs are dramatically reduced in the twin-roll method. Low yield rates and limited castable alloy scale are among its disadvantages [8]. In the twin roll casting method; solidification and

deformation together. In this method, the molten liquid metal is transferred between two counter-rotating and continuously cooled rollers with water. Solidification begins as soon as the molten metal comes into contact with the rollers. The thickness of the solidified metal decreases as the metal passes through the rollers [9]. In this study, rolling direction due to TRC method was considered to determine anisotropic behavior of material. At the last stage of manufacturing process final heat treatment process carried out.

Mechanical properties of material were shown in Table 1, with respect to rolling direction.

Table 1: Mechanical Properties of AA1050 H0

Direction	Thickness (mm)	Width (mm)	Yield Stress (MPa)	Tensile Stress (MPa)
0	0.69	12.42	37	73
45	0.69	12.42	38	77
90	0.69	12.42	35	73

Yield stress ratios of AA1050-H0 in different direction were shown in Table 2.

Table 2: Yield Stress Ratios

Material	r0	r45	r90
AA1050 - H0	0.724	0.465	0.94

Lankford parameters of material is given Table 3.

Table 3: Lankford Parameters of AA1050 H0

Material	F	G	H	L	M	N
AA1050 - H0	0.4468	0.58	0.4199	1.5	1.5	0.9908

4. Results

As a result of experimental tests, earing height is measured at 0°, 45°, 90° and 135° of rolling direction of blank. Table 4 indicates earing amount of experimental test results.

Table 4: Earing amount of experimental test results

Rolling Direction [°]	Earing Amount [mm]
0	19.08
45	17.44
90	18.77
135	17.9

Experimental results and FEM results were compared. Fig. 3 indicates comparison of FEM and experimental results. Experimental data was obtained from formed specimen with electronic measurement tools. Fig 4 represents experimental and FEM results.

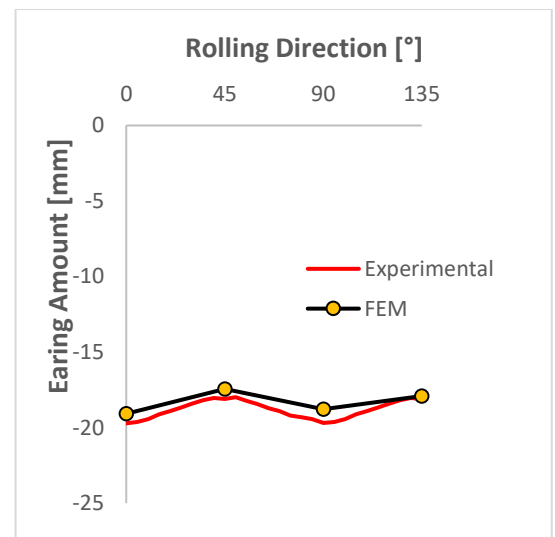


Fig 3: Measured earing amount

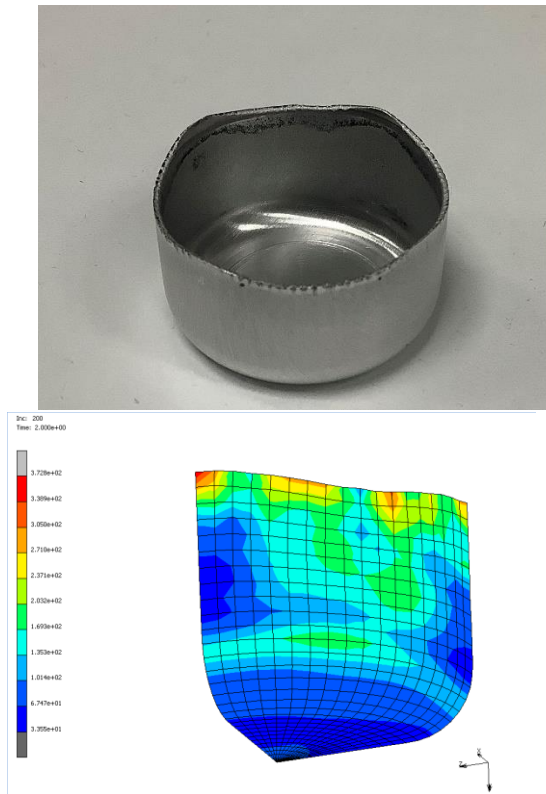


Fig 4: Presentation of experimental results and FEM results

It is shown that, experimental results and FEM results are very close with each other. But there are some differences between both results. Difference amount between results are given in Table 5.

Rolling Direction [°]	Earing Amount - Experimental [mm]	Earing Amount - FEM [mm]	Difference Amount (%)
0	19.08	19.71	3.22
45	17.44	18.10	3.63
90	18.77	19.70	4.70
135	17.9	18.10	1.09

Table 5: Solution comparison

5. Conclusion

In the present study, AA1050 H0 aluminum alloy was modelled with FEM and deep drawing test was performed. Hill yield criteria was used as yield criterion. It is seen that; FEM results and experimental results are very close. Used FE model and yield criteria predicted earring amount with

accuracy. For more accurate results, some results should be investigated such as thickness difference and stress concentration.

References

[1] Şener, B. , Akşen, T. A. & Fırat, M. (2021). On the Effect of Through-Thickness Integration for the Blank Thickness and Ear Formation in Cup Drawing FE Analysis . *European Mechanical Science* , 5 (2) , 51-55 . DOI: 10.26701/ems.781175

[2] Hill, R. (1948). A theory of the yielding and plastic flow of anisotropic metals. *Proceedings of the Royal Society of London Series A Mathematical and Physical Sciences*, 193: 281-297. doi: 10.1098/rspa.1948.0045

[3] Y. Özçetin, 3005 ALÜMİNYUM ALAŞIMI LEVHALARIN DERİN ÇEKİLME KABİLİYETİNİN ARAŞTIRILMASI

[4] J. M. Mark Clogan, «Deep drawing process: analysis and experiment,» *Journal of Materials Processing Technology*, vol. 132(1), pp. 35-41, 2003.

[5] BOUCHAËLA, K., ESSADIQI, E., MADA, M., GHANAMEH, M. F., FAQIR, M., MEZIANE, M. (2018). Prediction of earring in cylindrical deep drawing of aluminum alloys using Finite Element Analysis. *International Journal of Mechanical and Production Engineering*, 6(10).

[6] Patel, R., Dave, H., & Raval, H. (2015). Study of earring defect during deep drawing process with finite element simulation. *Key Engineering Materials*, 639, 91–98. <https://doi.org/10.4028/www.scientific.net/kem.639.91>

[7] Akşen, T. A., & Fırat, M. (2021). Blank thinning predictions of an aluminum alloy in hole expansion process using finite element method. *SN Applied Sciences*, 3(3). <https://doi.org/10.1007/s42452-021-04336-7>

[8] Alper G, Alüminyum Sürekli Döküm Yöntemi ile Üretilmiş 5052-5182 Alüminyum Alaşımlarının Şekillendirilebilirlik Kabiliyetinin Belirlenmesi

[9] Sun, N., Patterson, B. R., Suni, J. P., Simielli, E. A., Weiland, H., & Allard, L. F. (2006). Microstructural evolution in twin roll cast AA3105 during homogenization. *Materials Science and Engineering: A*, 416 (1-2), 232- 239. doi:10.1016/j.msea.2005.10.018

REDUCING ENERGY CONSUMPTION DURING HEAT TREATMENT OF CAST ALUMINUM ALLOYS – OPTIMIZATION OF PROCESS PARAMETERS THROUGH CALPHAD

Emre ÇINKILIÇ¹, Esra DOKUMACI ALKAN², Bilge Nur KAVALCI², Şevval ANAVATAN²,
Başak YAŞAR², Gizem AMMAS²

¹Hakkari University, ²Dokuz Eylül University
Türkiye

Keywords: Al-Alloys, Pandat, Heat Treatment

Abstract

In this study, the effect of solution heat treatment temperature and time on the artificial aging response of an EN233 aluminum alloy is investigated. CALculation of PHase Diagrams analysis using Pandat from CompuTherm LLC is performed to evaluate the phase equilibria for different solution treatment conditions. Samples extracted from cylinder head castings provided by an industry partner are subjected to different solution heat treatment conditions that are selected by CALPHAD analysis. The effect of solution treatment conditions on artificial aging response and energy consumption are evaluated.

1. Introduction

The mechanical properties of cast aluminum alloys are strongly influenced by the presence of precipitates dispersed in the microstructure. Precipitation hardening allows engineers to tune the mechanical properties of aluminum alloys by tailoring the alloy microstructure. The energy consumption associated with the heat treatment procedure, especially the high temperature solution treatment step, increases the carbon footprint of the produced aluminum cast components.

2. Materials and Methods

In this study, cylinder heads made of EN 233 (AlSi10Mg(Cu)) alloy were used. Cylinder heads are produced by casting followed by T6 heat treatment. Firstly, the microstructural properties were studied by using an optical microscope. The solution treatments and aging processes were carried out at different durations and temperatures. The phase equilibrium diagram given in Figure 1 was used to determine temperatures of the solution treatment. After the solution treatment and aging process, the mechanical properties were determined by Vickers microhardness tests.

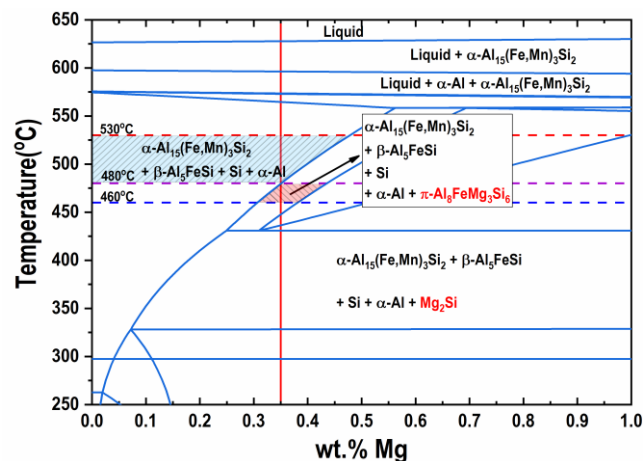


Figure 1. The phase diagram of Al-9.55Si-xMg-0.59Fe-0.47Mn-0.11Cu system (EN 233).

3. Conclusions

In addition to primary α -Al dendrites, eutectic Si particles, π -Al₈FeMg₃Si₆ and Mg₂Si phases are seen in the as-cast structure. In heat-treated samples, Si particles become spherical, α -Al₁₅(Fe,Mn)₃Si₂ phase precipitates into the structure at 490 °C, and β -Al₅FeSi phase also precipitates into the structure at 520 °C.

Acknowledgment

The authors are pleased to acknowledge the sample support for this research from NEMAK Izmir Döküm Sanayi A.S.



INVESTIGATION OF MICROSTRUCTURE OF HOMOGENIZED ALUMINUM ALLOYS IN THE BATCH HOMOGENIZATION PLANT AND CONTINUOUS HOMOGENIZATION PLANT

Murat DOĞAN^{1,2}, Deniz KAVRAR ÜRK^{2,3}, Büşra GEDİK^{4,5}, Gökçen GÖKÇE²

¹Yıldız Technical University, ²Sistem Teknik, ³Istanbul Technical University, ⁴Şeyh Edebalı University, ⁵Arslan Aluminium
Türkiye

Keywords: 6063 alloy, homogenization, microstructure evaluation

Abstract

Vertical direct chill casting (VDC) is an advanced method for producing wrought aluminium alloys in billets and slabs. However, as-casted aluminium alloys have low formability due to some microstructure inhomogeneities such as micro-segregation, grain boundary segregation, low melting point eutectics and brittle intermetallic compounds. That's why, homogenization process has to be performed cast billets to partly or completely eliminate in the structure. After homogenization process, cast billets can be easily formable by extrusion process. Commercially, there are two different types of homogenization plants in the modern cast house: batch-type homogenization and continuous homogenization plant. For 6xxx series aluminium alloys, continuous homogenization process is most preferable by most of customers because of lowest labour costs, lowest energy consumption and straightness of billets. On the other hand, the batch-type homogenization process is favoured for the large billet diameter and some special aluminium alloys having long holding times. The principle aim of this study is to investigate the comparison of microstructures of homogenized billets in the batch and continuous homogenization process. These two plants were installed as well by Sistem Teknik Industrial Furnace LTD. The results were used in the development of two facilities in terms of microstructure and energy consumption.

1. Introduction

The major goal of homogenization heat treatment after casting is to eliminate the effects of dendritic segregation and the dissolution of coarse eutectic intermetallic phases, which reduce the fracture toughness of the aluminum alloys. In this way, β -AlFeSi can be transformed to more workable α -AlFeSi particles with homogenization process [1, 2].

The cooling rate in homogenization process has significant impact on the ductility of aluminum alloys [3]. In homogenization process if the cooling rate is slow, the material becomes more ductile. Furthermore, homogenization also has beneficial impact. Alloying element micro segregation is decreased, and soluble precipitates are returned to solid solution thanks to homogenization. As α -AlFeSi has lower Fe:Si ratio, the concentration of Si in solid solution increases as a result of the phase transition. As a result, the Al matrix, which has Mg in solution, will precipitate a greater volume fraction of Mg₂Si depending on cooling conditions. In this study, casted 6063 alloys in same batch were subjected to homogenization process in the batch and continuous homogenization. Then, microstructures of homogenized billets were compared with each other with regard to homogenization rate and energy consumption.

2. Materials and Methods

Table 1 shows the chemical composition of the 6063-alloy sample. Thermo Scientific's ARL 3460 optical emission spectrometer was used to determine the chemical composition of alloys. The alloys are supplied in billet form from direct chill (DC) casting. After DC casting, continuous and batch-type homogenization furnaces were used to homogenize the billets. The samples were ground from 240 till 2000 grade, polished, and finally etched. Metallographic examinations were carried out with an optical microscope.

Table 1. Chemical analysis of the Material (wt%)

Fe	Si	Cu	Mn	Zn	Mg
0.19	0.42	0.01	0.04	0.02	0.50

3. Conclusion

β -AlFeSi to α -AlFeSi transition rate observed 92.22% for a 6-inch diameter billet with microstructure analysis after continuous homogenization. For batch type homogenization, this rate is revealed as only 81.28%. The total heating and soaking time of a continuous homogenization furnace are shorter 204 minutes than a batch homogenization furnace. For one cycle, it provides 80Nm³ energy saving.

Acknowledgment

The authors would like to thank Mr. Uğur Doma from ARSLAN Alüminyum AŞ. and all R&D researchers of Sistem Teknik Industrial Furnace LTD. for their supports.

References (if needed)

- [1] G. Mrówka-Nowotnik and J. Sieniawski, Journal of Materials Processing Technology, 162–163 (2005) 367–372.
- [2] K. B. S. Couto, S. R. Claves, Materials Science and Technology, 21(2) (2005) 263–268.
- [3] M. B. Karamış, I. Halici, Materials Letters, 61(4-5) (2007) 944–948.



PARAMETRIC APPROACH OF A NOVEL HEAT TREATMENT ON Al-Mg-Si ALLOYS: RETROGRESSION AND RE-AGING

Almina DEVECİ¹, Nilgün BÖYÜKULUSOY¹, Mehmet Buğra GÜNER^{1,3},
Görkem ÖZÇELİK^{2,3}, Rıdvan GECÜ¹

¹Yıldız Technical University, ²Sakarya University of Applied Sciences, ³ASAŞ Aluminum Türkiye

Abstract

The method of rapidly heat-treating locally or along their length at various tempers using induction heating methods to return or approach their highly ductile state is termed retrogression. The process, which is a sequential combination of retrogression and re-aging heat treatments, which provides an increase in corrosion resistance with a relative loss of mechanical properties, is called RRA. With their good weldability, good strength/weight ratio, and excellent formability, 6XXX series aluminum alloys appeal to many sectors but are mostly used in building sector applications. The improvement provided by the RRA process in corrosion resistance and the effective gains that this improvement will provide in the construction sector, where 6XXX series alloys are frequently used, have been the objectives for the results of the experimental process in the study. In this context, an experimental setup was prepared in which EN AW 6063 (Al - (0.75-0.8%) Mg₂Si) alloys were used as samples in order to investigate the effect of aging parameters for the RRA application. Various times and temperatures were chosen for re-aging under constant retrogression parameters. The microstructural investigation, mechanical testing, and conductivity measurements have been done to gain knowledge and build links about precipitation characteristics of extruded Al-Mg-Si alloy over mechanical and electrical properties by changing microstructure.

Keywords: Retrogression and re-aging, Al-Mg-Si Alloys, extrusion

Introduction

Aluminum alloys have a wide range of industrial use with their good weldability, corrosion resistance, and good strength/weight ratios. Aluminum alloys, which are divided into two groups casting and forging according to their processing processes, can respond to many different thermal processes depending on their phase solubility [1].

6XXX series Al-Mg-Si alloys, which are frequently preferred in the extrusion industry and can be treated with aging, have an ever-increasing variety of uses

with versatile applications in many fields from the construction industry to the maritime, from the automotive to the aviation industry. While the majority of aluminum alloys produced by extrusion are 6XXX series alloys, AA6063 alloys, which have been examined experimentally in this study for their good surface finish properties, coating ability, and mechanical properties that can be improved by heat treatment; are the most used alloys in the 6XXX series [1] [2].

The basic components of the AA6063 alloy are Si and Mg, and these elements form the Mg₂Si intermetallic compound in the structure, and the stoichiometric Mg:Si ratio in this compound is 1.73. The numbers, crystal structures, and precipitate sizes of these metastable precipitate phases formed in the phase transitions of Al-Mg-Si alloys play a role in the change of strength values such as hardness and strength. The retrogression and re-aging (RRA) heat treatment, which is the basis of the study, is aimed to improve the corrosive properties of the alloy by dissolving these precipitated phases in the continuous network structure at the grain boundaries that cause intergranular corrosion [3] [4] [5].

In this study, various times and temperatures were chosen for re-aging under constant retrogression parameters, and mechanical, electrical, and corrosive properties of AA6063 specimens were investigated.

Experimental

In this study, 80*80*2 millimeters and 20 centimeters long EN AW 6063 (Al - (0.75-0.8%) Mg₂Si) alloy was retrogressed at 200°C for 10 minutes, and then the samples were re-aged at 160-180-200 °C for 4-8 hours. Parameters was given in Table 1.

For the determination of mechanical and physical properties and corrosion values of heat-treated samples, tensile test under DIN EN ISO 6892-1 standard conditions at a pulling speed of 10 mm/min in the 0° direction, hardness test under ASTM E10 - EN ISO 6506 standard conditions with 62.5 kP load and 2.5 mm ball diameter tip, corrosion test under

ISO 11846 (Method B) standard conditions with 30 g of NaCl, 960 mg of distilled water, 10 ml of HCl-containing solution for 24-72 hours, DIN EN Conductivity test was carried out under 2004-1 standard conditions. For microstructure investigations, the Sanding process was carried out using 600, 800, 1000, and 1200 mesh SiC sandpapers, then the samples were polished with diamond paste. After polishing, the solution was prepared with 85 ml of distilled water, 10 ml of H₂SO₄, and 5 ml of HF, and the etching process was applied between 1-4 minutes, depending on the heat treatment condition. The macro/microstructure properties of the samples were observed under an optical microscope.

Table 1. RRA heat treatment parameters

Initial Status	Retrossion		Re-Ageing	
	Temperature	Time	Temperature	Time
T6	200 °C	10 min.	160 - 180 - 200 °C	4,8 h

Results and Discussion

During the applied re-aging process, the precipitates dispersed in the matrix cause the purification of the matrix structure. With the increasing RRA time and temperature, the precipitates formed in the structure reduce the cohesion in the lattice, thus a decrease in the lattice stress occurs. The decrease in the lattice stress causes an increase in the electrical conductivity values. Figure 1 shows the change graph of conductivity values according to RRA parameters.

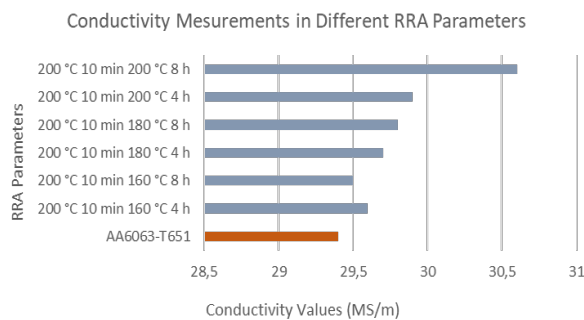


Figure 1. Conductivity measurement results of samples with different re-aging parameters

As seen in Figure 2, with the high RRA values applied, a decrease in hardness values is observed as new precipitates are formed, and the volume ratios of existing precipitates increase.

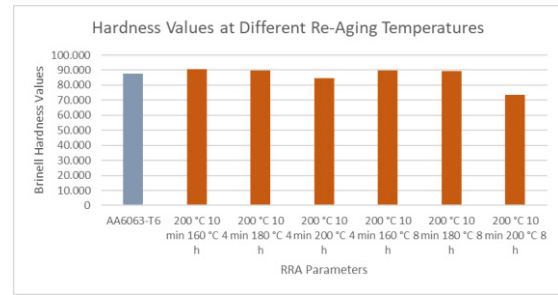
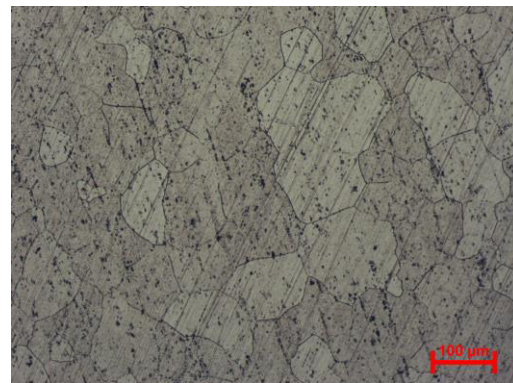
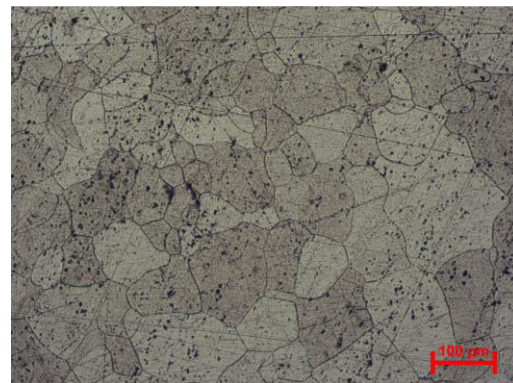


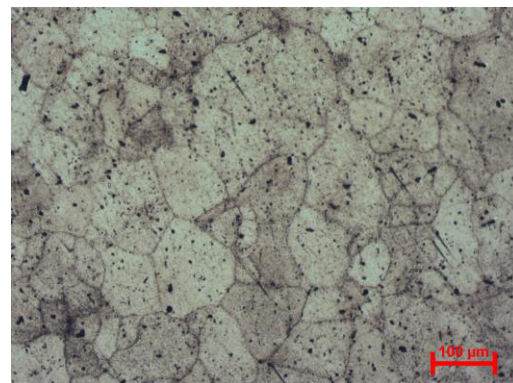
Figure 2. Hardness values at different re-aging temperatures



(a)

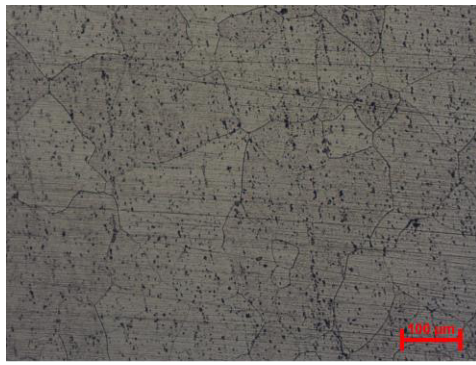


(b)

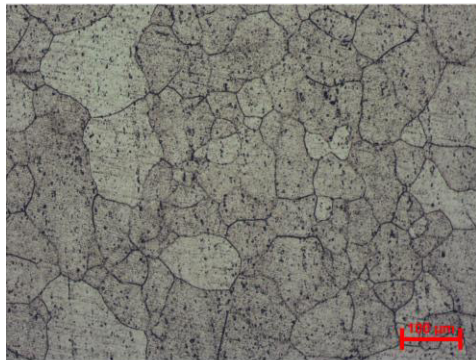


(c)

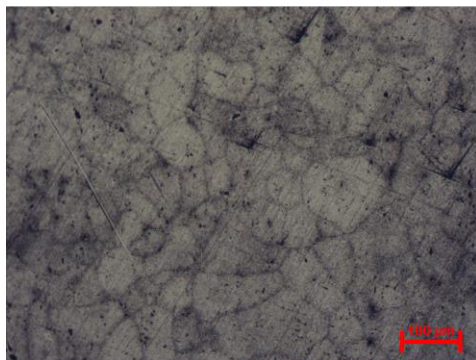
Figure 3. 200 °C 10 min. Retrogression 160 °C 4 hours Re-Aging (a), 200 °C 10 min. Retrogression, 180 °C 4 hours Re-Aging (b), 200 °C 10 min. Retrogression 200 °C 4 hours Re-Aging (c)



(a)



(b)

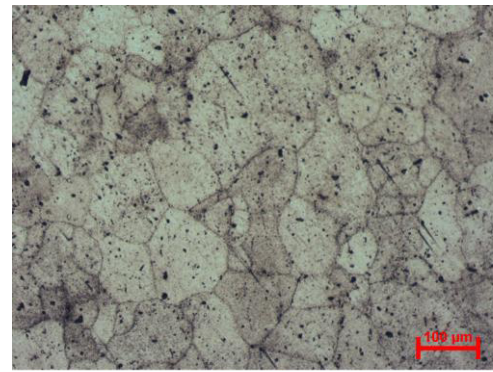


(c)

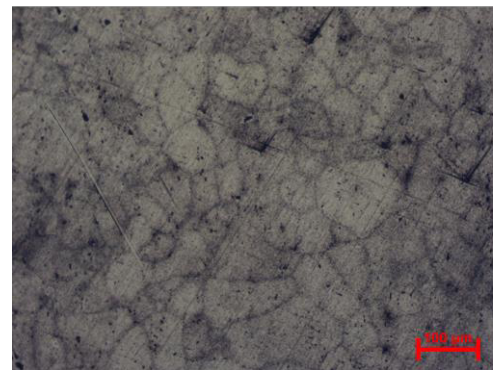
Figure 4. 200 °C 10 min. Retrogression 160 °C 8 hours Re-Aging (a), 200 °C 10 min. Retrogression, 180 °C 8 hours Re-Aging (b), 200 °C 10 min. Retrogression 200 °C 8 hours Re-Aging (c)

As can be seen in Figures 3 and 4, the grain boundaries are fine, and a coarse grained structure is observed in the sample treated at low re-aging temperature. The coarsening of grain boundaries and precipitates and reduction in grain sizes were observed in the sample where the processing temperature increased.

From the samples shown in Figure 5, it was observed that the dimensions of the precipitates formed in the matrix in the microstructure with a long re-aging time increased, and their homogeneous distribution in the matrix disappeared.



(a)



(b)

Figure 5. 200 °C 10 min. Retrogression 200 °C 4 hours Re-Aging (a), 200 °C 10 min. Retrogression, 200 °C 8 hours Re-Aging (b)

Conclusion

- ✓ According to the test data, the highest hardness value was obtained after aging at 160 °C - 8 hours, and a decrease in hardness values was observed with increasing heat treatment time.
- ✓ According to the tensile test results, a decrease in tensile strength was observed with increasing re-aging temperature and time.
- ✓ The yield strength values decreased with increasing temperature and the highest yield strength was obtained by re-aging at 160 °C - 4 hours.
- ✓ It was observed that the highest weight loss was in the 200 °C - 4 s re-aging parameter in the corrosion weight tests performed by keeping it in solution for 24 hours, and the highest weight loss was observed in the 180 °C - 4s parameter in the test applied by keeping it in solution for 72 hours. Therefore, the lowest corrosion resistance values were obtained in these parameters.
- ✓ It was determined that all conductivity values measured after RRA were higher than the sample in T6 state.

References

- [1] P. Mukhopadhyay, “Alloy Designation, Processing, and Use of AA6XXX Series Aluminium Alloys”, *ISRN Metall.*, c. 2012, ss. 1–15, Nis. 2012, doi: 10.5402/2012/165082.
- [2] H. H. Uğurlu, “Titanyum İle Alüminyum-magnezyum-silisyum Alaşımlarının Yapı Kontrolü”, İstanbul Teknik Üniversitesi, İstanbul, 2009.
- [3] H. Aydın, M. Şendeniz, ve A. H. Demirci, “EKSTRÜZYON ÖNCESİ VE SONRASI UYGULANAN ISIL İŞLEMLERİN AA 6063 ALÜMİNYUM ALAŞIMININ MEKANİK ÖZELLİKLERİ ÜZERİNDEKİ ETKİSİ”, *Uludağ Üniversitesi Mühendislik-Mimarlık Fakültesi Derg.*, c. 14, sayı 2, ss. 1–10, 2009.
- [4] M. Türkmen vd., “Al-Mg-Si ALAŞIMININ MİKROYAPI VE MEKANİK ÖZELLİKLERİNE SOĞUMA HIZININ ETKİSİ THE EFFECT OF COOLING RATE ON MICROSTRUCTURE AND MECHANICAL PROPERTIES OF Al-Mg-Si (6063) ALLOY”, c. 21, sayı 1, ss. 11–14, 2015, doi: 10.5505/pajes.2014.30075.
- [5] K. Turbalioglu ve Y. Sun, “The improvement of the mechanical properties of AA 6063 aluminum alloys produced by changing the continuous casting parameters”, *Sci. Res. Essays*, c. 6, sayı 13, ss. 2832–2840, 2011, doi: 10.5897/SRE11.471.



INFLUENCE OF Mg CONTENT ON THE MICROSTRUCTURE AND MECHANICAL PROPERTIES OF EN AW 6082 ALLOYS

Aleyna GÜMÜŞSOY, Hilal ÇOLAK, Işık KAYA, Emrah Fahri ÖZDOĞRU

TRI Metalurji A.Ş.
Türkiye

Keywords: EN AW 6082, Mg Addition, Heat Treatment, Microstructure, Mechanical Properties

Abstract

EN AW 6082 is one of the most popular high strength Al-Mg-Si alloys for structural profiles. In the present study, it is aimed to investigate the influence of Mg addition on the mechanical properties of EN AW 6082. Commercial 6082 alloy and pure Mg (99.9%) ingot were used for alloying and laboratory scale casting experiments. The final composition was measured by arc spark optical emission spectroscopy. As-cast samples were solution heat treated at 560°C for 3 hours in order to dissolve soluble elements from the alloy into solid solution followed by water quenching. The solution heat treated/water quenched samples were aged at 185°C for 1, 2, 4, 6, 8 and 10 hours followed by air cooling in order to improve mechanical properties. Brinell hardness measurements of as-cast, solution heat treated and aged samples were performed on the polished cross sections and measurements were taken from 5 different points. The hardness increased from 110 to 120 HBW due to the addition of Mg, at the optimum aging conditions (185°C, 6 hours) for Mg-added 6082 alloys. The morphologies of the intermetallic of the alloys were analyzed by scanning electron microscopy (SEM). The results indicated that hardness of the alloy increase with increasing Mg content and with low cycle aging time.

1. Introduction

Aluminum alloys have superior mechanical properties due to having low density, high specific strength, high corrosion resistance, and ability to improve their

mechanical properties. Those properties make them useful in many industries such as automotive, transportation, aviation-space, electronics, machinery and manufacturing. Especially in the automotive, aerospace and aviation sectors (drone application), it plays a very important role in providing fuel savings and preventing air pollution by reducing weight due to their low density. Recently, EN AW 6082 has been receiving a lot of attention as a high-strength alloy for use in automotive extrusion profiles because of its mechanical properties and superior corrosion resistance [1].

The T6 heat treatment is usually applied to these alloys in order to improve the mechanical properties [2]. Besides the heat treatment, small addition of various alloying elements such as Mg, also modifies the microstructure of the alloys to improve the mechanical properties [3].

Precipitation hardening occurs as a result of artificial ageing where the alloy is first heated to a temperature above the solvus line, however still below the eutectic temperature to avoid local melting of the alloy. This first initial step is known as solution heat treatment and followed by quenching to room temperature. All alloying elements are then in solid solution and are said to be in a supersaturated solid solution (SSSS) [4]. The second step is artificial aging, which involves heating the alloy to an intermediate temperature, usually 150-190°C. During artificial aging a series of meta-stable phases will precipitate with increasing holding time, until the

equilibrium phase β (Mg_2Si) forms if the alloy is over-aged [5]. The precipitation sequence may be written as: SSSS \rightarrow solute clusters \rightarrow GP-zones \rightarrow β'' \rightarrow β' \rightarrow β (Mg_2Si)

In the present study, the effect of Mg addition on the mechanical properties of EN AW 6082 alloys were investigated using optical microscopy, scanning electron microscopy (SEM), and hardness tests.

2. Experimental Procedure

In this study, high-purity Mg (99.9%) was added as the additional alloying element in the commercial EN AW 6082 alloy. Laboratory scale melting and alloying experiments were performed in alumina crucible placed in electric resistance furnace at 750°C and after that the melt was subsequently poured into a steel mould to form rod. Chemical compositions of the commercial and Mg-added 6082 alloys were measured by arc spark optical emission spectroscopy and given in Table 1 and 2, respectively.

Table 1. Chemical composition of the commercial EN AW 6082 alloy (wt.%)

Si	Fe	Cu	Mn	Mg
0.95	0.181	0.012	0.469	0.62

Table 2. Chemical composition of the Mg-added EN AW 6082 alloy (wt.%)

Si	Fe	Cu	Mn	Mg
0.97	0.175	<0.012	0.469	0.74

As-cast samples were solution heat treated at 560°C for 3 hours in order to dissolve soluble elements from the alloy into solid solution followed by air cooling. The solution heat treated/water quenched samples were aged at 185°C for 1, 2, 4, 6, 8 and 10 hours followed by air cooling in order to improve mechanical properties.

The surfaces of the as-cast, solution heat treated and aged samples were prepared using standard metallographic sample preparation steps including grinding and polishing and etched with HF (5%) for microstructural analysis.

Hardness measurements of the samples were performed by a Brinell hardness tester (HBW 2.5/62.5) with the load of 62.5 kp, 2.5 mm diameter.

The morphologies of the intermetallic of the as-cast and aged samples were investigated by scanning electron microscopy (SEM).

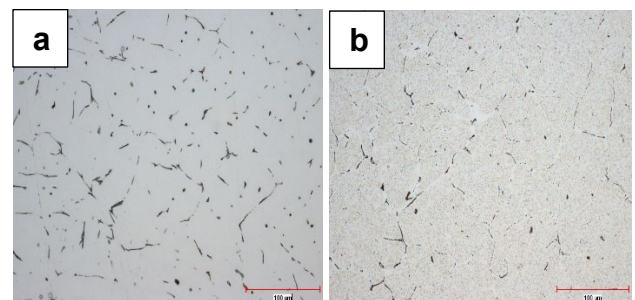
3. Results and Discussion

3.1. Microstructural Analysis

The microstructure of the as-cast samples (Figure 1a and Figure 2a) consists of Al-rich solid solution dendrites while the intermetallic phases are segregated at the secondary dendrite arm boundaries.

In comparison to as cast state, after homogenization and water quenching (Figure 1b and Figure 2b) dissolution of significant amount of the Mg_2Si particles and defragmentation of $AlFe(Mn)Si$ particles is observed. In the case 6082-Mg, with higher Mg and Si content, after homogenization at the temperature of 560°C, the number of Mg_2Si particles is greater.

After aging treatment, however, the main difference in microstructure among the two alloys is the precipitates and precipitation is highly dependent on the Mg/Si ratio [6].



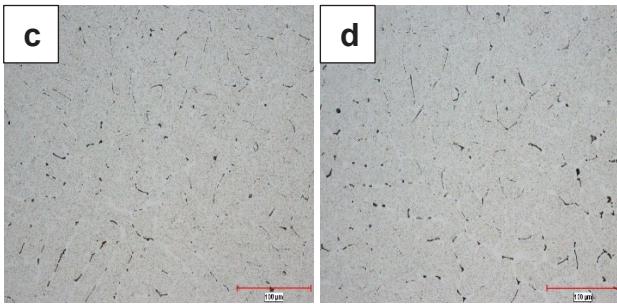


Figure 1. Microstructure of commercial 6082 alloy (a) in as-cast, (b) after solution heat treatment, (c) after 2 hours aging at 185°C, (d) after 6 hours aging at 185°C (100X)

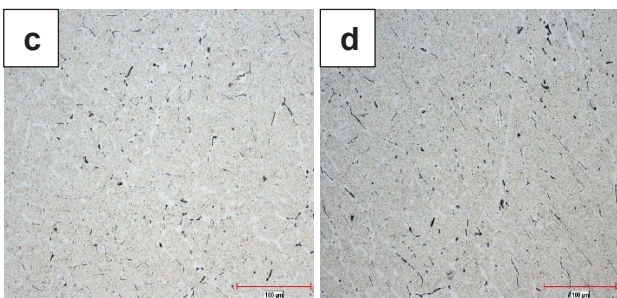
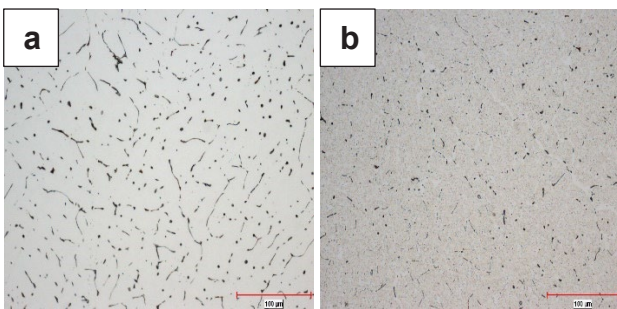


Figure 2. Microstructure of Mg-added 6082 alloy (a) in as-cast, (b) after solution heat treatment, (c) after 2 hours aging at 185°C, (d) after 6 hours aging at 185°C (100X)

3.2. Hardness Measurements

Figure 3 shows the Brinell hardness values of commercial and Mg-added 6082 alloys depending on the various aging times at 185°C. These results show that 6082 alloy with higher Mg content and Mg/Si ratio (6082-Mg), has higher hardness values at all aging times. Han et al., (2009) investigated the effect of Mg/Si ratio on the mechanical properties of Al-Mg-Si alloys and explained that the alloy

with higher Mg/Si ratio has a higher hardness value [6]. In this study, Mg/Si ratio were calculated for 6082 and Mg-added 6082 alloys as 0,984 and 1,168, respectively. The hardness results that are obtained in the scope of this study are compatible with the literature data.

The other important output from the hardness curve is that the hardness requirements from the alloy is defined in EN 755-2 as 95 Hardness of Brinell and after Mg addition, the target hardness is easily caught with 2 hours aging cycle which is two times less than the standard 6082 alloys.

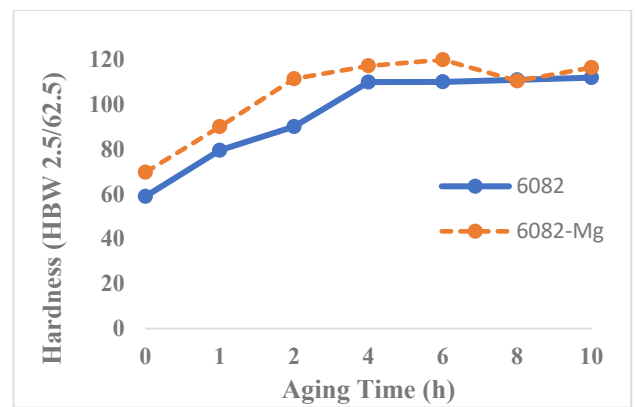


Figure 3. Hardness measurements of the commercial and Mg-added 6082 alloys

3.3. SEM Analysis

In the SEM microstructure of both as-cast alloys (Figure 4a and Figure 5a), two types of particles are observed: Mg₂Si (black) and AlFe(Mn)Si (white). The AlFeMnSi based dispersoid have characteristic needle shape and are located mainly on grains boundaries and Mg₂Si particles are located inside the grain.

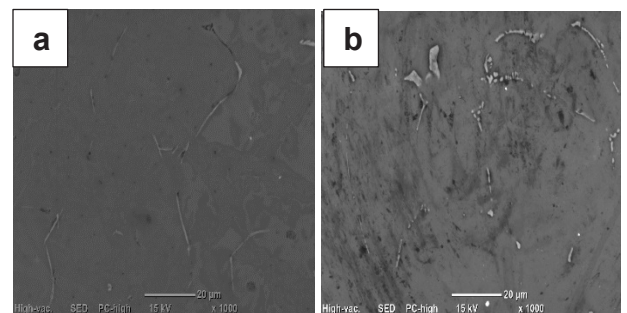


Figure 4. SEM microstructure of the commercial 6082 (a) as-cast state, (b) after 6 hours aging at 185°C. (1000X)

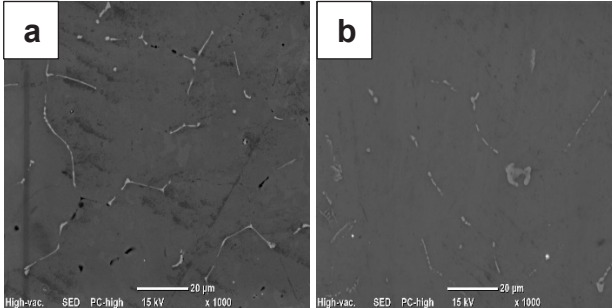


Figure 5. SEM microstructure of the 6082-Mg (a) as-cast state, (b) after 6 hours aging at 185°C. (1000X)

4. Conclusion

The results can be summarized as follows:

- The main difference in microstructure among the two alloys is the precipitates and precipitation is highly dependent on the Mg/Si ratio (0,984 and 1,168, respectively)
- Hardness measurements performed following the T6 heat treatment process for all the samples showed that hardness values of the Mg-added samples are higher than those of the commercial 6082 alloy samples.
- With the addition of Mg, higher hardness values are achieved at lower heat treatment times. This allows time and energy savings in industrial applications.

Acknowledgement

This work is financially supported by the Scientific and Technological Research Council of Turkey (TÜBİTAK) with project number TEYDEB 7210183.

References

- [1] Y. Birol, “Effect of Cr and Zr on the Grain Structure of Extruded EN AW 6082 Alloy,” vol. 20, no. 4, pp. 727–732, 2014.
- [2] G. Mrówka-Nowotnik, “Influence of chemical composition variation and heat treatment on microstructure and mechanical properties of 6xxx alloys,” *Arch. Mater. Sci. Eng.*, vol. 46, no. 2, pp. 98–107, 2010.
- [3] C. H. Caceres, C. J. Davidson, J. R. Griffiths, and Q. G. Wang, “The effect of Mg on the microstructure and mechanical behavior of Al-Si-Mg casting alloys,” *Metall. Mater. Trans. A Phys. Metall. Mater. Sci.*, vol. 30, no. 10, pp. 2611–2618, 1999.
- [4] P. Hidalgo-Manrique, S. Cao, H. R. Shercliff, R. D. Hunt, and J. D. Robson, “Microstructure and properties of aluminium alloy 6082 formed by the Hot Form Quench process,” *Mater. Sci. Eng. A*, vol. 804, no. November 2020, p. 140751, 2021.
- [5] P. Noga, A. Piotrowicz, T. Skrzekut, A. Zwoliński, and P. Strzpek, “Effect of various forms of aluminum 6082 on the mechanical properties, microstructure and surface modification of the profile after extrusion process,” *Materials (Basel)*, vol. 14, no. 17, 2021.
- [6] Y. Han *et al.*, “Effect of Mg/Si ratio on the microstructure and hardness–conductivity relationship of ultrafine-grained Al–Mg–Si alloys,” *J. Mater. Sci.*, vol. 52, no. 8, pp. 4445–4459, 2017.



GOLD EXTRACTION FROM OXIDE GOLD ORES BY GLYCINE LEACHING

Umay ÇINARLI¹, Gabriel UĞURGEL¹, M. Barış DARYAL², M. Hakan MORCALI³,
Ahmet TURAN¹

¹Yeditepe University, ²Gama Composite Engineering & Products, ³Gaziantep University
Türkiye

Keywords: Cyanide-free process; Glycine leaching; Oxide gold ore; Hydrometallurgy; Gold; Silver; Adsorption

Abstract

Gold is a yellow-coloured metal with the greatest ductility and malleability. Except for selenic acid, simple acids do not dissolve gold. However, in the presence of oxidants such as nitric acid, oxygen, manganese dioxide, hydrochloric acid dissolves gold. The basic system used to extract gold from its ores is the process in which gold is dissolved in cyanide and oxygen is used as the oxidant. In this study, leaching experiments were carried out using glycine, a non-toxic reagent.

1. Introduction

Methods such as flotation and gravity are used in the processing of gold. However, the most common of these is the cyanidation method. To date, approximately 1 billion tons of gold has been processed by cyanidation. During this process, highly toxic and dangerous HCN gas is released. In addition, there is a very serious public pressure on the use of this method and legal regulations are needed. Glycine, a non-toxic and the simplest amino acid, it is also dissolving selectively precious metals. Currently, the use of glycine is a promising process in gold extraction [1, 2]. In this study, gold extraction from oxide gold ore samples with glycine at increasing concentrations (1-3 M) and reaction times (4-60 hours) were investigated.

2. Materials and Methods

Standard oxide gold ore (National Geophysical Research Institute, India) was used in the experiments. In leaching experiments, agricultural and non-analytical grade glycine (97% pure, Biorad) was used as a leaching agent. Depending on the literature research, some experimental conditions were determined. The reaction temperature was determined at 60°C and the pH of the solution was adjusted to around 11-12. In addition, the dry air flow rate was kept constant at 1 L/min and the mixing speed at 350 rpm. The average particle size of the oxide gold ore used was 70.7 µm, based on analysis with the Mastersizer. After the extraction experiments, adsorption studies were carried out using 0.06 g/10 mL and 0.12 g/10 mL coconut-based activated carbon with increasing time (from 15 minutes to 120 minutes).

3. Conclusion

According to the experimental results, the highest gold extraction result (81.41%) was obtained at 3M glycine concentration after 48 hours at 350 rpm at 60°C. As expected, moderate silver solubility was obtained and, the extraction yield was 44.50% at the same conditions. However, Fe solubility (7.71%) was lower compared to precious metals (i.e. gold and silver). It was observed that glycine concentration and reaction time positively affected the dissolution of oxide gold ore. The gold leaching process with glycine, it appears to be a sustainable and more environmentally friendly approach and may be used to extract gold and silver selectively from oxide ore/oxidized wastes bearing precious metals. The gold content in the pregnant solution was 311.1 mg/L and, it was decreased to an amount less than 250 mg/L after a single step adsorption for both activated carbon to solution ratios (0.06 g/10 mL and 0.12 g/10 mL) and after 120 minutes duration. It was observed that 0.12 g/10 mL adsorbent ratio was slightly more effective particularly in the beginning stage of the adsorption experiments. Adsorption were reached an equilibrium after the duration of 60 minutes for both adsorbent ratios. Activated carbon showed a performance which is suitable for the adsorption of gold from alkaline glycine systems.

Acknowledgment

Authors thank to Mehmet Üçışık (Yeditepe U.) for Mastersizer analysis and, Samet Kaplan and M. Şeref Sönmez (ITU) for ICP-MS analyses in adsorption stage.

References

- [1] E.A. Oraby, J.J. Eksteen, Hydrometallurgy 152 (2015) 199-203.
- [2] P. Altinkaya, Z. Wang, I. Korolev, J. Hamuyuni, M. Haapalainen, Minerals Engineering 158 (2020) 106610.



AN UPDATE FOR CRITICAL RAW MATERIALS (CRMS)

Erman CAR¹, Umay ÇINARLI², Ahmet TURAN², Onuralp YÜCEL³

¹Insertec Thermal Solutions, ²Yeditepe University, ³Istanbul Technical University
Türkiye

Keywords: Critical raw materials; Sustainability; European Commission

Abstract

Raw materials form the industrial basis of various products and applications used in modern technologies and in daily life. Minerals, mineral concentrates, compounds and metallic semi-products are among these raw materials which have to be used to sustain all activities by human beings. Although economic importance and supply risk have been well-known features since the time humankind passed from being hunter-gatherer to being agriculture-assisted, calculation of those aspects have been a relatively new concept (over the last two decades) to point out sustainable development of the nations which utilize raw materials for industrial production. This concept is called “Critical Raw Materials” (CRMs). The first CRMs list was released by the European Commission in 2011 containing 14 raw materials and, the number of raw materials was increased up to 30 in 2020 by the EU. In the present study, historical background, development of the EU’s CRM list and the calculation of CRM list in the EU perspective are given in detail with the properties of the raw materials in the list. Moreover, 2020 updated CRMs list is introduced in detail.

1. Introduction

CRMs contain all raw materials except the raw materials for energy production and agricultural products. They are very important for the sustainable production in mega sectors both conventional and advanced such as green technology, space exploration, aviation, medical devices, transportation, defence, telecommunications, microelectronics. There are global trends suggesting that the demand for CRMs will increase significantly in the near future because of the demand. It has been estimated that this increase will be approximately 250% in the next 10 years. Therefore, CRMs cause concerns in the EU and around the world. For this reason, the European Commission has released a list of CRMs for the EU that is subject to regular updating and review. The list contained 14 items in 2011, 20 items in 2014, and 27 items in 2017. The fourth list of CRMs for the EU was published in 2020 and included 30 raw materials. Lithium, titanium, bauxite and strontium are the materials added to the list for the first time in 2020 (Table 1).

Table 1. CRMs list released in 2020, new raw materials are present in bold in comparison to 2017 list [1].

Antimony	Cobalt	Hafnium	Natural graphite	Phosphorus	Vanadium
Baryte	Coking coal	Heavy Rare Earth Elements	Natural rubber	Scandium	Bauxite
Beryllium	Fluorspar	Light Rare Earth Elements	Niobium	Silicon metal	Lithium
Bismuth	Gallium	Indium	Platinum Group Metals	Tantalum	Titanium
Borate	Germanium	Magnesium	Phosphate rock	Tungsten	Strontium

To accept a raw material as CRM, it is necessary to meet with following aspects: Limited resources; High economic value for key industries in the EU such as environmental, automotive, defence, medical, electronics; High import dependency; Deposits (or resources) of a raw material located in a few countries across the world; Raw materials which are not easy to find substitutional materials in the near future.

2. Conclusion

In the next 20 years, it is predicted that the demand on the raw materials will remarkably increase due to the need in energy and the fossil fuel dependency of the energy production. As an annual average, raw material consumption rates increase between 3-5%. Also, it is necessary to enhance the efficiency of mining operations to mitigate the pressure on natural resources. Moreover, recycling rates will increase for other metals like Mg, Be, Ga, Li and the rare earth metals.

References

[1] European Commission, Critical Raw Material List, 2020.

ENVIRONMENTAL IMPACT OF HYDROMETALLURGICAL ZINC PRODUCTION

Georgi PATRONOV

University of Plovdiv "Paisii Hilendarski"
Bulgaria

Keywords: Environmental Impact, Hydrometallurgical Zinc Production, Emissions, Sustainability, Exergy Analysis

Abstract

The present study aims to examine and assess the environmental impact of a typical hydrometallurgical zinc production technology. As an example, a real operating installation in KCM - SA, Plovdiv, Bulgaria is considered. KCM is the largest producer of zinc and lead for South-Eastern Europe. The exergy method of thermodynamic analysis was used as a research method. A precise exergy assessment of the basic chemical-technological units as well as of the overall system has been obtained.

1. Introduction

Technological processes consume raw materials and energy resources from nature and at the same time release a significant amount of waste in it. Sustainable development of the system technology - nature can be achieved only by maintaining the state of consumption of resources, less than their recovery from the environment, as well as when waste emissions do not disrupt the biogeochemical cycles of the earth.

The criteria for sustainable technological process (from an ecological point of view) focus on the ratio between the use of renewable, non-renewable and re-used resources, the quantity and quality of waste released into the environment, and energy-technological efficiency of processes. The subject of the present study is the environmental impact of hydrometallurgical zinc production. The exergy method of thermodynamic analysis is a possible option for characterizing the technogenic load on the environment. It takes into account the interaction of each system with the environment. Exergy can be seen as a link between energy, the environment and sustainable development.

Exergy is a general criterion by which the resources and energy entering the production system can be evaluated. Exergy can also be used to quantify the environmental sustainability of the external environment in terms of the waste emitted in it, i.e. to show the norm of what nature can "recycle" [1-6].

The object of the analysis is a real functioning system - the zinc production plant in KCM - SA, Plovdiv. KCM is the largest lead and zinc Production Company in South Eastern Europe and exports to almost the entire world [7, 8]. The choice was made due to the complexity of the process (diversity in the raw materials used, products and waste; the use of different chemical-technological

processes) and its great economic, social and ecological importance [9-13].

2. Experimental Procedure

The studies were carried out on a real functioning system for the production of zinc by the hydrometallurgical method with a waelz process for the processing of waste zinc cakes, namely the one in KCM - SA, Plovdiv.

Fig. 1 shows the scheme of interaction of the production system "Hydrometallurgical extraction of zinc" with the surrounding ecosphere.

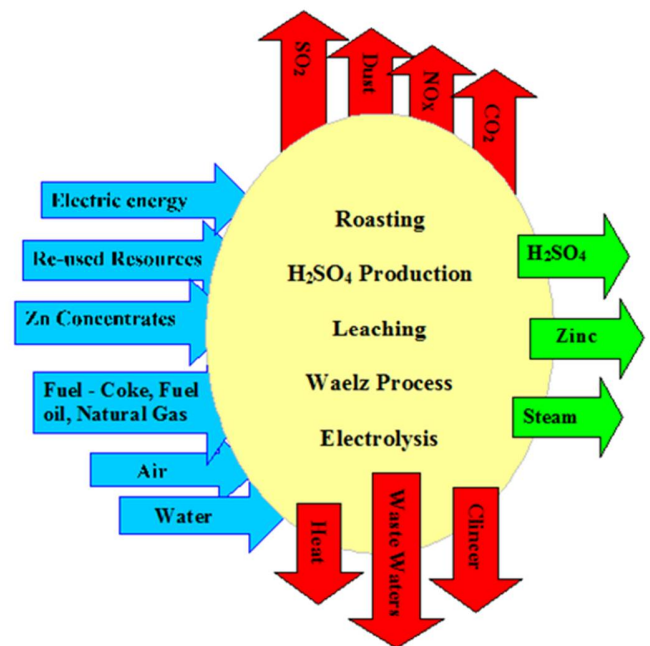


Figure 1. Flow chart of the interaction between the hydrometallurgical zinc production industrial system and the ecosphere surrounding it

This hydrometallurgical method is also called RLE (roast-leach-electrowin). RLE is a continuous process. The technological scheme includes the following processes: roasting of the zinc sulfide concentrates in a fluidized bed furnace, sulfuric acid leaching of the obtained calcine, purification of the zinc-bearing solution from undesirable impurities, zinc electrowinning, processing SO₂-containing roasting gases into H₂SO₄

using the DKDA method (“double contact – double absorption”), processing the waste zinc cakes from leaching via waelz process.

Weak acid from sulfuric acid production is neutralized to technical gypsum in two stages, namely neutralization to pH 2–3 with a limestone solution and gypsum separation, and neutralization to pH 9 with lime slurry and precipitation of heavy metals as hydroxides. The cake obtained proceeds further to Waelz processing while the wastewater enters the purification station of the Metallurgical Works to be purified.

The main raw materials in zinc production are zinc sulphide concentrates, air and water. An important role is played by electricity - most of it is consumed during the electroextraction process. Coke, fuel oil and natural gas are used as fuel. Activated carbon, potassium ethyl xanthogenate, potassium permanganate, zinc powder, etc. are imported as auxiliary materials. Zn-containing secondary raw materials, the amount of which has been increasing in recent years, are processed in the Waelz furnace.

We can divide the emissions into the environment from the hydrometallurgical zinc production technology under consideration as follows: gas emissions; waste water; solid waste; heat emission.

Historically, the main environmental problem associated with the production of zinc from sulphide concentrates has been the emission of sulfur dioxide into the air from the roasting process. This problem is effectively solved by high sulfur fixation and production of sulfuric acid by the DKDA method.

The main emissions to air from hydrometallurgical zinc production are – sulfur dioxide and acid mists; carbon dioxide (CO₂); metals and their compounds; dust. The sources of emissions depend on the process used can be – transport and handling of material; roasting and sulphuric acid plant; waelz process; leaching, purification and electrolysis; mechanical treatments like grinding, milling and granulation. Diffuse emissions are also important and need to be considered for all of the process stages.

The main pollutants emitted into the water are metals and their compounds - Zn, Cd, Pb, Cu, Ni, Co and to a lesser extent Hg, Se, As and Cr. Other significant substances that are emitted to water are sulfates, chlorides and fluorides. The possible waste water streams are – waste water from roasting and gas-cleaning steps; accidental spillage from various hydrometallurgical processes; collected and reused as filter washing water; anode and cathode washing liquid effluent; water from general operations, including cleaning of equipment, floors, etc. The waste water from the zinc plant and the sulfuric acid plant enters the treatment plant for neutralization and purification.

The production of zinc results in the generation of several by-products, residues and waste. Solid residues obtained from different processes can have possible

destinations such as recycling in or before the process, downstream processing for the recovery of other metals - for example cadmium, final disposal after processing to ensure safe disposal. The main solid wastes generated are clinker and spent vanadium catalyst. Clinker is a waste from the waelz process. Proceed to extract the useful components (Cu) in it. It also contains FeO, SiO₂, Al₂O₃, CaO, MgO, etc. Spent vanadium contact mass is a waste product from the sulfuric acid plant. The waste is sent for vanadium extraction or recycling.

Environmental controls require systems to fix sulfur dioxide, control of particulates and gases emissions into the atmosphere, safe disposal of waste, maintain a safe work environment in the plant, and limit liquid wastewater discharges to environmentally acceptable levels of harmful substances. Air and water emissions, waste management and energy considerations are among the key factors influencing the modernization of the production process [7, 9 and 14].

The environmental impact of the considered chemical-technological system "Hydrometallurgical extraction of zinc" was evaluated by means of the exergy method of thermodynamic analysis. The exergy analysis was carried out according to the methodology described in [15]. The absolute losses (irreversible and effluent) and the relative exergy characteristic (exergy efficiency) of the individual stages as well as of the system as a whole were estimated.

The irreversible losses D_{irr} were calculated from the difference in the exergy values of the input ($\sum \varepsilon_{i, input}$) and the output ($\sum \varepsilon_{i, output}$) flows of each considered stage.

$$D_{irr} = \sum \varepsilon_{i, input} - \sum \varepsilon_{i, output} = T_0 \Delta S \quad (1)$$

The effluent losses D_{effl} include the exergy of the unusable material and energy flows penetrating into the environment.

The exergy efficiency η_e was determined through the ratio of the exergy of the usable output flows (ε_{ut}) to the exergy of the input flows ($\sum \varepsilon_{i, input}$):

$$\eta_e = \frac{\varepsilon_{ut}}{\sum \varepsilon_{i, input}} \times 100\% = \frac{\varepsilon_{ut}}{\varepsilon_{ut} + D_{irr} + D_{effl}} \times 100\% \quad (2)$$

The exergy losses and the thermodynamic degree of perfection characterize the corresponding chemical-technological system quantitatively and qualitatively [1, 3 and 15].

3. Results and Discussion

The impact of zinc production on the environment can be considered in the following two directions - consumption of material and energy resources and emissions entering the environment.

The main raw material with which zinc is imported is zinc sulfide concentrate - 1.4 t/t Zn. According to the presented data, about 24% of the zinc raw materials are secondary Zn-containing resources. The tendency is for

this percentage to grow to 30%. The processed secondary raw materials averaged 442 kg/t Zn. Their composition includes dust from electric arc steelmaking and cast iron-making; ashes, bottom and top dross from the galvanizing industry; old roofing and other sheet materials; non-ferrous fractions from the shredding of old cars and of other products mainly containing steel; residues from the chemical uses of zinc and other. The zinc content in them varies from 35% to 70%. They also contain iron, copper, lead, chlorine, etc. [9, 14].

The energy requirements vary to a large extent. They depend on the quality of the feed and the products, the use of latent or waste heat and the production of by-products. The use of natural gas instead of fuel oil and coke, as well as low-sulfur fuel oil (sulfur content up to 1%) leads to a reduction in SO₂ and CO₂ emissions. The utilization of the heat of the off-gas flows increases the energy efficiency of the processes. Modernization and gasification of the existing waelz furnaces are currently underway.

The consumed electricity amounts to 3924 kWh/t Zn.

All emission limits imposed by national legislation as well as by best available techniques are met for gaseous emissions, waste water and solid waste. The application of the DKDA process for the extraction of sulfuric acid from SO₂-containing gases allows reducing SO₂ emissions to 140 – 280 mg/m³ with a conversion rate of 99.8%. The implementation of "cleaner" production processes and effective measures against pollution leads to an economic and ecological effect at the same time [9, 14].

The first step in performing the exergy analysis is the calculation of the exergy value of the raw materials, electricity and fuels introduced into the system and the resulting products and waste. These values are presented in Table 1.

Table 1. Exergy values of the main resources, products and emissions in hydrometallurgical zinc production

	Flow	GJ/t Zn
Resources	Zinc Concentrates	9.785
	Re-used Resources	0.719
	Coke	15.400
	Fuel Oil	0.636
	Natural Gas	0
	Electric Energy	14.126
Products	Zinc	5.187
	Sulphuric Acid	1.971
	Steam	1.920
Emissions	Off-gases (H ₂ SO ₄ Production)	0.059
	Off-gases (Waelz Process)	1.381
	Clinker	5.375
	Heat	2.673

The values of the absolute and the relative exergy characteristics D_{irr} , D_{effl} and η_e of the individual technological stages are presented in Table 2 and Figure 4. While determining the individual indices for each technological unit, the exergy of the input flows was accepted to be 100 %.

Table 2 - Exergy characteristics for the principal stages in hydrometallurgical zinc production

№	Stage	Losses			
		D_{irr}		D_{effl}	
		MJ	%	MJ	%
1.	Roasting	3 876	38.2	213	2.1
2.	H ₂ SO ₄ Production	2 789	53.7	415	8.0
3.	Leaching	1 016	37.0	107	3.9
4.	Electrolysis	4 462	37.8	597	5.1
5.	Waelz Process	9 957	53.7	7 822	42.2

The distribution of irreversible and effluent losses by separate stages is presented in Figure 2 and Figure 3.

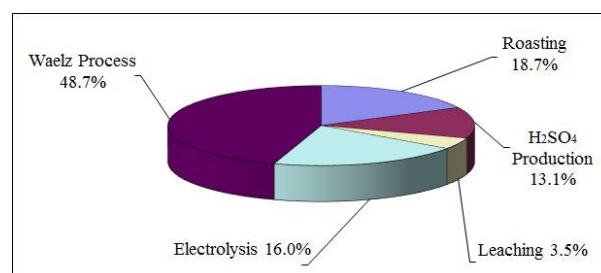


Figure 2. Distribution of irreversible losses by separate stages of the chemical-technological system "Hydrometallurgical extraction of zinc"

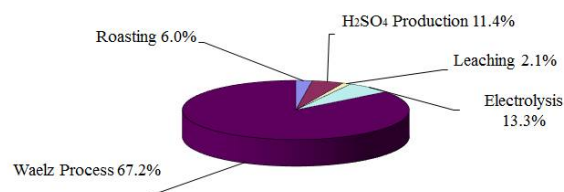


Figure 3. Distribution of effluent losses by separate stages of the chemical-technological system "Hydrometallurgical extraction of zinc"

The overall exergy efficiency of the chemical-technological system "Hydrometallurgical extraction of zinc" is comparatively low, only about $\eta_e = 22.3$ %. The value is typical of metallurgical processes, but higher than that of the same chemical-technological system, without processing or to a lesser extent of secondary raw materials. [3, 16 – 17].

The main part of the losses of available energy are the irreversible ones $D_{irr} = 54.4\%$, the remaining part are the effluent ones – $D_{effl} (\varepsilon_{off-gases} + \varepsilon_{clinker} + \varepsilon_{heat}) = 23.3\%$ (Tables 1 and 2, Figures 2 – 4).

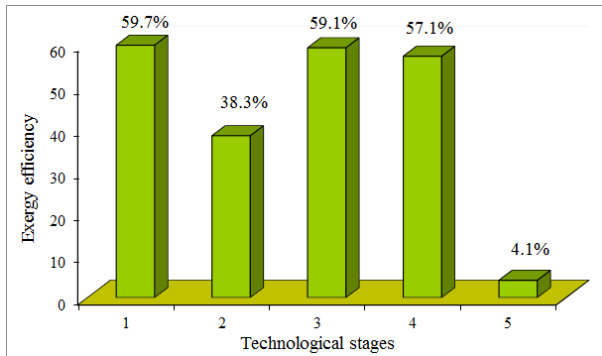


Figure 4. Exergy efficiency in the main technological stages of the chemical-technological system "Hydrometallurgical extraction of zinc": 1 - Roasting, 2 - H_2SO_4 Production, 3 - Leaching, 4 - Electrolysis, 5 - Waelz Process

The waelz process for treatment zinc cakes is energy inefficient. It has a low exergy efficiency – only 4.1%. The low values of the main exergy characteristics for this process are mainly determined by the nature of the irreversible chemical processes taking place in the furnace (burning of fuel, reduction of metal oxides) and heat exchange with the environment. The higher degree of extraction of Zn from zinc concentrates, the recovery of part of the solid waste (clinker) and the possible processing of secondary raw materials of various composition and origin are the reason for the presence of this chemical-technological stage in the scheme of hydrometallurgical zinc production.

4. Conclusion

An energy-technological study and assessment of the impact on the environment of the production system "Hydrometallurgical extraction of zinc with the application of a waelz process for the processing of waste cakes and secondary raw materials" was carried out. The exergy method of thermodynamic analysis was applied.

The overall exergy efficiency of the system under study is comparatively low – 22.3 %, i.e. 77.7 % of the available input energy in the system practically degrades. The main exergy losses are irreversible – 54.4 % while the effluent losses amount to 23.3 %.

The possibilities for increasing energy-technological efficiency and limiting the harmful impact of hydrometallurgical zinc production on the environment are a higher degree of use of renewable energy and secondary raw materials, a higher degree of solid waste processing and extraction of useful components, reduction of specific energy consumption.

Acknowledgment

The author would like to express their sincere gratitude to the Managing Board of KCM – SA, Plovdiv, especially Eng. St. Stoychev, for their valuable cooperation and help in carrying out the analysis.

References

- [1] I. Dinçer, M.A. Rosen, Exergy: energy, environment and sustainable development, 2nd Edition, Elsevier, 2012, Amsterdam, pp. 10-13, 31-39, 51-69.
- [2] O. Ignatenko, A. van Schaik, M. Reuter, Minerals Engineering 20 (2007) 862–874.
- [3] Vl. Stepanov and S. Stepanov, Energy Convers. Mgmt 39 (1998), 1803–1809.
- [4] B. Boryczko, A. Hołda, Z. Kolenda, Journal of Cleaner Production 84 (2014) 313–321.
- [5] Hernandez, R. Lupton, C. Williams, J Cullen, Applied Energy 218 (2018) 232–245.
- [6] E. Van Genderen, M. Wildnauer, N. Santero and N. Sidi, Int J Life Cycle Assess 21 (2016) 1580–1593.
- [7] <<https://www.kcm2000.eu/>> Dated: 03. 07. 2022
- [8] Metallurgy in Bulgaria in the year 2020, <<https://bami.bg/en/facts/analyses/>> Dated: 03. 07. 2022
- [9] D. Sancho, S. Roudier, F. Farrell et al., Best available techniques (BAT) reference document for the non-ferrous metals industries: Industrial Emissions Directive 2010/75/EU (integrated pollution prevention and control), European Commission, Joint Research Centre, Publications Office, 2017 <<https://data.europa.eu/doi/10.2760/8224>> Dated: 03.07. 2022.
- [10] St. Dudka and D. Adriano, Journal of Environmental Quality 26 (1997) 590–602.
- [11] T. Norgate, S. Jahanshahi, W. Rankin, Journal of Cleaner Production 15 (2007) 838–848.
- [12] N. Antunano, J. Cambra, P. Arias, Process Safety and Environmental Protection, 129 (2019) 308–320.
- [13] D. Stewart, A. Barron, Resources, Conservation & Recycling, 157 (2020) 104746.
- [14] <<https://www.moew.government.eu/>> Dated: 03. 07. 2022
- [15] G. Patronov, S. Magaeva, Chemical Papers, 61 (6) (2007) 457 – 463.
- [16] G. Patronov, S. Magaeva, Scientific Papers, Plovdiv University – Bulgaria, 37 (5) (2010) 155 – 162 (in Bulgarian).
- [17] G. Patronov, B. Boyanov, Exergy assessment of the sustainability of zinc production, 48th International October Conference on Mining and Metallurgy, 28 September - 01 October 2016, Bor Lake, Bor, Serbia, pp. 120-123.



INDUSTRIAL SCALE EXTRACTION OF LITHIUM CARBONATE AND RARE EARTH ELEMENTS FROM DOMESTIC SOURCES

Arzu S. SATILMIŞ¹, Herkail ÖZEN¹, Furkan E. ÖZEL¹, M. Şeref SÖNMEZ²

¹ASOS Process Engineering, ²Istanbul Technical University
Türkiye

Abstract

Extraction of lithium carbonate and rare earth production from domestic resources was explained in this study. Lithium carbonate extraction was carried out by using brines obtained from Tuz Lake, while rare earths was synthesised from Beylikova. Optimal conditions of hydrometallurgical extraction of lithium carbonate were determined. Crushing, screening, grinding, dimensional classification, leaching, solvent extraction (SX), impurity removal, and precipitation stages of rare earth extraction was stated.

Synthesis of Lithium Carbonate from Tuz Lake

In recent years the number of electric vehicles and devices significantly increasing. This demand has also increased the need for long-lasting batteries for electrical devices. With the increase in battery demand, the demand for lithium also increases [1]. Lithium can be extracted either from brines or mineral rocks. Brines remain the main source of lithium, representing more than 50% of globally identified reserves. Lithium has been extracted from brines in industrial scale in some countries such as Chile, Argentina, Bolivia, China, Russia and America. The electric vehicle revolution has been accelerated by government incentives and decisions to ban internal combustion engines. For example, countries such as France, India, China, Ireland, the Netherlands, Slovenia, Sweden, the United Kingdom and Norway, as well as the US state of California, announcing their EE related targets; stating that they will end the production of internal combustion engine vehicles by 2030-2040 [2, 3]. In this context, the optimisation of Li_2CO_3 synthesis from Tuz Lake was carried out in this study. Lithium recovery studies were carried out with different brine solutions taken from Tuz Lake. The lithium concentration in the brine solution varies between 200-350 ppm. In addition, there are 25-40 g/L magnesium (Mg), 15-50 g/L potassium (K), 90-110 g/L sodium (Na) in the solution. Such high alkali and alkaline metal concentrations make it difficult to obtain lithium. In the literature, it has been reported that the Mg/Li ratio in the solution concentration should be less than 6 in order to achieve economical Li recovery from brine solutions [4]. Cyanex 272, D2EHPA, Aliquat 336, Versatic 10 and TBF was used as in solvent extraction for the separation of Mg and Li. In addition, ion exchange was applied using selective adsorbent resin. 90% efficiency was obtained for the separation of Mg and Li using selective adsorbent resin. Optimal conditions were determined as 100 mL of resin volume and 5 BV of brine.

REE Synthesis from Domestic Resources

Rare-Earths (REE) are composed of fifteen lanthanides and seventeen elements consisting of yttrium and scandium. They are classified as heavy (Sc, Y, Eu, Gd, Tb, Dy, Ho, Er, Tm, Yb and Lu) and light (La, Ce, Pr, Nd, Pm and Sm) rare earth elements. Due to their application areas, REEs are called indispensable as technological material especially in energy applications. Although the amount of use in mass composition is not very high, it is preferred because of the high-level mechanical, optical, magnetic, and electrical properties [5]. Due to the strategic importance of rare earth elements, reserve research in our country has been deepened and geological and mining operations have been increased specially in the Eskişehir - Beylikova region where REE exist. In this study, both laboratory and pilot scale experiments were conducted to extract REE from domestic raw materials. It is planned to establish a production facility in Beylikova region by the end of 2022 containing crushing, screening, grinding, dimensional classification, leaching, solvent extraction (SX), impurity removal, and precipitation stages for the extraction of REE.

References

1. Ulusoy, M. (2016). Geleceğin Petrolü Lityum mu? Türk Mühendis ve Mimar Odaları Birliği Metalurji Ve Malzeme Mühendisleri Odası, Metalurji Sayı:178 Şubat, 4.
2. Kavanagh, L., Keohane, J., Cabellos, G. G., Lloyd, A., & Cleary, J. (2018). Global Lithium Sources— Industrial Use and Future in the Electric Vehicle Industry: A Review. 29.
3. Heredia, F., Martinez, A. L., & Urtubey, V. S. (2020). The importance of lithium for achieving a low-carbon future: Overview of the lithium extraction in the ‘Lithium Triangle’. 25.
4. Zhao, Z.; Si, X.; Liu, X.; He, L.; Liang, X. Li Extraction from High Mg/Li ratio Brine with LiFePO_4 / FePO_4 as Electrode Materials. *Hydrometallurgy* 2013, 133, 75–83
5. Gupta, C. K., Krishnamurthy, N., *Extractive Metallurgy of rare Earths*, (2005), CRC Press, ISBN 0-203-41302-4



TRANSFORMATION IN MINING AND GREEN METALS

Fevzi YILMAZ

Fatih Sultan Mehmet Vakıf University
Türkiye

Key words: AI in Mining, Deep Sea Mining, Metals in low-carbon economy, Batteries, Green Metals

Abstract

We are witnessing a fundamental shift in mining. Non availability of rich deposits of mine, logistic obstacles, and difficulty of exploring mines from politically instable countries are three of the problems. Automation and robotics in mining, shortly working smarter, are very attractive and highly beneficial. Deep sea mining is one of most innovative area in this field.

Green technologies have one thing in common: more intensive use of metals in products and systems. Usage of metals in carbonless economy should increase substantially by 2050 to meet climate policy. Top seven metals for green technologies are aluminium, copper, cobalt, silver, lithium, zinc, and nickel. Demand for some metals, like lithium, could increase 500% in decades. An inadequate response from production, heavy price volatility, or lower needs than anticipated could result in a misaligned supply and demand, upward or downward price changing in metals and commodities.

1. Introduction

Mining industry have limited credibility/profitability, diminishing investment returns and rising political/environmental risks. It is comparatively tiny sector and has sustainability problems, even big miners have difficulty to find big project. Worsening quality of mineral deposits and relying on scarce minerals are two other facts. For example Chilean copper has fallen by 30% over the past 15 years, to 0.7% Cu (above 1% Cu preferable). Lower grades are pushing up extraction and processing costs (and carbon emissions). Today, we use 16 times more energy to make same kilograms of copper as we did 100 years ago [1,2]. Tesla, an electric car maker, has intended to buy future nickel production of mines in Australia for securing scarce mineral supply[1,2]. Recently, Artificial Intelligence (AI) equipped marine robot has managed to collect nickel-cobalt-manganese mixture from sea bed for battery-metal mining

startup. This last one is an example for advanced scientific development in mining[3].

Green technologies are often used to describe renewable energies, electric vehicles, and material recycling methods. We are defining green technologies as all technologies, services and goods which have the potential to reduce our environmental footprint. This definition makes it possible to include renewable energies, batteries, and the electrification of society in green. The main objective is obeying to the Paris Climate Agreement: i.e., keeping the rise in global temperature to less than 2 °C from pre-industrial levels. The International Renewable Energy Agency (IRENA) expects the proportion of energy produced from renewable energies to rise from 13% in 2017 to 65% in 2050. While the electricity produced from hydro, geothermal and other sources would increase, the main drivers of this growth would be solar and wind power[1]. Dozens of metals, including lithium and graphite have rising use of wind, solar and batteries. According to one scenario the number of electric vehicles on the road could go from 8 to 140 million from 2019 to 2030. In the more aggressive scenario, in which the energy transition rolls out quickly, the number of electric vehicles on the road could hit 245 million in 2030. Low-carbon future would see strong demand for a wide range of base and precious metals. Alongside of aluminum and copper this includes nickel, silver, zinc, cobalt, lithium with high priority. Low-carbon technologies would need over 600 million tonnes (Mt) more metal resources up to 2050 in a 2°C scenario, compared to a 6°C scenario where fossil fuels use continues on its current path [2].

This study does not intend to give economic outlook to the future; instead, it explores development in mining and impacts of carbonless economy on the metal market.

2. Paradigm Transformation in Mining

The US Geological Society (USGS) assesses of more than 100 minerals and metals, key for low-carbon technologies. Moreover, it is expected that more than 200 mines will exhaust their reserves by 2035, and some, like Grasberg in Indonesia, and Chuquibambilla in Chile, will have to shift from open-pit mining to underground tunnels, because the easily accessible deposits will have been depleted. Mining operations in tunnels are more complex [1,2]. In human history, we have used more elements, in more combinations, and in increasingly refined amounts. The supply could be restructured in terms of the production methods used in the coming years, which could limit production while new technologies are integrated. Governments green plans, on the other hand, give importance on secondary production along with primary production by mining [1-3].

China is spending a lot for mining. Copper mining has instability due to turbulent demand and pricing. Chile is debating nationalising copper and lithium. Congo's cobalt mining barefoot children workers greet all foreigners. In Indonesia Chinese miners are demaging rainforest to dig out nickel. In Africa, Chinese groups closing 10,000 in numbers have napped most big commercial mineral deposits. Before Chinese influence, western mining companies dominated Africa. Lead mining and smelting (as well as calcinating) work run by one of British Co. in Zambia-Kabwe had legacy of wrongdoing. Kabwe leadwork had nationalised by Zambian Government at 1970 and closed down 25 years ago. Lead astray and toxic soil, lead unreturned environmental hazards and health problems. Problems are still prevail [4-7].

Top seven metals for green technologies are aluminium, copper, cobalt, silver, lithium, zinc, and nickel. World Bank's expanded list (2017) however cover nearly 20 elements or group of elements. This is true approach for our low-carbon future. Coming decades we would see strong demand for a wide range of base and precious metals. Additional list was made by Chromium, Indium, Iron (cast), Iron (magnet), Lead, Manganese, Molybdenum, REEs (Neodymium), Steel (Engineering) and Graphite. The world is fast becoming as dependent on those metals mentioned above as it is on oil and gas in the past.

Mining firms are giving priority to driverless trucks and unmanned drilling rigs and trains these days. The development of zero-emissions autonomous haul trucks for use in mining operations is other development. Many of their operations use remotely operated land rovers and drones to do risky jobs and keep people safe – like checking high walls in open pits and parts inside big machinery. They also take truck operators out of harm's way, reducing the risks associated with working around heavy machinery [8].

Data is one of our most valuable assets. Every day automated drills, trucks, shovels, conveyors, trains and ships produce huge amounts of valuable data. By combining this data with clever analytics, artificial intelligence, machine learning and automation, mining business is made safer and more productive. Mining companies have also set up Centres of Excellence focused on analytics, automation, asset management, energy and climate change, ore body knowledge, underground mining, surface mining and processing.

As demand for EVs rises, so too does the need for the metals that go into their batteries. Nickel, cobalt, aluminium, copper, manganese, silver and lithium metals are main constituents of battery. So far, these metals have been produced land based mining. Land based mines production generally has an allegations of environmental and human-rights abuses. Alternatives are in front of the door. Mining companies are looking to the Pacific Ocean, where trillions of potato-like nuggets made up of nickel, cobalt, and manganese are strewn across the floor of the Clarion-Clipperton Zone. After granting licenses by International Seabed Authority (ISA) extraction of minerals will be commercialized. According to mining companies, the polymetallic nodules could be vacuumed up with minimal environmental impact. Marine biologists disagree and imposing necessity of further research. BMW, Google, Samsung, and Volkswagen have supported study of undersea mining and side effects. Land-based metal mining, which destroys ecosystems generally leave a toxic legacy of tailings ponds (like leftover materials). AI-equipped marine robots can be programmed to recognize sea life. Sponges, worms and bacterias can be protected during mining. Impossible Mining Co. initiated sea bed study without using heat and harmful acid that leave toxic waste. ISA is already in the process of establishing an undersea mining code that includes robust environmental issues and requirements[3].

As a conclusion, researchers reckon \$2trn must be spent on green-metal exploration and production (E&P) by 2040 [2].

3. Green Metals

The International Energy Agency (IEA), an official forecaster, predicts that wind and solar could account for 70% power generation by 2050, up from 9% in 2020. That means huge demand for the metals that are vital for from EVs to all renewables. Market size of green metals would increase almost seven-fold by 2030. Like fossil-fuel reserves, these commodities are distributed unevenly (Figure 1). Some countries have none at all. Others blessed with vast deposits. Top ten producing countries' share of revenues are expected to change in coming years. Projection for 2040 can be seen in Figure 1.

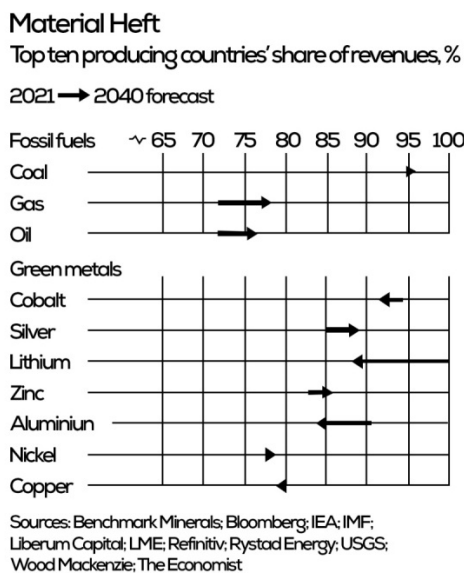


Figure 1. Top ten producing countries [2].

New players are expected for some green metals production (like cobalt, lithium and aluminium). Present producers' share of silver and zinc metals most probably will increase. Top ten producing countries' share of gas expands from 72% today to 77% in 2040. However lithium shrinks 100% today to 89% in 2040. This means other countries are able to mine new mineral deposits.

Australia has deposits of every metal. Chile is home to 42% of the world lithium reserves and a quarter of its copper deposits. Congo has 46% of global cobalt reserves (and produces 70% of World's output today). China is home to aluminium, copper, silver and lithium. Indonesia sits on mountains of

nickel. Peru holds nearly a quarter of the world's silver[2].

Many metals are used to a larger or smaller extent in clean-energy production and low-carbon technology. China's production, demand and export of commodities and metals (particularly green metals) should be examined. In Figure 2, average 60 % world consumption share of Chinese market for four metals (aluminium, copper, steel, nickel) and iron ores can be seen. Urbanisation, industrialisation and electrification in China lead over use of green metals. Chinese leadership supported industry and give them loan with low interest. Spot marketing, different stock exchange policy and on shore business make Chinese different than the rest of the world [9,10].

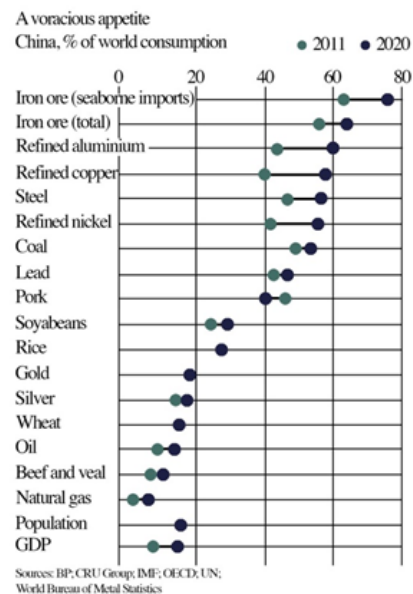


Figure 2. China's consumption change [4].

4. Conclusions

1) The phrase of "Make Mining Green" is used for the earth's sake. Land-based mining already passed their peak level and by the help of AI technologies, industry is changing and deep sea mining is becoming alternative.

2) Decarbonizing the world is likely to be the job of decades. Researchers suggest that the world will be less reliant on energy-related resources in 2040 than it is today. Wind and sunshine, the source of future, are free. The metals demand will not be as big as the coal-oil-gas boom after the second world war. The revenue from green metals rises from 0,5 % (today) to 0,7 % (2040) of world GDP. Seven



metals (aluminium, copper, cobalt, lithium, nickel, silver and zinc) obviously are critical to building an electricity economy.

3) Two things are going to guide the future of mining and metal world. i) Political risks and ii) Climate catastrophe. The worry now is that history repeats itself.

References

- [1] M.A. Dumont, “Green Technologies and Metals”, Desjardins Economic Viewpoint Economic Studies, May 6, 2021, 1-5 .
- [2] “Green commodities”, The Economist, March 26th 2022, 61-63.
- [3] “Make Mining Green”, TIME, April 25/May 2, 2022, 54,55.
- [4] “China and commodities”, The Economist, March 26th 2022, 65,66.
- [5] “Material moves”, The Economist, January 29th 2022, 60,61.
- [6] “Lead Astray”, The Economist, December 12th 2020, p:31,32.
- [7] J.Joly, “D.R. Congo”, The Guardian Weekly, 10 January 2020, 28.
- [8] <https://www.riotinto.com/en/about/innovation/automation> (June 2022).
- [9] “Fortified but not enriched”, The Economist May 28th 2022, p:13-15.
- [10] F.Yılmaz, “New Normal and Carbon Border Adjustments”, 10th International Aluminium Symposium, İstanbul, 03.03.2022



EFFECT OF HEAT TREATMENT ON MICROSTRUCTURE AND CORROSION BEHAVIORS OF ADDITIVE MANUFACTURED Ti-6Al-4V USING SLM TYPE 3D PRINTER

Yusuf Atilla SADIKOĞLU¹, Şeyma KÜÇÜK¹, Özkan GÖKÇEKAYA², Takayoshi NAKANO¹, Hakan YILMAZER¹

¹Yıldız Technical University, ²Osaka University
Türkiye, Japan

Keywords: Additive Manufacturing, Selective Laser Melting, Ti-6Al-4V Alloy

Abstract

In this study, the effect of the production parameters was investigated on the Ti-6Al-4V (Ti64) samples produced using a Selective Laser Melting (SLM) 3D printer. Microstructure, corrosion resistance and hardness values of Ti64 samples produced by SLM technique respectively. Optical microscope images were taken for microstructure characterization, and micro-Vickers hardness measurement was performed for the determination of mechanical properties. A 3-electrode technique was used for corrosion resistance measurement. The corrosion test was carried out with anodic potentiodynamic polarization (PDS) and electrochemical impedance spectroscopy (EIS) tests in 3.5% NaCl solution at room temperature and XRD analysis. As a result of the investigations, the effects of energy volume, which is the output of production parameters, and the effects of corrosion resistance were analyzed.

1. Introduction

Additive manufacturing (AM) has many advantages over traditional manufacturing. AM largely eliminates the need for any casting line installation, additional operations such as turning, or welding lines for joining parts, especially in critical areas such as aerospace and defense. As a result, both the carbon gas emissions that cause the climate crisis are reduced and printing can be carried out within hours. Although they seem far from each other, the common alloy of the aerospace and defense industry and the medical implant industry is additively manufactured Ti-6Al-4V (Ti64). The powder bed fusion (PBF) is an AM technique. Selective Laser Melting (SLM) is an PBF technique. The parts that produced by SLM cools faster than produced parts by casting. As a result, the parts produced by SLM have higher hardness and yield strength. On the other hand, SLMed parts shows lower corrosion resistance than TMed parts. There is lack of literature about heat treatment for investigations on corrosion resistance of SLMed parts. In this study, we search effect of heat treatment on microstructure, corrosion resistance, and hardness of the SLMed Ti64 alloys.

2. Materials and Methods

2.1 Sample Preparation

Commercial Ti64 alloy powders which was fabricated for AM by gas atomization. The investigations were performed on Ti64 samples powder bed melting samples with a dimension of 10x10x10 mm was fabricated by SLM 3D printer, with energy volume of 37.5 (J/mm³). Hereafter, the SLM process parameter were design to have energy volume of 62.5 J/mm³. However, due to the expected 60% efficiency of laser process. So, 60% of 62.5 J/mm³ is equal to 37,5 J/mm. Heat treatment was applied in tube furnace under argon atmosphere. Also, holding temperature is 1050°C, while 3 different holding time such as 0.5h, 1h, and 2h applied. After heat treatment, samples were cooled in the furnace until 25°C.

2.2 Characterizations

The specimens for the optic microscope (OM) analysis were mechanically polished and then etched in a Kroll's reagent consisting of 2 vol. % HF, 6 vol. % HNO₃, and 92 vol. % H₂O. Microstructure investigations have been carried out by optical microscope.

The samples prepared for corrosion test, micro-Vickers hardness testing, and X-ray Diffraction (XRD) analysis were mechanically polished by 2500grit sandpaper. The corrosion behavior of the samples will be examined by open circuit potential (OCP) and potentiodynamics scanning (PDS) in a 3,5 % NaCl solution using 3 electrode corrosion testing. The micro-Vickers hardness testing carried out under 1kg weight and 20 second dwelling time.

3. Conclusion

- Before heat treatment, SLM microstructure dominated by prior beta grain boundaries elongated build direction and Widmanstätten needle-like alpha plates. After heat treatment, prior beta grain boundaries transform alfa grain boundaries. And needle-like alpha plates were expand. With increasing holding time this alfa grain and alpha platelets were expand.
- The hardness values were decrease with heat treatment process. Decrease in hardness values is independent of holding time.
- The corrosion rate was decreased with increasing energy volumes of as built SLM samples.
- The corrosion rate was increased with increasing holding temperature. Also, resistance of passive layer was decrease gradually.

Acknowledgment

This study was funded by the Scientific and Technological Research Council of Turkey (TUBITAK) BİDEB 2209B Grant No: 1139B412100784

EFFECT OF HF ADDITION ON THE STRUCTURAL PROPERTIES, MICROHARDNESS AND OXIDATION BEHAVIOUR OF Co-Al-W SUPERALLOYS

Emre DAMAR, Mehmet Şahin ATAŞ, Mehmet YILDIRIM

Konya Technical University
Türkiye

Keywords: Co-based superalloys, Microhardness, Structural properties, Cyclic oxidation

Abstract

The effect of 2 at. % Hf addition and time and temperature of aging treatment on the microstructural and mechanical properties of Co-9Al-6W (at. %) superalloy was investigated. The study has two main aims: (i) the alteration of the microstructural features such as amount, size, distribution and morphology of the constituent phases w.r.t Hf content and aging treatment; (ii) the effect of microstructural alterations on microhardness and oxidation behavior.

1. Introduction

Nickel- and Cobalt-based superalloys are potential materials to produce components in the jet engine turbines and land-based power generation gas turbines due to their high strength, corrosion resistance, toughness, and good creep resistance at elevated temperatures. The excellent physical and mechanical properties of superalloys mainly depend on their unique microstructure composed of γ -matrix phase and coherent γ' -Co₃(Al,W) precipitates. The lifetime of these alloys strongly depends on the microstructure and its temporal evolution. The microstructural properties are directly affected by alloy composition and proper heat-treatment. In this study, it is aimed to produce Co-Al-W based superalloys and investigate the effect of aging time and 2 at. % Hf addition on the structural properties, hardness and oxidation resistance in detail.

2. Materials and Methods

Co-based superalloys were investigated with a nominal composition of Co-9Al-6W and Co-9Al-6W-2Hf (at. %). The superalloys were produced by arc-melting using a non-consumable tungsten electrode and a water-cooled copper tray under a partial Ar atmosphere to minimize oxidation. High purity Co (99.90 wt%), Al (99.9 wt%), W (99.95 wt%) and Hf (99.95 wt%) were used as starting materials. Samples were remelted three times and reversed between each melting step to achieve greater composition homogeneity. The weight loss during the arc-melting process was less than 0.5 wt%. Then, specimens were homogenized (at 1250 °C for 24 h) and subsequently aged (at 650, 750 ve 1000 °C for 16 and 64 hours) to form stable γ/γ' particles. The microstructures of the alloys were investigated by optical microscope and scanning electron microscope (SEM), while phase analysis was performed by x-ray diffraction (XRD) and energy dispersive x-ray spectroscopy (EDS). Mechanical properties were determined by Vickers microhardness measurements.

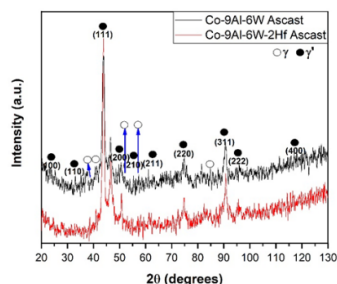


Figure 1. XRD analysis of Co-9Al-6W and Co-9Al-6W-2Hf superalloys.

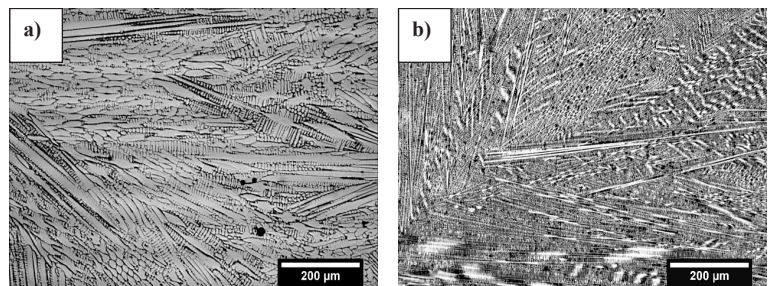


Figure 2. Optical microstructure of casting a) Co-9Al-6W and b) Co-9Al-6W-2Hf superalloys

3. Conclusion

The structural properties, microhardness, and oxidation behaviour of the ternary Co-9Al-6W and quaternary Co-9Al-6W-2Hf superalloys were investigated, and the important conclusions can be reported as follows: After heat treatment, the microstructure of the ternary Co-9Al-6W alloy transformed to coarse-grained and annealed twins. After heat treatment, the eutectic mixture exhibited coarsening behavior in the microstructure of the quaternary Co-9Al-6W-2Hf alloy and transformed to particles. With addition of Hf, the hardness of increased twice.

References (if needed)

- [1] J. Sato, T. Omori, K. Oikawa, I. Ohnuma, R. Kainuma, and K. Ishida, *Science*, 312 (2006), 90-91.
- [2] J. E. Saal, ve C. Wolverton, *Acta materialia*, 61 (2013), 2330-2338.
- [3] M. Ooshima, K. Tanaka, N. L. Okamoto, K. Kishida, and H. Inui, *Journal of Alloys and Compounds*, 508 (2010), 71-78.
- [4] T. Omori, K. Oikawa, J. Sato, I. Ohnuma, U. R. Kattner, R. Kainuma, and K. Ishida, *Intermetallics*, 32(2013), 274-283.
- [5] A. F. Dinler, *Synthesis and structural characterization of Co-Al based superalloys*, M.Sc. Thesis, Middle East Technical University, 2019, Ankara, Turkey, pp. 34-69.



HOMOGENIZATION OF THE CuNi12Zn24 ALLOY PRODUCED BY HORIZONTAL CONTINUOUS CASTING

Umut YILDIZ¹, Alptekin KISASÖZ², Çağlar YÜKSEL³, Mustafa YILDIZ¹,
Serdar Osman YILMAZ⁴

¹Kayalar Bakır Alaşımları, ²Kırklareli University, ³Atatürk University, ⁴Namık Kemal University
Türkiye

Keywords: CuNi12Zn24, Copper, homogenization, horizontal continuous casting, porosity

Abstract

This research has been focused on the properties of CuNi12Zn24 alloy after homogenization treatment that has been produced in horizontal continuous casting. The existence of impurities such as oxygen, and sulfur based in liquid metal induces surface and internal tensions, as also hot tearing and cracks formed during casting, and hot and cold rolling. The alloy has been produced with a thickness of 18mm, a width of 660 mm, and a length of 50 meters. The milling process has been applied in order to increase the surface quality, following the casting process. Then in order to eliminate the discontinuities and impurities, homogenization annealing has been performed at different temperatures and duration. The microstructure of the homogenized samples has been investigated with optical microscopy and image analysis, and also porosity level of the samples has been determined. Moreover, mechanical properties of the samples have been investigated by the hardness tests.

1. Introduction

CuNi12Zn24 alloy is a copper alloy with 12% Ni and 24% Zn. Nickel addition copper alloys are used for a wide variety of applications due to copper's excellent electrical and thermal conductivity. CuNi12Zn24 alloy is used for the production of money stamps and strips. Nickel-added copper alloys are one of the important commercial alloy groups in the coin industry due to their electrical conductivity, atmospheric corrosion resistance, and formability. The susceptibility of this alloy to stress corrosion cracking is much lower compared to other copper alloys. [1] [2] [3]

Nickel – Silvers are a copper-nickel-zinc alloy with an alpha phase structure. The alloy has good corrosion resistance to rural, industrial, and marine

atmospheres and fresh water. It has good cold formability and an attractive soft ivory-white color. The most commonly used forged forms are sheet, strip, rod, tube and wire. Other applications are in electrical, mechanical and miscellaneous (musical instrument and camera parts) uses. The alloy has excellent cold forming properties, on the other hand, its hot formability is limited. The annealing temperature of this alloy is typically between 620 and 700°C. A stress relieving heat treatment between 300-350°C is possible to reduce the presence of internal stress. [2] [4]

Serious plastic deformation processes such as cold working with high deformation rates are used in the production of coins. Hardness, microstructure, and mechanical properties are critical to the coin industry. The material is rolled and its thickness is reduced by cold deformation processes to be able to come to the money stamping processes. After the rolling process, the hardness increases, and the grains elongate. However, in order to reach the final thickness, it is necessary to perform the cold rolling process again. For this reason, strip recrystallization process is applied. Recrystallization annealing to continue cold working can solve various problems. Recrystallization annealing after cold forming is a heat treatment method. This method is an annealing process like stress relief annealing, normalizing, or soft annealing. Since grain boundaries migrate due to diffusion processes, grains can regenerate during recrystallization annealing. When the grains return to their original shape, the material regains its ductility and ability to form. The major concern with recrystallization annealing is that it is often done at high temperatures (600 – 700 °C) for copper alloys. [4]

2. Experimental Procedure

CuNi12Zn24 was used in experimental studies. The chemical composition of this alloy is given in **Table 1**. CuNi12Zn24 alloy is cast with a thickness of 18 mm and a width of 660 mm with the horizontal continuous casting method. Since the surface precision of these strips, which are approximately 50 meters in size, is important for quality, they are milled after casting. After the milling process of approximately 3 mm, the strips are reduced to 5 mm by the cold rolling process. By recrystallization annealing at 630°C after 5 mm, the grains are homogenized and the material is given ductility and the ability to shape. In the last cold rolling process, where the final thickness is given, micro-level discontinuities occur, and a solution is sought for this problem with homogenization annealing.

Table 1. Chemical composition of CuNi12Zn24 alloy (wt%)

Alloy	Cu	Ni	Zn	Pb	Mn
%	65,4	12,4	Rest	0,02	0,4
Alloy	Fe	P	S	Si	As
%	0,15	0,003	0,004	0,01	0,002

In order to eliminate the discontinuities mentioned in the subject, it is aimed to eliminate possible segregations by performing the homogenization process as annealing after horizontal casting. The macrostructures of the samples taken after horizontal casting were examined and the center line was interpreted by taking vertical sections. SEM-EDS analysis was performed on one of the samples after casting and the causes of micro-macro cracks were investigated. In addition, SEM and EDS analyses were performed on the crack surface and the impurity elements that could cause the crack was determined. Images were taken from the sample surface and elemental analysis results are reported. After the samples were rolled up to 5 mm, they were annealed at 630°C for 7 hours. The material, which was reduced to 2 mm after the rolling processes, was annealed at 800°C for 10 hours. For porosity analysis, the sample was ground and then polished with 1 mm diamond paste. Sample microstructure and grain size were examined using an optical microscope. Vickers microhardness tests and analysis after annealing were measured using a hardness measuring device with the HV10 method according to ASTM E384.

3. Results and Discussion

As a result of the macrostructural examinations, it was noted that the center line was not in the center, as can be seen in **Figure 2**. It is defined as centerline segregation due to reasons such as sudden dispersion of phases due to temperature difference in this region. In addition, it has been determined that there are differences between grain sizes as seen in the macrostructures of the samples taken from different strips from the same points.

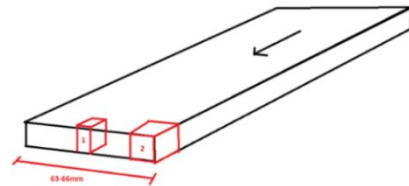


Figure 1. Sample schematic representation



Figure 2. Macrostructural investigations of samples taken from strip edges

SEM and EDS analysis were applied on sample number one. In order to reveal the phases in the structure more clearly, SEI (Secondary Electron Image) and BEI (Backscatter Electron Image) images were taken separately.



Figure 3. Sample image

SEM images taken for the sample coded as No. 1 are given in **Figure 4**.

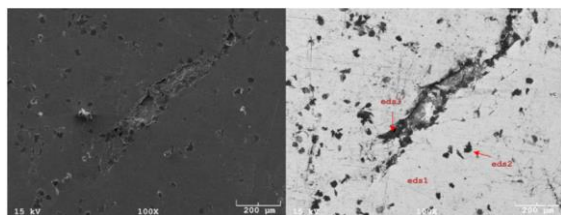


Figure 4. SEI and BEI image of 1 coded sample

The points where EDS analysis was performed are shown on the BEI image of the sample number 1 given in **Figure 4**. 3 EDS points have been determined and the matrix of the number 1 EDS structure delivers a different phase in the EDS structure number 2, the EDS crack region number 3. EDS results are given in **Table 2-3-4**.

Table 2. EDS result 1

Elt.	Line	Intensity (c/s)	Atomic %	Conc	Units
Ni	Ka	37,4	15,408	14,295	wt. %
Cu	Ka	105,64	59,280	59,543	wt. %
Zn	Ka	33,45	25,311	26,162	wt. %
			100,000	100,000	wt. %

As a result of EDS number 1, it was observed that the matrix of the structure was Cu, Zn and Ni.

Table 3. EDS result 2

Elt.	Line	Intensity (c/s)	Atomic %	Conc	Units
C	Ka	24,83	29,722	9,952	wt. %
O	Ka	56,6	18,058	8,055	wt. %
Si	Ka	61,69	4,776	3,739	wt. %
Cl	Ka	84,37	4,36	4,309	wt. %
K	Ka	58,03	2,946	3,212	wt. %
Ni	Ka	45,43	6,454	10,56	wt. %
Cu	Ka	125,84	24,029	42,569	wt. %
Zn	Ka	37,,57	9,656	17,604	wt. %
			100,00	100,00	wt. %

When the result of EDS number 2 was examined, it was observed that there were oxide structures.

Table 4. EDS result 3

Elt.	Line	Intensity (c/s)	Atomic %	Conc	Units
C	Ka	9,92	17,443	5,416	wt. %
O	Ka	49,35	22,832	9,443	wt. %
Si	Ka	51,18	5,84	4,24	wt. %
Cl	Ka	59,36	4,544	4,165	wt. %
K	Ka	31,39	2,35	2,375	wt. %
Ca	Ka	32,56	2,534	2,625	wt. %
Mn	Ka	18,79	2,192	3,112	wt. %
Fe	Ka	18,1	2,391	3,452	wt. %
Ni	Ka	26,59	5,737	8,705	wt. %
Cu	Ka	91,06	25,974	42,669	wt. %
Zn	Ka	0,00	0	0	wt. %
			91,838	86,203	wt. %

As a result of the EDS number 3 given in **Table 3**, when the fractured region is examined, it is observed that there are different elements except Cu, Zn and Ni, as well as 9% oxygen. Therefore, these different elements are thought to be in the oxide structure. No intermetallic phase or foreign particles were found. When the process is examined in general, this sulfur in the structure can be caused by dirty and not well cleaned scrap. The solubility of sulfur in copper is 0.023% by weight. Therefore, it can exist in copper in solid solution and can generate stress during rolling or deformation operations. It also shows phase transformations at 103, 435 and 1061°C. The sulfur in the Cu separates from the solution with heating and precipitates at the grain boundaries as highly segregated. Especially during deformation, they cause problems such as crack formation by causing both cold and hot tearing.

The hardness values of 5 mm samples after cold working (rolling) and samples annealed at 630°C for 7 hours are given in the chart. The hardness values of the materials, which were reduced from 5 mm to 2 mm by cold rolling again, were also given. It was annealed for 10 hours at 800°C at 2 mm. These values are the average of seven hardness test results made on the samples. As can be seen from the graph, there is a decrease of approximately 17 HV10 between the 5 mm unannealed material and the annealed material. In the hardness tests made on 2 mm material, a decrease of about 30 HV10. The main purpose of this is to prevent micro-macro

cracks in the internal structure and surface of the material during the cold workability of the material, to increase the ductility, to prevent the formation of cracks and to reduce the tension in the internal structure and ensure easy processing of the material. In addition, thanks to annealing, a homogeneous grain structure is obtained and segregations are prevented. As can be seen in the graph, the hardness values of the material decreased to 2 mm after cold rolling increased.

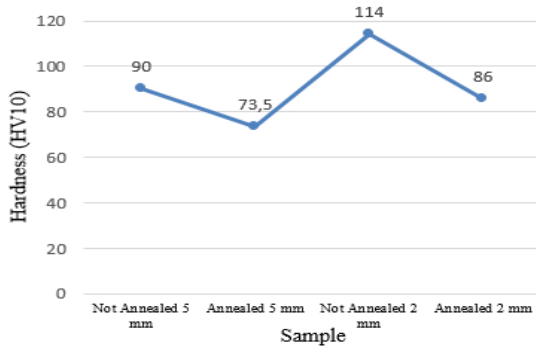


Figure 5. Hardness values of sample

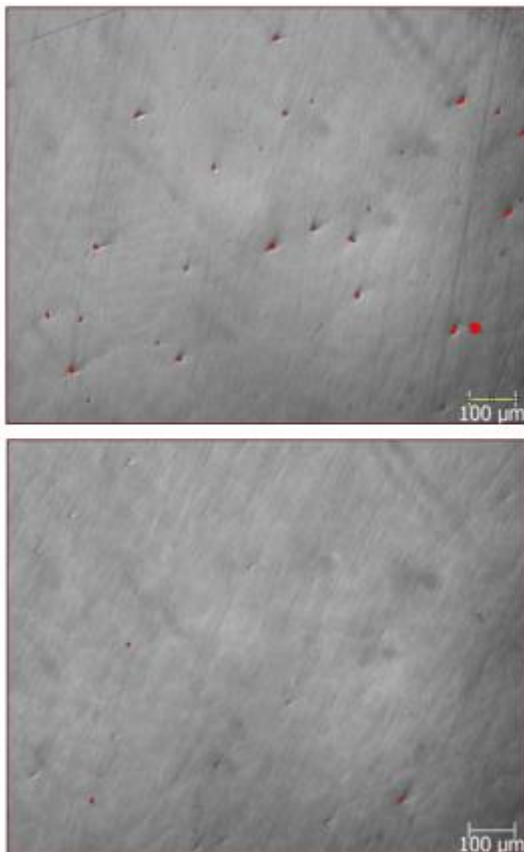


Figure 6. Porosity analyzes images before annealing (up) and after annealing (down)

After porosity analyzes, A great decrease was observed in the porosity amount of the annealed material. Also porosity count, total area and feret have been proven that the amount of porosity decreases.

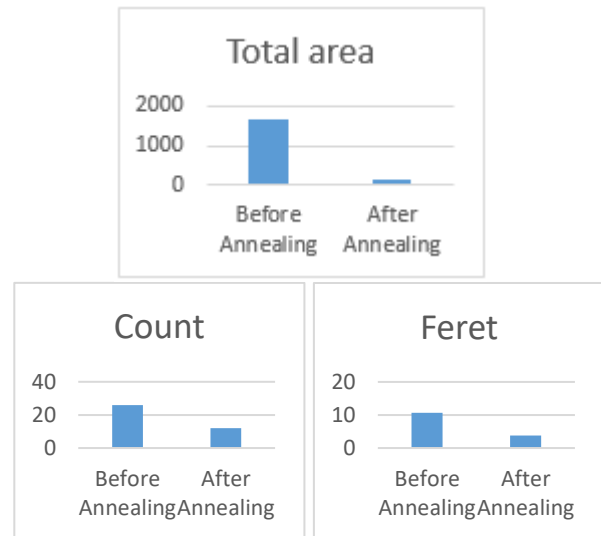


Figure 7. Porosity analyzes

4. Conclusion

In this study, the effect of annealing on the hardness and porosity behavior of cold-rolled CuNi12Zn24 was investigated. Results can be concluded as below:

1. The causes of crack formation are due to the high oxide and sulfur content in the structure.
2. The hardness value of CuNi12Zn24 was significantly reduced by annealing with an increasing reduction ratio.
3. After annealing, the amount of porosity decreases.

References

- [1] ASM Speciality Handbook, Copper and Copper Alloys, ASM International, 2001, 10-118
- [2] <https://www.copper.org/resources/properties/microstructure/ni_silver.html> Dated: 21.08.2013
- [3] Seungman Sohn, Tak Kang, The effects of tin and nickel on the corrosion behavior of 60Cu-40Zn alloys, 2001.
- [4] ASM Handbook, Heat Treating of Nonferrous Alloys, ASM International, 2016.
- [5] https://www.substech.com/dokuwiki/doku.php?id=wrought_copper-nickel_alloys_and_nickel_silver Dated: 04.06.2013



THERMODYNAMIC AND EXPERIMENTAL APPROACH OF THE PHASE FORMATIONS IN Ti-Nb-Ta-Zr-Mo HIGH ENTROPY ALLOYS

Gökhan POLAT¹, Yunus Eren KALAY²

¹Necmettin Erbakan University, ²Middle East Technical University
Türkiye

Keywords: High Entropy Alloys, Phase Prediction, Thermodynamic, Mechanical Properties

Abstract

Thermodynamical approaches, including enthalpy of mixing (ΔH_{mix}) and Thermo-Calc software, were used to estimate the formation of matrix and secondary phases in Ti-Nb-Ta-Zr-Mo high entropy alloys (HEAs). The overall phase formation of the HEAs was estimated by the thermo-physical calculations and compared with the Thermo-Calc results. Both techniques showed similar outputs in terms of phase predictions for the matrix phase. However, the overall thermo-physical calculations failed to estimate minor secondary phases' formation. Binary mixing enthalpies of the substances were used to predict the secondary phases. The experimental studies were conducted on the Ti-Nb-Ta-Zr-Mo HEAs to confirm the secondary phases in the matrix. The HEAs were produced using a vacuum arc melter and analyzed by the X-ray diffraction (XRD) technique. XRD analyses showed dual body-centered cubic (BCC) phases in the microstructure of the HEAs. The increasing Mo content in the HEAs also increased the amount of secondary BCC phase. The results well agreed with the results obtained from Thermo-Calc software. The hardness tests were conducted to reveal the effect of the secondary BCC phase on the mechanical properties of the HEAs. The results showed that the hardness of the HEAs enhanced from 368 to 524 HV with the increasing secondary BCC ratio.

1. Introduction

There are a limited number of binary engineering alloys commercially used in the industry, and most of these alloys are based on one principal element. These alloys can include solid solutions and intermetallic compounds in the microstructure [1], [2]. On the other hand, Yeh et al. [3], [4] suggested a novel alloy concept, so-called high entropy alloys (HEAs), pointing to the well-known thermodynamic fact that the configurational entropy (ΔS_{conf}) of a binary alloy is maximum when the elements are in equal atomic ratios

which makes an alloy stable thermodynamically. Since HEAs consist of at least 5 principle elements and the ratios of the elements are between 5 to 35 at. %, it significantly affects the phase formation kinetics, lattice distortion, and thus, the properties. The high mixing entropy increases the solubility between the constituent elements and leads to the formation of unexpected simple phases and microstructures. This simplification due to the high entropy effect is therefore significant in such multicomponent alloys. Thus, many theories, possible novel materials, and applications are predicted in the 21st century [5].

Yeh et al. [3], [4] suggested that owing to the high mixing entropy, disordered and partially ordered solid solutions could be expected in the HEAs. The formation of the type and number of the phases are the most critical issue in the alloy design strategy of the HEAs. Recently, intensive research has been conducted on the phase formation rules of the HEAs using parameters such as mixing enthalpy, configurational entropy, and atomic size difference between the principal elements. In addition, computational thermodynamic methods such as CALPHAD are also used to predict the phases of the HEAs by constructing the phase diagrams as a function of temperature [5].

HEAs are the most crucial candidates for high-temperature applications to improve the properties of traditional alloys such as Ni-based alloys. Gou et al. [6] studied the phase stability of the MoNbHfZrTi HEA using the differential scanning calorimetry (DSC) method. They showed that the room temperature phases of MoNbHfZrTi remained stable up to 1743 K temperature exposures. In the studies carried out by the same group, a yield strength of 1719 MPa was observed in the as-cast MoNbHfZrTi HEA at room temperature, and it was decreased to 1575 MPa after the homogenization [6]. In addition, Senkov et al. [7] studied the effect of Al on HfNbTaTiZr HEA. They

showed that the Al addition increased the room temperature hardness by 29 %, reduced the density of the HEA by 9 %, and enhanced the compressive yield strength by 98%. The researchers extensively conducted similar studies, including the elements such as Hf, Nb, Ta, Ti, and Zr elements, to investigate the structural and mechanical properties of the HEAs [8]–[11]. These studies show that HEAs are critical alloys, particularly for high-temperature applications.

In the present work, systematic Mo addition from 5 to 35 at. % into the TiNbTaZr was investigated using a thermodynamic approach (thermo-physical calculations and Thermo-Calc software) to reveal the phase formation hierarchy. The HEAs were then produced experimentally by melting and compared with the thermodynamic calculations and simulation. The results showed that the Mo addition triggered the formation of the secondary BCC phase in the microstructure, and the corresponding hardness values increased.

2. Experimental Procedure

5, 20, and 35 at. % Mo was added into TiNbTaZr HEA systematically to investigate its effect on the thermodynamic, structural, and mechanical properties.

The enthalpy of mixing (ΔH_{mix}), the entropy of mixing (ΔS_{mix}), and atomic size difference (δ) values of the HEAs were calculated using the thermo-physical calculations to reveal the formation of solid solution phases [5], [12], [13]. Furthermore, the valence electron concentration (VEC) of the HEAs was calculated to estimate the crystal structure of the alloy [14]. The hierarchy of solidified phases in the HEAs was calculated using equilibrium stepping calculation by a Thermo-Calc (version 2019b) software employing a TCHEA2 (High Entropy Alloys version 2.1.1). The simulations were conducted using temperature intervals of with 1-degree.

The HEAs were produced experimentally from high-purity (>99.9 wt.%) Ti, Nb, Ta, Zr, and Mo chunks. The melting was conducted under Ar atmosphere at 5–8 mbar pressure using Edmund Buhler MAM-1 copper hearth arc-melting equipment. Since the elements in the HEAs have high melting points, the alloys were remelted at least 5 times to ensure chemical homogeneity. The samples were flipped upside down in each melting step.

The phases present in the HEAs were determined by Bruker D8 Advance X-ray diffractometer using Cu-K α radiation. The hardness of the samples was investigated under 4.903 N force using the Vickers microhardness (HV) test with a diamond pyramid indenter.

3. Results and Discussion

5, 20, and 3 at. % Molybdenum (Mo) element was added to TiNbTaZr HEA, which has been widely studied in the literature, to examine its effect on the thermodynamic, structure, and mechanical properties. That is, (TiNbTaZr)_{100-x}Mo_x (x=5, 20, 35 at. %) was designed and investigated in detail.

Thermo-physical calculation results of HEAs are given in Table 1. As seen in the table, values such as atomic size difference, ΔS_{mix} , do not change significantly with the gradual Mo addition. However, the ΔH_{mix} value of the HEAs changes from positive to negative with the increasing Mo content due to the binary negative values of Mo with the remaining elements [15]. The transition of this value to the negative scale causes the formation of secondary phases, particularly intermetallic compounds, in the microstructure [16]. Although the thermo-physical calculations can be used to estimate the formation of solid solution phases, it should be noted that it does not provide information about the number of the phases having the same crystal structure. Therefore, it is expected to obtain a single-phase body-centered cubic (BCC) crystal structure for all the HEAs with changing Mo compositions depending on the average VEC value given in Table 1. That is, more than one phase having the same crystal structure could be expected in the HEAs.

Table 1. Thermo-physical calculations of (TiNbTaZr)_{100-x}Mo_x (x=5, 20, 35 at. %)

HEA	δ (%)	ΔH_{mix} (kJ/mol)	VEC	ΔS_{mix} (kJ/mol.K)	T (K)	Crystal Structure
(TiNbTaZr) ₉₅ Mo ₅	3.6	1.3	4.6	12.6	2536	BCC
(TiNbTaZr) ₈₀ Mo ₂₀	3.4	-1.8	4.8	13.4	2592	BCC
(TiNbTaZr) ₆₅ Mo ₃₅	3.0	-3.7	5.0	12.9	2648	BCC

Thermo-Calc Software is used to estimate the types and number of the phases upon solidification of the HEAs. The equilibrium stepping calculation module was used to predict the corresponding solidification paths and the relative amounts of the phases present in the HEAs during the solidification from the liquid. It

should be noted that preliminary experiments were conducted to reveal the dominant phases in the HEAs, and the remaining phases were eliminated based on these experiments to obtain the most reliable simulations.

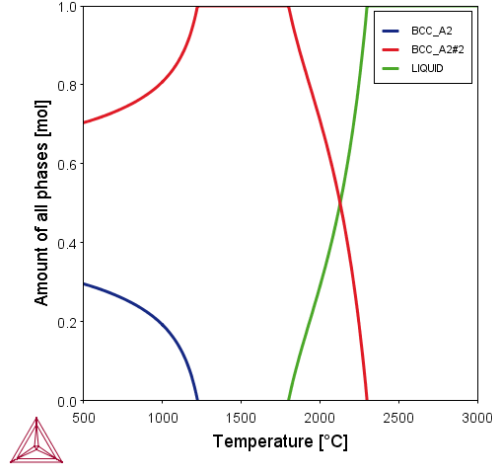


Figure 1. Equilibrium stepping calculation of $(\text{TiNbTaZr})_{65}\text{Mo}_{35}$ HEA

The mole fractions of the phases as a function of temperature are shown in Figure 1. The equilibrium stepping calculation of $(\text{TiNbTaZr})_{65}\text{Mo}_{35}$ shows a single primary BCC (A2) phase up to a temperature of around 1200 °C. However, the further decrease in the temperature causes a systematic decomposition of the primary BCC phase into a secondary BCC up to room temperature. That is, a microstructure including primary BCC (BCC-1) and secondary BCC (BCC-2) with values of around 67 and 33 vol. % could be expected after the equilibrium solidification. These results show that the thermo-physical calculation may not be reliable in estimating the second phases having the same crystal structure in the microstructure. However, since the ΔH_{mix} values of Mo-containing HEAs are between 1.3 and -3.7 kJ/mol (Table 1), only solid solution phases could be estimated in the HEAs. In addition, the decreasing atomic size difference below 6.6 % triggers the formation of solid solution phases. These values are between 3.0 and 3.6 % in the present study, as seen in Table 1. It means that the parameters restrict the formation of intermetallic compounds (ICs) in the Mo-containing HEAs. The melting points estimated from the Thermo-Calc software thermo-physical calculation are almost the same, with a value of around 2650 K.

The HEAs were produced experimentally using an arc melter to investigate their structure and compare them with the thermodynamic calculations and simulation.

Therefore, the cylindrical samples were cut into pieces and investigated by the X-ray diffraction (XRD) technique. XRD results given in Figure 2 show the effect of Mo on the structure of TiNbTaZr HEA. It can be seen from the XRD patterns that 5 at. % Mo addition causes a single BCC phase in the microstructure. However, the increasing Mo content up to 35 at. % triggers the formation of secondary BCC phases in addition to primary BCC in the HEAs. The formation of the secondary BCC may be attributed to the segregation of Mo-rich phases in the alloy. Nevertheless, these phases well agree with the phases estimated by Thermo-Calc results.

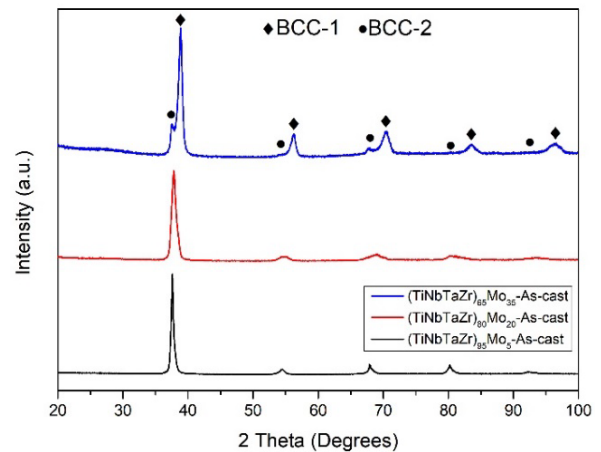


Figure 2. XRD patterns of as-cast $(\text{TiNbTaZr})_{100-x}\text{Mo}_x$ ($x=5, 20, 35$ at. %) HEA

Figure 3 shows the change in the Vickers hardness with the systematic addition of Mo to the TiNbTaZr HEA. The results show that 5 at. % Mo addition results in a hardness value of 368 (± 10) HV. However, 20 and 35 at. % Mo addition caused a gradual increase in the hardness with the values of 469 (± 2.5) and 524 (± 10) HV, respectively.

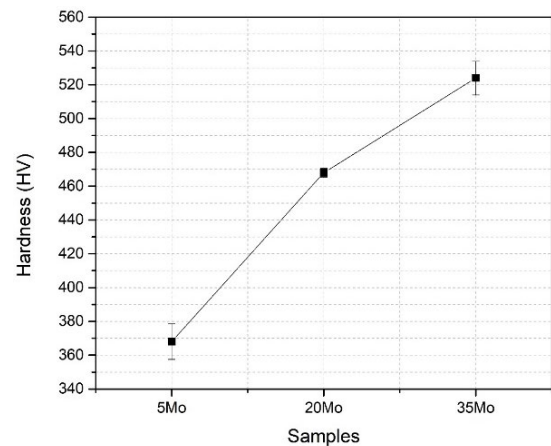


Figure 3. Hardness of as-cast $(\text{TiNbTaZr})_{100-x}\text{Mo}_x$ ($x=5, 20, 35$ at. %) HEA

The change in hardness can be explained by the correlation of Thermo-Calc results (Figure 1) and the XRD pattern (Figure 2). As can be seen from the figures, the Mo addition causes the formation of the secondary BCC phase (BCC-2) in the microstructure with a value of around 33 vol. % for 35 at. % Mo. That is, the systematic increase in the hardness could be attributed to the formation of a relatively hard BCC-2 phase in the microstructure. Furthermore, since increasing Mo raises the amount of the BCC-2 phase, the hardness of the HEAs increases proportionally.

4. Conclusion

In this study, the effect of Mo on the structural properties of TiNbTaZr was investigated by thermo-physical calculations, Thermo-Calc simulation, and experimental studies. The experimental results showed the dominant phases were well agreed with the simulation, and a single BCC phase was observed in the HEA containing 5 at. % Mo. However, increasing Mo up to 35 at. % caused the formation of the secondary BCC phase along with the primary BCC. The hardness tests were conducted on the HEAs to reveal the effect of the secondary BCC phase on the mechanical properties. The hardness results showed a dramatic increase from 368 to 524 HV with the increasing amount of Mo from 5 to 35 at. %, respectively.

Acknowledgment

The research reported in this paper was supported by Middle East Technical University, Turkey, through the Scientific Research Projects Coordination Unit (BAP) under project number GAP-308-2020-10325.

References

- [1] B. S. Murty, *High-entropy alloys*. Butterworth-Heinemann, 2014.
- [2] B. S. Murty, J. W. Yeh, S. Ranganathan, and P. P. Bhattacharjee, "High-entropy alloys: basic concepts," in *High-Entropy Alloys*, Elsevier, 2019, pp. 13–30.
- [3] J. W. Yeh *et al.*, "Nanostructured high-entropy alloys with multiple principal elements: Novel alloy design concepts and outcomes," *Adv. Eng. Mater.*, vol. 6, no. 5, pp. 299–303, 2004.
- [4] J. W. Yeh, "Alloy design strategies and future trends in high-entropy alloys," *Jom*, vol. 65, no. 12, pp. 1759–1771, 2013.
- [5] B. S. Murty, J. W. Yeh, S. Ranganathan, and P. P. Bhattacharjee, "High-entropy alloys: basic concepts," *High-Entropy Alloy.*, pp. 13–30, 2019.
- [6] N. N. Guo *et al.*, "Microstructure and mechanical properties of refractory MoNbHfZrTi high-entropy alloy," *Mater. Des.*, vol. 81, pp. 87–94, 2015.
- [7] O. N. Senkov, S. V. Senkova, and C. Woodward, "Effect of aluminum on the microstructure and properties of two refractory high-entropy alloys," *Acta Mater.*, vol. 68, pp. 214–228, 2014.
- [8] D. B. Miracle and O. N. Senkov, "A critical review of high entropy alloys and related concepts," *Acta Mater.*, vol. 122, pp. 448–511, 2017.
- [9] S. Gorsse, D. B. Miracle, and O. N. Senkov, "Mapping the world of complex concentrated alloys," *Acta Mater.*, vol. 135, pp. 177–187, 2017.
- [10] H. Dobbstein, E. L. Gurevich, E. P. George, A. Ostendorf, and G. Laplanche, "Laser metal deposition of a refractory TiZrNbHfTa high-entropy alloy," *Addit. Manuf.*, vol. 24, no. October, pp. 386–390, 2018.
- [11] Y. Zhang, X. Yang, and P. K. Liaw, "Alloy design and properties optimization of high-entropy alloys," *Jom*, vol. 64, no. 7, pp. 830–838, 2012.
- [12] S. Guo, Q. Hu, C. Ng, and C. T. Liu, "More than entropy in high-entropy alloys: Forming solid solutions or amorphous phase," *Intermetallics*, vol. 41, pp. 96–103, 2013.
- [13] D. B. Miracle and O. N. Senkov, "A critical review of high entropy alloys and related concepts," *Acta Mater.*, vol. 122, pp. 448–511, 2017.
- [14] S. Guo, C. Ng, J. Lu, and C. T. Liu, "Effect of valence electron concentration on stability of fcc or bcc phase in high entropy alloys," *J. Appl. Phys.*, vol. 109, no. 10, 2011.
- [15] A. Takeuchi and A. Inoue, "Classification of Bulk Metallic Glasses by Atomic Size Difference, Heat of Mixing and Period of Constituent Elements and Its Application to Characterization of the Main Alloying Element," *Mater. Trans.*, vol. 46, no. 12, pp. 2817–2829, 2005.
- [16] G. Polat, Z. A. Erdal, and Y. E. Kalay, "Design of Novel Non-equiatomic Cu-Ni-Al-Ti Composite Medium-Entropy Alloys," *J. Mater. Eng. Perform.*, vol. 29, no. 5, pp. 2898–2908, May 2020.



INTEGRATED PROCESSING OF $Al_xCoCrFeNi-Cu_a$ ($0.5 \leq x \leq 3$, $a=0.5,1$) HIGH-ENTROPY ALLOYS: FROM MASTER ALLOY SYNTHESIS TO SHAPING

Faruk KAYA¹, Albek ERŞAN², Sajjad ALIAKBARLU¹, Gül İpek SELİMOĞLU², Bora DERİN¹

¹Istanbul Technical University, ²Eskisehir Technical University
Türkiye

Keywords: High-entropy alloys, Thermochemical modelling, Combustion synthesis, SHS, Master Alloys, Suction-Casting, Cold/Hot Rolling, Microstructure, Hardness, Deformability

Abstract

In this study, an integrated manufacturing process for the lab scale production of semi-finished bars and sheets of $Al_xCoCrFeNi-Cu_a$ ($0.5 < x < 3$), ($a=0.5,1$) high-entropy alloys was investigated. The manufacturing steps start at cost and time-efficient pyrometallurgical combustion synthesis of master alloys from oxides through a self-sustained aluminothermic reduction reaction. Post-synthesis metallurgical processes include refining the selected master alloys by remelting, suction-casting via vacuum arc melting, and hot (1000 °C) and cold (25 °C) rolling. Thermochemical modelling via FactSage™ has been applied intensively both during synthesis and post-synthesis steps for precisely tuning the composition of the master alloys and the discussion of the thermodynamic aspects of the phase diagrams for non-equilibrium and final equilibrium conditions. The compositions, phase constituents and microstructure of the alloys were characterized through XRF, XRD, SEM-EDX, and TEM analyses. Mechanical properties were obtained through microvickers and nanoindentation tests.

1. Introduction

High-entropy alloys (HEAs) have revolutionized the alloy concept with the unique equimolar approach and have been studied extensively over the last ten years. Alloys with at least five principal elements with equal or near-equal compositions have been reported to exhibit superior properties over traditional alloys. $Al_xCoCrFeNi$ and $Al_xCoCrFeNiCu_a$ alloys are two of the most studied HEAs owing to their superior mechanical, chemical, and physical properties [1–5]. However, efforts toward the cost-efficient synthesis and processing of these promising alloys are rather scarce. Given that most of the engineering alloys are processed through hot and cold rolling into finished and semi-finished products, studies focusing on the comparison of hot and cold rolling capacities, and microstructural and mechanical property evaluation of these HEAs are crucial [6].

2. Materials and methods

The oxides Fe_2O_3 , NiO , Cr_2O_3 and Co_3O_4 of at least %98 purity whose amounts were carefully determined via FactSage™, were reduced by metallic Al in a self-propagating high-temperature synthesis (SHS) reactor [7]. Cu on the other hand was added to the SHS mixture in metallic form. Pieces of 5-6 g from each master alloy were refined and suction casted into a 4x4x30 mm square prism Cu mold by using a Vacuum Arc Melter (Edmund Bühler GmbH) under Ar atmosphere. Then the as-cast alloys were hot and cold rolled (25 °C) via Durston FSM-160 double roller. Hot rolled alloys were reheated in the furnace and held for 10 min to maintain the temperature between each pass.

3. Results and Conclusion

The master alloys were successfully synthesized and their compositions were acceptable for the casting/rolling processes according to XRF results. FCC-based alloys of $Al_{0.5}CoCrFeNi$ exhibited %185 CR deformation with significant work hardening (109%) without failure. However, in HR condition the max. thickness reduction was %93 due to extensive BCC-B2 precipitation. HR also had superior effects on the $Al_{0.5}CoCrFeNiCu$ alloy with a significant %70 increase in the hardness despite the recrystallization. The precipitation of the ordered BCC-B2 phase were found to have a profound effect on the thermomechanical properties of the alloys.

References

- [1] Y.-F.F. Kao, T.-J.J. Chen, S.-K.K. Chen, J.-W.W. Yeh, Microstructure and mechanical property of as-cast, -homogenized, and -deformed $Al_xCoCrFeNi$ ($0 \leq x \leq 2$) high-entropy alloys, *J. Alloys Compd.* 488 (2009) 57–64. doi:https://doi.org/10.1016/j.jallcom.2009.08.090.
- [2] W.-R.R.W.-L.L. Wang, W.-R.R.W.-L.L. Wang, J.-W.W. Yeh, Phases, microstructure and mechanical properties of $Al_xCoCrFeNi$ high-entropy alloys at elevated temperatures, *J. Alloys Compd.* 589 (2014) 143–152. doi:10.1016/j.jallcom.2013.11.084.
- [3] Q.H. Li, T.M. Yue, Z.N. Guo, X. Lin, Microstructure and Corrosion Properties of $AlCoCrFeNi$ High Entropy Alloy Coatings Deposited on AISI 1045 Steel by the Electrospark Process, *Metall. Mater. Trans. A.* 44 (2013) 1767–1778. doi:10.1007/s11661-012-1535-4.
- [4] C.P. Lee, Y.Y. Chen, C.Y. Hsu, J.W. Yeh, H.C. Shih, The Effect of Boron on the Corrosion Resistance of the High Entropy Alloys $Al_{[sub 0.5]}CoCrCuFeNiB_{[sub x]}$, *J. Electrochem. Soc.* 154 (2007) C424. doi:10.1149/1.2744133.
- [5] Z.Y. Lv, X.J. Liu, B. Jia, H. Wang, Y. Wu, Z.P. Lu, Development of a novel high-entropy alloy with eminent efficiency of degrading azo dye solutions, *Sci. Rep.* 6 (2016) 34213. doi:10.1038/srep34213.
- [6] J. Li, H. Yang, W.Y. Wang, H. Kou, J. Wang, Thermal–Mechanical Processing and Strengthen in $Al_xCoCrFeNi$ High-Entropy Alloys, *Front. Mater.* 7 (2021) 1–17. doi:10.3389/fmats.2020.585602.
- [7] F. Kaya, M. Yetiş, G.İ. Selimoğlu, B. Derin, Influence of Co content on microstructure and hardness of $AlCo_xCrFeNi$ ($0 \leq x \leq 1$) high-entropy alloys produced by self-propagating high-temperature synthesis, *Eng. Sci. Technol. an Int. J.* 27 (2022). doi:10.1016/j.jestch.2021.05.007.



THE EFFECT OF COOLANTS ON THE SURFACE QUALITY OF ALUMINIUM PRESSURE DIE-CASTING ALLOYS IN MACHINING PROCESS

Edin NURAY¹, Kaan GENÇER¹, Alptekin KISASÖZ², Çağlar YÜKSEL³

¹PTC Kimya, ²Kırklareli University, ³Ataturk University
Türkiye

Keywords: coolants, surface quality, high pressure die-casting, machining, recycle

Abstract

In the aluminium casting industry, high pressure die-casting is indispensable due to higher production rate, reduced section thickness, improved mechanical properties, and so on. In this study, the effects of two coolants, namely environmentally friendly boron and biocide-free (duaLCys™) were investigated within machining process fabricated via high pressure die-casting process which is widespread alloy for several components in the automotive industry. The specimens were characterized via scanning electron microscope and energy dispersive spectrum.

1. Introduction

In the high pressure die casting (HPDC) method, a high amount of production is offered in a short time. For this reason, it is used in many industrial areas. In the casting of light metals, almost 50% of the amount produced in the world is produced by this method [1]. In the HPDC method, especially aluminum alloys are preferred in the automotive industry, as they can show features such as lightness, good machinability, aesthetic appearance and high corrosion resistance [2]. One of the issues that affect the surface properties of the metal part, especially the improving quality of appearance and corrosion resistance, is the coolants used during machining process. Coolant fluids are generally used to minimize friction, dissipate heat, and remove metal chips or swarf in a variety of manufacturing processes. The completion of these tasks improves process stability, improves work piece quality, and extends tool life [3]. In traditional technologies, mineral-based oil products are used together with biocide supplements in cooling fluids [4]. Biocide additives carry the risk of skin and eye irritation, allergies and contamination of the process water [5]. In this study, environmentally friendly biocide-free coolants were used and their effects on the quality of metal surfaces were investigated.

2. Materials and Methods

Metalworking and cooling fluids are a triple molecular structure consisting of water molecule, oil molecule and emulsifiers that bind them together. This triple structure formed after attachment is called 'micelle'. In machining operations with traditional emulsion technologies, due to the higher micelle size, the emulsion adheres more to the part and chip surface, which causes higher product consumption compared to micro-emulsion technologies. In micro emulsion technologies, it is possible to produce with lower consumption, since less amount of product will be adhered to the surface of the part due to the small micelle size. Concerning the examined parts, the make-up and top-up concentrations of the emulsion with traditional emulsion technology and micro-emulsion technology are given in Table 1.

Table 1. Comparison of concentrations

	Traditional Emulsion Technologies	Micro-emulsion Technologies
Make up Concentration	9	7
Top-up Concentration	3	1,5

When scanning electron microscope (SEM) coupled energy dispersive spectrometry (EDS) analyzes are examined (Fig. 1), it is detected some impurities such as sodium and calcium originated from previous operations. There is a problem of yellowing/yellowish in the region (Fig. 2) where aforementioned elements occur due to the effect of the metal working fluids. In the machining operations performed with traditional emulsion technologies, such an effect is not observed in the machining operations performed with micro emulsion technologies.

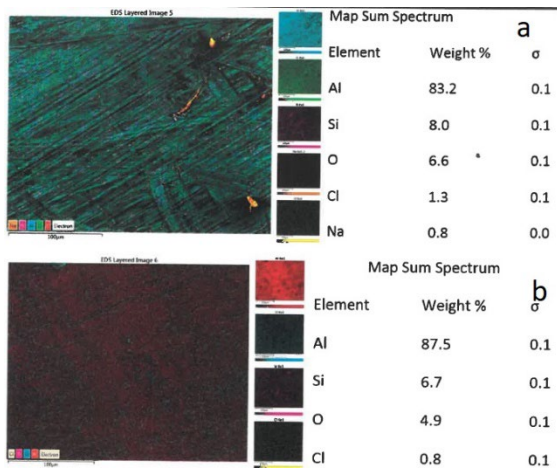


Figure 1. SEM-EDS Result of the examined part
a) Defective Area b) Defect-free Area

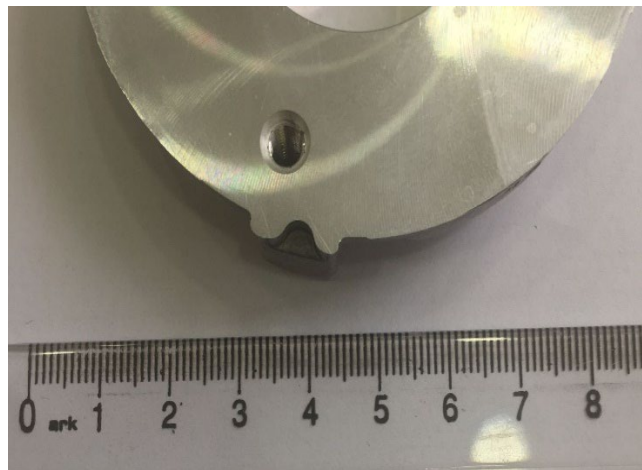


Figure 2. Macro image of the part processed with micro-emulsion technology.

3. Conclusion

- It was not very likely to encounter such an error at the same point in every part, as the impurities contained during the part filling would be randomly positioned in the mold.
- When such an error is encountered, yellowing/yellowish occurs on the machining surface with conventional machining fluids. On the other hand, processing with micro emulsion technologies, it was not observed any problematic areas on the casting part surfaces.
- With these new generation technologies, higher quality surfaces can be obtained without impurities.
- In addition, less waste of the coolants could be arised due to recyclable of biocide-free machining fluids.

References

- [1] F. Bonollo, N. Gramegna, and G. Timelli, "High-pressure die-casting: Contradictions and challenges," *Jom*, vol. 67, no. 5, pp. 901–908, 2015, DOI: 10.1007/s11837-015-1333-8.
- [2] H. Cao, M. Hao, C. Shen, and P. Liang, "The influence of different vacuum degree on the porosity and mechanical properties of aluminum die casting," *Vacuum*, vol. 146, pp. 278–281, 2017, DOI: 10.1016/j.vacuum.2017.09.048.
- [3] E. Brinksmeier, C. Heinzl, and M. Wittmann, "Friction, cooling and lubrication in grinding," *CIRP Ann. - Manuf. Technol.*, vol. 48, no. 2, pp. 581–598, 1999, DOI: 10.1016/S0007-8506(07)63236-3.
- [4] H. B. Schreyer, "Biological treatment of waste semi-synthetic metalworking fluid using a fluidized-bed bioreactor," 1997.
- [5] M. Winter, R. Bock, C. Herrmann, H. Stache, H. Wichmann, and M. Bahadir, "Technological evaluation of a novel glycerol-based biocide-free metalworking fluid," *J. Clean. Prod.*, vol. 35, pp. 176–182, 2012, DOI: 10.1016/j.jclepro.2012.05.048.

THE EFFECT OF JET-COOLING APPLICATION ON MICROSTRUCTURAL PROPERTIES OF THE OVERHEATING AREAS IN HIGH PRESSURE DIE CASTING PARTS

Kaan GENÇER¹, Yasin AYYILDIZ², Süleyman ŞENTÜRK³, Alptekin KISASÖZ⁴, Çağlar YÜKSEL⁵

¹PTC Chemical, ²Arslan Makina Döküm, ³PTC Technic, ⁴Kırklareli University, ⁵Ataturk University Türkiye

Keywords: Jet Cooling, HPDC, Aluminum Die Casting.

Abstract

In this study, the aluminum part demands of the industry are met in the high pressure die casting process. Some problems are encountered in the production of complex shaped parts in the high-pressure casting process. The effect of jet cooling application was investigated to find solutions to the problems encountered because of overheating of the mold due to the figure shape. High temperature zones of the mold cause defect such as porosity and shrinkage on the part. In addition, the temperature difference that the mold steel is exposed to affects the steel life negatively. For this reason, parts were produced by applying jet cooling, which is a kind of fast cooling system. The produced samples were characterized by optical microscope, X-ray and thermal images of the mold during the production phase.

1. Introduction

High pressure die-casting (HPDC) is particularly suitable for high production rates and net shaped parts production for metals and alloys, esp. light alloys[1]. It is applied in many industrial fields; In fact, about half of the world's light metal casting production is obtained with this technology [2], [3]. High production rates, which are mentioned as an advantage in this process, bring some limits. The basis of these limits is the solidification process of aluminum. When producing at high speed, causes of waste due to solidification arise [4]. In order to improve the solidification processes over time, technologies that provide thermal intervention such as spray, cooling channels, jet cooling have been developed.

Due to the complex part figure, parts such as pins and cores rise to high temperatures in some molds. In general, it has been stated in academic studies that the mold release agents used in the process work

optimally at 150-250 °C [5]. Above these temperatures, there is an adhesion problem due to the deterioration of the film layer. At the same time, the hot regions are also the cause of the shrinkage problem. Jet cooling technology is also used to intervene in the solidification process in order to solve the problems experienced due to high temperature. The main task of jet cooling; While solidification is taking place, it allows the solidification to be directed by cooling the area quickly at the user's request. In addition, it ensures to control the system by performing a leak test after each casting.

In this study, the solution of the rejection problem experienced in the production of 46000 aluminum casting alloy in a mold with a complex figure by high pressure casting method has been examined.

2. Experimental Procedure

46000 Al alloy is produced in Zitai 560-ton machine. The content of the alloy used is given in the table.

Table 1. Chemical composition of 46000 Al alloy

Chemical Composition of 46000 Al Alloy		
Elements	Min.	Max.
Si	8	11
Fe	0,6	1,1
Cu	2	4
Mn	-	0,55
Mg	0,15	0,55
Cr	-	0,15
Ni	-	0,55
Zn	-	1,2
Pb	-	0,35
Sn	-	0,15
Ti	-	0,2

The jet cooling system is used for the 'controlled' cooling of the core pins in high pressure casting machines with the molds inside.

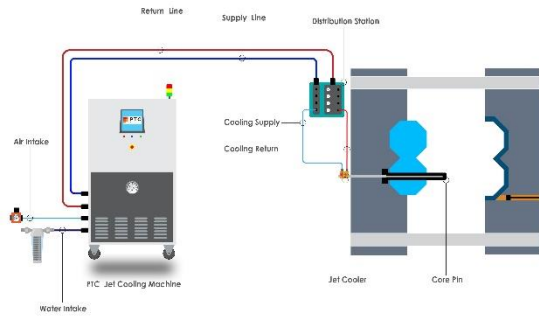


Figure 1. Schematic view of the jet cooling machine

The system is given schematically in Figure 1. The system is used for the 'controlled' cooling of the core pins in the molds in high pressure casting machines with high pressurized water. Working principle of the machine; A pump system performs the cooling process by circulating the pressurized cooling water (in the range of 3 to 20 bar) for a certain period in the circuits of small diameter injectors placed on certain core pins. As a result of the process, the pneumatic system gives air flow to the injector circuits to clean the small channels, and thus the cleaning process is carried out. In this way, the cycle, ie cooling and cleaning, is repeated at the desired time interval.

Details of jet cooling application are given in the table below. Due to the high temperatures of the machining surface in the middle of the part, jet cooling was applied to the pin. During the experiment, 3 different times were tried on the water flow time. Evaluations of these trials are made based on rejection rates. Comparisons were made with the parameter that gave the best results and the product without jet cooling on x-ray, macro- and microstructure and thermal images.

Table 2. Machine parameters.

Machine Parameters	
Min. Test Pressure	3 bar
Max. Temperature	60 °C
Min. Pressure	12 bar
Max. Pressure	18 bar

Table 3. Test parameters

The Flow Time of Water		
10 secs	12 secs	20 secs

3. Results and Discussion

During the experiments on the mass production cycles, 3,926 castings were made with the

application of jet cooling. Details of three different Jet-cooling settings;

- The flow time of water, which is the 1st setting, is 20 sec. 106 parts were 100% sealed and 8 rejections from the package.
- The second setting, the flow time of water, is 12 sec. 210 pieces were separated into 100% sealing and 1 rejection from the package.
- 3. The set flow time of water is 15 sec. 3.349 parts were 100% controlled; 6 sealing operations and 70 package operations were wasted due to the casting gap.

All jet cooling parameters have been successful within acceptable limits. All jet cooling parameters have been successful within acceptable limits. Before the jet cooling application, the rejection rate of the part was 20%. As a result of the Third Adjustment, the casting void rejection rate in sealing and packaging was reduced to 2.2%.

Figure 2 shows the macro view of the cross-sectional area of the part. As can be clearly seen in the image, the jet cooled pin removed the pores from the machining and sealing surface after the sudden cooling.



Figure 2. Macro image of the parts. (a. jet cooling application, b. no jet cooling.)

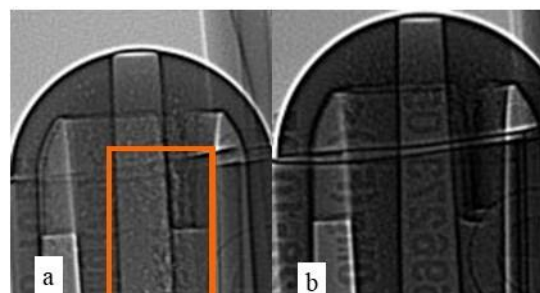


Figure 3. X-ray image of the casting parts. a. no jet cooling application, b. a jet cooling application

In Figure 2, the X-Ray image used for regular control in the company is given. It is seen that a similar macro image appears.

In Figure 3, it is seen that the pin zone was 277 °C before the application of jet cooling, and it decreased to 191 °C after the application of jet cooling

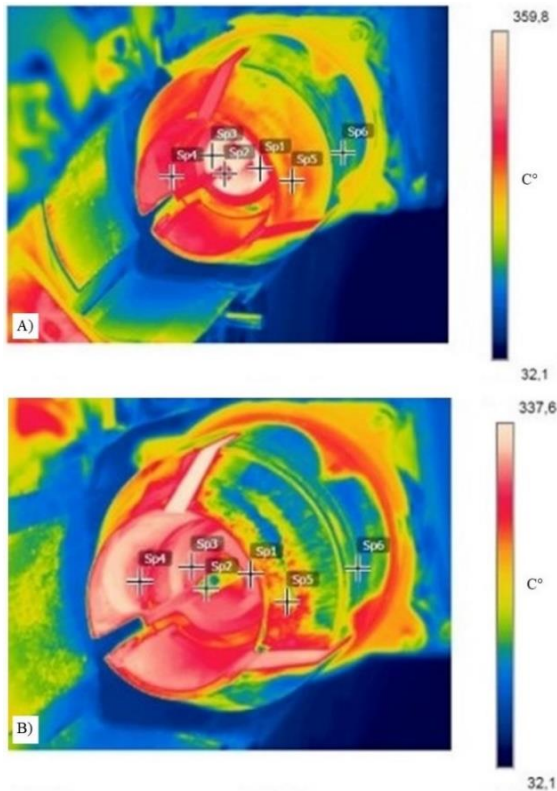


Figure 4. Thermal image of the casting parts. a. no jet cooling application, b. a jet cooling application.

In Figure 4, cross-sectional images were taken from approximately the same areas at 20x and 50x scales. In addition to the detection of many pores in the microstructure formed before jet cooling, it is clearly seen that particles in the microstructure are also formed. It was observed that the grain boundaries increased, and the pores decreased after rapid cooling.

Table 4. Temperature results of dieTemperature measurement results C°		
Area	Without Jet Cooling (C°)	With Jet Cooling (C°)
Sp1	361,2	309,4
Sp2	277,3	191,7
Sp3	353,4	307,9
Sp4	258,6	303,1
Sp5	257,3	271,6
Sp6	186,9	185,3

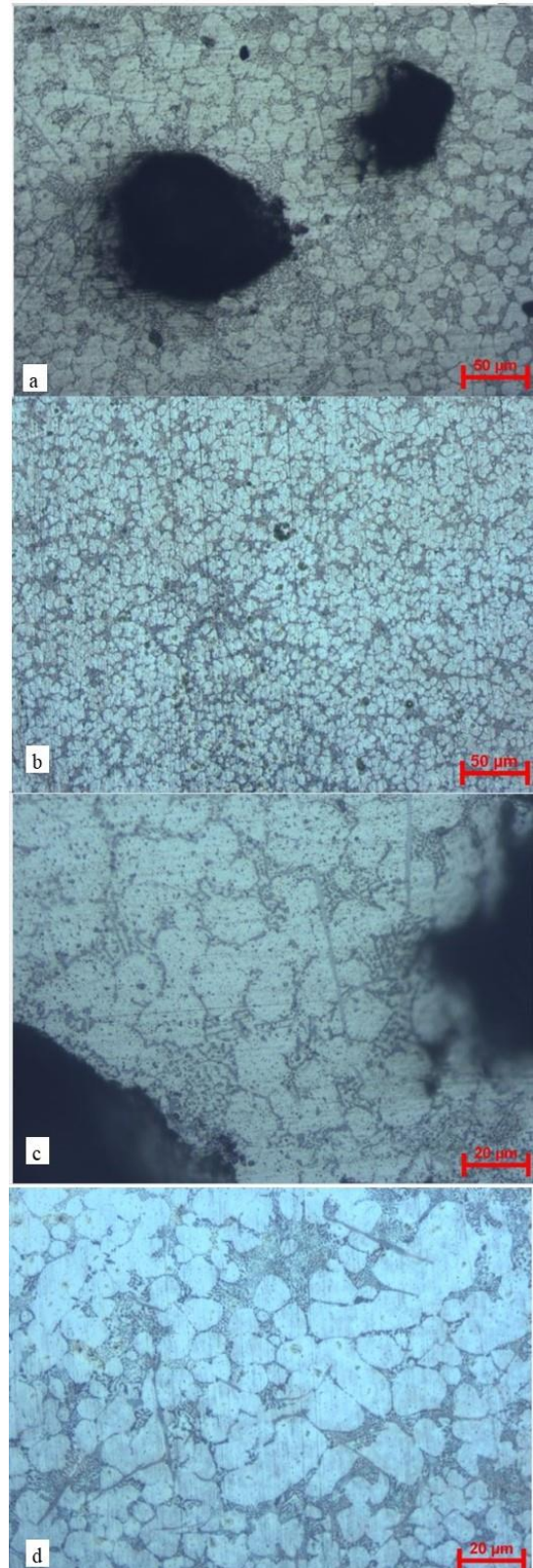


Figure 5. Micrography image of parts (a&c - there is no jet cooling application, b&d - there is a jet cooling application.)

4. Conclusion

In this study, the effect of jet cooling, which is one of the new generation cooling technologies, on the HPDC process was investigated.

As a result of the studies, it was observed that jet cooling application decreased the rejection rates in all different water flow times compared to before (From 20% to 2.2%).

A temperature drops of 31% occurred on the pin where jet cooling was applied. This has also been beneficial in preventing the aluminum from sticking to the mold. It also ensures that the mold is less exposed to thermal shocks.

As stated in the study of Pull et al., new generation cooling systems provide advantages in terms of both part quality and mold life.[4] As stated in the literature, it has been determined that the use of Jet cooling technology in areas with high temperatures is advantageous in terms of both saving rejection rates and preventing thermal shocks in the mold.

References

- [1] D. D. Apelian and D. M. M. Makhoulf, High Integrity Aluminum Die Casting: (Alloys, Processes, and Melt Preparation). NADCA.
- [2] F. Bonollo, N. Gramegna, and G. Timelli, "High-pressure die-casting: Contradictions and challenges," *Jom*, vol. 67, no. 5, pp. 901–908, 2015, doi: 10.1007/s11837-015-1333-8.
- [3] X. P. Niu, B. H. Hu, I. Pinwill, and H. Li, "Vacuum assisted high pressure die casting of aluminium alloys," *J. Mater. Process. Technol.*, vol. 105, no. 1–2, pp. 119–127, 2000, doi: 10.1016/S0924-0136(00)00545-8.
- [4] G. S. Phull, S. Kumar, and R. S. Walia, "Conformal cooling for molds produced by additive manufacturing: A review," *Int. J. Mech. Eng. Technol.*, vol. 9, no. 1, pp. 1162–1172, 2018.
- [5] N. Ekmen, "The Effect Of Mold Release Oil Used In High Pressure Casting On Die Temperature And Parts Quality," Sakarya University of Applied Sciences, 2021.

THE EFFECT OF NITROGEN GAS PURGING ON THE MECHANICAL PROPERTIES OF VERTICAL SEMI-CONTINUOUS CASTING

Mustafa YILDIZ¹, Çağlar YÜKSEL², Alptekin KİSASÖZ³, Umut YILDIZ¹,
Serdar Osman YILMAZ⁴

¹Kayalar Bakır Alaşımları, ²Atatürk University, ³Kırklareli University, ⁴Namık Kemal University
Türkiye

Keywords: CuAl6Ni2, Al-bronze, vertical semi-continuous casting, porosity, inert gas, tensile strength

The casting has been done in a vertical semi-continuous casting (slab) furnace. It has high mechanical properties, acid and corrosion resistance, due to excessive use of raw material and exposed to the air to molten material porosity occurred and this is one of the main problems that has been faced for this alloy during casting. These porosities cause shells and laminations that affect the material adversely on the surface of the final product. In order to eliminate the porosity problem, inert gas (nitrogen) has been carried out to the furnace during melting.

1. Introduction

Copper alloys are widely used today due to their corrosion resistance, high thermal conductivity, low loss in electrical conduction, easy production, and high wear resistance. In the production of copper alloys, the copper concentration in the slag is lost due to the formation of copper oxide on the surface of the liquid metal due to melting in an open environment to the atmosphere. [1] [2]

2. Materials and Methods

It is thought that homogenizing the microstructure will improve the mechanical properties of the material to eliminate these problems that occur during casting and increase the mechanical properties. The effect of degassing by inert gas in CuAl6Ni2 alloy on tensile strength and ductility was investigated. Experimental studies were tried on CuAl6Ni2, the alloy with the most porosity problem, and experimental studies were carried out at 1200 °C, which is the casting temperature of the alloy. The chemical composition of the samples, which no gas and nitrogen gas was given in **Table 1**.

Table 1. Chemical composition of CuAl6Ni2 alloy (wt.%)

Process	Alloy	Cu	Al	Ni	Zn	Fe	Other
0 min.	%	91,5	5,95	1,98	0,3	0,004	Rest
3 min.	%	91,6	5,94	1,99	0,4	0,003	Rest

Nitrogen gas was given to the holding furnace for 3 minutes and gas flow rate 2,8 l/min. Six tensile samples were taken from the positions shown in **Figure 1** from the castings that were not given nitrogen gas and were given nitrogen gas for 3 minutes. It is thought that the amount of porosity directly affects the tensile strength. For this reason, the relationship between porosity and gassing was investigated by examining the tensile strengths.



Figure 1. Schematic representation of samples

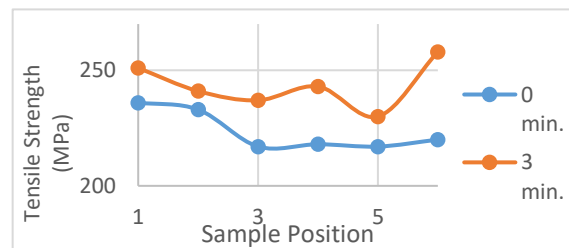


Figure 2. Tensile strength results of samples (0 min. = not given nitrogen and 3 min. nitrogen given)

3. Conclusion

As a result, it was observed that the use of nitrogen gas after casting increased the mechanical properties of the material. The lowest increase is observed in the 2 positions and is around 3.5%. The highest increase is in position 6, around 20%. It is thought that there is a decrease in the amount of porosity due to the increase in the mechanical properties of the material.

References

- [1] ASM Speciality Handbook, Copper and Copper Alloys, ASM International, 2001, 10-118
[2] Mehmet Ali Topçu, Aydın Rüßen, Bora Derin, Minimizing of copper losses to converter slag by a boron compound addition, 2019.



NICKEL RECOVERY FROM OLIVINE BY HYDROMETALLURGICAL METHOD

Şeyma YÜKSEL SAĞMAN¹, Hande ARDIÇOĞLU¹, Hasan NİZAMOĞLU²,
Mehmet Deniz TURAN², Ali KESKİN¹, Erdoğan KARİP¹, Gökhan BAŞMAN¹

¹Eti Chrome, ²Fırat University
Türkiye

Keywords: Olivine, Leaching, Ni recovery

Abstract

In this study, the Ni recovery and the change in the Fe ratio in its content were investigated by using olivine separated from the magnetic separator in Elazig, Eti Krom INC. The effects of acid leaching, time, roasting and mechanical activation on Ni recovery were investigated. In Eti Krom INC. it is aimed to add value to the waste material by recovering metal from olivine, which is in waste state.

In order to examine the effect of temperature on %Ni recovery, 3 different temperatures (45 °C, 65 °C, 85 °C) were carried out with using 2 different acids. In order to examine the effect of mixing time, 6 different time (15 min, 60 min, 120 min, 180 min, 360 min, 480 min) were tried. The effects of roasting and mechanical activation on leaching were also investigated. During the study we also followed the % Fe solubility which has the highest solubility in olivine, has the most impurity, dissolves easily and passes into the solution easily with Ni, which is the target metal.

As a result of this study, the % Ni recovery is 32.8%. The % Fe solubility is 40.181%. In all studies, the recovery did not exceed 32%, but the % Fe solubility was extreme high. Secondly, the highest yield % Ni recovery is 26.82% and % Fe solubility are 12.90%.

1. Introduction

Nickel has found a wide area of use in industry due to its superior qualities such as corrosion and heat resistant, high melting temperature. In addition, Nickel - Chromium - Iron alloys find wide use as stainless steel. The reason for its use in this area is; In addition to the good mechanical and physical properties of nickel, it is highly resistant to corrosion. Nickel does not become brittle at high temperatures. Nickel, which is ferromagnetic in the cold, loses this property at 370 °C. It can be made into wire and

sheet. Powdered nickel is an important reduction catalyst [1].

2. MATERIAL AND METHODS

2.1. Material

In this study, Ni recovery by hydrometallurgical method using olivine raw material separated as a by-product from high field strength dry magnetic separator in Eti Krom INC. and the change of Fe ratio in olivine content were investigated.

2.2. Method

2.2.1. Effect of Temperature on Ni Recovery from Olivine by Acid Leaching

To determine the effect of temperature, leaching experiment parameters using H₂SO₄ and HCl stock solution are given in Table 2.1

2.2.2. Effect of Mixing Time on Ni Recovery from Olivine by Acid Leaching

To determine the effect of mixing time, leaching test parameters using 3 M H₂SO₄ and 5 M HCl stock solution are given in Table 2.2

2.2.3 Effect of Roasting Process on Ni Recovery from Olivine by Acid Leaching

Roasting with 3 M H₂SO₄ stock solution and then leaching using 1 M H₂SO₄ stock solution are given in Table 2.3.

2.2.4 Effect of Mechanical Activation on Ni Recovery from Olivine by Acid Leaching

After the mechanical activation process applied to the olivine raw material at different times (5 min, 15 min, 60

min) leaching was carried out at 65 °C for 120 minutes using 3 M H₂SO₄.

Table 2.1 Leaching experiment parameters using H₂SO₄ and HCl stock solution to determine the effect of temperature

H ₂ SO ₄ Molarity	HCl Molarity	Solid:Liquid	Test Temperature (°C)	Mixing Speed (rpm)	Mixing Time (min)
3	3	1:10	45	400	120
3	3	1:10	65	400	120
3	3	1:10	85	400	120
5	5	1:10	45	400	120
5	5	1:10	65	400	120
5	5	1:10	85	400	120
7	7	1:10	45	400	120
7	7	1:10	65	400	120
7	7	1:10	85	400	120

Table 2.2. Leach experiment parameters using 3 M H₂SO₄ and 5 M HCl stock solution to determine the effect of mixing time

H ₂ SO ₄ Molarity	HCl Molarity	Solid:Liquid	Test Temperature (°C)	Mixing Speed (rpm)	Mixing Time (min)
5	3	1:10	65	400	15
5	3	1:10	65	400	60
5	3	1:10	65	400	120
5	3	1:10	65	400	180
5	3	1:10	65	400	360
5	3	1:10	65	400	460

Table 2.3 Test parameters of roasting with H₂SO₄ stock solution and then leaching using 1 M H₂SO₄

Molarity	Roasting Rate (Solid: Liquid) (Olivine:H ₂ SO ₄)	Roasting Temperature (°C)	Roasting Time (min)	Leaching Rate (Solid:Liquid) (Olivine:H ₂ SO ₄)	Leaching Temperature (°C)	Leach Time (min)
3	1:1	100	60	1:10	65	120
3	1:1	150	60	1:10	65	120
3	1:1	200	60	1:10	65	120
3	1:1	250	60	1:10	65	120

3. CONCLUSION

In this study, the recoverability of nickel in olivine separated from magnetic separator in Eti Krom INC. was

investigated. In this study, after enriching with literature and patents, experimental studies were carried out. The

effects of parameters such as temperature, time, roasting, mechanical activation for Ni recovery were investigated.

When all the results obtained in this study are examined, the highest yield is the roasting process at 100 °C and 60 minutes with H₂SO₄ before leaching, followed by water leaching at 65 °C for 120 minutes. As a result of this study, % Ni recovery is 32.8%. The % Fe solubility is 40.181%. In all studies, the yield did not exceed 32%, but the % Fe solubility is undeniably high. Secondly, the highest yield % Ni recovery is the leaching process with 3 M H₂SO₄ at 65 °C for 360 minutes. The % Ni recovery is 26.82% and the % Fe solubility is 12.90%.

While examining the % Ni recovery, we also followed the % Fe solubility, which easily dissolves into the solution with Ni, which is the target metal, which has the highest solubility in olivine, has the highest impurity feature, and easily dissolves. The % Fe solubility is important because even if we cannot obtain pure Ni, knowing how much Fe is dissolved together with Ni when we do economical H₂SO₄ leaching will guide us both now and for future projects.

One of the reasons why we could not gain Ni at the desired yield may be due to the fact that we could not break the bonds due to the refractory feature of the olivine. During the study, economic concerns were considered. H₂SO₄, the cheapest leaching reactant in the world, was used. Alternatively, HCl has been used in acid, but chloric acid solutions are always the 2nd option next to H₂SO₄ due to its high corrosion properties.

Looking at the patent and literature, leaching can be done under pressure in a reactor to increase the solubility of metal, such as Ni, which is in inclusions in refractory materials such as olivine. It is foreseen that the Ni extraction efficiency can be further increased. This study was carried out under atmospheric conditions, but if there is an increase in Ni prices, a leaching process under pressure can be tried to increase the amount of Ni recovery in the olivine. When evaluated economically, both investment and operating costs are high in leaching under pressure.

REFERENCES

1. Ağaayak, T., (2008), *Karaçam (Eskişehir) Lateritik Nikel Cevherinin Fiziksel Ve Kimyasal Yöntemlerle Zenginleştirilmesi*, Doktora Tezi, Selçuk Üniversitesi, Fen Bilimleri Enstitüsü



INVESTIGATION OF ROASTING BEHAVIOR AND MINERALOGICAL TRANSFORMATION OF TITANOMAGNETITE CONCENTRATE AT DIFFERENT TEMPERATURES

Ismail Emre YILDIZ¹, Zeynep Hazal YAZĞAN¹, Mikail BAŞYİĞİT¹, Elif UZUN KART¹, Abdullah BUHUR²

¹Marmara Üniversitesi, ²ARGETEST
Türkiye

Keywords: Titanomagnetite concentrate (TMC), roasting, mineralogical transformation

Abstract

The demand for titanium metal and its compounds is constantly increasing. Titanium's versatility, technological advancements, and increasing human population drive nations to demand more. This thirst for metals and exploiting mineral resources forces civilizations to harvest low-grade deposits. Titanium is no exception, thanks to its versatility and wide range of applications. There are two commercial titanium minerals, rutile and ilmenite, widely used in industrial applications. However, the decrease of this high-grade ore also causes the evaluation of low-grade ore as a resource. Therefore, titanomagnetite concentrate (TMC), with 4–8 Ti%, 50–54 Fe%, and 0.38–0.58% V content, is a high potential reserve in terms of Ti and V and, obtained by the magnetic enrichment method, has been an alternative source to high-grade ore. However, due to the high iron content of TMC, producing titanium metal and its compounds from these resources is difficult and costly. Thus, removal of the iron minerals, which is one of the major constituents and impurities, is necessary. Since for further metallurgical processes, concentrated and/or enriched materials are needed, titanium enrichment is important. While there are several methods to remove iron minerals, magnetic separation is one of the most effective methods. Despite its easiness and effectiveness, it has a crucial constraint, namely magnetic susceptibility. While some iron minerals such as magnetite and wustite are ferromagnetic and easy to separate with magnetic separators, others like hematite have low magnetic susceptibility. Therefore, they are not suitable for magnetic separation. Fortunately, this drawback can be overcome with a particular solution: magnetization roasting. Through the roasting process, it is possible to convert hematite into magnetite and wustite. In this study, TMC was primarily roasted at 9 different temperatures (from 200 to 1000 °C with 100 °C increments). After roasting, the effects of temperature on the mineralogical transformation were investigated by X-ray diffraction to obtain ideal/optimum experimental parameters. X-ray diffraction patterns show that magnetization takes place between 200–600 °C and peaks at 600 °C. Until

this temperature, hematite–magnetite conversion is evident. At this point, the magnetite/hematite ratio reaches 2.75. However, after this point, conversion goes reverse, and hematite occurrence takes place instead of the magnetite formation. At 1000 °C, the magnetite/hematite ratio drops to 0.45. Therefore, according to the findings of this study, 600 °C is optimal for magnetization and following the magnetic separation process.

1. Introduction

Titanomagnetite ore (TMO) which is an alternative to rutile and ilmenite ore, is a high-potential ore used for the production of Ti metal, TiO₂ (pigment), metallic iron, and vanadium compounds [1],[2]. TMO consists of phases mainly of ilmenite (FeO.TiO₂) and magnetite (FeO.Fe₂O₃). consisting of dissolved ilmenite in its matrix. Moreover, titanomagnetite concentrate (TMC), with 4–8 Ti%, 50–54 Fe%, and 0.38–0.58% V content, which is a high potential reserve in terms of Ti and V, has been obtained by the magnetic enrichment method. Türkiye's Ti-V-Fe-containing TMO research has finalized the existence of reserves on the coastline of our country but cannot be operated because it is not economical compared to the old and traditional methods [1]. To make it possible to realize the best benefits of ore, it is very important to perform phase analysis after some special process is used to detect the specific mineral phases of the ore [3]. Therefore, TMC primarily was roasted at 9 different temperatures (from 200 to 1000°C with 100°C increments). After roasting, the effects of temperature on the mineralogical transformation were investigated by X-ray diffraction to obtain ideal/optimum experimental parameters. The mineralogical phase transformations of TMC were investigated after roasting at different temperatures (from 200 to 1000 °C with 100 °C increments). After roasting, the effects of temperature on the mineralogical transformation were investigated to lay a foundation for the better development and utilization processing of the ore resources [3].

2. Experimental Procedure

2.1. Materials and Analysis

In experimental studies, the TMC sample was taken from a Turkey/Black Sea Region coastline placer-type deposit and concentrated with the wet magnetic separation method. The quantitative mineralogical and elemental analysis of the TMC sample was carried out by using X-ray diffraction (XRD) and inductively coupled plasma atomic emission spectroscopy (ICP-AES), respectively. The mineralogical composition of the TMC is given in Figure 1, and its chemical composition is given in Table 1. It has been determined that the TMC sample mainly consists of hematite and magnetite phases (Figure 1). ICP-AES analyses revealed that 50.17% Fe, 4.05% Ti, 1.02% Mg, and 0.28% V were present. When the XRD pattern was examined, although liberated rutile and ilmenite mineral peaks containing titanium could not be detected, it was detected that TMC had a content of 4.05 % Ti. This situation emphasizes that the titanium minerals such as rutile and ilmenite are in hematite and magnetite [1].

After roasting, the effects of temperature on the mineralogical transformation were investigated by XRD.

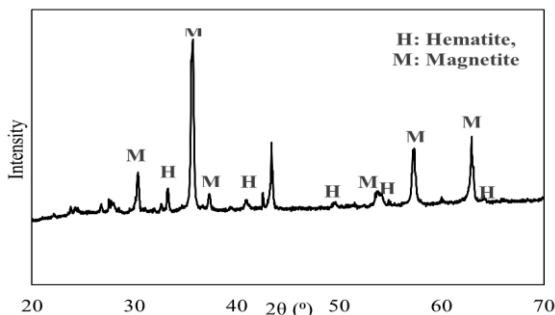


Figure 1. XRD pattern of raw TMC

Table 1. Chemical composition of TMC

Element	Fe	Ti	Mg	Al	V
%	50.17	4.05	1.02	1.44	0.28

2.2. Roasting Method

20 g TMC sample was used after removing the physical water at 105°C for 24 hours, and after keeping it stored in vacuum containers. The roasting temperature was determined as the variable parameter by keeping a constant time in the experimental study. TMC sample was roasted for 1 hour at varying temperature parameters, which were 200–1000 °C by increasing the temperature by 100 degrees in each experiment. After completing the roasting experiment, roasted TMC (R-TMC) was weighed and the resulting weight changes are given in Table 2.

Table 2. Roasting of TMC experimental parameters and R-TMC weights.

Roasting Temperature, °C	Roasting Time, h	Amount of TMK, g	Roasted TMK, g
200	1	20.00	19.86
300	1	20.00	19.87
400	1	20.00	19.96
500	1	20.00	19.95
600	1	20.00	19.92
700	1	20.00	19.95
800	1	20.00	19.99
900	1	20.00	20.05
1000	1	20.00	20.07

3. Results and Discussion

The XRD patterns of the R-TMC that were obtained after roasting applied to TMC at different temperatures are given in Figure 2. It is explained in the literature that TMC consists of magnetite (Fe_3O_4) phases that include dissolved ilmenite in its crystal structure [1], [2].

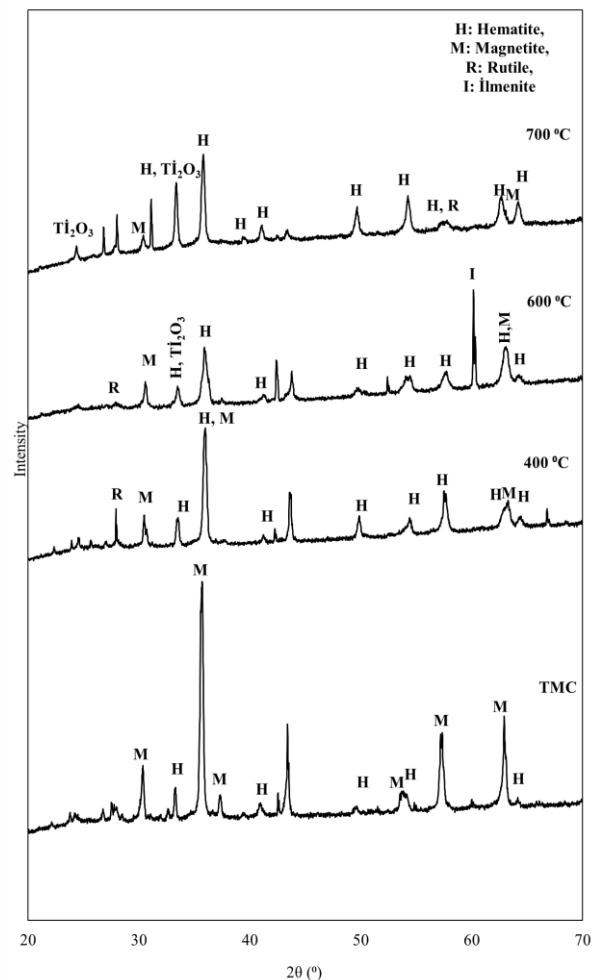


Figure 2. XRD patterns of R-TMC obtained different temperature

Therefore, the liberation behavior of titanium minerals such as ilmenite and rutile with the effect of increasing temperature was investigated. To determine this situation, it is crucial to examine the mineralogical transformation behavior of magnetite under increasing temperatures. For this reason, the percentages (%) of iron minerals were given in Figure 3 alongside corresponding temperatures. When Figure 3 is examined, it is observed that the conversion of magnetite to hematite intensely occurs at 600 °C. Therefore, it was considered adequate to examine XRD patterns in the roasting process at 400 °C, 600 °C, and 700 °C in the scope of the present study. When the XRD patterns were examined (Figure 2), It was discovered that magnetite was converted into hematite at 35 2θ at 400 °C, as well as rutile at 28 2θ (ref. code: 01-082-0514) at 400 °C and ilmenite at 60 2θ (01-075-1211) at 600 °C. Thus, new rutile and ilmenite peaks confirm that the rutile and ilmenite are in magnetite. In this case, as the conversion of magnetite to hematite increased, the liberation of titanium minerals was confirmed by XRD patterns. In Figure 2, the ilmenite peak at 60 2θ at 600 °C is not detected at 700 °C. However, the formation of hematite peaks at 39 2θ and rutile peaks at 58 2θ at 700 °C was observed. The reason for this situation is that the ilmenite transformed into hematite and rutile based on the reaction in Equation (1) [4]:



The fact that the hematite ratio at 700 °C in Figure 3 is higher than at 600 °C can be due to ilmenite transformation. Also, the magnetite/hematite ratio depending on the temperature increase is given in Figure 4. In Figure 4, it was also seen that the magnetite/hematite ratio increasingly decreased from 700 °C.

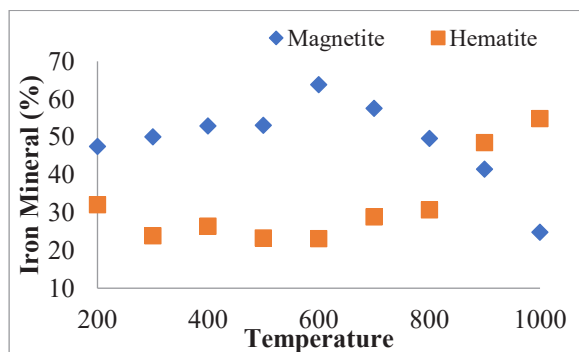


Figure 3. Effect of the temperature on iron minerals (%)

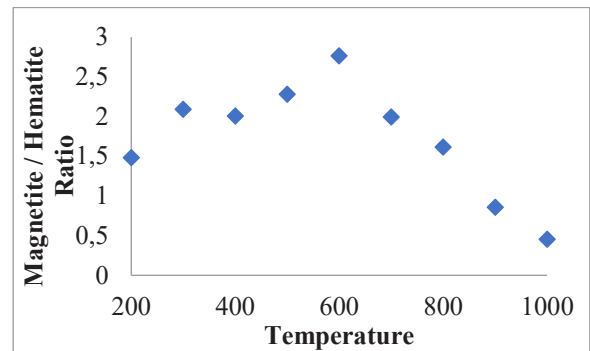


Figure 4. Effect of the temperature on magnetite/hematite ratio

Depending on the increased temperature, it is explained in the literature that transformation to sub-oxides phases Ti_3O_5 , Ti_2O_3 , and TiO of rutile takes place [5]. Therefore, after roasting at 700 °C, while the rutile peak at 28 2θ (01-082-0514) disappears, Ti_2O_3 conversion occurs at 24 and 33 2θ (ref. code: 01-07-1055). In addition, the decrease in intensity value of the rutile peak at 28 °C at 600 °C confirms that the transformation has taken place.

4. Conclusion

Increasing demand for titanium and diminishing titanium resources increase the importance of the low-grade ore. Therefore, it is a necessity to understand the behavior and structure of low-grade ore to extract precious metals with economic margins. In this context, this study aims to determine the optimum roasting temperature for TMC.

The findings of this study can be listed as follows;

- The roasting process is effective until 600 °C. The major iron element is magnetite, with higher magnetic susceptibility. Thus, the roasting can assist with the iron removal and titanium enrichment from the TMC.
- After the 600 °C a sharp decline occurs and the magnetite percentage drastically falls while the percentage of hematite increases. Therefore, this temperature can be selected as the optimum roasting point.
- Over roasting is not a viable option since while the process consumes more energy, it is not effective. Furthermore, beyond 900 °C the low magnetic susceptible mineral namely hematite is the major iron mineral.

References

- [1] E. U. Kart and M. Kirman, "Extraction of titanium from Ti-doped seaside magnetite concentrate in HO media," *Gospod. Surowcami Miner. / Miner. Resour. Manag.*, vol. 37, no. 4, pp. 79–96, 2021, doi: 10.24425/gsm.2021.139736.

- [2] B. Zhong, T. Xue, L. Zhao, H. Zhao, T. Qi, and W. Chen, "Preparation of Ti-enriched slag from V-bearing titanomagnetite by two-stage hydrochloric acid leaching route," *Sep. Purif. Technol.*, vol. 137, pp. 59–65, 2014, doi: 10.1016/j.seppur.2014.09.021.
- [3] S. Q. Wan, D. J. Lan, H. B. Han, and C. L. Zhou, "The phase analysis of Panzhihua vanadic titanomagnetite ore before and after heat treatment," *Adv. Mater. Res.*, vol. 807–809, pp. 2110–2114, 2013, doi: 10.4028/www.scientific.net/AMR.807-809.2110.
- [4] Z. Zulhan, R. Dinillah, T. Yulianton, I. Santoso, and T. Hidayat, "Carbothermic Reduction of Ilmenite Concentrate with Sodium Carbonate Additive to Produce Iron Granules and High Titania Containing Slag," *Metals (Basel)*, vol. 12, no. 6, p. 963, 2022, doi: 10.3390/met12060963.
- [5] N. a El-Hussiny, T. a Lasheen, and M. E. H. Shalabi, "Kinetic Reduction of Rosetta Ilmenite with Coke Breeze and Beneficiation of the Product," *J. Ore Dress.*, vol. 10, no. January 2008, pp. 17–23, 2008.

THE EFFECT OF THE SCALE FACTOR ON ALCOCRFENI BASED HIGH-ENTROPY ALLOYS PRODUCED VIA A SELF-PROPAGATING HIGH-TEMPERATURE SYNTHESIS METHOD

Murat ALKAN¹, Esra DOKUMACI ALKAN¹, Emre ÇINKILIÇ²

¹Dokuz Eylül University, ²Hakkari University
Türkiye

Keywords: High-Entropy Alloys, SHS, Scale Factor

Abstract

In this study, high-entropy alloys (HEA) having AlCoCrFeNi stoichiometry were produced via a self-propagating high-temperature synthesis (SHS) method starting from their metal oxide powder mixtures. The effects of the initial weights of raw materials (100-200-300-500-1000 g) on metal recovery values, chemical composition and properties of the final alloys were investigated.

1. Introduction

High-entropy alloys (HEA) are a moderately new group of alloys. The production processes of HEA are generally grouped into three main categories depending on the physical states of raw materials: liquid state, solid state and gaseous state. The self-propagating high-temperature synthesis (SHS) method is a fast and economically feasible process for the production of different kinds of materials. The production is realized by the spontaneous movement of a combustion flame, which is formed as a result of a highly exothermic reaction, on the raw material powder mixtures.

2. Materials and Methods

The self-propagating high-temperature synthesis was selected for the production of HEA. The raw materials were the mixtures of metal oxide powders with metallic aluminum powder (100 % stoichiometric amount). A copper crucible was used in SHS reactions. A resistance wire was placed at the top of the crucible and the reaction realized by passing current through the wire. The obtained SHS products were discharged from the crucible after cooling. The weights of the products were given in Table 1, and the metal recovery values obtained with the usage of different amount of raw materials was given in Figure 1.

Table 1. The mass of the raw materials and the products.

Raw mixture, g	Alloy, g	Slag, g	Scattered Ratio, %
100	49.9	49.4	0.7
200	102.5	90.5	3.5
300	156.3	128.6	5.0
500	267.0	223.0	2.0
1000	536.4	442.0	2.2

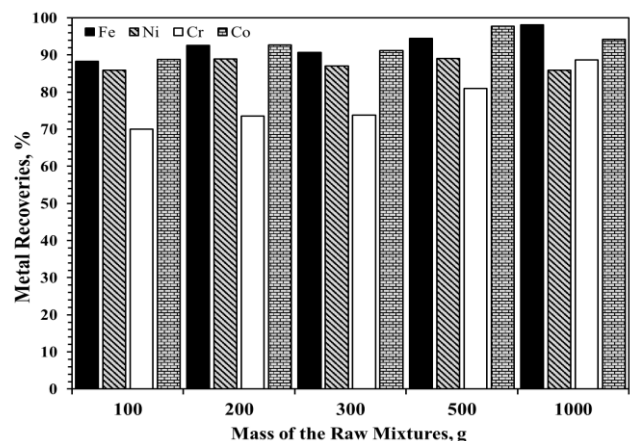


Figure 1. The metal recovery values.

3. Conclusions

The metal recovery efficiencies in the SHS production method were at higher levels in Fe, Ni and Co. These ratios were estimated to decrease due to the reduction potential of the elements and the low vapor pressures of the metal oxides. It has been determined that AlCoCrFeNi alloy has a disordered BCC structure. The highest metal recovery values were obtained where 1000 g of initial mixture was used.

Acknowledgment

The authors are pleased to acknowledge the financial support for this research from TUBITAK (Project No. 118M204).

THERMODYNAMIC AND MICROSTRUCTURAL INVESTIGATIONS OF AlCoCrFeNi(Ti)_x BASED HIGH-ENTROPY ALLOYS

Esra DOKUMACI ALKAN, Murat ALKAN, Oğuzhan DİRİCAN, Mehmet Nurullah KÖSE, Abdulkafi KARTOPU

Dokuz Eylul University
Türkiye

Keywords: High-Entropy Alloys, Eutectic, Vacuum Arc Melting

Abstract

In this study, it is aimed to produce AlCoCrFeNi(Ti)_x (x=1, 1.2, 1.4, 1.6, 1.8, 2) HEA by vacuum arc melting (VAM) method using high purity metal powder mixtures. The aim of this study is to obtain eutectic structure and to reveal the effects on mechanical properties in case the alloys produced have different eutectic phase ratios.

1. Introduction

High entropy alloys (HEA) are a group of alloys that have been studied extensively in recent years due to their superior properties such as high strength/hardness, superior wear resistance, exceptional high temperature resistance, high structural stability, good corrosion and oxidation resistance.

2. Materials and Methods

The high-entropy alloys based on AlCoCrFeNiTi_x (x=1.0-2.0) stoichiometry were produced by using a vacuum arc melting furnace. High purity (over 99.5%) metal powders having a fine-grain size were used as raw materials. HEAs were characterized by various techniques: scanning electron microscope (SEM) with an energy dispersive spectrometer (EDS), X-ray diffractometer (XRD), and Vickers microhardness tests. The thermodynamic investigations were performed to predict the phases present within as HEAs by using Thermo-Calc 2021a Software and its TCHEA4 database. SEM micrographs of the produced alloys are given in Fig. 1.

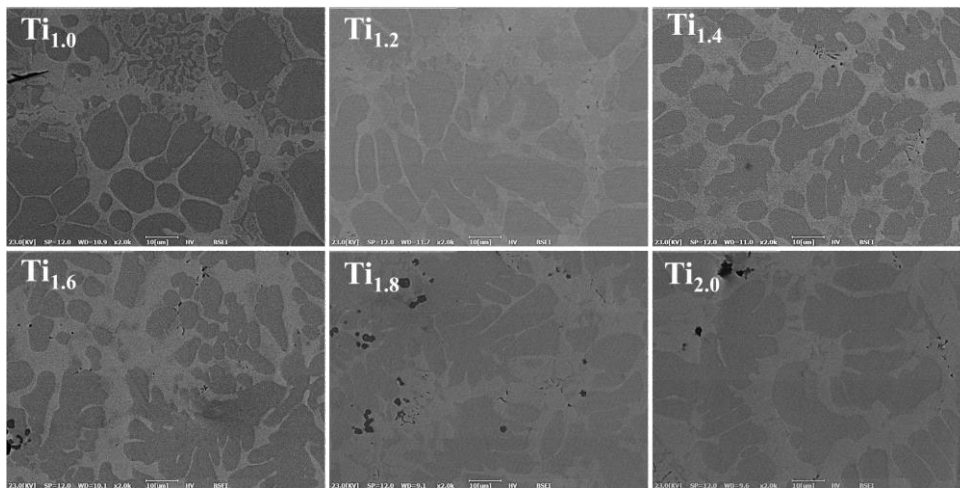


Figure 1. The microstructures of vacuum arc melted HEAs having different Ti contents.

3. Conclusions

When the microstructure and XRD results were compared, it was determined that BCC, B2, Laves and Heusler phases were present in the structure of the alloys. As the Ti content in the alloy increased, an increase was observed in the hardness values. Dendritic solidification has occurred in the alloys and eutectic structures have been determined at different rates.

Acknowledgment

The authors are pleased to acknowledge the financial support for this research from TUBITAK (Project No. 118M204).

DEVELOPMENT OF OXIDE DISPERSION STRENGTHENED INCONEL 718 ALLOY BY CALPHAD METHOD AND PRODUCTION OF DESIGNED NOVEL ODS ALLOY BY LASER POWDER BED FUSION

M. Yeşim YALÇIN¹, A. Alkım GÖKBAYRAK¹, C. Bora DERİN², Eda AYDOĞAN¹,
Bahattin KOÇ³

¹Middle East Technical University, ²Istanbul Technical University, ³Sabancı University
Türkiye

Keywords: Oxide dispersion strengthening, nano-oxides, Inconel 718, FactSage, Laser powder bed fusion

Abstract

IN718-YF (IN718 – Y₂O₃ – FeO) and IN718-YFH (IN718 – Y₂O₃ – FeO – Hf) alloy compositions were determined by CALPHAD approach. Designed ODS alloys were produced by selective laser melting (SLM) method. FeO and Hf additions have resulted in an increase of number densities of Y-Ti-O & Y-Hf-O nano-oxides and a decrease in nano-oxide particle size distributions. In-situ tensile tests were conducted to obtain high-temperature mechanical behaviors of alloys. Experimental results showed that an increase in nano-oxide number density and a decrease in nano-oxide size distribution improved the tensile strength of the IN718-ODS alloy.

1. Introduction

Inconel 718 alloy is a Nickel base superalloy which is hardened by precipitation hardening.[1] However, strengthening precipitates start to dissolve in matrix phase above 700°C which results in a sudden decrease in mechanical properties. In oxide dispersion strengthening, nano-oxides are homogeneously dispersed in the matrix phase, so they inhibit dislocation motion by Zener pinning, contribute mechanical and microstructural stabilities at elevated temperatures.[2,3] In this study, two different ODS-IN718 alloys were produced by SLM.

2. Materials and Methods

To determine the alloy composition, thermochemical simulations have been carried out based on FactSage 8.0. After mechanical alloying of powders, alloys were produced by SLM method. A novel heat treatment was applied (1050°C – 1 h). Microstructures of ODS alloys were examined by using optical microscopy, scanning electron microscopy and transmission electron microscopy. In-situ tensile tests were conducted according to ISO 6892-1 and ISO 6892-2 standards.

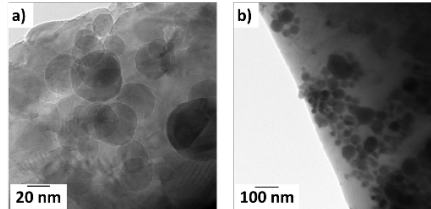


Figure 1. TEM images of a) IN718-YF and b) IN718-YFH alloys in heat treated condition

3. Conclusion

It is observed FeO and Hf additions have promoted nano-oxide formation and reduction of nano-oxide dispersoid sizes. For both alloys, above 99% densification and an increase in hardness were observed. In situ tensile tests showed that high-temperature stabilities and strengths of alloys were improved by nano-oxides.

Acknowledgement

The financial support provided by the Scientific and Technological Research Council of Turkey (TUBITAK) under grant No: 219M500 is greatly acknowledged.

References

- [1] H. Zhang, C. Li, Q. Guo, Z. Ma, H. Li, Y. Liu, *Scr. Mater.*, 164 (2019) 66–70.
- [2] M. Nganbe, M. Heilmaier, *Mater. Sci. Eng. A* 387–389 (2004) 609–612.
- [3] M. Yesim Yalcin, B. Derin, E. Aydogan, *J. Alloy. Compd.* 914 (2022), Article 165193

COMPARISON OF MICROSTRUCTURE AND MECHANICAL PROPERTIES OF COCRFENIMN HIGH-ENTROPY ALLOYS BY UNIAXIALLY PRESSING-SINTERING AND VACUUM HOT PRESSING-SINTERING METHODS

Burak KÜÇÜKELYAS¹, Cantekin KAYKILARLI¹, İhsan ÇAHA³, Alexandra C. ALVES³, Fatih TOPTAN⁴, Sebahattin GÜRME², Deniz UZUNSOY¹

¹Bursa Technical University, ²Istanbul Technical University, ³University of Minho, ⁴Izmir Institute of Technology
Türkiye, Portugal

Keywords: High Entropy Alloys, Mechanical Alloying, Vacuum Hot Pressing, Uniaxial Pressing

1. Introduction

Since its discovery in 2004, there has been a growing interest in high entropy alloys (HEA). HEA are multicomponent alloys in which each component has high concentration, or in which there is no longer a difference between solvent and solute. Initially, researchers concentrated on single-phased HEA compositions, such as the quinary equimolar CoCrFeNiMn, commonly known as the Cantor alloy. CoCrFeNiMn HEA has been manufactured primarily by arc melting/casting. However, due to the problems of diseconomy and restrictions in the shape and size of the end products, these processes are unsuited for industrial manufacture. Powder metallurgy is a more convenient alternative. This method for producing HEA consists of two steps: mechanical alloying (MA) and sintering. MA can produce nanocrystalline HEA powders with homogeneous constituents. From the as-milled powders, bulk HEAs with ultra-fine or nano-sized grain sizes can be easily generated during subsequent sintering. In the present study, powders of a high entropy CoCrFeNiMn alloy were produced in a planetary ball mill, and high-entropy CoCrFeNiMn bulk samples were obtained by two different processes: uniaxial pressing-pressureless sintering (UNPS) and vacuum hot pressing sintering (VHPS).

2. Materials and Method

As starting powders, a size of 325 mesh, highly pure metals were used. Using iron balls of various diameters, 54 hours of mechanical alloying were conducted in a planetary ball mill (Retsch PM 200). As a process control agent, n-heptane was used. The obtained powder characteristics were analyzed using X-ray Diffraction (XRD) and Scanning Electron Microscopy (SEM). XRD phase analysis was done by Bruker AXS D8 Discover and SEM analysis was done by Carl Zeiss/Gemini 300 SEM. Separate processes, (UNPS and VHPS), were utilized to obtain high-entropy CoCrFeNiMn bulk samples. VHPS was employed at 850 °C for 2 h and UNPS was performed under 1.2 GPa, followed by pressureless sintering at 1200 °C for 2 h under an argon atmosphere. The bulk samples were investigated with the same XRD and SEM equipment. The bulk samples are mechanically characterized by microhardness measurements and dry sliding wear tests. At least ten microhardness measurements were conducted using the Qness Q10 Microhardness Tester under conditions of 200 g load for 15 s, and the mean values were determined based on these measurements. Sliding wear tests were conducted by using Bruker UMT2 Tribometer under 4 N of load and 5 mm/s of speed over a total distance of 10 m against a chrome steel balls (ASTM E52100) with a 5 mm diameter.

3. Conclusion

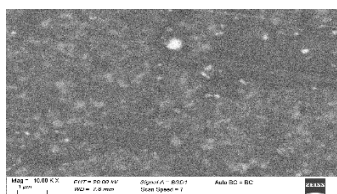


Figure 1: SEM image of bulk sample after VHPS

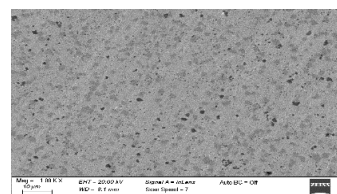


Figure 2: SEM image of bulk sample after UNPS

- The mechanically alloyed HEA powders were consisted of the FCC phase.
- Both VHPS and UNPS samples were presented two different precipitation phases.
- The EDS results indicated that the darker precipitates were the σ (sigma) phases rich in Cr, Fe and Mn elements and the other precipitated phase is rich in chromium.
- While the precipitates in VHPS sample were formed at nanoscale, they were formed larger than micron size in UNPS sample. For UNPS sample, the high temperature during sintering caused the precipitate grains to grow.
- The average microhardness values obtained are 211 HV for the UNPS samples and 445 HV for the VHPS samples. This excessive difference is due to the nanoprecipitates in VHPS samples.
- The coefficient of friction (COF) value of the VHPS sample was 0.66 and the UNPS sample was 0.54. The VHPS sample showed a slightly higher friction coefficient, which may be due to the resistance effect of smaller nanoprecipitates.

References

- [1] H. Cheng, Y.C. Xie, Q.H. Tang, R.A.O. Cong, and P.Q. Dai, Transactions of Nonferrous Metals Society of China, 28(7) (2018) 1360-1367.
- [2] M. Laurent-Brocq, P.A. Goujon, J. Monnier, B. Villeroy, L. Perrière, R. Pirès, and G. Garcin, Journal of Alloys and Compounds, 780 (2019) 856-865.



CWS

Corrosion and Wear Symposium

Korozyon ve Aşınma
Sempozyumu

INVESTIGATION OF THE INFLUENCE OF AGE HARDENING ON THE CORROSION RESISTANCE AND HARDNESS OF A NANOCRYSTALLINE AA2024 ALLOY

Furkan ÖZDEMİR¹, Hasan OKUYUCU¹, Rajeev GUPTA²

¹Ankara Yıldırım Beyazıt University, ²North Carolina State University
Türkiye, USA

Keywords: Nanocrystalline alloys, aluminum alloys, corrosion, hardness

Abstract

The objective of this work is to investigate the influence of age hardening on the corrosion and hardness of a nanocrystalline AA2024 alloy. Nanocrystalline AA2024 specimens were prepared by high-energy ball milling of gas atomized AA2024 powder and subsequent compaction under 3GPa of uniaxial pressure at room temperature. Influence of age hardening conditions on the corrosion behavior of AA2024 was analyzed along with the mechanisms that provide superior hardness.

1. Introduction

The simultaneous presence of high-strength and corrosion resistance is a rare virtue in aluminum alloys, where high strength after strengthening efforts resulted in low corrosion performance in commercial alloys such as AA2024[1,2]. Nanocrystalline Al alloys produced by high energy ball milling (HEBM) have been recently reported to demonstrate simultaneous ultra-high strength and significant corrosion resistance [3,4]. The effects of age hardening, on the hardness and corrosion of AA2024 are investigated herein.

2. Materials and Methods

AA2024 master alloy powder was high energy ball milled for 100 hours and then cold compacted. Loading and sealing of the materials were performed under controlled atmosphere. Heat treatment was performed at 150°C for 1-48 h. The 1 h, 8 h, and 48 h heat treated samples are termed as underaged (UA), peak aged (PA) and overaged (OA), respectively. The microstructure is characterized by X-ray diffraction (XRD) and Scanning electron microscopy (SEM). Cyclic potentiodynamic polarization (CPP) experiments and Vickers microhardness tests were performed to evaluate corrosion and hardness, respectively.

3. Conclusions

Age hardening modified the significantly improved corrosion resistance and hardness of the high energy ball milled AA2024 (Figure 1). Peak aging resulted in enhanced hardness and corrosion performance among applied heat treatments.

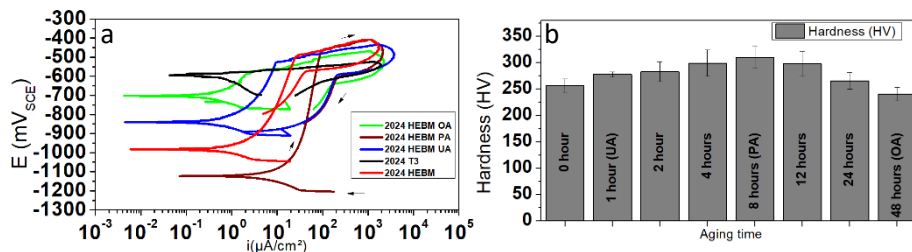


Figure 1. a) CPP b) Hardness test results of the age hardened high-energy ball milled AA2024

Acknowledgement

F.O Acknowledges the financial support from TUBITAK.

References

- [1] J.R. Davis, Corrosion of aluminum and aluminum alloys, Asm International, 1999.
- [2] I. Polmear, Light Alloys, From Traditional Alloys to Nanocrystals, 4th ed., Butterworth-Heinemann, 2006.
- [3] R.K. Gupta, B.S. Murty, N. Birbilis, An Overview of High-energy Ball Milled Nanocrystalline Aluminum Alloys, Springer, 2017.
- [4] F. Ozdemir, C.S. Witharamage, A.A. Darwish, H. Okuyucu, R.K. Gupta, Corrosion behavior of agehardening aluminum alloys produced by high-energy ball milling, J. Alloys Compd. 900 (2022) 163488.

CAN HIGH-STRENGTH STEEL BECOME STAINLESS ALSO WITH LOW CHROMIUM CONTENT?

Beste PAYAM, Mustafa Kamil ÜRGEN, Cem ÖRNEK

Istanbul Technical University
Türkiye

Keywords: High-Strength Steel, Corrosion Resistance, Low-alloyed Stainless Steel

Abstract

High-strength steels are used in demanding applications where a high strength-to-weight ratio is a primary concern. This steel group offers tensile strengths higher than 1000 MPa but is susceptible to environmentally-induced degradation, such as corrosion or hydrogen embrittlement. Hybrid steel is a new-generation low-alloyed high-strength steel that offers exceptionally high corrosion resistance. We performed electrochemical potentiodynamic polarization measurements in 0.1 M and 0.01 M near-neutral sodium chloride solution at room temperature and found that 5Cr-5Ni-2Al Hybrid steel shows similar corrosion behavior to 14% chromium-containing martensitic stainless steel (grade 420). In addition, Hybrid steel was seen to undergo pitting corrosion and indicated spontaneous passivity similar to stainless steel. The exceptional corrosion resistance stems from the mixed oxide of Al, Cr, Ni and Mo species. Our work has shown that steel can also be made stainless without needing a minimum chromium content of 10.5 per cent.

1. Introduction

Stainless steels contain a minimum of 10.5 wt.-% Cr with often other alloying elements, such as Mo, Ni and N, and offer high corrosion resistance and passive properties in halide media. However, due to the high alloying concentration, stainless steels are expensive. Hy55 Hybrid steel is novel steel containing relatively low alloying elements (see table below), providing a cheaper option for meeting the high strength needs in ball-bearing applications. Hybrid steel offers a double precipitation hardening of a martensitic microstructure offering a hardness of 55 HRC. During tempering, sub-micrometer-sized carbides and nanometer-sized nickel aluminides form finely dispersed in the microstructure. This combination of microstructure design and chemical composition brings superior material properties. In addition, the production of Hybrid steel also offers a green production process due to the zero CO₂ emission policy of the manufacturer (OVAKO AB, Sweden) and the use of fewer alloying elements, resulting in extensive cost reduction.

2. Materials and Method

The chemical composition (wt.-%) of the investigated steels is shown in the table below:

Material	C	Mn	Cr	Ni	Mo	Al	Fe
Hybrid Steel	0.18	0.3	5	5	0.7	2	Bal.
420 Stainless Steel	0.3	0.42	14.1	0.12	0.03	0.006	Bal.

The corrosion behavior of the materials was investigated in 0.01 M and 0.1 M NaCl at room temperature by potentiodynamic polarization using the conventional three-electrode setup. The obtained polarization diagrams are shown in Figure 1. Hybrid steel was seen to show spontaneous passive behavior since a Tafel fitting was not possible, indicating that the anodic dissolution occurred under mass control dominance. Furthermore, a steep rise in anodic current density at around 0 mV vs Ag/AgCl (sat.) occurred, indicating the protective surface film breakdown. After the polarization experiments, the corrosion morphology examined by optical and scanning electron microscopy revealed that the corrosion morphology was localized corrosion with clear signs of pitting (Figure 2).

3. Conclusions

The work has shown that Hybrid steel offers similar corrosion resistance to a counterpart of high-strength stainless steel and, hence, provides a cheaper and more sustainable solution for engineering applications. In addition, steel can also be made stainless with chromium content lower than 10.5 weight per cent.

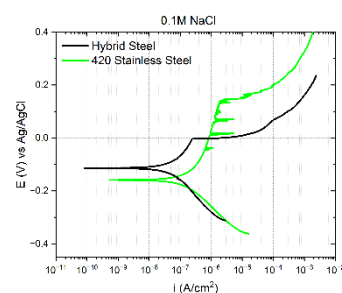


Figure 2. Polarization curves of Hybrid steel and 420 stainless steel in 0.1 M NaCl.

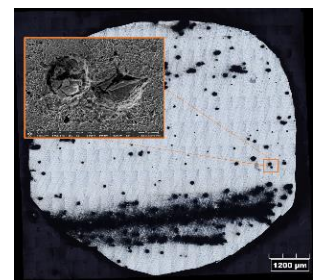


Figure 1. Corrosion morphology under an optical and scanning electron microscope (image inset).

TRIBOCORROSION PROPERTIES OF ELECTROLESS NICKEL-BORON COATINGS FROM STABILIZER-FREE BATH

Muslum YUNACTI¹, Alex MONTAGNE², Mariana Henriette STAIA², Véronique VITRY¹

¹Université de Mons, ²Arts et Métiers Institute of Technology
Belgium, France

Abstract

Electroless nickel-boron coatings were produced in a stabilizer-free bath. Its properties were investigated in a tribocorrosion test. It is found that its potential slightly increased after sliding. A lower and stable friction coefficient (COF) was observed during the tribocorrosion test when it was compared to the dry sliding test.

1. Introduction

Electroless nickel-boron coatings have excellent hardness and wear resistance, thickness uniformity, shape compliance, etc. Recently, a new electroless nickel-boron coating, which is produced in a bath exempt from toxic heavy metal, was developed by the Metallurgy Department of Mons University. This coating presents properties close to those of the conventional electroless nickel-boron coating, but noticeably, it exhibits a much-improved corrosion resistance [1]. Tribocorrosion is a phenomenon that concerns the degradation of materials under a variety of wear conditions in corrosive environments. Synergies therefore must be taken into account when corrosion and wear act simultaneously.

2. Materials and Methods

The coatings were synthesized on mild steel (ST 37-DIN 17100) in the shape of sheet coupons with 25*50*1 mm³. Coatings were produced in the stabilizer-free bath with the conditions: of 95 °C, duration of 1h, and 300 rpm mechanical agitation. Optical microscopy and SEM were used for the investigation of coating morphology. Tribocorrosion tests were carried out in UMT Tribolab, under the following conditions: the normal load of 2 N, speed of 10 cm/s, and the electrolyte of NaCl (0.1 M). The test duration was set as 140 mins: 60 mins before sliding, 20 with sliding, and 60 mins after sliding.

3. Conclusion

During the tribocorrosion test, a slight increase in the potential (see figure 1a) was observed when sliding started. This slight increase could be attributed to the corrosion product formed during 1h of immersion. As there is no decrease in the potential, it could be said that coating hindered the electrolyte reach the substrate which has a lower potential than the coating. It is seen in figure 1a, the COF obtained during the tribocorrosion test is lower than the one from the dry sliding test, which could be due to the lubricating effect of electrolyte solution. It is also observed that the coating presents stable COF during the tribocorrosion test.

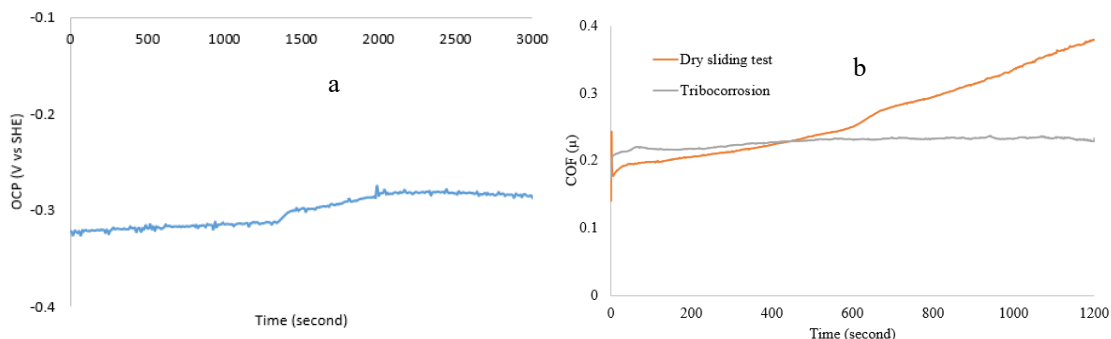


Figure 1: (a) OCP evolution during the tribocorrosion test, (b) COF from tribocorrosion and dry sliding tests

References

1. Yunacti, M.; Mégret, A.; Staia, M.H.; Montagne, A.; Vitry, V. Characterization of electroless nickel–boron deposit from optimized stabilizer-free bath. *Coatings* **2021**, *11*, 576, doi:10.3390/coatings11050576.

EFFECT OF B AND SR ADDITION TO TRIVALENT CHROMIUM PROCESS (TCP) COATED Al-Si CAST ALLOYS ON CORROSION RESISTANCE

Berkay SAVAŞKAN^{1,2}, Muammer MUTLU², Özgül KELEŞ¹

¹Istanbul Technical University, ²Mita Kalıp ve Dokum Sanayii
Türkiye

Keywords: Aluminum foundry alloys, Micro-galvanic corrosion, Tafel extrapolation, Copper Intermetallics

Abstract

The corrosion resistance of cast aluminum alloys (EN AC 4xxxx series) is a vital characteristic asked by customers, especially in automotive industry. The alloying elements of aluminum casting alloys directly affect their corrosion resistance. The corrosion resistance of copper-containing aluminum alloys is poor due to micro-galvanic corrosion caused by copper in the alloy. In this study, the effects of EN AC 46000 (Cu ~ 2.5 wt.%) and EN AC 43400 (Cu ~ 0.1% wt.) alloys on the corrosion resistance of both before and after the Trivalent Chromium Process (TCP) with the addition of Sr and B were investigated. Electrochemical Impedance Spectroscopy (EIS) analyzes was applied to compare their corrosion resistance.

1. Introduction

The corrosion resistance of aluminum casting alloys varies depending on the amount of alloying elements. Particularly, the presence of copper element reduces corrosion resistance considerably. Due to the fact that copper is a more noble metal than aluminum, copper intermetallics in aluminum alloys can corrode its surrounding areas that is called microgalvanic corrosion phenomena [1]. There is a lot of corrosion protection techniques. And chemical conversion coating is the one of them. Trivalent Cr(III) conversion coating or Trivalent Chromium Process (TCP) is one of the most widely used corrosion protection methods in automotive industry.

2. Materials and Methods

EN AC 43400 (Cu: 0.1 wt.%) and EN AC 46000 (Cu: 2.5% wt.) alloys are used in this study. Samples are produced by high pressure die casting (HPDC) process. Grain refinement and eutectic modifier agents (B & Sr) were added to alloy before casting by 200ppm & 250 ppm respectively. Casted samples are characterized by optic microscope and SEM in order to determine effectiveness of B and Sr addition to alloys. Total 6 different samples (EN AC 46000 & EN AC 43400 with *no addition*, *B added* and *Sr added*) are produced. After casting process and TCP coating process is applied. TCP coating process parameters are 4 min. & 70 °C for degreasing, 3 min. for desmutting and 4 min. & 35 °C for trivalent chromium conversion coating. EIS is carried out TCP coated samples in the 3.5% NaCl solution. EIS parameters are frequency range and potential amplitude 10⁵ Hz to 1 Hz and 10mV, respectively.

3. Conclusion

Table-1: Electrochemical parameters obtained by EIS model fitting with experimental results

Alloy Type	Sample	Rs (Ohm)	Rp (Ohm)	Yo _p , Ss ⁿ	n1	Rct (Ohm)	Yo _{ct} , Ss ⁿ	n2
EN AC 46000	No addition	3.601	6.477	10.12 x10 ⁻⁶	0.895	122.0 x10 ³	6.019 x10 ⁻⁶	0.880
	B added	4.526	447.1	23.49 x10 ⁻⁶	0.850	56.65 x10 ³	25.28 x10 ⁻⁶	0.832
	Sr added	4.566	47.73	7.083 x10 ⁻⁶	0.939	130.2 x10 ³	3.769 x10 ⁻⁶	0.970
EN AC 43400	No addition	4.431	8.840	3.202 x10 ⁻⁶	0.976	199.2 x10 ³	3.327 x10 ⁻⁶	0.948
	B added	4.726	13.88	3.194 x10 ⁻⁶	0.952	1073 x10 ³	2.852 x10 ⁻⁶	0.949
	Sr added	4.846	11.88	3.250 x10 ⁻⁶	0.948	138.9 x10 ³	3.789 x10 ⁻⁶	0.944

EIS results shows that TCP coated EN AC 43400 samples have higher corrosion resistance than the TCP coated EN AC 46000 samples according to charge transfer resistance (Rct) values (table-1). Also, EN AC 43400 B added sample has higher Rct than the other samples. On the other hand, the EN AC 46000 Sr added sample has a higher Rct value than the other samples.

4. Reference

[1] Y. Guo, G.S. Frankel (2012). Characterization of trivalent chromium process coating on AA2024-T3, *Surface and Coatings Technology*, 206:19–20, s. 3895-3902.

THE EFFECT OF BORON ADDITION ON THE MICROSTRUCTURE AND MECHANICAL PROPERTIES OF HCX TOOL STEEL

N. Şeyma NEVCANOĞLU, Akay NEVCANOĞLU, H. Özkan GÜLSOY

Marmara University
Türkiye

Keywords: HCx Tool Steels, Microstructure, Hardness, Boron Doping

Abstract

This work handles enhancing hardness and microstructural properties of HCx tool steel owing to doping FeB. FeB was doped as boron source. Samples were prepared by using conventional powder metallurgy techniques. Samples were sintered on different conditions. While one group did not include boron, the other one had % 1.5 wt FeB. Two different sintering temperature and time were used to figure out the objective effect of boron doping. Sintered density results, hardness scores and microscope images were provided. Analyses were related to each other. The sample on best condition was detected owing to analyses. Characterization methods were executed to this sample. Analyse and characterization info revealed that was a remarkable increase on sintered density and hardness. The factors that led to this improvement were discussed.

1. Introduction

Tool steels were advanced in early years of 1960s to provide various engineering properties that were required in industrial applications. It was a breakthrough in materials science, since it let machining and shaping materials simply. Tool steels serve advanced engineering properties owing to their Cr, W, V, Co, Mo contents contrary to non-alloyed steels. Tool steels can be designed for the purpose of providing mechanical properties such as; hardness, strength, ductility, wear resistant. However, the purpose also can be bringing in engineering properties such as; corrosion resistance, advanced surface properties and increased thermal or electrical conductivity. Tool steels are used in various areas such as; manufacturing of casting and press moulds, machining parts, hand tools, agricultural tools, polymer injection moulds [1–3].

HCx tool steel was produced by requirement of wear and corrosion resistance at high temperatures and in contaminated working environments. HCx presents the properties above owing to its high Cr content along with conventional tool steel elements such as; Mo, Co, W and V. HCx is generally used as valve inserts in automobile engines and as milling shafts. HCx is also preferred on manufacturing of

pressure cooker, since it serves wear and corrosion resistance at high temperature. General Electric Co. uses HCx steel as grinding parts on vertical mills. It is illustrated in Fig. 1. The compressibility is the leading challenge for HCx PM products. However, HCx tool steel is manufactured by PM methods mostly. Boron takes attention with its enhancing effect on steels regarding with hardening even it is used in trace amounts. Furthermore, its enhancing wear resistant and lubricating effect is known also [4–7].



Fig. 1. GE Grinding Material HCx Parts [8].

Tool steels reach their final hardness properties after proper heat treatment. The heat treatment includes heating to austenite temperature, holding on this temperature and then quenching. After quenching, the microstructure of tool steel is organized to serve the highest hardness. Thus, the final hardness reached is directly related with the microstructure. Hardening is generally followed by a normalization heat treatment to reduce the stress on matrix. The microstructure before hardening generally presents reticulated carbides in perlite matrix. The reticulated cementite (Fe_3C) is illustrated in Fig. 2a. After hardening heat treatment, perlite matrix changes into

martensite phase, while carbides separate in matrix as fine precipitations. The microstructure that is presented in Fig. 2b serves the highest hardness depending on C content, alloying metals and austenitization temperature [9–12].

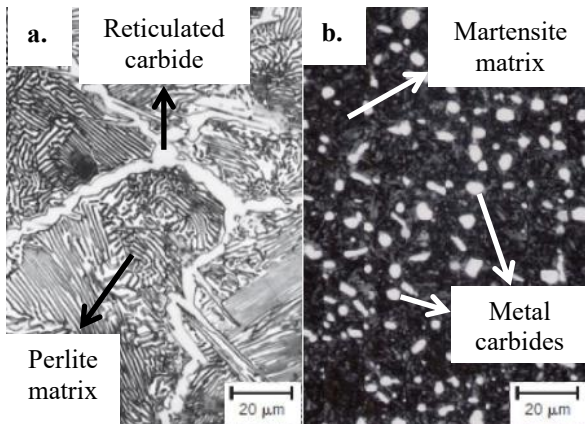


Fig. 2a. Reticulated Fe_3C in perlite matrix [13] and **b.** Carbides in M42 martensite matrix [14].

Hardening ability is primarily controlled by C content. Austenitization temperature decreases with increasing % C ratio that dramatically determines the heat treatment conditions. The alloy composition of tool steel also effects hardening ability. Thus, all type of tool steels requires unique hardening mechanism. The primary and secondary metal carbides occur with separating of reticulated carbides as a result of hardening heat treatment. The carbides of conventional tool steel elements form as fine precipitations. MC , M_2C and M_6C type metal carbides are called as primary carbides and the size of carbide precipitations are under $5\ \mu m$. M_7C_3 and $M_{23}C_6$ types are secondary carbides and precipitation sizes are measured on nanometer scales [15–17].

Boron addition to steels has been studied by several researchers. Boron is known by its hardening and effect of increasing hardenability. The detailed known effect of boron addition to steels is increasing mechanical properties owing to liquid phase sintering mechanism. Erden at. al. [18] proved that % 0.1 - 0.5 wt elemental boron addition increased yield strength and hardness dramatically. Özgün at. al. [19] reached the highest hardness without hardening owing to elemental boron addition up to % 1 wt on D2 tool steel. Gülsoy [20] handled the corrosion behaviour of boron doped 17-4 PH stainless steel. Results present convincing increase in corrosion resistance. HBHSS (High Boron High Speed Steels) are obtained by % 4 wt boron addition to HSS (High Speed Steels). HBHSS serve 1700 HV hardness. This score is reached only by W and V containing HSS. HBHSS are preferred to HSS on several applications because of its lower production cost [21–24].

Limited numbers of studies exist in literature about HCx stainless tool steel. The researchers that studied this material generally focused on its corrosion behaviour. Hitachi Ltd. executed a rare study which

dealt with mechanical properties of HCx. Hot rolling mills made from HCx were used in the study. Ono at. al. [7] detected that shaping regime was regulated and milling speed was increased owing to HCx using. The corrosion behaviours of HCx doped PM steels were investigated by Gordo at. al. [4–6] mostly. They indicated that the HCx doping to steels served convincing corrosion behaviour while decreased total costs of production powder. In this work, cylindrical shaped samples were prepared by conventional PM methods. The Archimedeian density determinations, hardness measurements and microstructure observations were applied. Optical Microscopy (OM) and Scanning Electron Microscopy (SEM) methods were used on microstructure observations. It is aimed to figure out effect of boron addition on hardness and microstructural properties of HCx. Additionally, it is predicted to enrich insufficient literature about HCx tool steel.

2. Experimental Procedure

The powder mixture consisted of % 0.5 wt Acrawax - C as the lubricant ingredient, % 1.5 wt FeB as boron source and balancing HCx. The irregular shaped HCx powder was provided by Höganäs Limited (Great Britain), while the spherical shaped FeB powder were bought from F. W. Winter Inc. & Company. The chemical composition info of HCx is given in Table 1. The particle contribution of HCx powder was reported as D_{50} : 150 - 180 μm by its supplier. The supplier of FeB powder declared the composition as wt % 19 B - %81 Fe and the median particle size D_{50} : 10.65 μm . The morphology of powders can be observed in Fig. 3a and b [25, 26].

Table 1. The chemical composition of HCx [25].

Alloy (%wt)	Fe	Cr	Mo	W	V	C	Si
min	Balance	22	2.8	2.8	1.8	1.5	0.5
max		25	3.2	3.2	2.2	1.7	1.5

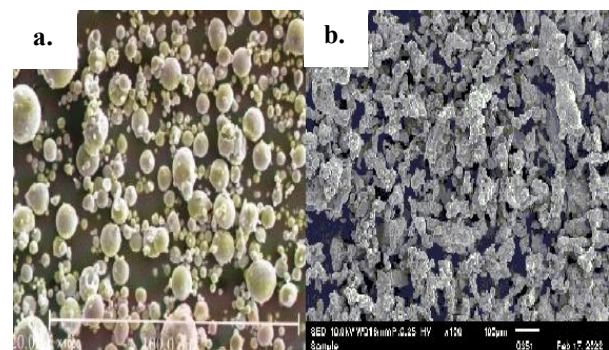


Fig. 3a. SEM image of FeB powder and **b.** SEM image of HCX powder.

A schematic illustration of the whole production process is given in Fig. 4. The determined powder composition was adjusted by a precise balance. The powders were blended in a Turbula mixer for 60 minutes. Green samples were provided owing to hydraulic press in 600 MPa. Sintering processes were

carried out under high purity H_2 atmosphere, since boron has high oxygen affinity. The sintering conditions in this work were appointed with reference to previous researchers [20–24] who experienced conventional sintering of boron doped tool steels. Thus, 1150°C and 1200°C was selected as sintering temperature while sintering times were 60 and 90 minutes. The sintering conditions and composition info of samples are listed in Table 2. Sintering processes provide de-bonding of the binder ingredient at first stage. Instant temperature rises can cause contamination in samples owing to burning of binder ingredient. Rapid cooling caused thermal shocks are not desired to avoid distortion of samples. Since eliminate these risks, the heating and cooling regime was chosen as 10 °C/minutes.

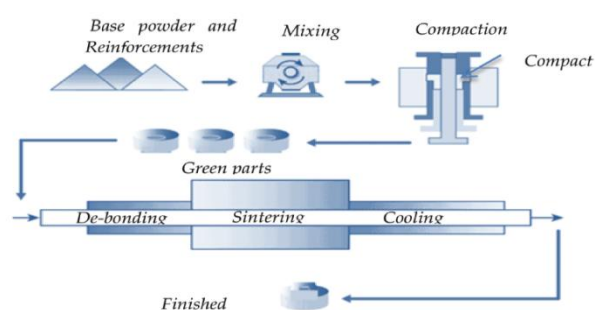


Fig. 4. Conventional PM production process [27].

Table 2. The determined conditions of samples.

Sample Name	FeB Content (% wt)	Sintering Temperature (°C)	Sintering Time (min)
a	0	1150	60
b	1.5	1150	60
c	0	1200	60
d	1.5	1200	60
e	0	1200	90
f	1.5	1200	90

The density was calculated by Archimedes density measurement method. Precisa 205 is a precise balance which has Archimedean density kit was used measurement of sample densities. The hardness determination of samples was executed by Instron Wolpert which is adjusted in Rockwell B (HRB) scale. Repetitive at least three hardness measurements were applied for each sample to provide consistent hardness results. Samples were polished as standard metallographic procedures. Microstructures were obtained by Olympus-BX51M (OM) and Jeol-JSM-IT100 SEM after polishing and etching.

3. Results and Discussion

3.1. Sintered density measurements

Sintered density results for all samples were increasing by boron content, sintering time and sintering temperature as expected. The sample (f) which was doped % 1.5 wt FeB and sintered at 1200°C for 90 minutes achieved the highest density. Density of sample d proved effect of boron doping on sintered density showed approximately % 4.63 increase that was considerable when compared with the free boron one (c). Sintered density results indicated that the sintering time for 90 minutes and sintering temperature at 1150°C provided negligible improvement on density. The samples sintered at 1150°C (a, b) served the lowest density owing to higher porosity ratio. Microstructure observations were also supportive with this phenomenon as illustrated in Fig. 7a and 8a.

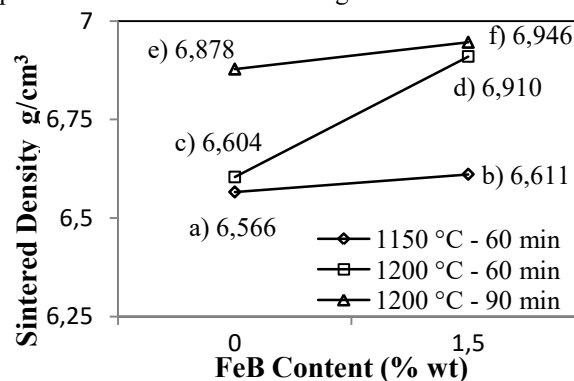
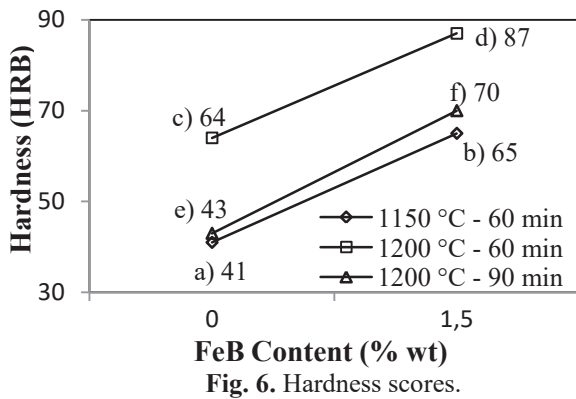


Fig. 5. Sintered density evolution.

The sintered density evolution by parameters can be attributed to resulting in advanced contact of particles, thus enhancing the mass transfer. This fact was detected by many researchers. Miramontes et al. [28] indicated that density increased by boron content on sintered 409Nb stainless steel at 1150°C. Selecká et al. [29] investigated boron effect on Ni, Cr and Mo alloyed structural steels. They declared an increase up to % 10 on sintered density by % 0.1 - 0.6 wt ferroboron addition. Sercombe [30] showed that the highest density was provided by % 0.4 wt FeB addition on SLS (Selective Laser Sintering) product 18Ni(350) maraging steel.

3.2. Hardness measurements

The hardness scores differed with the sintered density measurements. The sample (d) sintered at 1200°C for 60 minutes with FeB served the highest hardness. This fact was commented as a result of excess the grain growth for 90 minutes sintering. The grain growth can be observed in Fig. 7 and 8. The hardness scores of boron free samples revealed that sintering at 1200°C for 60 minutes was the optimum parameters in terms of hardness. Sample c served approximately % 50 higher hardness when compared with samples a and e. The hardness increased by FeB content as expected. The hardness score of sample d (87 HRB) was remarkable.



The hardening feature of boron addition to steels is mentioned in number of works [19,22–24,31] on the literature. Gülsoy [32] indicated that hardness increased approximately % 47 owing to % 1 wt FeB doping on 17-4 PH stainless steel. Miramontes et al. [28] claimed the highest hardness score they reached was 78 HRB when % 1.2 wt B doped to 409Nb stainless steel.

3.3. Microstructure observations

The micrographs of free boron samples (a, e, c) captured on 50X magnification presented the grain growth by sintering time and temperature. The excess grain growth for 90 minutes sintering (Fig. 7c) was revealing the hardness decrement when c and e samples compared (Fig. 6). The black areas in the microstructure of free boron samples were commented as porosity. The porosity ratio was decreasing by increasing sintering temperature and time as seen in Fig. 7a, b and c. The density measurements for free boron samples proved this fact as in general literature (Fig. 5) [20,22,31].

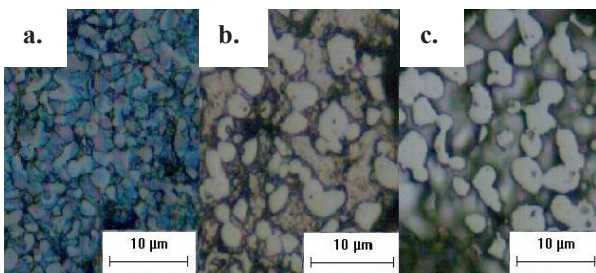


Fig. 7a. %wt 0 FeB, sintered at 1150°C for 60 min.
b. %wt 0 FeB, sintered at 1200°C for 60 min.
c. %wt 0 FeB, sintered at 1200°C for 90 min.

The micrographs of % 1.5 wt FeB doped samples showed same properties with free boron ones, except including fine precipitations. The microstructures of doped samples were captured on 100X magnification to observe the fine precipitations simpler. They were commented as primary carbides, since they caused the hardness increase as seen in Fig. 6. The decrease of porosity ratio and the grain growth can also be observed in Fig. 8a, b and c. The microstructure of sample d, measured 87 HRB of hardness had intensive precipitation as seen in Fig. 8b.

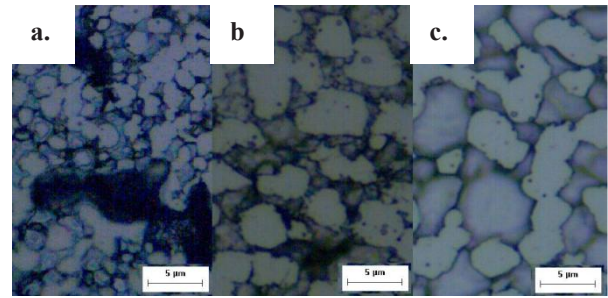


Fig. 8a. %wt 1.5 FeB, sintered at 1150°C, 60 min.
b. %wt 1.5 FeB, sintered at 1200°C, 60 min.
c. %wt 1.5 FeB, sintered at 1200°C, 90 min.

The primary carbide precipitations can be observed in SEM images, on higher magnifications, in Fig. 9b. The SEM images were captured on 200X magnification. The hardness enhancement owing to primary carbide occurrence on were investigated by several researchers [4,12,23,33].

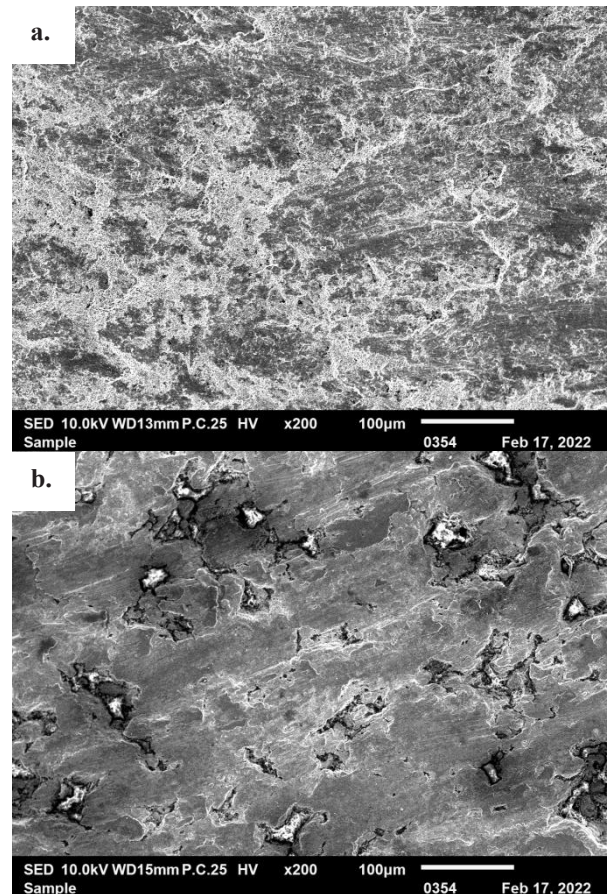


Fig. 9a. %wt 0 FeB, sintered at 1200°C, 60 min.
b. %wt 1.5 FeB, sintered at 1200°C, 60 min.

4. Conclusions

This study clarified that the FeB addition to HCx tool steel is considerable in terms of density and hardness. The optimum parameters for FeB doped HCx were detected as sintering at 1200°C for 60 min. Sintered density was increased approximately to 7 g/cm³, while 87 HRB was achieved by FeB doping to HCx tool steel.

References

- [1] Dey AK. Most Common Types of Steel | Grades of Steel (PDF) Grades of Steel Types of Steel based on Chemical Composition n.d.:1–7.
- [2] Hakan Koçak. Takım Çelikleri El Kitabı 2006;31.
- [3] Dr.C.Ergun. Engineering Materials. Notes, 2007, p. 1–30.
- [4] Gordo E, Khattab N, Torralba JM. Sinterability and properties of HCx PM steel diluted with stainless steels. Rev Metal 2005;SPEC. VOL.:95–100. <https://doi.org/10.3989/revmetalm.2005.v41.extra.1005>.
- [5] Gordo E, Jimenez-Morales A, Khattab N. Oxidation and corrosion behaviour of high-alloyed steels based on HCx steel. Proc Euro Powder Metall Congr Exhib Euro PM 2007 2007;1:97–102.
- [6] Khattab N, Gordo E, Torralba JM, Trabadelo V, Iturriza I. Development Of Hcx Stainless Steel - Based Materials For Its Application As Valve Seat Inserts In Diesel Engines n.d.
- [7] Ono, H; Watanabe, T; Yoshimoto, K; Kaga, S [Hitachi, Ltd. T (Japan)]. Industrial Application of HCX-MILL to Hot Strip Mills. Hitachi Hyoron; J 1996:9–16.
- [8] General Electric. HCX™ Grinding Elements for Vertical Mills. 2017.
- [9] Zhou, Xue-feng Di L iu, Wang-long Zhu, F eng Fang, Yi-you Tul j ian-q in g j ia ng. Morphology , microstructure and decomposition behavior of M2C carbides in high speed steel. ScienceDirect 2017;21:15–21.
- [10] Mustafa TAYANÇ GZ. YÜKSEK HIZ ÇELİKLERİNİN İÇ YAPI VE ISIL İŞLEM ÖZELLİKLERİ. BAÜ Fen Bilim Enstitüsü Derg 2000;2:103–22.
- [11] Yasin SUBAŞI. DÖKÜM YÜKSEK HIZ ÇELİKLERİNDE MİKROYAPISAL KARAKTERİZASYON; MİKROYAPI-MEKANİK ÖZELLİKLER İLİŞKİSİNİN BELİRLENMESİ. 2006.
- [12] Chaus AS, Dománková M. Precipitation of Secondary Carbides in M2 High-Speed Steel Modified with Titanium Diboride. J Mater Eng Perform 2013;22:1412–20. <https://doi.org/10.1007/s11665-012-0407-9>.
- [13] ÖZTÜRK PDS. Faz diyagramları Ders Notları, KTÜ, Metalurji ve Malzeme Mühendisliği Bölümü; n.d.
- [14] Voort G Vander. Metallographic Characterization of the Microstructure of Tool Steel Five - Step Method for Preparing Tool Steel, Lake Bluff, Illinois USA: Buehler Ltd; n.d.
- [15] Hou TP, Wu KM, Liu WM, Peet MJ, Hulme-Smith CN, Guo L, et al. Magnetism and high magnetic-field-induced stability of alloy carbides in Fe-based materials. Sci Rep 2018;8:1–10. <https://doi.org/10.1038/s41598-018-20910-3>.
- [16] Jaworski J, Kluz R, Trzepieciński T. Influence of heat treatment on content of the carbide phases in the microstructure of high-speed steel. Arch Foundry Eng 2017;17:59–62. <https://doi.org/10.1515/afe-2017-0091>.
- [17] KALAFATOĞLU İE, S. Nuran ÖRS. 21. YÜZYILDA BOR TEKNOLOJİLERİ VE UYGULAMALARI. BAÜ Fen Bil Enst Derg 2003:1–23.
- [18] ERDEN MA, TÜRKMEN M, KARABULUT H, GÜNDÜZ S. Effect of Boron Nitride Addition on the Microstructure and Mechanical Properties of PM Steels. Afyon Kocatepe Univ J Sci Eng 2017;17:185–91. <https://doi.org/10.5578/fmbd.48591>.
- [19] Özgün Ö, Erçetin A, Balalan Z, Özkan Gülsoy H, Uzun M. Bor İlavesinin Toz Metal D2 Takım Çeliğinin Mikroyapı ve Mekanik Özelliklerine Etkisi. Fırat Üniv Müh Bil Derg Sci Eng J Fırat Univ 2017;29:87–96.
- [20] Gülsoy HÖ. Dry sliding wear in injection molded 17-4 PH stainless steel powder with nickel boride additions. Wear 2007;262:491–7. <https://doi.org/10.1016/j.wear.2006.05.003>.
- [21] Madan DS. Role of Some Ferroalloy Powders in Enhancing Sintering and Improving Properties of Ferrous P/M Compacts. Adv Powder Metall 1991;4:103–13.
- [22] You J, Kim HG, Lee J, Kang K, Lee HM, Kim M, et al. Microstructure Modification of Liquid Phase Sintered Fe–Ni–B–C Alloys for Improved Mechanical Properties. Metall Mater Trans A Phys Metall Mater Sci 2021;52:4395–401. <https://doi.org/10.1007/s11661-021-06392-5>.
- [23] Napara-Volgina SG, Baglyuk GA, Orlova LM, Kud VK, Khomenko AI, Kostenko AD. Structure and properties of sintered iron-boron-carbon alloys with different carbon contents. Powder Metall Met Ceram 2011;50:67–72. <https://doi.org/10.1007/s11106-011-9304-2>.
- [24] Liu J, Cardamone A, Potter T, German RM, Semel FJ. Liquid phase sintering of iron-carbon alloys with boron additions. Powder Metall 2000;43:57–61. <https://doi.org/10.1179/pom.2000.43.1.57>.
- [25] Unit M. Product specification. vol. 21. Londra: n.d. <https://doi.org/10.1080/09613219308727250>.
- [26] Gülsoy HÖ, Bilici MK, Bozkurt Y, Salman S. Enhancing the wear properties of iron based powder metallurgy alloys by boron additions. Mater Des 2007;28:2255–9. <https://doi.org/10.1016/j.matdes.2006.05.022>.
- [27] HG PK, M AX. Processing of Graphene/CNT-Metal Powder. Powder Technol., 2018. <https://doi.org/10.5772/intechopen.76897>.

- [28] Cabral Miramontes JA, Barceinas Sánchez JDO, Almeraya Calderón F, Martínez Villafañe A, Chacón Nava JG. Effect of boron additions on sintering and densification of a ferritic stainless steel. *J Mater Eng Perform* 2010;19:880–4.
<https://doi.org/10.1007/s11665-009-9544-1>.
- [29] Selecká M, Šalak A, Danninger H. The effect of boron liquid phase sintering on properties of Ni-, Mo- and Cr-alloyed structural steels. *J Mater Process Technol* 2003;141:379–84.
[https://doi.org/10.1016/S0924-0136\(03\)00421-7](https://doi.org/10.1016/S0924-0136(03)00421-7).
- [30] Sercombe TB. Sintering of freeformed maraging steel with boron additions. *Mater Sci Eng A* 2003;363:242–52.
[https://doi.org/10.1016/S0921-5093\(03\)00645-2](https://doi.org/10.1016/S0921-5093(03)00645-2).
- [31] Narasimhan KS, Semel FJ. Sintering of powder premixes - A brief overview. *Adv Powder Metall Part Mater - 2007, Proc 2007 Int Conf Powder Metall Part Mater PowderMet 2007* 2007:51–524.
- [32] Gülsoy HÖ. TOZ ENJEKSİYON KALIPLAMA METODU İLE ÜRETİLMİŞ 17-4 PH PASLANMAZ ÇELİK PARÇALARA YAPILAN İKİ TİP BOR İLAVESİNİN MİKROYAPI VE MEKANİK ÖZELLİKLERE ETKİSİ. 2003.
- [33] El-Rakayby AM, Mills B. On the microstructure and mechanical properties of high-speed steels. *J Mater Sci* 23 1988;23:40–4.



CORROSION BEHAVIOUR OF FEW-LAYERED-GRAPHENE (FLG) REINFORCED AL-4 WT.%CU METAL MATRIX COMPOSITES PROCESSED BY MECHANICAL ALLOYING

Cantekin KAYKILARLI, Burak KÜÇÜKELYAS, Taha Yasin EKEN, Nazlı AKÇAMLI, Deniz UZUNSOY

Bursa Technical University
Türkiye

Keywords: Aluminium, Metal Matrix Composites, Graphene, Corrosion

1. Introduction

Aluminium matrix composites (AMCs) have high tensile strength, elastic modulus and toughness, low density, and excellent corrosion and wear resistance, among other advantages. The transportation, maritime, and aviation industries typically use heat treatable aluminium (Al) alloys because of their advantageous combinations of high strength-to-weight ratio, toughness, fatigue resistance, and weldability, notably those in the 2xxx series (Al-Cu type). SiC, BN, Al₂O₃, B₄C, TiC, graphene, graphite, fullerene, and carbon nanotubes are just a few of the reinforcements used by the AMCs. Due to its exceptional properties, graphene distinguishes out from other reinforcing materials. Some of its properties are high specific surface area, excellent tensile strength, and Young's modulus. Despite being highly resistant to corrosion in air environments, aluminium and its alloys are not immune to corrosion in chlorinated and alkaline media. In this study, different proportions of few-layered graphenes (FLG) were mechanically alloyed at different times. The effect of these FLGs on the corrosion behaviour of reinforced aluminum is investigated with electrochemical tests.

2. Materials and Method

In this study, FLG (0, 0.25 and 0.5 wt.%) reinforced AMCs are produced with powder metallurgy routes. FLG were fabricated via the arc discharge method in our laboratory. Prepared powder mixtures were mechanically alloyed for 5, 7 and 9 hours in a planetary ball mill. The mechanically alloyed (MA'ed) powders were compacted via a hydraulic press under uniaxial pressure of 300 MPa. The sintering process was performed at 590°C for 3 h under argon gas flow. Corrosion properties were determined by the Tafel exploration method and tests were conducted using a standard three-electrode cell configuration and a CH InstrumentsTM CHI608 electrochemical workstation. The electrolyte solution is made with NaCl (Merck > 99.9% purity) salts of high purity. The samples are prepared with SiC papers of grit sizes of 100, 500, 800 and 1200, respectively and polished with colloidal silica. The surfaces were cleaned with isopropyl alcohol in an ultrasonic cleaner. As a respective reference, counter, and working electrodes, Ag/AgCl, platinum, and the samples are employed. All measurements are conducted in a NaCl solution containing 3.5% by weight. The samples were kept in electrolyte for 75 min before polarisation tests. The polarization curves are acquired at a scan rate of 1 mV/s and potential ranges of -400 to +400 mV with respect to the samples' open circuit potential (OCP).

3. Conclusion

The OCP behaviours of all specimens were determined to be close to each other and as -0.695 V vs. Ag/AgCl. Specimens reached equilibrium potential after 5 min., but to ensure the result, each sample was kept in the OCP test for 75 min., and the equilibrium potential did not change. According to the Tafel results, pit formation was observed at -0.72 V in all samples. The E_{corr} values were close, but it was observed that the corrosion resistance tended to increase as the amount of graphene increased.

Table 1. E_{corr} values of the FLG reinforced aluminium alloys with different mechanical alloying (MA) duration.

Specimens	MA Duration		
	5 h	7 h	9 h
Al ₄ Cu Bare	-0.807 V	-0.804 V	-0.819 V
Al ₄ Cu 0.25 wt. % FLG	-0.818 V	-0.801 V	-0.790 V
Al ₄ Cu 0.5 wt. % FLG	-0.808 V	-0.766 V	-0.781 V

References

- [1] J. Mohapatra, S. Nayak and M.M. Mahapatra, Journal of Alloys and Compounds, 11 (2018) 703-711.
- [2] G. Asan and A. Asan, Journal of Molecular Structure, 1201 (2020) 127184.

CHANGE IN FRICTION COEFFICIENT OF CU15NI8SN MATERIAL IN DRY AND OILY ENVIRONMENT ACCORDING TO CASTING METHOD

Talip ÇITRAK, Orçun ZİĞİNDERE, Edanur KASAP, Feriha BİROL, Ümit KAPLAN

Sağlam Metal
Türkiye

Keywords: Cu15Ni8Sn alloy, permanent mold casting, centrifugal casting, friction and wear.

Abstract

There are many plain bearing materials used commercially in the industry. Copper alloys are also included in these materials and the most used copper alloy as bearing material is bronze. Cu15Ni8Sn alloy, also known as C96900, is a spinodally hardened alloy and exhibits very good bearing properties in both lubricated and dry sliding conditions. Because of their excellent properties, these copper alloys are found in a wide variety of applications as bearing materials, especially in the aerospace and mining industries. There are many different casting methods for the C96900 material.

In this study, C96900 material was produced by two different casting methods, permanent mold casting and centrifugal casting. Solution and spinodal hardening heat treatments were applied to both materials according to the TX00 standard at the temperatures we obtained from our previous scanning and achieved optimum values. Pin-on-disc wear tests were carried out on the heat-treated samples using 440C stainless steel (60 HRC) balls with a diameter of 6 mm, at a speed of 0.30 m/s under 2 N force, in dry and oily environments. An oil with a viscosity of 200 cSt was used for the oily medium. According to the casting method, the hardness, electrical conductivity, and friction coefficients of the samples in dry and oily environments were examined comparatively.

1. Introduction

There are many plain bearing materials used commercially in the industry. Copper alloys are also included in these materials and the most used copper alloy as bearing material is bronze. Cu15Ni8Sn alloy, also known as C96900, is a spinodally hardened alloy and exhibits very good bearing properties in both lubricated and dry sliding conditions. Because of their excellent properties, these copper alloys are found in a wide variety of applications as bearing materials, especially in the aerospace and mining industries [1-3].

The C96900 material are produced by using many different casting methods such as permanent molding, horizontal or vertical continuous casting, centrifugal

casting. Casting method could affect microstructure of the alloy, resulting in changes material properties [4].

Friction and wear behavior of rolling bearings vary depending on many factors such as material pair properties, environment, load type etc. Material properties depends on directly production history such as production method, heat treatment etc. [5].

In this study, friction coefficient and wear loss behavior of Cu15Ni8Sn alloy, produced by two different casting methods and spinodally aged according to TX00 standard, was investigated in a pin-on-disc based wear device under dry and oily environment conditions.

2. Experimental Procedure

2.1. Material

In this study, a standard Cu15Ni8Sn casting alloy was used as a reference material. The chemical composition of the alloy was determined by Hitachi Inspire the Next brand spectral analyzer and is given in Table 1.

Table 1. Chemical composition of material C96900 (wt.%).

Cu	Ni	Sn	Zn	Mn	Fe
Balance	14,5	7,6	0,23	0,18	0,07

The material, whose chemical composition is given, was heat treated according to the TX00 standard, under optimum conditions determined as a result of our own studies.

2.2. Microstructural Investigations

Microstructure characterizations were performed using Nikon Eclipse MA100 model inverted optical microscope. The chemical etching of the samples was done by immersion in 100 ml of distilled water containing 95 ml of C₂H₅OH, 5 ml of HCl and 5 g of FeCl₃.

2.3. Mechanical Properties

The mechanical properties of the alloys were characterized with hardness test. Vickers microhardness

tests were conducted using a Future-Tech FM800e device under 500 g load.

2.4. Wear Test

Friction and wear tests of casting materials were carried out with a pin-on-disc type CSM Instrument Tribometer. The samples were tested under 2N load and 0.30 m/s sliding speed. The sliding distance in each condition was determined as 200 m and the rotation speed as 0.30 m/s. Wear depth and friction coefficients were calculated.

3. Results and Discussion

3.1. Microstructural Investigations

Microstructural investigation of C96900 spinodal alloy produced by two different casting method was carried out. Centrifugal casting and permanent mold casting material microstructures are given in Figure 1 comparatively.

The optical microscope images of the alloys casted by different methods were examined. It was determined that the centrifugal casting had a smaller grain size than the permanent mold casting. In addition, more precipitation was observed at grain boundaries in permanent mold casting.

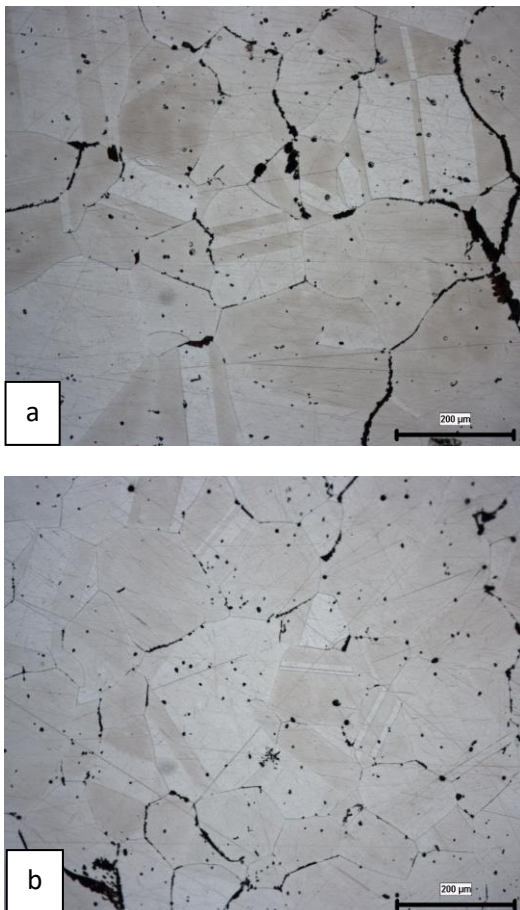


Figure 1. Optical microscope image of C96900 alloy (Casting method: a) Permanent Mold Casting, b) Centrifugal Casting) (100X magnification).

3.2. Mechanical Properties

Measured hardness values of the samples were given in the Table 2. These values meet the value required in the standard ASTM B505.

Table 2. Hardness values of C96900 material according to casting methods.

Casting Methods	Load (gf)	Average Value (HRC)
Centrifugal Casting	500	35,15
Permanent Mold Casting	500	37,05

3.3. Wear Test Results

The wear test results of the materials were revealed in the Table 3. The coefficient of friction and depth of wear penetration were determined. As a result of the high coefficient of friction in the experiments carried out in dry conditions, more wear was observed on the samples. In the experiments carried out in dry environment, there was more wear in centrifugal casting. However, it has been observed that centrifugal casting gives better results than permanent mold casting in experiments performed in a lubricating medium (Table 3).

Table 3. Average friction coefficient values of C96900 material according to casting methods and wear environment.

	Average Friction Coefficient	
	Permanent Mold Casting	Centrifugal Casting
Dry	0,643	0,752
Oil	0,206	0,193

Within the scope of the study, the graphs of the time-dependent penetration depth and friction coefficient of the C96900 alloy are given below (Figure 2, Figure 3, Figure 4, Figure 5). While very high friction coefficient values were obtained in the tests performed in dry conditions, low friction coefficients were obtained in the tests performed in oil environments with 200 cSt viscosity, and this change continued throughout the sliding distance. It is seen that the friction coefficient decreases considerably in the tests carried out in the lubricating environment.

When casting methods are compared, permanent mold casting has a lower friction coefficient than centrifugal casting in tests performed in dry conditions. In an oily environment, the opposite is true. Centrifugal casting has a lower coefficient of friction than permanent mold casting. Centrifugal casting has a smaller grain structure as it cools faster than permanent mold casting. In this case, the C96900 alloy used as the plain bearing material has a lower coefficient of friction in centrifugal casting in lubricating environments.

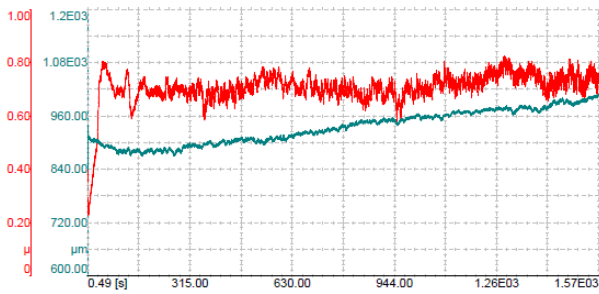


Figure 2. Abrasion test graph in dry environment of the permanent mold casting material. (red line: coefficient of friction, blue line: depth of wear)

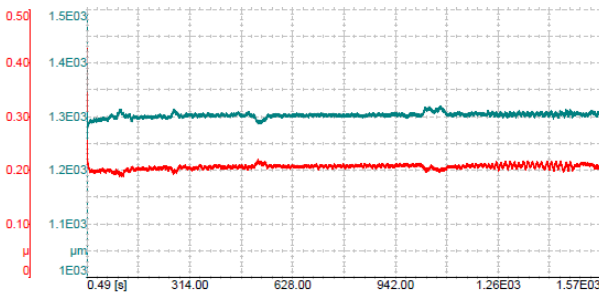


Figure 3. Abrasion test graph in oily environment of the permanent mold casting material. (red line: coefficient of friction, blue line: depth of wear)



Figure 4. Abrasion test graph in dry environment of the centrifugal casting material (red line: coefficient of friction, blue line: wear depth)

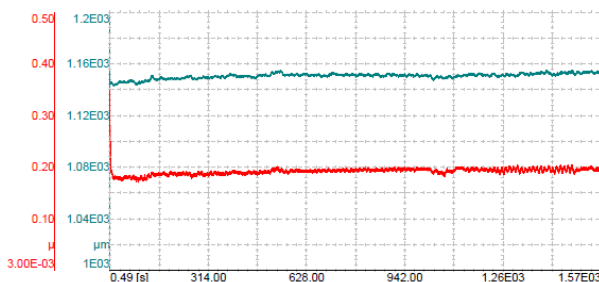


Figure 5. Abrasion test graph in oily environment of the centrifugal casting material (red line: coefficient of friction, blue line: wear depth)

4. Conclusions

In this study, the following results were obtained in the wear tests of C96900 spinodal alloy (Cu15Ni8Sn) performed in different working environments according to the centrifugal and permanent mold casting methods:

1. The friction coefficient and wear losses of the C96900 alloy in oily environments are lower than in dry environments.
2. In the experiments performed in dry environment, lower friction coefficient and wear depth were obtained in the samples obtained from permanent mold casting.
3. In the experiments conducted in oily environment, lower friction coefficient and wear depth were obtained in the samples obtained from centrifugal casting.
4. The lowest friction coefficient and wear depth were obtained in the centrifugal casting wear test performed in an oil medium with a kinematic viscosity of 200 cSt.
5. The hardness of permanent mold casting (37.5 HRC) under 500 gf load was higher than the hardness of centrifugal casting (35.15 HRC).
6. It has been observed that centrifugal casting has smaller grain size.
7. In permanent mold casting, precipitation at the grain boundaries are more in the microstructure.

References

- [1] Güngör, K. (2016). Sinterlenmiş bronz esaslı kaymalı yataklarda polimer kullanımının tribolojik özelliklere etkisi.
- [2] Guo, C., Shi, Y., Chen, J., Xiao, X., Liu, B., Liu, J., & Yang, B. (2021). Effects of P addition on spinodal decomposition and discontinuous precipitation in Cu-15Ni-8Sn alloy. *Materials Characterization*, 171, 110760.
- [3] Wang, Y. H., Wang, M. P., & Hong, B. (2005). Microstructures of Spinodal Phases in Cu-15Ni-8Sn Alloy. *International Journal of Minerals, Metallurgy and Materials*, 12(3), 243-247.
- [4] Davis, J. R. (Ed.). (2001). *Copper and copper alloys*. ASM international.
- [5] Singh, J. B., Cai, W., & Bellon, P. (2007). Dry sliding of Cu-15 wt% Ni-8 wt% Sn bronze: Wear behaviour and microstructures. *Wear*, 263(1-6), 830-841.



CGRS

Ceramics, Glass, Refractory Materials Symposium

Seramik, Cam, Refrakter
Malzemeleri Sempozyumu

SYNTHESIS OF Li_4SiO_4 AS A SOLID SORBENT FOR CARBON CAPTURE VIA SOLUTION COMBUSTION ROUTE

Kagan BENZESİK¹, Ahmet TURAN², Şeref SÖNMEZ¹, Maria Teresa IZQUIERDO³, Onuralp YÜCEL¹

¹Istanbul Technical University, ²Yeditepe University, ³Instituto de Carboquímica ICB-CSIC
Türkiye, Spain

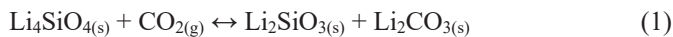
Keywords: SCS, Carbon capture, Solid sorbent

Abstract

Li_4SiO_4 is a critical material for both CCS technologies and fusion reactors. Conventionally and commercially Li_4SiO_4 is synthesized via solid-state synthesis. This technique requires very high energy consumption to heat up the reactant materials (Li_2CO_3 and SiO_2) resulting in synthesized powders having very large particle size and crystallite size. Combustion synthesis methods provide synthesized ceramic powders with low energy requirement and in nano-size. With this study, Li_4SiO_4 powders as solid sorbent for post-combustion carbon capture were synthesized via solution combustion technique using LiNO_3 as lithium source, TEOS as silicon source and citric acid as the fuel. CO_2 uptake characteristics of the synthesized powders were fully investigated. The sorbent showed a sorption performance as 29.5 wt.% CO_2 uptake value, in thermobalance test under 92 vol% CO_2 (N_2 balance) gas concentration at 600 °C.

1. Introduction

Li_4SiO_4 appears as a suitable material for CO_2 capture at high temperatures. The reaction of this solid is attributed to the mechanism by which the Li_2O within the crystal structure of Li_4SiO_4 reversibly reacts with CO_2 , as given by Eq. (1).



The advantages of this solid include a relatively high capture capacity (theoretical value of 36.7 wt%) at temperatures of 450–700°C, fast kinetics of carbonation/decarbonation, good mechanical properties and also the possibility of use in repeated carbonation/decarbonation cycles.

In this study, Li_4SiO_4 powders were synthesized via solution combustion route instead of the conventional solid-state synthesis method.

2. Materials and Methods

Lithium nitrate (LiNO_3) and tetraethyl orthosilicate (TEOS) were used as the oxidizers, respectively. Citric acid monohydrate ($\text{C}_6\text{H}_8\text{O}_7 \cdot \text{H}_2\text{O}$) was used as the reducer (fuel) for the SCS reactions. SCS experiments were carried out using a hot plate. After the combustion in aqueous media, the resulted powders were subjected to a following calcination step in a muffle furnace. Calcination took place at 650 °C for 4, 5 and 6 hours. Then the CO_2 uptake characteristics of the calcined powders were investigated using a thermogravimetric analyzer.

3. Conclusion

The XRD and CO_2 uptake results of the synthesized powders are given in Fig. 1 and Fig. 2, respectively.

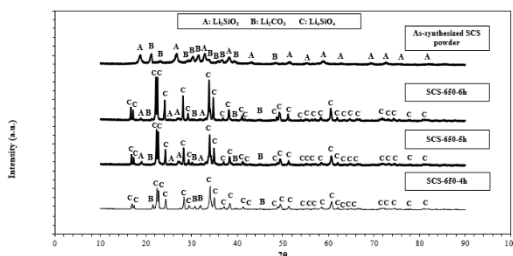


Fig. 1. XRD results of the synthesized powders.

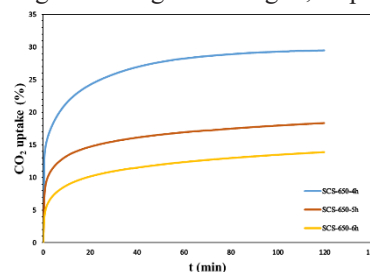


Fig. 2. CO_2 uptake values of the synthesized powders.

4. References

- [1] Y. Zhang *et al.*, "Recent advances in lithium containing ceramic based sorbents for high-temperature CO_2 capture." doi: 10.1039/c8ta08932a.
- [2] Y. Hu, W. Liu, Y. Yang, X. Tong, Q. Chen, and Z. Zhou, "Synthesis of highly efficient, structurally improved Li_4SiO_4 sorbents for high-temperature CO_2 capture," doi: 10.1016/j.ceramint.2018.06.094.

Nb-Co CO-DOPED BARIUM TITANATE DIELECTRIC CERAMICS FOR MULTILAYERED CERAMIC CAPACITORS

Berkay ÖZGÜR¹, N. Kaan ÇALIŞKAN¹, Abdullah ÖZTÜRK²

¹Tübitak SAGE, ²Middle East Technical University
Türkiye

Keywords: Dielectric Constant, Capacitance, Barium Titanate, Dielectric loss, Doping

Abstract

Niobium (Nb) and Cobalt (Co) co-doped barium titanate (BaTiO₃) ceramics were prepared to stabilize ferroelectric-tetragonal phase transformation of BaTiO₃. Preparation of ceramics started with mixing BaTiO₃, niobium oxide and cobalt oxide powders at predetermined concentrations varying from 1 to 3 atomic percentage. The mixing was done at wet conditions using distilled water with alumina balls at 50 rpm for 24 h in a ball mill. Then, the mixtures were compacted into 15 mm diameter and 4 mm thick disc shaped pellets by uniaxial pressing at 150 MPa. After that the discs were sintered at various temperatures ranging from 1230 °C to 1290 °C for various durations ranging from 30 min to 4 h. Sintered pieces were characterized using XRD, SEM, EDS, and DSC characterization techniques. Electrical properties namely dielectric constant, dielectric loss and temperature coefficient of capacitance were measured. Experimental results revealed that the co-doping of BaTiO₃ with Nb and Co lead to broaden permittivity peaks and temperature stability. A high dielectric constant of 3258 at 1 kHz is obtained at room temperature, along with +%10 and -%17 variation over temperature ranging between -30 and +150 °C. Also, the dramatic change in crystal structure of BaTiO₃ at 10 °C and 121 °C is suppressed.

Introduction

Barium titanate (BaTiO₃) is the first ferroelectric and piezoelectric ceramic developed for commercial piezoelectric applications such as sensors, and piezoelectric motors. It also plays an important role in design and manufacture of multilayer ceramic capacitors since it has large room temperature dielectric constant (as high as 7000), though other ceramics have values between 20 and 70 [1]. Smaller parts and high power density capacitors are successfully fabricated from BaTiO₃ based ceramics by cheap processing methods [2].

Dependence of relative dielectric constant to temperature in BaTiO₃ ceramics is the unfavorable property for capacitor applications. Kishi [3] reported that at least two dopants are needed to be able to overcome this deficiency and to produce reliable capacitors with long lifetime. First dopant is an acceptor such as Mn²⁺, Mg²⁺, Ca²⁺, Co²⁺ to substitute Ti site to prevent degradation of BaTiO₃ during sintering [4]. Second dopant could be the ions with intermediate ionic radius such as Y³⁺, Ho³⁺, Nb⁵⁺ which substitutes both Ba and Ti site to obtain shell region [3]. Burn [5] reported that Nb addition leads to broaden permittivity peaks of BaTiO₃. Also, Co addition is necessary to decrease temperature dependence of relative permittivity. Chazano [6] states the importance of firing temperature and composition on temperature dependence and dielectric constant. Chen [7] stated that Nb/Co ratio is very important for controlling grain growth and provide effective core shell structure to gain optimal dielectric properties through temperature range of -50 +125 °C. It has been reported that core-shell structures in BaTiO₃ is favored by slow volume diffusion of Nb [8].

Differential scanning calorimetry (DSC) could be used to detect phase transitions of samples. Since the main reason of dielectric constant change of BaTiO₃ based ceramics is the allotropic changes at certain temperatures, i.e., ~5 °C and ~120 °C, DSC could be employed to detect the allotropic changes with respect to temperature variations [9]. Although DSC curves of BaTiO₃ are available [10-11], the DSC data on the Nb-Co co-doped BaTiO₃ ceramics has not been reported in the open literature till now.

The purposes of this study are to prepare Nb-Co co-doped BaTiO₃ ceramics with controlled microstructure at temperatures between 1250 and 1290 °C by conventional mixed-oxide route and, to suppress the phase transformation at temperatures between -30 and +125 °C so that dielectric properties are improved.

Experimental Procedure

Ceramic capacitor samples were prepared by conventional mixed-oxide route. Three different powders used in this study were Barium titanate (BaTiO_3) (>99.5% Entekno), Niobium Oxide (Nb_2O_5) (99.99% Sigma-Aldrich), and Cobalt Oxide (Co_3O_4) (99.5% Sigma-Aldrich). In order to see the effects of Nb and Co co-doping on dielectric properties of BaTiO_3 , 1 or 3 at% Nb and 1 at % Co were co-doped to BaTiO_3 . Hereafter, the co-doped ceramics were named as Nb1Co1 and Nb3Co1, respectively. First the starting powders were weighed to yield a ceramic with predetermined composition. Then, the powders were wet mixed in a ball mill using distilled water and ZrO_2 balls for 24 h. Powder mixture was dried and mixed with 2 g of 5% PVA solution. Disk shaped pellets were pressed in a hardened steel die at 3 tonnes of uniaxial pressure. The nominal dimensions of the green pellets were 15 mm in diameter and 3 mm in height. Sintering was done at temperatures of 1250, 1270, and 1290 °C for 30, 60, and 120 min in air.

Crystal structure and phase analysis of pristine and Nb and Co co-doped BaTiO_3 ceramics were identified by X-Ray diffraction (XRD) (MiniFlex 300/600) using $\text{Cu K}\alpha$ radiation ($\lambda = 1.5418 \text{ \AA}$) with operating voltage of 40 kV and current of 15 mA. Scan speed was 0.5 °/min between 20-80°. XRD patterns were investigated by PDXL integrated XRD software.

Microstructure of starting powders and sintered ceramic bodies were examined using a scanning electron microscopy (Zeiss MERLIN Field Emission Gun). Operation voltage was 15 kV. All the samples were coated with Gold-Palladium conductive layers.

Particle size analysis of starting powders was done using Malvern Instruments Mastersizer 2000 particle size analyzer. Dispersant used in laser measurements was distilled water. Measurable particle size range was 0.020 to 2000 μm .

Dielectric constant and the tangent loss values of BaTiO_3 based ceramics were measured with Hioki IM3536 Impedance analyzer. Prior to measurement, surfaces of the samples were polished to get flat and parallel surfaces. MD-Dac was used for polishing with suitable suspensions.

Surfaces of the specimens were printed with Heraeus silver paste by screen printing method. Then, the silver on pellets was dried in an oven at 80 °C for 1 h. After that, the silver was cured at 950 °C for 30 min to adhere onto surface. Finally, the wires are connected to the silver coated surfaces with soldering process. The wires soldered to the surface of sample connected to the impedance analyzer

Density of pellets were measured by Archimedes' method using a OHAUS PR series precision digital balance with ± 0.0001 accuracy. Samples were saturated with xylene for 8 h for density measurements.

Results and Discussion

Density measurements of Nb3Co1 ceramics sintered at different temperatures revealed that the ceramics sintered at 1250 °C have the lowest relative density with the average sintered density of 87.3%. The ceramics sintered at 1290 °C have the highest relative density with the average sintered density of 96.2%. The increase in relative density becomes smaller after 1270 °C because densification mechanism slows down exponentially. Therefore, 1270 °C was selected the optimum sintering temperature.

Figure 1 shows the XRD patterns of pristine BaTiO_3 (BTO), Nb1Co1, and Nb3Co1 ceramics sintered at 1270 °C for 60 min. XRD patterns suggest that all co-doped ceramics have nearly the same peak positions with BTO. The XRD peaks of Nb1Co1 ceramic shifted 0.1° to the left whereas, that of Nb3Co1 ceramic shifted 0.15° to the left as compared to the XRD peak positions of BTO.

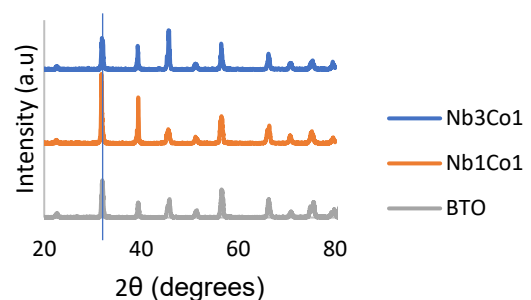


Figure 1. XRD pattern of BTO, Nb1Co1, and Nb3Co1 ceramics sintered 1270 °C.

The 1st and 3rd peaks in the XRD pattern of Nb3Co1 have similar intensity while the same peaks in the XRD of Nb1Co1 have large difference in terms of the intensity. This finding is interpreted as that both ceramics have been doped with different amount of dopants so that the crystal structures are different.

Figure 2 shows the representative microstructures of the Nb3Co1 ceramic sintered at 1250, 1270, and 1290 °C. The images were taken from the polished surface. The main difference in the images is the porosity present in the samples. Porosity amount and size decrease gradually with increasing temperature.

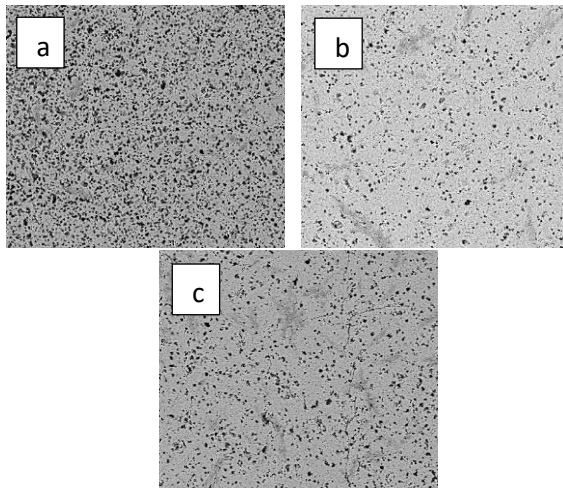


Figure 2. Microstructure of Nb₃Co₁ ceramic sintered at (a) 1250 °C, (b) 1270 °C, and (c) 1290 °C.

Figure 3 shows the variation of the dielectric constant (ϵ_r) with temperature from -30 to +130 °C for Nb₃Co₁ ceramic sintered at different temperatures. The variation of ϵ_r with temperature in the same temperature range for BTO ceramic was shown for comparison purpose. Dielectric constant at room temperature gradually increases with increasing sintering temperature. It is obvious that Nb₃Co₁ ceramic sintered at different temperatures did not show an abrupt change in ϵ_r , suggesting that the ferroelectric-tetragonal phase transformation was suppressed. Nb₃Co₁ ceramic sintered at 1250 °C have the smallest ϵ_r through measurement temperature range implying that the densification of the sample was not enough to have desirable dielectric performance. Nb₃Co₁ ceramic sintered at 1290 °C have the highest ϵ_r value at elevated temperatures but, at lower temperatures ϵ_r shows gradual decrease. This phenomenon could be caused by the collapse of the core-shell structure.

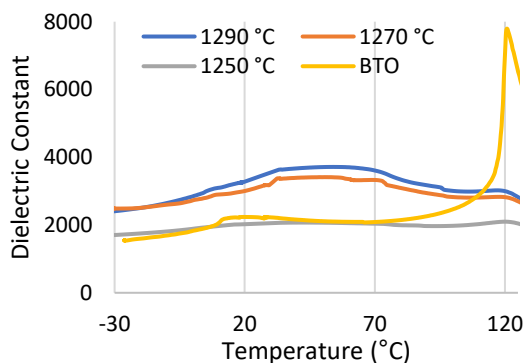


Figure 3. Temperature vs dielectric constant graph of BTO and Nb₃Co₁ ceramics sintered at 1250, 1270, and 1290 °C.

A decrease in ϵ_r is an undesirable property since the change in charge storage capacity becomes larger [12]. Nb₃Co₁ ceramic sintered at 1270 °C exhibited a desirable change in ϵ_r within the temperature range of -30 to +130 °C.

Table 1 shows the dielectric properties of Nb₃Co₁ ceramic sintered at different temperatures in the temperature range studied. In terms of the dielectric properties, the most consistent ceramic is the one sintered at 1250 °C but, its dielectric constant at room temperature is 33% lower than the Nb₃Co₁ ceramics sintered at 1270 and 1290 °C. Since the most common usage of capacitors is at room temperature, a sample with higher dielectric constant should be preferred. A high ϵ_r of 3258 at 1 kHz is obtained at room temperature, along with +10 and -17% variation over temperature ranging between -30 and +150 °C.

Table 1. Dielectric properties of Nb₃Co₁ ceramic sintered at different temperatures.

Property	Temperature (°C)		
	1290	1270	1250
Max ϵ_r	3713.891	3355.123	2098.065
Min ϵ_r	2177.495	2486	1711
ϵ_r at Room Temperature	3258	2950	2015
+% ϵ_r change	13.97	13.73	4.12
-% ϵ_r change	-33.18	-15.73	-15.08
Tan δ (1 Hz)	0.41	0.27	0.18

Also, the tan δ (dielectric loss) value for the Nb₃Co₁ ceramics sintered at 1290 °C is ~50% higher than that for the Nb₃Co₁ ceramics sintered at 1270 °C. Dielectric loss in capacitance materials should be as low as possible [12]. When the two properties are taken into consideration, the Nb₃Co₁ ceramics sintered at 1270 °C is preferred.

Experimental results reveal that the co-doping of Nb and Co atoms into the BaTiO₃ structure suppress the structural changes in BTO. The suppression of structural changes was proved by DSC measurements. The variation of heat flow with temperature in the range of -50 to +150 °C for Nb₃Co₁ ceramic sintered at 1270 °C for 60 min shown in Figure 4. The variation of the heat flow with temperature in the same temperature range for BTO ceramic was also shown for comparison purpose.

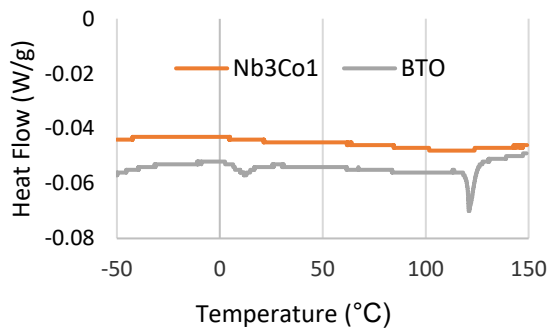


Figure 4. DSC Measurements of BTO and Nb₃Co₁ ceramics sintered at 1270 °C for 60 min.

Conclusion

It is possible to produce Nb-Co co-doped BaTiO₃ ceramics with mixed-oxide method. Nb and Co co-doping plays an important role on the development of porosity that is mostly related to sintering temperature in BaTiO₃ ceramics. Higher sintering temperatures leads higher relative density. Results shows that controlling Nb/Co ratio could increase the dielectric constant stability over temperature range. Dielectric constant values at room temperature increase by increasing sintering temperatures but the dielectric losses and temperature dependency of dielectric constant increases. Relative density of 94.5%, dielectric constant variation of $\sim\pm 15\%$ throughout the temperature range of -30 to +125 °C, that is a boundary for commercially used Y7R type capacitors, dielectric loss of 0.27 are obtained for Nb-Co co-doped BaTiO₃ ceramics at Nb/Co atomic ratio of 3% when sintered at 1270 °C for 60 min. DSC measurements shows that the doping of BaTiO₃ suppress the structural changes in the temperature ranging from -50 to +125 °C.

Acknowledgment

The authors greatly acknowledge Division of Fundamental Material Technologies Application at TÜBİTAK-SAGE for providing the facilities and the financial support for this study.

References

- [1] V. Buscaglia, M. T. Buscaglia, and G. Canu, BaTiO₃-based ceramics: Fundamentals, properties and applications, *Encyclopedia of Materials: Technical Ceramics and Glasses*, (2021) pp. 311–344,
- [2] C. A. Randall, R. E. Newnham, and L. E. Cross, History of the first ferroelectric oxide, BaTiO₃. Materials Research Institute, The Pennsylvania State University, 2004, University Park, Pa, USA, 1.
- [3] H. Kishi, Y. Mizuno, and H. Chazono, Base-metal electrode-multilayer ceramic capacitors: Past, present and Future Perspectives, *Japanese Journal of Applied Physics*, vol. 42, no. Part 1, No. 1, 2003, pp. 1–15.
- [4] S. Sato, Y. Nakano, A. Sato, and T. Nomura, Mechanism of improvement of resistance degradation in Y-doped BaTiO₃ based mlccs with ni electrodes under highly accelerated life testing, *Journal of the European Ceramic Society*, vol. 19, no. 6-7, 1999, pp. 1061–1065.
- [5] I. Burn, Temperature-stable barium titanate ceramics containing niobium pentoxide, *Electro Component Science and Technology*, vol. 2, no. 4, 1976, pp. 241–247.
- [6] H. Chazono and H. Kishi, Sintering characteristics in the BaTiO₃-Nb₂O₅-Co₃O₄ ternary system: II, stability of so-called CoreShell structure, *Journal of the American Ceramic Society*, vol. 83, no. 1, 2000, pp. 101–106.
- [7] R. Chen, X. Wang, L. Li, and Z. Gui, Effects of Nb/Co ratio on the dielectric properties of BaTiO₃-based X7R Ceramics, *Materials Science and Engineering: B*, vol. 99, no. 1-3, 2003, pp. 298–301.
- [8] H. Chazono and H. Kishi, Sintering characteristics in BaTiO₃-Nb₂O₅-Co₃O₄ ternary system: I, electrical properties and microstructure, *Journal of the American Ceramic Society*, vol. 82, no. 10, 2004, pp. 2689–2697.
- [9] D. F. K. Hennings and B. S. Schreinemacher, Temperature-stable dielectric materials in the system BaTiO₃-Nb₂O₅-Co₃O₄, *Journal of the European Ceramic Society*, vol. 14, no. 5, 1994, pp. 463–471.
- [10] F. Baeten, B. Derks, W. Coppens, and E. van Kleef, Barium titanate characterization by differential scanning calorimetry, *Journal of the European Ceramic Society*, vol. 26, no. 4-5, 2006, pp. 589–592.
- [11] A.A. Guzhova, M.F. Galikhanov, Yu.A. Gorokhovatsky, D.E. Temnov, E.E. Fomicheva, E.A. Karulina, T.A. Yovcheva, Improvement of polyactic acid electret properties by addition of fine barium titanate, *Journal of Electrostatics*, Volume 79, 2016, pp 1-6.
- [12] G. S. Gudavalli and T. P. Dhakal, “Simple parallel-plate capacitors to high-energy density future supercapacitors,” *Emerging Materials for Energy Conversion and Storage*, 2018, pp. 247–301.

PRODUCTION OF ACTIVATED CARBON FROM OLIVE SEED

Derya AKBULUT, Ali Osman KURT

Sakarya University
Türkiye

Keywords: Activated carbon, physical activation, micro/nano size porosity

Abstract

In this study, activated carbon has a surface area of over 600 m²/g was produced from olive seeds with a single process in two steps of carbonization and physical activation process, which have a minimal economic and environmental impact.

1. Introduction

Activated carbon (AC) is a synthetic type of adsorbent that can hold solid, liquid and gas molecules within its body thanks to its large surface area, strong attraction forces and pore volumes. Application areas of activated carbon are energy storage, purification of medicines in medicine, removal of dyestuffs in textiles, industrial and domestic water purification filters [1]. Conversion of the said wastes into activated carbon also provides important contributions in terms of environmental health.

2. Materials and Methods

In this study, olive seeds normally discarded or disposed of as fuel were used as a carbon source. They were washed, dried, ground and sieved before the carbonization process. Effects of raw materials' particle size, holding time and temperature on the final product of AC were examined. Raw materials between 150 µm and 1 – 3 mm were used in our experimental studies. Single process in two steps heating was used as 2 hours at 500 to 600°C with 12L/h nitrogen gas (N₂) flow for carbonization and 2 hours at 700°C at 6L/h CO₂ gas flow for the activation process.

3. Conclusion

Micro-sized activated carbon with surface areas over 600 m²/g was obtained from waste olive seeds by performing a one-step physical activation process that almost the same results reported in the literature with two-step physical activation [2, 3, 4]. The effects of raw material grain size along with temperature were given in Figure 1. Our studies carried out in CO₂ flow with carbonization and physical activation (one-step physical activation process) have a minimal environmental impact and support the production of activated carbon suitable for continuous production. It is the advantage of running a single-step physical activation process since it is low cost and low energy consumption, time-saving and sustainable compared with two-step processes.

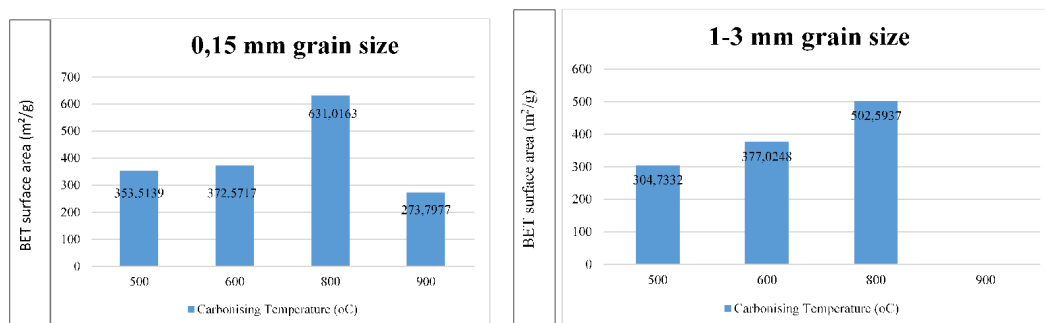


Figure 1. Effect of grain size on surface area

Acknowledgment

The authors thank Sakarya University Scientific Research Projects Unit (SAÜ-BAP) for financial support (project no 2022-7-25-43). Derya would also like to thank you for the scholarship from YÖK (100/2000 program).

References

- [1] S. Aslan, Fırat Üniversitesi Müh. Bil. Dergisi, 33(1), 2021, 193-201.
- [2] S. Mopoung, N. Dejang, "Activated carbon preparation from eucalyptus wood chips using continuous carbonization–steam activation process in a batch intermittent rotary kil", 2021 <https://doi.org/10.1038/s41598-021-93249-x>.
- [3] S. Bachrun, A.R. Noni, S.H. Annisa, and A. Hidayat, 2016. "Preparation and characterization of activated carbon from sugarcane bagasse by physical activation with CO₂ gas", Chemical Engineering Department, 105, 012027.
- [4] Lopes, G.K.P., Zanella, H.G., Spessato, L., Ronix, A., Viero, P., Fonseca, J.M., Yokoyama, J.T.C., Cazetta, A.L., Almeida, V.C., 2021. "Steam-activated carbon from malt bagasse: Optimization of preparation conditions and adsorption studies of sunset yellow food dye", Arabian Journal of Chemistry, 14(3), 103001.



THE USE OF OLIVINE IN THE PRODUCTION OF MINERAL WOOL

Akın ODABAŞI¹, Gökhan BAŞMAN², Hülya KAFTELEN ODABAŞI¹, Hande ARDIÇOĞLU²

¹Firat University, ²Etikrom Inc.
Türkiye

Keywords: Olivine, mineral wool, XRF analysis

Abstract

The rapid development and industrialization of mineral wool insulation material started in the early 20th century with the ability to produce two distinctive features, low density and high porosity. Mineral wool can be produced in different forms according to its intended use such as a blanket, pipes, exterior wall insulation, and board. The general features required to meet the intended use of mineral wool in all its forms are energy saving or thermal insulation, fire prevention, sound absorption and noise reduction on the applied surface. Olivine, $(\text{Mg}^{2+}, \text{Fe}^{2+})_2\text{SiO}_4$, is a major component in most basic rocks and it found mostly in the earth's crust. Olivine has attracted great interest as a potential material for various industrial applications such as the hot metal and refractory industries due to its chemical compositions (MgO and SiO₂ contents), low-cost, high refractoriness and low thermal expansion, thermal shock resistance and high chemical stability, etc. Hot metal industries are one of the major consumers of olivine products which are widely used for slag conditioner, molding sand, tap hole filler, and coating materials. In refractory industries, it is particularly used as a raw material to produce forsterite refractories, to manufacture cordierite kiln by addition of clay system, in silo burners lined with its sand. Besides, the high liquidus temperature of olivine provides a heat insulation material with a high temperature resistance, making olivine superior to asbestos wool for utilization in eco-friendly mineral wool. Olivine, which is extracted as a by-product with chromite ore, is a material that has the raw material potential for mineral wool applications with its high MgO and SiO₂ contents (86-89%) and low iron content. In this contribution, we investigate the potential use of olivine and its opportunities for thermal insulation in the safe and efficient manner of mineral wool.

1. Introduction

Olivine is a general term used to denote a group of orthosilicates in a solid solution series that combines magnesium and iron $(\text{Mg,Fe})_2\text{SiO}_4$ [1] and is one of the most widely distributed minerals in the earth's crust (i.e., >50 % of the upper mantle). Due to its excellent physical, mechanical and thermal properties, olivine has many different applications [2] such as slag remover, refractory material, foundry sand, coating material in underwater pipes and cables, and also sandblasting in the steel industry. Olivine is an important raw material source for the production of mineral wool is used as thermal, fire and acoustic insulation in building and industrial applications. Rock wool or stone wool is the main mineral wool with fine and intertwined fibers produced by spinning molten rock at high speed, similar to making cotton candy, typically between 1300-1500 °C [3].

In rock wool production, the fluidity of the melt has a critical importance in fiber production [3]. The fluidity behavior generally changes as a function of the chemical composition of the raw material, hence the mineral content. Stone wool quality can be determined by two important properties that must be present in the raw material [4, 5]: one is the acidity modulus (M_a) and the other is the CaO/MgO ratio (≥ 0.5). Additionally, only acidic type basalts (over 46% SiO₂) satisfy the conditions for fiber preparation.

At Etikrom Inc. magnetic separation plant, the amount of olivine mineral released as a by-product with chromite ore is approximately 500 tons per month, and 25 tons of olivine mineral and the same amount of chromite ore are extracted from 50 tons of ore. However, the high MgO content (about 50 wt. %) in olivine are challenges for wool production due to the higher melting temperature required for industrial processing. Therefore, we applied the acid digestion techniques to adjust the modulus of acidity keeping the CaO/MgO ratio constant and providing the CaO

amount from the cement as binder. This work presents the investigation that undertaken the potential use of olivine, a by-product of Etikrom Inc., as raw materials in fabrication of the mineral wool.

2. Experimental Procedure

In this study, olivine containing particles of size smaller than 300 μm was used as a starting material extracted as a by-product with chromite ore in Etikrom Inc. (Elazığ, Turkey). 100 g of olivine sand was mixed with two different HCl solutions (8M and 9M in 250 ml) using a magnetic stirrer. Each solution containing olivine sand was placed on a hot plate and stirred continuously at three different conditions: (a) room temperature for 1h, (b) 60 °C for 30 min and (c) and 60 °C for 1h. Powder samples were designated depending on the HCl acid solution concentration, temperature, and time parameters; for example, 8M/25-1 stands for 9M HCl solution treated olivine powders at room temperature (25 °C) for 1h. After completion of HCl treatment, the unreacted solid particles are filtered and washed with distilled water several times to remove the impurities and then dried using an oven at 150 °C for 24 h. The chemical compositions of the samples after HCl treatment The dried samples should be examined using X-ray fluorescence (XRF, Rigaku™ Primus II) analysis.

The phase compositions of olivine and the HCl treated powders were evaluated using XRD investigations conducted in a Rigaku Powder Diffractometer with $\text{CuK}\alpha$ (1.54060 Å) radiation in the 2θ range of 10-70° with 0.02° steps at a rate of 2°/min. The Rietveld method was carried out using HighScore Plus XRD software to identify the composition (wt.-%) of the crystalline phases. The morphology of powders was characterized using a scanning electron microscope (Zeiss™ Evo) equipped with an energy dispersive spectrometer (EDS, Bruker). Prior to the SEM investigations, powder samples were cold mounted and polished using standard metallographic techniques and

powder samples sputtered with Au-Pd to obtain conductive surface.

3. Results and Discussions

Table 1 gives the XRF analysis results of the olivine and 8M and 9M HCl solution treated olivine powders at different times and temperature. As can be seen from Table 1, the amount of MgO in the olivine weight percentage decreased from 50 to 7.8 after the olivine was treated in 9M HCl solution at 60 °C for 1 h. At the same time, the percentage of Al_2O_3 increased from 1.48 to 22.85 %, while the percentage of SiO_2 increased from 37 to 49.62%. Chemical analysis of sample 9M/60-1 is comparable to that of basalt rock composition given by Isnugroho et al. [1], which is used as a raw material in the production of rock wool.

As mentioned in the introduction section, the modulus of acidity (M_a) plays important role for producing the high quality of mineral wool fibre. The M_a is calculated according to the following equation [5]:

$$M_a = m\text{SiO}_2 + m\text{Al}_2\text{O}_3 / m\text{CaO} + m\text{MgO} \quad [1]$$

where m: mass content of oxides (wt.%)

The modulus of acidity (M_a) should be higher than 1.8 [5] in order to obtain the high-quality mineral wool fibre, i.e., the higher the M_a of the raw basalt, the better quality in terms of strength, corrosion, temperature resistance and thermal insulation is the wool fibre as a final product.

Based on the Equation (1) and the XRF results, the calculated M_a value for 9M/60-1 sample found as 5.5 which is higher than 1.8 indicating that this value meet the high-quality rock wool characteristics. The CaO/MgO ratio was kept constant to equal 1. Furthermore, the SiO_2 percentage of this sample greater than 46 wt.% indicates that it is an acidic material, which complies with the parameters required for the production of good quality mineral wool.

Table 1: The chemical analysis of olivine , 8M and 9M HCl treated powder samples.

	MgO	Al2O3	SiO2	Fe2O3	CaO	NiO	Fe	Cr2O3	C	S
Olivine	50.69	1.48	37.41	6.45	0.94	0.75	4.48	1.73	-	<0.001
8M/25-1	22.09	20.44	30.19	21.37	0.14	-	-	5.27	0.06	<0.001
8M/60-30	13.69	21.93	38.43	20.21	0.14	-	-	5.11	0.09	<0.001
8M/60-1	19.32	20.88	37.15	17.37	0.13	-	-	4.66	0.08	<0.001
9M/25-1	12.66	22.06	33.97	25.02	0.18	-	-	5.6	0.08	<0.001
9M/60-30	26.20	19.80	32.43	16.25	0.12	-	-	5.71	0.22	<0.001
9M/60-1	7.18	22.85	49.67	15.31	0.13	-	-	4.36	0.12	<0.001

Comparisons of the diffraction patterns of the raw olivine and HCl solution treated olivine powder samples were given in Figure 1, indicating that a new phase, quartz appears at around $2\theta = 26^\circ$ (indicated by an arrow) after HCl treatment of the raw olivine. All of the samples mainly consisted of forsterite

($\text{Fe}_{0.24}\text{Mg}_{1.76}\text{O}_4\text{Si}$, orthorhombic), chromite (cubic) and lizardite ($\text{H}_4\text{Mg}_3\text{O}_9\text{Si}_2$) phases.

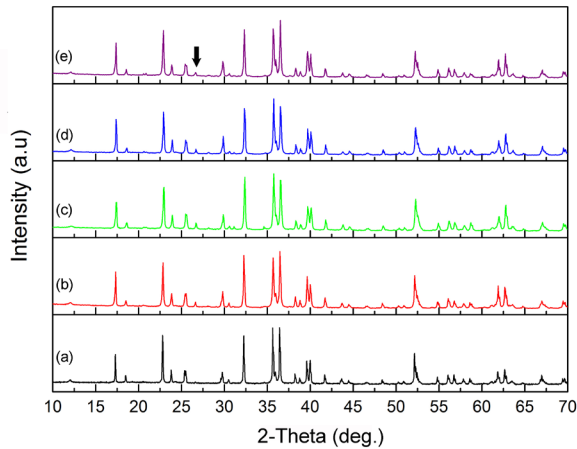


Figure 1: XRD diffractograms of (a) raw olivine and HCl solution treated (b) 8M/25-1 (c) 8M/60-1 (d) 9M/25-1 and (e) 9M/60-1 olivine powder samples.

Rietveld refinement method was crucial in determining the phase identity and in estimating weight fractions. In this study, the crystalline phase fractions (wt.-%) were quantitatively analyzed with HighScore Plus XRD software based on the Rietveld method. Figure 2 gives the Rietveld refinement results of the raw olivine and 9M/60-1 powder sample.

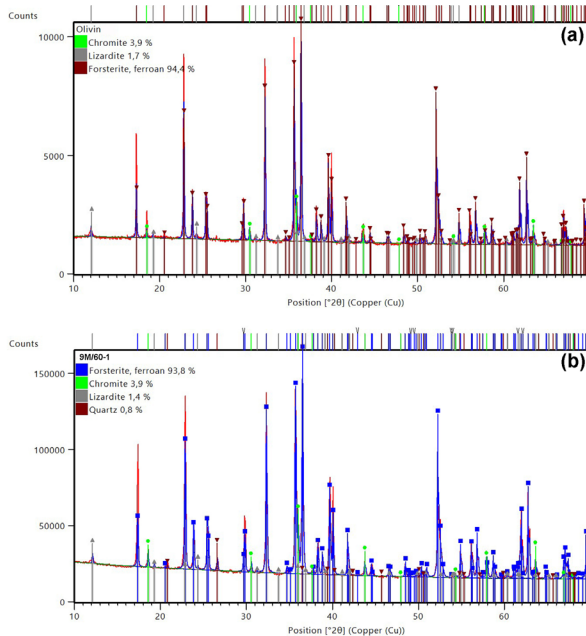


Figure 2: Rietveld analysis for X-ray powder diffraction of (a) raw olivine and (b) 9M/60-1 powder sample

Rietveld results show that 94.4% forsterite and 1.7% lizardite phase are present in raw olivine, while 9M/60-1 powder sample contains 93.8% forsterite, 1.4% lizardite, 3.9% chromite, 0.8% quartz phase. The fact

that the amount of forsterite phase has decreased as a result of the HCl solution treatment indicates that it is dissolved by reacting with MgO and HCl acid solution, and there is also free quartz formation as a result of 1 h reaction in 9M HCl solution. Note that the peaks belonging to the quartz phase are also present in all HCl-treated powders.

Energy-dispersive X-ray (EDX) spectroscopic maps provide useful information on the distribution of elements within the overall microstructure. In order to determine the elemental distribution of olivine powders after 8M HCl treatment for 1h at room temperature (25 °C), map data were collected from the whole area given in Fig. 3(a) which was investigated for distributions of Mg, Si, Fe, Al and Cr. The superimposed phase distribution map is shown in Fig. 3(b). Leafy structured particles adjacent to angular shaped particles contains Al-rich phases as shown in Fig. 3(c), while light gray particles indicated by arrows in Fig. 3(a) contains Cr-rich phases.

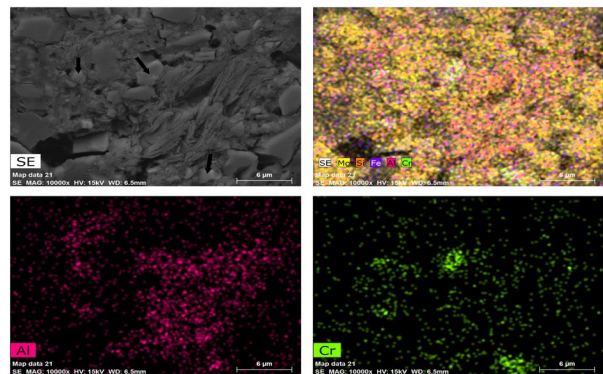


Figure 3: High magnification SEM micrograph of the 8M/25-1 powder and element distribution map showing the pixels indexed as Mg (yellow), Si (orange), Fe (purple) and Al (pink), Cr (green) separated elemental distribution maps for Al and Cr.

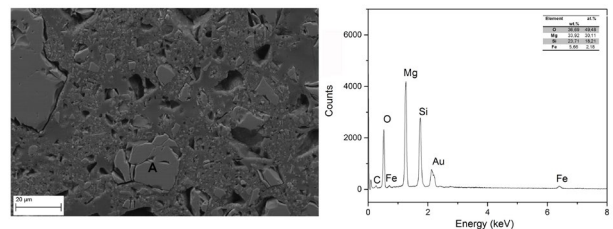


Figure 4: SEM micrograph of the 8M/60-1 powder and corresponding EDS analysis taken from Mg rich phases (point A).

Figure 4 taken from olivine powders after 8M HCl treatment at 60 °C for 1 h, reveals presence of angular shaped particles as labelled A. EDS spectra from the angular shaped particles show mainly Mg (30.11 at.%), Si (18.21 at.%), and O (49.48 at.%) elements with

small amounts of other element Fe (2.18 at.%). Note that the signal about 2 keV belongs to coating materials, Au.

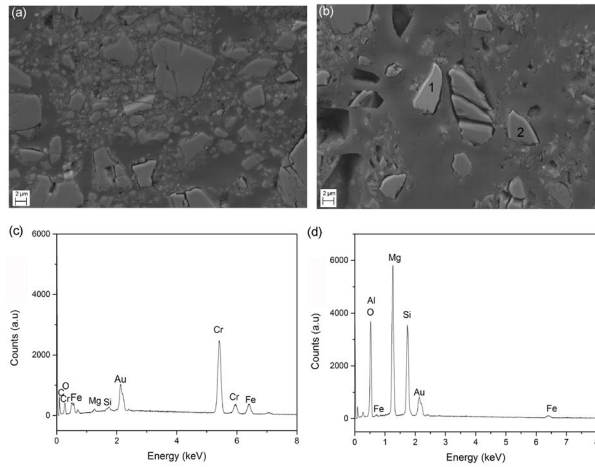


Figure 5: Backscatter SEM micrographs of (a) 9M/25-1 and (b) 9M/60-1 power samples and corresponding EDS analysis (c) taken from point 1, and (d) point 2.

Figure 5(a) and 5(b) show the SEM micrographs in BSE modes of the olivine powders after 9M HCl treatment for 1 h at room temperature and 60 °C, respectively. EDX spectra (Fig. 5c) taken from the light appearing particle (marked as 1) in Fig. 5(b) indicates that the particle consists of mainly Cr phase with Mg, Si and Fe, while EDX spectra presented in Fig.5(d) from point 2 in (b) reveals that magnesium-aluminium-silicate present in olivine, which is confirmed by Rietveld refinement results (Figure 2).

4. Conclusion

The aim of this work was to evaluate the possible use of olivine as a raw material for the production of mineral wool. For this purpose, olivine powders treated in two different concentrations of HCl solution to make the chemical composition of olivine suitable for

mineral wool production were examined by XRD, XRF and electron microscopy.

XRD analysis showed that forsterite as major phases in all olivine powder samples and low amount of chromium and lizardite phases are also present. Rietveld refinement results of raw olivine and the HCl solution treated powders showed that the amount of forsterite phase decreases most likely as a result of the dissolution of Mg phases, and as a result, quartz phase was formed. SEM investigations showed that the general microstructures of olivine samples contain Mg, Si, Fe, Al and Cr elements, as well as iron-containing magnesium aluminum silicate particles, iron-containing magnesium aluminum silicate particles and chromium-rich particles. Studies have shown that only the 9M/60-1 sample meets the acidity modulus value required to obtain mineral rock wool due to its low MgO content (7.18wt.%) and high SiO₂ content (49.67 wt.%). Additionally, the HCl acid used in the digestion process is completely recoverable and provides a source of usable energy.

References

- [1] K Isnugroho et al IOP Conf. Ser.: Mater. Sci. Eng. 285 (2018) 012014.
- [2] R. Sarkar, Olivine—The Potential Industrial Mineral: An Overview, Transactions of the Indian Ceramic Society, 61:2, (2002) 80-82, DOI: 10.1080/0371750X.2002.10800031
- [3] Yap, Z.S.; Khalid, N.H.A.; Haron, Z.; Mohamed, A.; Tahir, M.M.; Hasyim, S.; Saggaff, A. Waste Mineral Wool and Its Opportunities—A Review. Materials 2021, 14, 5777. <https://doi.org/10.3390/ma14195777>.
- [4] Fomichev S V, Babievskaya I Z, Dergacheva N P, Noskova O A and Krenev V A (2010) Inorganic Materials 46(10) 1121 - 5.
- [5] Farouk, M., Soltan, A, Farrag, A., El Kammar, A., Hamzawy, E. Egyptian Journal of Geology, v. 64, (2020), pp.155-165.

THE UTILIZATION OF CITRATE GEL METHOD IN COBALT BORIDE SYNTHESIS

Buse BİTİKÇİ, Çağan Berker İYİ, Hülya BİÇER

Kütahya Dumlupınar University
Türkiye

Keywords: cobalt boride, citrate-gel synthesis, carbothermal reduction

Abstract

Studies on cobalt boride have been extensively performed for corrosion and wear-resistant surface coating. Recently, cobalt boride nanoparticles have drawn attention as a significant potential catalyst for hydrogen storage and fuel cell applications. Size, size distribution, shape, and agglomeration state of the synthesized powder have a significant impact on the microstructure and final properties of the materials. In the conventional wet chemistry methods, cobalt boride nanoparticles with narrow size distribution and controlled shapes can be successfully synthesized. In the present study, a cobalt salt (either $\text{Co}(\text{NO}_3)_2 \cdot 6\text{H}_2\text{O}$ or $(\text{CH}_3\text{COO})_2\text{Co} \cdot 4\text{H}_2\text{O}$) as the cobalt source, boric acid (H_3BO_3) as the boron source, and citric acid ($\text{C}_6\text{H}_8\text{O}_7$) as a chelating agent were used. The characterization analysis of powders by XRD, FTIR and SEM will be presented.

1. Introduction

Borides exhibit appealing properties and can be used either as structural materials or as catalyst [1, 2]. A wide variety of boride structures are known. Cobalt borides are inorganic borides with the general formula Co_xB_y (common ones are CoB and Co_2B). Cobalt borides are important candidates for corrosion and wear resistant surface coatings due to their outstanding resistance to oxidation [3]. In recent years, cobalt boride nanoparticles have been objects of extensive studies by a variety of disciplines as potential catalysts for electrochemical water splitting and fuel cell applications. In most conventional wet chemistry methods, cobalt salts are spontaneously reduced by boron based reducing agent to form cobalt boride which shows excellent catalytic activity in the hydrolysis reaction [2, 4, 5]. $\text{CoCl}_2 + \text{NaBH}_4$ system has been extensively studied, however, the nature of Co_xB_y structure is still not fully understood and the synthesis of nanoparticles with high purity is a challenge. In this study, formation conditions and mechanism of cobalt boride are evaluated when citrate-gel method is utilized. To our knowledge, no prior study on the synthesis of cobalt boride by citrate-gel method has been performed.

2. Materials and Method

Cobalt boride formation mechanisms were thermodynamically modeled by taking the oxidation state of Co (2+ or 3+) into consideration in accordance with the possible reactions at certain temperature. Figure 1 summarizes all possible yielding reactions through various mechanisms. Boric acid, citric acid and Cobalt(II) acetate/nitrate were dissolved in deionized water separately with various molar ratios. The solutions were then all mixed in a beaker on hot plate setting the temperature at 85°C with a rotation speed of 400 rpm. Prior to the merely evaporation of water, chelation initiated in terms of increase in the viscosity. Subsequent abandoning of water from the structure, dry chelate powder was collected. Consequently, raw powder was installed in tube furnace in order to obtain Co_xB_y through carbo/borothermic steps in a broad range of dwell temperature (500-1100 °C) on the purpose of distinguishing the formation temperature.

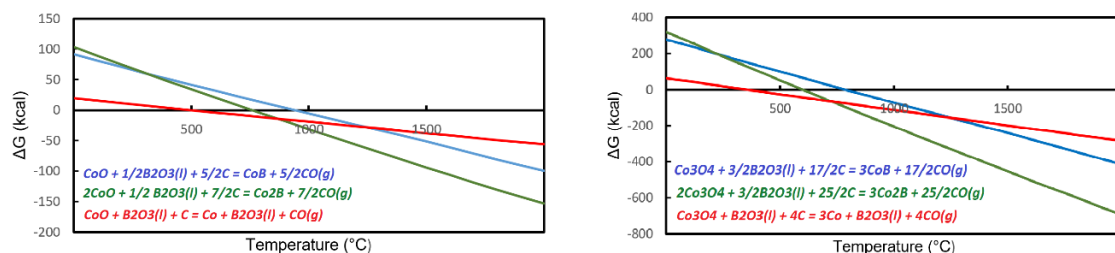


Figure 1. Comparing the change in Gibbs free energy based on the oxidation state of Co with respect to temperature.

3. Conclusion

The main objective of this study is to observe formation mechanisms of cobalt boride(s) and assess an accurate stoichiometry for the precursors addressing side reactions in addition to the main carbo/borothermic reactions. In pursuit of obtaining cobalt borides via citrate-gel method, following conclusions can be made:

- Oxidation state of cobalt (Co^{2+} or Co^{3+}) is the deterministic factor influencing the formation temperature. Over 900°C , CoO is the stable oxide. For both borides (CoB and Co_2B), higher oxidation state (Co^{3+}) yields a more feasible carbothermal reduction taking place at lower temperatures, as expected.
- Over 400°C , Co easily gets reduced by C, in contrast to some other 3d metals such as Cr, Ti and V, complicating the process.
- According to the preliminary studies, Co_{23}B_6 and $\text{Co}_2(\text{B}_2\text{O}_5)$ phases are observed whereas the rest forms Co^0 .



References

- [1] B. Golla, A. Mukhopadhyay, B. Basu and S.K. Thimmappa, *Progress in Materials Science*, 111 (2020) 100651.
- [2] Z. Chen, X. Duan, W. Wei, S. Wang, Z. Zhang, B.J.Ni, *Nano Research*, (2020) 1-22.
- [3] M. Dong and B.L. Shen, *Surface and Coatings Technology* 236 (2013): 102-106.
- [4] Liu, B. H., Li, Z. P., & Suda, S. (2006). Nickel-and cobalt-based catalysts for hydrogen generation by hydrolysis of borohydride. *Journal of Alloys and Compounds*, 415(1-2), 288-293.
- [5] Masa, J., Weide, P., Peeters, D., Sinev, I., Xia, W., Sun, Z., ... & Schuhmann, W. (2016). Amorphous cobalt boride (Co₂B) as a highly efficient nonprecious catalyst for electrochemical water splitting: oxygen and hydrogen evolution. *Advanced Energy Materials*, 6(6), 1502313.
- [6] Göçmez, C. Tuncer, M. Yeniçeri, Y. S. (2014). Low temperature synthesis and pressure less sintering of nanocrystalline zirconium diboride powders , *Ceramics International*, 40, 12117–12122.



EFFECT OF HOT ISOSTATIC PRESSING ON DENSIFICATION, MICROSTRUCTURE AND ELECTRICAL PROPERTIES OF $Mg_{0.95}Ca_{0.05}TiO_3$ CERAMIC

Selin GÜNTOP^{1,2}, Hakan DER¹, N. Kaan ÇALIŞKAN¹, M. Kaan PEHLİVANOĞLU¹,
Abdullah ÖZTÜRK²

¹Tübitak SAGE, ²Middle East Technical University
Türkiye

Keywords: MgCaTiO₃ ceramic, densification, hot isostatic pressing, microstructure, electrical properties

Abstract

The effect(s) of hot isostatic pressing (HIP) on densification, microstructure, and electrical properties of $Mg_{0.95}Ca_{0.05}TiO_3$ (M0.95CT) ceramic was researched. M0.95CT ceramic was prepared by the conventional mixed oxide method. The powder mixture of the oxide components in appropriate molar ratios was compacted in a stainless steel die by double action pressing. The square shaped compacts with nominal dimensions of 35 mm in size and 4 mm in thickness were pressureless sintered in air at temperatures of 1300, 1350, and 1400 °C. HIP sintering was applied on the pressureless sintered ceramics at ~1200 °C for 1 h. The differences on the characteristics and electrical properties of M0.95CT ceramic was evaluated on the samples produced by application of HIP and without HIP. Results revealed that HIP sintering has a profound influence on densification, microstructural development, and electrical properties especially on insulating behavior of M0.95CT ceramic.

1. Introduction

Magnesium calcium titanate ($MgCaTiO_3$, MCT) dielectric ceramics take place an important position in modern communication devices since they offer good electrical properties such as quality factor (Q), dielectric constant (ϵ_r) and near-zero temperature coefficient of resonant frequency (τ_f). [1] They are required to have optimum combinations of these properties if they are to be used in special applications such as mobile phones, antennas, and global positioning systems. Although many microwave dielectric ceramics exhibit good properties, high starting material and preparation costs limit their

utilization. $CaLaTi_4O_{15}$, $Ba(Y_{1/2}Ta_{1/2})O_3$, and $NdAlO_3$ ceramics are among the examples for such cases. [2] $MgTiO_3$ ceramics not only have low material cost but also show good microwave properties including high Q, high ϵ_r . However, the τ_f value, which symbolizes the change of the resonance frequency with temperature, is negative for $MgTiO_3$. [3] Also, a large τ_f value imposes a limitation of $MgTiO_3$ ceramics for sensitive applications where the temperature change is high. For that reason, small amount of $CaTiO_3$ that has positive τ_f value is incorporated to bring the τ_f value of $MgTiO_3$ ceramics closer to zero. The $Mg_{0.95}Ca_{0.05}TiO_3$ (M0.95CT) composition meets the desired microwave dielectric properties with its high Q (56.000 GHz), suitable ϵ_r (20-21), and low τ_f (≈ 0 ppm/°C) values. [4]

Dielectric properties of ceramics are also highly dependent on microstructural factors such as second phase, grain size and porosity. [5] Compared to second phases and grain size, porosity indicate more detrimental effect on the desired properties since their properties are generally nearly zero. Therefore, grained structure with nearly full density and homogeneous distribution of pores are required to obtain desirable dielectric properties. It is hard to make ceramic materials completely dense. Open or closed pores are commonly seen after the sintering process. The distribution, amount and morphology of the pores adversely affect the mechanical performance of ceramic materials as well as their dielectric properties. [6] Hot isostatic pressing (HIP) sintering is applied to pressureless sintered parts in order to eliminate or minimize the porosity in an inert atmosphere. While an increase in density is expected with HIP sintering, the structural and physical properties of M0.95CT

ceramic are also expected to be improved by the reduction of the partial oxygen pressure. [7]

The purpose of this research is to see the effect(s) of HIP on the microstructural development hence to optimize the process parameters for the production of M0.95CT dielectric ceramic. The motivation was to gain information and practice on the production of M0.95CT dielectric ceramic so that foreign dependency on dielectric ceramics could be avoided.

2. Experimental Procedure

Reagent grade MgO, CaCO₃, and TiO₂ powders supplied from Merck were used as starting materials for the production of M0.95CT ceramic. Particle size of the starting powders varied in the range of 1-5 μm. The oxide components in appropriate amounts to yield the predetermined molar ratios were wet mixed using isopropyl alcohol ~60 rpm in a ball mill. Alumina balls and alumina jar were used as balling medium. The powders ball milled were calcined in air at ~1100 °C. The calcined powder in chunk form was crushed and ground by mortar with pestle. The ground powder was mixed with poly vinyl alcohol, employed as binder. Compaction of the powder was accomplished in a tool steel die at 80-150 MPa pressure by double action pressing. The square shaped compacts with nominal dimensions of 35 mm in size and 4 mm in thickness were pressureless sintered in air at temperatures of 1300, 1350, and 1400 °C. HIP sintering was applied on the pressureless sintered ceramics at ~1200 °C for 1 h. Microstructural features such as pore and grain amount, size, and distribution as well as the compositional differences of the ceramics produced by the application of HIP and without HIP was investigated by scanning electron microscope (SEM, Zeiss Merlin/Feg-SEM) and X-ray diffraction (XRD, Rigaku Miniflex 600) analyses. The samples were sputter coated with gold before SEM analysis. XRD measurements were done using Cu-Kα radiation at 40 kV between 2θ = 10 and 90° at a scan rate of 2°/min.

Density measurement was done in accord with Archimedes method using Xylene. Dielectric constant measurement was done with parallel electrode method using LCR Meter. Resistivity measurement was done at temperatures between 25 and 400 °C and Hall-Effect measurement was done using four probe method.

3. Results and Discussion

The XRD analyses of the M0.95CT ceramics sintered at different temperatures were almost the same. No major difference in the phases developed during sintering was noted. Figure 1 represents the variation of relative density and dielectric constant with

sintering temperature. It is an expected behavior that the relative density increases with increasing temperature. When the energy required for atomic diffusion is provided, neck formation begins between the powder particles and lower energy solid-solid interfaces are obtained. [8] Therefore, the determination of the sintering temperature is very important in terms of getting high sintered density. Dielectric constant value also increases with increasing temperature since the amount of pores in the sample decreases. The dielectric constant of air is approximately 1 [9], and has a rather small value compared to M0.95CT ceramic. Since the reduction of pores causes a decrease in air volume, dielectric constant increases.

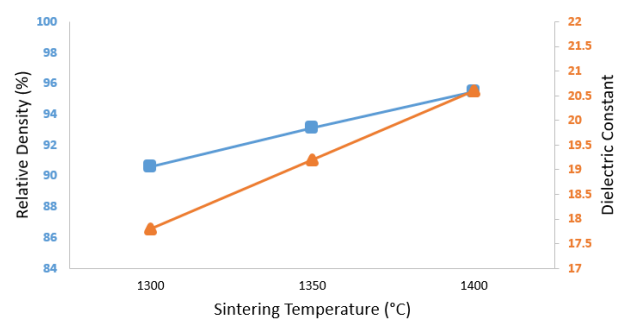


Figure 1. Variation in relative density and dielectric constant with sintering temperature for M0.95CT ceramic

A noticeable difference between density values of M0.95CT ceramics sintered with and without HIP was recognized. Improvement of relative density is observed after HIP sintering process. The density values of the HIP applied M0.95CT (MCT-HIP) ceramic varied in a wide range from 95.56 to 97.17. Although the processing parameters were the same.

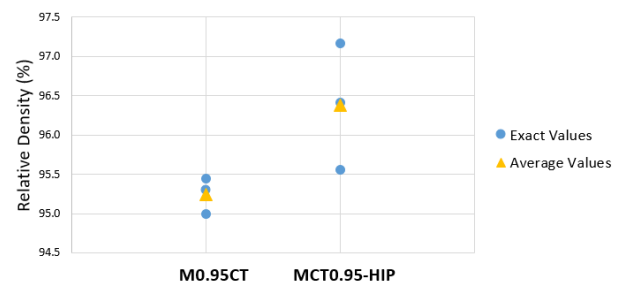


Figure 2. Relative density of M0.95CT and M0.95CT-HIP ceramics.

After HIP sintering, there is no distinguished difference in the XRD patterns of the samples, implying that the phases present in M0.95CT ceramic did not disappear and no new phase was developed during HIP processing as seen in Figure 3. Nevertheless, the amount and size of the pores present in the microstructure of M0.95CT ceramic considerably decreased as seen in the SEM images shown in Figure 4.

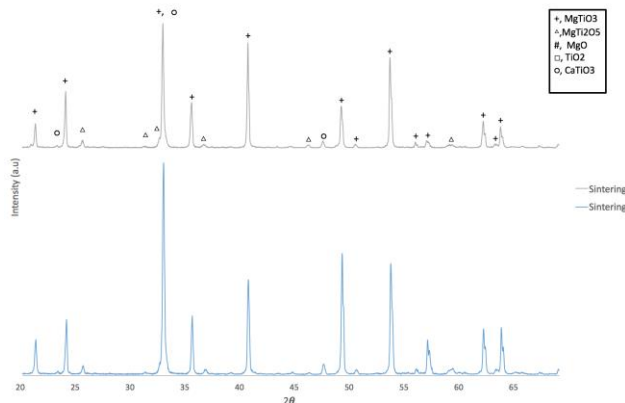


Figure 3. XRD pattern of M0.95CT and M0.95CT-HIP ceramics.

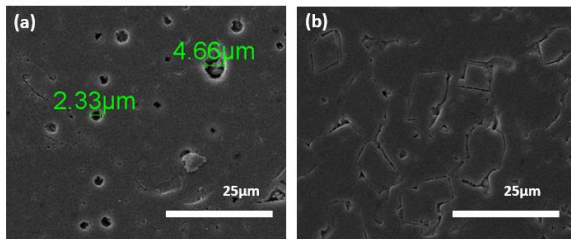


Figure 4. SEM images of (a) M0.95CT and (b) M0.95CT-HIP ceramics. X2000.

Back scattered-SEM (BS-SEM) investigation was done for the identification of the phases present in the structure. A representative BS-SEM image of M0.95CT ceramic is shown in Figure 5. The EDS analysis results taken from various spots in the structure is shown in Table 1. For spot number 1, the atomic percentages of Mg and Ti are close to each other, suggesting that the matrix phase is $MgTiO_3$. For spot number 2, Ti to Mg ratio is close to 2. This is an indication that this structure is $MgTi_2O_5$. The result is in accord with the XRD analysis where small amount of $MgTi_2O_5$ phase was detected, EDS analysis of the white spots in Figure 5 is assumed to be $CaTiO_3$ since the Ca/Ti ratio is approximately 1.

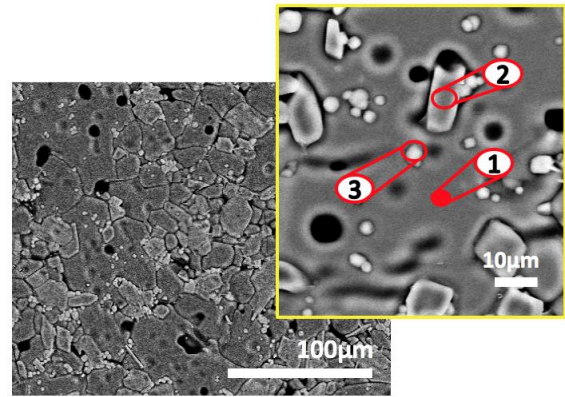


Figure 5. BS-SEM image of M0.95CT ceramic.

Table 1. The EDS analysis results taken from various spots in the image shown in Figure 5.

	Element (atomic %)				
	O	Mg	Al	Ca	Ti
Spot 1	20.73	38.70	1.88	2.07	44.56
Spot 2	13.47	24.29	3.81	0.97	55.22
Spot 3	13.38	8.11	1.12	31.65	43.02

Resistivity measurement was done for both M0.95CT and M0.95CT-HIP ceramics. No current flowed into M0.95CT ceramic. Therefore, the measurement could not be taken. It can be interpreted as the sample has a very high resistance over 200 MΩcm. Resistivity values of semiconductor materials range from 10^{-2} to 10^8 Ωcm [10]. For M0.95CT-HIP ceramic, an increase in conductivity was observed compared to M0.95CT ceramic as shown in Figure 6. Especially, after 200 °C, conductivity increases significantly, and resistivity reaches to approximately 10^3 Ωcm at 400 °C.

Hall- Effect measurement is carried out at 27 °C to determine whether electrons or holes are majority carriers. Figure 7 suggest that holes are the majority carriers. Thus, it can be interpreted that M0.95CT-HIP ceramic is a p-type semiconductor with high energy band gap.

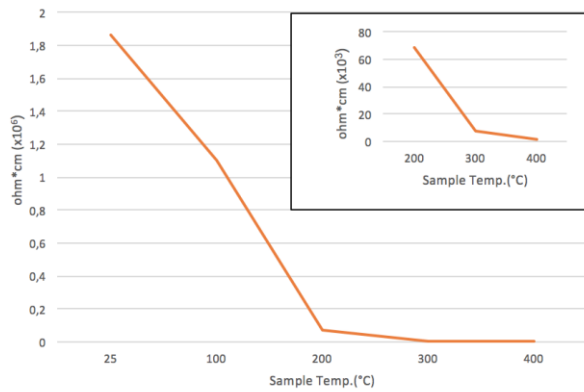


Figure 6. Resistivity measurement results for M0.95CT-HIP ceramic.

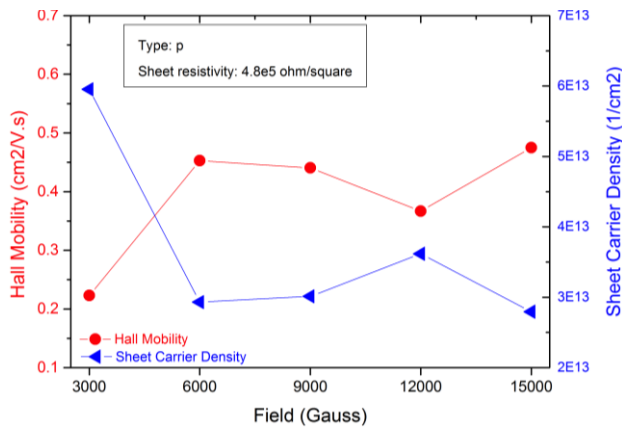


Figure 7. Hall-Effect measurement results for M0.95CT-HIP ceramic.

4. Conclusion

Dielectric constant, resistivity, and Hall-Effect measurements were done to find out the effects of HIP sintering on electrical properties of M0.95CT ceramic. Although an improvement in sintered density and in the amount of closed porosity was experienced, the insulation behavior of M0.95CT ceramic changed from insulator to semiconductor particularly at high temperatures from 200 to 400 °C. The M0.95CT-HIP ceramic produced was specified as p-type semiconductor. It is concluded that addition of HIP sintering to the production steps of M0.95CT ceramic changes electrical properties. The results revealed that an insulator material could be converted to a semiconductor material by HIP sintering.

Acknowledgment

Division of Fundamental Material Technologies Application at Tübitak SAGE is greatly acknowledged for the measurements and financial support.

References

- [1] M. T. Sebastian, Dielectric Materials for Wireless Communication, Elsevier, Ed., India: National Institute for Interdisciplinary Science & Technology (NIIST), (2008) p. 425.
- [2] W. K., Z. H. S. W. C. X. and R. H. , Solid-State Reaction Mechanism and Microwave Dielectric Properties of 0.95MgTiO₃-0.05CaTiO₃ Ceramics, J Mater Sci: Mater Electron, 25 October 2017.
- [3] Y. Liou, -C. and S.-L. & Yang, Calcium-Doped MgTiO₃-MgTi₂O₅ Ceramics Prepared Using a Reaction-Sintering Process., Material Science and Engineering, pp. 142(2-3),(2007) 116-120.
- [4] C. C., P. Z., X. L. B. K. and & F. X., Microwave Dielectric Properties of Novel (1-x) MgTiO₃-xCa_{0.5}Sr_{0.5}TiO₃ Ceramics, Journal of Material Science: Materials in Electronics, (2020) p. 31(16).
- [5] Z. Hou, F. Ye and L. Liu, "Effects of pore shape and porosity on the dielectric constant of porous SiAlON ceramics," Elsevier, 2015.
- [6] K. A., "TP3 Sintering 1 TP3-ceramics: Sintering and Microstructure Responsible," Practical Classes "Ceramics & Colloids", 2013.
- [7] F. S., P. V. P., O. N., P. V., K. Maca and & P. V. B., "The impedance analysis of sintered MgTiO₃ Ceramics.," Journal of Alloys and Compounds, pp. 107-115, 2017.
- [8] S. Hampshire, "2.01 - Fundamental Aspects of Hard Ceramics," Elsevier, vol. 2, pp. 3-28, 2014.
- [9] L. G. Hector and H. L. & Schultz, "The Dielectric Constant of Air at Radiofrequencies," Physics ,(1936), pp. 133-136.
- [10] <<https://eng.libretexts.org>>. Dated: 06 07 2021.

PRODUCTION AND CHARACTERIZATION OF CERAMICS FOR MICROWAVE APPLICATIONS

Melike DÖNMEZ, Cihangir DURAN

Ankara Yıldırım Beyazıt University
Türkiye

Keywords: Dry Pressing, Dielectric Ceramics, Dielectric and Microwave Measurements, Characterization

Abstract

New research and developments on microwave communication result in a rising demand for dielectric resonators used in wireless communication devices. Dielectric oxide ceramics are used as filters, oscillators in a variety of applications from mobile phones to global positioning systems. It has also played an important role in the microwave wireless communications industry by reducing the size and cost of antenna components. The essential properties for a dielectric resonator are high dielectric constant (ϵ_r), high quality factor (Q) and near-zero temperature coefficient of resonance frequency (τ_f). In this study, dielectric ceramic compositions (e.g., MgNb_2O_6 , $\text{Ba}_2\text{Ti}_9\text{O}_{20}$, $0.68\text{CaTiO}_3\text{-}0.32\text{Ca}(\text{Zn}_{1/3}\text{Nb}_{2/3})\text{O}_3$ and $\text{Ba}_{6-3x}(\text{Nd}_{1-y}\text{Bi}_y)_{8+2x}\text{Ti}_{18}\text{O}_{54}$ $x=2/3$ and $y=0.07$) with various dielectric constants were synthesized by solid state method and successfully fabricated by dry pressing for microwave resonator applications. Densification and phase formation were investigated for each composition sintered at least 3 temperatures to optimize dielectric properties. All sintered samples had a relative density $>97\%$. Dielectric constants at optimum sintering temperatures for each composition were 20.27 for MgNb_2O_6 , 39.20 for $\text{Ba}_2\text{Ti}_9\text{O}_{20}$, 89.63 for $0.68\text{CaTiO}_3\text{-}0.32\text{Ca}(\text{Zn}_{1/3}\text{Nb}_{2/3})\text{O}_3$ and 90.83 for $\text{Ba}_{6-3x}(\text{Nd}_{1-y}\text{Bi}_y)_{8+2x}\text{Ti}_{18}\text{O}_{54}$ $x=2/3$ $y=0.07$.

1. Introduction

1.1. Microwave Dielectric Ceramics

With the development of communication technology, the importance of dielectric ceramic materials in microwave devices is continuously increasing. Microwave dielectric materials are used in mobile phones, global positioning systems, military radars and satellite communication systems. Applications and electromagnetic spectrum are shown in Figure 1. Microwave region falls in the spectrum between 300 MHz and 300 GHz. Microwaves have higher frequency and lower wavelength than radio waves. As a result of its huge bandwidth capacity in comparison to radio waves, its information carrying capabilities are high [1, 2].

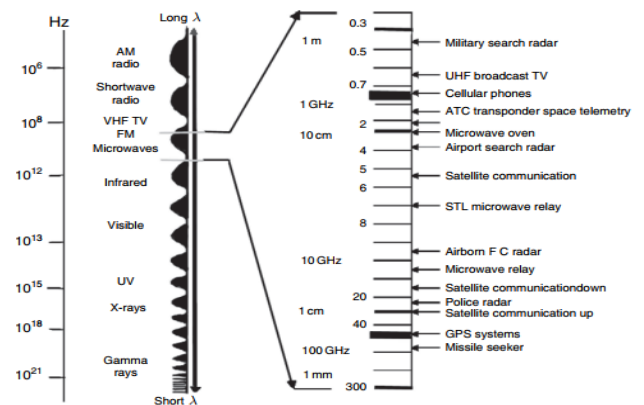


Figure 1 Applications of microwave frequencies and electromagnetic spectrum [2].

Microwave applications require special devices for transport and filtering due to cable response time and transport time. Conventional transistors, integrated circuits and cables cannot be used to carry these waves. Due to the high resistance that occurs in conventional circuits at high frequencies, the signal is lost before reaching the desired location. For this reason, ceramic materials find use in microwave circuits due to their dielectric properties. Ceramics used in this field are used in the production of parts such as resonators and oscillators [3].

The dielectric material spectrum is practically limited to about $20 < \epsilon_r < 100$. To ensure maximum signal identification, the dielectric loss ($\tan\delta$) should be less than 10^{-3} [4]. This is closely related to the quality factor (i.e., $Q=1/\tan\delta$), which should generally be maximized. However, experimental studies have shown that Q is not an independent parameter [5]. In fact, since the product of Q and the resonance frequency (f_0) for a given material is almost constant, a general knowledge of the material's Q value has emerged. That is, the Q factor is always based on the measured (resonant) acquisition frequency. Nowadays, $Q > 30,000$ at 1 GHz is required for many practical applications. Especially in communication systems, in order to ensure a certain temperature balance, the resonator's temperature coefficient of resonance

frequency (τ_f) must be around $\sim \pm 2$ ppm/ $^{\circ}\text{C}$ so that the signal does not shift during operation [6, 7].

Dielectric ceramic materials with $\epsilon_r \leq 25$ are used for microwave circuit elements in substrate material and missile tracking systems. $\epsilon_r = 25-50$ are used to improve signal-to-noise ratios in satellite communications and cell phone base stations. $\text{BaMg}_{1/3}\text{Ta}_{2/3}\text{O}_3$ and $\text{BaZn}_{1/3}\text{Ta}_{2/3}\text{O}_3$ are prominent members of this group. $\epsilon_r \geq 50$ are used for miniaturization such as mobile phones. The most important member of this group is $\text{Ba}_{63}\text{xR}_{8+2\text{x}}\text{Ti}_{18}\text{O}_{54}$ ($\text{R}=\text{Pr, Sm, La}$) dielectric ceramics [8, 9]. The size of the resonator proportional to $\lambda_0 / \sqrt{\epsilon_r}$ where λ_0 is free-space wavelength at the resonant frequency [10]. The dielectric constant (ϵ_r) should be as large as possible since the size of the resonator is inversely proportional to the square root of the dielectric constant.

2. Experimental Procedure

MgNb_2O_6 , $\text{Ba}_2\text{Ti}_9\text{O}_{20}$, $0.68\text{CaTiO}_3-0.32\text{Ca}(\text{Zn}_{1/3}\text{Nb}_{2/3})\text{O}_3$ and $\text{Ba}_{6-3\text{x}}(\text{Nd}_{1-\text{y}}\text{Bi}_{\text{y}})_{8+2\text{x}}\text{Ti}_{18}\text{O}_{54}$ $\text{x}=2/3$ $\text{y}=0.07$ powders were synthesized by the solid state method. Dry pressing was used as the shaping method in all ceramic compositions and the steps followed in the experimental studies are given in Figure 2.

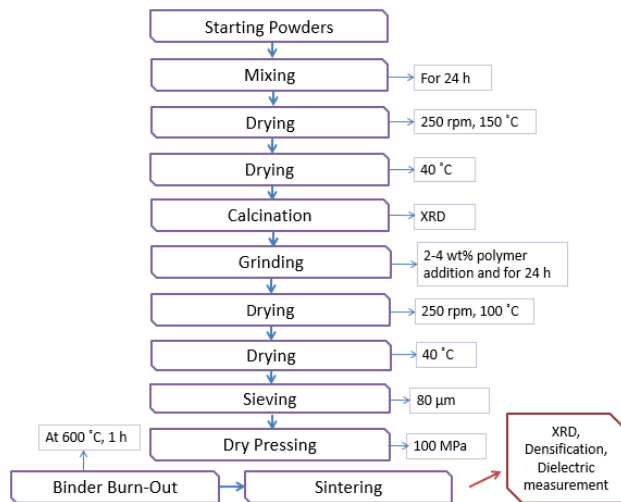


Figure 2. Flowchart of the sample preparation steps.

Also, the materials used for ceramic compositions are tabulated with their trade names and properties in Table 1.

Table 2 summarizes the starting components and calcination conditions. The mixed powders were weighed at stoichiometric ratios and ball milled in ethanol for 24 hours at 185 rpm using 0.5 cm diameter yttria stabilized zirconia balls. The mixtures were dried on a hot plate at 150 $^{\circ}\text{C}$ at 250 rpm, and then oven dried at 40 $^{\circ}\text{C}$. Commercial MgNb_2O_6 and CaTiO_3 powders were used as-received.

Table 1. The ceramic materials used in experiments.

Raw powders	Trade name	Property
MgNb_2O_6	Commercial powder, China	99.9% purity
BaCO_3	Sigma-Aldrich, Germany	$\geq 99\%$ purity
TiO_2	Aeroxide, Germany	P25 (20 nm, 35-62 m^2g^{-1})
CaO	Nanografi, Türkiye	99.9% purity
ZnO	Nanografi, Türkiye	99.99% purity
Nb_2O_5	Sigma-Aldrich, Germany	99.9% purity
CaTiO_3	Commercial powder, China	99.5% purity
Bi_2O_3	Nanografi, Türkiye	99.99% purity
Nd_2O_5	Commercial powder, China	99.99% purity

Table 1. The calcination conditions of $\text{Ca}(\text{Zn}_{1/3}\text{Nb}_{2/3})\text{O}_3$, $\text{Ba}_2\text{Ti}_9\text{O}_{20}$ and $\text{Ba}_4(\text{Nd}_{0.93}\text{Bi}_{0.07})_{28/3}\text{Ti}_{18}\text{O}_{54}$ ceramics.

Starting Components	Final Components	Calcination Conditions
$\text{CaO} + 1/3\text{ZnO} + 1/3\text{Nb}_2\text{O}_5$	$\text{Ca}(\text{Zn}_{1/3}\text{Nb}_{2/3})\text{O}_3$	1300 $^{\circ}\text{C}$ - 3 hours [11]
$2\text{BaCO}_3 + 9\text{TiO}_2$	$\text{Ba}_2\text{Ti}_9\text{O}_{20}$	1250 $^{\circ}\text{C}$ - 3 hours [12]
$4\text{BaCO}_3 + 4.34\text{Nd}_2\text{O}_5 + 0.326\text{Bi}_2\text{O}_3 + 18\text{TiO}_2$	$\text{Ba}_4(\text{Nd}_{0.93}\text{Bi}_{0.07})_{28/3}\text{Ti}_{18}\text{O}_{54}$	1100 $^{\circ}\text{C}$ - 3 hours [13]

Before shaping, 4 wt% vinyl-based binder solution (MSE Teknoloji, Türkiye) was added as a binder to the calcined powders given in Table 2, $0.68\text{CaTiO}_3-0.32\text{Ca}(\text{Zn}_{1/3}\text{Nb}_{2/3})\text{O}_3$ powder mixture and MgNb_2O_6 powder. The slurries were dried on a hot plate at 100 $^{\circ}\text{C}$ at 250 rpm with continuous stirring. All the ethanol was evaporated in the drying oven at 40 $^{\circ}\text{C}$ for 24 hours. The dried powders were then ground with a mortar and passed through an 80-micron sieve. The sieved powders were compacted at 100 MPa to disc shaped. The pellets were burned-out at 600 $^{\circ}\text{C}$ for 1 h with heating rate of 0.5 $^{\circ}\text{C}/\text{min}$. Then, they were sintered at different temperatures in the range of 1150 $^{\circ}\text{C}$ –1300 $^{\circ}\text{C}$ for 2 h for MgNb_2O_6 , 1250 $^{\circ}\text{C}$ –1350 $^{\circ}\text{C}$ for 3 h for $\text{Ba}_2\text{Ti}_9\text{O}_{20}$, 1350 $^{\circ}\text{C}$ –1450 $^{\circ}\text{C}$ for 4 h for $0.68\text{CaTiO}_3-0.32\text{Ca}(\text{Zn}_{1/3}\text{Nb}_{2/3})\text{O}_3$ and 1280 $^{\circ}\text{C}$ –1350 $^{\circ}\text{C}$ for 3 h for $\text{Ba}_{6-3\text{x}}(\text{Nd}_{1-\text{y}}\text{Bi}_{\text{y}})_{8+2\text{x}}\text{Ti}_{18}\text{O}_{54}$ $\text{x}=2/3$ $\text{y}=0.07$ in air with a heating and cooling rate of 5 $^{\circ}\text{C}/\text{min}$. The bulk density was measured using Archimedes' method. The phase

formation of the calcined powders was checked by X-ray diffraction (XRD), (Miniflex600, Rigaku) with a scan rate was 2°C/min and a step interval of 0.02°C. The parallel surfaces with coated with an air-dry silver ink before dielectric measurements. Dielectric properties were measured at 5 MHz at room temperature using an impedance analyzer (HIOKI IM3570).

3. Results and Discussion

3.1. Phase formation

The XRD pattern of $\text{Ca}(\text{Zn}_{1/3}\text{Nb}_{2/3})\text{O}_3$ powder calcined at 1300°C for 3 hours is given in Figure 3. According to the XRD pattern result, $\text{Ca}(\text{Zn}_{1/3}\text{Nb}_{2/3})\text{O}_3$ powder was matched with the literature and a perovskite phase was formed in 3 hours at 1300°C [11].

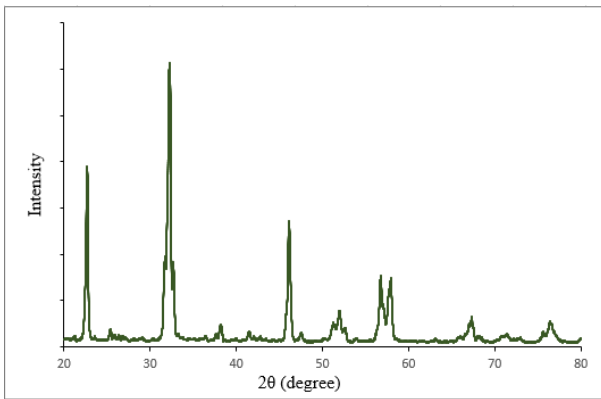


Figure 3 XRD pattern of $\text{Ca}(\text{Zn}_{1/3}\text{Nb}_{2/3})\text{O}_3$ powder calcined at 1300°C for 3 h.

Figure 4 shows $\text{Ba}_2\text{Ti}_9\text{O}_{20}$ powder calcined at 1250°C for 3 hours. A pure $\text{Ba}_2\text{Ti}_9\text{O}_{20}$ powder was obtained (PDF Card No: 01-076-1424). The same results were also attained in the literature [12].

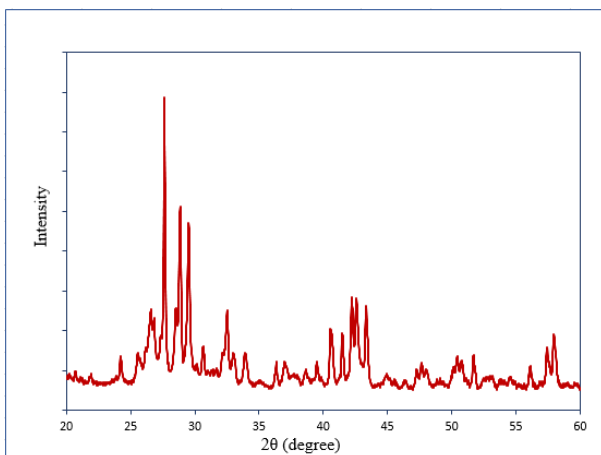


Figure 4 XRD pattern of $\text{Ba}_2\text{Ti}_9\text{O}_{20}$ powder calcined at 1250°C for 3 h.

The XRD result of $\text{Ba}_4(\text{Nd}_{0.93}\text{Bi}_{0.07})_{28/3}\text{Ti}_{18}\text{O}_{54}$ powder calcined at 1100°C for 3 hours is shown in Figure 5. The pattern matched with the literature and was defined as a tungsten bronze type solid solution [13].

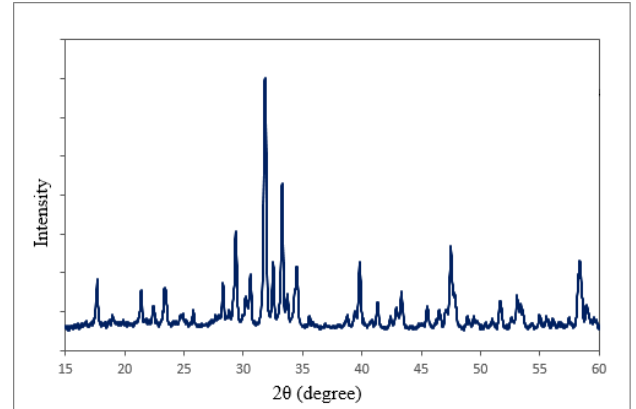


Figure 5 XRD pattern of $\text{Ba}_4(\text{Nd}_{0.93}\text{Bi}_{0.07})_{28/3}\text{Ti}_{18}\text{O}_{54}$ powder calcined at 1100°C for 3 h.

3.2. Densification and Dielectric Properties

All ceramics were fabricated using dry pressing method. The ball mill was applied both to mix powders and reduce particle size. The bulk and relative densities and dielectric properties of sintered MgNb_2O_6 , $\text{Ba}_2\text{Ti}_9\text{O}_{20}$, 0.68CaTiO_3 - $0.32\text{Ca}(\text{Zn}_{1/3}\text{Nb}_{2/3})\text{O}_3$ and $\text{Ba}_4(\text{Nd}_{0.93}\text{Bi}_{0.07})_{28/3}\text{Ti}_{18}\text{O}_{54}$ compositions as a function of temperature are shown in Table 3, 4, 5 and 6, respectively.

Table 3 shows the densification and dielectric properties of MgNb_2O_6 ceramics sintered between 1150°C and 1300°C. After 1250°C, the density value decreased due to grain growth during sintering [14]. Averaged relative density values were recorded as 96.34% at 1300°C, 97.97% at 1250°C, 98.32% at 1200°C and 91.62% at 1150°C. Hence, the optimum temperature was determined as 1200 °C for 2 h. The dielectric constant increased and the dielectric loss relatively decreased where the densification was high. Also, the relative density value was quite high and the dielectric properties were low at 1150°C due to the lower densification.

Table 3. The density and dielectric properties of MgNb_2O_6 samples

Sintering Temperature (°C), Time (h)	Bulk Density, g/cm ³	Relative Density, %	Dielectric Constant, 5 MHz	Dielectric Loss, 5 MHz
1150, 2	4.58	91.62	17.98	0.0068
1200, 2	4.91	98.32	20.27	0.0049
1250, 2	4.89	97.97	20.31	0.0043
1300, 2	4.81	96.34	20.09	0.0051

Table 4 tabulates the densification and dielectric properties of $\text{Ba}_2\text{Ti}_9\text{O}_{20}$ ceramics sintered between 1250°C and 1350°C. The bulk densities of all samples were recorded between 4.45-4.53 g/cm^3 , which ensured relative densities >96%. It has been determined that as the temperature decreased, the density of the samples increased, which enhanced the dielectric properties. The $\text{Ba}_2\text{Ti}_9\text{O}_{20}$ samples sintered at 1250°C showed maximum densification (98.11%) and dielectric constant (39.20).

Table 4. The density and dielectric properties of $\text{Ba}_2\text{Ti}_9\text{O}_{20}$ samples

Sintering Temperature (°C), Time (h)	Bulk Density, g/cm^3	Relative Density, %	Dielectric Constant, 5 MHz	Dielectric Loss, 5 MHz
1250, 3	4.53	98.11	39.20	0.0026
1300, 3	4.50	97.60	39.14	0.0025
1350, 3	4.45	96.59	38.31	0.0037

Table 5 indicates the densification and dielectric properties of $0.68\text{CaTiO}_3\text{-}0.32\text{Ca}(\text{Zn}_{1/3}\text{Nb}_{2/3})\text{O}_3$ ceramics sintered between 1350°C and 1450°C. All samples showed very close densities with relative densities >97%. At highest density and dielectric constant, the optimum temperature was determined as 1400 °C for 4 h.

Table 5. The density and dielectric properties of $0.68\text{CaTiO}_3\text{-}0.32\text{Ca}(\text{Zn}_{1/3}\text{Nb}_{2/3})\text{O}_3$ samples

Sintering Temperature (°C), Time (h)	Bulk Density g/cm^3	Relative Density, %	Dielectric Constant, 5 MHz	Dielectric Loss, 5 MHz
1350, 4	4.16	97.20	86.28	0.0047
1400, 4	4.17	97.35	89.63	0.0035
1450, 4	4.15	97.04	86.78	0.0037

Table 6 gives the densification and dielectric properties of $\text{Ba}_4(\text{Nd}_{0.93}\text{Bi}_{0.07})_{28/3}\text{Ti}_{18}\text{O}_{54}$ ceramics sintered between 1280°C and 1350°C. The sintered samples at 1320°C for 3 hours showed maximum density and dielectric constant. The sintered samples at 1280°C reacted with the alumina substrate, and broken. The dielectric properties followed the densification path and the optimum properties were obtained at 1320 °C.

Table 6. The density and dielectric properties of $\text{Ba}_4(\text{Nd}_{0.93}\text{Bi}_{0.07})_{28/3}\text{Ti}_{18}\text{O}_{54}$ samples

Sintering Temperature (°C), Time (h)	Bulk Density g/cm^3	Relative Density, %	Dielectric Constant, 5 MHz	Dielectric Loss, 5 MHz
1280, 3	5.75	98.21	90.04	0.0068
1320, 3	5.77	98.50	90.83	0.0065
1350, 3	5.75	98.31	90.06	0.0069

Overall, one of the features sought in microwave dielectric ceramic compounds is to obtain high bulk density to control dielectric properties [14]. It has been reported in literature that the dielectric constant increases with increasing density due to elimination of porosity [6]. Relative densities $\geq 97\%$ were successfully obtained for all samples.

4. Conclusions

MgNb_2O_6 , $\text{Ba}_2\text{Ti}_9\text{O}_{20}$, $0.68\text{CaTiO}_3\text{-}0.32\text{Ca}(\text{Zn}_{1/3}\text{Nb}_{2/3})\text{O}_3$ and $\text{Ba}_{6-3x}(\text{Nd}_{1-y}\text{Bi}_y)_{8+2x}\text{Ti}_{18}\text{O}_{54}$ $x=2/3$ $y=0.07$ ceramics in the dielectric constant range of 20-100 were successfully prepared by solid state method for microwave dielectric resonator applications. XRD results of the calcined powders indicated phase-pure compositions. Maximum densification was attained at 1200°C for 2 hours (relative density of 98.32%) for MgNb_2O_6 , 1250°C for 3 hours (relative density of 98.11%) for $\text{Ba}_2\text{Ti}_9\text{O}_{20}$, 1400°C for 4 hours (relative density of 97.35%) for $0.68\text{CaTiO}_3\text{-}0.32\text{Ca}(\text{Zn}_{1/3}\text{Nb}_{2/3})\text{O}_3$ and 1320°C for 3 hours (relative density of 98.50%) for $\text{Ba}_{6-3x}(\text{Nd}_{1-y}\text{Bi}_y)_{8+2x}\text{Ti}_{18}\text{O}_{54}$ $x=2/3$ $y=0.07$. The dielectric constant (loss) values at optimum sintering temperatures were 20.27 (0.0049) for MgNb_2O_6 , 39.20 (0.0026) for $\text{Ba}_2\text{Ti}_9\text{O}_{20}$, 89.63 (0.0035) for $0.68\text{CaTiO}_3\text{-}0.32\text{Ca}(\text{Zn}_{1/3}\text{Nb}_{2/3})\text{O}_3$ and 90.83 (0.0065) for $\text{Ba}_{6-3x}(\text{Nd}_{1-y}\text{Bi}_y)_{8+2x}\text{Ti}_{18}\text{O}_{54}$ $x=2/3$ $y=0.07$ ceramics. Dielectric properties were found to depend on densification levels for all ceramics, which is critical for microwave applications.

References

- [1] Cohen, S.B. (1968). Microwave band pass filters containing high Q dielectric resonators, IEEE Microwave Theory and Techniques MMT,16,218-227
- [2] M. T. Sebastian, "CHAPTER ONE-INTRODUCTION," in *Dielectric materials for wireless communication*, Amsterdam: Elsevier, 2008, pp. 1–10.
- [3] Shriey, H.M. (2002). Low Temperature Synthesis of the Microwave Dielectric Material, Barium

Magnesium Tantalate (BMT). Pittsburgh University, Pittsburgh, USA.

- [4] Wersing, Wolfram. "Microwave ceramics for resonators and filters." *Current Opinion in Solid State and Materials Science* 1.5 (1996): 715-731.
- [5] Korkmaz, E. (2010). Effect of different dopants on the sintering behaviour and dielectric properties of $\text{Ba}(\text{Zn}_{1/3}\text{Nb}_{2/3})\text{O}_3$ microwave dielectric ceramics. Marmara University, İstanbul
- [6] R. Freer, F. Azough, Microstructural engineering of microwave dielectric ceramics, *Journal of the European Society* 28(2008), 1433-1441.
- [7] Surenderan, K.P. (2004). Investigations on low loss dielectric ceramic materials for wireless communication. Kerala University, Ceramic Technologies Department, Kerala, India
- [8] H. Ohsato et al., "Microwave-millimeterwave dielectric materials," 2004, doi: 10.4028/www.scientific.net/kem.269.195
- [9] Ohsato, H. (2011). Perovskite Materials: Synthesis, Characterization, Properties and Applications, ExLi4EvA, Open Access
- [10] Keyrouz, S., Caratelli, D. (2016). Dielectric resonator antennas: basic concepts, design guidelines, and recent developments at millimeter-wave frequencies. *International Journal of Antennas and Propagation*, 2016.
- [11] Chen, X. M., et al. "Microstructures and microwave dielectric characteristics of $\text{Ca}(\text{Zn}_{1/3}\text{Nb}_{2/3})\text{O}_3$ complex perovskite ceramics." *Journal of the American Ceramic Society* 87.12 (2004): 2208-2212.
- [12] C. L. Huang, M. H. Weng, C. T. Lion, C. C. Wu, Low temperature sintering and microwave dielectric properties of $\text{Ba}_2\text{Ti}_9\text{O}_{20}$ ceramics using glass additions. *Materials research bulletin*, 35(14-15), 2445-2456, (2000).
- [13] Wu, Y. J., & Chen, X. M. (2001). Structures and microwave dielectric properties of $\text{Ba}_{6-3x}(\text{Nd}, \text{Bi}_y)_{8+2x}\text{Ti}_{18}\text{O}_{54}$ ($x=2/3$) solid solution. *Journal of Materials Research*, 16(6), 1734-1738.
- [14] Ma, J., Fu, Z., Tang, X., Li, Y. (2016). Characterization and microwave dielectric properties of $\text{Mg}_4\text{Nb}_2\text{O}_9$ ceramics produced via using nanopowders. Retrieved May 20, 2022.



PHASE ANALYSIS AND DIELECTRIC CHARACTERISTICS OF BST CERAMICS PRODUCED BY CONVENTIONAL AND MICROWAVE ASSISTED SOLID-STATE REACTIONS

Başar SÜER, Özlem AYDIN ÇİVİ, Arcan F. DERİCİOĞLU

Middle East Technical University
Türkiye

Abstract

Ferroelectrics like $Ba_xSr_{1-x}TiO_3$ (BST) draw great attention for applications in tunable devices such as antennas, frequency-selective surfaces (FSS) and tunable filters that are commonly used in electronics industry. In this study, the effect of Sr content and heating method on lattice parameters, volumetric phase percentages (tetragonal ferroelectric and cubic paraelectric) and tetragonality factor (c/a) were extensively investigated using X-ray diffraction (XRD). Individual lattice parameters, volumetric phase percentages and tetragonality factors were calculated using Rietveld refinement software MAUD for both tetragonal ferroelectric phase and cubic paraelectric phase of BST. Ferroelectric to paraelectric phase transition temperatures of the samples were determined using differential scanning calorimetry (DSC).

Keywords: barium strontium titanate, tunable dielectrics, Rietveld, microwave-assisted synthesis

1. Introduction

Ferroelectric behavior originates from the spontaneous distortion of the cubic structure along a certain direction below Curie temperature (T_C), above which the ferroelectric properties are lost due to the formation of the paraelectric phase. The displacement of the cation along the same direction is responsible for the polarity that provides ferroelectric characteristics to the perovskites, which is rather crucial for electromagnetic applications. In order to investigate the factors affecting ferroelectricity, $Ba_xSr_{1-x}TiO_3$ ceramic powders were produced using conventional as well as microwave heating via solid-state reaction route at different temperatures and times. Curie temperatures (T_C) of the samples were determined using DSC. Extensive and careful examinations through Rietveld refinement indicated co-existence of tetragonal and cubic phases in the synthesized BST ceramics.

2. Materials and Methods

BST powders were synthesized by mixed-oxide route using barium and strontium carbonates and titanium dioxide as precursors. Ball milling was applied in 2-propanol as the milling medium, where 1:5 powder to ball ratio was selected. With the proper amount of precursors mixed according to the stoichiometric ratios using ball milling in a planetary centrifugal mixer (Thinky Mixer ARE-250 CE), powder mixture was left in a drying oven for 24 hours followed by grinding and pelletizing for the heat treatment. Calcination was carried out by conventional as well as microwave heating at 900 and 1200 °C for varying durations of 15 min and 2 h. Characterization of the powders was conducted using Rigaku DMAX2200 (XRD), FEI NOVA NANO 430 (SEM), Perkin Elmer DSC for phase identification, morphological examination and phase transition temperature determination, respectively.

3. Conclusion

Lattice parameters of the samples showed a linear relation with the Ba fraction up to $x = 0.6$, which indicated a constant tetragonality factor (c/a). c/a ratio started to increase when $x > 0.6$ suggesting the formation of tetragonal ferroelectric phase. BST powders prepared using microwave heating resulted in more cubic paraelectric phase compared to conventional heating in terms of volumetric percentage due to faster cooling, obstructing phase transition at low temperatures due to slow solid-state kinetics.

EXPERIMENTAL PHASE STUDIES IN THE QUASI-BINARY BaCeO₃-SrCeO₃ SYSTEM

Hanifi Eray KORKMAZ, Nuri SOLAK

Istanbul Technical University
Türkiye

Keywords: Perovskite Structure, Ceramic Conductor, Metal Oxides, Quasi-binary section

Abstract

In recent years, ceramic oxides with the structure of the perovskite have gained considerable attention due to their technological applications in fuel cells and oxygen permeable membranes. The BaCeO₃-SrCeO₃ solid oxide solution exhibited exemplary behavior in ionic conductivity-driven applications. The structure, stability and phase formation in the system control the materials properties. In the literature, limited phase stability data is available, therefore, this work aims to investigate the mutual solubility in the BaCeO₃-SrCeO₃ quasi-binary section at various temperatures.

1.Introduction

For better performance of solid oxide fuel cells, operating temperatures are increased. On the other hand, high operating temperatures are cramps for good thermodynamical stability of the anode, cathode, and electrolyte in solid oxide fuel cells. The different electrolytes are used in solid oxide fuel cells for decreasing operation temperature and increasing conductivity like BaCeO₃, SrCeO₃, BaZrO₃, CaZrO₃, Y₂O₃ and SrZrO₃. In this study, BaCeO₃-SrCeO₃ solid oxide solution perovskite structure was selected as these kinds of the ionic conductor because of look promising conductivity properties. (Ba_xSr_{1-x})CeO₃ perovskite structure was selected to investigate phase characteristics and the sintering ability of ceramic structure at 1300°C.

2.Materials and Method

Samples were prepared using the conventional oxide mixing route and also sol-gel based wet-chemistry (Fig. 1). X-ray diffraction, electron microscopy and thermal analysis techniques were used to characterize samples. Representative results are given below.

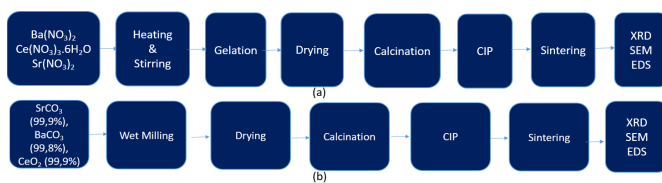


Figure1: Powder Production and Characterization Flow

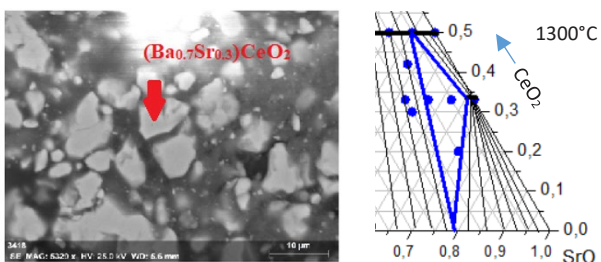


Figure3: Example SEM image, SrO-rich phase diagram.

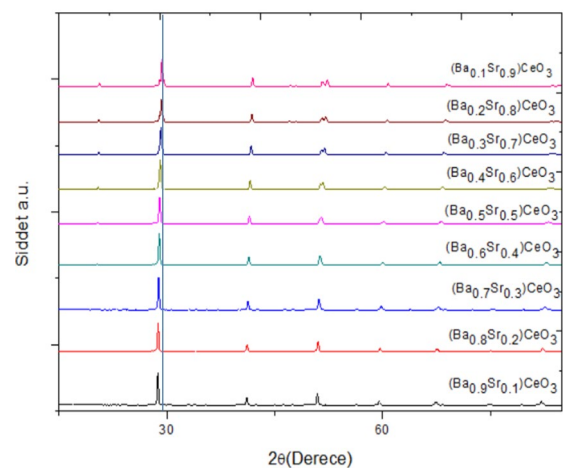


Figure2: XRD Results at 1300°C Sintering

3.Conclusion

The 1300°C SrO-rich isothermal sections of the ternary oxide system has been constructed. The effect of temperature on solubility was limited. Extended BaO solubility in SrCeO₃ and limited solubility in Sr₂CeO₄ phases were observed and shown on the phase diagram.



EFFECT OF h-BN AMOUNT ON Al₂O₃/GLASS COMPOSITES FOR LTCC APPLICATIONS

Oğuzhan BİLAÇ, Cihangir DURAN

Ankara Yıldırım Beyazıt University
Türkiye

Key words: Al₂O₃/glass composite, hexagonal boron nitride, low temperature co-fired ceramics, thermal properties, dielectric properties

Abstract

(SiO₂-Al₂O₃-CaO)-based glass (55 wt% glass)/ceramic (45 wt% Al₂O₃) composites with nano-hBN (0–10 wt%) addition were investigated. Al₂O₃/glass/hBN composites were fabricated for the LTCC applications. Alignment and homogeneous distribution of the platelet hBN particles during tape casting allowed high hBN (5 wt%) loading as well as facilitated densification at 800°C (density of 2.65 g/cm³, apparent porosity of 0.7%). Dielectric constant of the dense composites decreased (or, alternatively, enhanced) with increasing hBN content from 7.3 for the 0 wt% hBN to 6.55 for the 5 wt% hBN at 5 MHz. In addition, hBN addition strongly improved the mean thermal conductivity from 1.86 W/m·K for the 0 wt% hBN to 2.43 W/m·K for the 5 wt% hBN between 75°C and 250°C.

Introduction

Thin, lightweight and multifunctional electronic components are attracting considerable attention due to the rapid growth of wireless communication systems and microwave devices such as those used in the automotive, medical and telecommunication. Low temperature co-fired ceramic (LTCC) technology allows manufacturing of 3D ceramic modules with embedded components and metal electrodes [1].

Materials and Methods

A composition of 45 wt% Al₂O₃ and 55 wt% glass mixture (hereafter called as A55) was mixed with hBN at 1, 2.5, 5 and 10 wt% by ball milling for 24 h. Samples were produced by dry pressing, CIP and tape casting method. Then, samples characterized some properties such as densification, phase formation, thermal and dielectric properties.

Conclusion

Al₂O₃/glass/hBN composites were successfully fabricated for the LTCC applications. Maximum densification was attained at 800°C for the 0–2.5 wt% hBN composites and at 900°C for the 5–10 wt% hBN composites. The 5 wt% hBN composite was densified at 800°C when the fabrication method was changed to tape casting due to alignment and homogeneous distribution of the hBN particles within the Al₂O₃/glass structure. XRD results proved that hBN neither chemically reacted with the other phases nor decomposed with temperature, which was critical to increase thermal conductivity to decrease dielectric constant at the same. The Al₂O₃/glass/hBN composites a promising candidate for the LTCC application.

[1]Sebastian MT, Jantunen H. Low loss dielectric materials for LTCC applications: A review. Int Mater Rev. 2008;53(2):57–90.

METHYLENE BLUE REMOVAL BY PHASE SEPARATED POROUS GLASS

Emre Burak ERTUŞ¹, Çekdar Vakıf AHMETOĞLU², Abdullah ÖZTÜRK³

¹KTO Karatay University, ²İzmir Institute of Technology, ³Middle East Technical University
Türkiye

Keywords: Porous glass, Methylene Blue, Adsorption.

Abstract

In this study, it was aimed to utilize Porous glass (PG) as an adsorbent in MB removal from wastewater. PG powders were produced by melting and phase separation of an alkali borosilicate glass followed by selective leaching in HCl and an additional alkali treatment. The scanning electron microscope and N₂ adsorption/desorption techniques were applied to characterize the pore architecture of the PGs. Methylene blue (MB) adsorption efficiency was investigated from the change in MB concentration in the MB aqueous solutions with various concentrations through the absorbance of the solution at a wavelength of 664 nm monitored on a UV-Vis spectrometer. Results showed that the structure and textural properties of PG was evidently altered via alkali treatment hence affected its adsorption performance. The maximum adsorption capacity for alkali treated PG in the concentration ranges studied was 60.6 mg/g. The isotherm analysis indicated that the equilibrium data were well fitted to the Freundlich isotherm model.

1. Introduction

The usage of dyes in textile and chemical industry generates colored wastewaters, which often cause significant environmental problems. The dye-containing runoffs are hazardous for the biological stability of neighboring ecosystems and can be carcinogenic and mutagenic. Methylene blue (MB) is a cationic dye and commonly used for dyeing cotton, silk, and wood. MB can have various harmful effects on human being and animals [1]. Several methods including chemical oxidation [2], biodegradation [3], flocculation-coagulation [4], and adsorption [5] are available for the removal of dyes from industrial wastewaters. Among them, adsorption is a comparatively cheap and effective method in the removal of dyes from wastewaters [5].

So far, the most popular adsorption materials are activated carbon, clays, and agricultural solid wastes

[6]. Among these adsorbents, phase separated PG is distinguished from other porous solids by its distinctive sponge-like interconnected porous structure, suitability for low cost mass production, reusability of waste glass, and mechanical integrity [7, 8]. Pore topology, volume, size, the surface area can be tailored via processing parameters [7]. PGs are produced in a variety of forms such as powder, beads, monoliths, fibers, or tubes. It is also known that PG does not cause catalyst poisoning. [9, 10]. Several studies have investigated the adsorption properties of PG. Kuznetsova et al. [11] examined the adsorption of iron ions by PG in diluted solutions of iron(III) chloride. Zhang et al. [12] studied the MB adsorption performance of polyvinylidene fluoride (PVDF)/porous glass composite membrane. To the best of the authors knowledge, no study has been reported on the MB adsorption behavior of phase separated PG.

The purpose of this study was to evaluate the MB adsorption performance and to analyze equilibrium adsorption isotherms of phase separated PG.

2. Experimental Procedure

2.1. Porous glass preparation

Porous glasses (PGs) were produced in accord with our previous study. Readers are referred to reference [13] for the details in the production. A sodium borosilicate glass with nominal composition of 55.7SiO₂-33.6B₂O₃-9.2Na₂O-1.5Al₂O₃ (wt%) was produced by conventional melt-quenching technique using an electric furnace. To provide phase separation, the as cast glass was heat treated at 525 °C for 9 h. Later, the heat-treated glass pieces were acid leached using 1M HCl solution at 80 °C for 24 h. To remove the silica clusters precipitated in the pore channels, the acid leached porous glass (PG1) was additionally alkaline leached at room temperature using 0.5M NaOH solution for 2 h (PG2). After each leaching process, PGs were washed with distilled water and after all dried at 200 °C for 3 h. These modifications were followed to induce different pore architecture, surface

functionality and to observe their effect on the MB adsorption efficiency. All crushed and ground in an agate mortar with pestle. Finally, the resulting material was sieved in the size of less than 28 μm (500 mesh).

2.2 Characterization

The pore characteristics of PGs were measured via nitrogen (N_2) adsorption-desorption method using Quantachrome Autosorb-6 instrument. Prior to the measurement, the PGs were evacuated at 200 $^\circ\text{C}$ for 3 h. Brunauer–Emmett–Teller (BET) equation was used to calculate the specific surface areas from the adsorption isotherm. The total pore volume was obtained from the amount of gas adsorbed at the relative pressure $P/P_0 = 0.99$. The desorption branch of the nitrogen sorption isotherm was used to determine pore size distributions of PGs according to the BJH (Barrett, Joyner, Halenda) method, depended on the Kelvin equation, which relates the pore size with critical condensation pressure assuming a straight cylindrical pore model [14]. The structure of the pores was investigated by a scanning electron microscope (FE-SEM, Nova Nanosem 430, Hillsboro OR, USA).

To evaluate the adsorption properties of PGs Methylene Blue (MB), a cationic dye, was used as the adsorbed media. Before the experiments, 240 mg/L MB/ deionized water solution was prepared and diluted to the desired concentration. Adsorption tests were conducted in a glass container. 50 mg PGs and 50 mL MB solution (concentration between 20 and 240 mg/L with 40 mg/L increment) were added to the glass container than the mixture was magnetically stirred for an hour at room temperature. The suspension was centrifuged for 30 min at 4500 rpm and then supernatant was analyzed to determine MB adsorption change at the wavelength of 665 nm using a UV spectrophotometer (Agilent, Cary60). The concentration of MB was calculated referring to the calibration curve of MB. The amount of methylene blue uptake by PGs, q_e (mg/g) and the adsorption rate R (%) was calculated according to equations (1) and (2) respectively.

$$q_e = \frac{V(C_0 - C_e)}{W} \quad (1)$$

$$R = \frac{C_0 - C_e}{C_0} \times 100 \quad (2)$$

where V (L) is the volume of MB solution and W (mg) is the mass of PGs. C_0 and C_e (mg/L) are the initial and equilibrium concentrations of the MB in the solution, respectively. Freundlich [15] and Langmuir [16] equations were used to describe the equilibrium characteristics of adsorption, which are given in equations (3) and (4), respectively.

$$\log q_e = \log k_F + \frac{1}{n} \log C_e \quad (3)$$

$$\frac{C_e}{q_e} = \frac{1}{k_L q_{\max}} + \frac{C_e}{q_{\max}} \quad (4)$$

In Freundlich equation, k_F ($(\text{mg}/\text{m}^2)(\text{L}/\text{mg})^{1/n}$) is indicative of the adsorption capacity, and n (dimensionless) is the empirical parameter representing the energetic heterogeneity of the adsorption sites. For Langmuir type adsorption process q_{\max} (mg/g) is the maximum monolayer adsorption capacity and k_L is a constant related to the energy of adsorption. The efficiency of the adsorption process could be predicted by the equilibrium parameter, R_L (dimensionless), using equation (5) [17].

$$R_L = \frac{1}{1 + C_0 K_L} \quad (5)$$

3. Results and Discussion

The N_2 sorption isotherms for PGs are shown in **Fig. 1(a)**. The isotherms are of the Type IV(a) according to the IUPAC classifications, indicated that all glasses include mesoporosity. PGs exhibits the combination of H1 and H2 type hysteresis loop that is associated to pore-blocking/percolation in a narrow range of pore necks (ink-bottle pore model) or to cavitation-induced evaporation [14]. Isotherms exhibiting double hysteresis (two cycles) indicate a bimodal pore size distribution [18].

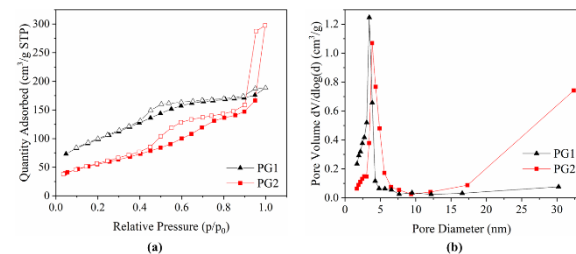


Figure 1. (a) N_2 adsorption-desorption isotherms, and (b) pore size distribution data for PGs.

The pore size distribution curves, shown in **Fig. 1(b)**, illustrate that the micro and mesopores coexists in PGs prepared, indicating that the pores formed hierarchical porosity. The pores around 4-5 nm are associated with the inter-particle spaces in between the channel walls and silica clusters (themselves as well). Also, the mesopores developed in a wider range up to 35 nm are related with the silica rich interconnected open-pore structure left behind the acid leaching what is called “liquation channels” [19, 20]. As a result of the following alkali treatment the size of the pores in the mesoporous range further increased, also some of the micropores diminished due to particle and/or surface dissolution of silica clusters [21].

The pore volume (V_p) and the specific surface area (SSA) values as calculated from N_2 adsorption-desorption analysis for PG1 and PG2 were listed in **Table 1**. Associated with the findings about pore

size alteration, the SSA of PG2 decreased while V_p increased relative to PG1, as a result of the removal of silica clusters and enlargement of liquation channels.

Table 1. The specific surface area (SSA) and total pore volume (V_p) of PGs.

Adsorbent	SSA (m ² /g)	V_p (cm ³ /g)
PG1	350.6	0.291
PG2	199.0	0.459

Fig. 2 shows the SEM images taken from the surfaces of the PGs produced at a magnification of 100,000x. The characteristic “worm-like” porous structure observed in both PGs. The liquation channels were better distinguishable than pores derived from silica clusters. The liquation channels i.e., silica skeleton of the PG2 deformed and the pores grew because of alkali leaching, proving the results of the N₂ sorption analysis.

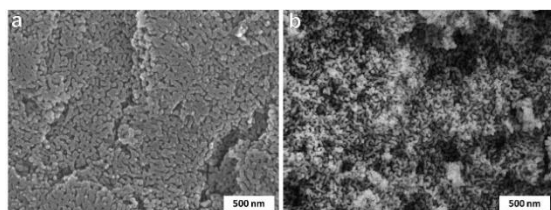


Figure 2. SEM images of (a) PG1 and (b) PG2.

Fig 3 (a) shows the relationship between initial MB concentration and the adsorption rate. At the initial MB concentration of 20 mg/L, PG2 exhibited higher adsorption rate (99.5%) than PG1 (60.1%). As the initial MB concentration was increased up to 240 mg/L, the adsorption rates of PG1 and PG2 decreased to 16.6% and 27%, respectively. It is related to the amount of active adsorption sites at PG pore walls. With increasing dye concentration, the active adsorption sites on the adsorbing surface become saturated with dye molecules [12]. Therefore, a decrease in the removal efficiency observed as the initial MB concentration increased. The adsorption rate for PG2 was higher than that for PG1 for all concentrations studied. As mentioned previously, removing the silica clusters by alkaline leaching increased the pore volume and enlarged the liquation channels. A higher adsorption rate for PG2 may be explained by easy diffusion of the aqueous MB solution through the porous structure and alteration of the surface functionality. That is, it is assumed that alkali treatment increased the surface adsorption sites or changed their nature, causing a superior adsorption performance. [22, 23].

Fig 3 (b) shows the nonlinear fitting of experimental adsorption data to the Freundlich and Langmuir models. The calculated values for the corresponding parameters are given in **Table 2**. According to correlation coefficient (R^2) it is suggested that the

adsorption of MB on PGs is fitted well to both equations with R^2 values greater than 0.9. It can be considered that the adsorption is intermediate between Langmuir and Freundlich isotherm models. But, Freundlich isotherm model which has greater R^2 values was more suitable to describe this adsorption process. The better fit with the Freundlich model suggests that the adsorption process to be multilayer and the heterogeneity of active sites on the surface of the adsorbent i.e., the sites involved in the adsorption process were not in the same type. It is known that PGs have a negative surface charge and slightly acidic character due to silanol (Si-OH) groups on their surface [8]. MB adsorption is simply due to the electrostatic attraction between the negatively charged PG surface and the positively charged MB molecules in solution. In addition, the hydrogen bonding between the amine group of MB molecule with Si-OH groups on PG surface is effective [24]. The diversity of active groups on the surface of PG is thought to explain the heterogeneity. Surface active groups can be in the form of (i) isolated free silanol, (ii) geminal free silanol, and (iii) vicinal groups. Also, siloxane and borate groups can be formed on PG surface [8, 25]. Values of n between 1 and 10 implies favorable adsorption. For PG1 and PG2, n values are greater than 1 confirmed the favorably adsorption of MB on PGs and more favorable for PG2. On the other hand, $1/n$ values smaller than 1 in the Freundlich model, indicates a monolayer adsorption. The k_F value is a relative indicator of the adsorption capacity and PG2 has superior k_F than PG1 [25].

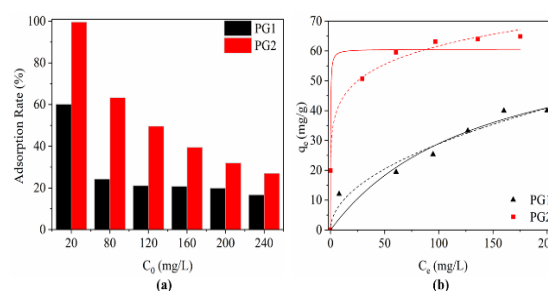


Figure 3. (a) The effect of initial MB concentration on adsorption rates of PGs and (b) equilibrium adsorption isotherms of MB onto PGs with simulations by Freundlich (dashed line) and Langmuir (solid line) isotherm models.

Table 2. Langmuir and Freundlich adsorption isotherm constants and correlation coefficients.

Adsorbent	Langmuir model			
	q_{max}	k_L	R_L	R^2
PG1	69.71±22.8	0.007	0.3731	0.93
PG2	60.69±2.31	5.9	0.0007	0.96
Adsorbent	Freundlich model			
	n	k_F	R^2	
PG1	2.04	2.89	0.94	
PG2	6.66	30.5	0.98	

For Langmuir isotherm model, R_L value indicates the type of the isotherm as either unfavorable ($R_L > 1$), linear ($R_L = 1$), irreversible ($R_L = 0$), or favorable ($0 < R_L < 1$) [17]. Values of R_L were between 0 and 1 for PGs implying that the adsorption process was favorable. The R_L value of PG2 is very close to 0, suggesting a higher degree of irreversible adsorption than PG1. Also, the k_L value of PG2 indicates that MB has a higher interaction with PG2 than PG1. Although all other data show that the adsorption performance of PG2 is better than PG1, the calculated q_{max} value of PG2 (60.69 ± 2.31 mg/g) was lower than PG1 (69.71 ± 22.8 mg/g). It is considered that this calculation is not very reliable due to the high curve fit error value.

4. Conclusions

- Hierarchically porous glasses (PGs) were produced by selective acid leaching processes conducted on a sodium borosilicate glass. The alkaline treatments have intense effects on the pore structure, the total pore volume increased (0.459 cm³/g), and specific surface area decreased (199 m²/g) with successive alkaline treatment.
 - Freundlich isotherm model was more suitable to describe MB adsorption process and the diversity of active groups on the surface of PG is thought to explain the heterogeneity of adsorption model.
 - R_L values between 0 and 1 for PGs implied that the adsorption process was favorable, that is related to the hierarchically (micro-meso) porous structure, high V_p , and SSA combined with the negatively charged silanol residues on the surface of this structure. The R_L value of PG2 is very close to 0, indicating a higher degree of irreversible adsorption than PG1 may be explained by easy diffusion of the aqueous MB solution through the porous structure and altered surface functionality.
 - The results obtained showed that the PGs are an appropriate adsorbent for removal of cationic dyes from aqueous solutions.
- Allen, S. and B. Koumanova, Journal of the University of Chemical Technology and Metallurgy, 2005. **40**(3): p. 175-192.
 - Rafatullah, M., et al., Journal of hazardous materials, 2010. **177**(1-3): p. 70-80.
 - Enke, D., F. Janowski, and W. Schwieger, Microporous and mesoporous materials, 2003. **60**(1-3): p. 19-30.
 - Schüth, F., K.S.W. Sing, and J. Weitkamp, *Handbook of porous solids*. 2002: Wiley-Vch.
 - Yanagida, S., et al., Catalysts, 2019. **9**(1): p. 82.
 - Aubry, E., et al., Surface and Coatings Technology, 2007. **201**(18): p. 7706-7712.
 - Kuznetsova, A., et al., Glass Physics and Chemistry, 2018. **44**(1): p. 41-46.
 - Zhang, Y., et al., Journal of the European Ceramic Society, 2019. **39**(15): p. 4891-4900.
 - Ertuğ, E.B., C. Vakıfahmetoğlu, and A. Öztürk, Ceramics International, 2020. **46**(4): p. 4947-4951.
 - Thommes, M., et al., Pure and Applied Chemistry, 2015. **87**(9-10): p. 1051-1069.
 - Freundlich, H., J. Phys. chem, 1906. **57**(385471): p. 1100-1107.
 - Langmuir, I., Journal of the American Chemical Society, 1918. **40**(9): p. 1361-1403.
 - Weber, T.W. and R.K. Chakravorty, AIChE Journal, 1974. **20**(2): p. 228-238.
 - Li, W.C., et al., Chemistry—A European Journal, 2005. **11**(5): p. 1658-1664.
 - Kreisberg, V., V. Rakcheev, and T. Antropova, Glass Physics and Chemistry, 2006. **32**(6): p. 615-622.
 - Toquer, G., et al., Journal of Non-Crystalline Solids, 2011. **357**(6): p. 1552-1557.
 - Lyubavin, M., T. Burkat, and V. Pak, Inorganic Materials, 2008. **44**(2): p. 203-206.
 - Müller, R., et al., Talanta, 2013. **107**: p. 255-262.
 - Lei, S., et al., Carbon, 2006. **44**(10): p. 1884-1890.
 - N. Yuan, H. Cai, T. Liu, Q. Huang, X. Zhang, Adsorpt. Sci. Technol. 2019. **37** 333–348.
 - Khraisheh, M., et al., Water Research, 2005. **39**(5): p. 922-932.

Acknowledgment

The authors thank Middle East Technical University for the partial financial support through project number BAP-03-08-2016-004.

References

- Khan, S. and A. Malik, 2014, Springer. p. 55-71.
- Dutta, K., et al., Journal of hazardous materials, 2001. **84**(1): p. 57-71.
- Bharti, V., et al., Environmental research, 2019. **171**: p. 356-364.
- Alizadeh, M., et al., Iranian Journal Of Chemistry And Chemical Engineering, 2015. **34**(1): p. 39-47.

VALUABLE SOURCES OF RAW MATERIAL FOR ACTIVATED CARBON; HAZELNUT HUSK AND PUMPKIN SHELL

Mürüvet Hazel UYSAL, Ali Osman KURT

Sakarya University
Türkiye

Keywords: Activated carbon, hazelnut husk, pumpkin shell, waste, disposal.

Abstract

Hazelnut husk (HH) and pumpkin shell (PS) wastes, formed after agricultural activities and processing in the Sakarya region in Türkiye, are generally disposed via burning illegally. Finding an economical and environmentally friendly disposal method such as converting them into value-added product / activated carbon (AC) might be a good alternative solution for their disposal problem. Within the scope of this study, HH and PS wastes were tried to be converted with a low cost, easy and environmentally friendly method to activated carbon, as an alternative to commercially produced AC products.

1. Introduction

Environmental pollution is a major issue of the today's society. Scientists have found many kind of techniques to remove contaminants and hazardous chemicals. Adsorption is one of the most common and suitable applied methods for removal of the pollutant due to its high efficiency, simply operating, being convenient, fast and having low initial costs. Activated carbon (AC) is the robust adsorbent that is most frequently used in adsorption processes especially for the purification of hazardous compounds in drinking or waste water and removal of pollutants in air [1, 2]. AC is derived from coal, agricultural residues, wood and a range of biomass materials via pyrolysis followed by chemical and/or physical activation or via directly physical activation in a single step. Among biomasses, the use of agricultural wastes preparing adsorbents would be a better alternative, because they are abundant, renewable and low price [3].

2. Materials and Methods

In this work, HH and PS wastes were used as a carbon source after washing, drying, grinding and sieving processes. AC was produced via physical activation process in a single step using mullite tube furnace. CO₂ gas with a constant flow rate of 8 lt/h was used in all tests for sweeping exhaust gases in the system and also for activation. After carbonization and activation process, products obtained from HH and PS were analyzed with BET and FESEM.

3. Conclusion

Single step process as carbonization and physical activation was carried out at 800°C for 2 hours for HH and 850°C for 1 hour for PS was enough to obtain ACs with porous structures (Figure 1). Heating and cooling rate was constant as 10°C/min for all tests. HH at 800°C for 2 hours and PS at 850°C for 1 hour gave the best results for BET value of 392,84m²/g and 679,54 m²/g, respectively. It was shown in this study that the abundant wastes may be disposed safely by converting them in a valuable product.

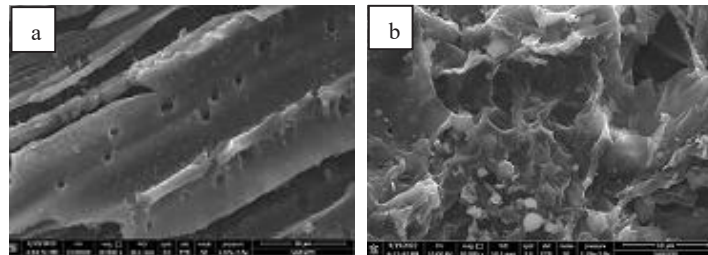


Figure 1. FESEM images (X10.000) of AC from a) HH and b) PS.

Acknowledgment

First author is thankful for their kind support from TÜBİTAK through BİDEB 2211-A grant and Council of Higher Education (YÖK) for the 100/2000 program grant.

References

- [1] M. Gupta, H. Gupta, D.S. Kharat, "Adsorption of Cu(II) by low cost adsorbents and the cost analysis", *Environ. Technol. Innovat.* 10 (2018) 91-101.
- [2] D. Bergna, H. Romar, S. Tuomikoski, H. Runtti, T. Kangas, P. Tynjälä, & U. Lassi, "Activated Carbon from Renewable Sources: Thermochemical Conversion and Activation of Biomass and Carbon Residues from Biomass Gasification." *Waste Biomass Management – A Holistic Approach*, Springer, 2017, 187-213.
- [3] E. Unur, "Functional nanoporous carbons from hydrothermally treated biomass for environmental purification." *Microporous and Mesoporous Materials*, 168, 2013, 92-101.



THE EFFECT OF SINTERING PARAMETERS ON THE PROPERTIES OF IR TRANSPARENT ZnS PRODUCED BY SPARK PLASMA SINTERING

Zeynep ÖZTÜRK, M. Kaan PEHLİVANOĞLU, N. Kaan ÇALIŞKAN

Tübitak SAGE
Türkiye

Keywords: ZnS, Spark Plasma Sintering, Infrared, Optical Transmission

Abstract

In this study, spark plasma sintering (SPS) was used to produce optical grade zinc sulfide (ZnS), by using different temperatures, times and pressures. Sintering temperature was between 750 and 900 °C, sintering time was between 5 and 10 minutes and pressure was increased from 16 MPa to 50 MPa between two steps. The results showed that SPS can effectively be used in optical grade ZnS production when these SPS parameters were optimized. As far as the results of this study is concerned, optimum sintering temperatures seem to be around 850 °C with relatively short sintering times. Microstructure analysis revealed that grain size has remained rather small around 1-8 µm, which might contribute to mechanical property improvement. Optical transmission values were found to vary with specimen thickness and ranged from 15 to 63% within the 3-12 µm infrared wavelength spectrum, depending on sintering time and temperature. Selected samples hot isostatic pressed (HIP) after SPS have shown that HIPing has resulted in a significant improvement on optical transmission, reaching 75% transparency.

1. Introduction

Zinc sulphide (ZnS) is a wide band gap II-VI semiconductor compound that can be used in optics, electronics and photocatalysis industry [1]. Due to the transmittance in the infrared (IR) wavelengths, it is widely used in defense applications as infrared windows and missile domes. Below 1020 °C, ZnS has a cubic structure which has a good transparency, above 1020 °C cubic structure transforms to hexagonal structure and transparency becomes reduced [2]. ZnS can be transparent at two different wavelength spectra, it is called standard ZnS (s-ZnS) when transparent between 8-12 µm and multispectral ZnS (m-ZnS) when transparent between 1-12 µm [3]. Mainly chemical vapor deposition (CVD) method is used for mass production of standard ZnS with high purity [4].

Multispectral ZnS is usually obtained from this grade by subsequent hot isostatic pressing operation, which makes it more costly. s-ZnS produced by CVD method has low mechanical properties for tough conditions [5]. In visible spectrum and medium wavelength IR region (3-5 µm), transmittance is poor. m-ZnS, on the other hand, has superior optical transmission but even lower mechanical properties.

It is a long-lasting demand and goal among academic and industrial community to produce high quality ZnS with multispectral optical characteristics and high mechanical properties. In this respect, powder metallurgical production methods seem to provide a big opportunity. CVD method can be more convenient to large size products, while powder metallurgy can be applied to smaller products that were desired to have higher mechanical properties. Spark plasma sintering (SPS) as one of the powder sintering techniques can be used for ZnS production and studies using SPS suggest that this method may provide higher mechanical properties along with good optical characteristics through a faster and cheaper production route for this material [6].

In this study, optical grade ZnS was tried to be produced by SPS method. The effects of the SPS parameters such as sintering temperature, sintering time, pressure and heating rate on the microstructural and optical characteristics of produced ZnS samples were investigated and the results were compared with those of a reference m-ZnS material.

2. Experimental Procedure

Commercial ZnS powder with an average particle size of 3-4 micrometer and commercial reference m-ZnS sample was used in this study. The reference m-ZnS sample was produced through the conventional CVD+HIP route. Powders were sintered by SPS method and sintering parameters are given in Table 1. All of the

sintering operations were carried under Argon (Ar) atmosphere. Powders were placed in a graphite mold with a diameter of 2 cm and sintered to obtain final thicknesses ranging between 1-3 mm. Pressure was 16 MPa at first heating ramp, increased to 50 MPa during second heating ramp and remained constant at 50 MPa during sintering step for all experiments. For specimens A and C, sintering steps also included heating ramps. For specimen C, sintering was concluded manually when piston travel becomes constant. As a supplementary study, selected samples, namely samples B and F, were subjected to hot isostatic pressing (HIP) under Ar atmosphere at 900 °C and 150 MPa pressure for 3 hours, with platinum foil used as an encapsulant.

Scanning electron microscopy (SEM, FEI NOVA NANO SEM 430) was used for morphology and size analysis of ZnS powders and microstructure analysis of sintered ZnS specimens. Polishing and etching was applied in order to reveal the microstructure of sintered ZnS. In order to analyze the phases of powder and phases formed after different sintering parameters, X-ray diffraction (XRD, Rigaku Miniflex 600) analysis were done, sintered specimens were pulverized for analysis. Voltage was 40 kV, diffraction angle 2θ was from 20° to 70° and the scanning rate was 2 °/min. Finally, optical transmission spectra of specimens were measured by Fourier-transform infrared spectroscopy (FTIR) between 1 and 15 μm IR region.

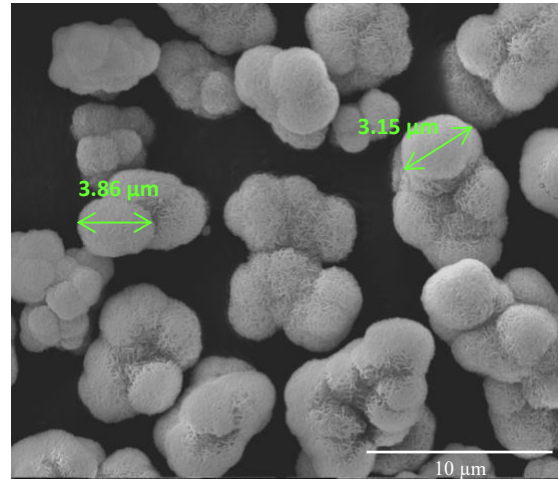


Figure 1. SEM image of ZnS powders used in the study

The microstructure of SPSed samples were examined in SEM together with the reference m-ZnS sample. The results of the microstructural analysis are shown in Figure 2 for selected samples. SEM analysis had shown that there is a large grain size difference between reference m-ZnS and ZnS samples sintered with SPS. It can be seen in Figure 2 that average grain size of m-ZnS is around 175 μm whereas specimen A has 8 μm , specimen B has 1.5 μm and specimen G has 2 μm . Owing to the advantageous properties provided by SPS such as relatively low sintering temperature and short sintering time, grain size generally does not increase as it does in other techniques such as CVD, hot pressing and pressureless sintering. Grain size of ZnS produced by CVD method is cited to be between 3-10 μm in the literature [1,7], however by SPS, 1-2 μm , and even lower grain sizes can be achieved, as also seen in this study. Also, it is known from literature that the grain size of m-ZnS produced through CVD+HIP route can reach to very high values such as hundreds of micrometers. The high grain size of the reference m-ZnS sample investigated in the study is attributed to this fact. As seen in Figure 2, pores can be observed in all of the SPSed specimens, however it is significantly less in specimen B. It was also seen that reference m-ZnS sample was essentially pore-free.

XRD results of the studied samples are given in Figure 3, together with that of the reference m-ZnS sample. The XRD peaks belonging to the cubic and hexagonal ZnS phases are labeled on the figure. As can be seen, hexagonal phase peaks can be observed in specimen A more prominently, indicating that this sample has significant amounts of the hexagonal phase in its microstructure. For the other SPSed specimens, the most pronounced peak of the hexagonal phase whose 2θ is 27° was not eliminated, suggesting that these samples also contain the hexagonal ZnS phase in their microstructure to some extent, in an essentially cubic

Table 1. SPS parameters of the Studied Samples

No.	Heating Ramp 1 (at 16 MPa)		Heating Ramp 2 (at 50 MPa)		Sintering Step (at 50 MPa)		
	HR (°C/min)	T (°C)	HR (°C/min)	T (°C)	HR (°C/min)	T (°C)	t (min)
A	100	450	100	650	10	900	5
B	100	650	10	850	-	850	10
C	100	450	100	650	10	750	-
D	100	650	10	850	-	850	10
E	100	650	10	850	-	850	10
F	100	650	10	900	-	900	10

*HR: Heating Rate, T: Temperature, t: time

3. Results and Discussion

The morphology and size of the ZnS powders used in the study was investigated in SEM. SEM images of the studied powders are given in Figure 1. As can be seen in the figure, the average particle size was measured to be around 3-4 μm . The figure also reveals that the powders had agglomerated to some extent and had a fibrous inner morphology.

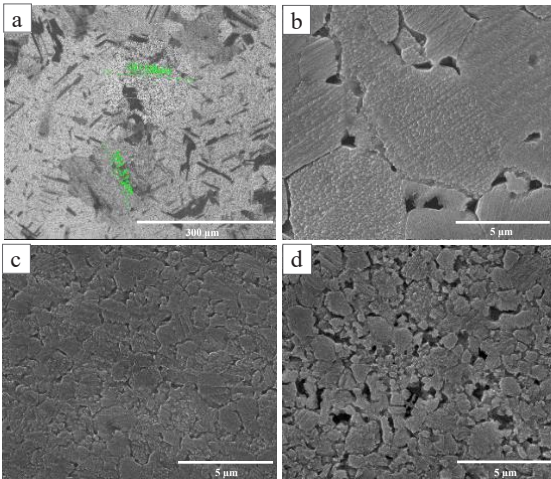


Figure 2. SEM images of a) commercial multispectral ZnS, b) specimen A, c) specimen B, d) specimen F

ZnS matrix. Reference m-ZnS, on the other hand, does not seem to have any hexagonal peak. The reason why sample A has a higher amount of the hexagonal phase in its microstructure might be related to the difference in the pressure and temperature application scheme applied to this sample in SPS. When compared to the other SPSed samples, the faster rising rate of the pressure to 50 MPa in the second heating ramp and the application of a higher sintering temperature for a relatively shorter time seems to favor the formation and/or persistence of the hexagonal phase for sample A, which is the stable phase at higher temperatures for ZnS.

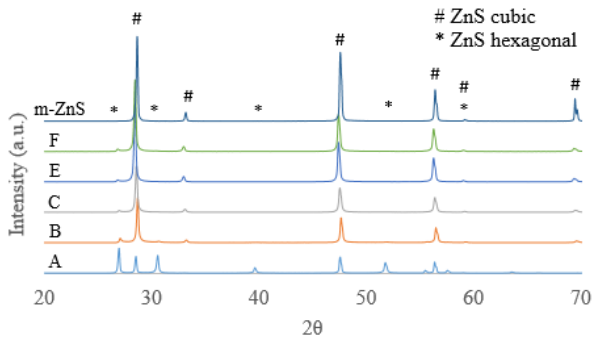


Figure 3. XRD results of the samples investigated

The optical transmission spectra of the samples investigated and the reference m-ZnS are given in Figure 4. As can be seen in this Figure, Specimen B showed a maximum of 63% transmittance at 9 μm wavelength, which was the highest transmittance observed in this study relative to the other SPSed specimens. Also, the overall transmittance of this sample within the whole 1-15 μm IR range was superior. The essentially pore free microstructure (see Figure 2) and a low amount of the highly scattering hexagonal phase (see Figure 3) is thought to contribute to the achievement of these good optical characteristics for this sample. Although the

same SPS parameters as that of sample B were applied, similar good results could not be obtained for specimens D and E. The noticeable differences between samples B, D and E were in the sintered sample thickness and microstructure. The sintered sample thickness was 1 mm for sample B, and 2 mm for samples D and E. Besides, the microstructures of samples D and E were found to resemble that of sample F (see Figure 2), rather than that of sample B, that is, a microstructure with relatively higher porosity. Owing to the peculiar electrical working principle of SPS, different sample thicknesses might result in different microstructures, and hence different optical characteristics, under the application of the same SPS parameters. The exploration of this phenomenon, however, is beyond the scope of this study and the explanation of the observed discrepancy among samples B, D and E requires further investigation. To get further insight into the effect of the sample thickness, sample F was prepared with a thickness of 2.7 mm at a slightly higher sintering temperature and thinned out by grinding and polishing to 1.5 mm. The results of this experiment are given in Figure 5, in comparison to samples B and D. The results have shown that a considerable increase in optical transmission can be obtained with decreasing sample thickness. Within the limits of this study, the main factor contributing to the degrading of the optical performance is thought to be scattering, which is caused by the presence of pores, grain boundaries and the hexagonal phase in the microstructure of the samples. Since the light transmitting through a sample will encounter less of these defects, it is rather expected that optical transmission will be enhanced with decreasing sample thickness.

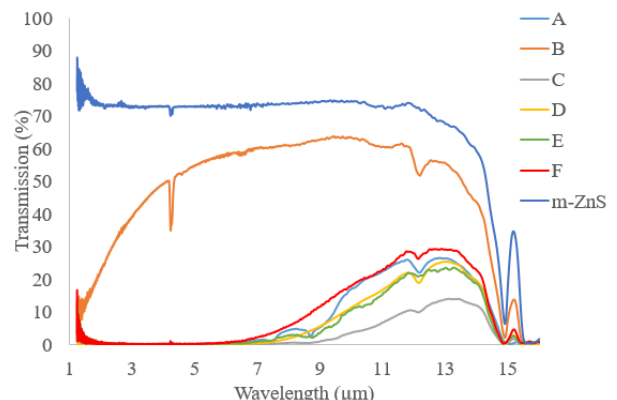


Figure 4. FTIR optical transmission spectra of the studied samples

The healing effect of HIPing on the optical transmission characteristics of s-ZnS is well documented in the literature. To examine whether such an effect can also be obtained on the SPSed samples, preliminary HIPing experiments have been conducted on samples B and F.

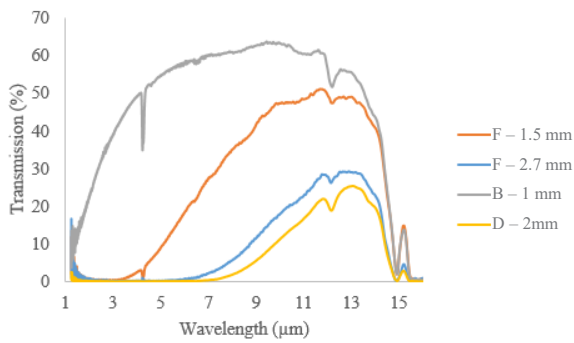


Figure 5. Effect of sample thickness on the optical transmission spectra

An examination of the results given in Figure 7, together with Figures 4 and 5, shows that the optical transmission was remarkably increased in the IR range by HIPing, especially for sample B, reaching that of the reference m-ZnS sample. In addition, the optical transmission is also enhanced in the visible range, as shown in Figure 6.

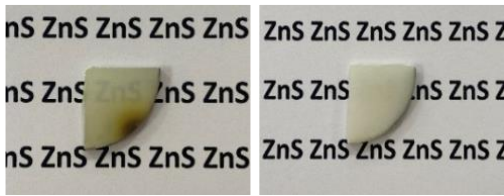


Figure 6. Photographs of HIPed specimen B (left) and specimen F (right), showing the effect of HIPing on the optical transmission characteristics in the visible range

The relatively strong absorption peak observed in the optical transmission spectra of most of the samples around 4.8 μm is known to be due to water vapor (gaseous H_2O). Although it may also be due to water contained in the samples, its presence is most probably an experimental artifact caused by the remnant water vapor entrapped inside the FTIR spectrometer during the optical transmission experiments.

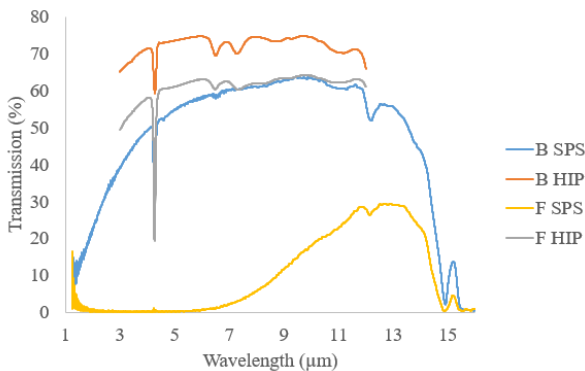


Figure 7. The effect of HIPing on the optical transmission characteristics in the IR range

Conclusion

The results of this study have shown that optical grade ZnS can be produced by SPS method, by optimizing the SPS parameters such as sintering temperature, sintering time, pressure and heating rate. Within the limits of this study, optimum sintering temperatures seem to be around 850 $^{\circ}\text{C}$ with relatively short sintering times. HIPing after SPS was found to have a considerable effect in enhancing the optical properties.

References

- [1] E. V. Yashina, *Inorganic Materials*, (2003) 786–792.
- [2] D. C. Harris, *Proc. of SPIE*, vol. 6545, (2007).
- [3] D. W. Blodgett, M.E. Thomas, D.V. Hahn, S.G. Kaplan, Longwave infrared absorption and scatter properties of ZnS and ZnSe, *Proc. SPIE 5078, Window and Dome Technologies VIII*, 26 September 2003, Orlando, Florida, pp. 137-147.
- [4] J. Khaled, T. Sato, M. Koide, H. Sato, Development of near-net dome shaped ZnS window for the infrared region using Spark Plasma Sintering technique, *Proc. SPIE 11740, Infrared Imaging Systems: Design, Analysis, Modeling, and Testing XXXII*, 12 April 2021,
- [5] W.K. Jung, J. Hong, D.H. Choi, *Journal of Ceramic Processing Research*, 22 (2021) 86-90
- [6] Y. Chen, L. Zhang, J. Zhang, P. Liu, T. Zhou, H. Zhang, D. Gong, *Optical Materials*, 50 (2015) 36–39.
- [7] D. C. Harris, M. Baronowski, L. Henneman, L. LaCroix, C. Wilson, S. Kurzius, B. Burns, K. Kitagawa, J. Gembarovic, S. M. Goodrich, C. Staats, J. J. Mecholsky, Jr., *Optical Engineering*, vol. 47, (2008).



IMPROVEMENT OF OXIDATION RESISTANCE OF CARBON FIBER WITH Bn-B₄C COATINGS

Cennet YILDIRIM^{1,2}, Muhammet Nasuh ARIK¹, Nuri SOLAK²

¹Boron Research Institute (TENMAK), ²Istanbul Technical University
Türkiye

Keywords: Boron Carbide, Boron Nitride, Fibers, Oxidation Resistance, Coatings

Abstract

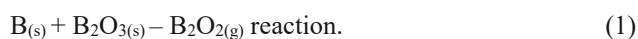
In order to improve the oxidation resistance of carbon fibers, a B₄C and BN-B₄C multilayers coatings were deposited with a chemical vapor deposition process by generating boron oxide gas species (BO-CVD). The samples were characterized by XPS, SEM, XRD, FTIR and RAMAN. The oxidation behavior of B₄C and BN- B₄C coated carbon fibers was evaluated using DTA/TG with flowing air up to 1500 °C.

1. Introduction

Carbon fibers are easily oxidized when the temperature is higher than especially 450 °C [1]. After that, their mechanical properties decrease. At present, the main high-temperature protective coating materials for the carbon fibers include silicon carbide (SiC) and boron carbide (B₄C) [2]. During the oxidation process, a protective glassy boron oxide film on the surface is formed which hinders the further oxidation. At the same time, newly formed B₂O₃ heals the surface defects such as pores and cracks on the substrate [3]. This phenomenon may help protect the mechanical properties at elevated temperature with respect to bare carbon fiber. In this work, the B₄C and BN/ B₄C coatings on carbon fibers have prepared using the boron oxide gas species during CVD (BO-CVD).

2. Materials and Methods

The PAN-based carbon fibers were selected as the substrate material. Before coating process, the epoxy coating on fiber surfaces was removed by heat treatment at 1100 °C for 6 hours. Afterwards, the mixture of B₂O₃ and B powders in 1:1 molar ratio was loaded on an alumina crucible. The substrate carbon fibers were placed on top of the alumina crucible. Subsequently, the coating process were realized in a tube furnace at different temperatures (1100, 1200, 1300, and 1400 °C) under flowing Ar gas. During the coating process, B₂O_{2(gas)} was produced as a result of;



Finally, in order to further improve the oxidation resistance, remaining surface boron oxide species was turned into BN via NH₃ gas reaction. This process was implemented at 1400 °C for 2 hours.

3. Conclusion

The B₄C/C_f and BN/B₄C/C_f were prepared by BO-CVD technique. It is observed that the B₄C coatings have formed with a uniform morphology along the surface, yet remained some boron oxide species in the upper most surface. It is later evaluated through TG analysis that these oxide species hinder the true potential of the coatings. XRD analysis revealed the B₄C formation and the BN presence was detected through Raman and FTIR analysis. As a result of these studies, it was found that the oxidation resistance of carbon fiber was improved upon coating the samples with B₄C and BN/ B₄C.

Acknowledgment

We would like to thank TENMAK-Boron Research Institute and their laboratory staff for their support during this research.

References

- [1] K. Kobayashi, K. Maeda, H. Sano, Y. Uchiyama, High temperature oxidation of carbon/SiC/B₄C composite in different atmospheres. Tanso, 1992(151), 20-26.
- [2] Q. Zhang, X. Zuo, Y. Liu, L. Zhang, L. Cheng, & X. Liu, Oxidation behaviors and mechanisms of CVD Si-B-C ceramic in wet oxygen from 700 °C to 1400 °C. Journal of the European Ceramic Society, 2016, 36(15), 3709-3715.
- [3] S. Fan, L. He, C. Yang, H. Li, S. Wang, Y. Lin, L. Cheng, Effect of B₄C on the microstructure and properties of B₄C modified three-dimensional needled C/C-SiC composites. Materials Science and Engineering: A, 2017, 706, 201-210.



SYNTHESIS OF B₄C-Al₂O₃ COMPOSITE POWDER VIA ALUMINOTHERMIC REDUCTION

Emre TOY, Oğuz KARAAHMET, Buğra ÇİÇEK

Yıldız Technical University
Türkiye

Keywords: Carbon Black, Boron Oxide, B₄C, Al₂O₃, In-situ, Composite

Abstract

Boron carbide (B₄C) is one of the well-known hardest materials used in industrial applications but it has some limitations in sintering. B₄C has poor densification ability because of its strong covalent bonds, low plasticity, and high resistance to grain boundary sliding. Therefore, high temperature and/or pressure are required for fully dense B₄C products and this process is costly. To overcome this disadvantage, aluminum oxide (Al₂O₃) can be added to the B₄C sintering powder for improving the densification ability of B₄C significantly, and also the addition of B₄C to Al₂O₃ increases hardness and fracture toughness by grain boundary pinning effect. In our study, we investigated the in-situ synthesis of B₄C-Al₂O₃ composite powder via aluminothermic reduction by examining the mechanism between aluminum and raw materials used in B₄C synthesis. Boron oxide (B₂O₃) carbon black, and metallic aluminum were used as reactants. The raw materials were mixture and the prepared mixtures were homogenized by a horizontal roller ball milling. The homogenized powders were pressed into cylindrical pellets and placed into graphite crucibles with perforated lids. The pellets were subjected to heat treatment in a controlled atmosphere furnace at 1400-1600 °C for 3 hours with an argon gas flow rate of 3l/min. As a result, the phases and microstructures of final products were characterized and B₄C-Al₂O₃ composite powder was synthesized.

1. Introduction

Boron carbide (B₄C) is one of the well-known hardest materials formed by covalent bonds of boron and carbon [1–4]. Thanks to its high hardness (~31.5 GPa Hv micro-hardness at 1 N load), elastic modulus (~450 GPa) [5–8], melting point (~2450 °C) [9–12], low density (2.52 g/cm³) [8,12] and neutron absorption capability [1,13], B₄C is

highly preferred in engineering applications such as lightweight composites, light armors, bulletproof applications, abrasives, and nozzles [13,14]. B₄C is sintered by using different types of methods such as pressureless, hot pressing, spark plasma, and isostatic press [15–20]. Due to the poor sinterability of B₄C, in studies, some additives were added to the composition to improve the sintering properties of B₄C [15,17,18,21]. In literature, Y₂O₃ and Al₂O₃ were used as densification additives to increase the density of sintered B₄C [21–23]. Furthermore, B₄C can be synthesized by using different methods such as carbothermal reduction, metallothermic reduction, synthesis from the elements, vapor phase reactions, synthesis from polymer precursors, liquid-phase reactions, and ion beam synthesis [1,24,25]. In literature, magnesiothermic and aluminothermic reduction methods which are metallothermic reduction methods were used to synthesize B₄C [26–28]. In these methods, the final products include metal oxides and borides. As a result of the aluminothermic reduction of boron oxide, aluminum oxide or aluminum borides can be obtained [26,27,29,30]. In this study, we investigated the synthesis of B₄C-Al₂O₃ composite powder via the aluminothermic reduction method by using metallic aluminum and carbon black at temperatures of 1400-1600 °C. Aluminum was used to reduce B₂O₃ to boron and obtain Al₂O₃ as sintering additives. In addition, we examined the effects of aluminum and B₂O₃ contents on the free carbon and properties of final products such as structures and compositions.

2. Experimental Procedure

The materials used were B₂O₃ (purity 98%, <200 μm), metallic aluminum powders (purity >99%, <180 μm) and carbon black (purity 99%, Dv(90) 10 μm). B₂O₃ and

metallic aluminum were used as purchased. Carbon black granules were milled to obtain powder form.

Table 1. Composition of mixtures prepared with carbon black

Code	C:B ₂ O ₃ ratio	Al (wt.%)	Code	C:B ₂ O ₃ ratio	Al (wt.%)
CB–Al0	3:1	0	XCB–Al0	1.5:1	0
CB–Al10	3:1	10	XCB–Al10	1.5:1	10
CB–Al20	3:1	20	XCB–Al20	1.5:1	20

Two compositions were prepared and these were C:B₂O₃=3:1 and C: B₂O₃=1.5:1. The reason for preparing C:B₂O₃=1.5:1 composition by adding B₂O₃ to B₂O₃=3:1 composition was to prevent the loss of boron source during the reaction. At temperatures between 1050 and 1270 °C, the B₂O₃ transforms into volatile sub-oxides, which causes the boron sources to be discharged from the furnace by the flue. To adjust the boron content in the reaction area, some samples were prepared with excess boron oxide. The mixtures were homogenized via horizontal roller ball milling machines for 10 hours and the ball/powder ratio was used as 5:1. After homogenization, the powders were formed into cylindrical pellets. The pellets were heat-treated at temperatures between 1400 and 1600 °C for 3h in an inert atmosphere with 3l/min argon gas flow. The heating and cooling rates were 15 °C/min and 3°C/min, respectively.

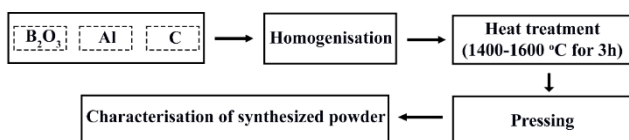


Figure 1. Flowchart of the experimental study

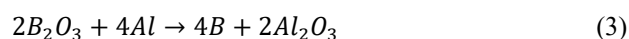
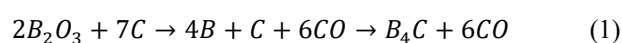
X-ray diffraction (XRD) analyses were used to determine phases in the final products. Bruker D8 Advance diffractometer was used for XRD analysis and the measurement parameters were Cu K α radiation with a step size of 0.02° (2 θ).

3. Results and Discussion

The effects of aluminum on B₄C–Al₂O₃ synthesis were examined. The heat treatments were carried out at 1400, 1500, and 1600 °C. Metallic aluminum was added with a ratio of 10/20 wt.% to the raw material mixture which was C:B₂O₃=3:1 and C:B₂O₃=1.5:1. The addition of aluminum caused the formation of different phases such as aluminum oxides and aluminum borides. Metallic aluminum couldn't observe in the final product but high carbon peaks

were observed in XRD analysis. The reason for free carbon was the lack of sufficient boron sources which is necessary to obtain B₄C. During heat treatment, B₂O₃ was transformed into vapor boron suboxide at about 1100 °C and this vapor escapes from the flue as gas. However, since the aluminum addition forms aluminum borate phases, it prevents the decrease in the amount of B₂O₃ and evaporation. Thus, B₂O₃ didn't escape from the reduction area and reacted with carbon to form B₄C. So that, the amount of free carbon decreased. Liu et. al. explained that reaction (4) is convenient above 1227 °C, as thermodynamically [31].

The overall reactions are given below [26,31],



The final products synthesized at 1400–1600 °C were examined by XRD for determining phases. In Fig. 2, XRD diffractograms of samples heat-treated at 1400 °C were given and the phases were indicated on diffractograms. Different phases were observed in Fig. 2 because of the amount of aluminum. And also, these differences depended on the boron oxide and carbon ratio. When the C and B₂O₃ ratio was 3:1, there were Al₂O₃ peaks for containing aluminum sample but there weren't any peaks in the samples have a ratio of 1.5:1. The reason for this can be an insufficient amount of B₂O₃. When aluminum was increased, the intensity of carbon peaks decreased and Al₂O₃ and Al₁₈B₄O₃₃ phases were increased. The increasing amount of B₂O₃ caused a decrease in free-carbon peak intensity.

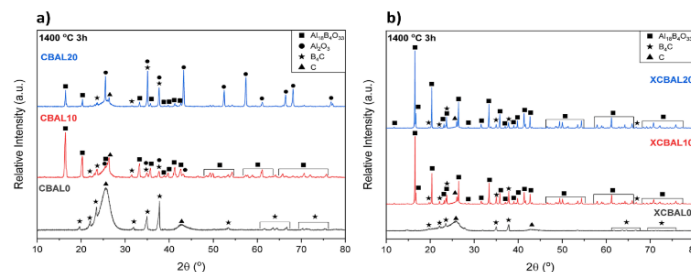


Figure 2. XRD analysis results of samples heat-treated at 1400 °C for 3 h (a) CB–Al0/10/20, (b) XCB–Al0/10/20

XRD diffractogram of samples heat-treated at 1500 °C was given in Fig. 3 and phases were indicated on diffractograms. Differently from samples heat-treated at 1400 °C, the samples hadn't $\text{Al}_{18}\text{B}_4\text{O}_{33}$ peaks. These results indicated that the aluminum borate phases decomposed at a temperature of 1500 °C. Similar to Fig. 2, the increasing B_2O_3 ratio caused to decrease in free-carbon peaks intensity. The samples with aluminum had a lower intensity of free-carbon peaks for all.

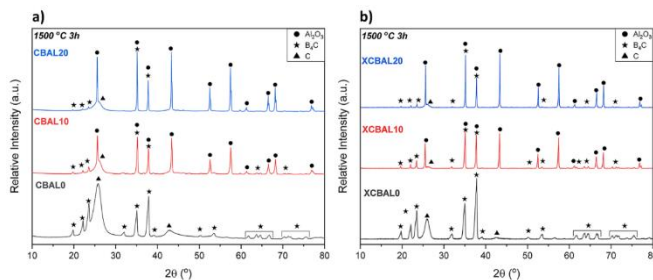


Figure 3. XRD analysis results of samples heat-treated at 1500 °C for 3 h (a) CB–Al10/10/20, (b) XCB–Al10/10/20

Similar to Fig. 3, the XRD results of samples heat-treated at 1600 °C were given in Fig. 4 and the phases are indicated on the diffractogram. Similar to Fig. 3, there weren't any peaks on $\text{Al}_{18}\text{B}_4\text{O}_{33}$ in samples, and increasing the B_2O_3 ratio caused decreasing free-carbon peaks intensity. This decrease could indicate the formation of boron carbide phases.

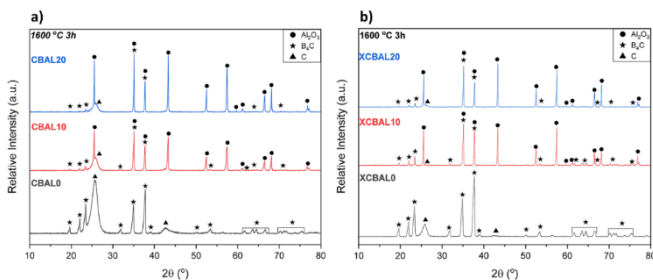


Figure 4. XRD analysis results of samples heat-treated at 1600 °C for 3 h (a) CB–Al10/10/20, (b) XCB–Al10/10/20

4. Conclusion

In this study, the synthesis of $\text{B}_4\text{C}-\text{Al}_2\text{O}_3$ composite powder via the aluminothermic reduction method was investigated. The effects of metallic aluminum amount, C: B_2O_3 ratio, and synthesis temperature on the obtained phases and free carbon amount were examined. B_4C , Al_2O_3 , $\text{Al}_{18}\text{B}_4\text{O}_{33}$, and carbon phases were observed as a result of syntheses. All the mentioned phases were observed in samples heat-treated at 1400 °C, while B_4C ,

Al_2O_3 , and carbon phases were observed in samples heat-treated at 1500 and 1600 °C. The $\text{Al}_{18}\text{B}_4\text{O}_{33}$ phase wasn't found at temperatures of 1500 and 1600 °C. This indicated that the $\text{Al}_{18}\text{B}_4\text{O}_{33}$ phase decomposes to B_2O_3 and Al_2O_3 at temperatures higher than 1500 °C. When B_2O_3 was increased by %100 for aluminum-free samples, the carbon peak intensities were decreased and the B_4C peak intensities were increased. The addition of aluminum increased the formation of B_4C and Al_2O_3 . The decreasing of free carbon peak intensities indicated the formation of B_4C . Boron sub-oxide transformation was prevented by $\text{Al}_{18}\text{B}_4\text{O}_{33}$ phase formation. So that, the escaping of boron source from the reaction area was prevented. Briefly, the increase of B_2O_3 and metallic aluminum increased the formation of B_4C and Al_2O_3 . $\text{B}_4\text{C}-\text{Al}_2\text{O}_3$ composite powders were synthesized at temperatures between 1500-1600 °C.

References

- [1] A.K. Suri, C. Subramanian, J.K. Sonber, T.S.R.C. Murthy, Synthesis and consolidation of boron carbide: A review, *Int. Mater. Rev.* 55 (2010) 4–40.
- [2] D. Emin, Unusual properties of icosahedral boron-rich solids, *J. Solid State Chem.* 179 (2006) 2791–2798.
- [3] M. Bouchacourt, F. Thevenot, The melting of boron carbide and the homogeneity range of the boron carbide phase, *J. Less-Common Met.* 67 (1979) 327–331.
- [4] F.X. Zhang, F.F. Xu, T. Mori, Q.L. Liu, A. Sato, T. Tanaka, Crystal structure of new rare-earth boron-rich solids: $\text{REB}_{28.5}\text{C}_4$, *J. Alloys Compd.* 329 (2001) 168–172.
- [5] J.H. Gieske, T.L. Aselage, D. Emin, Elastic properties of boron carbides, in: *AIP Conf. Proc.*, AIP, 1991: pp. 376–379.
- [6] K.A. Schwetz, W. Grellner, The influence of carbon on the microstructure and mechanical properties of sintered boron carbide, *J. Less-Common Met.* 82 (1981) 37–47.
- [7] D. Gerlich, G.A. Slack, Elastic properties of β -boron, *J. Mater. Sci. Lett.* 4 (1985) 639–640.
- [8] V. Dornich, S. Reynaud, R.A. Haber, M. Chhowalla, Boron Carbide: Structure, Properties, and Stability under Stress, *J. Am. Ceram. Soc.* 94 (2011) 3605–3628.
- [9] A. Alizadeh, M. Mahoodi, Investigation of the effect of argon flow on the morphology of B_4C nanoparticles synthesized by the VLS method, *J. Nanostructures.* 9 (2019) 510–520.
- [10] Y.Q. Li, T. Qiu, Oxidation behaviour of boron carbide powder, *Mater. Sci. Eng. A.* 444 (2007)

- 184–191.
- [11] L. Nikzad, T. Ebadzadeh, M.R. Vaezi, A. Tayebifard, Effect of milling on the combustion synthesis of ternary system B₂O₃, Mg and C, *Micro Nano Lett.* 7 (2012) 366.
- [12] Ian Crouch, *The Science of Armour Materials*, in: 1st Editio, Woodhead Publishing, 2016: pp. 331–393.
- [13] A.W. Weimer, *Carbide, Nitride and Boride Materials Synthesis and Processing*, in: Springer Netherlands, Dordrecht, 1997: p. 696.
- [14] T. Gray, N. Mann, Summary for Policymakers, in: *Intergovernmental Panel on Climate Change (Ed.), Clim. Chang. 2013 - Phys. Sci. Basis*, Cambridge University Press, Cambridge, 2013: pp. 1–30.
- [15] H. Biçer, M. Tuncer, Conventional and two-step sintering of boron carbide ceramics with a sintering additive, *J. Aust. Ceram. Soc.* 58 (2022) 21–27.
- [16] M.F. Toksoy, W. Rafaniello, K.Y. Xie, L. Ma, K.J. Hemker, R.A. Haber, Densification and characterization of rapid carbothermal synthesized boron carbide, *Int. J. Appl. Ceram. Technol.* 14 (2017) 443–453.
- [17] N. Firshtman, S. Kalabukhov, N. Frage, Effect of boron carbide composition on its densification behavior during spark plasma sintering (SPS), *Ceram. Int.* 44 (2018) 21842–21847.
- [18] M. Mashhadi, E. Taheri-Nassaj, V.M. Sglavo, Pressureless sintering of boron carbide, *Ceram. Int.* 36 (2010) 151–159.
- [19] G.I. Kalandadze, S.O. Shalamberidze, A.B. Peikrishvili, Sintering of boron and boron carbide, *J. Solid State Chem.* 154 (2000) 194–198.
- [20] R.N.J. Taylor, Novel powder processing of sintered boron carbide, *Key Eng. Mater.* 264–268 (2004) 45–48.
- [21] K.Y. Xie, M.F. Toksoy, K. Kuwelkar, B. Zhang, J.A. Krogstad, R.A. Haber, K.J. Hemker, Effect of Alumina on the Structure and Mechanical Properties of Spark Plasma Sintered Boron Carbide, *J. Am. Ceram. Soc.* 97 (2014) 3710–3718.
- [22] X. Lyu, Z. Zhao, H. Sun, X. Jiang, C. Hu, T. Song, Z. Luo, Influence of Y₂O₃ contents on sintering and mechanical properties of B₄C-Al₂O₃ multiphase ceramic composites, *J. Mater. Res. Technol.* 9 (2020) 11687–11701.
- [23] F. Zhang, Z. Fu, J. Zhang, H. Wang, W. Wang, Y. Wang, J. Shi, Fast densification of B₄C ceramics with Al₂O₃ as a sintering aid by spark plasma sintering, *Mater. Sci. Forum.* 620 622 (2009) 395–398.
- [24] O. Karaahmet, USE OF PARTIALLY HYDROLYZED PVA FOR BORON CARBIDE SYNTHESIS FROM POLYMERIC PRECURSOR, *Ceram. - Silikaty.* 64 (2020) 434–446.
- [25] B. Cicek, O. Karaahmet, *Bor Karbür ve Düşük Sıcaklık Bor Karbür Sentezleme Yöntemleri*, 1. Edition, Nobel Akademik Yayıncılık, 2018.
- [26] O. Torabi, R. Ebrahimi-Kahrizsangi, Synthesis of B₄C, Al₂O₃, and AlB₁₂ reinforced Al matrix nano composites via mechanochemical method, *J. Compos. Mater.* 46 (2012) 2227–2237.
- [27] A. Atasoy, The aluminothermic reduction of boric acid, *Int. J. Refract. Met. Hard Mater.* 28 (2010) 616–622.
- [28] F. Farzaneh, F. Golestanifard, M.S. Sheikhaleslami, A.A. Nourbakhsh, New route for preparing nanosized boron carbide powder via magnesiothermic reduction using mesoporous carbon, *Ceram. Int.* 41 (2015) 13658–13662.
- [29] R. Ebrahimi-Kahrizsangi, O. Torabi, Combination of mechanochemical activation and self-propagating behavior for the synthesis of nanocomposite Al₂O₃/B₄C powder, *J. Alloys Compd.* 514 (2012) 54–59.
- [30] O. Torabi, R. Ebrahimi-Kahrizsangi, Effect of the aluminum content on the mechanochemical behavior in ternary system Al-B₂O₃-C, *Int. J. Refract. Met. Hard Mater.* 36 (2013) 90–96.
- [31] Y. Liu, S. Yin, Z. Guo, L. Hoyi, Aluminum borate in the combustion synthesis of alumina/boride composite, *J. Mater. Res.* 13 (1998) 1749–1752.



EMS

Energy Materials Symposium

Enerji Malzemeleri
Sempozyumu

THE EFFECT OF IRON CONCENTRATION IN ELECTRODEPOSITED SOLUTION AND PH OF ELECTROLYTE ON PHOTOELECTROCHEMICAL HYDROGEN PRODUCTION EFFICIENCY OF HEMATITE (α - Fe_2O_3) PHOTOANODE

Ersan DOĞAÇ, İlkan KARUL, Seyedsina ALYASİN, Ömer DOĞAÇ, Fatma Betül YILMAZ, Cevat SARIOĞLU

Marmara University
Türkiye

Keywords: Hematite, Photoelectrochemical Characterization, Thermal Oxidation, Electrodeposition

Abstract

In this study, photoelectrochemical performance (PEC) of Hematite (α - Fe_2O_3) photoanode, fabricated with thermal oxidation of electrodeposited iron at 450 °C for 24 hrs. was investigated. The effect of iron concentration (0.02M, 0.04M and 0.06M $\text{FeSO}_4 \cdot 7\text{H}_2\text{O}$) in solution of iron sulfate, boric acid (H_3BO_3), and sodium sulfate (Na_2SO_4) on the PEC performance of the hematite photo anode were studied. The PEC characterization of hematite (α - Fe_2O_3) was carried out with I-V, photo voltage, PEIS, and Mott Schottky analysis in 0.1 NaOH (pH=13) solution. The best photo current of 0.22mA/cm² at 0.6 V vs. SCE was found for 0.04M $\text{FeSO}_4 \cdot 7\text{H}_2\text{O}$ the sample with 50 sec. coating time at pH 13 after optimization of Fe concentration and coating time because of determined higher donor density of $40.3 \times 10^{18} \text{ cm}^{-3}$. Photo current measured for different pH such as 7, 11, 13 and 14 were respectively 0.02, 0.11, 0.16 and 0.21 mA/cm² at 0.6 V vs. SCE. As the pH increased the photo current density increased.

1. Introduction

Nowadays many Scientists' aiming to minimize the effects of global warming by adding alternative ways. Therefore, studies in this domain have been started to reduce the usage of the fossil fuels, for instance scientists are studying hydrogen energy as an alternative to fossil fuels. Hydrogen energy is a type of renewable energy that can be easily obtained and has almost no harm to the environment.[1] There are two general pathways for converting solar energy into useful forms of energy: solar photothermal and photoelectrochemical water separation (PEC). In this process, with a help of solar energy, electrolysis of water is taken place to dissociate water into hydrogen and oxygen. [2]

Hematite is a very common iron oxide mineral (Fe_2O_3) that is found in rocks throughout the world. It is the most mined ore of iron. Because of its substantial light absorption (ideal bandgap of 1.9-2.2 eV), abundance, non-toxicity, and maximum theoretical STH efficiency of 16 % with a theoretical photocurrent of 12.6 mA/cm², hematite is an attractive material for use in photoanode. Despite its promising features, hematite performed poorly in prior investigations (maximum known photocurrent value 6 mA/cm² at 1.23V vs. RHE) when compared to theoretical values (12.6 mA/cm²) because to restrictions such as poor electrical conductivity, short hole diffusion length, and high overvoltage need.[3]

Nanostructuring synthesis techniques have been widely implemented to solve some of the limitations associated with the short hole diffusion length and poor light absorption of standard hematite photoanodes. These include atomic layer deposition, solution-based colloidal, spray pyrolysis, anodization, hydrothermal, electrochemical deposition, atmospheric pressure chemical vapor deposition and thermal oxidation. [4-8].

The thermal oxidation method is a single-step, simple, and cost-effective manufacturing technique. This procedure does not involve the use of specific or expensive equipment. In the literature, several researchers have concentrated on the growth and manufacturing of hematite nanowire and nanorod nanostructures fabricated using thermal oxidation approach after depositing Fe film on FTO substrate using PVD or electrodeposition. When iron or steel is oxidized at high temperatures, the oxide consists of multilayer scales in the sequence Fe/FeO/Fe₃O₄/Fe₂O₃. According to the iron oxygen system, the phase FeO does not occur above 570 °C. The thermal oxidation technique was used to oxidize iron or steel samples in various environment conditions such as water vapor, oxygen, air, inert and mixed gases (SO₂, CO₂, NO₂). [9-11]

Aim of this work is to study the effect of iron concentration in electrodeposited solution, coating time, and pH of electrolyte on photoelectrochemical hydrogen production efficiency of hematite (α - Fe_2O_3) photoanode.

2. Experimental Procedure

1. Prepare three coating solution with only free variable molarity of iron alloy with pH=13 and coating time of 50 sec. Solution consists of 0.02M, 0.04M, and 0.06M of Iron (II) Sulphate Heptahydrate with 0.5M Boric Acid, 0.5M Sodium Sulphate and 100ml distilled water. To investigate the effect of coating time interval is taken as 25-50-75 and 100 seconds. To study the effect of pH of electrolyte solution the pH is used between 7, 11,13 and 14. Hold up at least 2 days for the solution to rest.
2. Cleaning the FTO in ultrasonic device with 3 different materials, each for approximately 20 minutes, namely water with detergent, ethyl alcohol and acetone and at last polishing with soft cotton to avoid any remaining scratches.

- The coating or electrodeposition process is carried out with use of potansiostat. The system consists of a reference electrode, a counter electrode, and a working electrode. Connect FTO (Fluorine-Doped Tin Oxide) as working electrode. Connect Platinum as the reference and counter electrode. Also use 2 dummy before main samples.
- Thermal oxidation parameters are 450°C for 24 hours. After the thermal oxidation, allow the samples cooling.
- For the electrode preparation, link a cable about 10 cm to FTO with silicon gun.
- To characterize PEC performance of the samples, use calomel (mercury chloride) as the reference electrode and platinum as the counter electrode. FTO is connected to the working electrode part.
- Apply Open Circuit Voltage (OCV), Nyquist and Bode Impedance, Linear Sweep Voltage (LSV) and Mott-Schottky by Biologic E-C Lab.
- First, apply OCV to ensure that the material is reached out to steady state, and then carry out Nyquist and Bode Impedance analyses. Both OCV and impedance tests have to be performed with the light on and off, after that the LSV has to be applied with the light on and off at 15 second intervals, and finally the Mott-Schottky analysis has to be examined with the light on and off. For calculating the donor density and flatband potential, dielectric constant surface area, frequency and temperature are the parameters and taken as 80, 1.0 cm², 1.0 kHz, 25°C respectively.
- Sample naming is performed by considering the morality of iron, pH, duration, process, and light condition, respectively. (For example, the Mott-Schottky result of the 0.04 (named B) molar sample at pH 13, which is coated for 25 seconds at non-illuminated state, is called B1325M-0). "M" for Mott-Schottky, "P" for Impedance, "O" for OCV, "L" for LSW, and finally "1" for illuminated state and "0" for non-illuminated state.

3. Results and Discussion

The effect of concentration of iron in solution and coating time and pH on PEC performance of Hematite ($\alpha\text{-Fe}_2\text{O}_3$) was studied. The results were given below.

3.1. Effect Of Iron Concentration In Solution

To examine the effect of the molarity of the iron on PEC performance of Hematite ($\alpha\text{-Fe}_2\text{O}_3$), 3 different molarity of iron solution samples were used (pH=13 coating duration is 50 seconds) and they are 0.02M, 0.04M, 0.06M called as A1350, B1350 and C1350 respectively. LSV data of these samples were examined in Figure 1. Photo current density was determined from Figure 1 at 0.6V and tabulated in Table 1. The result indicted that the best photocurrent density of 0.22mA/cm² amongst these three samples was B1350 (50 sec coating time, pH=13 and 0,04M). The sample A1350 exhibited similar photo current value of 0.19mA/cm². This is because of similar coating thickness obtained for 0.02M and 0.04M solution during electrochemical deposition of Fe film. In Figure 1, increasing iron concentration from 0.04 M to 0.06 M

decreased the photocurrent density. Liang et al. suggested that higher concentrations for electrodeposition showed lower photocurrent density, possibly because of the non-uniformity of the electrodeposited Fe film [12].

Table 1. Photocurrent density of A, B and C samples at 0.6V vs SCE

Sample	Photocurrent Density (mA/cm ²)
A1350	0.19
B1350	0.22
C1350	0.12

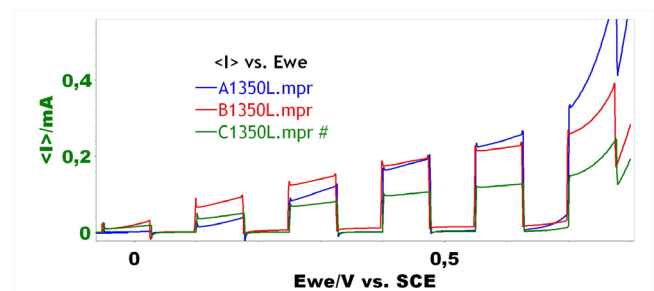
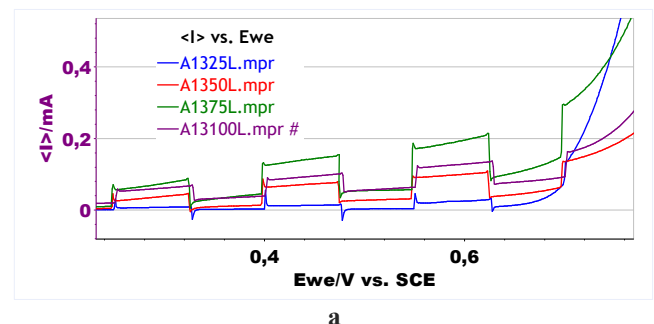


Figure 1. IV-curve of A1350(Blue), B1350(Red), C1350(Green)

3.2. Effect of Coating Time

To study the effect of coating time, 25, 50, 75 and 100 seconds were used as coating durations for both A and B samples.

In Figure 2, when the photocurrent density of the materials was examined as shown in Table 2, the photo current initially increased with coating time, then decrease after reaching maximum value. According to the literature, the moderate thickness of hematite film is essential to light absorption and charge transfer in PEC applications [12]. In this study, the highest photocurrent density for 0.04M (Iron (II) Sulphate) was found in B1350 (50 s) while for 0.02M (Iron (II) Sulphate solution) the highest photo current was found in A1375 (75s), Table 2. These results were consistent with the coating thickness of the samples. As the coating thickness increased with coating time, the photo current increased first and then when it became too thick it decreased, Table 2.



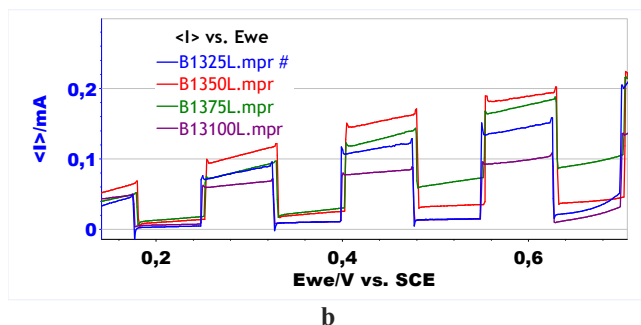


Figure 2 IV-Curve of a) A samples b) B samples at 25s,50s,75s, and 100s

Table 2. Photocurrent density of A and B samples at 0.625V vs SCE

Sample	Photocurrent Density (mA/cm ²)
A1325	0.02
A1350	0.07
A1375	0.12
A13100	0.06
B1325	0.14
B1350	0.16
B1375	0.11
B13100	0.10

3.3. The Effect of pH of Electrolyte Solution

To show the effect of pH solution on photoelectrochemical performance (PEC) of Hematite ($\alpha\text{-Fe}_2\text{O}_3$) photoanode, pH 1, 7, 11, 13 and 14 were investigated and results were presented below. The Hematite ($\alpha\text{-Fe}_2\text{O}_3$) photoanode was dissolved in solution at pH=1, therefore no data were determined for pH =1 solution.

Table 3. Photocurrent Density of Different Samples at 0.625V vs SCE

Samples	Photocurrent Density (mA/cm ²)
B775	0.03
B1175	0.11
B1375	0.16
B1475	0.21

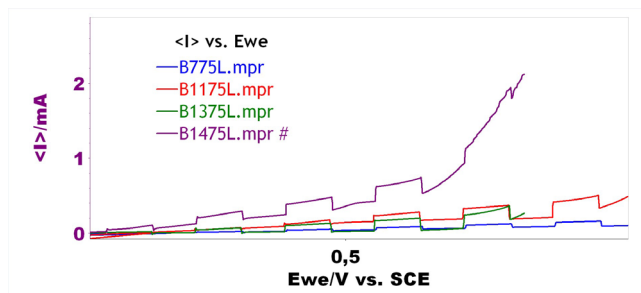


Figure 3. IV curve of samples B775(Blue), B1175(Red), B1375(Green) and B1475(Purple)

As shown in Figure 3 and Table 3, for the potential of 0.6V B775, B1175, B1375, and B1475 samples indicated that there was no significant differences between B1175, B1375 and, B1475 as 0.11, 0.16 and 0.21 mA/cm² respectively while, B775 remained at very low level of photo current density of 0.03 mA/cm². In agreement with the literature, the results showed that increasing the electrolyte pH from 7 to 14 causes the photocurrent values to increase up to 0.21 mA/cm² [13]. The highest photo current density value was obtained for the solution with pH=14. To investigate further the reason for this result, Mott-shottkly analysis were performed as shown in Figure 4. The defect concentration ($218.0 \times 10^{18} \text{ cm}^{-3}$), as indicated in Table 4 was the highest for the pH=14 solution in agreement with photo current density value in Table 3.

Table 4. Flatband Potentials and Donor Densities of Samples

Samples	Flatband Potential (V)	Donor Density (cm ⁻³)
B775M-1	-1.082	4.9×10^{18}
B1175M-1	-0.684	50.6×10^{18}
B1375M-1	-0.680	19.4×10^{18}
B1475M-1	-0.850	218.0×10^{18}

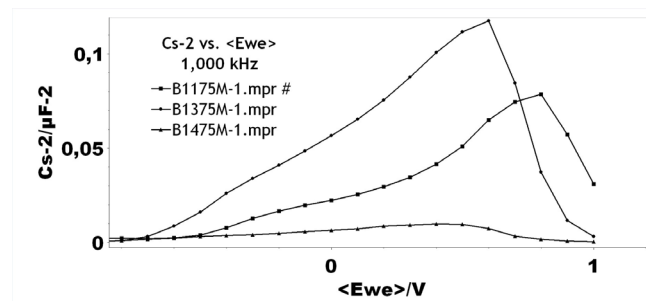


Figure 4. Mott-Schottky analysis of B1175, B1375 and B1475 in illuminated state

4. Conclusion

- A (0.02M Fe) and B (0.02M Fe) samples with 50 sec coating time exhibited the highest photocurrent density as about 0.19, and 0.22 mA/cm² respectively at 0.6 V vs. SCE for pH=13.
- As coating thickness increased with increasing coating time, the photo current initially increased with coating time, then decreased after reaching maximum value. The highest photocurrent density for 0.04M (Iron (II) Sulphate) was found in B1350 (50 s) while for 0.02M the highest photo current was found in A1375 (75s), Table 2.

- In case of pH analyses, the results indicated that as the pH increased the photocurrent density increased up to 0.21 mA/cm² for pH=14.

Acknowledgment

The completion of this Term Project Presentation could not have been possible without the participation and assistance of so many people whose names may not all be enumerated. Their contributions are sincerely appreciated and gratefully acknowledged. However, our group would like to express their deep appreciation and indebtedness particularly to the following:

MARMARA UNIVERSITY for inspiring guidance, constant encouragement with our work during all stages, to bring this article into fruition, Research assistants Alaaddin Cem OK, Şükrü KAYA and Fatma Betül YILMAZ for their inspiring guidance. Above all, to the Great Almighty, the author of knowledge and wisdom, for his countless love. Thank you.

References

- [1] W.B. Ingler, S.U.M. Khan, *Int. J. Hydrogen Energy* 30 (2005) 821
- [2] Jeon TH, Moon G, Park H and Choi W. Ultra-efficient and durable photoelectrochemical water oxidation using elaborately designed hematite nanorod arrays. *Nano Energy* (2017), 39:211- 218,
- [3] Sivula, K., Formal, F. L., Grätzel, M., *Solar Water Splitting: Progress Using Hematite (α -Fe₂O₃) Photoelectrodes*, *ChemSusChem* (2011), 4, 432-449,
- [4] Y. J. Lin, Y. Xu, M. T. Mayer, Z. I. Simpson, G. McMahon, S. Zhou and D. W. Wang, *J. Am. Chem. Soc.*, (2012), 134, 5508-5511,
- [5] Bak, T.; Nowotny, J.; Rekas, M.; Sorell, C. C.; *Int. J. of Hydrogen Energy*, (2002), 27, 991- 1022
- [6] M. A. Waghmare, V. Kadam, P. Patil, P. Sonone, *Spray Pyrolytic Deposition of Zirconium Oxide Thin Films: Influence of Concentration on Structural and Optical Properties*, *Engineered Science*, (2018), 10.30919/es8d622
- [7] C. Jorand Sartoretti, M. Ulmann, B.D. Alexander, J. Augustynski, A. Weidenkaff, *Chem. Phys. Lett.* 376 (2003) 194.
- [8] H.E. Prakasam, O.K. Varghese, M. Paulose, G.K. Mor, C. a Grimes, *Synthesis and photoelectrochemical properties of nanoporous iron (III) oxide by potentiostatic anodization*, *Nanotechnology* 17 (2006) 4285–429
- [9] Demirci, S., Tünçay, M.M., Dikici, T., Sarioğlu, C., *Effect of Thermal Oxidation Atmosphere on Photoelectrochemical (PEC) Water Splitting of Hematite Produced from Electrodeposited Fe Film*, *International Metallurgy and Materials Congress*, (2018).
- [10] Yılmaz FB and Sarioğlu C., *The effect of thermal oxidation atmosphere and temperature on PEC efficiency of hematite photoanode produced by oxidation of electrodeposited Fe thin films*, 6th IHTEC, (2022) 186-188.
- [11] André LMF, Waldemir M, Carvalho JR and Flavio LS., *Enhanced water oxidation efficiency of hematite thin films by oxygen deficient atmosphere*. *J. Mater. Res.* (2015) 30:3595-3604.
- [12] Liang P., Li L., Liu C., Wang W., Zhang H., Mitsuzaki N. and Chen Z., *Effects of cathodic electrodeposition conditions on morphology and photoelectrochemical response of α -Fe₂O₃ photoanode*, *Thin Solid Films*, (2018) 666:161-171.
- [13] Liu Y., Formal F.L., Boudoire F. and Guijarro N., *Hematite photoanodes for solar water splitting: A detailed spectroelectrochemical analysis on the pH-dependent performance*, *ACS Appl. Energy Mater.* (2019) 2:6825-6833.

THE THERMOCHEMICAL HEAT STORAGE PROPERTIES OF COMPOSITE STRUCTURES PRODUCED DIFFERENT MATRIX AND SORBENT SALTS

Behiye YÜKSEL¹, Esra AYAN², Gökhan ORHAN²

¹Halic University, ²Istanbul University-Cerrahpasa
Türkiye

Keywords: thermochemical heat storage, composite, salt in porous matrix.

Abstract

Thermochemical Heat Storage (THS) systems have a lot of attention for heat storage with the development and improvement of composite materials as storage mediums. In this study, composite materials were prepared by impregnating sorbent salt (CaCl₂, LiCl) into three different matrix materials as anodic aluminum oxide (AAO) template, vermiculite (V) and pumice (P). The cyclical heat storage behaviors of the obtained composites were investigated with the laboratory scale thermochemical heat exchanger prototype system and heat storage behaviors of different salts impregnated with different porous host materials were compared.

1. Introduction

In recent years, when energy storage has become important for the efficient use of energy, composite materials obtained by impregnated sorbent salt into a porous host matrix are among the prominent storage materials for THS systems. Many sorbent salts such as CaCl₂, LiCl, LiNO₃, MgCl₂ are used for heat storage. In addition to host matrix are widely used in the literature such as zeolite, silica gel, and vermiculite, new generation porous materials have also attracted attention in recent years [1,2].

In this study, anodic aluminium oxide templates, vermiculite and pumice used as porous host matrix. Composite materials were prepared by impregnating mono and mixed sorbent salts (CaCl₂, LiCl) into host materials. The cyclic energy density (E_d) of the obtained composite materials were investigated with the thermochemical heat exchanger prototype system.

2. Materials and Method

AAO templates with regular pore structure were obtained by applying two-step anodization method to high purity (99.99%) aluminium plates. Salt impregnation was carried out under vacuum for AAO and in open atmosphere for vermiculite and pumice. Composite materials obtained as a result of salt impregnation were characterized by a prototype. Experiments were carried out as three successive discharge-charge cycles and the cyclic behaviour of composites were investigated. Figure 1 and Figure 2 shows the cyclic energy density (E_d) values of composites over three discharge cycles.

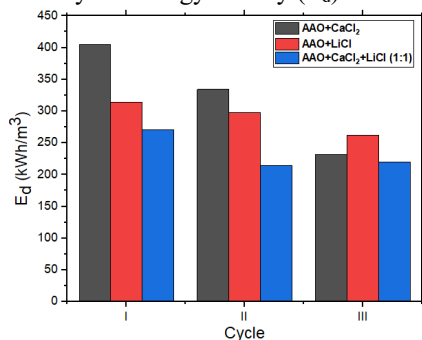


Figure 1. E_d values of AAO composites

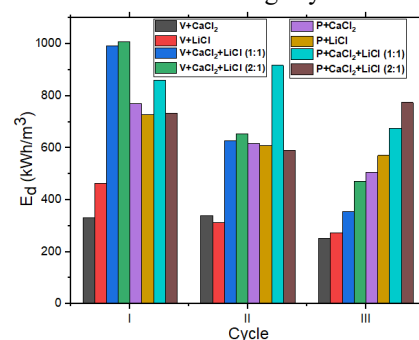


Figure 2. E_d values of natural rock composites

3. Conclusion

According to the results, E_d values of composites decreased with increasing cycle number and higher E_d was obtained for the mixed salt composites (excluding AAO) for the first cycle.

Acknowledgement

This study was supported by the Scientific and Technological Research Council of Turkey (TUBITAK) (Project No: 119M073).

References

- [1] N. Yu, R.Z. Wang and L.W. Wang, Progress in Energy and Combustion Science, 39 (2013) 489-514.
- [2] D. Aydin, S.P. Casey and S. Riffat, Renewable and Sustainable Energy Reviews, 41 (2015) 356-367.

ADVANCED MATERIAL SOLUTIONS FOR SAFER AND LONG-LASTING HIGH CAPACITY COBALT FREE BATTERIES FOR STATIONARY STORAGE APPLICATIONS (CoFBAT)

Kamil Burak DERMECI, Kato DAEMS, Joeri Van MIERLO, Maitane BEREIBAR

Vrije Universiteit Brussel
Belgium

Keywords: Li-ion Batteries, LNMO, Gel Polymer Electrolytes, Si, TiNb₂O₇

Abstract

The CoFBAT project aims to use LNMO cathodes, Si or metal oxide-based anodes and a gel type electrolyte to improve the power performance, energy density (750 Wh/L), lifetime, safety, recycling and reduce the cost (0.03 €/kWh/cycle) of the batteries. CoFBAT combines the expertise of material development, battery science, large-scale battery producers, life cycle assessment and recycling by combining Multiphysics based continuum scale modelling with experimental validation and manufacturing of battery cells.

1. Introduction

Nowadays, the need for decentralization of the energy production within Europe is increasing day by day. In order to strengthen competitiveness in advanced materials and nanotechnologies related to energy storage value chain, Europe should become more independent from raw materials supply towards recycling and metal recovery in the Li-ion battery industry.

Cobalt is a key material for the production of Li-ion batteries. According to the latest studies, there will not be enough cobalt in the near future to meet the market needs due to rapid growth of its demand. The EU targets for stationary storage and electromobility are at risk. In this sense, CoFBAT project offers an alternative solution by introducing high voltage spinel Li₁Ni_{0.5}Mn_{1.5}O₄ (LNMO) cathodes with no cobalt used. Thanks to the high-voltage gel polymer electrolytes and next generation anodes (Si and TiNb₂O₇); longer lifetime (up to 10,000 cycles), lower costs (down to 0.03 €/kWh/cycle), improved safety and more efficient recycling (>50%) is expected with 30Ah cells.

2. Materials and Methods

The CoFBAT project uses KPI's defined by industrial partners to meet the market needs of battery technologies. Optimized battery materials will be characterized, evaluated and manufactured in a coin cell, monolayer pouch cell and a stacked pouch cell. Advanced characterization techniques are used for morphological, structural, physico-chemical and electrochemical analysis of the cell components and their interfaces. A Multiphysics based model to understand the mechanisms and influence of parameters is created to give feedback for cell development. One cell chemistry will be chosen to scale up for large prismatic cells and validate by electrical, mechanical and thermal assessment. Figure 1 shows overall CoFBAT concept.

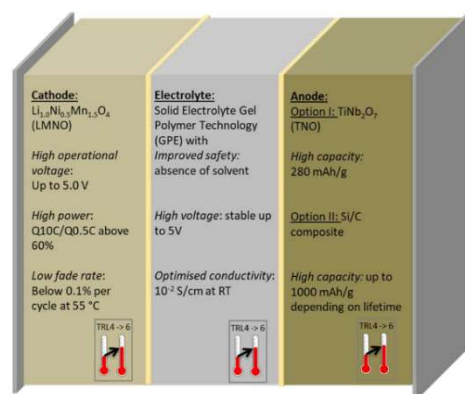


Figure 1. CoFBAT concept

3. Conclusion

The ultimate goal for the CoFBAT project is to achieve a superior battery by creating, validating and optimizing LNMO cathode, Si and TNO anodes and gel polymer electrolyte materials. A product process plan for mass production, life cycle assessment and recycling process will be developed for the resulting CoFBAT battery.

Acknowledgement

This project has received funding from the European Union's Horizon 2020 Research and Innovation Programme under Grant Agreement No 875126.



MATERIAL SUPPLY RISK FOR THIN FILM SOLAR CELLS AND IMPORTANCE OF RECYCLING

Ioanna TEKNETZI, Burçak EBİN

Chalmers University of Technology
Sweden

Keywords: photovoltaic waste, thin film solar cells, material supply, recycling, extraction

Abstract

This research focuses on two crucial points; the metal need of the thin film PV industry and their impacts on the market and recycling of these metals from manufacturing and end-of-life waste. The analysis clearly showed that silver, indium, and gallium supplies are the bottlenecks of the industry due to resource limitations and the importance of the other industrial applications of these metals. Considering recycling of copper-indium-gallium-diselenide thin-film solar cells, hydrometallurgical approach is the only direction for the recovery of critical and valuable metals. One step acidic leaching results indicate that 100% Ag and 55% In extractions are possible, but purification stages are needed to reuse the metals in the PV industry.

1. Introduction

Solar energy is accepted as the key to a clean energy future and limiting the effects of climate change. The energy transformation from fossil fuels to renewable sources has significant challenges due to raw material shortages. International Energy Agency has an ambitious target to reach photovoltaic (PV) solar panel capacity that covers more than 20% of the global energy demand. The cumulative installed worldwide PV capacity has been increasing exponentially since 2010 and it will continue in the same trend to meet the energy need.

Although policymakers and manufacturers draw a bright future, natural source limitation is a nightmare for PV technology. Especially, silver (Ag) and indium (In) are critical metals for the industry considering their other usages. Additionally, end-of-life solar panels will dramatically affect the waste stream, and currently, there is no sustainable recycling for their waste. Thus

2. Materials and Methods

The required metal supply for the thin film PV industry was studied by literature investigations covering scientific papers, technology and market news, state and company reports, and also interviews were conducted with related stakeholders from academia and industry.

Waste thin film CIGS solar cells and modules were supplied by a solar cell manufacturer. Nitric acid leaching at room temperature was applied to recover valuable metals with a focus on silver (Ag), indium (In) and gallium (Ga). The elemental composition of the waste and extracted metal amounts were analyzed by inductively coupled plasma optical emission spectroscopy (ICP-OES).

3. Conclusion

Silver is accepted as a key element for PV technologies and is used in busbars and fingers due to its high electrical conductivity. PV manufacturers are aware of its supply risk and working on reducing its consumption in the cells, as well as investigating different materials such as copper and graphene to replace with silver. However, reducing the silver amount in PV modules decreases the recoverable material value dramatically, thus becoming a significant obstacle to developing a feasible recycling process.

Indium compounds have critical importance for thin-film, heterojunction, and tandem PV technologies as transparent conductive oxide and absorber layer. Considering the increased demand in its main usage area which is electronic screen technologies and zero recycling from end-of-life products, its long-term supply and price stability is a challenge for the industry.

Silver and indium are recovered from CIGS solar cells together with other valuable metals by nitric acid leaching at room temperature. The recovery rates reached 100% for silver and 55% for indium. However, the obtained leachate should be further treated to purify the valuable metals.

Acknowledgment

This research was funded by Swedish Energy Agency, Project No: 49349-1.

AN INDUSTRIAL ECOLOGY PERSPECTIVE OF BATTERY TECHNOLOGIES FOR ELECTROMOBILITY: LCA OF SOLID-STATE LIS BATTERY

Burak ŞEN¹, Ahsen AKBULUT¹, Abdulkadir KIZILASLAN¹, Mahmud TOKUR¹, Murat KÜÇÜKVAR², Nuri Cihat ONAT², Hatem AKBULUT¹

¹Sakarya University, ²Qatar University
Türkiye, Qatar

Keywords: Solid-state battery, lithium sulfur battery, life cycle assessment, sustainable transportation, electromobility

Abstract

This study investigates the sustainability of an emerging lithium-based battery technology (i.e., lithium sulfur battery, LiS) from the perspective of industrial ecology. According to the results, the use of argon and sulfuric acid in the production of LiS pouch cells may cause adverse environmental impacts.

1. Introduction

New battery chemistries capable of outperforming LIBs not only electrochemically but also environmentally are needed to facilitate the electrification of transportation. LiS technology is a promising option among other technologies, given their higher theoretical energy density, cost-effective production, and more sustainable profile relative to LIBs. Life cycle assessment (LCA) is a methodological framework from the IE toolbox widely used to assess the potential environmental impacts of a product or service system from a systems perspective.

2. Methods and materials

The LCA framework has been employed to investigate the sustainability implications of manufacturing a solid-state LiS battery (546.17 Wh/kg). The developed battery uses $\text{Li}_7\text{P}_3\text{S}_{11}$ as the solid electrolyte, graphene sulfur composite (GSC) as the cathode, and lithium as the anode. A battery configuration model has been configured to scale a solid-state LiS pouch cell up to a LiS battery pack and constructed a life cycle inventory (LCI) for the configured pack, as shown in Figure 1.

3. Results & conclusions

The manufacturing of a solid-state LiS battery pack that provides 1 kWh requires the supply of 20 kg of energy resources. More than 90% of this demand is attributable to the production of solid-state LiS pouch cell and approximately 5% of it is attributable to the Turkish electricity grid mix. The use of argon accounted for about 35% of the climate change impact (i.e., GWP), as shown in Figure 2.

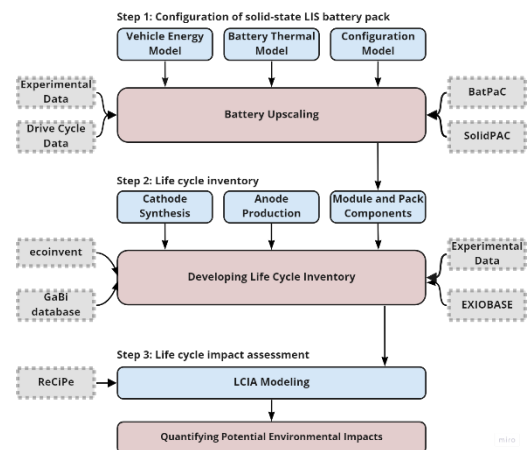


Figure 1. The modeling framework employed

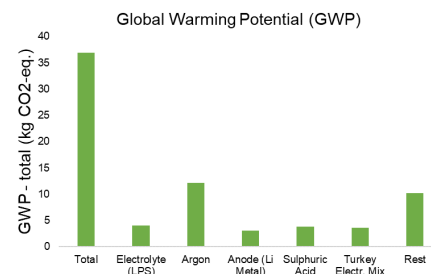


Figure 2. LCA results for a 1kWh of LiS battery



ELECTROCHEMICAL NOISE MEASUREMENT IN BATTERIES WITH METALLIC LITHIUM ANODES

Gözde KARAOĞLU, Burak ÜLGÜT

Bilkent University
Türkiye

Keywords: Electrochemical Noise, Lithium, Primary Batteries

1. Introduction

Electrochemical noise measurements are well known in corrosion literature. From the measurements, it is possible to identify the mode of corrosion and distinguish between localized corrosion types and the uniform ones when it is analyzed in conjunction with post-mortem studies. In recent years, the increase in the use of lithium-ion batteries demands the development of tests that are faster, easier, cheaper and, if possible, non-destructive and non-perturbing. Noise measurements are an ideal candidate as they are fully benign, only passively measuring without any excitations. Although some electrochemical noise studies have begun to be carried out on batteries, the literature on this subject is scarce and questionable. Electrochemical noise measurement of Li batteries can be ultimately used as a non-invasive tool to diagnose the battery health and we have already shown that non-rechargeable batteries with Li/MnO₂ chemistry shows increase in voltage noise after being exposed to a short circuit. As a result, morphological changes on metallic lithium can be detected by electrochemical noise measurements and this method can be used as non-invasive diagnosis tool.[1] Lithium metal-based chemistries have a much higher energy density than the currently commercial rechargeable chemistries because of the use of Lithium-aluminum alloy in rechargeable chemistries, as opposed to metallic Lithium used at the anode. It is known that charging of lithium metal electrode can result in the formation of lithium dendrites. These dendrites can disrupt the separator separating the anode from the cathode, exposing the battery to a short circuit or even causing the battery to burn or explode. For this reason, the pre-detection of any potential dendrite formation is both academically interesting and industrially important. Some preliminary studies show that noise level increase drastically after charging. Moreover, the anodes of the charged batteries were also examined with SEM and serious deterioration was observed in the anode of the battery after charging. Just like noise measurements on non-rechargeable batteries with lithium chemistry exposed to short circuits, it is worthy to study on and develop pre-detection method for in lithium batteries that are prone to form dendrite during charging and discharging cycles by using electrochemical noise measurements. For this reason, we also conduct noise studies with symmetrical and asymmetric cells (Li/Li, Cu/Cu and Li/Cu) prepared in the glove box and examine the details of the noise increase in a controlled and detailed manner.

2. Materials and Methods

CR2032 Li/MnO₂ coin cells were subjected to the electrochemical noise analysis

3. Conclusion

In this talk, we will discuss details of electrochemical noise of metallic lithium-based batteries. These details involve measurement methods, reasons for increase and sources of the noise. We will present both noise measurements and imaging with optical microscope in situ and post-mortem with spectroscopic analysis.

References

[1] Karaoglu G; Uzundal CB; Ulgut B; “Uneven Discharge of Metallic Lithium Causes Increased Voltage Noise in Li/MnO₂ Primary Batteries upon Shorting, submitted.

INVESTIGATING THE ELECTROCHEMICAL PERFORMANCE OF DOUBLE SHELL CATHODE ACTIVE MATERIALS FOR LITHIUM ION BATTERIES

Elif SARİKAS, Ipek TUNC, Ozgul KELES

Istanbul Technical University
Türkiye

Keywords: Cathode active materials, Core-shell structure, NMC

1. Introduction

The increasing effects of global warming force humans to decrease their carbon footprint and CO₂ emissions in all fields. Transportation makes up a large part of carbon footprint. In this field, electric cars provide an opportunity to fulfil this aim [1]. Producing a rechargeable battery with high performance, long cycle life and capacity retention is the aim of many researchers. As the limiting factor of performance in lithium ion batteries, cathode active materials with desired properties must be developed [2].

2. Materials and Methods

In this study, lithium nickel cobalt manganese oxide (NMC) as cathode active material is synthesized via co-precipitation method. The active material composition is designed to be in double shell structure as NMC 811/721/622 and 811/622/111 for core, inner shell, and outer shell, respectively. The change in composition is obtained by modifying the stoichiometry of the transition metal solution. NaOH solution is used as precipitating agent and NH₄OH solution is used to adjust the chelating agent. The precipitate is collected and mixed with LiOH, then calcined at 500 °C for 6 hours and at 850 °C for 12 hours. The crystal structure of synthesized NMC 811/721/622 core-shell active materials before and after calcination is investigated by X-ray diffraction method and results are given in Figure 1. The electrochemical performance is investigated by galvanostatic tests, cyclic voltammetry and impedance analysis. Preliminary galvanostatic test results for NMC 811/721/622 could be seen in Figure 2.

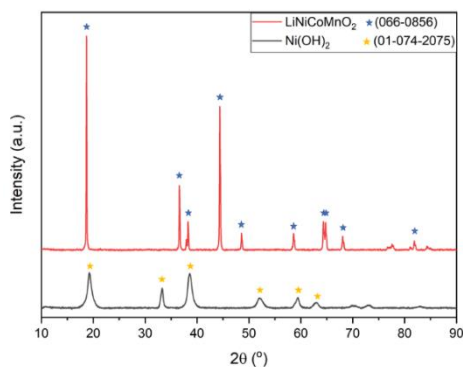


Figure 1. XRD patterns of synthesized powder

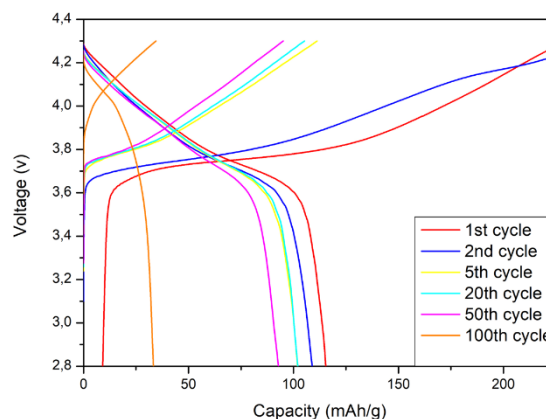


Figure 2. Preliminary galvanostatic test results of NMC 811/721/622 double shell active materials

3. Conclusion

Due to high proportion of nickel presenting in the structure, the XRD pattern of pre-calcination is matching with nickel hydroxide as expected. After calcination all peaks are found to be suitable with NMC811. The initial discharge capacity of the active material was determined as 115 mAh/g.

The present study aims to develop cathode active materials with improved structural stability and capacity retention due to double shell design.

References

- [1] Lamb, W. F., Wiedmann, T., Pongratz, J., Andrew, R., Crippa, M., Olivier, J. G., Minx, J. (2021). A review of trends and drivers of greenhouse gas emissions by sector from 1990 to 2018. *Environmental Research Letters*, 16(7), 073005. doi:10.1088/1748-9326/abee4e
- [2] Liu, C., Neale, Z. G., & Cao, G. (2016). Understanding electrochemical potentials of cathode materials in rechargeable batteries. *Materials Today*, 19(2), 109-123. doi:10.1016/j.mattod.2015.10.009.



COMPOSITE ELECTRODES PRODUCTION USING NICKEL-TITANIUM ORTHODONTIC WASTE AND INVESTIGATION OF THEIR USES IN LITHIUM ION BATTERIES (LIBS)

Humza ASHRAF¹, B. Deniz KARAHAN^{1,2}

¹Istanbul Medipol University, ²Istanbul Technical University
Türkiye

Keywords: Biomedical Waste, Metal Recovery, Composite Fabrication, Anode Material, Lithium-Ion Batteries

Abstract

Limited metal deposits on Earth and a rise in energy prices cause the value of the metals, produced by the primary method, to be increased continuously in the metal market. Therefore, instead of primary production, recycling and recovery become more important. In this study, an economical, and practical method for extracting nickel and titanium, as their oxides form, has been proposed by leaching the orthodontic waste (nickel-titanium wires) with sulfuric acid. In this scope, firstly an optimization of leaching has been realized then TiO₂ rich and NiO rich powders have been fabricated, from the leachate, by chemical precipitation at pH 1 and 10, respectively. Moreover, these powders have been mechanically mixed with a weight ratio of 1:6 (TiO₂: NiO). Then, all fabricated powders have been characterized structurally, chemically, and morphologically. The possible uses of these powders have been studied as anode material in lithium-ion batteries based on their potentiostatic and galvanostatic test performances. This study defines another way to coop with biomedical waste efficiently and solves the problem of waste management as well as their inexpensive but practical use as energy storage anode material in LIB.

1. Introduction

The requisite of clean renewable power sources and revolution in research and technology gave birth to many different power alternatives. Among them, lithium-ion batteries (LIB) are the most renowned ones due to their features such as having lightweight, excellent energy density, and long cycle life [1][2]. Because of that LIBs are utilized in almost all areas of our daily life and their demands are increased exponentially. It is estimated that the market of LIB is going to expand up to \$300 billion by 2050 and per year power production requirement will achieve 4-12 TWh [3]. For the satisfaction of this energy demand and power production through LIB, 19-50 metric tons of raw material (anode and cathode) must be produced annually [3]. The continual depleting metal

reserves and increased energy cost have raised the per ton production cost of metal through primary routes. As a result of expensive metal prices and elevated energy demands recycling and recovery of values from different waste is found to be promising. The biomedicine market involves the consumption of valuable metals in vast quantities. According to a survey, the total amount of metals used in the biomedical application, constitutes more than 57% of iron, 21% of titanium, and 6% of other metals like nickel [4]. These metals can be recovered from waste by designing an economical and practical method. Then after the recovery, they may be structured to be re-utilized in different applications such as electrode material for lithium-ion batteries. In the near past, the recovery of valuable materials from different wastes and structuring them for energy storage material in LIB have been reported [5][6]. But no effort has been found in the open literature to fabricate electrode materials from NiTi orthodontic waste.

Up to now, Özgün et al [7] recovered titanium dioxide and nickel oxide by chemical precipitation from the leached solution of orthodontic waste and reported each powder properties. Then, Ans et al [8] leached NiTi wires and optimized the Ni recovery efficiency by design of experiment.

Unlikely, herein, firstly biomedical (orthodontic) waste has been leached with sulfuric acid with 100% efficiency, then selective metal recovery, through chemical precipitation, was done at two different pHs. Afterward, first time in the open literature, a composite powder was fabricated by high-energy ball milling of these two powders to be able to utilize them effectively as electrode material for lithium-ion batteries.

2. Experimental

2.1. Experimental procedure

Orthodontic waste was first cleansed in a sonication bath with water at 60°C for 2 hours. Then, an optimization in the leaching efficiency was realized. A 100% leaching

efficiency was achieved when 5M H₂SO₄ solution was used at 90°C, with a solid to liquid ratio of 1:50 for 4 hours, in the reflux system under magnetic stirring conditions. After that TiO₂-rich and NiO-rich powders were chemically precipitated separately, using 14M NaOH solution, at pH 1 and 10 respectively. After washing them, these powders were dried in a vacuum oven at 80°C overnight then at 300°C for 2 hours. Then the composite was fabricated using high-energy ball milling (VARSAN) of two powders in the weight ratio of 1:6 (TiO₂: NiO) at 300 RPM for 2 hours in an argon environment. Ball to powder ratio was kept at 20:1 and ethanol was used as a process control reagent (PCR) for 5% of the weight of the powder. Then composite was dried in a vacuum oven at 80°C overnight.

2.2. Morphological, structural, and chemical characterizations of powders

The morphologies of three samples were observed by using a scanning electron microscope (SEM, Zeiss Gemini 500), and chemical analysis was realized by XRF. The structural analysis was performed with an X-ray diffractometer (XRD, Bruker AXS/Discovery D8) between 10°-90° by Cu K α with a scanning rate of 0.02°/sec.

2.3. Electrochemical characterization

For the electrode fabrication, the uniform slurry was prepared by blending 60%wt active material, 25%wt Timcal-C64 as conductor, and 15%wt polyvinylidene difluoride (PVDF, Gelon) as a binder in solvent N-Methyl-Pyrrolidone (NMP, EMPLURA®). Coin cell (using CR2032, MTI Corp.) assembly was realized in an Ar-filled glovebox (LABmaster Pro, MBRAUN, <0.1 ppm H₂O and O₂) as defined in our previous work [5]. Galvanostatic tests were conducted using Neware Battery Analyzer under a current load of 50 mA g⁻¹ between 10mV-3V vs. Li/Li⁺. Then, the lithiation mechanism of each electrode was studied by cyclic voltammetry (CV) at a scan rate of 0.2V s⁻¹ between 1mV-3V (vs Li/Li⁺) (Gamry Interface1000E), and electrochemical impedance spectroscopy (EIS) of each electrode was measured at 10mV, from 0.01Hz to 100kHz in symmetrical cells, as suggested by Chen et al. [9], for the elimination of intrusion by Li during impedance testing.

3. Results and Discussion

3.1. Morphological, structural, and chemical characterizations of powders

Powders' shape and morphology were analyzed by scanning electron microscopy. SEM analysis shows that TiO₂-rich, NiO-rich, and composite powders are comprising of nano-sized, irregular-shaped particles which tend to agglomerate and form relatively bigger particles (Figure 1). But it can be observed that for

composite, particle size is much smaller and uniform than the two parent powders. These nano sized particles are beneficial to have as they provide higher surface area, offer higher sites for lithium intercalation/insertion, and improves electrolyte-powder contact interface. Figure 2 shows that at pH 1 titanium ions are selectively precipitated and at pH 10 nickel ions are precipitated, respectively. XRF results (Table 1) agree with XRD outcomes. The fact that at pH:1 not all titanium is recovered from the leachate, at pH 10 some amount of Ti is found to be present along with Ni. XRD pattern of composite powder contains all those peaks of the two parent samples. Herein it is worth noting that some peaks related to NiO are lost ($2\theta = 22.6^\circ, 23.6^\circ, 46.2^\circ$) and new peaks ($2\theta = 28.3^\circ, 29.4^\circ$) appear in the composite powder. The latter shows that ball milling promotes partial phase transformation in the composite powder.

3.2. Electrochemical characterization

Fig.3 (a-c) show that the 1st discharge capacities, of TiO₂-rich, NiO-rich, and the composite powders :281 mAhg⁻¹, 331 mAhg⁻¹, and 517.9 mAhg⁻¹, respectively. In every sample, a remarkable decrease in the capacity is noted similar to the literature [10][11]. After 50 cycles the capacities delivered by three electrodes were 147 mAhg⁻¹, 187.9 mAhg⁻¹, and 363 mAhg⁻¹, respectively. Pure NiO has high theoretical capacity (718 mAh g⁻¹) but could not get the breakthrough in LIB due to its poor ionic and electrical conductivity, large volumetric expansion, and low lithiation kinetics of conversion type reaction [12]. On the other hand, TiO₂ possesses good capacity retention, incredible cycle stability, low volume expansion (less than 4%), higher coulombic efficiency, and faster Li intercalation kinetics as it offers suitable sites for intercalation and provide better electric conductivity [12][13][14]. But its low capacity restricted its utilization.

Moreover, when the voltage capacity curves of TiO₂ (inset Figure 3a) and NiO-rich (inset Figure 3b) electrodes are studied, the first one exhibits lower capacity with excellent capacity retention but the later exhibit relatively higher capacity with poor capacity retention, as expected. Therefore, composite fabrication of these two powders proved to be a profitable attempt as the composite electrode delivers higher capacity with enhanced capacity retention than those of NiO (inset Figure 3b). This shows that in the composite powder TiO₂ not only avoids particle agglomeration, improves electronic conductivity and promotes the Li⁺ diffusion by controlling SEI layer formation [12], but also acts as barrier to volumetric change in NiO and imparts structural stability which eventually enhances electrochemical performance [14][15].

In voltage-capacity curves of TiO_2 , mainly two plateaus are observed at 1.75V and 1.9V in discharge and charge curves, respectively. These two are the characteristics plateaus representing the insertion of Li^+ in tetrahedral sites and the extraction of Li^+ from octahedral sites, following the reaction given by equation (1) [16]. A slight bend is observed at around 0.75V, which got vanished in succeeding cycles. This bend can be attributed to irreversible SEI formation [17]. For the voltage-curve of the NiO-rich sample, a remarkable plateau is noted at around 0.75V in 1st discharge curve due to the conversion reaction of NiO with Li given by equation (2), and SEI formation [11]. This plateau got shifted to around 1V in subsequent cycles due to polarization effect. In the charge curve, two bends at 1.45V and 2.25V are due to SEI decomposition and reaction between Ni and Li_2O [18]. These results are consistent with the previous studies [16][11]. When, the voltage capacity curves of the composite are observed, almost all plateaus are found in the curves of those constituent powders but the performance of NiO powder is more dominant as its weight ratio is larger than that of TiO_2 .

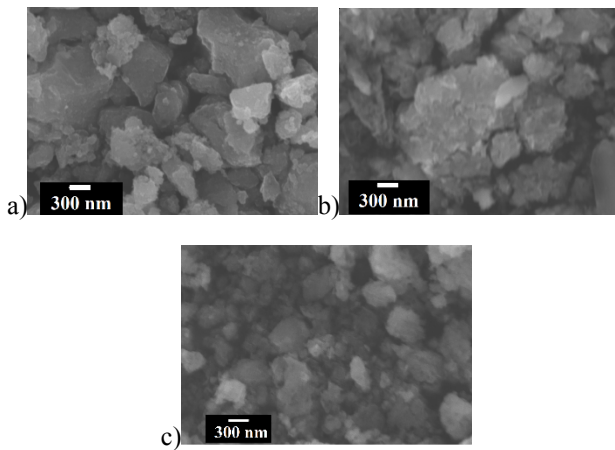


Figure 1. SEM images of a) TiO_2 b) NiO-rich & c) 1:6 (TiO_2 : NiO) composite

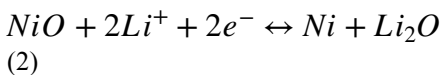
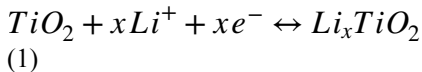


Figure 4 exhibits the cyclic voltammogram of the powders. In the first cathodic scan of TiO_2 -rich sample an intense peak at 1.75V is appeared representing the insertion of Li^+ in TiO_2 (see Eq (1)), and the other peak appeared around 0.73V due to the irreversible SEI formation got wiped out in later cycles. In the anodic scan, only an intense peak appeared at 2V representing the extraction of Li from Li_xTiO_2 [10] [16]. Then for NiO

rich powder, a cathodic peak appearing at 0.7 V signifies the SEI formation and the reduction of NiO. These peaks later got weakened and shifted around 1V due to polarization [11]. In an anodic scan, two humps are observed at 1.45V and 2.25V. The first hump reflects the decomposition of the electrolyte but the second hump corresponds to the oxidation reaction of Ni with Li_2O [18]. These CV outcomes are in agreement with the voltage capacity curves. Likewise, the CV of the composite powder (Fig.4c) contains all the characteristic peaks of its parent constituents, but the NiO character is more dominant due to its excess quantity.

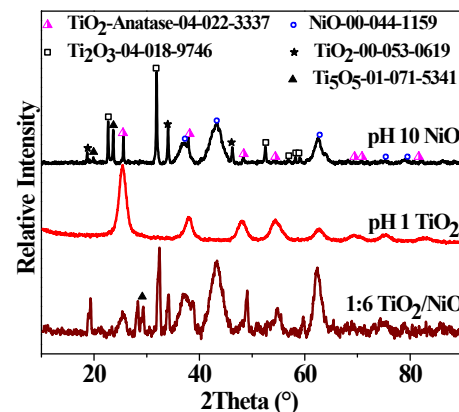
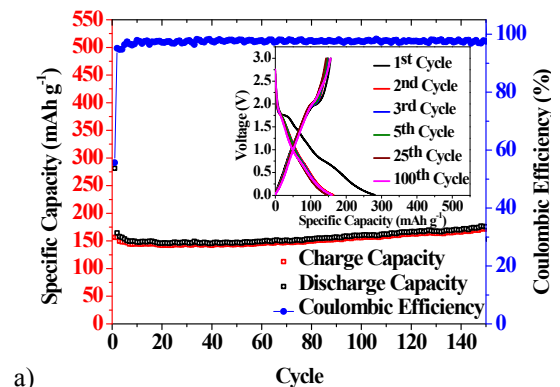


Figure 2. XRD pattern of TiO_2 -rich powder, NiO-rich powder, and the composite powder

Table 1. XRF analysis of fabricated powder (wt%)

Powder	Ni	Ti	Fe	S	Cr
TiO_2 -rich powder	0.17	94.55	1.4	3.55	0.17
NiO-rich powder	84.76	0.5	1.28	12.2	0.36



a)

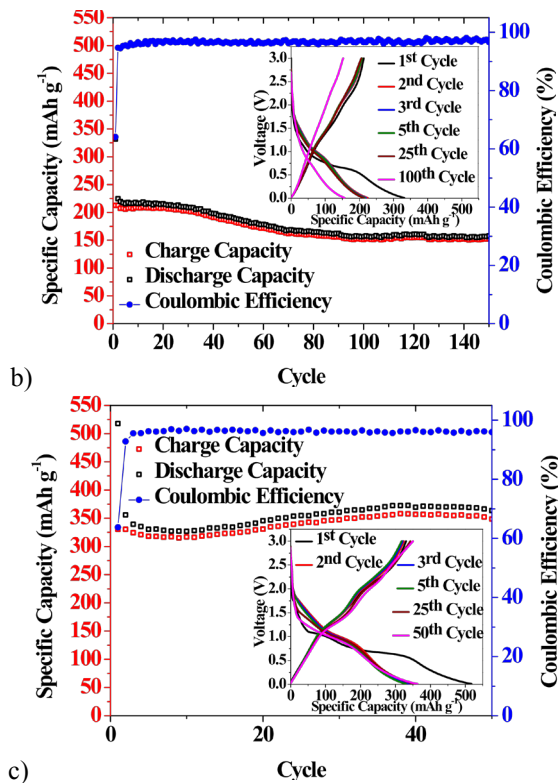


Figure 3. Galvanostatic charge-discharge and Voltage capacity curves of a) TiO₂-rich powder, b) NiO-rich powder, and c) the composite powder

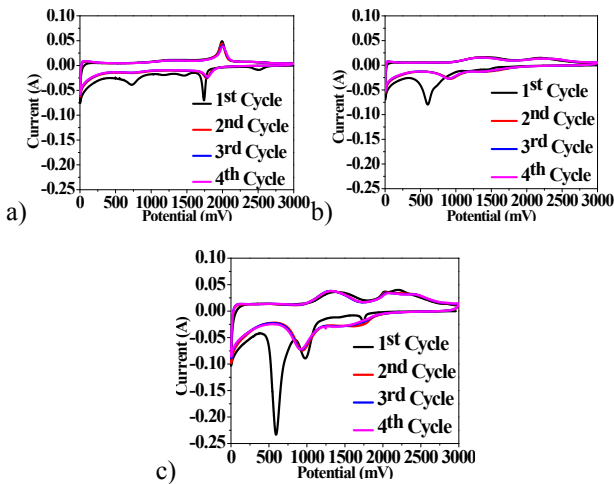


Figure 4. Cyclic voltammety curves of a) TiO₂-rich powder, b) NiO-rich powder, and c) the composite powder

Fig.5 shows the EIS results of the three electrodes at their fully lithiated states. The results show that the composite has lower charge transfer resistance which also explains its improved cycle performance.

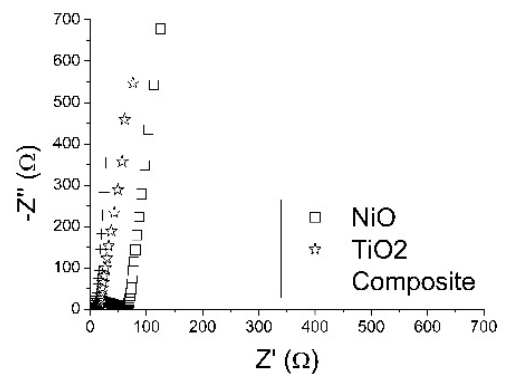


Figure 5. EIS of TiO₂-rich powder, NiO-rich powder, and the composite powder

4. Conclusion

In this research, biomedical waste was successfully leached out with 100% efficiency. TiO₂-rich and NiO-rich powders were obtained after the selective precipitation at different pHs and the composite was formed by ball milling them with 1:6 ratios. It was found that the composite performed better than that of each individual constituent powder. This study sets an example for the recovery of valuable metals from biomedical wastes and structuring them to utilize in an energy storage application.

Acknowledgment

The authors acknowledge appreciatively Dr. Halenur from Medipol Mega Hospital for providing the raw material (orthodontic waste), Arçelik for AAS and XRF analyses; and REMER for SEM and XRD characterizations.

References

- [1] Y. Ding, Z. P. Cano, A. Yu, J. Lu, and Z. Chen, "Automotive Li-Ion Batteries: Current Status and Future Perspectives," *Electrochem. Energy Rev.* 2019 21, vol. 2, no. 1, pp. 1–28, Jan. 2019, doi: 10.1007/S41918-018-0022-Z.
- [2] M. Qadrdan, N. Jenkins, and J. Wu, "Smart Grid and Energy Storage," *McEvoy's Handb. Photovoltaics Fundam. Appl.*, pp. 915–928, Jan. 2018, doi: 10.1016/B978-0-12-809921-6.00025-2.
- [3] L. Usai, J. J. Lamb, E. Hertwich, O. S. Burheim, and A. H. Strømman, "Analysis of the Li-ion battery industry in light of the global transition to electric passenger light duty vehicles until 2050," *Environ. Res. Infrastruct. Sustain.*, vol. 2, no. 1, p. 011002, Mar. 2022, doi: 10.1088/2634-4505/AC49A0.
- [4] "Biomedical Metal Market - Global Forecasts and Opportunity Assessment by Technavio | Business Wire." <https://www.businesswire.com/news/home/20170620006368/en/Biomedical-Metal-Market---Global-Forecasts-and-Opportunity-Assessment-by-Technavio> (accessed Aug. 11, 2022).
- [5] M. F. Gülcan and B. D. Karahan, "Upcycling of industrial iron scale waste for reutilization as anode material in lithium ion batteries," *Mater. Chem. Phys.*, vol. 276, p. 125270, Jan.

2022, doi: 10.1016/J.MATCHEMPHYS.2021.125270.

by metal nickel dotted NiO–graphene composites,” *J. Mater. Sci.*, vol. 54, no. 2, pp. 1475–1487, Jan. 2019, doi: 10.1007/S10853-018-2882-3.

- [6] B. D. Karahan, “Carbon coated electric arc furnace dust prepared by one-pot pyrolysis: An efficient, low carbon footprint electrode material for lithium-ion batteries,” *Mater. Chem. Phys.*, vol. 287, p. 126178, Aug. 2022, doi: 10.1016/J.MATCHEMPHYS.2022.126178.
- [7] M. İ. Özgün, A. Terlemez, M. E. Acma, Y. R. Eker, and A. B. Batıbay, “Recovering of Disposed Nickel – Titanium Rotary Endodontic Files via Sulphuric Acid Leaching Treatments,” *El-Cezeri*, vol. 8, no. 1, pp. 1–10, Jan. 2021, doi: 10.31202/ECJSE.741512.
- [8] M. Ans, M. Atif Makhdoom, M. Faisal Irfan, and A. Al Abir, “Optimized modelling and kinetic analysis of nickel recovery from waste orthodontic implants using response surface methodology,” *Miner. Eng.*, vol. 175, p. 107279, Jan. 2022, doi: 10.1016/J.MINENG.2021.107279.
- [9] C. H. Chen, J. Liu, and K. Amine, “Symmetric cell approach and impedance spectroscopy of high power lithium-ion batteries,” *J. Power Sources*, vol. 96, no. 2, pp. 321–328, Jun. 2001, doi: 10.1016/S0378-7753(00)00666-2.
- [10] S. B. Patil, H. Phattepur, B. Kishore, R. Viswanatha, and G. Nagaraju, “Robust electrochemistry of black TiO₂ as stable and high-rate negative electrode for lithium-ion batteries,” *Mater. Renew. Sustain. Energy*, vol. 8, no. 2, pp. 1–10, Jun. 2019, doi: 10.1007/S40243-019-0147-Y/FIGURES/11.
- [11] C. Liu, C. Li, K. Ahmed, Z. Mutlu, C. S. Ozkan, and M. Ozkan, “Template Free and Binderless NiO Nanowire Foam for Li-ion Battery Anodes with Long Cycle Life and Ultrahigh Rate Capability,” *Sci. Reports 2016 61*, vol. 6, no. 1, pp. 1–8, Jul. 2016, doi: 10.1038/srep29183.
- [12] H. Zhang, B. Tian, J. Xue, G. Ding, X. Ji, and Y. Cao, “Hierarchical non-woven fabric NiO/TiO₂ film as an efficient anode material for lithium-ion batteries,” *RSC Adv*, vol. 9, no. 43, pp. 24682–24687, Aug. 2019, doi: 10.1039/C9RA04947A.
- [13] S. Paul, M. A. Rahman, S. Bin Sharif, J.-H. Kim, S.-E.-T. Siddiqui, and M. A. M. Hossain, “TiO₂ as an Anode of High-Performance Lithium-Ion Batteries: A Comprehensive Review towards Practical Application,” *Nanomater. 2022, Vol. 12, Page 2034*, vol. 12, no. 12, p. 2034, Jun. 2022, doi: 10.3390/NANO12122034.
- [14] Z. Chen *et al.*, “TiO₂/NiO/reduced graphene oxide nanocomposites as anode materials for high-performance lithium ion batteries,” *J. Alloys Compd.*, vol. 774, pp. 873–878, Feb. 2019, doi: 10.1016/J.JALLCOM.2018.10.010.
- [15] S. H. Choi, J. H. Lee, and Y. C. Kang, “One-pot rapid synthesis of core-shell structured NiO@TiO₂ nanopowders and their excellent electrochemical properties as anode materials for lithium ion batteries,” *undefined*, vol. 5, no. 24, pp. 12645–12650, 2013, doi: 10.1039/C3NR04406H.
- [16] W. H. Ryu, D. H. Nam, Y. S. Ko, R. H. Kim, and H. S. Kwon, “Electrochemical performance of a smooth and highly ordered TiO₂ nanotube electrode for Li-ion batteries,” *Electrochim. Acta*, vol. 61, pp. 19–24, Feb. 2012, doi: 10.1016/J.ELECTACTA.2011.11.042.
- [17] J. Chen *et al.*, “CNTs–C@TiO₂ composites with 3D networks as anode material for lithium/sodium ion batteries,” *J. Mater. Sci.*, vol. 54, no. 1, pp. 592–604, Jan. 2019, doi: 10.1007/S10853-018-2814-2/FIGURES/7.
- [18] J. Chen *et al.*, “Enhanced lithium storage capability enabled



MODULATION OF CATION COMPOSITION FOR LITHIUM STORAGE OF SPINEL-STRUCTURED HIGH ENTROPY OXIDES

Deniz Okan BAYRAKTAR^{1,2}, Ersu LÖKÇÜ³, Çiğdem TOPARLI¹

¹Middle East Technical University, ²ASPİLSAN Enerji, ³Eskişehir Osman Gazi University
Türkiye

Keywords: Energy Storage, Lithium – Ion Batteries, High Entropy Oxides

Abstract

Various high entropy spinel oxides with non-equimolar composition have been produced via co-precipitation method with the purpose of investigating lithium storage capability and electrochemical behavior. Acquired results were compared in terms of electrochemical performance.

Introduction

The hunt for improved materials for increasingly demanding applications in the energy storage industry continues as the present generation of lithium-ion batteries reaches maturity. A novel family of materials has recently evolved that exhibits exceptional features when compared to current lithium-ion battery materials. Because of their high configurational entropy, these materials are referred to as high entropy materials.

The high entropy rock – salt oxide ($\text{Co}_{0.2} \text{Cu}_{0.2} \text{Mg}_{0.2} \text{Ni}_{0.2} \text{Zn}_{0.2}$)O material has been studied extensively in recent years, with greater specific capacities than graphite [1-4]. The 2-D channel for ionic lithium transport is enabled by the rock–salt structure. The spinel structure, on the other hand, offers for a three-dimensional channel for lithium transport [5].

Materials and Methods

Co-precipitation method was used to synthesize $(\text{Fe}_{0.2} \text{Co}_{0.2} \text{Mn}_{0.2} \text{Cr}_{0.2} \text{Zn}_{0.2})_3\text{O}_4$, $(\text{Fe}_x \text{Co}_{0.3} \text{Mn}_y \text{Cr}_z \text{Zn}_t)_3\text{O}_4$, and $(\text{Fe}_x \text{Co}_y \text{Mn}_z \text{Cr}_t \text{Zn}_{0.3})_3\text{O}_4$ (where $x + y + z + t \leq 0.7$) high entropy spinel oxide (HESO) materials. The HESO materials were characterized structurally, morphologically, and electrochemically.

Conclusion

HESO materials with non-equimolar cation composition have shown distinctly different electrochemical behavior. With this knowledge it is believed that for future generation of batteries very fine tuning of electrochemical behavior may be enabled in a more structured manner.

References

- [1] A. Sarkar, B. Breitung, H. Hahn, Scripta Materialia 187 (2020) 43-48.
- [2] C. M. Rost, E. Sachet, T. Borman, A. Moballegh, E. C. Dickey, D. Hou, J. L. Jones, S. Curtarolo, J. P. Maria, Nature Communications 6 (2015) 8485
- [3] M. Moździerz, J. Dąbrowa, A. Stępień, M. Zajusz, M. Stygar, W. Zając, M. Danielewski, K. Świerczek, Acta Materialia 208 (2021) 116735
- [4] P. Ghigna, L. Airoidi, M. Fracchia, D. Callegari, U. Anselmi-Tamburini, P. D'Angelo, N. Pianta, R. Ruffo, G. Cibin, Danilo Oliveira de Souza, E. Quartarone, ACS Applied Materials & Interfaces 12 (2020) 50344-50354
- [5] C. M. Julien, A. Mauger, K. Zaghib, H. Groult, Inorganics 2 (2014) 132-154.



INVESTIGATION OF NI EFFECT ON Mn-Fe-BASED MULTI-TRANSITION METAL LAYERED CATHODE MATERIALS FOR SODIUM-ION BATTERIES

Burcu KALYONCUOĞLU¹, Sebahat ALTUNDAĞ², Serdar ALTIN², Metin ÖZGÜL¹

¹Afyon Kocatepe University, ²Inonu University
Türkiye

Keywords: Energy storage, Sodium-ion batteries, Fe-Mn based Cathode materials, Ni doping.

Abstract

In this study, Ni-doped NaMnFeAlO₂ cathode materials with different stoichiometric ratios were synthesized successfully by a modified solid-state technique using high purity oxide powders. X-ray Diffraction (XRD) and Scanning Electron Microscope (SEM) are used for structural analyses of the materials. Galvanostatic charge-discharge tests, Cyclic Voltammetry (CV), and Electrochemical impedance spectroscopy (EIS) are used for electrochemical characterization of cells. Based on the results, better capacity was obtained with Ni-doping than that of the undoped composition.

1. Introduction

Researchers continue to investigate alternatives to lithium-ion batteries due to several restrictions such as the limited reserves and high cost. Sodium-ion batteries (SIBs) are regarded as one of the most promising alternative candidates to lithium-ion batteries. Na_xMnO₂ and Na_xFeO₂ single transition metal layered oxide cathode materials will lead to the poor electrochemical performance due to some problems such as low stability and performance. On the other hand, recent studies show that double and multi-transition metal layered oxide cathode materials can exhibit better electrochemical performance than Fe-based and Mn-based systems [1-2]. In this perspective, a new improved multi-transition metal layered oxide cathode material was synthesized.

2. Materials and Methods

Ni-substituted NaMnFeAlO₂ cathode materials with different stoichiometric ratios were synthesized successfully by a modified solid-state technique using high purity oxide powders. The cathode materials were fabricated by combining the active material, carbon black, and PVdF binder in a weight ratio of 70:20:10 using N-methyl-pyrrolidone as a solvent. Cr2032 type coin cells were assembled by using synthesized cathode materials under an inert atmosphere and the electrochemical properties of cells were investigated. The battery capacity performance of the cells was measured by C/3-rate up to 100 cycles.

3. Conclusion

The major results of the study;

- Ni-doped NaMnFeAlO₂ multi-transition metal layered cathode materials with different stoichiometric ratios were synthesized successfully.
- The electrochemical performance of Ni-doped NaMnFeAlO₂ multi-transition metal layered cathode materials improved to a certain extent compared with the undoped NaMnFeAlO₂ materials.
- It has been observed that Ni-doped NaMnFeAlO₂ multi-transition metal layered cathode materials are one of the promising candidates for SIBs.

Acknowledgment

The authors would like to thank both TUBITAK for financial support by the contract number of 220N335 and by Afyon Kocatepe University, Scientific Research Projects Commission with number 21.FEN.BİL.40.

References

- [1] Zhou, D., Zeng, C., Xiang, J., Wang, T., Gao, Z., An, C., & Huang, W. Review on Mn-based and Fe-based layered cathode materials for sodium-ion batteries. *Ionics*, (2022), 1-12.
- [2] Liu, Q., Hu, Z., Chen, M., Zou, C., Jin, H., Wang, S., ... & Dou, S. X. Recent progress of layered transition metal oxide cathodes for sodium-ion batteries. *Small*, 15(32), (2019), 1805381.



THE EFFECT OF IMPREGNATION CONDITIONS ON ACTIVE METAL SIZE AND DISTRIBUTION PROFILES OF Ni/Al₂O₃ SUPPORTED CATALYST

Emine ERSEZER¹, Cem AÇIKSARI², Elif ERDİNÇ², Serdar ÇELEBİ², Servet TURAN¹,
Umut SAVACI¹

¹Eskisehir Technical University, ²TUPRAS R&D Center
Türkiye

Keywords: heterogeneous catalyst, Al₂O₃ support, Ni catalyst, characterization

Abstract

The impregnation step in the manufacturing process of shaped catalysts strongly effects the final quality of the catalyst, which depends mainly on the specific impregnation method and the drying conditions. The distribution of the metal nanoparticles within the porous support critically affects the performance of shaped catalysts. This study investigates the effects of varying impregnation conditions on active metal dispersion profiles of spherical-shaped γ -Al₂O₃ supports impregnated with Ni catalysts by incipient wetness and wet impregnation methods. In order to understand the effect of impregnation conditions on catalyst properties, the Ni/Al₂O₃ shaped catalysts were investigated via SEM-EDX, XRD, XRF, TEM, FTIR and TPR analyses.

1. Introduction

Catalysts in which catalytically active metal nanoparticles are dispersed on a support material own to a high surface area and porous structure are defined as supported catalysts. The support provides the shape and size of the catalyst bodies and thus determines the external surface area, the mechanical strength, and the porous structure. As a catalytic support gamma(γ)-Al₂O₃ has great properties such as highly uniform pore channels, narrow pore size distribution and large surface area which results in high activity of the surface for a catalyst support. In large-scale industrial applications the choice of the metal precursor is also crucial, Ni-based catalysts are considered the most promising catalysts in many reactions due to high catalytic activity and affordable cost. In industrial reactions, shaped heterogeneous catalyst bodies are preferred instead of powder form in order to prevent pressure drops during the reaction. The impregnation step in the manufacturing process of shaped catalysts strongly effects the final quality of the catalyst, which depends mainly on; the impregnation method and conditions, the metal-support interaction, catalyst particle properties and the drying conditions. The distribution of the metal nanoparticles within the porous support critically affects the performance of shaped catalysts. In many cases, a uniform distribution of the catalyst nanoparticles throughout the support body is the most attractive profile, especially for reactions that are kinetically controlled [1]. This study aimed to investigate the effects of varying impregnation and drying conditions on active metal size and dispersion profiles of spherical-shaped γ -Al₂O₃ supports impregnated with Ni catalysts by incipient wetness and wet impregnation methods.

2. Materials and Methods

The alumina-supported Ni catalysts were prepared by incipient wetness and wet impregnation using 2.5 mm diameter-spherical γ -Al₂O₃ support (SASOL Inc.) with Ni(NO₃)₂·6H₂O aqueous solution of the appropriate concentration to obtain a 10 wt% Ni content. After then, the Ni impregnated γ -Al₂O₃ samples were dried in three steps under vacuum in rotary evaporator at 25°C, then oven drying at 60°C for 15h and followed by 2h drying at 90°C. Dried samples were then calcined in air for 4h at 500°C which calcination temperature was determined by considering the results of thermogravimetric analysis. Finally, SEM-EDX, XRD, XRF, TEM, FTIR and TPR analyses were performed to characterize the Ni/Al₂O₃ catalysts produced in this study.

3. Conclusion

In this study, the effects of varying impregnation and drying conditions on active metal dispersion profiles of spherical-shaped γ -Al₂O₃ supports impregnated with Ni catalysts were investigated. As supported by the SEM-EDX and XRF analyses, incipient wetness impregnation is insufficient at achieving uniform distribution. On the other hand, uniform metal distribution profile along the cross-section of support surface having 10 wt% nickel content was successfully obtained by using wet impregnation technique in the various solvent amounts. It is well known that the formation of NiAl₂O₄ spinels during calcination due to excessive calcination temperature (above approximately 800°C) has generally been considered to results in the deactivation of Ni/Al₂O₃ catalysts [2]. Therefore, the optimum calcination temperature was determined by considering the results of thermogravimetric analysis. Consequently, XRD results revealed that while sufficient NiO formation was observed thanks to the appropriate calcination temperature, the presence of NiAl₂O₄ spinels was not detected.

References

- [1] Regalbuto, John. Catalyst Preparation Science and Engineering. CRC Press, 2007, 375-400.
- [2] J. R. H. Ross, Catal. Today 2005, 100, 151 – 158.



TEMPERATURE-DEPENDENT GALVANOSTATIC EIS OF SPIRAL AND BOBBIN Li/SOCl₂ BATTERIES

Gökberk KATIRCI, Fazlı Eren CİVAN, Burak ÜLGÜT

Bilkent University
Türkiye

Keywords: Lithium Thionyl Chloride, Electrochemical Impedance Spectroscopy

Electrochemical Impedance Spectroscopy (EIS) is a powerful tool that enables us to understand the electrochemical properties of the studied cell. It can reveal the thermodynamic and kinetic characteristics of electrochemical processes in batteries when paired with a temperature-dependent experimental setting[1]. We have been investigating the impedance of Li/SOCl₂ batteries and published several papers on this topic[2][3].

One interesting property of Li/SOCl₂ batteries is that they provide a stable discharge voltage (~ 3.6V) throughout their usage. This can be explained by the reaction governing the battery.



This makes it attractive in addition to the high energy density because of the solvent working as the cathode active material as well.

The Li oxidation and delivery of Li⁺ to the electrolyte via the Solid Electrolyte Interface (SEI) is one of the most fundamental and important components of Li batteries. Future Li anode research is optimized and developed as a result of further study of these features. In order to comprehend the Li⁺ transport via the SEI, specifically with metallic lithium anodes, we have investigated Lithium Thionyl Chloride (Li/SOCl₂) batteries at different architectures (namely bobbin and spiral).

To describe these processes, equivalent circuit fits were made on the observed EIS spectra. To obtain an Arrhenius relation with regard to temperature, the charge transfer resistances were then plotted inversely. The Activation Energies (E_A) of several electrochemical processes can be determined from the slope of these plots. The transportation of Li⁺ through the SEI is studied. The passivation layer, which forms when a reactive electrolyte or solvent comes into contact with a metallic Li anode, is also investigated. We also demonstrated that this layer can occur right after the measurements and can be broken with high discharge current before each measurement. Due to this property, certain battery types are able to have an incredibly long shelf-life.

We have also investigated two different architectures of Li/SOCl₂ batteries which are spiral and bobbin. Spiral type has a larger electrode area but has less amount of electrolyte and active material. Higher currents can be withdrawn from the battery since the current density is distributed over the large electrode area. The drawback of the spiral type is its low capacity. On the other hand, bobbin-type of batteries are specifically designed for higher capacity at moderate and low discharging currents. The amount of electrolyte in the bobbin type is significantly higher than the spiral type. As a result, higher capacities are reached.

Even though the chemistries of anode, cathode and electrolyte are the same in both battery types in addition to both being C size, we have encountered different activation energies. The impedance data are not only exhibiting different features but also shows a different behavior against increasing temperature.

Our findings demonstrate that the Li⁺ transport processes are non-Arrhenius, demonstrating their complexity. We shall discuss the specifics of Li⁺ movement within the SEI as a result of our findings.

References

- [1] M. A. Zabara and B. Ulgut, "Electrochemical impedance spectroscopy based voltage modeling of lithium thionyl chloride (li\ socl2) primary battery at arbitrary discharge," *Electrochimica Acta*, vol. 334, p. 135584, 2020.
- [2] M. A. Zabara, C. B. Uzundal, and B. Ulgut, "Linear and nonlinear electrochemical impedance spectroscopy studies of li/socl2 batteries," *Journal of The Electrochemical Society*, vol. 166, no. 6, p. A811, 2019.
- [3] M. A. Zabara, H. Göçmez, A. Karabatak, and B. Ulgut, "Characterization of different electrolyte composition lithium thionyl chloride reserve battery by electrochemical impedance spectroscopy," *Journal of The Electrochemical Society*, vol. 168, no. 5, p. 050529, 2021.



AN INNOVATIVE APPROACH FOR ELECTROLYTE RECYCLING FROM LITHIUM-ION BATTERIES

Nils ZACHMANN, Burçak EBİN

Chalmers University of Technology
Sweden

Keywords: lithium-ion battery waste, electrolyte, organic recovery, pyrolysis, supercritical CO₂

Abstract

In this study, electrolyte recovery was investigated by two different processes which are low temperature pyrolysis and supercritical CO₂ to compare the recovery efficiencies and effectiveness of the process. The results showed that dimethyl carbonate (DMC), ethyl methyl carbonate (EMC), and ethylene carbonate (EC) were successfully recovered by low temperature thermal treatment. However toxic exhaust gases, hydrogen fluoride (HF), and phosphoryl fluoride (POF₃), due to the decomposition of LiPF₆ were detected. On the other hand, DMC and EMC were effectively recovered by the supercritical CO₂ method and no toxic compound formation was observed.

1. Introduction

Creating a reliable raw material supply chain for the Li-ion battery industry has been becoming more important not only for the material shortage to meet the increasing demand but also for environmental concerns. Although the main research direction focuses on the recycling of valuable metals from battery waste, electrolyte recovery is as significant as metals to reduce the environmental impact of the battery industry and increase the feasibility of the existing recovery processes.

The liquid electrolyte in Li-ion batteries is a multi-component system composed of a conductive salt, mostly LiPF₆, dissolved in a mixture of (volatile) linear and cyclic carbonates and potential additives. Electrolyte recovery is also important concerning environmental pollution and safety aspects. Severe threats can be potentially induced by the inflammable, toxic, and hazardous components of its organic solvents and fluorinated decomposition products of the conductive salt. Electrolyte uncontrollably evaporates and/or decomposes during the pretreatment stage which increases workplace safety and health risk as well as the organic residue affects the following recycling processes and contaminates the water sources.

There is limited study on electrolyte recycling and scientific and industrial know-how is limited to implement a process stage to the battery recycling process. Thus the investigation of electrolyte recycling is precious for widespread industrialization of battery recycling and sustainable development.

2. Materials and Methods

Spent lithium-ion battery pouch cells (NMC/graphite) of an EV application were used in this study. In pyrolysis experiments, batteries were treated in a tube furnace between 90 to 150°C process temperatures under N_{2(g)} constant flow. The exhaust gas that carries the recovered electrolyte is analyzed in-situ by Fourier transform infrared spectroscopy (FTIR).

Supercritical CO₂ studies were conducted using different pressures, temperatures, and durations to investigate the effects of the parameters on electrolyte recovery. FTIR was used to analyze recovered electrolyte solvents.

3. Conclusion

The linear and cyclic carbonates dimethyl carbonate (DMC), ethyl methyl carbonate (EMC), dimethyl carbonate (DEC), and ethylene carbonate (EC) which are used as the organic solvent in the electrolyte were successfully recovered by the suggested low temperature pyrolysis process. Although hazardous HF and POF₃ gaseous were formed during the recovery process due to the decomposition of electrolyte salt, LiPF₆, HF, and phosphoric acid were produced from these gases by exhaust gas washing.

The results of electrolyte recovery by supercritical CO₂ showed that the linear carbonates dissolve in the process environment and separated from battery waste in high purity. Dissolution and recovery of EC by supercritical CO₂ is possible at relatively high pressures and temperatures. However, a creative design of a co-solvent and CO₂ system is required to recover EC and LiPF₆ in economically and environmentally acceptable process conditions.

Acknowledgment

This research was funded by Swedish Energy Agency, Project No: 50124-1.



FAHTS

Failure Analysis and Heat Treatment Symposium

Hasar Analizi ve Isıl İşlem
Sempozyumu

DETERMINATION OF THE AUSTENIZATION TEMPERATURE VIA COMPUTATIONAL METALLURGY APPROACH FOR AN ALLOYED DUCTILE IRON

**Barış ÇETİN¹, Ayşe ERKAN², Ümmihan T. YILMAZ³, Buğra ATASOY¹, Caner YALÇINER¹,
Caner ŞİMŞİR^{4,5}**

¹FNSS Savunma Sistemleri, ²Döksen Isıl İşlem, ³Kırıkkale University, ⁴Middle East Technical University, ⁵Simultura Malzeme Teknolojileri
Türkiye

Keywords: Ductile iron, normalization, induction hardening, phase fraction

Abstract

Normalization heat treatment which should be performed slightly above the A_{cm} temperature generally has a homogenization, grain refinement and relaxation effect on the ferrous materials. Furthermore, for a ductile cast iron this, treatment may also alter the phase fractions as like the pearlitic-ferritic microstructure. Tuning the phase fractions may have some crucial effects in specific processes as in the case of induction hardening. In this study, an alloyed ductile iron grade was inspected with the quantitative metallography approach and the success of the normalization heat treatment was assessed by the final microstructure. In particular, the initial ferrite volume fraction was tried to be decreased. To perform the normalization, the needed austenization temperature was calculated with computational metallurgy approach which was decided to be a more proper solution instead of using some conventional rule-of-thumb methods.

1. Introduction

Since for most of the defense industry application, the components encounter with high loads and stresses, ductile iron (DI) grades could often be used owing to their superior mechanical properties compared to conventional lamellar graphite cast iron [1]. Regarding DI grades, it can be said that the mechanical properties could be altered, in other words DI with different quality grades could be casted in the foundry by basically differing the chemical composition and phase fractions of ferrite/pearlite. In particular, the changes in the chemical composition barely effects the microstructure, i.e. the volume fraction of the phases (ferrite, pearlite, graphite particles). In some specific designs, an alloyed DI may also be the proper solution. The alloying content for most of the cases, they don't have any tendency in carbide precipitation (as like Ni or Co) serve as a tool in increasing the hardenability or enhancing the ductility of the final product [2-3]. Moreover, alloying content can also provide remarkable advantages related to the surface treatment such as induction hardening. Finally, as the normalization process effects the micro-structural composition and homogenization of the grain size

distribution, it can be used to increase the strength level of the material while sacrificing some of the ductility and modify the microstructure to enhance hardenability ability regarding induction process [4]. Especially, it is well-known fact that Ni addition increase impact strength, machinability and toughness of DI [5].

In this study, an alloyed DI grade which conforms to 80-55-06 grade (ASTM A536) was studied. In order to obtain a microstructure which is more prone to be induction hardened, was aimed to be obtained. For that purpose, a proper normalization heat treatment was applied where the austenization temperature of the material was determined by computational metallurgical approach. In particular, Pandat software was used to determine the phase compositions in different temperature regimes which aligned the experimental effort by estimating the austenization temperature.

2. Experimental Procedure

The chemical composition of the studied material is shown in Table. 1.

Table 1. Chemical analysis of the studied DI (wt%)

C	Si	Mn	Cr	Ni
3.53	2.61	0.22	0.06	1.00
Cu	Mo	Ti	Al	Fe
0.58	0.04	0.01	0.02	Balance

Furthermore, the micrograph is also depicted in Figure. 1. Fig. 1 shows that as-cast micro-structure has a ferrite dominant character. This finding ends up with a significantly low tendency to be induction hardened. For this reason, the material was decided to be normalized to increase the pearlite fraction by performing a normalization operation where the austenization temperature was determined by Pandat software. This software is capable of determining phase equilibria and thermodynamic properties of multi-component, multi-phase systems [6].

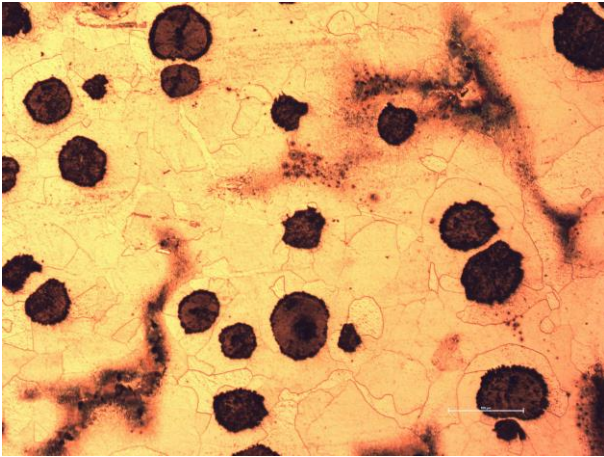


Figure 1. Variation of specific surface area with % addition

2.1. Determination of Austenization Temperature with Pandat Software

The series of analysis, related with the austenitization temperature determination within the scope of this study, are conducted by utilizing Pandat Software. At first, the equilibrium condition between 500-1300 °C is investigated to determine the temperature range at which austenite transformation takes place. Subsequently, aforementioned temperature range is divided into steps of 50 degrees, starting from 850 °C to 1050 °C, then compositions of the phases present at these temperatures are calculated, separately. Following this, new systems with graphite phase-suppressed are defined by using the chemical compositions belonging to austenite phases present at these different temperatures and the equilibrium conditions are examined within the temperature range of 500-1100 °C, separately. Afterwards, the most convenient temperature is specified by considering the final microstructure intended to be obtained in accordance with the purpose of the project. The aforementioned computation efforts uncover that at 920 °C there is approximately %100 austenite phase (apart from very limited MB2). Thus, the austenitization operation was planned to be processed at 920 °C and 120 minutes. Fig. 4 displays the phase diagram of the studied DI whereas Fig 5 and Table-2 monitors the real (graphite suppressed) compositions.

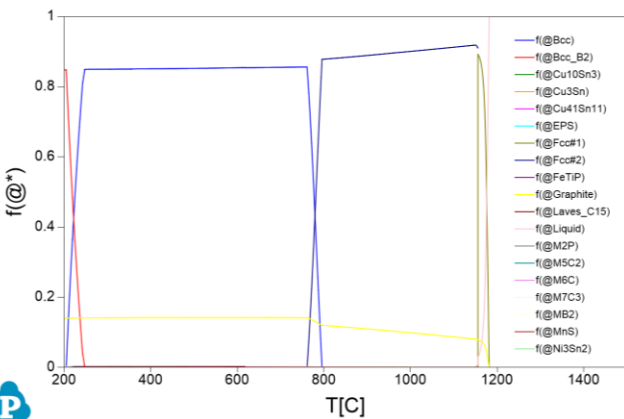


Figure 2. Phase diagramme predicted by Pandat (with graphite)

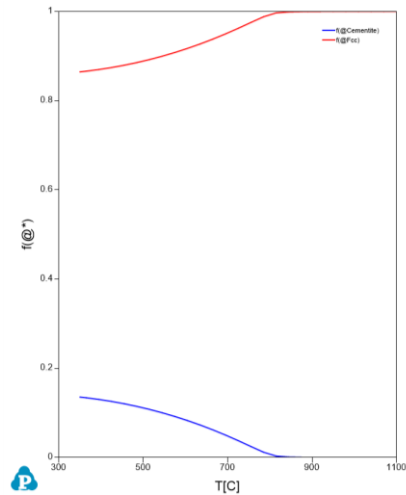


Figure 3. Phase diagram predicted by Pandat (without graphite)

Table 2. Phase Fractions with respect to temperature for the graphite suppressed case

T (°C)	Phase name	Fe3C (%)	FCC (%)
350	FCC+Fe3C	0.1355	0.8645
365	FCC+Fe3C	0.1339	0.8661
395	FCC+Fe3C	0.1301	0.8699
425	FCC+Fe3C	0.1257	0.8743
455	FCC+Fe3C	0.1205	0.8795
485	FCC+Fe3C	0.1145	0.8855
515	FCC+Fe3C	0.1078	0.8922
545	FCC+Fe3C	0.1003	0.8997
575	FCC+Fe3C	0.0919	0.9081
605	FCC+Fe3C	0.0827	0.9173
635	FCC+Fe3C	0.0727	0.9273
665	FCC+Fe3C	0.0619	0.9381
695	FCC+Fe3C	0.0502	0.9498
725	FCC+Fe3C	0.0377	0.9623
755	FCC+Fe3C	0.0246	0.9754
785	FCC+Fe3C	0.0118	0.9882
815	FCC+Fe3C	0.0032	0.9968
845	FCC+Fe3C	0.0009	0.9991
875	FCC+Fe3C	0.0003	0.9997
890	FCC+Fe3C	0.0001	0.9999
920	FCC	0	1

3. Results and Discussion

The samples were prepared with proper metallography techniques. The etching operation was carried out with Picral (%4) etchant. The micro-structure after the normalization heat treatment was displayed in Fig.2. When Fig. 2 is compared with Fig,1, it is clear that the microstructure was modified and the pearlite volume fraction was increased significantly.

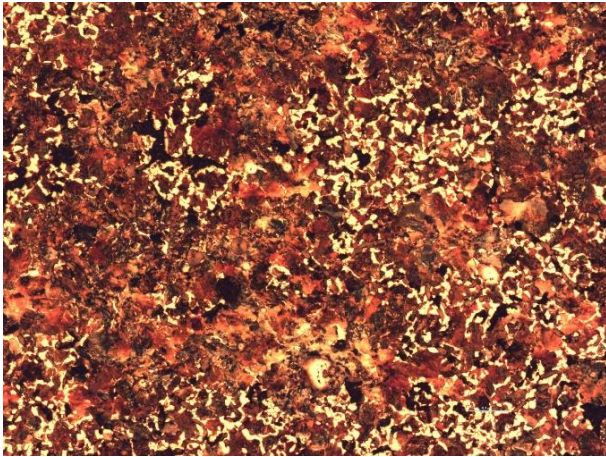


Figure 4. Variation of specific surface area with % addition

In order to obtain quantitative results, the micrograph was analyzed with ImageJ software [7]. By means of proper thresholding strategy, the ferrite volume fraction was determined as %49,81 and %16,43 before and after the normalization process respectively. The analysis pictures with thresholding were given in Figure 5-6. Thus, it can be concluded that the austenization temperature (i.e., normalization heat treatment) was determined with a reasonable precision level. Also, it is worth the declare that normalization duration is seemed to be sufficient.

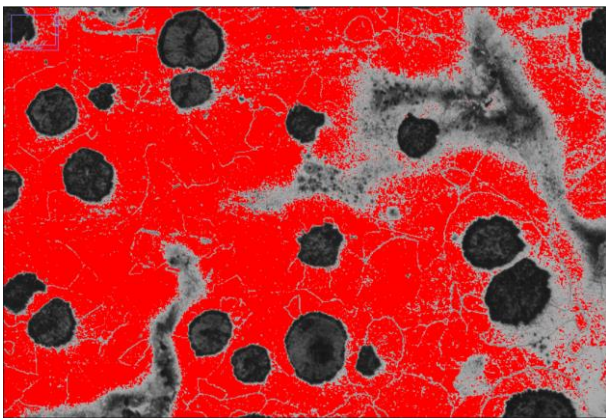


Figure 5. Picture with thresholding before the normalization (Red zones are accepted as ferritic)

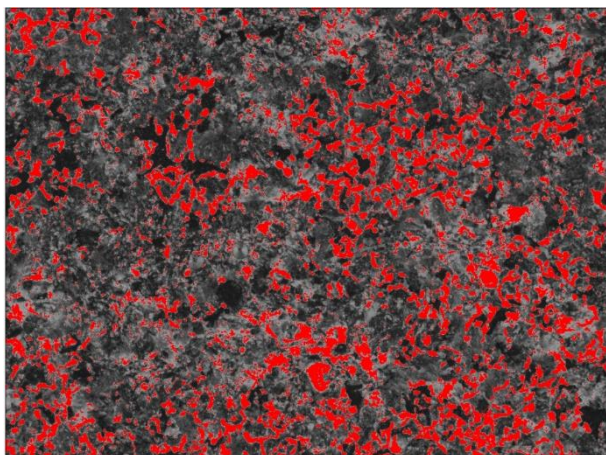


Figure 6. Picture with thresholding after the normalization (Red zones are accepted as ferritic)

Finally, tensile tests were conducted on blocks which were normalized with the batch. This test verified the improved strength values which is explicitly given in Fig.7 and Table-3. Before the normalization process the yield and ultimate tensile strength of the studied ductile iron was determined as 378 and 610 MPa respectively.

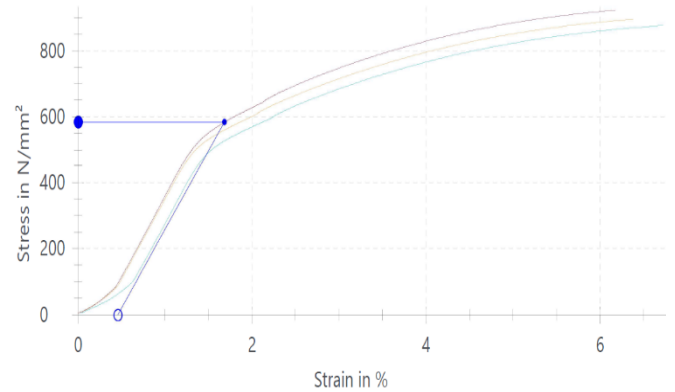


Figure 7.

Table.2

Sample No	Rp0.2 [MPa]	Rm [MPa]	TE (%)
1	550	896	6,0
2	544	877	6,2
3	583	924	6,3

The tensile tests revealed that as it is expected the strength values of the material were significantly improved while sacrificing from the total elongation in the acceptable limit. In other words, the microstructural transformation ended up with a desired strength increase either.

4. Conclusion

In this study, the austenization temperature of an specific alloyed ductile iron grade was determined by computational metallurgy approach with Pandat software aiming to design the proper normalization heat treatment. The experimental tensile tests and microstructural analysis which was used to determine phase fractions revealed that the proposed approach provide sufficiently well results. In particular, an austenization temperature of 920 °C and duration of 120 minutes lead to the desired mechanical and microstructural properties.

References

- [1] B. Çetin, H. Meço, K. Davut, E. Arslan, M.C. Uzun, Hittite Journal of Science and Engineering, 3 (1) (2016), 29-34.
- [2] M.I Boulifa, A. Hadji, Frattura ed Integrità Strutturale, 56 (2021) 74-83.
- [3] J. Sertucha, J. Lacaze, J. Serrallach, R. Suarez, F. Ramon, Material Science and Technology, 28 (2012) 184-191.



- [4] O. Adetunji, P. Aiyedun, I. Olasunkanmi, M. Alao, *Journal of Minerals and Materials Characterization and Engineering*, 11 (2021) 832-835
- [5] M. Ashraf Sheikh ,Effect of Nickel on Tensile Strength of Ductile Iron, *International Conference on Mechanical, Industrial, and Manufacturing Technologies*, 22-24 January 2010, Sanya China, pp.
- [6] S-L. Chen, S. Daniel, F. Zhang, Y.A. Chang, X-Y. Yan, F.-Y. Xie, R. Schmid-Fetzer, W.A. Oates, *Calphad* 26 (2) (2002) 175-188.
- [7] S. Toraman, T. Coşgun, B. Alkan, B. Çetin, Ö. Akyıldız, *Mugla Journal of Science and Technology*, 5(1) (2019) 137-142.



THE DAMAGE ANALYSIS OF THE DIAMOND PARTICLE IN THE CUTTING NATURAL STONE PROCESS

Berrak BULUT

Istanbul Technical University
Türkiye

Keywords: Diamond, Diamond cutting tools, Natural stone cutting, Micro-fractured diamonds, Pull-out diamonds

Abstract

Natural stone production in open mining is carried out in the form of cutting the natural stone from the bedrock with different methods and reducing it to the desired dimensions. The diamond cutting wire and saws are the newest and most advantageous method, which has the most application area among the block natural stone production methods. The segments are composed of binder, diamond grain and metal matrix and the segments are prepared with powder metallurgy process. There are many geological and physico-mechanical factors affecting the field performance of the diamond cutting tools; machine power, hardness and abrasiveness of the stone to be cut, operator experience, diamond segment design and production technology. In addition to these parameters, the most important factor affecting the cutting performance is the selection of the metal matrix composition of the diamond tools and the determination of the properties of the diamond such as concentration, grain size and coating type.

During stone cutting, contacting between diamond grits and stone surfaces is obvious that it results in on impact force on diamond grits. By liquid in the environment that carries hard abrasives of tiny rock detritus, erosive wear occurs on metal binder surfaces in diamond tools. The diamonds is subjected to varied forces during the sawing process and the diamonds get damages under the load. The damages of the diamond grit can be classified into three categories; micro-fractured diamond grits, abrasion diamond grits and pulled-out diamond grits. The aim of this study determine the effects of the concentration of the diamond for controlling the damages, reducing wear of segments, increasing life and precision machining of the diamond tools. In this study, two different diamond concentrations were determined C42 and C75 and the metal matrix is chosen cobalt based.

The microstructures of the samples were examined by scanning electron microscope (SEM) and X-ray diffraction (XRD) analysis. The density and hardness of the samples were determined. The field performances of the samples were examined at cutting marble stones. After the field tests, the diamonds were investigated by SEM. It was observed that the serving life of the diamond cutting tools was increased with increasing diamond concentration. The diamond damage was observed much more intensely at lower diamond concentration.

1. Introduction

Owing to its high hardness, high sharpness, good wear resistance, good high-temperature resistance and good chemical inertness, synthetic diamond has been commonly used as abrasives of grinding or cutting tools, which are increasingly employed for the machining of hard and/or brittle materials as natural stones [1]. The diamond cutting tools are available in the form of wire, circular and linear saw. The circular and linear saw blades are welded with diamond segment. The segments are composed of binder, diamond grain and metal matrix and the segments are prepared with powder metallurgy process [2,3]. The diamond tools are developed as per the requirements of variety properties of the stone available in queries or ceramic materials to be cut [4].

The size of the diamond grains used in the segment is in the range of 18-60 mesh. 20/30 mesh diamond size is for cutting very low hardness and coarse grained stones such as limestone and sandstone, 30/40 mesh diamond size is for cutting medium hard marble stone, 40/50 mesh diamond size is for cutting hard and fine grained stones such as granite and basalt, and 50/ 60 mesh diamond grain size is preferred for cutting flint and very hard granite type stone [5,6]. As the diamond grain size gets thinner, the impact strength increases. Although high cutting speeds can be achieved with coarse-grained diamonds, fine-grained diamond is preferred as the hardness of the cut stone increases [7]. In addition to diamond grain size, another characteristic that affects cutting performance is its concentration. Concentration refers to the volume of diamond in the insert mix and is calculated by the weight of the diamond in the metal matrix layer. The high diamond concentration provides high wear resistance for the diamond tools, even at high loads. However, a large contact surface requires lowering the grinding intensity. In this case, a lower diamond concentration should be used [8,9].

During stone cutting, contacting between diamond grits and stone surfaces is obvious that it results in on impact force on diamond grits. This force is more in gang saw blades and generates impact wear mechanism. By liquid in the environment that carries hard abrasives of tiny rock detritus, erosive wear occurs on metal binder surfaces in diamond tools [10]. The sawing force change periodically with the time, only half of the time in a cycle has the sawing force and the other half is zero. The blades are in the condition of

sawing stone, separating stone and after a period of time, the blades contact with the stone for sawing again and separating stone [11].

Diamonds in the segments can wear due to the force and hard field conditions they are exposed to during the production of natural stone. The damages occurring in diamond grains can be classified under four headings; new grains, broken grains, worn grains and spilled grains. The new diamond grains retain their sharp-edged structure and the cutting process continues as the diamond surface is not damaged. When broken grains, thermal stress and subsequent rapid cooling, combined with mechanical load, breakage occurs at the tips of the diamond grain and new sharp corners are formed. Thus, the diamond grains can continue the cutting process. In worn diamonds, the diamonds lose their sharp corners as a result of friction, resulting in rounded, flattened cutting edges that do not contribute to the cutting action. These diamond grains are known as atrophied or vitrified diamonds. Finally, in cases where the holding force of the bond between the diamond and the matrix is not sufficient, the diamond grains are shed. Diamond metal matrix, which continues the cutting process or completes its task, leaves the structure with wear [12,13].

The aim of this study determine the failure of the diamonds while cutting beige marble with gang saws and investigate the effects of the concentration of the diamond for controlling the damages, reducing wear of segments, increasing life and precision machining of the diamond tools.

2. Experimental Procedure

The metal matrix of the diamond tools segment was consisted of 85 wt% cobalt powder and 15 wt% aluminium 7075 alloys (Al_{7075}). The grit size of the diamonds used in the segments was 40/50 and 50/70 Mesh. Two different diamond concentrations were determined C42 and C75 and the samples were referenced as their concentration value. Figure 1 shows the effect of diamond concentration on matrix distribution and table 1 presents the concentration of the C42 and C75.

The metal powders and diamonds were mixed in a 360° rotating chamber. The metal powders and diamond compositions were compacted in a cold press, and the green samples were sintered via Spark Plasma Sintering method at 750°C and 30 MPa pressure. The microstructures of the samples were examined by a Zeiss Evo 18 scanning electron microscope (SEM) and X-ray diffraction (XRD) analysis was used for the quantitative identification of the phases and was carried out with a Bruker D8-Advanced X-ray diffractometer using $Cu\ K\alpha$ radiation. The measurements were performed with a step size 0.02° and a scan rate of 1 step/min. The 2θ range was set to 10- 90°. The density of the samples was determined by the Archimedes method. Hardness measurements were carried out with a Shimadzu HMV-2 micro hardness tester using a Vickers indenter by the application of a 300 g load for 15 sec. The gang saw group used in the cutting tests was consisted of 45 blades. The blades had 28 impregnated diamond segments with unequal spacing.

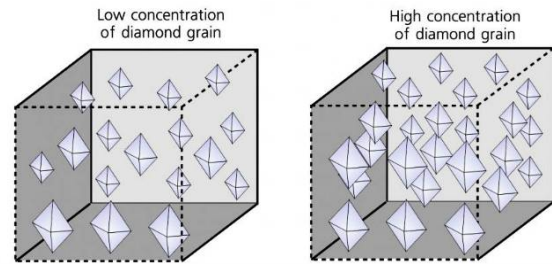


Figure 1. The diamond concentrations on the matrix distributions.

Table 1. The diamond concentration by weight in the metal matrix layer of the segment.

Reference Name	Diamond weight in carats per 1 cm ³ of the diamond layer	
	Carat (ct/cm ³)	Gram (g)
C42	1.85	0.37
C75	3.30	0.66

3. Results and Discussion

The XRD patterns of the investigated samples are given in Figure 2. The acquired peaks for the C42 and C75 samples correspond to Co and $MnAl_6$. The peaks obtained at the C42 and C75 had approximately the same intensity. No effect of the concentrations of the diamonds was observed on the phases formed in the structure.

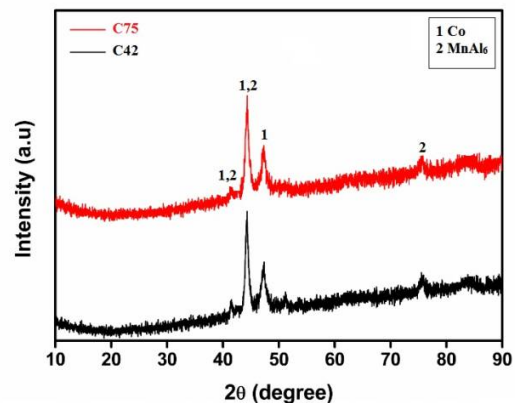


Figure 2. The XRD pattern of the samples.

Figure 3 present the optical microscopy and SEM images of the samples. The distribution of the increasing diamond concentration in the metal matrix and the diamond density difference are shown in Figure 3.

The relative densities of the C42 and C75 samples are 99.0 ± 0.042 and 99.7 ± 0.048 , respectively. The hardness values are of the C42 and C75 samples are $428 \pm 1.05\ HV_{0.3}$ and $433 \pm 1.05\ HV_{0.3}$, respectively. With the increasing diamond concentration, the porosities in the metal matrix structure decreased and in parallel, the density and hardness values of the metal matrix increased. It was observed that the hardness value increased by 1.2 % when the concentration was increased from C42 to C75 concentration.

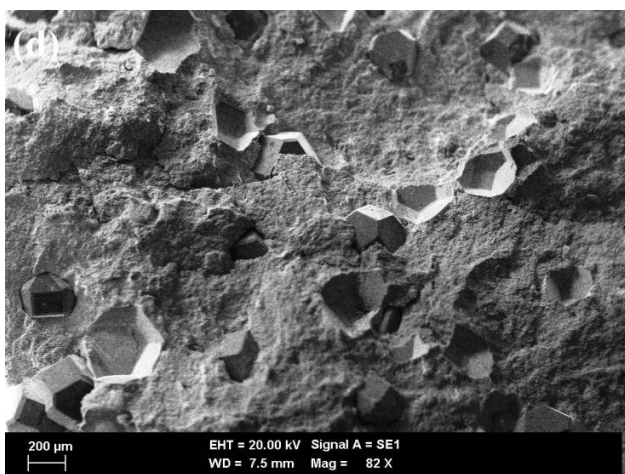
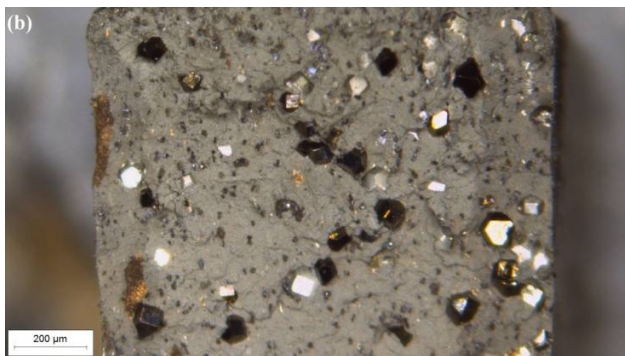
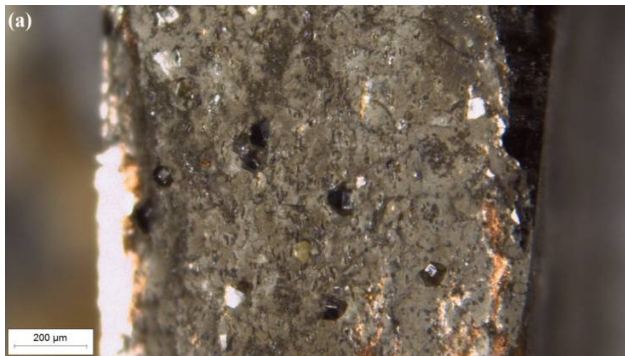


Figure 3. The optical microscopy and SEM images of the fractured surface of the samples a-c) C42 b-d) C75.

The field tests were carried out on industrial scale with the C42 samples that are currently used commercially and the C75 samples prepared in this study to improve the cutting performance and service life of the gang saws. Sawing tests were performed using a multi-block cutting machine. The segment topographies were inspected with optical microscopy and SEM after sawing the entire block. The optical microscopy and SEM images of diamonds of each sample after the cutting process are given in Figure 4 and 5, respectively.

There are many pulled-out diamond particles at the samples of C42. When the diamond grains and the metal matrix interface are examined, cavities are seen at the root of the diamonds where the metal matrix is attached. The excessive load that occurs during cutting natural stone causes pitting and damage to the diamond bottoms. The result of pitting is the pull-out of diamonds that have not completed their cutting task. The diamond grains of the C75 samples have a large height of excrescence and minimum surface damage and have the very good cutting performances. With the increasing diamond concentration, the load on a diamond during cutting was reduced, pitting damage at the diamond-matrix interface was prevented and the premature shedding problem in diamonds was terminated.

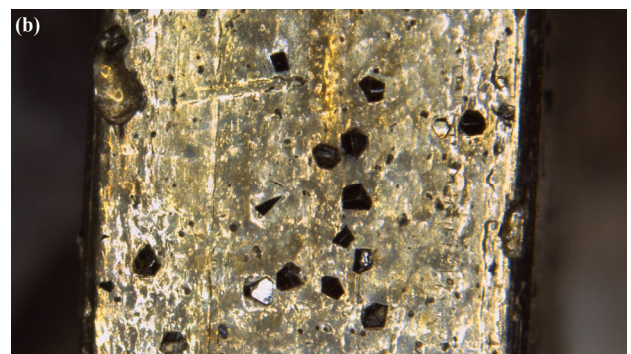
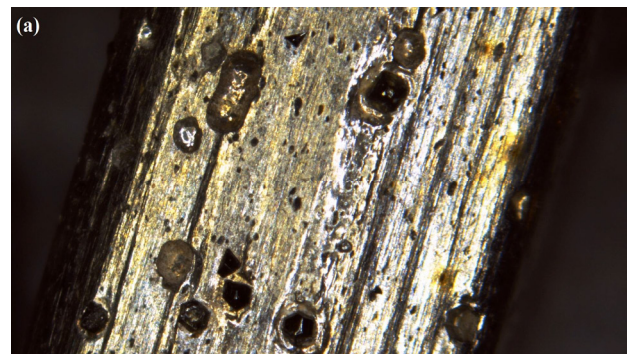


Figure 4. The optical microscopy images after field tests a) C42 b) C75.

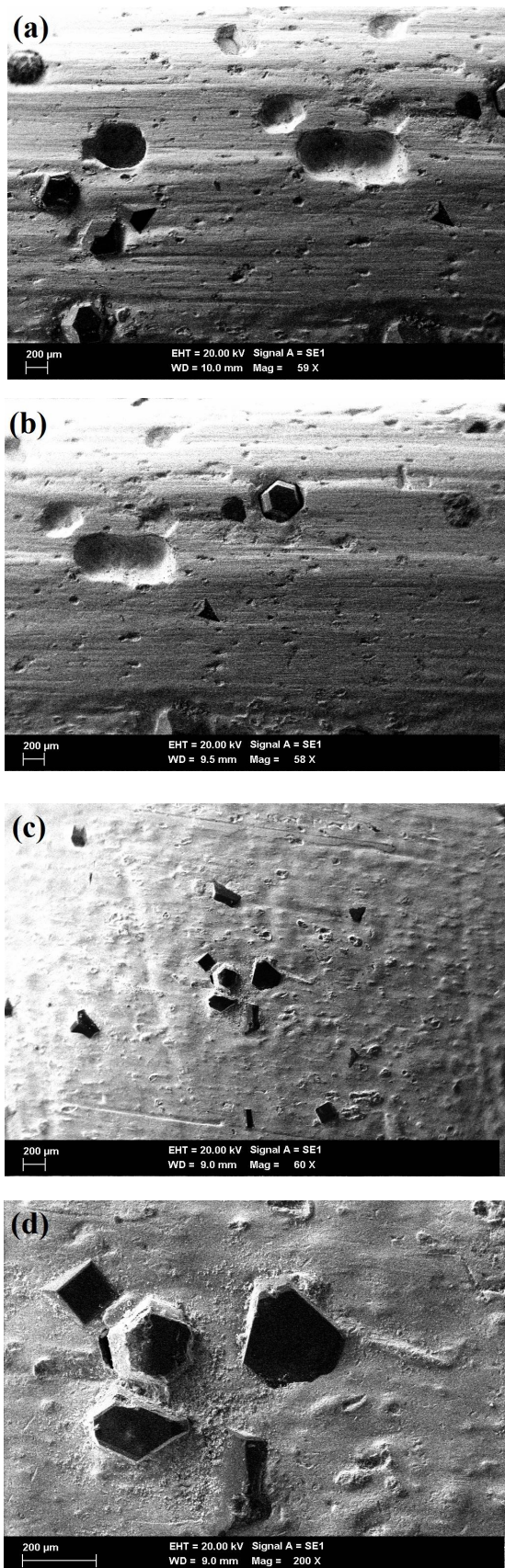


Figure 5. The SEM images after field tests a-b) C42 c-d) C75.

4. Conclusion

At low concentration C42 samples, only a few diamonds were involved in the cutting process due the working principal of the gang saw machines. The only few diamonds have been acted from the cutting forces of the machine and this situation have been caused pull-out of the diamond grits. Because of the high load and the pull-out of diamond, subsequent frictional forces appeared between the surface of the natural stone and the gang saws. With higher concentration C75 samples, the cutting ability was higher, because more diamond grits have been involved in the cutting process. In addition, tool life was longer at higher concentration. In this study, the fauilre mechanism at during cutting process in low concentration saw blades was determined. The effects of diamond concentration increase on this failure mechanism were investigated and it was determined that with the increased diamond concentration, diamond spill failure was eliminated and the service life and field performance of diamond cutting saws were increased.

References

- [1] M. Mostofi, T. Richard, L. Franca and S. Yalamanchi, *Wear*, 410-411 (2018) 34–42.
- [2] N. Yang, W. Huang and D. Lei, *Procedia CIRP*, 71 (2018) 140–143.
- [3] S.J. Zhang, S. To and G.Q. Zhang, *Journal of Advanced Manufacture Technology*, 1 (2017) 4.
- [4] H.K. Tonshoff, B. Denkena and H.H. Apmann, *Key Engineering Materials*, 250 (2003) 33–40.
- [5] L.G. Rosa, J.C. Fernandes, C.A. Anjinho, A. Coelho and P.M. Amaral, *Journal of Refractory Metals and Hard Materials*, 49 (2015) 276–282.
- [6] A. Ersoy, S. Buyuksagis and U. Atici, *Wear*, 258 (2005) 1422–1436.
- [7] L.J. Oliveira and M. Filgueira, *Material Science Forum*, 591-593 (2008) 241–246.
- [8] M. Zeren and S. Karagoz, *Materials Design*, 28 (2007) 1055–1058.
- [9] N.B. Dhokey, K. Utpat, A. Gosavi and P. Dhoka, *Journal of Refractory Metal Hard Materials*, 36 (2013) 289.
- [10] A.J. Gant, I. Konyashin, B. Ries, A. Mckie, R.W.N. Nilen and J. Pickles, *Journal of Refractory Metal Hard Materials*, 71 (2018) 106–114.
- [11] J. Yan, Z. Zhang and T. Kuriyagawa, *International Journal of Machine Tools Manufacture*, 49 (2009) 366–374.
- [12] N.S. Delgado, A.R. Rey, L.M.S. Rio, I.D. Sarria, L. Calleja and V.G.R. Argandona, *International Journal of Rock Mechanism and Mineral Science*, 42 (2005) 161–166.
- [13] A.L.D. Skury, G.S. Bobrovitchii, M.G. Azevedo and S.N. Monteiro, *Materials Science Forum*, 727–728 (2012) 305–309.



INVESTIGATION OF EPDM MATERIALS USED IN MILK TANKER

Yıldız YARALI ÖZBEK¹, Emin Emre GÖKTEPE^{1,2}

¹Sakarya University, ²Tırsan Treyler
Türkiye

Key Words: EPDM, crack, ductility

Abstract

In this study, it was conducted to investigate the ideal material for solving the cracking problems of EPDM materials used in long vehicles. The effect of three different Ethylene Propylene Diene (EPDM) materials on the mechanical properties of the material, depending on the change in their chemical content, was investigated. The materials were subjected to X-Ray Diffraction (XRD) analysis in order to determine their chemical composition. Scanning Electron Microscope (SEM) and Energy Dispersive Spectroscopy (EDS) techniques were used to investigate the homogeneous distribution of material contents. Tensile tests were applied to determine the mechanical properties of the materials.

1. Introduction

Milk tankers are road vehicles that transport milk from farms to production facilities. Milk, which is one of the most nutritious substances in the world, contains many beneficial and harmful bacteria, yeast and mold fungi. [1]. Milk is a product that needs to be transported cold due to its perishable nature. Therefore, milk tankers usually have an insulated structure to reduce thermal conductivity. The thermal conductivity value should be below 0.7. In addition, the selection of materials used in tankers is of great importance in the production of tankers, since the organic structures in them interact with the materials. For this reason, stainless steels form the main structure in milk tankers.

Since milk tankers are included in the liquid transportation class, they are exposed to high dynamic loads in the main structure and chassis matching areas. In order to prevent the stress intensity and deformation in these areas, intermediate damping materials are used. Generally, rubber derivatives are preferred as intermediate dampers in the sector. The properties of rubber materials such as shock and vibration damping, being an insulator, having superior elasticity, tensile absorption capacity under constant deformation and

being easy to process make the material suitable for use as this intermediate damping element.

Rubber is a material that has many applications in the field of rubber material manufacturing industry. Rubber material can be defined as a material obtained naturally from the milky sap (latex) of some tropical plants or artificially as a result of mixing petroleum and alcohol. [2] These tropical plants are predominantly composed of *Hevea brasiliensis*, a tall, soft tree originating from Brazil, suspended in a milky liquid. In the study, Ethylene Propylene Diene (EPDM) synthetic rubber type, known for its resistance to ozone, sunlight and weather conditions, was examined. Ethylene Propylene Diene (EPDM) is a type of polymer produced together with rubber propylene and unsaturated diene. It is among the reasons why it is preferred because of its excellent durability under static and dynamic loads and its ability to absorb incoming loads.

EPDM rubber have been reported in early literatures due to its excellent elasticity. EPDM rubber has been used in the automotive seal systems [1] and the white side walls of tires [2]. Compared with Polytetrafluoroethylene (PTFE) and/or metal, EPDM rubber is a viscoelastic material and its friction properties are sensitively affected by its amount of ingredients and the operating conditions, including the sliding velocity, the surface roughness, the environment temperature and the cycles for rubber sliding. It is especially visible that the elasticity of EPDM rubber presents a remarkable reduction trend with the increase in temperature, which in turn exacerbates the friction and wear of seals and even leads to the failure of seals [3,4]. Study has reported that about 80% failures in seals are from the friction behaviors, causing enormous economic loss [5]. Therefore, it is indeed necessary to explore the friction behaviors for designing reasonable seals. The friction behaviors of rubber originate from its ingredients and

the interaction between two contact surfaces during relative sliding.

Damping of vibration in automotive fields has been an area of focus for improving the life of a particular component. The damping materials are usually made of natural rubber with some reinforcement because of its tendency of increased elastic modulus, tensile strength and hysteresis. The behavior of this rubber is generally hyper-elastic which is characterized by large deformations and strains [6].

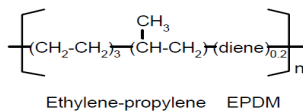


Figure 1. EPDM Molecular Structure [3]

These Hyper-elastic models are based on strain energy density function that relates strain energy density of a material to its deformation gradient. Rubbers can withstand high strains without failing because they have long molecular chains and properties such as extensibility, resilience, and durability. The reason for this is when damping is applied it gives as some type of contact between the member and material to be damped.

2. Experimental Procedure

3 different samples were purchased, which are considered to be preferred for the truck parts with constant breaking and cracking problems. It was investigated which sample was more ductile. First of all, the contents of EPDM materials were analyzed with the help of XRD. Microstructure investigations were made with SEM and EDS.

Tensile tests were carried out, especially since the mechanical properties of the materials are very important. The samples were prepared in accordance with the tensile test. Surfaces suitable for hardness have been prepared.

3. Results and Discussion

Cracking problems are constantly observed in the parts used in the damper part of milk transport vehicles. For the problem of continuous cracking when vibration is experienced, 3 materials with different contents were investigated instead of the problem part. 3 polymeric based materials were compared with the help of various tests. It is thought that the problem of vibration-induced cracking, especially seen in brittle materials, can be solved by being a more ductile material. Experimental data in the research are aimed at producing more ductile materials.

The results of XRD sample R1 are given in Figure 2. SiO₂, ZnO, CaCO₃, SiC phases were found in sample R1 while containing CaCO₃, SiO₂ and ZnO phases. Figure 3 shows result of tensile test sample R1 and R2. Phases ingredient on samples were mechanical

properties. This samples have very high ductility for damping problem.

This part, which is used in trucks, breaks and creates a problem in vehicles that are constantly in motion. It is thought that the reason for this especially mechanical problem is the inability of the material to withstand vibration.

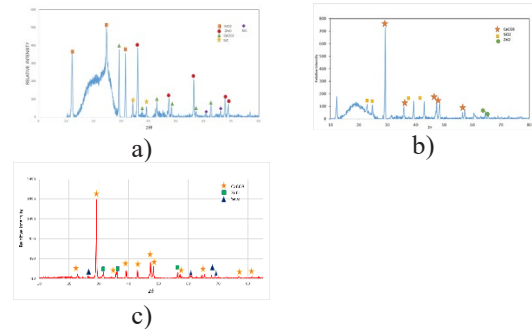


Figure 2. XRD analyses of sample of a) R1, b) R2, c) T1

Figure 2c. shows results of XRD of sample T1. Although the XRD results of the T1 sample show the presence of the same phases as the others, the peak intensities are different.

Although the xrd results of the T1 sample show the presence of the same phases as the others, the peak intensities are different. It is considered that the content ratios are different when preparing EPDM mud.

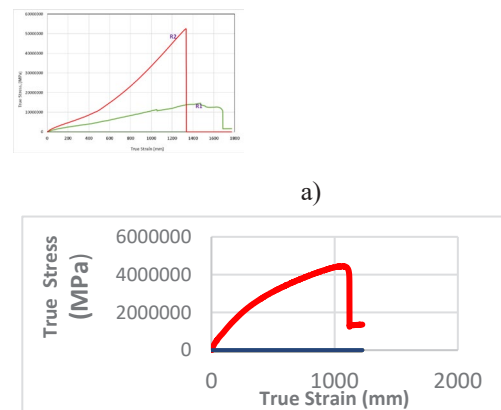


Figure 3. Result of tensile test of samples a) R1 and R2, b) T1

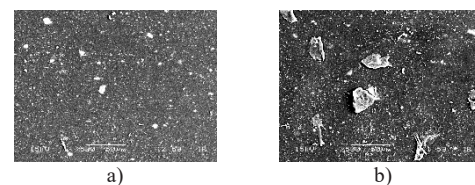


Figure 4. The SEM microstructures of sample R1

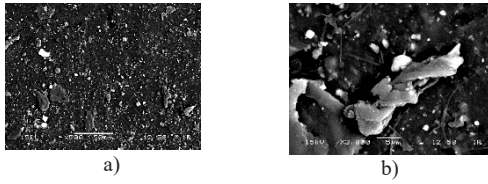
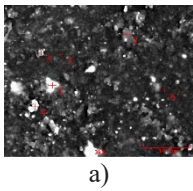


Figure 5. The SEM microstructures of sample R2

The SEM microstructure of R1 and R2 are seen in Figure 4-5. Thin reinforcing structures are seen in the R2 structure. these reinforcements are not homogeneously distributed in the structure. The R1 microstructure is more ductile than the R2 sample structure. In terms of microstructure, R1 is more uniform and homogeneous. R2 structure is more scattered and reinforcement additions in complex



a)

Elt.	1(wt.%)	2(wt.%)	3(wt.%)	4(wt.%)	5(wt.%)	6(wt.%)
C	12.815	71.012	78.150	75.249	71.321	67.837
O	33.765	17.254	13.192	14.074	15.282	14.272
Na	0.402	0.808	0.000	0.391	0.833	0.817
Al	0.353	1.793	1.023	1.173	2.492	5.023
Si	0.474	2.607	1.677	1.887	3.355	6.060
S	0.466	3.288	3.371	3.734	3.268	2.778
Ca	50.568	0.446	0.396	0.751	0.249	0.340
Zn	1.158	2.792	2.190	2.741	3.200	2.874

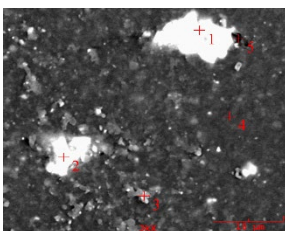
geometr
y are
seen.

Figure 6. a) The SEM b) EDS analyses of sample

R1

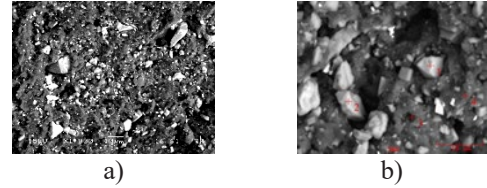
Figure 6, 7 and Figure 8 shows EDS analyses of sample R1, R2 and T1. When we look at the EDS point analysis results, it is seen that the dough contents and content ratios are very different. The content and ratio changes of EPDM materials caused these material groups to have different ductile properties. It is very important that the material is very ductile, especially in order to solve the cracking problem.

SEM micrograph of sample T1 shows in Figure 8a. T1 sample was prepared as a new mud since other R1 and R2 samples could not solve the crack problem in some aspects and were insufficient. The build content is different. It is understood that the reinforcement and content of the mud are different.



4	1(wt.%)	2(wt.%)	3(wt.%)	4(wt.%)	5(wt.%)
C	5.259	9.062	60.245	78.054	39.239
O	39.726	41.888	22.583	13.324	31.954
Na	0.057	0.265	1.012	0.000	1.851
Al	0.027	0.081	1.670	0.319	0.323
Si	0.290	0.163	2.434	0.632	1.861
S	0.238	0.211	3.122	3.999	2.195
Ca	52.740	47.438	5.130	0.343	19.273
Zn	1.664	0.892	3.805	3.329	3.305

Figure 7. EDS analyses of sample R2



a)

b)

Elt.	1 (wt.%)	2 (wt.%)	3 (wt.%)	4 (wt.%)
C	12.829	12.829	43.716	52.467
O	53.261	53.261	9.806	17.892
Mg	0	0.240	0	0.599
Si	0.240	0.238	3.207	2.363
S	0.238	0.485	15.242	8.597
Ca	0.485	32.046	14.815	12.809
Zn	32.046	0.901	13.215	5.273

Figure 8. a) SEM, b)EDS analyses of sample T1

T1 sample microstructure and reinforcement geometry are very different from other samples R1 and R2 (Fig.8).

4. Conclusion

Three different materials have been proposed to prevent vibration-induced cracks in EPDM material used in long vehicles such as trucks. The microstructures of these three submitted materials were examined, and their contents were investigated. These three material groups, produced by changing the contents of EPDM materials, showed different mechanical properties depending on their contents. It has been observed that the general properties of T1 material are much better than other materials, especially among the materials recommended for the crack problem. It is thought that the ductility of the T1 material is sufficient to prevent cracking issues, especially in material groups that have continuous severe vibration problems

REFERENCES

[1] Günhan, T., Çiftlik tipi soğutma performans değerlerinin deneysel olarak belirlenmesi. (2006)



[2] Mazlum U., Experimental investigation of the stress relaxation behaviors of epdm synthetic rubbers, 2015

[3] Peter A. Ciullo, Norman Haber, The Rubber Formulary, William Andrew,

ISBN: 9780815514343,0815514344, (1999)

[4] Chuanbing Zhang, Jian Wu, Fei Teng, Benlong Su, Youshan Wang, Hongrui A, Theoretical and experimental characterization for macro-micro friction behaviors of EPDM rubber, Polymer Testing 99 (2021) 107213

[5] V.B.S.Rajendra Prasad, Dr.G.VenkataRao, Mohammed Idrees, Identification of Damping Characteristics of EPDM-RUBBER with applications to sandwiched beams and considerations to Engine Mounts for Performance Evaluation, Materials Today: Proceedings 24 (2020) 628–640

FAILURE EVALUATION OF COMPRESION STEEL SPRING WIRES AND FACTORS AFFECTING BREAKING

Y. Ziya SALIK¹, Ekrem ALTUNCU²

¹Çelik Halat ve Tel Sanayii, ²Sakarya University of Applied Sciences
Türkiye

Keywords: Steel spring, Wire drawing, Failure analysis, Fracture, Fatigue Cracking,

Abstract

Automotive springs, which are one of the important application areas of compression springs, are safety parts with critical life. In compression springs, provided that it remains in the elastic region of the material, the energy that is compressed and stored due to a force acting in the direction of the spring's axis can be recovered later. These springs, operating under dynamic repetitive loading conditions, must have a certain cycle life. In this study, failure analysis studies were carried out on a 5.30mm and 0.83C steel (EN-10270-1) broken spring, which was cold drawn and then subjected to patenting heat treatment, and the factors affecting the breakage were discussed. Failure analysis studies, internal structural control (segregation, decarburization, capillary crack, inclusion), fracture zone and surface examinations under electron microscopy (SEM-EDX) and hardness measurements, and factors affecting the fracture were investigated after the metallographic preparation of the material. All production stages were observed throughout the study, and as a result, it was concluded that the formation of microcracks on the surface due to the unsuitable or insufficient cold deformation and lubrication conditions in the wire drawing process, the fracture occurred as a result of the development of these cracks with the increasing number of cycles and it had a limited life. It has been determined that the crack that occurs on the wire surface and causes breakage is in the form of a V crack, which is defined as a crow's foot.

1. Introduction

Commercial wire drawing usually starts with a coil of hot rolled 11–9 mm diameter wire rod. Steel wires produced by cold drawing are used in many critical engineering applications such as motor tyre bead, electrodes, springs, wire ropes, mesh, and so forth [1-7]. In general, steel wires are produced from control cooled or patented wire rods by single or multi pass cold drawing operations. Compression springs, as one of the primary elastic members of the pedal system of vehicles, are widely used in automobile industry. They elastically and store the energy to absorb and smooth out shocks that are received by driving conditions. This cyclic service loading condition often results in fatigue crack failure of the pedal spring in a variety of ways. The types of wire breakages that occur during cold drawing may be attributed by improper input wire rod quality in terms of microstructure, inappropriate

combinations of die angle, lubrication break down, excessive reduction in cold drawing, and others [3].

Raw materials (Wire rod, Ø11mm) defects, surface imperfections, improper heat treatment (patenting), corrosion, segregation and decarburization are generally recognized causes of fatigue cracking failure of spring wires [1-4]. In service, the residual stresses on the surface of spring is the position of maximum stress and surface imperfections in materials and surface integrity that serve as stress concentration points bringing about crack initiation [3]. The above summary shows that a variety of factors may cause breakage failure of compression springs in engineering spring applications. In fact, it is often the concurrent acts of several of the above causes that results inspring fatigue. This experimental study about on failure analysis of a compression springs and emphasized fractographic analysis of the fracture surface, microstructure and chemical analysis of the spring material [4,5].

2. Experimental Procedure

Investigations and failure analysis studies were carried out on the failed spring sample (Fig. 1), which was determined not to have sufficient life under test conditions. The chemical composition of the steel wire used in the construction of the compression spring is given in Table I. Generally, steel wires with carbon percent of 0.83 are used. The increase in the carbon ratio increases the elastic properties of the steel. Fatigue crack formations in the mechanical strength of these springs operating under cyclic loads determine the service life of the spring. In order to increase the deformation ability of steel wires, it is aimed to obtain a suitable microstructure by providing the formation of fine pearlite in the microstructure by subjecting them to the patenting heat treatment process in a fluid sand bed below about 500 °C after austenitization at high temperatures (1030 °C). This patenting process provides good formability and ductility to steel wires. The patented wire withstands large degrees of compression and acquires much higher properties after drawing. The patented wire has higher strength and elasticity than hardened and tempered wire after drawing. The deformable wires are then converted into a spring products.

Metallographic analysis and microstructural examinations were made from the transverse and longitudinal sections of the sample pieces taken from the broken spring in the life performance test. 3% nital (HNO_3) solution was used as etching reagent to reveal the microstructure. Fragments taken from the fracture site were examined with an optical microscope (OM) and a scanning electron microscope (SEM-EDX).

Table 1. Chemical analysis of the Steel Material (wt%)

Element	C	Mn	Si	P
wt %	0.83	0.51	0.19	0.013
Element	S	Cu	Cr	Ni
wt%	0.017	0.015	0.031	0.011



Figure 1. Failed spring and fracture zone

3. Results and Discussion

Failure analysis studies are based on a systematic and hierarchical series of observations. After macro examinations on the spring, microstructural examinations on the cross-section and surfaces and detailed microscopic findings in the fracture zone are examined. First of all, the chemical composition and structural discontinuities in the raw material are checked for compliance with the relevant standard (EN10270-1). It is also recommended to check possible working or test conditions before failure. While the spring performance life is expected to be $>2 \times 10^6$, it has been found that under the test conditions, breakage occurs below 10^3 cycles.

The presence of structural discontinuities (segregation, inclusion and decarburization) in the wire cross-section

was checked (Fig 2.). The standard in the examinations made observed in the range. No structural discontinuity was observed at the macro scale. The etched condition shows drawn pearlite typical structure of cold drawn spring.

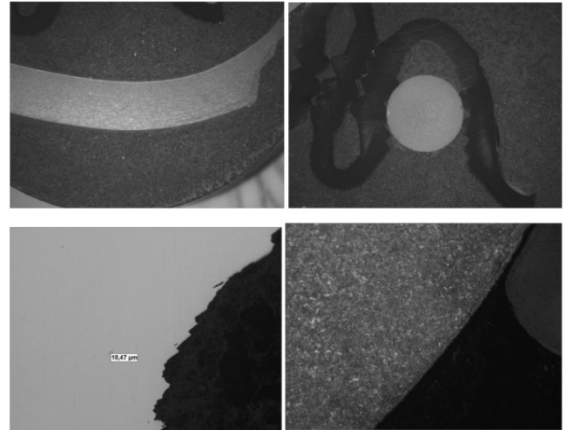


Figure 2. Microstructural analysis of wire a,b:segregation, c. inclusion d. decarburization

Crack formation in the fracture zone in the form of crow's feet and deep crater on the surface, traces of wire drawing die are clearly visible (Fig. 3). Horizontal crack formations generally depend on the die angle and geometry, and the appropriate reduction ratio and it may occur if the speed cannot be determined and/or due to insufficient lubrication effect. As can be seen in figure 3b, crow's feet type discontinuities continue along the wire.

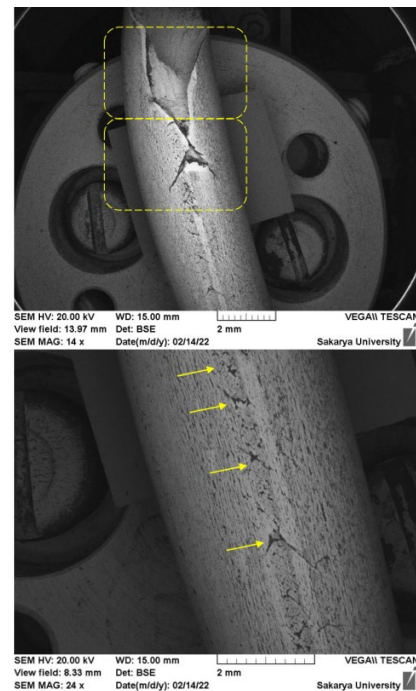
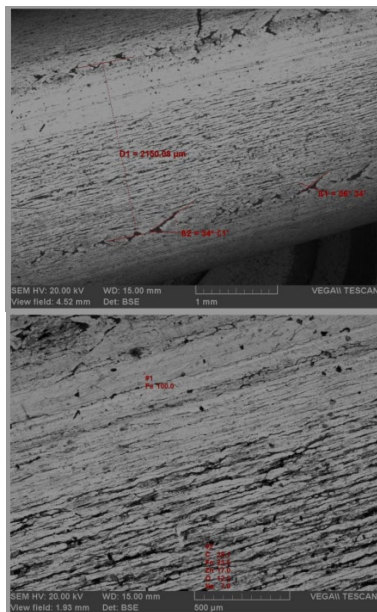


Figure 3. a.Fracture zone and b.crow feet tracks and

poor lubrication regions of failed spring
A series of crow's feet cracks (Fig. 4a) are observed on the surface of wire. It is observed that the die traces, on which the phosphate layer is scraped, deepen on the surfaces just below the V type cracks.



a. Crow feet cracks



b. Poor lubrication sites

Figure 4. SEM images of crow's feet tracks (top) and poor lubrication sites on wire (bottom)

In the EDX analysis, only Fe element is observed in the scraping region, and Fe, Zn, O and P elements are observed in the other region (Fig 4b). In microhardness control, the hardness of the inner zone is $410 \pm 10 \text{ HV}_{0.1}$,

the hardness of the near-surface zone is $560 \pm 15 \text{ HV}_{0.1}$ was measured. It is clearly observed that the fracture is brittle fracture (Fig 5.).

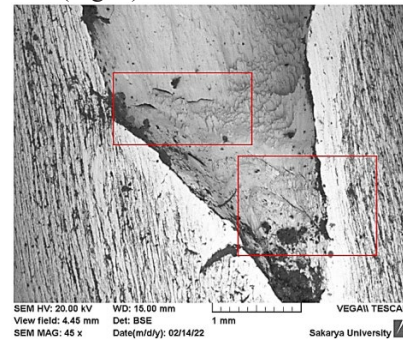


Figure 5. Brittle fracture zone

4. Conclusion

The results of the failure analysis examinations on the $\varnothing 5,30 \text{ mm}$, $\%0,83 \text{ C}$ broken steel wire spring are presented: The surface of the wire passing through the wire drawing die without sufficient lubrication surface tensions and notches formed by scraping the layer of as a result, cracks formed on the surface were detected. Die scratch tracks, horizontal cracks and crow's feet act as crack initiation site clearly observed in our SEM examinations. Improper die angles, depending on the result of the combination of the deficiency of the lubrication process in addition to the die geometry as a result, the wire could not elongate sufficiently (deformation, hardened) due to this. Crow feet crack formation and grow has been caused to brittle fracture. The failure analysis has showed crack associated with crow feet and high surface stresses. The presence of crow feet like surface defect acted as stress concentration for fatigue crack initiation. With the effect of increasing cyclic stresses, surface defects develop cracks and cause fracture. Surface defects can be significantly reduced by a versatile die design and lubrication process improvement.

References

- [1] Y. Prawoto, M. Ikeda, S.K. Manville, A. Nishikawa, *Eng Fail Anal*, 15 (2008), pp. 1155-1174
- [1] S. Das, J.Matur, T. Bhattacharyya, S.Bhattacharyya, *Engineering Failure Analysis* 27 (2013), 333-339.
- [2] S. Das, J.Matur, T. Bhattacharyya, S.Bhattacharyya *Case Studies in Engineering Failure Analysis*, 1 (2013) 32-36.
- [3] P. Palit, S. Das, J.Matur, *Case Studies in Engineering Failure Analysis* 4 (2015) 83-87.
- [4] Y.Zhu, Y. Wang, Y. Huang, *Case Studies in Engineering Failure Analysis* 2 (2014) 169-173.
- [6] F. Bergh, G. Cordeiro Silva, C. Silva, P. Paiva, *Engineering Failure Analysis* 129 (2021), 105679.
- [7] M.T. Todinov, *International Journal of Mechanical Sciences*, 41,3,(1999),357-370.

INVESTIGATION OF FORGING PROCESS FAILURES AND SOLUTIONS IN THE PRODUCTION OF STEERING AND SUSPENSION SYSTEM PARTS

Sefer KOÇAK

Ditaş Doğan Yedek Parça
Türkiye

Keywords: Forging, Mold, Burr, Plastic Deformation

Abstract

Forging process includes metallic material, temperature, mold, lubrication, dimensional, human factor. These factors sometimes constitute an element of their own, and sometimes error modes as an element among themselves. Since these errors can be critical safety parts according to their application, special controls and prevention of these errors occur as an important element for people and other living things. The reasons for the origin of these errors in the forging process are addressed based on the standardization principles in order to eliminate the faults that have been handled one by one and to avoid duplication of these errors.

1.Introduction

Forging is the process of giving plastic shape to the part, usually hot, semi-hot or cold, under the influence of only compressive forces. Many parts are shaped by forging when high strength is required. It is the plastic shaping process applied to give the desired shape to the metal, reduce the grain size and improve the mechanical properties by providing a controlled plastic deformation under impact and pressure. Most forging is done hot and has a history of 4000 years or more.

Forging is used today in aerospace, automotive, hand tools, etc. used in many industries. In many industries, bolts, rivets, rods, turbine shafts, coins, medals, gears and various material groups are forged elements.

2. Errors that may occur during the forging process

2.1 Temperature Errors

Temperature is one of the most important issues for forging, and it is critical that it is not adjusted correctly in order not to make an erroneous measurement. Waiting after temperature measurement is one of the mistakes made in the process, but other factors such as the correct measurement of the measuring device, measurement, etc. should be considered.

The most commonly used heating methods before forging

- Induction heating method, Induction heating is non-contact heating process. In this method, electrically conductive metals, carbon-based materials are heated precisely and precisely using high-frequency electricity. Its measurements are mostly made with various pyrometers, it is the most suitable heating method for mass production.

2.1.1 Extremely high Forging Temperature

The deterioration of the material's internal structure (overgrowth of the grain size), the layering of the material, the melting at the grain boundary, and early mold deformations cause problems. The most critical situation among these errors is the excessive growth of grain size and the initiation of melting at the grain boundary. The error that may occur in this case is the breakage of the part during use. For example; As seen in Figure 2.1.1, a material that has risen above the required 850-1250°C temperature was broken during use, and this error was noticed in the SEM analysis when a study was conducted on this subject. It can be seen in Figure 2.1.2.



Figure 2.1.1 Fracture of forged material at high temperature

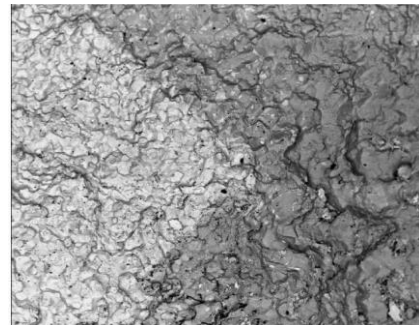


Figure 2.1.2 SEM image of the material that has started melting at the grain boundary

2.1.2 Low Forging Temperature

A low forging temperature may lead to multiple errors, some of these errors are seen in the forged part and some occur in the forging die, in this case the errors that occur are as follows:

- As a result of insufficient material flow, the material does not fill the forging mold,



- Insufficient temperature reduces the ductility of the material and accordingly, cracks in the materials in the parts of the compression force coming to the material.
- Due to the loss of ductility of the part during forging, the breaking of the mold as a result of the force coming to the mold

The results are visible. In order to avoid these results, it should be ensured that the temperature is set correctly and that the measuring instrument measuring the temperature is measured correctly.

As an example, when we examine the effect of the forged material on the mold with the temperature lower than the required value, the mold was broken as seen in Figure 2.1.3.



Figure 2.1.3 Breakage in the mold forged at low temperature

2.2 Defects from Mold

2.2.1 Mold Processing Errors

Errors that may occur during mold processing can be directly reflected on the forged parts, and unwanted errors may occur on the surface of the part.

- Insufficient radius and sharp corners will cause folds as seen in Figure 2.2.1
- Traces of cutting tools during mold processing

- Surface roughness being more than the desired values are the main mold processing errors.

Figure 2.2.1 Plication formation in the part

2.2.2 Mold Deformation Errors

One of the problems that occur during the forging of parts is the deformation of the mold. These deformation causes are given in Figure 2.2.2 and their explanations are as follows:

- Plastic deformations; Sharp corners are also a common error type
- Thermal fatigues; It is the type of error that occurs most during cooling and heating of the part.
- Mold cracks; It is the type of error that occurs in the deepest parts of the mold.
- Mold wears; It is the type of error that occurs in the parts where the part is in contact for the longest time.

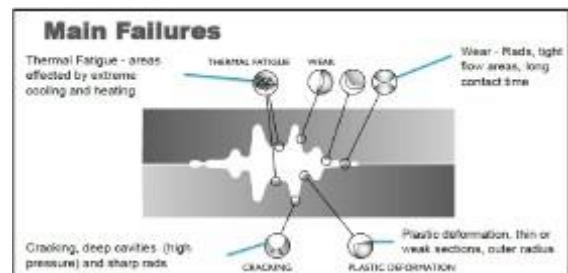


Figure 2.2.2 Die deformation types in hot forging

2.3 Faults from The Forging Process

Although the tattoo process is rapidly moving towards new technologies, robotization and automation systems, there are many elements related to the human factor. Even if the precautions are taken against these factors, they occur during forging, control stages, the next processing stage, and assembly stages in many subjects today.

2.3.1 Ensuring mold centering on the horizontal axis

In forging, first of all, after the upper mold is fixed and the mold is connected, the lower mold is centered according to the upper mold. In the meantime, if the lower mold is not centered less than 1 mm from the upper mold, a situation called lateral misalignment occurs in the horizontal axis of the part coming from the lower mold (Figure 2.3.1).



Figure 2.3.1 Side offset image

2.3.2 Ensuring Mold Centering on the Vertical Axis

During the adjustment of the lower mold according to the upper mold after the upper mold is attached to the anvil, if the lower mold is ahead or behind the upper mold, mold centeredness will not be achieved in the vertical axis, in this case an error called oversize will occur (Figure 2.3.2). In order to avoid this situation, various methods are used in mold designs. These methods must be ensured that mold centrality is ensured by adding a transition and pin system to the mold corners. (Figure 2.3.2)



Figure 2.3.2 Pin system that ensures mold centeredness

If the centrality is not ensured, skewness will occur, and at the same time, if the sharp corners of the mold come across, breakages may occur.

Making sure that the centering of the pins that ensure the centeredness during the mold clamping is done without certainty will create great risks. While the pins escaping from the center, hitting the mold surface and splashing will put occupational health and safety at risk, there is a high risk of damaging the molds.



Figure 2.3.3 Overhead display

2.3.3 Surface distortion error

The material to be forged is brought to the austenite temperature for steels, and because the oxidation resistance of the material is very low at this temperature, a continuously increasing scale layer is formed at each contact time with oxygen. In order to prevent the scale layer formed, it is necessary to use an atmosphere-controlled heating method with the help of gas such as Nitrogen, Argon, etc., and it is necessary to do the forging process in a very short time from the moment the heated part starts to come into contact with oxygen.

If the scale layer seen on the material surface is not removed just before forging, it will cause surface deterioration after the scale adheres to the piece during forging. For this reason, care should be taken to ensure that no scale remains in the mold and the part.



Figure 2.3.4 The scale layer seen in the form of a crust



Figure 2.3.5 Surface disorder image

2.3.4 Diameter and length errors of the material used

Before a part is forged, its technical drawing and model are looked at first and then the surface area of the part to be forged is calculated. According to this calculation, first of all, which type of tattoo machine to use is determined and how much tonnage is required.

Accordingly, after determining whether the material to be forged is square or round, the thickness and length of the piece is one of the most important points. Errors to be made here may have a negative effect on the tattoo machine and molds, and may result in incorrect removal of the part.

After the geometric shape of the material to be forged is determined, cutting or crushing process is started. It should be +5 mm more than the specified length. As this measure increases,

- As shown in Figure 2.3.6, the burr will increase and the rate of used material will increase.
- Mold will resist more material, its life will be reduced
- The forging machine will be damaged by creating pressure force on more material.

It is absolutely necessary that it is not less than -5 mm from the specified length. In case of shortage of material,

In machines with overlapping die surfaces, especially in screw forging machines, it can cause damage to the moving system called ram, causing it to run up.

As the material is insufficient, the flow will be insufficient and the part will not completely fill the mold as shown in Figure 2.3.7



Figure 2.3.6 Excess burr of the part with excess material used



Figure 2.3.7 Not filling the missing material used part

3. Conclusion

The forging process should be pre-processed according to the dimensions of the material to be used with the crushing or cutting method, the cut length and thickness must be ensured, the temperature setting is suitable for the type of material to prepare the parts for forging and it has been clearly verified that the temperature gauge measures correctly. Before starting the forging process, the dies were checked in terms of dimensions using the light scanning system before the forging process was started, visual checks were made, and the desired surface quality was reached by checking whether there were any superficial defects. During the start of the forging process, it was reviewed whether there was an error in the clamping of the die, it was confirmed that the machine type to be used was correct and in accordance with the working principles, and the forging process was started with the right equipment. Attention was paid to the importance of the lubrication process during forging, and all errors that may occur due to lubrication errors were carefully checked on site. These controls were performed by collecting the data of the errors, an error-free forging operation was carried out, the causes of the errors were spread to other elements, and standardized to prevent the repeating of the errors.

Acknowledgment

References

- [1] ALTINTAŞ, A. and Murat KARAHAN, SDU International Technologic Science (2015) Vol. 7, No 3, December, pp. 16-26
- [2] < <http://www.ekoendustri.com/assets/pdf/15.pdf> > Dated:
- [3] < https://www.123rf.com/photo_76328331_high-precision-hot-forging-product-automotive-part-production-by-hot-forging-process-automatic-line.html > Dated:
- [4] < <https://www.indiamart.com/proddetail/forging-die-15258262348.html> > Dated:

INVESTIGATION OF THE AA6005-A ALLOY'S CORROSION BEHAVIOR IN DIFFERENT AGING CONDITIONS

Murat DOĞAN^{1,2}, İbrahim TÜTÜK¹, Kubilay ÖZTÜRK¹, Serhat ACAR¹,
Kerem Altuğ GÜLER¹

¹Yıldız Technical University, ²Sistem Teknik
Türkiye

Keywords: AA6005-A, Corrosion, Heat-Treatment,
Aluminium

Abstract

Using a potentiodynamic polarization test in a 3.5 percent NaCl solution, the effects of aging conditions on the corrosion behavior of AA 6005-A were examined in this study. Microstructural investigations and hardness testing supported the results. The potentiodynamic polarization experiments were performed with a scanning speed of 0.5 mV/s at 250 mV below and above the observed open circuit potential values. Using the Tafel curves obtained, the corrosion potential (E_{corr}) and corrosion current (I_{corr}) values were calculated. Vertical direct-chill cast billets (228 mm) were solution heat treated for 2 hours at 550 °C, then water quenched to room temperature. After the solution heat treatment, the samples were aged at 180 °C for 4 hours, 8 hours, and 24 hours. The experimental results showed that varied aging parameters had a significant impact on the alloy's main corrosion characteristics, such as E_{corr} and I_{corr} . Corrosion resistance increased and began late in the over-aged sample. In under-aged sample, corrosion resistance decreased and started early.

1. Introduction

With an oxide film, aluminum has a great resistance to corrosion. Because this oxide film is only stable in the pH range of 4 to 9, aluminum should only be used in neutral conditions. Due to the fact that this oxide film forms rapidly when aluminum is exposed to the atmosphere, aluminum can protect itself from further oxidation by using it as a protective layer. The principal alloying components of 6xxx alloys are silicon and magnesium. These heat-treatable alloys are often used in mechanical, automotive, marine, and architectural extrusions [1-3].

2. Materials and Methods

The chemical composition of the AA6005-A sample is displayed in Table 1. The chemical composition of alloys was determined using the ARL 3460 optical emission spectrometer from Thermo Scientific. Direct chill (DC) casting produces billet form of the alloys for supply. After DC casting, the billets were homogenized and following a two-hour solution heat treatment at 550 °C, the samples were water quenched to room temperature. The samples were ground in grades ranging from 240 to 2000, polished, and then etched. An optical microscope was used for the metallographic exams. The AA 6005-A specimen performed a potentiodynamic polarization test in a 3.5 percent NaCl solution at room temperature. Each sample's polished and ground surface was adjusted to a 1 cm² area. The Brinell hardness test with a 2.5 mm indentation ball tip was applied to the samples under 62.5 kg load. The hardness test was repeated 5 times for each sample and their average values were given in Table 2.

Table 1. Chemical analysis of the Material (wt%)

Fe	Si	Cu	Mn	Mg
0.26	0.61	0.09	0.14	0.51

Table 2. The Brinell hardness (HB) values of the AA6005-A

As-Cast	4h	8h	24h
56.1	94.6	95.4	88.8

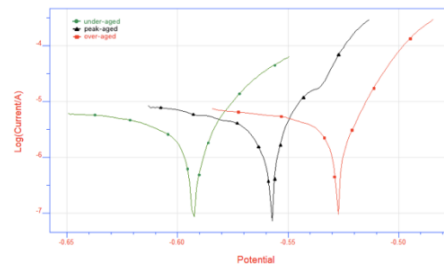


Figure 1. Tafel curves in 3.5% NaCl solution for 6005-A samples; aged for different times at 180 °C.

3. Conclusion

Corrosion potential (E_{corr}) and corrosion current (I_{corr}) values were calculated by using obtained Tafel curves; E_{corr} -4h: -0.5909, I_{corr} -4h: 6.59×10^{-3} , E_{corr} -8h: -0.5560, I_{corr} -8h: 8.09×10^{-3} , E_{corr} -24h: -0.5263, I_{corr} -24h: 7.51×10^{-3} . The maximum I_{corr} values correspond to the peak hardness. AA6005-A with the under-aged conditions shows more negative E_{corr} values and corrosion resistance decreased with starting early.

Acknowledgment

It is acknowledged that Arslan Aluminium A.S. provided the necessary materials.

References

- [1] J.R. Davis, Corrosion of aluminum and aluminium alloys, ASM International, 1999, OH, USA.
- [2] M. C. Reboul and B. Baroux, Materials and Corrosion, 62 (2011) 215-233.
- [3] H. Ezuber, A. El-Houd, and F. El-Shawesh, Materials and Design, 29 (2008) 801-805

FAILURE ANALYSIS OF A BROKEN REDUCER SHAFT

M. Eriş DURMUŞOĞLU, Ali KOCA

İskenderun Demir ve Çelik A.Ş.
Türkiye

Keywords: Failure Analysis, Steel, Metals

Abstract

Reducer shafts may fail for a number of causes sometimes before the expected service period ends. This study is about the analysis work carried out on a broken reducer shaft made from 17CrNiMo6, has failed by breaking into two at a reduced section, showing evident beach marks on the fracture surface, which are typical signs of fatigue failure, at a service period much shorter than expected (2 months for 5 years). Information collected on working conditions evidences, chemical, mechanical and metallographic findings supported us to make an evaluation and gave ideas about how it can be avoidable.

1. Introduction

Mechanical components on the production lines have a critical role on the performance of a production plant. Although manufactured with great care, they have limited service lives which is closely affected by the material properties as well as the working conditions. Reducer shaft in a raw material preparation line has a critical role on the continuity of the material feeding to the Blast Furnace in an integrated steelmaking factory. This paper is about our search for the possible causes of the reducer shaft (Fig.1) failure using failure analysis methods.

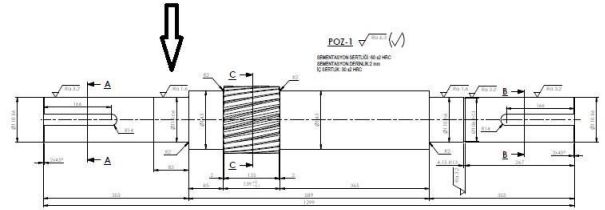
The material quality was declared to be 17CrNiMo6 steel, with a typical chemical composition as given in Table 1.

Table 1. Typical chemical analysis of the material used.

C	Mn	Si	Ni	Cr	Mo
0.15 - 0.20	0.40 - 0.60	0,40 max	1,40 - 1,70	1.50 - 1.80	0.25 - 0.35

Working rate was given as 1000 rpm, expected service period 5 years, and only in 2 months became out of service because of breaking. Point of failure is as marked on Fig.1.

The piece brought for examination were partly cut on one side, so field of examination was partly restricted. However, it was enough to give plenty of valuable information.



For comparison purposes, samples from a non-failed shaft were also taken.

Figure 1. Reducer Shaft

2. Experimental Procedure

- Fracture surface and its edges were examined visually at macro scale.
- Sample for chemical analysis was taken from a point far from fracture surface and analyzed via spectroscopy.
- Sections cut out of selected regions of fracture surface were examined by metallographic methods, under light microscope and SEM, including non-metallic inclusion rating.
- Hardness measurements were done on shaft sections along its radius.

3. Results and Discussion

3.1. Failed Shaft sample

Chemical analysis of the failed shaft sample matches the declared quality (17CrNiMo6).

Table 2. Chemical analysis of the failed shaft sample.

C	Mn	Si	Ni	Cr	Mo	Nb
0,14	0,54	0,27	1,59	1,68	0,28	0,026

Beach marks that are located in more than one direction were detected on the fracture surface, as an evidence for fatigue

failure. Torsional deformation was visible. Type of fracture was observed to be ductile.

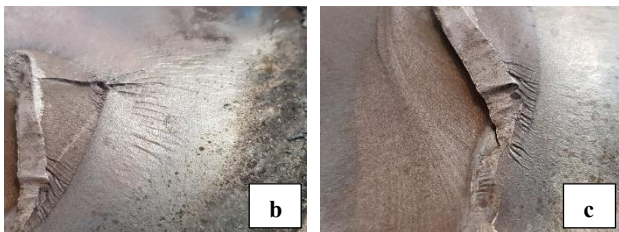
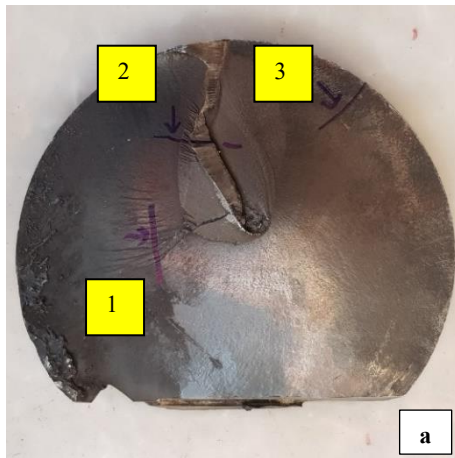


Figure 2. Beach marks on the fracture surface, macro view

Micro structure examinations, parallel bands lying along the length of shaft including brittle type of phases were noted (Fig.3). On the section taken from the final separated region, branched cracks down from the fracture surface were detected. Signs of plastic deformation supports the observation for ductile fracture.

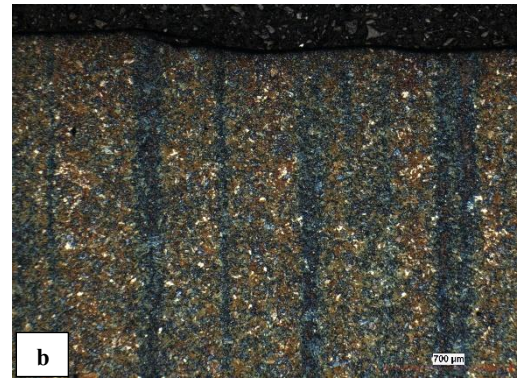
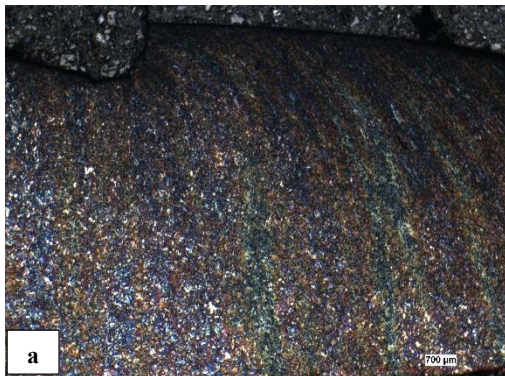


Figure 3. Parallel bands view, (a) for plan-2 at Fig.2-a, (b) for plan-1 at Fig.2-a; 25x

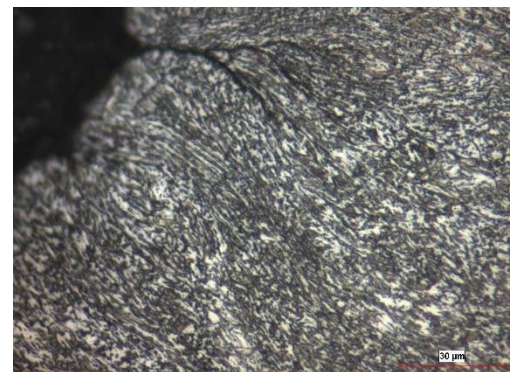


Figure 4. Branched crack, for plan-2 at Fig.2-a ; 500x

Sulfide, alumina and globular type of inclusions were detected in the matrix (Table 3).

Table 3. Inclusion levels acc. to ASTM E45 Method A.

Sulfide A		Alumina B		Silicate C		Globular D	
Thin	Heavy	Thin	Heavy	Thin	Heavy	Thin	Heavy
1,25	1,00	0,75	0,75	0,00	0,00	1,25	0,50



Figure 5. Sulfide inclusion, length near 200µm ; 100x

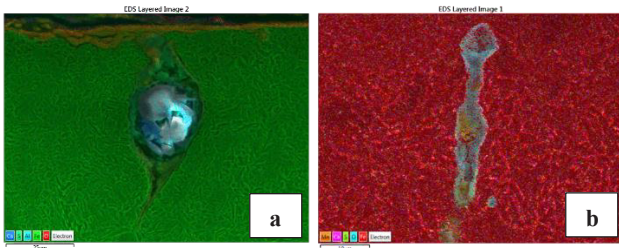


Figure 6. SEM images of the detected inclusions, (a) globular type of inclusion with Al-Mg-Ca surrounded by S, dia 25 μm, (b) sulfide type of inclusion with S-Mn -Al-O, length 40 μm

3.1. Non-Failed Shaft sample

The material was seen to chemically match 17CrNiMo6.

Table 4. Chemical analysis of the non-failed shaft sample.

C	Mn	Si	Ni	Cr	Mo	Nb
0,16	0,53	0,17	1,70	1,69	0,27	<0,01

Micro structure includes banding formation with brittle phases, similar to the other sample.

Same types of inclusions but at lighter levels were detected.

Table 5. Inclusion levels for non-failed shaft, acc. to ASTM E45 Method A.

Sulfide A		Alumina B		Silicate C		Globular D	
Thin	Heavy	Thin	Heavy	Thin	Heavy	Thin	Heavy
0,50	0,50	0,25	0,00	0,00	0,00	1,00	0,00

3.3. Evaluation

Sample for the failed shaft did not give a clear clue about how the failure have started, the missing cut out piece could do so probably. Very clear forms of fatigue were seen.

Comparing with the non-failed shaft, chemically it does not include Nb, whereas there existed Nb in the composition of failed shaft. Nb is known to combine with high C levels and also N, forming carbides and nitrides on the grain boundaries which act as stress concentrators so raise the failure probability. No such situation was found for the non-failed shaft.

Hardness measurements resulted in higher averages for the non-failed shaft, which is not directly related to earlier breaking.

Although inclusion ratings do not seem to be high, some individual ones may lead to uncontrolled deformation.

Location of failure being close to the mounting side makes one think there could be triggering situations such as overload, high friction etc.

4. Conclusion

In this work which we have searched the possible reasons that lead failure of a reducer shaft in early stages of its service life, showing clear signs of fatigue. The broken sample was compared with a non-failed one and a few differences that could open paths for precautions not to face a new case, were detected.

None of the findings are strong enough to cause a failure individually but combination of them could do so. Checking material properties at purchasing period and showing care during commissioning, also following the symptoms during service can keep away work losses

References

- [1] ASM Handbook Vol.11, Failure Analysis and Prevention, p.2301

FAILURE ANALYSIS OF A BROKEN DESCALER PUMP SHAFT AT THE HOT STRIP MILL FACILITIES

Mehmet Eriş DURMUŞOĞLU, Ali KOCA

İskenderun Demir ve Çelik A.Ş.
Türkiye

Keywords: Failure Analysis, Hot Strip Mill, Steel, Metals

Abstract

Descaler Pump shaft made from DIN 1.4313 martensitic stainless steel, at İsdemir Hot Strip Mill line, has failed by breaking into two at a reduced section, showing evident beach marks on the fracture surface, which are typical signs of fatigue failure, at a service period much shorter than expected (7 months for 5 years). Information collected on working conditions evidences, chemical, mechanical and metallographic properties supported us to make an evaluation and gave ideas about how it can be avoidable.

1. Introduction

Mechanical components on the production lines have a vital role on the performance of a production plant. Although manufactured with great care, they have limited service lives which is closely affected by the material properties as well as the working conditions. Descale pump shaft in a hot strip mill has a critical role on the surface quality of the steel coil, responsible for pushing away the scale layer that is formed during rolling process with pressurised water. This paper is about our search for the possible causes of the pump shaft failure (Fig.1) using failure analysis methods.

In this study, fracture surface and its edges were examined visually at macro scale.

The material is DIN 1.4313 martensitic stainless steel, with a typical chemical composition as given in Table 1.

Table 1. Typical chemical analysis of the material used. (in wt%)

C	Mn	Si	Ni	Cr	Mo
0,07	1,50	1,0	3,5-5,0	12,0-13,5	0,7
max	max	max			max



Figure 1. Broken shaft piece and main body (left to right)

2. Experimental Procedure

- Fracture surface and its edges were examined visually at macro scale.
- Work site was visited for surveying.
- Sample for chemical analysis was taken from a point far from fracture surface and analyzed via spectroscopy.
- Sections cut out of selected regions of fracture surface were examined by metallographic methods
- Hardness measurements were done at HV0,3.

3. Results and Discussion

Visual examination of the fracture surface made us see the beach marks which is the typical sign of the fatigue failure. As fatigue failure may have several different origins, details needed to be revealed by metallographic work.

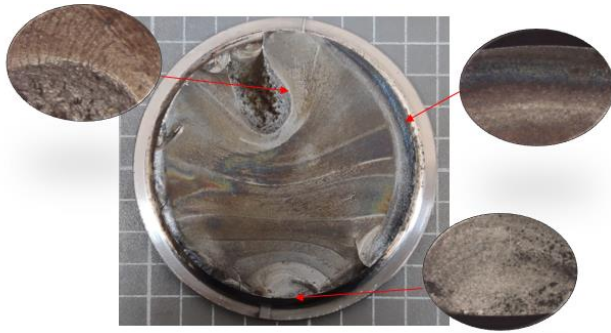


Figure 2. Beach marks on the fracture surface

Key points of failure are shown on Fig.2 with magnified details. Starting point of fatigue seems to be 6 o'clock direction. Moving counter clock wise, 2nd view shows the edge region with a bluish mark resembling local heat input, and 3rd is the final point of fracture. (See Fig. 3 for details)

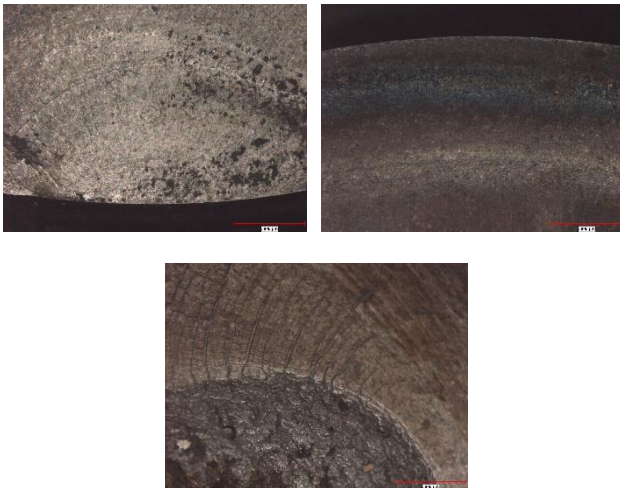


Figure 3. Details of the key points in Fig.2, the same order.

Breaking point is very near to the section change region where any surface discontinuity here may be the potential root cause. Macroscopic and microscopic views did not show any sign on that probability.

The two-piece ring (Fig.3) working very close to the point of failure was also examined. No remarkable damage was observed inside the rings.



Figure 3. The two-piece ring

Hardness measurements through the section taken from the edge of the fracture surface (6 o'clock direction for Fig.2) which looks like the initiation region of deformation gave values varying from 300 to 281 inwards from surface, as a clear structural sign for deformation (Fig.5, Fig.6).

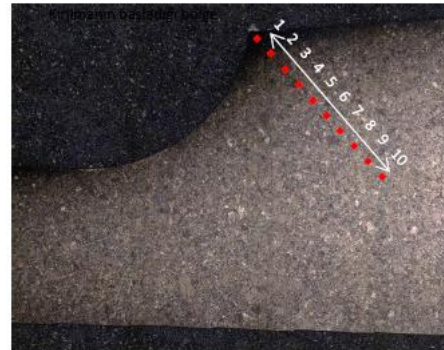


Figure 4. Hardness measurement points.

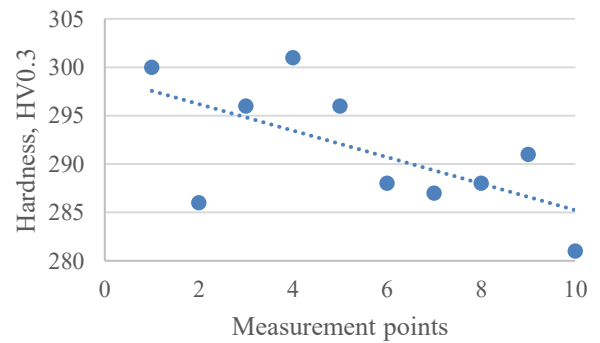


Figure 5. Hardness values.

Sequence of the flow marks seen on the fracture surface matches unidirectional bending deformation (Fig.6-h), which is thought to have started the surface crack that finally lead to fatigue failure. The probable origin of the surface defect that grew into crack form is the wear conditions that may come from either the service conditions or manufacturing phase before service.

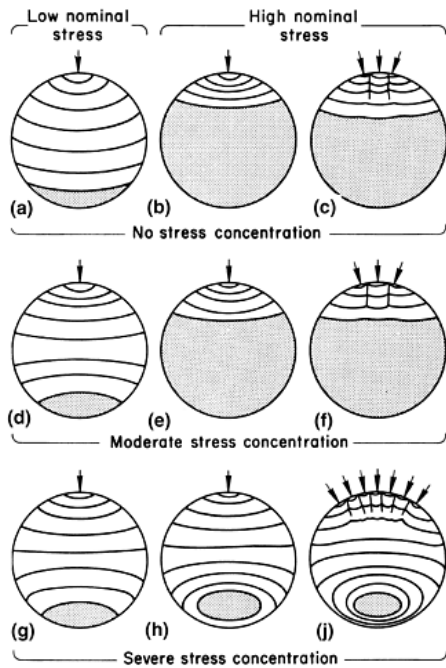


Figure 6. Beach mark models according to stress concentration levels

The service history of this equipment was reviewed, information on the previous failures at different step points of the shaft (that is, rear locations acc. to Fig7) and the last one we were investigating being the first time at that location made us think the possible overloads or rotation tolerances



Figure 7. Descaler Pump Shaft (replacement after failure)

4. Conclusion

Results of the tests and observations are evaluated below:

- Material type was verified through chemical analysis as DIN 1.4313, martensitic stainless steel.
- Microstructure controls and hardness measurements results did not show any deflections that can be a clue to resolve the origin of this failure.
- Since the location of break is very close to section step point, possible effect of radius finish was checked, it was found curvy enough to avoid notch effect, so eliminated from the possible causes list.
- Considering the flow of the beach marks, the failure is speculated to have happened because of a crack that have formed though a minor surface discontinuity under cyclic loading that leads to bending deformation. The surface discontinuity may originate from the manufacturing step, however, fretting wear during operation and also load distribution balance on the shaft may be effective as well.



Below points were suggested for further examination:

- Since failures of the past shafts were reported to have happened at different step points of the body, positioning, linearity and rotation tolerances of the shaft
- Because located very close to the breaking region, lubrication conditions of the shaft at contact point with the two-piece ring.

References

[1] ASM Handbook Vol.11, Failure Analysis and Prevention, p.2301

INVESTIGATION OF THE AUSTEMPERING DURATION AT 400°C ON SILICON SOLUTION STRENGTHENED DUCTILE IRON

Soner Özden ERTÜRK¹, Levent Cenk KUMRUOĞLU², Ahmet ÖZEL³

¹HEMA Otomotiv Sistemleri, ²İskenderun Teknik Üniversitesi, ³Sakarya Üniversitesi
Türkiye

Keywords; solution strengthened ductile iron, austempering, heat treatment, silicon

Abstract

Silicon Solution Strengthened Ductile Irons (SSSDI)/(EN GJS 500-14), which has been developed in recent years, is an important material in engineering terms due to its advantages such as high yield strength, ductility and machinability. However, the effect of heat treatment processes such as austenitizing-austempering temperature and austempering duration on mechanical properties and microstructure has not been studied sufficiently. In this study, the austempering behavior of a new ductile iron grade material SSSDI has been investigated. Considering the inhibition effect of silicon on iron carbide formation and solution strengthening effect of ductile iron in ductile iron, ductile iron containing wt.3.7% silicon was produced, then austenitizing was performed at 950 °C, followed by austempering processes at 400 °C during 5,15,30,60, 90 and 120 minutes. The austempering capability of this high silicon ductile cast iron was investigated by hardness, tensile tests and OM, SEM, XRD. Austenitization tests have shown that 950 °C is an ideal austenitizing temperature for solid solution strengthened cast iron due to 3.7% Si. It was observed that the tensile strength was 1464 MPa, the hardness increased to 463 HBN and the elongation amount to 4.1. With the increase in austempering time, the tensile strength decreased partially, while the elongation value increased.

1.Introduction

General customers of Ductile casting products are automotive, machinery, agriculture and construction equipment industry. This is due to its mechanical properties such as high tensile strength, good wear resistance, high ductility, as well as its practical and low cost in foundry engineering, such as low melting temperature, high fluidity and producing close-to-net shape components. The mechanical strength of ductile iron is close to steel properties and it is an advantageous material that offers ease of manufacture of cast irons. Meeting the demands of machine part designers from a component poses many challenges in foundry practice. The increased strength and elongation at break allow the designer to provide a lightweight component with high functionality [1]

Solution strengthened ferritic ductile irons (SSFs) are strengthened by high silicon (3.2–4.3 wt%) with ferritic microstructure and have the combination of properties as high; yield and tensile strength, higher % elongation at rupture, castability, machinability and low production cost [2]. In recent years, this new grade material has gained interest from cast parts designers also as a result from foundries because of exhibiting higher % elongation at rupture and yield strength as same with tensile properties, comparing with ferritic/pearlite grades of ductile irons [3].

With the increase in the content of silicon (3.0-4.3%) solution reinforced ferritic ductility, a single ferrite phase of cast iron, cast matrix structure is obtained and the tensile properties are increased to 450-600 as tensile, and the % elongation at rupture values increases by 10%. Pearlite can participate on the grain boundaries, where it has an important influence on the mechanical properties. By heating of the ductile iron above the Ac1 point has no influence on mechanical properties, as only traces of pearlite are removed. Holding the middle silicon ductile iron at temperatures above the Ac1, causes carbon to dissolve in the grains of iron-silicon solution. After cooling, the iron has a higher tensile strength but lower impact strength. [4]

Austempered Ductile Iron is an engineering material with ductile and high strength and good properties as wear resistance, fatigue life and fracture toughness [5]. Matrix structure is called ausferrite which is a result of heat treatment at a two steps, called as austempering. Generally, austempering heat treatment begin with austenitization at 880-950 °C and isothermal holding in salt bath at the temperature range in 260-400 °C. By adjusting the temperature of austempering, ferrite and austenite phase fractions of matrix is adjusted at lower temperatures favoring strong ferrite structure while at higher heat treatment temperatures, increase the amount of austenite which is leading to lower strength but higher (elongation) ductility. With increase in the content of silicon from the 2.0 to 2.5 wt% to S.S.F ductile irons, i.e. 3.7 to 4.3 wt%, it is possible to achieve austempered ductile irons with higher strength without reduction in the ductility by the formation of bainitic carbides [6]. In addition, the increased silicon content is the widening the process window of

austempering heat treatment at higher temperatures due to inhibited cementite formation at longer holding times [7].

Heat treatment is an effective way to improve engineering properties by changing the internal structure of the material, and SSSDI grade iron is a material that meets the heat treatment criteria. Ductile cast iron with ferritic structure has been widely used as a structural material recently [Larker et al] by taking silicon into the solution [8].

In the literature, the effect of austenization time of ductile iron containing 3.7% silicon on the mechanical and microstructure has been investigated. In this study, the effect of holding time on the properties of mechanical and microstructure of the austenization process at 400 ° C was examined and the data were examined.

2.Experimental Procedure

For the experimental study, commercial EN GJS-500-14 melt was selected. Chemical composition of the final part is presented in Table 1. In addition to the elements, the melt iron was treated for getting spheroidal graphite with nodularity higher than 80%, with ferro-magnesium alloy which contains La. The melt was prepared the same basic charge—40% steel and 60% pig iron. The material for experiment was cast in Y-blocks. The Y-blocks were cut and milled for mechanical testing and austemperability experiments. Y-blocks were first machined down to diameter of 20 mm and height of 20mm bars before austempering experiments. Also tensile specimens machined from Y-blocks were used in austempering experiments (Fig.1.). Optical micrograph of etched ductile iron specimen in the as-cast is shown in Figure 2. (Fully ferritic) The as-cast specimen has a fully ferritic microstructure with nodular graphite's distributed in the microstructure.

Table 1. Chemical compositions of the SSSDI

C	Si	Mn	Cu	P	S
%wt	%wt	%wt	%wt	%wt	%wt
3,22	3,7	0,17	0,07	<0,02	<0,009

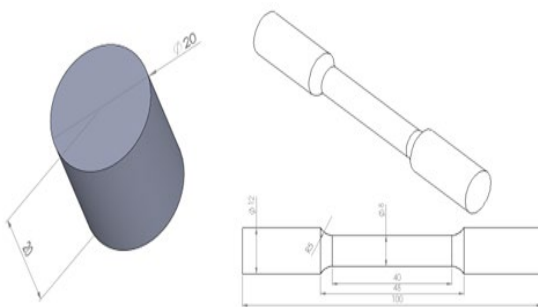


Figure 1. Tensile test specimen dimensions

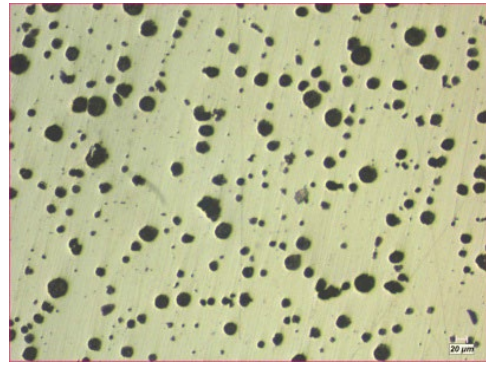


Figure 2. The as-cast specimen has a fully ferritic microstructure with nodular graphite's

For mechanical testing, austenitisation of ductile iron grade of EN GJS 500-14 (SSSDI) was carried out at $T_{\gamma}=950$ °C. Austenitisation time was held constant at $t_{\gamma}=60$ minutes after furnace achieved this temperature. Test samples were austempered at $T_{\text{aust}}=400$ °C in salt bath ($\text{KNO}_3 - \text{NaNO}_2$) holding time with; 5, 15, 30, 60, 90 and 120 minutes respectively. The simulated cooling curves of sample (temperature change in the center of specimen) of 5 & 60 mins austempering presented in figure3. Two bars and three tensile specimens were heat treated in a group and tensile tests were carried out in room temperature. Samples were cut in half from the middle for hardness tests. Samples were etched with echtant with 2% Nital to observe the microstructure of ausferritic and non-ausferritic structures. SEM-Jeol 7100F-EBSD FEG SEM was used as electron microscopy and X-ray diffraction (XRD) studies were completed on samples prepared from these cylindrical pieces per austempering heat treatment time to measure phase fraction, lattice constants. In order to predict the heat transfer and phase transformation of the austempering process, heat distribution simulations of the cast samples were made with a computer-aided simulation program. The simulation results of the samples with 5 minutes and 60 minutes of austempered are given in Fig.3. According to the results, it was concluded that the sample, which was austempered for 60 minutes, was kept at 400 C in a more stable manner and the phase transformation took place throughout the sample.

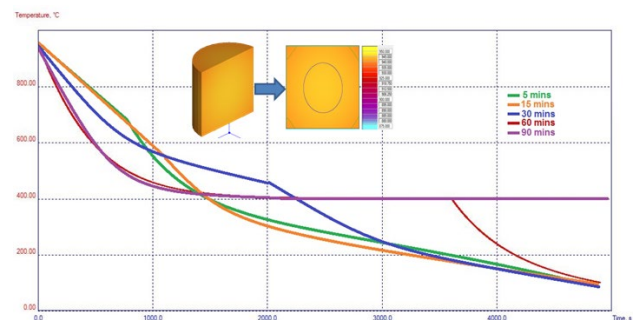


Figure 3. The simulated cooling curves of sample (temperature change in the center of specimen) from 5 to 90 mins austempering

3. Results and Discussion

Results of hardness and tensile test results are presented in Table 2 for each austempering time. The shown results are mean values of three measurements. Results show highest strength with 30 min. austempering time. The hardness is also one of the highest result shown in table. With the increase in austempering time the hardness decreases. The maximum % elongation determined in the sample with 15 min. austempered.

Table 2. Results of hardness & tensile tests

t(min) Austempering	Hardness HB	Tensile MPa	% Elongation	*Toughness (10-3 J/mm3)
5	540	953	4,05	38,6
15	465	1425	6,2	88,35
30	463	1464	3,4	49,7
60	402	1248	5,2	64,9
90	405	1299	2,3	29,9
120	410	1227	2,1	25,8

In 5 mins sample, no austenite phase determined that means 5 minutes is not enough for formation any residual austenite phase and open air cooling after austempering provided fast cooling to eliminate this residual phase formation. In SEM images some martensite phase formations has been determined. That proved that the maximum hardness measurement on this sample.

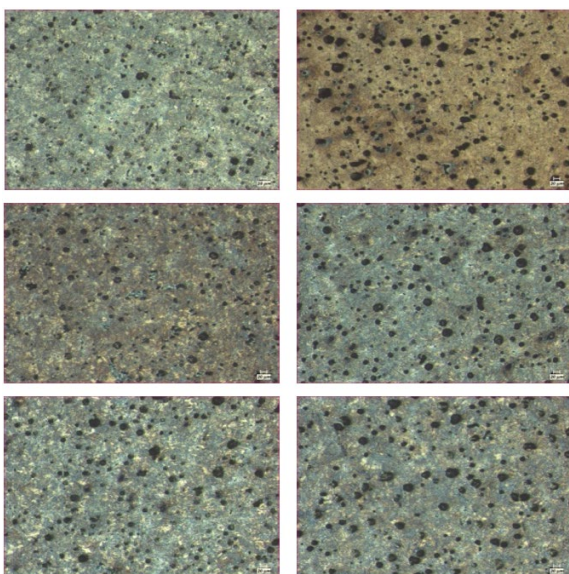


Figure 4. Optical Microscope View of Austempered 5,15,30,60,90 & 120 mins respectively SSSDI's

At 400 ° C, mechanical values such as hardness and tensile strength increase with increasing austempering time. At 400 ° C, the tensile strength of SSDI that 15 minutes austempered is higher compared to 30 minutes, 60 minutes. With increasing austempering time of more than 60 minutes, the hardness increases and the elongation value decreases. It can be concluded that the SSDI sample has the best properties at 15 minutes of austempering time and the hardness properties at this temperature decrease as the austempering time increases. This might be because of the formation of carbide. When we calculate the toughness as the product of tensile strength (in MPa) by elongation at fracture (in mm/mm); at 15 minutes of austempering time the maximum toughness has been achieved.

The microstructures are composed of spherical graphite in a matrix of acicular ferrite and stabilized austenite (called ausferrite). The structures showing the acicular ferrite matrix and stabilized austenite (called ausferrite). The structures of the samples that were austempered for 15 minutes at 400 ° C were characterized by fine ausferrite needles, while samples that were austempered for 90 and more at 400 ° C were characterized by coarse ausferrite platelets. As the austempering time increased, a significant coarsening of the ausferrite was observed. Figures 4 to 5 were Optical Microscopy, SEM micrographs of the samples that austempered at the different durations.

As with the optical micrograph, fine ausferrite needles characterized the structure of the samples austempered for 15 minutes, while the structure of the samples at 60, 90 and 120 minutes' times were characterized by coarser ausferrite. In increasing time, fine ausferrite needles turn into coarse platelets [9].

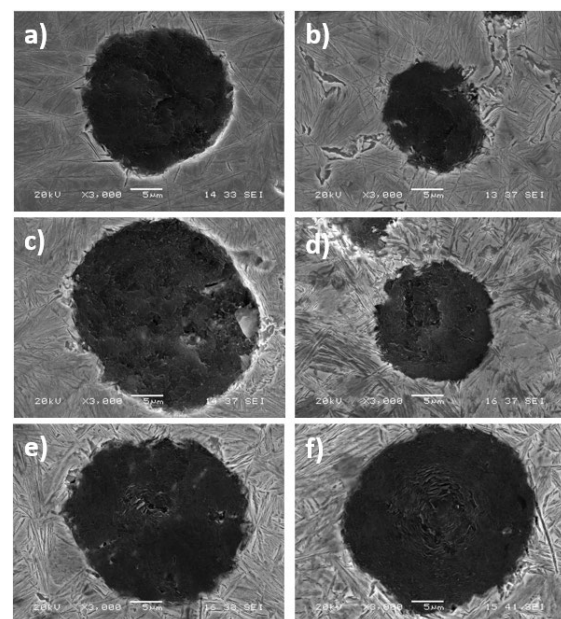


Figure 5. 3000X magnification SEM images of samples that were austempered at 400 °C for 5-15-30-60-90 and 120 minutes after austenitized at 950 °C

The XRD patterns of produced SSDI were as presented in Figures 6 also confirmed that the phases predominantly consist of ausferrite structure. From the pattern, the peak values were predominantly austenite (γ) and ferrite (α) phases. The austenite (γ) phase was observed on (111) plane at 2θ of 43, (002) plane at 2θ of 50 and (220) plane at 2θ of 75 for the produced SSDI samples at different austempering parameters. The ferrite (α) phase was observed on (110) plane at 2θ of 44.5, (200) plane at 2θ of 65 and (211) plane at 2θ of 82 for the produced SSDI samples at different austempering parameters.

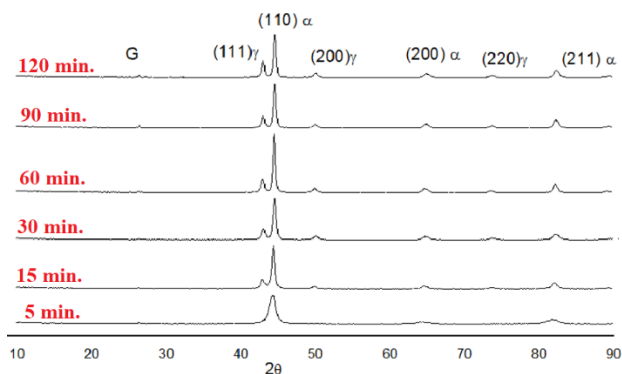


Fig.6. XRD patterns of SSSDI specimens

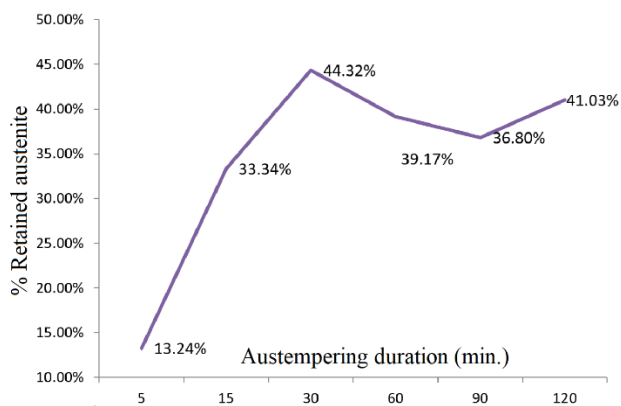


Fig.7. Retained austenite percentages austempering duration graph

4. Conclusion

Austempering time is an important factor in terms of mechanical properties and microstructure transformation. Not only the retained austenite level has impact on the mechanical values. Acicular structure, texture, grain size and in homogeneity of nodularity which is a handicap for these low C containing material grade, has also impact the mechanical properties. The phase transformation of the produced Silicon Solution Strengthened Ductile Irons takes place with the increase in the austempering time,

as the coarsening of the ausferrite, this coarsening begins after 30 minutes. XRD analysis reveals a microstructure containing austenitic (γ) and ferrite (α) phases, spherical graphite as predominant phases. Calibrated diffraction peaks demonstrate that cementite does not appear during the heat treatment process. No carbide was detected, because of the 3,7% Si content could inhibit the formation, subsequently causing the carbon-enriched retained austenite and austempered ferrite.

Acknowledgment

The authors would like to thank management of Hema Automotive Systems Company (A group company of Hema Endüstri A.Ş.) for supporting this study.

References

- [1] Herfurth, K., Gorski, R., Beute, K., Hering, M. (2011). GOPAG C 500 F, Gontermann-Peipers, Germany.
- [2] de La Torre U, Loizaga A, Lacaze J and Sertucha J 2014 As cast high silicon ductile irons with optimised mechanical properties and remarkable fatigue properties Mater. Sci. Technol. 30 1425–31
- [3] Stets W, Löblich H, Gassner G and Schumacher P 2014 Solution strengthened ferritic ductile cast iron properties, production and application Int. J. Metalcast. 8 35–40
- [4] J.Piaskowski. Ductile Iron Containing ~3,9% Silicon, Advanced Materials & Processes, Feb. 2003:35-37
- [5] E. Dorazil, High strength austempered ductile cast iron. Prentice Hall, 1991
- [6] Kaisu Soivio, Austempering Experiments of Production Grade Silicon Solution Strengthened Ductile Iron, Materials Science Forum ISSN: 1662-9752, Vol. 925, pp 239-245 doi:10.4028/www.scientific.net/MSF.925.239
- [7] A. Kochański, A. Krzyńska, T. Radziszewski, Highsilicone Austempered Ductile Iron, Arch.Foundry Eng. 14 (1) (2014) 55–58.
- [8] Larker R. Solution strengthened ferritic ductile iron ISO 1083/JS/500-10 provides superior consistent properties in hydraulic rotators. China Foundry. 2009;6(4):343–351. Heat Treatment Studies For Improving The Solution Strengthened Ferritic Ductile Iron Cast Material EN GJS 500-14
- [9] Abioye et al. International Journal of Applied Engineering Research ISSN 0973-4562 Volume 12, Number 23 (2017) pp. 13435-13441 © Research India Publications.



CPS

Composite and Polymer Materials Symposium

Kompozit ve Polimer
Malzemeler Sempozyumu



SURFACE MODIFICATION OF GLASS FIBER WOVEN FABRICS BY INDIUM TIN OXIDE COATINGS AND ELECTROMAGNETIC CHARACTERIZATION OF THEIR MULTILAYERED GRADED COMPOSITES IN X-BAND FREQUENCY RANGE

Merve ÖZDİL DARICIOĞLU, Caner DURUCAN, Arcan F. DERİCİOĞLU

Middle East Technical University
Türkiye

Keywords: Indium tin oxide, Graded type absorber, EM absorption, X-band frequency range

Abstract

In this study, the main objective was to develop a guideline for designing an electromagnetic (EM) wave absorbing composite which is a combination of Jaumann and graded type absorber effective in the X-band frequency range (8-12 GHz). Within the scope of this aim, the effects of conductivity and cascading order of indium tin oxide (ITO) coated glass fiber woven fabrics on the electromagnetic properties of hybrid type multilayered graded composite design was investigated. The spray pyrolysis technique was used to deposit ITO sols on glass fiber woven fabrics, and the electrical properties of these layers were varied to achieve the desired amount of EM wave absorption. EM characteristics of the ITO-modified fabrics were measured experimentally using free space set-up in the X-band frequency range, and data obtained from the measurements were introduced to AWR microwave software to design multilayered graded type absorber composites by cascading ITO-modified fabrics with different conductivity gradients. A composite design with the highest performance has been formed by cascading six ITO-modified fabrics with a gradually increasing conductivity gradient from the front to back layer of the composite and ~85% and ~93% average absorption was achieved without and with a metal sheet placed at the back of the composite.

1. Introduction

The increase in application areas of electromagnetic devices results in electromagnetic interference (EMI) which creates a growing need for electromagnetic shielding materials and structures. That's why materials and systems that can suppress the EMI by absorbing the incident electromagnetic waves have been studied by many researchers, and a variety of different materials or systems have been used for the purpose of EMI shielding [1]. Indium tin oxide (ITO) has promising potential among all EMI shielding materials due to its electrical, optical and electromagnetic properties. Besides its high electrical conductivity and transparency in visible light, ITO exhibits high chemical and mechanical stability while being nontoxic. ITO can also absorb ultraviolet and infrared waves which are desirable for good EMI shielding [2]. Multilayered graded type composite design is the preferable one among the other structures, since it has large bandwidth and minimum reflectivity over a wide frequency range due to its gradually changing multilayered structures.

2. Materials and Methods

ITO coating sols with different molarity were prepared by using sol-gel technique and were deposited on pre-cleaned and surface heated (300°C) glass fiber woven fabrics by spray pyrolysis technique. Sol was manually sprayed to the substrates by scanning laterally to cover the whole sample surface. Subsequently, the same procedure was applied rotating the substrate by 90°, and alternating layers were deposited until the whole coating sol was consumed. After the coating procedure, a post-heat treatment operation was carried out at 500 °C for 1 h in open air using a chamber furnace. Finally, necessary characterization techniques were applied to these single-layer surface-modified fabrics, and they were used to design multilayered graded composite structures.

3. Conclusion

In the present study, it was observed that the best design was achieved when cascading ITO-modified fabrics with gradually increasing surface conductivity. In this way, the front layer provided impedance matching between air and the receiving surface of the composite which minimizes the surface reflection. Highly conductive layers at the back prevented the transmission of the incident wave through the protected material. In the end, these led to high overall EM wave absorption.

References

- [1] D. C. T. F. S. Geetha, K. K. Satheesh Kumar, Chepuri R. K. Rao, M. Vijayan, "EMI Shielding: Methods and Materials—A Review," *Journal of Applied Polymer Science*, vol. 116, 2010, doi: 10.1002/app.29812.
- [2] M. Zhu, C. Xiong, and Q. Lee, "Research on ITO transparent electromagnetic shielding coatings for E-O system," *3rd International Symposium on Advanced Optical Manufacturing and Testing Technologies: Advanced Optical Manufacturing Technologies*, vol. 6722, p. 67223Y, 2007, doi: 10.1117/12.783569.

SYNTHESIS AND CHARACTERIZATION OF GRAPHENE REINFORCED AL-7.5 WT.% ZN MATRIX COMPOSITES

Berk ŞENYURT¹, Gökçe BORAND¹, Duygu AĞAOĞULLARI², Nazlı AKÇAMLI¹, Deniz UZUNSOY¹

¹Bursa Technical University, ²Istanbul Technical University
Türkiye

Keywords: Metal-Matrix Composites, Aluminum, Graphene

1. Introduction

The use of aluminum and its alloys in the automotive, aerospace and defense industries, especially in areas where advanced material properties are needed, is limited due to their low strength and durability. To improve their mechanical properties, alloying elements and reinforcement additives are added into the aluminum matrix. Zinc is one of the important alloying element for the Al-matrix for improving strength and enabling precipitation hardening. Graphene, which is one of the strongest materials per unit weight with nanoparticle size, has the potential to be an important reinforcement material for metal matrix composites. Among carbon-based reinforcement elements, graphene has a higher dispersibility in the matrix compared to carbon nanotubes thanks to its wrinkled surface structure, and it can transfer its high mechanical properties to the structure by holding on to the matrix better [1–3].

2. Materials and Method

In this study, few-layered graphene (FLG) reinforced Al-7.5 wt.% Zn-xFLG (x= 0, 0.5, 1, 2 and 5 wt.%) alloys are fabricated via powder metallurgical route from their elemental powders and the effect of FLG amount and milling time were investigated. To prepare composite powders, mechanical alloying method was applied in a SPEX-type ball mill with 1200 rpm and 8:1 ball-to-powder ratio. Powders were compacted under 650 MPa pressure and samples were subjected to debinding treatment to at 425 °C for 2 hours in a tube furnace under flowing Ar atmosphere and they were pressurelessly sintered at 565°C for 2 hours in a tube furnace under flowing Ar gas at a 5 °C/min heating and cooling rate. The microstructural investigations on the mechanically alloyed (MA'ed) and as-blended (non-MA'ed) powders were conducted via XRD and SEM. Sintered samples were characterized in terms of microstructural and mechanical properties via XRD and SEM analyses, density via Archimedes' density method and microhardness (Vickers), reciprocating wear and compression tests.

3. Conclusion

According to the phase and microstructural analyses results, FLG-reinforced Al-Zn alloy powders with an average particle size of 1 to 40 microns were successfully fabricated via mechanical alloying process. Zinc particles were homogenously distributed in the Al matrix according to the SEM-EDX analysis. According to the XRD analysis, a small amount of aluminum carbide formation was determined in the matrix after sintering. The hardness values of alloys increased from 80 HV up to 180 HV with increasing amount of FLG in the Al-Zn matrix.

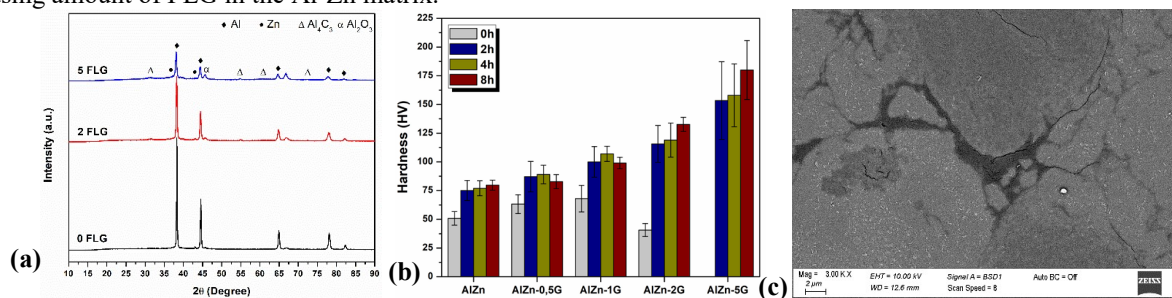


Figure 1: (a) XRD patterns of Al-Zn-xFLG (x= 0, 2 and 5%), (b) hardness values of Al-Zn-xFLG (x=0, 0.5, 1, 2 and 5%) by MA hours and (c) SEM image of 4 h-MA'ed and sintered Al-Zn-2FLG sample.

References

- [1] S.F. Bartolucci, J. Paras, M.A. Rafiee, J. Rafiee, S. Lee, D. Kapoor, N. Koratkar, Graphene-aluminum nanocomposites, *Mater. Sci. Eng. A.* 528 (2011) 7933–7937. <https://doi.org/10.1016/j.msea.2011.07.043>.
- [2] G. Borand, N. Akçamlı, D. Uzunsoy, Structural characterization of graphene nanostructures produced via arc discharge method, *Ceram. Int.* 47 (2021) 8044–8052. <https://doi.org/10.1016/j.ceramint.2020.11.158>.
- [3] B.V. Ramnath, C. Elanchezian, R.M. Annamalai, S. Aravind, T.S.A. Atreya, V. Vignesh, C. Subramanian, Aluminium metal matrix composites - A review, *Rev. Adv. Mater. Sci.* 38 (2014) 55–60.



MECHANICAL PROPERTIES OF Si_3N_4 REINFORCED Ti6Al4V COMPOSITE FOAM

Ömür Ekrem GÜNTÜRK, Mevlüt GÜRBÜZ

Ondokuz Mayıs University
Türkiye

Keywords: Ti6Al4V, Composites, Foams, Powder metallurgy, Space holder technique

Abstract

In this study, Ti6Al4V (Ti64) foams and Ti64- Si_3N_4 composite foams were produced with a porosity of 70% by volume by powder metallurgy and space holder method. The effects of Si_3N_4 reinforcement ratios (1%, 3%, 5% and 7% by weight) on % relative density ratio, % porosity ratio, hardness, compressive strength and microstructure properties of composite foams were investigated comparatively. As a result of the analysis, the highest increase in compressive strength compared to Ti64 foam materials was observed with an increase of 35.34% in Ti64- Si_3N_4 composite foams reinforced with 1% Si_3N_4 . The best hardness value was obtained with 7% Si_3N_4 reinforced Ti64 matrix composite foams with an increase of 111.60% compared to Ti64 foams.

DOI number will be given to the 4 page manuscripts.

1. Introduction

Today, with the rapidly developing industrialization, composite materials have started to be produced in order to meet the superior performance requirements (high strength, hardness) [1]. It has been realized that by taking models found in nature as an example, technologies with the potential for longer-lasting use can be created even from the materials used today. Foams that can contain various physical and mechanical properties together with a high amount of mechanical energy absorption capacity, which are used for functional and structural purposes in nature, and other materials with high porosity rates can be shown as an example to this situation. Artificially developed materials are also produced in this context [2]. One of the most common methods used to obtain the foam structure is the space holder method. In the space holder method, low density material is obtained by mixing metal powder and space holder material in order to obtain a porous structure [3]. The strength of polymers in materials to be produced for structural function purposes is insufficient to meet the desired properties. The fact that ceramic materials are fragile in nature causes problems. For these reasons, metal materials are the most appropriate option for the production of load bearing foams [2]. The reason for the low density and lightness of metallic foam materials is the large amount of air spaces formed thanks to the pores they contain. In

addition to these features, these materials have high compressive strength, their shock and vibration damping properties are also highly developed. Thanks to these various important properties, these materials are used in fields such as health, automotive and space technologies [4].

Composite materials are materials have superior mechanical properties such as high strength, modulus of elasticity and fracture toughness, good wear and fatigue strength. Composite materials are divided into three main classes as polymer, metal and ceramic matrix composites depending on the matrix type [5]. Powder metallurgy (PM) is one of the most suitable production methods to produce materials for the properties of composite materials. The PM method is a suitable production method to produce components with good mechanical properties, such as strength and hardness [6]. Metal matrix composites (MMC) consist of a matrix material consisting of metal or its alloy and a reinforcement element, which is usually particulate. Ti, Al and Mg are generally used as matrix materials. In addition, materials such as TiC, SiC, Si_3N_4 , B_4C and WC are used as reinforcements to produce MMC [7]. Titanium (Ti) and its alloys are frequently preferred in the biomedical, automobile and aircraft industries due to their high specific strength and biocompatibility [8]. Pure Ti and Ti6Al4V are generally preferred in orthopedic surgery [9]. Ti foams, on the other hand, are generally used in industries such as healthcare, automotive and aerospace. Thanks to its high melting point, Ti foams are preferred even at high temperatures. Fatigue properties and superior biocompatibility allow Ti foams to be used in biomedical industries as well [10]. Foam materials produced from pure Ti are generally used in dental implants, while foam materials produced from Ti alloys are preferred in bone implants [3].

Silicon nitride (Si_3N_4) ceramics, which is one of the important structural materials, has a wide application area due to its properties such as high hardness and superior fracture toughness [11]. Si_3N_4 as a reinforcing element is a ceramic with suitable mechanical and chemical properties. Si_3N_4 shows favorable properties for cell interaction supporting its good biocompatibility [12].

In this study, non-reinforced and Si_3N_4 reinforced composite foam materials were produced using PM and

space holder methods. Composite foams produced were analyzed in terms of microstructure and mechanical properties.

2. Experimental Procedure

In this study, Ti64 was used as matrix material and Si_3N_4 at different ratios (1%, 3%, 5% and 7% by weight) as reinforcement material. Urea (carbamide) has been used as a space-forming material. The production of composite materials was carried out by PM method. The used Ti64 matrix powder has 99%+ purity, $\geq 43 \mu\text{m}$ size range and 4.43 g/cm^3 density. Si_3N_4 , which is used as a reinforcement material, has a purity of 99.9%+, < 325 mesh and 3.25 g/cm^3 density. Urea, which has a chemical formula ($\text{CH}_4\text{N}_2\text{O}$) and is used as a space-forming material, has a purity of 98.5%, a density of 1.32 g/cm^3 and a grain size of 1-2 mm.

To obtain non-reinforced Ti64 foam samples; A urea powder mixture was prepared that will contain 70% urea and 30% Ti64 powder by volume. Raw samples are obtained by shaping the urea and powder mixture in a uniaxial hydraulic press with an average pressure of 630 MPa. In order to remove urea from the obtained raw samples, the crude samples were kept in water at 150°C for 90 minutes. The samples, for which urea removal was performed, were dried in an oven at 45°C for 120 minutes. In the next step, the samples were sintered at 1250°C for 120 minutes in an argon gas atmosphere. The final samples obtained after the sintering process were analyzed mechanically, chemically and physically. Sample codes are given in Table 1.

Table 1. Sample codes

Composition	Sample Code
Ti6Al4V	Ti64
Ti6Al4V-%1 Si_3N_4	Ti64-SN1
Ti6Al4V-%3 Si_3N_4	Ti64-SN3
Ti6Al4V-%5 Si_3N_4	Ti64-SN5
Ti6Al4V-%7 Si_3N_4	Ti64-SN7

A homogeneous distribution of Si_3N_4 reinforcement material with ethanol in an ultrasonic bath at 25°C for 15 minutes was achieved. Si_3N_4 ethanol mixture was put into the ball mill chamber and mixed for 15 minutes at 800 rpm in a high-speed vibratory mill. After this process, Si_3N_4 reinforcement powder was filtered from the balls and Ti64 matrix material in powder form was added, and the processes performed in the ultrasonic bath and ball mill were repeated. Filtering was carried out in order to remove ethanol from the Ti64- Si_3N_4 powder mixture taken from the ball mill and this mixture was dried in an oven at 40°C for 22 hours. The dried powder mixture was passed through a $200 \mu\text{m}$ sieve and mixed to form a mixture of 70% urea and 30% powder by volume. Raw samples were obtained by shaping the prepared urea-powder mixture under a pressure of 630 MPa by means of a uniaxial hydraulic press. The shaped samples were kept in water at

150°C for 90 minutes in order to remove the urea from the obtained raw samples, and the samples that were freed from the urea were dried at 45°C for 120 minutes. The dried raw samples were sintered in an argon gas atmosphere at 1250°C for 120 minutes. The final samples, whose sintering process was completed, were analyzed mechanically, physically and chemically.

3. Results and Discussion

3.1. Porosity and Density

In this part of the study, the % relative density and % porosity values of unreinforced Ti64 composite foam and Si_3N_4 reinforced composite foams were investigated comparatively. The % relative density values are given in Figure 1. % porosity values are given in Figure 2.

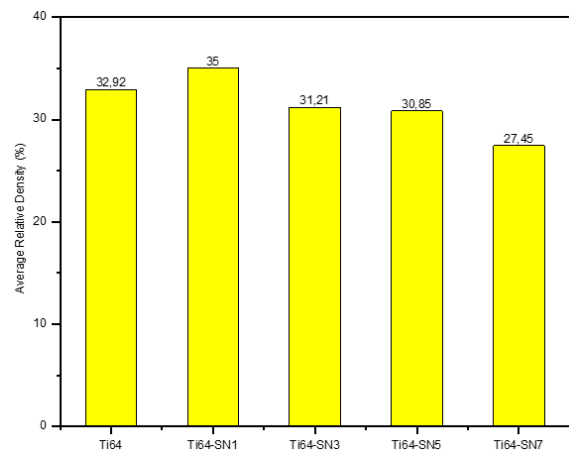


Figure 1. % relative density values

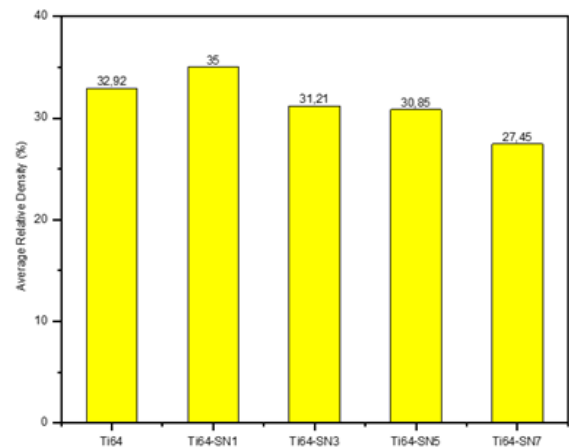


Figure 2. % porosity values

It is seen that the average relative density value of the composite foam material decreases gradually with the increase in the reinforcement ratio in the composite foam materials obtained by the Si_3N_4 reinforcement to the Ti64 matrix. The fact that the density of Si_3N_4 is lower than the density of the Ti64 matrix causes an increase in the % average relative density as the reinforcement ratio increases.

It is seen that the sample with the code Ti64-SN1 has the highest % average relative density value (35%). When the % average relative density values are examined, it is seen that there is not a big difference between the values, and the density decreases somewhat with the increasing ceramic ratio. The reason for this is that the ceramic powder clumps with increasing amount and homogeneous powder distribution is difficult.

The average porosity ratio of Ti64 and Si₃N₄ reinforced Ti64 matrix composite foam materials is given in the graph, the highest average porosity value (72.55%) is seen in Ti64-SN7 coded samples due to the inverse relationship between fill and porosity.

3.2. Hardness Of Foam Wall

In this section, the change in hardness values with the addition of Si₃N₄ to the Ti64 matrix at varying reinforcement rates (1%, 3%, 5% and 7% by weight) was investigated. Cell wall vickers hardness values are given in Figure 3.

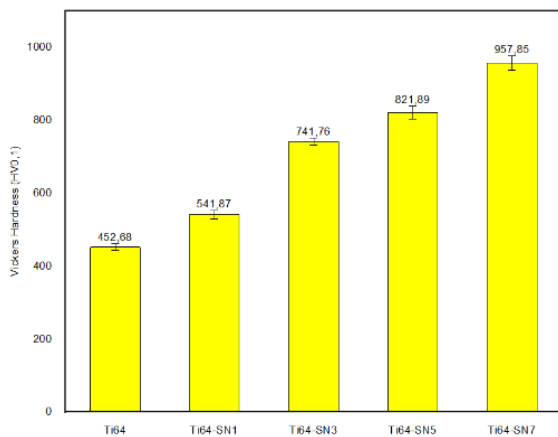


Figure 3. Hardness of foam wall

When the hardness values of the unreinforced Ti64 and Si₃N₄ reinforced Ti64 composite foam materials are examined on a graphic, it is seen that the hardness value increases with the reinforcement ratio in Si₃N₄ reinforced composite foam materials as the reinforcement ratio increases. The highest hardness value was measured with 957.85±20 HV0,1 in composite foam material coded Ti64-SN7. As the reinforcement ratio of Si₃N₄ reinforcement increases, it causes an increase in the hardness value with the increasing reinforcement ratio due to the high hardness of the ceramic in the structure.

3.3. Compressive Strength and Toughness

In this section, the maximum compressive strength and toughness values of non-reinforced Ti64 and Si₃N₄ reinforced composite foam materials were investigated. Maximum compressive strength values are given in Figure 4.

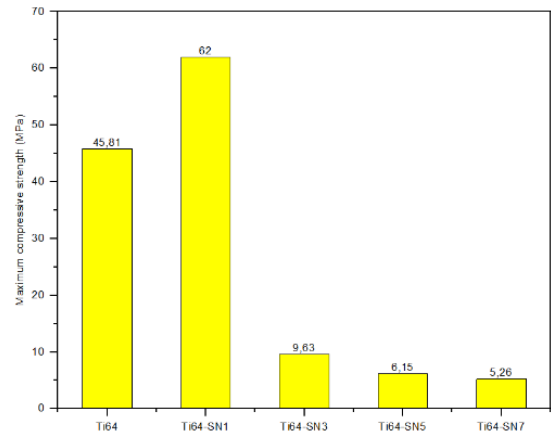


Figure 4. Maximum compressive strength

It is observed that the compressive strength of the composite foam sample increased with the addition of Si₃N₄ to Ti64. With the increase in the reinforcement ratio, the compressive strength values gradually decrease. The main reason for this situation is that Si₃N₄ is a ceramic material with a brittle structure and the tendency to agglomerate increases with increasing reinforcement value. The best compressive strength is seen in the sample coded Ti64-SN1. Toughness values are given in Figure 5.

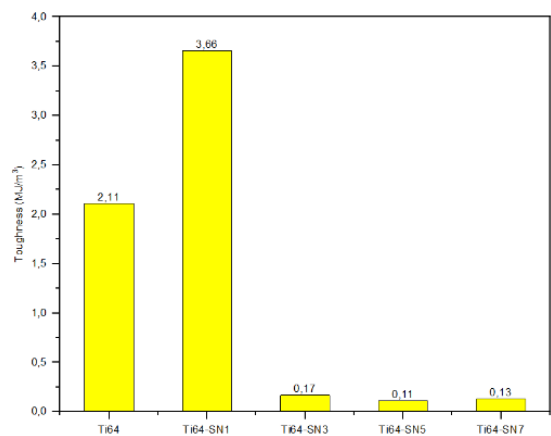


Figure 5. Toughness values

It is observed that the toughness value of the 1% Si₃N₄ reinforced Ti64 matrix composite foam sample increased with Si₃N₄ reinforcement. It is seen that the toughness value decreases as the reinforcement ratio increases. The highest toughness value of 62 MJ/m³ is seen in Ti64-SN1 coded material.

The reason for the increase in the mechanical properties with low amount of ceramic reinforcement can be given that the ceramic particles are homogeneously dispersed in the structure and the compressive strength of the ceramic is high. The reason for the decrease in the mechanical properties with the increasing ceramic ratio is due to the increase in the agglomeration tendency of

Si_3N_4 and the decrease in the density with the increase in the Si_3N_4 reinforcement ratio. In addition, the increase in the Si_3N_4 reinforcement ratio is due to the fact that the agglomerated ceramic on the cell walls of the composite foam sample becomes more brittle and low in toughness due to its more brittle structure under compression load.

3.4. Microstructure

In this section, microstructural analysis of Si_3N_4 reinforced composite foams at different ratios (1%, 3%, 5% and 7% by weight) has been carried out. The SEM image of the Si_3N_4 reinforced composite foam material is given in Figure 6. From the images, it is seen that the grains in Ti64 composite material reinforced with 1% Si_3N_4 by weight from the cell wall are homogeneously dispersed and have a strong neck formation. In the following figures, it has been observed that the porosity and agglomeration increase in the structure due to the increase in the Si_3N_4 reinforcement ratio (Figure 6-d). EDX element distribution maps of Ti64-SN1 coded composite foam sample are given in Figure 7.

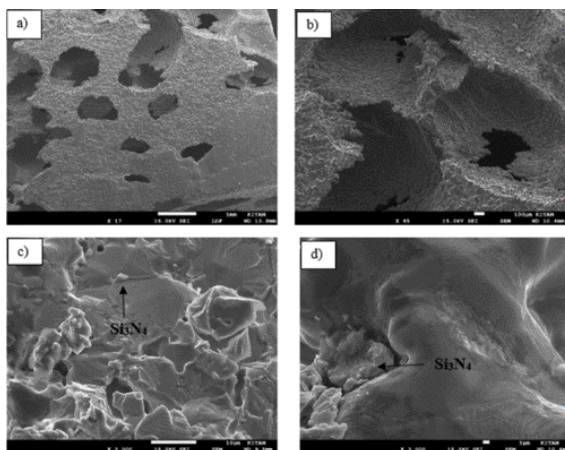


Figure 6. a) Ti64-SN1 cell pores b) Ti64-SN1 fracture surface cell wall c) SEM image of Si_3N_4 homogeneously dispersed in Ti64-SN1 structure at 2000 magnification d) SEM image of agglomerated Si_3N_4 in Ti64-SN5 structure at 3000 magnification

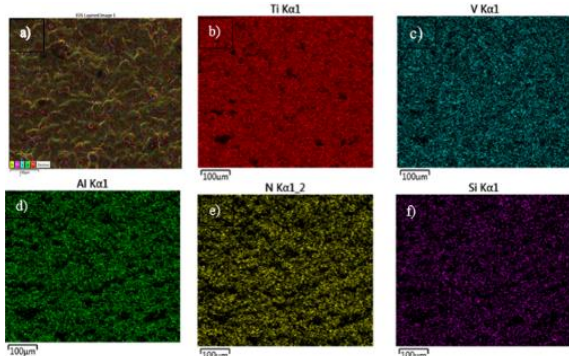


Figure 7. (a-f) EDX element distribution maps of

Ti64SN1 coded composite foam sample

These figures show how the Si_3N_4 reinforcement material is dispersed in the Ti64 matrix and its presence in the composite material. In addition, as a result of the EDS analysis, the expected Ti, Al, V, N and Si are found in the structure, and it is also seen from the map analysis that the ceramics are homogeneously distributed.

4. Conclusion

In this study, it is aimed to improve the mechanical properties of Ti64 foams. Composite foam materials were produced by adding Si_3N_4 to Ti64 at different rates (1%, 3%, 5% and 7% by weight) and by using powder metallurgy method and space holder method. As a result of the mechanical tests, it was observed that the hardness value increased as the Si_3N_4 reinforcement ratio increased. It has been observed that the composite foam material obtained by adding Si_3N_4 to the Ti64 matrix improves the compressive strength and toughness values. The reason for the decrease in compressive strength and toughness values with the increase in the reinforcement ratio is due to the agglomeration of Si_3N_4 in the structure.

References

- [1] M.C. Şenel, M. Gürbüz and E. Koç, Universal Journal of Materials Science, 5 (2017) 95-101.
- [2] N. Tunçer, Gözenekli Titanyumda Yapı-Özellik İlişkisi, Ph. D. Thesis, Anadolu University, 2011, Eskişehir, Turkey, pp. 1-21.
- [3] Z. Esen, Production And Characterization Of Porous Titanium Alloys, Ph. D. Thesis, Middle East Technical University, 2007, Ankara, Turkey, pp. 27-35.
- [4] M.F. Ashby, A. Evans, M. N.A. Fleck, L.J. Gibson, J.W. Hutchinson and H.N.G. Wadley, Metal Foams: A Design Guide, BH, 2000, Burlington MA, United States of America, pp. 3-5, 40-52.
- [5] A. Kalemtaş, Putech & Composites, (2014) 18-30.
- [6] M. Meignanamoorthy and M. Ravichandran, Mechanics and Mechanical Engineering, 22 (2018) 65-76.
- [7] M. C. Şenel, M. Gürbüz and E. Koç, Mühendis ve Makina, 59 (2018) 33-46.
- [8] D.B. Lee, I. Pohrelyuk, O. Yaskiv and J.C. Lee, Nanoscale Research Letters, 7 (2012) 1-5.
- [9] G. He and M. Hagiwara, Materials Science and Engineering: C, 26 (2006) 14-19.
- [10] D.C. Dunand, Advanced engineering materials, 6 (2004) 369-376.
- [11] D. Yao, Y. Xia, K. Zuo, D. Jiang, J. Günster, Y. Zeng and J.G. Heinrich, Journal of the European Ceramic Society, 34 (2014) 3461-3467.
- [12] F. Mussano, T. Genova, P. Rivolo, P. Mandracci, L. Munaron, M.G. Faga and S. Carossa, Journal of Materials Science, 52 (2017) 467-47.

BIODEGRADABLE POLYMER NANOCOMPOSITES USING MODIFIED CELLULOSE NANOCRYSTALS

Onur Nuri ARSLAN, Yonca ALKAN GÖKSU, Mohammadreza NOFAR

Istanbul Technical University
Türkiye

Keywords: Cellulose Nanocrystal, Surface Modification, PBAT

Abstract

Cellulose nanocrystal (CNC) can be a good nanofiller in polymer matrices thanks to its superior properties. However, its hydrophilic nature cause agglomeration in polymer matrices. To eliminate this, poly(glycidylmethacrylate) (PGMA) modification on CNC surface was carried out in this study. After that, poly (butylene adipate-co-terephthalate) (PBAT) was used as polymer matrix to understand the improvement of CNC dispersion. Also, it is aimed to improve the rheological and other properties of PBAT by improving dispersion. Thanks to PGMA modification, chemical bridge can be created between CNC and polymer matrix and hydrophilicity can be decreased with PGMA chains on CNC surface. CNC dispersion quality in nanocomposites were compared through rheological analysis. Also, TGA and DSC analysis were conducted to determine thermal properties.

1. Introduction

Although cellulose nanocrystal has numerous superior properties such as abundant sources and high mechanical properties, it has also some drawbacks to be used in polymer matrices such as low thermal degradation temperature and hydrophilic nature [1]. Due to hydroxyl groups on CNC surface, it has hydrophilic nature however, these groups can give reaction with different chemical groups and consequently numerous modification methods can be applied on CNC surface [2].

2. Materials and Methods

Materials

Spray-dried CNCs were provided by CelluForce (Montreal, Canada). Potassium persulfate (KPS) was used as initiator and was provided from Sigma Aldrich. Glycidyl methacrylate was used as monomer and polymerized on CNC surface. It was provided from Sigma Aldrich. The PBAT (Ecoflex® F Blend C1200) was provided from BASF.

Preparation of CNC-g-PGMA

To prepare CNC grafted PGMA(CNC-g-PGMA), an amount of CNC was dispersed in water. Reflux condenser system was prepared and the temperature was set to 70 °C. System was purged by using nitrogen environment and potassium persulfate(KPS) was added in the reaction environment. After that, glycidyl methacrylate (GMA) was added slowly and polymerization took place for 3 hours. The reaction was terminated by the addition of methanol and centrifugation was carried out and products were mixed in THF to get rid of homopolymers.

Production of PBAT/CNC specimens

3 wt. % of neat CNC, PGMA and CNC-g-PGMA were added in PBAT matrices and PBAT was produced without CNC by using melt mixer. Production step was performed for 5 minutes at 160 °C.

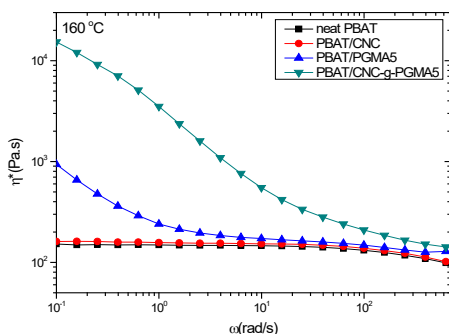


Figure 1. Complex viscosity of specimens

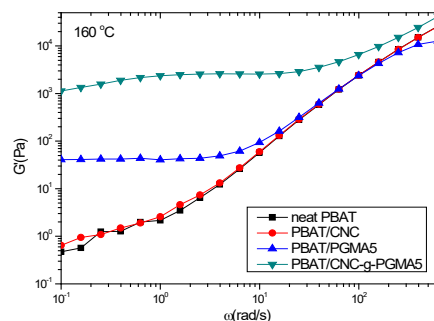


Figure 2. Storage Modulus of specimens

3. Conclusion

CNC was modified successfully with polymerization of GMA on CNC surface and rheological properties were increased dramatically thanks to presence of PGMA especially at low frequencies. On the other hand, when CNC-g-PGMA5 and PGMA5 were compared, positive effects of CNC was observed. Modification of CNC with PGMA contributes to obtain a remarkable nanofiller especially in biodegradable polymer matrices. The green nanocomposites can be used instead of non-degradable polymers in commodity applications.

References

- [1] Tang, J., Sisler, J., Grishkewich, N., & Tam, K. C. (2017). Functionalization of cellulose nanocrystals for advanced applications. *Journal of colloid and interface science*, 494, 397-409
- [2] Habibi, Y. (2014). Key advances in the chemical modification of nanocelluloses. *Chemical Society Reviews*, 43(5), 1519-1542.



INVESTIGATION OF THE EFFECT OF COPPER ALLOY REINFORCEMENT ON THE PHYSICAL PROPERTIES OF POLYMER MATRIX COMPOSITE

Ömer Alparslan KAYA¹, Talip ÇITRAK¹, Serdar TOZKOPARAN¹, Edanur KASAP¹,
Münir TAŞDEMİR², Feriha BİROL¹

¹Sağlam Metal, ²Marmara Üniversitesi
Türkiye

Extended Abstract

Polymer materials are used in many sectors such as automotive, machinery, aviation and medical due to their easy forming, recycling, reuse and strong characteristic properties with their affordable cost. The properties of polymer materials such as thermal, mechanical and electrical conductivity can be improved by using these materials as polymer-metal, polymer-polymer, polymer-fiber composites. This makes polymer composites the preferred material for many specific applications. In this study, PE and PP were used as matrix materials. Reinforced copper alloy CuCrZr powder particles were added at a rate of 0.5%-1%-3%-5% by weight. The materials were granulated using a twin screw extruder. Then, test coupons were printed with an injection machine. Molded samples; melt flow index, moisture absorption, thermal distortion temperature, vicat softening temperature, wear rate, static and dynamic friction coefficient and scanning electron microscopy (SEM) tests were carried out. The results of the tests were examined and the effects of copper powder supplementation on polyethylene and polypropylene were investigated. According to the results of the tests, it was determined that with the increase of copper powder ratio in the matrix, the moisture absorption value decreased, while the thermal distortion temperature, vicat softening temperature, melt flow index, friction coefficient and wear rate values increased.

Keywords: PE, PP, Copper Powder, Metal Powder, Polymer composite, Physical Properties.

In recent years, polymer composites are attractive materials for the medical, automotive and aerospace industries. [1]. Composite materials are formed from two or more materials to achieve the desired properties. Thermoset and thermoplastic materials are used as matrix in most advanced composite materials. Studies are carried out to meet the needs of different sectors, such as metal and ceramic powders as an additive. [2,3,4]. Additional materials are used to improve thermal, mechanical, electrical and physical properties.[5-6] These properties depend on the volume, forms and types of the additive materials in the matrix, the production method and the interface compatibility[7]. In this study, 0.5%, 1%, 3%, 5% by weight copper powder was used as additive and

polyethylene and polypropylene were used for the polymer matrix. After the composite production, the physical properties were investigated experimentally.

1. Experimental Produce

1.1 Compositon and Material

Copper powder was added in polyethylene and polypropylene material at the rates of 0.5%-1%-3%-5% by weight. Samples with no addition of each polymer material were included in the study as reference and a total of 10 groups were investigated. The company from which the polyethylene and polypropylene materials used were supplied did not share information due to commercial concerns. Copper powder was supplied from CNPC POWDER GROUP CO., LTD. The powder size is between 15-53 micrometers and its density is 5.3 g/cm³.

Polyethylene and polymer raw materials are supplied in sheets, therefore the sheet materials were crushed into granules for extruder. The granule sizes are in the range of 3-5 mm. The granules were dried in a Yamato ADP-31 type oven at 105°C for 24 hours to remove moisture. Then, polymer composites were prepared by melting in a twin screw extruder (Mikrosan) under 25-35 bar pressure, 25 rpm-1 rotation speed and temperatures between 200-240°C. After that it was dried in the oven at 85°C for 12 hours and the test samples were printed in an injection machine (Yonca machine) with a temperature of 200-240°C, a pressure of 700-900 bar and a screw rotation speed of 25 rpm.

1.2 Characterization

HDT test was carried out according to ISO 75 standard and Vicat softening temperature ISO 307 standard with Ceast brand tester. The load applied to the samples in the thermal distortion temperature test was determined by the formula below.

$$F=2.\sigma.b.h^2/3L \quad (1)$$

σ : Bending strength (MPa), b: Sample width (mm), h: Sample thickness (mm), L: Distance between supports (mm), F: Force applied to sample (N).

In the Vicat test, a load of 10 N was applied to the sample. The size of the samples used here is taken as 20x20x4mm.

The MFI test was performed with a Zwick 4100 device according to ISO 1133 standard. Here, 230°C temperature was applied to the sample and it was forced to flow under a load of 2.16 kg. The MFI value was determined using the formula below. m is the total weight of the sample flowing in a certain time (gr) and t is a certain time (sec).

$$MFI = m \cdot 600 / t \quad (2)$$

Moisture absorption tests are carried out according to ASTM D6980. The dimensions of the sample used here are 10x10x4 mm.

Abrasion tests were carried out according to DIN 53 516 standard. The rotation speed of the drum is set as 40 rpm. A load of 10 N was applied to the samples (FN) and the etching distances (L) were adjusted to be 20-40-60 and 80 meters. In order to find the weight loss (Δm) caused by wear, the weights of the samples before the test (M_1) and after the test (M_2) were weighed with a balance with an accuracy of 0.0001 g, and the weight loss was calculated with the formula given below.

$$\Delta m = M_1 - M_2 \quad (3)$$

The weight loss of the samples was measured after the etching process and the wear rates were calculated with the formula given below.

$$W_s = \Delta m / \rho \cdot FN \cdot L \quad (4)$$

Δm : Weight loss, ρ : Density, FN: Applied load and L: Abrasion distance. To determine the wear rates, 3 samples were tested and their arithmetic averages were taken.

The following formulas were used to determine the static and dynamic friction coefficient. Three samples from each group were tested and their average values were taken. Where F_s -static friction force, static friction coefficient and μ_s -dynamic friction coefficient.

$$\begin{aligned} \mu_s &= F_s / FP \\ \mu_d &= F_d / FP \end{aligned} \quad (5)$$

Samples for SEM-Scanning electron microscope were coated with gold/palladium alloy in Polaron brand coating device and were examined with Jeol brand scanning electron microscope under 10 kV.

2. Results and Discussion

2.1 2.1 Physical and Wear Properties

2.2 Vicat softening temperature of the composite obtained by adding copper powder in different

weight ratios into polyethylene and polypropylene polymer is given in Figure 3.1. In Figure 3.1, it is seen that the addition of copper powder increases the vicat temperature of the polyethylene samples. The same situation is observed in polypropylene samples as the copper addition rate increases

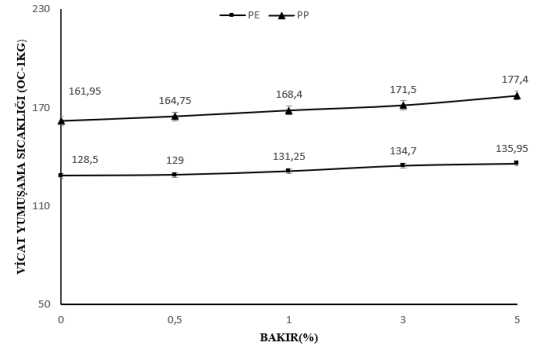


Figure 3.1 Vicat softening temperature graph of PE-PP/Cu composite

The melt flow index is a parameter of high importance in the production of polymer-based products. In polyethylene samples, the highest value was obtained in the sample with 5% copper addition, 1.706 gr/10 min. It was observed in the samples with 5% copper addition in the polypropylene samples. Melting flow index increased with the increase of copper addition.

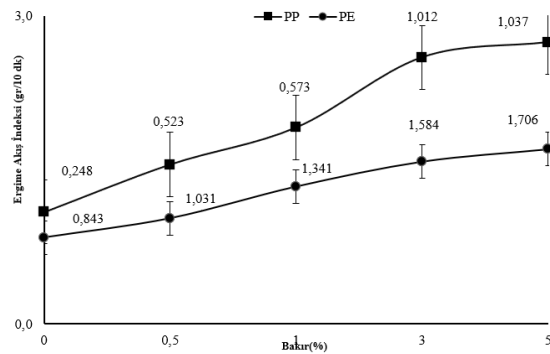


Figure 3.2 Melt flow index graph of PE-PP/Cu composite

It is seen in Figure.3.2 that the dehumidification rate of the polyethylene composites decreases from 0.613 in to 0.517 as the copper addition increases while it declines from the value of 0.817 to 0.453 in the polypropylene samples with the increasing of the copper ratio. A decrease of 16% was observed in polyethylene samples and 45% in polypropylene samples. The less moisture retention of metals compared to polymers causes the dehumidification rate in the samples to decrease as the

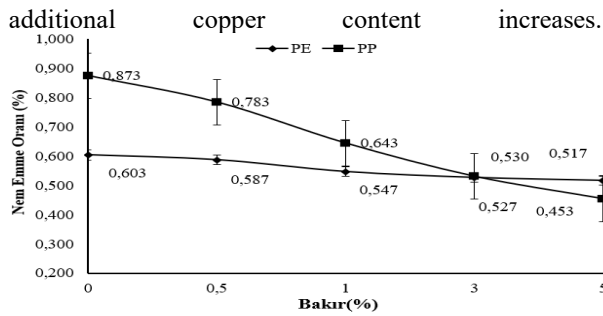


Figure 3.3 Moisture absorption rate of PE-PP/Cu composite

Two different methods were applied to measure the friction coefficient of the composites obtained. In the friction test, loads of 1.96 - 2.94 - 3.92 - 4.9 and 6.86 N were applied. Then static and dynamic friction coefficients of the polymer composite were calculated.

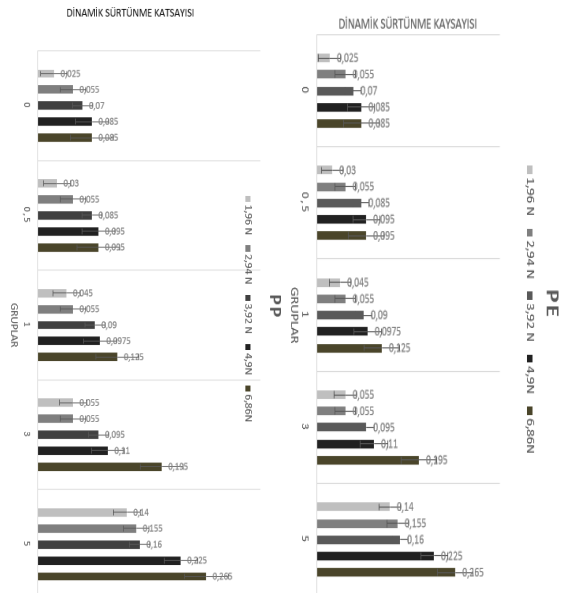


Figure 3.4 Dynamic friction coefficient of PE-PP/Cu composite

The test results of the dynamic and static friction coefficients of polyethylene and polypropylene composites as increase of distance as well. In a study by Öksüz et al., it was determined that the wear rate values increased with the increase of the wear distance in the PP matrix polymer composite (Öksüz, Taşdemir, 2018). Aka et al. (Aka et al., 2019), Ulutaş et al. (Ulutaş et al. 2019), and Taşdemir et al. (Taşdemir, Kaştan, 2021) found in their studies that the wear rate values increased with the increase in the amount of applied load.

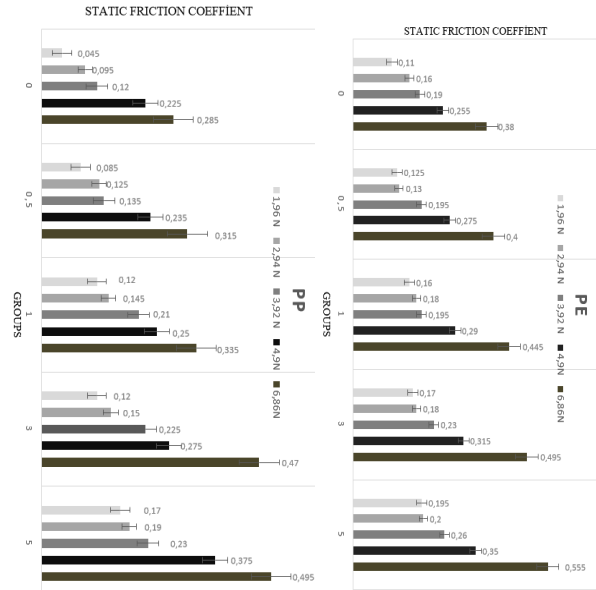


Figure 3.5 Static friction coefficient of PE-PP/Cu composite

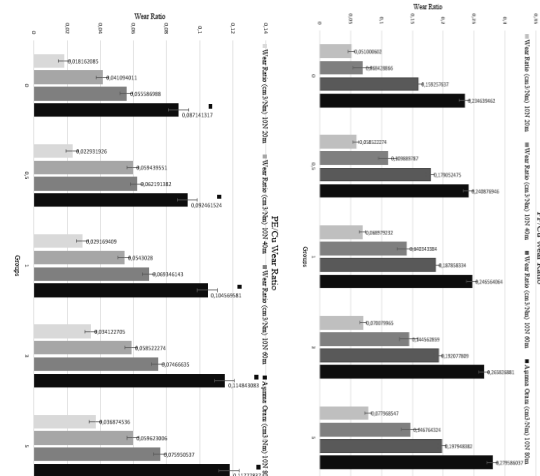


Figure 3.6 Wear rate of PE-PP/Cu composite

In Figure 3.6, it is seen that the addition of copper powder increases amount of wear of polyethylene and polypropylene composites as increase of distance as well. In a study by Öksüz et al., it was determined that the wear rate values increased with the increase of the wear distance in the PP matrix polymer composite (Öksüz, Taşdemir, 2018). Aka et al. (Aka et al., 2019), Ulutaş et al. (Ulutaş et al. 2019), and Taşdemir et al. (Taşdemir, Kaştan, 2021) found in their studies that the wear rate values increased with the increase in the amount of applied load.

3.2 Morphological Features

SEM images of the composites of polyethylene and polypropylene with the addition of 0.5%-1%-3%-5% copper powder are given in Figure 3.7.

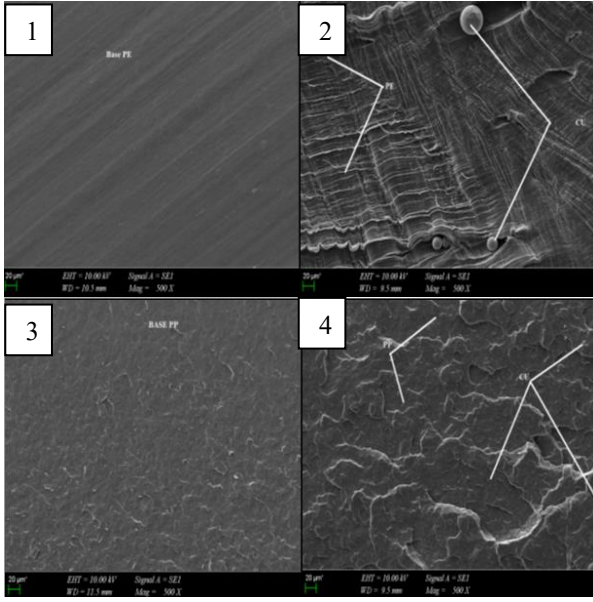


Figure 3.7 SEM images of PE-PP/Cu composite (1: pure pe, 2: 5%Cu/pe, 3: pure pp,4:%5Cu/pp)

4. Conclusion

The test results of the prepared composite samples can be summarized as follows:, when the test results of the composites with 0.5%-1%-3%-5% copper addition are examined,

- The increase in the addition of copper to both polymers increases their dynamic and static friction coefficient.
- At the same way, the vicat softening temperature increased with the copper addition rate as well.
- Addition of copper powder into both polymers affects the melt flow index of the copposites. As the addition of copper amount increases, the melt flow indexes of the composites increase.
- However, the dehumidification rate decreased in both polymer materials with the additional copper content.

5. Acknowledgment

This work was supported by Marmara University BAPKO. Project No: FYL-2022-10444. Sağlam Metal San. ve Tic. Inc. Thank you for your financial support and guidance.

6. References

- [1] Hollaway, L. C. (2004). Advanced Polymer Composites for Structural Applications in Construction: ACIC, (The University of Surrey, UK).
- [2] Mamunya, Y. P., Davydenko, V. V., Pissis, P., and Lebedev, E. V., European Polym. J. 38, 1887 (2002).
- [3] Tavman, I. H., Powder Tcehnology 91, 63 (1997).
- [4] Tavman, I. H., J. Appl. Poly. Sci. 62, 2161 (1996).
- [5] Zois, H., Apekis, L., and Mamunya, Y. P., Macromaol. Symp. 194, 351 (2003).

[6] Mamunya, Y. P., Zois, H., Apekis, L., and Lebedev, E. V., Powder Technol. 140, 49 (2004). [7] Zhu, K. and Schmauder, S., Computational Materials Sci. 28, 743 (2003).

[7] Aka A, Tekerek AY, Güler G, Taşdemir M, 2019. High density polyethylene/uncarbonized and carbonized waste corn husk polymer composites: physical and wear behaviors. 35th International conference of the polymer processing society (PPS-35), 26 - 30 May 2019, İzmir/Turkey.

[8] Akbaş S, Güleç T, Tufan M, Taşcıoğlu C, Peker H, 2013. Fındıkkabuklarının polipropilen kompozit üretiminde değerlendirilmesi. Artvin Çoruh Üniversitesi, Orman Fakültesi Dergisi, 14(1): 50-56.

[9] Banat R, 2019. Olive pomace flour as potential organic filler in composite materials: A brief review. American Journal of Polymer Science, 9(1):10-15.

[10] Demir M. E., Çelik Y. H. ve Kılıçkap E., 2019. Cam ve Karbon Elyaf Takviyeli Kompozitlerde Elyaf Cinsinin, Yükün, Kayma Hızı ve Mesafesinin Abrasiv Aşınmaya Etkisi. Politeknik Dergisi, 22(4): 811-817.

[11] Karakuş K, Başboğa İH, Mengeloğlu F, 2014. Termoplastik esaslı polimer kompozitlerin üretilmesinde orman budama atıklarının değerlendirilmesi. II. Ulusal Akdeniz Orman ve Çevre Sempozyumu, 22-24 Ekim 2014, Isparta, sayfa:801-807.

[12] Kızıltas A, Gardner DJ, Han Y, Yang HS, 2010. Determining the mechanical properties of microcrystalline cellulose (MCC) filled PET/PTT blend composites. Wood Fiber Sci. 42(2), 165-176.

[13] Korkmaz B, Özhan A, Peksanlı A, Tepeyurt GN, Taşdemir M, 2018. Investigation on phsical and mechanical properties of high density polyethylene/artichoke leaf powder polymer composites. International conferance on physical chemisry and functional materials, Fırat University, Elazığ-Turkey, pp:136-140, june 10-21, 2018.

[14] Öksüz A, Taşdemir M, 2018. Değişik oranlarda cam elyaf takviyeli polipropilen polimer kompozitine etilen vinil asetat ilavesi ile mekanik değerlerdeki değişimlerin incelenmesi. International Conference on Multidisciplinary Sciences (icomus), sayfa 1014-1023, 15-16 Aralık 2018, İstanbul Medipol Üniversitesi/İstanbul/Türkiye



MICROCELLULAR HEMP FIBRE REINFORCED POLYPROPYLENE MATRIX COMPOSITES

Yeşim ASLAN¹, Munir TAŞDEMİR², Yeliz ALBRECHTSEN¹, İsmail MUTLU¹

¹Tekkan Plastik, ²Marmara University
Türkiye

Keywords: Chemical Foaming Agent, Hemp Fibre, Microcellular Composites, Natural Fiber, Plastic Injection.

Abstract

Microcellular nature fiber reinforced polymer materials have significant application especially automotive industry because of their advantages such as their reducing weight and improving strength of components through microcellular structure, process and product. This research investigates chemical foaming agent types and their contents (1-2-3%wt.) impacts on physical properties of hemp fibre reinforced PP composites. Water absorption test, melt flow index test (MFI), density, Vicat softening temperature, heat deflection temperature (HDT), water absorption test would done. The morphology of the microcellular hemp fibre composites were examined using scanning electron microscopy (SEM) to observed cell morphology cell size, shape, and distribution of cells account for physical properties behavior.

1. Introduction

The sustainability of the plastics processing industry market requires innovation to save materials and minimize production costs. Due to new improvements methods and products are come out by studies [1]. Microcellular foam is a material that reduced material consumption, process temperatures, the viscosity of melt polymer, the density of products [2]. Due to the decrease in the density microcellular foaming agent is significant for the automotive industry [3]. It is possible to foam many commercially important polymers using physical or chemical foaming agents. Three methods of producing polymer foams take place in the literature: chemical foaming, physical foaming (mucell), and glass bubble. Chemical foaming has some advantages as particularly, no extra equipment is necessary for the chemical foaming process whereas the physical foaming process needs for example metering system and gas cylinder. The raw material costs are lower compared to glass bubbles [4], [5].

Injection molding is one of the most significant fabrication processes for thermoplastics [6]. Production thermoplastic foam polymers is known for many years by injection molding because of some advantages such as reduction of cycle time, lower viscosity. However, industrial applications of microcellular foamed thermoplastic polymers are rare because processing parameters are extensive. Besides, most studies have not applied for industrial scale [7].

The invention in the 20th-century polymers revolution laid environmental problems because of the lack of

non-biodegradable polymers waste management. Today, material science focus on biodegradable resources, such as natural fibers as hemp, wood, sisal and, flax, cotton. Hemp is green, eco-friendly which is one the most widely used natural fiber because of high aspect ratio (length/diameter ratio) and lower density as reinforcement in composites [8]-[10]. Natural polymer reinforced composite materials are reduced the weight of materials usage areas. Polymer matrix natural fiber reinforced bio-composites have recently drawn great attention in fundamental research and industrial applications for their ecological and economic advantages. Besides, environmental concerns, natural fiber reinforced polymer bio-composites provide a unique combination such as high performance, great versatility, and processing advantages at favorable costs [11], [12].

The effects of the microcellular foaming agent on natural fiber reinforced polypropylene composites in the injection molding process were described in the previous papers. Due to the previous studies, with high crystallinity, weak strain, and hardening behavior challenging production microcellular foaming agent polypropylene compound. And another parameter is low melt strength is inadequate to retain foaming gases in melt processes. And the melt strength is the main parameter in polymer foaming because of its effects on bubble size, bubble growth [13]-[16].

The scope of this study is to investigate the effects of chemical foaming agent content on the physical and morphological properties of microcellular natural fiber reinforced polypropylene composites. Therefore, reducing the consumption of plastic material used, reducing the total molding cycle time, using less tonnage injection molding machines, and thus reducing the energy costs are the purpose of this study which used the microcellular foaming process hemp fibre reinforced polypropylene matrix composites.

2. Experimental Procedure

A commercial %20 hemp fiber reinforced polypropylene compound (NAFIlean-PF2 555, Karel Kalıp SAN.A.Ş., Turkey) was used in this work. A commercial ITP was included not only as a nucleating agent but also chemical foaming agent (ITP825-818, HYDROCEROL, Clariant A.S.).

The commercial natural fiber-reinforced recycled composite

polypropylene which given Fig. 1(a), was dried in an oven at 105°C for 24 hours. Fig. 1(b) shown Hydrocerol. Afterward, %20 hemp fibre reinforced polypropylene and Hydrocerol (ITP 818-825) were mixed by the calculated seven different ratios which each prepared 2 kg specified in Table. I Each mixture was charged to plastic injection molding which was given Fig.1(c), Table. II was shown the process condition. From injection molding, liquid mixture was poured into the molds and test samples were obtained.

Table I. Samples ratios

Groups	PP+%20 Hemp fiber (wt.%)	ITP 825 (wt.%)	ITP 818 (wt.%)
1	100	-	-
2	99	1	-
3	98	2	-
4	97	3	-
5	99	-	1
6	98	-	2
7	97	-	3

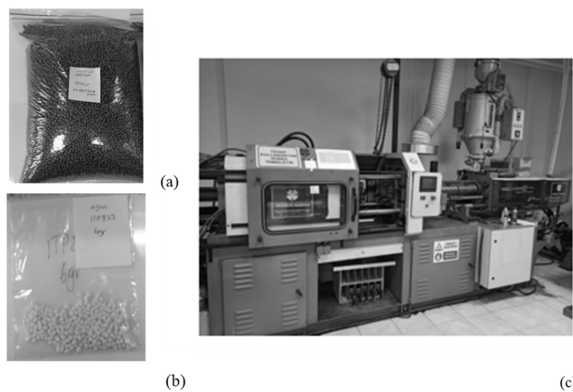


Fig. 1. Sample Preparation: (a): The commercial %20 hemp fiber reinforced polypropylene, (b): Hydrocerol, (c): Plastic injection molding machine

Heat deflection temperature (HDT) and Vicat softening point test were applied according to ISO 75 and ISO 307 standards, (CEAST 6521). Melt flow index (MFI) was carried out by ISO 1133 standard (Zwick 4100 MFI). Water absorption (WA) test was carried out according to ISO 62. The conditioned specimens were entirely immersed for 1 day in a container of water at 24°C. At the end of immersion time, the specimens were taken out from the water and all surface water was removed with a clean dry cloth. The specimens were immediately weighed to the nearest 0.01 g. According to the test method specified in ISO1183-1. Three specimens for each type of composite were used in the density measurement.

Table II. Process condition

Process Condition	Injection
Temperature (°C)	190-220
Pressure (bar)	75
Waiting time in mold (s)	8.6
Screw speed (rpm)	75
Mold temperature (°C)	-

3. Results and Discussion

Fig. 2 is given altering density behavior by chemical foaming contribution. %20 hemp fibre reinforced PP composite density is 0.98 g/cm³. The density of group 5 does not change. However, in group 6 and group 7 ITP 818 contribution increases, density is decreasing to 0.90 g/cm³ and 0.89 g/cm³. Not only ITP 818 but also ITP 825 decrease of the %20 hemp fibre reinforced PP density such as from 2.8 g/cm³ to 2.1 g/cm³ and 2.2 g/cm³. Thus, both types of chemical foaming agents may be created bubbles in the compound successfully.

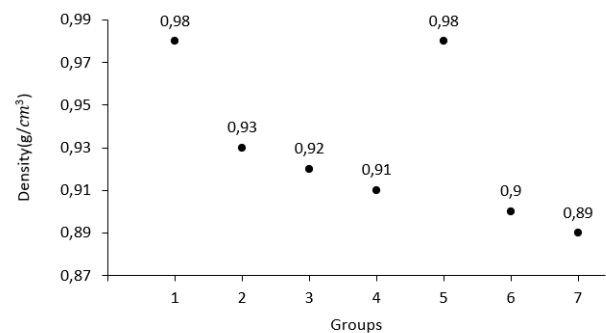


Fig. 2. Density of 20% hemp fiber reinforced d PP with different ITP loading.

The average water absorption (WA) values of each type of sample are presented in Fig. 3. The WA of the 20% hemp fibre reinforced PP, which shows as group 1 in the table, is obtained at 1.6 g/m². The WA values of the ITP 818 contribution, which shows group 5, group 6 and group 7 samples are decreased (1,2,3 %wt) 3,79 g/m² to 3.1 g/m² and 2.2 g/m² respectively. On the other hand, group 2, group 3, and group 4 that dopped ITP 825 samples are decreased greater than ITP 818 from 2.8 g/m² to 2.12 g/m² and 2.16 g/m² more 20% hemp fibre reinforced polypropylene may be become more hydrophobic by ITP contributions.

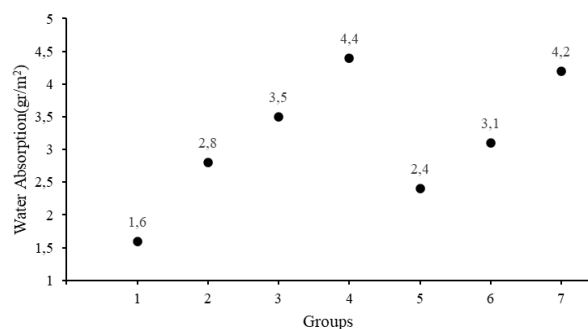


Fig. 3. One-day water absorption (WA) of the of 20% hemp fiber reinforced PP with different ITP loading

Fig. 4 shows the heat deflection temperature of the 20% hemp fibre reinforced PP and different quantities of ITP 825 and ITP 818 (1,2,3 %wt.). In this work, the HDT of group 1 %20 hemp fibre reinforced PP is found to be 83°C. In general addition of both types of ITP is decreased HDT of %20 hemp

fibre reinforced. However, group 4 and group 7 (3%wt. both types of ITP) have been greater decreased of the HDT. On the other hand, 1%wt. of ITP 825 is dropped HDT temperature from 83 °C to 81°C. These results led us to believe that the foaming agent created bubbles decrease of heat deflection temperature is obtained.

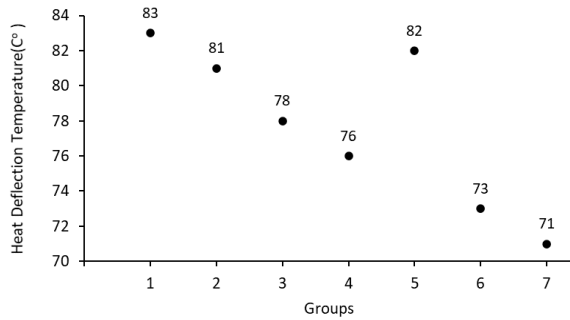


Fig. 4. Heat deflection temperature properties of 20% hemp fiber reinforced PP with different ITP loading.

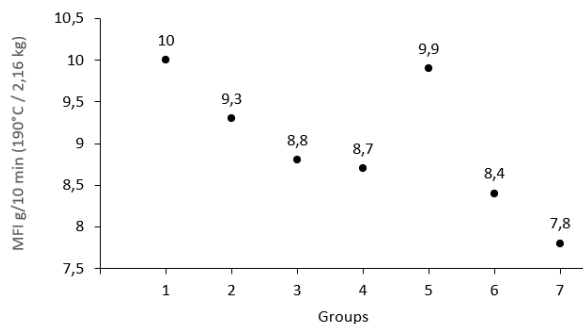


Fig. 5. Melt flow index of 20% hemp fiber reinforced PP with different ITP loading.

The relationship between the melt flow index (MFI) and the percentage of chemical foaming agents addition in the %20 hemp fibre reinforced to PP composites are shown in Fig. 5. With the inclusion of ITP in the composites the MFI values of the are found to be decreasing. For instance, group 2, group 3, and group 4 MFI values are measured as 9.3 g/10 min, 8.8 g/10 min, and 8.7 g/10 min respectively. The MFI value of group 1 is 10.0 g/10 min. Group 5, group 6 and group 7 MFI values decrease from 9.9 g/10 min to 8.4 g/10 min and 7.8 g/10 min, respectively. Hence, compounds flow decrease related to ITP consisted of bubbles. That suggests, 3 %wt. ITP 818 may not disperse homogeneously.

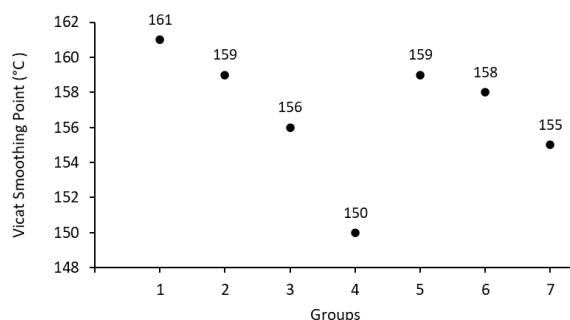


Fig. 6. Vicat properties of 20% hemp fiber reinforced PP with different ITP loading.

Fig. 6 shows Vicat softening behavior properties 20% hemp fibre contents PP and Hydrocerol (ITP 818 and ITP 825) loading. The Vicat softening point of group 2, group 3, and group 4 is decreased from 161 g/cm³ and 159 g/cm³ to 156 g/cm³ and 150 g/cm³, by ITP 825 chemical foaming agent, respectively. The Vicat softening point of group 5, group 6, and group 7 dropped from 161g/cm³ and 159 g/cm³ to 158 g/cm³ and 155 g/cm³ loaded by ITP 818. Because ITP creates bubbles in the compound, Vicat softening points have been decreased. The Vicat softening point is a more pronounced decrease for the samples loaded with ITP 825.

Fig. 7 (a) illustrates group 1, which is %20 hemp fibre reinforced PP composite, morphology structure. Fig. 7 (b) is group 3 given the pore size of about 60µm and irregular. On the other hand, Fig. 7 (c) shows group 4, which is 3%wt. ITP 825 addition, cell size between 60-140 µm. It can be seen that the content of ITP 825 has obvious influence on the pore structure of the composite foams. Fig. 7 (d) and Fig. 7 (e) show in group 6 and group 7, where ITP 818 contribution 2 and 3 %wt. respectively. When the foaming agent is further increased, the walls between the holes are in contact with each other, and the shape of bubbles is irregular.

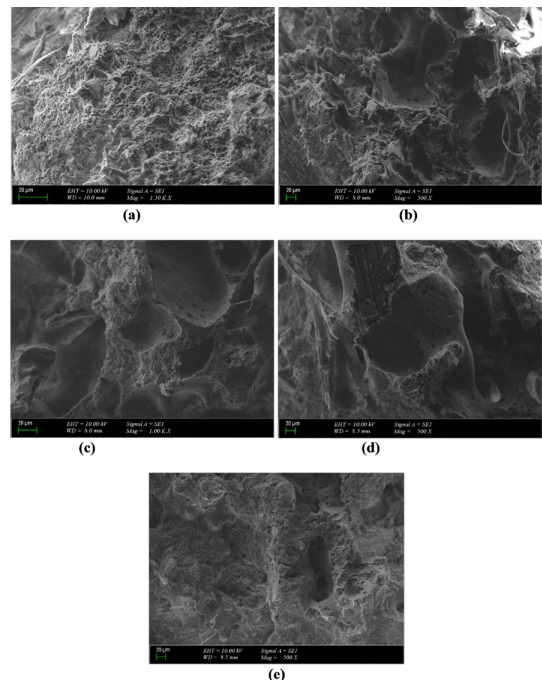


Fig. 7. Micrograph photo of 20% hemp fiber reinforced PP with different ITP loading

4. Conclusion

The effect of chemical foaming agents (ITP 818 and ITP 825) on the Vicat softening point, HDT, melt flow index, density, water absorption, of %20 hemp fibre reinforced PP were investigated. Hydrocerol was used as a potential foaming agent in the polypropylene and polypropylene matrix composites. The following results were obtained: Melt flow index, Heat deflection temperature, Vicat softening points of %20 hemp fibre reinforced PP decreased as both types of chemical foaming agents concentration increased. According to morphological analysis, the foaming

agents showed to create pores on the microstructure. Chemical foaming agent types and ratio affects the pore's size and distribution on the morphology of the composite depending upon the physical properties of %20 hemp fibre reinforced PP.

References

- [1] A. K. Bledzki and O. Faruk, Microcellular injection molded wood fiber-PP composites: Part I - Effect of chemical foaming agent content on cell morphology and physico-mechanical properties, Dec. 2006, *J. Cell. Plast.*, vol. 42, no. 1, pp. 63–76.
- [2] A. K. Bledzki, H. Kirschling, M. Rohleder, and A. Chate, Correlation between injection moulding processing parameters and mechanical properties of microcellular polycarbonate, *J. Cell. Plast.*, Nov. 2012, vol. 48, no. 4, pp. 301–340.
- [3] M. Kozłowski, Lightweight Plastic Materials, *Thermoplast. Elastomers.*, Mar. 2012, vol. 14, no. 1, pp. 291–318.
- [4] M. AKKOYUN, İ. BADEM, M. E. ÖZTOKSOY, and Y. ASLAN, Polypropylene/Chemical Blowing Agent Foams: Effect of the Injection Speed and Core Back Distance on Microstructure and Mechanical Properties, June 2020, *Uluslararası Muhendis. Arastırma ve Gelistirme Derg.*, pp. 638–647.
- [5] F. L. Jin, M. Zhao, M. Park, and S. J. Park, Recent trends of foaming in polymer processing: A review, *Polymers (Basel)*, June 2019, vol. 11, no. 6.
- [6] A. K. Bledzki and O. Faruk, Microcellular wood fiber reinforced PP composites: Cell morphology, surface roughness, impact, and odor properties, *J. Cell. Plast.*, Nov. 2005, vol. 41, no. 6, pp. 539–550.
- [7] A. K. Bledzki, M. Rohleder, H. Kirschling, and A. Chate, “Correlation between morphology and notched impact strength of microcellular foamed polycarbonate, *J. Cell. Plast.*, Sept. 2010, vol. 46, no. 5, pp. 415–440.
- [8] A. Shahzad, Hemp fiber and its composites - A review, *J. Compos. Mater.*, Sept. 2012, vol. 46, no. 8, pp. 973–986.
- [9] A. K. Bledzki and O. Faruk, Wood fibre reinforced polypropylene composites: Effect of fibre geometry and coupling agent on physico-mechanical properties, *Appl. Compos. Mater.*, June 2003 vol. 10, no. 6, pp. 365–379.
- [10] A. K. Bledzki, O. Faruk, and V. E. Sperber, Cars from bio-fibres, *Macromol. Mater. Eng.*, Apr 2006, vol. 291, no. 5, pp. 449–457.
- [11] E. Bodros and C. Baley, Study of the tensile properties of stinging nettle fibres (*Urtica Dioica*), *Mater. Lett.*, May 2008, vol. 62, pp. 2143–2145.
- [12] G. Sui, M. A. Fuqua, C. Ulven, and W. Zhong, A plant fiber reinforced polymer composite prepared by a twin-screw extruder, *Bioresour. Technol.*, Nov. 2008, vol. 100, pp. 1246–1251.
- [13] A. K. Bledzki and O. Faruk, Injection moulded microcellular wood fibre-polypropylene composites, *Compos. Part A Appl. Sci. Manuf.*, Aug. 2006, vol. 37, no. 9, pp. 1358–1367.
- [14] F. A. Soares and S. M. B. Nachtigall, “Effect of chemical and physical foaming additives on the properties of PP/wood flour composites,” *Polym. Test.*, Feb. 2013, vol. 32, no. 4, pp. 640–646.
- [15] G. Llewelyn, A. Rees, C. A. Griffiths, and M. Jacobi, A novel hybrid foaming method for low-pressure microcellular foam production of unfilled and talc-filled Copolymer Polypropylenes, *Polymers (Basel)*, Nov. 2019, vol. 11, no. 11.
- [16] A. K. Bledzki, W. Zhang, and O. Faruk, Microfoaming of flax and wood fibre reinforced polypropylene composites, *Holz als Roh- und Werkst.*, Dec. 2005, vol. 63, no. 1, pp. 30–37.



A STUDY ON THE MATERIAL PROPERTIES OF CARBON NANOTUBES DOPED GLASS FIBER REINFORCED NANO COMPOSITES

Bahadır TÜRKYAMAN¹, Mehmet Fatih ÖKTEM²

¹Tübitak SAGE, ²Ankara Yıldırım Beyazıt University
Türkiye

Keywords: Carbon Nanotubes, Glass Fibers, Spray and Mechanical Mixing Methods

Abstract

Fiber based laminated composites show relatively low out of plane/through thickness properties because of weak fiber/matrix interphase. In this study, it has been aimed to improve the through thickness properties of Multi Walled Carbon Nanotubes (MWCNTs) doped Glass Fiber Reinforced Polymers (GFPCs) produced by using different production methods such as Mechanical Mixing Method and Spray Method. Also, surfactant has been used to distribute MWCNTs more homogeneously. To see the effects of these methods on the properties of the composite materials, several mechanical testing and material characterization have been conducted. As a result of the conducted studies, best flexural strength and flexural modulus are obtained by Spray Method with the aid of surfactant. Also, increases observed on hardness of composite materials produced by both Spray and Mechanical Mixing Methods as compared to control sample. The SEM images revealed that the best dispersion of MWCNTs in the structure are obtained with Spray Method.

1. Introduction

Nano composite materials have constituted a new scientific field for researchers, scientists and engineering industry with their specific high strength, high resistance to corrosion, low weight and other important features in today's technology. Composite materials have two distinct phases that are matrix and reinforcement phases. Also, between these phases, there is another important phase exist which is called as interphase. This phase directly allows load transferring from matrix to reinforcement phase, so it is important to get closer to theoretical values [1], [2].

Glass fibers are one of the most important fibers used as reinforcement for all polymer matrix composites and, they are commonly used as reinforcement phase

in the industry. Their outstanding properties in terms of excellent impact resistance, high strength to weight ratios and high corrosion resistance make the glass fibers one of the most significant candidates [3]. Glass fiber reinforced epoxy composite materials show excellent in-plane mechanical properties, but out of plane/through thickness properties of these composites is significantly low due to weak fiber/matrix interphase. This weak interphase directly affects z-axis properties such as interlaminar shear strength, flexural strength, delamination resistance etc. So, it is important to enhance the fiber/matrix interphase to reach maximum mechanical strengths. In recent years, these drawbacks have drawn the attention of researchers to use carbon nanoparticles in order to enhance interface between glass fiber and polymer matrix. Carbon nanotubes (CNTs) are one of the significant candidates due to their excellent mechanical, electrical, thermal properties and enormous surface area [4], [5], [6].

In the literature, many studies were conducted by researchers to demonstrate effect of CNTs on interface between glass fiber and polymer matrix phases. In 2019, Panchagnula et al. [7] studied effect of multi-walled CNTs (MWCNTs) on glass fiber reinforced polymers (GFRP). The results of this study showed that nearly 39.41% increases in the flexural strength of MWCNTs grafted GFRP composites is observed from neat epoxy with addition of 0.3% MWCNT that improved interfacial adhesion between glass fiber and matrix. Also, another study on the improvement of interfacial strength of glass fiber reinforced polyphenylene sulfide composites with grafting MWCNTs, was conducted by Li et al. [8]. According to the results of this study, it was demonstrated that with the addition of MWCNTs to the composite materials enhance was observed in interface by improving contact area between glass fiber and matrix

and, bending strength of composite material increased from 67 to 85 MPa.

In this study, it has been aimed to improve the through thickness properties of Glass Fiber Reinforced Composites (GFPCs) by doping Multi Walled Carbon Nanotubes (MWCNTs) that was produced by using different production methods such as Mechanical Mixing and Spray Methods.

2. Experimental Procedure

2.1. Materials and Methods

In the experimental part of this study, Twill Woven 2/2 Glass Fiber is used as reinforcement phase. As matrix phase, epoxy is used that consists of resin (A) and hardener (B). To improve fiber/matrix interfacial strength, MWCNTs are used as a doping nano-material. Also, to disperse MWCNTs homogenously in the structure and to prevent agglomeration problem, surfactant is used in the study.

To produce composite materials, two different methods are applied in this study. These are Spray and Mechanical Mixing Methods. During production, all the ratios are kept constant to see the effect of production methods on the out of plane properties. Followed production path is given in **Figure 1**.

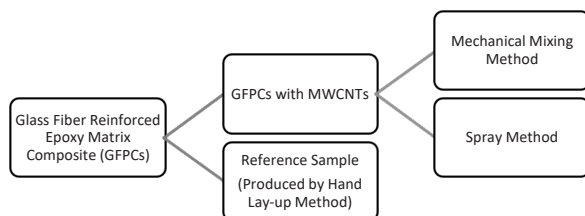


Figure 1. Followed Path for Production of Glass Fiber Composite Materials.

During production processes, firstly, control sample is produced with hand lay-up method to check changes in flexural properties with addition of MWCNTs in the structure. Resin and hardener are mixed by using high shear mixer. Also, in all production processes, hand lay-up and vacuum bagging methods are used.

In this study, Spray Method is used as one of the methods to disperse nanoparticles homogeneously. In this method, MWCNTs are sprayed on the glass fibers and hand lay-up process is applied to produce composite material. The ratio of MWCNTs has been chosen as 1.5 wt.% in this study.

Another method used in this study is Mechanical Mixing Method. In this method, MWCNTs are directly mixed with resin and hardener mixture. Then, hand lay-up process is applied to produce composite material.

2.2. Three Point Bending Test

To see the effects of MWCNTs and different composite production methods along the z-axis/through thickness properties of glass fiber composite materials, Three-Point Bending Test has been conducted to composite specimens in accordance with ASTM D 7264 Standard Test Method for Flexural Properties of Polymer Matrix Composite Materials- Procedure A. Flexural Stress values are calculated for any point on the load-deflection curve by the following equation given in Equation (1) [9]:

$$\sigma = 3PL/2bh^2 \quad (1)$$

where; σ is the stress at the outer surface at mid-span, MPa [psi], P is the applied force, N [lbf], L is the support span, mm [in.], b is the width of the beam, mm [in.] and h is the thickness of the beam, mm [in.].

2.3. Fractographic Analysis

To evaluate distribution of MWCNTs in epoxy system and on glass fiber, Scanning Electron Microscopy (SEM) has been used. Before the analysis, all samples have been covered with gold to provide the conductivity to get the desired image.

3. Results and Discussion

In this study, three-point bending tests have been conducted for three specimens of each production methods to get valid test results. Flexural Strength (MPa) vs. Deformation (mm) curves given in **Figure 2**.

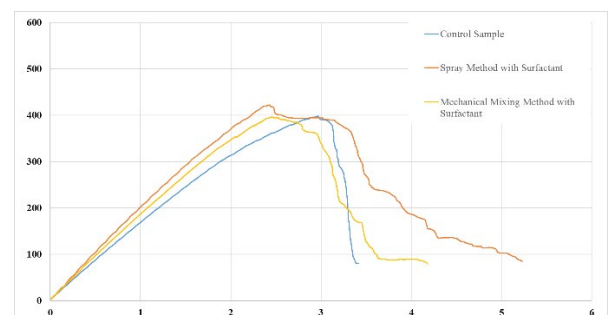


Figure 2. Flexural Strength vs. Deformation Curve for Samples [1].

It is observed that from **Figure 2**, the composite material produced with neat resin quickly failed after reaching its maximum strength value. When MWCNTs have been added to GFECs, it is observed on composite materials produced by different production methods that slight decrease in load after reaching its maximum strength value. It is clearly seen that best average flexural strength and flexural modulus value is obtained in composite material produced by using Spray Method. Flexural strength and modulus are increased about 4.30 and 17.70% respectively as compared to control sample and about 10.00 and 7.50% respectively as compared to mechanical mixing method.

To see effects of Spray and Mechanical Mixing Methods on the dispersion of MWCNTs on the glass fiber reinforced epoxy matrix composite SEM has been used. SEM images taken from composite materials produced by using Spray and Mechanical Mixing Methods are given in **Figure 3** and **Figure 4**.

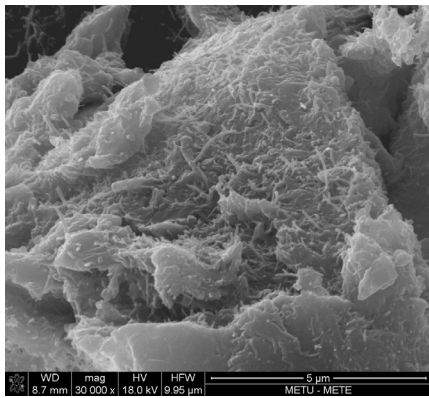


Figure 3. SEM Image of Composite Material Produced by Mechanical Mixing Method [1].

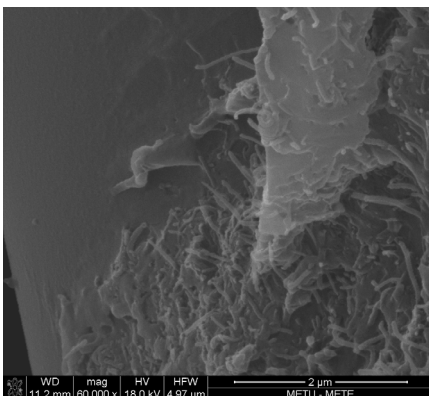


Figure 4. SEM Image of Composite Material Produced by Spray Method [1].

When the **Figure 3** and **Figure 4** are compared in terms of dispersion of MWCNTs in the structures, it is clearly seen from SEM images that better dispersion of MWCNTs was observed with Spray Method. This dispersion directly related to flexural properties. The results of three-point bending test performed on these composite materials to obtain flexural properties overlap with the SEM images obtained. It is obtained from three-point bending tests that better flexural properties are obtained with Spray Method as compared to Mechanical Mixing Method.

4. Conclusion

In these study, to see the effects of these methods on the composite materials Three-Point bending test and Scanning Electron Microscopy (SEM) analyses have been conducted. As a result of conducted studies, the best flexural strength and modulus are obtained with Spray Method. Flexural strength and modulus are increased about 4.30 and 17.70% respectively as compared to control sample and about 10.00 and 7.50% respectively as compared to mechanical mixing method. Also, SEM images revealed that the best MWCNTs dispersion is observed with Spray Method.

Acknowledgment

I would like to express my deep thankfulness to Asst. Prof. Dr. Mehmet Fatih ÖKTEM for supporting and encouraging this study. I would like to express my very great appreciation to Dr. Necmettin Kaan Çalışkan for helping me finalize my project with their valuable ideas in difficult situations. I owe my thanks to my company TÜBİTAK SAGE which I am proud to be a member of, for opportunities and great support provided to me.

Reference

- [1] Türkyaman B., Comparison of Flexural and Physical Properties of Multi-Walled Carbon Nanotubes Added Glass Fiber Reinforced Polymer Composites Produced by Conventional Direct Mixing and Innovative Spray Method, M.Sc. Thesis, Ankara Yıldırım Beyazıt University, 2020
- [2] Karger-Kocsis, J., Mahmood, H., and Pegoretti, A., Recent advances in fiber/matrix interphase engineering for polymer composites, Prog. Mater. Sci., vol. 73, 1–43, 2015.
- [3] Khan, M. S., Glass Fiber Composites | Properties of Glass Fiber | Manufacturing of Glass Fiber | Applications of Composite Glass Fiber, Textile



Learner, <https://textilelearner.blogspot.com/2012/09/glass-fiber-composites-properties-of.html>, 18-Feb-2020.

[4] Wang, Y., Pillai, S. K. R., Che, J., and Chan-Park, M. B., High Interlaminar Shear Strength Enhancement of Carbon Fiber/ Epoxy Composite through Fiber- and Matrix-Anchored Carbon Nanotube Networks, *ACS Appl. Mater. Interfaces*, 9(10), 8960–8966, 2017.

[5] Fan, Z., Santare, M. H. and Advani S. G., Interlaminar shear strength of glass fiber reinforced epoxy composites enhanced with multi-walled carbon nanotubes, *Compos. Part A Appl. Sci. Manuf.*, 39(3), 540–554, 2008.

[6] Yao, Y. and Chen, S., The effects of fiber's surface roughness on the mechanical properties of fiber-reinforced polymer composites, *J. Compos. Mater.*, 47(23), 2909–2903, 2012.

[7] Panchagnula, K. K. and Kuppan, P., Improvement in the mechanical properties of neat GFRPs with multi-walled CNTs, *J. Mater. Res. Technol.*, 8(1), 366–376, 2019.

[8] Li, J., Qiao, Y., Li, D., Zhang, S., and Liu, P., Improving interfacial and mechanical properties of glass fabric/polyphenylene sulfide composites via grafting multi-walled carbon nanotubes, *RSC Adv.*, 9(56), 32634–32643, 2019.

[9] ASTM International, “D7264/D7264M: Standard Test Method for Flexural Properties of Polymer Matrix Composite Materials,” *Annu. B. ASTM Stand.*, 2015, doi: 10.1520/D7264.

INVESTIGATION OF THE MECHANICAL PROPERTIES OF THERMOPLASTIC BASED SANDWICH STRUCTURES PRODUCED BY FUSED DEPOSITION MODELING (FDM) TECHNIQUE

Hurşit Sefa AYDIN, Cihan KABOĞLU, Deniz UZUNSOY

Bursa Technical University
Türkiye

Keywords: Sandwich Structures, FDM, 3D, Thermoplastic

1. Introduction

Lightweight sandwich structures are used widely in the aerospace and automotive industries due to its high energy absorption capacity, superior thermal insulation, high impact and bending resistance. The sandwich structures basically consist of core and surface layers. The basis of core structures which developed as a result of numerous analytical and experimental studies consists of porous cellular geometries. Recently, conventional fabrication techniques are insufficient due to production of complex cellular core structures and reduction of the core sizes geometrically. Therefore, the desired core topologies have started to be produced by using the fused deposition modeling (FDM) technique which is one of the additive manufacturing (AM) methods. FDM three-dimensional (3D) technologies, which are superior to conventional fabrication methods with their features such as reducing costs, manufacturing complex products with high precision and eliminating additional processes provide many advantages.

In this study, sandwich structures with auxetic and tetrachiral core geometry were manufactured using acrylonitrile butadiene styrene (ABS) and polystyrene (PS) thermoplastic materials by using an FDM-based 3D printer. The mechanical behavior of the produced sandwich structure samples was determined by applying compression test and three-point bending test.

2. Materials and Methods

The materials used in this study were chosen as ABS and PS filaments with a diameter of 1.75 mm which are suitable for use in FDM 3D printers. Sandwich panels to be manufactured as compression and three-point bending specimens are designed respectively according to ASTM C393/C393M-16 and ASTM D7336/7336M-16 standards. 3D process parameters for the production of sandwich samples were determined as respectively 255°C printing temperature, 115°C built plate temperature, 0.4 mm nozzle diameter, 0.3 mm layer height and 60 mm/sec printing speed.

3. Conclusion

Sandwich structure samples with auxetic and tetrachiral core geometries were successfully manufactured by FDM technique as shown in Figure 1. According to the results of compression and three-point bending tests, PS sandwich structure sample with tetrachiral core geometry showed the highest compressive force value of 17616,43 N and ABS sandwich structure sample with auxetic core geometry showed maximum bending force value of 996 N.

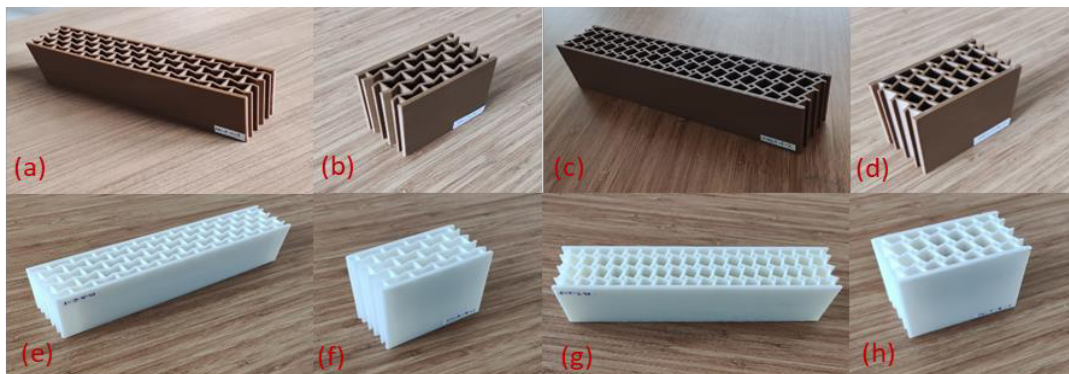


Figure 1. Images of the manufactured sandwich structures. (a) three-point bending test specimen with auxetic core geometry, (b) compression test specimen with auxetic core geometry, (c) three-point bending test specimen with tetrachiral core geometry, (d) compression test specimen with auxetic core geometry manufactured using ABS filament. (e) three-point bending test specimen with auxetic core geometry, (f) compression test specimen with auxetic core geometry, (g) three-point bending test specimen with tetrachiral core geometry, (h) compression test specimen with auxetic core geometry manufactured using PS filament.

Acknowledgment

This study was financially supported by “Bursa Technical University Coordinatorship of Scientific Research Projects (BTÜ-BAP)” with the project number of 211N007.

MECHANICAL CHARACTERIZATION OF GRAPHENE NANOPATELETS/Al₂O₃ REINFORCED EPOXY HYBRID COMPOSITES

Cantekin KAYKILARLI^{1,2}, Aygül YEPREM², Deniz UZUNSOY¹

¹Bursa Technical University, ²Yıldız Technical University
Türkiye

Keywords: Polymer Matrix Composites, Epoxy, Graphene, Aluminum Oxide

1. Introduction

The development of composite materials has allowed engineers to replace traditional materials in the majority of engineering fields, ranging from terrestrial to space applications. One of the most economical ways to enhance mechanical, tribological, and physical characteristics of polymeric materials is to add nanofillers to them. Epoxy is one of the most significant thermosetting polymers used in a variety of applications due to its superior mechanical properties, ease of manufacture, low cost, superior thermal stability, low moisture absorption, good adherence to a variety of substrates, and high electrical, corrosion, and chemical resistance. Graphene's superior properties, such as extraordinary tensile strength, a large surface area and excellent elastic modulus, making it an ideal reinforcement for epoxy-based composites.

2. Materials and Method

In this study, graphene nanoplatelets (GNP) and aluminum oxide (Al₂O₃) reinforced epoxy matrix composites are produced with sonication and magnetic stirring routes. All composites produced with the same methodology. Firstly, The reinforcements dispersed in acetone via Sonicator (Bandelin Sonoplus HD 3200) for 30 min. Epoxy resin has been added to the solution and sonicated for another 30 min. After the sonication process, the mixture was stirred with magnetic stirring at 70°C overnight. The curing agent is added to the reinforcements-epoxy resin mixture and poured into moulds. The epoxy composites were degassed under vacuum at room temperature for 90 min and cured at room temperature for 24 hours. The post curing process is applied at 60°C for 15 h in the oven. Mechanical, microstructural characterization of epoxy composites were investigated using X-ray diffraction (XRD), hardness and tensile tests.

Conclusion

Firstly, Al₂O₃ reinforced epoxy composites were prepared and determined to optimum Al₂O₃ amount. According to the hardness and tensile test results, the optimum amount of Al₂O₃ observed was 3 wt.%. Afterwards, epoxy-3 wt.% Al₂O₃- xGNP (x:0.25, 0.5 and 1 wt.%) composites were produced. XRD patterns, hardness values and tensile strength of the neat epoxy and epoxy hybrid composites are shown in Figure 1. The C peak could be detected in the XRD patterns with increasing GNP amount. 0.25 wt.% GNP reinforced specimen showed the highest hardness value, with an increase of 22% compared to neat epoxy. According to the tensile test results, reinforcing 3 wt.% Al₂O₃ to epoxy improved their ultimate tensile strength increased by 38%, 45.55 to 62.83 N/mm². However, a dramatic decrease in tensile strength occurred with the addition of GNP. The lowest tensile strength was found for the 0.5 wt.% GNP reinforced composites.

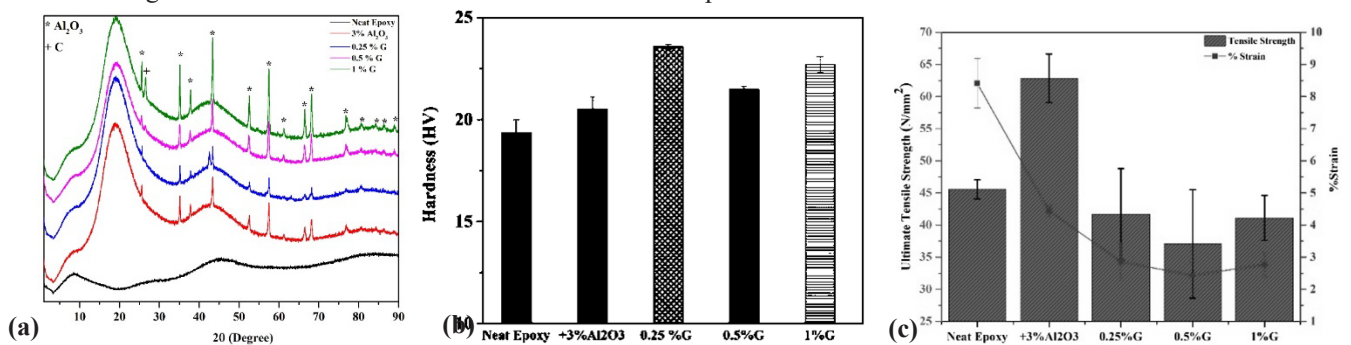


Figure 1: (a) XRD patterns of composites (b) hardness (c) tensile strength of composites

References

- [1] S. Ahmad, S. Ali, M. Salman and A.H. Baluch, *Ceramics International*, 47 (2021) 33956-33971.
- [2] R.K. Upadhyay, A. Kumar, *Colloid and Interface Science Communications*, 33 (2019) 100206.
- [3] C. Bao, Y. Guo, L. Song, Y. Hu, *Journal of Materials Chemistry*, 21 (2011) 13942-13950.
- [4] Kesavulu, A. Mohanty, *Materials Research Express*, 6 (2019) 125329.



INVESTIGATION OF MICROSTRUCTURE AND MECHANICAL PROPERTIES OF DP QUALITY STEELS WELDED WITH DIFFERENT HEAT INPUTS

Kardelen YILMAZ¹, Bilgehan ÖGEL², Caner BATIGÜN²

¹Middle East Technical University, ²METU Welding Technology and Non-Destructive Testing Centre
Türkiye

Keywords: DP Steels, MAG and TIG welding, Microstructure and Mechanical Properties

Abstract

Due to climate changes, Automobile industry reduces the weight of automobiles. It causes the increasing usage of High Strength Steel. DP steel is a part of high-strength steel. Welding is an essential key role in that industry. The welding methods are investigated TIG and MAG which includes CMT and pulse arcs. TIG and MAG have different heat inputs that cause different microstructure and mechanical properties. These investigation purposes are that compare the welding methods and understand metallurgical changes and mechanical properties in structure.

1. Introduction

DP steel assembling issue has been investigated since usage beginning in the industry. GTAW and GMAW are used in assembling from arc-type welding for this type of steel. These arc weldings have many advantages in it. The arc-type welding is very advantageous for penetration rate, weld quality and thickness of the steel. Heat inputs of welds can be ordered for this examination: GTAW >GMAW Pulse>GMAW CMT. The purpose of this investigation compares the heat input and martensite content in structure.

2. Materials and Methods

DP500 and DP700 30*15 cm 12 steel pieces by two pieces are welded at different heat speeds that cause different heat input. DP 500 pieces are 1,5 mm and DP 700 pieces are 1.4mm in thickness. TIG welding is done if it is welded with wire whose composition is WG₃Si. 100% Ar gas environment was used during the experiment. Welds are done manually.

Moreover, DP 500 and DP 700 steel pieces are welded in different welding parameters. In MAG welding pulse and CMT arc are used. The gas environment is 18% CO₂ and 82% Ar gas mixture. Pulse and CMT arc technology are used. Steel pieces manually are welded.

Welding is done in different voltages, amperes, and speeds. This creates a different heat input in the structure. The total heat input in welding is calculated and evaluated. This evaluation is done by comparing the parameters of welds.

Microstructural analyses are done. The microstructural examination is done by grinding from 120 micron to 1200 micron paper, polishing 6 micron to 1 micron and 2% Nital etching. From analyses, HAZ₁, HAZ, fusion zone and base metal region are observed. These regions change by heat input and cooling rates. Phase changing is observed from microstructural analyses.

The tensile test is done with ASTM E8 standard in the transverse direction of the weld structure. The welded structure shows higher strength than the initial strength of the metal. It is applied to two pieces of backbone from the welded structure.

Bending test is applied per four pieces from the welded structure with ASTM E190-21 standard. Welded structures are evaluated and determine the quality of the weld structure is done.

The heat inputs and cooling rates were evaluated with microstructural and mechanical analyses.

3. Conclusion

GMAW and GTAW welding process is applied to DP500, and DP 700 quality steels and then different heat inputs and cooling rates are obtained. Welded specimens are investigated in microstructural, hardness, tensile test and bending test. These tests determine the quality, mechanical and microstructural characteristics of these welding techniques.

References

- [1] N. Fonstein, in Automotive Steels, 2017, Chapter 7 Dual Phase Steels.
- [2] Kou, S. (2021). Welding Metallurgy. Wiley.



THE EFFECT OF PROCESS PARAMETERS ON BEAD GEOMETRY, HARDNESS AND MICROSTRUCTURAL PROPERTIES ARMOUR STEEL WELDS PERFORMED BY ROBOTIC GAS METAL ARC WELDING

Ceren ÇELİK¹, Recep Murat KURT¹, Ozan ÇOBAN¹, Hakan BAYKAL², H. Kübra AKBEN¹, Uğur GÜROL^{1,2}

¹Istanbul Gedik University, ²Gedik Welding
Türkiye

Keywords: Robotic MIG welding, Armor steel, Bead-on-plate weld, Process parameter, Penetration

Abstract

The robotic welding operations have received a great deal of attention since they are highly appropriate both to increase in production rate and quality for desired products used in defence industry. Therefore, selection of an optimum combination of welding parameters is critical in achieving high weld quality and productivity. In this study, the effects of robotic gas metal arc welding (GMAW) process parameters such as current and welding speed on bead geometry, hardness and microstructural properties of the weldment were investigated. The bead on plate technique was used to deposit weld metal on the Protection 500 series armour steel plates having 6 mm thickness. The ER307 austenitic solid wire with a diameter of 1.2 mm according to AWS A5.9 standard were used as filler metal under the 97.5 % Ar + 2.5 % CO₂ mixture of shielding gas atmosphere. The welded plates were first subjected to visual inspection and radiographic examination to detect any imperfections described in ISO 5817 and ISO 10675-1, respectively. Then detailed characterization of the sectioned samples was conducted using a stereo microscope, optical microscope, and micro-hardness tester. As a result; the different responses such as depth of penetration, reinforcement area, bead width, heat-affected zones, and hardness profiles were compared and results were correlated with microstructures. The obtained results revealed that process parameters have significant effect on bead geometry and hardness values.

1. Introduction

The use of armor steels is of great importance for the defense industry. These steels are used for armoured vehicles such as tanks, tracked vehicles and armoured personnel carriers due to their superior mechanical and ballistic performance as well as its weldability. Thermal cycles that occur due to heat input in welding processes of armor steels cause detrimental change in the microstructure. Extreme hardness and softening zones occur in the heat-affected region due to microstructural changes. Therefore, optimization of welding parameters is of great importance.

Gas Metal Arc Welding (GMAW) method is the most used method in welding processes of armor steels. The GMAW method stands out due to its high toughness, high deposition rate and ease of industrial application [1-3]. In addition, gas tungsten arc welding (GTAW), laser disc welding (LDW), hybrid plasma arc welding (HPAW), cold metal transfer (CMT) are also studied [4-7]. Austenitic and ferritic filler metals can be preferred in the welding processes of armor steels. The ferritic filler metals provide higher strength in the welded structure and higher hardness in the weld metal while the austenitic filler metal provides high impact toughness and low hydrogen induced cracking damage. However, heterogeneous microstructure formation because of elemental migration resulted by dissimilar joint configuration and internal stress problems may occur due to thermal conductivity difference [8-17]. Therefore, many studies have been carried out recently on the effect of heat input on microstructure and mechanical properties to optimize welding parameters [17-25]. The most important parameters affecting the heat input are welding current and travel speed. In this study, bead-on-plate welding was applied to Protection 500 armour steel by robotic GMAW method. Upon the complication of welding processes, the welding defects were examined by visual inspection and radiographic examination according to the ISO 5817 and ISO 10675-1, respectively. By performing microhardness tests, the hardness of the weld metal and different HAZ regions at different current and welding speed values were examined and the most accurate current and welding speed values were determined. The obtained results are associated with microstructural changes and the effects of current and welding speed changes are revealed.

2. Experimental Procedure

In this study, Protection 500 quality steel plate was used. The plate thickness was 6 mm and it has been produced by Miilux OY company. The composition of Protection 500 is shown in Table 1. The filler wire used in experimental studies is GeKa austenitic ER307 with 1.2 mm diameter. The

composition of the filler wire is given in Table 2. The welding method used is robotic gas metal arc welding and the bead-on-plate welding process parameters are shown in Table 3.

Table 1 Chemical composition of Miilux Protection 500 armour steel (wt%)

	C	Mn	Si	Cr	Ni	Mo	P	S
Base Metal	0.26	0.95	0.4	0.5	0.4	0.3	0.00	0.00
			2	3	4		7	2

Table 2 Chemical compositions of ER 307 filler metal, (wt%)

	C	Si	Mn	Mo	Ni	Cr	Fe
ER307	0.07	0.55	6.41	0.02	8.52	17.7	balanced

Table 3 Welding process parameters

Welding Parameters	Value (s)
Welding Current (A)	160 – 200 - 240
Welding Voltage (V)	24
Polarization Type	DC+
Welding Speed (mm/s)	3 – 4 – 5 – 6 – 7 - 8
Protective Gas	ARCO2.5 (Ar + 2.5% CO ₂)
Gas Flow Rate (l/min)	16
Torch Angle (°)	90

Before bead on plate welding was performed, the plates are grinded, and demagnetization process was applied in order to provide stable and uniform arc during the welding process. Radiographic inspection, metallographic sample preparation, macrostructural analysis, microstructural analysis and microhardness tests were applied and welded structures were characterized. The etchants used in metallographic sample preparation are given in Table 4. Microstructure images were obtained with LEICA DMi8 optical microscope and macrostructure images were obtained with Nikon SMZ745T macro imager. Hardness measurements were made on EMCOTEST DuraScan 70 G5 device using the Vickers hardness measurement method with 0.5 kgf load (HV0.5) and with 0.25 mm intervals.

Table 4 Etchants used for metallographic sample preparation

Etchant	Content	Purpose and Usage
Marshall Reagent	50 ml water + 2,5 ml H ₂ SO ₄ + 55 ml 30% H ₂ O ₂ + 4 g oxalic acid	Micro etching for HAZ and base metal (vertically immersed for 20 seconds, pre-etched for 3 seconds with Nital 3)
Nital 3	3 ml HNO ₃ + 97 ml ethanol	Macro etching. By swabbing.
NaOH	25 g NaOH + 75 g water	Electrolytically etched for weld metal. 6V, 20 seconds.

3. Results and Discussion

3.1. Radiographic inspection

The results obtained for different current values depending on the changing welding speeds were evaluated according to the ISO 5817 and ISO 10675-1, respectively. Accordingly, no defects were detected for all speed values for 160A and 200A. However, some porosities that reaching the acceptance criteria of the related standards were found at 240A, especially at low welding speeds. Results are given in Figure 1-3.

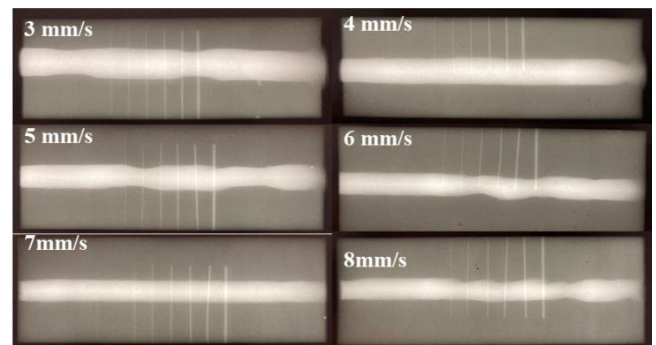


Figure 1. Radiographic inspection results of 160A samples

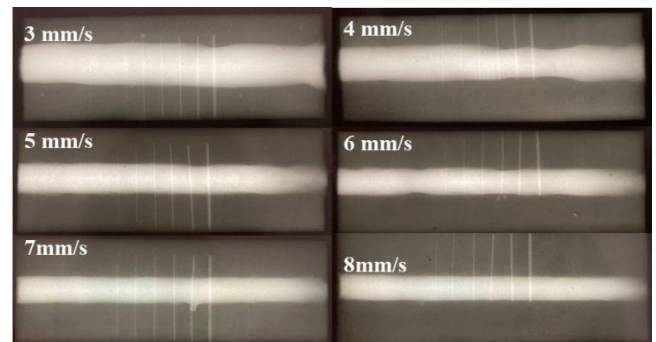


Figure 2. Radiographic inspection results of 200A samples

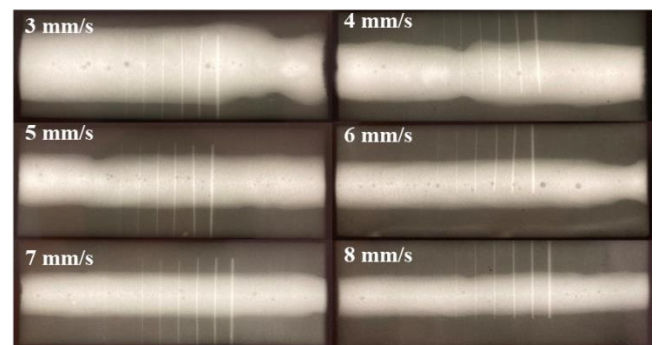


Figure 3. Radiographic inspection results of 240A samples

3.2. Macrostructural analysis

The macrostructure results obtained as a result of bead-on-plate welding performed with different current and welding speed are given in Figure 4. It has been determined that as the current value increases, the bead width increases and the

bead reinforcement decreases. The penetrating zone width decreases at high current and low welding speed values.

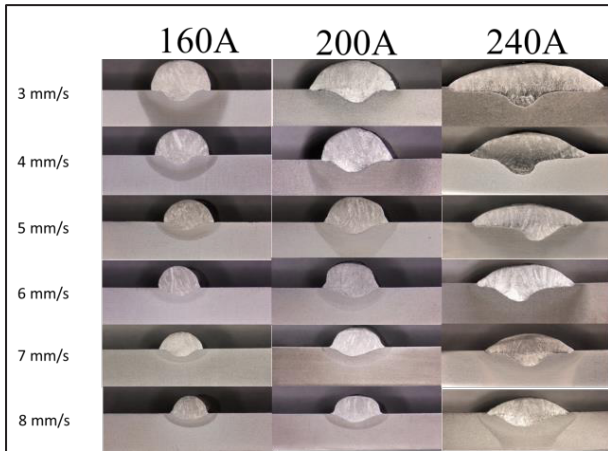


Figure 4. Macrostructural analysis results

The variation of penetration depths depending on the welding speed for different current values is shown in Figure 5. The increase in the current value increased the penetration depth as it increased the heat input. It has been determined that increasing the welding speed decreases the penetration depth and the change is higher at high current values.

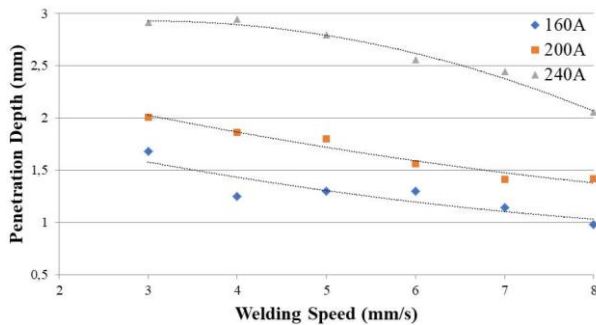


Figure 5. Penetration depth change over welding speed for varying currents

3.3. Microstructural analysis

From the weld metal to the base metal, different zones are formed along the heat affected zone (HAZ), where different peak temperatures and cooling rates occur, and these zones formed in armour steels are shown in Figure 6a. Weld metal (WM) consisted of delta ferrite inside austenite matrix. In the region close to the fusion line, a coarse grained zone (CGHAZ) is formed in the zone corresponding to very high peak temperatures. As can be seen in Figure 6b, coarse needle martensite (NM) and some tempered martensite (TM) are formed within the prior austenite grain boundary (PAGB) in this region with a grain size of approximately 50 μm . In the zone where the peak temperatures occur slightly above the A_3 line, the grain refinement occurs and this zone is called FGHAZ. As can be seen in Figure 6c, in this region where the grain size has decreased to 15-20 μm , the structure consists of TM and some bainite (B) phase. In the zone where the peak temperatures coincide between the A_3 and A_1

lines, partial transformation takes place. In this region, which is called the intercritical heat affected zone (ICHAZ), there is the formation of MA constituents consisting of martensite and austenite, which can be located both inside the grain and on the grain boundaries, as can be seen in Figure 6d [21]. Acicular ferrite (AF) / bainite (B) formation is observed inside the grain. Some researchers have defined these phases as AF and some as B [1, 17]. At temperatures below the A_1 line, the martensitic base metal is tempered, and this region is called as sub-critical heat affected zone (SCHAZ) as can be seen in below side of Figure 6d.

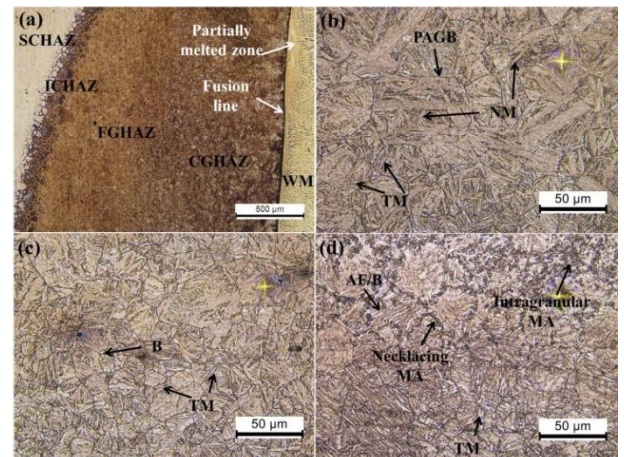


Figure 6. Microstructures of armour steel weld zones; (a) WM and HAZ, (b) CGHAZ, (c) FGHAZ, (d) ICHAZ and SCHAZ

3.3. Microhardness

According to the radiographic examination and macrostructural analysis, microhardness test was performed on the samples with parameters meeting the standards. Hardness distributions from weld metal to base metal according to varying welding speeds for 160 A and 200 A are given in Figure 7 and Figure 8, respectively. As can be seen from both, in general, hardness increases in CGHAZ and FGHAZ starting from the fusion line and decreases dramatically in ICHAZ and reaches to minimum between ICHAZ and SCHAZ regions. Hardness starts to increase in the SCHAZ region towards the base metal. Here, the distance to reach the base metal hardness is of great importance and according to the MIL-STD-1185 military standard [26], this distance from the any toe of the weld should be a maximum of 15.9 mm. Therefore, it is very important to reduce the width of the HAZ. As can be seen from Figure 7 and Figure 8, CGHAZ, FGHAZ and ICHAZ shrink as the welding speed increases (SCHAZ is partially investigated in this study) due to the decrease in heat input. As can be seen in Figure 7, where the hardness results of 160 A specimens are given, the softening zone is very wide in ICHAZ, where the hardness decreases too much (310 HV) at a welding speed of 5 mm/s. At 7 mm/s velocity value, it is seen that the hardness of this region increases to 350 HV and narrows. Considering the importance of reducing brittleness in CGHAZ + FGHAZ, where high hardnesses occur, it can

be considered that the 6 mm/s sample also gives good results due to the narrow softening zone. It has been determined that the hardness of the weld metal is close to each other at all speed values.

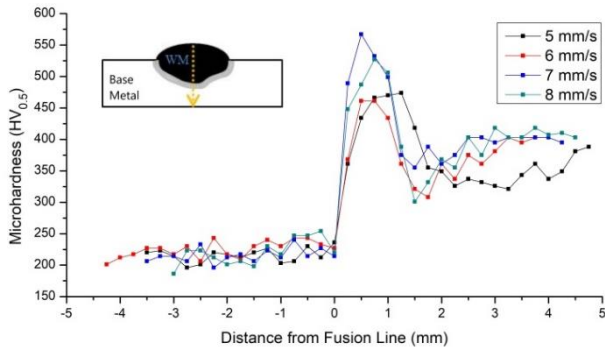


Figure 7. Microhardness distribution over WM and HAZ for varying welding speed for 160 A current

The results of the microhardness test performed on the welded samples performed at 200 A current and different speeds are given in Figure 9. The hardness values of the CGHAZ and FGHAZ regions are close to each other for all welding speeds. When the softening zone is examined, it is seen that the minimum hardness at 5 mm/s and 6 mm/s velocity values decrease to 300 HV and 250HV, respectively. In addition, the decrease in hardness continues. This shows that the softening zone is quite large. It has been determined that these hardness values are around 350 HV and fixed at 7 mm/s and 8 mm/s of welding speeds. When the weld metal hardness is examined, it is observed that the weld metal hardness increases slightly with increasing welding speeds.

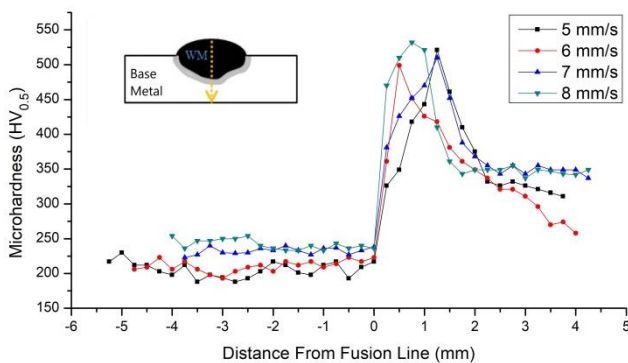


Figure 8 Microhardness distribution over WM and HAZ for varying welding speed for 200 A current

In Figure 9, the hardness test results of optimum welding speed values for 160A and 200A current values are given together. It has been determined and evaluated that samples of 200 A - 8 mm/s due to high weld metal hardness and lower softening in ICHAZ-SHAZ, and 160 A - 7 mm/s due to high ICHAZ hardness and narrow softening zone give optimum results.

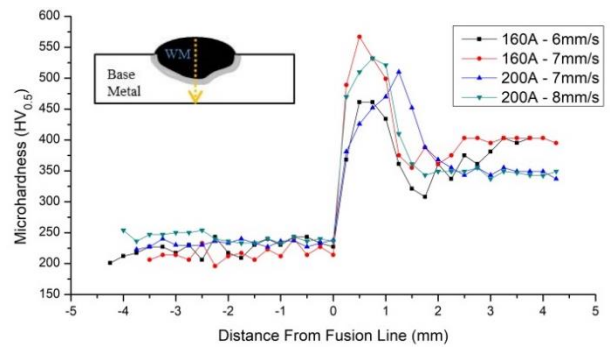


Figure 9. Microhardness distribution over WM and HAZ for optimized samples

The effect of welding speed was investigated on 160 A samples and the microstructures of different HAZ regions are given in Figures 10a-f for 6 mm/s and 7 mm/s welding speed. As can be seen from Figure 10a,b, needle martensite was formed in CGHAZ instead of tempered martensite due to the increase in cooling rate with increasing welding speed. This caused the hardness value to increase from 460HV to 570HV. As can be seen from Figure 10c,d, in FGHAZ, the increase in welding speed caused a decrease in grain size due to faster cooling, a change in the martensite morphology in the direction of needle-like structure, and an increase in hardness from 460 HV to 500 HV. The ICHAZ microstructures given in Figure 10e,f showed that increasing the welding speed decreased the volume fraction of intragranular MA Constituents and caused the hardness to increase from 310 HV to 360 HV.

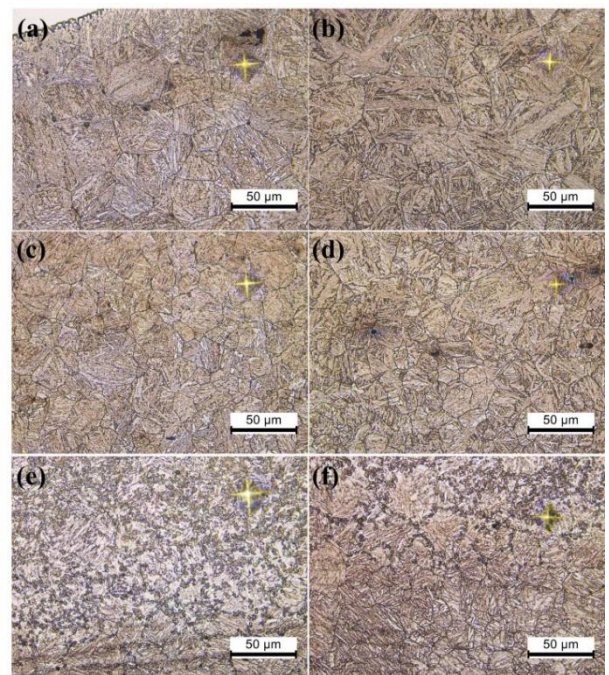


Figure 10 Microstructures showing the HAZ regions of 160A samples; (a), (c), (e) 6 mm/s welding speed, (b), (d), (f) 7 mm/s welding speed

In order to investigate the effect of the current parameter on the microstructure, CGHAZ (Figure 11a) and FGHAZ (Figure 11b) microstructures obtained at 200 A current, and 7 mm/s welding speed are given in Figure 11. Compared to the CGHAZ and FGHAZ microstructures of 160A sample given in Figure 11b,d, it was determined that the increase in current caused an increase in the amount of retained austenite and the formation of tempered martensite instead of needle martensite for both regions, acicular ferrite and some bainite due to slower cooling in FGHAZ. It was observed that the hardness values of CGHAZ and FGHAZ decreased from 570 HV to 450 HV and from 500 HV to 450 HV, respectively, with the increase in current value

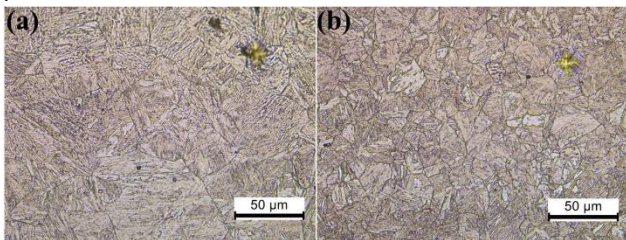


Figure 11. Microstructures of 200A – 7mm/s sample (a) CGHAZ, (b) FGHAZ.

4. Conclusion

In this study, the effects of 6 mm thickness Protection 500 armor steel on the radiographic examination result, macro and microstructure and microhardness were investigated in bead-on-plate welding with robotic GMAW method.

According to the obtained results.

- Welding porosities occurred at high welding speeds (6-8 mm/s) with a current value of 240 A.
- The hardness values increased significantly with the increase of welding speed due to the formation of needle martensite in CGHAZ, decrease in grain size and increase in martensite needles in FGHAZ, and decrease in MA volume fraction in ICHAZ. With the increase of the current value, it was observed that the hardness values decreased significantly due to the formation of retained austenite, acicular ferrite and bainite.
- The optimum hardness test results in terms of narrowing the softening zone, keeping the hardness of the minimum hardness zone high and increasing the hardness of the weld metal are obtained at a welding speed of 7 mm/s at 160A and at a welding speed of 8 mm/s at 200A.

It can be concluded that the current and welding speed parameters have a significant effect on the microstructure which results significant changes on the mechanical and ballistic properties of armor steels. Therefore, optimization of current and welding speed parameters for fillet welding, butt welding, or repair welding to be applied to armor steels has a real significance, especially for the defense industry.

Acknowledgement

This study has been supported by Scientific and Technological Research Council of Turkey (TUBITAK) under the scope of “TUBITAK-1505” (University-Industry Cooperation Support Program) with the project number 5210029. Authors wish to thank Miilux OY Steel for the provisions of the steel plates under the technical and research cooperation programme between Miilux OY and Gedik Welding.

References

- [1] L. Kuzmikova, An investigation of the weldability of high hardness armor steel, PhD Thesis, University of Wollongong, 2013, Australia.
- [2] G. Magudeeswaran, V. Balasubramanian, G. M. Reddy, Mater Des 29 (2008) 1821.
- [3] G. Magudeeswaran, V. Balasubramanian, G. M. Reddy, Def Technol 10 (2014) 47.
- [4] A. Günen, S. Bayar, M. Karakaş, Journal of Engineering Materials and Technology, 142 (2019) 1-23. 10.1115/1.4045569.
- [5] Mesut Yücel Doğrugiden, Farklı Kaynak Metotları İle Birleştirilen Zırh Çeliklerinin Kırılma Tokluk Değerlerinin İncelenmesi, M.Sc. Thesis, Uşak Üniversitesi Fen Bilimleri Enstitüsü, 2019.
- [6] D. Janicki, Archives of Metallurgy and Materials, 59(4) (2014) 1641-1646. DOI: 10.2478/amm-2014-0279 ; ISSN 1733-3490
- [7] A. Saxena, A. Kumaraswamy, G. M. Reddy, V. Madhu, Defence Technology 14 (2018) 188-195. <https://doi.org/10.1016/j.dt.2018.01.005>.
- [8] G. Madhusudhan Reddy, T. Mohandas, G.R.N. Tagore, Journal of Materials Processing Technology, 49 (1995), 213-228
- [9] P. Deb, K. D. Challenger, D.R. Clark, Materials Science Engineering, 77 (1988) 155-167
- [10] H.B. Cary Modern welding technology (3rd ed.), Prentice-Hall, Inc., London (1994)
- [11] G. Magudeeswaran, V. Balasubramanian, G. Madhusudhan Reddy, International Journal of Hydrogen Energy, 33 (2008) 1897-1908
- [12] G. Magudeeswaran, V. Balasubramanian, G. Madhusudhan Reddy, Defence Technology, 10(1) (2014) 47-59, ISSN 2214-9147, <https://doi.org/10.1016/j.dt.2014.01.005>.
- [13] N. K. Sabramani, V. Balasubramanian, S. Malarvizhi et al., Transactions of Indian Institute of Metals 74 (2021) 909–921. <https://doi.org/10.1007/s12666-021-02197-7>
- [14] N. K. Sabramani, V. Balasubramanian, S. Malarvizhi et al., Influence of Welding Consumables on Ballistic Performance of Gas Metal Arc Welded Ultra-high Hard Armor Steel Joints. 10(1) (2021) 443-462. DOI: 10.1520/MPC20200150
- [15] C. Evci, H. Işık, E. Değirmenci, Materials Testing, 56 (2014) 812-817, DOI: 10.3139/120.110634.
- [16] T. Özdemir, International Journal of Engineering Research and Development, 12 (1) (2020) 166-175. DOI: 10.29137/umagd.488104



- [17] U. Gürol, T. Karahan, S. Erdöl et al., Transactions of the Indian Institute of Metals 75 (2022), 757–770. <https://doi.org/10.1007/s12666-021-02464-7>
- [18] O. Coban, U. Gurol, S. Erdol, M. Kocak, Effect Of Plate Thickness On The Microstructure And Hardness Of Robotic Fillet Welded Armour Steels, 6th International Conference on Welding Technologies and Exhibition (ICWET'21), 13-15 October 2021, Hatay-Turkey, Paper ID-46.
- [19] S. Kumar, C. Pandey, A. Goyal, International Journal of Pressure Vessels and Piping, 185(5) (2020) 104128. DOI: 10.1016/j.ijpvp.2020.104128.
- [20] A. K. Maurya, C. Pandey, R. Chhibber, International Journal of Pressure Vessels and Piping, 192 (2021) 104439.
- [21] V. E. Danilchenko, V. Mazanko, V. E. Iakovlev, Nanoscale Research Letters 9 (2014) 322
- [22] D. J. Abson, Science and Technology of Welding and Joining 23 (2018) 635.
- [23] J. Xu, Y. Peng, S. Guo, Q. Zhou, J. Zhu, X. Li, Journal of Materials Engineering and Performance 28 (2019) 6669.
- [24] E. Souza, R. Weber, S. Monteiro, S. Oliveira, Materials 14(19) (2021) DOI: 10.3390/ma14195789
- [25] B. Savic, A. Cabrilo, Materials 14 (2021) 3617.
- [26] MIL-STD-1185, Department of Defense Manufacturing Process Standard: Welding, High Hardness Armor (31 Dec 1979) [Supersedes Mil-W-62162]

DESIGN OF HIGH STRENGTH AND HIGH TORQUE RESISTANCE WIRE ROPE

Fatih DUMAN¹, Emel TABAN², Sevim Gökçe ESEN¹

¹Çelik Halat ve Tel Sanayii A.Ş., ²Kocaeli University
Türkiye

Keywords: High strength, Torque factor, Rotational resistance, Steel wire rope

Abstract

Steel wire ropes are critical load bearing elements in a wide range of applications such as elevators, cranes, mining operations, bridges and ships. The aim of this study is the design of wire rope, prototype production, performance measurements and the development of a wire rope with commercialization potential, especially in mobile cranes operating over 60 meters. Outputs of this study have provided torque-rotation resistance and strength properties above the performance properties of imported steel ropes used in mobile cranes and become a product with commercialization potential. The products that are equivalent to the rope in question have a high Sunday share in Asia, Europe and America, and there are limited compositions and limited production opportunities in our country.

1.Introduction

The new generation multi-strand high-strength and high-torque resistant steel ropes have been used as a lifting rope for telescopic cranes, crawler cranes, offshore cranes, ship deck cranes, tower cranes and mobile cranes. [1]

During loading of the steel ropes at the rate of safety factor, the torque forces applied by the strands to each other must be balanced. For this reason, steel ropes used beyond 60 meters should not show rotational behaviour under load. In this study, new design and torque-rotation test studies were carried out to balance the torque behaviour of the wire and wire mesh angles of the steel rope. [2]

Steel wire ropes are a mechanism consisting of mobile parts (wires) that work in integration with each other. Steel Ropes consist of wires, strands and a core. The main component is wires. Strands are knitted with wires. Ropes are formed by knitting the knitted strands around a core again in rope machines. [3]

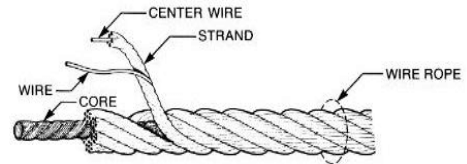


Figure 1 Wire rope components. [4]

Steel rope, the general purpose of which is to lift weights, is produced in different compositions and used in many sectors. The wires forming the ropes are in contact with each other and the systems are used due to their circular cross-sections. [5]

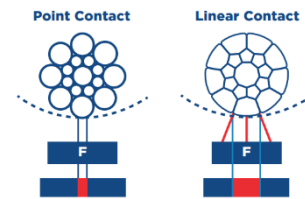


Figure 2 Point contact and Linear Contact. [5]

The wires of non-compact ropes (see figure 2) have point contact with each other. Compact ropes are produced by reducing the diameter of the strands by the rolling system. Since the strands are subjected to a certain amount of force, their circular contact between each other became a linear shape contact. [6]

As a result of this, when compared compacted steel wire ropes which have the same diameter and structure with non-compact steel wire ropes, compacted steel wire ropes have a greater metallic cross-sectional area. As a result of obtaining the thicker wires, compacted ropes have higher breaking forces. [1]

When steel ropes are subjected to load, two types of forces are encountered due to the winding shape. These forces are tensile forces and torque forces. The tensile forces act parallel to the beam axis and cause the steel ropes to elongate with increasing loads. [6]

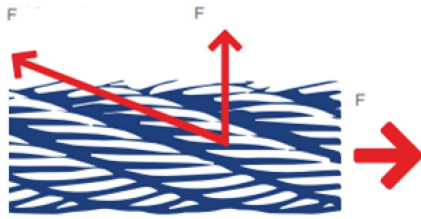


Figure 3 The forces acting on the steel rope. [5]

The first step in the work was the design of the wire rope composition. In the design phase of steel ropes, there are many parameters such as number of wires, number of wires, wire and wire relationship, diameters, layer structures and the engineering approaches used during the selection of these parameters directly affect the situation. For high strength and high wear performance, which is the expected performance criteria of the rope to be designed. The cross section has been increased by compressing it. Wear resistance and service life performance have been increased by distributing the pressure forces generated as a result of increasing the contact surface area of the rope.

2. Experimental Procedure

This study is about the development of a rotation resistant rope design. Ropes tend to spin under load. Rotation resistant ropes perform their duties safely by showing a minimum twisting tendency. In this paper, rotational resistant steel ropes used worldwide and in Turkey were examined. In line with the examined equivalent products and theoretical calculations, the original steel rope design was carried out. The rope design was verified by means of the package program. The rope designs, which are the first step of the design, were created in the rope design program. Strand designs have been selected considering the effect of the strand type on the rope, with flexibility and torque resistance for the designed rope. The 3D view of the new generation rope designed is presented in Figure 4.



Figure 4 3D view of the new generation rope designed

The steel core forming the heart of the rope has been developed with a unique design, very different from the

analysed equivalent products. Considering the cross-sectional occupancy rate for the central strand of the rope, a 21-wire filament strand was preferred.

In order to serve as the outermost layer of the steel core, the 1+6 strand filler, a lower layer was knitted to fill the valley gaps of the 19 Simple Warrington strand. This provided the cross-section fill rate and the amount of wire per unit area both to increase, thus contributing to the strength of the rope in a positive means. In the second layer of the steel core, Simple Warrington strands were preferred. The main reason why Simple Warrington strand was preferred here is that the rope is expected to have a flexible structure compared to its equivalents. This results with an increase in bending fatigue resistance and flexibility. In addition, adhering to this design, only wire with the same diameter value was used instead of the 1 + 6 composition filler wire in the steel core. The purpose of this is to alleviate the workforce in mass production and to reduce set-up times. Torque resistance is calculated as 0.22% when wire is used instead of strand. This value gives 68% better performance than the rope produced with the strand. Rope strength remained almost the same in theory. The section view of the ropes to be produced is given in Figure 6 below.

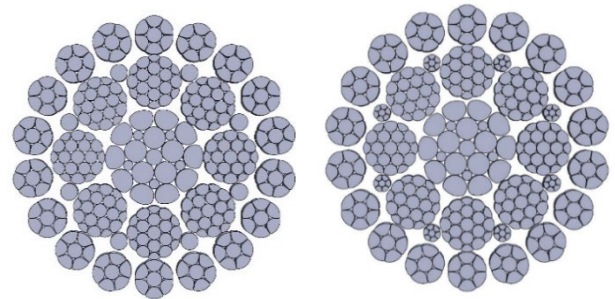


Figure 6 Section view of the designed ropes.

The prototype production of the designed steel rope was provided with a diameter of 16 mm. Wire drawing processes were carried out for the prototype production of the developed rotation resistant rope design. In addition, 2 meters of samples were taken to be examined at the end of production for quality purposes. After the wire production, the bundling phase was started. The following table shows the strands types.

Table 1 Strands production detail

	21 Fillers	19 Simple Warrington	1+6 Filler Strand	1+6 Outer Strand
Diameter Ø (mm)	5.70	3.17	1	2.28
Compact %	14	14	9	18

After the strand knitting, rope knitting was started. Rope prototype production was produced in 4 different ways over a total of 200 meters. Each sample was produced at 50 meters.

Table 2 Steel wire rope production detail

1	18xk7 with 6.80 lay rate
2	18xk7 with 6.80 lay rate and compression roller
3	18xk7 with 6.50 lay rate
4	18xk7 use of wire instead of strand with 6.80 lay rate

3. Results and Discussion

Wire performance tests were carried out. Target values have been achieved.

Table 3 Wire performance tests

Wire Diameter Ø	Measured wire diameter Ø (mm)	Tensile Strength (kg/mm ²)	Torsion (Turns)
0.33	0.33	232	-
0.39	0.39	216	-
0.98	0.99	209	48
0.57	0.58	221	51
0.77	0.77	215	48
0.74	0.74	227	47
0.81	0.81	200	51
1.38	1.39	211	36
0.58	0.58	221	50
1.3	1.31	203	34
0.81	0.81	202	49
0.90	0.90	208	50

Tensile tests and torsion tests were performed on the produced wires. Torsion tests were carried out according to ISO 7800. Tensile tests were carried out according to ISO 7892. All values are within the given spec ranges.

After the rope production, the appearance of the rope was examined. No problem was encountered during the rope production. The appearance of the rope produced is given in Figure 7.



Figure 7 Wire rope with 6.80 lay rate and rope section

Rope breaking load results have been successful.

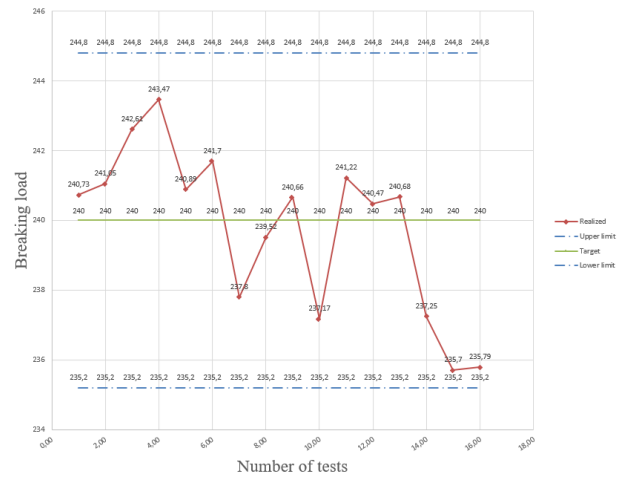


Figure 8 Breaking load results

The breaking load results are within the expected values. The targeted value in the rope design program was determined as 243 kN. The most successful result in the produced samples was 243.47 kN and the sample with 6.80 lay ratio produced with a compression roller.

According to this, it was observed that the results of the tests applied to the samples with ratios of 6.80 and 6.50 were very close to each other. The breaking load values of the samples, in which wire was used instead of the filler strand, were close to the lower limit compared to the other samples.

Torque tests were performed on 4 different rope samples at Çelik Halat ve Tel Sanayii A.Ş. The expected rotational performance of ropes with resistance to rotation is calculated based on the torque value measured at 20% of the breaking load of the rope.

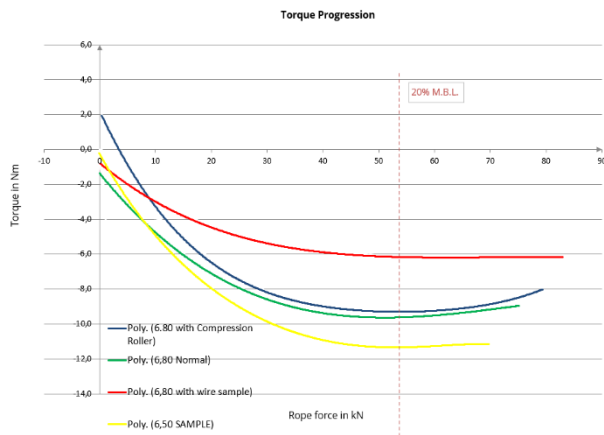


Figure 9 Torque test results

The sample produced with wire instead of filler strand gave the best torque resistance performance. According to the theoretical calculations made from the rope design program, this was expected. The decrease in torque resistance with decreasing lay rate has been verified by experiments. 17% better torque resistance was measured compared to the 6.50 lay ratio of the sample with 6.80 lay ratio.

According to the University of Dresden, Germany, 40% better torque resistance was obtained in Çelik Halat ve Tel Sanayii A.Ş. than the best non-rotating rope produced in this class.

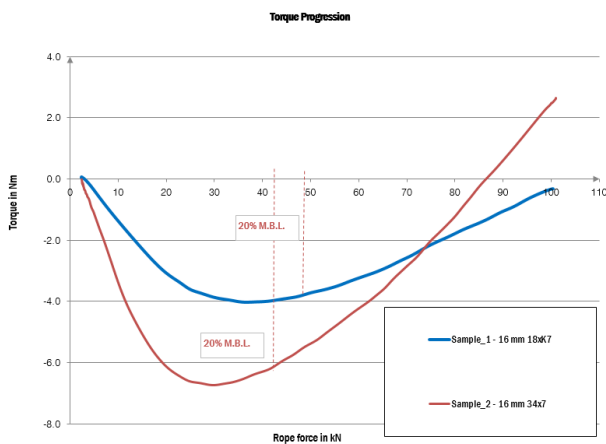


Figure 10 According to the test results conducted at the Technical University of Dresden, Germany

4. Conclusion

Steel ropes tend to rotate under load due to their structure. The steel rope that is the subject of the study is in the class of rope that is resistant to rotation. In this paper, a specially designed steel rope was designed and performance tests were carried out. Here, the effects of the lay rate of the steel ropes and the compression roller on the rope strength and torque resistance were observed. This study reveals that the designed new generation steel rope has 14% better strength and 40% better torque resistance than the rope produced in the existing company.

Acknowledgements

This study was supported by Tubitak with the project no.113B412101189. Authors would like to acknowledge Tubitak for the support.

References

- [1] Yilmaz, M. (2007). Structural Steel Wire Ropes and Applications in the Mining Industry, Master Thesis, Eskisehir Osmangazi University, Eskisehir Osmangazi University, Eskişehir, 178984.
- [2] Bridon Ropes. (1992). Steel Wire Ropes and Fittings
- [3] Verreet, R. (1998). Calculating the service life of running steel wire ropes. Germany.
- [4] Mercuri, V. (2014), Shape Memory Alloys Strands: Conventional 3D FEM Modelling and Simplified Models, The University of Pavia, Faculty of Engineering, Department of Civil Engineering and Architecture
- [5] Çelik Halat ve Tel Sanayii A.Ş. (2020). Product Catalog Turkey.
- [6] Feyrer, K. (2007). Wire ropes: tension, endurance, reliability. Springer. Berlin.



EFFECTS OF BUILD ORIENTATION AND PROCESS PARAMETERS ON MECHANICAL BEHAVIOR OF IN718 COMPONENTS MANUFACTURED BY SELECTIVE LASER MELTING METHOD

Tuğçe KALELİ¹, Aydın YAĞMUR², C. Hakan GÜR¹

¹Middle East Technical University, ²EOS GmbH Electro Optical Systems
Türkiye

Abstract

In recent years, additive manufacturing techniques have created new opportunities for the production of critical metallic components having extremely complex shapes and functionally graded layers. IN718 has gained importance in aerospace, nuclear, and energy industries due to its excellent mechanical behavior at elevated temperatures. In additive manufacturing of IN718, localized fast-melting/solidification, micro segregation, etc. create several risks such as anisotropic behavior and reduced mechanical properties. In addition, the presence of the brittle Laves and acicular δ phases affect machinability negatively. The aim of this study is to investigate the effects of build orientation and process parameters on the microstructure and mechanical properties of IN718 alloy manufactured via Selective Laser Melting.

Keywords: Additive manufacturing, Selective Laser Melting, IN718, Mechanical properties

1. Introduction

Additive manufacturing (AM) technologies have been preferred over the past few years since they allow the production of critical metallic components with an extreme degree of complexity and functional part optimization. However, the knowledge on relationship between microstructure and property in this technique is still being developed. Selective laser melting (SLM) that is one type of AM techniques allows producing complex geometries with a fast solidification rate. Qualification, verification, and industry adoption of AM parts are dependent upon process parameters, post-heat treatment processes and the capability of NDE [1-3]. In this study, it is aimed to investigate the effect of post processing heat treatment and building direction on microstructure and so desired mechanical properties at room temperature.

2. Materials and Methods

IN 718 specimens were fabricated with vertically and horizontally built direction and special process parameters by EOS GmbH Electro Optical Systems in Germany and SENTEZBİR in İzmir. The energy input (EI) per volume of produced parts is 52 W.sec/mm³. As-processed specimens were analyzed by OM, SEM and XRD for microstructural analysis. Several heat treatment procedures were applied to the as-built specimens. Hardness measurement and tensile tests were done at room temperature.

3. Conclusion

- Heat treatment does not eliminate texture completely, because it does not change completely the elongated shape and crystallographic orientation of the solid solution grains.
- Yield strength, tensile strength and hardness values of aged, SLM-fabricated alloy are slightly higher than those for a wrought material. In as-built condition, the highest tensile strength (945 MPa) is achieved with horizontally built samples.
- Direct aging leads to improve tensile strength significantly (~50% increase). Horizontally built samples have higher tensile strength in both as-built and direct-aged condition. The dissolution of Laves phase contributes to the improvement of ductility and the precipitation of strengthening phases in the aging treatment.

Acknowledgement

The authors gratefully appreciate to sample support from the EOS, Germany and SENTEZ-BİR, İzmir.



References

- [1] J.M. Waller, B.H. Parker, K.L. Hodges, E.R. Burke, J.L. Walker, Nondestructive evaluation of additive manufacturing: state-of-the-discipline report, NASA/TM-2014–218560, (2014), 10.13140/RG.2.1.1227.9844.
- [2] Lucas William Koester, J Bond Leonard, Hossein Taheri, Peter C. Collins, Additive Manufacturing for the Aerospace Industry: Non-Destructive Evaluation of Additively Manufactured Metallic Parts: In-Situ and Post Deposition, Ed. F. Froes and R. Boyer, Elsevier (2019), pp. 401-417, doi.org/10.1016/B978-0-12-814062-8.00020-0.
- [3] Amin, Peter; The present non destructive examination techniques for metal additive manufacturing parts and components and their future, NDE 2018 Conference and Exhibition of ISNT, 19-21 , 2018, Mumbai, India.

THE EFFECT OF HEAT INPUT ON MECHANICAL PROPERTIES OF TRIP STEELS IN GMAW AND TIG WELDING

Gökhan ERİAN¹, Adem KURT²

¹Turkish Accreditation Agency, ²Gazi University
Türkiye

Keywords: TRIP Steel, Thermal Cycle, Welding Speed, GMAW, TIG Welding, ISO/IEC 17025

Abstract

The effect of heat input on mechanical properties was investigated in GMAW and TIG welding of TRIP steels. To ensure the effectiveness of the developed procedure, all TRIP steel plates were single-pass welded and thermal cycle data were recorded from different points located on the surface of the welded plates. In the experimental part, thermal cycle profiles were obtained by taking temperature measurements at a distance of 1-2-3-5 mm from the fusion line in GMAW applications and 3-5-7-9 mm from the fusion line in TIG welding applications, taking into account the heat input. Thermal cycles were obtained by using 4-channel k-type thermocouples at different welding speeds. Mechanical tests and microstructural examination were carried out in accordance with the ISO/IEC 17025 standard. The results were discussed to evaluate the effect of heat input on the thermal cycle profiles of GMAW and TIG welded TRIP Steel sheets as a function of welding speed.

1. Introduction

In the 1980s, Low Carbon (LC) TRIP steels with total elongation up to 30% and ultimate tensile strength (UTS) more than 1000MPa was announced by Matsumura. LC TRIP steels having chemical composition of Fe-0.4C-1.5Si-0.8Mn, had microstructure containing retained austenite, ferrite and bainite [1].

As seen on figure 1 there exists two routes, Route-A and Route-B for Production of LC TRIP steels. Main goal of LC TRIP steel production is to form allotriomorphic ferrite at first and then forming bainite phase in this ferritic matrix by controlling the cooling rate. In Route-A, allotriomorphic ferrite and bainite are obtained in order. Using route-A, enables to reach the desired microstructure at a lower cost with single cooling stage without applying intercritical annealing. The final product obtained by Route-A thickness of 3mm. This plate thickness is unacceptable to use in the automotive industry. Later cold working decreases the amount of retained austenite and deteriorates the TRIP effect. In Route B, intercritical annealing has applied to LC TRIP alloy containing

ferrite and perlite. After intercritical annealing, rapid cooling applied considering the bainite transformation temperature. During this rapid cooling austenite has enriched with carbon, and some of it turns into martensite, yet there exists retained austenite at room temperature in the final microstructure [2, 3].

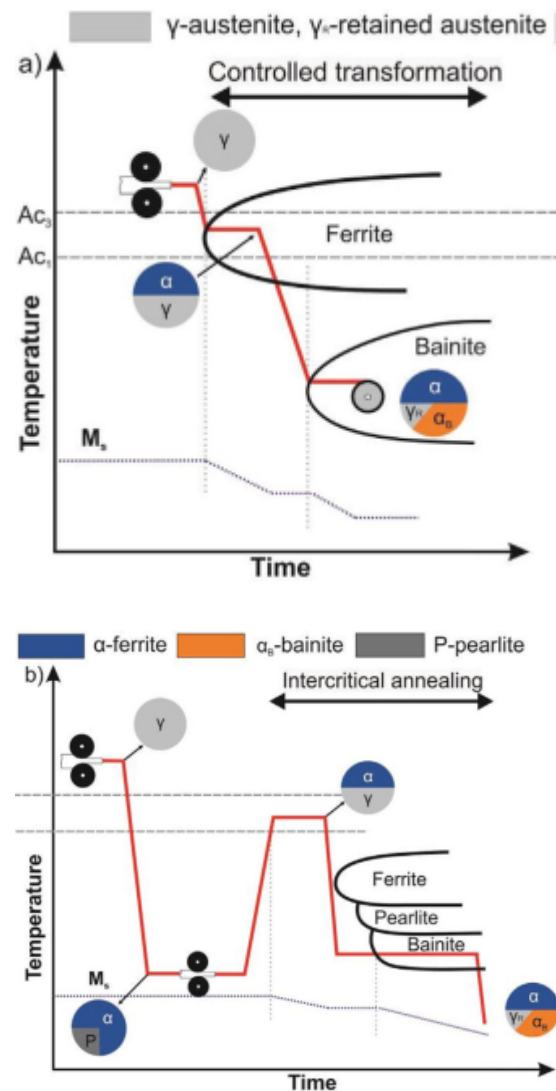


Figure 1. LC TRIP steel production process a) Route A, b) Route B [2]

LC TRIP steel plates produced by Route B used for engine cradle and B-columns in the automotive industry. Main purpose of using TRIP steel in automotive industry is to reduce weight and sustain strength and ductility together. In addition, another advantage is the high energy absorption rate of TRIP steels considering the sudden deformation like crash [4]. Considering the body in white production of unibody chassis primary welding technique used is resistance spot welding (RSW) [5]. However, cross members of truck chassis cannot be joined together with RSW. To perform RSW punch holes are required because two sides of the work piece is needed [6]. To overcome this problem, lap joint welding performed. Several studies were done about strength and fatigue performance of TRIP steel lap joints [7-9]. Studies done with ER309LSi welding wire revealed that in low heat input conditions alternating bands of martensite and austenite were visible in the weld metal. That made ER309LSi a good candidate for GMAW applications of TRIP steel in order to achieve TRIP effect in the weldments [10]. LC TRIP steels used in automotive industry such as TRIP690 and TRIP780, were prepared according to VDA 239-100 and EN 10338 standards.

The aim of this study is to determine the effect of heat input on the thermal cycle and mechanical properties of TRIP 800 steel lap joint weldments with different welding speeds for both GMAW and TIG welding.

2. Experimental Procedure

In this study, effect of heat input and the resultant thermal cycle on mechanical properties in GMAW and TIG welding were investigated in a TRIP800 Steel. The base material (TRIP800 steel) had yield strength (YS) of 496MPa, UTS of 840MPa and total elongation (TE) of %32. The chemical composition of the base material with a thickness of 1.5mm was given in Table 1. For GMAW, K-type thermocouples were placed 1mm, 2mm, 3mm, and 5mm away from end of TRIP800 steel plate 1 adjacent to TRIP800 steel plate 2 respectively. Similarly, for TIG welding K-type thermocouples were placed 3mm, 5mm, 7mm, and 9mm away from end of the plate 1 adjacent to the plate 2 respectively. Heat Affected Zone (HAZ) regions of TIG weldments were wider than GMAW applications due to given heat input. As a result, thermocouples were located in different positions.

Table 1. Chemical comp. (wt.%) of TRIP 800 steel

C	Si	Mn	P	S	Cr
0.21	1.66	1.71	0.0096	0.0042	0.0216
Ni	Cu	Al	Mo	V	Nb
0.0239	0.0095	0.0464	0.0075	0.0038	0.0009

Table 2. Welding parameters and heat input

Code (cm.min ⁻¹)	GMAW			TIG Welding	
	72	102	150	9.5	12
U(V)	18	19	20	10.5	10.2
I(A)	141	166	211	50	50
V(cm.min ⁻¹)	72	102	150	95	120
WFS(m.min ⁻¹)	3.5	4.5	6.5	-	-
h (efficiency)	0.8	0.8	0.8	0.7	0.7
E	0.212	0.186	0.169	0.332	0.255
Q (kJ.mm ⁻¹)	0.169	0.148	0.135	0.232	0.179
Tp	25	22	22	29	33
F2	0.9	0.9	0.9	0.9	0.9
F3	0.67	0.67	0.67	0.67	0.67
d(mm)	1.5	1.5	1.5	1.5	1.5
$\Delta t_{8/5}$ thin plate (sec) (Calculated)	12.9	9.9	8.2	24.5	14.5
$\Delta t_{8/5}$ thin plate (sec) (measured)	12.4	9.7	-	21.6	-
Measured Peak Temp (°C)	920.2	870.2	770.3	1034.5	743.2

WFS: Wire Feed Speed; LWS: Linear Weld Speed; E: Line energy; $E = (I \times U) / \text{Weld speed}$
Q: Effective Line Energy

$$\Delta t_{8/5} = (4300 - 4.3 \cdot T_p) \cdot 10^5 \cdot \frac{Q^2}{d^2} \cdot \left(\frac{1}{(500 - T_p)^2} - \frac{1}{(800 - T_p)^2} \right) \cdot F_2 \quad (1)$$

Welding parameters for both GMAW and TIG welding were given on table 2. The lap joints of TIG welding were done autogenous with pure argon protective environment. The lap joints of GMAW application were done by using ER309LSi electrode with a protective environment of 82%Ar and %18 CO₂ gas mixture. For both GMAW and TIG welding applications, welding parameters, calculated and measured $\Delta t_{8/5}$ values and calculated heat input values were given in Table 2. $\Delta t_{8/5}$ values are calculated using the equation 1 for thin plate weldments. In order to

avoid angular distortion, all the weldments were clamped. Weldment pieces were prepared in the size of 170 x 150 x 1.5 mm was given at figure 2. Mechanical tests were conducted by laboratory accredited from TS EN ISO/IEC 17025. Tensile tests were conducted according to TS EN ISO 6892-1 and Vickers Hardness measurements were conducted according to TS EN ISO 6507-1. Chemical composition is determined according to ASTM E 415. Measurement uncertainty determined for tensile testing was $\pm 12,81$ MPa and for hardness testing was ± 4 HV. For Metallographic examination of both GMAW and TIG welding applications of HAZ region and Base metal first 4% Picral and HCl solution than 10% Metabisulfite solution were applied to samples. For GMAW weld metal examination separate set were prepared and electro-etched with %40 NaOH solution.

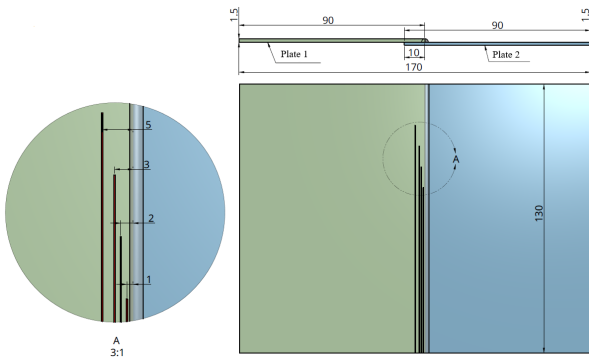


Figure 2. Schematic layout of K-type thermocouples in GMAW application

3. Results and Discussion

Thermal cycle analysis results of TIG weldments for welding speed of 9.5 cm.min^{-1} and 12 cm.min^{-1} , and GMAW applications for welding speed of 72 cm.min^{-1} , 102 cm.min^{-1} and 150 cm.min^{-1} were given at figure 3 respectively. For TIG weldments peak temperatures of 1034.5°C and 743.2°C were obtained from K-type thermocouples were placed 3mm away from end of TRIP800 steel plate 1 adjacent to TRIP800 steel plate 2 for welding speed of 12 cm.min^{-1} and 9.5 cm.min^{-1} respectively. For GMAW applications peak temperatures of 920.2°C , 870.2°C and 770.3°C were obtained from K-type thermocouples were placed 1 mm away from end of TRIP800 steel plate 1 adjacent to TRIP800 steel plate 2 for welding speed of 72 cm.min^{-1} , 102 cm.min^{-1} and 150 cm.min^{-1} respectively. For High-Si TRIP steel with similar composition to TRIP 800 steel used in this project, A_{c1} and A_{c3} were determined as 735°C and 915°C respectively [11].

Microstructural examinations revealed that GMAW applications with the welding speed of 150 cm.min^{-1} had alternating bands of martensite and austenite on weld metal microstructure. This microstructure was not obtained none of the other GMAW and TIG weldments. In this welding conditions, lowest heat input was considered as the key factor to achieve such microstructure.

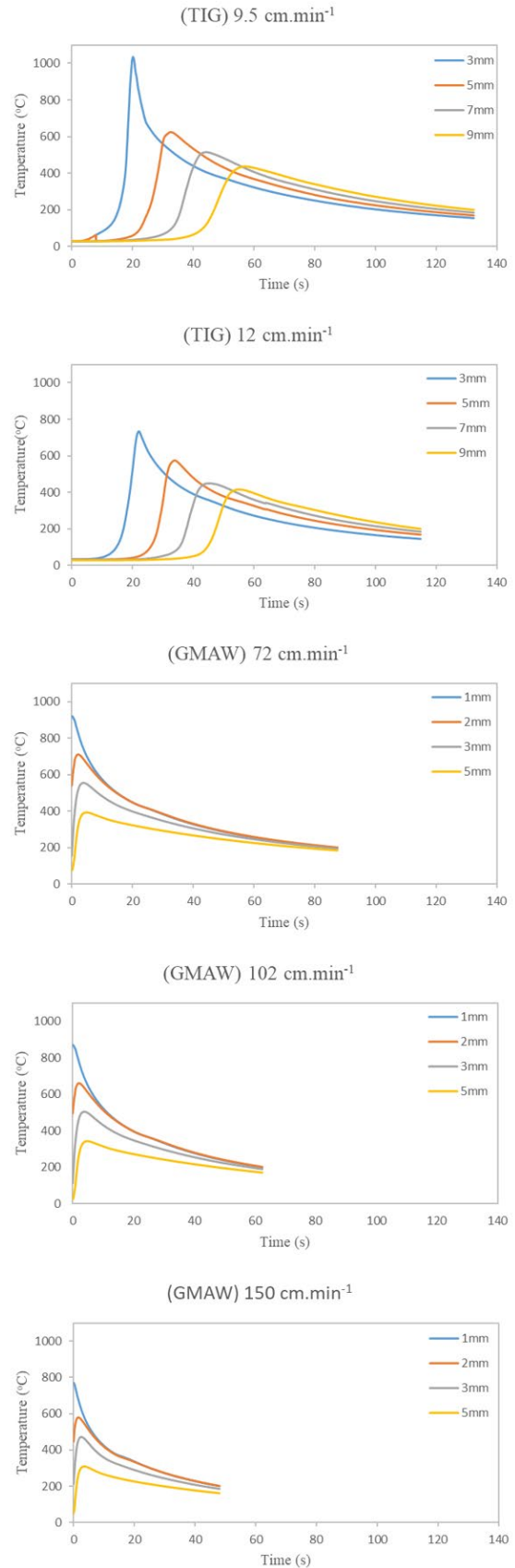


Figure 3. Thermal cycle analysis results of TIG weldments for welding speed of 9.5 cm.min^{-1} and 12 cm.min^{-1} , and GMAW applications for welding speed of 72 cm.min^{-1} , 102 cm.min^{-1} and 150 cm.min^{-1}

For TIG Weldment with welding speed of 9.5 cm.min⁻¹ where K-type thermocouple placed 3 mm away from the end of plate and for GMAW application with welding speed of 72 cm.min⁻¹ where K-type thermocouple placed 1 mm away from end complete austenization were occurred. Respectively for the other GMAW and TIG weldments where peak temperature achieved 1 mm and 3 mm away from the end of plate 1, partial austenization occurred. Heat Affected Zone (HAZ) regions of TIG weldments were wider than GMAW applications due to given heat input. As a result, thermocouples were located in different positions.

Weldment joint efficiency curve according to welding speed for both GMAW and TIG weldments was given at figure 4. Although the tensile test results of TIG weldments were not very low compared to the UTS of the base material, the % elongation amounts remain relatively low. TRIP effect was not achieved for TIG weldments. Highest efficiency among both GMAW and TIG weldments was obtained for the GMAW application with welding speed of 150 cm.min⁻¹. For GMAW application with welding speed of 150 cm.min⁻¹, UTS was measured as 730,8 MPa and % elongation value was measured as 17.4. TRIP effect successfully achieved. For the other GMAW applications with welding speed of 72 cm.min⁻¹ and 102 cm.min⁻¹, UTS were measured as 394.8 MPa and 504 MPa respectively and which was very low compared to the base metal UTS of 840 MPa. For those weldments % elongation values were measured as 4.9% and 5.3 percent which were also very low compared to the base metal's % elongation of 32.2%.

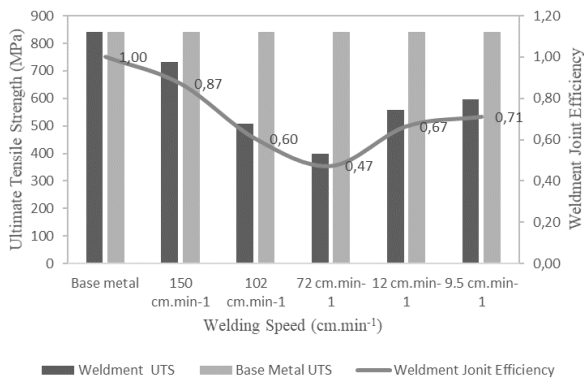


Figure 4. Weldment joint efficiency curve according to welding speed for both GMAW and TIG weldments

4. Conclusion

This paper presents the effect of successive heat inputs on the thermal cycle of TRIP800 steel. In this project, for both GMAW and TIG weldments as welding speed increases heat input due to welding operation decreases. As a result, peak temperature at the HAZ region decreased. Decreased heat input is beneficial to both the mechanical properties and weldment joint efficiency. None of the welded TRIP800 steel sample

fractured from the base metal. Tensile test samples with welding speed of 150 cm.min⁻¹ with the lowest heat input were fractured from the section of the HAZ close to base metal. For GMAW application with welding speed of 150 cm.min⁻¹, alternating bands of martensite and austenite on weld metal microstructure enhanced TRIP effect on weld metal. Other samples for different welding speeds for both GMAW and TIG weldments were fractured from weld metal. Considering the mechanical tests and metallography examinations of the samples, it is concluded that most efficient weldment joint in mechanical properties and TRIP effect had successfully been achieved for the GMAW application with welding speed of 150 cm.min⁻¹.

References

- [1] O. Matsumura, Y. Sakuma and H. Takechi, Transactions of the Iron and Steel Institute of Japan, 27 (1987) 570-579.
- [2] B. Wolfgang, G. Xiaofei and M. Yan, Steel Research international, 88 (2017) 1-21.
- [3] M. Takahashi and H. K. D. H. Bhadeshia, Materials Science and Technology, 6 (1990) 592-603.
- [4] R. Kuziak, R. Kawalla and S. Waengler, Archives of Civil and Mechanical Engineering, 8 (2008) 103-117.
- [5] <<https://www.autolist.com/guides/body-on-frame-vs-unibody>> Dated: 25.03.2021.
- [6] K Tomita, T. Shiozaki, T. Urabe and A. Yoshitake, Development of 780 MPa Grade High Strength Hot Rolled Steel Sheet, SAE 2000 World Congress, 6 March 2000, Detroit, Michigan-USA, pp. 308-317.
- [7] A. Joaquin, A. Elliott, C. Jiang, V. Rajan, D. Hartman and C. Karas, SAE Technical Paper Series, (2007) 2007-01-1360.
- [8] J. J. F. Bonnen, R. Mandapati, H. Kang, R. M. Iyengar, A. K. Khosrovaneh, M. A. Amaya and H. C. Shih, SAE International Journal of Materials and Manufacturing, 2 (2009) 155-171.
- [9] R. Iyengar, J. J. F. Bonnen, E. Young, D. Maatz, M. Soter, M. Amaya and H. S. Shih, SAE Technical Paper Series, (2009) 2009-01-1549.
- [10] M. Rowe, T. Nelson and J. Lippold, Welding Journal, 8 (1999) 31-37.
- [11] N. Fonstein, N. Pottore, S. Lalam and D. Bhattacharya, Phase Transformation Behavior During Continuous Cooling and Isothermal Holding Of Aluminum and Silicon Bearing TRIP Steels. Materials Science and Technology 2003 Meeting Chicago, IL-USA, 9-12 November 2003; pp. 549-561.



THE EFFECT OF BRAZING PARAMETERS ON THE MICROSTRUCTURAL FEATURES OF ALUMINA-COPPER JOINTS

Ece Naz YURTSEVEN^{1,2}, N. Kaan ÇALIŞKAN¹, M. Kaan PEHLİVANOĞLU¹

¹Tübitak SAGE, ²Middle East Technical University
Türkiye

Keywords: ceramic brazing, metallization, microstructure, diffusion

Abstract

Oxygen free copper and alumina ceramic are brazed by using filler alloy with composition 72 wt% silver and 28 wt% copper under high vacuum ($\sim 10^{-5}$ mbar) conditions. Different brazing temperatures and times are experimented for this study to see the effect on microstructure and unity of the joints because these are the main parameters influencing elemental diffusion.

1. Introduction

In ceramic-metal joints, alumina is most often brazed to kovar or oxygen free copper to obtain hermetically sealed microelectronics. Alumina is preferred for its high abrasion and wear resistance, and for being electrically insulator. Also, oxygen free copper is selected for electronic applications because it is more resistant to shorts and corrosion [1], [2], [3].

The requirements for filler material are being compatible with the substrates to be brazed and the fixture material if used, to wet the base materials, to make a strong bond, to have a chemical composition for providing sufficient homogeneity and stability [2], [4]. For the joint of alumina and oxygen free copper, silver-copper alloy is very suitable as filler material. The eutectic alloy of silver copper is selected because of two reasons; the first one is being most widely used utility filler material, the latter is being a eutectic, lower melting point alloy with respect to other brazing materials.[5] Lower melting point fillers are more feasible due to economic concerns.

The surface of the alumina ceramic tube has to be metallized in order to be brazed because of the lack of wettability of the molten filler alloy. The molybdenum-manganese metallization is preferred because it is the most widely used type for alumina ceramics. Moreover,

in order to increase wettability and bonding in joints, metallized ceramics are also nickel plated. [2], [4], [6]

Since the soundness and integrity of the joints are very important in the applications, in this study all experimental variables/brazing parameters (temperature and time) are selected to see the effect on microstructure and uniformity. Moreover by proper heat treatment – meaning adjusting temperature and time- thermal expansion coefficient difference problem is compensated. The results have shown that brazing temperature and time have a remarkable effect on the microstructural features of the joint, and these concerns are discussed experimentally in this paper [3], [7].

2. Experimental Procedure

Materials to be brazed are alumina ceramic tubes conforming to ASTM D2442 Type IV and oxygen free copper conforming to ASTM B152-C10200. They are chemically cleaned before brazing. For removing oxides from coppers NaOH+NaCN solution is used. For chemical cleaning of alumina tubes, 1:1 HF+HCl solution is applied [8].

For the metallization of ceramics, molybdenum-manganese conductor paste purchased from Ceronics Inc. is used. Metallization heat treatment starts with drying at 260 °C for thirty minutes under argon atmosphere and continues with metallizing at 1400 °C for one hour under wet hydrogen atmosphere (70 °C dew point.) The heat treatment is applied by using Protherm PTF 17/75/400. The resultant metallization layer thickness is averaging about 13 - 17 µm. The metallized tubes are then coated with 4 – 8 µm nickel electrolytically, applying 150 mA current for 10 minutes in TÜBİTAK SAGE laboratories.

The brazing paste used in the experiments are Ag72Cu28 (-500 mesh) named BVAg-8, purchased from Prince

Izant Company in the paste form and its composition is 72wt%silver and 28wt%copper. For applying the brazing paste, a template is designed to make sure 50 μm thickness of paste is applied. This paste thickness was selected, because it is generally cited in open literature as an optimal braze clearance value. For integration of coppers and nickel coated metallized alumina ceramics and to maintain this integrity during the heat treatment procedure, a fixture is designed in TÜBİTAK SAGE. The brazing heat treatment is applied to the specimens in the Narbertherm Cold Wall Water Furnace, VHT/-GR H2.

All of the brazing treatments are under high vacuum ($\sim 10^{-5}$ mbar). Peak temperatures and times experimented on this study are 810 and 835 $^{\circ}\text{C}$ and 1,5,10 minutes respectively. The brazing temperatures are selected according to the data sheet provided by Prince Izant Company. 810 $^{\circ}\text{C}$ is the lowest temperature and 835 $^{\circ}\text{C}$ is the highest temperature in the recommended working range. [9] The aim of choosing these boundary conditions is to observe the effects on the diffusion of elements and see the difference clearly. The selected brazing temperatures and times and the specimen naming are seen in Table 1.

Table 1. The brazing temperatures and times applied in the study and the specimen naming

Time (min.) \ Peak Brazing Temperature ($^{\circ}\text{C}$)	810 $^{\circ}\text{C}$	835 $^{\circ}\text{C}$
	1	810-1
5	810-5	835-5
10	810-10	835-10

To characterize the specimens, microstructural evaluation by optical and scanning electron microscopy, EDS and elemental line analysis are used. Optical microscope used in this study is Zeiss Axioskop 2 Mat, placed in TÜBİTAKSAGE. EDS and elemental line analysis are conducted through SEM study by Zeiss Gemini 2 placed in Atılım University.

3. Results and Discussion

The microstructural difference in between peak brazing temperatures and times are seen in

Figure 1. The effects of brazing temperature and time are clearly seen in this figure. The brazing alloy diffuses more in the specimens treated at high temperature. Comparing Figure 1.a and b, one can observe that temperature effect is more dominant than the time effect. This is expected since the brazing process is diffusional.

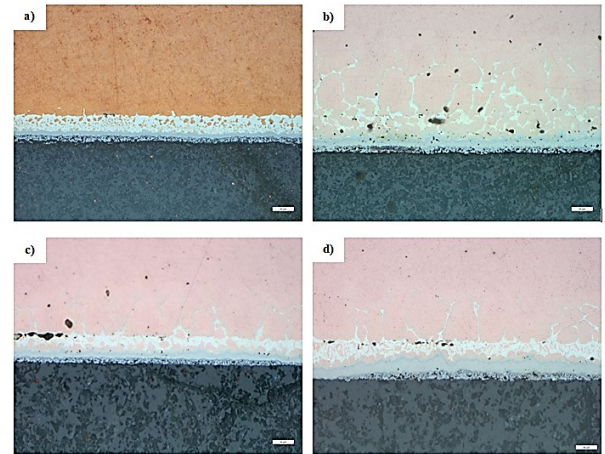


Figure 1. The micrographs obtained through optical microscopy belonging the specimens a)810-1 b)835-1 c)810-10 d)835-10

Similar trend is observed in the SEM images for the same specimens, as seen in Figure 2. However, it is more observable in the SEM images that the distance of diffusion zone in between the metallization and the band formation of silver rich phase seem to increase with increasing temperature and time.

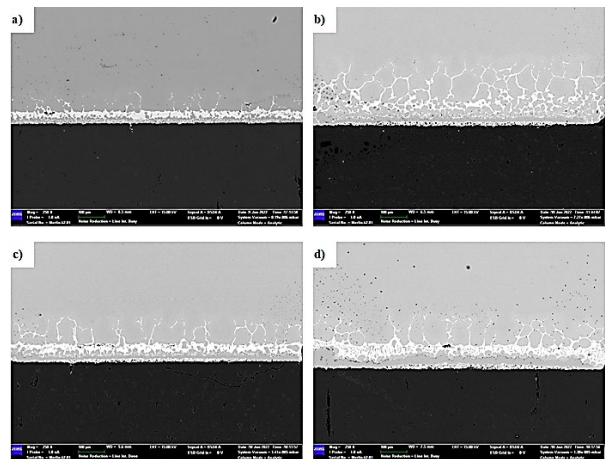


Figure 2. The SEM images belonging the specimens a)810-1 b)835-1 c)810-10 d)835-10

EDS analysis is conducted during electron microscopy and the phases obtained are shown in labels on the

optical micrograph given in Figure 3 as an example. The porosities are generally believed to be as a result of excessive diffusion because in experiments conducted in low temperatures and times less porosity is observed. (see Figure 1)

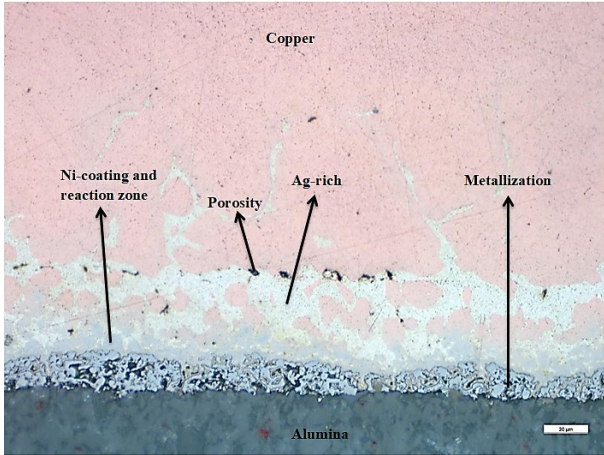


Figure 3. The phases observed in the braze joint microstructure in all of the samples studied (shown on the micrograph of 810-5 as an example)

Moreover, to observe the details of elemental diffusion, elemental line analysis is conducted for each specimen. As an example, the analysis belonging to 810-5 specimen is shown in Figure 4, in comparison to Figure 3. In Figure 4, alumina ceramic, metallized region, silver rich and copper rich regions are seen clearly. Also, the nickel coating and the diffusion of nickel are seen on the yellow line.

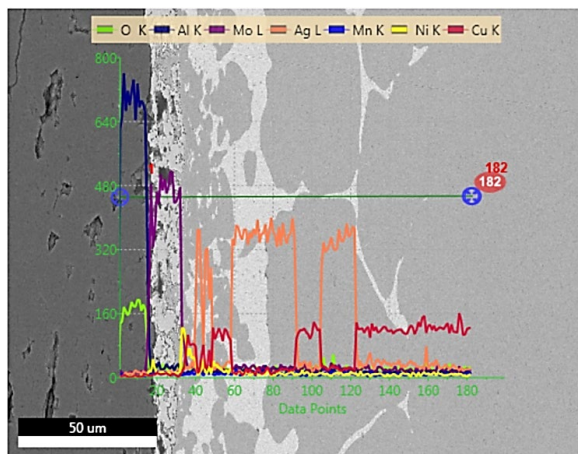


Figure 4. Elemental line scan results of 810-5

The elemental line analysis results belonging to the boundary conditions in brazing temperature and time are

shown in Figure 5. The results suggest that the diffusion mechanism is the same for all specimens. The diffusion depths are changing depending on mainly temperature and also time. Based on Figure 5, for all the samples studied, one can see that nickel diffuses into the braze alloy for a certain depth, but not to the interior of copper. However, the braze alloy seem to penetrate intergranularly in copper matrix in each temperature, considerably.

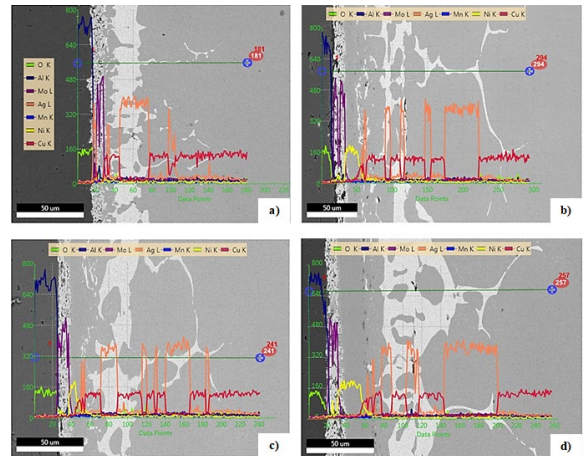


Figure 5. The elemental line scan results belonging to the specimens a)810-1 b)835-1 c)810-10 d)835-10

For the determination of the metallization layer thickness and diffusion depth values, measurements are conducted via SEM for each specimen. To signify the values, a naming is applied to each reaction zone thickness. The naming is shown on the SEM image seen in Figure 6.

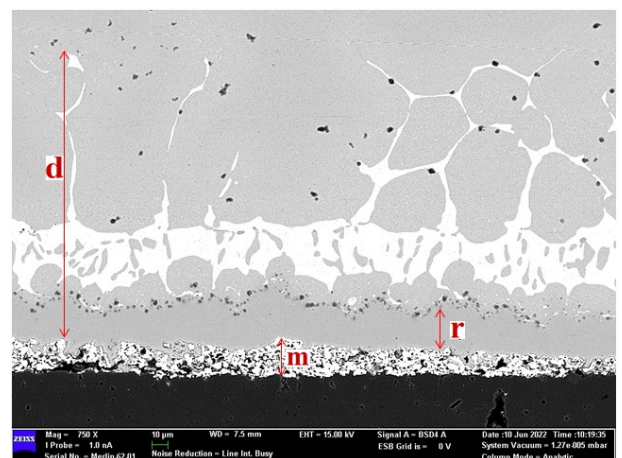


Figure 6. The measurement naming for the observed reaction zones, shown on SEM image of 835-10

The thickness measurements are made by SEM imaging and named as m, r and d meaning ‘metallization layer thickness’, ‘Ni-braze alloy reaction zone thickness’ and ‘Ni-braze alloy–copper reaction zone thickness’ respectively. The results are tabulated in Table 2.

Table 2. The thickness measurements belonging to the reaction zones described in the text

Thickness Specimen	m (μm)	r (μm)	d (μm)
810-1	14.4	11.0	112.4
810-5	13.2	8.8	123.4
810-10	14.3	17.7	160.1
835-1	15.4	17.6	236.5
835-5	13.2	15.4	166.7
835-10	15.1	22.0	196.1

By graphical representation of Table 2, given in Figure 7, the variation in the reaction zone thicknesses can be realized more clearly. As can be seen in Table 2 and Figure 7, the metallization thickness, ‘m’ is similar for all the specimens because the same amount of molybdenum-manganese paste is applied to all the specimens. On the other hand, reaction zone thickness ‘r’ and ‘d’ have shown an increasing trend with increasing temperature and time.

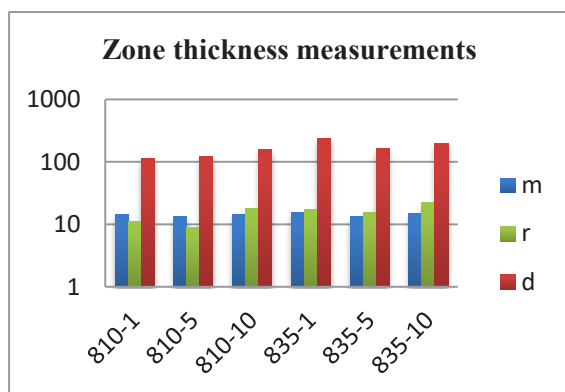


Figure 7. Graphical representation of reaction zone thickness measurements in logarithmic scale

Evaluated as a whole, the results of the study have shown that higher brazing temperatures and times might result in excessive diffusion and somewhat faulted microstructures. Therefore, it might be more appropriate to apply lower brazing temperature and times for obtaining a brazing joint with optimal soundness.

4. Conclusion

In this study, the effects of brazing temperature and time on the microstructural evolution and structural integrity of alumina-copper joints is examined. The optimal brazing conditions seem to be accomplished in the low temperature regime experimented in the study, and for relatively short brazing times, considering the unity of microstructure and lack of porosity.

Acknowledgement

Special thanks to Dr. M. Kaan PEHLİVANOĞLU for his deep knowledge and guidance throughout this study.

Fundamental Material Technologies Division at TÜBİTAK SAGE greatly acknowledged for the financial support of this study.

References

- [1] D. P. Sekulić, *Advances in brazing: Science, technology and applications*. 2013.
- [2] D. M. Jacobson and G. Humpston, *Principles of Brazing*. .
- [3] O. M. Akselsen, *Advances in brazing of ceramics*, *J. Mater. Sci.*, vol. 27, no. 8, pp. 1989–2000, 1992, doi: 10.1007/BF01117909.
- [4] M. M. Shwartz, *Brazing: Second edition*. 2003.
- [5] R. Andersson, T. Holm, S. Wiberg, and A. Åstrom, *Brazing of Metals*, no. 4, p. 43.
- [6] J. Szczurek and J. Kowalewski, *Issues in vacuum brazing*, *Proc. 3rd Int. Brazing Solder. Conf.*, vol. 2006, pp. 326–333, 2006.
- [7] E. Wulf, H. Bachmann, K. Möhwald, R. Eifler, and H. J. Maier, *The influence of brazing temperature and surface roughness on the wettability of reactive brazing alloys*, *Int. J. Mater. Res.*, vol. 105, no. 3, pp. 240–248, 2014, doi: 10.3139/146.111022.
- [8] S. Ghosh, K. S. Pal, N. Dandapat, S. Datta, and D. Basu, *Interfacial properties of metallized alumina ceramics*, *Met. Mater. Int.*, vol. 18, no. 4, pp. 625–630, 2012, doi: 10.1007/s12540-012-4010-2.
- [9] T. Prince and I. Company, *BVAg-8 data sheet* Prince Izant, pp. 1–2.



NON-DESTRUCTIVE DETECTION OF FLAWS IN CONDUCTIVE SEALANT APPLICATIONS WITH A METAMATERIAL BASED ANTENNA

Elif Gaye ERKİ¹, Mete BAKIR¹, Oğuzhan AKGÖL²

¹TUSAS, ²Iskenderun Technical University
Türkiye

Keywords: Conductive sealant, Flaw detection, Metamaterials, Antennas, Fillers, Non-destructive measurements

Abstract

In this study, we have designed a metamaterial based antenna which can be used to determine application errors for conductive sealant on metal plates. This type of applications are common on aircrafts to maintain conductivity on the surface. During the application of conductive sealant, there might be some holes with different shapes and imperfection which must be determined particularly through non-destructive methods. In this method, the imperfections on the application of conductive sealant on metal plates and around fasteners are determined using the resonance frequency changes on the metamaterial-based antenna. In order to increase the sensitivity of the determination system, the magnitude changes on return loss behavior of the designed antenna are also considered for different error scenarios. These scenarios include different shapes and location of errors on the application of conductive sealant between two metallic plates and around a fastener. In all scenarios, the imperfections on the application of conductive sealant can be determined highly effectively without damaging the applied area by only placing the measurement system close to the area to be measured. Another advantage of the designed system is that it can be adopted to other fillers in order to determine application error for different applications.

1. Introduction

In aerospace industry, magnetic field resulting from electronic hardware cause aerospace systems subject to high current due to static electric and lightning issues. In order to diminish this effect, conductivity shall be provided in the structure of the airplanes. Moreover, requirements for electronic systems are becoming stringent in military and commercial aerospace systems.

Composite materials are far more lightweight and durable when compared to metallic structures. This leads composite materials to be widely used in aerospace industry. However, by decreasing the conductivity with the usage of composite materials, additional precautions such as usage of conductive materials; sealants, and coatings for increasing the conductivity shall be taken. Low impedance interface can be obtained by using these types of materials between joints and are used for providing conductivity where continuity and/or electro-magnetic shield or ground are demanded.

Additionally, metallic, composite and titanium plates are attached to the airplane structures with several threaded fasteners. It is important to decrease the radar cross section for stealth military aircrafts. Between these plates and fasteners, gaps and level differences are treated with sealants, especially with conductive sealants for stealth properties. Therefore, it is very critical to measure fastener profile accurately with respect to the aircraft surface.

There is a lack of study on how to determine application errors for conductive or non-conductive sealants with a non-destructive or destructive test methods.

Henry Chan et.al [1] investigated the fatigue cracks occurred in multilayered structures in aerospace by using ultrasonic waves. They performed the measurements the growth of fatigue cracks using laser during cyclic loading procedure.

Bullen, G. [2] studied on hole inspection systems for composite structures. The study defines new non-destructive inspection method using laser without touching the structure for evaluating the holes and flaws in aerospace parts made up with composite materials.

In another study, B. T. Gibson et.al. [3] investigated the errors in applications made by sealants like gaps and/or tiny spots. The process they have developed involves analyzing the process forces along with their frequencies and decreasing the data size using known algorithms for detection. Experimental method includes welded aluminum alloy faying surfaces with cured and uncured non-conductive sealant configurations.

The designed structure in this study includes a metamaterial (MTM) PCB antenna. Metamaterials are man-made materials providing unique and extraordinary properties that are not readily available in nature. The idea of MTM was first introduced by a Russian Physician Victor Veselago with his pioneer work on negative refractive index [4]. Several years later, such extraordinary materials were realized by Pendry et al. and Smith et al. [5-7]. These scientists successfully achieved to have structures providing negative refraction index. Due to their unusual and extraordinary features, such materials called metamaterials (MTM).

In the related literature, there are numerous studies on the use of MTM based antennas for determining different types of parameters in various industries from agriculture to aerospace.

In one of these studies, Bakir et al. [8] investigated a

sensor based on chiral metamaterials for determining pressure, density, temperature and moisture content. In their study, they used chiral nihility medium.

In another study, Sabah et al. [9] studies a Metamaterial based microwave biosensor for determining marrowbone temperature. They used a diamond shaped MTM operating at microwave frequencies for their sensor that can be used for biosensing applications.

With the developing technology, the use of microwave techniques on determining different types of parameters has been gradually increased. In such an interesting study, Ozturk et al. [10] investigated a method for determining physical properties of concrete having various water/cement ratios. They tried to find out a relationship between electrical and mechanical properties of concrete.

2. Materials and Methods

Electromagnetic measurement setup is used to determine the dielectric coefficients (electrical permittivity- ϵ and magnetic permeability- μ) of the conductive sealant applied on metal surfaces. This measurement setup includes a vector network analyzer (VNA), two linearly polarized and wideband horn antennas and also sample holder to keep the sample under test fixed. Return loss parameters (S11) of the sample placed in the middle of the distance between two antennas are measured and used to calculate the dielectric coefficients of the material. The detailed measurement setup can be seen in the following figure (Figure 1).

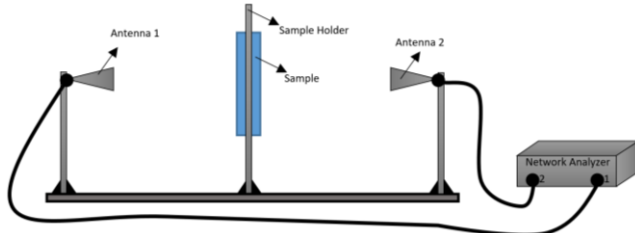


Figure 1. Free-Space Electromagnetic Measurement Setup

By using the free-space measurement setup shown in Figure-1, scattering parameters of the sample manufactured in dimensions appropriate for the sample holder were determined. Although there are several ways to calculate dielectric coefficients from scattering parameters, Debye method was preferred to determine the dielectric coefficients since the conductive sealant applied on a metal plate. In this method, electrical permittivity- ϵ and magnetic permeability- μ values are calculated by using the return loss parameter (S11). Because of the metallic ground plane of the conductive sealant, it is assumed that there is no transmission. For Debye method, the following equations are used.

$$S_{11} = \frac{\mu \tanh(itk_0\sqrt{\mu\epsilon}) - \sqrt{\mu\epsilon}}{\mu \tanh(itk_0\sqrt{\mu\epsilon}) + \sqrt{\mu\epsilon}} \quad (1)$$

$$\epsilon = \epsilon_{inf} + \frac{\epsilon_s - \epsilon_{inf}}{1 + i\frac{\omega}{\omega_\epsilon}} \quad (2)$$

$$\mu = \mu_{inf} + \frac{\mu_s - \mu_{inf}}{1 + i\frac{\omega}{\omega_\mu}} \quad (3)$$

where,

t =Material thickness,

ϵ_s =Static Epsilon,

ϵ_{inf} =Infinite epsilon value,

μ_s =Static Mu,

μ_{inf} =Infinite Mu,

ω =Wave number.

One can see from the equations that the material thickness and reflection parameters are very important parameters in the calculation of the dielectric coefficient. In addition, an initial value is entered for magnetic permeability- μ , which was entered as “1” for our case.

Electromagnetic properties of the conductive sealant used as a filler were obtained through the method mentioned above and the corresponding data were transferred into the electromagnetic simulation program (CST Microwave Studio). A metamaterial (MTM) based loop antenna was designed in accordance with the obtained electromagnetic properties of the material. Possible error scenarios that can be seen in the application of conductive sealant were then simulated. The loop antenna was designed to be manufactured as a printed circuit board and copper was used for the loop and FR-4 dielectric material was selected for the substrate. At the back side of the antenna twenty-one MTM cell structures were placed as shown in the following figure (Figure 2).

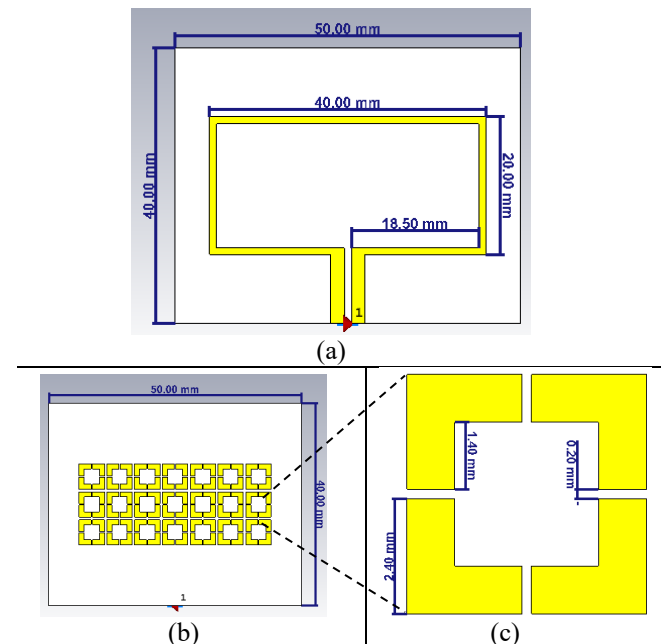


Figure 2. Metamaterial based loop antenna dimensions, front (a), back (b) view and the MTM (c)

The obtained return loss graph (S11) and far field radiation pattern of the antenna are given in the following figure (Figure 3). As seen in the figure, the antenna operates at about $f=2.1$ GHz. In the far-field radiation pattern, one can see that the radiation pattern is omnidirectional and the antenna has 1.71 dBi gain with 94 degree half-power beamwidth which can also be used for sensor purposes.

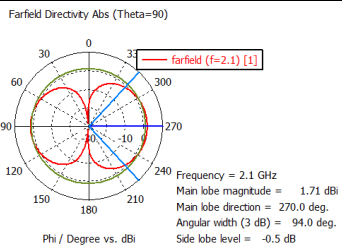
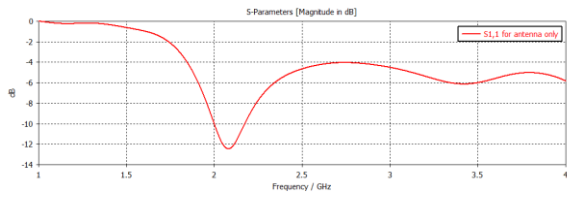


Figure 3. Return loss (a) and far-field radiation pattern (b) of the designed MTM loop antenna

3. Results and Discussion

3.1. Detecting flaws on and around a steel fastener

The designed antenna structure can be used to determine the application error of conductive sealant applied around fasteners and between metal plates. In this respect, conductive sealant filler applied around a fastener has been simulated first, the filler between two metal plates was examined in the second phase. The fastener and the ground on which the fastener was applied were chosen as steel. The empty spaces in the structure was filled with conductive sealant with determined electromagnetic properties.

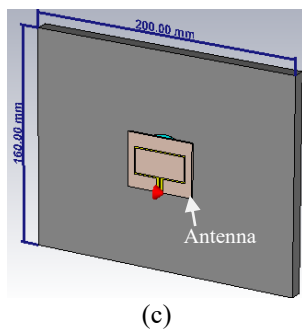
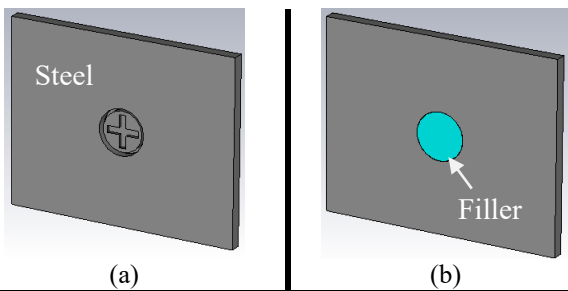


Figure 4. Fastener on steel plate (a), filler made with conductive sealant (b), placement of the MTM based loop antenna (c).

In order to show that the designed MTM based loop antenna can be used to determine the size of the defect in filling made by conductive sealant on fastener, a circular

shape filler scenario was used. A cylindrical shape with different sizes was removed from the conductive sealant in each cases.

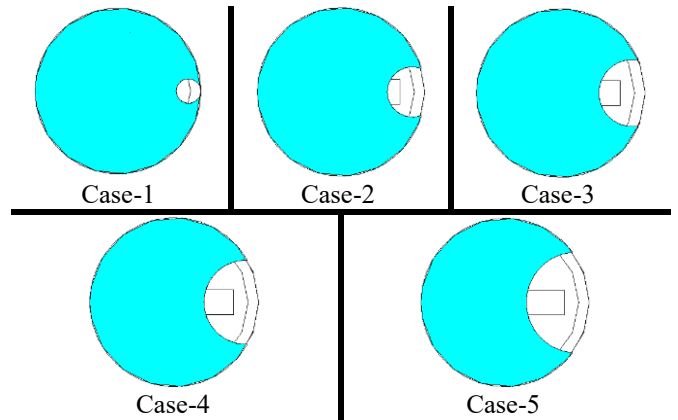


Figure 5. Different cases for the sizes of the imperfect filling.

The size of the cylinder increased gradually in each case and the return loss graphs of the designed structure have been obtained (Figure 6). As seen in the figure, the bigger the gap size, the higher the resonance frequency. The increase in the frequency axis is almost linear which allows a very effective determination of the size of the filler flaws.

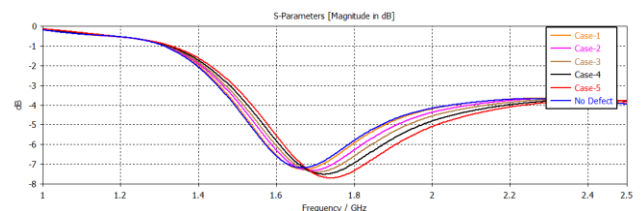


Figure 6. Free-Space Electromagnetic Measurement Setup

For better understanding, the frequency shifts depending on the flaw sizes were tabulated in Table 1 below. As seen in the table, both frequency and magnitude changes can be used to determine the flaw sizes.

Table 1. Chemical analysis of the Material (wt%)

	No Defect	Case-1	Case-2	Case-3	Case-4	Case-5
Frequency (GHz)	1.666	1.672	1.690	1.705	1.720	1.738
Magnitude (dB)	-7.17	-7.25	-7.32	-7.39	-7.50	-7.69

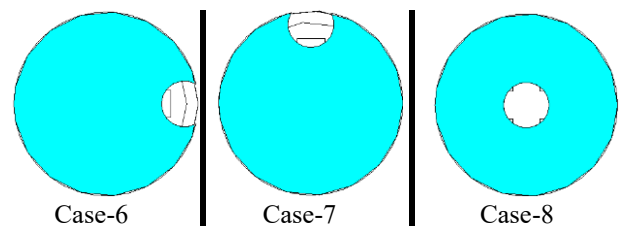


Figure 7. Different locations of flaws in sealant application.

The designed structure can also be used to determine the location of the filler failures. For this purpose, three cases have been simulated on filler applied using conductive sealant on a fastener (Figure 7).

The return loss graphs for Cases 6-8 are given in Figure 8 below. As seen in the figure, not only the frequency points but also the magnitude values of the return loss graphs changed allowing us to determine the flaws location in conductive sealant application.

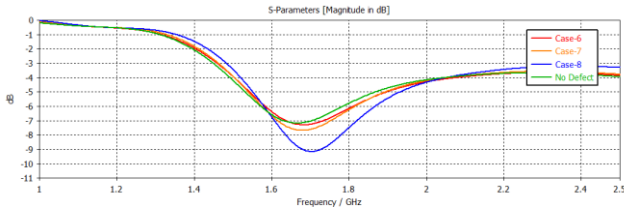


Figure 8. Return loss graph corresponding to different location of filling errors.

3.2. Detecting flaws between two metal plates

In another scenario, two steel plates made up with steel were included in the structure and conductive sealant material defined previously was assigned as the filler between the steel plates. In this respect, flaws on the conductive sealant application between two metal plates have been simulated using the designed MTM based loop antenna. The following figure demonstrates the flaw types simulated (Figure 9). The cases includes the removal of 5mm long cylinders having 1.5 mm, 3 mm and 5 mm radius, respectively.

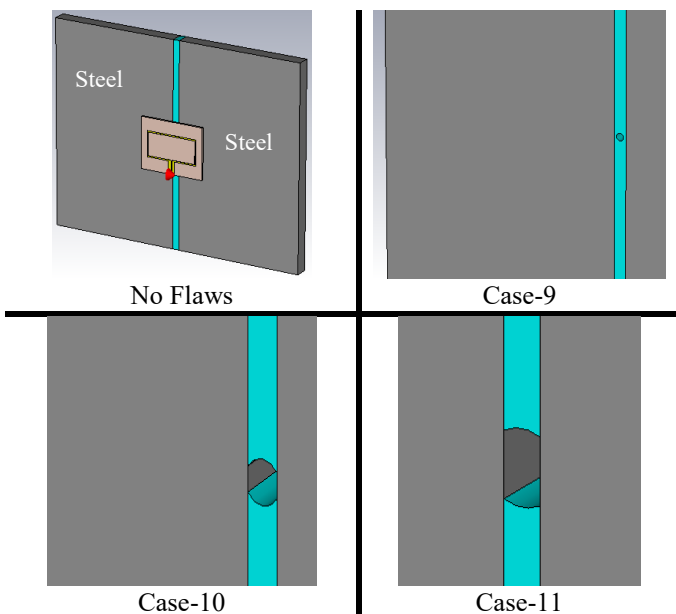


Figure 9. Different sizes of sealant flaws applied between metal plates.

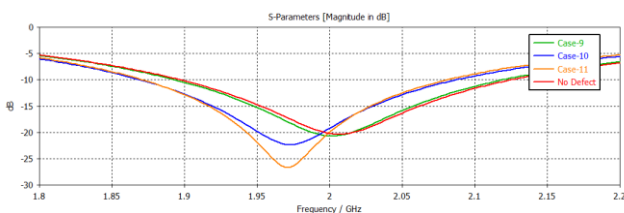


Figure 10. Return loss graph corresponding to different sizes of flaws in sealants applied between metal plates.

Return loss graphs for the cases stated in Figure 9 are given

in Figure 10 below. When the size of the flaw increases, the magnitude of the return loss decreases which can be used to estimate the flaw sizes.

4. Conclusion

In conclusion, flaw detection in conductive sealant used as a filler on steel fasteners and gaps between metallic plates has been investigated using a MTM based PCB loop antenna operating at around $f=2.1\text{GHz}$. It was shown that the designed structure can be used for determining not only the defect size but also the flaw location in filling applications made by conductive sealant particularly for steel fasteners and gaps between steel plates.

Acknowledgment

We would like to thank Mr. Adem Can USAK for his assistance in the measurement process of the sealant used in the study.

References

- [1] Henry Chan, Bernard Masserey, and Paul Fromme, "High frequency guided ultrasonic waves for hidden fatigue crack growth monitoring in multi-layer model aerospace structures", Smart Materials and Structures, 23 January, 2015.
- [2] Bullen, G., "Non-Contact Measurement of Aerospace Fastener Holes, Using Ring Laser Adaptive Optics," SAE Technical Paper 2015-01-2497, 2015.
- [3] B. T. Gibson, D. M. Wilkes, G. E. Cook, and A. M. Strauss, "In-Process Detection of Faying Surface Sealant Application Flaws in Friction Stir Welding", Journal of Aircraft, Vol. 50, No. 2, March–April 2013.
- [4] Veselago, V.G.: The electrodynamic of substances with simultaneously negative values of ϵ and μ . Sov. Phys. Usp., 10 (4) (1968), 509–514.
- [5] Pendry, J.B.; Holden, A.J.; Stewart, W.J.; Youngs, I.: Extremely low frequency plasmons in metallic mesostructures. Phys. Rev. Lett., 76 (1996), 4773–4776.
- [6] Pendry, J.B.; Holden, A.J.; Robbins, D.J.; Stewart, W.J.: Magnetism from conductors and enhanced nonlinear phenomena. IEEE Trans. Microw. Theory Tech., 47 (1999), 2075–2084.
- [7] Smith, D.R.; Padilla, W.J.; Vier, D.C.; Nemat-Nasser, S.C.; Schultz, S.: Composite medium with simultaneously negative permeability and permittivity. Phys. Rev. Lett., 84 (2000), 4184–4187.
- [8] Bakir, M., Karaaslan, M., Akgol, O. and Sabah C.; Multifunctional metamaterial sensor applications based on chiral nihility. Opt Quant Electron (2017) 49:346.
- [9] Sabah, C., Dincer, F., Karaaslan, M. Bakir, M., Unal, E. and Akgol, O.: Biosensor applications of chiral metamaterials for marrowbone temperature sensing. Journal of Electromagnetic Waves and Applications, 29 /17 (2015), 2393-2403.
- [10] Ozturk, M., Sevim, U.K., Akgol, O., Unal, E. and Karaaslan, M.: Determination of physical properties of concrete by using microwave nondestructive techniques. ACES JOURNAL, Vol. 33, No. 3 (2018).



PROPERTIES OF LASER WELDED 3003 ALUMINUM ALLOY

Abdullah CEBEÇİ¹, Emel TABAN²

¹Assan Hanil Otomotiv, ²Kocaeli Üniversitesi
Türkiye

ABSTRACT

Technological developments in the production industry have led to the improvements for welding processes. Despite the disadvantage of high initial setup cost, laser welding method is on the rise due to its advantages such as increasing the amount of work done per unit second, increasing the quality of welding, and no requirement of consumable, amongst the fusion type of welding processes.

In this study, similar welds have been produced by fiber laser welding using 1.4 mm thick 3003 series aluminum alloys. The optimization of the welding parameters is accomplished by Taguchi method and the mechanical and microstructural properties of the welded joints have been examined.

Keywords: Fiber laser welding, aluminum, mechanical properties, microstructural properties

1. Introduction

The use of aluminum alloys, which is an easily processed and corrosion resistant material, in automobile body production continues to increase every year. Automotive manufacturers are trying to lighten vehicles as a result of their efforts to

minimize the emission values of vehicles. The aim should be accomplished without reducing the rigidity and impact resistance of the vehicle [1-3].

Welding is a frequently used process for joining components in automotive manufacturing. The rate of applying laser welding has increased considerably in recent years since it allows ease of automation, high welding speeds, high power density, narrow heat affected zone, high weld penetration and low thermal distortions [1-4]

The biggest difference of the laser beam from other energy sources is that it can easily reach the desired point on the part. In this way, the desired amount of energy can be sent locally to the region to be joined with the source. Figure 1 shows schematically a laser beam device. Light is pumped to the laser active material by a powerful lamp connected to the energy source. The pumped light accelerates the atoms of the material, causing them to produce photons in the form of magnetic waves. Here, the laser active substance can be in solid, liquid and gas phase. The laser beams emanating from the laser medium are converted into a powerful light beam with the help of resonator mirrors. The light beam is transmitted to the desired location by means of mirror and lens systems or with the help of a light cable, depending on the laser type [1-4].

In order to determine the mechanical properties of the joints, tensile test was applied to the samples, SEM images were taken in the fracture zones of the samples with the highest and lowest tensile strength as a result of the tensile test, and the hardness values were examined.

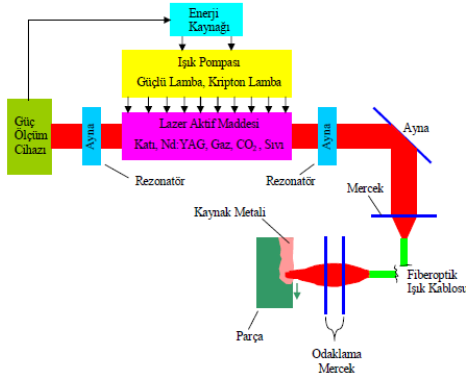


Figure1. Schematic of the laser beam

Table 1. Chemical and mechanical properties of the material

Alloy	Yield Strength (Mpa)	Tensile Strength (Mpa)	Chemical composition(%)						
			Si	Fe	Cu	Mn	Ti	Zn	Al
3003 - H24	Max. 115	Max. 180	0.18	0.7	0.13	1.2	0.14	0.01	98

Laser systems, which are mostly used in laser beam welding method, are collected in two groups. These are; solid state laser systems and gas laser systems. The important parameters affecting the laser source are; laser power, welding speed, focusing distance, shielding gas properties. In laser welding, it is essential that the concentrated energy emanating from the laser beam generator is focused on the weld groove of the two materials with the help of various optical materials, and this zone melts as a result of overheating and the two materials are joined. With the use of laser welding technology, welding parameters and welding quality can also be measured. Due to this advanced welding technology, a well controlled welding operation and a good welding quality can be created.

2. Experimental Procedure

In this study, 3003 H24 series sheets with a thickness of 1.4 mm were used as test material (Table 1). 18 pieces of 3003 series aluminum sheets were joined by laser welding process and the experimental parameters were determined by taguchi method and 9 sample welded joints were obtained.

After the materials were cut in the laser cutting machine in accordance with the current standard rules, the surfaces to be welded were sanded and then cleaned with acetone. It is welded by pressing the clamps at 3 points in the welding fixture. The robot settings were controlled and progressed in each piece assembly. (Figure 2-3)

Table 2. Experimental Settings

Symbol	Welding Parameter	Level-1	Level-2	Level-3
A	Power	2800	3100	3300
B	Speed	20%	17%	14%
C	Focus Point	0	+3	+6

Power, speed and focus point distance were determined as welding parameters. 2800,3100,3300 in power. Rate 20%, 17%, 14%. 0, +3, +6 is set as the focal point (Table 2).

3003-H24 plates were welded with the help of the taguchi method with the parameters determined by the L9 orthogonal test matrix. The L9 matrix is shown in Table 3.



Figure 2. Sample Connection

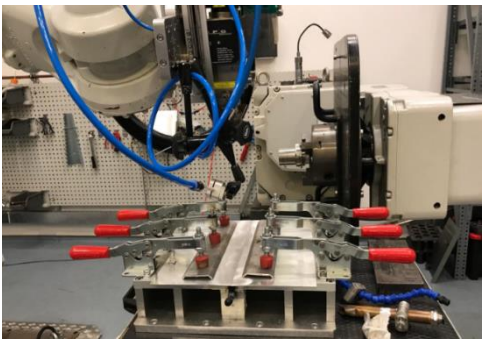


Figure 3. Robot position

3. Results and Discussion

Tensile Testing

For the tensile test, 3 samples were taken from each plate. For tensile test max. Z250 model Zwick brand universal tensile tester with 250 kN capacity is used. All experiments were carried out at 25°C. Tensile test results are given in Table 4.

When the welded samples were evaluated, it was observed that the tensile values increased when the strength value increased.

At the robot speed, it was seen that the 17% speed was the most ideal speed values.

As a result of the tensile test, it was seen in plate weld number 8 with the highest average tensile value.

Table 3. L9 orthogonal test matrix

Sample No	Power	Speed	Focus Point
1	2800	20%	0
2	2800	17%	+3
3	2800	14%	+6
4	3100	20%	+3
5	3100	17%	+6
6	3100	14%	0
7	3300	20%	+6
8	3300	17%	0
9	3300	14%	+3

Table 4. Tensile strenght result

Sample No	Power	Speed	Focus Point	Tensile Strength N/mm2			Avarage Tensile St. N/mm2
				1	2	3	
1	2800	20%	0	119.75	125.79	127.26	124.3
2	2800	17%	+3	119.73	119.73	129.19	122.9
3	2800	14%	+6	120.41	123.1	123.59	122.4
4	3100	20%	+3	86.29	121.35	114.93	107.5
5	3100	17%	+6	111.56	123.07	126.42	120.4
6	3100	14%	0	107.45	125.84	123.56	119.0
7	3300	20%	+6	121.2	129.92	123	124.7
8	3300	17%	0	121.05	132.03	127.29	126.8
9	3300	14%	+3	118.74	115.67	123.25	119.2

Analysis of SEM Images

In the SEM analysis, the fracture surfaces of the welded plates with the highest tensile strength value and the lowest tensile strength value of the tensile plates were examined. (Figure 4a – 4b)

Acknowledgments

The authors would like to sincerely acknowledge Dr. Onur Binbaşar, Cankat Kuş, Cihan Gürbüz, Süleyman Kahraman for technical support.

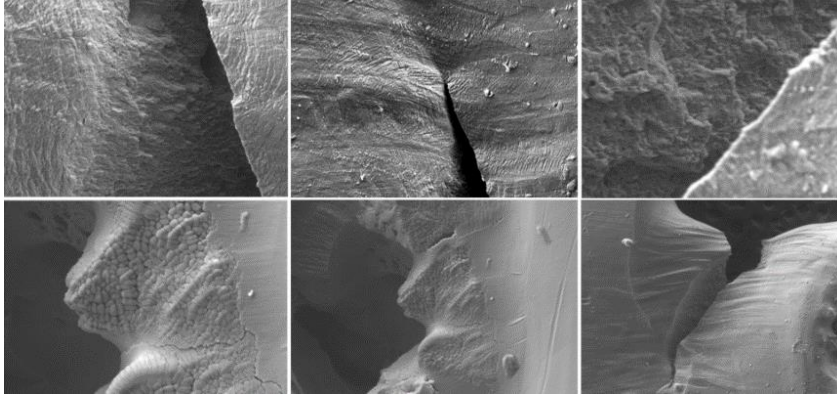


Figure 4a. SEM image of low value tensile test sample

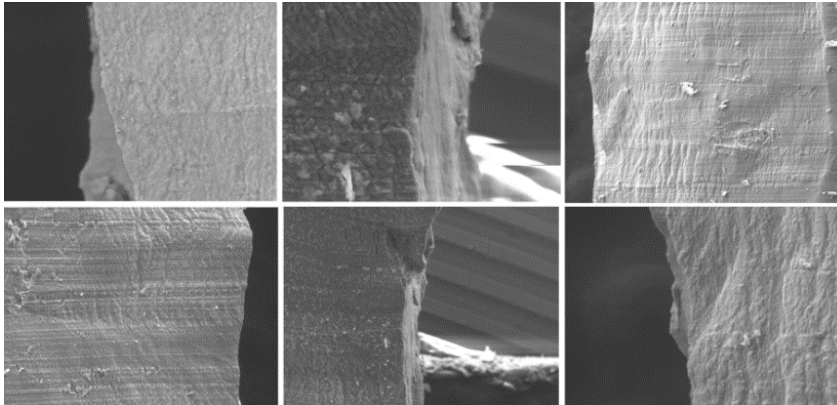


Figure 4b. SEM image of high value tensile test sample

References

4. Conclusion

When the strength values of welded joints are examined, it is seen that the tensile strength value increases with the increase in the strength value. In the robot speed value, it was observed that the plates with a value of 17% had higher tensile strength values in their own groups compared to other speeds. At the focal distances, the highest tensile strength value was obtained between the test plates at the 0 point and high power value.

- [1] O. Oladimeji, E. Taban, Trend and innovations in laser beam welding of wrought aluminum alloys, 2016, 1-43
- [2] O.O. Ojo, E. Taban, Loop travel path of fiber laser welded Alclad AA2219-O alloy, Journal of Materials Processing Technology, Vol. 251, p.118-126, 2018
- [3] T.Alpar, O. Çelenk ve K.Çavdar, Yüksek Mukavemetli Çeliklerde Lazer Kaynağı Uygulamaları, 2021, 1-20
- [4] K.Aydın, İ.Karaağaç Lazer Kaynağı ve Lazer Kaynağının Başlıca Uygulamaları, 2018, 3-14

EFFECT OF POST WELD STRESS RELIEVING HEAT TREATMENT ON 6XXX SERIES ALUMINUM ALLOYS

Furkan YALÇINKAYA¹, Barış KARA², Cem KAHRUMAN¹

¹Bursa Technical University, ²Yeşilova Holding
Türkiye

Keywords: Welding of aluminium, stress relieving, MIG welding, 6xxx alloys

Abstract

6XXX series aluminum alloys are alloys containing aluminum, magnesium, silicon with relatively higher mechanical properties and can be heat treated. The strength losses that will occur after welding these alloys can be eliminated by heat treatment. In this study, two 6082 aluminum alloys in the form of plates were welded by MIG method and stress relieving heat treatment was applied for 30 minutes at 175°C, which is the parameters used in industrial painting. It has been determined whether the temperature has an effect during the dyeing process in the bake hardening process. Then, rupture, hardness and microstructure analyzes were performed on the samples. According to the test results, stress relieving heat treatment at the specified parameters after welding decreased the shear force and elongation, while increasing the hardness in the weld base metal and the weld area.

1. Introduction

Thanks to its lightness, mechanical properties and corrosion resistance, aluminum and its alloys have a wide range of uses in the automotive, aviation, ship, construction, transportation, food and packaging industries. 6XXX series alloys have excellent formability from simple to complex profiles by extrusion method. Mg and Si are the main alloying elements that increase the strength of the alloy by precipitation hardening. T6 heat treatment, which consists of solution heat treatment, artificial aging and quenching steps, is a widely used method to increase the mechanical properties of the alloy. Among aluminum alloys, 6082 is one of the most widely used alloys. Its mechanical properties are given in Table 1. Solution heat treatment is first carried out at 500°C to obtain a supersaturated α solid solution. Artificial aging is achieved by heating to about 200°C for various times and leads to precipitation of different phases (β phase). Hardness and strength are determined by the type of precipitate, its density and size [1].

Tungsten Inert-Gas (TIG) and Metal Inert-Gas (MIG) welding processes are preferred for welding aluminum alloys due to their high quality welding.

Table 1. Mechanical properties of 6082 aluminum alloy [1]

Temper	Proof Stress (MPa)	Tensile Strength (MPa)	Shear Strength	%Elongation	Hardness Brinell	Hardness Vickers
O	60	130	85	27	35	35
T1	170	260	155	24	70	75
T4	170	260	170	19	70	75
T5	275	325	195	11	90	95
T6	310	340	210	11	95	100

Stress relieving is a process applied to reduce internal stresses that occur as a result of processes such as welding, casting, heat treatment and cold forming. Residual stresses in metallic materials are elastic stresses that arise when a workpiece is not subjected to any load, and the maximum value it can reach is limited by the yield stress of the material. If a residual stress is large enough to exceed the yield limit, it will deform the part, causing deformation. This is what is called distortion in the industry[2].

Post-weld heat treatment has been successfully applied to improve the properties of welded parts. Jie YI et al. investigated the effect of post-weld heat treatment on the microstructure and mechanical properties of 6061-T6 aluminum alloy welded joints [3]. The hardness of the weld zone increased with the increase of post-weld heat treatment time and temperature. It is already known that the mechanical properties of weld joints are severely reduced due to aggregation and coarsening of Mg_2Si particles under the weld thermal cycle. The reason for the improvement of mechanical properties after artificial aging at 160°C after welding for 18 hours was

explained by the precipitation of a certain number of Mg₂Si particles of appropriate size in the HAZ. Fadaeifard et al. investigated the effect of post-weld heat treatment on the microstructure and mechanical properties of gas tungsten arc welded AA6061-T6 alloy. They stated that they obtained a surface between fragile and ductile [3-6].

2. Experimental Procedure

5 mm thick 6082 aluminum plates were welded using 4043 welding wire by MIG method, in an argon gas atmosphere with overlap welding. Welding parameters are given in Table 1. After welding parts, weld areas cut in an abrasive cutting device were sanded and penetration measurements were made in Struers brand microscope according to TS EN ISO 10042 standard. Afterwards, heat treatment was applied to the samples in a Nüve FN 500P brand oven at 175°C for 30 minutes. The samples were divided into two groups: heat treated samples as T group and non-heat treated samples as N group. The obtained samples were subjected to tensile test in Shimadzu brand tensile-compression device and hardness tests in Q10M microhardness device, microstructure studies were carried out and the effect of heat treatment was examined.

Table 2. Welding parameters

Current	Voltage	Wire feed speed	Shielding Gas
150A	20V	8,9 mm/s	Ar

3. Results and Discussion

3.1. Penetration measurements

Penetration depth measurements were made by taking 3 samples according to TS EN ISO 10042 standard. By forming an isosceles triangle, the a value was calculated by using the leg lengths. The value a indicates the amount of penetration.

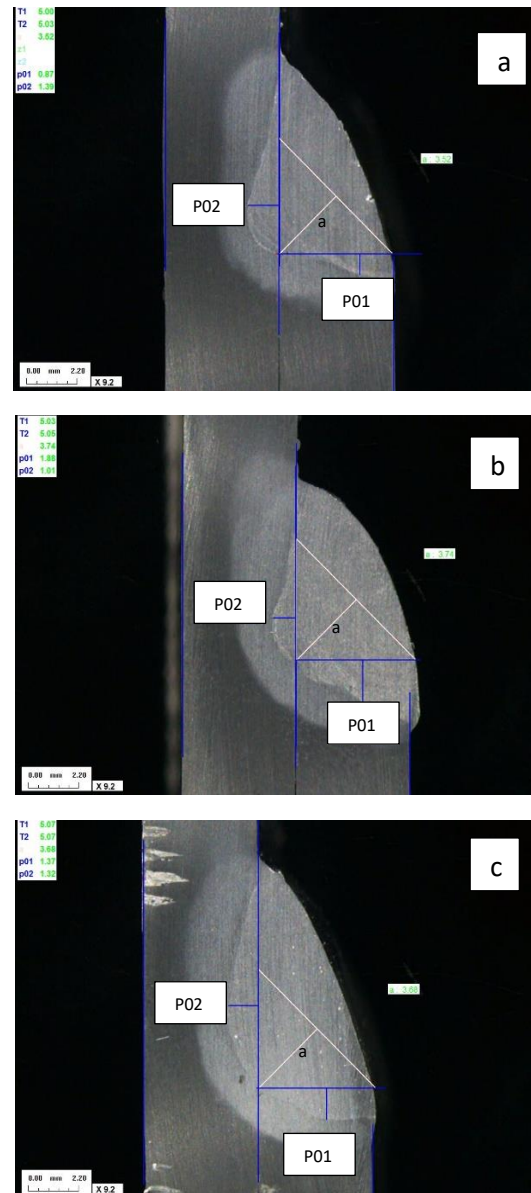


Figure 1. Three different penetration measurements of a,b,c 6082 alloy

Table 3. Penetration measurement results (Min: indicates the minimum value specified in the standard)

	Min	a	b	c
P01	0,52	0,87	1,88	1,37
P02	0,52	1,39	1,01	1,32
a	2,4	3,52	3,74	3,68

3.2. Tensile Test Results

N series shows untreated samples, T series shows post weld heat treated samples. Tests were carried out by taking 4 of each. The tests were carried out at a tensile speed of 5mm/min. According to the test results, the heat treatment applied for 30 minutes at

175°C decreased the shear force and elongation amount.

Table 4. Tensile Test Results

Samples	Force (kN)	Strain(%)
N-1	19,4	3,04
N-2	18,5	2,45
N-3	20,5	2,81
N-4	14,8	2,47
T-1	14,8	2,98
T-2	16,5	1,84
T-3	15,9	2,16
T-4	14,7	1,86

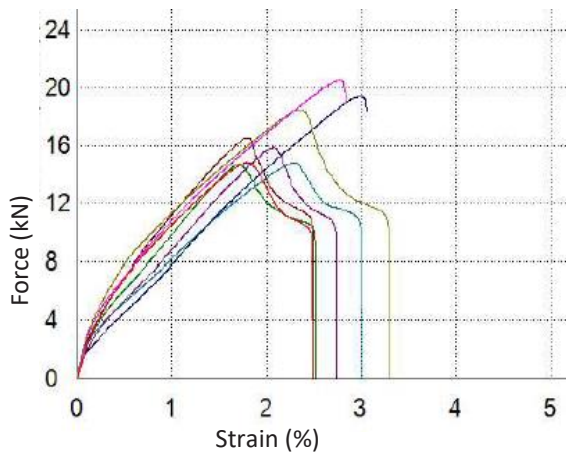


Figure 2. Force-elongation graph (force graph is given since the strength values are very close)

3.3. Hardness Results

The hardness tests were taken from three different zones: weld zone, heat affected zone and base metal. In the heat treatment carried out after welding, an increase in hardness was observed in the region between the weld metal and the base metal. In addition, as expected, a decrease in hardness was observed in the weld zone.

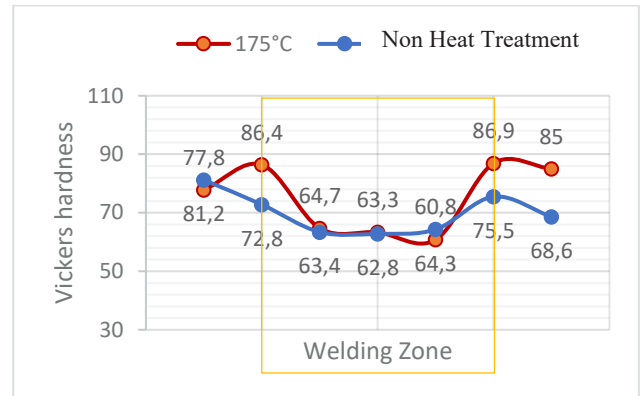


Figure 3. Hardness values of base metal and HAZ zone in welded parts

3.4. Microstructure analyzes

Stress relieving heat treatment applied at 175 °C for 30 minutes helped to arrange the grains in the heat-effective region in the microstructure.



Figure 4. Microstructure image of untreated sample (N1)



Figure 5. Microstructure image of heat treated sample (T1)

4. Conclusion

In the specified MIG welding parameters, penetration above the minimum values of P01: 0.52, P02:0.52 and a:2.4 in the TS EN ISO 10042 standard was provided for the 6082 alloy (Table 3)

Heat treatment applied for 30 minutes at 175°C after welding decreased the force and elongation amount.

In the heat treatment carried out after welding, an increase in hardness was observed in the region between the weld metal and the base metal. The effect of this result could not be seen as it broke from the weld area in the tensile test. The wire alloy 4043 used is an alloy with lower strength than the base metal.

References

- [1] M.El- Shennawy, Kh. Abdel-Aziz and A.A. Omar, Metallurgical and Mechanical Properties of Heat Treatable Aluminum Alloy AA6082 Welds, 11 (2017). 2832-2839
- [2] Demirpolat H., Alüminyum İşlem Alaşımalarında T651 Isıl İşlemi Uygulamaları ve Etkilerinin Araştırılması Investigation Of T651 Heat Treatment Applications And Effects In Aluminum Wrought Alloys Seracettin Akdı1.
- [3]Jie Y11,Effect Of Post-Weld Heat Treatment On Microstructure And Mechanical Properties Of Welded Joints Of 6061-T6 Aluminum Alloy. 2018
- [4] Bo Wang, Songbai Xue, Chaoli Ma, Jianxin Wang and Zhongqiang Lin. Effects of Porosity, Heat Input and Post-Weld Heat Treatment on the Microstructure and Mechanical Properties of TIG Welded Joints of AA6082-T6. 2017
- [5] Firouz Fadaeifard, Khamirul Amin matorı1, Farhad Garav, Muath Al-Falahı ,Gholamreza V. Effect Of Post Weld Heat Treatment On Microstructure And Mechanical Properties Of Gas Tungsten Arc Welded AA6061-T6 Alloy, Trans. Nonferrous Met. Soc. China 26(2016) 3102–3114.
- [6] M.N. Gusseva,*, N. Sridharana,b, M. Norfolk, K.A. Terrania, S.S. Babua, Effect of post weld heat treatment on the 6061 aluminum alloy produced by ultrasonic additive manufacturing, 684 (2017),606-618.



BMS

Biomaterials Symposium

Biyomalzemeler
Sempozyumu



SURFACE MODIFICATION OF 3D-PRINTED POROUS 316L STAINLESS STEEL

Azade YELTEN^{1,2}, Batur ERCAN²

¹Istanbul University-Cerrahpasa, ²Middle East Technical University
Türkiye

Keywords: DMLS Method, 316L Stainless steel, Anodization, Surface modification, Topography

Abstract

Metallic biomaterials are extensively used to meet the demands in orthopedic applications. For patient specific implant fabrication, three-dimensional (3d) printing systems have been investigated in the last decade. In fact, 3d printing allows fabrication of metallic implants that match the anatomy of the damaged hard tissue, which enabled improved bone regeneration for the patients. Aside from the appropriate implant geometry, surfaces of the implants also play an essential role in integration of the implant with juxtaposed bone tissue (osseointegration). To enhance the interactions between the implant and bone tissue, implant surface can be modified. One of the promising techniques to modify the surfaces of metallic implants is anodization. Anodization can be used to modify the surfaces of metallic implants in the nanoscale. In fact, the surface of the 316L stainless steel (316L SS), a commonly-used low-cost metallic implant material having appropriate mechanical properties and high machinability, can be altered via anodization to provide nanostructured surface topography.

In this study, porous 316L SS samples were manufactured with Direct Metal Laser Sintering (DMLS) method. For this purpose, computer-aided design (CAD) model of the sample was sketched and porous parts were printed according to this design. A porous morphology with 700 μm pore size was selected to reduce the elastic modulus difference between the bone and implant material. Moreover, the porous structure of the implant material was expected to improve the osseointegration between the bone tissue and the implant material. Afterwards, the printed porous 316L SS samples were anodized. Different process parameters were implemented to observe the structures forming on the material surfaces. These parameters were the electrolyte concentrations, applied voltage and anodization duration. The formed structures on the anodized samples were examined with Scanning Electron Microscope (SEM). It is observed that columnar shaped nanostructures developed on the surface according to the altered process parameters.

1. Introduction

Metallic biomaterials play a critical role in filling the increasing demand for orthopedic implants in the world. Fabrication of the metallic patient-specific implants that are designed in digital platforms through the three dimensional (3d) printing systems provide new opportunities in the orthopedic field. 316L SS is frequently used in orthopedic applications depending on its essential features, such as optimal mechanical properties (elastic (E) modulus, fracture toughness, fatigue strength), good machinability, being cost-effective and widely available [1-4]. However, the large difference between E-modulus of the bone and full-density 316L SS lead to the stress shielding problem, which causes weakening and density loss of the bone in time. Fabrication of porous implants lowers the E-modulus of the material so that the applied stress can be shared more uniformly between the bone tissue and implant material [3,5]. It is not easy to ensure the harmony and coherency in pore sizes and pore dispersion within the porous implants that are prepared according to the conventional production methods. Mechanical properties of the implant materials are negatively affected when reproducibility and homogeneous pore features are not enabled. On the contrary, materials can be achieved one-to-one compatible with the determined dimensions and design owing to the rapid prototyping approach [6,7].

Aside from the pore size and porosity content, the interactions between the bone tissue and material is another critical factor that influences osseointegration. Among various surface modification techniques, anodic oxidation (anodization) is ideal for orthopedic applications in terms of its versatility in controlling the surface in nanoscale. In this respect, porous 316L SS parts were fabricated by employing 3d printing, i.e. Direct Metal Laser Sintering (DMLS) technique, and then the surfaces of the samples were modified in nanoscale via anodization. Thus, it is aimed to enhance the material-bone tissue interactions by providing better fixation between the implant and bone tissue.

2. Experimental Procedure

Porous 316L SS samples were manufactured with the DMLS method using the EOS M290 3d-printer. DMLS technique is based on processing the metal powder bed layer-by-layer with the laser beam according to the computer-aided design (CAD). For this purpose, a CAD model of the octahedron (eight-faced) unit cells with interconnected open pores was sketched. A porous morphology with 700 μm pore size was selected to reduce the E-modulus difference between the bone and implant material. The chemical composition of the 316L SS powders used in the printing process is 17-19% Cr, 13-15% Ni, 2,25-3% Mo, $\leq 2\%$ Mn, $\leq 0,75\%$ Si, $\leq 0,5\%$ Cu, $\leq 0,1\%$ N, $\leq 0,03\%$ C, $\leq 0,01\%$ S, $\leq 0,025\%$ P, and balance % Fe. 316L SS powders had a spherical morphology and the average particle size of the powders was $\sim 20 \mu\text{m}$. Porous implants (**Fig. 1**) were 3d-printed by repeating the defined unit cells until reaching the actual part sizes (d: 1.2 cm and h: 0.45 cm).

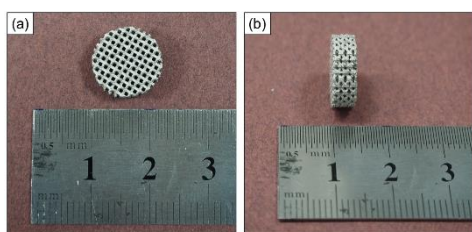


Figure 1. (a) Upper surface and (b) lateral surface of 3d-printed porous 316L SS samples.

3d-printed porous 316L SS samples were then ultrasonically cleaned in acetone, ethanol, and distilled water for 20 min, respectively prior to anodization. A platinum mesh was used as the cathode, while 3d-printed porous 316L SS sample was the anode. The distance between the anode and cathode was adjusted as 4 cm [2,8,9]. Electrolyte was composed of ethylene glycol (EG, $\text{C}_2\text{H}_6\text{O}_2$ (Isolab, Extra pure, $\geq 99\%$) and perchloric acid (HClO_4 , Sigma-Aldrich, puriss, p.a., ACS reagent). The temperature of the electrolyte was kept as 4-5 $^\circ\text{C}$ in order to tolerate the temperature rise that occurs due to the current increase. The electrochemical cell used in the experiments can be seen in **Fig. 2**.

Different process parameters were implemented to observe the structures that form on the material surfaces. These parameters were the electrolyte concentrations (vol. 5% HClO_4 containing EG solution and vol. 6.66% HClO_4 containing EG solution), applied voltage (30V and 40V) and anodization duration (5 min, 10 min, and 15 min).

The formed structures on the anodized samples were examined with FEI Nova Nano 430 model Scanning Electron Microscope (SEM).

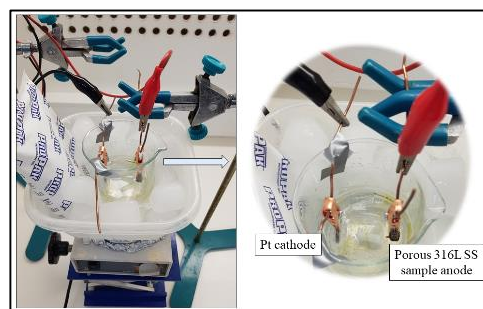


Figure 2. Experimental set-up used for anodizing the 3d-printed porous 316L SS samples.

3. Results and Discussion

SEM images (**Fig. 3**) of the samples anodized in EG solution containing vol. 5% HClO_4 showed columnar shaped structures forming on the sample surfaces. However, it was realized that these structures did not possess a distinct order. Actually, non-homogeneous formation and dispersion of the nanostructures were determined when 30V was applied as the potential. Initial development of nanostructures with different morphologies was observed only in the pore wall regions rather than on the surface of the samples (**Fig. 3 (a-c)**). Since the mentioned regions draw higher amount of current due to their geometry, anodization reactions firstly became apparent on the pore walls. The maximum current value recorded as 0.28A when 30V was applied.

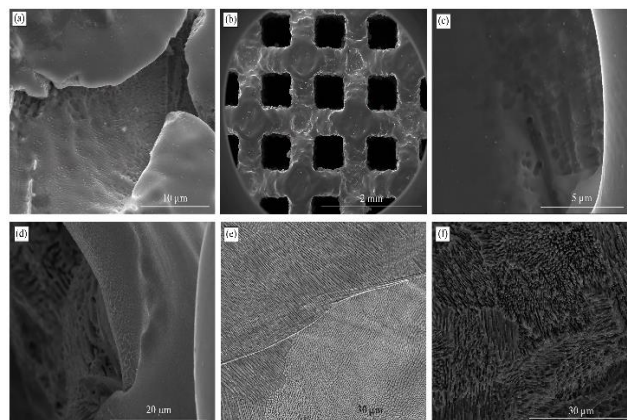


Figure 3. SEM images of the 3d-printed porous 316L SS samples anodized in the 5% HClO_4 containing EG solution (a) 30V 5min, (b) 30V 10min, (c) 30V 15min, (d) 40V 5min, (e) 40V 10min, and (f) 40V 15min.

It was recognized from the SEM images (**Fig. 3e**) that an applied voltage of 40V yielded nanostructures with rod-like morphology on the sample surface. We have not encountered any studies explaining the fabrication of columnar shaped nanostructures via anodization on 3d-printed porous 316 SS samples. This observation confirms the novelty of the obtained data.

When vol. 6.66% HClO₄ containing EG solution was used as the electrolyte, 30V still did not modify the whole surface but caused changes in the pore walls. As can be understood from the SEM images in **Fig. 4 (a and b)**, the rod-like nanostructure formation initially started from the pore walls, however, no significant change took place on the struts. This situation was clearly shown in **Fig. 3c**, where the struts with smooth surfaces appeared without any morphological changes. Conversely, 40V led to a pitting on the sample surfaces (**Fig. 4 (c and d)**).

It was also important to optimize the anodization time to manage the current that the system drew. As expected, the current value of the anodization system reached such high values as 1A in very short durations when higher voltages were applied. Moreover, when the larger surface area of the material due to its porous morphology was anodized with higher voltage values, the formation of non-homogeneously developed and dispersed nanostructures occurred. Optimization studies are ongoing to achieve uniform and properly-dispersed nanostructures on the surface of the 3d-printed porous 316L SS samples.

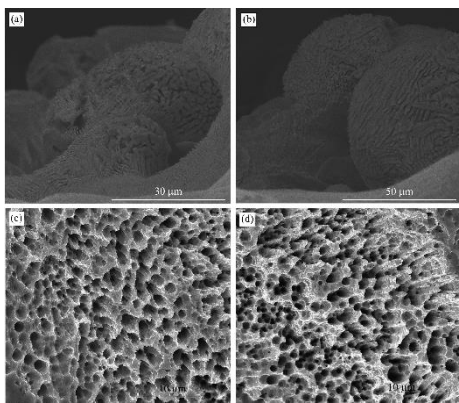


Figure 4. SEM images of the 3d-printed porous 316L SS samples anodized in the 6.66% HClO₄ containing EG solution. **(a)** 30V 10min, **(b)** 30V 15min, **(c)** 40V 10min, and **(d)** 40V 15min.

4. Conclusion

Some critical facts about this research are summarized below:

- ✓ Porous 316L SS parts were fabricated by DMLS technique, and afterwards the surfaces of the samples were modified in nanoscale via anodization.
- ✓ It was aimed to enhance the material-bone tissue interactions by controlling the surface in nanoscale through anodization.
- ✓ Various parameters were considered to analyze their effects on formation of nanostructures on the surface of the material.
- ✓ 30V as the voltage value was not effective in forming nanostructures with different morphologies either in

vol. 5% HClO₄ containing EG solution or 6.66% HClO₄ containing EG solution.

- ✓ Anodization time was another critical process parameter that influenced the nanostructure formation.
- ✓ 5 min. was not sufficient to create a prominent change, however, 15 min. induced formation of pits on the material surface especially when 6.66% HClO₄ containing EG solution was used as the electrolyte.
- ✓ SEM images demonstrated that when 40V was applied, rod-like nanostructures formed on the 3d-printed porous 316L SS sample surfaces. This interesting data emphasized the novelty of the study among the reports in the literature.

Acknowledgement

This work was supported by the Scientific and Technological Research Council of Turkey under the project TÜBİTAK 2218 - National Postdoctoral Research Fellowship Programme, Project No. 118C497.

References

- [1] F. Mat Noor, K.R. Jamaludin and S. Ahmad, Fabrication of porous stainless steel 316L for biomedical applications, MATEC Web of Conferences (ICME'17), 135 (2017) 00062.
- [2] S. Ni, L. Sun, B. Ercan, L. Liu, K. Ziemer and T.J. Webster, A mechanism for the enhanced attachment and proliferation of fibroblasts on anodized 316L stainless steel with nano-pit arrays, Journal of Biomedical Materials Research B: Applied Biomaterials, 102B (6) (2014) 1297-1303.
- [3] X. Wang, S. Xu, S. Zhou, W. Xu, M. Leary, P. Choong, M. Qian, M. Brandt and Y.M. Xie, Topological design and additive manufacturing of porous metals for bone scaffolds and orthopaedic implants: a review", Biomaterials, 83 (2016) 127-41.
- [4] X.P. Tan, Y.J. Tan, C.S.L. Chow, S.B. Tor and W.Y. Yeong, Metallic powder-bed based 3D printing of cellular scaffolds for orthopaedic implants: A state-of-the-art review on manufacturing, topological design, mechanical properties and biocompatibility, Materials Science and Engineering C, 76 (2017) 1328-43.
- [5] A. El-Hajje, E.C. Kolos, J.K. Wang, S. Maleksaeedi, Z. He, F.E. Wiria, C. Choong, A.J. Ruys, Physical and mechanical characterization of 3D-printed porous titanium for biomedical applications, Journal of Materials Science: Materials in Medicine, 25 (2014) 2471-80.
- [6] G.E. Ryan, A.S. Pandit and D.P. Aptsidis, Porous titanium scaffolds fabricated using a rapid prototyping and powder metallurgy technique, Biomaterials, 29 (2008) 3625-35.
- [7] S. Van Bael, G. Kerckhofs, M. Moesen, G. Pyka, J. Schrooten and J.P. Kruth, Micro-CT-based improvement of geometrical and mechanical controllability of selective laser melted Ti6Al4V porous structures, Materials Science and Engineering A, 528 (2011) 7423-31.
- [8] A. Jagminas, K. Mazeika, N. Bernotas, V. Klimas, A. Selskis and D. Baltrunas, Compositional and structural characterization of nanoporous films produced by iron anodizing in ethylene glycol solution, Applied Surface Science, 257 (2011) 3893-97.
- [9] Z. Cong, M. Wang, X. Sun, L. Liu and H. Sun, Optical and dielectric properties of anodic iron oxide films, Applied Surface Science, 503 (2020) 144159.

CHARACTERIZATION OF COPPER NANOPARTICLE-DEPOSITED BIOCERAMIC COATINGS FABRICATED ON ZIRCONIUM

Tuba YILDIZ^{1,2}, Salih DURDU³, Kadriye OZCAN³, Metin USTA¹

¹TUSAS, ²Iskenderun Technical University
Türkiye

Keywords: Copper nanoparticle (CuNPs), Bioceramic coatings, Micro arc oxidation (MAO), Electrochemical deposition (ED), Antibacterial surface.

Abstract

The commercial pure zirconium (Zr) was coated by micro arc oxidation (MAO) in solution, consisting of calcium acetate and β -calcium glycerophosphate salt. Then, copper nanoparticles (CuNPs) were deposited at different by electrochemical deposition (ED). The phase structure, surface morphology, elemental composition and wettability of both coatings were characterized by XRD, SEM, EDS and contact angle goniometer, respectively. The XRD results indicated that zirconia, calcium zirconate and hydroxyapatite were detected on the surfaces. The coating surfaces were rough and porous. Also, CuNPs was randomly distributed through the whole surface. In vitro antibacterial test of all surfaces was carried out for Gram positive (*S. aureus*) and Gram negative (*E. coli*) bacteria.

1. Introduction

Zirconium and its alloys are one of the best choices for dental and orthopedic implant materials due to their superior chemical and mechanical properties such as good corrosion resistance, chemical stability, high fracture toughness, high bending and flexural strength and low toxicity [1]. The elastic modulus of zirconium is 92 GPa and it causes minimal stress shielding effect of the bone to be implanted, compared to other metallic implants such as stainless steel, CoCr and Ti and its alloys. MAO offers more advantages as it produces well-adhered, crystalline, dense and thick coating layers with high tribological performance and high thermal-chemical stability [2], the electrochemical deposition process can be carried out under a mild experimental condition at a relatively low temperature, thus avoiding undesired phase changes. This method also produces highly crystalline coatings with low solubility in body fluids and low residual stress [3]. Cu one of the essential trace elements, plays vital role in humans [4]. Cu was recognized by the United States Environmental Protection Agency (EPA) in 2008 as the first effective metallic antimicrobial agent with broad-spectrum antimicrobial properties against bacteria, fungi and viruses [5].

2. Materials and Methods

In this study, as a first step, bioceramic coatings of 30 min durations were fabricated on Zr (commercially pure zirconium) in an electrolyte based on calcium acetate and β -calcium glycerophosphate salt with MAO. Then, as a second step, the CuNPs were deposited with ED on the MAO surface. The phase compositions of the Cu-based MAO coatings were scanned by powder XRD (X-ray diffractometer, Bruker D8 Advance) (Fig. 1). The surface morphologies of plain MAO and Cu-deposited MAO coating are seen in Fig.2 a and b, respectively.

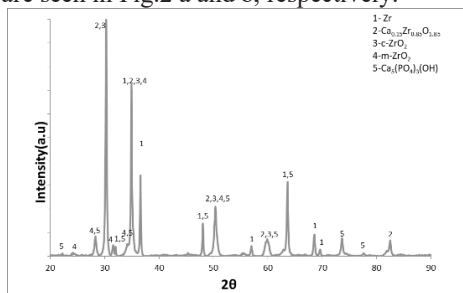


Figure 1. Powder-XRD spectra of the Cu-deposited MAO coatings.

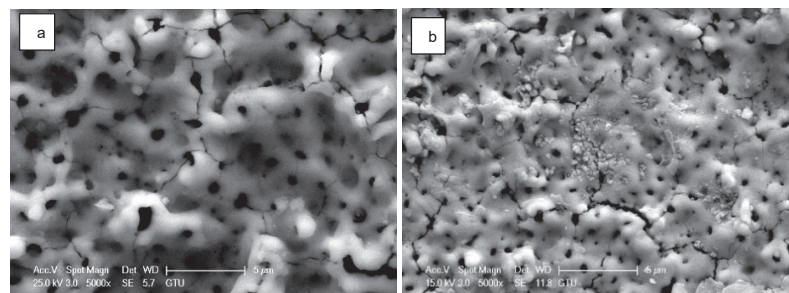


Figure 2. Surface morphologies of the coatings (30 min): a) plain MAO coating and b) Cu-deposited MAO coating.

3. Conclusion

In this study, after MAO and MAO + ED processes, all elements such as Ca, P, O, Zr and Cu were uniformly distributed through the whole surface. The surfaces of the both coatings were rough and porous. The bacterial adhesion on the CuNPs-coated MAO surfaces was reduced compared to bare MAO and Zr substrate.

Acknowledgment

Mr. A. Nazim for running SEM and EDS analyses and Mr. A. Sen for running powder-XRD at Gebze Technical University.

References

- [1] A. G. Sanchez, W.D.G. Schreiner and S. Ceré, Appl. Surf. Sci., 257(15) (2011) 6397–6405.
- [2] S. Durdu and M. Usta, Ceram. Int., 40(2) (2014) 3627–3635.
- [3] N. N. C. Isa, Y. Mohd and N. Yury, APCBEE Procedia, 3 (2014) 46–52.
- [4] X. Zhang, Mater. Sci. Eng. C., 82 (2018) 110–120.
- [5] R. Bai, L. Peng, Q. Sun, Y. Zhang, L. Zhang, Y. Wei and B. Han, Materials, 13(20) (2020) 4594.

PRODUCTION AND CHARACTERIZATION OF BIOACTIVE GLASS-CERAMICS FROM SODA-LIME-SILICA AND BOROSILICATE WASTE GLASSES

Merve Şeyma SÜREL¹, İremnur AKÇAKOCA¹, Şeniz Reyhan Kuşhan AKIN²,
Gülsüm TOPATEŞ¹

¹Ankara Yıldırım Beyazıt University, ²Çankaya University
Türkiye

Keywords: Waste SLS and borosilicate glass, Glass-ceramic, Crystalline-amorphous ratio, Bioactivity, Solubility

Abstract

In this study, bioactive glass-ceramics are aimed to be produced by waste glasses to ease bioactive glass-ceramic production and transform waste glasses into high-valued products. Two bioactive glass compositions have been studied; the first one is the well-known 45S5 and the second one is the newly determined 23B23S. Also, compositions from pure oxides were prepared to compare with waste glasses. High degradation rate and hydroxyapatite (HA) layer formation was observed after (simulated body fluid) SBF immersion. The formation of a thicker layer was observed with increasing soaking time.

1. Introduction

Reuse (recycle or upcycle) rate of two major glasses (soda-lime-silica (SLS) and borosilicate) is very limited despite higher production rates. [1] Bioactive glasses were discovered in 1970 and the very first of them was 45S5 which consisted of 45% SiO₂, 24.5% Na₂O, 24.5% CaO, and 6% P₂O₅. [2] In recent years, several elements such as boron have been including glass composition, and effect of boron on promoting bone healing was announced. [3] The degradation range can be diversified by replacing SiO₂ with B₂O₃ to match the degradation rate of bioactive glass with the bone degradation rate. [2] Waste SLS and borosilicate glasses are suitable to use in bioactive glass-ceramics. There are limited studies about the production of bioactive glasses from waste glasses. The first study was made by Abbasi and Hashemi (2014) which was the fabrication of bioactive glass-ceramics using waste SLS glass which resulted in crystallinity of bioactive glass-ceramic affecting the bioactivity. [4]

2. Materials and Methods

To use borosilicate waste glass, a new boron-containing composition was determined based on the mol % of 45S5. Half of the SiO₂ in 45S5 was replaced with B₂O₃ and it was named 23B23S. Samples with four different compositions were heat treated between 500°C - 1000°C for 0.5 hours. Firing shrinkage and weight loss values were calculated. To observe in vitro degradation, samples were soaked in Tris-HCl buffer solution at 37°C for 1-7 days. XRD was performed to identify phases and calculate the crystal phase amount. Microstructure of the samples heat-treated at highest temperatures and samples after SBF were observed via SEM-EDX.

3. Conclusion

Phase analysis of samples showed that several Na-Ca-silicate phases which show bioactive response have been formed for all samples. Boron-containing samples also included tricalcium (bis)borate. SEM images of 45S5 and 23B23S from waste glasses were given before and after the SBF test in Figure 1. For all samples, a very dense structure was produced as a result of the glassy phase. EDX analyses after SBF proved the formation of a HAP-like layer with different morphologies. As a result of in vitro degradation tests, a high amount of degradation between 65.6 – 99.2% was observed in bioactive glass-ceramic powders.

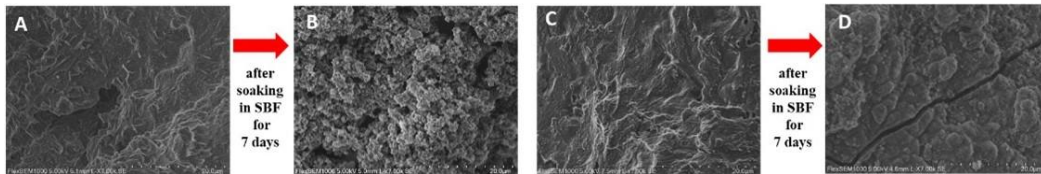


Figure 1. SEM images of before (a) 45WS5, (c) 23WB23S and after SBF immersion (b) 45WS5, (d) 23WB23S

Acknowledgments

The financial support for this study is provided by TÜBİTAK within the 2209-A - Research Project Support Programme for Undergraduate Students.

References

- [1] Topateş, G., Applied Ceramic Technology, 17 (2020) 555-561.
- [2] Rahaman, M.N., et. al., Acta Biomaterialia, 7 (2011) 2355-2373.
- [3] Balasubramanian, P., et. al., Journal of the European Ceramic Society, 38 (2018) 855-869.
- [4] Abbasi, M., Hashemi, B., Materials Science and Engineering C, 37 (2014) 399-404.



ESSENTIAL OIL-LOADED POLYMERIC FOAMS VIA GREEN ROUTE

Fatma Nur PARIN

Bursa Technical University
Türkiye

Keywords: polymeric foam, citral essential oil, wound dressing, antibacterial activity, polyvinyl alcohol (PVA), collagen

Abstract

An ideal wound dressing in the wound healing process should be able to create biocompatible structured matrixes that can retain moisture, prevent bacterial adhesion, and prevent environmental threats. In this study, collagen and biocompatible polyvinyl alcohol (PVA), which have recently been used quite widely in wound healing processes, will be used as a matrix material. Although PVA and collagen polymers are used alone as matrix materials for the purpose of ideal wound dressing, their combined use will contribute to the development of the physical properties of the final wound dressing to be produced. However, since PVA/collagen (PVA/COL) wound dressings cannot provide all the requirements and it is necessary to obtain topical foams by enriching them with the active ingredient citral essential oil. In this study, the morphological, thermal, spectroscopic analysis, and antibacterial activities of the foam materials that will be obtained according to different amounts of essential oils by preparing Pickering emulsions will be evaluated.

1. Introduction

Essential oils are volatile components generated as bioactive molecules by aromatic plants and are commonly utilized in agriculture, medical, cosmetic, pharmacological, and food applications [1]. Because of their antibacterial properties, essential oils have a high potential for application in medical. However, they are quickly oxidized, resulting in decreased bioactivities [1,2]. Citral ($C_{10}H_{16}O$) is a type of monoterpene aldehyde which is a combination of two geometric isomers, geranial and neral. It has been found in a number of experimental and clinical investigations to have anti-inflammatory and anti-corrosive properties, and there is considerable evidence that it works as a fungicidal and bactericidal agent [3]. Especially, citral has an antibacterial activity against both gram-positive and gram-negative bacteria in both oil and vapor state, as

well [4]. Similar to other essential oils, it is sensitive to environmental conditions and also has hydrophobic nature, for this reason its antibacterial activity may soon be lost. Pickering emulsions are a novel and new way of stabilizing emulsions, i.e., oil/water mixtures, that use solid particles rather than surfactants [5]. Solid particles are highly adsorbed at the oil/water interface in Pickering emulsions, producing a permanent barrier that limits coalescence. Stable colloidal emulsions also offer stronger evaporation resistance to volatile oils than systems stabilized with the surfactant, extending their shelf life and providing a controlled release mechanism that provides the essential oil's effectiveness [6]. Although various inorganic particles, such as silica, clay, and titanium dioxide, have been utilized as Pickering emulsifiers, other research has modified cellulose, protein, and starch to enhance biocompatibility. β -cyclodextrin (β -CD) with a hollow conical structure acts as a very good Pickering emulsifier at room temperature. Because of its hydrophobic interior hole, it may form non-covalent host-guest inclusion complexes with a variety of lipophilic chemicals, such as essential oils [7].

In this study, polymer foams were produced by Pickering emulsions of bio-based PVA/collagen (PVA/COL) matrix and β -CD/citral essential oil (citral) to use in wound applications. It was investigated the changes of the morphological, thermal morphological, physical and antibacterial activities in the resultant foams due to the various ratio of the β -CD/citral complexes.

2. Experimental Procedure

The polyvinyl alcohol (PVA) was purchased from YellowX Company (Turkey). Collagen (Type 1-3) were used which were purchased from Hammadesepeti Corporation (Turkey). β -cyclodextrin (β -CD) cyclodextrin (β -CD) (Cavamax W7 HP Pharma) was donated by Wacker Chemie (Germany). Citral (99% purity) was kindly donated by ElsoKimya Chemical

Company (Turkey) and APS was donated by Borakay Chemical Company (Turkey). Glycerin was bought from LIFE IN Company (Turkey). Distilled water was used in the experiments and all of the reagents were used without any purification.

2.1. Synthesis of Essential oil-loaded PVA/Collagen Foams

PVA granules were dissolved in distilled water at 90°C to produce a homogenous 10% (w/v) PVA solution. Then, MBAm crosslinker was added in the PVA solution to mixed for 24 h. Collagen powders and glycerol were added respectively in the polymer solution produce a uniform PVA/collagen blend solution. This solution poured into the teflon mould and it was kept in the oven for 1 day.

To synthesis of essential oil-loaded polymer foams, blend solutions mixed with in mechanical stirrer. In this scope, glycerol was added PVA/collagen blend solutions and mixed with 260 rpm. After, citral essential oil was added in the mixture drop by drop in varying concentration. Finally, beta-cyclodextrin and KPS was put in the mixture and mixed with 700 rpm for 5 min. As in the production of neat PVA/collagen solution, the foam solution poured into the teflon mould and it was kept in the oven for 1 day. (Figure 1).

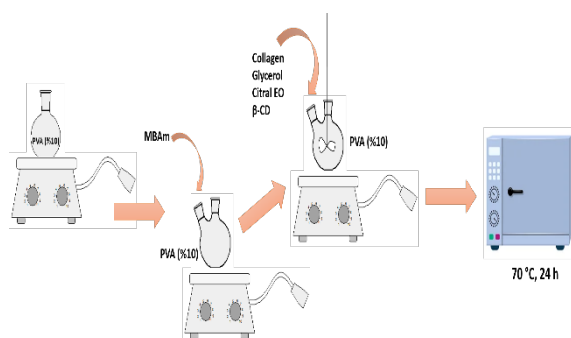


Figure 1. Schematic illustration of citral EO-loaded PVA/collagen foams.

2.2. Characterization of the Foams

Morphological Analysis of the Foams

The polymer foams and neat film were also characterized using stereomicroscope (Leica-M125) with 8 X magnification and optical microscope with 10 kX, respectively.

Thermal Analysis

Thermal analysis was performed using a TA/SDT650 TGA (USA). TGA analysis was carried out in a nitrogen atmosphere with a heating rate of 10 °C min⁻¹ and a temperature range of 30-600 °C, and in an oxygen atmosphere with a heating rate of 10 °C min⁻¹ and a temperature range of 600 - 900 °C.

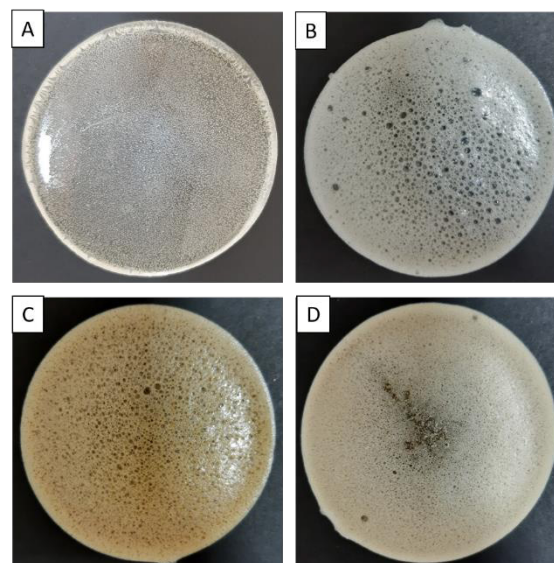


Figure 2. Digital photographs of neat PVA/COL film and Pickering PVA/COL/CIT foams.

Spectroscopic Analysis

FT-IR data were obtained in the 4000-500 cm⁻¹ range using an ATR (Attenuated Total Replication) adapter (Smart Orbit Diamond, USA) spectrometer, with 16 scans recorded at 4 cm⁻¹ resolutions using a ThermoNicolet iS50 FT-IR (USA) spectrometer.

Antibacterial Activities

As positive controls, antibacterial activities of the polymer foams were evaluated against standard strains of *Escherichia coli* ATCC® 25922 and *Staphylococcus aureus* ATCC® 25923. To revive the lyophilized bacterial strains, Trypton Soy Agar (8 g) medium was mixed with distilled water (75 mL) and melted in the microwave oven. The pH of the mixture was set to 7.2 and sterilized in an autoclave for 15 minutes at 121°C. It was autoclaved and then warmed to 45-50 °C before being put on petri dishes. Bacterial strains were inoculated on solid agar after the petri dishes had cooled. Afterwards, the plates were incubated in an aerobic environment for 18 hours (37 °C). Liquid suspensions of bacterial colonies in a 0.9 % isotonic NaCl solution.

3. Results and Discussion

Optical Microscope

Figure 3 depicts the surface morphology of the neat film and Pickering sponges. Surface defects (bubbles) appear on pure films (Figure 2A). The other images showed Pickering foams with different ratio of β -CD/citral inclusion complexes (Figure 2B-2D). When the ratio of the β -CD/citral inclusion complex was 1:8, the foam structure was breakdown and no Pickering film was obtained. For this reason, the heterogeneous film structure is seen in Figure 2E.

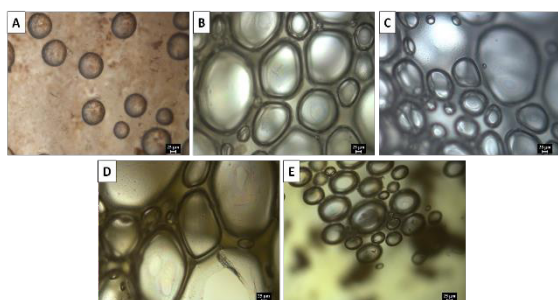


Figure 3. Optical images of A. Neat PVA/COL film, B. PVA/COL/CIT 1:1, C. PVA/COL/CIT 1:2, D. PVA/COL/CIT 1:4 and E. PVA/COL/CIT 1:8 foams (10X).

Stereo-microscope

In Figure 5, the surface images of neat film and Pickering foams clearly were appeared. In this scope, bubbles in the neat film (Figure 3A) and little pores in the PVA/COL/CIT 1:1 foams were observed. Moreover, with an increase in the amount of the β -CD/citral inclusion complex, the pores have grown and a heterogeneous pore structure has been formed. As with the optical microscope, the distorted foam structure in the PVA/COL/CIT 1:8 sample appears more clearly (Figure 4E). Overall, the amount of oil prevents the formation of foam after a certain value.

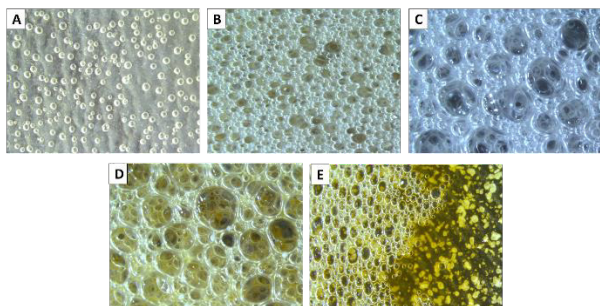


Figure 4. Stereo-microscope images of A. Neat PVA/COL film, B. PVA/COL/CIT 1:1, C. PVA/COL/CIT 1:2, D. PVA/COL/CIT 1:4 and E. PVA/COL/CIT 1:8 foams (8X).

TGA Analysis

TGA was used to evaluate the thermal stability of neat PVA/COL polymer film and PVA/COL/CIT Pickering foams and the TGA thermograms are shown in Figure 4. All Pickering foams and neat film lost weight at temperatures ranging from 30 to 100 °C (initial stages) due to moisture loss from the materials. From the TGA curve of neat sample, it can be seen that the sample has a 4-step decomposition (except for moisture loss). The other sequential weight losses were recorded at the range of 150-500 °C [8]. This is due to the decomposition of PVA side chains and the nature of collagen decomposition

caused by the collagen chain backbone. The last step is (600 - 650 °C) observed the breakdown of PVA's C-C bonds. These data are consistent with the literature [8,9]. It is observed that the thermal resistance decreases with the addition of citral essential oil to the structure. The TGA degradation profile of PVA/COL/CIT 1:4 differs from other CIT-containing samples and has started to degrade earlier. This can be attributed to the fact that essential oils are sensitive to temperature and oxidation.

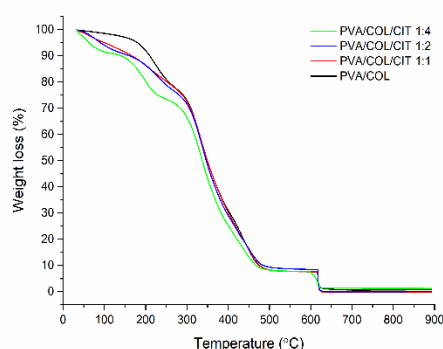


Figure 5. TGA thermograms of neat PVA/COL film and PVA/COL/CIT foams.

FT-IR Analysis

The chemical structure of the neat PVA/COL films and Pickering foams were analyzed by FT-IR (Figure 6). According to literature, PVA's spectra shows the following absorption bands: 3299 cm^{-1} (-OH stretching), 2955 cm^{-1} and 2861 cm^{-1} asymmetric and symmetric (-CH stretching), 1418 cm^{-1} (-OH or -CH bending), 1087 cm^{-1} (C-C stretching and -OH bending), and 840 cm^{-1} (CH_2 rocking) [8,9]. Furthermore, a peak at 1726 cm^{-1} was related to a C=O stretching vibration band from carbonyl functional groups presence of residual acetate groups remaining after PVA manufacture from polyvinyl acetate hydrolysis or oxidation during preparation and processing [8]. The characteristic FTIR bands of collagen were observed in the neat PVA/Col films, including bands at 3296 cm^{-1} (amide A, -NH stretching, and -OH stretching), 2938 cm^{-1} (amide B, the asymmetrical stretching of CH_2 vibration), 1655 cm^{-1} (amide I, hydrogen bonding between -NH stretching and -CO), 1549 cm^{-1} (amide II, -NH bending and -CN stretching), and 1200-1350 cm^{-1} (amide III bands corresponded to -CN stretching and -NH in plane bending vibration (deformation) [8-10]. The existence of these bands suggested that collagen had been absorbed into the PVA blended films, as did triple helix structure of collagen. With the addition of β -CD/citral inclusion complexes to PVA/COL solutions, changes were observed in the FTIR spectrum, especially in the 650-1700 cm^{-1}

band. This indicates the presence of characteristic peaks of citral in the Pickering foams.

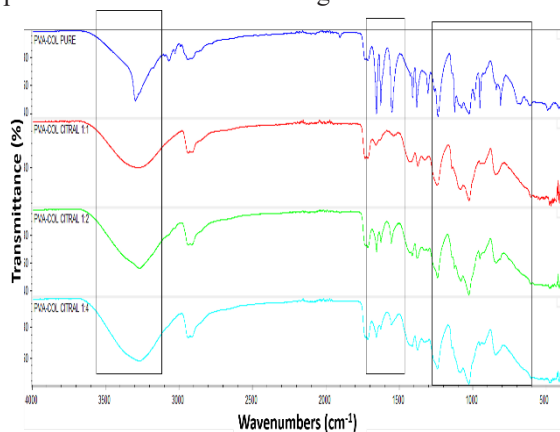


Figure 6. FT-IR spectra of neat PVA/COL film and citral EO-loaded PVA/collagen foams.

Antibacterial Activities

The antibacterial activity of PVA/COL neat film and Pickering PVA/COL/St foams were applied using a disk diffusion technique against gram negative (*E.coli*) and gram positive (*S. aureus*) bacteria. two different microbial species. Bacterial infections appear to be a major healthcare problem as a result of the growth and spread of multi-drug resistant bacteria, which has stimulated significant interest in the development of new antimicrobial treatments [11]. In this scope, many researchers found that citral has antimicrobial property against pathogenic and food-spoilage microorganisms such *E. coli*, *Salmonella Typhimurium*, *Listeria monocytogenes*, and *Staphylococcus aureus*. Furthermore, in a study with antibacterial activity of citral against *C. sakazakii*, it was not exactly appointed [1]. In this study, all PVA/COL Pickering foams with β -CD/citral inclusion complexes displayed antibacterial activity against only *S. aureus* bacteria. This may be due to the Gram-negative bacteria are often more resistant to plant extracts, oils than gram-positive bacteria [12].



Figure 7. Antibacterial activity of the foams against *S. aureus* bacteria.

4. Conclusion

Briefly, PVA/COL/CIT foams were successfully produced by Pickering emulsion route. The obtained

foams were investigated by optical and stereo microscopes, FTIR, TGA analyses and antibacterial activities. The results showed β -CD/citral ratio directly effects antibacterial activity and also structure of PVA/COL/CIT foams. The study led the future therapeutic uses for wound healing applications.

Acknowledgment

The author gratefully acknowledge Dr. Uğur Parin for his kind help in the antibacterial measurements of the foams and Aydın Adnan Menderes University of Faculty of Veterinary Science, Microbiological Department.

References

- [1] M. Mokarizadeh, H. S. Kafil, S. Ghanbarzadeh, A. Alizadeh, & H. Hamishehkar *Research in Pharmaceutical Sciences*, 12(5), 409, (2017).
- [2] I. H. N. Bassolé, & H. R. Juliani, *Molecules*, 17(4), 3989-4006 (2012).
- [3] C. Shi, K. Song, X. Zhang, Y. Sun, Y. Sui, Y. Chen, & X. Xia, *Plos one*, 11(7), e0159006 (2016).
- [4] C. Argyropoulou, D. Daferera, P. A. Tarantilis, C. Fasseas, & M. Polissiou, *Biochemical Systematics and Ecology*, 35(12), 831-837 (2007).
- [5] J. W. Hu, M. W. Yen, A. J. Wang, & I. M. Chu, *Colloids and Surfaces B: Biointerfaces*, 161, 51-58 (2018).
- [6] A. G. de Souza, J. de Souza Marciano, R. R. Ferreira, E. R. de Oliveira & D. dos Santos Rosa, (2021). Researchsquare.
- [7] C. Li, X. Luo, L. Li, Y. Cai, X. Kang, & P. Li, *International Journal of Biological Macromolecules*, 209, 344-355 (2022).
- [8] B. Iqbal, N. Muhammad, A. Rahim, F. Iqbal, F. Sharif, S. Z. Safi, & I. U. Rehman, *International Journal of Polymeric Materials and Polymeric Biomaterials*, 68(10), 590-596 (2019).
- [9] S. El Moujahed, F. Errachidi, H. Abou Oualid, A. V. Botezatu-Dediu, F. O. Chahdi, Y. K. Rodi, & R. M. Dinica, *RSC advances*, 12(7), 4175-4186 (2022).
- [10] N. N. Bailore, B. K. Sarojini, B. Pushparekha, & B. Kabiru, (2020, June). In *AIP Conference Proceedings* (Vol. 2244, No. 1, p. 020003). AIP Publishing LLC.
- [11] N. G. Vasconcelos, J. Croda, & S. Simionatto, *Microbial pathogenesis*, 120, 198-203 (2018).
- [12] D. Trombetta, F. Castelli, M. G. Sarpietro, V. Venuti, M. Cristani, C. Daniele, & G. Bisignano, *Antimicrobial agents and chemotherapy*, 49(6), 2474-2478 (2005).

PRODUCTION AND CHARACTERIZATION OF Ti-6Al-4V SLURRY FOR TRABECULAR DENTAL IMPLANTS PRODUCED BY REPLICA IMPREGNATION METHOD

Aynur İNAN ÜSTÜN, Gülsüm TOPATEŞ, Yasin Sinan ERTEM, Hasan OKUYUCU

Ankara Yıldırım Beyazıt University
Türkiye

1. Introduction

In recently, metallic foams are in demand for several application because of their superior properties such as lightweight, high compression strength, low thermal conductivity, and good energy absorption. The trabecular implants, made of titanium and its alloys, have some important properties such as high corrosion resistance, suitable mechanical properties, good biocompatibility, etc, have been extensively used as biomaterials. According to the literature, trabecular implant provides the bone to move into the implant and thus better anchoring, result in a long life of implant can be ensured [1]. We aim to obtain a stable slurry and examine the binder and pH effect on the slurry.

In this study, the slurries for the metallic foam to be used in implants were produced with Ti6Al4V alloys. This slurry will be used in replica impregnation method that is relatively easy and cheap. We aimed to examine binder effect on sedimentation of slurry and pH effect on viscosity of slurry.

2. Materials and Methods

Ti-6Al-4V powders with high purity ($\geq 99.5\%$) were used as a base material. The powders have 15 μm size and spherical shape. Water was used as a solvent, polyethylene glycol and methylcellulose were used as a binder, carboxylic acid solution was used as a dispersant, and NaOH solution was used as a pH regulator. The five slurries were prepared. The first two slurries contain 15,5 % distilled water, 77,5 % Ti-6Al-4V powders, 1 % carboxylic acid solution, 2,3 % NaOH. However, they have different binder quantity and types. The first one contains 3,1 % polyethylene glycol and 0,5 % methyl cellulose, the second one contains only 3,6 % polyethylene glycol. The sedimentation rate of these slurries were examined. Then, pH effect on viscosity of slurry were examined. Three different pH were tried and optimum pH was found for the slurry. For the slurries, firstly binder and water were mixed and then dispersant and powders were added and finally NaOH was added. Finally, first two slurries were poured to the glass tubes, sedimentation rate measured. Then, second three slurries were measured the viscosity.

3. Results and Discussion

According to the results, binder type have effect on the sedimentation rate. The slurry with added methylcellulose provided better stability than without methylcellulose (see Figure 1). Because methylcellulose has longer molecular chain and this property inhibits sedimentation of the powders. pH is important parameter for the slurry [2]. Three different pH were tried. They were 9,33, 11 and 12,25 respectively. The highest viscosity was at 9,33 pH and the lowest viscosity was 12,25 pH (see Figure 2).

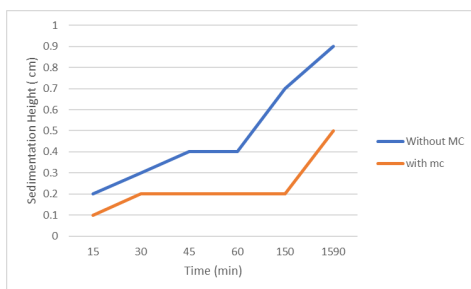


Figure 1. Sedimentation rate

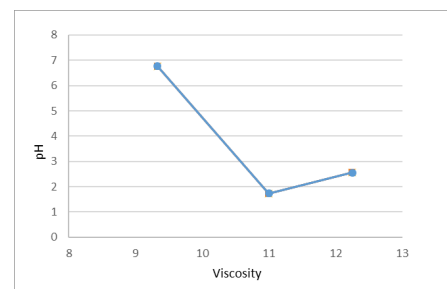


Figure 2. Viscosity versus pH

4. Conclusions

Binder type and pH are important parameters for the slurry. For the stable slurry optimum pH and binder type must be found.

References

- [1] J. Lario, et al. (2019) Corrosion behaviour of Ti6Al4V ELI nanotubes for biomedical applications. - ScienceDirect?. Journal of Materials Research and Technology, 8 (6), 5548-5556.
- [2] J. P. Li, et al. (2004). Factors having influence on the rheological properties of Ti6Al4V slurry. Journal of Materials Science: Materials in Medicine, 15, 951-958.

SURFACE INVESTIGATION OF ANTIBACTERIAL COPPER-INCORPORATED BIOACTIVE SURFACES FABRICATED ON COMMERCIAL PURE TITANIUM

Salim Levent AKTUĞ¹, Kemal KORKMAZ¹, Sıtkı AKTAŞ², Salih DURDU²

¹Gebze Technical University, ²Giresun University
Türkiye

Keywords: Micro-arc oxidation (MAO); Thermal evaporation (TE); Bioceramic coatings.

Abstract

In this study, as a first step, a copper (Cu) thin film layer was deposited on cp-Ti (Grade-2) by thermal evaporation-physical vapor deposition (TE-PVD). And then, the Cu-based titanium surface was coated by micro-arc oxidation (MAO). The phase structure, surface morphology, elemental composition, functional groups, wettability and surface topography of both coatings were characterized by XRD, SEM, EDS-mapping, contact angle goniometer, ATR-FTIR and surface profilometer, respectively. The XRD results indicated that anatase and rutile were detected on the surface after MAO and TE+MAO. Both coatings' surfaces were rough and porous due to plasma chemical reactions on micro discharge channels. The Cu-incorporated MAO coating exhibited much more hydrophilic character than MAO coating, and the Cu was homogeneously distributed through the surface.

2. Materials and methods

The rectangular cp-Ti (Grade-2) substrates with the sizes of 65 mm x 25 mm x 5 mm were prepared for the coating processes by water jet device. A copper (Cu) thin film layer was deposited on the cp-Ti surface at a base pressure of 3×10^{-5} mbar at room temperature by the TE-PVD process (Vaksis PVD/2T) in a vacuum evaporation system. In order to measure the average thickness of Cu film with about 20 nm, XTM integrated to TE device was run. Afterward, the Cu vapor products were deposited onto cp-Ti surfaces. In order to provide reproducibility, three Cu layers were deposited on three cp-Ti surfaces by the same PVD-TE parameters as written above.

An AC MAO system (MDO-100WS could be run up to 100 kW) was used to coat oxide structures on cp-Ti and Ag deposited Ti. The alkaline electrolyte was prepared by sodium silicate and potassium hydroxide in distilled water. The MAO process was carried out at 0.260 A/cm^2 for 15 min.

The phase structures of all coatings were analyzed by XRD (X-ray diffractometer, Bruker D8 Advance) with $\text{Cu-K}\alpha$ radiation at a scanning speed of $0.1^\circ \text{ min}^{-1}$ from 20° to 90° . The surface morphologies and the elemental amount of the coatings were examined by SEM (Scanning electron microscope, Philips XL30S FEG) and EDS (Energy dispersive spectrometer) attached to the SEM, respectively. The wettability and average contact angles of both surfaces were evaluated by using CAG (Contact Angle Goniometer, Dataphysics OCA 15EC) sessile drop technique at room temperature.

3. Results and discussion

The phase structures of the MAO and Cu-incorporated MAO coatings formed on cp-Ti metallic titanium, anatase- TiO_2 and rutile- TiO_2 on both surfaces were detected by XRD.

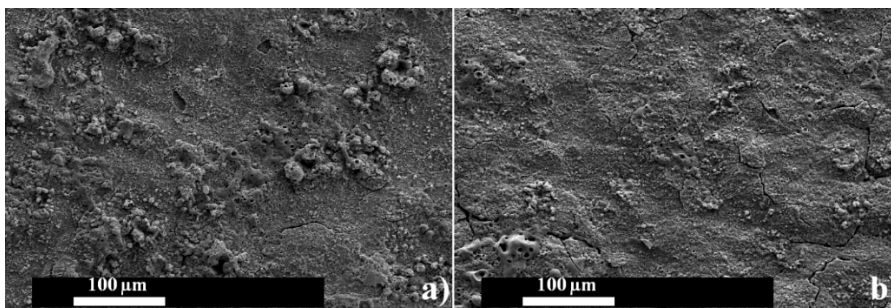


Figure 1. The surface morphology of the MAO and Cu-incorporated MAO coatings

As seen in Fig. 1, the surface morphologies of both coatings are completely different from each other, whereas they are fabricated on cp-Ti and nano-Cu coated cp-Ti substrates. The surface of Cu-incorporated MAO is more homogeneous than the one of the MAO. The MAO coatings that contain local micro-crater structures up to $20 \mu\text{m}$ have non-homogeneous surface structures. However, the micro-pores are well separated over the Cu-incorporated Ti surface.

ANTIMICROBIAL PROPERTIES OF ELECTROSPUN NANO-SIZED Ag AND TiO₂ BLENDED PVA NANOFIBERS

Merve OCAKTAN¹, Fatih ÇİFTÇİ², Nilüfer EVCİMEN DUYGULU¹

¹Yildiz Technical University, ²Fatih Sultan Mehmet Vakif University
Türkiye

Keywords: Electrospinning, PVA, Ag, TiO₂, Nanofiber, Antimicrobial

Abstract

In the present study, the effect of concentration and electrospinning parameter variations on poly (vinyl alcohol) (PVA) nanofibers was investigated. The diameters and morphological properties of the obtained nanofibers were determined using scanning electron microscopy (SEM), and the average fiber size was measured with the Image J program. The optimum PVA nanofiber production conditions were determined as 425.30 ± 58.59 nm, for %10 wt./v concentrations at 0.5 ml/h and 9kV. Nano-sized silver (Ag) and titanium oxide (TiO₂) were blended into PVA solution with different concentrations and electrospun at optimum conditions. Additionally, the antimicrobial attitude of Ag and TiO₂ blended PVA nanofibers was analyzed by using the agar disc diffusion method, and antimicrobial activity against gram – (Escherichia coli; ATCC 25922) and gram + (Staphylococcus aureus; ATCC 25923) was observed.

1. Introduction

Electrospinning is one of the electrohydrodynamic methods used to achieve enhanced nanofibers quality at a low cost. These nanofibers can be assembled as membranes and can be used in various potential applications such as biomedical, sensors, energy, and so on. [1] Especially, in biomedical and biocompatible fields, PVA is one of the preferable polymers due to its biocompatible, biodegradable, non-toxic, and hydrophilic behavior. [2] Blending PVA polymer with nanoparticles provides an improvement in the functionality of fibers. Among these nanoparticles TiO₂; oxidizer, photoactive, biocompatible,[3] and Ag; antibacterial, electrically resistive are preferable ones. [4]

2. Materials and Methods

The production steps of PVA and doped nanofibers are given in Fig.1. Both the PVA and nanoparticle doped solution preparations were stirred by using magnetic string. The physical properties of the solutions are given in Table 1.

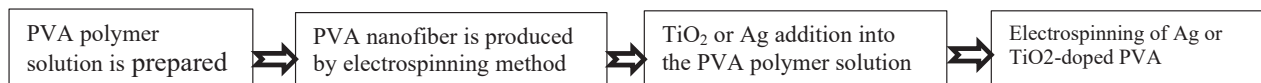


Figure 1. Production steps of PVA and nanoparticle doped nanofibers.

The nanofibers were obtained at 9 kV voltage and 0.5 ml flow rate the morphologic observations with the histogram are shown in Fig.2 Figure 3 shows photographs of agar plates grown with S. Aureus (ATCC 25923) treated with E. coli (ATCC 25922), TiO₂ blended PVA, Ag blended PVA and PVA control samples.

Table 1. Physical properties; conductivity, pH and viscosity variations of polymer solutions.

	PVA	TiO ₂ Blended PVA	Ag Blended PVA
Conductivity (μS)	440	517.25	486
pH	7.77	6.995	7.0175
Viscosity(Cp)	44.85	63.5	42.98

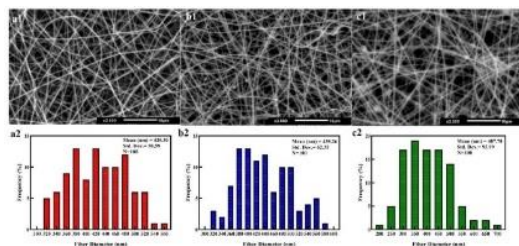


Figure 2. SEM images of PVA, TiO₂ and Ag blended PVA electrospun nanofibers and fiber

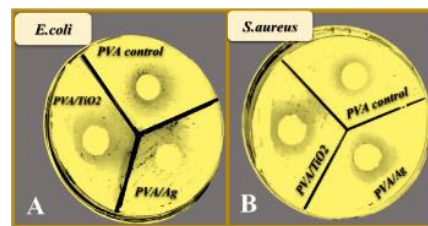


Figure 3. Antibacterial Analysis Test Results

3. Conclusion

For %10 PVA concentrations electrospun at optimum conditions; 9 kV voltage, 0.5 ml/h flow rate has been detected. The fiber size was measured as 425.30 ± 58.59 nm. For %1 TiO₂ blended PVA fiber size was 439.26 ± 62.35 nm and for %1 Ag blended PVA fiber size was measured as 407.70 ± 95.99 nm. The bacteria were incubated in a growth medium with the pure PVA and the composites. This result shows the usability of nanoparticle TiO₂ doped PVA nanofiber work in biomedical applications.

Acknowledgment

This work has been supported by Yildiz Technical University Scientific Research Projects Coordination Unit under project number # FYL-2022-5221..

References

- [1] J. Nathanael I, Encapsulation of Calcium Phosphates on Electrospun Nanofibers for Tissue Engineering Applications ,2021
- [2] M. Singh, D. Chauhan, A. K. Das, Z. Iqbal, and P. R. Solanki, PVA/PMMA polymer blended composite electrospun nanofibers mat and their potential use as an anti-biofilm product, J. Appl. Polym. Sci., 2021
- [3] N.Evcimen Duygulu, Production of Nano Sized TiO₂ Blended PLA Nano Fiber with Electrospinning Method,2019
- [4] Y. J. He, "Powder Technol. " 147 ,2004 Wang, Xue Ping, Li, Wei Dong,2012, Nanofibers: Synthesis, Properties

A GREEN MANUFACTURING METHOD IN SKIN TISSUE ENGINEERING

Merve SIRTİKARA, Emir ERIŞÇİ, Sevda Nur TEBERDAR, Mustafa ŞENGÖR

Marmara University
Türkiye

Keywords: Scaffold, 3D Printing, Freeze-dry, Skin Tissue, Biomaterial

Abstract

In this study, sodium caseinate/gelatin-based scaffolds were fabricated and crosslinked with microbial transglutaminase (mTg) (4% w/w). Sodium caseinate (NaC) was mixed at a concentration of %16 (w/w) inside deionized water. The dynamics of enzymatic cross-linking activity was evaluated with different concentrations of sodium caseinate. Apart from many other enzymes, microbial transglutaminase has the ability to be active even below freezing temperatures. By keeping it at -59°C for 24 hours, the enzymes were still active to complete the post-crosslinking process. Cell activity and characterization tests were conducted and it was observed that these scaffolds could have very promising applications in skin tissue engineering.

1. Introduction

The skin is one of the biggest features that protects the body from various environmental conditions. It can deteriorate due to various reasons such as infections, armed conflicts, chemicals and medical operations. Sponge dressings, on the other hand, create an environment where cells can adhere and proliferate thanks to their high porous structures. Hydrogels are three-dimensional cross-linked networks of water-soluble polymers that have many of the desirable properties of an ideal wound dressing. Enzymatically crosslinked hydrogels can provide useful systems for tissue engineering applications due to their flexible nature, green cross-linking conditions, low cytotoxicity, and having mechanical properties similar to natural tissues.

2. Materials and Methods

The first solution was prepared with 16% (wt.) NaC addition inside de-ionized water. The solution was stirred in a sealed glass for 4 hours at $50 \pm 5^{\circ}\text{C}$. After 4 hours, 4% (wt.) mTG was added to the solution and the final solution was obtained by mixing in the same sealed glass for 2 hours. Prepared hydrogels were then gently poured into 3D printed cylindrical molds (10x40 mm) and rectangular molds (10x45x5 mm) to test their compression and tensile mechanical performances, respectively, followed by crosslinking by keeping at room temperature for 4 hours. Samples that were molded and kept for 4 hours were frozen at -20°C for 12 hours. For the freeze-dry process, the freeze-drier was set to sublimation at -59°C . The samples, which were kept in freeze-dry for 24 hours, were kept for 24 hours in an environment saturated with water vapor at 37°C for secondary crosslinking reaction.

3. Conclusions

There is a dramatic difference between the double-stage and single-stage crosslinking methods in terms of the mechanical, physical, and chemical properties of the scaffolds. Morphology of the cells seeded on the scaffold and mechanical test performances can be observed in Fig.1.

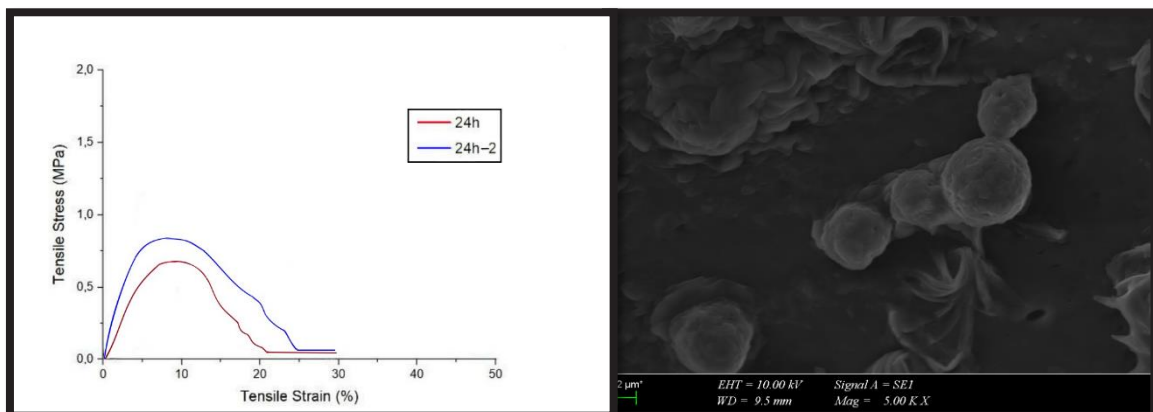


Figure 1: Morphology of the cells seeded on the scaffold and mechanical test performances



NMS

Nanomaterials Symposium

Nanomalzemeler
Sempozyumu

PRODUCTION OF NANO STRONTIUM HEXAFERRITE BY SOLUTION COMBUSTION SYNTHESIS

Ceren ÇALIŞKAN, Raşit SEZER

Karadeniz Technical University
Türkiye

Keywords: Strontium hexaferrite, permanent magnets, solution combustion synthesis

Abstract

In this study, we produced strontium hexaferrite magnets with different metal doped via solution combustion synthesis technique using strontium nitrate ($\text{Sr}(\text{NO}_3)_2$), iron (III) nitrate ($\text{Fe}(\text{NO}_3)_3$) and citric acid ($\text{C}_6\text{H}_8\text{O}_7$). Calcium nitrate tetrahydrate ($\text{Ca}(\text{NO}_3)_2 \cdot 4\text{H}_2\text{O}$), chromium (III) nitrate nonahydrate ($\text{Cr}(\text{NO}_3)_3 \cdot 9\text{H}_2\text{O}$) and manganese (II) nitrate tetrahydrate ($\text{Mn}(\text{NO}_3)_2 \cdot 4\text{H}_2\text{O}$) were used as additives in the production of doped magnets. Magnets produced during the studies were annealed at different temperatures and various analyzes were made. X-Ray Diffraction (XRD) was used to determine the phases in strontium hexaferrite ($\text{SrFe}_{12}\text{O}_{19}$), Master Sizer analysis to determine grain sizes, and Fourier Transform Infrared Spectrometer (FTIR) analysis to determine chemical bonds

1. Introduction

Magnetism has been known since ancient times and has attracted the attention of mankind. The present decades have witnessed the enormous expansion of magnetic applications. Over the course of the century, science, which developed especially in Europe, became available for use in the industrialized world. Advances in permanent magnetization, magnetic recording, and high-frequency materials form the basis for advances in computers, communications equipment, and consumer products that most people around the world enjoy. Permanent magnets are back to replace the electromagnets found in the one billion small motors produced each year. Magnetic storage is driving the information revolution and the internet. Groundbreaking advances in geology, medical imaging, and the theory of phase transformations can be attributed to magnetism.

The general formula of ferrite (ceramic) permanent magnets is $\text{M}_0.6\text{Fe}_2\text{O}_3$. Here M can be barium, strontium, or a combination of both [1]. M-type strontium hexaferrites were discovered in Philips laboratories in the 1950s. It is offered under the trade

name Ferroxdure. Soon after, the compound was developed and started to be used in permanent magnet applications by using strontium instead of barium. It attracts a lot of attention compared to rare earth compounds with its favorable magnetic properties, chemical stability and low cost [2]. Strontium ferrites are widely used as permanent magnets due to their abundant raw materials and low production costs [3]. However, the magnetic characteristics of these magnets may differ from this standard on the basis of manufacturers. Generally, tolerances for magnetic properties of magnetic materials according to manufacturers; residual flux density is $\pm 5\%$ for B_r , coercive force is $\pm 8\%$ for H_c , energy production $(\text{BH})_{\text{max}}$ is $\pm 10\%$. In MMPA standards, materials have MMPA abbreviation according to their maximum normal energy production and intrinsic coercive forces. In this system, the short designation of a material with a maximum normal energy production of 5.0 megagauss-oersted (MGO) and an intrinsic coercive force of 2000 Oersted (2 kO_c) is 5.01/2.0. Most permanent magnets lack ductility and are inherently brittle. For this reason, the measurement of properties such as hardness and tensile strength is not applicable. The physical properties of hard ferrite magnets are shown in Table 1 [1].

Table-2: Physical properties of hard ferrite magnets [1].

Characteristic	Value
Density	4,9 gr/cm ³
Vertical to orientation	10x10 ⁻⁶ cm/cm.°C
parallel to orientation	14x10 ⁻⁶ cm/cm.°C
thermal conductivity	0,029 Wb/cm.°C
Electrical resistance	106 ohm.cm
Porosity	5%
Elastic module	1,8x10 ¹¹ Pa
Poisson's ratio	0,28
Compression resistance	895x10 ⁶ Pa
Tensile strength	34 x10 ⁶ Pa
Bending strength	62 x10 ⁶ Pa
Hardness (Mohs)	7

Combustion synthesis (CS) is an important technique that can be used in the production of advanced ceramics, catalysts, composites, alloys, intermetallic compounds and nanomaterials. CS, which is an exothermic redox reaction, is divided into sub-branches such as high temperature synthesis, low temperature combustion synthesis or solution combustion synthesis, according to the nature of the reacting materials (solid, liquid, gas) and flame temperature. SCS, which is included in the combustion syntheses, was found by chance as a result of the reaction between aluminum nitrate, NH_4NO_3 and urea, $\text{CH}_4\text{N}_2\text{O}$, about 30 years ago and has become a very preferred position due to its superiority over other methods [4-5]. SCS is a very simple, fast and low-cost method compared to other methods that produce nano-sized materials, and it is a prominent method in terms of producing homogeneous and pure metal oxides. It is an exothermic reaction that progresses spontaneously by heating the homogeneous mixture of the oxidizer and fuel in the solution environment in suitable proportions to the initial temperature (150-300°C).

2. Experimental Procedure

In this study, calcium, chromium and manganese are added to strontium hexaferrite magnets separately. By doping, 3 different magnet powders were obtained.

2.1. Production Method

Produced strontium hexaferrite powders were produced by solution combustion synthesis. The production flow is shown in figure 1.

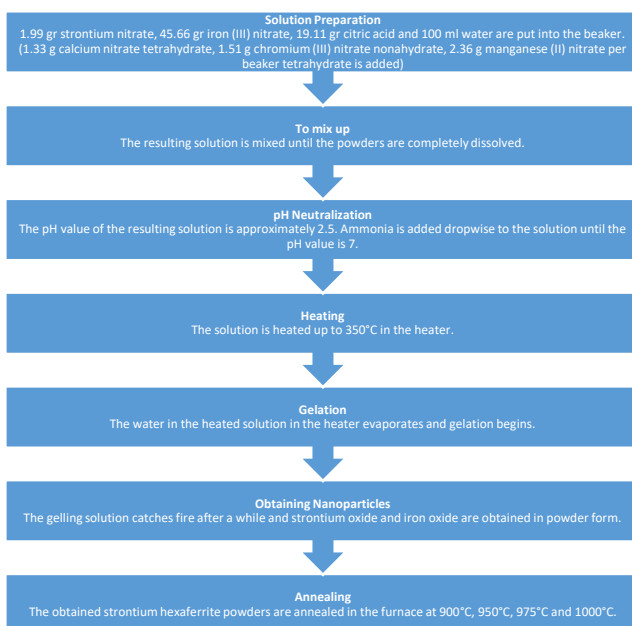


Figure-1: Production scheme of strontium hexaferrite.

To produce 10 g of strontium hexaferrite, 1.99 g of strontium nitrate, 45.66 g of iron (III) nitrate, 19.11 g of citric acid were used. To provide calcium, chromium and manganese additives, 1.33 g calcium nitrate tetrahydrate, 1.51 g chromium (III) nitrate nonahydrate, 2.36 g manganese (II) nitrate tetrahydrate were used.

100 ml of distilled water was put into each beaker. Then, strontium nitrate, iron (III) nitrate were added to beakers, respectively, and calcium nitrate tetrahydrate, chromium (III) nitrate nonahydrate and manganese (II) nitrate tetrahydrate were added to each beaker separately. At this stage, the color of the solution began to darken due to the iron.

After adding 19.11 g of citric acid as fuel into the beakers, it was mixed with magnetic fish and mixing continued until the added powders were completely dissolved. The pH values of the solutions obtained after the mixing process was completed were approximately 2.5. To neutralize these solutions, ammonia was added dropwise with a micro pipette. 35.5 ml of ammonia was used for calcium added solution, 40.5 ml for chromium added solution and 41 ml for manganese added solution. After these processes, the magnetic fish in the beakers were removed and the beakers were placed in the heater. The water in the solutions heated up to 350°C in the heater started to evaporate and gelation took place after a while. As a result of these processes, combustion occurred and strontium hexaferrite (with added calcium, chromium and manganese) and iron oxide in powder form were obtained. The obtained strontium hexaferrite powders were annealed in the furnace at 900°C, 950°C, 975°C and 1000°C.

3. Results and Discussion

At this stage of the study, X-Ray Diffraction (XRD) Analysis, Grain Size (Master Sizer) Analysis and Fourier Transform Infrared Spectrometer (FTIR) Analysis were performed.

3.1. X-Ray Diffraction (XRD) Analysis

X-Ray Diffraction (XRD) analysis was performed for the determination of phases in strontium hexaferrite ($\text{SrFe}_{12}\text{O}_{19}$). The phases found as a result of this analysis are shown in figure 2.

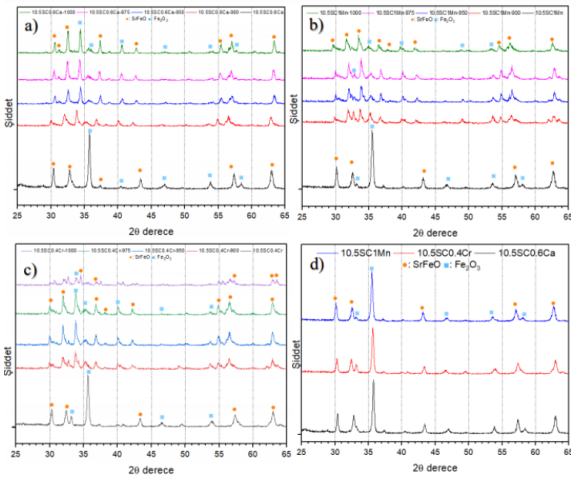


Figure-2: XRD patterns of magnets; (a) Ca, (b) Mn and (c) Cr doped, annealed at different temperatures and (d) non-annealed.

As can be seen from the graph (Figure 2), hematite and strontium oxide phases are observed in doped strontium hexaferrites. It is observed that the intensity of some hematite phases decreases with the increase in temperature. Although calcium, manganese and chromium are added to strontium hexaferrite, there is no peak on the calcium, chromium and manganese phases in the XRD graph. The reason for this is that the ratios of Ca, Cr and Mn are quite low in the compound.

In Figure 2 (d), the XRD graph of Mn, Cr and Ca calcium doped strontium hexaferrites ($\text{SrFe}_{12}\text{O}_{19}$) at room temperature, which has not been subjected to any annealing process, is given. Hematite and strontium oxide phases are seen in all three powders.

3.2. Grain Size (Master Sizer) Analysis

Master Sizer analysis was performed to determine the particle size of the produced strontium hexaferrite ($\text{SrFe}_{12}\text{O}_{19}$) powders. As a result of this analysis, the average grain sizes (d50) are given in figure 3.

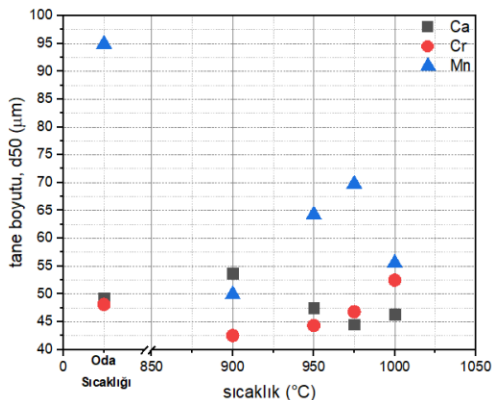


Figure 3: Grain size (Master Sizer) analysis of strontium hexaferrite ($\text{SrFe}_{12}\text{O}_{19}$) doped with Ca, Cr and Mn and annealed at different temperatures.

Table 2: Grain sizes of calcium doped strontium hexaferrite annealed at room temperature and at different temperatures

	Calcium Added				
	At room temperature	Annealed at 900 °C	Annealed at 950 °C	Annealed at 975 °C	Annealed at 1000 °C
d10	16,430 μm	16,928 μm	15,924 μm	15,812 μm	16,676 μm
d50	49,236 μm	53,695 μm	47,514 μm	44,559 μm	46,379 μm
d90	99,623 μm	112,332 μm	100,016 μm	89,529 μm	91,901 μm

Table 3: Grain sizes of chromium doped strontium hexaferrite annealed at room temperature and at different temperatures

	Chromium Added				
	At room temperature	Annealed at 900 °C	Annealed at 950 °C	Annealed at 975 °C	Annealed at 1000 °C
d10	16,912 μm	13,549 μm	16,926 μm	17,251 μm	17,374 μm
d50	48,115 μm	42,537 μm	44,334 μm	46,808 μm	52,487 μm
d90	48,115 μm	82,242 μm	85,358 μm	93,335 μm	125,255 μm

Table 4: Grain sizes of chromium doped manganese hexaferrite annealed at room temperature and at different temperatures

	Manganese Added				
	At room temperature	Annealed at 900 °C	Annealed at 950 °C	Annealed at 975 °C	Annealed at 1000 °C
d10	35,736 μm	17,712 μm	20,989 μm	22,645 μm	18,917 μm
d50	94,903 μm	49,918 μm	64,249 μm	69,752 μm	55,559 μm
d90	198,630 μm	102,477 μm	133,110 μm	148,712 μm	114,533 μm

As can be seen in Figure 3, with the increase in temperature in all three powders with Ca, Cr and Mn additives, the grain size decreases first and then growth occurs. However, this observed grain reduction is not a predictable situation. Since the grains will become larger as the annealing temperature increases under normal conditions, it is not expected that these powders will decrease in grain size with the increase in temperature. As seen in the XRD graphs (Figure 3), no amorphous structure was formed in any of the strontium hexaferrite ($\text{SrFe}_{12}\text{O}_{19}$) powders. Therefore, it is seen

that no glassy phase is formed by melting in the annealing processes. It is possible to say that the grain shrinkage seen in Figure 3 with the increase in temperature is due to measurement errors.

3.3. Fourier Transform Infrared Spectrometer (FTIR) Analysis

Fourier Transform Infrared Spectrometer (FTIR) analysis was performed for the determination of chemical bonds in strontium hexaferrite (SrFe₁₂O₁₉). The chemical bonds found as a result of this analysis are shown in Figure 4.

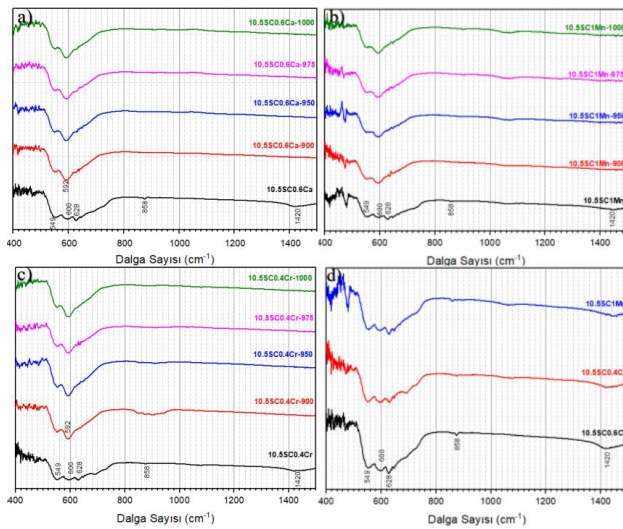


Figure 4: Fourier Transform Infrared Spectrometer (FTIR) analysis of strontium hexaferrite (SrFe₁₂O₁₉) doped with Ca, Cr and Mn and annealed at different temperatures.

These graphs represent the characteristic peak of 549 cm⁻¹ strontium hexaferrite. It is also seen that there is no change in this peak with the increase in temperature. Uptake of hematite (Fe₂O₃) instead of magnetite (Fe₃O₄) is indicated by absorption bands at 600 cm⁻¹. Due to the acceleration of this uptake with the increase in temperature, this peak, which is at 592 cm⁻¹ at room temperature, occurs at 549 cm⁻¹ when strontium hexaferrite begins to anneal. Well-established absorption bands at 549 cm⁻¹ indicate the formation of strontium ferrite. 858 cm⁻¹ is attributed to SrCO₃, which appears to be a transitional phase before the formation of strontium ferrite. Since SrCO₃ decomposes with the increase in temperature, this peak is not observed in the annealed samples. The peak at 1420 cm⁻¹ refers to magnetite (Fe₃O₄). This peak is not seen in the annealed samples since magnetite will turn into hematite with the increase in temperature. These results are in agreement with the XRD results (Figure 4).

4. Conclusion

Calcium, chromium and manganese additives were made separately to the strontium hexaferrite powders produced by solution combustion synthesis. These powders were then annealed at different temperatures. It is observed that with the increase in annealing temperature, some hematite phases in the structure disappear, that is, the hematite phase undergoes complete transformation (Figure 2). In addition, it is expected that the grain sizes will increase with the increase in the annealing temperature, but this growth is not observed at every annealing temperature due to some measurement errors (such as insufficient grinding of the samples, placing too many samples in the device to be measured, inhomogeneity of the sample placed) (Figure 3). Again, as the magnetite turns into hematite in the FTIR graph as a result of the increase in annealing temperature, this peak is not seen in the annealed samples (Figure 4). All results obtained are consistent.

References

- [1]. MMPA Standard No: 0100-00, 1964 Standart specifications for permanent magnet materials, Magnetic Materials Producers Association, Chicago
- [2] Zi Z. F., et al., 2008, "Structural and magnetic properties of SrFe₁₂O₁₉ hexaferrite synthesized by a modified chemical co-precipitation method," Journal of Magnetism and Magnetic Materials, vol. 320, pp. 2746-2751
- [3] Wang, Y. F. et al., 2009, "Preparation and magnetic properties of different morphology nano-SrFe₁₂O₁₉ particles prepared by sol-gel method," Journal of Alloys and Compounds, vol. 467, pp. 284-287.
- [4] Alves, K. A., Bergmann, C. P., Berutti, F. A., (2013) Chapter 2 Combustion Synthesis, Novel synthesis and characterization of nanostructured materials, Berlin Heidelberg, (11-22).
- [5] Patil, K. C., Aruna, S. T., Mimani, T. (2002). Combustion synthesis: an update, Current Opinion in Solid State and Materials Science, 6(6), (507-512).

PHASE ENGINEERING OF SEMICONDUCTOR NANOSCALE MATERIALS

Selim DEMİRCİ, Mehmet Masun TÜNÇAY

Marmara University
Türkiye

Keywords: TiO₂, Phase Transformation, Thermal Expansion, Phase Fraction, Phase Engineering.

Abstract

It is well known that phase structures and their fractions for nanoscale materials affect the efficiency of output in different application areas in a positive way. Therefore, the utilization of materials with different phases and their fractions together is very intense. Intensive studies are carried out to produce hybrid structures with different phases and/or fractions in order to boost nanoscale materials application. In this context, the adjustment and calculation of phase transformation and ratios by applying the thermal expansion method for powder materials has been evaluated. The results obtained from thermal expansion method were compared with the results of XRD technique in order to confirm. The results showed that the adjustment of phase fractions might be performed during the process without using XRD.

1. Introduction

The physical and chemical properties of nanoscale semiconductor materials are greatly dependent on the crystal phase structures in energy and environmental applications. The design and construction of crystal phase structure of nanoscale semiconductor materials is the key how to enhance the performance of semiconductors in energy and environmental applications [1]. The rational design and construction of crystal phase structure of nanoscale semiconductors stimulate the harvesting of the light, separation charge transfer and adsorption and activation of reactant molecules [2]. The junction structures composed by semiconductors with similar or the same lattice structures are most favorable due to the little lattice mismatching and continuity of chemical bonding, therefore homojunctions are the most desirable [3]. Dilatometer is one of the method to determine phase fraction for materials. When transforming from one phase to another phase, changes occur in the thermal expansion curves. Thanks to this change, the ratios of the phases can be determined [4]. In this context, the adjustment and calculation of phase transformation and ratios by applying the thermal expansion method for powder materials has been evaluated.

2. Experimental Section

Anatase TiO₂ nanopowders (99.55%) were obtained. (Nanografi, Turkey). The particle size of powders was 38 nm. Then, the powders were

pressed forming pellets with a uniaxial press at 150 MPa. The dimensions of the prepared pellets were 10 mm in diameter and 2.5 mm in height. Finally, the prepared pellets were sintered at 750 °C for 10 h with a ramp rate 5 °C/min. After that, the pellets were placed dilatometry machine. High temperature horizontal push-rod type dilatometer was used. The dilatometry measurements were carried out by dilatometer (NETZSCH DIL 402C). The dilatometric phase transformation of the pellets was measured as a function of temperature up to 1300 °C at heating rates of 10 °C/min under air atmosphere. Phase identification and crystal structures of the samples were performed by X-ray diffractometer (XRD, Rigaku ULTIMA 3-Rint 2200/PC).

3. Result and Discussion

Fig. 1 showed the image of sintered pellet in dilatometry machine. As seen in Fig. 1, the sintered sample was transferred to furnace of dilatometry machine and alumina push rod was adjusted to touch the sintered sample.



Fig. 1. The images of sintered pellet and dilatometry machine.

Fig. 2 exhibited the shrinkage curve of sintered pellet. As seen in Fig. 2, firstly, there was an abrupt drop in thermal expansion curve which was related to sintering process of pellet because of by the compaction behavior after approximately 800 °C. Secondly, a linear thermal expansion was observed between around 900 and 1100 °C. This linear thermal expansion was regarding the phase transition of TiO₂ from anatase to rutile. Thirdly, the compaction of pellet still continued after at around 1100 °C. The lever rule is usually used to

compute the phase fraction from the dilatometry curves as seen in Fig. 2.

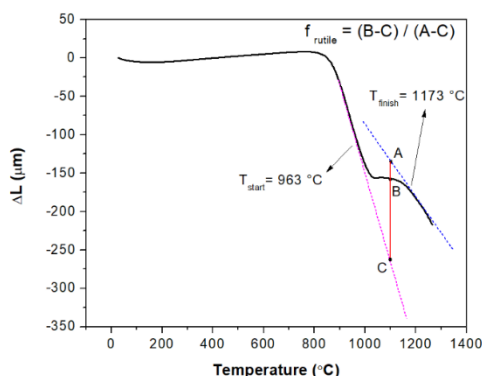


Fig. 2. Dilatometer shrinkage curve and lever rule for phase fraction calculation.

The principle of the method is described in Fig. 2. Two linear segments of a dilatometric curve are first extrapolated. Then, the phase fraction of the formation phase at a given temperature (T) is evaluated by the difference of the measured dilatometric curve between these two extrapolated lines. The authors point out that due to its nature, the lever rule method does not enable an accurate estimation of the phase content in the boundaries of the dual phase domain (i.e. from 0 to 10% and from 90 to 100% of phase) [5]. Based on the extrapolation curves, the starting and ending temperature from anatase to rutile transformation were determined to be 963 and 1173 °C, respectively. Rutile phase fractions were calculated with the applying lever rule at 970 and 1100 °C as shown in Eq.1 and 2.

Determination of the rutile phase fraction for 970 °C:

$$f_{rutile} = \frac{-109.591 - (-113.984)}{-73 - (-113.984)} = 0.107 \rightarrow 10.7\% \quad \text{Eq.1}$$

Determination of the rutile phase fraction for 1100 °C:

$$f_{rutile} = \frac{-156.539 - (-260.605)}{-135.044 - (-260.605)} = 0.828 \rightarrow 82.8\% \quad \text{Eq.2}$$

The phase fractions of rutile obtained from dilatometry curve are good agreement with XRD results. XRD patterns of the anatase TiO₂ nanopowders after annealing process at the certain temperature according to the dilatometry curve were revealed. As seen in Fig. 3, the formation of high crystalline TiO₂ phases occurred after the annealing. The Fig. 3(a) belonged to the untreated anatase TiO₂ nanopowders. As expected, only anatase phase was detected in Fig. 3(a). Fig. 3(b) corresponded to TiO₂ nanopowders that were annealed at 970 °C. According to Rietveld analysis performed by MAUD (Materials Analysis Using Diffraction) program in Fig. 3(b), the weight

fractions of anatase and rutile TiO₂ phases were calculated to be 95.95 % and 4.05 %, respectively. Fig. 3(c) matched the TiO₂ nanopowders that were annealed at 1100 °C. The weight fractions of anatase and rutile TiO₂ phases were found to be 89.65 % and 10.35 %, respectively.

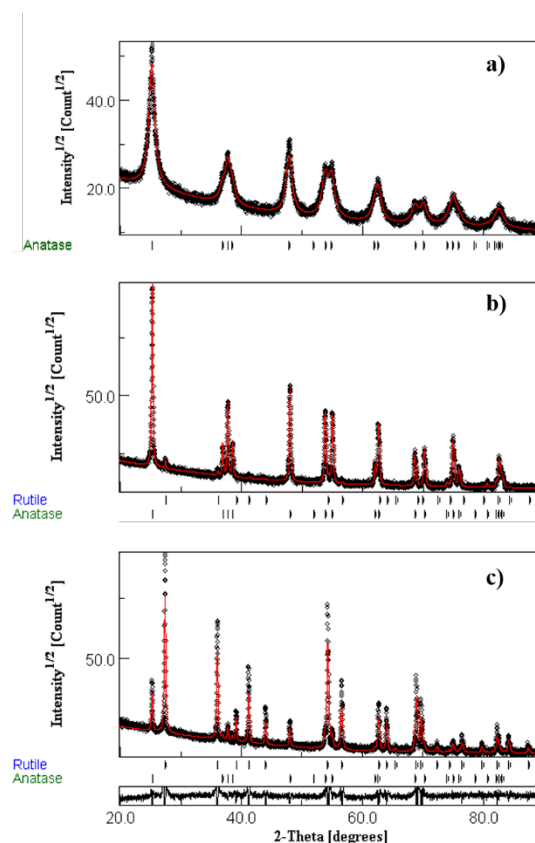


Fig. 3. XRD and Rietveld analysis of TiO₂ nanopowders.

As seen in Fig. 3(b) and (c), the weight fraction of phases are very close to the fractions which were determined by lever rule depending on thermal expansion curve in dilatometry machine. The shift between the determined value can be acceptable. Because, some energy needing for transformation was consumed in sintering process for pellet sample. It can be deduced that thermal expansion curve can be used to adjust phase fraction of samples.

4. Conclusion

In this present work, TiO₂ nanopowders were purchased to study whether the phase fraction can be adjusted by thermal expansion curve in dilatometric analysis. The results showed that the phase fraction based on dilatometric analysis could fit well to XRD analysis at the sample temperature.



References

- [1] S. Wang, C. Huang, L. Pan, Y. Chen, X. Zhang, F. Aleem and J. Zou, *Catalysis Today*, 335 (2019) 151-159.
- [2] S. Bai, C. Gao, J. Low, and Y. Xiong, *Nano Research*, 12 (2019) 2031-2054.
- [3] L. Pan, J. Zou, S. Wang, Z. Huang, X. Zhang, L. Wang, *Appl. Sur. Sci.* 268 (2013) 252–258.
- [4] T. Liu, M. Long, H. Fan, D. Chen, H. Chen, H. Duan, W. Jiang and W. He, *J. Mater. Res.*, 33 (2018) 967-977.
- [5] T. Jailin, N. Tardif, J. Desquines, M. Coret, M.-C. Baiuto, V. Georghum, *Materials Characterization*, 162 (2020) 110199.

EFFECT OF STARTING COMPOSITION ON THE MORPHOLOGY OF SOL-GEL SYNTHESIZED BORON CARBIDE (B₄C) PARTICLES

Selin TÜMKAYA, Suna AVCIOĞLU, Figen KAYA, Cengiz KAYA

Yıldız Technical University
Türkiye

Keywords: Boron Carbide, Sol-Gel, Carboxylic Acids, Practice Morphology

Abstract

In the present work, the effect of the starting materials and composition on the B₄C formation and its final particle morphology was investigated. The particle size and shape of boron carbide powders were tailored by controlling the polymeric network of the gel using carboxylic acids with different molecular structures. Polymeric gels were fabricated using boric acid, glycerin, mandelic acid, and tartaric acid as starting materials in different ratios. The pyrolysis process of the synthesized gels was carried out at 675 °C, followed by heat treatment on pyrolyzed processors at 1500°C for 5h in an Ar atmosphere. The results showed that the formation of fiber, rod, plate, and equiaxed boron carbide particles was observed. In addition to morphology, acids and their ratios were also found to be effective in boron carbide transformation.

1. Introduction

In recent years advanced carbide ceramics are in high demand right, especially B₄C because of its unique properties, as well as its high melting temperature, low specific weight, excellent hardness, outstanding chemical stability, and high thermal neutron absorption crosssection [1]. The following processes are widely used to synthesize boron carbide: magnesiothermic reduction, synthesis from elements, liquid-phase reactions, vapor-phase reactions, synthesis from polymer precursors, ion beam synthesis, and carbothermic reduction. As these processes require high synthesis temperatures and involve some difficulties in controlling the size, morphology, and purity of the final product, the development of low-temperature synthesis techniques has been focused on to achieve low-cost production. Accordingly, the sol-gel method is known as one of the most important techniques for production of boron carbide [1–3]. Synthesis of crystalline B₄C powder at low temperatures using organic precursors derived from boric acid (H₃BO₃) and polyols such as cellulose and glucose, citric acid, glycerin, and poly(vinyl alcohol) (PVA) has been investigated. The formation of B-O-C bonds in a gel precursor using the sol-gel process enables more homogeneous dispersion of H₃BO₃ and polyol as the boron and carbon sources, respectively [4,5].

In this work, tartaric acid and mandelic acid was used as a modifier and carbon source. The effect of the different carboxylic acid types and starting composition on the B₄C formation and its final particle morphology was investigated.

2. Experimental Procedure

2.1. Synthesis of B₄C Powders

Analytic grade boric acid (H₃BO₃), glycerin (C₃H₈O₃), tartaric acid (C₄H₆O₆) and mandelic acid (C₈H₈O₃) were used as starting materials. All chemicals were purchased from E.Merck and used without further purification. For fabrication of condensed gels, boric acid was dissolved directly in glycerin, followed by addition of tartaric acid and mandelic acid in different amounts (5% wt. and 10% wt.) into the mixture to observe the efficiency of the carboxylic acids. After the dissolution of boric acid and carboxylic acids in glycerin, the mixture was mixed continuously by a magnetic stirrer at 150 °C, where gelation has started to occur by condensation reaction. In order to investigate the effect of starting materials and composition on gel formation, gel properties, and final boron carbide powders, different carboxylic acids with different molecular structures were used. The schematic representation of the molecular structures of carboxylic acids is shown in Fig. 1.

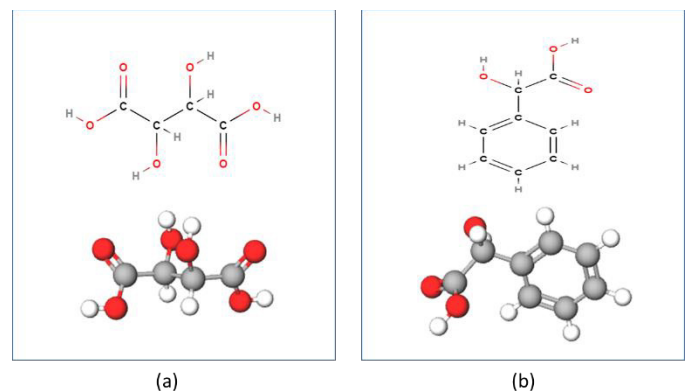


Figure 1. The schematic representation of the molecular structures of carboxylic acids; (a) tartaric acid; (b) mandelic acid

In total, four different samples were prepared in accordance with the amount of tartaric and mandelic acid additions. Sample codes and ratios were given in **Table 1**.

Table 1. Sample codes and ratios.

Sample Code	Tartaric Acid (% wt.)	Mandelic Acid (% wt.)
GT5	5	-
GT10	10	-
GMd5	-	5
GMd10	-	10

The pyrolysis process of the synthesized gels is carried out at 675 °C for 6 h. in atmospheric conditions. After pyrolysis, precursors were ground to powder form by using an agate mortar. Final heat treatment of the B₄C precursors was performed in graphite crucibles at 1500 °C for 5 h in an argon flow (500 ml/min) at a heating rate of 10 °C /min.

2.2. Characterization

In order to identify chemical bonding of condensed gels Fourier Transform infrared (FT-IR) analysis were carried out in the 400–4000 cm⁻¹ wavenumber region using a Bruker Tensor 27 spectrometer. The phase assembly of synthesized powders were established by X-ray diffraction analysis (XRD) with Cu K α radiation ($\lambda = 1.540 \text{ \AA}$) from 10° to 80° and a scanning speed of 1°/min. The morphology of the powders was characterized by scanning electron microscopy (SEM) technique. The elemental point analysis of the samples was also obtained through the EDX detector attached to SEM.

3. Results and Discussion

FT-IR spectra of condensed gel samples were shown in **Fig. 2**. The wavenumber regions where the absorption peaks of the bonds O-H, C=O, B-O, C-H, BO-H, and B-O-C are observed are consistent with previous studies [6, 7]. As can be seen, for all samples, the formation of borate ester bonds (B-O-C) was successful. The absorption peaks of borate ester bonds (B-O-C) formed by dehydration and condensation reactions were most notable at 1080 and 1020 cm⁻¹. It was observed that the borate ester (B-O-C) peak intensity seen around 1100 cm⁻¹ in both samples containing mandelic acid was higher than the samples containing tartaric acid, and the intensity (B-O-H) seen around 1130 cm⁻¹ was lower. This means that adding mandelic acid to the starting composition promotes dehydration and condensation reactions more than adding tartaric acid.

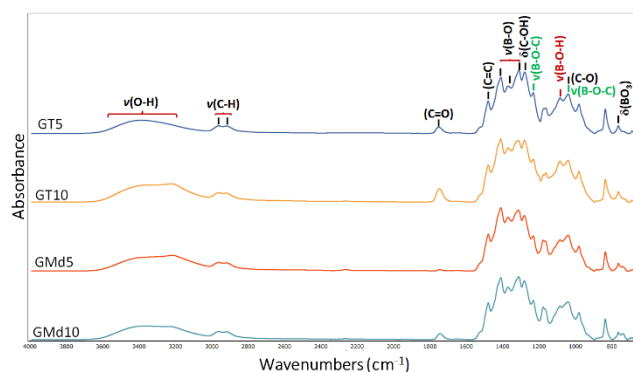


Figure 2. FT-IR spectra of condensed gels.

The X-ray diffraction patterns of the final products after heat treatment at 1500°C for 5h. in Ar flow were given in **Fig. 3**. While both samples contain approximately similar excess carbon content in the form of graphite and excess boron oxide, the sample coded GT10 contains higher excess carbon content compared to the sample coded GT5. After the washing process, it was determined that the residual boron oxide in the samples was completely removed. However, it was observed that this process did not reduce the amount of excess graphite/carbon. The XRD analysis results of the samples prepared with compositions containing 5 %wt. and 10 %wt. mandelic acid are showed that boron carbide conversion did not occur completely in both samples. By increasing the mandelic acid ratio to 10 %wt., residual boron oxide was removed, but a very high ratio of residual graphite remained in the system. The fact that the peaks of boron carbide are so low reveals the importance of the acids and their ratios used in the starting composition.

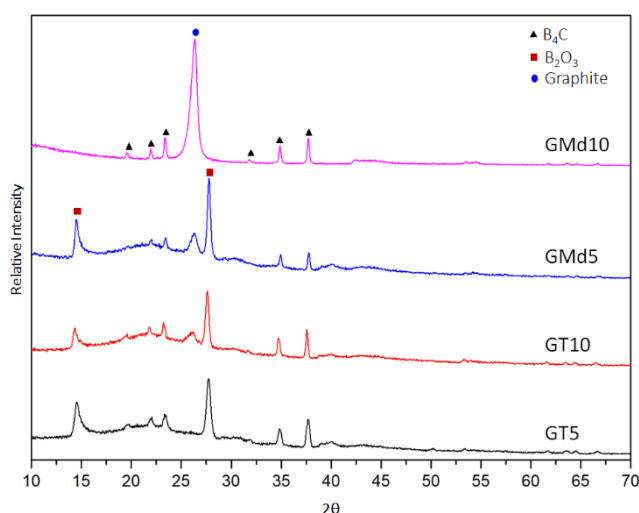


Figure 3. The X-ray diffraction patterns of the final products after heat treatment at 1500°C for 5h

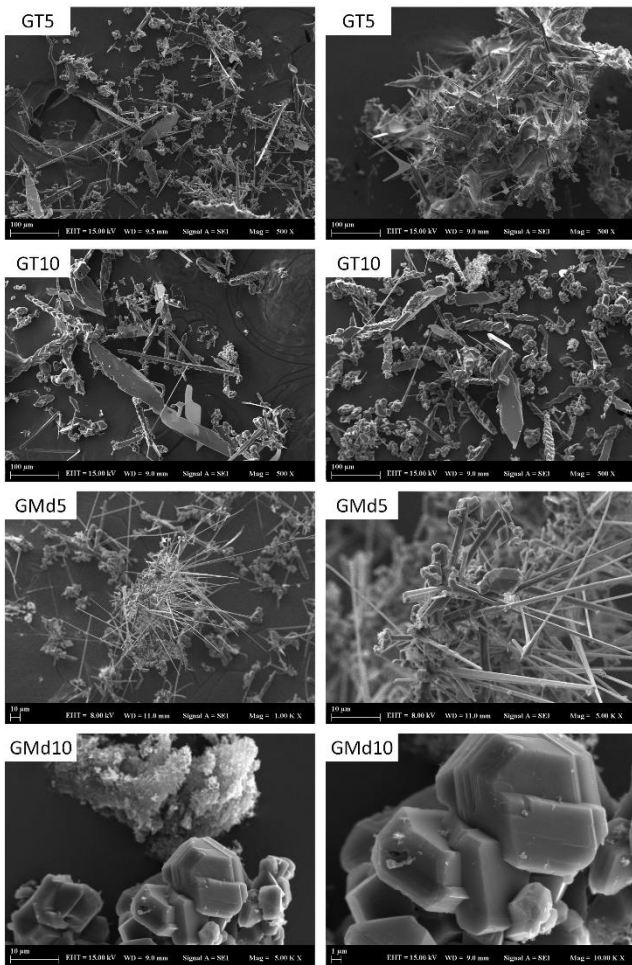


Figure 4. SEM images of the B₄C particles after heat treatment at 1500°C for 5h

The SEM images of the B₄C powders shown in **Fig. 4**. Indicates that B₄C samples consist of variety of particle morphologies. In the GT5 sample with 5 %wt. tartaric acid addition, it was observed that complex shaped and equiaxed particles were formed as well as high fiber and platelike B₄C particles on the incompletely consumed precursor particle. It was seen that increasing the amount of tartaric acid from 5 %wt. to 10 %wt. decreases particle formation in fiber morphology. While it was determined that a high proportion of B₄C was formed in the GMd5 sample, the images showed that the boron carbide fiber and rod-like particles in the sample were formed by the lateral growth mechanism from the equiaxed roots. In addition to the absence of fiber formation in the GMd10 sample, the size of the equiaxed particles was larger than the GMd5 coded sample. These findings showed that the use of more than 5 %wt. mandelic acid additive was not ideal for B₄C production with the designed method described here.

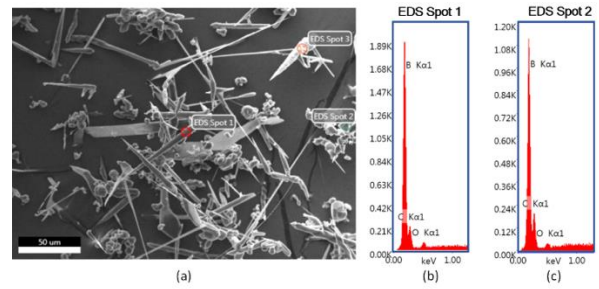


Figure 5. SEM-EDS results of GT5

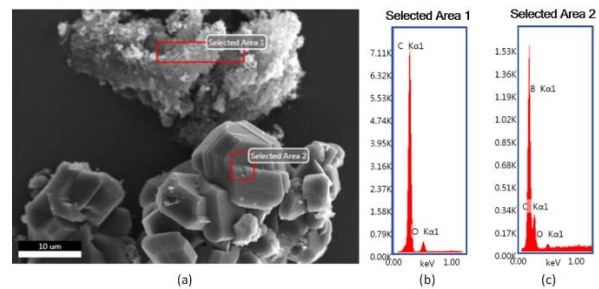


Figure 6. SEM-EDS results of GMd10

SEM-EDX point analysis confirm that all varied shaped particles were B₄C. Taken spectrum positions and EDX results of GT5 and GMd10 shown in **Figs. 5 and 6** indicated that the pyramid-like structures detected in the SEM images of the GT5 sample were more carbon-rich compared to the equiaxed particles. The results confirmed that the spongy parts seen in the GMd10 sample were residual graphite and the equiaxed particles were boron carbide.

4. Conclusions

B₄C particles with varied morphologies (fiber, plate, equiaxed and rod-like) were fabricated by heat treatment at 1500°C for 5 h. It was found that by modifying the glycerin and boric acid-based polymeric gel network structure with carboxylic acids, the formation of borate ester (B-O-C) in the gel network structure could be supported. Therefore, the starting composition has a great influence on the morphology and phase ratio of synthesized B₄C powders. It was observed that the rate of particle formation in fiber morphology decreased with the increase in the amount of additives for both carboxylic acid types. Additionally, both samples contain approximately similar excess carbon content in the form of graphite and excess boron oxide that reveals the importance of the acids and their ratios used in the starting composition.

Acknowledgements

The authors are grateful for the financial support from the Scientific and Technological Research Council of Turkey (TUBITAK) under the contract numbers of 120M651.

References

- [1] A. Najafi, F. Golestani-Fard, and H. R. Rezaie, “Sol-gel synthesis and characterization of B₄C nanopowder,” *Ceram. Int.*, vol. 44, no. 17, pp. 21386–21394, 2018, doi: 10.1016/j.ceramint.2018.08.196.
- [2] S. Gao, X. Li, S. Wang, P. Xing, J. kong, and G. Yang, “A low cost, low energy, environmentally friendly process for producing high-purity boron carbide,” *Ceram. Int.*, vol. 45, no. 3, pp. 3101–3110, 2019, doi: 10.1016/j.ceramint.2018.10.202.
- [3] M. Kakiage, N. Tahara, Y. Tominaga, S. Yanagidani, I. Yanase, and H. Kobayashi, “Effect of molecular structure of polyols with different molecular characteristics on synthesis of boron carbide powder,” *Key Eng. Mater.*, vol. 534, pp. 61–65, 2013, doi: 10.4028/www.scientific.net/KEM.534.61.
- [4] S. Avcioglu, F. Kaya, and C. Kaya, “Synthesis of High Purity Boron Carbide Powders via Sol-Gel Method,” *UCTEA Chamb. Metall. Mater. Eng. Train. Cent.*, pp. 450–453, 2018.
- [5] N. Tahara, M. Kakiage, I. Yanase, and H. Kobayashi, “Effect of addition of tartaric acid on synthesis of boron carbide powder from condensed boric acid-glycerin product,” *J. Alloys Compd.*, vol. 573, pp. 58–64, 2013, doi: 10.1016/j.jallcom.2013.03.255.
- [6] S. Avcioglu, F. Kaya, C. Kaya, Effect of elemental nano boron on the transformation and morphology of boron carbide (B₄C) powders synthesized from polymeric precursors, *Ceram. Int.* 46 (2020) 17938–17950, <https://doi.org/10.1016/j.ceramint.2020.04.104>.
- [7] S. Avcioglu, F. Kaya, C. Kaya, Non-catalytic synthesis of boron carbide (B₄C) nano structures with various morphologies by sol-gel process, *Mater. Lett.* 249 (2019) 201–205, <https://doi.org/10.1016/j.matlet.2019.04.056>

THE SYNTHESIS & CHARACTERIZATION OF HOMOGENOUS HIGH-QUALITY GRAPHENE ENCAPSULATED METALLIC POWDERS VIA PLASMA ENHANCED ROTATING CVD

Deniz ÇAKIR¹, Ömer Refet ÇAYLAN^{1,2}, Tarık Can TÜRKÖĞLU¹, Oğulcan AKGÜN³,
Günce DUGAN³, Halil Onat TUĞRUL³, Benat KOÇKAR³, Gökür CAMBAZ BÜKE¹

¹TOBB University of Economics and Technology, ²Bilkent University, ³Hacettepe University
Türkiye

Key Words: Graphene, Copper, Metal Powder, PECVD

Abstract:

Graphene, the two-dimensional allotrope of carbon, holds a great potential to be a solution for various problems faced by both scientists and industries owing to its superior mechanical properties, electrical and thermal conductivity. Recently, graphene encapsulated powders have attracted attention since it is possible to harvest graphene's potential on a large scale; however, current processing techniques are limited to top-down methods and do not match all the requirements; especially synthesis of high-quality graphene without undesired functional groups and defects, large-scale production, and low cost. In this study, a cost effective and novel method is proposed to synthesize high quality graphene encapsulated metal powders at low temperature *via* plasma enhanced chemical vapor deposition (PECVD). The mechanical properties are measured with compression and tension tests and thermal resistivity of graphene encapsulated powders are studied with laser flash method. The results are compared with the samples without graphene.

1. Introduction

Copper (Cu) is the one of the most widely used metals in the industry due to its numerous advantages such as low cost and high electrical and thermal conductivity. However, low mechanical strength of Cu limits its applications. Compared with traditional reinforcements such as ceramics, carbon materials are more favorable as reinforcements for Cu-based materials because of their lightweight and high strength. Recently, graphene/Cu composites with high mechanical and electrical properties have received significant attention. Graphene is regarded as an ideal reinforcement for Cu-based composites due to its high strength and electrical properties, such as large theoretical specific surface area, high electron mobility, Young's modulus and thermal conductivity.

2. Materials and Method

The steps of growing graphene on copper powders with PECVD are as follows: 15 g of as-received Cu powder is put into the crucible made of Cu foil. The prepared powder-filled Cu crucible is placed in the quartz tube. It is heated while flowing H₂ and Ar gas up to 400 °C. By flowing H₂ and Ar gas at 400 °C, the natural oxide layer on the Cu powders is cleaned with 200 W plasma. Then, graphene is grown on Cu powders with CH₄, H₂, and Ar at 400 °C with 200 W CH₄ plasma for 60 minutes. The test specimens are produced by cold pressing and applying 400 MPa pressure with a 10 mm diameter mold to have test specimens with 10 mm height. The obtained green products are sintered at 1000 °C for 1 hour in the Ar atmosphere. Samples were characterized with SEM and Raman Spectroscopy. Mechanical tests were conducted at room temperature (RT), 200, and 400 °C.

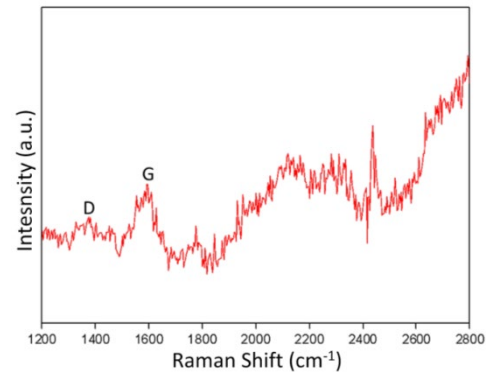


Figure 1. Raman Signal

3. Conclusion

Raman signal from graphene encapsulated Cu powder shows D and G peaks that indicate carbon structure (Fig.1). The results show that the yield strength (YS) and stress values of samples with graphene powders are significantly higher than samples without graphene: The YS of the graphene samples increased by about 3 times at RT, and the stress values obtained at 30 percent constant strain increased by about 2 times.

Acknowledgement

This study is supported by TUBITAK grant number 118F491.



PRODUCTION OF TIN NANOWIRES VIA AAO TEMPLATE METHOD AND INVESTIGATION OF THEIR PERFORMANCE AS CATALYSIS FOR ELECTROCHEMICAL CO₂ REDUCTION

Dilan ER^{1,2}, Eleni ROSOLYMOU³, Mustafa URGEN¹

¹Istanbul Technical University, ²Arcelik Global, ³National Technical University of Athens
Türkiye, Greece

Keywords: AAO, nanowire, electrochemical CO₂ reduction, catalysis, formate

Abstract

Electrochemical CO₂ reduction is known as one of the promising methods to deal with anthropogenic CO₂ at the atmosphere. However, insufficient current density obtained during the reduction continues to keep this technique a step back in large scale applications when compared to the electrolyzer and fuel cell systems. To overcome this problem, production of nanostructured electrocatalyst having high surface to volume ratio has been proposed. An easy and low-cost technique for fabrication of nanostructured electrocatalyst is a highly desirable goal. Anodic oxidation of aluminum is a versatile way to produce uniform and highly-ordered patterns for serving as a template for nanostructured materials. However, formation of barrier non-conductive oxide layer at the bottom of the pores on AAO film has to be eliminated to perform electrodeposition on the pattern. In this study, tin nanowire electrodes were produced using AAO templates to obtain electrocatalysis having high effective surface area for electrochemical reduction of CO₂ to formate. To perform an efficient electrodeposition of tin using AAO template, zincating process, which was proposed firstly in our group as an alternative way to handle the barrier oxide layer, was used. The self-standing tin nanowires produced by electrodeposition into zincated AAO template gave substantially higher currents per geometric surface area than the bulk electrodes with the same geometrical area. Moreover, the amount of formate produced during electrochemical CO₂ reduction was 4 times higher than the bulk tin plate electrodes. This work indicated that tin nanowires produced this method can be a strong candidate as electrocatalysts for CO₂ reduction.

Introduction

Each passing day, anthropogenic CO₂ formed via human-based activities including burning fossil fuels and deforestation rises significantly [1]. To deal with the excessive CO₂ amount at the atmosphere, several approaches such as capture and conversion have been proposed [2]. Among these proposed techniques, electrochemical CO₂ reduction that produces value-added chemicals as a result of reduction, steps forward. In addition to the ability to produce valuable products, operating at ambient conditions, having abundant catalysis and easy setup, etc. are the other advantages of the method [3]. However, conversion of CO₂ based on this method in commercial scale has not been

accomplished yet. One of the drawbacks preventing to run the system in large scale is the low current efficiency of the system [1,4,5]. To overcome this problem, production of electrodes having large effective surface area is one of the promising approaches. At this point, nanostructured materials open a door to achieve high surface to volume ratio and provide high catalytic performance [6]. Anodic aluminum oxide (AAO) has been used as a template for producing uniform regular patterns of nanowires [7]. Easy production, low-cost, and possibility for altering structure (pore diameter, length, etc.) make AAO a highly desirable template for obtaining nanostructured materials [7,8]. The challenging point of AAO method is the barrier layer at the bottom of pores, which serves as an insulator and make electrodeposition on the pattern difficult [8].

In this study, we aimed to produce tin nanowires via AAO template method to obtain tin nanowire electrocatalysis for electrochemical CO₂ reduction with high surface area. The difficulty resulting from insulating barrier layer is resolved by zincating of AAO. The self-standing Sn nanowires produced with this method made possible to produce formate with relatively high faradaic efficiency and high formate production.

1. Experimental Procedure

Experimental studies are divided as: (i) production of tin nanowire electrocatalysts and (ii) determination of their catalytic activity during electrochemical CO₂ reduction.

The production process of tin nanowires is given in Figure 1. At first, the anodic aluminum oxide membranes were produced using aluminum plates (99.99%), with 80x10 mm dimensions, that were annealed at 400°C in open atmosphere for 2 hours. Then, they were electropolished to obtain a mirror-like appearance. Afterwards, anodization was performed in 0.3 M oxalic acid using 70V (DC) constant potential at 5°C for 30 min. The elimination of barrier oxide layer at the bottom of the pores was achieved via zincating. Produced AAO membranes were immersed into the zincating solution at 30°C for 50 seconds. Then, samples were cleaned with distilled water at least three times to eliminate the residues of the zincating solution. The next step was electrodeposition of tin into AAO membranes. Electrodeposition was carried at -0.50 V (DC) for 3 hours in sulphate-based tin bath (Coventya, Stabac Crystal NPF™). A soluble tin anode was used for maintaining the tin ion concentration constant in the electrolyte during deposition.

After the samples were cleaned with distilled water, they were annealed at 150°C for 2h in open atmosphere to improve mechanical properties of tin nanowires. As the final step, etching of AAO membranes was performed in 3M NaOH solution in a temperature range of 50-55°C. Then, samples were washed with distilled water several times.

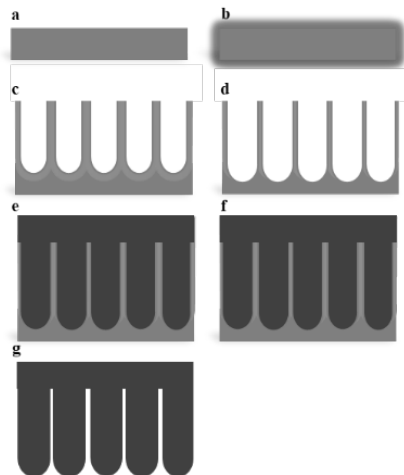


Figure 1. Production steps of tin nanowire electrodes. (a) annealing of aluminum substrate, (b) electropolishing, (c) anodization, (d) zincating, (e) electrodeposition of tin on AAO membrane, (f) annealing, (g) etching of AAO pattern.

As-produced samples were analyzed via SEM (FEG-SEM, Zeiss Supra 55VP) and XRD (Bruker's D8 Advance- with a Cu-K α radiation).

To determine the catalytic behavior of tin nanowire electrodes, electrochemical CO₂ reduction experiments were conducted via using Gamry Reference 3000 potentiostat/galvanostat. The performance of the electrodes was determined via determination of the amount of formate production rate and faradaic efficiency (Equation 1). CO₂ electrolysis was carried out in custom-made H-cell (Figure 2) consisting of platinumized titanium mesh as counter electrode, Ag/AgCl (3 M KCl) as reference electrode, and tin nanowires as working electrode. The geometric area of the tin working electrode was 1 cm². A cation exchange membrane (CEM, Nafion 117TM) was placed between anolyte and catholyte departments to prevent crossing over and oxidation of the produced formate. 0.1 M KHCO₃ solution (pH: 8.50±0.05) prepared with ultrapure water (UPW) was used as electrolyte, and it was saturated with CO₂ before each experiment until the pH of the solution reached to 6.8. CO₂ was continuously fed into the electrolyte throughout the experiment to keep CO₂ concentration stable. Electrochemical reduction experiments were performed at -1.4V (vs Ag/AgCl) for 60 min. At the end of each experiment, electrolyte sample was extracted from catholyte department for calculation of formate amount via ion chromatography (930 Compact IC Flex by Metrohm AG equipped with Metrosep A supp 17 – 250/4.0 column) analysis. To compare the catalytic performance of produced tin nanowire electrodes, electrochemical CO₂ reduction was also carried out on bulk tin plate (99.95%) electrodes having same geometrical area.

$$FE\% = \frac{n \cdot F \cdot e}{Q} \times 100 \quad (1)$$

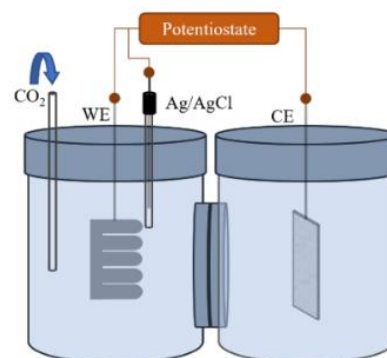


Figure 2. The custom-made H-cell setup used for electrochemical CO₂ reduction experiments.

2. Results and Discussion

The microstructure of produced anodic aluminum oxide film is given in Fig. 3. It was found that the average diameter of pores of AAO membrane is ~100 nm. However, increasing of pore diameters (approximately ~150 nm) was observed due to the zincating process. During zincating process, walls of the pores are dissolved besides the barrier oxide layer at the bottom of the pores is thinned. Therefore, zincating process results in expansion of pore diameter. Due to this phenomenon, optimization of zincating process is highly significant.

Figure 4 shows the SEM images of tin nanowires. As it can be seen, a self-standing nanowire pattern was obtained. The diameter and length of nanowires were found ~150 nm and ~7 μ m, respectively. It should be mentioned that there were loose and detached nanowires due to the aggressive gas formation during the etching of aluminum pattern (Fig. 4b). Annealing of tin nanowires before etching process serves as an improvement for mechanical strength of nanowires, but deformation of nanowires is inevitable.

Figure 5 indicates XRD analysis of as-received and annealed tin nanowire electrodes at 150 °C. The main peak of bulk tin film was observed at 55.4°, which is related to the (301) plane of the tetragonal (b-Sn) lattice. Tin nanowires indicated an intense peak at 30.6° standing for (200) plane of the tetragonal (b-Sn) lattice. Annealing of tin nanowires at 150 °C enhances the intensity of the (101) plane, accompanied also by the increase in the intensity of the (112) plane compared to the as-received nanowires.

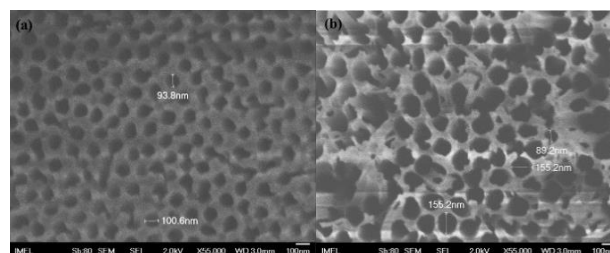


Figure 3. SEM images of AAO membrane (a) before zincating, (b) after zincating.

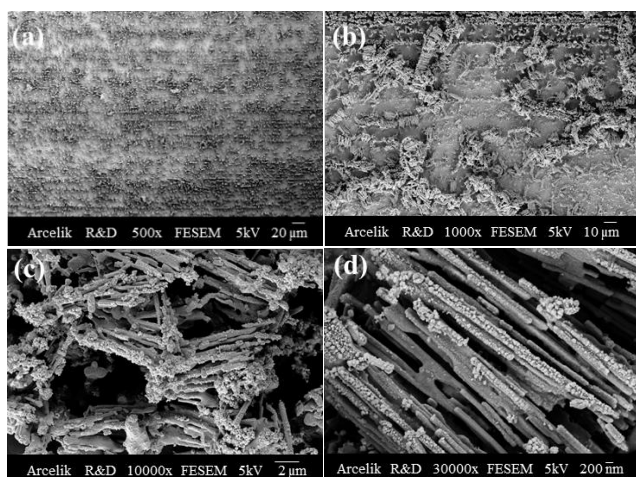


Figure 4. SEM images of tin nanowire electrode (a) uniform self-standing nanowires, (b) detached and loose nanowires, (c) interconnected and bundle structure of nanowires, (d) interconnected nanowires.

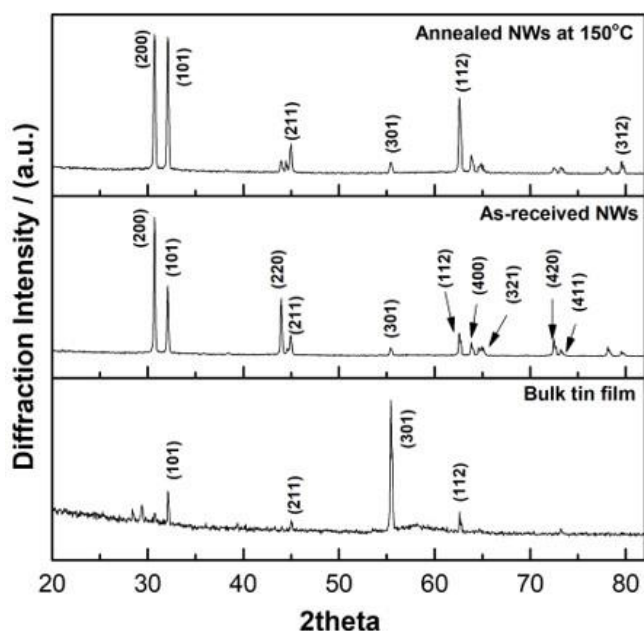


Figure 5. XRD analysis of bulk tin film and tin nanowire electrodes.

The electrocatalytic behavior of tin nanowire electrode was investigated via CO₂ reduction experiments. The current density was found as 5x higher compared to the tin plate (Fig. 6). This result was interpreted as the high surface to volume ratio of tin nanowire electrode. Moreover, the amount of formate produced was also found approximately 4x higher than tin plate electrode (Fig. 7).

The faradaic efficiency values of electrodes were found as 27.97 and 27.38 % for tin nanowire and tin plate, respectively.

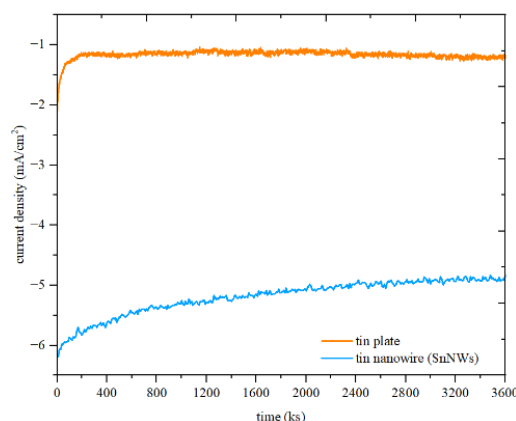


Figure 6. Current vs time plot of tin nanowire and tin plate electrodes at @-1.4V under CO₂ environment.

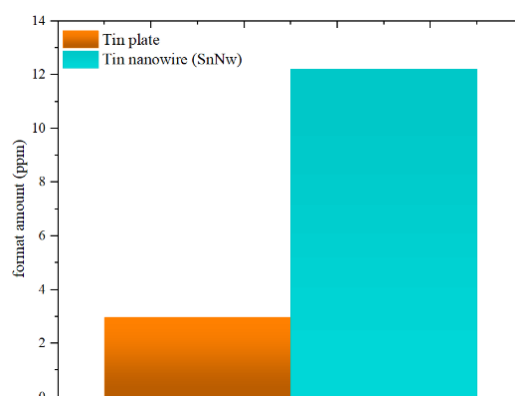


Figure 7. The amount of formate over tin plate and tin nanowires obtained under CO₂RR @-1.4V vs Ag/AgCl for 1h.

4. Conclusion

In this study, we aimed to use AAO membrane technique to produce tin nanowire electrodes and evaluate their performance as electrocatalysis for formate production under electrochemical CO₂ reduction conditions. The outcomes of this study were given below.

- (i) AAO membrane was produced successfully via anodization of aluminum under 70 V (DC) at 5°C for 30 min in 0.3 M oxalic acid solution.
- (ii) Zincating was found as an efficient technique to overcome the drawbacks of barrier layer at the bottom of pores on aluminum oxide layer. Our research group used this technique for the first time for thinning, eliminating the barrier layer and make it electrodepositable because of the thin zinc layer formed at the pore bottoms.
- (iii) Electrodeposition of tin on AAO template was performed at -0.5V (DC) for 2 hours. After annealing and etching processes, uniform and self-standing tin nanowires were obtained. The average diameter and length of nanowires were ~150 nm and ~7 μm, respectively.
- (iv) The electrocatalytic behavior of produced tin nanowire electrodes under CO₂RR conditions were investigated. At constant potential (-1.4V vs Ag/AgCl), tin nanowire electrode showed high catalytic effect. Almost 5 times higher current density was achieved over tin nanowire compared to bulk tin plate electrode. This outcome indicated that tin nanowire electrode has high surface area



- (v) and includes several active sites for CO₂RR. The amount of formate produced during electrochemical CO₂ reduction was found as 4 times higher on tin nanowire electrode. This result was attributed to the high surface area of tin nanowire, which provide high active sites for formate production at the same geometrical area.

Acknowledgment

We would like to thank to Arcelik A.Ş. for their support and Coventya A.Ş. for supplying the tin plating solution.

References

- [1] R. Chauvy and G. De Weireld, Energy Technology, 8 (2020).
- [2] J. Qiao, Y. Liu, F. Hong and J. Zhang, Chemical Society Reviews, 43 (2014) 631-675.
- [3] B. Khezri, A.C. Fisher, M. Pumera, Journal of Materials Chemistry A, 5 (2017) 8230-8246.
- [4] M.G. Kibria, J.P. Edwards, C.M. Gabardo, C. Dinh, A. Seifitokaldani, D. Sinton, and E. H. Sargent, Advanced Materials, 31 (2019).
- [5] F. Proietto, U. Patel, A. Galia and O. Scialdone, Electrochimica Acta, 389 (2021).
- [6] S. Zhao, S. Li, T. Guo, S. Zhang, J. Wang, Y. Wu and Y. Chen, Nano-Micro Letters, 11 (2019).
- [7] G.D. Sulka (Ed.), Nanostructured Anodic Metal Oxides, Elsevier, 2020, Cambridge, USA.
- [8] Z. B. Akıncı and M. Ürgen, ECS Electrochemistry Letters, 3 (2014) 46-49.

THE SYNTHESIS AND CHARACTERIZATION OF Mo_2CT_x MXENE BY HYDROTHERMAL ETCHING WITH DIFFERENT FLUORIDE SALTS FOR EMI SHIELDING APPLICATIONS

Elif OKAY¹, Ömer Refet ÇAYLAN¹, Begüm Beril İNCEÇİK², Göknur CAMBAZ BÜKE¹

¹TOBB University of Economics and Technology, ²Roketsan Missiles Industries
Türkiye

Key Words: Molybdenum Carbide, MXene, Hydrothermal Synthesis, EMI Shielding

Abstract:

Mxenes are the novel two-dimensional metal carbides or nitrides derived from their MAX phases. Recently discovered mxenes attracted the attention of many researchers and are widely studied for the applications of energy storage, catalysis, gas sensing, wastewater treatment etc. More than twenty Mxenes have been successfully synthesized and Mo_2CT_x holds great potential due to its theoretically predicted electrochemical, thermoelectric properties and chemical stability. Nonetheless, the long synthesis duration which can amount up to several days due to the strong bonding between the Mo-Ga atoms is challenging. In order to overcome this problem, in this study, hydrothermal etching has been used to lower the duration drastically.

1. Introduction

Hexagonal carbides and nitrides which have a layered structure are called MAX phases. M in the MAX stands for a transitional metal, A is an A group metal element and X is C or N. MXenes are obtained by selectively etching the A layer of their selected MAX phase. The general formula of MXenes are $\text{M}_{n+1}\text{X}_n\text{T}_x$ (n=1, 2 or 3). T_x in the general formula stands for various surface functional groups (-OH, -F, -O, -Cl groups). Generally, the etching process is done by etching the A layer with various chemicals. The most common etchant used is hydrofluoric acid (HF). The etchant attacks the weaker M-A bonds (relatively weaker than M-X bonds). The interest in mxenes have increased in areas such as catalysis, gas sensing, energy storage and wastewater treatment due to their layered structure, electrical and mechanical properties.

2. Materials and Methods

In this study, $\text{Mo}_2\text{Ga}_2\text{C}$ is used as the primary MAX phase. Gallium is removed by using hydrochloric acid (HCl) with different fluoride salts (LiF, BaF_2 , MgF_2 and MnF_4) and only HCl via hydrothermal reaction. MAX powder was put in a hydrothermal reactor (autoclave). Etchant mixture was prepared separately, poured onto MAX powders, and put into a box furnace. The autoclave was held at 140 and 160 °C for 24 h (5,6 and 7 days for only HCl). Later, the mixture was centrifuged and washed with distilled water (DIW) several times until the pH of the mixture reached 6. The obtained solution was probe-sonicated with DIW to obtain delaminated Mo_2CT_x . Mo_2CT_x /Epoxy composites were obtained by mixing Mo_2CT_x within an epoxy matrix by hand. Different weight percentages of Mo_2CT_x were used for the composites. Then the Electromagnetic Shielding Effectiveness of them were measured in accordance with "ASTM D4935 Standard Test Method for Measuring the Electromagnetic Shielding Effectiveness of Planar Materials" using a vector network analyser in the frequency range of 1.5–10 GHz.

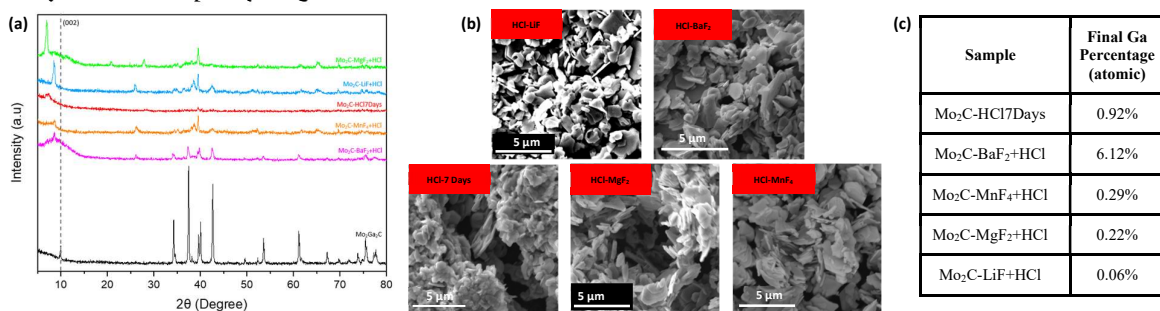


Figure 1: a) XRD analysis, b) SEM images and c) atomic Ga percentages of synthesised samples at 140 °C.

3. Conclusion

To summarize, this study has focused on faster and safer methods to synthesize Mo_2CT_x from its $\text{Mo}_2\text{Ga}_2\text{C}$ MAX phase. Different fluoride salts with HCl and only HCl was used as etchants. In Fig 1., the $\text{Mo}_2\text{Ga}_2\text{C}$ peaks in XRD were mostly gone and there has been a significant broadening and shift in the (002) peak. Which revealed that there has been an increase in the interlayer spacing and gallium was successfully etched away. The disappearance of gallium was also proven by EDX (elemental mapping). The best results were obtained from the only HCl etchant and HCl with LiF samples. The etching efficiency differed according to the cation radiuses and solubilities of the fluoride salts.



EFFECT OF CALCINATION TEMPERATURE ON $MgAl_2O_4$ NANOPARTICLES PRODUCTION BY SOL-GEL METHOD

Duygu YEŞİLTEPE ÖZÇELİK, Sebahattin GÜR MEN

Istanbul Technical University
Türkiye

Keywords: $MgAl_2O_4$, Sol-gel, Catalyst, Characterization, Spinel nanoparticles

Abstract

Spinel $MgAl_2O_4$ nanoparticles have attracted considerable research interest since they can be used in a wide variety of applications such as refractory linings, catalysis and sensors. In this study, $MgAl_2O_4$ nanoparticles were prepared by sol-gel method. Crystal growth and structural properties of $MgAl_2O_4$ nanoparticles obtained after different calcination temperatures (600–800 °C) for 3 h were investigated. The prepared powders were characterized by differential thermal analysis (DTA), X-ray diffraction (XRD), scanning electron microscopy (SEM) and energy dispersive spectroscopy (EDS), Fourier transform infrared spectroscopy (FT-IR).

1. Introduction

$MgAl_2O_4$ spinel has attracted significant attention because of its high melting point (2135 °C), good mechanical strength, high corrosion resistance against chemical attack and low dielectric constant and excellent optical properties [1,2]. In particular, $MgAl_2O_4$ spinel has also caught much attention in catalyst support for various organic reactions such as dehydrogenation, alkane reforming and petroleum processing, because of its good properties [2]. The solid-state, sol-gel, spray drying, pechini method and co-precipitation are the most conventional methods for preparation of $MgAl_2O_4$ spinel [1,3]. The sol-gel technique has been widely adopted because of its simple setup, low cost, and chemical homogeneity outcomes [1,4].

2. Materials and Methods

$MgAl_2O_4$ nanoparticles were prepared by sol-gel method using 0.1 M concentration prepared from the high purity $Al(NO_3)_3 \cdot 9H_2O$ and $Mg(NO_3)_2 \cdot 6H_2O$ salts as starting materials, 10-20 ml 0.1 M citric acid as a chelating agent, 10-30 ml 25% NH_4OH as a precipitation reagent. The solution was stirred at 400 rpm, at room temperature, for 2 hours in a magnetic stirrer, and after mixing, it was left for 1 day and then filtered. The powders were dried at room temperature and ground in a mortar. For the determination of the thermal decomposition (calcination) temperature for obtaining nanocomposite oxide powder from the obtained powders DTA-TG analysis.

3. Conclusion

As a result of the DTA-TG analysis of the Mg-Al hydroxide powder obtained for the production of $MgAl_2O_4$, it was observed that there was no weight loss after 600 °C. 600, 700, 800 °C calcinations were made to examine the effect of temperature. The crystal structure of the obtained samples was applied with XRD. It was determined that the peaks were compatible with JCDPS No: 00-005-0672 of $MgAl_2O_4$. FT-IR analysis results confirmed the existence of the $MgAl_2O_4$ spinel structure. The SEM results showed that nanoparticles had spherical morphologies and the particles size increase due to the growth of particles with increasing calcination temperature from 600 to 800 °C and the particles a little agglomerated.

Acknowledgment

This work was supported by Istanbul Technical University, Scientific Research Projects Coordination Unit (Project ID: 43781).

References

- [1] Y. Wen, X. Liu, X. Chen, Q. Jia, R. Yu, T. Ma, Effect of heat treatment conditions on the growth of $MgAl_2O_4$ nanoparticles obtained by sol-gel method, *Ceramics International*, 43, (2017), 15246–15253.
- [2] Q. Wu, G. Feng, L. Miao, Z. Tang, W. Jiang, J. Liang, J. Liu, Preparation of mesoporous petal-like $MgAl_2O_4$ via molten-salt assisted nonhydrolytic sol-gel method, *Chemical Physics Letters*, 778, (2021), 138794.
- [3] N. Habibi, Y. Wang, H. Arandiyani, M. Rezaei, Low-temperature synthesis of mesoporous nanocrystalline magnesium aluminate ($MgAl_2O_4$) spinel with high surface area using a novel modified sol-gel method, *Advanced Powder Technology*, 28 (4), (2017), 1249-1257.
- [4] S. Sanjabi, A. Obeydavi, Synthesis and characterization of nanocrystalline $MgAl_2O_4$ spinel via modified sol-gel method, *Journal of Alloys and Compounds*, 645, (2015), 535–540.



COMPARATIVE STUDY OF MICROSTRUCTURAL CHANGES AND HARDNESS OF NANOSTRUCTURED FECOCRNI HIGH ENTROPY ALLOYS AFTER DIFFERENT CONSOLIDATION ROUTES

Mustafa TEKİN¹, Ali Rıza BALOĞLU², Hasan KOTAN²

¹KTO Karatay University, ²Necmettin Erbakan University
Türkiye

Keywords: High entropy alloys; High energy mechanical alloying; Hardness; Sintering; Spark plasma sintering; Microstructure; Grain growth

Abstract

In this work, mechanically alloyed nanocrystalline FeCoCrNi HEAs were consolidated via cold compaction following conventional sintering and spark plasma sintering. The results showed that spark plasma sintering yielded higher density with increasing temperature. Microstructurally, SPS route resulted in increased amount of Cr-rich carbide second phases in the microstructure, which yielded higher hardness, when compared to the conventional sintering route.

1. Introduction

HEAs contains at least 5 elements in equimolar or near equimolar ratios with stabilized structures and enhanced properties [1, 2]. High Energy Mechanical Alloying (HEMA) is solid state process that leads to homogeneous structures which increases the strength of materials [3]. Spark plasma sintering (SPS) method is defined as production route which requires shorter processing time and immensely effective process [4]. After SPS, samples generally ensures high density, better nanocrystallinity, and homogenized compositions [5]. Resultantly FeCoCrNi HEA powders, produced by mechanical alloying with nanocrystalline structures, followed by conventional sintering and spark plasma sintering. A comparative study of microstructural properties and hardness of FeCoCrNi alloys were investigated as a function of different consolidation routes.

2. Experimental Procedure

Nanocrystalline FeCoCrNi was produced with HEMA via SPEX 8000D shaker for a duration of 20 h with the 10 to 1 ball to powder ratio. Samples then sintered for a duration of 1h at the temperatures of 900, 1000, and 1100 °C. Subsequent to mechanical alloying, powders were consolidated by spark plasma sintering (SPS) method at 1000 °C with 30 MPa pressure for 8 min and at 1100 °C 50 MPa pressure for 10 min under vacuum. X-ray diffraction (XRD), focused ion beam microscopy (FIB), and transmission electron microscopy (TEM) were used to investigate the microstructures of as-milled and annealed HEAs as a function of sintering route.

3. Conclusions

Nanostructured FeCoCrNi HEAs were prepared by HEMA and effect of different consolidation routes on the microstructural evolution, density, and hardness of alloys were investigated in this study. The results showed that SPS lead to higher density and the densities increased with higher temperatures. Structural analyses shown that the fcc obtained after HEMA was retained after different sintering routes. Microstructurally, SPS yielded increased amount of Cr-rich second phases in the microstructure, which lead to retain smaller grain size and yielded higher hardness.

Acknowledgement

This research was supported by Necmettin Erbakan University, TURKEY, through the Scientific Research Projects Coordination Unit (BAP) under project number 211219004. The authors also would like to thank to Dr. Erhan Ayas and Kübra Gürcan Bayrak for SPS process from Eskişehir Technical University.

References

- [1] M. Tekin, G. Polat, Y.E. Kalay, H. Kotan, Grain size stabilization of oxide dispersion strengthened CoCrFeNi-Y2O3 high entropy alloys synthesized by mechanical alloying, *Journal of Alloys and Compounds* 887 (2021) 161363.
- [2] M. Tekin, G. Polat, H. Kotan, An investigation of abnormal grain growth in Zr doped CoCrFeNi HEAs through in-situ formed oxide phases, *Intermetallics* 146 (2022) 107588.
- [3] E. Salur, M. Acarer, İ. Şavkliyildiz, Improving mechanical properties of nano-sized TiC particle reinforced AA7075 Al alloy composites produced by ball milling and hot pressing, *Materials Today Communications* 27 (2021) 102202.
- [4] S. Deng, R. Li, T. Yuan, S. Xie, M. Zhang, K. Zhou, P. Cao, Direct current-enhanced densification kinetics during spark plasma sintering of tungsten powder, *Scripta Materialia* 143 (2018) 25-29.
- [5] M. Zhang, T. Yuan, R. Li, S. Xie, M. Wang, Q. Weng, Densification mechanisms and microstructural evolution during spark plasma sintering of boron carbide powders, *Ceramics International* 44(4) (2018) 3571-3579.

DEVELOPMENT OF GRAPHENE/SILICON COMPOSITE BASED LITHIUM ION BATTERY ANODE

Tarık Can TÜRKÖĞLU, Eren ATLI, Ömer Refet ÇAYLAN, Göknur CAMBAZ BÜKE

TOBB University of Economics and Technology
Türkiye

Key Words: Graphene, Silicon, Li-Ion Battery, Anode

Abstract:

The need for energy storage devices is growing constantly, requiring the development of more efficient, high-capacity batteries. Due to their superior properties compared to conventional batteries, lithium-ion battery cells have become the most popular energy storage units, and they are now widely used. The Li-ion battery cells used in electric cars are expected to have a short charging time, a long cycle life, a low weight/volume, and a large storage capacity. The anode structure of Li-ion batteries should be enhanced to obtain these features. Because of its large surface area, mechanical and electrical capabilities, and chemical resistance, graphene has potential to solve challenges. Top-down processes such as high vacuum furnaces, and the flash method are used to make Gr for Gr/Si composites.

1. Introduction

Li-ion battery cells have become the most common energy storage devices. To obtain desirable properties such as rapid charging, a long cycle life, a low weight/volume, and a large storage capacity, the Li-ion battery anode structure must be improved. Graphite is a common active material in battery anode structures. However, its limited charge capacity and limited surface area require further development. Silicon is another popular Li-ion battery component, but anodes built of Si instead of graphite degrade faster and have a shorter service life due to structural fragmentation caused by the volume changes during charge and discharge cycles. Graphene (Gr), 2D carbon allotrope, has potential to address these issues due to its vast surface area, mechanical and electrical properties, and chemical resistance. Therefore, the objective of this study is to obtain a Gr/Si composite structure to enhance the energy storage capacity, mechanical properties, and chemical resistance of the battery anode.

2. Materials and Method

For the production of Gr for Gr/Si composites, top-down processes such as high vacuum furnaces and flash method are used. In order to produce Gr/Si composites, two different approaches are followed. Vacuum decomposition of different sized SiC powders were annealed at high vacuum furnace at different temperatures (1400, 1500, 1600, and 1700°C) for different durations (30 and 60 minutes) without any gas flow. At further steps, during vacuum annealing at high temperatures CH₄ gas is introduced to the system with different amounts (5, 10, 15, and 20 sccm). After the vacuum decomposition process, samples were analyzed with SEM and Raman Spectroscopy and all samples were compared.

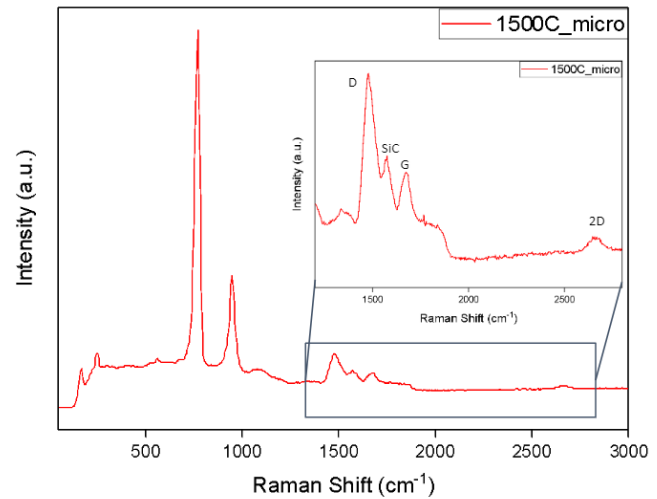


Figure 1. Micropowder SiC Raman Signal

3. Conclusion

Raman signals from micron-sized SiC powders that was annealed at 1500 °C shows significant D, G and 2D peaks which indicates the presence of graphene structure. Additionally, it can be seen that one of the SiC peaks also seen between D and G peak of graphene structure.

References

[1] Kayali, E. (2016). DEVELOPMENT OF CARBON BASED ELECTRODE MATERIALS FOR LITHIUM ION BATTERY APPLICATIONS (Master's thesis, TOBB ETU Graduate School of Science).

LASER INDUCED GRAPHENE STRUCTURES FOR ELECTROCHEMICAL SENSING DEVICES

Murat DEMİREL, Ömer Refet ÇAYLAN, Tarık Can TÜRKÖĞLU, Göknur CAMBAZ BÜKE

TOBB University of Economics and Technology
Türkiye

Keywords: Humidity Sensor, Laser Induced Graphene, Nail Polish

Abstract

Flexible electronic devices demonstrate great impact in wearable electronics and sensors therefore they are attracting significant attention from both academia and the industry. Humidity sensors are the most important members of these devices due to their fast response speed, low cost and outstanding stability with high performance, since the demands in various applications have been increasing such as water status tracking of plants, health monitoring via respiration detectors, environmental monitoring. In this study, 3D porous graphitic carbonaceous structure is synthesized and patterned on nail polish *via* laser induced graphene (LIG) technique with 405 nm Nichia blue laser to fulfill the demands of the humidity sensor properties. In addition, commercial humidity sensors are coated with LIG and the performance difference between as-received sensor and LIG coated sensor is compared with the arduino electronic platform.

1. Introduction

Possessing high electrical mobility and small dimensions are attracting significant attention towards the utilization of these materials for humidity sensors. Van der Waals forces in the 2-D structure of graphene sheets causes restacking and aggregation which prevent having high surface area and dispersion stability in solvents. These problems severely affect the application of the graphene in the sensors. Therefore, to fulfill the required material properties of humidity sensors, such as high precision, easy-to-process, and without complicated synthesis or fabrication processes, LIG method is used to produce porous 3D graphitic carbon structure on nitrocellulose film resulting in with high conductivity, superior electrochemical activity, tunable composition and large surface area. Since GO contains hydroxyl (-OH), carboxyl (-COOH), and epoxy (=O), the hydro-philicity of the GO is enhanced and as a result of this, it can be used in humidity sensor applications. However, in nail polish derived films further processes have to be applied for humidity sensing. Apart from that, coating nitrocellulose film on commercial humidity sensors results in better humidity measurements, as read from arduino code, which can be utilized under the soil for measuring humidity.

2. Materials and Methods

In this study, 1.2 mL nitrocellulose solution received from commercial nail polish is coated on the 5x5 mm² square PET *via* spin coating process carried out at 400 rpm for 2 minutes. The PET sheet was then placed on the laser engraving machine platform. Laser input voltage is 5V and laser is charged from 500 mA to 1A. As a result, during the experiment the surface was exposed to laser power from 2.5 W – 5 W. To obtain porous graphitic carbon structure required parameters are tested such as burning time (mS) and cycles (repetition of carving process with same parameters). All of the experiments are conducted in atmospheric pressure, open air and at room temperature. Resulting interdigitated electrode patterns with average 150 µm can be seen in Figure 1.

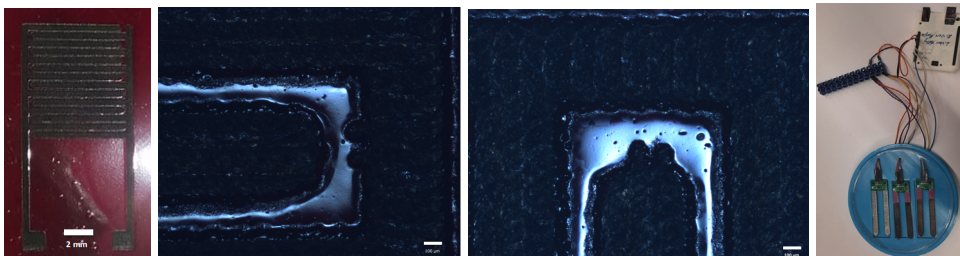


Figure 1. Interdigitated electrode pattern on nail polish, optical image in 50x in each image scale bar is 20 µm, arduino measurement experimental setup and system from left to right.

3. Conclusion

In this study, desired interdigitated patterns were engraved on commercial nail polish *via* LIG method. Properties related with the experiment parameters will be characterized with Raman and SEM for future work. LIG sample is compared and tested with commercial analog humidity sensors and from arduino measurements it is shown that the humidity sensing is improved when LIG coating is used on commercial humidity sensors.



PHOTOLUMINESCENCE PROPERTY OF NaYF₄: Yb/ Er/ Pr UPCONVERSION NANOPARTICLES IN THE NEAR INFRARED REGION

Mahla SHAHSAVAR, Ayşe DULDA

Yeditepe University
Türkiye

Keywords: Synthesis, Upconversion nanoparticles, Near-infrared emission, photoluminescence

Abstract

Near-Infrared emitted upconversion nanoparticles having particle size around 20 nm in hexagonal phase synthesized via the thermal decomposition technique. The research focused on the investigation of the photoluminescence property of NaYF₄: Yb³⁺/ Er³⁺ nanoparticles doped with different concentrations of Pr^{x3+} (x = 0, 0.1, 0.5,1) under 980nm excitation laser. Emission peaks have been observed in 520 nm, 540 nm, 654nm, 810, and 840 nm under the radiation of 980 nm excitation. Increasing the Pr³⁺ ions concentration weakens the emission energy peaks in NaYF₄: Yb³⁺/ Er³⁺/ Pr³⁺ matrix and reported no enhancement in emission peaks located in the NIR region.

1. Introduction

Upconversion nanoparticles (UCNPs) have become a potential type of light-emitting nanomaterial because of their unique properties, which allow them to overcome many of the issues that appeal to traditional fluorescence probes. Under near-infrared (NIR) radiation, up-conversion nanoparticles (UCNPs) emit not only (UV/Vis) light but also have the potential to emit near-infrared light. Various types of near-infrared emission nanoparticles have been demonstrated for excitation (NIR I) and emission in the infrared range (NIR-I, NIR-II). UCNP emission in the NIR regions represents essential advantages such as low toxicity, deep tissue penetration, and excellent photostability that are proposed as promising options for biomedical NIR I-II sensing and imaging. This work attempted to develop the luminescence emission in the NIR region by introducing different dopant concentrations of Pr³⁺ ions in NaYF₄: Yb³⁺/ Er³⁺ nanoparticles.

2. Materials and Methods

β-NaYF₄:Yb³⁺, Er³⁺ crystals synthesized by Thermal decomposition technique that is known as one of the best ways to achieve high-quality nanoparticles. Aqueous Ln(Ac₃) (Ln = Y³⁺, Yb³⁺, Er³⁺/Pr³⁺) was mixed with OA and ODE, and procedures were completed by heat treatment steps in controlled time [1]. The obtained pure NaYF₄:Yb³⁺, Er³⁺ nanocrystals were finally dispersed in cyclohexane. Typical dopant concentrations of 20% for Yb³⁺ ion and 2% for the Er³⁺ ion dopant concentrations give rise to an intense Er³⁺ green UCL [2]. To achieve enhancement in the NIR region, different concentrations of Pr³⁺ (0.1%, 0.5%, 1%) were applied in the synthesis of nanoparticles for comparison purposes. The size and morphology of the synthesized nanoparticles were characterized by Transmission Electron Microscope (TEM), and Crystallographic information of samples recorded through X-ray diffraction (XRD).

3. Conclusions

In this work, the upconversion luminescence properties of NaYF₄ doped with Yb³⁺, Er³⁺, and Pr³⁺ under 980nm laser excitation were studied. Synthesized upconversion nanoparticles were achieved in pure hexagonal phase and a size range of ~ 20 nm. Photoluminescence properties of nanoparticles were reported under a 980nm excitation laser, emission peaks have been observed at 520 nm, 540nm, 654nm, 810, and 840nm which corresponded to only Er³⁺ ions. The effect of different Pr³⁺ contents on the luminescence intensity was investigated, and it was found that by increasing the Pr³⁺ concentration, a reduction was observed in all peak intensities that indicates Pr³⁺ ions make no positive contribution to the upconversion emission of Er³⁺ under 980nm excitation laser. Pr³⁺ ions have a quenching effect on the Er³⁺ upconversion emissions that can be deduced from the results.

References

- [1]. Wang, Y., Li, Y., & Fan, D. (2017). *ChemistrySelect*, 2(28), 8874-8879.
- [2]. Haase, M., & Schäfer, H. (2011). *Angewandte Chemie International Edition*, 50(26), 5808-5829

THE SYNTHESIS & CHARACTERIZATION OF CARBON NANOTUBES ON SiC VIA VACUUM DECOMPOSITION

Erhan GÜRPINAR, Ömer Refet ÇAYLAN, Derya KARADENİZ, Erkin Köseoğlu, Göknur CAMBAZ BÜKE

TOBB University of Economics and Technology
Türkiye

Keywords: Carbon nanotubes, Vacuum Annealing, Field Emitters

Abstract

Due to their unique properties such as excellent electrical and thermal conductivity, high mechanical strength, good chemical stability, and a high aspect ratio, carbon nanotubes (CNTs) have been considered as the most promising candidate for field emitters. Vacuum annealing of silicon carbide, one of the most popular synthesis methods of CNTs, is advantageous in many aspects since it does not require the use of a catalyst, enabling producing CNTs with high purity and adhesion strength, among other properties. In this work, carbon structures (graphite, graphene, and CNTs) have been synthesized on silicon carbide using vacuum annealing, and the effects of different process parameters such as synthesis duration, temperature, pressure, gas mixtures, and flow rates on the synthesized structures are investigated. The morphology of carbon structures is examined using SEM, and Raman spectroscopy.

1. Introduction

Carbon nanotubes (CNTs), a one-dimensional structure composed of carbon atoms, have been studied for many years and used in various applications owing to their high electrical conductivity, mechanical strength, and thermal conductivity. The electrical properties of the CNTs can be tuned by changing the number of walls of the synthesized structures to exhibit metallic or narrow-band semiconductor behavior. Hence, CNTs are an excellent candidate for field emission applications as an electron source due to the mentioned properties. However, in such applications, high quality and controlled nanotube growth is required. In the literature, aligned CNTs are mostly synthesized by the chemical vapor deposition (CVD) method. However, this method poses a problem for field emission applications due to the fact that it contains a catalyst and has low adherence performance to the substrate. Another important technique, the decomposition of SiC, eliminates these problems. With this method, CNT synthesis can be performed at high temperatures without using a catalyst.

2. Materials and Methods

4H-SiC wafers were used for experiments. To clean the wafer, it was sonicated with acetone and ethanol for 5 minutes each. Then, to get rid of the surface oxide, it was kept in HF solution (5% concentration) for 15 minutes and was purified with distilled water. In the experiment, as-received samples were first pre-annealed at 1250 °C for 30 minutes. Then, annealing was carried out for 1 hour at 4 different temperatures (1400 °C, 1500 °C, 1600 °C, 1700 °C) under low vacuum ($\sim 10^{-5}$ torr) conditions. All samples were investigated by using SEM and Raman Spectroscopy.

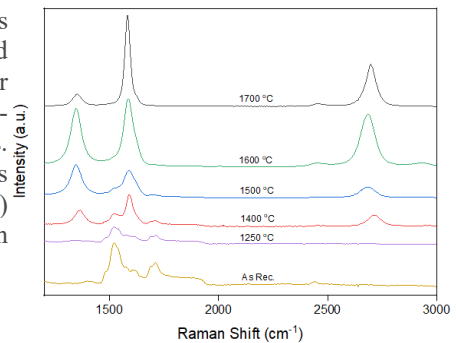


Figure 1. Raman Spectra of C-Face SiC wafers under different experiment temperatures.

3. Conclusion

Raman spectroscopy analysis (Figure 1) shows the presence of carbon structures on the SiC wafer at 1400 °C and above. In addition, when it comes to 1700 °C, a more ordered carbon structure formation is seen with a significant decrease in the D (disorder-induced) band around 1400 cm^{-1} compared to other temperatures.

Acknowledgment

This study is supported by the Air Force Office of Scientific Research grant number FA9550-19-1-7048.



CSS

Casting Symposium

Döküm
Sempozyumu

CIRCULAR ECONOMY IN METAL FOUNDRY SECTOR: FROM EUROPE TO TÜRKİYE

Semih ATEŞ¹, Kerem Can DİZDAR¹, Tunçağ Cihangir ŞEN², Serter Koray HATİPOĞLU²,
Cevat Fahir ARISOY¹

¹Istanbul Technical University, ²Turkish Foundry Association
Türkiye

Abstract

The circular economy is a new economical behavior system to reduce the wasting of all components of a system that includes reducing, reusing, recycling, and refurbishing-remanufacturing. The compound annual growth rate of global resource extraction is realized as 1.8% from 1980s to 2020. Minerals, metals, glass and plastics, paper, and wood are recycled, composted, and/or reused as 43.8%, 4.3%, 1.1%, and 3.6%. Linearity occurs in the metal casting sector that wastes can be summarized as glue, sand, slag, catalyst, gas-washing fluent and cleaning consumables 4.61%, 4.53%, 4.37%, 4.33%, 4.23%, 4.19% of total waste, respectively. Green deal is a milestone of new and updated process designs. In consonance with green deal protocols, European Union generates more than 25 communications, directives and regulations which are consisting of bans on plastic materials in daily life, regulating the waste collection and recycling method, and eco-design requirements. Also, Türkiye follows European Union Green Deal approaches and there are many different projects implemented via the Ministry of Environmental and Urbanization supported projects that can be implemented from micro to macro levels. Also, The Circular Economy Platform was established in 2016 with the support of the Business Council for Sustainable Development Türkiye (BCSD Türkiye) and the European Bank for Reconstruction and Development. In this study, circular economy approaches, and main concepts are reviewed per metal foundry process.

1. Introduction

The supply-demand chain of the world is classified in the linear economy that is directly connected to the production and consumption relation. Linear Economy (LE) is focused on *using* renewable or non-renewable resources and products are thrown away after use [1]. The economic system tries to close this linearity with the circulation which is called Circular Economy (CE) approach [2]. Mainly CE approach can be described as *derive*. The sources are used for production, but wastes are used as a new source for the same or another

process. The general difference between LE and CE chains is given in Figure 1.

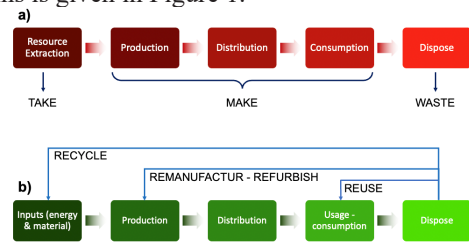


Figure 1. General process flows of a) Linear economy (LE), b) Circular economy (CE) [3]

According to Ellen MacArthur Foundation replaces the “end-of-life” concept with restoration and regeneration. P. Ghisellini, C. Cialani, and S. Ulgiati (2016) worked on a review for the CE according to more than 100 studies. They revealed that CE is an environmental protection card instead of steady-state-oriented economic systems such as regular consumption patterns. They separated CE into three stages: micro, meso, and macro. Each stage described spheres of influence [4]. J. Kirchherr, D. Reike, and M. Hekkert (2017) made a detailed literature review regarding the definitions of CE and they revealed that there were 114 different definitions and they vary from each other. Only 40% of papers showed the conceptualism of CE from a system perspective and there was a clear lack at the point of conceptual thinking about CE. Also, system perspective and environmental quality were added to conceptualisms after about 30 years from the first definition of CE which was about the 1930s [5]. The circularity is not only for materials, and consumables but also for humans. The CHRM (Circular Human Resource Management Project, see: [6]) is funded by the Erasmus+ Programme of the EU, which focuses on converting material circularity approaches for human resources to obtain circular thinking and conceptualization. Moreover, Türkiye has an active role in the CHROMAFOR project (Skills and Competencies for a Circular Human Resource Management in the Foundry Sector, see [7]) which is funded via the Erasmus+ Programme of the EU. This project is aimed to develop a training module for adapting human resource management as a key player

to obtain circularity in foundries. Thus, circularity can only be used as a permanent methodology system when provided for both material and humans.

The circular economy is based on 3R (reduce, reuse, recycle) principles that reveal the environmental relations [8], [9]. However, the main 3R can be separated into three groups and extended to 9R (refuse, rethink, reduce, reuse, repair, refurbish, remanufacture, repurpose, recycle, recover). The groups are smarter product use and manufacture (refuse, rethink, reduce), extend the lifespan of product its parts (reuse, repair, refurbish, remanufacture, repurpose), useful application of materials (recycle, recover) [9], [10].

2. Circular Economy in Europe

It is reported in World Economic Forum that only the consumer goods sector spends 80% of the US\$ 3.2 trillion material value irrecoverably each year because of the linear economic approach [11]. McKinsey reported (2017) that CE provides a 3% increment by 2030 for European resource productivity that promotes 6000€ billion cost savings per year and 1.8€ trillion more in other economic benefits [10]. The general ecosystem can be divided into 24 subgroups which are feeding the production chain. The groups were given in Figure 3.

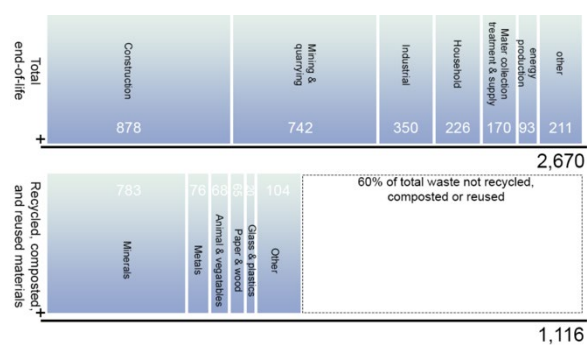


Figure 2. 2011 Eurostat waste statistics in million tons [1].

EU Green Deal (see: [12]) which is a compilation of policies for obtaining a neutral climate in the EU, 2050. It contains 10 communications, 8 directives, and 8 regulations. The impact area of the Green Deal is clean energy, sustainable industry, building and renovation, farm to fork, eliminating pollution, sustainable mobility, biodiversity, and sustainable finance. These have eco-design working plans, CE actions, action plan implementations, plastic product impact reduction reports, packing and its waste directives, ecological design requirements for household/refrigerators or dishwashers, welding equipment directives, etc. The report of M. Gribaudo and his friends (2020) states that homologation

constraint is promoted by designing 95% recyclable and recoverable vehicles and designing a new process without using heavy metals (Pb, Cd, Hg, Cr, etc.). Also, the European directive (200/53) promoted the guarantee for the customer to demolish their cars after end-of-life. The goal is that the recovery ratio increment is from 85% to 95% by weight ratio of wastes [13].

L. Holappa, M. Kekkonen, A. Jokilaakso and J. Koskinen (2021) reported a study about CE perspective for stainless steelmaking slags. Stainless steel production (SS) had an annual growth rate of 5.33% between 1980 – 2019. The total slag of SS was estimated as 15 – 17 Mt/year including electric arc furnace (EAF) melting, argon-oxygen-decarburization (AOD), and vacuum-oxygen-decarburization (VOD) converting, ladle operations, and casting. The CE implementations of SS making are focused on not only the company implementations and steel recovery but also the recovery of high-value elements such as Cr, Ni, Mo, Ti, and V. From the economic viewpoint, landfilling of SS slags causes expenses because of disposal taxation and handling cost. On the contrary, according to product groups of slags circularity, landfilling was found as the best solution for quick actions and very low investment costs. However, transforming this material into Ca-based products (like food additives) are estimated as having the highest cash flow rate. Another high-return investment can be provided via geopolymers and low-carbon cement. Also, fillers and aggregates followed the others. Surprisingly, they found that the exact relative cash flow of geopolymers and low carbon cement is higher than Ca-based products. They revealed that the SS slags can be converted into valuable products because of their adjusted chemistry and properties. Precipitated Calcium Carbonate (PCC) is an example of a valuable product for the paper industry. However, it can be used as a binder for CO₂, hence it lowers the carbon footprint for SS production [14].

T.A. Branca, V. Colla et. al. (2020) studied the reuse and recycling of by-products of the steel sector as CE and Industrial Symbiosis (IS) in Europe. IS focuses on developing collaboration between different sectors via generating new business opportunities. Thus, by-products can be used as a raw material for different sectors according to IS approaches. The by-products of steelmaking were categorized as slag, dust, and process gases. There are several methods for recovering zinc from dust and slags that can be used in cement, fertilizers, roadstone, and asphalt. Process gases are used in electricity and heating, others can be used in pencil pitch, plastics, and paints. These IS approaches can be an example for both new facilities and new job opportunities as circular human resource management. In the metal foundry sector, recent

actions are focused on used foundry sand recycling. For example, the combination of used foundry sand and electric arc furnace slag and bottom ash (taken from Municipal Solid Waste Incineration) in different percentages are used in road foundations [15]. Foundries and metal casting technology provide possible recycling and reusing of a significant portion of metals that have reached the end of their life to produce new products. In electric furnaces, the proportion of recycled materials utilized to replace virgin raw materials has risen significantly in recent years and presently stands at 75%. The water used to cool the furnaces is finally recycled and utilized 95%. Regarding the effects of production on the environment, the First Sustainability Report of the industry dedicated 28.5% of all investments to environmental issues in 2015. This amount is higher than average for manufacturing as a whole (2%) and it provides a significant reduction in waste output per ton of casting material (-26.6% between 2000-2015) and dust emissions (-65% since 2003). As per the CE action plans, Italian foundries have joined Assofond's Effige Project (Environmental Footprint for Improving and Growing Eco-Efficiency) which is funded by the EU and aims to test the PEF (Product Environmental Footprint) method, a system for calculating the environmental footprint of products throughout their entire life cycle to identify the production stages that have the greatest negative effects on the environment and to identify and introduce solutions that can lessen their incidence [17].

3. Circular Economy in Türkiye

According to European Environmental Departments and Institutes for the CE report, Türkiye is defined as a country that faces great challenges because of accelerated increments in the manufacturing industry. However, each municipality carries out its waste management system. According to the 2018 records of TEMA (the Türkiye foundation for combating erosion reforestation and the protection of natural habitats), Türkiye produced 32.2 million tons of waste overall per year and 1.16kg per capita/day. Also, Türkiye has 2223 waste disposal and recovery facilities in 2018, the average recycling rate is 12.3%. Türkiye started Zero Waste Management Action Plan in 2017 but it will be implemented by 2023 (announced in 2019), fully. 18750 public institutions were joined to this project by 126 tons of paper, 8.7 tons of glass, and 9.1 tons of organic waste according to 2019 reports.

P. Özuyar (2011) observed the Türkiye's CE practices. First of all, it was stated that Türkiye has microsystems for promoting CE approaches such as organized industrial zones (OIZ) which have improved access to basic services and provide easy regulations and practicing opportunities. Türkiye has 349 OIZs in 76

cities. In addition to this, Türkiye developed Technology Development Zones that have an indirect effect on CE but are very organic systems for CE implementations [17].

M.Y. Kılıç and M. Tüylü (2019) studied the usage of foundry sand wastes in Bursa, as a raw material for concrete. They stated that 4-5 tons of sand are used for 1-ton metal casting. According to the Guide for Casting Sector Document which is published by the Republic of Türkiye Ministry of Environment, Urbanization and Climate Change, 0.2-0.5 tons of waste is observed at 1-ton metal casting and the foundry sand waste is up to 65% of total waste. The annual ratio of cast metal/waste, cast metal/waste sand, and sand/waste was close to constant between 2006 and 2015. This study calculated the aggregate of concrete by using foundry sand as aggregate. They found that 8840 tons of waste sand usage save 20% cost of aggregate. To produce 100000 m³, 44200 tons of aggregate are consumed. Thus, the concrete company will save 58.694\$ because of foundry sand waste usage. The metal foundry will save 293.471\$ because of not covering the disposing cost of Bursa Municipality Regular Solid Waste Storage which was 4.18\$/ton for non-hazardous waste sand, in 2019 [18]. According to the "55th World Casting Statistics 2020", the Turkish Metal Casting Industry ranks as the 9th largest casting producer in the world and 2nd in Europe with a total production of 2,17 million tons. During the pandemic process and constantly changing conditions, the Turkish Metal Casting Industry had one of its brightest periods in 2021 as well with the effect of increasing orders and production output.

Besides the problems being experienced in the logistics sector and the rise in energy costs, the Green Deal Action Plan and the approval of the Paris Climate Agreement bring important responsibilities to all Turkish stakeholders in terms of reducing greenhouse gas emissions and carbon footprint.

At this point, it is essential that all stakeholders of the Metal Casting industry, official institutions, and authorities, come together and develop common solutions to become fully adapted to a circular economy model which is very critical for the sector to maintain its global position and sustainability.

Türkiye Circular Economy Platform was established in 2016 with the support of the Business Council for Sustainable Development Türkiye (BCSD Türkiye) and the European Bank for Reconstruction and Development. The CE Action of BCSD Türkiye is promoted by 32 companies. Also, the Turkish Materials Marketplace (TMM) was established within the project, also supported by TUDOKSAD The Turkish Foundry Association. It provides a platform for workshops, research, and exchange investments to waste minimization.

4. Conclusion

The circular economy is a new economic action pattern that will provide a more productive world for increasing demands. The circulation has already provided nearly at foundries via using scrap metals thanks to nature. The scraps can be gathered in ferrous or non-ferrous forms from many sources such as cars that completed their economic life, reinforced steels of demolished buildings, and metal shaping metallic residues. Both EU and Türkiye implement directives for closing the loops. There is less study focused on circularity in the foundry sector. Also, Türkiye should improve the collected data on waste and waste recycling. OIZs provide quick action possibilities for Türkiye, which are in the range of the Green Deal Programme of the EU and the Zero Waste Programme of Türkiye. Also, These OIZs bring Türkiye to the fore in actions within the scope of the CE. However, data collection of the foundry sector in Türkiye should be improved and classified in detail in order to generate value for evaluations. This study shows the current status of the circular economy in the metal foundry sector of the EU and Türkiye according to the basics of CE and other implementation examples.

References

- [1] J. Potocnik, "Towards the Circular Economy", Ellen MacArthur Foundation, 2013.
- [2] A. Valavanidis, "Concept and Practice of the Circular Economy", *Scientific Reviews*, sy July, 2018, [online]. acs.: <http://chem-tox-ecotox.org/concept-and-practice-of-the-circular-economy/>
- [3] A. Adam, "Circular economy: now or never", *Sostenibilidad*, 17 February 2021. <https://blogs.iadb.org/sostenibilidad/en/circular-economy-now-or-never/> (25 June 2022).
- [4] P. Ghisellini, C. Cialani, ve S. Ulgiati, "A review on circular economy: The expected transition to a balanced interplay of environmental and economic systems", *Journal of Cleaner Production*, c. 114, ss. 11-32, 2016, doi: 10.1016/j.jclepro.2015.09.007.
- [5] J. Kirchherr, D. Reike, ve M. Hekkert, "Conceptualizing the circular economy: An analysis of 114 definitions", *Resources, Conservation and Recycling*, c. 127, ss. 221-232, 2017, doi: 10.1016/j.resconrec.2017.09.005.
- [6] "Enhancing Circular Skills and Jobs Through Human Resource Management Training". <https://erasmus-plus.ec.europa.eu/node/4153> (29 June 2022).
- [7] "Skills and Competencies for a Circular Human Resources Management in the Foundry Sector". <https://erasmus-plus.ec.europa.eu/node/4153> (29 June 2022).
- [8] A. Heshmati, "A review of the circular economy and its implementation", *International Journal of Green Economics*, c. 11, sy 3-4, ss. 251-288, 2017, doi: 10.1504/IJGE.2017.089856.
- [9] Q. Z. Yang, J. Zhou, ve K. Xu, "A 3R Implementation Framework to Enable Circular Consumption in Community", *International Journal of Environmental Science and Development*, c. 5, sy 2, ss. 217-222, 2014, doi: 10.7763/ijesd.2014.v5.481.
- [10] P. Ekins, T. Domenech, P. Drummond, R. Bleischwitz, N. Hughes, ve L. Lotti, "The Circular Economy: What, Why, How and Where. Managing environmental and energy transitions for regions and cities", *OECD/EC Workshop on 5 July 2019 "Managing environmental and energy transitions for regions and cities" Paris*, ss. 1-89, 2019.
- [11] W. E. Forum, "Future of Reusable Consumption Models", World Economic Forum, 2021.
- [12] "A European Green Deal", *European Commission - European Commission*. https://ec.europa.eu/info/strategy/priorities-2019-2024/european-green-deal_en (29 July 2022).
- [13] M. Griboudo, D. Manini, M. Pironti, ve P. Pisano, "Circular Economy: A Performance Evaluation Perspective", *PervasiveHealth: Pervasive Computing Technologies for Healthcare*, ss. 196-199, 2020, doi: 10.1145/3388831.3388858.
- [14] L. Holappa, M. Kekkonen, A. Jokilaakso, ve J. Koskinen, "A Review of Circular Economy Prospects for Stainless Steelmaking Slags", *J. Sustain. Metall.*, c. 7, sy 3, ss. 806-817, Eyl. 2021, doi: 10.1007/s40831-021-00392-w.
- [15] T. A. Branca vd., "Reuse and recycling of by-products in the steel sector: Recent achievements paving the way to circular economy and industrial symbiosis in europe", *Metals*, c. 10, 2020, doi: 10.3390/met10030345.
- [16] "Life Effige - Environmental Footprint for Improving and Growing Eco-Efficiency", *Life Effige*. <https://www.lifeeffige.eu/> (erişim 29 Haziran 2022).
- [17] ASSOFOND, "Foundries and circular economy [FoundryGate]". <https://foundrygate.com/en/noticias/ver/5225/foundries-and-circular-economy> (29 June 2022).
- [18] M. Yalili Kiliç ve M. Tüylü, "Bursa'daki Atık Döküm Kumlarının Endüstriyel Simbiyoz İle Hazır Beton Üretiminde Ham Madde Olarak Kullanımı", *Uludağ University Journal of The Faculty of Engineering*, c. 24, sy 1, ss. 99-110, April 2019, doi: 10.17482/uumfd.463234.



OPTIMIZING THE AMOUNT OF FLUX USED IN THE CASTING PROCESS OF EN AW 6082 ALUMINUM ALLOY IN PROFILE PRODUCTION

Sena ERDOĞAN^{1,2}, Selçuk ERKUL, Zekeriya MUTLU¹, Rabia Şevval AKAN^{2,3}, Ayberk UZER^{2,3}, Muhammet ULUDAĞ^{2,3}

¹PMS Metal Profile Aluminum, ²Bursa Technical University, ³ULUCON R&D and Consulting Türkiye

Key Worlds: EN AW 6082, Degassing, Different Flux Amount, Bifilm Index, Liquid Metal Quality

Abstract

The use of quality melt is necessary to obtain a product with the high mechanical properties. In order to improve the quality of the molten metal, an efficient degassing process must be applied to remove slag and oxides from aluminum alloys prior to casting. In the degassing process, parameters such as gas, degassing time, degassing flow rate, amount of flux used affect the efficiency of the process. Various fluxes (casting chemicals) are used in order to remove oxidized structures, impurities and unwanted elements in the melt, to make the melt suitable for casting and to cut off its contact with the atmosphere. Within the scope of the study, the effect of the flux ratios used on the efficiency of the profile production process was examined. In this direction, all other parameters in the degassing process were kept constant, the effects of flux ratios at different rates were determined. In the study, EN AW 6082 aluminum alloy was used. In the degassing process, 3 different parameters (5, 8.5 and 10 kg) were applied. In line with the samples obtained, tests and analyzes such as bifilm index calculation, determination of density values, tensile test, hardness test, chemical analysis, microstructure analysis were carried out. In the results of working, the optimum flux usage amount was determined. The problems that occur as a result of the use of flux have been eliminated. Thus, a more efficient degassing process has been realized.

1. Introduction

Aluminum is a metal with high electrical and thermal conductivity, easy production, low specific gravity and high alloying properties [1]. Many desired properties can be added to aluminum by adding elements such as magnesium (Mg), silicon (Si), copper (Cu), zinc (Zn), nickel (Ni) and titanium (Ti) [2]. 6xxx series aluminum alloys with alloying elements Mg and Si have properties such as weldability, high formability, high corrosion resistance, high rolling and extrusion ability [3,4]. EN AW 6082 is the alloy with the highest strength

value among the 6xxx series aluminum alloys. Thanks to its features, it is frequently preferred in the automotive industry [5].

Aluminum liquid metal quality affects the final product's mechanical properties. The type of alloy or scrap used and the process applied affect the liquid metal quality. If a high-quality casting part is to be obtained, the gas content in the liquid metal must be minimized. In this direction, there are some applications such as degassing and the use of flux to clean the liquid metal [6-8]. Features such as the amount of flux to be used in the application, its chemical composition and morphology also affect the process [9]. The fluxing process is usually carried out by adding various compounds, chemicals and gases consisting of inorganic salts to the liquid metal. The purpose of the process is to reduce oxidation, to remove gases and inclusions from the liquid metal [10].

The aim of the study is to conduct research to optimize the amount of flux used in the casting process of the profiles to be produced using EN AW 6082 alloy. Studies were carried out with the use of flux at different rates.

2. Experimental Procedure

EN AW 6082 alloy was used within the extent of the study. Aluminum was melted at 705 ± 15 °C. After the melting process, the alloying process was carried out. It is ensured that the alloy is obtained in the desired chemical composition. In order to improve the liquid metal quality, degassing was applied. Degassing was carried out using nitrogen gas and flux. Within the extent of the study, the degassing process time was kept constant for 15 minutes. The use of flux at different rates, 5, 7.5 and 8.5 kg, was investigated. In order to determine the liquid metal quality, sampling was carried out in the reduced pressure test (RPT) mold simultaneously with the casting. In addition, samples were taken from the tensile test die. Obtained samples were subjected to microstructure examination, mechanical tests and

bifilm index analysis. In order to microstructure analysis, metallographic sample preparation steps were applied to the samples. Sample sizes were reduced by rough cutting. Then, the bakelite process was carried out to facilitate the surface preparation processes. The samples were sanded with grit numbers 400, 600, 800, 1200 and 2500. 6 and 1 micron diamond solutions were used for polishing. As a final step, the samples were etched with Keller's solution. Tensile tests were carried out in accordance with EN 755-2 standard. Eight repetitions were performed for each parameter. The analysis was done by taking the average of the obtained results. Brinell hardness test was applied to the samples. Hardness values of 55 HB with the addition of 5 kg flux, 55.33 HB with the addition of 7.5 kg flux and 53.33 HB with the addition of 8.5 kg flux were obtained. The densities of the samples obtained from the RPT mold were measured with the Archimedes principle. Then, the samples were divided into two in the middle and one surface was sanded. The surface was transferred to the computer using the scanner. Bifilm index analysis was realized on the image with the help of Sigma Scan program. Obtained results were calculated and interpreted.

3. Results and Discussion

The chemical composition of the EN AW 6082 alloy used in the study is given in Table 1.

Table 1. Chemical analysis of the Material (wt%)

Si	Fe	Cu	Mn	Mg
0,7-1,3	Max. 0,5	Max. 0,1	0,4-1	0,6-1,2
Cr	Zn	Ti	Al	
Max. 0,25	Max. 0,2	Max. 0,1	Rem.	

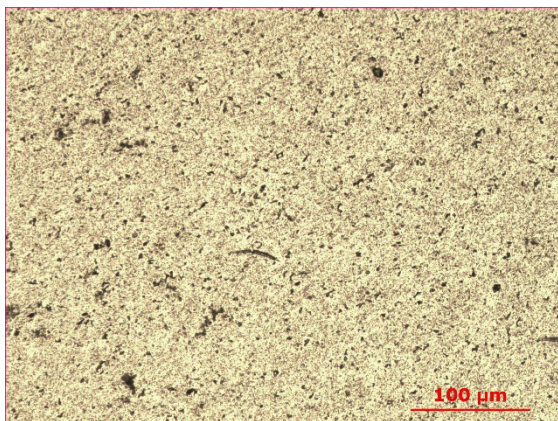


Figure 1. Representative microstructure images for 5 kg flux

The microstructure image obtained from the addition of 5 kg flux used in casting is given in Figure 1. When the microstructure image is examined, it is seen that the phase distribution is homogeneous. It is seen that equiaxial structures are obtained. It is seen that Mg₂Si phases precipitate in the microstructure. As a result of homogeneous distribution, acceptable values were obtained in mechanical values.

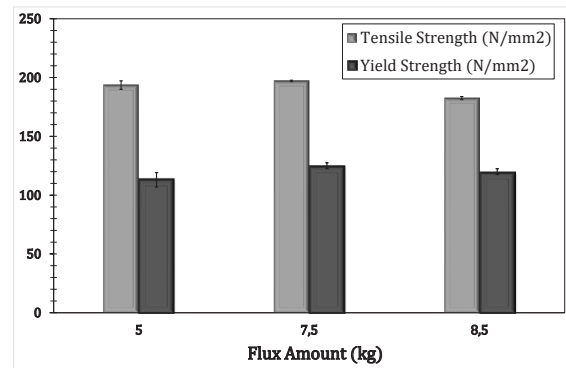


Figure 2. Tensile and yield strength values depending on different flux amounts

In Figure 2, the tensile strength and yield strength values obtained depending on different flux amounts are given. When the figure is examined, it is seen that the tensile strength values are 193.61 MPa with the use of 5 kg flux, 197.11 MPa with the use of 7.5 kg flux, and 182.53 MPa with the use of 8.5 kg flux. When the flux amount is increased from 5 kg to 7.5 kg, an increase in the tensile strength value occurs. With the increase of the flux amount to 8.5 kg, a decrease in the strength value occurs. In this case, it can be interpreted that the use of 8.5 kg flux damages the liquid metal. A similar situation is observed in the yield strength values. Strength values of 113.87 MPa at 5 kg, 124.80 MPa at 7.5 kg and 119.63 MPa at 8.5 kg were obtained.

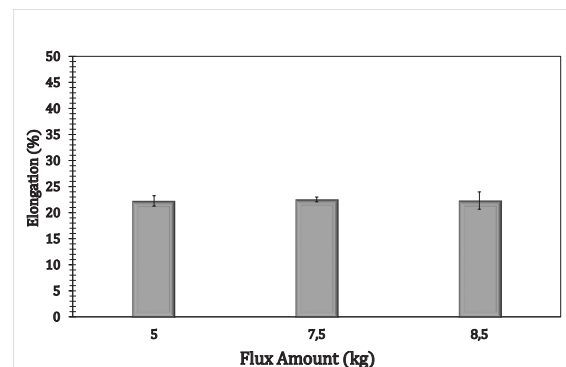


Figure 3. Elongation values obtained depending on different flux amounts

When Figure 3 is examined, the % elongation values were obtained as 22.25% in the addition of 5 kg flux, 22.54% in the addition of 7.5 kg of flux and 22.32%

in the addition of 8.5 kg of flux. The highest elongation value was obtained with the addition of 7.5 kg flux. The lowest elongation value was obtained with the addition of 5 kg flux.

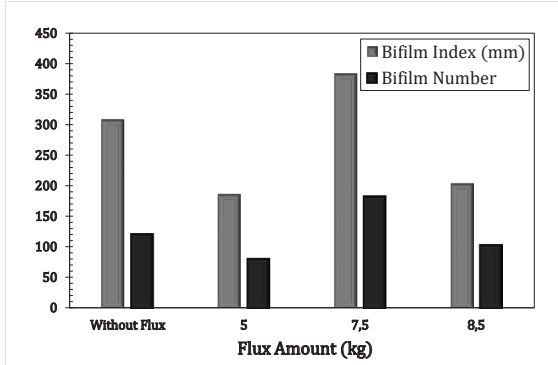


Figure 4. Bifilm index and bifilm number values obtained at different flux amounts

In Figure 4, bifilm index and bifilm number values are given depending on different flux amounts. When the data obtained are examined, it is seen that the bifilm index values of the alloy without flux addition decreased with the addition of flux. It is seen that the bifilm index length is at the lowest level with the addition of 5 kg flux, and the bifilm lengths increase with the increase in the flux ratio. Simultaneously, the number of bifilms increases with the increase of flux amount. Increasing the amount of flux reduces the quality of the liquid metal and damages the liquid metal. This can be understood by the increasing number and length of bifilms. For this reason, since the mechanical values are close to each other, it is appropriate to determine the 5 kg addition as the optimum parameter.

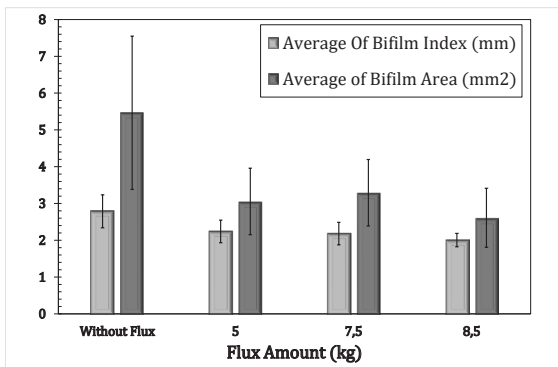


Figure 5. Average bifilm index and average bifilm area values depending on different flux amounts

Average bifilm index length and area values are given in Figure 5 depending on different flux ratios. When the values are examined, it is seen that the average bifilm index length values in liquid metal without flux are decreased with the addition of 5 kg flux. With the increase of flux addition, the average

bifilm index length values decrease. It is seen that for the average bifilm index area values, there is a decrease with the increasing amount of flux.

4. Conclusion

Within the scope of the study, the effect of using flux at different rates on the liquid metal quality was investigated. As a result of the work carried out;

- It has been observed that the use of flux with the degassing process has a higher liquid metal quality than the alloy without flux.
- Considering the mechanical values, it is seen that the results obtained from the addition of 7.5 kg of flux are higher compared to 5 kg. However, the values are close to each other.
- When the Bifilm values are examined, the values obtained from the addition of 7.5 kg are the highest values.
- Considering the bifilm values and mechanical values, it is thought that the optimum flux amount is 5 kg.

References

- [1] Shi-Gang X. And Li-Xin S., 2006. Composition and thermal properties of the coating containing mullite and alumina, *Materials Chemistry and Physics*, 97, 132–136.
- [2] Schultz, R. and W. Haupricht, Trends in aluminum use for passenger cars and light trucks in North America. *Light metal age*, 1999. 57(1-2).
- [3] Gavali M, Totik Y, Sadeler R. “The Effect of Artificial Aging on Wear Properties of AA 6063 Alloy”. *Materials Letters*, 57(24-25), 3713-3721, 2003.
- [4] Zvinys, J.,Kandrotaite Janutiene, R., Meskys, J., Juzenas, K., 2012, Investigation of thermo mechanical effect on structure and properties of aluminium alloy 6082, *Machines, Technologies, Materials : International Virtual Journal For Science, Technics And Innovations For The Industry*, 9, 3-6, Lithuania.
- [5] Zvinys, J., et al. Investigation of thermo mechanical effect on structure and properties of aluminium alloy 6082. In: *Scientific Proceedings IX International Congress on Machines, Technologies, Materials*. 2012. p. 13-16.
- [6] Zhao, Lei, et al. Degassing of aluminum alloys during re-melting. *Materials Letters*, 2012, 66.1: 328-331.



[7] Xu, Hanbing, et al. Degassing of molten aluminum A356 alloy using ultrasonic vibration. *Materials letters*, 2004, 58.29: 3669-3673.

[8] Utigard, T. A. The properties and uses of fluxes in molten aluminum processing. *Jom*, 1998, 50.11: 38-43.

[9] Majidi, O.; Shabestari, S. G.; Aboutalebi, M. R. Study of fluxing temperature in molten aluminum refining process. *Journal of Materials Processing Technology*, 2007, 182.1-3: 450-455.

[10] Gaustad, Gabrielle; Olivetti, Elsa; Kircham, Randolph. Improving aluminum recycling: A survey of sorting and impurity removal technologies. *Resources, Conservation and Recycling*, 2012, 58: 79-87.



REDUCING THE ENERGY COSTS FOR GREEN CONVERSION BY COATING THE SURFACES OF THE CRUCIBLES USED IN HPDC METHOD WITH BORON REINFORCEMENT CELLULOSE

Ümmet AYYILDIZ^{1,2}, Songül KILINÇ^{1,3}

¹Prometal, ²Bilecik Şeyh Edebali University, ³Bursa Technical University
Türkiye

Keywords: Aluminum Casting, High Pressure Casting Method, Holding Furnace, Cellulose Added Boron, Coating Process.

Abstract

Due to their weight/strength properties, aluminum alloys are widely used in the automotive, aviation, home appliance, hardware, etc. sectors, where weight reduction is very important. In addition to the production of aluminum alloys with various production methods, high pressure casting method (HPDC) is widely preferred in terms of its suitability for mass production. The melted liquid metal in the melting pot is taken to the holding pot and kept at a constant temperature value. While the liquid metal is kept in the crucible, it is necessary to keep the crucible at a constant temperature in order to prevent problems that will affect the product quality due to the frequent wear of the materials on the surfaces of the crucible, and most importantly, the high heat transfer inside the crucibles. It takes a lot of energy for this system. It is desired to reduce this excess energy and the associated cost. In this study, in order to reduce the carbon footprint and reduce energy costs within the scope of sustainability, cellulose added boron material was coated as an intermediate layer in the crucible. In order to carry out the trials, a crucible was built in the size that the applications can be made. The inner surface of the crucible is filled with coating material. The coating material consists of cellulose wool obtained from the recycling of newspaper papers and boron additives produced entirely by domestic means. The coating material is natural, organic and also has heat and sound insulation properties. As long as it does not come into direct contact with the liquid metal, its thermal insulation and flammability are very low. In addition to having a low thermal conductivity coefficient, it provides high efficiency thermal insulation by keeping the heat of the air-conditioned environments for a longer time with its high heat storage capacity. In the sound

tests, it was seen that as the thickness increases according to the coating thickness, the sound permeability of the crucible improves by 30%, while it provides significant gains in thermal insulation. While the study continues, it is thought that it will provide a significant gain, especially in terms of sustainability and energy costs, especially when evaluated in terms of sectoral preference.

Introduction

High-pressure die casting (HPDC) is especially suitable for high production rates, and it is applied in several industrial fields; actually, approximately half of the world production of light metal castings is acquired by this HPDC technology. This process is used to produce nonferrous and low-melting point base alloys parts, thus aluminium, zamak, brass and tin [1] These constituents can range from a few grams up to 25 kg [2]. In the HPDC of aluminum alloys, cold chamber die casting machines are typically used, in which the metal injection system is only in contact with the molten metal for a short period. Liquid metal, maintained in a holding pot at a production temperature [1]. By using high speed along with high pressures to inject liquid metal into a die, a reusable metallic mould, thin-walled products with high geometry complexity and surface hardness (SH) [3], excellent surface finish (by casting standards) [4]. All these extraordinary conditions that the molten metal is exposed and the difficulty to maintain process parameters make HPDC a failure creative process [5]. Well know that abrasion is one of most common failure for refractory used in light high metal melting crucible And this solid particles are added in rapidly moving molten aluminium [6]. In the other hand, While the liquid metal is kept in the crucible, it is necessary to keep the crucible at a constant temperature in order to prevent

problems that will affect the product quality due to the frequent wear of the materials on the surfaces of the crucible, and most importantly, the high heat transfer inside the crucibles. This physical process, can be defined as the second law of thermodynamics. In 1850, Clausius described the law with an expression that it is impossible to construct a device that operates in a cycle and produces no effect other than the transfer of heat from a cold body to a high body [7]. For this reason, it is necessary to keep the crucible at a constant temperature in order to prevent problems that will affect the product quality due to the high heat transfer in the ladle.

Automotive manufacturing is energy-intense process which consumes a significant quantity of raw materials. To sustain competitive, automotive original equipment manufacturers (OEMs) have to strive for outperform product quality by continuously improving their production process and driving towards low-carbon emissions and enhanced sustainability [8].

Experts have argued that a transition genuinely based on sustainability, equity, and capability [9] Zero carbon emissions are included in the 2030 targets of all countries, especially the United Nations. [10,11]. We need to reduce our carbon emissions in order to exist in the whole world order and to create our products under the standards determined by our supplies. We must do our duty for future generations.

In this study, in order to reduce the carbon footprint and reduce energy costs within the scope of sustainability, cellulose added boron material was coated as an intermediate layer in the crucible. With this process, thermal insulation in the crucibles will be ensured and excess energy consumption will be stopped. Thus, an increase in the wear times on the crucibles will be detected. Accordingly, the crucible costs will decrease. Most importantly, reductions in the energy values spent will be detected.

Experimental Procedure

Studies will be carried out for the use of cellulose added boron material, which is supplied from YALIBOR company, which can provide heat, sound, fire ve dump insulation at the same time, in the casting sector and industrially.



Figure 1. Cellulose added boron material

It consists of cellulose wool obtained from the recycling of waste newspaper paper and Boron additives produced entirely with domestic facilities.

This material thermal conductivity value of cellulose added boron is $\lambda = 0.037 \text{ W/m.K}$. With its low thermal conductivity coefficient and high heat storage capacity, it retains the heat of the air-conditioned environments for a longer period of time and performs high-efficiency thermal insulation. The heat permeability resistance is $1.35 \text{ m}^2\text{K/W}$ at 50 mm thickness. As a result of the application, high efficiency results are obtained without the formation of a thermal bridge. It can be applied by spraying method for insulation purposes on roof, ceiling, floor, wall and similar places. Acoustically sound absorption is excellent. Sound absorption coefficient is 1.0- sound absorption class A. It has a soundproof feature up to 70dB when used with suitable building elements and appropriate thickness.

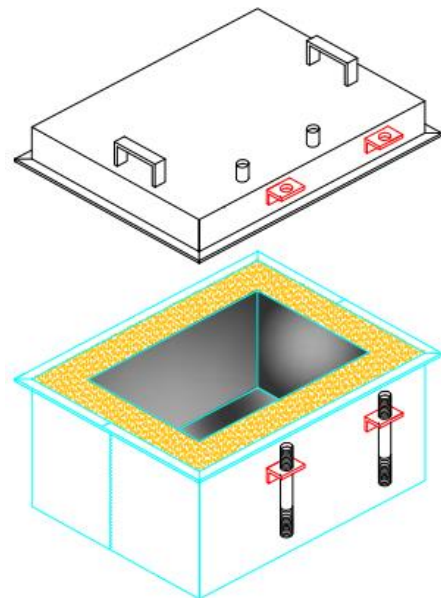


Figure 2. technical drawing of the crucible

In order to carry out experiments and to observe the change of heat transfer depending on the time, the construction was carried out by designing a pot (Figure 3) Cellulose-added boron material is sandwiched between the outer and inner parts of the crucible. The heat transfer test will be done in this crucible.



Figure 3. A - Cellulose added boron material, B - Inner surface of the crucible

A system was set up for sound insulation tests and tests were carried out under the same conditions using insulation materials of different thicknesses. It is designed to have a carrying cover on the crucible from both sides. The melting process will be done with the help of the resistances placed in the cover area. Temperature measurements will be made with a thermocouple to be placed from the cover to the inside.



Figure 4. a) Experiment box with a 5 cm interlayer, b) Experiment box with a 10 cm interlayer

The sound experiment was carried out by creating an intermediate block with a thickness of 2.5cm, 5cm, 7cm and 10cm in a closed experiment box (Figure 4).

Results and Discussion

The abbreviations based on sound test results are listed below.

The sound experiment was repeated 3 times and the average was taken. Experiments were repeated in the same quiet environment.

Table 1. Ambient sound value according to thickness (dB)

A(cm)	B _I (dB)	B _{II} (dB)
2,5	100,90	99,43
5	88,20	86,60
7,5	86,67	87,57
10	87,03	85,63

Parameters

A: Thickness

B_I: Cellulose added boron materials

B_{II}: Pressed cellulose added boron materials

Ambient sound measurement = 49 dB

Ambient sound measurement with alarm= 110,5 dB

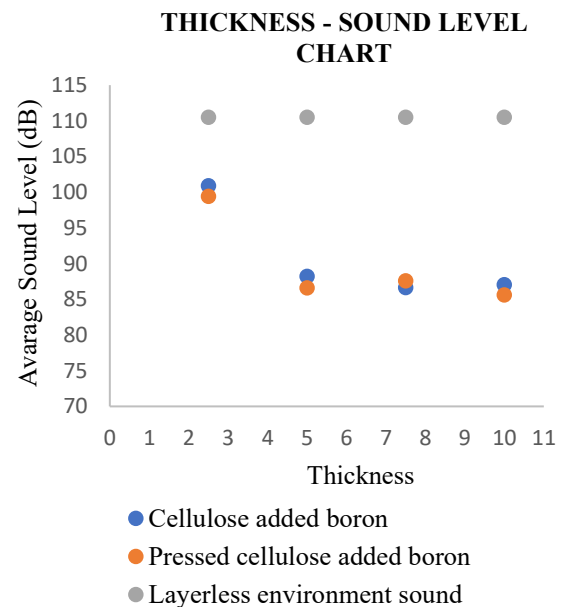


Figure 4. Comparison of average sound values with thickness

In sound trials, pressed cellulose added boron materials trials gave better results than unpressed cellulose added boron materials.

The liquid metal placed in the crucible covered with the coating will be melted, closed at the specified temperature, and the amount of heat lost in the specified time will be calculated. The same process will be applied for the uncoated crucible.

Conclusion

It was concluded that the sound absorption measurements made by creating a barrier with pressed cellulose-doped boron are much better than the measurements made without a barrier. With the cellulose-doped boron layer, the ambient sound value provided 30% absorption.

These studies have been carried out in order to reach the zero carbon target, which is among the targets in 2030, to put a stop to the climate crisis in the world and to minimize our carbon footprint.

With this system change in the crucibles, we plan to reduce our carbon footprint target by 25% for the end of 2022.

Acknowledgment

We would like to thank all the PROMETAL family who contributed to the construction of our works. In addition, we would like to thank YALIBOR for their contributions and guidance.

References

- [1] Larsen, D., & Colvin, G. (1999). Vacuum-Die casting titanium for aerospace and commercial components. *JOM*, 51(6), 26-27.
- [2] Vinarcik, E. J. (2002). *High integrity die casting processes*. John Wiley & Sons.
- [3] Singh, R. (2014). Modeling of surface hardness in hot chamber die casting using Buckingham's π approach. *Journal of Mechanical Science and Technology*, 28(2), 699- 704. doi:10.1007/s12206-013-1133-4.
- [4] Peti, F., & Grama, L. (2011). Analyze of the possible causes of porosity type defects in aluminium high pressure diecast parts. *Scientific Bulletin of the "Petru Maior" University of Targu Mures*, 8(1), 41.
- [5] Bonollo, F., Gramegna, N., & Timelli, G. (2015). High-Pressure Die-Casting: Contradictions and

Challenges. *JOM*, 67(5), 901-908. doi:10.1007/s11837-015-1333-8

[6] Ntakaburimvo, N., & Allaire, C. (2004). Abrasion wear of aluminosilicate refractories. *CIREP-CRNF, Ecole Polytechnique, Montreal*.

[7] Zhao, K. H., & Luo, W. Y. (2002). *Thermotics*. Beijing: Higher Education Press, 1–222

[8] Vaz, C. R., Rauen, T. R. S., & Lezana, Á. G. R. (2017). Sustainability and innovation in the automotive sector: A structured content analysis. *Sustainability*, 9(6), 880.

[9] UNFCCC. The Paris Agreement. United Nations Framework Convention on Climate Change. In *Proceedings of the 21st Paris Climate Change Conference, Paris, France, 12 December 2015*; Available online: <https://unfccc.int/documents/9064> (accessed on 6 April 2016).

[10] Anderson, K., Broderick, J. F., & Stoddard, I. (2020). A factor of two: how the mitigation plans of 'climate progressive' nations fall far short of Paris-compliant pathways. *Climate Policy*, 20(10), 1290-1304.

[11] Jackson, T. (2019). Zero Carbon Sooner—the case for an early zero carbon target for the UK. *CUSP Working Paper No. 18*.



MICROSTRUCTURE EVOLUTION OF THE THREE-PHASE Al-Al₂Cu- Ag₂Al EUTECTIC SYSTEM UPON DIRECTIONAL SOLIDIFICATION

Merve KEVKİR¹, Arash KAZAZİ², Samira MOHAGHEGHİ³, Melis ŞEREFÖĞLÜ¹

¹Marmara University, ²Koç University, ³Istinye University
Türkiye

Keywords: Solidification, crystal growth, eutectics, interphase boundaries, directional solidification

1. Introduction

Fundamental understanding of the microstructure formation during solidification is of interest from scientific and practical perspectives since the microstructure determines many properties of the materials. In addition to the process parameters such as the choice of solidification method, velocity, and temperature gradient, gravity-induced effects have dramatic impacts on microstructure formation. While many studies have been focused on single-phase and two-phase microstructures, the microstructure evolution during the solidification of multi-phase alloy systems is less understood. The multiplicity of phases and associated interphase boundaries makes it more difficult to understand the formation dynamics of complex solidification microstructures. In this study, Al-Al₂Cu-Ag₂Al three-phase eutectic system is used as a model alloy to tackle questions on multi-phase microstructure formation under microgravity conditions. The existence of an invariant ternary eutectic point, as well as reliable thermodynamic databases, make this system an ideal one to investigate the evolution of three-phase eutectic microstructures.

2. Materials and Methods

Bridgman-type setup was utilized to directionally solidify cylindrical samples at a constant temperature gradient and various velocities. The solidified samples were metallographically prepared for microstructural analysis. The existence of three phases and three interphase boundaries leads to various complex microstructure formation which in turn results in challenges in the quantitative characterization of the microstructures. We first developed a method to define the eutectic spacing in the most observed microstructure, so-called chain-like structure, and correlated the eutectic spacing to the solidification velocity. Subsequently, we defined morphological parameters to distinguish various microstructures. In addition to the effect of the experimental control parameters (Ex: velocity) on the microstructure, we observed a severe effect of gravity *i.e.* on Earth, under 1g conditions, elemental segregation and enhanced convection in the liquid resulted in different microstructures than the ones obtained in space, under microgravity conditions. This effect was more pronounced in the experiments that were run for a relatively long time.

3. Conclusion

On Earth, under 1g conditions, thermo-solutal convection and buoyancy forces affect the microstructure evolution severely. Understanding the three-phase eutectic growth and characterization of the solidification microstructures without eliminating the effects of gravity would be deficient. Therefore, this alloy system is used to perform directional solidification experiments on board of the International Space Station (ISS) under μ g condition. Preliminary data analysis shows that the most observed microstructure, *i.e.* chain-like structure, was formed under μ g condition as well. Ongoing investigations on μ g-microstructures along with the analysis of the microstructures obtained under 1g conditions shall shed light on the formation and stability of the various three-phase eutectic microstructures. A better fundamental understanding of three-phase microstructure formation and evolution will provide the physical data essential to the development of models, which will, in turn, further improve our capability to explore, control, and design materials with original microstructures and outstanding properties.

OPTIMIZATION OF THE HEAT TREATMENT PARAMETERS DEPENDING ON THE THICKNESS IN PLATE PRODUCTS MADE OF EN AW 1050 AL ALLOY

Sena ERDOĞAN^{1,2}, Selçuk ERKUL¹, Zekeriya MUTLU¹, Rabia Şevval AKAN^{2,3}, Ayberk UZER^{2,3}, Muhammet ULUDAĞ^{2,3}

¹PMS Metal Profile Aluminum, ²Bursa Technical University, ³ULUCON R&D and Consulting Türkiye

Keywords: EN AW 1050 Al Alloy, Heat Treatment, Plate Production, Mechanical Properties, Microstructure.

Abstract

Many of the engineering metals and alloys become industrially usable after one or more heat treatments. Heat treatment is a process applied to improve the mechanical properties (hardness, strength, etc.) of metals. Aluminum sheet material can be produced in many different thicknesses according to the usage area. Plates with different thicknesses produced from the same alloy should be heat treated with different parameters, because as it is known, the thickness of the material is one of the parameters affecting the heat treatment. Within the scope of the study, optimization of the heat treatment process parameters to be applied to 0.80 mm and 1.65 mm thick plate products made of EN AW 1050 (H24 condition) aluminum alloy used in the plate production facility was provided. The heat treatment parameters to be applied are: temperature parameter of 270 °C and 280 °C, and time parameter of 3 and 6 hours for each temperature. Mechanical and chemical tests and analyzes (bifilm index calculation, density calculation, tensile test, hardness test, chemical analysis, microstructure analysis) were applied to the non-heat-treated and heat-treated samples. As a result, optimum heat treatment temperature and duration were determined for plates with different thicknesses.

1.Introduction

Aluminum and its alloys have desirable properties such as lightness, corrosion resistance, durability, good thermal property, good electrical conductivity. Due to these properties, it is the preferred engineering material in the industry (electrical-electronics, defense, construction, food industry,..) [1-3]. 1xxx series Al alloys are alloys with a purity of 99.00% or higher. They are widely preferred in the fields of electricity and chemistry, thanks to their corrosion resistance, high thermal and electrical conductivity, and excellent machinability [4]. In addition, 1050 Al alloys are widely used in electrical coatings and thermal insulation [5]. In addition, this group of Al alloys is used in the aerospace and automotive industries because it has a high strength-to-weight ratio and high wear resistance [6].

The twin roll continuous casting process (TRC) is used for the production of flat rolled products used in many different industries. The continuous casting method, in which net shaped products close to the final product shape can be produced, causes high capital costs and also has a low operating cost [7,8]. With this process, less deformation and mechanical operations are required, which gives the continuous casting process an advantage in terms of energy and cost compared to other alternative processes [9]. Compared to the traditional casting method, the productivity is 15-20% higher and the material consumption is 1.5-2% lower [10]. When the literature is examined, studies have been carried out on process optimization for thermomechanical and annealing processes in aluminum alloys produced by TRC method [11,12]. In these studies, concentration changes that usually occur during TRC were investigated.

In this study, optimization of the heat treatment process parameters to be applied to 0.80 mm and 1.65 mm thick plate products made of EN AW 1050 (H24 condition) aluminum alloy has been achieved.

2.Experimental Procedure

In the study, EN AW 1050 aluminum alloy was used. The representation of the chemical composition of the alloy according to the TS EN 573-3 standard is given in Table 1. The melting process was carried out in a 25-ton furnace. The temperature of the melt is 817 °C.

Table 1. Chemical composition values of EN AW 1050 alloy - according to TS EN 573-3 standard (wt%)

Si	Fe	Cu	Mn	Mg	Cr	Ni	Zn	Ti	Ga	V	Al
0.25	0.4	0.05	0.05	0.05	-	-	0.07	0.05	-	-	99.5

In order to improve melt quality, degassing was applied. The degassing process was carried out using nitrogen gas for 10 min (by using 8-12 kg flux). RPT samples were taken using the RPT device before and after degassing. Then the melt was transferred to the holding furnace with a capacity of 15 tons. The temperature of the melt transferred to the holding furnace is 800 °C. The degassing process was carried out in the melt transferred to the holding furnace

(with the use of nitrogen gas for 10 minutes and the use of 5-7 kg flux.). RPT samples were taken before and after degassing in the holding furnace. The liquid metal was transferred to the rollers and rolled into coils. The rolling process of the coils was carried out in three steps. The final thickness of 0.80 mm and 1.65 mm was obtained in the last step. After the rolling process, samples were taken for testing and analysis. Some of the samples were annealed under different parameters. The annealing parameters are as follows; 3 and 6 hours at 270 °C, 3 and 6 hours at 280 °C. Tests and analyzes such as density measurements, bifilm index calculation, microstructure analysis, chemical analysis, hardness test, tensile test were carried out on the untreated and heat-treated samples. Tensile test specimens were prepared according to TS EN ISO 6892-1 standard. The conformity of the results of the tensile test and hardness tests was examined according to the TS EN 485-2 standard. Interpretation was made by taking the average of the numerical results obtained.

3. Results and Discussion

3.1 Chemical analysis measurements

In Table 2, the chemical analysis values obtained from the product with a thickness of 0.80 mm are given. When the measurements are examined, it is noticed that the AI values are in the desired value band in all three measurements. When the values are examined, it is seen that the obtained values are at the rate of 99.5%.

Table 2. Chemical analysis values obtained for 0.80 mm thickness (wt%)

Analyzes	Si	Fe	Cu	Mn	Mg	Cr	Ni	Zn	Ti	Ga	V	AI
1.	0.138	0.234	0.004	0.017	0.0053	0.0009	0.0037	0.0029	0.024	0.01	0.019	99.517
2.	0.138	0.236	0.0041	0.017	0.0053	0.001	0.0035	0.0024	0.024	0.01	0.019	99.514
3.	0.137	0.234	0.0037	0.017	0.0052	0.0007	0.0032	0.0026	0.024	0.01	0.02	99.52

Table 3 shows the chemical analysis values obtained from the material with a thickness of 1.65 mm. When the measurements are examined, it is seen that the AI values are close to the desired value in all three measurements. The values obtained are 99.5%.

Table 3. Chemical analysis values obtained for 1.65 mm thickness (wt%)

Analyzes	Si	Fe	Cu	Mn	Mg	Cr	Ni	Zn	Ti	Ga	V	AI
1.	0.129	0.215	0.0032	0.011	0.0037	0.0002	0.0035	0.0024	0.027	0.01	0.018	99.554
2.	0.132	0.212	0.0035	0.011	0.0034	0.0003	0.0036	0.002	0.025	0.0098	0.018	99.554
3.	0.13	0.212	0.0034	0.011	0.0033	0.0002	0.0036	0.0019	0.026	0.0099	0.018	99.556

3.2 Density measurements

In Figure 1, the density values of the RPT samples taken from the melting and holding furnace are shown. The lowest density value was obtained from the melting furnace (2.4 g/cm³). The highest value belongs to the sample taken from the holding furnace (2.64 g/cm³). A total of 2 degassing processes were applied to the melt in the holding furnace. Therefore,

the amount of oxide in the melt in the holding furnace is less. As a result, the density value of the melt in the holding furnace is higher.

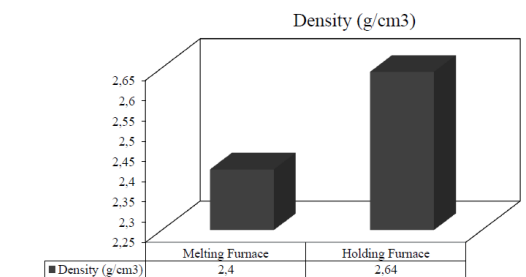


Figure 1. Density values of samples taken from melting and holding furnace

3.3 Bifilm index values

In Table 4, the bifilm index, bifilm number and total bifilm area values of the RPT samples taken from the melting and holding furnace are given. The highest value belongs to the sample before degassing from the melting furnace (69.48 mm). The lowest bifilm index value is 14.56 mm, this value was obtained from the RPT sample taken after degassing from the holding furnace. Dispinar, many studies have been carried out on aluminum alloys and he has revealed a scale [13,14]: 0-10 mm is the best quality, 10-50 mm is good quality, 50-100 mm is medium, 100-200 mm is bad, 200 and above is very bad. Considering that the obtained bifilm index number is 14.56 mm, it is determined that the melt quality is a good quality melt.

Table 4. Bifilm index values of RPT samples taken from the melting and holding furnace

		Bifilm Index (mm)	Number of Bifilms	Total Bifilm Area (mm ²)
Melting Furnace	Before Degassing	69.476	41.667	68.567
	After Degassing	61.643	33.2	65.211
Holding Furnace	Before Degassing	21.51	15.667	9.318
	After Degassing	14.558	11.75	5.422

3.4 Microstructure analysis

In Figure 2, the microstructure images of the unheated and heat-treated samples with thicknesses of 0.80 mm and 1.65 mm are shown. When the images without heat treatment in the figure are examined, it is noticed that the phase particles are aligned in the direction of the rolling. It can be noticed from the visual that the obtained structures exhibit heterogeneous distribution. When the microstructure image of the samples (Figure 2-b-g) subjected to heat treatment at 270 °C for 3 hours is examined, it is noticed that the grains are finer and coaxial. In the microstructure image of samples subjected to heat treatment for 6 hours at 270 °C (Figure 2-c-h), the presence of finer grains and the homogeneous distribution of the structure are noticed. For 0.80 mm thickness; It can be said that

the particle size decreased and the number increased in the 3 hour parameter at 280 °C (Figure 2-d). It is noticed that the grains in the microstructure at 6 hours at 280 °C begin to coarsen (Figure 2-e). For 1.65 mm thickness; There is heterogeneous distribution in the microstructure (Figure 2-i) of the sample, which was heat treated at 280 °C for 3 hours. It can be said that the particle size decreased and the number increased in the 6 hour parameter at 280 °C (Figure 2-j).

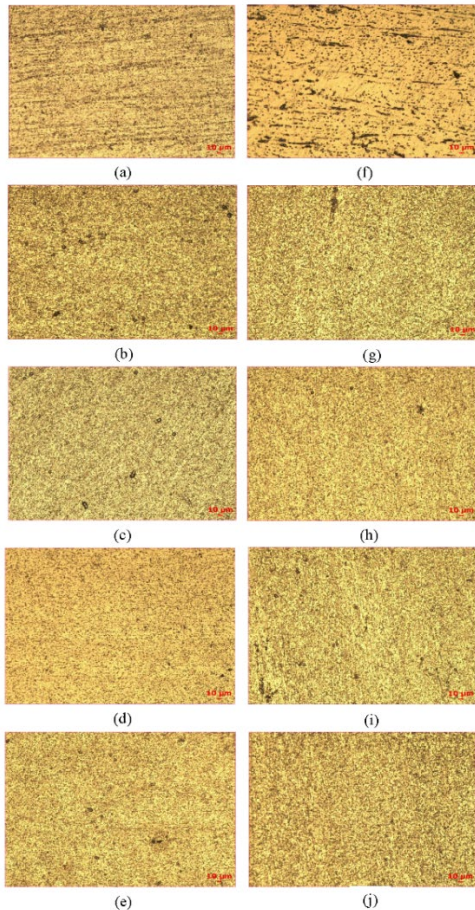


Figure 2. Optical microscope images taken under 200x magnification. 0.80 mm thickness: (a) No heat treatment (b) 270°C-3 hours, (c) 270°C-6 hours, (d) 280°C-3 hours, (e) 280°C-6 hours; 1.65 mm thickness: (f) Without heat treatment (g) 270°C-3 hours, (h) 270°C-6 hours, (i) 280°C-3 hours, (j) 280°C-6 hours

3.5 Tensile test

Figure 3 shows the tensile strengths of the untreated and heat-treated samples under different parameters. The highest tensile strength value was obtained from the sample with a thickness of 0.80 mm and without heat treatment, the value is 189.216 MPa. The lowest tensile strength value belongs to the sample with a thickness of 0.80 mm, which was heat treated at 280 °C - 6 hours (125.346 MPa). When the values are examined in general, the plate product with a thickness of 0.80 mm has a higher value in all parameters except the 280°C-6 hours heat treatment

parameter. The obtained values are compatible with the literature. To explain; When the annealing time is kept constant and the temperature is increased, the tensile strength decreases. When the annealing temperature is increased, the dislocations are activated and the tensile strength of the material decreases [15]. In another study, it was observed that the strength of the materials decreased as the annealing time increased [16].

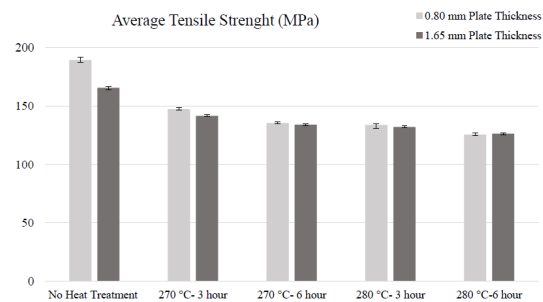


Figure 3. Tensile strength values of samples

Figure 4 shows the yield strength values of the samples that were not heat treated and heat treated in different parameters. When the values were examined, the highest yield strength value was obtained from the 0.80 mm thick sample without heat treatment (179.31 MPa). The lowest value belongs to the sample with a thickness of 0.80 mm and heat treated at 280 °C for 6 hours (115.364 MPa). When the samples taken from cold rolling are compared; It is seen that the yield strength of the 0.80 mm thick material is higher than the 1.65 mm thick material. This situation is compatible with the study examined in the literature, because the material with a thickness of 0.80 mm is subjected to more deformation, so the dislocation density occurring in the material is higher. This prevents the dislocation movement and plastic deformation of the material becomes difficult [17].

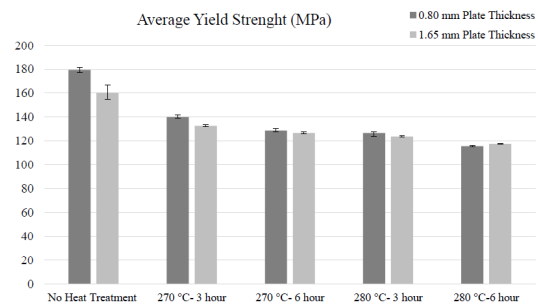


Figure 4. Yield strength values of samples

In Figure 5, the % elongation at break values of the samples without heat treatment and with different heat treatment parameters are shown. When the values were examined, the lowest elongation at break value was obtained from the 0.80 mm thick

sample without heat treatment (4.304 %). The highest elongation at break was obtained from the sample with a thickness of 0.80 mm, and the value was 14.642 %. It has been stated in the literature that with increasing temperature, the materials become ductile and increase in % elongation values [18]. When the results are evaluated in general, it is confirmed that they are compatible with the literature.

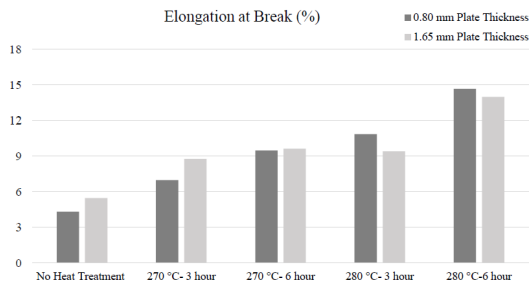


Figure 5. Elongation at break (%) values of samples

Figure 6 shows the hardness values of the samples obtained after the hardness test. When the graph is examined, it is noticed that samples with a thickness of 0.80 mm have higher hardness values than samples with a thickness of 1.65 mm. It is determined that the hardness value range of the samples with a thickness of 0.80 mm is between 60 and 40 HB. It can be seen from the graph that the hardness values of the sample with a thickness of 1.65 mm are between 57-39 HB.

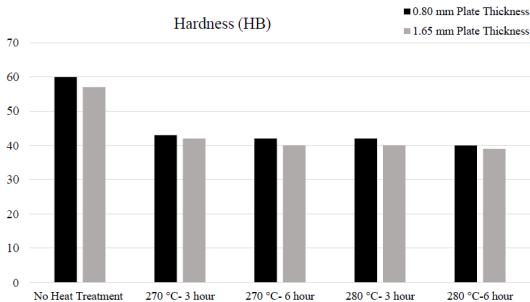


Figure 6. Hardness values values of samples

4. Conclusion

Within the scope of the study, optimization of the heat treatment process parameters of 0.80 mm and 1.65 mm thick plate products produced from EN AW 1050 aluminum alloy used in plate production was carried out.

In the experimental results, it was found that the yield and tensile strength values of 1050 aluminum alloy (with H24 condition) decreased when the annealing time was kept constant and the annealing temperature was increased, the % elongation at break increased. It was observed that the strength value of the materials decreased when the annealing time at constant temperature increased.

When the mechanical results and microstructure images of the annealing process at different temperatures and times are compared with each other, it is determined that the efficient annealing temperature is 270 °C and the annealing time is 6 hours in both thicknesses. Because; When the mechanical results were compared according to the TS EN 485-2 standard, it was determined that the tensile strength values of the samples that were heat treated for 3 hours at 270 °C were not within the standard range. The values obtained at other annealing temperatures and times are in compliance with the standards. However, since the temperature values are higher than 270 °C, it is determined that the efficient parameter is 270 °C 6 hours in order to take advantage of the temperature and time.

References

- [1] Cengiz, N. M. (2018). İkiz merdane yöntemi ile 1XXX serisi ve 3XXX serisi alüminyum levha üretimindeki proses parametrislerinin özellikler üzerindeki etkisi (Master's thesis, Kütahya Dumlupınar Üniversitesi/Fen Bilimleri Enstitüsü).
- [2] Rooy, E. L., & Kaufman, J. G. (2004). Aluminum Alloy Castings: Properties, Processes, and Applications (No. B-ASM-002). SAE Technical Paper.
- [3] Marsh, K., & Bugusu, B. (2007). Food packaging—roles, materials, and environmental issues. *Journal of food science*, 72(3), R39-R55.
- [4] Davis, J. R. (Ed.). (2001). *Alloying: understanding the basics*. ASM international.
- [5] Emley, E. F. (1976). Continuous casting of aluminium. *International metals reviews*, 21(1), 75-115.
- [6] Stojanovic, B., & Epler, I. (2018). Application of aluminum and aluminum alloys in engineering. *Applied Engineering Letters*.
- [7] Yun, M., Lokyer, S., & Hunt, J. D. (2000). Twin roll casting of aluminium alloys. *Materials Science and Engineering: A*, 280(1), 116-123.
- [8] Barekar, N., & Dhindaw, B. (2014). Twin-roll casting of aluminum alloys—an overview. *Materials and manufacturing processes*, 29(6), 651-661.
- [9] Sanders, R. E. (2012). Continuous casting for aluminum sheet: a product perspective. *JOM*, 64(2), 291-301.
- [10] Ahmed, M. I. (2017). Increasing Of Aluminum Continuous Casting Line Production Quality Via Improvement Of The Control Of Technological Parameters. *Journal Of Chemical Technology And Metallurgy*, 52(2), 235-241.

- [11] Sun, N., Patterson, B. R., Suni, J. P., Simielli, E. A., Weiland, H., & Allard, L. F. (2006). Microstructural evolution in twin roll cast AA3105 during homogenization. *Materials Science and Engineering: A*, 416(1-2), 232-239.
- [12] Zhou, S. X., Zhong, J., Mao, D., & Funke, P. (2003). Experimental study on material properties of hot rolled and continuously cast aluminum strips in cold rolling. *Journal of materials processing technology*, 134(3), 363-373.
- [13] Dispınar, D., & Campbell, J. (2007). Effect of casting conditions on aluminium metal quality. *Journal of materials processing technology*, 182(1-3), 405-410.
- [14] Dispınar, D., & Campbell, J. (2011). Porosity, hydrogen and bifilm content in Al alloy castings. *Materials Science and Engineering: A*, 528(10-11), 3860-3865.
- [15] Aydın, H., Gören, R., & Cengiz, N. M. (2020). İkiz Merdane Yöntemi İle 1xxx Serisi Alüminyum Levha Üretimindeki Proses Parametrelerinin Özellikler Üzerindeki Etkisi. *Mühendislik Bilimleri ve Tasarım Dergisi*, 8(1), 146-152.
- [16] Demiray Cucurachi, Y. İkiz merdane döküm yöntemi ile alüminyum AA5754 alaşımı levha üretimi, döküm ve termomekanik proses parametrelerinin etkilerinin araştırılması (Doctoral dissertation, Fen Bilimleri Enstitüsü).
- [17] Akdoğan, V. U., Işıksaçan, C., Altuner, H. M., Birbaşar, O., & Günyüz, M. (2019). Influence of Strip Thickness on As-Cast Material Properties of Twin-Roll Cast Aluminum Alloys. In *Light Metals 2019* (pp. 1137-1141). Springer, Cham.
- [18] Davis, J. R. (Ed.). (2001). *Alloying: understanding the basics*. ASM international.

UNDERSTANDING THE SOLIDIFICATION DYNAMICS OF COMMERCIAL ALUMINIUM ALLOYS PRODUCED BY TWIN-ROLL CASTING

Arash KAZAZI¹, Onur MEYDANOĞLU², Cemil IŞIKSAÇAN²,
Hatice MOLLAOĞLU ALTUNER², Melis ŞEREFİOĞLU³

¹Koç University, ²Assan Alüminyum, ³Marmara University
Türkiye

Keywords: Directional solidification, Twin-roll casting, Rapid solidification, Microstructure evolution, Aluminum alloys

1. Introduction

Twin-roll casting (TRC) is a proven technology for producing aluminum sheets. In TRC, due to the nature of the process, the cooling rate differs through the thickness of the sheet metal. The microstructure, and therefore, properties are strongly affected by this difference. The change in the cooling rate encountered through the thickness of the rapidly solidifying metal results in heterogeneous distribution of secondary phase particles (SPP) which have various morphological features. Unfortunately, there is no detailed study that directly relates the effects of cooling rate on microstructure evolution through the thickness of the TRC strips. In this study, Bridgman-type directional solidification (DS) setup with liquid metal cooling (LMC) was used to achieve high cooling rate values to be able to mimic the microstructure and hence, estimate the through-thickness cooling rates of commercial 1xxx and 8xxx aluminum alloys produced by the TRC process.

2. Materials and Methods

1xxx and 8xxx commercial aluminum alloys with and without grain refiner were used for this study. Cylindrical samples with 5 mm diameter were directionally solidified with velocities 1, 10, 25 and 50 mm/s. The microstructures both in transverse and longitudinal sections were investigated and morphological characterizations were performed. Additionally, the microstructure of the TRC strips were also investigated through the thickness of the strip. The secondary dendrite arm spacing and SPP were characterized to compare the cooling rates for 8xxx and 1xxx aluminum alloys, respectively.

3. Conclusion

It is observed in both DS and TRC samples that the shape of the isotherms affects the temperature gradient and hence, cooling rate at different locations of samples. The dendritic microstructures obtained from 8xxx alloy by TRC, and DS are shown in Figure 1. It is concluded that using directional solidification with high cooling rates is a promising method to achieve microstructures similar to that of a TRC strip. By varying the directional solidification velocity, we could characterize the morphological features through the thickness of the TRC.

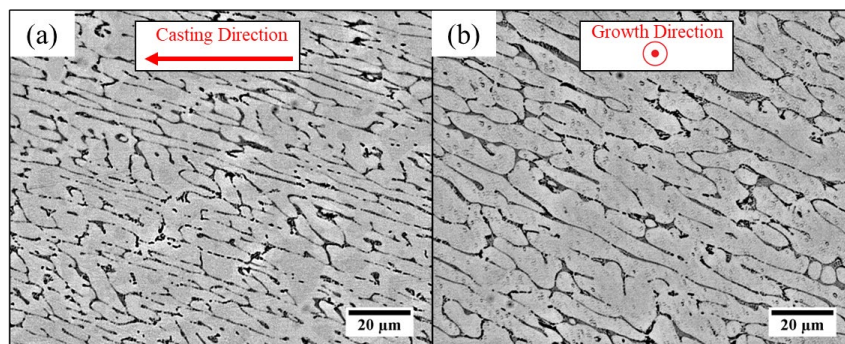


Figure 1. Microstructure of 8xxx alloy (a) TRC strip, quarter section and (b) DS sample growth with 25 mm/s velocity. Growth length = 50 mm.

Acknowledgment

This work is funded by TÜBİTAK 1505 (Grant no: 5210011). Authors would like to thank H. Kayaçetin and N. Yılmaz, technicians of Assan Aluminium Laboratory, for their valuable help with cast house operations and metallographic studies.

EFFECT OF CHROMIUM ON WEAR RESISTANCE OF CARBIDIC AUSTEMPERED DUCTILE IRON (CADI)

Barbaros SENSES¹, Ummihan T. YILMAZ², Ayse ERKAN¹, Gökhan SAĞLAM¹

¹Döksan Heat Treatment and R&D Center A.S., ²Kırıkkale University
Türkiye

Keywords: CADI, Wear, Chromium, Carbides, Austempering, Ductile Iron, Impact Toughness

Abstract

Carbide austempered ductile iron (CADI) is a type of ductile iron (DI) that contains carbides, providing strengthened wear behavior, compared to traditional austempered ductile iron (ADI). The presence of carbides in the structure increases the wear resistance. However, it was found that ADI has a better impact toughness than CADI.

1. Introduction

This present study focuses on the determination of the abrasive wear behavior of 2 types of CADI material, obtained by adding chromium wt. 0.5 % and 1.0 %, respectively. Austempering heat treatment temperature and time values are common for all samples. In this study also, microstructure examination, impact toughness, and hardness values were studied. The results were compared with each other in terms of weight loss according to heat treatment conditions and chromium contents.

2. Materials and Methods

In this work, GJS 600 samples were heat treated by austenitizing for 90 minutes at 900 °C followed by the austempering process at 360 °C for 120 minutes. As a result, the ausferrite structure was obtained (Figure 1). The wear resistance test was performed in a dry friction environment with the pin-on-disc method according to the ASTM G99-17 standard. The impact toughness test was carried out at room temperature by using standard unnotched samples.

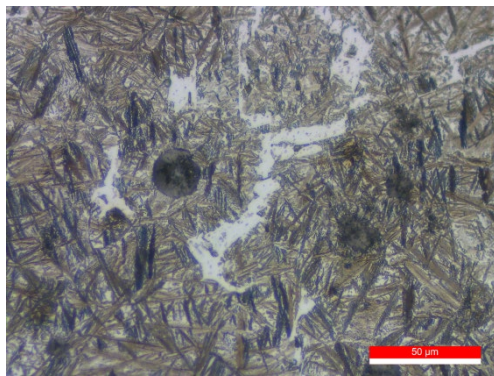


Figure 1. Microstructure for HT-1.0 % Cr (Etchant: Nital and Sodiummetabisulfite) (X500)

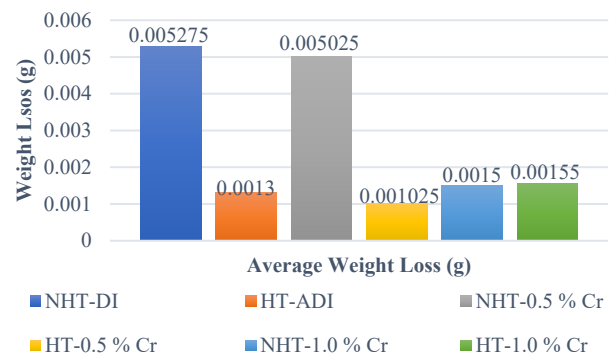


Figure 2. Average weight loss (HT: Heat Treated, NHT: Not Heat Treated)

3. Conclusions

The minimum average weight loss in the without heat-treated samples was measured as 0.0015 g for NHT-1.0 %Cr. This value is 3.5 times less than the NHT-DI with 0,005275 g. NHT-DI and the NHT-0.5 %Cr were measured as 0.005275 g and 0.005025 g, respectively, very close to each other. Also, in the heat-treated samples, the minimum value was measured as 0.001025 g in HT-0.5 %Cr. This value is 1.5 times less than the HT-1.0 %Cr which is the highest amongst heat-treated samples (0.00155 g). HT-0.5 %Cr (0.001025 g) showed approximately 5 times less weight loss than NHT-0.5 %Cr (0.005025 g). NHT-ADI and HT-1.0 %Cr were measured very close to each other as 0.0013 g and 0.00155 g, respectively. HT-0.5 %Cr (0.001025 g) showed 5 times less weight loss than NHT-DI (0.005275 g). NHT-1.0 %Cr and HT-1.0 %Cr are close to each other 0.0015 g and 0.00155 g, respectively (Figure 2). In the study, it was determined that the impact toughness decreased as the Cr or carbide content increased.



21st International Metallurgy and Materials Congress
21. Uluslararası Metalurji ve Malzeme Kongresi

CONGRESS PROCEEDINGS E-BOOK

KONGRE BİLDİRİLER E-KİTABI

6-8 October / Ekim
2022, ISTANBUL

TÜYAP Fair and Congress Center
TÜYAP Fuar ve Kongre Merkezi

 www.immc-mtm.com

 immc@immc-mtm.com

